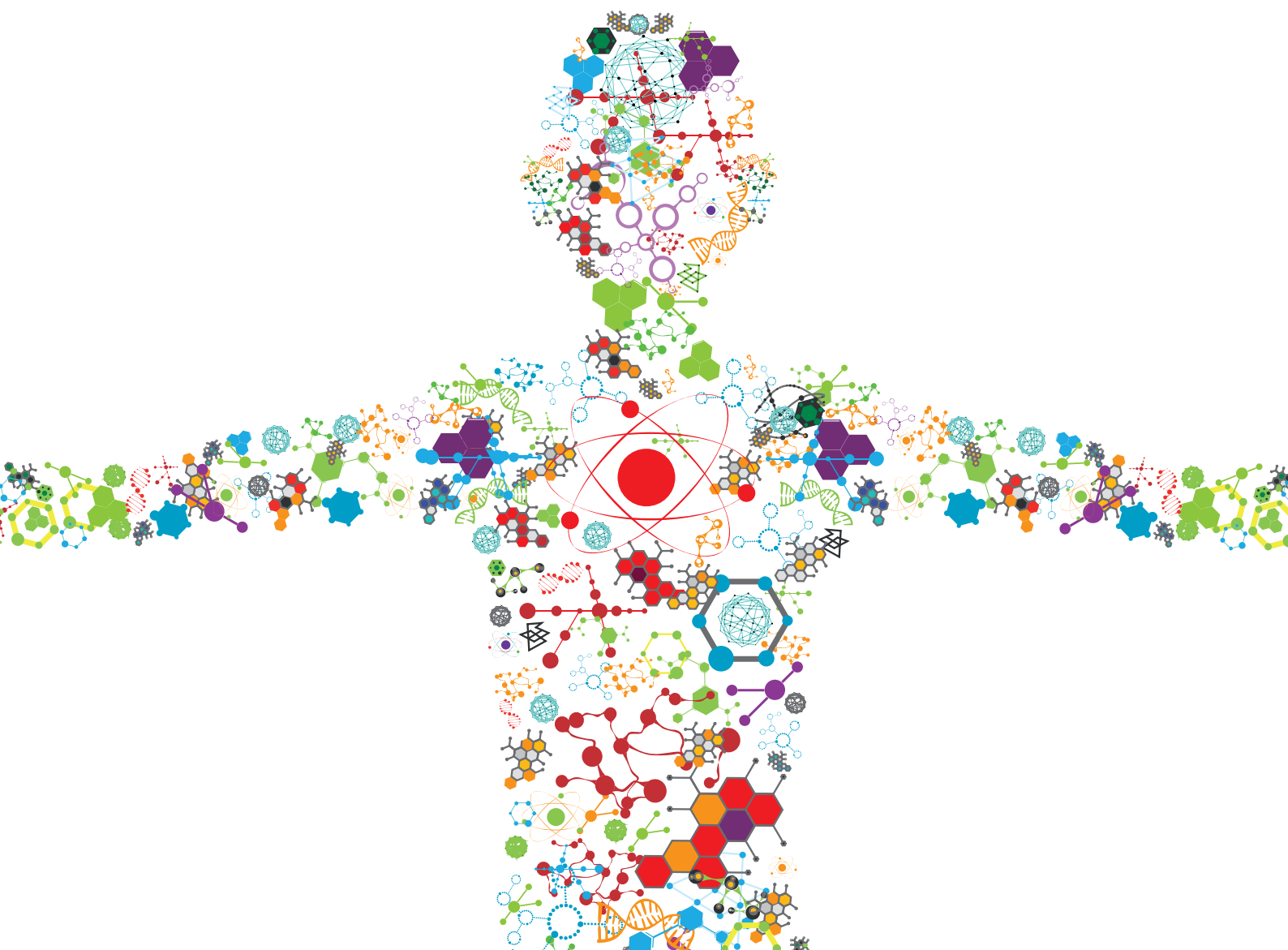


# SHORT-TERM VERSUS LONG-TERM CHALLENGES IN FUNCTIONAL BIOMATERIALS INTERFACING LIVING SYSTEMS: TWO SIDES OF THE COIN

EDITED BY: Davide Ricci, Christian Bergaud, Elisa Castagnola and  
Valentina Castagnola

PUBLISHED IN: Frontiers in Bioengineering and Biotechnology





# frontiers

## Frontiers eBook Copyright Statement

The copyright in the text of individual articles in this eBook is the property of their respective authors or their respective institutions or funders. The copyright in graphics and images within each article may be subject to copyright of other parties. In both cases this is subject to a license granted to Frontiers.

The compilation of articles constituting this eBook is the property of Frontiers.

Each article within this eBook, and the eBook itself, are published under the most recent version of the Creative Commons CC-BY licence.

The version current at the date of publication of this eBook is CC-BY 4.0. If the CC-BY licence is updated, the licence granted by Frontiers is automatically updated to the new version.

When exercising any right under the CC-BY licence, Frontiers must be attributed as the original publisher of the article or eBook, as applicable.

Authors have the responsibility of ensuring that any graphics or other materials which are the property of others may be included in the CC-BY licence, but this should be checked before relying on the CC-BY licence to reproduce those materials. Any copyright notices relating to those materials must be complied with.

Copyright and source acknowledgement notices may not be removed and must be displayed in any copy, derivative work or partial copy which includes the elements in question.

All copyright, and all rights therein, are protected by national and international copyright laws. The above represents a summary only. For further information please read Frontiers' Conditions for Website Use and Copyright Statement, and the applicable CC-BY licence.

ISSN 1664-8714

ISBN 978-2-88971-245-8

DOI 10.3389/978-2-88971-245-8

## About Frontiers

Frontiers is more than just an open-access publisher of scholarly articles: it is a pioneering approach to the world of academia, radically improving the way scholarly research is managed. The grand vision of Frontiers is a world where all people have an equal opportunity to seek, share and generate knowledge. Frontiers provides immediate and permanent online open access to all its publications, but this alone is not enough to realize our grand goals.

## Frontiers Journal Series

The Frontiers Journal Series is a multi-tier and interdisciplinary set of open-access, online journals, promising a paradigm shift from the current review, selection and dissemination processes in academic publishing. All Frontiers journals are driven by researchers for researchers; therefore, they constitute a service to the scholarly community. At the same time, the Frontiers Journal Series operates on a revolutionary invention, the tiered publishing system, initially addressing specific communities of scholars, and gradually climbing up to broader public understanding, thus serving the interests of the lay society, too.

## Dedication to Quality

Each Frontiers article is a landmark of the highest quality, thanks to genuinely collaborative interactions between authors and review editors, who include some of the world's best academicians. Research must be certified by peers before entering a stream of knowledge that may eventually reach the public - and shape society; therefore, Frontiers only applies the most rigorous and unbiased reviews.

Frontiers revolutionizes research publishing by freely delivering the most outstanding research, evaluated with no bias from both the academic and social point of view. By applying the most advanced information technologies, Frontiers is catapulting scholarly publishing into a new generation.

## What are Frontiers Research Topics?

Frontiers Research Topics are very popular trademarks of the Frontiers Journals Series: they are collections of at least ten articles, all centered on a particular subject. With their unique mix of varied contributions from Original Research to Review Articles, Frontiers Research Topics unify the most influential researchers, the latest key findings and historical advances in a hot research area! Find out more on how to host your own Frontiers Research Topic or contribute to one as an author by contacting the Frontiers Editorial Office: [frontiersin.org/about/contact](http://frontiersin.org/about/contact)



# SHORT-TERM VERSUS LONG-TERM CHALLENGES IN FUNCTIONAL BIOMATERIALS INTERFACING LIVING SYSTEMS: TWO SIDES OF THE COIN

Topic Editors:

**Davide Ricci**, University of Genoa, Italy

**Christian Bergaud**, Laboratoire d'analyse et d'architecture Des Systèmes (LAAS), France

**Elisa Castagnola**, University of Pittsburgh, United States

**Valentina Castagnola**, Italian Institute of Technology (IIT), Italy

**Citation:** Ricci, D., Bergaud, C., Castagnola, E., Castagnola, V., eds. (2022).

Short-Term Versus Long-Term Challenges in Functional Biomaterials

Interfacing Living Systems: Two Sides of the Coin. Lausanne: Frontiers Media SA.

doi: 10.3389/978-2-88971-245-8

# Table of Contents

- 05 Editorial: Short-Term Versus Long-Term Challenges in Functional Biomaterials Interfacing Living Systems: Two Sides of the Coin**  
Valentina Castagnola, Elisa Castagnola, Christian Bergaud and Davide Ricci
- 09 Personalized Graphene Oxide-Protein Corona in the Human Plasma of Pancreatic Cancer Patients**  
Riccardo Di Santo, Luca Digiacomio, Erica Quagliarini, Anna Laura Capriotti, Aldo Laganà, Riccardo Zenezini Chiozzi, Damiano Caputo, Chiara Cascone, Roberto Coppola, Daniela Pozzi and Giulio Caracciolo
- 20 Microfluidic Multielectrode Arrays for Spatially Localized Drug Delivery and Electrical Recordings of Primary Neuronal Cultures**  
Giulia Bruno, Nicolò Colistra, Giovanni Melle, Andrea Cerea, Aliaksandr Hubarevich, Lieselot Deleye, Francesco De Angelis and Michele Dipalo
- 31 Biocompatibility of a Conjugated Polymer Retinal Prosthesis in the Domestic Pig**  
José Fernando Maya-Vetencourt, Stefano Di Marco, Maurizio Mete, Mattia Di Paolo, Domenico Ventrella, Francesca Barone, Alberto Elmi, Giovanni Manfredi, Andrea Desii, Walter G. Sannita, Silvia Bisti, Guglielmo Lanzani, Grazia Pertile, Maria Laura Bacci and Fabio Benfenati
- 50 In vitro Label Free Raman Microspectroscopic Analysis to Monitor the Uptake, Fate and Impacts of Nanoparticle Based Materials**  
Hugh J. Byrne, Franck Bonnier, Esen Efeoglu, Caroline Moore and Jennifer McIntyre
- 66 A Plant Bioreactor for the Synthesis of Carbon Nanotube Bionic Nanocomposites**  
Giulia Magnabosco, Maria F. Pantano, Stefania Rapino, Matteo Di Giosia, Francesco Valle, Ludovic Taxis, Francesca Sparla, Giuseppe Falini, Nicola M. Pugno and Matteo Calvaresi
- 73 Hydrogels for 3D Neural Tissue Models: Understanding Cell-Material Interactions at a Molecular Level**  
Catalina Vallejo-Giraldo, Martina Genta, Olivia Cauvi, Josef Goding and Rylie Green
- 87 Real-Time Fast Scan Cyclic Voltammetry Detection and Quantification of Exogenously Administered Melatonin in Mice Brain**  
Elisa Castagnola, Elaine M. Robbins, Kevin M. Woeppel, Moriah McGuier, Asiyeh Golabchi, I. Mitch Taylor, Adrian C. Michael and Xinyan Tracy Cui
- 100 Colorimetric Nanoplasmonics to Spot Hyperglycemia From Saliva**  
Paolo Donati, Tania Pomili, Luca Boselli and Pier P. Pompa
- 109 Dexamethasone-Enhanced Microdialysis and Penetration Injury**  
Andrea Jaquins-Gerstl and Adrian C. Michael
- 125 Disentangling Biomolecular Corona Interactions With Cell Receptors and Implications for Targeting of Nanomedicines**  
Aldy Aliyandi, Inge S. Zuhorn and Anna Salvati

- 139** *Methods to Scale Down Graphene Oxide Size and Size Implication in Anti-cancer Applications*  
Immacolata Tufano, Raffaele Vecchione and Paolo Antonio Netti
- 173** *A Review: Electrode and Packaging Materials for Neurophysiology Recording Implants*  
Weiyang Yang, Yan Gong and Wen Li
- 204** *Interactions Between 2D Materials and Living Matter: A Review on Graphene and Hexagonal Boron Nitride Coatings*  
João Santos, Matteo Moschetta, João Rodrigues, Pedro Alpuim and Andrea Capasso
- 229** *Advances in Engineering Human Tissue Models*  
Chrysanthi-Maria Moysidou, Chiara Barberio and Róisín Meabh Owens
- 264** *Foreign Body Reaction to Implanted Biomaterials and Its Impact in Nerve Neuroprosthetics*  
Alejandro Carnicer-Lombarte, Shao-Tuan Chen, George G. Malliaras and Damiano G. Barone
- 286** *Explant Analysis of Utah Electrode Arrays Implanted in Human Cortex for Brain-Computer-Interfaces*  
Kevin Woeppel, Christopher Hughes, Angelica J. Herrera, James R. Eles, Elizabeth C. Tyler-Kabara, Robert A. Gaunt, Jennifer L. Collinger and Xinyan Tracy Cui



# Editorial: Short-Term Versus Long-Term Challenges in Functional Biomaterials Interfacing Living Systems: Two Sides of the Coin

Valentina Castagnola<sup>1,2\*</sup>, Elisa Castagnola<sup>3\*</sup>, Christian Bergaud<sup>4\*</sup> and Davide Ricci<sup>5\*</sup>

<sup>1</sup> Center for Synaptic Neuroscience and Technology, Istituto Italiano di Tecnologia, Genoa, Italy, <sup>2</sup> IRCCS Ospedale Policlinico San Martino, Genoa, Italy, <sup>3</sup> Department of Bioengineering, University of Pittsburgh, Pittsburgh, PA, United States, <sup>4</sup> MEMS Group, Laboratoire d'analyse et d'architecture des systèmes (LAAS-CNRS), University of Toulouse, Toulouse, France, <sup>5</sup> DITEN, University of Genoa, Genoa, Italy

**Keywords:** functional biomaterial, nanomedicine, nanoparticle, neural interface devices, drug delivery & targeting

## Editorial on the Research Topic

### Short-Term Versus Long-Term Challenges in Functional Biomaterials Interfacing Living Systems: Two Sides of the Coin

#### OPEN ACCESS

##### Edited and reviewed by:

Hasan Uludag,  
University of Alberta, Canada

##### \*Correspondence:

Valentina Castagnola  
valentina.castagnola@iit.it  
Elisa Castagnola  
elc118@pitt.edu  
Christian Bergaud  
bergaud@laas.fr  
Davide Ricci  
davide.ricci@unige.it

##### Specialty section:

This article was submitted to  
Biomaterials,  
a section of the journal  
Frontiers in Bioengineering and  
Biotechnology

**Received:** 10 June 2021

**Accepted:** 21 June 2021

**Published:** 04 August 2021

##### Citation:

Castagnola V, Castagnola E,  
Bergaud C and Ricci D (2021)  
Editorial: Short-Term Versus  
Long-Term Challenges in Functional  
Biomaterials Interfacing Living  
Systems: Two Sides of the Coin.  
Front. Bioeng. Biotechnol. 9:723451.  
doi: 10.3389/fbioe.2021.723451

Functional biomaterials (FBMs) have been increasingly adopted as a key element in all sorts of biomedical devices for innovative diagnostic and therapeutic solutions, as they can be tailored for specific applications while being highly tolerated by living systems. Thanks to their versatility, FBMs have been used as vehicles for targeted pharmaceutical delivery to address cancer and tissue/bone degenerations, engineered as scaffolds for musculoskeletal, cardiovascular, and nerve regeneration, or employed as electrode coatings to enhance sensing/modulation of specific signals and stability, as well as biodegradable encapsulations/substrates for the attenuation of host tissue responses.

Tailoring biomaterial properties for such a plethora of applications is a challenge that requires a merging of knowledge across chemistry, pharmacy, biology, physics, and engineering.

Clinical applications often involve opposing requirements in terms of FBMs' lifetimes. In some cases, the FBMs should be stable and efficiently interact with the biological environment for many years after implantation, while in others they may need to be safely biodegraded or gradually bio-absorbed once their restorative or delivery functions have been accomplished. Sometimes a combination of the two approaches is desirable.

In this special issue we focus on a number of key aspects that allow to better understand interactions between biomaterials and living cells, improving our ability to tailor FBM properties for specific applications. The following topics are covered:

- effects of biomolecular corona on the nanomaterials' surface
- optimization of 3D *in vitro* models of human tissues
- strategies for long-term implants of neural devices for recording, detection, and drug delivery
- 1-D and 2-D nanomaterial interactions with living systems and the impact of the fabrication methods.

## EFFECTS OF BIOMOLECULAR CORONA ON THE NANOMATERIALS' SURFACE

Nanoparticles represent an extraordinary tool for targeted therapeutics and diagnostics. Still, despite recent advances, only a few nanoformulations underwent successful clinical translation.

It is well-known that the discrepancy between *in vitro* and *in vivo* results originated from the formation of the biomolecular corona on the nanomaterials' surface, which defines a new biological identity masking the originally engineered surface chemistry. Therefore, the understanding of the mechanisms occurring at the nanomaterials-cell interface, mediated by the biomolecular corona, is a priority for a fast translation of functional nanomaterials into clinical applications.

The review article “Disentangling biomolecular corona interactions with cell receptors and implications for targeting of nanomedicines” of Aliyandi et al., gives an overview of our knowledge to date on the mechanisms of biocorona interaction with the cell machinery with the aim of exploiting it to develop novel targeting strategies.

While the biomolecular corona represents a challenge in nanomedicine, it can also be turned into a weapon in the field of diagnostics. In the article “Colorimetric nanoplasmonics to spot hyperglycemia from saliva” of Donati et al. a non-invasive colorimetric (naked-eye) sensing platform to identify hyperglycemia from saliva is reported, exploiting the plasmonic properties of gold nanostructures. Here the protein corona forming from biomolecules present in saliva seems to play a role in improving the performances and promoting the reshaping process responsible for the colorimetric change (Figure 1A).

## OPTIMIZATION OF 3D *IN VITRO* MODELS OF HUMAN TISSUES

Parallel efforts to reduce the *in vitro/in vivo* mismatch must be made on the biological models. The review article “Advances in Engineering Human Tissue Models” of Moysidou et al. (Figure 1B) covers the recent advances in 3D *in vitro* models of human tissues, highlighting the fact that this technology has the potential to fill the gap between *in vivo* studies and human physiological and diseased models, a necessary step for clinical translation. In the article “Hydrogels for 3D neural tissue models: Understanding cell-material interactions at a molecular level” of Vallejo-Giraldo et al. a poly(vinyl alcohol) biosynthetic hydrogel functionalized with gelatin and sericin was used to promote the development of complex neural networks. Here the role of the astrocytic support on the neural outgrowth was analyzed at the molecular level, giving important indications for future hydrogels designs.

## STRATEGIES FOR LONG-TERM IMPLANTS OF NEURAL DEVICES FOR RECORDING, DETECTION, AND DRUG DELIVERY

It is well-known that the main challenge faced by implantable neural devices is their long-term functionality and biocompatibility. The implant instability is mainly attributed to the foreign body response, neural degeneration, poor long-term material functionality and biocompatibility, mechanical mismatch between the brain tissue and the implant (Fattahi et al., 2014; Wellman et al., 2018). The review article “Foreign body reaction to implanted biomaterials and its impact in

nerve neuroprosthetics” of Carnicer-Lombarte et al. provides an extensive summary of the current nerve neuroprosthetic technologies and discusses how their long-term functional stability is limited by the foreign body reaction (FBR). Additionally, it provides an overview of different strategies, such as material properties, pharmacological therapies, or the use of biodegradable materials, that may be exploited to minimize FBR and improve the long-term stability of neuroprosthetic nerve interfaces.

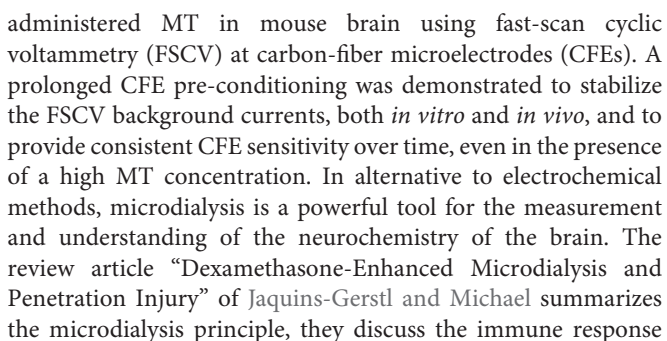
The choice of the material for device fabrication and the surgical delivery procedure become a critical factor in minimizing the damage to the tissue and providing a reliable and accurate functionality of a neural interface. Different intrinsic material properties (strength, flexibility, conductivity, and chemical inertness) and design parameters (geometry, size, packaging) must be considered. The review article “A Review: Electrode and Packaging Materials for Neurophysiology Recording Implants” of Yang et al. summarizes the state of the art of neural tissue implants for neurophysiological recording *in vivo* (Figure 1C). Particular attention has been dedicated to reviewing the different strategies adopted to tune the structural, functional, and dimensional properties of the different components of the implanted devices with the aim to match the mechanical, chemical, and electrical properties of the nervous system, improving the device-tissue interaction and longevity.

The research article “Explant analysis of recording and stimulating Utah electrode arrays implanted in human cortex for brain-computer-interfaces,” focuses on the evaluation of the long-term stability of Utah electrode arrays implanted in the human brain for bi-directional brain-computer interface application. Specifically, the authors examined six explanted arrays from two human participants and assessed the degrees of material degradation and fibrous encapsulation. Changes in the extent of material degradation and encapsulation were observed based on the length of implantation, but these changes did not correlate with recording performance prior to explantation.

The research article “Biocompatibility of a Conjugated Polymer Retinal Prosthesis in the Domestic Pig” of Maya-Vetencourt et al., reports about their progress toward human translation of biocompatible conjugated polymer retinal prosthesis, previously tested in rodents. They detailed the fabrication and *in vivo* testing of multi-layer fully organic prosthesis implanted subretinally in the eye of domestic pigs. Their findings highlight the biocompatibility of this new generation of retinal prosthesis and their potential suitability for subretinal implantation in patients suffering from degenerative blindness.

When a device is interfaced with deep brain structures for electrochemical neurotransmitter sensing, there are additional aspects to be considered, such as achieving stable sensitivity *in vivo*. Thus, the microelectrodes need to be electrochemically stable and resistant to chemical and biological fouling, other than presenting good adsorption properties and fast electron transfer kinetics. The research article “Real-Time Fast Scan Cyclic Voltammetry Detection and Quantification of Exogenously Administered Melatonin in Mice Brain” of Castagnola et al., shows a successful real-time drift-free detection of exogenous





Finally, the article “Microfluidic Multielectrode Arrays for Spatially Localized Drug Delivery and Electrical Recordings of Primary Neuronal Cultures” of Bruno et al. calized drug delivery and cell signaling recording of spontaneous and chemically stimulated activity in primary neuronal networks. This platform shows the capability to examine the effect of biochemical agents on the desired portion of cell culture.



## 1-D AND 2-D NANOMATERIAL INTERACTIONS WITH LIVING SYSTEMS AND THE IMPACT OF THE FABRICATION METHODS

In recent years 1-D and 2-D nanomaterials have been increasingly proposed as functional biomaterials offering an extremely wide spectrum of potential applications that rely not only on contrasting properties such as short or long-term lifetime, but even on opposite biological effects such as cytotoxicity vs. promotion of cell proliferation and differentiation. For this reason, they offer a very interesting case-study for investigating mechanisms of interaction with living systems.

The review article “Interactions Between 2D Materials and Living Matter: A Review on Graphene and Hexagonal Boron Nitride Coatings” of Santos et al. addresses the fundamental question on why two-dimensional material coatings exhibit complex and controversial interactions with biological matter, having shown in different contexts to induce bacterial cell death and contribute to mammalian cell growth and proliferation *in vitro* and tissue differentiation *in vivo*. After considering morphological, chemical, and electronic properties of materials described in state-of-the-art literature, a picture of their correlation with functionality emerges, usefully guiding future applications.

More specifically, the implications of a 2-D nanomaterial size (graphene oxide) on anti-cancer applications is addressed in the review article “Methods to Scale Down Graphene Oxide Size and Size Implication in Anti-cancer Applications” of Tufano et al. It presents a thorough description of the main methods to reduce and homogenize in nanometric scale the lateral dimensions of graphene oxide, either during production or *via* post-processing, together with a discussion of the implication of the small size in cancer treatment by exploiting GO nanocarriers as an effective

theragnostic tool. On the same subject of graphene oxide, the original research paper “Personalized Graphene Oxide-Protein Corona in the Human Plasma of Pancreatic Cancer Patients” of Di Santo et al., provides a proof of concept that exposing nanomaterials to plasma samples under “optimal dilution conditions” could be a good strategy to amplify personalization of protein corona and, in turn, to exploit it to distinguish between different classes of donors (e.g., cancer vs. non-cancer patients) (Figure 1D).

One of the greatest challenges for exploiting nanomaterials in living beings is the development of appropriate pathways for their biofunctionalization. The original research work presented in “A Plant Bioreactor for the Synthesis of Carbon Nanotube Bionic Nanocomposites” of Magnabosco et al., by incorporating functionalized single-walled carbon nanotubes within the roots of living plants producing a bionic composite material, poses the basis for *in vivo* synthesis of new materials taking advantage of the living organism as a reactor.

At last, the key issue of ensuring the ability to directly monitor and evaluate the interactions of the novel nanoparticle (NP) based functional materials with living systems is addressed in the review “*in vitro* Label Free Raman Microspectroscopic Analysis to Monitor the Uptake, Fate and Impacts of Nanoparticle Based Materials” of Byrne et al., where it is demonstrated that the—well-known to material scientists—Raman Microspectroscopy technique, is capable of confirming the intracellular localization of NPs in cells, monitoring the NP trafficking in subcellular vesicles and, monitoring NP degradation catabolization, identifying and tracking cellular response pathways, all in a single, label-free, measurement protocol.

## AUTHOR CONTRIBUTIONS

All authors listed have made a substantial, direct and intellectual contribution to the work, and approved it for publication.

## REFERENCES

- Fattahi, P., Yang, G., Kim, G., and Abidian, M. R. (2014). A review of organic and inorganic biomaterials for neural interfaces. *Adv. Mater.* 26, 1846–1885. doi: 10.1002/adma.201304496
- Wellman, S. M., Eles, J. R., Ludwig, K. A., Seymour, J. P., Michelson, N. J., McFadden, W. E., et al. (2018). A materials roadmap to functional neural interface design. *Adv. Funct. Mater.* 28:1701269. doi: 10.1002/adfm.201701269

**Conflict of Interest:** The authors declare that the research was conducted in the absence of any commercial or financial relationships that could be construed as a potential conflict of interest.

**Publisher’s Note:** All claims expressed in this article are solely those of the authors and do not necessarily represent those of their affiliated organizations, or those of the publisher, the editors and the reviewers. Any product that may be evaluated in this article, or claim that may be made by its manufacturer, is not guaranteed or endorsed by the publisher.

Copyright © 2021 Castagnola, Castagnola, Bergaud and Ricci. This is an open-access article distributed under the terms of the Creative Commons Attribution License (CC BY). The use, distribution or reproduction in other forums is permitted, provided the original author(s) and the copyright owner(s) are credited and that the original publication in this journal is cited, in accordance with accepted academic practice. No use, distribution or reproduction is permitted which does not comply with these terms.



# Personalized Graphene Oxide-Protein Corona in the Human Plasma of Pancreatic Cancer Patients

## OPEN ACCESS

### Edited by:

Valentina Castagnola,  
Italian Institute of Technology (IIT), Italy

### Reviewed by:

Cristiana Tanase,  
Victor Babes National Institute  
of Pathology (INCDVB), Romania  
Monica Neagu,  
Victor Babes National Institute  
of Pathology (INCDVB), Romania  
Ester Polo,  
University of Santiago  
de Compostela, Spain

### \*Correspondence:

Daniela Pozzi  
daniela.pozzi@uniroma1.it  
Giulio Caracciolo  
giulio.caracciolo@uniroma1.it

<sup>†</sup> These authors have contributed  
equally to this work

### Specialty section:

This article was submitted to  
Biomaterials,  
a section of the journal  
Frontiers in Bioengineering and  
Biotechnology

**Received:** 18 February 2020

**Accepted:** 28 April 2020

**Published:** 25 May 2020

### Citation:

Di Santo R, Digiacomo L,  
Quagliarini E, Capriotti AL, Laganà A,  
Zenezini Chiozzi R, Caputo D,  
Cascone C, Coppola R, Pozzi D and  
Caracciolo G (2020) Personalized  
Graphene Oxide-Protein Corona  
in the Human Plasma of Pancreatic  
Cancer Patients.  
Front. Bioeng. Biotechnol. 8:491.  
doi: 10.3389/fbioe.2020.00491

**Riccardo Di Santo<sup>1†</sup>, Luca Digiacomo<sup>1†</sup>, Erica Quagliarini<sup>2</sup>, Anna Laura Capriotti<sup>2</sup>, Aldo Laganà<sup>2</sup>, Riccardo Zenezini Chiozzi<sup>3,4</sup>, Damiano Caputo<sup>5</sup>, Chiara Cascone<sup>5</sup>, Roberto Coppola<sup>5</sup>, Daniela Pozzi<sup>1\*</sup> and Giulio Caracciolo<sup>1\*</sup>**

<sup>1</sup> Nanodelivery Lab, Department of Molecular Medicine, Sapienza University of Rome, Rome, Italy, <sup>2</sup> Department of Chemistry, Sapienza University of Rome, Rome, Italy, <sup>3</sup> Biomolecular Mass Spectrometry and Proteomics, Bijvoet Center for Biomolecular Research and Utrecht Institute for Pharmaceutical Sciences, Utrecht University, Utrecht, Netherlands, <sup>4</sup> Netherlands Proteomics Centre, Utrecht, Netherlands, <sup>5</sup> General Surgery Unit, University Campus Bio-Medico di Roma, Rome, Italy

The protein corona (PC) that forms around nanomaterials upon exposure to human biofluids (e.g., serum, plasma, cerebral spinal fluid etc.) is personalized, i.e., it depends on alterations of the human proteome as those occurring in several cancer types. This may be relevant for early cancer detection when changes in concentration of typical biomarkers are often too low to be detected by blood tests. Among nanomaterials under development for *in vitro* diagnostic (IVD) testing, Graphene Oxide (GO) is regarded as one of the most promising ones due to its intrinsic properties and peculiar behavior in biological environments. While recent studies have explored the binding of single proteins to GO nanoflakes, unexplored variables (e.g., GO lateral size and protein concentration) leading to formation of GO-PC in human plasma (HP) have only marginally addressed so far. In this work, we studied the PC that forms around GO nanoflakes of different lateral sizes (100, 300, and 750 nm) upon exposure to HP at several dilution factors which extend over three orders of magnitude from 1 (i.e., undiluted HP) to 10<sup>3</sup>. HP was collected from 20 subjects, half of them being healthy donors and half of them diagnosed with pancreatic ductal adenocarcinoma (PDAC) a lethal malignancy with poor prognosis and very low 5-year survival rate after diagnosis. By dynamic light scattering (DLS), electrophoretic light scattering (ELS), sodium dodecyl sulfate-polyacrylamide gel electrophoresis (SDS-PAGE) and nano liquid chromatography tandem mass spectrometry (nano-LC MS/MS) experiments we show that the lateral size of GO has a minor impact, if any, on PC composition. On the other side, protein concentration strongly affects PC of GO nanoflakes. In particular, we were able to set dilution factor of HP in a way that maximizes the personalization of PC, i.e., the alteration in the protein profile of GO nanoflakes between cancer vs. non-cancer

patients. We believe that this study shall contribute to a deeper understanding of the interactions among GO and HP, thus paving the way for the development of IVD tools to be used at every step of the patient pathway, from prognosis, screening, diagnosis to monitoring the progression of disease.

**Keywords:** protein corona, nanoparticles, graphene oxide, pancreatic ductal adenocarcinoma, precision medicine

## INTRODUCTION

Upon exposure to biological milieu, nanomaterials are coated by a dynamic protein envelope, which is referred to as protein corona (PC) (Lundqvist et al., 2008; Barrán-Berdón et al., 2013). After a decade of intense research, we have clearly established that PC is shaped by several concomitant factors such as NPs' synthetic identity, protein source and environmental factors (Pozzi et al., 2015; Ke et al., 2017). The most relevant implication is that protein patterns surrounding nanomaterials do not merely reflect the composition of the human proteome in which about twenty plasma proteins represent 99% of the total plasma volume (Schwenk et al., 2017). On the other side, PC works as “nano-concentrator” of biomolecules with an affinity for the particle surface (Zheng et al., 2015). A turning point was achieved when Mahmoudi and coworkers introduced the concept of “personalized” and “disease-specific” protein corona (Hajipour et al., 2015), i.e., they demonstrated that exposing nanomaterials to human plasma (HP) obtained from healthy subjects and patients with various diseases, induced considerable alterations in the corona profile of NPs. This is especially relevant in early detection of several cancer types where protein alteration is a hallmark of tumorigenesis and the humane proteome evolves in time as a function of the disease progress (Jimenez et al., 2018). However, no previous studies explored the concomitant effect of protein source (e.g., HP from cancer vs. non-cancer patients) and concentration on the personalization of the PC. According to previous literature (Caracciolo et al., 2011), one may expect that adjusting protein concentration by plasma dilution may modulate corona composition. For diagnostic purposes, optimal dilution factors for HP samples may be defined as those boosting differences in PC composition between different classes of donors. Among technologies under development, nanoparticle-enabled blood (NEB) tests are emerging as a fast, cheap and user-friendly tool for early cancer detection (Caputo et al., 2017; Papi and Caracciolo, 2018; Caputo and Caracciolo, 2019; Papi et al., 2019). NEB tests are based on the characterization of size, surface charge and composition of the NP-PC by benchtop techniques such as dynamic light scattering (DLS), micro-electrophoresis (ME) and one-dimensional (1D) sodium dodecyl sulfate polyacrylamide gel electrophoresis (SDS-PAGE). Due to high specific surface area and the presence of carboxylic and epoxydic groups on its surface, GO exhibits high protein binding (Liu et al., 2011) through electrostatic and hydrophobic interactions (Wang et al., 2011; Chung et al., 2013). These properties makes GO an ideal candidate to differentiate blood human samples derived from different classes of individuals thus representing a logical choice for the development of new

variants of the NEB test with optimized sensitivity and specificity (Lesniak et al., 2010; Castagnola et al., 2018). Recent studies have investigated molecular interactions of GO with human blood plasma proteins (Wang et al., 2018). It was demonstrated the existence of size-dependent interactions between GO nanoflakes and albumin, fibrinogen and globulin (Kenry et al., 2016). However, factors affecting adsorption from single protein solutions may be ruled out in HP by the simultaneous presence of thousands of proteins with an affinity for the particle surface. In this work we investigated the effect of GO lateral size and protein concentration on PC composition. To this end, we exposed GO nanoflakes of three different sizes (~100, 300, and 750 nm) to diluted plasma samples with dilutions factors ranging from 1 (i.e., undiluted HP) to  $10^3$ . Human plasma samples were collected from 20 subjects, half of them diagnosed with pancreatic ductal adenocarcinoma (PDAC) and half of them being healthy subjects. PDAC was chosen as a model of aggressive malignancy that is predicted to become one of the leading causes of cancer-related death in the near future (Rahib et al., 2014; Caputo and Caracciolo, 2019). Surgery can increase survival rates, but regrettably, only a minority of PDACs are diagnosed early enough for resection. In the early stage the tumor is asymptomatic or symptoms can be confused with common indicators of other diseases (Caputo and Caracciolo, 2019). Therefore, the development of novel tools for the early detection of PDAC is urgently needed. Here we show that GO lateral size has no appreciable effect on PC composition. On the other hand, we demonstrate that protein concentration has a major effect on PC composition and personalization. At high protein concentration (i.e., at low plasma dilution), the PC formed in the plasma of PDAC patients was indistinguishable from that formed in the plasma of healthy subjects. On the other side, at low protein concentration (i.e., at high plasma dilution) PC of PDAC patients was significantly different from that of healthy donors. Our results suggest that concentration of plasma samples should be properly tuned to boost personalization of PC. This may be a fundamental step to improve sensitivity and sensibility of the NEB tests and other IVD technologies based on direct characterization of PC.

## EXPERIMENTAL SECTION

### Demographic Characteristics

Demographic characteristics (age, sex), tumoral markers (CEA, Ca 19.9) and gamma-globulin levels for both PDAC subjects and healthy volunteers have been evaluated (**Supplementary Tables S1, S2**). PDAC diagnosis was obtained

in all cases with endoscopic ultrasonographic guided fine needle aspiration biopsy (EUS-FNAB). All PDAC patients were staged according to the AJCC TNM system eight edition (Chun et al., 2018). Among PDAC patients those who underwent surgery according to the good clinical practice received a pathological stage, while those who unfit for surgery received only clinical stage.

## Preparation of Graphene Oxide Nanoflakes

Graphene Oxide was purchased from Graphenea (San Sebastián, Spain). GO solutions were subjected to sonication (Vibra cell sonicator VC505, Sonics and Materials, United Kingdom) and centrifugation (Hermle Z 216 MK, Hermle Labortechnik, Germany), to obtain large, medium and small GO nanoflakes. To prepare large nanoflakes, a GO solution was subjected to a sonication of 1 min at 125 W, followed by centrifugation at 14,850 RCF for 15 min; after that the supernatant was removed, and the pellet was resuspended. To prepare medium size nanoflakes, a GO solution was sonicated (10 min, 125 W) and centrifuged two times. The first centrifuge was performed at 7,700 RCF for 30 min, then the supernatant was recovered and centrifuged again for 30 min at 18,620 RCF. Finally, the supernatant was removed, and the pellet was resuspended. Lastly, small size GO nanoflakes were obtained by sonicating three times a GO solution for 180 min at 125 W. After each sonication, the resulting solution was centrifuged at 10,000 RCF for 15 min and the final supernatant was collected. GO concentration was estimated by UV-Vis spectrometry experiments using the characteristic GO absorption peak, which is located at 230 nm (Jasim et al., 2016; Di Santo et al., 2019).

## Size and Zeta-Potential Experiments

For size and zeta-potential measurements, GO was dispersed in ultrapure water (nominal pH within 2.2–2.5). Size and zeta-potential experiments were carried out through a NanoZetaSizer apparatus (Malvern, United Kingdom) equipped with a 633 nm He–Ne laser and a digital logarithmic correlator. Size measurements were performed by using Malvern micro cuvettes (ZEN0040), while zeta-potential measurements were performed by using a Dip Cell Kit (ZEN1002). Results are reported as average  $\pm$  standard deviation of three independent measurements.

## Preparation of GO-Protein Corona Complexes

Human plasma (HP) was purchased from Sigma–Aldrich, Inc. (Merk KGaA, Darmstadt, Germany). GO-protein complexes were obtained by incubating 100  $\mu$ l of GO nanoflakes (0.25 mg/ml) with 100  $\mu$ l of commercial HP (60 min, 37°C) at several dilution factors ranging 1–10<sup>3</sup>, as indicated in **Supplementary Table S3**. For further experiments, blood samples from 10 healthy donors and 10 PDAC patients were collected and stored according to an established protocol (10/12 ComET CBM and further amendments), which was approved

by the Ethical Committee of the University Campus Bio-Medico di Roma. Blood plasma was obtained by centrifugation at 37°C for 15 min at 15,000 RCF. GO-PC complexes were obtained by incubating 100  $\mu$ l of GO nanoflakes with 100  $\mu$ l of blood plasma at different dilution factors, as indicated in **Supplementary Table S3**.

## 1D SDS PAGE Experiments

GO-PC complexes were subjected centrifugation at 18,620 RCF for 15 min at 4°C. Next, the pellet were washed with ultrapure water to eliminate free proteins (Papi et al., 2019). This procedure was repeated three time. After the washing step, the pellet was resuspended in 20  $\mu$ l of Laemmli loading buffer 1 $\times$ , boiled at 100°C for 10 min and centrifuged at 18,620 RCF for 15 min at 4°C. Finally, 10  $\mu$ l of supernatants were recovered and loaded on a stain–free gradient polyacrylamide gel (4–20% TGX precast gels, Bio–Rad, Hercules, CA, United States) and run at 100 V for about 150 min. Gel images were obtained with a ChemiDoc™ imaging system (Bio–Rad, Hercules, CA, United States) and were processed by ImageLab Software and custom Matlab (MathWorks, Natick, MA, United States) scripts to evaluate the one-dimensional intensity distribution function of each sample and obtain the corresponding one-dimensional molecular weight (MW) distribution. On each of the gel images, background was preliminary removed to prevent unwanted baselines affect the resulting curves. In detail, a rolling ball subtraction was carried out, row by row with a fixed rolling ball radius. Sampled intensity  $I(x,y)$  of the original image was therefore converted into a new two-variable function  $I'(x,y)$ :

$$I(x, y) \rightarrow I'(x, y)$$

where the  $y$ -displacement is related to protein MWs,  $x$ -displacement is a discrete sample index and the intensity value is proportional to the detected protein amount. The projection ( $P$ ) of the two-variable function over a plane orthogonal to the image is the resulting protein pattern of the generic lane ( $j$ ):

$$P_j(y) = I'(x_j, y)$$

Then,  $y$ -displacements were converted into MW values, by fitting the location of known proteins (ladder lane) to the following non-linear equation:

$$MW(y) = a_1 e^{b_1 y} + a_2 e^{b_2 y}$$

The resulting one-dimensional profiles represent the MW distributions of the corresponding samples and were finally normalized to 1. Normalized distributions were subdivided into MW ranges, within which the corresponding definite integrals were computed. Further details can be found elsewhere (Digiacoimo et al., 2019).

## Nano Liquid Chromatography Tandem Mass Spectrometry

GO nanoflakes were incubated with HP (1:200 vol/vol) for 1 h at 37°C. Then, samples were centrifuged three times for 15 min at 18,620 RCF at 4°C. Pellets were vigorously washed, each time,



with ultrapure water to remove loosely bound proteins. After washes, pellets were subjected to protein denaturation, digestion, and desalting following a robust protocol which is generally applied to isolate unbound and loosely bound proteins from bio-coronated materials (Chetwynd et al., 2019). Finally, the samples were lyophilized using a Speed-Vac device (mod. SC 250 Express; Thermo Savant, Holbrook, NY, United States), reconstituted with 0.1% HCOOH solution and stored at  $-80^{\circ}\text{C}$  until use. Tryptic peptides were investigated by using a nano-liquid chromatography apparatus (Dionex Ultimate 3000, Sunnyvale, CA, United States) connected to a hybrid mass spectrometer (Thermo Fisher Scientific, Bremen, Germany) and equipped with a nanoelectrospray ion source. Xcalibur (v.2.07, Thermo Fisher Scientific) raw data files were submitted to Proteome Discover (1.2 version, Thermo Scientific) for a database search using Mascot (version 2.3.2 Matrix Science). Data were searched against the SwissProt database (v 57.15, 20 266 sequences) using the decoy search option of Mascot and protein quantification was performed using Scaffold software. For each identified protein, the mean value of the normalized spectral countings (NSCs) was normalized to the protein molecular weight (MWNsc) to obtain the relative protein abundance (RPA). For each identified protein, the reported RPA is the mean of three independent technical replicates  $\pm$  standard deviation.

## RESULTS

### Effects of GO Lateral Size on PC Composition

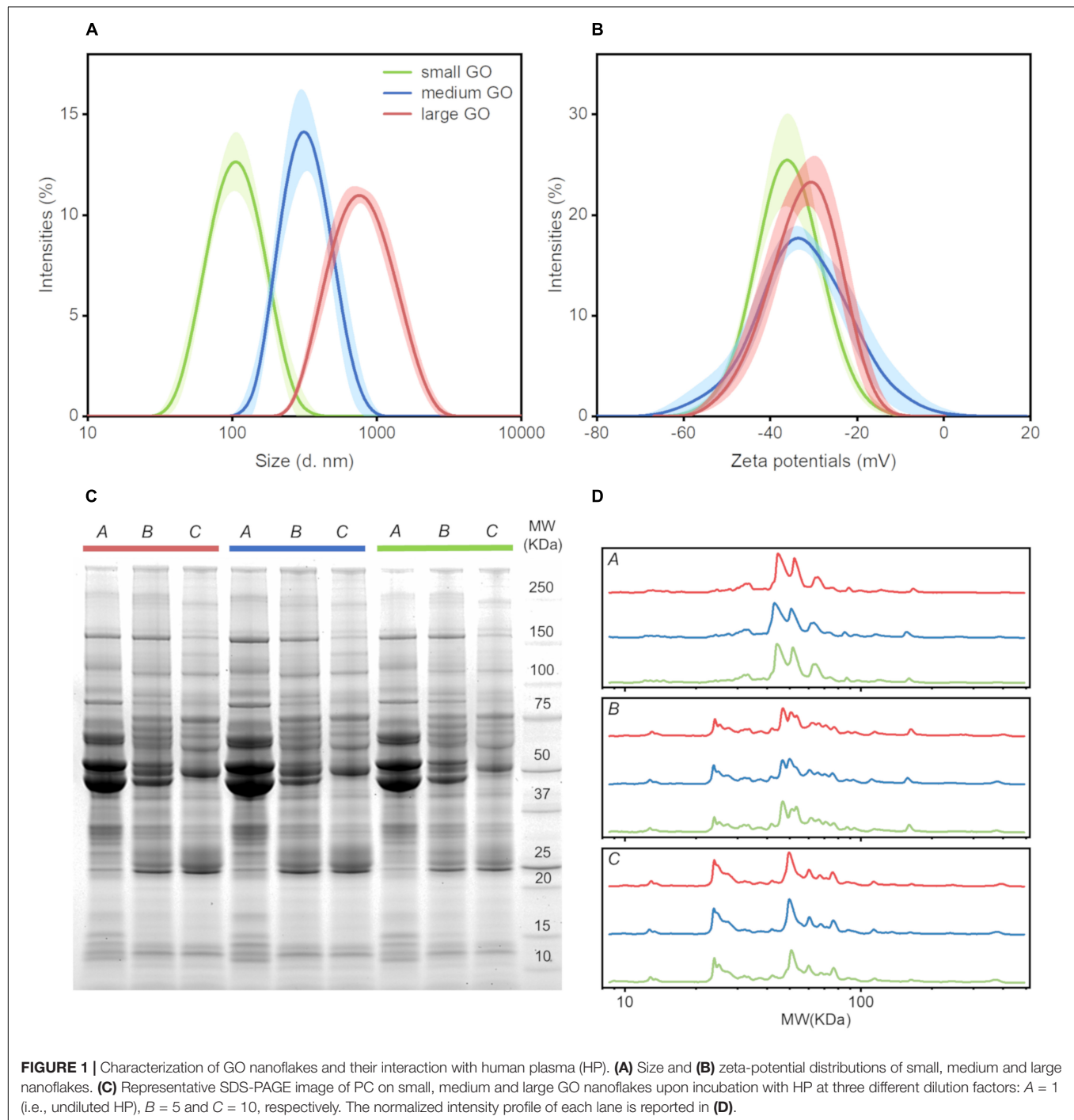
Our first aim was to investigate the effect of GO lateral size on PC composition. To this end, we used small, medium and large GO nanoflakes with size distribution centered at  $\sim 100$ , 300, and 750 nm respectively (**Figure 1A**). To explore whether surface charge of GO nanoflakes was influenced by lateral size, zeta-potential experiments were performed. It was interesting to observe that no variation in surface charge was caused by changing the lateral size. In fact, zeta-potential distributions of small, medium and large GO nanoflakes were comparable and peaked around  $-30$  mV (**Figure 1B**). Next, we evaluated whether the molecular interactions between GO and blood plasma proteins were affected by GO lateral size. To this end, GO nanoflakes were incubated with HP at different dilution factors. SDS-PAGE results (**Figure 1C**) indicate that PC formed around GO nanoflakes was affected by protein concentration, but not by GO lateral size. In **Figure 1D** we report normalized MW distributions of protein patterns. The three boxes regroup the intensity profiles for each plasma dilution at the three different sizes of GO nanoflakes. As expected by the visual inspection of the gel image, profiles trends are almost superimposable for small, medium and large GO-protein complexes but strongly distinct for dilution conditions (dilution factors  $A = 1$ ,  $B = 5$ ,  $C = 10$  respectively). Thus, we demonstrated that the molecular interactions between GO and proteins are strongly influenced by protein concentration and not influenced by the GO lateral size. As a consequence, in the following experiments only large size GO nanoflakes were used.

### Effects of Protein Concentration on Protein Corona Composition

Motivated by results of **Figure 1** we characterized PC of GO nanoflakes in a much wider protein concentration range. To accomplish this issue, GO nanoflakes were incubated with HP at 12 dilution factors ranging from dilution factor  $A = 1$  (i.e., undiluted HP) to dilution factor  $L = 10^3$ . Intensity profiles corresponding to each dilution factor are reported in **Figure 2**. At the lowest protein concentration (i.e., at the highest dilution factor,  $L = 10^3$ ) the intensity profile exhibited a single evident peak around 25 kDa. On the other side, the complexity of the protein pattern increased with increasing protein concentration. Furthermore, **Figure 2** also shows that MW distribution of corona proteins is markedly shaped by plasma dilution. This finding may have relevant implications for cancer detection. Indeed, it is a hallmark of tumorigenesis that cancer induces relevant changes in concentration of several blood plasma proteins with different MW (Shruthi and Palani Vinodhkumar, 2016). The situation is even more complex if one considers that these alterations may be also influenced by cancer stage and clinical treatment. As a consequence, one may predict that only exposing nanomaterials to HP at certain plasma dilution factors may promote enrichment of plasma proteins whose blood concentration has been altered by cancer onset and progression. To explore this further, we exposed GO nanoflakes to plasma samples from PDAC patients and healthy subjects under different dilution conditions and compared the emerging coronas.

### Personalized Protein Corona in PDAC Patients

GO nanoflakes were exposed to diluted plasma samples from 10 healthy HP donors and 10 PDAC patients. A representative gel image is presented in **Figure 3A**. For better comparison, we also performed a densitometric analysis of each gel lane. In **Figure 3B** we compare the intensity profiles derived from PDAC patients and healthy donors (yellow and black curves respectively). Vertical solid lines indicate two MW ranges where protein profiles were differentiated. Between 20 and 30 kDa a sharp peak is present in healthy profiles, while it is definitely less pronounced in PDAC patients. In the second MW range (from 40 to 65 kDa), slighter but significant variations were detected. To compare coronas of PDAC patients and healthy volunteers, we calculated the integral areas of the experimental distributions within the two selected MW ranges. **Figure 4A** shows that the gap between the integral area of healthy donors and PDAC patients in the first MW range (20–30 kDa) increases with increasing plasma dilution. An opposite trend was found in the second MW range (40–65 kDa) (**Figure 4B**). Then, we calculated the relative differences by subtracting the areas derived from healthy donors from those derived from PDAC patients (**Figures 4C,D**). Comparing results of **Figures 4C,D** one may speculate that at high dilution (dilution factor  $J = 200$ ) PDAC induces reduction in relative abundance of plasma proteins with MW between 20 and 30 kDa that is compensated by simultaneous enrichment of proteins with MW comprised between 40 and 65 kDa. In conclusion, SDS-PAGE results indicate that PDAC can induce



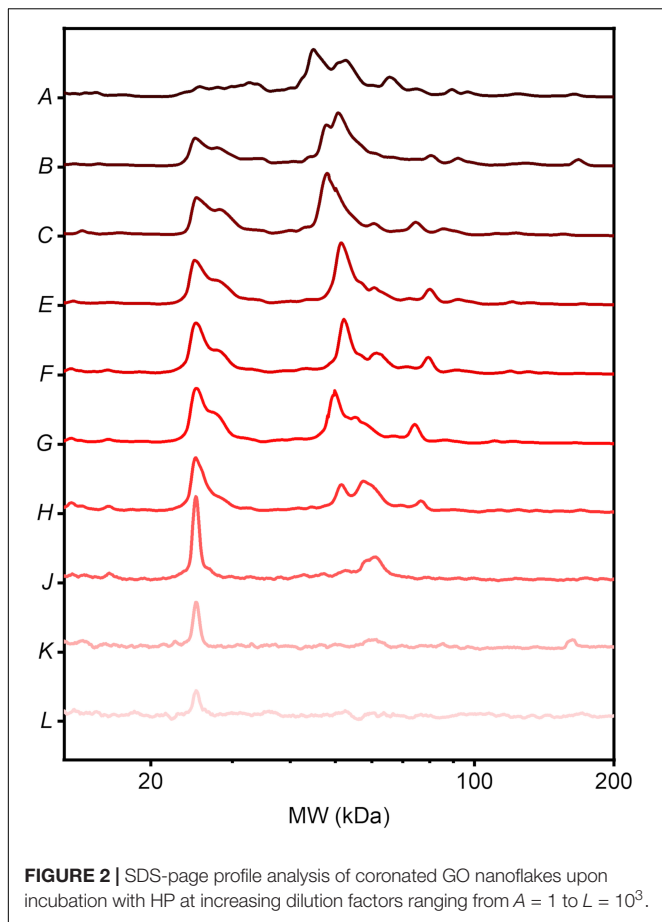
personalization of the PC that forms around GO nanoflakes in HP. Most importantly, the occurrence and relevance of this process is markedly influenced by protein concentration.

## Liquid Chromatography Tandem Mass Spectrometry

As a next step, we performed nano-LC MS/MS experiments to identify and quantify proteins enriching the coronas of GO

nanoflakes following exposure to plasma samples of 10 PDAC patients and 10 healthy volunteers. According to SDS-PAGE results, dilution factor 200 (condition J) was chosen as it boosts differences in PC composition. 199 proteins were detected on the studied samples (**Supplementary Table S4**), but only 20 of them represented the most abundant parts of the coronas, with a cumulative relative protein abundance (RPA) that reached about 88 and 90%, for healthy and PDAC samples respectively. Those 20 proteins were the only ones with RPAs larger than 1%. Their





gene names are reported around the pie charts in **Figure 5A**, which shows the measured distributions of the corona proteins according to their MW. Interestingly, healthy PCs were more enriched by low-MW proteins than PDAC counterparts. In detail, differences of about 3% were detected within the first two MW ranges (i.e., <20 and 20–30 kDa). Apolipoprotein A1 was one of the most abundant proteins (second largest RPA, after human serum albumin) and exhibited a manifest decrease in PDAC samples. On the other hand, alpha-1-antitrypsin (serpina1) and serum albumin were more abundant in PDAC coronas with respect to the healthy ones. Indeed, the former was 2.5 times more enriched for PDAC and the latter exhibited the highest absolute difference (about 5%). Finally, to take into account proteins that may show significant differences despite their small RPAs, we compared the PDAC-to-healthy fold-change of the measured RPAs and the corresponding *p*-value from Student's *t* test, for each of the detected corona protein. Data are shown in **Figure 5B**, as a Volcano plot. Each protein is represented by a dot, whose location is determined by the abundance's excess in healthy (left region) or PDAC (right region) coronas and the corresponding statistical significance (with the commonly employed thresholds  $p < 0.05$  and  $p < 0.001$ ). Black and yellow dots correspond to potential biomarkers for PDAC as they indicate proteins that were found to be strongly downregulated (black) or upregulated (yellow) in healthy and cancer corona respectively.

## DISCUSSION

Physical-chemical properties of pristine nanomaterials are the main factors driving the interactions of NPs in biological environments. In fact, size, curvature radius, surface charge, surface chemistry and functionalization represent some of the interdependent features that co-determine NP behavior in biological media, as those properties affect protein adsorption on NP surface, thus formation and composition of the resulting PC and the subsequent physiological response. This could be important for early detection of several human conditions that cause alteration in the proteome. A paradigmatic example is provided by cancer where protein alteration is frequently associated to the disease onset and progression. Moreover, recent research has suggested that systematic comparisons of corona patterns of nanoparticles recovered from cancer patients and healthy individuals may help to discover new insights on the biology and stage of distinct types of cancer (Caputo et al., 2018; Caracciolo et al., 2019). Nanomaterials coated by a disease-specific PC could be therefore designed to develop cancer detection technologies aligned to the ASSURED criteria stated by the World Health Organization for cancer screening and detection. More in depth investigations on larger cohorts are needed to validate clinical applicability of PC-based detection technologies, and to evaluate the factors that may influence their specificity and sensitivity. This study was aimed at providing new insights on the role of GO lateral size and plasma protein concentration on the personalization of the PC. For two-dimensional materials, previous studies explored size effects on the interactions of the designed NPs with single plasma proteins (Kenry et al., 2016) and living systems (Ma et al., 2015). Here, we firstly studied the role of GO lateral size on the composition of the PC that was formed upon exposure to HP. GO solutions were obtained by an iterative sonication/centrifugation procedure, therefore surface chemistry and oxidation state were maintained the same for all the resulting samples, which differed only for their lateral size. **Figures 1A,B** clearly show that we were able to separate the starting batch of GO solution into three distinct populations with different lateral size and almost equal zeta potential. Then, after exposure to human plasma (HP), we evaluated the protein patterns of the PC formed on small, medium and large GO sheets by 1D SDS-PAGE experiments. Interestingly, we found that GO lateral size have minor impact, if any, on PC composition, whereas protein concentration strongly affected the measured protein patterns (**Figures 1C,D**). This outcome was relatively surprising, as it seemed to be in disagreement with previous findings. As an instance, Kenry et al. studied adsorption, binding kinetics, conformational stability and structural change of single proteins interacting with GO and concluded that molecular interactions between GO and plasma proteins are significantly dependent on the lateral size distribution of GO sheets (Kenry et al., 2016). Our results suggest that despite the molecular interactions of single proteins may be affected by GO lateral size, those size effects become negligible in physiological environments, where single GO-protein binding parameters represent only a portion of a greater description, which involves protein-protein interactions and competitive

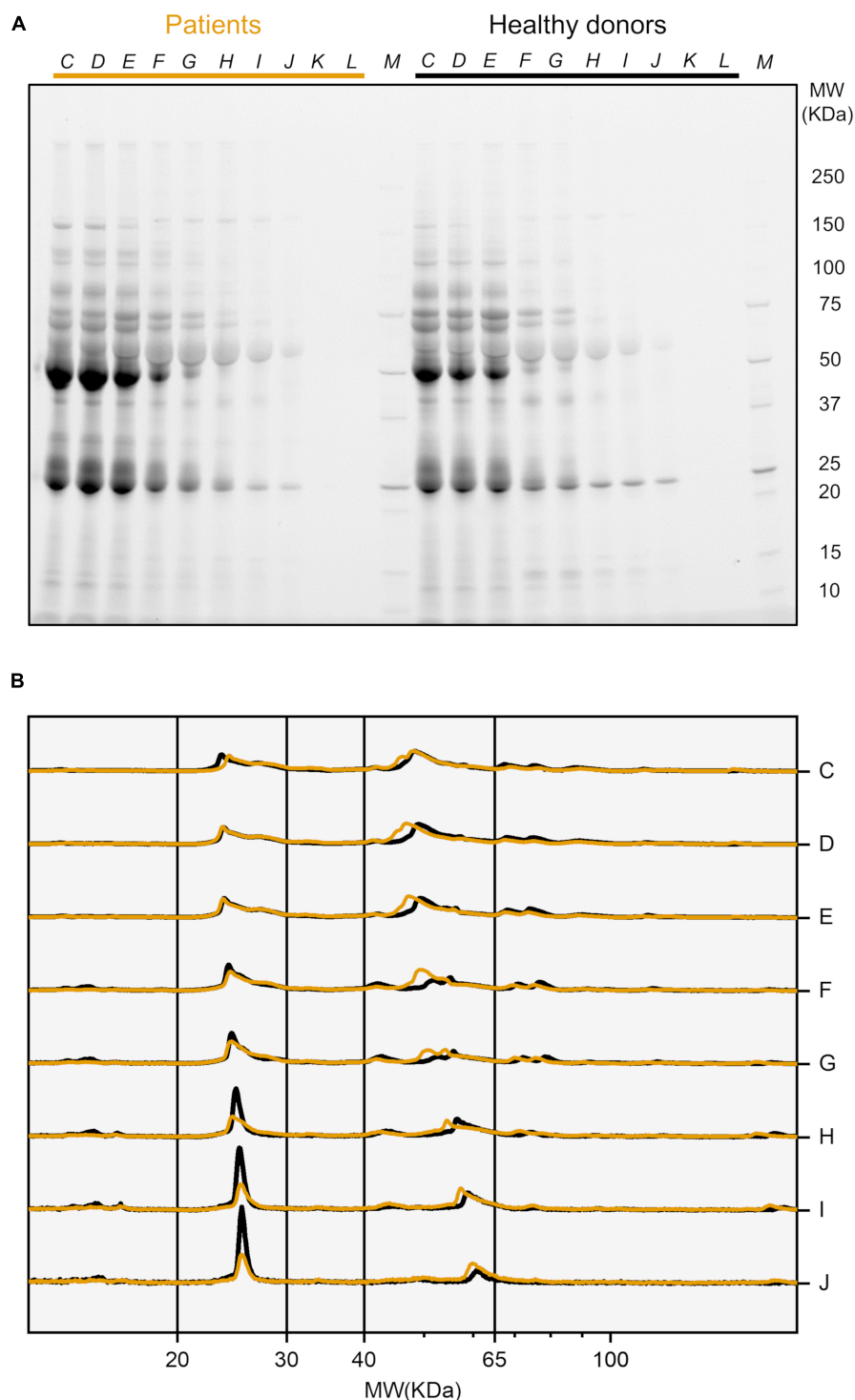
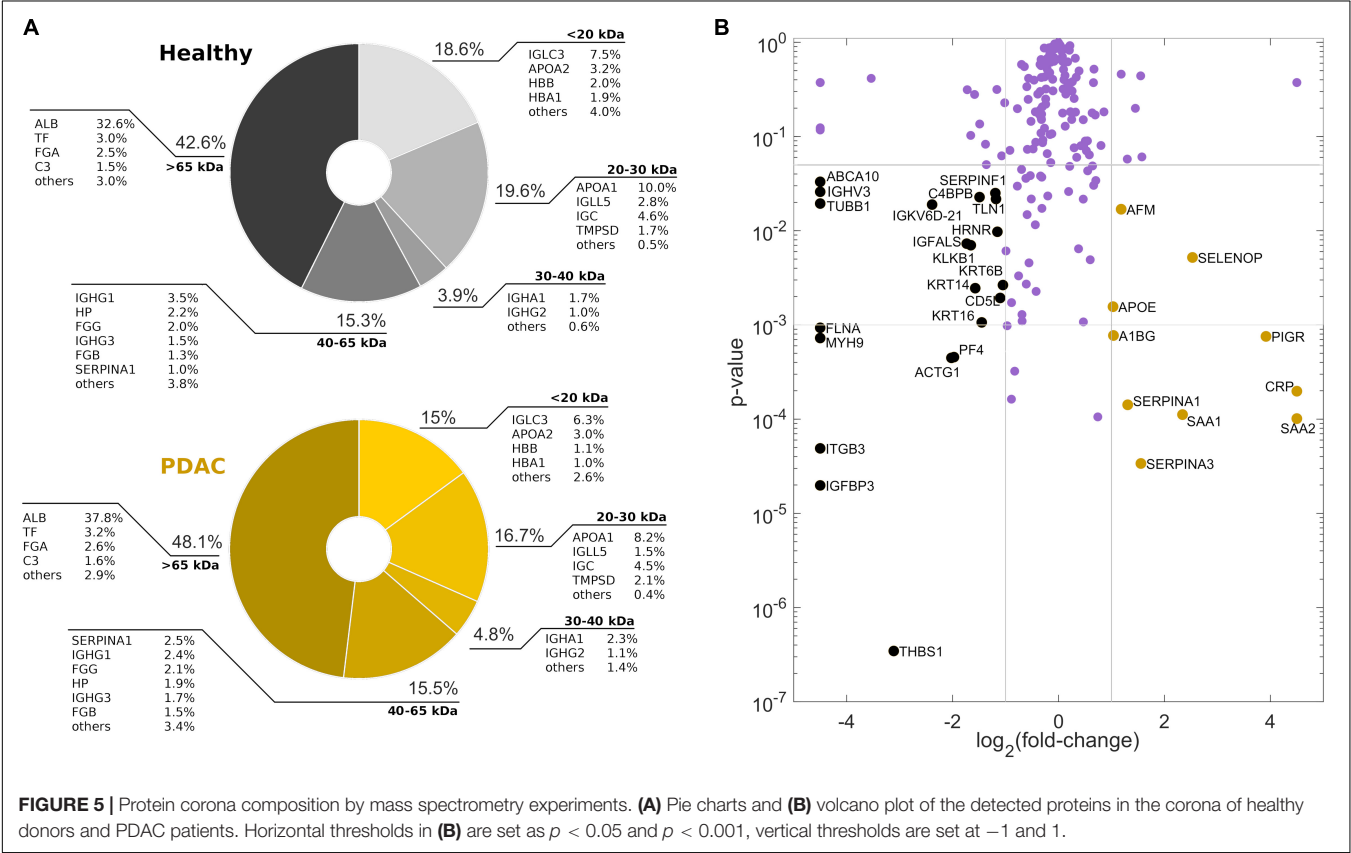
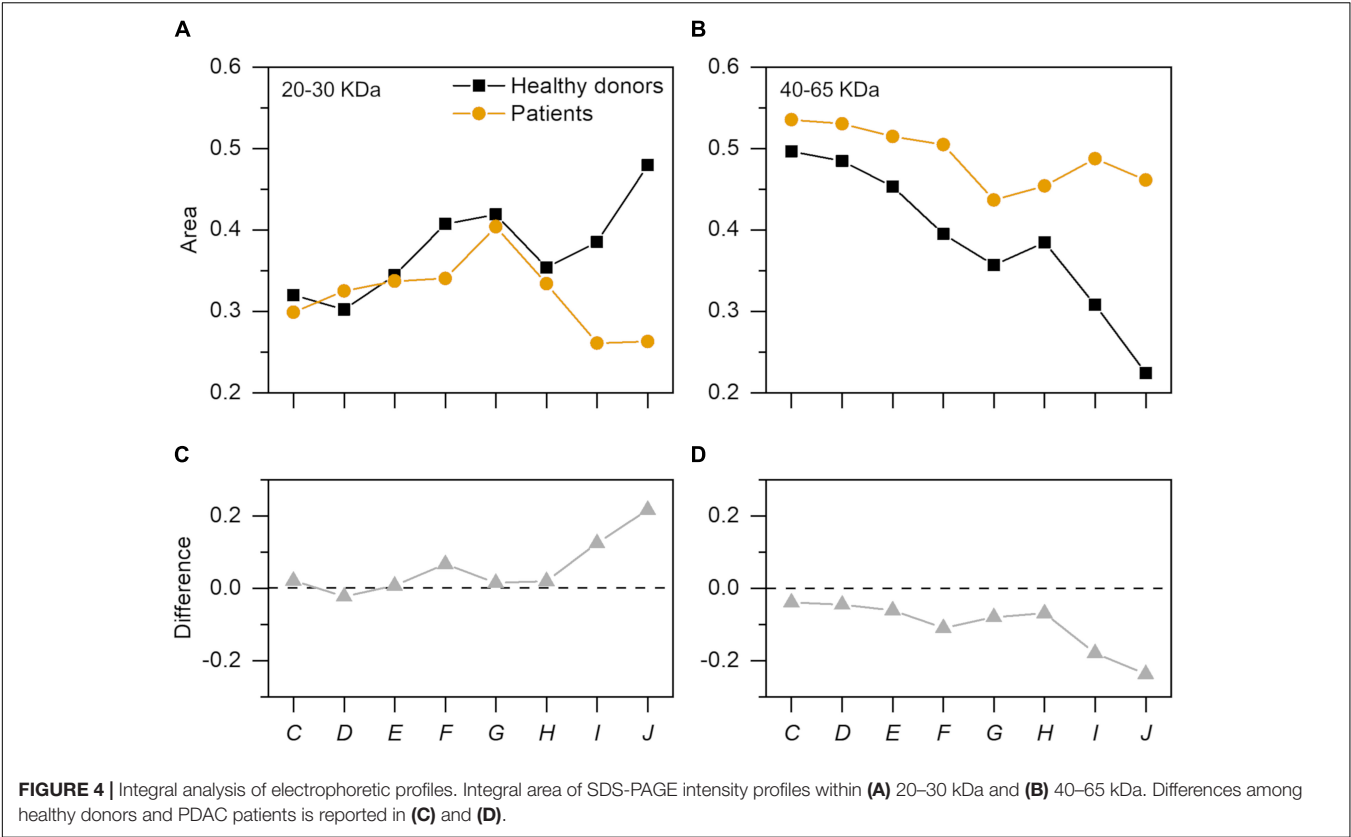


**FIGURE 3 | (A)** Representative SDS-page image of biocoronated GO nanoflakes upon incubation with human plasma from PDAC patients and healthy volunteers. Plasma samples were diluted with dilution factors ranging from C = 10 to L =  $10^3$ . **(B)** One-dimensional protein profiles obtained by densitometry analysis of SDS-PAGE results. Profiles K and L are not reported because their low signal-to-noise ratio compromised the analysis.

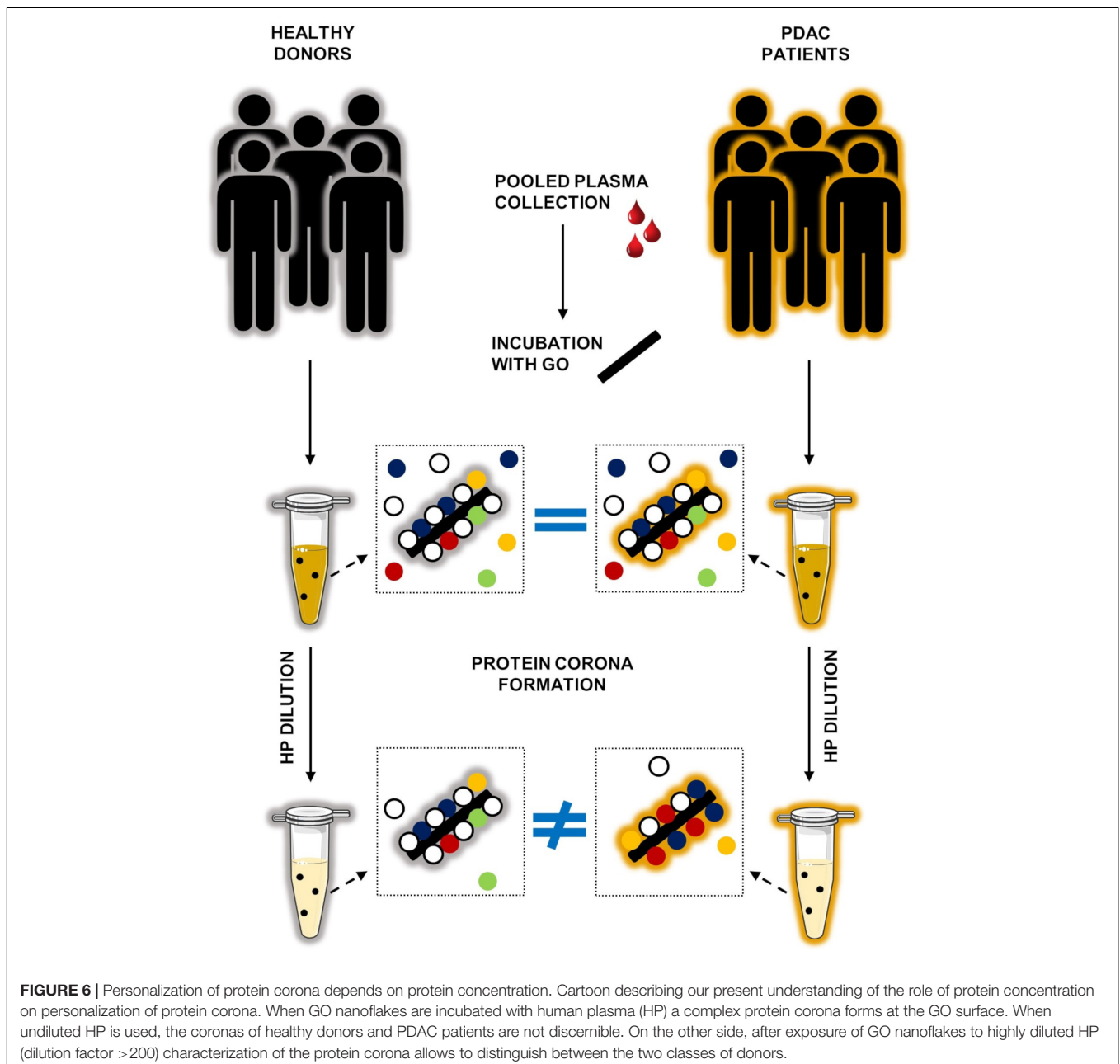
adsorption mechanisms. Our evidence shows that in a complex and crowded protein source such as HP, the overall composition of the PC does not depend on GO lateral size, at least within

the explored size range. Furthermore, even for the smallest GO sheets population (lateral size  $\sim 100$  nm), the available surface area for protein adsorption is much greater than the average



cross section of any single protein. Indeed, under both rough and more detailed approximations, the Stokes radius of proteins (modeled as spherical objects) (Erickson, 2009) is on average more than one order of magnitude smaller than the smallest GO population employed in this work. Therefore, it is reasonable to suppose that possible size dependence of protein adsorption, if any, may be due to edge effects that become negligible as GO lateral size increases. On the other hand, protein concentration is a determining factor involved in formation and shaping of the PC on manifold nanomaterials (Lesniak et al., 2010; Caracciolo et al., 2011; Castagnola et al., 2018) and this trend has been already confirmed for graphene-based systems. As an instance, Castagnola et al. founded that the electrophoretic protein profile

of Graphene-PC complexes was not modified only above a certain threshold of protein concentration (50% v/v) (Castagnola et al., 2018). In agreement with that work, our findings extend the explored incubation conditions, spanning a very broad range of plasma concentration (Figure 2). Interestingly, the obtained electrophoretic patterns exhibited clear trends, especially within 20–30 and 40–65 kDa (Figures 3, 4). To further clarify SDS-PAGE results, we identified proteins enriching PC by nanoLC MS/MS. In particular, within 20–30 kDa proteins apolipoprotein A1 (APOA1) was found to be the most enriched plasma protein (Figure 5A). By recent experimental evidence, it is known that apolipoprotein A1 has a high affinity to graphene and GO surface (Castagnola et al., 2018; Alnasser et al., 2019), and, interestingly,



that protein is recognized as a potential biomarker for PDAC (Koomen et al., 2005; Brand et al., 2011; Lin et al., 2016). Within the other MW ranges, some representative proteins are serum albumin (ALB), hemoglobin (subunit B and A1, HBB and HBA1 respectively) and alpha-1-antitrypsin (SERPINA1). In previous studies, SERPINA1 was identified as a clinically useful biomarker for prognostic or therapeutic purposes in metastatic pancreatic cancer (Koomen et al., 2005; Thakur et al., 2008). Interestingly, in our analysis SERPINA1 was among those corona proteins that had a significant PDAC-to-healthy RPA fold-change, despite their low abundance (**Figure 5B**). This particular group includes also serum amyloid proteins (SAA1 and SAA2), apolipoprotein E (APOE) and alpha 1B glycoprotein (A1BG). SAA is an acute-phase protein involved in tumor pathogenesis and might be included in a group of non-specific biomarkers for cancers, including PDAC (Malle et al., 2009). APOE has been found to be up-regulated in the sera of patients with PDAC and has been proposed as a potential PDAC-related biomarker, alone or in combination with others (Chen et al., 2013; Lin et al., 2016). Finally, A1BG is a plasma glycoprotein, whose function is not clear yet but its overexpression has been detected and quantified in cancerous pancreatic juice (Tian et al., 2008). These are some representative examples of known potential biomarkers for cancers that were detected by GO protein corona. In principle, the list could be enlarged with other proteins, which exhibit variations in the personalized coronas but to date are not yet known to have a role in the tumor biology of PDAC.

## CONCLUSION

In conclusion, we have shown that the protein corona that forms around GO nanoflakes in human plasma does not depend on GO lateral size but is strongly affected by protein concentration. The latter result may be relevant to exploit the personalized protein corona for diagnostic purposes. Indeed, we could demonstrate that the protein corona of pancreatic cancer patients differs significantly from that of healthy individuals only at very low protein concentration, i.e., upon 200-fold dilution of human plasma. The main limitation of the present study is undoubtedly the use of pooled samples. Although employment of non-pooled samples is a key issue for the validation of PC-based diagnostic tests, this is far beyond the scope of the present investigation. We indeed see this work as the proof of concept that exposing nanomaterials to plasma samples under 'optimal dilution conditions' could be a good strategy to amplify personalization of the protein corona and,

in turn, to exploit it to distinguish between different classes of donors (e.g., cancer vs. non-cancer patients) (**Figure 6**). We underline that identification of optimal dilution factors may be not trivial as it may depend simultaneously on synthetic identity of nanomaterials, the protein source and environmental factors. We envision that exploring the interactions among nanomaterials and HP will offer unprecedented opportunities for the development of sophisticated IVD technologies to be used at every step of the patient pathway, from diagnosis to monitoring the progression of disease and individual response to treatment.

## DATA AVAILABILITY STATEMENT

The datasets generated for this study are available on request to the corresponding author.

## ETHICS STATEMENT

The studies involving human participants were reviewed and approved by Ethics Committee of the University Campus Bio-Medico di Roma. The patients/participants provided their written informed consent to participate in this study.

## AUTHOR CONTRIBUTIONS

DC, RC, AL, GC, and DP: conceptualization. GC and DP: methodology, project administration, and funding acquisition. LD: software and data curation. RD and LD: formal analysis, writing – original draft preparation, and visualization. RD, LD, EQ, CC, and AC: investigation. DC, RZ, GC, and DP: resources and writing – review and editing. AL, GC, and DP: supervision.

## FUNDING

The research leading to these results has received funding from AIRC under IG 2017 – ID. 20327 project – P.I. GC. LD is recipient of a FIRC/AIRC fellowship (ID 24143; 2019).

## SUPPLEMENTARY MATERIAL

The Supplementary Material for this article can be found online at: <https://www.frontiersin.org/articles/10.3389/fbioe.2020.00491/full#supplementary-material>

## REFERENCES

- Alnasser, F., Castagnola, V., Boselli, L., Esquivel-Gaon, M., Efeoglu, E., McIntyre, J., et al. (2019). Graphene nanoflake uptake mediated by scavenger receptors. *Nano Lett.* 19, 1260–1268. doi: 10.1021/acs.nanolett.8b04820
- Barrán-Berdón, A. L., Pozzi, D., Caracciolo, G., Capriotti, A. L., Caruso, G., Cavaliere, C., et al. (2013). Time evolution of nanoparticle-protein corona in human plasma: relevance for targeted drug delivery. *Langmuir* 29, 6485–6494. doi: 10.1021/la401192x
- Brand, R. E., Nolen, B. M., Zeh, H. J., Allen, P. J., Eloubeidi, M. A., Goldberg, M., et al. (2011). Serum biomarker panels for the detection of pancreatic cancer. *Clin. Cancer Res.* 17, 805–816. doi: 10.1158/1055-9965.EPI-18-0483
- Caputo, D., and Caracciolo, G. (2019). Nanoparticle-enabled blood tests for early detection of pancreatic ductal adenocarcinoma. *Cancer Lett.* 470, 191–196. doi: 10.1016/j.canlet.2019.11.030
- Caputo, D., Cartillone, M., Cascone, C., Pozzi, D., Digiacomo, L., Palchetti, S., et al. (2018). Improving the accuracy of pancreatic cancer clinical staging by exploitation of nanoparticle-blood interactions: a pilot study. *Pancreatol.* 18, 661–665. doi: 10.1016/j.pan.2018.06.002



- Caputo, D., Papi, M., Coppola, R., Palchetti, S., Digiacomo, L., Caracciolo, G., et al. (2017). A protein corona-enabled blood test for early cancer detection. *Nanoscale* 9, 349–354. doi: 10.1039/c6nr05609a
- Caracciolo, G., Pozzi, D., Capriotti, A. L., Cavaliere, C., Foglia, P., Amenitsch, H., et al. (2011). Evolution of the protein corona of lipid gene vectors as a function of plasma concentration. *Langmuir* 27, 15048–15053. doi: 10.1021/la202912f
- Caracciolo, G., Vali, H., Moore, A., and Mahmoudi, M. (2019). Challenges in molecular diagnostic research in cancer nanotechnology. *Nano Today* 27, 6–10.
- Castagnola, V., Zhao, W., Boselli, L., Giudice, M. L., Meder, F., Polo, E., et al. (2018). Biological recognition of graphene nanoflakes. *Nat. Commun.* 9, 1–9.
- Chen, J., Chen, L.-J., Yang, R.-B., Xia, Y.-L., Zhou, H.-C., Wu, W., et al. (2013). Expression and clinical significance of apolipoprotein E in pancreatic ductal adenocarcinoma. *Med. Oncol.* 30:583. doi: 10.1007/s12032-013-0583-y
- Chetwynd, A. J., Wheeler, K. E., and Lynch, I. (2019). Best practice in reporting corona studies: minimum information about nanomaterial biocorona experiments (MINBE). *Nano Today* 28:100758.
- Chun, Y. S., Pawlik, T. M., and Vauthey, J.-N. (2018). of the AJCC cancer staging manual: pancreas and hepatobiliary cancers. *Ann. Surg. Oncol.* 25, 845–847. doi: 10.1245/s10434-017-6025-x
- Chung, C., Kim, Y.-K., Shin, D., Ryoo, S.-R., Hong, B. H., and Min, D.-H. (2013). Biomedical applications of graphene and graphene oxide. *Acc. Chem. Res.* 46, 2211–2224. doi: 10.1166/jnn.2014.9571
- Di Santo, R., Digiacomo, L., Palchetti, S., Palmieri, V., Perini, G., Pozzi, D., et al. (2019). Microfluidic manufacturing of surface-functionalized graphene oxide nanoflakes for gene delivery. *Nanoscale* 11, 2733–2741. doi: 10.1039/c8nr09245a
- Digiacomo, L., Palchetti, S., Giulimondi, F., Pozzi, D., Chiozzi, R. Z., Capriotti, A. L., et al. (2019). The biomolecular corona of gold nanoparticles in a controlled microfluidic environment. *Lab Chip* 19, 2557–2567. doi: 10.1039/c9lc00341j
- Erickson, H. P. (2009). Size and shape of protein molecules at the nanometer level determined by sedimentation, gel filtration, and electron microscopy. *Biol. Proced. Online* 11:32. doi: 10.1007/s12575-009-9008-x
- Hajipour, M. J., Raheb, J., Akhavan, O., Arjmand, S., Mashinchian, O., Rahman, M., et al. (2015). Personalized disease-specific protein corona influences the therapeutic impact of graphene oxide. *Nanoscale* 7, 8978–8994. doi: 10.1039/c5nr00520e
- Jasim, D. A., Lozano, N., and Kostarelos, K. (2016). Synthesis of few-layered, high-purity graphene oxide sheets from different graphite sources for biology. *2D Mater.* 3:014006.
- Jimenez, C. R., Zhang, H., Kinsinger, C. R., and Nice, E. C. (2018). The cancer proteomic landscape and the HUPC cancer proteome project. *Clin. Proteomics* 15:4. doi: 10.1186/s12014-018-9180-6
- Ke, P. C., Lin, S., Parak, W. J., Davis, T. P., and Caruso, F. (2017). A decade of the protein corona. *ACS Nano* 11, 11773–11776.
- Kenry, K. P. L., and Lim, C. T. (2016). Molecular interactions of graphene oxide with human blood plasma proteins. *Nanoscale* 8, 9425–9441. doi: 10.1039/c6nr01697a
- Koomen, J. M., Shih, L. N., Coombes, K. R., Li, D., Xiao, L.-C., Fidler, I. J., et al. (2005). Plasma protein profiling for diagnosis of pancreatic cancer reveals the presence of host response proteins. *Clin. Cancer Res.* 11, 1110–1118.
- Lesniak, A., Campbell, A., Monopoli, M. P., Lynch, I., Salvati, A., and Dawson, K. A. (2010). Serum heat inactivation affects protein corona composition and nanoparticle uptake. *Biomaterials* 31, 9511–9518. doi: 10.1016/j.biomaterials.2010.09.049
- Lin, C., Wu, W.-C., Zhao, G.-C., Wang, D.-S., Lou, W.-H., and Jin, D.-Y. (2016). ITRAQ-based quantitative proteomics reveals apolipoprotein AI and transferrin as potential serum markers in CA19-9 negative pancreatic ductal adenocarcinoma. *Medicine* 95:e4527. doi: 10.1097/MD.00000000000004527
- Liu, Z., Robinson, J. T., Tabakman, S. M., Yang, K., and Dai, H. (2011). Carbon materials for drug delivery & cancer therapy. *Mater. Today* 14, 316–323.
- Lundqvist, M., Stigler, J., Elia, G., Lynch, I., Cedervall, T., and Dawson, K. A. (2008). Nanoparticle size and surface properties determine the protein corona with possible implications for biological impacts. *Proc. Natl. Acad. Sci. U.S.A.* 105, 14265–14270. doi: 10.1073/pnas.0805135105
- Ma, J., Liu, R., Wang, X., Liu, Q., Chen, Y., Valle, R. P., et al. (2015). Crucial role of lateral size for graphene oxide in activating macrophages and stimulating pro-inflammatory responses in cells and animals. *ACS Nano* 9, 10498–10515. doi: 10.1021/acs.nano.5b04751
- Malle, E., Sodin-Semrl, S., and Kovacevic, A. (2009). Serum amyloid A: an acute-phase protein involved in tumour pathogenesis. *Cell. Mol. Life Sci.* 66:9. doi: 10.1007/s00018-008-8321-x
- Papi, M., and Caracciolo, G. (2018). Principal component analysis of personalized biomolecular corona data for early disease detection. *Nano Today* 21, 14–17.
- Papi, M., Palmieri, V., Digiacomo, L., Giulimondi, F., Palchetti, S., Ciasca, G., et al. (2019). Converting the personalized biomolecular corona of graphene oxide nanoflakes into a high-throughput diagnostic test for early cancer detection. *Nanoscale* 11, 15339–15346. doi: 10.1039/c9nr01413f
- Pozzi, D., Caracciolo, G., Capriotti, A. L., Cavaliere, C., La Barbera, G., Anchordoquy, T. J., et al. (2015). Surface chemistry and serum type both determine the nanoparticle–protein corona. *J. Proteomics* 119, 209–217. doi: 10.1016/j.jpro.2015.02.009
- Rahib, L., Smith, B. D., Aizenberg, R., Rosenzweig, A. B., Fleshman, J. M., and Matrisian, L. M. (2014). Projecting cancer incidence and deaths to 2030: the unexpected burden of thyroid, liver, and pancreas cancers in the United States. *Cancer Res.* 74, 2913–2921. doi: 10.1158/0008-5472.CAN-14-0155
- Schwenk, J. M., Omenn, G. S., Sun, Z., Campbell, D. S., Baker, M. S., Overall, C. M., et al. (2017). The human plasma proteome draft of 2017: building on the human plasma PeptideAtlas from mass spectrometry and complementary assays. *J. Proteome Res.* 16, 4299–4310. doi: 10.1021/acs.jproteome.7b00467
- Shruthi, B. S., and Palani Vinodhkumar, S. (2016). Proteomics: a new perspective for cancer. *Adv. Biomed. Res.* 5:67.
- Thakur, A., Bollig, A., Wu, J., and Liao, D. J. (2008). Gene expression profiles in primary pancreatic tumors and metastatic lesions of Ela-c-myc transgenic mice. *Mol. Cancer* 7:11. doi: 10.1186/1476-4598-7-11
- Tian, M., Cui, Y.-Z., Song, G.-H., Zong, M.-J., Zhou, X.-Y., Chen, Y., et al. (2008). Proteomic analysis identifies MMP-9, DJ-1 and A1BG as overexpressed proteins in pancreatic juice from pancreatic ductal adenocarcinoma patients. *BMC Cancer* 8:241. doi: 10.1186/1471-2407-8-241
- Wang, M., Gustafsson, O. J., Siddiqui, G., Javed, I., Kelly, H. G., Blin, T., et al. (2018). Human plasma proteome association and cytotoxicity of nano-graphene oxide grafted with stealth polyethylene glycol and poly (2-ethyl-2-oxazoline). *Nanoscale* 10, 10863–10875. doi: 10.1039/c8nr00835c
- Wang, Y., Li, Z., Wang, J., Li, J., and Lin, Y. (2011). Graphene and graphene oxide: biofunctionalization and applications in biotechnology. *Trends Biotechnol.* 29, 205–212. doi: 10.1016/j.tibtech.2011.01.008
- Zheng, T., Pierre-Pierre, N., Yan, X., Huo, Q., Almodovar, A. J., Valerio, F., et al. (2015). Gold nanoparticle-enabled blood test for early stage cancer detection and risk assessment. *ACS Appl. Mater. Interfaces* 7, 6819–6827. doi: 10.1021/acsami.5b00371

**Conflict of Interest:** The authors declare that the research was conducted in the absence of any commercial or financial relationships that could be construed as a potential conflict of interest.

Copyright © 2020 Di Santo, Digiacomo, Quagliarini, Capriotti, Laganà, Zenezini Chiozzi, Caputo, Cascone, Coppola, Pozzi and Caracciolo. This is an open-access article distributed under the terms of the Creative Commons Attribution License (CC BY). The use, distribution or reproduction in other forums is permitted, provided the original author(s) and the copyright owner(s) are credited and that the original publication in this journal is cited, in accordance with accepted academic practice. No use, distribution or reproduction is permitted which does not comply with these terms.





# Microfluidic Multielectrode Arrays for Spatially Localized Drug Delivery and Electrical Recordings of Primary Neuronal Cultures

Giulia Bruno<sup>1,2</sup>, Nicolò Colistra<sup>2</sup>, Giovanni Melle<sup>1,2</sup>, Andrea Cerea<sup>2</sup>, Aliaksandr Hubarevich<sup>2</sup>, Lieselot Deleye<sup>2</sup>, Francesco De Angelis<sup>2\*</sup> and Michele Dipalo<sup>2\*</sup>

<sup>1</sup> DIBRIS, Università degli Studi di Genova, Genoa, Italy, <sup>2</sup> Istituto Italiano di Tecnologia, Genoa, Italy

## OPEN ACCESS

### Edited by:

Davide Ricci,  
University of Genoa, Italy

### Reviewed by:

Robert Langer,  
Massachusetts Institute  
of Technology, United States  
Vanessa Maybeck,  
Helmholtz Association of German  
Research Centers (HZ), Germany  
Luca Maiolo,  
Italian National Research Council, Italy

### \*Correspondence:

Francesco De Angelis  
francesco.deangelis@iit.it  
Michele Dipalo  
michele.dipalo@iit.it

### Specialty section:

This article was submitted to  
Nanobiotechnology,  
a section of the journal  
Frontiers in Bioengineering and  
Biotechnology

**Received:** 18 February 2020

**Accepted:** 21 May 2020

**Published:** 16 June 2020

### Citation:

Bruno G, Colistra N, Melle G,  
Cerea A, Hubarevich A, Deleye L,  
De Angelis F and Dipalo M (2020)  
Microfluidic Multielectrode Arrays  
for Spatially Localized Drug Delivery  
and Electrical Recordings of Primary  
Neuronal Cultures.  
Front. Bioeng. Biotechnol. 8:626.  
doi: 10.3389/fbioe.2020.00626

Neuropathological models and neurological disease progression and treatments have always been of great interest in biomedical research because of their impact on society. The application of *in vitro* microfluidic devices to neuroscience-related disciplines provided several advancements in therapeutics or neuronal modeling thanks to the ability to control the cellular microenvironment at spatiotemporal level. Recently, the introduction of three-dimensional nanostructures has allowed high performance in both *in vitro* recording of electrogenic cells and drug delivery using minimally invasive devices. Independently, both delivery and recording have led to pioneering solutions in neurobiology. However, their combination on a single chip would provide further fundamental improvements in drug screening systems and would offer comprehensive insights into pathologies and diseases progression. Therefore, it is crucial to develop platforms able to monitor progressive changes in electrophysiological behavior in the electrogenic cellular network, induced by spatially localized injection of biochemical agents. In this work, we show the application of a microfluidic multielectrode array (MEA) platform to record spontaneous and chemically stimulated activity in primary neuronal networks. By means of spatially localized caffeine injection via microfluidic nanochannels, the device demonstrated its capability of combined localized drug delivery and cell signaling recording. The platform could detect activity of the neural network at multiple sites while delivering molecules into just a few selected cells, thereby examining the effect of biochemical agents on the desired portion of cell culture.

**Keywords:** microfluidics, multielectrode array, drug delivery, *in vitro* electrophysiology, neuron

## INTRODUCTION

Neurological and neurodegenerative conditions, such as Alzheimer, Parkinson disease, and multiple sclerosis, affect a large percentage of the world's population. These diseases involve the progressive loss of neural functions due to a variety of factors such as oxidative stress, protein aggregation, or misfolding in the central and peripheral nervous system (Barnham et al., 2004). Given the variability and complexity of causes and symptoms, the ability to treat, study, and understand these conditions is limited to the tools capable of probing the signaling complexity of neuronal networks.

Multielectrode array (MEA) devices are widely used for investigating electrogenic cell connectivity, physiology, and pathology in brain tissues and in 2D neuronal cultures. MEA technology represents a unique electrical interface for cultured cells, as they can be directly grown on top of the electrodes (Spira and Hai, 2013). The key advantage of this technique is the capability to record and stimulate large populations of excitable cells, without inflicting mechanical damage to the cells (Hammerle, 1998). Nevertheless, this technique lacks the ability to provide a more comprehensive modeling of neuronal networks, missing the capability of manipulating neural activity at chemical level with high spatial resolution.

On the other hand, microfluidic devices are necessary and useful *in vitro* systems for acquiring a comprehensive view of pathology and disease progression by means of well-controlled and localized delivery of bio-chemical agents (Park et al., 2006). Moreover, these systems have the potential to improve therapeutic drug approval rates by providing more physiological and patient-specific *in vitro* assays. Although the complete *in vivo* complexity cannot be captured yet, these systems could help in recapitulating and simulating it in *in vitro* models. This technology permits to control the amount and distribution of fluid directly on the device recreating microenvironments at tissue, cellular, and molecular levels (Gross et al., 2007; Lin and Levchenko, 2015). The physiologic and pharmacologic response of complex cellular systems can be investigated with precise control of the environment surroundings by controlling the reagent and factor distribution via the microfluidic channels. This specific aspect is relevant in studies involving the effect of the treatment on specific parts of cell culture. By optimizing the device design, it is even possible to create spatial concentration gradients of molecules in the same culture (Tsur et al., 2017; Coluccio et al., 2019).

This approach is useful in cancer therapeutics research (Saadi et al., 2006), growth factors studies on neuronal stem cells (Chung et al., 2005) or more generally, because of the complex interactions occurring among neural cells in *in vitro* studies of neuronal networks (Blasiak et al., 2017; Kamande et al., 2019). Polydimethylsiloxane (PDMS) is widely used for allowing compartmentalization of the culture on the device and strictly limiting the communication between those separate environments through microfluidic channels (Takayama and Kida, 2016). In this field, creating co-cultures or inducing co-pathological cell cultures, where the unaffected cell population is in contact with other cell populations in a disease state, is an important tactic in neurodegenerative studies and pharmaceutical tests (Kunze et al., 2011). In fact, studying the disease progression pattern from the unhealthy cell population to the healthy one could provide the ability to monitor time-variant changes in cell network morphology and electrophysiology during disease progression. In the vast majority of cases, the current methods for analyzing the electrophysiological responses in these systems are done using fluorescence. However, these techniques are cumbersome and the attached fluorescent compounds could interfere with binding sites of interactive molecules, thereby hampering the conformational changes of the molecules and increasing non-specificity. In other cases,

the evaluation is carried out by *a posteriori* methods that does not allow for simultaneous evaluation of the treatment and the disease evolution.

Therefore, combining microfluidic technologies with a MEA device would provide an immediate, label-free, and non-invasive procedure for investigating electrogenic cells response in the studied conditions. In this regard, Gladkov et al. (2017) designed two subpopulations of primary hippocampal neuronal cultures directly onto a MEA device with asymmetric channels. Morphological and functional connectivity between the two subpopulations could be analyzed thanks to the electrodes underneath the cell culture. Thereby, the unidirectional spiking pattern propagation through the microfluidic channels between the two sectors could be observed. These strategies provided powerful tools for advancing applications in therapeutics, diagnostics, and drug discovery.

Nevertheless, integrated and multiplex *in vitro* devices for neuronal modeling and disease therapeutics require the capability to achieve higher spatial resolution and tools for localized access to a specific cell environment (Pinto and Howell, 2007).

Despite the importance of this tool in medicine and therapeutics (Stewart et al., 2016), the selective and precise delivery of pharmaceutical agents including proteins, peptides, nucleic acid, or drugs into living cells remains a challenge in biosensing platforms.

In this context, the addition of nanostructures might increase the capabilities and specificity of a high throughput, label-free, non-invasive drug delivery. Different groups already focused on developing nanostructures such as gold nanotubes, nanopillar (Xie et al., 2012), and nanostraws (Xie et al., 2013) intended for highly specific and localized delivery of pharmaceutical agents on chip. In contrast with carrier mediated delivery methods, these nanostructures allow to carry molecules straight into the cells, enabling for a spatial, temporal, and dose-controlled delivery. Following this line, the N. Melosh group provided several advancements in the field. They culture cells onto nanostructured membranes forming tight cell-nanostraw interfaces (Xie et al., 2013). Cargoes are delivered from the fluid below the membrane, through the nanostraws directly into the cells, by either electrophoresis or diffusion. Their method supports an optimal delivery and ensures a low diffusion of the injected molecules into the external medium. However, the device does not allow for a direct electrophysiological evaluation of the cell response to the induced stimuli.

In this regard, further efforts were made in order to develop a functional approach that combines high precision cell response monitoring with a simultaneous molecule delivery. In previous work from our group, exploiting the multifunctional capabilities of hollow 3D nanostructures, we developed a tool able to monitor the bioelectrical activity of electrogenic cells while locally treating them with exogenous molecules (Cerea et al., 2018). Here, the hollow nanoantennas were used as a hybrid structure for intra- and extra-cellular recordings and as a nanoscale tool for selective and intracellular delivery. The microfluidic MEA (MF-MEA) device provided high quality intra- and extracellular recordings in human derived cardiac cells and in immortalized

cardiomyocytes from mouse (HL-1). As a proof of concept, the simultaneous intracellular delivery was also verified with the localized injection of molecules in the cardiomyocytes through the 3D hollow nanotubes. However, the injected molecules were basic fluorescent dyes that had no effect on the spontaneous electrical activity of the cells, preventing us from correlating the effects of delivered drugs on the electrophysiological response of the culture. Moreover, the cardiomyocytes required only up to 4–5 days in culture for acquiring spontaneous electrical activity. Therefore, the experiments did not give indications on the full biocompatibility of the MF-MEAs for sustaining long-term cultures for several weeks, as it would be required for neurons.

In this work, we show that MEAs with microfluidic channels and protruding 3D nanotubes can sustain cultures of both hippocampal and cortical primary neurons up to their maturation. The neurons could be cultured for more than 3 weeks *in vitro* and showed the functional maturation of a network with spiking and bursting activity, ensuring the reliability of the device with neuronal cells. The cultures were characterized by fluorescence microscopy and by electrophysiological recording of the network activity. Further, the device demonstrates the ability to deliver selectively a stimulant molecule, caffeine, which dynamically affects the electrical response of the neuronal networks. Specifically, the neurons were chemically stimulated by localized injection of caffeine through the 3D nanotubes, while simultaneously monitoring the electrophysiological response of the network. As a result, we demonstrated the ability to observe the specific changes in electrical signaling of the treated neurons, while maintaining the physiological conditions in the rest of the culture.

## MATERIALS AND METHODS

### Fabrication and Packaging of Microfluidic MEA

The MEA devices with microfluidic channels were fabricated with a technique explained in previous work by Cerea et al. (2018). Briefly, the membrane and nanochannels were fabricated on a 525  $\mu\text{m}$  thick silicon wafer with 500 nm  $\text{Si}_3\text{N}_4$  on both sides. A 400 nm Cr mask was sputter coated on one side in order to create nanochannels and membranes. Subsequently, a thin layer of photoresist was spin coated on top of it. The shape was defined with conventional UV photolithography (SÜSS MicroTec Mask Aligner) and subsequent Cr etching of the exposed areas. After dissolving the remaining photoresist in acetone, the wafer and the mask was exposed to reactive ion etching (RIE, SENTECH) in order to selectively etch the 500 nm layer of silicon nitride. After chemically removing the Cr mask, the 525  $\mu\text{m}$  of silicon were wet etched in a solution of KOH and deionized  $\text{H}_2\text{O}$  (1:2). After this procedure, the two 2 mm<sup>2</sup> membranes were defined and the sample was immersed in distilled water to remove residues.

The gold coated 3D nanoelectrodes were fabricated as described in Dipalo et al. (2015). Briefly, a 2  $\mu\text{m}$  thick layer of S1813 (MICROPOSIT S1813) was spin coated on top of

the  $\text{Si}_3\text{N}_4$  membrane. After the exposure and the following development in MF-319 (MICROPOSIT MF-319 DEVELOPER), 24 ti/au electrodes and conductive tracks were fabricated through electron beam evaporation. The unnecessary resist was lifted-off in hot remover-PG (MicroChem) and the residuals were removed by  $\text{O}_2$  plasma ashing. The 24 electrodes (100–900  $\mu\text{m}^2$ ) were defined opening apertures on a 1.2  $\mu\text{m}$  spin coated SU-8 photoresist in correspondence of each pad. The gold coated 3D nanoelectrodes were manufactured on the planar electrode through FIB (FEI NanoLab 600 dual beam system) lithography (with the exposure dose of 27  $\text{nC}\cdot\mu\text{m}^{-1}$ ) from the backside of the membrane, following the technique described in the work of De Angelis et al. (2013). The nanopillars decorate each electrode located on the  $\text{Si}_3\text{N}_4$  membranes. These structures have an external diameter of 600 nm, an internal diameter of 150 nm, and a height of 1.2  $\mu\text{m}$ . Each electrode contains an array with a variable number of nanostructures depending on the electrode dimensions and with a pitch of 4  $\mu\text{m}$  between each nanostructure. The two membranes on the platform include eight nanostructured electrodes each. The finished device is mounted on a PCB and covered with a 2 mm thick layer of PDMS. The area with the electrodes is not covered in PDMS, allowing the confinement of the cells to the sensible area of the device and thereby reducing the number of cells per device. A glass ring was placed on top of the device in order to form a container for the cell medium. On the bottom side of the device, a thick rectangular piece of PDMS was plasma bonded, acting as a connector for inlet and outlet tubing to the microfluidic channels.

### Culture of Cortical and Hippocampal Neurons

First, each side of the MF-MEAs was sterilized under UV for 20 min. Next, the devices were pre-conditioned 2 days before cell seeding by overnight incubation at 37°C, 5%  $\text{CO}_2$ , and 95% humidity in Primary Neural Growth Medium (PNGM), supplemented with 2 mM L-glutamine, GA-1000, and 2% Neural Serum Factor-1, in order to saturate the porous matrix of the culture well. Additionally, the tubing and microchannels at the bottom of the device were manually filled with PNGM using a sterile syringe. The following day, the PNGM was removed from the culture well to coat it with a solution of 30  $\mu\text{g}/\text{mL}$  poly-D-lysine (Sigma-Aldrich) and 2  $\mu\text{g}/\text{mL}$  laminin (Sigma-Aldrich) in phosphate-buffered saline (PBS) in order to enhance primary neuronal cells adhesion and proliferation on the devices. After coating, the device was again incubated for 4 h at 37°C, 5%  $\text{CO}_2$ , and 95% of humidity. After that, the substrates were washed extensively with sterile water four times and dried in sterile conditions overnight before cell seeding. Rat cortex and hippocampus neuronal cells (Lonza Walkersville, United States) were seeded on the PDL-laminin substrates at a density of 500 cells/ $\text{mm}^2$  and incubated at 37°C, 5%  $\text{CO}_2$ , and 95% humidity. Upon adhesion, after 2–2.5 h, PNGM was partially removed, leaving a small volume to ensure the cells do not dry, and fresh medium was added. Cultures were maintained for more than 3 weeks, while every 4 days, one-third of the medium was changed for fresh PNGM.

## Neuronal Network Activity Analysis

Data analysis was performed offline by using a custom software package named SpyCode (Bologna et al., 2010), developed in MATLAB (The Mathworks, Natick, MA, United States). Spike detection was performed by means of a threshold-based precise timing spike detection (PTSD) algorithm (Maccione et al., 2009). The algorithm requires three parameters: a threshold set to seven times the standard deviation of the baseline noise, a peak lifetime period (set at 2 ms), and a refractory period (set at 1 ms). To analyze and quantify the electrophysiological activity of cortex and hippocampal neuronal networks in both basal and caffeine-affected conditions, first order statistics were extracted. In particular, we evaluated the mean firing rate (MFR), i.e., the number of spikes per second from each channel, and the percentage of random spikes, i.e., the fraction of spikes outside bursts. Furthermore, burst detection was performed according to the method described by Pasquale et al. (2010). A burst is a sequence of spikes having an inter-spike interval (ISI, i.e., time intervals between consecutive spikes) smaller than a predefined reference value (set at 100 ms in our experiments), and containing at least a minimum number of consecutive spikes (set at five spikes). The parameters extracted from this analysis were the mean bursting rate (MBR) and the mean burst duration (MBD), which are, respectively, the frequency and the duration of the bursts at the single channel level.

Statistical analysis was carried out to determine significant differences between each sample pairs by using MATLAB. All data were presented as mean  $\pm$  standard error of the mean. Since the data do not follow a normal distribution (evaluated by the Kolmogorov–Smirnov normality test), statistical analysis was performed using a non-parametric Mann–Whitney *U*-test.

## Pumping System

To maintain a constant flow, a commercial pressure-driven microfluidic system (MFCS-EZ, FLUIGENT) was used. The system was connected tightly to reservoirs containing the molecules we needed to inject. The flow rate was  $100 \mu\text{L min}^{-1}$  to ensure a mild constant flow.

## Immunofluorescence Staining and Analysis, SEM Imaging

To acquire confocal fluorescence images, the culture medium was removed and the cell culture was washed using pre-heated PBS at 37°C. After washing, the cells were fixed through a 15 min incubation in paraformaldehyde (4% in PBS-1X) at room temperature (RT). Following fixation, cells were gently washed 4 times with 1X PBS, before permeabilization with 0.1% Triton in PBS for 15 min. Next, a blocking solution made of 5% FBS, 1% BSA in PBS was added for 30–45 min, before incubation with primary antibodies for 2 h at RT. Alpha Microtubule-Associated Protein (MAP2) polyclonal IgG (1:1000, Invitrogen PA5-17646) and alpha Glial Fibrillary Acidic Protein (GFAP) IgG2b (1:1000, Invitrogen PA1-9565) were used as primary antibodies and diluted in blocking solution. After primary antibody binding, the cells were washed three times for 5 min in PBS. Immediately after, the cells were incubated for 1 h in the dark at RT with

the corresponding secondary antibodies marked with Alexa Fluor 488 and Alexa Fluor 546 (Life Technologies, Italy). To finalize, the cells were washed four times in PBS and the incubation with the nuclear marker DAPI (Invitrogen P36931) was performed for 15 min in the dark at RT. Images from rat brain neurons were acquired and visualized with 20X and 60X objectives using the Leica TCS SP5 AOBS Tandem DM6000 upright confocal microscope (Leica Microsystems, Germany).

To perform fluorescence analyses, the images were converted to grayscale to enhance the signal-to-noise contrast, followed by the setting of a manual threshold. The same threshold was applied to all the pictures used for the same type of analysis. The “*analyze particles*” function from ImageJ software (version Fiji) was used in order to count nuclei in images stained with DAPI and to count neurons and glial cells in images stained with MAP2 and GFAP. The particles were identified according to their sizes and shapes. In particular, the average size of the neuronal soma was taken into account in order to avoid under or over estimation of the cell number. The “*measure*” tool was used to evaluate the covered surface of neurites in images stained with MAP2. The values of interest were extracted from nine visual fields randomly chosen in each culture.

To perform scanning electron microscopy (SEM) imaging, cells were fixed at 10 days *in vitro* (DIV) with glutaraldehyde 2% solution in deionized water for 40 min at RT. Subsequently, the cultures were sequentially dehydrated by changing the solution every 5 min to a solution with a higher percentage of ethanol in water (from 30 to 100%). The samples were left to dry overnight in Hexamethyldisilazane (HMDS, Sigma–Aldrich). The dry samples were then coated with a 10 nm thick gold layer and analyzed by SEM (FEI NanoLab 600 dual beam system).

## Electrophysiological Recordings and Electroporation

The electrophysiological signals were acquired with a custom-made MEA acquisition setup based on a RHA2032 amplifier from the company Intan Technologies (Los Angeles, CA, United States). The electronic board provides recordings from 24 channels multiplexed on an analog output. The sampling rate is 10 kHz for each channel.

For cell electroporation, a pulse train of 2 V peak-to-peak (100  $\mu\text{s}$  pulse duration, 20 Hz repetition rate) was applied for 10 s at the 3D hollow nanoelectrodes (Caprettini et al., 2017). Given the nanoscale nature of our 3D nanoelectrodes and the low voltage applied, the electroporation protocol allows to induce an effect limited to the cell(s) in immediate proximity of the nanoelectrode (Xie et al., 2013). After electroporation, we waited 1 min before recording the activity for 5 min.

## RESULTS

### Microfluidic Multielectrode Array Sensor

The used platform was described in detail in the recent work of Cerea et al. (2018) and it is focused on the idea of designing a flow-through MEA sensor for simultaneous recording and localized drug delivery. The approach enriches the



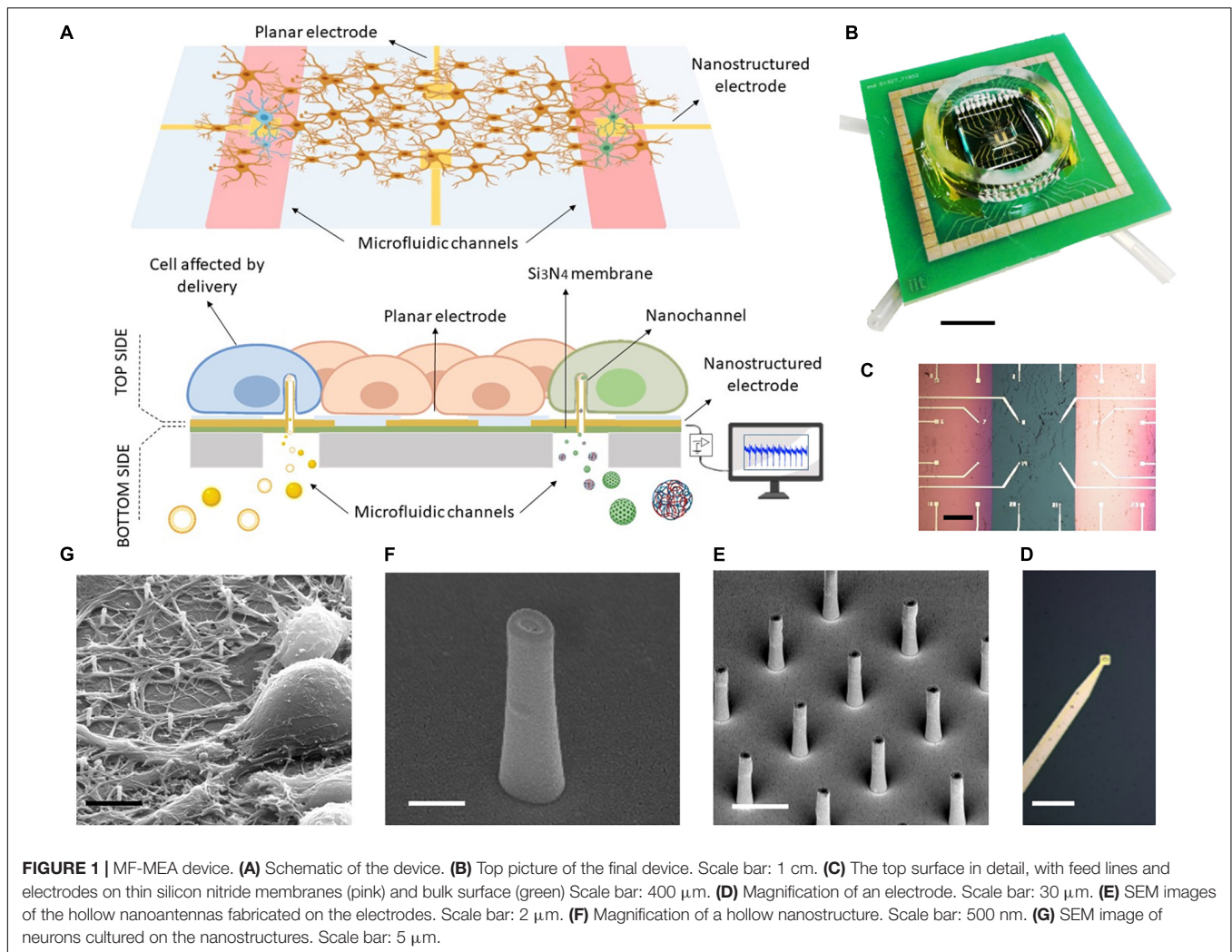


**FIGURE 1 | MF-MEA device. (A)** Schematic of the device. **(B)** Top picture of the final device. Scale bar: 1 cm. **(C)** The top surface in detail, with feed lines and electrodes on thin silicon nitride membranes (pink) and bulk surface (green). Scale bar: 400  $\mu\text{m}$ . **(D)** Magnification of an electrode. Scale bar: 30  $\mu\text{m}$ . **(E)** SEM images of the hollow nanoantennas fabricated on the electrodes. Scale bar: 2  $\mu\text{m}$ . **(F)** Magnification of a hollow nanostructure. Scale bar: 500 nm. **(G)** SEM image of neurons cultured on the nanostructures. Scale bar: 5  $\mu\text{m}$ .

well-established passive MEA concept, with the possibility of cell poration and localized and carrier-free drug delivery.

As depicted in **Figures 1A,B**, the MF-MEA is composed of a thin silicon nitride layer (green) on top of bulk silicon (gray) and two microfluidic channels that run underneath the surface. The 24 gold electrodes with an inter-electrode distance of 400  $\mu\text{m}$  are fabricated and precisely distributed on the top surface of the device, comprising the two separated 500 nm thick silicon nitride membranes and the bulk section in between (**Figure 1C**). Each membrane is connected to a microfluidic channel and tubing which work as inlet and outlet for compound and molecule injection (see **Figure 1B**). In this way, we could store the compounds in these separate chambers (highlighted in red in the schematic **Figure 1A**) and deliver molecules simultaneously in separate parts of the cell culture.

The electrodes fabricated on the membranes (**Figure 1D**) are nanostructured with focused ion beam lithography (see **Figures 1E,F**). In particular, the MF-MEA configuration has eight of these nanostructured electrodes on each membrane and eight electrodes fabricated on the bulk section. The latter are considered as control. Several hollow nanoantennas protrude

from each of these electrodes, providing an access from the lower compartment to the cells cultured on the top side (see **Figure 1E**). As described previously, these hybrid nanochannels allow for molecule delivery at their tip. The latter is in close contact with the cell membranes, thereby impeding the diffusion in other regions of the cellular network. The cellular medium will also not be contaminated by the fluid inserted into the microfluidic channels beneath, making it easy to wash the channels and switch to another molecule. A glass ring is attached on the device in order to contain the cellular medium when the cells are cultured on the surface (see **Figure 1B**). For completeness, **Figure 1G** shows an SEM image of a neuronal cell cultured and stained on such nanostructured electrode, following previously described protocols (Dipalo et al., 2017).

### Confocal Imaging of Neuronal Primary Cultures on Microfluidic Multielectrode Arrays

Hippocampal neurons were cultured at a density of 500 cells/ $\text{mm}^2$  on top of the MF-MEA platforms. These

cells are considered standard models to investigate physiological properties of neurons, such as development, aging, and death, and represent a powerful tool to study degenerative disorders (Ghosh and Greenberg, 1995; Gärtner et al., 2006; Arnold et al., 2011; Gresa-Arribas et al., 2012). To investigate the cell viability and the development of the neuronal networks on the platform under physiological conditions, confocal fluorescent images of the neurons on the surface were obtained after fixation and staining at 18 DIV.

The major microtubule associated protein is visualized with MAP2 marker (green), while glial cells are visualized with a GFAP marker (orange). Additionally, the nuclei were stained with nuclear marker DAPI (blue). Monitoring the viability and the development of the neurons on both the bulk surface and the surface with the membranes was important for evaluating the possible effects of a heterogeneous surface and the presence of nanochannels. For example, the part of the neuronal culture situated on the microfluidic channels could be affected by different dynamics of growth factors due to the presence of a fluidic connection (provided by the hollow nanostructures) to the fluid beneath the thin membranes. In **Figure 2A**, highly magnified images of the cells on the electrodes are shown in order to highlight the viability of the neurons in the presence of both nanostructured electrodes on the silicon nitride membranes and planar electrodes on the bulk section.

The collective network development on both the silicon nitride membranes and the bulk material section was evaluated from 20X upright fluorescence and bright field images (**Figures 2B,C** and **Supplementary Figure S1**). The MAP2 expression shows a healthy and homogeneous neurite growth on both surfaces, with no marked distinctions. In particular, we quantified the area covered by neurites (MAP2) using the “measure” tool from the ImageJ software. The neurites covered  $21 \pm 8$  and  $23 \pm 6\%$  of the surface, respectively, on the microfluidic and bulk parts of the MF-MEA (**Figure 2D**). This indicates that the heterogeneous surface and the presence of nanochannels did not hinder the normal network development, suggesting that the platform design does not affect the cell culture adhesion, the network development, and the processes formation. We also estimated the number of cells per unit area using images of the nuclei stained with DAPI and the “analyze particles” function from ImageJ. As shown in **Figure 2E**, this resulted in a density of  $430 \pm 60$  cells/mm<sup>2</sup> in the bulk section and  $423 \pm 43$  cells/mm<sup>2</sup> on the microfluidic section of the device. We further calculated the neuron/glia ratio in the two cases using the same tools. The count was performed individually on GFAP and MAP2 stained images. The ratio was  $1.9 \pm 0.4$  for the microfluidic region and  $2.0 \pm 0.4$  for the bulk section, as reported in **Figure 2F**.

## Electrophysiological Recordings of Spontaneous Neuron Activity on MF-MEA

To support the applicability of the device to neuronal electrophysiology, we performed several experiments after culturing either primary hippocampal or cortical neurons from

rat on our devices. As neuronal networks require approximately 3 weeks to reach maturation and bursting spontaneous activity, we started the recording sessions at 18 DIV (Ichikawa et al., 1993; Roppongi et al., 2017).

To examine the spontaneous electrophysiological activity of the network, the cells were kept at a controlled temperature of 37°C during recording. In order to preserve the sample sterility, a PDMS cap was placed on top of the glass ring. The so-constituted sensor was connected to the custom-made acquisition system that allows for acquiring signals from the 24 electrodes simultaneously.

The recorded activity showed temporal clusters and neuronal spiking patterns on the whole networks. We observed the behavior of the mature neuronal culture in physiological medium characterized by periodic firing and bursting activity. In particular, the analysis of MEA recordings indicates the presence of dominant spiking and bursting activity that occurred at the level of separated regions of the cultures, with no simultaneous activity taking place overall the complete cultures. This suggests that the neuronal networks presented separated clusters with little inter-cluster connectivity. **Figures 3A,B** depict 2-min long traces extracted from recordings on representative electrodes on the microfluidic channels, respectively, for hippocampal (20 DIV) and cortical (21 DIV) neuronal network activity. In total, we performed experiments on five MF-MEA devices. Three MF-MEA devices were used for cortical cultures, whereas the remaining two were used for hippocampal cultures. Each MF-MEA with cortical neurons was measured at 18, 21, and 22 DIV. Each MF-MEA with hippocampal neurons was measured at 19 and 20 DIV. The recordings lasted typically 5 min. The recorded extracellular spikes exhibited a good signal to noise ratio (SNR), allowing for a proper characterization of the bursting and firing activity of the cells on the electrodes. To analyze the electrical activity and the network's dynamical properties from the obtained spike trains, the following metrics have been computed for both cortical and hippocampal neuronal networks: MFR, percentage of random spikes, MBR, and MBD. The above-mentioned parameters were calculated as means of the average values obtained from all the active electrodes that exhibited a minimum value of spiking and bursting rate of, respectively, 0.1 spikes/s and 0.4 bursts/min. The MFR is calculated through the sum between intra- and extra-burst spiking activities.

Cortical networks showed a MFR of  $0.5 \pm 0.1$  spikes/s (mean  $\pm$  standard error of the mean) and a MBR of about  $3.1 \pm 0.9$  bursts/min. The hippocampal neurons exhibited a MFR and MBR of  $2.2 \pm 0.6$  spikes/s and  $16 \pm 4$  bursts/min, respectively. Regarding the burst duration, we found a MBD of  $212 \pm 23$  ms for cortical neurons and  $101 \pm 16$  ms for hippocampal neurons. We also evaluated the percentage of random spikes (i.e., the fraction of spikes outside bursts) for both culture types. In particular, cortical networks presented about  $65.4 \pm 2.1\%$  of random spiking. The hippocampal neurons showed a level of random spiking of  $15.1 \pm 4.0\%$ .

The calculated values are in line with those reported in literature for mature healthy rat cortical and hippocampal networks recorded *in vitro* (Cotterill et al., 2016; Napoli and Obeid, 2016). Therefore, as already suggested by our fluorescence



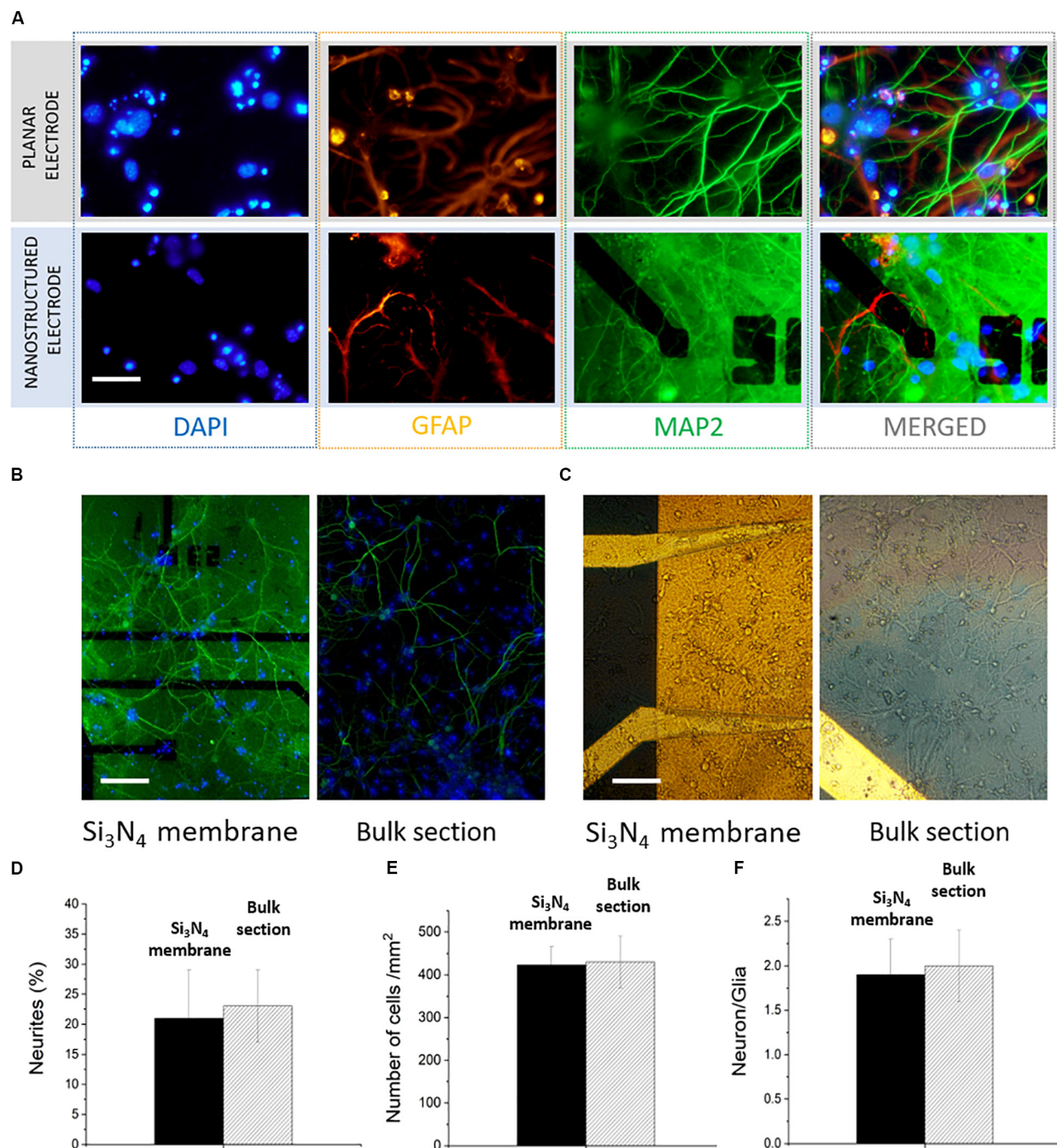
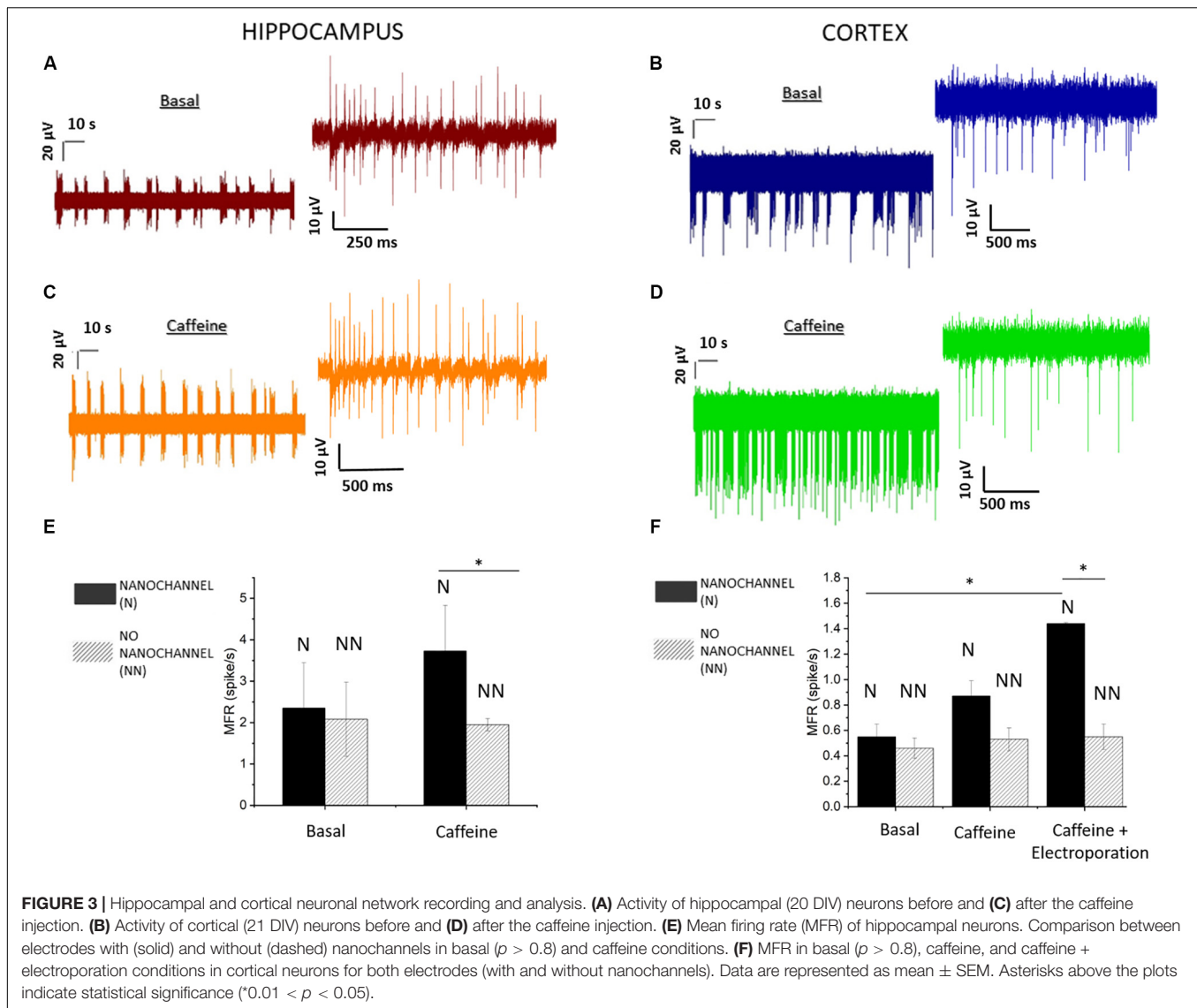


**FIGURE 2 |** Confocal images of hippocampal neurons of microfluidic MEA. **(A)** Comparison between a planar electrode on bulk surface and a nanostructured one on thin silicon nitride membrane. Scale bar: 30  $\mu\text{m}$ . **(B)** 20x image of the electrodes with microfluidic channel underneath (left) and the bulk surface (right). Scale bar: 100  $\mu\text{m}$ . **(C)** 20x bright field images of the network on both surfaces. Scale bar 100  $\mu\text{m}$ . **(D)** Percentage of neurites covering the device surface on the of bulk section and on the membrane. **(E)** Number of cells/mm<sup>2</sup>. **(F)** Comparison between the calculated neuron/glia ratios on the two sections of the device.

analysis, the presence of microfluidic channels and pass-through 3D hollow nanotubes on the electrodes did not alter the correct maturation of hippocampal or cortical neurons. This implies the suitability of the MF-MEA device for culturing neuronal cells up to their maturation state and subsequent proper characterization of the network activity.

## Spatially Resolved Delivery of Caffeine

Next, we evaluated the capability of the MF-MEAs for inducing a selective chemical change in the electrophysiological behavior of sub-populations of neuronal cultures. The experiments consisted of delivering a stimulant molecule, caffeine, through the 3D hollow nanotubes fabricated on the microfluidic channels.



Caffeine has multiple effects on the central nervous system, resulting in an increasing of neuronal activity. The main effects are mobilization of intracellular calcium, inhibition of phosphodiesterases, and antagonizing the adenosine receptors (Donato et al., 2003; Jackson and Thayer, 2006).

The hollow nanostructures enable a precise delivery in the few cells located on the nanostructured electrode area without affecting the remaining neuronal culture. Considering the typical cell dimension of  $100\text{--}200\text{ }\mu\text{m}^2$  and the distance between the 3D nanostructures ( $4\text{ }\mu\text{m}$ ), a single cell could typically interact with nine hollow nanostructures. Additionally, the branches from neighboring cells situated on this region could also be affected by the same delivery. Hence, a sub-population of neurons in immediate proximity of the electrodes are affected by the stimulation induced by the injected treatment. We have simulated the spatial and temporal dynamics of diffusion through the 3D hollow nanostructures. The results are reported in **Supplementary Section S2**. In particular, the simulations provide

an estimate of approximately  $40\text{ }\mu\text{m}$  as the maximum distance from the 3D nanostructure at which caffeine concentration is high enough to produce an effect. Therefore, we can consider the spatial resolution of the delivery to be within the area of the electrode itself. For comprehensiveness, in **Supplementary Section S2**, we also report further simulations of the molecule diffusion through the nanochannels in case of several starting concentrations (**Supplementary Figure S2.4**).

To assess the reproducibility of this selective delivery, the experiment was repeated on five different cultures. Caffeine, at a concentration of  $16\text{ mM}$  in PBS, was first pre-heated at  $37^\circ\text{C}$  and thereafter inserted into the microfluidic channels below the MF-MEA. After filling the two separated compartments underneath the device, the caffeine molecules are able to diffuse across the nanotubes to the upper chamber where the cells are cultured. The caffeine was let to diffuse for  $5\text{ min}$  in order to ensure a theoretical concentration of  $2\text{ mM}$  delivered to the cells, in correspondence of the electrodes (**Supplementary Section S2**).

The effect was investigated by observing the firing/bursting rates of the affected cells before and after the administration of caffeine, and comparing them to the values related to the electrodes without hollow structures, where caffeine delivery did not occur. In **Figures 3C,D**, we report typical recordings after the caffeine injection on hippocampal and cortical neurons at 20 and 21 DIV, respectively. To evaluate the effects, we calculated and compared the MFRs before and after caffeine delivery, separating regions on the microfluidic nanochannels (affected by delivery) from the regions on the planar surface (no delivery). **Figures 3E,F** show the difference from the basal case in terms of firing rate between the electrodes with and without hollow nanostructures. Furthermore, for cortical neurons, bursting analysis was performed on the electrodes presenting bursting activity. We report the MBRs and MBDs before and after caffeine delivery in the treated regions in **Supplementary Figure S3**.

Both cultures show increased activity after caffeine delivery only in the parts of the culture laying on the microfluidic channels (**Figures 3E,F**). In particular, the MFR increases on the electrodes with nanochannels by 60% in case of hippocampal neurons and by 45% in case of cortical neurons. Differently, no statistical difference is observed on the electrodes without nanochannels. Hence, the caffeine delivery did not produce measurable effects on the neurons situated on the planar/bulk section of the MF-MEA, where no delivery occurred. The absence of increased activity in the central part of the cultures could be explained by the observations made in Section “Electrophysiological Recordings of Spontaneous Neuron Activity on MF-MEA,” related to the fact that the cultures presented a fragmented and clustered connectivity. In other cultures in which the neurons would be well connected over the complete networks, we expect that the increased excitability would be observed also in regions outside the microfluidic channels by propagation through the synaptic connections. As the device enables molecules delivery only in the area of the microfluidic channels without a significant diffusion in the cellular medium, it might be useful for high-localized pharmacological delivery studies. Lastly, we further report the calculated percentage of random spikes after caffeine delivery. Cortical networks present  $43.9 \pm 16.0\%$  of random spiking, whereas the hippocampal neurons show a level of random spiking of  $10.6 \pm 3.1\%$ .

In addition, we also investigated the effects of caffeine on the cortical neuronal network activity in case of cellular electroporation, assessing the possibility of an enhanced delivery of caffeine aided by membrane permeabilization. The electroporation protocol was applied to the neurons following the details in the methods Section “Electrophysiological Recordings and Electroporation.” In these experiments, we observed a further increase of the firing rate by approximately 50% after electroporation in comparison to the case of caffeine delivery without electroporation, as shown in **Figure 3F**. Thus, the effects of caffeine were enhanced by cell membrane permeabilization, without compromising the collective behavior, nor damaging the cell culture. In addition, in the nanostructured electrodes, the MBR rises from  $4.8 \pm 1.1$  bursts/min (without electroporation) up to  $8.1 \pm 1.1$  bursts/min with electroporation, with a percentage of random spikes of  $36.3 \pm 8.3\%$ . The MBD

changed from  $281 \pm 25$  to  $324 \pm 26$  ms with the addition of electroporation (**Supplementary Figure S3**). A possible explanation for these results might be related to the binding of caffeine to intracellular caffeine-sensitive gated channels (Meldolesi and Pozzan, 1998; Verkhratsky and Petersen, 1998). Sample recordings after caffeine delivery are reported in **Supplementary Figure S4** with and without electroporation.

Similar experiments of membrane permeabilization by means of electroporation did not provide satisfactory results on hippocampal neurons, as no spontaneous activity could be recorded after electroporation. In this regard, further optimizations of the device design and of the electroporation protocol are needed to improve the success rate of membrane permeabilization on different cultures.

However, in perspective, the MF-MEA devices may also enable neuron membrane permeabilization by means of electroporation and simultaneous localized caffeine delivery to the network, without negatively affecting the neuronal cultures. This could be considered a first step toward internalization of non-permeant exogenous molecules or other specific materials into neurons using our platform. Given the possibility of simultaneous monitoring and localized injection, this approach might be useful in gene therapy, cellular reprogramming, or as an intracellular investigation probe.

## DISCUSSION

In this work, we demonstrated localized drug delivery in and simultaneous electrical recording of primary cortical and hippocampal neurons using the MF-MEA platforms. Confocal fluorescence microscopy and electrophysiology experiments ensured the ability of the device to sustain cultures of primary neurons up to their full maturation without effecting their expected activity. The images confirmed a homogeneous network development overall the surface of the platform, without distinction between the thin nitride membranes decorated with 3D nanostructures and the planar surface. Furthermore, the maturity of the network was supported by the spontaneous bursting activity recorded from the electrodes of the MF-MEAs. The MF-MEAs also enabled the localized delivery of neuronal stimulants that chemically affected the electrical response of sub-populations in the network. The molecules inoculated from the nanochannels did not affect the parts of the cultures laying on the bulk MEA region, ensuring high spatial localization of compounds in the cell cultures. Therefore, the device allows for chemically treating only a selected sub-population of neurons, while simultaneously analyzing the whole network response.

Additionally, we showed the possibility of applying a non-invasive electroporation protocol to the cultured neurons with parallel pharmacological delivery, further paving the way toward effective studies on intracellular neuronal drug delivery on chip. In fact, the delivery of nucleic acids and other molecules to examine or manipulate cellular processes or gene expression on chip could improve preclinical research. Minimal effect on cell growth and differentiation is essential for advancing biological research, especially for neuronal cells. Subsequently,



studying cells in their natural state, with spatial–temporal control, is extremely useful for examining and manipulating cellular processes and improve therapeutic drug potential.

At last, in this study, we focused on the devices' ability for passive diffusion of molecules inside the nanochannels to achieve localized delivery to neurons. However, the MF-MEA configuration could also support the active delivery of charged molecules, using, for example, electrophoresis. In this regard, an external electric driving force for highly controlled spatial delivery of single molecules through 3D hollow nanoelectrodes was recently used with a thin membrane configuration resembling the MF-MEA (Huang et al., 2019). In this case, an external electric driving force applied between the upper and bottom microfluidic compartments promotes the diffusion of the molecule. This force is achieved by bringing an extra electrode in contact with the fluid in the bottom chamber. By applying a similar methodology to MF-MEAs, one might also enable active translocation of nanoparticles into single selected neurons using an applied electric field.

## CONCLUSION

We believe that the proposed platform could improve the studies of neuronal mechanisms under physiological and pathophysiological conditions. Specifically, in the first place, the delivered molecules are spatially separated from the cell culture, allowing simple insertion using a pumping system or syringes. Second, the method provides selective and high spatial resolution delivery of these compounds in the neuronal network under study. Third, the platform demonstrated promising preliminary results of soft neuronal electroporation, opening the way to studies on localized transfection of neuronal cells directly on-chip. Moreover, as future perspective, the device design presents flexibility for integration of additional features such as, for example, drug delivery enhanced by electrophoresis.

## REFERENCES

- Arnold, B., Cassady, S. J., VanLaar, V. S., and Berman, S. B. (2011). Integrating multiple aspects of mitochondrial dynamics in neurons: age-related differences and dynamic changes in a chronic rotenone model. *Neurobiol. Dis.* 41, 189–200. doi: 10.1016/j.nbd.2010.09.006
- Barnham, K. J., Masters, C. L., and Bush, A. I. (2004). Neurodegenerative diseases and oxidative stress. *Nat. Rev. Drug Discov.* 3, 205–214. doi: 10.1038/nrd1330
- Blasiak, A., Kilinc, D., and Lee, G. U. (2017). Neuronal cell bodies remotely regulate axonal growth response to localized netrin-1 treatment via second messenger and DCC dynamics. *Front. Cell. Neurosci.* 10:298. doi: 10.3389/fncel.2016.00298
- Bologna, L. L., Pasquale, V., Garofalo, M., Gandolfo, M., Baljon, P. L., Maccione, A., et al. (2010). Investigating neuronal activity by SPYCODE multi-channel data analyzer. *Neural Networks* 23, 685–697. doi: 10.1016/j.neunet.2010.05.002
- Caprettini, V., Cerea, A., Melle, G., Lovato, L., Capozza, R., Huang, J. A., et al. (2017). Soft electroporation for delivering molecules into tightly adherent mammalian cells through 3D hollow nanoelectrodes. *Sci. Rep.* 7:8524. doi: 10.1038/s41598-017-08886-y
- Cerea, A., Caprettini, V., Bruno, G., Lovato, L., Melle, G., Tantussi, F., et al. (2018). Selective intracellular delivery and intracellular recordings combined in MEA biosensors. *Lab Chip* 18, 3492–3500. doi: 10.1039/c8lc00435h
- Chung, B. G., Flanagan, L. A., Rhee, W., Schwartz, P. H., Lee, A. P., Monuki, E. S., et al. (2005). Human neural stem cell growth and differentiation in a gradient-generating microfluidic device. *Lab Chip* 5, 401–406. doi: 10.1039/b417651k
- Coluccio, M. L., Perozziello, G., Malara, N., Parrotta, E., Zhang, P., Gentile, F., et al. (2019). Microfluidic platforms for cell cultures and investigations. *Microelectron. Eng.* 208, 14–28. doi: 10.1016/j.mee.2019.01.004
- Cotterill, E., Hall, D., Wallace, K., Mundy, W. R., Eglén, S. J., and Shafer, T. J. (2016). Characterization of early cortical neural network development in multiwell microelectrode array plates. *J. Biomol. Screen* 21, 510–509. doi: 10.1177/1087057116640520
- De Angelis, F., Malerba, M., Patrini, M., Miele, E., Das, G., Toma, A., et al. (2013). 3D hollow nanostructures as building blocks for multifunctional plasmonics. *NANO Lett.* 13, 3553–3558. doi: 10.1021/nl401100x
- Dipalo, M., Amin, H., Lovato, L., Moia, F., Caprettini, V., Messina, G. C., et al. (2017). Intracellular and extracellular recording of spontaneous action potentials in mammalian neurons and cardiac cells with 3D plasmonic nanoelectrodes. *NANO Lett.* 17, 3932–3939. doi: 10.1021/acs.nanolett.7b01523
- Dipalo, M., Messina, G. C., Amin, H., La Rocca, R., Shalabaeva, V., Simi, A., et al. (2015). 3D plasmonic nanoantennas integrated with MEA biosensors. *Nanoscale* 7, 3703–3711. doi: 10.1039/c4nr05578k

The above-mentioned key features make MF-MEA a promising device for studying dynamic cellular activities or alterations at multiple levels, enabling the observation of signal pathways during the selective inoculation of specific treatments. In fact, this will enable an easier and punctual manipulation of cell environment together with electrophysiological observations. For these reasons, the MF-MEA approach could be useful in basic neuroscience investigations, neurodegenerative diseases research, cancer therapeutics, or studies with neurons derived from human induced pluripotent stem cells (HiPSCs). Therefore, we believe that the MF-MEA will be useful for an improved understanding of the cellular mechanisms behind drug delivery, cell differentiation, disease progression, and treatment evolution at both network and single cell level.

## DATA AVAILABILITY STATEMENT

The datasets generated for this study are available on request to the corresponding authors.

## AUTHOR CONTRIBUTIONS

MD and FD conceived and planned the experiments. GB and AC carried out the samples preparation and experiments. NC and LD carried out the data analysis. GM performed the cell cultures and immunofluorescence protocols. AH performed the finite element simulations. All authors wrote the manuscript.

## SUPPLEMENTARY MATERIAL

The Supplementary Material for this article can be found online at: <https://www.frontiersin.org/articles/10.3389/fbioe.2020.00626/full#supplementary-material>

- Donato, R., Canepari, M., Lape, R., and Nistri, A. (2003). Effects of caffeine on the excitability and intracellular Ca<sup>2+</sup> transients of neonatal rat hypoglossal motoneurons *in vitro*. *Neurosci. Lett.* 346, 177–181. doi: 10.1016/S0304-3940(03)00568-8
- Gärtner, A., Collin, L., and Lalli, G. (2006). Nucleofection of primary neurons. *Methods Enzymol.* 406, 374–388. doi: 10.1016/S0076-6879(06)06027-7
- Ghosh, A., and Greenberg, M. E. (1995). Calcium signaling in neurons: molecular mechanisms and cellular consequences. *Science* 268, 239–247. doi: 10.1126/science.7716515
- Gladkov, A., Pigareva, Y., Kutyina, D., Kolpakov, V., Bukatin, A., Mukhina, I., et al. (2017). Design of cultured neuron networks in vitro with predefined connectivity using asymmetric microfluidic channels. *Sci. Rep.* 7:15625. doi: 10.1038/s41598-017-15506-2
- Gresa-Arribas, N., Viéitez, C., Dentesano, G., Serratos, J., Saura, J., and Solá, C. (2012). Modelling neuroinflammation in vitro: a tool to test the potential neuroprotective effect of anti-inflammatory agents. *PLoS One* 7:e0045227. doi: 10.1371/journal.pone.0045227
- Gross, P. G., Kartalov, E. P., Scherer, A., and Weiner, L. P. (2007). Applications of microfluidics for neuronal studies. 252, 135–143. doi: 10.1016/j.jns.2006.11.009
- Hammerle, H. (1998). A novel organotypic long-term culture of the rat hippocampus on substrate-integrated multielectrode arrays. *Brain Res. Brain Res. Protoc.* 2, 229–242. doi: 10.1016/S1385-299X(98)00013-0
- Huang, J. A., Capretini, V., Zhao, Y., Melle, G., MacCafferri, N., Deleye, L., et al. (2019). On-demand intracellular delivery of single particles in single cells by 3D hollow nanoelectrodes. *NANO Lett.* 19, 722–731. doi: 10.1021/acs.nanolett.8b03764
- Ichikawa, M., Muramoto, K., Kobayashi, K., Kawahara, M., and Kuroda, Y. (1993). Formation and maturation of synapses in primary cultures of rat cerebral cortical cells: an electron microscopic study. *Neurosci. Res.* 16, 95–103. doi: 10.1016/0168-0102(93)90076-3
- Jackson, J. G., and Thayer, S. A. (2006). Mitochondrial modulation of Ca<sup>2+</sup>-induced Ca<sup>2+</sup>-release in rat sensory neurons. *J. Neurophysiol.* 96, 1093–1104. doi: 10.1152/jn.00283.2006
- Kamande, J., Nagendran, T., Harris, J., and Taylor, A. M. (2019). Multi-compartment microfluidic device geometry and covalently bound poly-D-lysine influence neuronal maturation. *Front. Bioeng. Biotechnol.* 7:84. doi: 10.3389/fbioe.2019.00084
- Kunze, A., Meissner, R., Brando, S., and Renaud, P. (2011). Co-pathological connected primary neurons in a microfluidic device for Alzheimer studies. *Biotechnol. Bioeng.* 108, 2241–2245. doi: 10.1002/bit.23128
- Lin, B., and Levchenko, A. (2015). Spatial manipulation with microfluidics. *Front. Bioeng. Biotechnol.* 3:39. doi: 10.3389/fbioe.2015.00039
- Maccione, A., Gandolfo, M., Massobrio, P., Novellino, A., Martinoia, S., and Chiappalone, M. (2009). A novel algorithm for precise identification of spikes in extracellularly recorded neuronal signals. *J. Neurosci. Methods* 177, 241–249. doi: 10.1016/j.jneumeth.2008.09.026
- Meldolesi, J., and Pozzan, T. (1998). The endoplasmic reticulum Ca<sup>2+</sup> store: a view from the lumen. *Trends Biochem. Sci.* 23, 10–14. doi: 10.1016/S0968-0004(97)01143-2
- Napoli, A., and Obeid, I. (2016). Comparative analysis of human and rodent brain primary neuronal culture spontaneous activity using micro-electrode array technology. *J. Cell. Biochem.* 117, 559–565. doi: 10.1002/jcb.25312
- Park, J. W., Vahidi, B., Taylor, A. M., Rhee, S. W., and Jeon, N. L. (2006). Microfluidic culture platform for neuroscience research. *Nat. Protoc.* 1, 2128–2136. doi: 10.1038/nprot.2006.316
- Pasquale, V., Martinoia, S., and Chiappalone, M. (2010). A self-adapting approach for the detection of bursts and network bursts in neuronal cultures. *J. Comput. Neurosci.* 29, 213–229. doi: 10.1007/s10827-009-0175-1
- Pinto, M., and Howell, R. W. (2007). Concomitant quantification of targeted drug delivery and biological response in individual cells. *Biotechniques* 41, 64–71. doi: 10.1214/000112492
- Roppongi, R. T., Champagne-Jorgensen, K. P., and Siddiqui, T. J. (2017). Low-density primary hippocampal neuron culture. *J. Vis. Exp.* 2017:55000. doi: 10.3791/55000
- Saadi, W., Francis, S. W., and Jeon, N. L. (2006). A parallel-gradient microfluidic chamber for quantitative analysis of breast cancer cell chemotaxis. *Biomed. Microdevices* 8, 109–118. doi: 10.1007/s10544-006-7706-6
- Spira, M. E., and Hai, A. (2013). Multi-electrode array technologies for neuroscience and cardiology. *Nat. Nanotechnol.* 8, 83–94. doi: 10.1038/nnano.2012.265
- Stewart, M. P., Sharei, A., Ding, X., Sahay, G., Langer, R., and Jensen, K. F. (2016). In vitro and ex vivo strategies for intracellular delivery. *Nature* 538, 183–192. doi: 10.1038/nature19764
- Takayama, Y., and Kida, Y. S. (2016). In vitro reconstruction of neuronal networks derived from human iPS cells using microfabricated devices. *PLoS One* 11:e0148559. doi: 10.1371/journal.pone.0148559
- Tsur, E. E., Zimmerman, M., Maor, I., Elrich, A., and Nahmias, Y. (2017). Microfluidic concentric gradient generator design for high-Throughput cell-Based studies. *Front. Bioeng. Biotechnol.* 5:21. doi: 10.3389/fbioe.2017.00021
- Verkhratsky, A. J., and Petersen, O. H. (1998). Neuronal calcium stores. *Cell Calcium* 24, 333–343. doi: 10.1016/S0143-4160(98)90057-4
- Xie, C., Lin, Z., Hanson, L., Cui, Y., and Cui, B. (2012). Intracellular recording of action potentials by nanopillar electroporation. *Nat. Nanotechnol.* 7, 185–190. doi: 10.1038/nnano.2012.8
- Xie, X., Xu, A. M., Leal-Ortiz, S., Cao, Y., Garner, C. C., and Melosh, N. A. (2013). Nanostraw-electroporation system for highly efficient intracellular delivery and transfection. *ACS Nano* 7, 4351–4358. doi: 10.1021/nn400874a

**Conflict of Interest:** The authors declare that the research was conducted in the absence of any commercial or financial relationships that could be construed as a potential conflict of interest.

Copyright © 2020 Bruno, Colistra, Melle, Cerea, Hubarevich, Deleye, De Angelis and Dipalo. This is an open-access article distributed under the terms of the Creative Commons Attribution License (CC BY). The use, distribution or reproduction in other forums is permitted, provided the original author(s) and the copyright owner(s) are credited and that the original publication in this journal is cited, in accordance with accepted academic practice. No use, distribution or reproduction is permitted which does not comply with these terms.





# Biocompatibility of a Conjugated Polymer Retinal Prosthesis in the Domestic Pig

José Fernando Maya-Vetencourt<sup>1,2,3†</sup>, Stefano Di Marco<sup>1,2,4†</sup>, Maurizio Mete<sup>5†</sup>, Mattia Di Paolo<sup>4</sup>, Domenico Ventrella<sup>6</sup>, Francesca Barone<sup>6</sup>, Alberto Elmi<sup>6</sup>, Giovanni Manfredi<sup>7</sup>, Andrea Desii<sup>7‡</sup>, Walter G. Sannita<sup>1</sup>, Silvia Bisti<sup>4,8</sup>, Guglielmo Lanzani<sup>7§</sup>, Grazia Pertile<sup>5§</sup>, Maria Laura Bacci<sup>6§</sup> and Fabio Benfenati<sup>1,2\*§</sup>

## OPEN ACCESS

### Edited by:

Elisa Castagnola,  
University of Pittsburgh, United States

### Reviewed by:

Maureen Ann McCall,  
University of Louisville, United States

Magdalene J. Seiler,

University of California, Irvine,

United States

Tobias Peters,

University of Tübingen, Germany

### \*Correspondence:

Fabio Benfenati  
fabio.benfenati@iit.it

<sup>†</sup> These authors have contributed  
equally to this work

### \*Present address:

Andrea Desii,  
Smart Bio-Interfaces, Istituto Italiano  
di Tecnologia, Pontedera, Italy

<sup>§</sup> These authors share senior  
authorship

### Specialty section:

This article was submitted to  
Biomaterials,  
a section of the journal  
Frontiers in Bioengineering and  
Biotechnology

Received: 01 July 2020

Accepted: 18 September 2020

Published: 15 October 2020

### Citation:

Maya-Vetencourt JF, Di Marco S,  
Mete M, Di Paolo M, Ventrella D,  
Barone F, Elmi A, Manfredi G, Desii A,  
Sannita WG, Bisti S, Lanzani G,  
Pertile G, Bacci ML and Benfenati F  
(2020) Biocompatibility of a  
Conjugated Polymer Retinal  
Prosthesis in the Domestic Pig.  
Front. Bioeng. Biotechnol. 8:579141.  
doi: 10.3389/fbioe.2020.579141

<sup>1</sup> Center for Synaptic Neuroscience and Technology, Istituto Italiano di Tecnologia, Genova, Italy, <sup>2</sup> Istituto di Ricovero e Cura a Carattere Scientifico, San Martino Hospital, Genova, Italy, <sup>3</sup> Department of Biology, University of Pisa, Pisa, Italy, <sup>4</sup> Department of Biotechnology and Applied Clinical Science, University of L'Aquila, L'Aquila, Italy, <sup>5</sup> Department of Ophthalmology, Sacro Cuore Don Calabria Hospital, Negrar, Italy, <sup>6</sup> Department of Veterinary Medical Sciences, University of Bologna, Bologna, Italy, <sup>7</sup> Center for Nano Science and Technology, Istituto Italiano di Tecnologia, Milan, Italy, <sup>8</sup> Consorzio Interuniversitario INBB, Rome, Italy

The progressive degeneration of retinal photoreceptors is one of the most significant causes of blindness in humans. Conjugated polymers represent an attractive solution to the field of retinal prostheses, and a multi-layer fully organic prosthesis implanted subretinally in dystrophic Royal College of Surgeons (RCS) rats was able to rescue visual functions. As a step toward human translation, we report here the fabrication and *in vivo* testing of a similar device engineered to adapt to the human-like size of the eye of the domestic pig, an excellent animal paradigm to test therapeutic strategies for photoreceptors degeneration. The active conjugated polymers were layered onto two distinct passive substrates, namely electro-spun silk fibroin (ESF) and polyethylene terephthalate (PET). Naive pigs were implanted subretinally with the active device in one eye, while the contralateral eye was sham implanted with substrate only. Retinal morphology and functionality were assessed before and after surgery by means of *in vivo* optical coherence tomography and full-field electroretinogram (ff-ERG) analysis. After the sacrifice, the retina morphology and inflammatory markers were analyzed by immunohistochemistry of the excised retinas. Surprisingly, ESF-based prostheses caused a proliferative vitreoretinopathy with disappearance of the ff-ERG b-wave in the implanted eyes. In contrast, PET-based active devices did not evoke significant inflammatory responses. As expected, the subretinal implantation of both PET only and the PET-based prosthesis locally decreased the thickness of the outer nuclear layer due to local photoreceptor loss. However, while the implantation of the PET only substrate decreased the ff-ERG b-wave amplitude with respect to the pre-implant ERG, the eyes implanted with the active device fully preserved the ERG responses, indicating an active compensation of the surgery-induced photoreceptor loss. Our findings highlight the possibility of developing a new generation of conjugated polymer/PET-based prosthetic devices that are highly biocompatible and potentially suitable for subretinal implantation in patients suffering from degenerative blindness.

**Keywords:** retinal degeneration, retinitis pigmentosa, biomedical pig, retinal prosthesis, conjugated polymers

## INTRODUCTION

The development of therapeutic approaches for retinal degenerative diseases is a hot spot in vision science research (Scholl et al., 2016). In fact, the progressive degeneration of retinal photoreceptors (Wright et al., 2010; Dias et al., 2018) is a public health issue with a concerning incidence worldwide (Hartong et al., 2006; Wong et al., 2014). Although one gene therapy for RPE65-linked retinal dystrophies is available (Russell et al., 2017), clinical interventions to treat other widespread retinal dystrophies based on optogenetics (Simunovic et al., 2019) and stem cells (Maeda et al., 2019) are still in preclinical experimentation and/or in early phases of testing in humans.

The wide variety of genetic defects causing retinal degeneration poses some challenges for the development of therapeutic approaches. Therefore, alternative treatments for these pathologies have been reported (Frasson et al., 1999; Busskamp et al., 2010; Leveillard and Sahel, 2010; Pearson et al., 2012; Barber et al., 2013). Among them are strategies that aim at rescuing vision by using electronic devices able to stimulate spared retinal networks (Walter et al., 2005; DeMarco et al., 2007; Gerding et al., 2007; Yanai et al., 2007; Zrenner et al., 2011; Mathieson et al., 2012; Mandel et al., 2013; Ayton et al., 2014; Lorach et al., 2015). However, strategies that use microelectrode-based stimulation (Humayun et al., 2012; Dagnelie et al., 2017) or photodiodes-driven chips (Stingl et al., 2013; Lorach et al., 2015) need power supply and external camera. Moreover, mechanical mismatch with retinal tissues, poor biocompatibility, high resistance and heat production represent further drawbacks. The optimization of the current retinal prostheses is therefore necessary to restore high-quality visual capabilities in dystrophic patients.

Conjugated polymers have been recently introduced as interfaces for neuronal stimulation (Ghezzi et al., 2011, 2013; Gautam et al., 2014; Martino et al., 2015; Feyen et al., 2016). A few years ago, we reported the ability of a planar, photovoltaic, biocompatible, and fully organic retinal prosthesis to persistently restore visual functions in a rat model of progressive neuronal degeneration, the Royal College of Surgeons (RCS) rat (Antognazza et al., 2016; Maya-Vetencourt et al., 2017). Not only sensitivity to light significantly increased, but also spatial resolution and metabolic activity of the visual cortex were positively affected. More recently, we developed a second-generation nanoscale prosthesis that similarly reinstates visual functions in dystrophic RCS animals (Benfenati and Lanzani, 2018; Maya-Vetencourt et al., 2020). In the present work, we directed our efforts toward the transfer of the initial results obtained in rodents to the swine model, as a preliminary step before phase-1 experimentation in humans.

As compared to rodents, we first enlarged the active surface of the prosthesis in consideration of the elevated retinal surface in pigs. Then, we analyzed various types of substrates for the photoactive polymers, which satisfied the needs of the surgical implant procedures. We first considered electro-spun silk fibroin (ESF) to have prostheses with a broader area, a high conformability and a more uniform surface, with respect to the ones previously used in RCS rats fabricated with crystallized silk

fibroin (Maya-Vetencourt et al., 2017). Unexpectedly, the ESF caused a strong phlogistic reaction of the pig retina resulting in proliferative vitreoretinopathy (PVR). We therefore decided to use polyethylene terephthalate (PET) as substrate. Before the experimental tests in naive pigs, we confirmed that PET is an excellent biocompatible substrate in dystrophic rodents. The experimental results in pigs show the optimization both in shape and chemical composition of this novel retinal prosthesis and the set-up of a surgical implantation procedure ready to be translated to humans. Our findings demonstrate the biocompatibility and functionality of the device 10–30 days after implant in naive pigs.

## MATERIALS AND METHODS

### Engineering of the Active Layers

The planar implants were created using the spin coating technique. The first conductive layer was obtained spin coating a PEDOT:PSS water dispersion (Clevios PH-1000) containing specific additives over the substrate. Briefly, the additives used were dimethylsulfoxide (DMSO, 9% v/v) to increase the overall electrical conductivity, the surfactant Zonyl FS-300 (0.18% v/v) to promote dispersion wettability and facilitate the spin-coating process, the crosslinker 3-glycidoxypolytrimethoxysilane (GOPS, 0.9% v/v) to enhance the adhesion of the PEDOT:PSS layer to the substrate and avoid delamination. The solution was deposited twice at the speed of 1600 rpm and treated for 300 s at 120°C. The top layer of the implants was created using poly(3-hexylthiophene) (P3HT), a polymer widely recognized in the literature and used for the manufacture of planar prosthetic devices of photovoltaic nature (Ghezzi et al., 2013; Gautam et al., 2014; Antognazza et al., 2016; Feyen et al., 2016; Maya-Vetencourt et al., 2017). The polymer was dissolved in chlorobenzene (30 mg/ml) and subsequently deposited at the speed of 1600 rpm. This way, the resulting films have a thickness of 200 nm and good homogeneity. The overall thickness of PEDOT:PSS and P3HT layers obtained with this process is 550 nm.

### Engineering of the Prosthesis Substrate

We used two alternative substrates to support the polymeric layer, ESF and PET with distinct characteristics of flexibility, bending behavior. ESF, made from the same substrate used to fabricate the devices implanted in the rat (crystallized silk fibroin), provides an exceptionally uniform and flexible surface devoid of deformation memory.

Electro-spun silk fibroin substrates were produced as previously described (Alessandrino et al., 2008). Briefly, silk fibroin was autoclaved at 120°C, dissolved in LiBr (9.3 M) for 3 h at 60°C, and dialyzed against distilled water. The water solution has been drop-casted on petri dishes and the resulting films have been again dissolved in formic acid. The formic acid silk fibroin solution has been loaded in the electrospinning apparatus comprising two high voltage generators (F.u.G. Elektronik GmbH – HCN 35-12500), a syringe pump (Graseby Medical – MS 2000), and a stainless steel 0.5 mm wide spinneret. Positive potential was applied to spinneret and negative potential to

the collector plate. After the deposition, the electro-spun films were detached from the collector plate treating with water at 37°C for 5–10 min and isopropanol for 10 min, dried, and then treated with methanol to induce silk fibroin crystallization. The resulting fibroin fabric was characterized by an excellent layering of polymers and an easy curling for introduction in the posterior chamber of the pig eye, with the possibility to significantly increase of coverage area of the retina with respect to more rigid substrates.

Polyethylene terephthalate substrates, whose biocompatibility has already been widely verified in the biomedical field, were obtained from 23  $\mu\text{m}$  thick films (Hostaphan®, Mitubishi Polyester Film). Before use, the material was carefully cleaned through three sonication baths using milli-Q water, acetone and isopropanol. Substrate films were subjected to plasma treatment in air at 40 W to improve the adhesion of the polymeric layers.

We used laser cutting to give the devices their final shape. The light source was an amplified mode-locked Yb:KGW laser with emission at 1030 nm. The laser was frequency-doubled using a HIRO harmonic generator and operated at 500 KHz with a pulse width of 240 fs. The light beam was focused using a 20x objective and the incident power was 100 mW. Samples were mounted between two glass slides and placed on a three-axis micro-controlled stage; the stage was moved at 0.4 mm/s. The cut was repeated 10 times at different z-positions to facilitate the detachment of the sample from the glass slides. The final cut width was below 10  $\mu\text{m}$ .

## Experimental Animals and Ethical Considerations

The use of domestic pigs in this study (total  $n = 8$  of either sex; approx. 3 months of age) was regulated by two protocols approved by the Italian Ministry of Health (D.Lgs 116/92 and D.Lgs 26/2014) in accordance with the Association for Research in Visual Ophthalmology Statement for the Use of Animals in Ophthalmic and Vision Research. Commercial hybrid pigs [(Large White  $\times$  Landrace)  $\times$  Duroc] were enrolled in the study and housed in multiple boxes according to their origin dominance group to reduce stress and aggressiveness. Animals, kept at  $20 \pm 4^\circ\text{C}$  with a 12/12 h light/dark cycle were fed with standard swine diet (CESAC s.c.a. Conselice RA, Italy) twice a day and received water *ad libitum* (Barone et al., 2020). Chains and pieces of wood were used as environmental enrichment; no bedding materials were dispensed to guarantee good health conditions; every 2 days the animals received a small amount of straw as rooting material (Barone et al., 2018). Royal College of Surgeons inbred, pink-eyed dystrophic (RCS) rats (total  $n = 51$ ; either sex; approx. 3 months of age) and congenic non-dystrophic controls (RCS-rdy) were provided by M. M. La Vail (Beckman Vision Center, University of California, San Francisco, California) (LaVail and Battelle, 1975). All manipulations and procedures were performed in accordance with the guidelines established by the European Community Council (Directive 2012/63/EU of 22 September 2010) and were approved by the Italian Ministry of Health (Authorization no. 645/2015-PR). RCS rat colonies were bred

under standard conditions with food and water *ad libitum* under a 12:12 h light/dark cycle, as previously described (Maya-Vetencourt et al., 2017).

## Surgical Procedures in the Pig

Domestic pigs were weighted and sedated with an intramuscular (IM) injection of Tiletamine-Zolazepam (Zoetel, Virbac, Prague, Czechia) (5 mg/kg). After 15 min, general anesthesia was induced with 8% sevoflurane (SevoFlo, Esteve, Barcelona, Spain), administered through a mask in a 1:1 oxygen/air mixture and maintained with the same halogenated agent (3%) after orotracheal intubation (Elmi et al., 2019). Lactated Ringer infusion was set at a rate of 10 ml/kg/h through the auricular vein (left ear). Heart frequency rate, non-invasive blood pressure (NIBP), peripheral capillary oxygen saturation  $\text{SpO}_2$  and  $\text{CO}_2$  were strictly monitored along anesthesia (Ventrella et al., 2017). Local analgesia was granted by the application of oxybuprocaine hydrochloride eye drops (Novesina 0.4%, Visufarma s.r.l. Rome, Italy).

After shaving and disinfecting the periocular area with Povidone-Iodine 10%, a sterile drape was positioned and the eye exposed with a speculum. Two 23-gauge and one 20-gauge trocars were inserted 1.5 mm from the limbus and a chandelier light was positioned to allow bimanual surgery. After the induction of a posterior vitreous detachment by active suction of the cutter, vitrectomy was performed, paying attention to avoid the lens. The posterior retina was separated from the retinal pigmented epithelium (RPE) by injecting a balanced salt solution (Balanced Salt Solution; Alcon Laboratories, TX, United States) into the subretinal space through a 41-gauge subretinal cannula connected with the automated pump of the machine. One injection was fine to detach the temporal side of the visual streak. A 1.5 mm mid-peripheral retinotomy was performed with scissors (DORC International). The implant was inserted in the vitreous cavity through an injector, specifically designed for this purpose, that fitted on the 20-gauge trocar. Subsequently, it was inserted into the subretinal space using two intraocular forceps. Perfluorocarbon liquid (PFCL) was injected into the vitreous cavity enough to cover the retinotomy, drain the subretinal fluid and reattach the retina. Laser endophotocoagulation was performed around the edge of the retinotomy. A fluid/air exchange was carried out. The trocars were removed and the sclerotomies sutured with Vicryl 8-0. An isovolemic mixture of Sulfur Hexafluoride ( $\text{SF}_6$ ) gas was used as final tamponade. After surgery, all animals received an intra-conjunctival administration of triamcinolone acetonide (40 mg per eye, Kenacort, Bristol-Myers Squibb, New York, United States) and fuocinolone acetonide/neomycin eye drops (Iridex, Ceva Vete, Agrate Brianza, Italy).

## Surgical Procedures in the RCS Rat

Three months-old RCS rats of either sex were anesthetized with an intraperitoneal injection of diazepam (10 mg/kg) followed by intramuscular administration of xylazine (5 mg/kg) and ketamine (33 mg/kg). The sub-retinal implant of the prosthesis was carried out in a sterile room using a Leica ophthalmic

surgical microscope, as previously described (Maya-Vetencourt et al., 2017). Briefly, a 1.5 mm peritomy was made 2 mm posterior to the limbus, followed by a limbus-parallel incision through the sclera and choroid of approximately 1 mm. The retina was then gently detached from the choroid using a custom-designed spatula. Viscoelastic material was injected into the subretinal space and the device was inserted with the polymeric coating facing the retina. The edges of the sclerotomy were electrocoagulated and the conjunctiva apposed. At the end of the surgical intervention, the position of the device was evaluated by indirect ophthalmoscopy and antibiotic and cortisone were applied to both eyes.

## Optical Coherence Tomography Analysis

Pigs were anesthetized as described above and their pupils dilated with 1% tropicamide eye drops (Visumidriatic, Visufarma s.p.a. Rome, Italy) before image acquisition. Spectral domain optical coherence tomography (SD-OCT) was performed using the iVue device (Optovue, Fremont, United States) using  $840 \pm 10$  nm light with power at the pupil of 750  $\mu$ W. The depth of resolution in tissue is 5  $\mu$ m, and the transverse resolution is 15  $\mu$ m. Each image covered a  $6 \times 6$  mm area centered on the fovea, acquired at 26,000 A-scan/second and composed of 256 to 1024 A-scan/frame.

## Electrophysiological Recordings

The electrophysiological analysis in pigs was performed before and after the implant procedure, with the animals under general anesthesia induced with the protocol described above. Pupils were dilated with 1% tropicamide eye drops (Visumidriatic, Visufarma s.p.a. Rome, Italy). Two drops of oxybuprocaine hydrochloride (Novesina, Visufarma s.r.l. Rome, Italy) were used as a local anesthetic, then a Barraquer blepharostat was used and eyes were maintained in a central and stable position by two stay sutures. Corneal contact lenses electrodes (ERGjet, Universo Plastique, Switzerland) were used as active electrodes while dermal needle electrodes were used as reference and ground, during ff-ERG. A drop of 3% carbomer (Dacriogel, Alcon, Fort Worth, TX, United States) was applied to the inner surface of the lens electrodes to protect the cornea and to ensure good electrical contact. The International Society for Clinical Electrophysiology of Vision (ISCEV) Standards for ff-ERGs were used with the settings adjusted for the swine species, as previously described (Barone et al., 2020). We performed ff-ERG recordings using the light-adapted ERG 3.0 protocol because the retinal implant was surgically positioned in high cone density visual streak of the swine retina (Hendrickson and Hicks, 2002). Briefly, ERG recordings were filtered with a 2–500 Hz band-pass FFT filter. For ff-ERGs, the amplitude ( $\mu$ V) from “a” to “b” waves was measured. The adaptation/background light luminance and time were: 30  $\text{cd}/\text{m}^2$  and 10 min. The ff-ERG stimuli were produced by a Ganzfeld dome and the patterned stimuli by a screen connected to a pattern generator. The stimulus luminance was of 3  $\text{cd}/\text{s}/\text{m}^2$  with an inter-stimulus time of 1.1 Hz. The data were amplified and acquired by the WinAverager Software. The Ganzfeld dome, the pattern screen and generator, the amplifier, and the Software used were part of the BM6000-MAXI

Electrophysiology Unit (Biomedica Mangoni, Pisa, Italy). Both eyes were separately investigated while covering the opposite one to prevent light exposure during the electrophysiological recordings. Each experimental session, including the animals' preparation, lasted about 2 h. At the end of the electrophysiology sessions, the animals were gently recovered from anesthesia. The electrodes, the sutures and the blepharostat were removed and Chloramphenicol 10 mg-Sodium colistimethate 180,000 U.I.-Tetracycline 5 mg ophthalmic ointment (Colbiocin; SiFi, Catania, Italy) was applied on the conjunctiva. The animals were then moved to a dark and quiet room and the orotracheal tube was removed when the swallowing reflex reappeared. Pigs completely recovered from anesthesia within a maximum of 2 h were then moved back to their origin pen. As to the RCS dystrophic rats, the electrophysiological recordings of visually evoked potentials (VEPs) were performed as reported in Maya-Vetencourt et al. (2017). In the case of light sensitivity, visual stimuli were flashes of light (20  $\text{cd}\cdot\text{m}^{-2}$ ; 100 ms) whereas in the case of spatial acuity, visual stimuli were horizontal sinusoidal gratings of increasing spatial frequencies (0.1–1) cycles per degree of visual angle ( $\text{c}\cdot\text{deg}^{-1}$ ) at 0.5 Hz. Light sensitivity corresponded to the amplitude of the VEP response to flashes of light. Spatial acuity was obtained by extrapolation to zero (0) amplitude of the linear regression through the last 4–5 data points of VEP amplitude against the log spatial frequency. Electrophysiological traces were reconstructed and analyzed using the OriginPro 9.1 software.

## Immunohistochemistry

At the end of the experimental protocol, pigs were euthanized and eyes were immediately explanted and fixed with 4% paraformaldehyde buffer; a small incision at the limbus level was made to improve fixative permeability. After cornea and lens removal, each eye was cut in four quadrants (superior, inferior, temporal and nasal), embedded in mounting medium (Tissue Tek OCT compound; Sakura Finetek, Torrance, CA, United States) and snap-frozen in liquid nitrogen. Cryosections were cut at 20  $\mu$ m (CM1850 Cryostat; Leica, Wetzlar, Germany) and collected on gelatin and poly-L-lysine coated slides. Retinal sections were incubated with 10% bovine serum albumin (BSA, Merk, Darmstadt, Germany) to block non-specific binding sites and immunolabeled overnight at 4°C with primary antibodies (mouse monoclonal anti-FGF2 antibody, 1:200, Merk, Darmstadt, Germany; rabbit polyclonal anti-GFAP, 1:5000, Dakocytomation, Campbellfield, Australia; rabbit anti-IBA-1, 1:1000, Wako, Richmond, United States; mouse anti-Rhodopsin 1:200, Thermofisher, Waltham, United States). Tissues were then incubated with appropriate secondary antibodies conjugated to a fluorescent dye (Alexa Fluor 488, Alexa Fluor 594; Molecular Probes, Invitrogen, Carlsbad, CA, United States) for 2 h at 37°C. Nucleus staining dye, 4',6-diamidino-2-phenylindole (DAPI, Merk, Darmstadt, Germany), was used before slides coverslips apposition. Images were acquired with confocal microscopy (Leica TCS SP5 II) and analyzed with Fiji software (Wayne Rasband, NIH, United States). Photoreceptors' survival was estimated by measuring the outer nuclear layer (ONL) thickness in DAPI-stained images.



Quantification of fluorescence was obtained by measuring the integrated fluorescence intensity acquired from equivalent ROIs for FGF2 and IBA-1 in the entire ONL and for GFAP throughout the retina. The number of IBA-1-positive cells was manually evaluated by counting the nuclei both in the ONL and in the entire retina. The morphology of IBA-1-positive microglial cells was evaluated via Scholl analysis of sampled cells from the entire retina by using the free software Fiji default plugin.

## Statistical Analysis

The statistical analysis was performed using the Prism 6.0 software (GraphPad Prism, San Diego, CA, United States). The experiments of ff-ERG responses (PRE and POST) in pigs implanted with the PET-based device were analyzed using the paired Student's *t*-test. The analysis of visual functions (light sensitivity and visual acuity, respectively) in dystrophic RCS rats implanted with the PET-based device (single variable experiments) was performed using the one-way ANOVA/Tukey's test. The histological morphology of the retina, the astrocytic and microglial responses as well as the FGF2 expression in the pig retina after implantation of the PET-based device were analyzed, in different retinal areas (two variable experiments), using the two-way ANOVA/Tukey's test. Differences with  $p < 0.05$  were considered significant. The results were expressed as means  $\pm$  SD of the indicated *n* values. Regarding non-implanted naïve pigs and animals implanted with the ESF-based prosthesis, the data include an  $n = 2$  in each experimental design. As to the electrophysiological, histological, and immunohistochemical analysis, the data of pigs implanted with the PET-based prosthesis correspond to 4 independent animals each implanted in the left eye with the active device and in the right eye with the sham material. The data of controls include 4 eyes obtained from 2 naïve pigs.

## RESULTS

### Prosthesis Engineering and Surgical Implant and Recording Procedures in the Pig

Conductive (PEDOT:PSS) and semiconductive (P3HT) polymers (**Figure 1A**) were successively layered on top of the substrate of choice as described in the methods and the complete device was subjected to laser-assisted cutting with rounded edges to the final dimensions shown in **Figure 1B**. The prostheses in the final configuration showed an absorption spectrum that covered the entire visible spectrum with a peak in the green region (**Figure 1C**). ESF membrane used as passive substrates display at the scanning electron microscopy analysis a mesh of intermingled thin fibroin fibers (**Figure 1D**).

The optimization of the surgical procedure for the implant of the retinal prosthesis then took place. Since the first interventions conducted in pigs using the same procedure previously followed in rats (*trans-scleral* implantation) presented problems in the post-operative phase, we decided

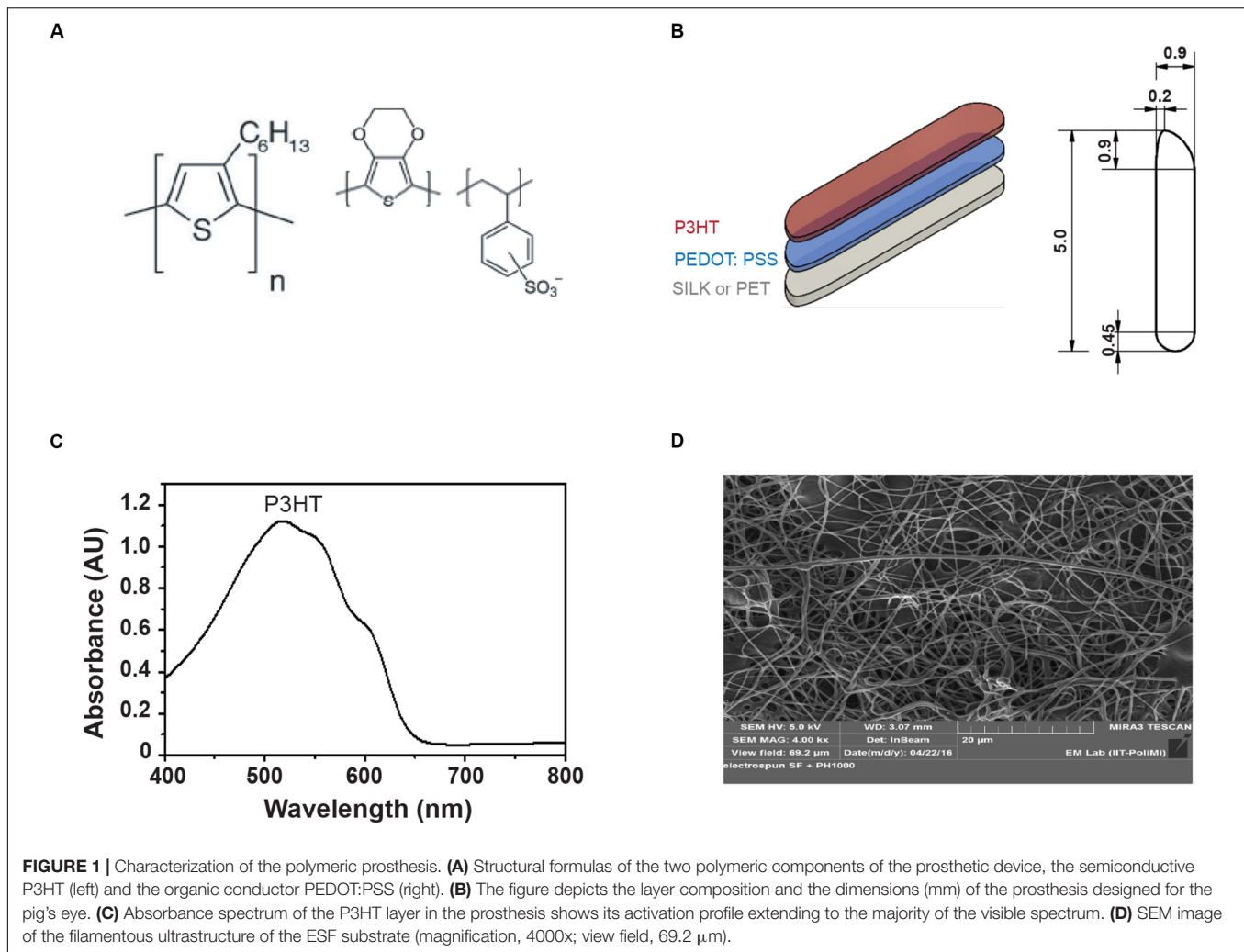
to access the retina through the posterior chamber. Thus, to introduce a sufficiently large device, the prosthesis substrate should be rolled up for insertion of the implant into the 20-gauge trocar, followed by unrolling inside the eye's posterior chamber.

To setup a standard evaluation of retina activation and physiological integrity, electroretinography was used in naïve pigs. Clear ff-ERG traces were obtained in adult anesthetized naïve animals. As expected, ff-ERG b-wave signals corresponding to the left and right eyes in the same animal were closely similar in both amplitude and latency (**Figures 2A,B**) and similar traces were obtained from independent experimental pigs (**Figure 2C**). This was confirmed by the SD-OCT images obtained immediately after the electrophysiological analysis, which showed full integrity of retinal layers (**Supplementary Figure S1A**).

### Implant of the Polymeric Device on ESF in the Pig

Since crystallized silk fibroin was demonstrated to be a harmless passive substrate after implantation in RCS rats (Antognazza et al., 2016; Maya-Vetencourt et al., 2017), we initially thought to adopt the same material for manufacturing the larger prostheses to implant in the pig's eye. However, crystallization could not achieve large planar surfaces. In addition, large crystallized fibroin surfaces do not have sufficient compliance to adapt to the retina curvature. For this reason, keeping the same source material, we generated electro-spun fibroin fibers organized in a mesh (**Figure 1D**) that was similar in behavior to silk fabrics. The resulting fibroin fabric was characterized by an excellent layering of polymers, a facilitated folding and unfolding during the surgical implant, with high potential to cover large areas of the retina.

Although this material had ideal physical-chemical characteristics to adopt an endo-vitreous approach, the experimental findings revealed that it was poorly biocompatible with the pig's retina and triggered adverse reactions. Indeed, the electrophysiological analysis following the surgical implant of 4 aligned ESF-based prosthesis per eye, showed a complete absence of the ff-ERG b-wave signal after 10 days of implant, from both the eyes implanted with the complete device (active; left eye) and the eyes implanted with the substrate only (sham; right eye) in the two tested animals (E2 and E3 pigs; **Figures 3A–D**), as compared to the respective initial recording sessions (PRE vs. POST; **Figures 3E,F**). Indeed, in the days following the operation indirect ophthalmoscopy and SD-OCT scans revealed marked alterations in outer retinal layers in direct contact with the prosthesis (**Supplementary Figure S1B**). Retrospective histochemistry confirmed the existence of an intense PVR with proliferation, curling, and incorporation of the device inside the reactive tissue (**Figures 4A–D**), in contrast with the excellent biocompatibility previously demonstrated for crystallized fibroin in the rat (Antognazza et al., 2016). Since the retinal reaction occurred in both eyes implanted with active or sham devices, it is possible that the local inflammatory reaction was caused by either the filamentous microstructure



of ESF or the progressive fibroin swelling and subsequent curling of the device.

## Replacement of ESF With PET and Functional Testing in the RCS Rats

In light of these findings, we decided to modify the nature of the passive substrate by using PET (**Figure 5A**). Although the biocompatibility of this material is well known, and PET is widely used in biomedical applications, we conducted preliminary functional tests in RCS dystrophic rats implanted for 1 month with a prosthetic device with the previously described geometry specifically designed for the rat eye (Maya-Vetencourt et al., 2017). To this end, electrophysiological recordings of visual evoked potentials (VEPs) in the binocular area of the primary visual cortex of dystrophic RCS animals were performed, as previously described (Maya-Vetencourt et al., 2017) by implanting either the complete device, or PET alone (sham). The amplitude of VEP responses to light flashes or the spatial discrimination of the responses evoked by patterned stimuli in implanted animals were compared with non- or sham-implanted dystrophic RCS rats and congenic non-dystrophic RCS-rdy rats

of the same age (**Figure 5B**). This analysis revealed the capability of PET-based retinal prostheses to improve visual functions in rats with neurodegenerative retinal dystrophy. Indeed, a significant enhancement of both light-sensitivity and spatial acuity (**Figure 5C**) was observed in RCS implanted rats as compared to both naïve and sham-implanted RCS controls, respectively. The functional rescue was in the same order of magnitude of that obtained using crystallized silk fibroin as substrate (Maya-Vetencourt et al., 2017), indicating that the passive substrate does not directly affect the activity of the overlying polymeric layers.

## Implant of the PET-Based Polymeric Device in Pigs

After optimizing the chemical composition of the prosthesis and testing it in rodents, we implanted 4 aligned pieces of PET-based devices per eye to increase retina coverage in the swine model. Unlike the ESF-based prosthesis, PET-based devices did not elicit overt adverse reactions in the retina of naïve pigs (**Figure 6**). In the four analyzed pigs, the amplitude of the ff-ERG b-wave was slightly, but significantly, decreased ( $p = 0.0182$ ,

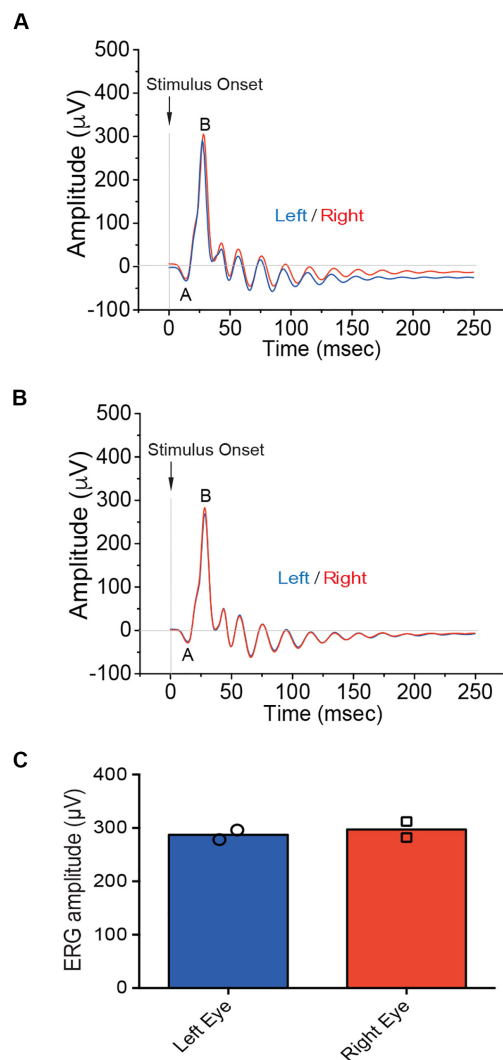


**FIGURE 2 |** Electrophoretic responses in naïve pigs. **(A,B)** Representative ff-ERG recordings in the left (blue trace) and right (red trace) eyes, respectively, from the G1 **(A)** and G2 **(B)** naïve pigs ( $n = 2$ ). **(C)** Bar plots (means with superimposed experimental points) depicting the amplitude of the ff-ERGs b-wave (μV) in the left and right eyes of the G1 and G2 pigs. The electrophysiological recordings of ff-ERGs show that b-wave amplitudes are not different in both naïve pigs validating the experimental approach used to assess retinal functionality.

paired Student's *t*-test) after the surgical procedure in the sham-implanted eye (**Figures 6A,B,E**). Notably, in the four eyes implanted with the active prosthesis, ff-ERG b-wave amplitudes did not significantly differ before and after the surgical procedure ( $p = 0.1492$ , paired Student's *t*-test) (**Figures 6C,D,F**). No significant difference in the latency of the ff-ERG b-wave signal was observed. In addition, SD-OCT scans obtained after the electrophysiological analysis, revealed full integrity of the retinal layers that were in tight contact with the implant (**Supplementary Figure S1C,D**). The decreased post-implant ERG responses in sham-implanted eyes, are consistent with a partial surgery-evoked impairment. On the other hand, the preservation of the

responses in eyes implanted with active devices, which underwent the same surgical implantation procedure, may signal an active compensation by the implanted device (**Figures 6E,F**).

## Biocompatibility of the PET-Based Implant

Based on the positive electrophysiological and OCT data, we next assessed in more detail the biocompatibility of the implanted PET-based device by analyzing the retina cellularity and performing immunohistochemical assays for various inflammatory/trophic markers. We compared untreated eyes collected from normal pigs with the eyes of animals that were subjected to bilateral surgery. After carefully dissecting the eyes, removing cornea, lens, and vitreous body, we checked the position of the implant and signs of a possible glial reaction caused by either the surgery or the chemical composition of the device. At the macroscopic level, we did not find marked signals of gliosis or signs of retinal detachment (**Figures 7A,B**). Both PET-based and sham devices were in subretinal position with no indication of movement after the insertion. To check for morphological changes or remodeling of the ONL due to the foreign body insertion between the photoreceptor layer and the RPE, we performed a nuclear staining with bisbenzimidazole in implanted (**Figure 7C**) and non-implanted (**Figure 7D**) eyes. We measured the ONL thickness in three positions of the retina: the area of the implant and the two neighboring areas of the Periphery/Optic disk axis that we refer to as "Peripheral" and "Central" areas (**Figure 7B**). An expected, thinning of the ONL in the "implant" area was observed in both active device and sham-device eyes, with no significant difference between the two eyes (**Figure 7E**). The thickness of the other two neighboring areas of the retina, in both sham-implanted and prosthesis-implanted eyes, was comparable to those of non-implanted animals (control; **Figure 7E**).

We then performed a series of immunohistochemical assays in sham- and prosthesis-implanted pig eyes to check for the expression of neuroinflammatory/trophic markers, namely: (i) the glial fibrillary acidic protein (GFAP); (ii) the ionized calcium-binding adapter molecule 1 (IBA-1); (iii) fibroblast growth factor 2 (FGF2) in the previously described "peripheral," "implant" and "central" areas.

Glial fibrillary acidic protein expression correlates with neuroinflammation (Brahmachari et al., 2006; Kim et al., 2016; Zhang et al., 2017). In the retina, GFAP is constitutively expressed in astrocytes and Muller cell's soma; it is upregulated following stress and, in Muller cells, translocated along their outer and inner branches (Lewis and Fisher, 2003; Edwards et al., 2016; Luna et al., 2016; Zhang et al., 2017; Lu et al., 2018) (**Figure 8A**). No significant changes in GFAP levels were found between sham- or prosthesis-implanted and control animals (**Figure 8B**).

Microglia are a resident glial cells population. They represent tissue macrophages that, in healthy retinas, play an essential role in homeostasis. Their normal localization is in the plexiform layers, GCL and nerve fiber layer, where they are responsible for immune surveillance and synapses homeostasis thanks to their extensive ramified processes. Interestingly, in healthy retinas,

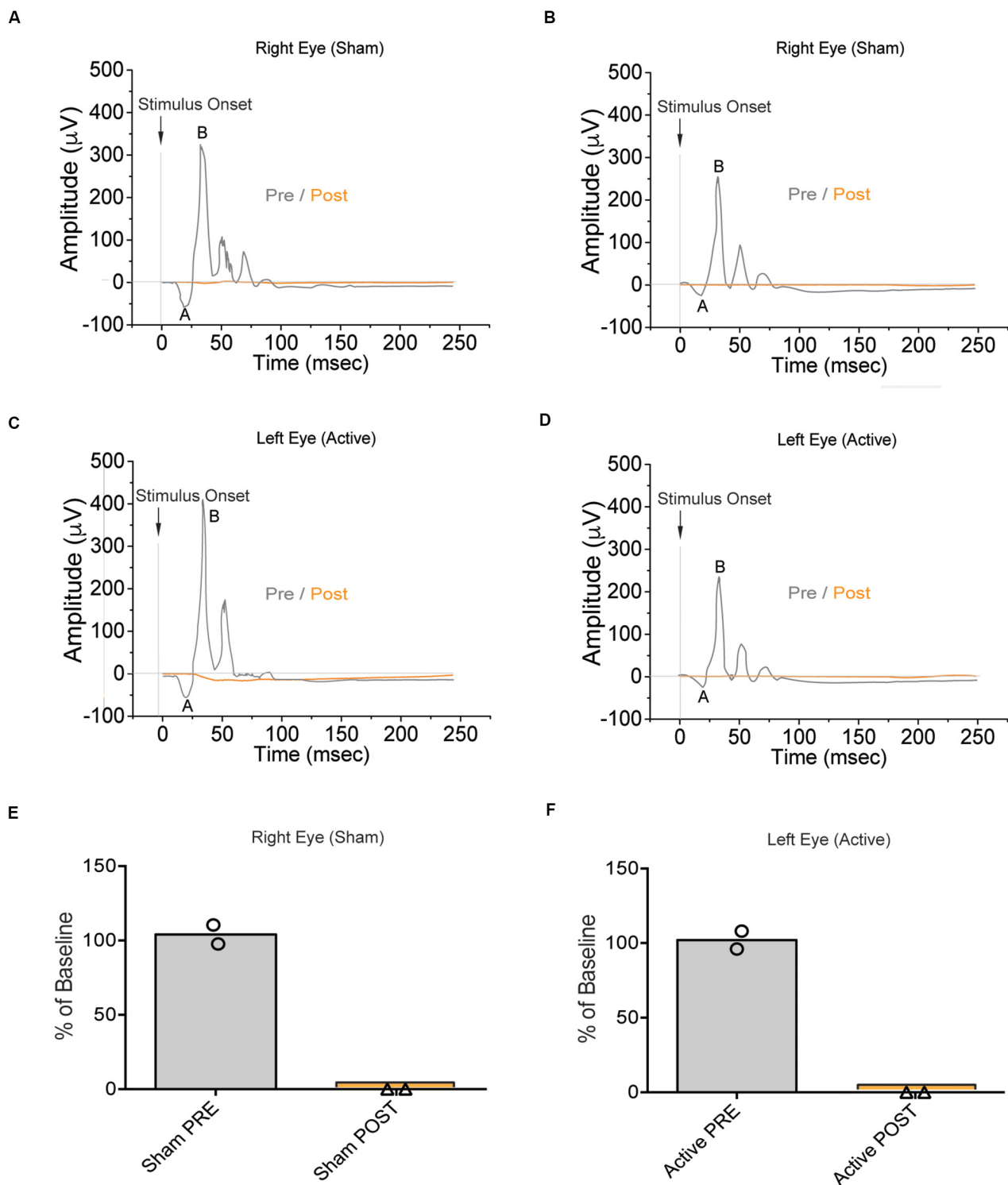
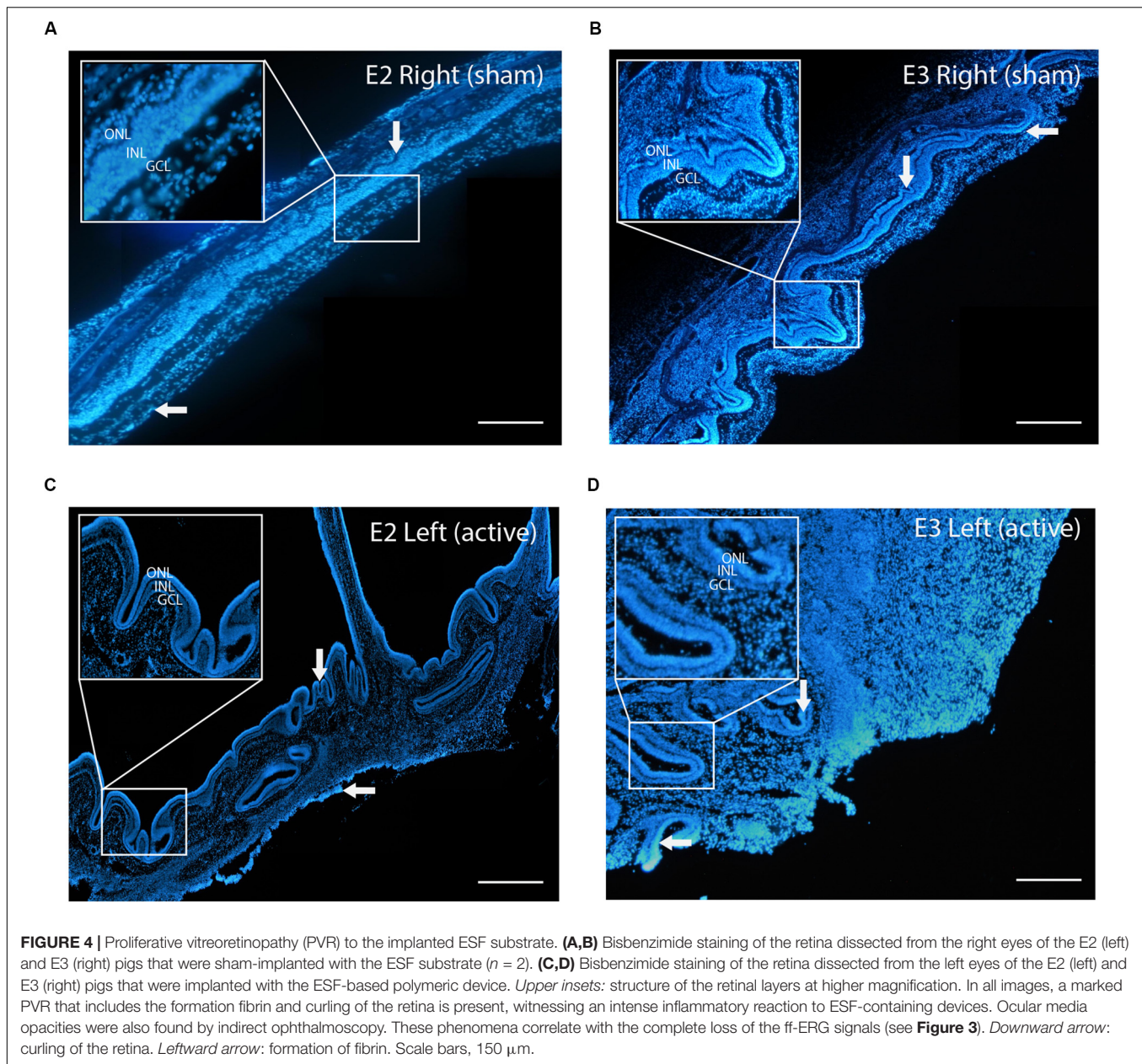


**FIGURE 3 |** Electrophoretic responses in naive pigs subretinally implanted with the ESF-based substrate. **(A,B)** Representative ff-ERG signals of the right eye of the E2 (left) and E3 (right) pigs before surgery (Pre, gray) and after (Post, orange) implantation of the sham ESF substrate alone. **(C,D)** Representative ff-ERG signals of the left eye of the E2 (left) and E3 (right) pigs before surgery (Pre, gray) and after (Post, orange) implantation of the ESF-based complete polymeric device (active). **(E,F)** Bar plots (means with superimposed experimental points) depicting the amplitude of the ff-ERGs b-wave before (Pre, gray) and after (Post, orange) the implantation of either sham substrate (right eye; E) or the active device (left eye; F) in the E2 and E3 pigs ( $n = 2$ ). Data are expressed as the percentage of baseline. The use of ESF as a substrate, irrespective of whether it was layered with the polymers or bare-implanted, had a detrimental impact on the visual response to light after implantation.





processes are highly dynamic structures that show a high degree of movement, which is not followed by the movement of their soma (Lee et al., 2008). Following stress or retinal injury, microglial cells start to extend their processes toward the injured area. In addition, microglial morphologies change from arborized to amoeboid shape. The morphological changes and soma migration toward the injured or stressed part of the retina are usually considered a clear sign of microglia activation (Lee et al., 2008; Cuenca et al., 2014; Di Marco et al., 2019; Rashid et al., 2019). For this reason, we considered microglia migration to the ONL and their changes in shape (evaluated with Scholl analysis) as markers for augmented reactivity following implant surgery. We counted, in all experimental groups, the number of IBA-1-positive cells in the ONL layer (**Figure 9A**).

We observed an increased number of IBA-1 positive cells in the “implant” region of both sham and prosthesis eyes with respect to non-implanted controls (**Figure 9B**). However, the total number of microglia did not change in the different samples (**Figure 9C**). When we performed Scholl analysis to quantify the activation of microglia in terms of number and extension of processes, microglial activation was closely similar between the experimental groups, with no signs of the harmful reactive microglia in the implanted retinas (**Figure 9D**).

Müller cells constitutively synthesize FGF2 that, following retinal insults such as optic nerve sectioning or photoreceptor damage, translocates to photoreceptors. There, FGF2 binds to its specific receptor (FGFR-1), increasing photoreceptor stability, survival, and reducing photoreceptor synaptic function

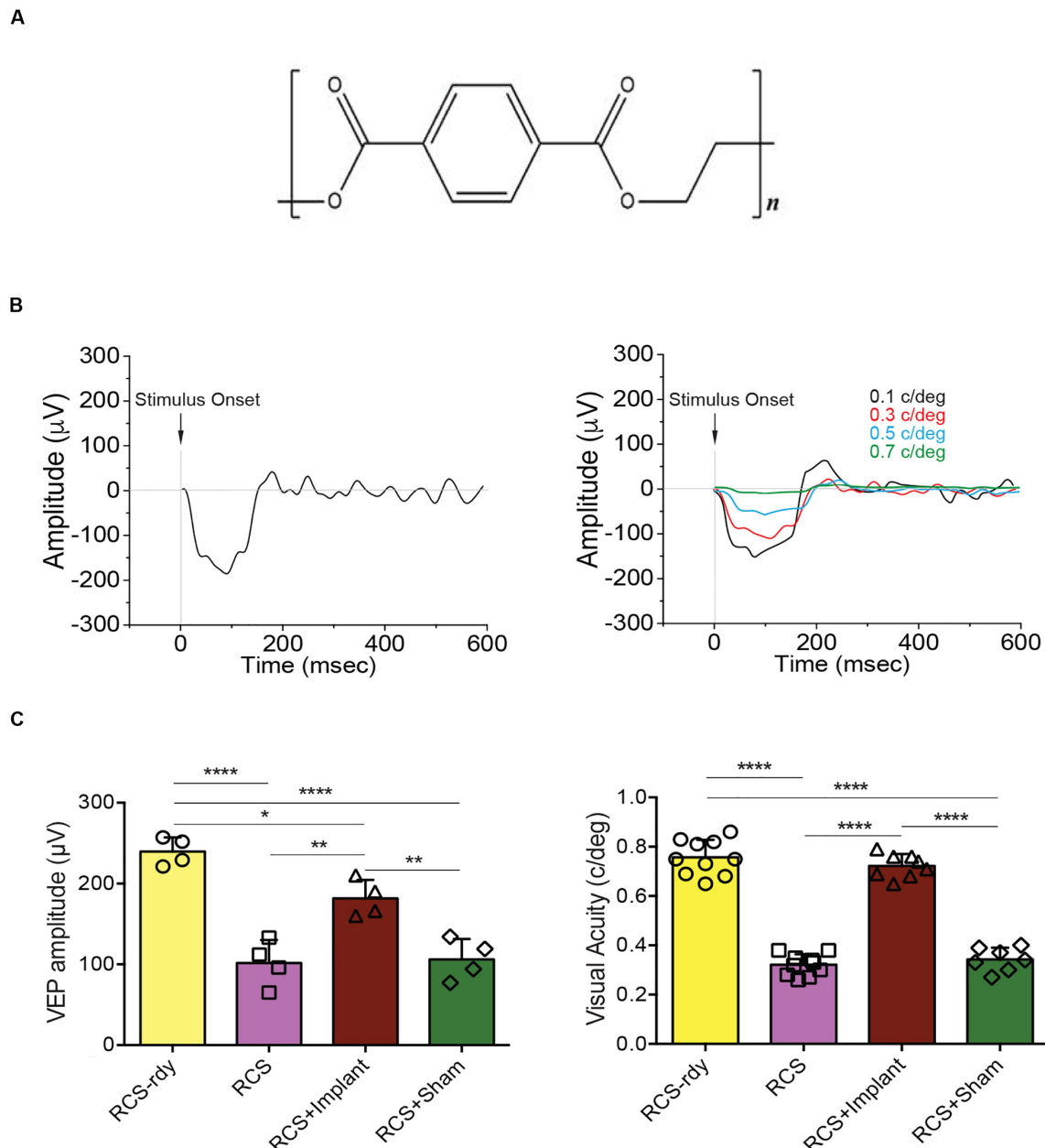


**FIGURE 5 |** Light sensitivity and visual acuity in adult dystrophic RCS rats implanted with the PET-based polymeric prosthesis. **(A)** Structural formula of polyethylene terephthalate (PET). **(B) Left:** representative trace of the visual evoked potential (VEP) recorded in the binocular area of the primary visual cortex in non-dystrophic RCS-rdy rats. **Right:** representative VEP traces in non-dystrophic RCS-rdy rats showing the progressive decrease of the signal amplitude that occurs with the increase of the spatial frequency of the visual stimulus. **(C) Left:** the VEP response to light in naïve RCS dystrophic rats (102 μV) was lower ( $p < 0.0001$ ) than that observed in RCS-rdy congenic controls (240 μV). Sensitivity to light increased significantly (182 μV) after 1 month of implant with the active device as compared to either non-implanted dystrophic RCS rats ( $p = 0.0024$ ) or sham-implanted dystrophic RCS rats ( $p = 0.0038$ ). Light sensitivity in sham-implanted RCS animals did not differ from that seen in naïve RCS rats ( $n = 4$  per experimental group). **Right:** visual acuity in naïve dystrophic rats (0.32 c/deg) was lower ( $p < 0.0001$ ) than that of RCS congenic controls (0.76 c/deg) but following 1 month of implantation with the PET-based prosthetic it significantly enhanced (0.72 c/deg) with respect to either naïve RCS animals ( $p < 0.0001$ ) or sham-implanted RCS rats ( $p < 0.0001$ ). Data are means  $\pm$  SD with superimposed experimental points. \* $p < 0.05$ ; \*\* $p < 0.01$ ; \*\*\*\* $p < 0.0001$ ; one-way ANOVA/Tukey's tests ( $n = 10$  for both RCS-rdy and RCS animals;  $n = 8$  for RCS + Implant;  $n = 7$  for RCS + sham).

(Gargini et al., 2004; Valter et al., 2005; Hochmann et al., 2012). We measured FGF2 intensity in all layers of the retina (Figure 10A), with special reference to the ONL. We found an increase of FGF2 level in the “peripheral” and “central”

ONL areas of sham- and prosthesis-implanted eyes and, to a lesser extent, in the “implant” area (Figure 10B). The lower FGF2 density seen in the “implant” area likely reflects the loss of photoreceptors. Both sham- and prosthesis-implanted eyes

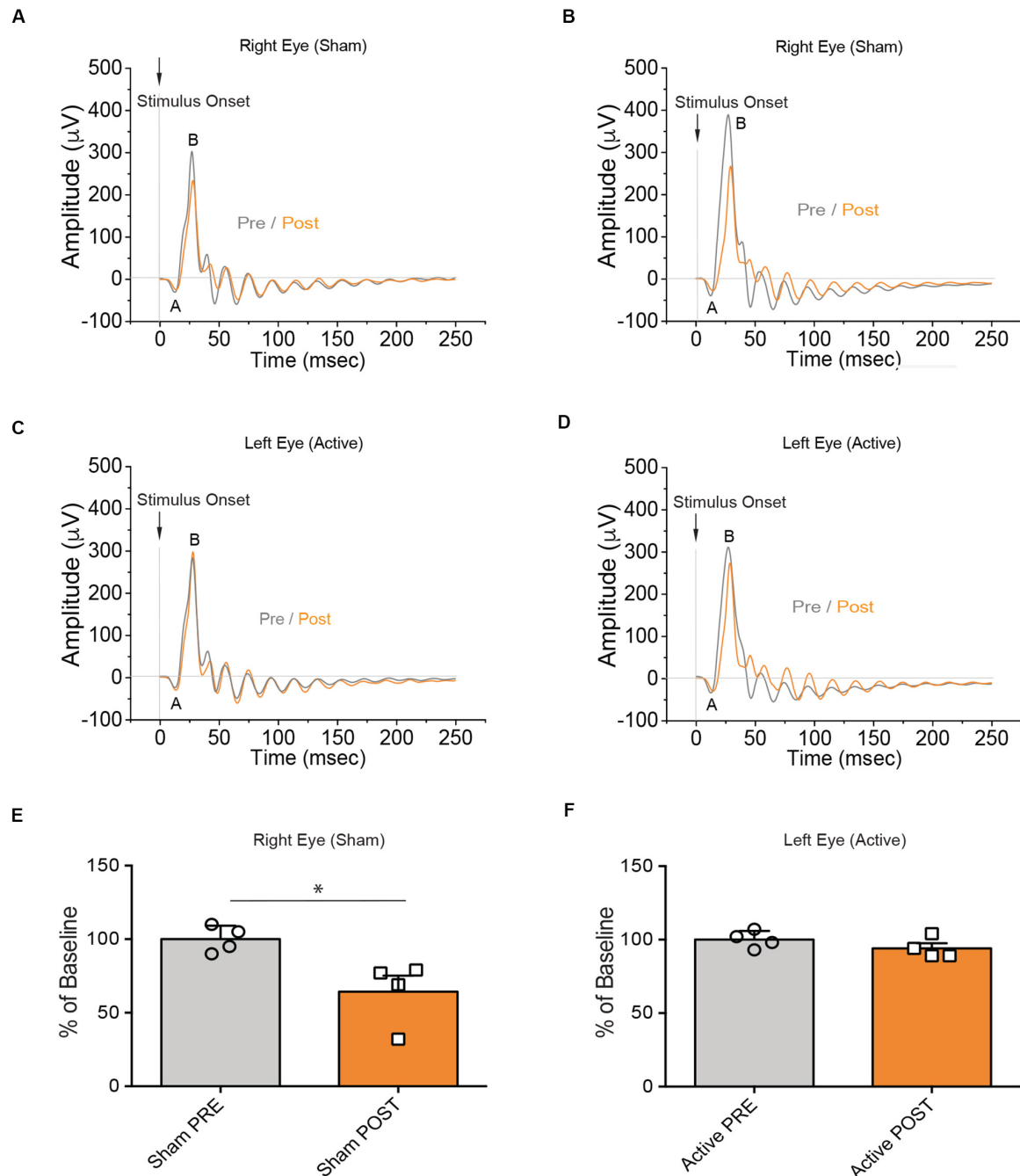


**FIGURE 6 |** Electrophysiological responses in naïve pigs subretinally implanted with the PET-based prosthesis. **(A,B)** Representative ff-ERG signals of the right eye of the E31 (left) and E34 (right) pigs before surgery (Pre, gray) and after (Post, orange) implantation of the sham PET substrate alone. **(C,D)** Representative ff-ERG signals of the left eye of the E31 (left) and E34 (right) pigs before surgery (Pre, gray) and after (Post, orange) implantation of the PET-based complete polymeric device (active). **(E,F)** Bar plots (mean  $\pm$  SD) depicting the amplitude of the ff-ERGs b-wave before (Pre, gray) and after (Post, orange) the implantation of either sham substrate (right eye; **E**) or the active device (left eye; **F**) in  $n = 4$  individual pigs. Data (means  $\pm$  SD with superimposed experimental points) are expressed as the percentage of baseline. Before the surgical intervention, the amplitude of the ff-ERG b-wave in the eyes of all pigs was normal. Notably, these signals were preserved after the subretinal implantation of the PET-based active prosthetics in all animals ( $p = 0.1492$ ). No rescue effect was observed in sham-implanted animals ( $p = 0.0182$ ). \* $p < 0.05$ , paired Student's  $t$ -test ( $n = 4$ ).

showed less fluorescence with respect to control retinas in the Muller cells soma (**Figure 10C**). The fluorescence levels in the GCL of the “central” region were higher in controls with respect

to sham- and prosthesis-implanted retinas, slightly higher in the peripheral area of prosthesis-implanted retinas, and equivalent to controls in all the other regions (**Figure 10D**).

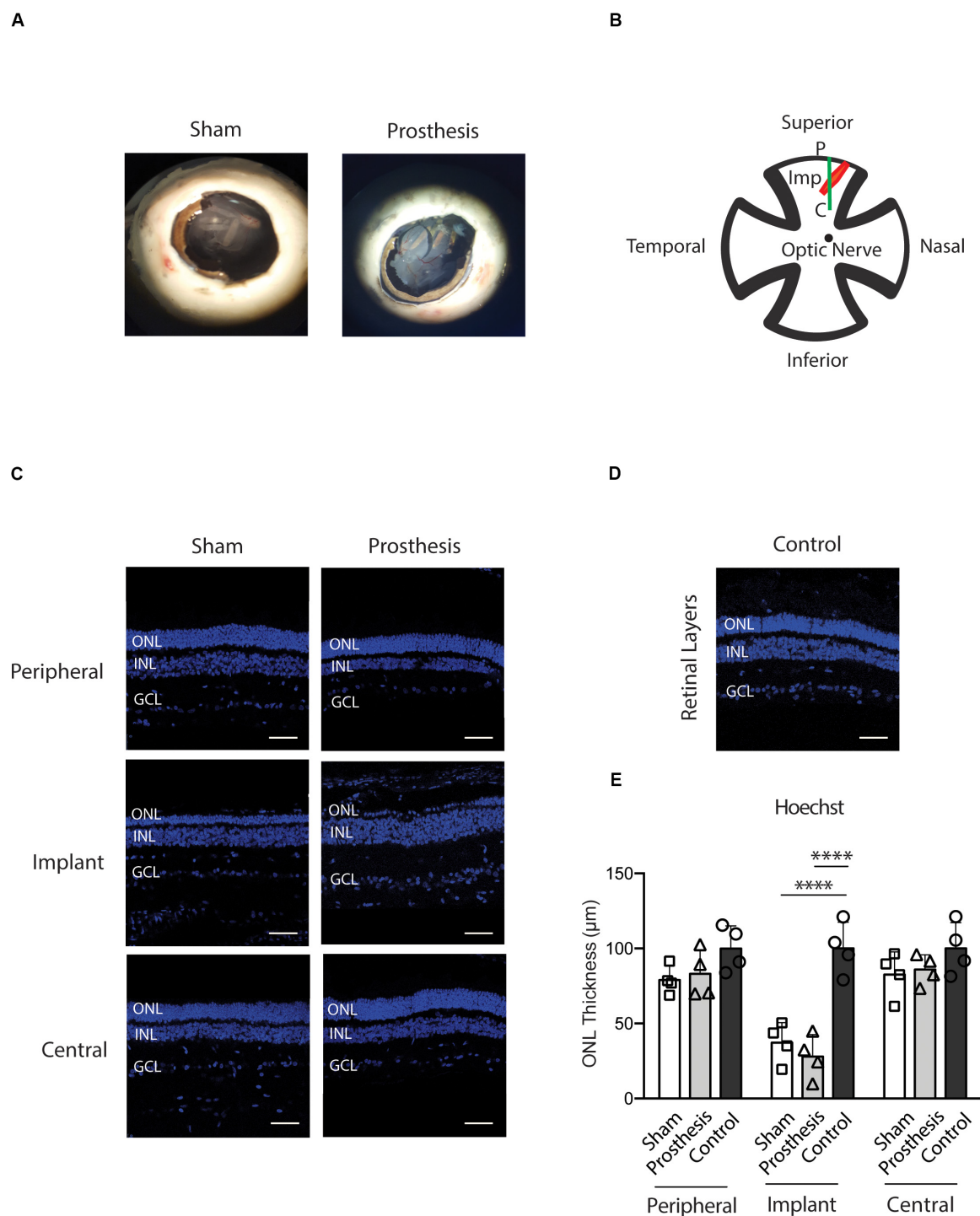


**FIGURE 7 |** Morphology of the ONL after implantation of PET-based devices in the pig. **(A)** Representative eyecups of sham- and prosthesis-implanted pigs. All the examined eyes had no overt signs of inflammatory reaction or displacement of the implants from the insertion place. **(B)** Cartoon depicting the retinal areas ("peripheral," "implant," and "central") that were sampled in sham- and prosthesis-implanted eyes. **(C,D)** Representative retina sections stained with bisbenzimidazole to show the thickness of nuclear layers in "peripheral," "implant," and "central" positions in sham- and prosthesis-implanted pigs **(C)** as well as in the non-implanted control group **(D)**. ONL, outer nuclear layer; INL, inner nuclear layer; GCL, ganglion cell layer; P, Peripheral; Imp, implant; C, central. Scale bars, 50  $\mu\text{m}$ . **(E)** Bar plots (means  $\pm$  SD with superimposed experimental points) showing the retinal ONL thickness measured in sham-implanted (white), prosthesis-implanted (light gray) and non-implanted control (dark gray) groups measured in the peripheral, implant and central retinal regions. In the implant area, a significant reduction in the ONL thickness of the sham ( $p < 0.0001$ ) and prosthesis ( $p < 0.0001$ ) group with respect to non-implanted controls was observed. No significant changes in retinal thickness in the other retinal regions were found. \*\*\*\* $p < 0.0001$ , two-way ANOVA/Tukey's tests ( $n = 4$  for each experimental group).



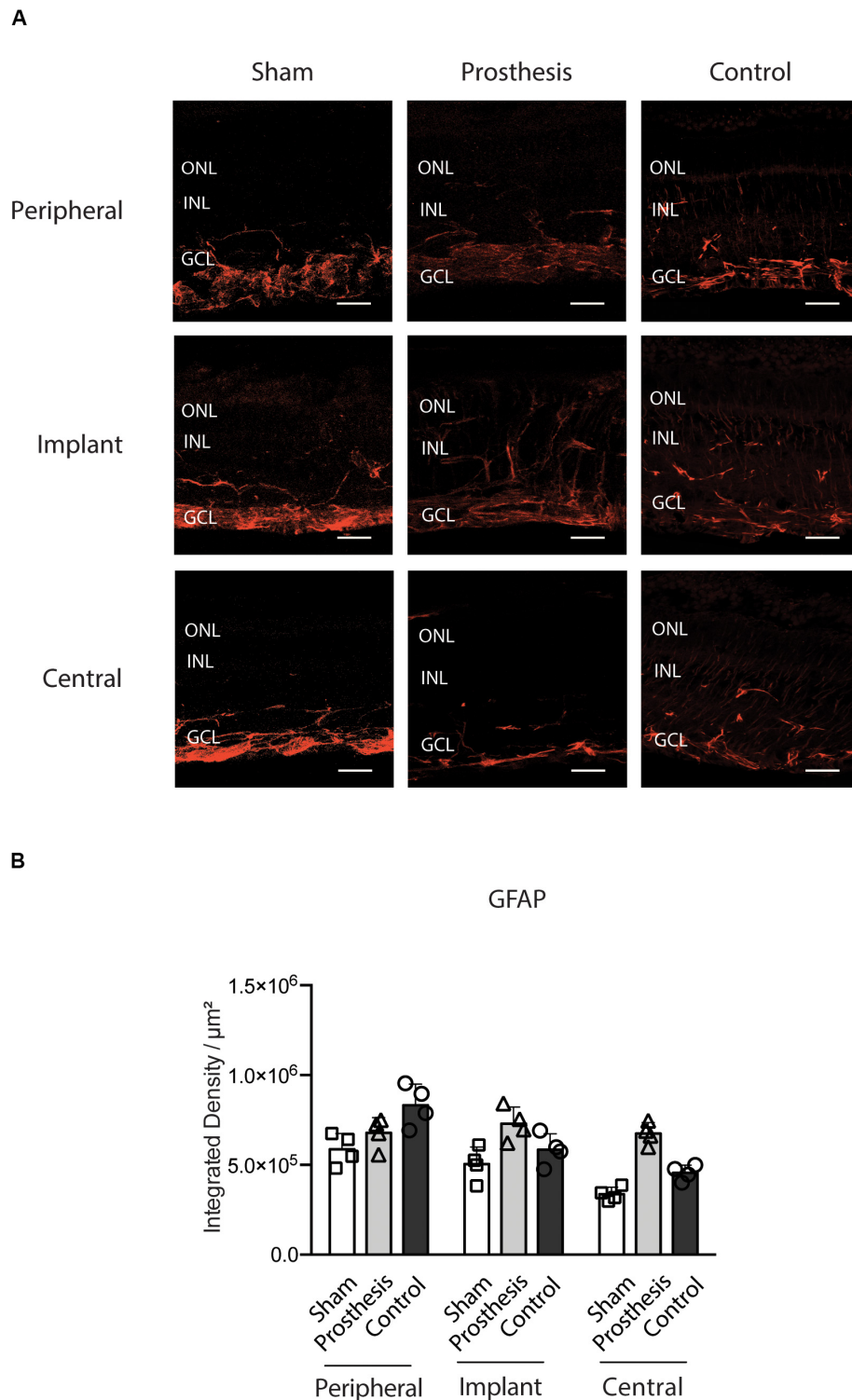


**FIGURE 8 |** Astrocytic response in the retina after implantation of PET-based devices in the pig. **(A)** Representative retinal sections stained with anti-GFAP antibody (red), labeling astrocytes. The immunoreactive areas were sampled as indicated in **Figure 7B**. ONL, outer nuclear layer; INL, inner nuclear layer; GCL, ganglion cell layer. Scale bars, 50  $\mu\text{m}$ . **(B)** Bar plots (mean  $\pm$  SD) displaying GFAP levels in the retinas of sham-implemented (white), prosthesis-implemented (light gray) and non-implemented control (dark gray) groups measured in the peripheral, implant and central retinal regions. All retinal areas showed comparable GFAP levels ( $p > 0.05$  for all comparisons between experimental groups; two-way ANOVA/Tukey's test,  $n = 4$ ), indicating the absence of a significant glial activation following the surgical implant.

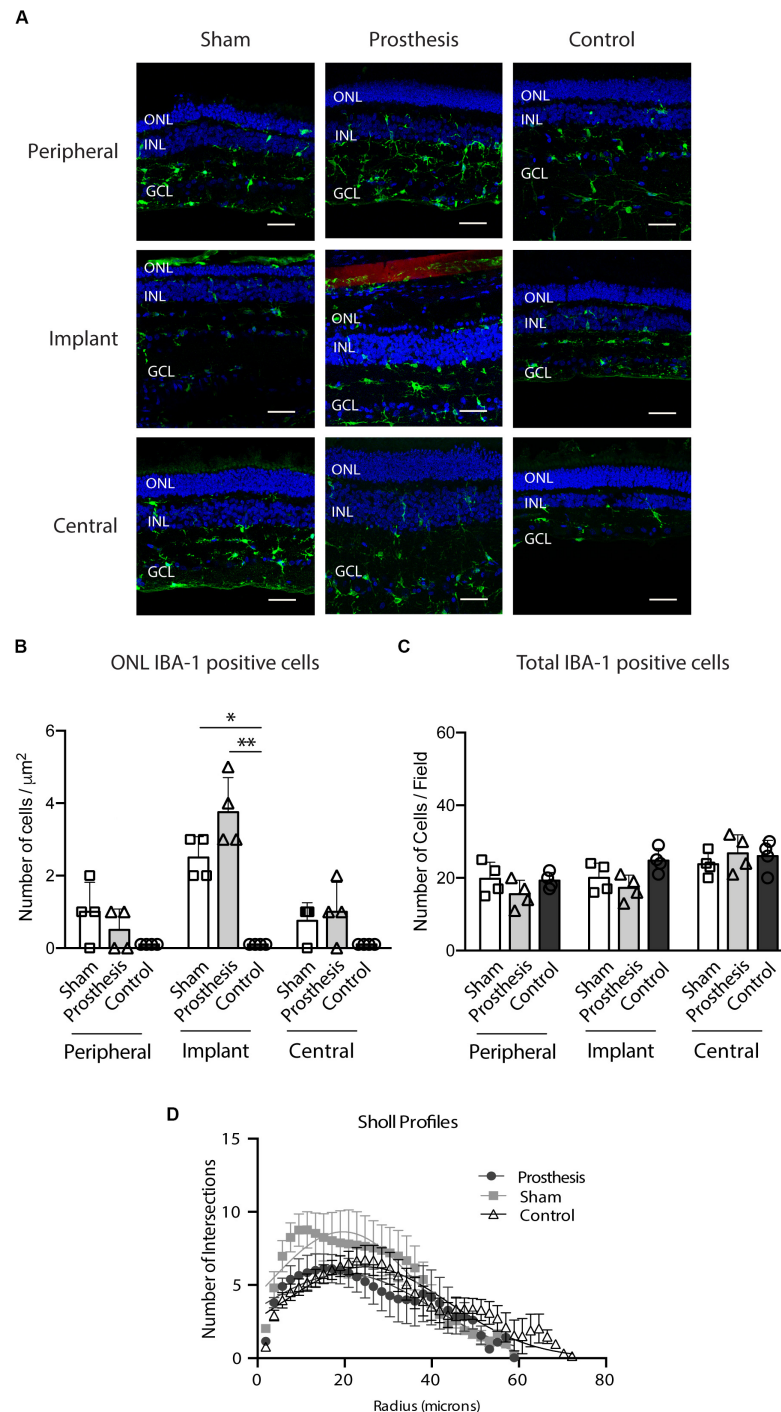


**FIGURE 9 |** Microglial response in the retina after implantation of PET-based devices in the pig. **(A)** Representative retinal sections stained with anti-IBA-1 antibody (green) and bisbenzimidazole (nuclei, blue). The PET-based active device was detected thanks to the P3HT fluorescence (red). The immunoreactive areas were sampled as indicated in **Figure 7B**. ONL, outer nuclear layer; INL, inner nuclear layer; GCL, ganglion cell layer. Scale bars, 50  $\mu\text{m}$ . **(B)** Bar plots (means  $\pm$  SD with superimposed experimental points) depicting the number of IBA-1-positive microglial cells in the ONL of sham-implanted (white), prosthesis-implanted (light gray) and non-implanted control (dark gray) groups measured in the peripheral, implant and central retinal regions. In the ONL, all groups show a similar number of IBA-1-positive cells, except for a significant increase of microglia in the implant area of both sham- and prosthesis-implanted groups with respect to control retinas ( $p = 0.0266$  and  $p = 0.0039$ , respectively). **(C)** Bar plots (means  $\pm$  SD with superimposed experimental points) depicting the number of IBA-1-positive microglial cells in the entire retina of sham-implanted (white), prosthesis-implanted (light gray) and non-implanted control (dark gray) groups measured in the peripheral, implant and central retinal regions. The total number of cells is not significantly changed. **(D)** Scholl analysis of microglial processes shows the number of intersections of the processes of IBA-1-positive cells in concentric circles centered on the cell body and drawn every 0.38  $\mu\text{m}$ . Morphological shapes are similar in all experimental groups, indicating the absence of a significant microglia activation. \* $p < 0.05$ ; \*\* $p < 0.01$ ; two-way ANOVA/Tukey's tests ( $n = 4$ ).

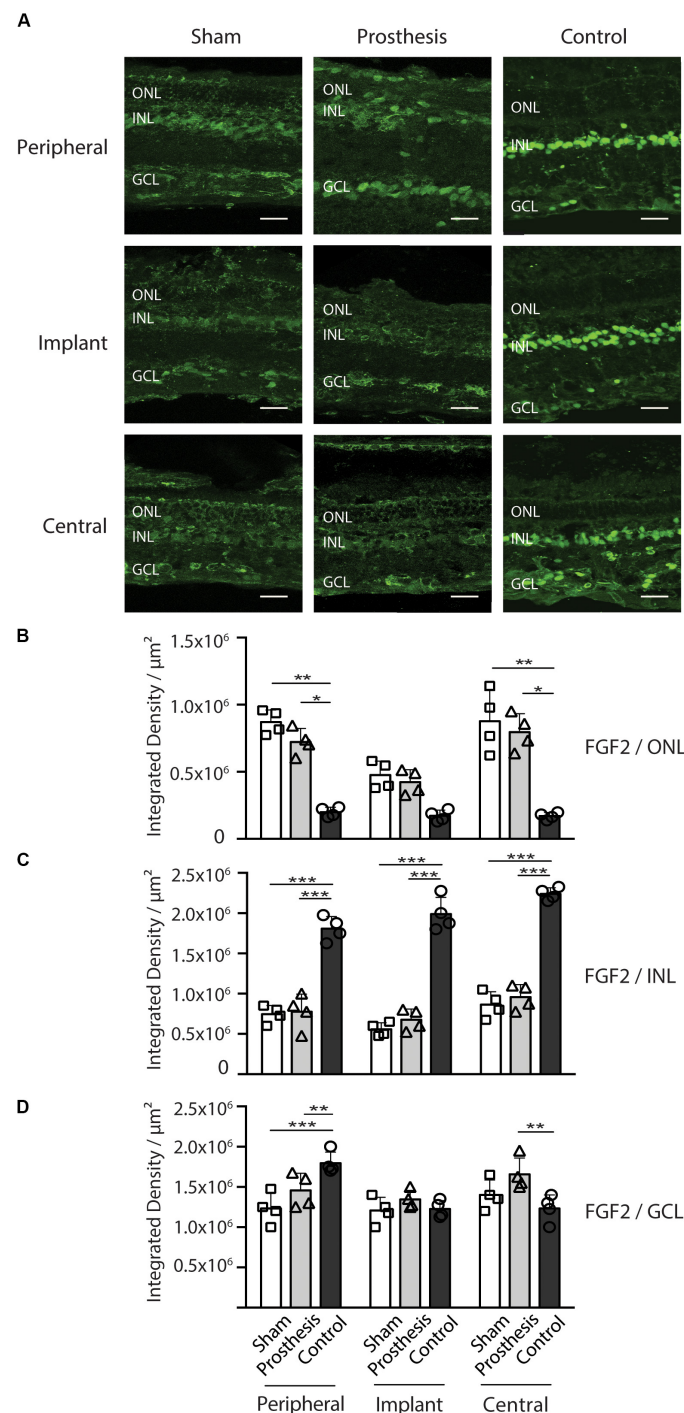


**FIGURE 10 |** FGF2 expression in the retina after implantation of PET-based devices in the pig. **(A)** Representative retina sections stained with anti-FGF2 antibody (green). The immunoreactive areas were sampled as indicated in **Figure 7B**. ONL, outer nuclear layer; INL, inner nuclear layer; GCL, ganglion cell layer. Scale bars, 50  $\mu\text{m}$ . **(B)** Bar plots showing the FGF2 levels in the ONL of sham-implanted (white), prosthesis-implanted (light gray), and non-implanted control (dark gray) groups measured in the peripheral, implant and central regions of the retina. In both the peripheral and central areas, prosthesis- and sham-implanted retinas are significantly more positive than the control retinas. **(C)** Bar plots showing the FGF2 levels in the INL of the same experimental groups shown in B. All areas of control retinas were significantly different from both sham- and prosthesis-implanted retinas. **(D)** Bar plots showing the FGF2 levels in the GCL of the same experimental groups shown in B. No variation of FGF2 immunoreactivity was observed between the implant area of both sham- and prosthesis-implanted eyes as compared to control eyes. A significant decrease of FGF2 expression was found in the peripheral area of both sham- and prosthesis-implanted eyes as compared to control eyes. In contrast, a significant increase of FGF2 was observed in the central area of prosthesis-implanted eyes with respect to controls. All data are means  $\pm$  SD with superimposed experimental points. \* $p < 0.05$ ; \*\* $p < 0.01$ ; \*\*\* $p < 0.001$ ; two-way ANOVA/Tukey's test ( $n = 4$ ).

## DISCUSSION

To evaluate the action of the polymeric prosthesis, successfully tested in the RCS rat, in the swine model, we used the bilateral subretinal implantation of the retinal prosthesis in naïve pigs as experimental paradigm. After initial unsuccessful attempts of retinal implantation by trans-scleral route, we decided to use an intravitreal approach. The prosthetic device initially used in rats (Maya-Vetencourt et al., 2017), consisted of 3 layers: P3HT, PEDOT:PSS, and crystallized silk fibroin as substrate. However, due to the intrinsic rigidity of the crystallized silk fibroin, we used the same starting material to ESF fabrics characterized by an extremely uniform surface, high flexibility and absence of memory after bending. The modification of the substrate was to facilitate the surgical implant procedure and, at the same time, to increase the area of retina coverage. Despite the technical success of the implant design, we found an undesired retinal reaction (PVR) to the ESF substrate, as assessed by indirect ophthalmoscopy and histology, associated with the complete disappearance of the ff-ERG b-wave signal in the implanted eyes. We then replaced the ESF with PET, while keeping the other layers of the prosthesis intact. To test the efficacy of this material, we performed control experiments in dystrophic RCS rats. In line with previous findings (Maya-Vetencourt et al., 2017), RCS dystrophic animals implanted with the PET-based prosthetic showed a significant rescue of both light sensitivity and visual acuity that was virtually absent from sham-implanted rats.

After testing the efficacy of the new prosthesis in rodents, we implanted subretinally the prosthesis or the substrate alone in pigs with normal vision. Following the surgical implant of the sham device, the ff-ERG b-wave amplitude was reduced with respect to the signal recorded before the implant, confirming the partial retinal dysfunction after surgery and testifying the degeneration of photoreceptors in the retinal area overlying the implant. Notably, the eyes that received the active prosthesis, equal in size as compared to the sham device and implanted with the same surgical procedure, displayed fully preserved ff-ERG b-wave amplitudes, in spite of the implant-induced local photoreceptor degeneration. This result indicates not only the absence of adverse inflammatory reactions to the implantation of the active device in the normal retina, but also a functional compensation of the induced photoreceptor degeneration carried out by the photosensitive prosthesis. Moreover, SD-OCT images revealed that the external retina remained in tight contact with the prosthetic, with only a limited reduction of the outer retina thickness in the “implant” area, but not in neighboring regions. These findings show that the optimized prosthetic does not induce severe tissue damage to outer layers of retina and that the surgical procedure for the subretinal prosthesis is well standardized.

Histological analyses revealed a moderate degree of stress in photoreceptors localized in the site of “implant,” in the absence of adverse effects on the retinal structure outside the implant area. In the retina, GFAP is constitutively expressed in astrocytes and Muller cells, and becomes upregulated under stress

conditions (Lewis and Fisher, 2003; Edwards et al., 2016; Luna et al., 2016; Zhang et al., 2017; Lu et al., 2018). Interestingly, we observed no changes in GFAP expression after 10 days of surgery in both sham-implanted and prosthesis-implanted eyes as compared to non-implanted controls. Furthermore, microglia activation assessed by IBA-1 immunoreactivity was significantly enhanced with respect to controls only at the “implant” area of both sham-implanted and prosthesis-implanted eyes, but not in the neighboring areas of the retina. Additionally, Scholl analysis unveiled no differences in the morphology of microglial cells among the various experimental groups, indicating the absence of microglia activation. Our experimental findings point toward the retinal recovery from the surgical stress associated with the prosthetic implant and to an excellent biocompatibility of the PET substrate.

Another important aspect in the field of vision science research is the trophic effect induced by retinal surgery, which could *per se* enhance photoreceptors' survival. To address this issue, we performed immunohistochemistry for FGF2, a trophic factor constitutively expressed in Muller cells and retinal ganglion cells (Walsh et al., 2001; Valter et al., 2002) whose upregulation and translocation to the ONL in the retina is a typical landmark of photoreceptor stress (Xiao et al., 1998, 1999; Sannita et al., 2004; Valter et al., 2005; Rutar et al., 2010; Hochmann et al., 2012). An induction of FGF2 levels, likely due to the surgical implantation procedure, was found in the neighboring areas of the retina. This finding, together with the fact that no functional recovery was seen in sham-implanted animals, confirms the previously described role of FGF2 in the retinal response after the surgery (Valter et al., 2005). Interestingly, no additional signs of retinal stress were detected. Neither an increase of GFAP-positive cells, nor a morphological activation of IBA-1-positive cells as assessed by Scholl analysis was observed in the area covered by the prosthesis. In humans, it was reported that ff-ERG suppression in the damaged retina correlates with the up-regulation of FGF2, but not with the extension of damaged area (Di Loreto et al., 2002). Notably, FGF2 upregulation has been found to be deleterious for visual responses to light in animal models (Gargini et al., 1999). The decrease of ff-ERG signals observed in animals sham-implanted with the PET-only devices indicates that the up-regulation of FGF2 levels in the “peripheral” and “central” areas of the retina 10 days after the implant reduced the retinal responses, by acting at the level of the first synapse photoreceptors-bipolar cell (Valter et al., 2002, 2005). On the other hand, the total preservation of visual responses after implantation of the fully active device, in spite of photoreceptor degeneration overlying the implant area, indicates that the polymers might compensate for this phenomenon by acting on second order neurons (bipolar cells) thus rendering the degenerated area of the retina light sensitive.

## CONCLUSION

Our findings obtained in a large animal model such as the biomedical pig highlight the possibility of developing a



new generation of photosensitive conjugated polymer/PET-based prosthetic devices that are highly biocompatible and suitable for subretinal implantation in patients suffering from degenerative blindness.

## DATA AVAILABILITY STATEMENT

The data that supports the plot within this paper together with other findings of this study are available from the corresponding author upon reasonable request.

## ETHICS STATEMENT

The animal study was reviewed and approved by the Italian Ministry of Health.

## AUTHOR CONTRIBUTIONS

FaB, MB, GL, and GP supervised, coordinated, and financed all the activities on pigs and rats. JFM-V performed the *in vivo* electrophysiology experiments in rodents and followed the electroretinographic analyses on pigs under the supervision of FaB. SD and MD carried out the immunohistochemical and histological analysis under the supervision of SB. MM executed the optical coherence tomography. GP and MM developed and performed the subretinal implantation of the prosthesis. GM and AD fabricated the prostheses and characterized them under the supervision of GL. DV, AE, and FrB performed all the procedures on pigs including general husbandry, anesthesia, electrophysiological analyses, and final samplings under the supervision of MB. WS supported the electroretinographic analysis on pigs. JFM-V, SD, and FaB wrote the manuscript. All authors discussed the experimental results and commented on the script.

## REFERENCES

- Alessandrino, A., Marelli, B., Arosio, C., Fare, S., Tanzi, M. C., and Freddi, G. (2008). Electrospun silk fibroin mats for tissue engineering. *Eng. Life Sci.* 8, 219–225. doi: 10.1002/elsc.200700067
- Antognazza, M. R., Di Paolo, M., Ghezzi, D., Mete, M., Di Marco, S., Maya-Vetencourt, J. F., et al. (2016). Characterization of a polymer-based, fully organic prosthesis for implantation into the subretinal space of the rat. *Adv. Healthc. Mater.* 5, 2271–2282. doi: 10.1002/adhm.201600318
- Ayton, L. N., Blamey, P. J., Guymer, R. H., Luu, C. D., Nayagam, D. A., Sinclair, N. C., et al. (2014). First-in-human trial of a novel suprachoroidal retinal prosthesis. *PLoS One* 9:e115239. doi: 10.1371/journal.pone.0115239
- Barber, A. C., Hippert, C., Duran, Y., West, E. L., Bainbridge, J. W., Warre-Cornish, K., et al. (2013). Repair of the degenerate retina by photoreceptor transplantation. *Proc Natl. Acad. Sci. U.S.A.* 110, 354–359. doi: 10.1073/pnas.1212677110
- Barone, F., Muscatello, L. V., Ventrella, D., Elmi, A., Romagnoli, N., Mandrioli, L., et al. (2020). The porcine iodoacetic acid model of retinal degeneration:

## FUNDING

The work was supported by the Italian Ministry of Health (project RF-2013-02358313 to GP, GL, and FB), Fondazione Cariplo (project 2018-0505 to GL, FB, and GP), H2020-MSCA-ITN 2019 "Entrain Vision" (project 861423 to FB) and EuroNanoMed3 (project 2019-132 "NanoLight" to FB). The support of the Ra.Mo. Foundation (Milano, Italy), Rare Partners srl (Milano, Italy) and Fondazione 13 Marzo (Parma, Italy) is also acknowledged. This project has received funding from the European Union's Horizon 2020 Research and Innovation Programme Graphene Flagship (Core 3; WP5) under grant agreement no. 881603.

## ACKNOWLEDGMENTS

The authors would like to thank Paola Bagnoli and Vittorio Porciatti for precious comments on the manuscript. They also thank M. M. La Vail (Beckman Vision Center, University of California, San Francisco, CA, United States) for providing RCS rats; G. Vijfinkel (Oftavinci BV, Geervliet, Netherlands) for manufacturing specific surgical tools for implantation; R. Ciancio, I. Dallorto, A. Mehili, R. Navone, and D. Moruzzo (Istituto Italiano di Tecnologia, Genova, Italy) for technical assistance.

## SUPPLEMENTARY MATERIAL

The Supplementary Material for this article can be found online at: <https://www.frontiersin.org/articles/10.3389/fbioe.2020.579141/full#supplementary-material>

**Supplementary Figure 1** | SD-OCT images of the eyes in the experimental pigs. **(A)** Representative SD-OCT scans of the left eyes in the G1 and G2 naïve animals, highlighting the optimal health state of retinal layers. **(B)** Representative images of the eyes of E2 and E3 pigs showing major morphological alterations in the external retinal layers after the ESF implant. **(C,D)** The implantation of the PET-based retinal prosthesis or PET alone (E31 and E34 pigs) causes no morphological alterations in external layers of the retina after the subretinal implant. Scale bars: 100  $\mu$ m.

- morpho-functional characterization of the visual system. *Exp. Eye Res.* 193:107979. doi: 10.1016/j.exer.2020.107979
- Barone, F., Nannoni, E., Elmi, A., Lambertini, C., Scorpio, D. G., Ventrella, D., et al. (2018). Behavioral assessment of vision in pigs. *J. Am. Assoc. Lab Anim. Sci.* 57, 350–356. doi: 10.30802/AALAS-JAALAS-17-000163
- Benfenati, F., and Lanzani, G. (2018). New technologies for developing second generation retinal prostheses. *Lab. Anim.* 47, 71–75. doi: 10.1038/s41684-018-0003-1
- Brahmachari, S., Fung, Y. K., and Pahan, K. (2006). Induction of glial fibrillary acidic protein expression in astrocytes by nitric oxide. *J. Neurosci.* 26, 4930–4939. doi: 10.1523/JNEUROSCI.5480-05.2006
- Busskamp, V., Duebel, J., Balya, D., Fradot, M., Viney, T. J., Siebert, S., et al. (2010). Genetic reactivation of cone photoreceptors restores visual responses in retinitis pigmentosa. *Science* 329, 413–417. doi: 10.1126/science.1190897
- Cuenca, N., Fernández-Sánchez, L., Campello, L., Maneu, V., De la Villa, P., Lax, P., et al. (2014). Cellular responses following retinal injuries and therapeutic approaches for neurodegenerative diseases. *Prog. Retin. Eye Res.* 43, 1–59. doi: 10.1016/j.preteyeres.2014.07.001
- Dagnelie, G., Christopher, P., Arditi, A., da Cruz, L., Duncan, J. L., Ho, A. C., et al. (2017). Performance of real-world functional vision tasks by blind subjects

- improves after implantation with the Argus(R) II retinal prosthesis system. *Clin. Exp. Ophthalmol.* 45, 152–159. doi: 10.1111/ceo.12812
- DeMarco, P. J. Jr., Yarbrough, G. L., Yee, C. W., McLean, G. Y., Sagdullaev, B. T., Ball, S. L., et al. (2007). Stimulation via a subretinally placed prosthetic elicits central activity and induces a trophic effect on visual responses. *Invest. Ophthalmol. Vis. Sci.* 48, 916–926. doi: 10.1167/iovs.06-0811
- Di Loreto, S., Spadea, L., Cencioni, S., Balestrazzi, E., Adorno, D., Cervetto, L., et al. (2002). Correlation between ERG changes and FGF2 mRNA Up-regulation in patients with choroidal melanoma. *Exp. Eye Res.* 75, 217–225. doi: 10.1006/exer.2002.2023
- Di Marco, S., Carnicelli, V., Franceschini, N., Di Paolo, M., Piccardi, M., Bisti, S., et al. (2019). Saffron: a multitask neuroprotective agent for retinal degenerative diseases. *Antioxidants* 8:224. doi: 10.3390/antiox8070224
- Dias, M. F., Joo, K., Kemp, J. A., Fialho, S. L., da Silva Cunha, A. Jr., Woo, S. J., et al. (2018). Molecular genetics and emerging therapies for retinitis pigmentosa: basic research and clinical perspectives. *Prog. Retin. Eye Res.* 63, 107–131. doi: 10.1016/j.preteyeres.2017.10.004
- Edwards, M. M., McLeod, D. S., Bhutto, I. A., Villalonga, M. B., Seddon, J. M., and Luty, G. A. (2016). Idiopathic preretinal glia in aging and age-related macular degeneration. *Exp. Eye Res.* 150, 44–61. doi: 10.1016/j.exer.2015.07.016
- Elmi, A., Ventrella, D., Laghi, L., Carnevali, G., Zhu, C., Pertile, G., et al. (2019). <sup>1</sup>H NMR spectroscopy characterization of porcine vitreous humor in physiological and photoreceptor degeneration conditions. *Invest. Ophthalmol. Vis. Sci.* 60, 741–747. doi: 10.1167/iovs.18-25675
- Feyen, P., Colombo, E., Endeman, D., Nova, M., Laudato, L., Martino, N., et al. (2016). Light-evoked hyperpolarization and silencing of neurons by conjugated polymers. *Sci. Rep.* 6:22718. doi: 10.1038/srep22718
- Frasson, M., Sahel, J. A., Fabre, M., Simonutti, M., Dreyfus, H., and Picaud, S. (1999). Retinitis pigmentosa: rod photoreceptor rescue by a calcium-channel blocker in the rd mouse. *Nat. Med.* 5, 1183–1187. doi: 10.1038/13508
- Gargini, C., Belfiore, M. S., Bisti, S., Cervetto, L., Valter, K., and Stone, J. (1999). The impact of basic fibroblast growth factor on photoreceptor function and morphology. *Invest. Ophthalmol. Vis. Sci.* 40, 2088–2099.
- Gargini, C., Bisti, S., Demontis, G. C., Valter, K., Stone, J., and Cervetto, L. (2004). Electroretinogram changes associated with retinal upregulation of trophic factors: observations following optic nerve section. *Neuroscience* 126, 775–783. doi: 10.1016/j.neuroscience.2004.04.028
- Gautam, V., Rand, D., Hanein, Y., and Narayan, K. S. (2014). A polymer optoelectronic interface provides visual cues to a blind retina. *Adv. Mater.* 26, 1751–1756. doi: 10.1002/adma.201304368
- Gerding, H., Benner, F. P., and Taneri, S. (2007). Experimental implantation of epiretinal retina implants (EPI-RET) with an IOL-type receiver unit. *J. Neural. Eng.* 4, S38–S49. doi: 10.1088/1741-2560/4/1/S06
- Ghezzi, D., Antognazza, M. R., Dal Maschio, M., Lanzarini, E., Benfenati, F., and Lanzani, G. (2011). A hybrid bioorganic interface for neuronal photoactivation. *Nat. Commun.* 2:166. doi: 10.1038/ncomms1164
- Ghezzi, D., Antognazza, M. R., Maccarone, R., Bellani, S., Lanzarini, E., Martino, N., et al. (2013). A polymer optoelectronic interface restores light sensitivity in blind rat retinas. *Nat. Photonics* 7, 400–406. doi: 10.1038/nphoton.2013.34
- Hartong, D. T., Berson, E. L., and Dryja, T. P. (2006). Retinitis pigmentosa. *Lancet* 368, 1795–1809. doi: 10.1016/S0140-6736(06)69740-7
- Hendrickson, A., and Hicks, D. (2002). Distribution and density of medium- and short-wavelength selective cones in the domestic pig retina. *Exp. Eye Res.* 74, 435–444. doi: 10.1016/exer.2002.1181
- Hochmann, S., Kaslin, J., Hans, S., Weber, A., Machate, A., Geffarth, M., et al. (2012). Fgf signaling is required for photoreceptor maintenance in the adult zebrafish retina. *PLoS One* 7:e30365. doi: 10.1371/journal.pone.0030365
- Humayun, M. S., Dorn, J. D., da Cruz, L., Dagnelie, G., Sahel, J. A., Stanga, P. E., et al. (2012). Interim results from the international trial of Second Sight's visual prosthesis. *Ophthalmology* 119, 779–788. doi: 10.1016/j.optha.2011.09.028
- Kim, G. H., Kim, H. II, Paik, S.-S., Jung, S. W., Kang, S., and Kim, I.-B. (2016). Functional and morphological evaluation of blue light-emitting diode-induced retinal degeneration in mice. *Graefes Arch. Clin. Exp. Ophthalmol.* 254, 705–716. doi: 10.1007/s00417-015-3258-x
- LaVail, M. M., and Battelle, B. A. (1975). Influence of eye pigmentation and light deprivation on inherited retinal dystrophy in the rat. *Exp. Eye Res.* 21, 167–192. doi: 10.1016/0014-4835(75)90080-9
- Lee, J. E., Liang, K. J., Fariss, R. N., and Wong, W. T. (2008). Ex vivo dynamic imaging of retinal microglia using time-lapse confocal microscopy. *Investig. Ophthalmol. Vis. Sci.* 49, 4169–4176. doi: 10.1167/iovs.08-2076
- Leveillard, T., and Sahel, J. A. (2010). Rod-derived cone viability factor for treating blinding diseases: from clinic to redox signaling. *Sci. Transl. Med.* 2:26s16. doi: 10.1126/scitranslmed.3000866
- Lewis, G. P., and Fisher, S. K. (2003). Up-regulation of glial fibrillary acidic protein in response to retinal injury: its potential role in glial remodeling and a comparison to vimentin expression. *Int. Rev. Cytol.* 230, 263–290. doi: 10.1016/s0074-7696(03)30005-1
- Lorach, H., Goetz, G., Smith, R., Lei, X., Mandel, Y., Kamins, T., et al. (2015). Photovoltaic restoration of sight with high visual acuity. *Nat. Med.* 21, 476–482. doi: 10.1038/nm.3851
- Lu, Y. Z., Fernando, N., Natoli, R., Madigan, M., and Valter, K. (2018). 670nm light treatment following retinal injury modulates Muller cell gliosis: evidence from in vivo and in vitro stress models. *Exp. Eye Res.* 169, 1–12. doi: 10.1016/j.exer.2018.01.011
- Luna, G., Keeley, P. W., Reese, B. E., Linberg, K. A., Lewis, G. P., and Fisher, S. K. (2016). Astrocyte structural reactivity and plasticity in models of retinal detachment. *Exp. Eye Res.* 150, 4–21. doi: 10.1016/j.exer.2016.03.027
- Maeda, A., Mandai, M., and Takahashi, M. (2019). Gene and induced pluripotent stem cell therapy for retinal diseases. *Annu. Rev. Genomics Hum. Genet.* 20, 201–216. doi: 10.1146/annurev-genom-083118-015043
- Mandel, Y., Goetz, G., Lavinsky, D., Huie, P., Mathieson, K., Wang, L., et al. (2013). Cortical responses elicited by photovoltaic subretinal prostheses exhibit similarities to visually evoked potentials. *Nat. Commun.* 4:1980. doi: 10.1038/ncomms2980
- Martino, N., Feyen, P., Porro, M., Bossio, C., Zucchetti, E., Ghezzi, D., et al. (2015). Photothermal cellular stimulation in functional bio-polymer interfaces. *Sci. Rep.* 5:8911. doi: 10.1038/srep08911
- Mathieson, K., Loudin, J., Goetz, G., Huie, P., Wang, L., Kamins, T. I., et al. (2012). Photovoltaic retinal prosthesis with high pixel density. *Nat. Photonics* 6, 391–397. doi: 10.1038/nphoton.2012.104
- Maya-Vetencourt, J. F., Ghezzi, D., Antognazza, M. R., Colombo, E., Mete, M., Feyen, P., et al. (2017). A fully organic retinal prosthesis restores vision in a rat model of degenerative blindness. *Nat. Mater.* 16, 681–689. doi: 10.1038/nmat4874
- Maya-Vetencourt, J. F., Manfredi, G., Mete, M., Colombo, E., Bramini, M., Di Marco, S., et al. (2020). Subretinally injected P3HT nanoparticles fully rescue vision in a rat model of retinal dystrophy. *Nat. Nanotechnol.* 15, 698–708. doi: 10.1038/s41565-020-0696-3
- Pearson, R. A., Barber, A. C., Rizzi, M., Hippert, C., Xue, T., West, E. L., et al. (2012). Restoration of vision after transplantation of photoreceptors. *Nature* 485, 99–103. doi: 10.1038/nature10997
- Rashid, K., Akhtar-Schaefer, I., and Langmann, T. (2019). Microglia in retinal degeneration. *Front. Immunol.* 10:1975. doi: 10.3389/fimmu.2019.01975
- Russell, S., Bennett, J., Wellman, J. A., Chung, D. C., Yu, Z. F., Tillman, A., et al. (2017). Efficacy and safety of voretigene neparvovec (AAV2-hRPE65v2) in patients with RPE65-mediated inherited retinal dystrophy: a randomised, controlled, open-label, phase 3 trial. *Lancet* 390, 849–860. doi: 10.1016/S0140-6736(17)31868-8
- Rutar, M., Provis, J. M., and Valter, K. (2010). Brief exposure to damaging light causes focal recruitment of macrophages, and long-term destabilization of photoreceptors in the albino rat retina. *Curr. Eye Res.* 35, 631–643. doi: 10.3109/02713681003682925
- Sannita, W. G., Acquaviva, M., Ball, S. L., Belli, F., Bisti, S., Bidoli, V., et al. (2004). Effects of heavy ions on visual function and electrophysiology of rodents: the ALTEA-MICE project. *Adv. Space Res.* 33, 1347–1351. doi: 10.1016/j.asr.2003.11.007
- Scholl, H. P., Strauss, R. W., Singh, M. S., Dalkara, D., Roska, B., Picaud, S., et al. (2016). Emerging therapies for inherited retinal degeneration. *Sci. Transl. Med.* 8:368rv366. doi: 10.1126/scitranslmed.aaf2838
- Simunovic, M. P., Shen, W., Lin, J. Y., Protti, D. A., Lisowski, L., and Gillies, M. C. (2019). Optogenetic approaches to vision restoration. *Exp. Eye Res.* 178, 15–26. doi: 10.1016/j.exer.2018.09.003
- Stingl, K., Bartz-Schmidt, K. U., Besch, D., Braun, A., Bruckmann, A., Gekeler, F., et al. (2013). Artificial vision with wirelessly powered subretinal electronic implant alpha-IMS. *Proc. Biol. Sci.* 280:20130077. doi: 10.1098/rspb.2013.0077

- Valter, K., Bisti, S., Gargini, C., Di Loreto, S., Maccarone, R., Cervetto, L., et al. (2005). Time course of neurotrophic factor upregulation and retinal protection against light-induced damage after optic nerve section. *Invest. Ophthalmol. Vis. Sci.* 46, 1748–1754. doi: 10.1167/iops.04-0657
- Valter, K., van Driel, D., Bisti, S., and Stone, J. (2002). FGFR1 expression and FGFR1-FGF-2 colocalisation in rat retina: sites of FGF-2 action on rat photoreceptors. *Growth Factors* 20, 177–188. doi: 10.1080/0897719021000057617
- Ventrella, D., Dondi, F., Barone, F., Serafini, F., Elmi, A., Giunti, M., et al. (2017). The biomedical piglet: establishing reference intervals for haematology and clinical chemistry parameters of two age groups with and without iron supplementation. *BMC Vet. Res.* 13:23. doi: 10.1186/s12917-017-0946-2
- Walsh, N., Valter, K., and Stone, J. (2001). Cellular and subcellular patterns of expression of bFGF and CNTF in the normal and light stressed adult rat retina. *Exp. Eye Res.* 72, 495–501. doi: 10.1006/exer.2000.0984
- Walter, P., Kisvarday, Z. F., Gortz, M., Altheheld, N., Rossler, G., Stieglitz, T., et al. (2005). Cortical activation via an implanted wireless retinal prosthesis. *Invest. Ophthalmol. Vis. Sci.* 46, 1780–1785. doi: 10.1167/iops.04-0924
- Wong, W. L., Su, X., Li, X., Cheung, C. M., Klein, R., Cheng, C. Y., et al. (2014). Global prevalence of age-related macular degeneration and disease burden projection for 2020 and 2040: a systematic review and meta-analysis. *Lancet Glob. Health* 2, e106–e116. doi: 10.1016/S2214-109X(13)70145-1
- Wright, A. F., Chakarova, C. F., Abd El-Aziz, M. M., and Bhattacharya, S. S. (2010). Photoreceptor degeneration: genetic and mechanistic dissection of a complex trait. *Nat. Rev. Genet.* 11, 273–284. doi: 10.1038/nrg2717
- Xiao, M., McLeod, D., Cranley, J., Williams, G., and Boulton, M. (1999). Growth factor staining patterns in the pig retina following retinal laser photocoagulation. *Br. J. Ophthalmol.* 83, 728–736. doi: 10.1136/bjo.83.6.728
- Xiao, M., Sastry, S. M., Li, Z. Y., Possin, D. E., Chang, J. H., Klock, I. B., et al. (1998). Effects of retinal laser photocoagulation on photoreceptor basic fibroblast growth factor and survival. *Invest. Ophthalmol. Vis. Sci.* 39, 618–630.
- Yanai, D., Weiland, J. D., Mahadevappa, M., Greenberg, R. J., Fine, I., and Humayun, M. S. (2007). Visual performance using a retinal prosthesis in three subjects with retinitis pigmentosa. *Am. J. Ophthalmol.* 143, 820–827. doi: 10.1016/j.ajo.2007.01.027
- Zhang, S., Wu, M., Peng, C., Zhao, G., and Gu, R. (2017). GFAP expression in injured astrocytes in rats. *Exp. Ther. Med.* 14, 1905–1908. doi: 10.3892/etm.2017.4760
- Zrenner, E., Bartz-Schmidt, K. U., Benav, H., Besch, D., Bruckmann, A., Gabel, V. P., et al. (2011). Subretinal electronic chips allow blind patients to read letters and combine them to words. *Proc. Biol. Sci.* 278, 1489–1497. doi: 10.1098/rspb.2010.1747

**Conflict of Interest:** The P3HT material studied in this paper is subject of the US patent application US 16/005248 ‘Eye-injectable polymeric nanoparticles and method of use therefor’ by Istituto Italiano di Tecnologia and Ospedale Sacrocuore Don Calabria, with JM-V, MM, GP, FaB, and GL as inventors.

The remaining authors declare that the research was conducted in the absence of any commercial or financial relationships that could be construed as a potential conflict of interest.

Copyright © 2020 Maya-Vetencourt, Di Marco, Mete, Di Paolo, Ventrella, Barone, Elmi, Manfredi, Desii, Sannita, Bisti, Lanzani, Pertile, Bacci and Benfenati. This is an open-access article distributed under the terms of the Creative Commons Attribution License (CC BY). The use, distribution or reproduction in other forums is permitted, provided the original author(s) and the copyright owner(s) are credited and that the original publication in this journal is cited, in accordance with accepted academic practice. No use, distribution or reproduction is permitted which does not comply with these terms.



# *In vitro* Label Free Raman Microspectroscopic Analysis to Monitor the Uptake, Fate and Impacts of Nanoparticle Based Materials

Hugh J. Byrne<sup>1\*</sup>, Franck Bonnier<sup>2</sup>, Esen Efeoglu<sup>1</sup>, Caroline Moore<sup>1</sup> and Jennifer McIntyre<sup>1</sup>

<sup>1</sup> FOCAS Research Institute, Technological University Dublin, Dublin, Ireland, <sup>2</sup> UFR Sciences Pharmaceutiques, EA 6295 Nanomédicaments et Nanosondes, Université de Tours, Tours, France

## OPEN ACCESS

### Edited by:

Valentina Castagnola,  
Italian Institute of Technology (IIT), Italy

### Reviewed by:

Satoshi Arai,  
Kanazawa University, Japan  
Marco P. Monopoli,  
Royal College of Surgeons in Ireland,  
Ireland

Michele Dipalo,  
Italian Institute of Technology (IIT), Italy

### \*Correspondence:

Hugh J. Byrne  
hugh.byrne@tudublin.ie

### Specialty section:

This article was submitted to  
Nanobiotechnology,  
a section of the journal  
Frontiers in Bioengineering and  
Biotechnology

**Received:** 27 March 2020

**Accepted:** 12 October 2020

**Published:** 29 October 2020

### Citation:

Byrne HJ, Bonnier F, Efeoglu E,  
Moore C and McIntyre J (2020)  
*In vitro* Label Free Raman  
Microspectroscopic Analysis  
to Monitor the Uptake, Fate  
and Impacts of Nanoparticle Based  
Materials.  
Front. Bioeng. Biotechnol. 8:544311.  
doi: 10.3389/fbioe.2020.544311

The continued emergence of nanoscale materials for nanoparticle-based therapy, sensing and imaging, as well as their more general adoption in a broad range of industrial applications, has placed increasing demands on the ability to assess their interactions and impacts at a cellular and subcellular level, both in terms of potentially beneficial and detrimental effects. Notably, however, many such materials have been shown to interfere with conventional *in vitro* cellular assays that record only a single colorimetric end-point, challenging the ability to rapidly screen cytological responses. As an alternative, Raman microspectroscopy can spatially profile the biochemical content of cells, and any changes to it as a result of exogenous agents, such as toxicants or therapeutic agents, in a label free manner. In the confocal mode, analysis can be performed at a subcellular level. The technique has been employed to confirm the cellular uptake and subcellular localization of polystyrene nanoparticles (PSNPs), graphene and molybdenum disulfide micro/nano plates (MoS<sub>2</sub>), based on their respective characteristic spectroscopic signatures. In the case of PSNPs it was further employed to identify their local subcellular environment in endosomes, lysosomes and endoplasmic reticulum, while for MoS<sub>2</sub> particles, it was employed to monitor subcellular degradation as a function of time. For amine functionalized PSNPs, the potential of Raman microspectroscopy to quantitatively characterize the dose and time dependent toxic responses has been explored, in a number of cell lines. Comparing the responses to those of poly (amidoamine) nanoscale polymeric dendrimers, differentiation of apoptotic and necrotic pathways based on the cellular spectroscopic responses was demonstrated. Drawing in particular from the experience of the authors, this paper details the progress to date in the development of applications of Raman microspectroscopy for *in vitro*, label free analysis of the uptake, fate and impacts of nanoparticle based materials, *in vitro*, and the prospects for the development of a routine, label free high content spectroscopic analysis technique.

**Keywords:** Raman microspectroscopy, nanoparticles, *in vitro* cytotoxicity, polystyrene nanoparticles, poly(amidoamine) dendrimers, molybdenum disulphide nano plates, high content spectroscopic analysis



## INTRODUCTION

Nanoscience and technology are novel, rapidly emerging fields which encompass the design, production, and exploitation of novel structures, processes and devices at the scale of 1–100 nm. Numerous applications based on nanoparticles have already been marketed, in products as diverse as industrial lubricants, advanced tires, self-cleaning glass, paints, semiconductor devices, medicines, cosmetics, sunscreens, nutraceuticals and food (Nano tech project, 2020). The international nanomaterials market was estimated to be \$14,741.6 million in 2015, and is expected to increase to \$55,016 million by 2022 (Allied market research, 2020). Specifically in the field of biomedicine, by 2015, nanotechnology had already created a 96.9 billion \$US market (Pattni et al., 2015) and is projected to continue to have a significant impact. Polymeric micro and nanoparticles (NPs) have been explored for a wide range of medical applications in diagnosis, tissue engineering, and as drug delivery vehicles (Storrie and Mooney, 2006; Ito et al., 2008; Naha et al., 2008, 2009; Gao et al., 2016; Thaxton et al., 2016). Understanding the interface of these functional biomaterials with living systems and tailoring their capacity to target and penetrate cells is a short term challenge, which, if met, could revolutionize targeted drug and nutrient delivery, as well as other therapeutic strategies. On the other hand, major concerns have been raised regarding the possible human and environmental effects of accidental, large scale, NP exposure, in the short and long term. Profiling the interactions of nano particulate materials with human cells, their uptake and fate, as well as the cellular responses induced, is therefore of paramount importance (Love et al., 2012; Anguissola et al., 2014; Ajdary et al., 2018).

Among the main challenges is to detect and identify nanoparticles that have traversed the cell membrane, and to monitor their trafficking and fate within the cell. One of the most commonly employed methods to do so, is that of confocal fluorescence microscopy, applied to imaging cells exposed to fluorescently labeled NPs *in vitro* (Roy et al., 2005; Cang et al., 2007; Naha et al., 2010a). Notably, however, not all NPs can be readily fluorescently labeled, and furthermore, it has been demonstrated that the label can be released into the surrounding cellular environment, such that the fluorescence distribution within the cell does not necessarily represent the presence or spatial distribution of the NPs (Suh et al., 1998; Yin Win and Feng, 2005; Salvati et al., 2011). It is also unclear whether the transport of NPs, particularly smaller ones, fluorescently labeled with anionic groups, is the same as that of their unlabeled counterparts. As an example, extrinsic labeling of bovine serum albumin with fluorescein-5-isothiocyanate has been reported to change its adsorption and diffusion behavior (Gajraj and Ofoli, 2000). Transmission Electron Microscopy (TEM) is also commonly used to visualize NPs and their surroundings within cells, but a considerable amount of sample processing (fixing and ultramicrotoming) is required, and, in order to visualize the NPs, they must have sufficient electronic contrast to the local environment of the cell (Davoren et al., 2007; Shapero et al., 2011). Ideally, techniques to localize and identify NPs internalized in cells, should be based on

their intrinsic chemical composition, rather than electronic contrast or the properties of extrinsic labels. Identification of the local subcellular environment of NPs in the cytoplasm (e.g., endosomes, lysosomes, endoplasmic reticulum) or nucleus could further advance the understanding of their intracellular trafficking and interaction mechanisms, and the resultant impact on the metabolism of the cell. Such impacts are commonly and routinely screened *in vitro* by conventional cytotoxicity assays, such as the colorimetric dye-based assays Alamar Blue, Neutral Red, MTT, etc, which can provide indications of impact on cell viability, proliferative capacity, metabolic activity, endosomal/lysosomal and mitochondrial activity (Mukherjee et al., 2010b). However, each assay reports on a single endpoint, such that multiple assays are required, at multiple time points, and doses. Furthermore, there have been numerous reports of false positive results of such assays, due to the extracellular interaction of the NPs with the *in vitro* cell culture medium (Casey et al., 2007a, 2008), and with the molecular constituents of the colorimetric cytotoxicity assays themselves (Casey et al., 2007b), highlighting the need for alternative methodologies (Herzog et al., 2007).

As an alternative technique, label free Raman microspectroscopy can provide a holistic, real-time representation of the biochemistry of the whole cell, at subcellular levels, and has previously been employed for characterization of the biochemical evolution underpinning cell culture and mitosis (Boydston-White et al., 2006; Matthäus et al., 2006), as well as cell proliferation (Short et al., 2005), differentiation and activation (Nottingham et al., 2004; Ami et al., 2008; Pavillon et al., 2018), cellular adhesion (Meade et al., 2007), death (Gasparri and Muzio, 2003), and invasion (Liu et al., 2001).

The Raman effect was first described in Raman and Krishnan (1928) and the principles and underlying theory are described in numerous excellent textbooks, notably that of Long (2002). Based on inelastic scattering of light due to coupling of energy of incident photons with vibrations of target samples, Raman spectroscopy is well established for chemically fingerprinting materials, with applications in, for example, forensics and the pharmacological industry (Hodges and Akhavan, 1990; Kneipp et al., 1999; Vankeirsbilck et al., 2002; Edwards and Vandenabeele, 2016). Modern instruments typically couple a laser to a microscope, which focuses the source light and also collects the scattered radiation. The sample can be rastered to produce a map of the sample, in a similar way to a laser scanning fluorescence microscope. Raman microspectroscopy can also be performed at UV, visible, or near IR wavelengths in a confocal mode and can provide detail at sub micrometer resolution. In this context, instrumentally, Raman microspectroscopy is similar to Confocal Laser Scanning Microscopy, except that the chemical specificity derives from the analysis of the spectrum of the scattered light, dispersed by a diffraction element (e.g., grating). Similar to infrared vibrational spectroscopic analysis and imaging, the technique therefore has the advantage of being truly label-free, producing a spectrum which comprises contributions from each molecular bond, and is a “signature” or “fingerprint” which is characteristic of a material, or changes associated with a physical or chemical process. In complex samples,

notably biological cells or tissue, the spectroscopic signature incorporates characteristics of all constituent functional groups of lipids carbohydrates, proteins and nucleic acids (Byrne et al., 2010). A comparison of the techniques of Infrared and Raman spectroscopic imaging for biomedical applications is provided in Byrne et al. (2010). Notably, however, the Raman effect, is intrinsically weak, requiring the highly sensitive detection of Charge Coupled Detector arrays, and the features of the spectrum can often be swamped by fluorescence or stray light scattering (Byrne et al., 2010). Depending on the nature of the sample, and the desired signal to noise ratio, a single spectrum is typically accumulated over a period of seconds, and therefore a spatial map of a sample can take minutes or hours, depending on the desired area to be mapped, and sampling step size. Although time resolved Raman spectroscopy using pulsed laser sources can be utilized to study reaction mechanisms and correlations between molecular structure and reaction rates (Sahoo et al., 2011), commercial instruments typically use steady state conditions, but can measure the temporal evolution of a system by measuring at specific time points. More sophisticated variants, such as surface enhanced Raman scattering, and coherent Raman scattering can enhance the sensitivity of the technique, and will be discussed in more detail in section “In vitro toxicity assessment using Raman Microspectroscopy.”

Raman microspectroscopy has attracted increasing attention for biological characterization and biomedical applications, and specific protocols have been described (Butler et al., 2016). *In vitro* cellular analysis can be performed at subcellular level, of fixed or live cells, in 2D and/or 3D culture environments (Meade et al., 2010; Bonnier et al., 2011; Gargotti et al., 2018). Screening of multiple cell lines has demonstrated a remarkable reproducibility of the subcellular signatures, elucidating, for example, the role of the nucleolus in discriminating different cancer cell lines (Farhane et al., 2015b). The reproducibility of the signatures was seen to also extend to the comprehensive and systematic analysis of drug uptake and mechanisms of action (Farhane et al., 2015a, 2017a,b, 2018a,b; Szafraniec et al., 2016), radiotherapy (Meade et al., 2016; Roman et al., 2019) and nanoparticle toxicity (Dorney et al., 2012; Efeoglu et al., 2015, 2016, 2017a,b, 2018), demonstrating potential applications for high content analysis for pre-clinical drug screening and toxicological applications (Byrne et al., 2018).

Raman microspectroscopy potentially offers a label free, high content probe of NPs within cells, which can potentially analyze their local environment, their fate, and ultimately changes in the cellular metabolism which can be correlated with cytotoxic responses, oxidative stress, or inflammation. Illustrated with specific examples from the published work of the authors, this paper will present the principles and methodology of cellular and subcellular analysis using Raman microspectroscopy, and will detail some examples of multivariate chemometric data mining to identify the uptake and localization of NPs within cells, and to explore the spectroscopically fingerprint of the local environment of trafficking, or degradation, over time. The dose and time dependent evolution of spectroscopic signatures, and their biochemical origin, will be described, and correlated with conventional cytotoxicological approaches. As well as mechanisms

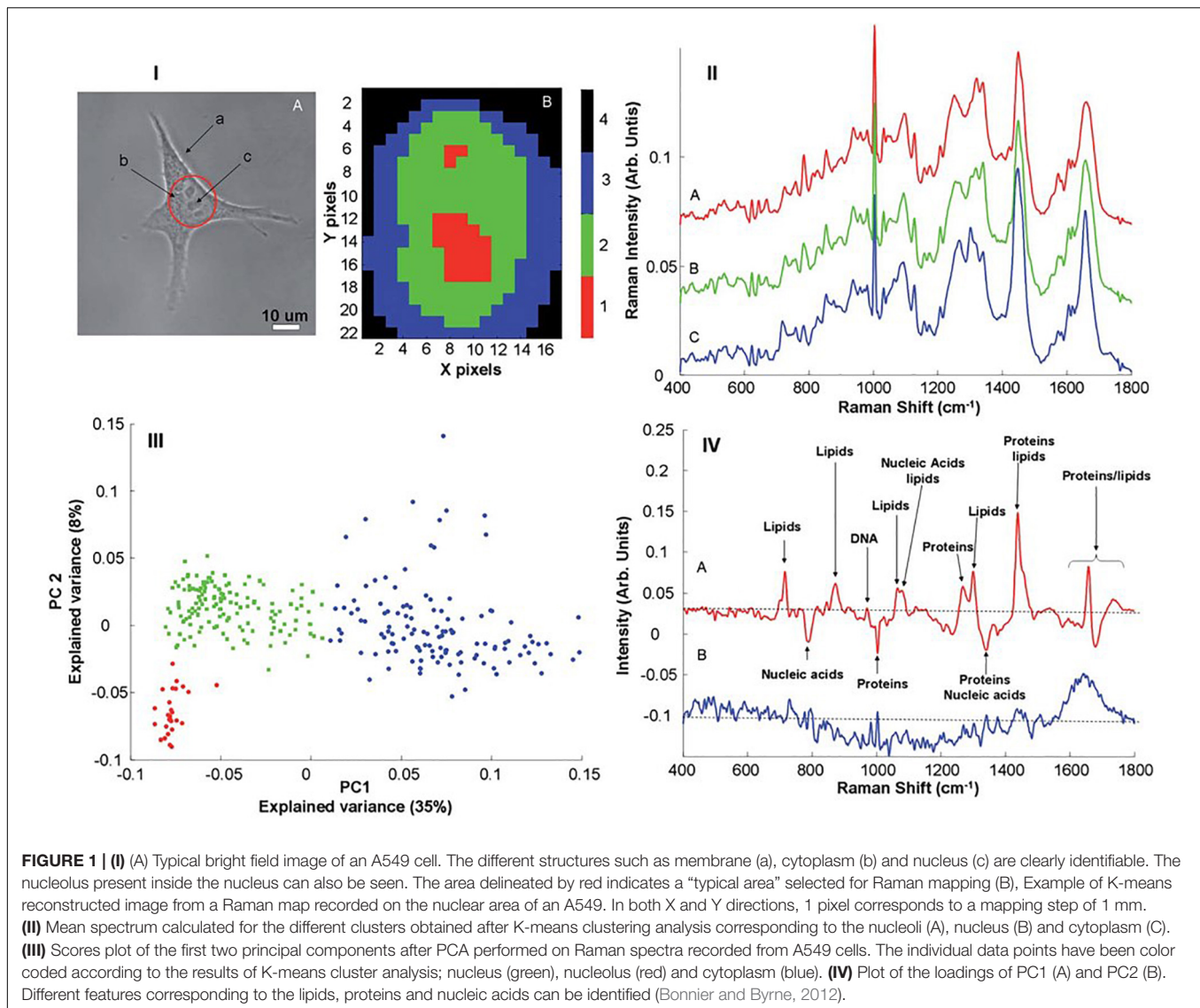
of acute cytotoxicological responses, genotoxic responses will also be explored.

## RAMAN MICROSCOPIC PROFILING OF CELLS

Raman microspectroscopic profiling of biological cells, *in vitro*, is typically performed by point mapping over a grid defined within the field of view of the objective. The cells can be profiled live, in the culture medium, although the presence of the dye phenol red can obscure the visual image, and so mapping in saline solution or phenol red free medium is often performed (Bonnier et al., 2010a). Measurement in immersion minimizes background scatter (Bonnier et al., 2011) and any photo-thermal degradation (Bonnier et al., 2012), and substrate contributions to the spectra can be avoided by culturing on 3D protein matrices such as collagen, such that high signal to noise/background spectra can be obtained, the background being the spectrum of water/medium (Bonnier et al., 2010b).

**Figure 1** shows examples of Raman microspectroscopic maps of an individual A549 human lung adenocarcinoma cell (Bonnier and Byrne, 2012). In the bright field image of **Figure 1(IA)**, the cell cytoplasm and nucleus are clearly visible, and nucleoli within the nuclear region can be identified. **Figure 1(IB)** shows a false color image of the same cell, after KMCA of the Raman spectroscopic data. A high degree of correspondence between the distribution of the clusters and the substructure of the cell can be clearly seen, and the nucleoli, nucleus and cytoplasm are associated with individual clusters. The spatial definition of the map is determined by the objective employed, and the mapping step size. The use of a 100x objective provides the maximum lateral resolution ( $\sim 1$   $\mu$ m) and provides visible images which elucidate the cell morphology. Decreasing the lateral step size from 1.5 to 0.75  $\mu$ m was seen to improve the definition of the subcellular structures (Dorney et al., 2012). Uzunbajakava et al. (2003) have reported that, using intervals 2–3 times smaller than the laser spot, optimal lateral sampling can be achieved, promising even higher definition of the subcellular features.

K-Means Clustering Analysis (KMCA) false color maps give a representation of the biochemical variability across the cell, each cluster representing regions of similar biochemical character. The biochemical information of each cluster is represented by its mean spectrum, in which characteristic bands of proteins, lipids, nucleic acids and carbohydrates can be identified. **Figure 1(II)** shows the mean spectra obtained from selected clusters of the KMCA image of **Figure 1(IB)** [nucleoli (A), nucleus (B), and cytoplasm (C)]. The characterization of live cells has been reported in a number of studies (Nottingham et al., 2003; Short et al., 2005; Nottingham and Hench, 2006; Swain et al., 2008; Bonnier et al., 2010a) and, assignments of the different peaks can be made, and are well cataloged in literature (Movasaghi et al., 2007). Differences between the mean spectra are subtle and not easily discernible, however, but can be better analyzed using Principal Components Analysis (PCA), by which the spectra of each individual cluster can be compared. **Figure 1(III)** shows a PCA scatter plot (PC 1 versus PC 2) for the spectra of the



clusters corresponding to the nucleus (green), nucleolus (red) and cytoplasm (blue). PC 1, representing 35% of the explained variance, indicates good discrimination between the spectra of the cytoplasm and those of the nuclear regions. The spectra of the two regions of the nucleus are partially differentiated by PC2, but can be more clearly discriminated in a pairwise analysis (Bonnier and Byrne, 2012).

The spectral loadings represent the variability described by a given PC, as a function of wavenumber, and are used to identify the key spectroscopic features which differentiate the respective clusters, which can in turn be associated with specific biochemical constituents of the cell. **Figure 1(IV)** shows the loading of PC1, which enables visualization of the spectral features responsible for discrimination between the cytoplasm and the nuclear regions. Positive contributions to the loading are associated with spectra which score positively according to the PC in the scatter plot, and vice versa for negative peaks (Bonnier and Byrne, 2012), and thus the features of the loading can be analyzed in terms

of reference spectra of known biomolecules. The prominence of, for example, DNA and RNA in the nucleus of the cell is clear, while lipidic features are stronger in the cytoplasm of the cell. It has been demonstrated that a pairwise PCA of datasets better facilitates the interpretation of the loadings, however, and enables differentiation of the subcellular nuclear regions based on nucleic acid content (Bonnier and Byrne, 2012).

Raman microspectroscopy, coupled with multivariate chemometric analysis, is clearly therefore a powerful, label free methodology for high content analysis of cells, with optical spatial resolution. However, a single cellular map can take anything between minutes to hours to complete (Bonnier et al., 2010a; Bonnier Knief et al., 2011), depending on the laser spot, step size and desired quality of signal, and, as a result, only a small proportion of the cell population is typically analyzed (Butler et al., 2016). In order to produce datasets of a larger cell population, a “point spectra” approach is commonly adopted, whereby the subcellular regions of nucleolus, nucleus and



cytoplasm of multiple cells in a cell culture are sampled, and subsequently data mined using multivariate analysis. Erring on the side of prolonged acquisition times for high quality spectral analysis, the cells are typically formalin fixed and air dried (Hobro and Smith, 2017). This methodology has been employed, for example, to understand the subcellular differentiation of lung cancer (Farhane et al., 2015b) and oral cancer cell lines (Carvalho et al., 2015), and to monitor the subcellular accumulation of, binding interactions, and subsequent cellular response to chemotherapeutic agents (Farhane et al., 2015a, 2017a,b, 2018c).

## LOCALIZATION AND TRAFFICKING OF NANOPARTICLES IN CELLS

The analysis protocols of Section 2 were employed to similarly profile A549 cells exposed to non-toxic polystyrene nanoparticles (PSNPs). In addition to clusters of the nucleoli (cluster 3), nucleus (cluster 6) and cytoplasm (clusters 1,2,4,8,9,10), KMCA identifies a spectral cluster (cluster 5) which has strong features which are characteristic of polystyrene, as shown in **Figure 2**. The spectral features of this cluster unambiguously confirm the localization of the NPs within the cytoplasmic and perinuclear region of the cell (Dorney et al., 2012). Notably, the mean spectrum of cluster 5 clearly also contains biological contributions, and so the analysis can potentially provide information about the local cellular environment of the NPs, and the *in vitro*, intra cellular trafficking process.

Efeoglu et al. (2015) using confocal laser scanning fluorescence microscopy and organelle staining, analyzed the uptake and localization of similar non-toxic carboxylated PSNPs in A549 cells, as a function of exposure time, confirming colocalization in endosomes (4 h), lysosomes (8 h), and endoplasmic reticulum (24 h). In parallel, Raman microspectroscopic profiling of multiple cells in a Raman mapping approach, combined with KMCA and PCA, was used to differentiate the local biochemical environment of the NPs at the different timepoints, and identify the spectroscopic signatures of the associated subcellular organelles (**Figure 3**). The contribution of the spectrum of the PSNPs themselves was calculated using a Least Squares analysis, and subtracted (Efeoglu et al., 2015).

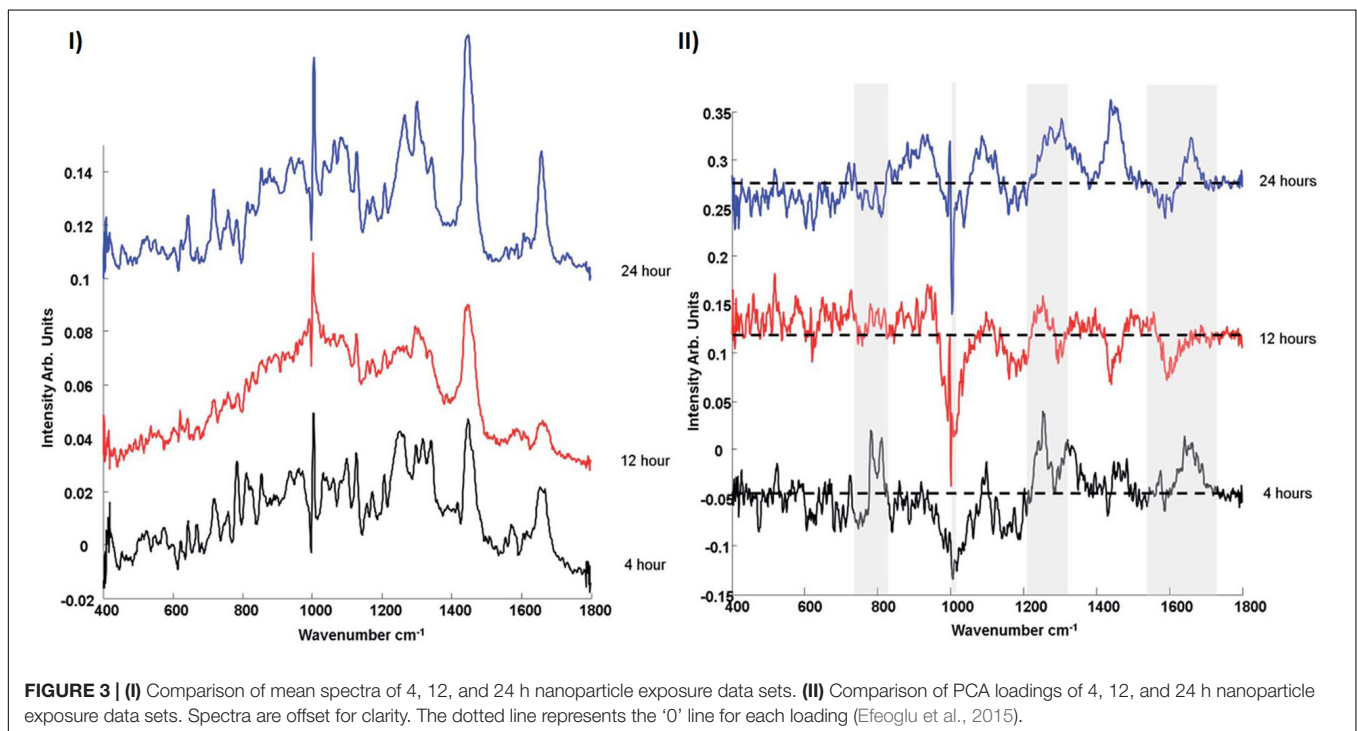
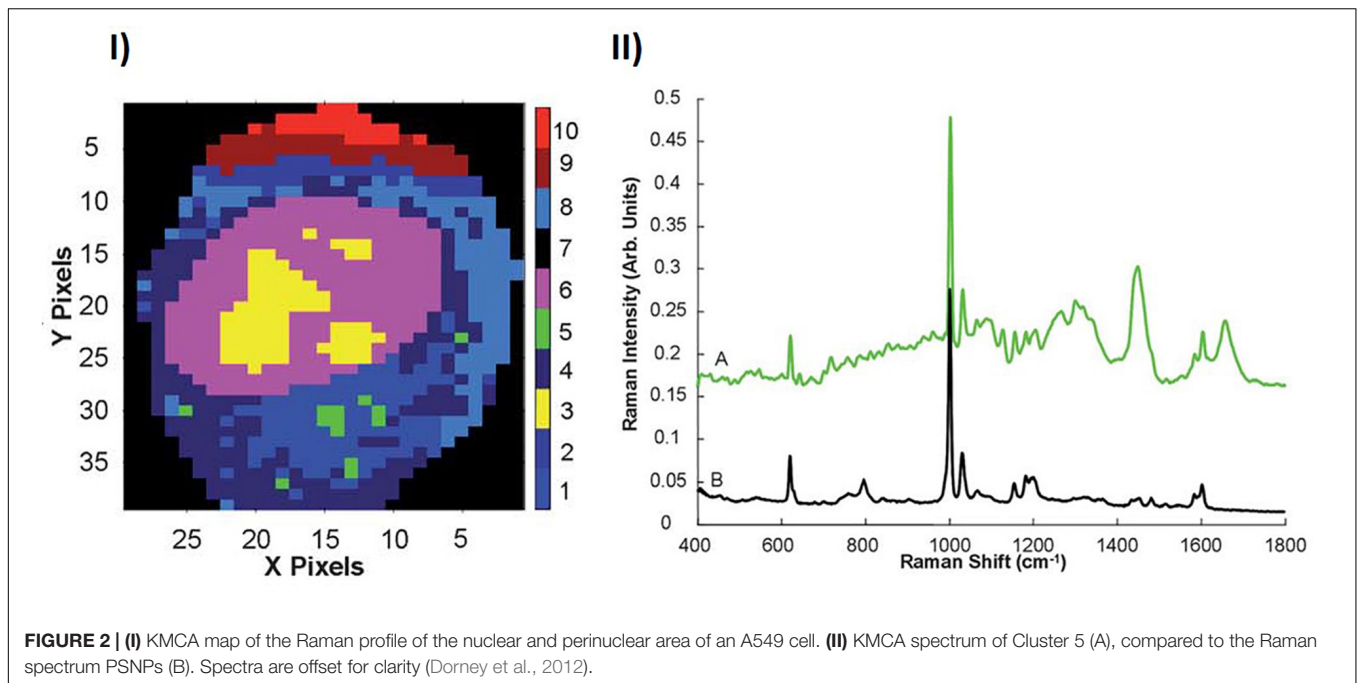
PSNPs are initially endocytosed by cells (Salvati et al., 2011), whereupon they are bound by membrane derived endosomal vesicles. After 4 h particle exposure, compared to spectra of 12 and 24 h particle exposure, the Raman spectrum is seen to exhibit strong bands attributed to proteins, within the range of 700–900  $\text{cm}^{-1}$ , which exist naturally in membrane structures (Terasaki and Jaffe, 1991; Notingher and Hench, 2006; Talari et al., 2015). Bands related to phospholipids ( $\sim 1080$ ,  $\sim 1656$   $\text{cm}^{-1}$ ) and phosphatidylcholine and membrane lipids ( $\sim 790$ ,  $\sim 718$   $\text{cm}^{-1}$ ) are consistent with membrane derived vesicles. Early endosomes are internally trafficked within the cytoplasm and are engulfed by lysosomes, which originate from the golgi apparatus and endoplasmic reticulum, and therefore show similar properties (Watson et al., 2005). The Raman signature which characterizes the 12 h exposure data set is similarly dominated by features of proteins and lipids, although

the their signatures are significantly different to those which characterize the early endosomes. Prominent bands related to phosphatidylinositol (519  $\text{cm}^{-1}$ ), phosphatidylethanolamine (759  $\text{cm}^{-1}$ ), C–C stretch of lipids (1130  $\text{cm}^{-1}$ ),  $\text{CH}_2$  twist of lipids (1304  $\text{cm}^{-1}$ ) and  $\text{CH}_{\text{def}}$  of lipids (1439  $\text{cm}^{-1}$ ) are observed. Compared to the 4 h, endosomal spectrum, the protein derived features in the range 700–900  $\text{cm}^{-1}$  disappear, whereas clear, protein related differences can now be observed in the amide I ( $\sim 1600$ – $1700$   $\text{cm}^{-1}$ ) and amide III ( $\sim 1200$ – $1300$   $\text{cm}^{-1}$ ) regions. PSNPs containing lysosomes are trafficked to the golgi apparatus or endoplasmic reticulum (Chang et al., 2008; Dorney et al., 2012). After 24 h, the mean spectrum, associated with the endoplasmic reticulum, is characterized by prominent bands of nucleic acids ( $\sim 785$   $\text{cm}^{-1}$  and 810  $\text{cm}^{-1}$ ), consistent with the presence of RNA required for protein synthesis within the perinuclear region and granular endoplasmic reticulum. Generally, the characteristic spectral profile is consistent with the protein lipid and rich nature of the endoplasmic reticulum.

Other studies have demonstrated the use of Raman imaging to visualize the uptake of nanoparticles, such as metallacarborane aggregates into single cells (Schwarze et al., 2020), and magnetic nanoparticles into erythrocytes (Soler et al., 2007). Carotene, an extremely strong Raman scatterer, was employed as a surface coating of carbon nanoparticles, such that their uptake could be readily visualized using Raman mapping of human melanoma and breast cancer cells, *in vitro* (Misra et al., 2016). Chernenko et al. (2009) also employed Raman microspectroscopy to monitor the intracellular delivery of two biodegradable nanoparticle systems, commonly used as drug delivery vehicles, poly( $\epsilon$ -caprolactone) and poly(lactic-co-glycolic acid), and their subcellular degradation patterns. The nanoparticles were identified in the subcellular environment of lysosomes, and the degradation pathway was mapped by shifts and intensity changes of the characteristic spectral profiles of the materials.

Label-free Raman micro-spectroscopy was similarly employed to confirm the intracellular localization and fate of molybdenum disulfide ( $\text{MoS}_2$ ) submicron plates, in differentiated THP-1 macrophage like cells, *in vitro* (Moore et al., 2020a). The field of 2D materials technology has significantly expanded since the isolation and characterization of monolayer graphene in 2004 (Novoselov et al., 2004) and the emergence of techniques for liquid phase exfoliation (Smith et al., 2011). It is critical, at this juncture, to understand how such materials interact with cells following exposure, and the influence of the cellular micro-environment on the physico-chemical properties of these particles. Macrophages play a crucial role in recognizing a foreign threat, causing a cascade of events designed to eliminate them from their environment and to maintain homeostasis (Gordon, 2007). Using sub-lethal doses (Moore et al., 2017), internalized  $\text{MoS}_2$  submicron plates were clearly identifiable in THP-1 cells by their characteristic Raman spectroscopic features, the  $\text{E}^{1}_{2g}$  (380  $\text{cm}^{-1}$ ) and  $\text{A}^1_g$  (407  $\text{cm}^{-1}$ ) peaks (Moore et al., 2020a). Using a combination of single cell mapping and multicellular point spectral Raman microspectroscopic analysis, three distinct local environments of the particulate material were identified in untreated THP-1 cells, and 4, 24, and 72 h after a 4 h exposure





to MoS<sub>2</sub> submicron plates, in a pulse chase approach. In all cases, white light microscopic images revealed that the cells were rich in vesicles of several microns diameter particularly in the perinuclear region (**Figure 4A**). Analysis of the spectra of the prominent vesicles in multiple cells, in a point spectra approach, indicated that those of untreated macrophage cultures were characterized by spectroscopic features of sphingomyelin lipids, normally prominent in the cell membrane, and are therefore

associated with the transport of the membrane lipid from the endoplasmic reticulum. In contrast, those of cells 4 and 24 h after exposure to MoS<sub>2</sub> were predominantly characterized by signatures of phosphatidyl lipids, and are therefore associated with phagosomes and/or phagolysosomes. Seventy two hours after exposure the population of intracellular lipidic vesicles was again dominated by those of a sphingomyelin character, indicating a return to homeostasis (Moore et al., 2020b).

Mapping individual cells, 4, 24, and 72 h after exposure, in addition to vesicles with prominent features of phosphatidyl lipids, another species of vesicle, with strong signatures of lysozyme, was identified (Moore et al., 2020a). Using Factor Analysis (Figure 4B), different spectral signatures of MoS<sub>2</sub> were identified (Figures 4Cii,Dii,Eii) distributed differently throughout the cell (Figures 4Ci,Di,Ei). The spectral profiles of the second two factors (Figures 4Dii,Eii) are consistent with those of degraded MoS<sub>2</sub>, using PCA, were associated with the phosphatidyl environment, after 24 h, but not in the lysosomal, suggesting that the activity of the enzyme is inhibited by the lipopolysaccharide (LPS) contaminant, previously identified on the surface of particulate material (Moore et al., 2017).

## IN VITRO TOXICITY ASSESSMENT USING RAMAN MICROSCOPY

The potential of Raman microspectroscopy to probe the *in vitro* cytotoxicity to nanoparticle exposure was first explored by Knief et al. (2009), for the example of exposure of A549 cells to single walled carbon nanotubes. Peak ratio analysis of modes of lipidic CH<sub>2</sub> deformation ( $\sim 1302\text{ cm}^{-1}$ ) as well as DNA bases guanine, adenine and thymine ( $\sim 1287$  and  $\sim 1338\text{ cm}^{-1}$ ) versus the amide III band ( $\sim 1238\text{ cm}^{-1}$ ), demonstrated a dose dependent response which correlated with previous toxicological studies (Davoren et al., 2007). Notably, these modes had previously been employed in a study of HgCl<sub>2</sub> toxicity to human keratinocytes, *in vitro* (Perna et al., 2007). PCA was employed to elucidate the dose dependent cellular response and associated characteristic spectroscopic signatures. To further illustrate the potential of Raman microspectroscopy in this field, partial least squares regression analysis combined with genetic algorithm feature selection were employed to demonstrate that the end points of the clonogenic assay (Herzog et al., 2007), as a measure of the toxic response, can be predicted from the Raman spectra of cells exposed to undetermined doses, potentially eliminating the requirement for time consuming and costly cytotoxicological assays. However, similar studies demonstrated that there was no evidence that the nanotubes were internalized in the cells (Davoren et al., 2007), and that an indirect toxicity, due to medium depletion (Casey et al., 2007a) was the most likely cause of the cellular response.

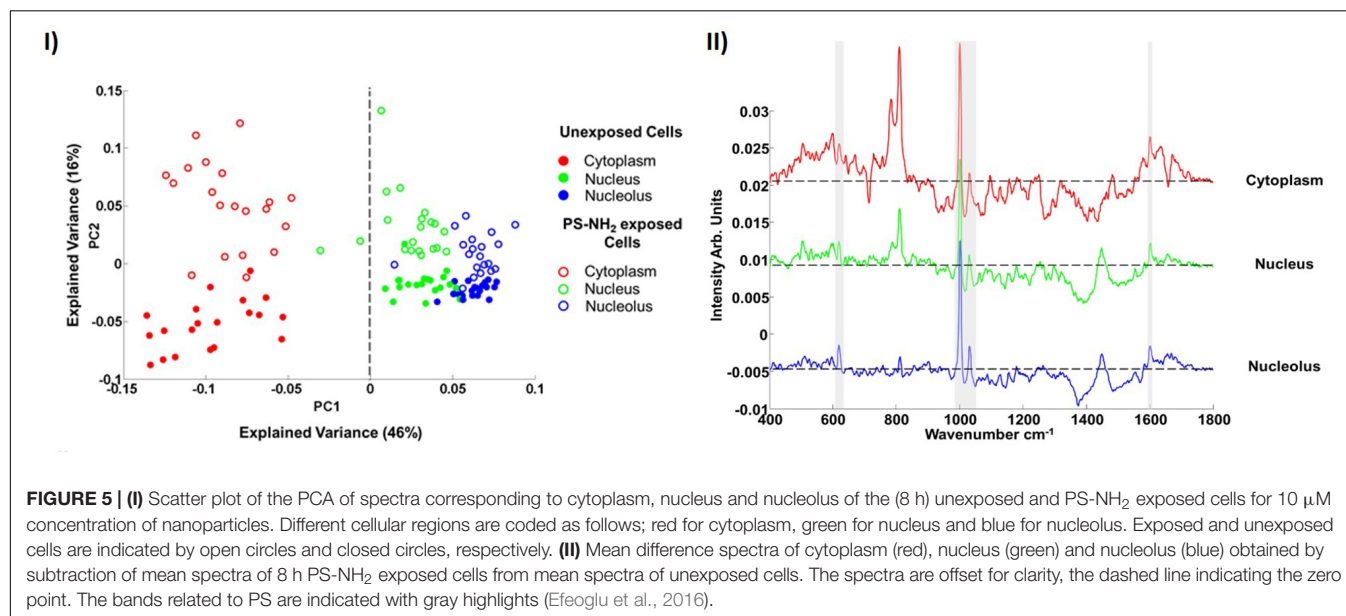
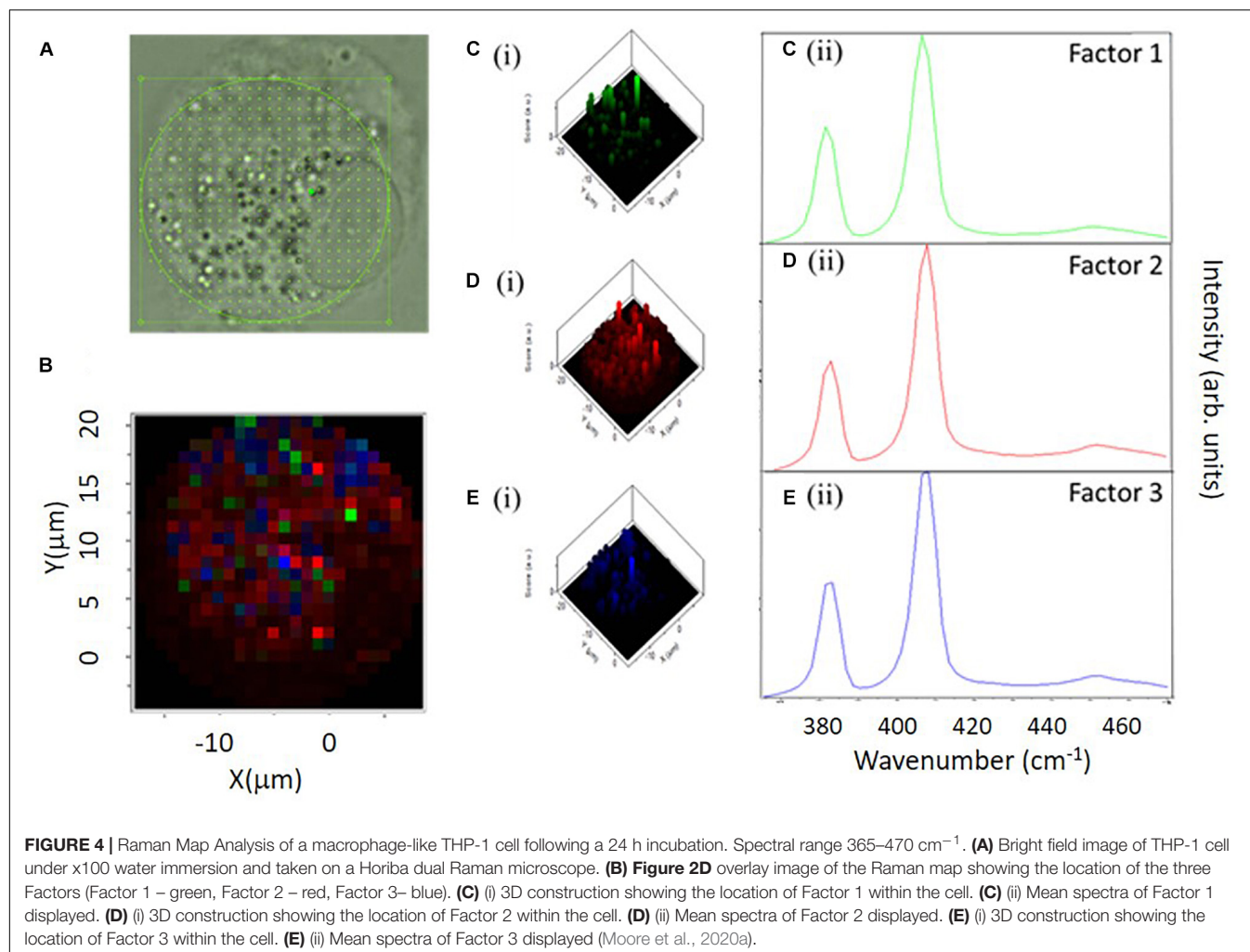
PSNPs serve as a model for NP uptake in cells (Anguissola et al., 2014), and can be fluorescently labeled for tracking and organelle co-localization studies (Salvati et al., 2011; Efeoglu et al., 2015). While their carboxylated counterparts are non-toxic, amine functionalized PSNPs (PS-NH<sub>2</sub>) elicit a well documented, dose and time dependent *in vitro* toxic response, associated with oxidative stress, and inflammatory cascades, leading to apoptosis (Anguissola et al., 2014; Maher et al., 2014). Using the protocol of point spectral analysis (cytoplasm, nucleus, nucleoli) of control and exposed cells, the dose and time dependent responses have also been monitored using Raman microspectroscopy, demonstrating the potential of the technique as a label free high content screening protocol (Efeoglu et al., 2016).

After an 8 h exposure to a 10  $\mu\text{M}$  concentration of nanoparticles, the spectra of each subcellular region of the cells can be differentiated, using PCA, from those of the control cells, as shown Figure 5I. Although subcellular vesicles are not specifically targeted, the mean difference spectra (Figure 5I) clearly show features of the PS-NH<sub>2</sub>, which are excluded from the analysis. The PCA loading (Figure 5II) also show clear biological signatures, particularly in the cytoplasmic region, which can be associated with the cytotoxic response, and ultimately correlated with conventional *in vitro* cytotoxicity assays.

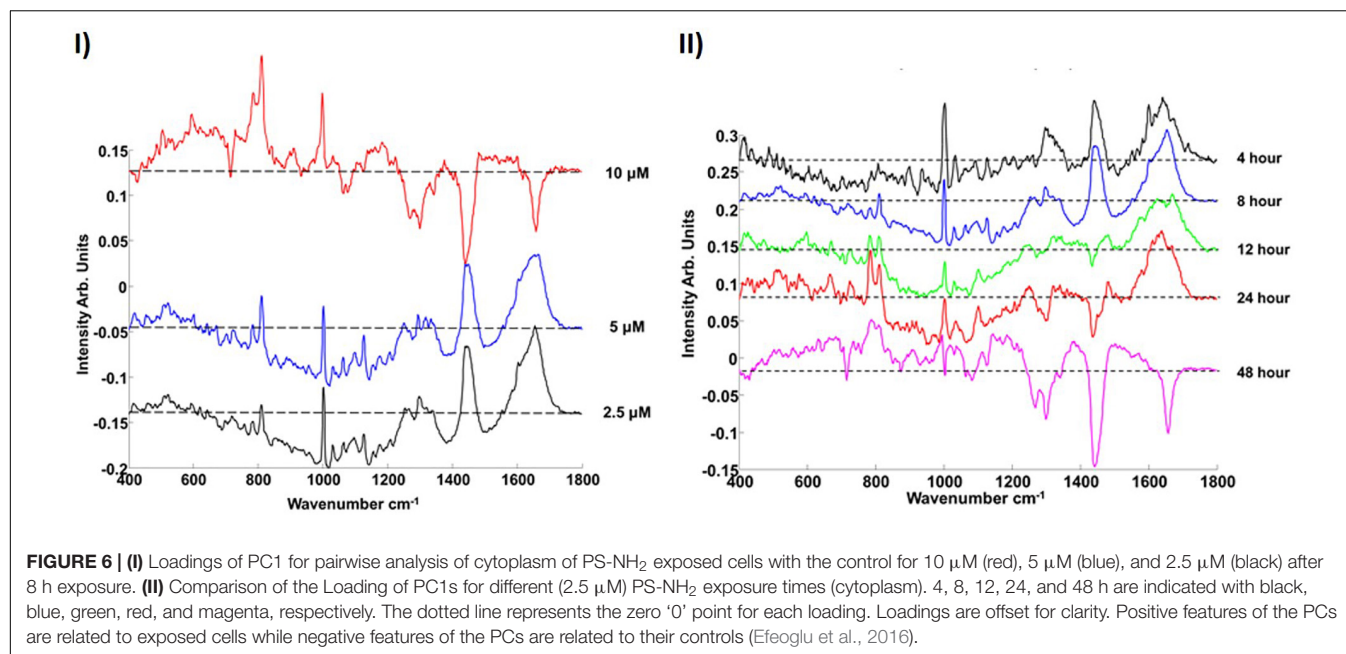
In the dose and time dependent responses of A549 cells to PS-NH<sub>2</sub> exposure, the most prominent spectral marker which differentiates the cytoplasm of the control and exposed cells is seen to be the a 'doublet' of peaks at 785 and 810  $\text{cm}^{-1}$  (Figure 6). The appearance of this feature is indicative of changes to the cytoplasmic RNA content associated with oxidative stress, and is observed in cells even at low doses, and short exposure times (4 h). The intensity of the band is seen to systematically and progressively change as a function of both NP dose and exposure time (Efeoglu et al., 2016) and its evolution is associated with concurrent and subsequent changes in protein (Amide I region,  $\sim 1600 - 1700\text{ cm}^{-1}$ ) and lipid (1229 and 1438  $\text{cm}^{-1}$ ) content and/or structure, indicative of proteolysis and lipotoxicity (Efeoglu et al., 2016, 2017a).

The potential of Raman microspectroscopy to delivering multi-parametric information by label free analysis was further explored by comparing the evolution of spectral markers in other cancerous and non-cancerous cells lines (Efeoglu et al., 2017a). Characteristic spectral markers of toxic events, including oxidative stress and lysosomal damage, have been identified and characterized as a function of time, and the analysis indicates that the spectral markers identified for cellular dependent events are consistent across multiple cell lines (Figure 7), potentially facilitating the identification of the mechanism of toxic response to the nanomaterial. Analysis of the presence and progression of spectral markers, especially in the low wavenumber region, also indicates the applicability of Raman spectral analysis to identification of cellular signatures characteristic of cell death pathways in cancerous and non-cancerous cell lines, differentiating between necrotic and apoptotic (Efeoglu et al., 2017a, 2018).

Aminated dendritic polymer nanoparticles, such as poly (amidoamine) (PAMAM) and poly (propylene imine), have been demonstrated to elicit a similar profile of toxic responses in mammalian cells, *in vitro*, involving endocytosis, oxidative stress, mitochondrial damage, inflammatory cascades, leading to apoptosis (Mukherjee et al., 2010a,b; Naha et al., 2010b; Maher et al., 2014; Khalid et al., 2016). Notably, under similar exposure conditions, A549 cells were shown to exhibit remarkably similar (differential) spectroscopic profiles in the cytoplasm of A549 cells, associated with acute cytotoxicity (Figure 7) (Efeoglu et al., 2017a). Notably, the significantly smaller PAMAM dendrimers ( $\sim 5-7\text{ nm}$ ) have been shown to elicit significant genotoxic responses *in vitro* (Naha and Byrne, 2013; Naha et al., 2018). In the case of A549 exposure to PAMAM dendrimers, a significant dose and time dependent response of the spectroscopic profile of







the nuclear region was observed, which may be associated with DNA damage and a genotoxic response (Efeoglu et al., 2017a).

In a study of the intracellular uptake and toxic response of silver and copper oxide nanoparticles in human lung cells, *in vitro*, and Raman spectroscopy was employed to monitor the cellular uptake, compared to the respective metal ionic species as well as the particle-cell interactions, although specific signatures of cellular responses were not identified (Cronholm et al., 2020). Raman spectroscopic imaging has also been employed in conjunction with microinjection of nanoparticles into cells, as a proposed tool for nanotoxicological studies (Candeloro et al., 2011).

Raman spectroscopy has also been employed to confirm the *in vitro* cytotoxicity, and therefore anti-cancer activity, of functionalized silica nanoparticles (Dhinasekaran et al., 2020). The surface of the silica nanoparticles was functionalized with 5-Fluorouracil by direct conjugation or chitosan mediated conjugation. Raman spectroscopy indicated changes in the nucleic acid spectral signature for cancer cell lines exposed to the formulation, rather than normal cells confirming a selective toxicity to cancer cells.

In a study of the impact of nanoparticle uptake on the biophysical properties of cells, Raman spectroscopy was employed in particular to analyze disruptions to the cell membranes (Rasel et al., 2019). The study indicated that nanoparticle uptake results in substantial perturbation of the fundamental structure of the cells, having implications for applications in biomedical engineering.

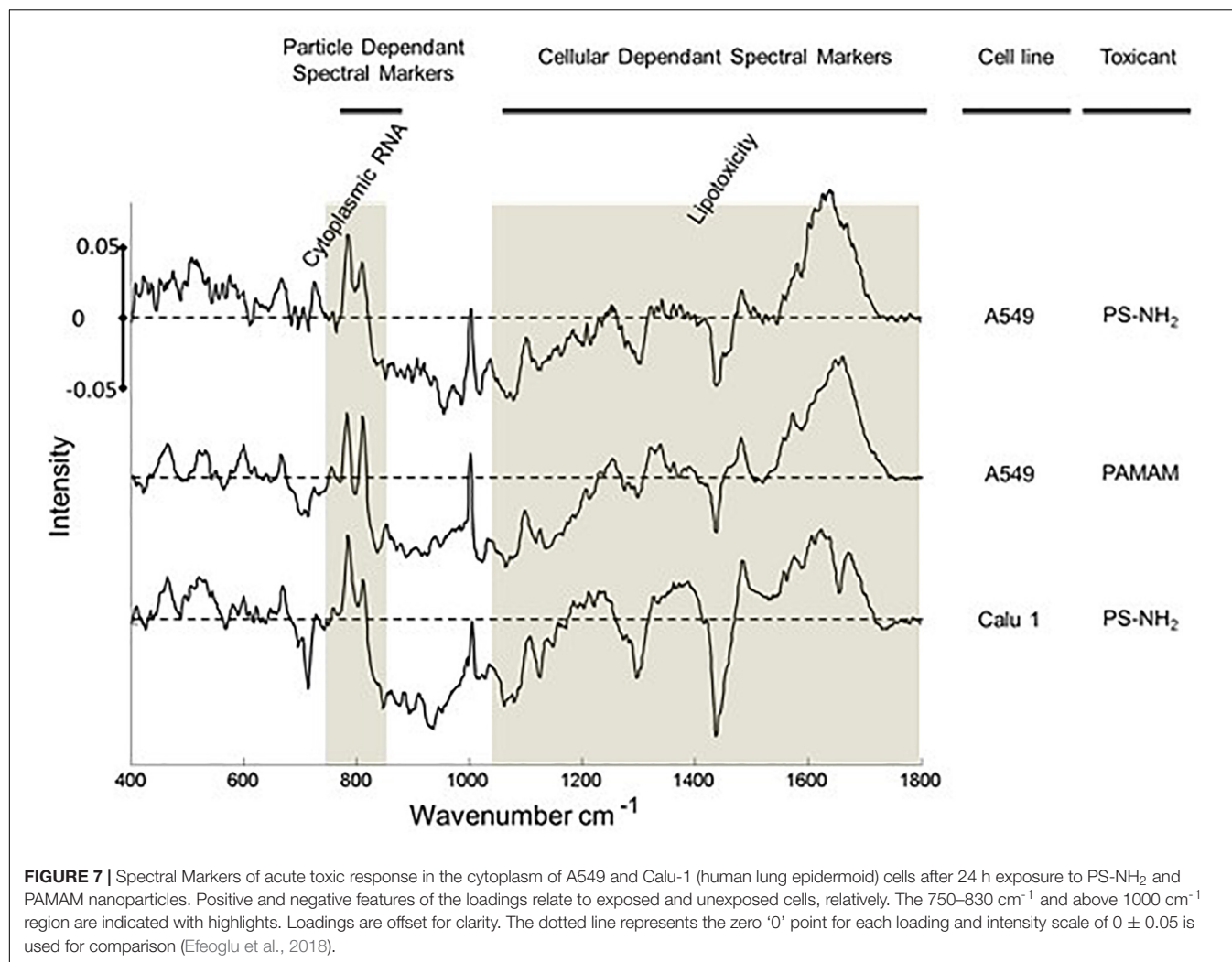
## DISCUSSION

Technological advances in recent decades have rendered confocal Raman microspectroscopy increasingly routine

amongst benchtop laboratory techniques for materials and process analysis. As it can be performed using optical sources of wavelength from the UV to near IR, it can provide submicrometer spatial resolution and therefore can image cells and processes at a subcellular level, and therefore a wealth of information about their biomolecular makeup, and changes to it due to external factors. As a label-free technique, it can unambiguously identify the presence of NPs within cells, on the basis of their intrinsic spectroscopic fingerprint, and can also profile the biochemistry of the local environment, differentiating endosomal, lysosomal and perinuclear compartmentalization in the course of NP uptake and trafficking by the cell. The stability of the NP material within the subcellular environment can also be probed, enabling mapping of catabolic pathways. In terms of the cytotoxic responses of the cells, clear dose and time dependent signatures, associated with oxidative stress, proteolysis and lipotoxicity, can be observed in the cytoplasm, and the processes of apoptosis and necrosis can be differentiated. In the nuclear regions, signatures of genotoxicity are indicated. The single, label-free technique can therefore provide *in vitro* high content spectroscopic screening of the process of NP uptake, trafficking, fate and acute cytotoxic and genotoxic responses. The technique is therefore ideally suited to address many of the short-term and long-term challenges of exploring the interface of functional (nano) materials with living systems, at least in the context of *in vitro* models.

An important consideration is the reproducibility and transferability of the signatures of the spectral response, across NPs of similar cytotoxic mechanisms, and different cell lines. Previously, it has been demonstrated that the differential spectroscopic signatures (PC loadings) which discriminate the subcellular regions of cytoplasm, nucleus and nucleoli, of different cell lines are remarkably similar, so much so that different lung cancer cell lines could only be discriminated



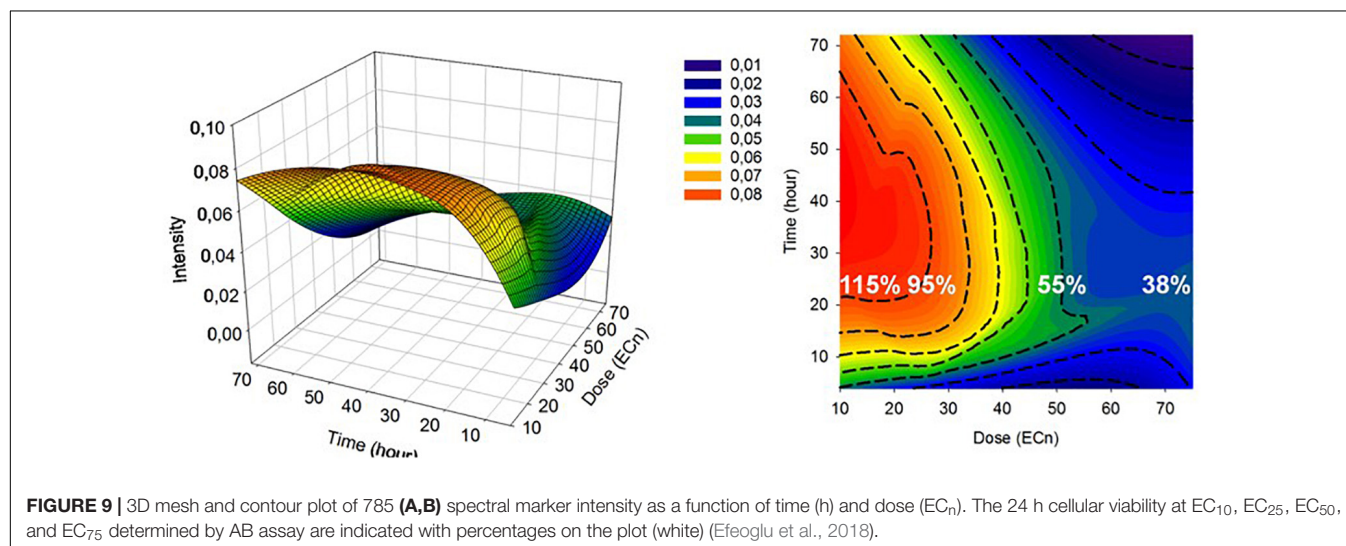
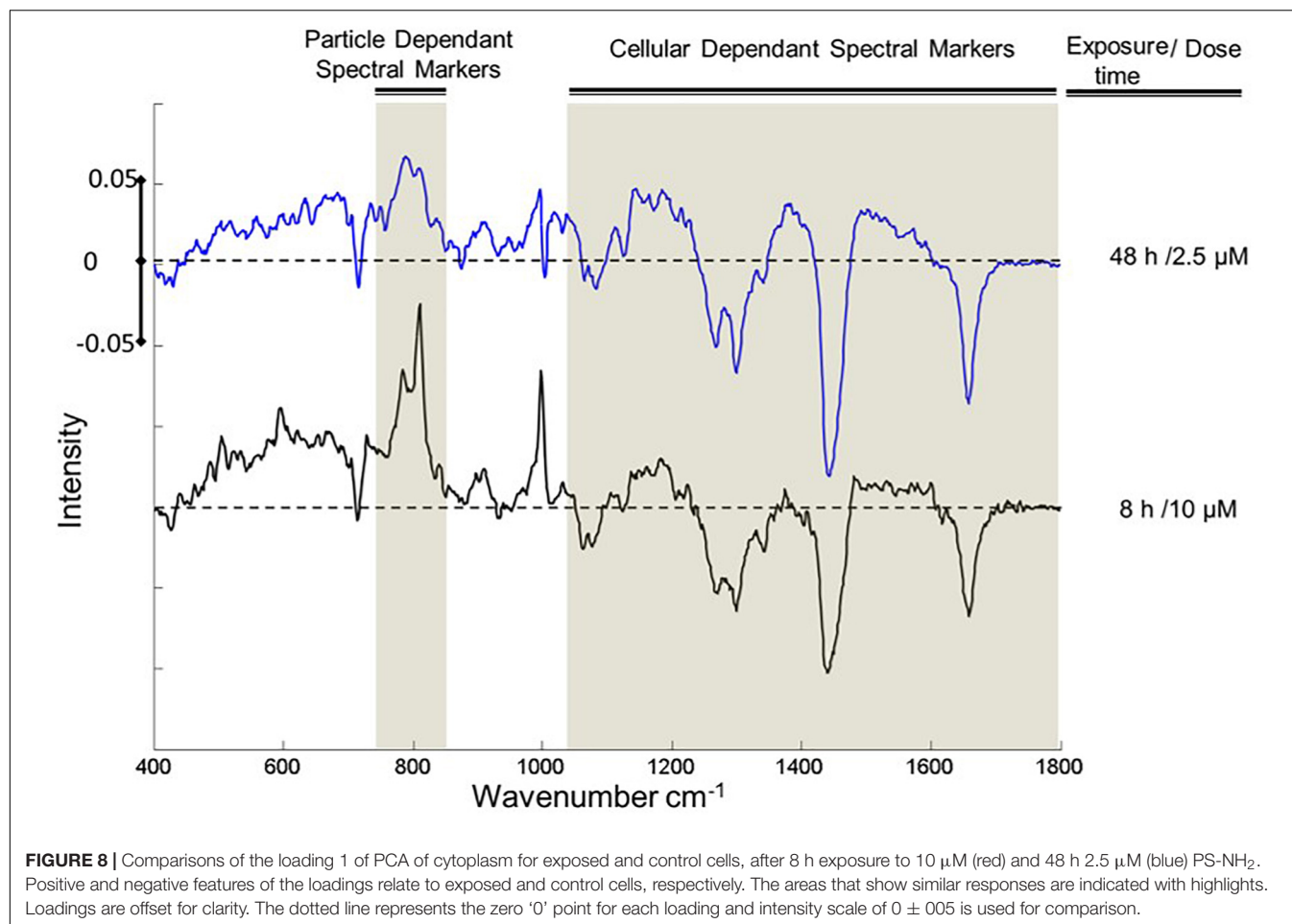


according to the signatures of the nucleoli (Farhane et al., 2015b). Furthermore, **Figure 7** clearly indicates similar spectroscopic responses for two different aminated polymeric particles, both known to initiate oxidative stress responses, in two different cell lines. As shown in **Figure 8**, for the case of exposure of A549 cells to PS-NH<sub>2</sub>, the differential spectral profiles of low dose/prolonged exposure and high dose/short exposure also show remarkable similarities (Efeoglu et al., 2018). The 3D nature of the dose and time dependent spectral signatures is consistent with previous modeling analysis of dose and time dependences of *in vitro* cytotoxic responses (Maher et al., 2014; Byrne and Maher, 2019). The 3D contour map of the spectral responses can also be correlated with the response of classical colorimetric cytotoxicity assays, as shown in **Figure 9**, for the example of the 785 cm<sup>-1</sup> feature of the response of A549 cells to PS-NH<sub>2</sub> exposure, and the dose response curve of AB at 24 h (Efeoglu et al., 2018).

The consistency of the responses indicates that the signatures of the multiparametric responses, composed of contributions of multiple biochemical constituents, are characteristic of the mode of action, supporting a “spectralomics” approach to high content spectroscopic analysis (Byrne et al., 2018; Efeoglu et al., 2018;

Farhane et al., 2018c). In **Figures 7, 8**, the lower wavenumber responses (~800 cm<sup>-1</sup>) are associated with oxidative stress, and so can be considered to be dependent on the initial NP dose and intrinsic toxicity (degree of amination). The higher wavenumber responses (1000–1800 cm<sup>-1</sup>) can be associated with the subsequent cascade of cellular responses. In the framework of the predictive toxicology approach of Adverse Outcome Pathways (OECD, 2017; Wittwehr et al., 2017), the characteristic “spectralome” of the initial response can be considered that of the Molecular Initiating Event. The subsequent adverse pathway of cell death is described by the respective characteristics of inflammatory responses and apoptosis or necrosis in the higher wavenumber region of the fingerprint.

Critical for realizing the potential of the technique is reliably data mining the evolution of the signatures which map out the temporal evolution, and spatial propagation, of the key events of the subcellular responses. While multivariate algorithms such as KMCA and PCA provide a detailed picture of the static state of the cellular system, compared to control, more sophisticated data mining techniques are required to monitor the kinetic evolution of



signatures of cellular response pathways. Algorithms such as Evolving Factor Analysis (EFA) (Keller and Massart, 1991) and Multivariate Curve Resolution Alternating Least Squares (MCR-ALS) (Felten et al., 2015) have been developed to similarly monitor the evolution of chemical

and photochemical reactions. Constraints based on kinetic evolution models allow identification of the characteristic spectral signatures of the products and intermediates (Vernooij et al., 2018). Although the approaches have not yet been extensively explored to analyze the evolution

of Raman spectroscopic signatures of cytological processes, initial applications to track the spectroscopic signatures of the *in vitro* action of the chemotherapeutic agent, doxorubicin, are promising (Perez-Guaita et al., 2020).

A number of technological variations on the basis of Raman spectroscopy have been developed to enhance the sensitivity of the technique. Surface Enhanced Raman Spectroscopy (SERS) was first observed in 1974 (Fleischmann et al., 1974; Jeanmaire and Van Duyne, 1977), and has been explored for the development of nanoparticle based analytical probes to monitor nanomaterials in a cellular environment (Kneipp et al., 2002, 2009). Incorporation of Raman reporters enables localization of the SERS probe within the subcellular environment, and such SERS nanosensors can be designed, for example to monitor pH changes in a cell at the different stages of the endocytic pathway (Kneipp et al., 2006, 2010; Wang et al., 2008). A number of studies have described novel SERS based probes for intracellular sensing and imaging (Kneipp et al., 2009), identification of biomarkers (Zhang et al., 2020) and to monitor intracellular delivery of single gold particles via 3D hollow nanoelectrodes (Huang et al., 2019). SERS has also been employed to probe cell surface receptors associated with cancer (Kong et al., 2012), in the isolation and non-invasive analysis of circulating cancer stem cells (Cho et al., 2018), and applications in cancer detection and tumor imaging have been extensively explored (Meola et al., 2018; Ravanshad et al., 2018).

The technique particularly exploits the enhanced local field of surface plasmon resonances in nanoparticles of, for example gold and silver. Only a small selection of nanoparticles can be exploited for such applications, however, and specific probes of specific cellular function are required, and therefore, in many cases, it is debatable whether the technique can really be considered label-free, although there have been notable examples of studies in which nanostructured gold/silver substrates have been used as SERS substrates for cellular investigation, in a label-free manner (Dipalo et al., 2015; La Rocca et al., 2015; Shalabaeva et al., 2017; Caprettini et al., 2018). The current manuscript highlights the applications of (unenanced) Raman microspectroscopy itself to probe, in a label free manner, the cellular uptake, distribution and fate of nanoparticles themselves, applicable to a broad range of chemical compositions and morphologies, and to, using the same measurement protocol, probe the cellular response.

It is acknowledged that, unenanced, the sensitivity of the technique is a potential limitation, resulting in prolonged analysis times for cellular imaging. Emerging techniques based on coherent Raman scattering, in the form of either coherent anti-Stokes Raman (CARS) or stimulated Raman scattering (SRS) promise to significantly enhance the sensitivity, and therefore reduce the sampling time, without compromising the label-free aspect of the technique. Although currently only commercially available in limited frequency ranges, full spectral coherent Raman microspectroscopic imaging has already been demonstrated (Camp et al., 2014), promising label free high content spectroscopic analysis of sub-cellular processes in real-time, and hitherto unrivaled visualization of cellular

processes and function. Indeed, CARS has been employed, in conjunction with electron microscopy to explore cell-nanoparticle interactions at nanometer resolution (Saarinen et al., 2019), while SRS using polymer nanoparticles has been employed for multiplexed live-cell imaging (Hu et al., 2017).

## CONCLUSION

Nanomaterials, and in particular nanoparticles, have become an important element of the drive for the development of functional biomaterials, and although their potential in therapeutics and diagnostics is already well established, the “other side of the coin,” that of potential harmful effects to human health and the environment, is equally evident. The associated short and long term challenge, pertinent to both sides of the coin, relates to the ability to directly monitor and evaluate the interactions of these novel functional materials with living systems, and particularly cells. While conventional microscopic techniques and cytological staining and assays can provide a limited picture of the process, the technique of Raman microspectroscopy has been demonstrated to be capable of; confirming the intracellular localization of NPs in cells, monitoring the NP trafficking in subcellular vesicles and, monitoring NP degradation catabolization, identifying and tracking cellular response pathways, all in a single, label free, measurement protocol. The studies strongly suggest that the spectroscopic signatures are characteristic of key initiating and pathway events, although exploration of more sophisticated, dynamic multivariate data mining techniques is required to map out cellular response pathways. However, further larger scale studies are required to verify the transferability of the characteristic “spectralomic” signatures, for a range of different NP and cell types. Applications can readily be envisaged in areas such as toxicological screening, to guide regulatory processes, *in vitro* pre-clinical candidate drug screening to guide synthetic strategies, and ultimately potentially even patient screening for drug resistance/sensitivity, as the basis for companion diagnostics.

## AUTHOR CONTRIBUTIONS

FB undertook the initial studies of PSNPs in cells. EE undertook the localization and toxicology studies of PSNPs, PS-NH<sub>2</sub>, and PAMAM in cells. CM and JM undertook the studies of MoS<sub>2</sub> in THP-1 cells. HB is the senior responsible scientist and drafted the manuscript, with input from all other authors. All the authors contributed to the article and approved the submitted version.

## FUNDING

Aspects of this work were funded by the Irish HEA PRTLI Cycle 4 “INSPIRE”, and by Science Foundation Ireland 11/PI/87. CM was funded by a DIT Fiosraigh Scholarship.

## REFERENCES

- Ajdary, M., Moosavi, M. A., Rahmati, M., Falahati, M., Mahboubi, M., Mandegary, A., et al. (2018). Health concerns of various nanoparticles: a review of their in vitro and in vivo toxicity. *Nanomaterials* 8:634. doi: 10.3390/nano8090634
- Allied market research (2020). *Nanomaterials Market Size, Share | Industry Forecast 2014-2022*. Available online at: <https://www.alliedmarketresearch.com/nano-materials-market> (accessed March 8, 2020). doi: 10.3390/nano8090634
- Ami, D., Neri, T., Natalello, A., Mereghetti, P., Doglia, S. M., Zaroni, M., et al. (2008). Embryonic stem cell differentiation studied by FT-IR spectroscopy. *Biochim. Biophys. Acta Mol. Cell* 1783, 98–106. doi: 10.1016/j.bbamcr.2007.08.003
- Anguissola, S., Garry, D., Salvati, A., O'Brien, P. J., and Dawson, K. A. (2014). High content analysis provides mechanistic insights on the pathways of toxicity induced by amine-modified polystyrene nanoparticles. *PLoS One* 9:e108025. doi: 10.1371/journal.pone.0108025
- Bonnier, F., Ali, S. M. M., Knief, P., Lambkin, H., Flynn, K., McDonagh, V., et al. (2012). Analysis of human skin tissue by Raman microspectroscopy: dealing with the background. *Vib. Spectrosc.* 61, 124–132. doi: 10.1016/j.vibspec.2012.03.009
- Bonnier, F., and Byrne, H. J. (2012). Understanding the molecular information contained in principal component analysis of vibrational spectra of biological systems. *Analyst* 137, 322–332. doi: 10.1039/c1an15821j
- Bonnier, F., Knief, P., Lim, B., Meade, A. D., Dorney, J., Bhattacharya, K., et al. (2010a). Imaging live cells grown on a three dimensional collagen matrix using Raman microspectroscopy. *Analyst* 135, 3169–3177. doi: 10.1039/c0an00539h
- Bonnier, F., Meade, A. D., Merzha, S., Knief, P., Bhattacharya, K., Lyng, F. M., et al. (2010b). Three dimensional collagen gels as a cell culture matrix for the study of live cells by Raman spectroscopy. *Analyst* 135, 1697–1703. doi: 10.1039/c0an00060d
- Bonnier, F., Mehmood, A., Knief, P., Meade, A. D., Hornebeck, W., Lambkin, H., et al. (2011). In vitro analysis of immersed human tissues by Raman microspectroscopy. *J. Raman Spectrosc.* 42, 888–896. doi: 10.1002/jrs.2825
- Bonnier Knief, P., Meade, A., Dorney, J., Bhattacharya, K., Lyng, F., Byrne, H. F., et al. (2011). "Collagen matrices as an improved model for in vitro study of live cells using Raman microspectroscopy" in *Proceedings of the SPIE Clinical and Biomedical Spectroscopy and Imaging II*, Munich.
- Boydston-White, S., Romeo, M., Chernenko, T., Regina, A., Miljkovic, M., and Diem, M. (2006). Cell-cycle-dependent variations in FTIR micro-spectra of single proliferating HeLa cells: principal component and artificial neural network analysis. *Biochim. Biophys. Acta Biomembr.* 1758, 908–914. doi: 10.1016/j.bbamem.2006.04.018
- Butler, H. J., Ashton, L., Bird, B., Cinque, G., Curtis, K., Dorney, J., et al. (2016). Using Raman spectroscopy to characterize biological materials. *Nat. Protoc.* 11, 664–687.
- Byrne, H. J., Bonnier, F., Casey, A., Maher, M., McIntyre, J., Efeoglu, E., et al. (2018). Advancing Raman microspectroscopy for cellular and subcellular analysis: towards in vitro high-content spectralomic analysis. *Appl. Spectrosc.* 72:E11.
- Byrne, H. J., and Maher, M. A. (2019). Numerically modelling time and dose dependent cytotoxicity. *Comput. Toxicol.* 12:100090. doi: 10.1016/j.comtox.2019.100090
- Byrne, H. J., Sockalingum, G. D., and Stone, N. (2010). "Raman microscopy: complement or competitor?" in *Biomedical Applications of Synchrotron Infrared Microspectroscopy. RSC Analytical Spectroscopy Series*, ed. D. Moss (London: Royal Society of Chemistry), 105–143. doi: 10.1039/9781849731997-00105
- Camp, C. H., Lee, Y. J., Heddleston, J. M., Hartshorn, C. M., Walker, A. R. H., Rich, J. N., et al. (2014). High-speed coherent Raman fingerprint imaging of biological tissues. *Nat. Photon.* 8, 627–634. doi: 10.1038/nphoton.2014.145
- Candeloro, P., Tirinato, L., Malara, N., Fregola, A., Casals, E., Puentes, V., et al. (2011). Nanoparticle microinjection and Raman spectroscopy as tools for nanotoxicology studies. *Analyst* 136, 4402–4408. doi: 10.1039/c1an15313g
- Cang, H., Xu, C. S., Montiel, D., and Yang, H. (2007). Guiding a confocal microscope by single fluorescent nanoparticles. *Opt. Lett.* 32:2729. doi: 10.1364/ol.32.002729
- Caprettini, V., Huang, J.-A., Moia, F., Jacassi, A., Gonano, C. A., Maccaferri, N., et al. (2018). Enhanced raman investigation of cell membrane and intracellular compounds by 3D plasmonic nanoelectrode arrays. *Adv. Sci.* 5:1800560. doi: 10.1002/adv.201800560
- Carvalho, L. F. C. S., Bonnier, F., O'Callaghan, K., O'Sullivan, J., Flint, S., Byrne, H. J., et al. (2015). Raman micro-spectroscopy for rapid screening of oral squamous cell carcinoma. *Exp. Mol. Pathol.* 98, 502–509. doi: 10.1016/j.yexmp.2015.03.027
- Casey, A., Davoren, M., Herzog, E., Lyng, F. M., Byrne, H. J., and Chambers, G. (2007a). Probing the interaction of single walled carbon nanotubes within cell culture medium as a precursor to toxicity testing. *Carbon N.Y.* 45, 34–40. doi: 10.1016/j.carbon.2006.08.009
- Casey, A., Herzog, E., Davoren, M., Lyng, F. M., Byrne, H. J., and Chambers, G. (2007b). Spectroscopic analysis confirms the interactions between single walled carbon nanotubes and various dyes commonly used to assess cytotoxicity. *Carbon N.Y.* 45, 1425–1432. doi: 10.1016/j.carbon.2007.03.033
- Casey, A., Herzog, E., Lyng, F. M., Byrne, H. J., Chambers, G., and Davoren, M. (2008). Single walled carbon nanotubes induce indirect cytotoxicity by medium depletion in A549 lung cells. *Toxicol. Lett.* 179, 78–84. doi: 10.1016/j.toxlet.2008.04.006
- Chang, M. Y., Shiau, A. L., Chen, Y. H., Chang, C. J., Chen, H. H. W., and Wu, C. L. (2008). Increased apoptotic potential and dose-enhancing effect of gold nanoparticles in combination with single-dose clinical electron beams on tumor-bearing mice. *Cancer Sci.* 99, 1479–1484. doi: 10.1111/j.1349-7006.2008.00827.x
- Chernenko, T., Matthäus, C., Milane, L., Quintero, L., Amiji, M., and Diem, M. (2009). Label-free raman spectral imaging of intracellular delivery and degradation of polymeric nanoparticle systems. *ACS Nano* 3, 3552–3559. doi: 10.1021/nn9010973
- Cho, H. Y., Hossain, M. K., Lee, J. H., Han, J., Lee, H. J., Kim, K. J., et al. (2018). Selective isolation and noninvasive analysis of circulating cancer stem cells through Raman imaging. *Biosens. Bioelectron.* 102, 372–382. doi: 10.1016/j.bios.2017.11.049
- Cronholm, P., Karlsson, H. L., Hedberg, J., Lowe, T. A., Winnberg, L., Elihn, K., et al. (2020). Intracellular uptake and toxicity of Ag and CuO nanoparticles: a comparison between nanoparticles and their corresponding metal ions. *Small* 9, 970–982. doi: 10.1002/sml.201201069
- Davoren, M., Herzog, E., Casey, A., Cottineau, B., Chambers, G., Byrne, H. J., et al. (2007). In vitro toxicity evaluation of single walled carbon nanotubes on human A549 lung cells. *Toxicol. Vitro* 21, 438–448. doi: 10.1016/j.tiv.2006.10.007
- Dhinasekaran, D., Raj, R., Rajendran, A. R., Purushothaman, B., Subramanian, B., Prakasara, A., et al. (2020). Chitosan mediated 5-Fluorouracil functionalized silica nanoparticle from rice husk for anticancer activity. *Int. J. Biol. Macromol.* 156, 969–980. doi: 10.1016/j.ijbiomac.2020.04.098
- Dipalo, M., Messina, G. C., Amin, H., La Rocca, R., Shalabaeva, V., Simi, A., et al. (2015). 3D plasmonic nanoantennas integrated with MEA biosensors. *Nanoscale* 7, 3703–3711. doi: 10.1039/c4nr05578k
- Dorney, J., Bonnier, F., Garcia, A., Casey, A., Chambers, G., and Byrne, H. J. (2012). Identifying and localizing intracellular nanoparticles using Raman spectroscopy. *Analyst* 137, 1111–1119. doi: 10.1039/c2an15977e
- Edwards, H. G. M., and Vandenabeele, P. (2016). Raman spectroscopy in art and archaeology. *Philos. Trans. R. Soc. A* 374, 1523–1844.
- Efeoglu, E., Casey, A., and Byrne, H. J. (2016). In vitro monitoring of time and dose dependent cytotoxicity of aminated nanoparticles using Raman spectroscopy. *Analyst* 141, 5417–5431. doi: 10.1039/c6an01199c
- Efeoglu, E., Casey, A., and Byrne, H. J. (2017a). Determination of spectral markers of cytotoxicity and genotoxicity using in vitro Raman microspectroscopy: cellular responses to polyamidoamine dendrimer exposure. *Analyst* 142, 3848–3856. doi: 10.1039/c7an00969k
- Efeoglu, E., Maher, M. A., Casey, A., and Byrne, H. J. (2017b). Label-free, high content screening using Raman microspectroscopy: The toxicological response of different cell lines to amine-modified polystyrene nanoparticles (PS-NH<sub>2</sub>)†. *Analyst* 142, 3500–3513. doi: 10.1039/c7an00461c
- Efeoglu, E., Keating, M., McIntyre, J., Casey, A., and Byrne, H. J. (2015). Determination of nanoparticle localisation within subcellular organelles in vitro using Raman spectroscopy. *Anal. Methods* 7, 10000–10017. doi: 10.1039/c5ay02661j
- Efeoglu, E., Maher, M. A., Casey, A., and Byrne, H. J. (2018). Toxicological assessment of nanomaterials: the role of in vitro Raman microspectroscopic analysis. *Anal. Bioanal. Chem.* 410, 1631–1646. doi: 10.1007/s00216-017-0812-x



- Farhane, Z., Bonnier, F., and Byrne, H. J. (2017a). Monitoring doxorubicin cellular uptake and trafficking using in vitro Raman microspectroscopy: short and long time exposure effects on lung cancer cell lines. *Anal. Bioanal. Chem.* 409, 1333–1346. doi: 10.1007/s00216-016-0065-0
- Farhane, Z., Bonnier, F., Maher, M. A., Bryant, J., Casey, A., and Byrne, H. J. (2017b). Differentiating responses of lung cancer cell lines to Doxorubicin exposure: in vitro Raman micro spectroscopy, oxidative stress and bcl-2 protein expression. *J. Biophoton.* 10, 151–165. doi: 10.1002/jbio.201600019
- Farhane, Z., Bonnier, F., and Byrne, H. J. (2018a). An in vitro study of the interaction of the chemotherapeutic drug Actinomycin D with lung cancer cell lines using Raman micro-spectroscopy. *J. Biophoton.* 11:e201700112. doi: 10.1002/jbio.201700112
- Farhane, Z., Bonnier, F., Howe, O., Casey, A., and Byrne, H. J. (2018b). Doxorubicin kinetics and effects on lung cancer cell lines using in vitro Raman micro-spectroscopy: binding signatures, drug resistance and DNA repair. *J. Biophoton.* 11:e201700060. doi: 10.1002/jbio.201700060
- Farhane, Z., Nawaz, H., Bonnier, F., and Byrne, H. J. H. J. (2018c). In vitro label-free screening of chemotherapeutic drugs using Raman microspectroscopy: towards a new paradigm of spectralomics. *J. Biophoton.* 11:e201700258. doi: 10.1002/jbio.201700258
- Farhane, Z., Bonnier, F., Casey, A., and Byrne, H. J. (2015a). Raman micro spectroscopy for in vitro drug screening: subcellular localisation and interactions of doxorubicin. *Analyst* 140, 4212–4223. doi: 10.1039/c5an00256g
- Farhane, Z., Bonnier, F., Casey, A., Maguire, A., O'Neill, L., and Byrne, H. J. (2015b). Cellular discrimination using in vitro Raman micro spectroscopy: the role of the nucleolus. *Analyst* 140, 5908–5919. doi: 10.1039/c5an01157d
- Felten, J., Hall, H., Jaumot, J., Tauler, R., De Juan, A., and Gorzsás, A. (2015). Vibrational spectroscopic image analysis of biological material using multivariate curve resolution-alternating least squares (MCR-ALS). *Nat. Protoc.* 10, 217–240. doi: 10.1038/nprot.2015.008
- Fleischmann, M., Hendra, P. J., and McQuillan, A. J. (1974). Raman spectra of pyridine adsorbed at a silver electrode. *Chem. Phys. Lett.* 26, 163–166. doi: 10.1016/0009-2614(74)85388-1
- Gajraj, A., and Ofoli, R. Y. (2000). Quantitative technique for investigating macromolecular adsorption, and interactions at the liquid-liquid interface. *Langmuir* 16, 4279–4285. doi: 10.1021/la9911436
- Gao, L., Liu, Y., Kim, D., Li, Y., Hwang, G., Naha, P. C., et al. (2016). Nanocatalysts promote *Streptococcus mutans* biofilm matrix degradation and enhance bacterial killing to suppress dental caries in vivo. *Biomaterials* 101, 272–284. doi: 10.1016/j.biomaterials.2016.05.051
- Gargotti, M., Efeoglu, E., Byrne, H. J., and Casey, A. (2018). Raman spectroscopy detects biochemical changes due to different cell culture environments in live cells in vitro. *Anal. Bioanal. Chem.* 410, 7537–7550. doi: 10.1007/s00216-018-1371-5
- Gasparri, F., and Muzio, M. (2003). Monitoring of apoptosis of HL60 cells by fourier-transform infrared spectroscopy. *Biochem. J.* 369, 239–248. doi: 10.1042/bj20021021
- Gordon, S. (2007). The macrophage: past, present and future. *Eur. J. Immunol.* 37(Suppl. 1), S9–S17.
- Herzog, E., Casey, A., Lyng, F. M., Chambers, G., Byrne, H. J., and Davoren, M. (2007). A new approach to the toxicity testing of carbon-based nanomaterials—The clonogenic assay. *Toxicol. Lett.* 174, 49–60. doi: 10.1016/j.toxlet.2007.08.009
- Hobro, A. J., and Smith, N. I. (2017). An evaluation of fixation methods: spatial and compositional cellular changes observed by Raman imaging. *Vib. Spectrosc.* 91, 31–45. doi: 10.1016/j.vibspec.2016.10.012
- Hodges, C. M., and Akhavan, J. (1990). The use of Fourier Transform Raman spectroscopy in the forensic identification of illicit drugs, and explosives. *Spectrochim. Acta Part A Mol. Spectrosc.* 46, 303–307. doi: 10.1016/0584-8539(90)80098-j
- Hu, F., Brucks, S. D., Lambert, T. H., Campos, L. M., and Min, W. (2017). Stimulated Raman scattering of polymer nanoparticles for multiplexed live-cell imaging. *Chem. Commun.* 53, 6187–6190. doi: 10.1039/c7cc01860f
- Huang, J. A., Caprettini, V., Zhao, Y., Melle, G., MacCafferri, N., Deleye, L., et al. (2019). On-demand intracellular delivery of single particles in single cells by 3D hollow nano-electrodes. *Nano Lett.* 19, 722–731. doi: 10.1021/acs.nanolett.8b03764
- Ito, F., Fujimori, H., Honnami, H., Kawakami, H., Kanamura, K., and Makino, K. (2008). Effect of polyethylene glycol on preparation of rifampicin-loaded PLGA microspheres with membrane emulsification technique. *Coll. Surf. B Biointerf.* 66, 65–70. doi: 10.1016/j.colsurfb.2008.05.011
- Jeanmaire, D. L., and Van Duyne, R. P. (1977). Surface raman spectroelectrochemistry. Part I. Heterocyclic, aromatic, and aliphatic amines adsorbed on the anodized silver electrode. *J. Electroanal. Chem.* 84, 1–20.
- Keller, H. R., and Massart, D. L. (1991). Evolving factor analysis. *Chemometr. Intellig. Lab. Syst.* 12, 209–224. doi: 10.1016/0169-7439(92)80002-1
- Khalid, H., Mukherjee, S. P., O'Neill, L., and Byrne, H. J. (2016). Structural dependence of in vitro cytotoxicity, oxidative stress and uptake mechanisms of poly(propylene imine) dendritic nanoparticles. *J. Appl. Toxicol.* 36, 464–473. doi: 10.1002/jat.3267
- Kneipp, J., Kneipp, H., McLaughlin, M., Brown, D., and Kneipp, K. (2006). In vivo molecular probing of cellular compartments with gold nanoparticles and nanoaggregates. *Nano Lett.* 6, 2225–2231. doi: 10.1021/nl061517x
- Kneipp, J., Kneipp, H., Rajadurai, A., Redmond, R. W., and Kneipp, K. (2009). Optical probing and imaging of live cells using SERS labels. *J. Raman Spectrosc.* 40, 1–5. doi: 10.1002/jrs.2060
- Kneipp, J., Kneipp, H., Wittig, B., and Kneipp, K. (2010). Following the dynamics of pH in endosomes of live cells with SERS nanosensors. *J. Phys. Chem. C* 114, 7421–7426. doi: 10.1021/jp910034z
- Kneipp, K., Haka, A. S., Kneipp, H., Badizadegan, K., Yoshizawa, N., Boone, C., et al. (2002). Surface-enhanced Raman spectroscopy in single living cells using gold nanoparticles. *Appl. Spectrosc.* 56, 150–154. doi: 10.1366/0003702021954557
- Kneipp, K., Kneipp, H., Itzkan, I., Dasari, R. R., and Feld, M. S. (1999). Ultrasensitive chemical analysis by Raman spectroscopy. *Chem. Rev.* 99, 2957–2975.
- Knief, P., Clarke, C., Herzog, E., Davoren, M., Lyng, F. M., Meade, A. D., et al. (2009). Raman spectroscopy - A potential platform for the rapid measurement of carbon nanotube-induced cytotoxicity. *Analyst* 134, 1182–1191. doi: 10.1039/b821393c
- Kong, K. V., Lam, Z., Goh, W. D., Leong, W. K., and Olivo, M. M. (2012). Carbonyl-gold nanoparticle conjugates for live-cell SERS imaging. *Angew. Chem. Int. Edn.* 51, 9796–9799. doi: 10.1002/anie.201204349
- La Rocca, R., Messina, G. C., Dipalo, M., Shalabaeva, V., and De Angelis, F. (2015). Out-of-plane plasmonic antennas for raman analysis in living cells. *Small* 11, 4632–4637. doi: 10.1002/smll.201500891
- Liu, K. Z., Jia, L., Kelsey, S. M., Newland, A. C., and Mantsch, H. H. (2001). Quantitative determination of apoptosis on leukemia cells by infrared spectroscopy. *Apoptosis* 6, 269–278.
- Long, D. A. (2002). *The Raman Effect: A Unified Treatment of the Theory of Raman Scattering by Molecules*. Hoboken, NJ: Wiley.
- Love, S. A., Maurer-Jones, M. A., Thompson, J. W., Lin, Y.-S., and Haynes, C. L. (2012). Assessing nanoparticle toxicity. *Annu. Rev. Anal. Chem.* 5, 181–205. doi: 10.1146/annurev-anchem-062011-143134
- Maher, M. A., Naha, P. C., Mukherjee, S. P., and Byrne, H. J. (2014). Numerical simulations of in vitro nanoparticle toxicity - the case of poly(amido amine) dendrimers. *Toxicol. Vitro* 28, 1449–1460. doi: 10.1016/j.tiv.2014.07.014
- Matthäus, C., Boydston-White, S., Miljković, M., Romeo, M., and Diem, M. (2006). Raman and infrared microspectral imaging of mitotic cells. *Appl. Spectrosc.* 60, 1–8. doi: 10.1366/000370206775382758
- Meade, A. D., Clarke, C., Draux, F., Sockalingum, G. D., Manfait, M., Lyng, F. M., et al. (2010). Studies of chemical fixation effects in human cell lines using Raman microspectroscopy. *Anal. Bioanal. Chem.* 396, 1781–1791. doi: 10.1007/s00216-009-3411-7
- Meade, A. D., Howe, O., Unterreiner, V., Sockalingum, G. D., Byrne, H. J., and Lyng, F. M. (2016). Vibrational spectroscopy in sensing radiobiological effects: analyses of targeted and non-targeted effects in human keratinocytes. *Faraday Discuss* 187, 213–234. doi: 10.1039/c5fd00208g
- Meade, A. D., Lyng, F. M., Knief, P., and Byrne, H. J. (2007). Growth substrate induced functional changes elucidated by FTIR and Raman spectroscopy in in-vitro cultured human keratinocytes. *Anal. Bioanal. Chem.* 387, 1717–1728. doi: 10.1007/s00216-006-0876-5
- Meola, A., Rao, J., Chaudhary, N., Sharma, M., and Chang, S. D. (2018). Gold nanoparticles for brain tumor imaging: a systematic review. *Front. Neurol.* 9:328. doi: 10.3389/fneur.2018.00328

- Misra, S. K., Mukherjee, P., Chang, H. H., Tiwari, S., Gryka, M., Bhargava, R., et al. (2016). Multi-functionality redefined with colloidal carotene carbon nanoparticles for synchronized chemical imaging, enriched cellular uptake and therapy. *Sci. Rep.* 6:29299.
- Moore, C., Harvey, A., Coleman, J. N., Byrne, H. J., and McIntyre, J. (2020a). In vitro localisation and degradation of few-layer MoS<sub>2</sub> submicrometric plates in human macrophage-like cells: a label free Raman micro-spectroscopic study. *2D Mater.* 7:025003. doi: 10.1088/2053-1583/ab5d98
- Moore, C., Harvey, A., Coleman, J. N., Byrne, H. J., and McIntyre, J. (2020b). Label-free screening of biochemical changes in macrophage-like cells following MoS<sub>2</sub> exposure using Raman micro-spectroscopy. *Spectrochim. Acta Part A Mol. Biomol. Spectrosc.* 246:118916. doi: 10.1016/j.saa.2020.118916
- Moore, C., Movia, D., Smith, R. J., Hanlon, D., Lebre, F., Lavelle, E. C., et al. (2017). Industrial grade 2D molybdenum disulphide (MoS<sub>2</sub>): an in vitro exploration of the impact on cellular uptake, cytotoxicity, and inflammation. *2D Mater.* 4:025065. doi: 10.1088/2053-1583/aa673f
- Movasaghi, Z., Rehman, S., and Rehman, I. U. (2007). Raman spectroscopy of biological tissues. *Appl. Spectrosc. Rev.* 42, 493–541. doi: 10.1080/05704920701551530
- Mukherjee, S. P., Davoren, M., and Byrne, H. J. (2010a). In vitro mammalian cytotoxicological study of PAMAM dendrimers - Towards quantitative structure activity relationships. *Toxicol. Vitro.* 24, 169–177. doi: 10.1016/j.tiv.2009.09.014
- Mukherjee, S. P., Lyng, F. M., Garcia, A., Davoren, M. B. H., Mukherjee, S. P., Lyng, F. M., et al. (2010b). Mechanistic studies of in vitro cytotoxicity of poly(amidoamine) dendrimers in mammalian cells. *Toxicol. Appl. Pharmacol.* 248, 259–268. doi: 10.1016/j.taap.2010.08.016
- Naha, P., Kanchan, V., Manna, P. K., and Panda, A. K. (2008). Improved bioavailability of orally delivered insulin using Eudragit-L30D coated PLGA microparticles. *J. Microencapsul.* 25, 248–256. doi: 10.1080/02652040801903843
- Naha, P. C., Bhattacharya, K., Tenuta, T., Dawson, K. A., Lynch, I., Gracia, A., et al. (2010a). Intracellular localisation, geno- and cytotoxic response of poly(N-isopropylacrylamide) (PNIPAM) nanoparticles to human keratinocyte (HaCaT) and colon cells (SW 480). *Toxicol. Lett.* 198, 134–143. doi: 10.1016/j.toxlet.2010.06.011
- Naha, P. C., Davoren, M., Lyng, F. M., and Byrne, H. J. (2010b). Reactive oxygen species (ROS) induced cytokine production and cytotoxicity of PAMAM dendrimers in J774A.1 cells. *Toxicol. Appl. Pharmacol.* 246, 91–99. doi: 10.1016/j.taap.2010.04.014
- Naha, P. C., and Byrne, H. J. (2013). Generation of intracellular reactive oxygen species and genotoxicity effect to exposure of nanosized polyamidoamine (PAMAM) dendrimers in PLHC-1 cells in vitro. *Aquat. Toxicol.* 132–133, 61–72. doi: 10.1016/j.aquatox.2013.01.020
- Naha, P. C., Kanchan, V., and Panda, A. K. (2009). Evaluation of parenteral depot insulin formulation using PLGA and PLA microparticles. *J. Biomater. Appl.* 24, 309–325. doi: 10.1177/0885328208096238
- Naha, P. C., Mukherjee, S. P., and Byrne, H. J. (2018). Toxicology of engineered nanoparticles: focus on poly(amidoamine) dendrimers. *Intern. J. Environ. Res. Public Health* 15:338. doi: 10.3390/ijerph15020338
- Nano tech project (2020). *CPI Home*. Available online at: <http://www.nanotechproject.org/cpi/> (accessed March 8, 2020).
- Nottingham, I., Bisson, I., Bishop, A. E., Randle, W. L., Polak, J. M. P., and Hench, L. L. (2004). In situ spectral monitoring of mRNA translation in embryonic stem cells during differentiation in vitro. *Anal. Chem.* 76, 3185–3193. doi: 10.1021/ac0498720
- Nottingham, I., and Hench, L. L. (2006). Raman microspectroscopy: a noninvasive tool for studies of individual living cells in vitro. *Expert Rev. Med. Devices* 3, 215–234. doi: 10.1586/17434440.3.2.215
- Nottingham, I., Verrier, S., Haque, S., Polak, J. M., and Hench, L. L. (2003). Spectroscopic study of human lung epithelial cells (A549) in culture: living cells versus dead cells. *Biopolym. Biospectrosc. Sect.* 72, 230–240. doi: 10.1002/bip.10378
- Novoselov, K. S., Geim, A. K., Morozov, S. V., Jiang, D., Zhang, Y., Dubonos, S. V., et al. (2004). Electric field effect in atomically thin carbon films. *Science* 306, 666–669. doi: 10.1126/science.1102896
- OECD (2017). *Joint Meeting of the Chemicals Committee and the Working Party on Chemicals Pesticides and Biotechnology*. ENV/JM/MONO(2013)6 Revised Guidance Document on Developing and Assessing Adverse Outcome Pathways. Available online at: <http://www.oecd.org/officialdocuments/publicdisplaydocumentpdf/?cote=env/jm/mono%282013%296&doclanguage=en> (accessed June 29, 2018).
- Pattini, B. S., Chupin, V. V., and Torchilin, V. P. (2015). New developments in liposomal drug delivery. *Chem. Rev.* 115, 10938–10966. doi: 10.1021/acs.chemrev.5b00046
- Pavillon, N., Hobro, A. J., Akira, S., and Smith, N. I. (2018). Noninvasive detection of macrophage activation with single-cell resolution through machine learning. *Proc. Natl. Acad. Sci. U.S.A.* 115, E2676–E2685.
- Perez-Guaita, D., Quintas, G., Farhane, Z., Tauler, R., and Byrne, H. J. (2020). Data mining Raman microspectroscopic responses of cells to drugs in vitro using multivariate curve resolution-alternating least squares. *Talanta* 208:120386. doi: 10.1016/j.talanta.2019.120386
- Perna, G., Lastella, M., Lasalvia, M., Mezzenga, E., and Capozzi, V. (2007). Raman spectroscopy and atomic force microscopy study of cellular damage in human keratinocytes treated with HgCl<sub>2</sub>. *J. Mol. Struct.* 27, 834–836.
- Raman, C. V., and Krishnan, K. S. (1928). A new type of secondary radiation. *Nature* 121, 501–502. doi: 10.1038/121501c0
- Rasel, M. A. I., Singh, S., Nguyen, T. D., Afara, I. O., and Gu, Y. (2019). Impact of nanoparticle uptake on the biophysical properties of cell for biomedical engineering applications. *Sci. Rep.* 9, 1–13.
- Ravanshad, R., Karimi Zadeh, A., Amani, A. M., Mousavi, S. M., Hashemi, S. A., Savar Dashtaki, A., et al. (2018). Application of nanoparticles in cancer detection by Raman scattering based techniques. *Nano Rev. Exp.* 9:1373551. doi: 10.1080/20022727.2017.1373551
- Roman, M., Wrobel, T. P., Panek, A., Efeoglu, E., Wiltowska-Zuber, J., Paluszkiwicz, C., et al. (2019). Exploring subcellular responses of prostate cancer cells to X-ray exposure by Raman mapping. *Sci. Rep.* 9, 1–13.
- Roy, I., Ohulchanskyy, T. Y., Bharali, D. J., Pudavar, H. E., Mistretta, R. A., Kaur, N., et al. (2005). Optical tracking of organically modified silica nanoparticles as DNA carriers: a nonviral, nanomedicine approach for gene delivery. *Proc. Natl. Acad. Sci. U.S.A.* 102, 279–284. doi: 10.1073/pnas.0408039101
- Saariinen, J., Gütter, F., Lindman, M., Agopov, M., Fraser-Miller, S. J., Scherließ, R., et al. (2019). Cell-nanoparticle interactions at (Sub)-nanometer resolution analyzed by electron microscopy and correlative coherent anti-stokes raman scattering. *Biotechnol. J.* 14:e1800413. doi: 10.1002/biot.201800413
- Sahoo, S. K., Umaphathy, S., and Parker, A. W. (2011). Time-resolved resonance Raman spectroscopy: exploring reactive intermediates. *Appl. Spectrosc.* 65, 1087–1115. doi: 10.1366/11-06406
- Salvati, A., Åberg, C., dos Santos, T., Varela, J., Pinto, P., Lynch, I., et al. (2011). Experimental and theoretical comparison of intracellular import of polymeric nanoparticles and small molecules: toward models of uptake kinetics. *Nanomed. Nanotechnol. Biol. Med.* 7, 818–826. doi: 10.1016/j.nano.2011.03.005
- Schwarze, B., Gozzi, M., Zilberfain, C., Rüdiger, J., Birkemeyer, C., Estrela-Lopis, I., et al. (2020). Nanoparticle-based formulation of metallacarboranes with bovine serum albumin for application in cell cultures. *J. Nanopart. Res.* 22, 1–22. doi: 10.19184/pk.v6i1.6609
- Shalabaeva, V., Lovato, L., La Rocca, R., Messina, G. C., Dipalo, M., Miele, E., et al. (2017). Time resolved and label free monitoring of extracellular metabolites by surface enhanced Raman spectroscopy. *PLoS One* 12:e0175581. doi: 10.1371/journal.pone.0175581
- Shaper, K., Fenaroli, F., Lynch, I., Cottell, D. C., Salvati, A., and Dawson, K. A. (2011). Time, and space resolved uptake study of silica nanoparticles by human cells. *Mol. Biosyst.* 7, 371–378. doi: 10.1039/c0mb00109k
- Short, K. W., Carpenter, S., Freyer, J. P., and Mourant, J. R. (2005). Raman spectroscopy detects biochemical changes due to proliferation in mammalian cell cultures. *Biophys. J.* 88, 4274–4288. doi: 10.1529/biophysj.103.038604
- Smith, R. J., King, P. J., Lotya, M., Wirtz, C., Khan, U., De, S., et al. (2011). Large-scale exfoliation of inorganic layered compounds in aqueous surfactant solutions. *Adv. Mater.* 23, 3944–3948. doi: 10.1002/adma.201102584

- Soler, M. A. G., Bão, S. N., Alcântara, G. B., Tib, V. H. S., Paludo, G. R., Santana, J. F. B., et al. (2007). Interaction of erythrocytes with magnetic nanoparticles. *J. Nanosci. Nanotechnol.* 7, 1069–1071. doi: 10.1166/jnn.2007.423
- Storrie, H., and Mooney, D. J. (2006). Sustained delivery of plasmid DNA from polymeric scaffolds for tissue engineering. *Adv. Drug Deliv. Rev.* 58, 500–514. doi: 10.1016/j.addr.2006.03.004
- Suh, H., Jeong, B., Liu, F., and Kim, S. W. (1998). Cellular uptake study of biodegradable nanoparticles in vascular smooth muscle cells. *Pharm. Res.* 15, 1495–1498.
- Swain, R. J., Jell, G., and Stevens, M. M. (2008). Non-invasive analysis of cell cycle dynamics in single living cells with Raman micro-spectroscopy. *J. Cell Biochem.* 104, 1427–1438. doi: 10.1002/jcb.21720
- Szafraniec, E., Majzner, K., Farhane, Z., Byrne, H. J., Lukawska, M., Oszczapowicz, I., et al. (2016). Spectroscopic studies of anthracyclines: structural characterization and in vitro tracking. *Spectrochim. Acta Part A Mol. Biomol. Spectrosc.* 169, 152–160. doi: 10.1016/j.saa.2016.06.035
- Talari, A. C. S., Movasaghi, Z., Rehman, S., and Rehman, I. U. (2015). Raman spectroscopy of biological tissues. *Appl. Spectrosc. Rev.* 50, 46–111. doi: 10.1080/05704928.2014.923902
- Terasaki, M., and Jaffe, L. A. (1991). Organization of the sea urchin egg endoplasmic reticulum and its reorganization at fertilization. *J. Cell Biol.* 114, 929–940. doi: 10.1083/jcb.114.5.929
- Thaxton, C. S., Rink, J. S., Naha, P. C., and Cormode, D. P. (2016). Lipoproteins and lipoprotein mimetics for imaging and drug delivery. *Adv. Drug Deliv. Rev.* 106, 116–131. doi: 10.1016/j.addr.2016.04.020
- Uzunbajakava, N., Lenferink, A., Kraan, Y., Willekens, B., Vrensen, G., Greve, J., et al. (2003). Nonresonant Raman imaging of protein distribution in single human cells. *Biopolym. Biospectrosc. Sect.* 72, 1–9. doi: 10.1002/bip.10246
- Vankeirsbilck, T., Vercauteren, A., Baeyens, W., Van der Weken, G., Verpoort, F., Vergote, G., et al. (2002). Applications of Raman spectroscopy in pharmaceutical analysis. *TrAC Trends Anal. Chem.* 21, 869–877.
- Vernooij, R. R., Joshi, T., Horbury, M. D., Graham, B., Izgorodina, E. I., Stavros, V. G., et al. (2018). Spectroscopic studies on photoinduced reactions of the anticancer Prodrug, trans,trans,trans-[Pt(N3)2(OH)2(py)2]. *Chem. A Eur. J.* 24, 5790–5803. doi: 10.1002/chem.201705349
- Wang, Z., Bonoio, A., Samoc, M., Cui, Y., and Prasad, P. N. (2008). Biological pH sensing based on surface enhanced Raman scattering through a 2-aminothiophenol-silver probe. *Biosens. Bioelectron.* 23, 886–891. doi: 10.1016/j.bios.2007.09.017
- Watson, P., Jones, A. T., and Stephens, D. J. (2005). Intracellular trafficking pathways and drug delivery: fluorescence imaging of living and fixed cells. *Adv. Drug Deliv. Rev.* 57, 43–61. doi: 10.1016/j.addr.2004.05.003
- Wittwehr, C., Aladjov, H., Ankley, G., Byrne, H. J. H. J., de Knecht, J., Heinzle, E., et al. (2017). No Title. *Toxicol. Sci.* 155, 326–336.
- Yin Win, K., and Feng, S. S. (2005). Effects of particle size, and surface coating on cellular uptake of polymeric nanoparticles for oral delivery of anticancer drugs. *Biomaterials* 26, 2713–2722. doi: 10.1016/j.biomaterials.2004.07.050
- Zhang, W., Liang, J., Lu, X., Ren, W., and Liu, C. (2020). Nanoparticle tracking analysis-based in vitro detection of critical biomarkers. *ACS Appl. Nano Mater.* 3, 2881–2888. doi: 10.1021/acsnm.0c00154

**Conflict of Interest:** The authors declare that the research was conducted in the absence of any commercial or financial relationships that could be construed as a potential conflict of interest.

The handling editor declared a past co-authorship with several of the authors, HB, EE, and JM.

Copyright © 2020 Byrne, Bonnier, Efeoglu, Moore and McIntyre. This is an open-access article distributed under the terms of the Creative Commons Attribution License (CC BY). The use, distribution or reproduction in other forums is permitted, provided the original author(s) and the copyright owner(s) are credited and that the original publication in this journal is cited, in accordance with accepted academic practice. No use, distribution or reproduction is permitted which does not comply with these terms.



# A Plant Bioreactor for the Synthesis of Carbon Nanotube Bionic Nanocomposites

Giulia Magnabosco<sup>1</sup>, Maria F. Pantano<sup>2</sup>, Stefania Rapino<sup>1</sup>, Matteo Di Giosia<sup>1</sup>,  
Francesco Valle<sup>3</sup>, Ludovic Taxis<sup>2</sup>, Francesca Sparla<sup>4</sup>, Giuseppe Falini<sup>1\*</sup>,  
Nicola M. Pugno<sup>2,5\*</sup> and Matteo Calvaresi<sup>1\*</sup>

<sup>1</sup> Dipartimento di Chimica “Giacomo Ciamician,” Alma mater Studiorum—Università di Bologna, Bologna, Italy, <sup>2</sup> Laboratory of Bio-Inspired, Bionic, Nano, Meta Materials and Mechanics, Department of Civil, Environmental and Mechanical Engineering, University of Trento, Trento, Italy, <sup>3</sup> Istituto per lo Studio dei Materiali Nanostrutturati (CNR-ISMN), Consiglio Nazionale delle Ricerche, Bologna, Italy, <sup>4</sup> Department of Pharmacy and Biotechnology, Alma mater Studiorum—Università di Bologna, Bologna, Italy, <sup>5</sup> School of Engineering and Materials Science, Queen Mary University of London, London, United Kingdom

## OPEN ACCESS

### Edited by:

Valentina Castagnola,  
Italian Institute of Technology (IIT), Italy

### Reviewed by:

Fabio Candonato Carniel,  
University of Trieste, Italy  
Amitava Mukherjee,  
VIT University, India

### \*Correspondence:

Matteo Calvaresi  
matteo.calvaresi3@unibo.it  
Giuseppe Falini  
giuseppe.falini@unibo.it  
Nicola M. Pugno  
nicola.pugno@unitn.it

### Specialty section:

This article was submitted to  
Nanobiotechnology,  
a section of the journal  
Frontiers in Bioengineering and  
Biotechnology

**Received:** 08 May 2020

**Accepted:** 14 October 2020

**Published:** 05 November 2020

### Citation:

Magnabosco G, Pantano MF,  
Rapino S, Di Giosia M, Valle F, Taxis L,  
Sparla F, Falini G, Pugno NM and  
Calvaresi M (2020) A Plant Bioreactor  
for the Synthesis of Carbon Nanotube  
Bionic Nanocomposites.  
Front. Bioeng. Biotechnol. 8:560349.  
doi: 10.3389/fbioe.2020.560349

Bionic composites are an emerging class of materials produced exploiting living organisms as reactors to include synthetic functional materials in their native and highly performing structures. In this work, single wall carboxylated carbon nanotubes (SWCNT-COOH) were incorporated within the roots of living plants of *Arabidopsis thaliana*. This biogenic synthetic route produced a bionic composite material made of root components and SWCNT-COOH. The synthesis was possible exploiting the transport processes existing in the plant roots. Scanning electrochemical microscopy (SECM) measurements showed that SWCNT-COOH entered the vascular bundles of *A. thaliana* roots localizing within xylem vessels. SWCNT-COOH preserved their electrical properties when embedded inside the root matrix, both at a microscopic level and a macroscopic level, and did not significantly affect the mechanical properties of *A. thaliana* roots.

**Keywords:** bionic synthesis, nanobio composite, nanobio interactions, carbon nanotubes, plant nanobioreactor

## INTRODUCTION

Nanocomposite materials are attracting growing attention in current research for their promising applications in relevant fields such as catalysis (Walsh et al., 2011), medicine (Magnabosco et al., 2015) and sensing (Zhang et al., 2010). Currently, their fabrication routes consist mainly in chemical- and physical- based techniques. The conditions used in these synthetic protocols are usually harsh and employ elevated temperatures and pressures, organic solvents and toxic and expensive chemicals. Living organisms can offer great assistance to chemists to synthesize new materials (Valentini et al., 2016; Ashfaq et al., 2018; Nguyen et al., 2018; Magnabosco et al., 2019; Pugno and Valentini, 2019). After all, living organisms are essentially “nano-factories.” The synthesis of nanomaterials/nanocomposites using biology can be far superior to other technological methods in terms of cost and their eco-friendly nature. Biological entities can control precisely the composition and morphology of nanocomposites while working in physiological conditions, close to neutral pH and at room temperature. The exploitation of living organisms to direct the syntheses of nanocomposites is extremely attractive for two main reasons: (i) the production of the materials takes place in conditions milder than those used in traditional materials-processing techniques;



(ii) the reduction of energy inputs and chemicals required to produce the nanocomposites makes bio-enabled syntheses inherently “green” processes. The latter is particularly relevant for *in vitro* or *in vivo* applications since the reagents that are used in chemical syntheses are often toxic and may remain as contaminants in the final product.

Composites made with carbon nanomaterials (CNMs) have been extensively studied to obtain new materials that exploit their chemical and physical proprieties (Calvaresi et al., 2013; Giosia et al., 2016). In particular, carbon nanotubes (CNTs) are one-dimensional (1-D) carbon nanoparticles having excellent electrical, thermal and mechanical proprieties. It is known that CNTs may interact with proteins and living organisms (Long et al., 2012; Calvaresi and Zerbetto, 2013; Wang et al., 2013; Dewi et al., 2015; Lukhele et al., 2015; Thakkar et al., 2016; Di Giosia et al., 2019, 2020); however, most of the work is limited to the study of their toxicity and does not explore their use as an additive to obtain new materials. The inclusion of CNM into plants, their organelles, and organelle components has the potential to enhance their functions (Faltermeier et al., 2014; Wong et al., 2016). For example, CNTs incorporated into isolated thylacoid enhance their maximum electron transport rates (Dewi et al., 2015). A pioneering study by Girardo et al. showed how the direct injection of functionalized CNT into *A. thaliana* leaves allows to prepare a bionic leaf which can be used as a NO sensor (Faltermeier et al., 2014).

Incorporation of nanomaterials inside a whole living plant to create innovative nanocomposites simply by growing the plants in a medium containing the additive is a big challenge.

In this paper, we demonstrated for the first time the possibility to incorporate single wall carboxylated carbon nanotubes (SWCNT-COOH) into the roots of living plants of *Arabidopsis thaliana* to obtain a bionic composite made of root material and SWCNT-COOH, by exploiting the transport properties of *A. thaliana* roots. The bionic incorporation of nanomaterials inside roots directly by using the plant as a “nanoreactor” represents a pioneering approach able to overcome the limitations of laboratory synthesis.

## MATERIALS AND METHODS

### Water Dispersion of SWCNT-COOH

SWCNT-COOH were purchased by Cheap Tubes (Short COOH Functionalized Single Walled-Double Walled Carbon Nanotubes 1–4 nm). Water dispersions of SWCNT-COOH were obtained by ultrasonication using a probe tip sonicator (Misonix XL2020; 500 W, 40% power) cooling the solution with ice bath, in pre-milliQ water at the concentration of 0.1 mg/mL for 20 min. Lower concentrations were obtained by dilution.

### Plant Growing Methods

**Germination.** The percentage of germination of *A. thaliana* (ecotype Columbia) seeds was calculated by counting seedlings at the emerging of the first true leaves (about 2 weeks after sowing). Seeds were sterilized with chlorine fumes for 4 h and then transferred into square plates (10 × 10 cm<sup>2</sup> Petri dishes

with grid) containing half-strength Murashige-Skoog medium (1/2MS medium; Micropoli, Milan, Italy), 8 g/L agar and SWCNT-COOH at different concentrations (0.1 mg/mL, 10 µg/mL, and 1 µg/mL). To avoid SWCNT-COOH precipitation, different concentrations of SWCNT-COOH were sterilized at 121°C for 20 min in presence of water-dispersed agar. A stock solution of 1/2MS medium 100× was sterilized separately, cooled to 40°C and then mixed with SWCNT-COOH/agar solutions to reach the correct final concentration. Four-day cold stratification (the seeds were subjected to both cold, 4°C, and moist conditions. *Arabidopsis thaliana* seeds require these conditions before germination) in the dark was applied prior to transfer seeds into growth chamber. Plants were cultured at 22°C, with cycle of 12-h light/12-h dark, and illuminated with a photosynthetic photon flux density of 110 µmol m<sup>-2</sup> s<sup>-1</sup>.

**Hydroponic Culture.** Plants were grown in 1/2MS medium (not supplemented with agar) in the condition described above. Seedholders were filled with 6.5 g/L sterile agarose and containing one seed each. Plants were grown for 28 days allowing the development of a long radical apparatus. After 28 days the plants were transferred to water solution supplemented with dispersed SWCNT-COOH at a concentration of 10 µg/mL, 1 µg/mL, 0.1 µg/mL, and pure water. Plants were kept for a further 6 days under the conditions mentioned above.

## Microscopic Characterization of the Plant Roots

**Scanning Electron Microscopy.** SEM images were collected on uncoated samples using a Phenom G2 and a Zeiss (LEO) 1530VP. The roots were fixed with glutaraldehyde 2.5% in PBS and then air dried. To obtain sections, roots were embedded into polydimethylsiloxane (PDMS) and cut. The root was sliced at the level of the mid-elongation zone, in between the apex and the stem.

**Atomic Force Microscopy.** Substrate surfaces used for AFM imaging were native Silicon Oxide (SiOx) functionalized with 3-Aminopropyltriethoxysilane (APTES). Briefly, the SiOx pieces were first cleaned by the sequential sonication in Acetone, Isopropyl alcohol, and milliQ water; then they were exposed to an oxygen plasma for 5 min. The fragments were then closed in a desiccator containing 10 µl APTES and 10 µl triethanolamine under a mild vacuum for 30 min; 5 µl of CNT solution was spotted onto the APTES-SiOx and dried. Images were performed using a Multimode VIII AFM (Bruker) equipped with a Nanoscope V controller and operated in Peakforce tapping mode; NSG01 probes (NT-MDT) were used. Images were processed by Gwyddion.

## Electrochemical Measurements

Scanning electrochemical microscopy (SECM) measurements were performed using an experimental setup coupling a 910B SECM (CH Instruments) with a Nikon ECLIPSE Ti inverted optical microscope. The stepper motors and the piezoelectric components of the 910B CHI instrument for the microelectrode displacement were removed from the original stage and mounted

on the plate of the inverted microscope. SECM measurements were performed on roots cross-section using ferrocenemethanol 1 mM as redox mediator in PBS. A 10  $\mu\text{m}$  platinum disk electrode with an  $\text{RG} = 10$  was used as working electrode, an  $\text{Ag}/\text{AgCl}$  (3 M KCl) and a platinum wire acted as reference and counter electrodes, respectively. Data analysis and approach curve fitting were performed using the software MIRA. Conductance was measured with a digimaster tester (DM39A) along 1 cm of root.

## Tensile Tests

Tensile tests were carried out on fresh roots, using the Nanotensile Tester T150 UTM by Agilent. Root samples with typical gage length of 13 mm were tested at room temperature and at a strain rate of  $0.001 \text{ s}^{-1}$ . The measurements were repeated for 6 different samples on control and SWCNT-COOH treated roots.

## RESULTS

### Germination Studies in Presence of SWCNT-COOH

Germination studies were performed to evaluate the *A. thaliana* seeds ability to germinate in presence of SWCNT-COOH (Supplementary Figures S1, S2) and to incorporate the SWCNT-COOH during this growth stage. The germination of *A. thaliana* was not affected by the presence of SWCNT-COOH in the examined interval of concentrations (1–100  $\mu\text{g}/\text{mL}$ ). SWCNT-COOH treated samples appear very similar to the control, suggesting that no incorporation of the SWCNT-COOH happened. SEM image analysis of the SWCNT-COOH/agar matrix showed that SWCNT-COOH are strongly embedded within the agar matrix (Supplementary Figure S3).

### Hydroponic Culture in the Presence of SWCNT-COOH

Twenty-eight day old plants were transferred in dispersions of SWCNT-COOH in deionized water at different concentrations (10  $\mu\text{g}/\text{mL}$ , 1  $\mu\text{g}/\text{mL}$ , 0.1  $\mu\text{g}/\text{mL}$ , pure water) for 6 days. After 6 days, roots changed coloration and some plants died (see Supplementary Figures S4, S5). All the samples treated with SWCNT-COOH showed an increased mortality compared to the control (Supplementary Figure S5). The effect of SWCNT-COOH on *A. thaliana* vitality was concentration dependent. At the maximum concentration (10  $\mu\text{g}/\text{mL}$ ) and at the lowest concentration (0.1  $\mu\text{g}/\text{mL}$ ), a minimum toxic effect was observed. At the intermediate concentration of SWCNT-COOH (1  $\mu\text{g}/\text{mL}$ ), a strong toxic effect was observed. As can be seen in Figure 1, after 6 days of SWCNT-COOH treatment, the aspect of roots of the survived plants changed visibly, became black and remained black also after repeated washing.

UV-vis analysis (Supplementary Figure S6) of the three solutions (10  $\mu\text{g}/\text{mL}$ , 1  $\mu\text{g}/\text{mL}$ , and 0.1  $\mu\text{g}/\text{mL}$ ) showed a signal

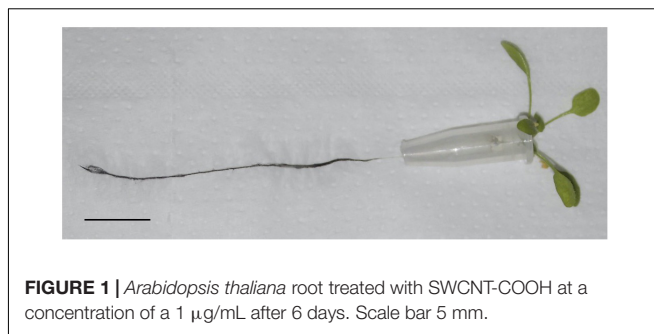


**FIGURE 1** | *Arabidopsis thaliana* root treated with SWCNT-COOH at a concentration of a 1  $\mu\text{g}/\text{mL}$  after 6 days. Scale bar 5 mm.

of the SWCNT-COOH absorbance proportional to the SWCNT-COOH concentration.

Analysis of the AFM images and relative height profile analysis revealed the dispersion state of the SWCNTs-COOH in deionized water at the different concentrations (Supplementary Figure S7). At the maximum concentration (10  $\mu\text{g}/\text{mL}$ ) SWCNTs-COOH are present in form of bundles of different sizes, while at the intermediate concentration (1  $\mu\text{g}/\text{mL}$ ) the SWCNT-COOH are monodispersed. At the lowest concentration, no clear SWCNT-COOH signal was detected, also at higher magnification, demonstrating the very low amount of SWCNT-COOH present in solution at this concentration (0.1  $\mu\text{g}/\text{mL}$ ), as confirmed also by the UV-vis spectra (Supplementary Figure S6).

### Microscopic Characterization of the SWCNT-COOH/Plant Roots Nanocomposite

The root slices were analyzed with scanning electron microscopy (SEM) and scanning electrochemical microscopy (SECM). The SECM technique enables spatially resolved imaging of SWCNT-COOH avoiding the use of probes and stimuli that may destroy the biological tissue, taking advantage of SWCNT-COOH electrical properties (Rapino et al., 2010, 2014; Lin et al., 2018). The presence of SWCNT-COOH was confirmed by SECM approach curves on the roots of treated and non-treated samples (Figure 2A). In fact, the approach curves on non-treated roots showed a typical insulating behavior described by the negative feedback model for insulating substrate, where a decrease of the faradic current is recorded when the sample is approached as an effect of the hindered diffusion of the redox mediator to the probe due to the physical presence of the insulating sample (Lin et al., 2018). On the contrary, the SWCNT-COOH treated samples act as electric conductors, described by the positive feedback model for conductive substrates, as the nanotubes present in the roots are able to regenerate the redox mediator in its pristine form by quickly exchanging electrons with it (Figure 2B) (Rapino et al., 2010). By overlapping a SECM map and a SEM image (Figure 3A) of the same region, it can be observed that the most conductive regions correspond to root vascular bundle. The incorporation of the SWCNT-COOH lowers the resistivity of the roots. In fact, non-treated root showed a resistance of 5.9  $\text{M}\Omega$  while a treated one has a resistance of 1.0  $\text{M}\Omega$ , measured with a tester along 1 cm of root. The SEM image of a SWCNT-COOH rich

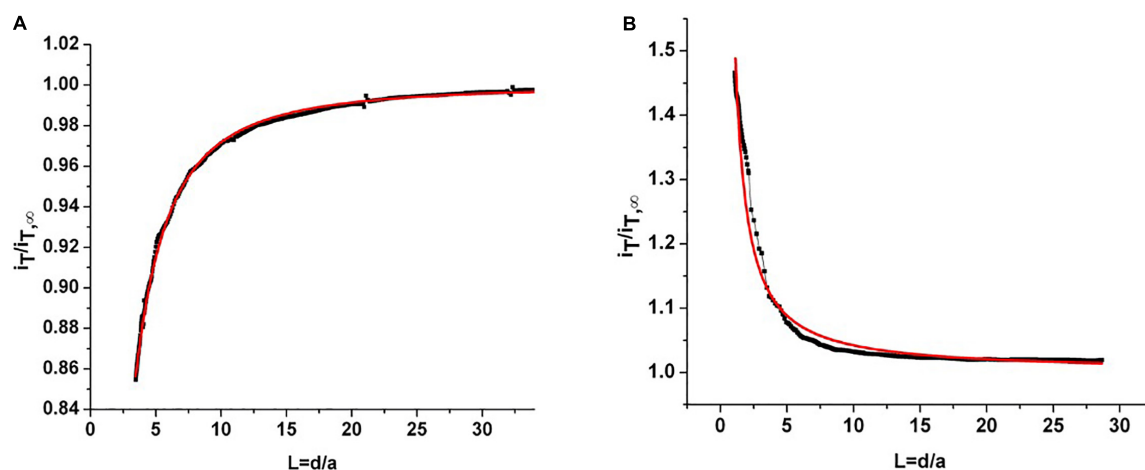


**FIGURE 2 | (A)** Experimental approach curve on non-treated root (black line) and fitted curve using a negative feedback model for insulating substrates (red line). **(B)** Experimental approach curve on root treated with SWCNT-COOH (black line) and fitted curve using a positive feedback model for conductor substrates (red line).  $i_T/i_{T\infty}$  is the current recorded at the probe divided by the current recorded at the probe in the bulk and  $L = d/a$  is given by the probe-sample separation divided by the ultramicroelectrode (probe) active radius.

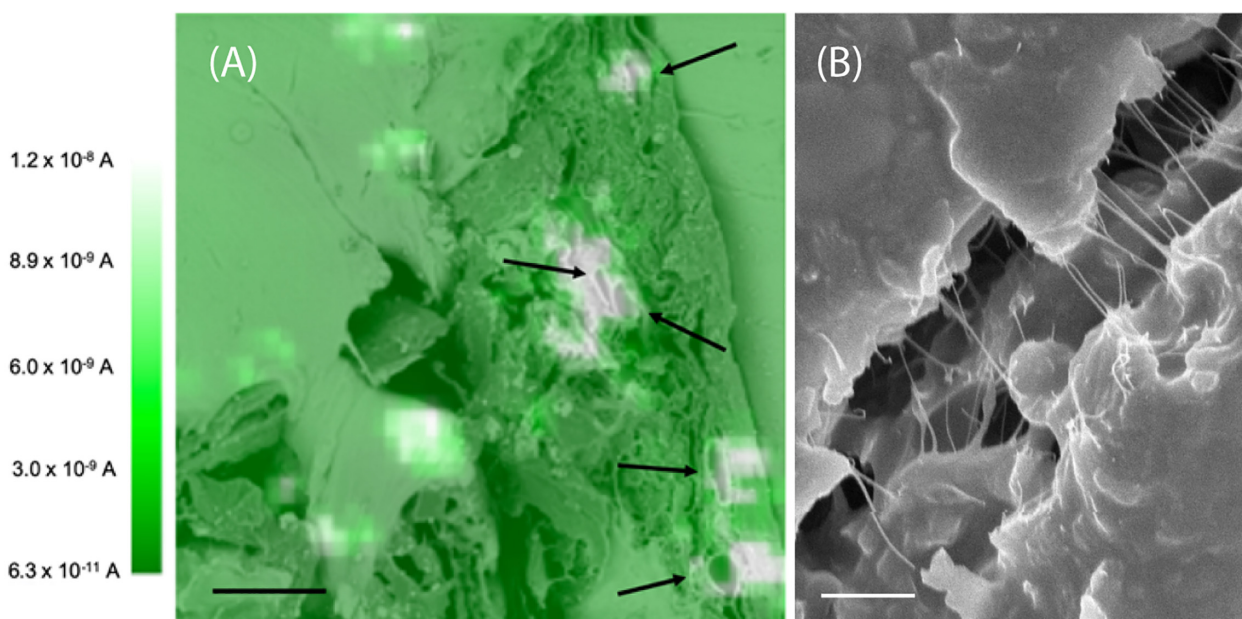


**FIGURE 3 | (A)** SECM image of an *A. thaliana* root section overlapped with SEM image. The white spots are conductive regions due to the presence of SWCNT-COOH. The black arrows indicate the plant vessels. These images are representative of the entire population of samples. Scale bar of 10  $\mu\text{m}$ . The SECM image was performed in 1 mM ferrocenemethanol in PBS, using a 10  $\mu\text{m}$  Pt working electrode,  $E = 0.5$  V versus Ag/AgCl (3 M KCl). **(B)** Scanning electron microscopy image of a SWCNT-COOH rich region of the *A. thaliana* root. Scale bar of 1  $\mu\text{m}$ .

region into the *A. thaliana* root (**Figure 3B**) shows that SWCNT-COOH bundles are incorporated within the root matrix.

### Mechanical Characterization of the SWCNT-COOH/Plant Roots Nanocomposite

Mechanical properties of the composite materials (**Supplementary Figure S8**) were derived through tensile

tests of root samples. Considering the high variability that always characterizes biological materials, there are no significant differences between treated and untreated roots in terms of Young modulus, fracture strain, and strength, where the presence of SWCNT-COOH results to affect slightly the mechanical properties of the *A. thaliana* roots. As it may happen in composite materials, this behavior, as observed in **Figure 4A**, indicates that a phase separation occurs



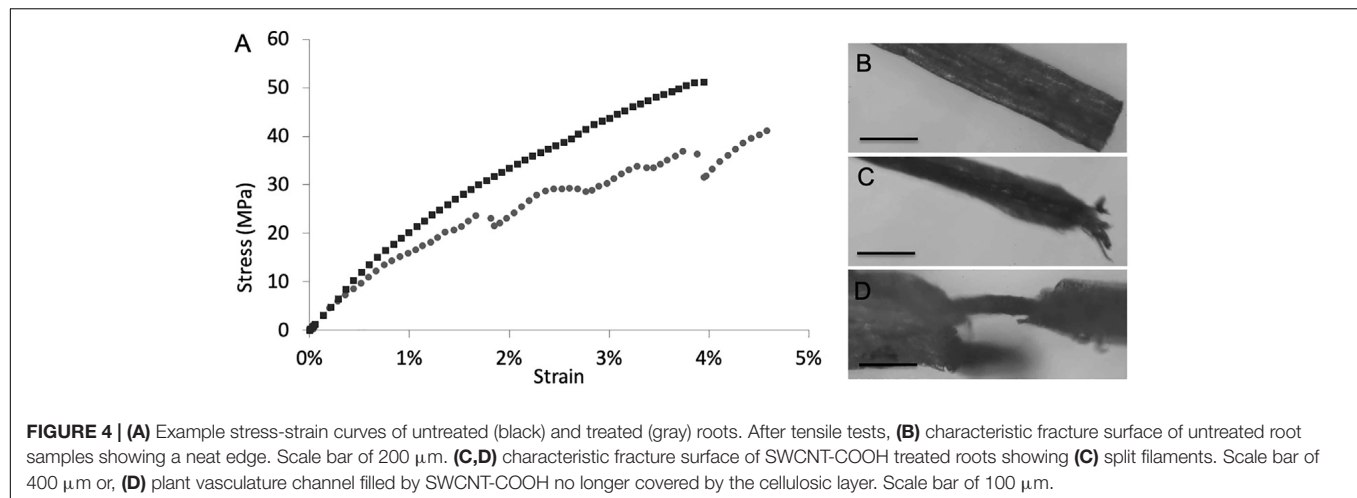


**FIGURE 4 | (A)** Example stress-strain curves of untreated (black) and treated (gray) roots. After tensile tests, **(B)** characteristic fracture surface of untreated root samples showing a neat edge. Scale bar of 200  $\mu\text{m}$ . **(C,D)** characteristic fracture surface of SWCNT-COOH treated roots showing **(C)** split filaments. Scale bar of 400  $\mu\text{m}$  or, **(D)** plant vasculature channel filled by SWCNT-COOH no longer covered by the cellulosic layer. Scale bar of 100  $\mu\text{m}$ .

and SWCNT-COOH do not interact uniformly with the biological matrix, that thus cannot take advantage of their higher mechanical performance. The treated samples often present a sequence of load drops, which can be ascribed to inhomogeneity in the sample, with stiffer and softer regions that reduce both the load standing and elongation capability. Such hypothesis is supported by optical investigation of samples after mechanical tests. In fact, as shown in **Figures 4B–D**, the fracture surface of untreated root samples usually showed a neat edge (**Figure 4B**), while in the fractured surface of SWCNT-COOH treated roots it is possible to see the external part of the root broken while the inner channels containing SWCNT-COOH are still intact, owing to their higher mechanical resistance (**Figures 4C,D**).

## DISCUSSION

For the biogenic incorporation of SWCNT-COOH into roots, we selected the plant *A. thaliana*, widely used as a model organism in plant biology. Initially, the toxicity of SWCNT-COOH toward the plant and the ability to incorporate SWCNT-COOH in the germination stage was verified. Water uptake is a critical step in seed germination. In fact, mature seeds are relatively dry and need a substantial amount of water to initiate cellular metabolism and growth. Imbibition is the physical process that marks the start of germination. The incorporation of SWCNT-COOH in the nascent plant may happen at that stage, as CNTs have been shown to penetrate the seed-coat and stimulate the seed germination due to more efficient water uptake induced by the CNT (Villagarcia et al., 2012). However, the germination of *A. thaliana* was not affected by the presence of SWCNT-COOH, suggesting that no incorporation of the SWCNT-COOH happened. The agar matrix present in the growth media entraps the SWCNTs-COOH (**Supplementary Figure S3**), and consequently, their effect on seed germination is limited.

Then, hydroponic culture was performed to study the effect of SWCNT-COOH on adult plants. Adult plants kept in

deionized water become turgid due to a massive internalization of water caused by the difference in osmotic pressure (Munns et al., 2000; Schopfer, 2006). This phenomenon was exploited to favor the uptake of SWCNT-COOH. All the samples treated with SWCNT-COOH showed an increased mortality compared to the control, meaning that at this stage of the life cycle SWCNT-COOH have a toxic effect on plants, due to SWCNT-COOH incorporation. Counterintuitively, at the maximum concentration (10  $\mu\text{g/mL}$ ) the minimum toxic effect was observed. This occurs because at high concentrations aqueous dispersion of SWCNT-COOH associate into bundles, see **Supplementary Figure S6** (Koh and Cheng, 2016), that are too big to be absorbed by the root. At the intermediate concentration of SWCNT-COOH (1  $\mu\text{g/mL}$ ) the maximum toxic effect was observed. At this concentration the SWCNT-COOH are well dispersed and can be internalized by the roots, causing a high mortality due to their toxic effect. Aggregation of the SWCNTs significantly affects their ability to interact with plants (Villagarcia et al., 2012). At the concentration of 0.1  $\mu\text{g/mL}$ , the toxic effect of SWCNT-COOH was greatly reduced.

Based on the mortality test results, the roots treated with 1  $\mu\text{g/mL}$  SWCNT-COOH were selected for further experiments, because when the maximum toxic effect is observed, a higher SWCNT-COOH incorporation is expected. After exposition to SWCNT-COOH, the roots of the survived plants became black. The obtained SWCNT-COOH/root composite was characterized.

Nanomaterials can be absorbed by primary and lateral roots or can be simply adsorbed on the surface of roots (Ma et al., 2010; Pérez-de-Luque, 2017). To discriminate between incorporation or surface adsorption, it is necessary to observe the inner vessels of the root (xylem and phloem), which can be accessible by slicing the root perpendicularly to its axis. The roots were sliced and analyzed with SEM and SECM.

Globally, non-treated roots showed a typical insulating behavior, while SWCNT-COOH treated samples behave as electric conductors, showing that the electrical properties of the conductive SWCNT-COOH are transferred to the insulating cellulose matrix, and demonstrating the fabrication of a biogenic



composite material. The incorporation of the SWCNT-COOH influences also the macroscopic proprieties of the material, lowering the resistivity of the roots of 6 times. The increased conductivity observed in well-defined regions of the root, as showed by the overlap of SECM map and a SEM image (**Figure 3A**), corresponding to root vascular bundles can be ascribed to the incorporation of the SWCNT-COOH in the plant vessels, characterized in the section by a circular region (indicated by black arrows in **Figure 3A**). Plant vascular bundle includes xylem and phloem that transport water and mineral ions (xylem) and photosynthates (phloem) from and to the roots, respectively. The above experimental data suggests that SWCNT-COOH can enter into root xylem and assembly orienting along their main axis. These results are in agreement with previous studies, where carbon nanotubes were detected in root xylem, suggesting that CNTs penetrated the epidermal tissue and root cap to enter the root xylem (Zhai et al., 2015).

As described for other carbon nanomaterials (Villagarcia et al., 2012; Zhai et al., 2015) and nanoparticles (Wang et al., 2012; Ma et al., 2017; Sun et al., 2020), SWCNT-COOH translocation takes place along with the uptake of water, then the nanoparticles are transported through the xylem.

Localization of SWCNT-COOH in the vascular bundles is also supported by mechanical studies. In fact, incorporation of SWCNT-COOH affects slightly the mechanical properties of the *A. thaliana* roots. However, the stress-strain curves of SWCNT-COOH treated roots shows a sequence of load drops, typical of composite materials. This behavior is also supported by optical investigation of samples after tensile tests. In fact, the characteristic fracture surface of untreated root samples shows a neat edge, while the fracture surface of SWCNT-COOH treated roots shows split filaments. The local fracture of the external layer (more or less severe and visible from optical inspection) can thus be correlated to the load drops observed in the stress-strain curve.

## CONCLUSION

This work demonstrates for the first time that it is possible to create a new bionic material by growing *A. thaliana* in a medium containing SWCNT-COOH. SWCNT-COOH can enter the vascular bundles of *A. thaliana* roots localizing within xylem vessels. The conductive electrical properties of the SWCNT-COOH are transferred to the root matrix, which is intrinsically insulating. SWCNT-COOH are internalized and

localized in the root's xylem giving rise to both micro- and macro-scale conductivity of the composite. Stress-strain tests demonstrated the typical behavior of a composite, with stiffer and softer regions evidenced by a more resistant inner channel and a less resistant external layer. Even if the use of plants as bioreactors may introduce technological issues due to biological variability as repeatability of the synthetic process, yield for cycle, and downstream processing, all the observations confirm the successful entrapment of SWCNT-COOH by *A. thaliana* roots and demonstrate the fabrication of a "bionic composite," posing the basis for the *in vivo* synthesis of new materials taking advantage of the living organism as a reactor.

## DATA AVAILABILITY STATEMENT

The raw data supporting the conclusions of this article will be made available by the authors, without undue reservation.

## AUTHOR CONTRIBUTIONS

GF, NMP, and MC contributed to the conception, design, and execution of this study. GM, MP, SR, LT, MD, FV, and FS executed the experiments described in this study. GF, NMP, and MC developed the analysis methodology. MC and GF drafted the manuscript with revisions contributed by all authors. All authors contributed to manuscript revision, and read and approved the submitted version.

## FUNDING

NMP was supported by the European Commission under the FET Open (Boheme), Grant No. 863179. GF and MC were supported by the European Commission under the Graphene Flagship Core 2, Grant No. 785219 (WP13, "Functional Foams and Coatings").

## SUPPLEMENTARY MATERIAL

The Supplementary Material for this article can be found online at: <https://www.frontiersin.org/articles/10.3389/fbioe.2020.560349/full#supplementary-material>

## REFERENCES

- Ashfaq, M., Iqbal, A., Naeem, K., Gul, H., Mahmood, N., Hasan, M., et al. (2018). Biological entities as chemical reactors for synthesis of nanomaterials: progress, challenges and future perspective. *Mater. Today Chem.* 8, 13–28. doi: 10.1016/j.mtchem.2018.02.003
- Calvaresi, M., Falini, G., Pasquini, L., Reggi, M., Fermani, S., Gazzadi, G. C., et al. (2013). Morphological and mechanical characterization of composite calcite/SWCNT-COOH single crystals. *Nanoscale* 5, 6944–6949. doi: 10.1039/c3nr01568h
- Calvaresi, M., and Zerbetto, F. (2013). The devil and holy water: protein and carbon nanotube hybrids. *Acc. Chem. Res.* 46, 2454–2463. doi: 10.1021/ar300347d
- Dewi, H. A., Sun, G., Zheng, L., and Lim, S. (2015). Interaction and charge transfer between isolated thylakoids and multi-walled carbon nanotubes. *Phys. Chem. Chem. Phys.* 17, 3435–3440. doi: 10.1039/c4cp04575k
- Di Giosia, M., Marforio, T. D., Cantelli, A., Valle, F., Zerbetto, F., Su, Q., et al. (2020). Inhibition of  $\alpha$ -chymotrypsin by pristine single-wall carbon nanotubes: clogging up the active site. *J. Coll. Interface Sci.* 571, 174–184. doi: 10.1016/j.jcis.2020.03.034
- Di Giosia, M., Valle, F., Cantelli, A., Bottoni, A., Zerbetto, F., Fasoli, E., et al. (2019). High-throughput virtual screening to rationally design protein - Carbon nanotube interactions. Identification and preparation of stable water dispersions of protein - Carbon nanotube hybrids and efficient design of new functional materials. *Carbon* 147:43. doi: 10.1016/j.carbon.2019.02.043

- Faltermeier, S. M., Reuel, N. F., McNicholas, T. P., Boghossian, A. A., Giraldo, J. P., Hilmer, A. J., et al. (2014). Plant nanobionics approach to augment photosynthesis and biochemical sensing. *Nat. Mater.* 13, 400–408. doi: 10.1038/nmat3890
- Giosia, M., Di Polishchuk, I., Weber, E., Fermani, S., Pasquini, L., Pugno, N. M., et al. (2016). Bioinspired nanocomposites: ordered 2D materials within a 3D lattice. *Adv. Funct. Mater.* 26, 5569–5575. doi: 10.1002/adfm.201601318
- Koh, B., and Cheng, W. (2016). The kinetics of single-walled carbon nanotube aggregation in aqueous media is sensitive to surface charge. *C J. Carbon Res.* 2:6. doi: 10.3390/c2010006
- Lin, T. E., Rapino, S., Girault, H. H., and Lesch, A. (2018). Electrochemical imaging of cells and tissues. *Chem. Sci.* 9, 4546–4554. doi: 10.1039/c8sc01035h
- Long, Z., Ji, J., Yang, K., Lin, D., and Wu, F. (2012). Systematic and quantitative investigation of the mechanism of carbon nanotubes toxicity toward algae. *Environ. Sci. Technol.* 46, 8458–8466. doi: 10.1021/es301802g
- Lukhele, L. P., Mamba, B. B., Musee, N., and Wepener, V. (2015). Acute toxicity of double-walled carbon nanotubes to three aquatic organisms. *J. Nanomater.* 2015, 1–19. doi: 10.1155/2015/219074
- Ma, X., Geiser-Lee, J., Deng, Y., and Kolmakov, A. (2010). Interactions between engineered nanoparticles (ENPs) and plants: phytotoxicity, uptake and accumulation. *Sci. Total Environ.* 408, 3053–3061. doi: 10.1016/j.scitotenv.2010.03.031
- Ma, Y., He, X., Zhang, P., Zhang, Z., Ding, Y., Zhang, J., et al. (2017). Xylem and phloem based transport of CeO<sub>2</sub> nanoparticles in hydroponic cucumber plants. *Environ. Sci. Technol.* 51, 5215–5221. doi: 10.1021/acs.est.6b05998
- Magnabosco, G., Giosia, M., Di Polishchuk, I., Weber, E., Fermani, S., Bottoni, A., et al. (2015). Calcite single crystals as hosts for atomic-scale entrapment and slow release of drugs. *Adv. Healthc. Mater.* 4, 1510–1516. doi: 10.1002/adhm.201500170
- Magnabosco, G., Hauzer, H., Fermani, S., Calvaresi, M., Corticelli, F., Christian, M., et al. (2019). Bionic synthesis of a magnetic calcite skeletal structure through living foraminifera. *Mater. Horizons* 6, 1862–1867. doi: 10.1039/c9mh00495e
- Munns, R., Passioura, J. B., Guo, J., Chazen, O., and Cramer, G. R. (2000). Water relations and leaf expansion: importance of time scale. *J. Exp. Bot.* 51, 1495–1504. doi: 10.1093/jexbot/51.350.1495
- Nguyen, P. Q., Courchesne, N. M. D., Duraj-Thatte, A., Praveschotinunt, P., and Joshi, N. S. (2018). Engineered living materials: prospects and challenges for using biological systems to direct the assembly of smart materials. *Adv. Mater.* 30, 1–34. doi: 10.1002/adma.201704847
- Pérez-de-Luque, A. (2017). Interaction of nanomaterials with plants: what do we need for real applications in agriculture? *Front. Environ. Sci.* 5:12. doi: 10.3389/fenvs.2017.00012
- Pugno, N. M., and Valentini, L. (2019). Bionocomposites. *Nanoscale* 11, 3326–3335. doi: 10.1039/c8nr08569b
- Rapino, S., Treossi, E., Palermo, V., Marcaccio, M., Paolucci, F., and Zerbetto, F. (2014). Playing peekaboo with graphene oxide: a scanning electrochemical microscopy investigation. *Chem. Commun.* 50, 13117–13120. doi: 10.1039/c4cc06368f
- Rapino, S., Valenti, G., Marcu, R., Giorgio, M., Marcaccio, M., and Paolucci, F. (2010). Microdrawing and highlighting a reactive surface. *J. Mater. Chem.* 20, 7272–7275. doi: 10.1039/c0jm00818d
- Schopfer, P. (2006). Biomechanics of plant growth. *Am. J. Bot.* 93, 1415–1425. doi: 10.3732/ajb.93.10.1415
- Sun, X. D., Yuan, X. Z., Jia, Y., Feng, L. J., Zhu, F. P., Dong, S. S., et al. (2020). Differentially charged nanoplastics demonstrate distinct accumulation in *Arabidopsis thaliana*. *Nat. Nanotechnol.* 15, 755–760. doi: 10.1038/s41565-020-0707-4
- Thakkar, M., Mitra, S., and Wei, L. (2016). Effect on growth, photosynthesis, and oxidative stress of single walled carbon nanotubes exposure to marine alga *Dunaliella tertiolecta*. *J. Nanomater.* 2016, 1–9. doi: 10.1155/2016/8380491
- Valentini, L., Bon, S. B., and Pugno, N. M. (2016). Microorganism nutrition processes as a general route for the preparation of bionic nanocomposites based on intractable polymers. *ACS Appl. Mater. Interfaces* 8, 22714–22720. doi: 10.1021/acsami.6b07821
- Villagarcia, H., Dervishi, E., De Silva, K., Biris, A. S., and Khodakovskaya, M. V. (2012). Surface chemistry of carbon nanotubes impacts the growth and expression of water channel protein in tomato plants. *Small* 8, 2328–2334. doi: 10.1002/smll.201102661
- Walsh, D., Kim, Y.-Y., Miyamoto, A., and Meldrum, F. C. (2011). Synthesis of macroporous calcium carbonate/magnetite nanocomposites and their application in photocatalytic water splitting. *Small* 7, 2168–2172. doi: 10.1002/smll.201100268
- Wang, H., Yang, S. T., Cao, A., and Liu, Y. (2013). Quantification of carbon nanomaterials in vivo. *Acc. Chem. Res.* 46, 750–760. doi: 10.1021/ar200335j
- Wang, Z., Xie, X., Zhao, J., Liu, X., Feng, W., White, J. C., et al. (2012). Xylem- and phloem-based transport of CuO nanoparticles in maize (*Zea mays* L.). *Environ. Sci. Technol.* 46, 4434–4441. doi: 10.1021/es204212z
- Wong, M. H., Giraldo, J. P., Kwak, S.-Y., Koman, V. B., Sinclair, R., Lew, T. T. S., et al. (2016). Nitroaromatic detection and infrared communication from wild-type plants using plant–nanobionics. *Nat. Mater.* 16, 264–272. doi: 10.1038/nmat4771
- Zhai, G., Gutowski, S. M., Walters, K. S., Yan, B., and Schnoor, J. L. (2015). Charge, size, and cellular selectivity for multiwall carbon nanotubes by maize and soybean. *Environ. Sci. Technol.* 49, 7380–7390. doi: 10.1021/acs.est.5b01145
- Zhang, T., Wang, W., Zhang, D., Zhang, X., Yurong, M., Zhou, Y., et al. (2010). Biotemplated synthesis of cold nanoparticle-bacteria cellulose nanofiber nanocomposites and their application in biosensing. *Adv. Funct. Mater.* 20, 1152–1160. doi: 10.1002/adfm.200902104

**Conflict of Interest:** The authors declare that the research was conducted in the absence of any commercial or financial relationships that could be construed as a potential conflict of interest.

Copyright © 2020 Magnabosco, Pantano, Rapino, Di Giosia, Valle, Taxis, Sparla, Falini, Pugno and Calvaresi. This is an open-access article distributed under the terms of the Creative Commons Attribution License (CC BY). The use, distribution or reproduction in other forums is permitted, provided the original author(s) and the copyright owner(s) are credited and that the original publication in this journal is cited, in accordance with accepted academic practice. No use, distribution or reproduction is permitted which does not comply with these terms.



# Hydrogels for 3D Neural Tissue Models: Understanding Cell-Material Interactions at a Molecular Level

Catalina Vallejo-Giraldo<sup>†</sup>, Martina Genta<sup>†</sup>, Olivia Cauvi, Josef Goding and Rylie Green\*

Department of Bioengineering, Imperial College London, London, United Kingdom

## OPEN ACCESS

### Edited by:

Davide Ricci,  
University of Genoa, Italy

### Reviewed by:

Jennifer Patterson,  
Instituto IMDEA Materiales, Spain  
PaYaM ZarrinTaj,  
Oklahoma State University,  
United States

### \*Correspondence:

Rylie Green  
rylie.green@imperial.ac.uk

<sup>†</sup>These authors share first authorship

### Specialty section:

This article was submitted to  
Biomaterials,  
a section of the journal  
Frontiers in Bioengineering and  
Biotechnology

**Received:** 01 September 2020

**Accepted:** 14 October 2020

**Published:** 06 November 2020

### Citation:

Vallejo-Giraldo C, Genta M,  
Cauvi O, Goding J and Green R  
(2020) Hydrogels for 3D Neural Tissue  
Models: Understanding Cell-Material  
Interactions at a Molecular Level.  
Front. Bioeng. Biotechnol. 8:601704.  
doi: 10.3389/fbioe.2020.601704

The development of 3D neural tissue analogs is of great interest to a range of biomedical engineering applications including tissue engineering of neural interfaces, treatment of neurodegenerative diseases and *in vitro* assessment of cell-material interactions. Despite continued efforts to develop synthetic or biosynthetic hydrogels which promote the development of complex neural networks in 3D, successful long-term 3D approaches have been restricted to the use of biologically derived constructs. In this study a poly (vinyl alcohol) biosynthetic hydrogel functionalized with gelatin and sericin (PVA-SG), was used to understand the interplay between cell-cell communication and cell-material interaction. This was used to probe critical short-term interactions that determine the success or failure of neural network growth and ultimately the development of a useful model. Complex primary ventral mesencephalic (VM) neural cells were encapsulated in PVA-SG hydrogels and critical molecular cues that demonstrate mechanosensory interaction were examined. Neuronal presence was constant over the 10 day culture, but the astrocyte population decreased in number. The lack of astrocytic support led to a reduction in neural process outgrowth from  $24.0 \pm 1.3 \mu\text{m}$  on Day 7 to  $7.0 \pm 0.1 \mu\text{m}$  on Day 10. Subsequently, purified astrocytes were studied in isolation to understand the reasons behind PVA-SG hydrogel inability to support neural network development. It was proposed that the spatially restrictive nature (or tight mesh size) of PVA-SG hydrogels limited the astrocytic actin polymerization together with a cytoplasmic-nuclear translocation of YAP over time, causing an alteration in their cell cycle. This was confirmed by the evaluation of p27/*Kip1* gene that was found to be upregulated by a twofold increase in expression at both Days 7 and 10 compared to Day 3, indicating the quiescent stage of the astrocytes in PVA-SG hydrogel. Cell migration was further studied by the quantification of MMP-2 production that was negligible compared to 2D controls, ranging from  $2.7 \pm 2.3\%$  on Day 3 to  $5.3 \pm 2.9\%$  on Day 10. This study demonstrates the importance of understanding astrocyte-material interactions at the molecular level, with the need to address spatial constraints in the 3D hydrogel environment. These findings will inform the design of future hydrogel constructs with greater capacity for remodeling by the cell population to create space for cell migration and neural process extension.

**Keywords:** hydrogels, 3D models, primary neuroprogenitors, mechanosensory, cell interaction, neural tissue engineering

## INTRODUCTION

The development of tissue-engineered, three dimensional (3D) neural tissue analogs has significant implications in the treatment of neurodegenerative diseases, *in vitro* assessment of material and device interactions, and the design of new approaches to engineering neural interfaces. Existing *in vitro* models poorly represent the complex cell interactions of the nervous system, with particular deficit in the central nervous system (CNS) (Gilmour et al., 2019). CNS models are often desired for *in vitro*, high throughput assessment of new materials and devices. Within the CNS, neuronal function is supported by the neighboring glia cells that present neurons with trophic and physical stimuli (Sofroniew, 2015; Gilmour et al., 2016). These include astrocytes, oligodendrocytes and microglia. The use of cell populations containing both neurons and glia, that can respond to injury and interact in 3D, is critical to enabling useful insights that can guide the development of next-generation materials and devices for neural interfaces.

The majority of 3D neural models rely on clonal cell lines (Mahoney and Anseth, 2006; Lowry Curley and Moore, 2017; Wang et al., 2019) that are highly proliferative, robust upon handling and have defined culture protocols. While clonal cell cultures are highly tunable through the control of cellular components and essential factors that present biosignaling cues to other cell types, they present a distinct disadvantage when used to assess the interaction between material scaffolds and cell development. Clonal cells differ genetically and phenotypically from their tissue of origin and show altered morphology over time. This variable cell behavior is exacerbated over longer time points, causing undesirable heterogeneity in the intended models (Ulrich and Pour, 2001). Hence, these models not only lack the native complexity of neural tissue necessary to recapitulate the neural milieu, but the immortalization of these cells often results in long-term genetic drifts (Kaur and Dufour, 2012).

Alternatively, primary cells can be used to establish models of neural tissue where the phenotype is well matched to the nervous system (Thomson et al., 2008; Gilmour et al., 2016). Primary neural cells are commonly harvested from rodent embryos and either isolated to single cell types or cultured in complex media to establish development of both neural and glial cells within a single well (Gilmour et al., 2019). Of note, long-term central nervous system (CNS) cell cultures in two dimensions (2D) have been established, with reports of neural network formation and maintenance over 90 days (Satir et al., 2020). Despite these promising results, there are limited reports of translation to 3D where more complex *in vivo* interactions can be effectively modeled. A critical hurdle to the development of primary 3D neural tissue analogs is the need to support multiple cell types within the same environment.

In 2D culture (clonal or primary) it is typical to use a layered or multistep process to combine cell types (Aregueta-Robles et al., 2019). This enables individual cell populations to be established by controlling the growth and differentiation cues, prior to combining. For example, astrocytes can be formed into a mature and confluent layer prior to addition of neurons (Schutte et al., 2018), ensuring that there is biologically mediated

mechanical and trophic support to encourage growth of the neural network. This is a time-consuming process, requiring weeks and sometimes months to establish a neural culture (Gilmour et al., 2019). Additionally, being constrained to planar (2D) substrates and potentially pseudo-3D scaffolds (such as open porous structures), this step wise approach can only model limited cell interactions. To achieve a true 3D model, encapsulation of neural cells within hydrogels represents an increasingly important and popular technique (Aregueta-Robles et al., 2014). However, hydrogel encapsulation necessitates the incorporation of all cells within the material at the same time. This means that the support and cues for multiple cell types must be provided at the outset, within the same material, but remain accessible by the cells as they develop into a functional tissue analog over the long-term.

While a few notable *in vitro* studies have shown neural outgrowth using primary cultures in 3D hydrogels (Suri and Schmidt, 2010; Edgar et al., 2017; Lam et al., 2020), these approaches have used constructs fabricated from biological polymers such extracellular matrix (ECM). While capable of supporting complex primary neural cell cultures, the natural variation of biological components results in batch-to-batch variability and an inability to systematically vary scaffold composition and properties (Serban and Prestwich, 2008). The complexity of ECM macromolecules also imposes a microenvironment which is a combination of mechanical, topographical, and biochemical cues. These complex cues that govern cell fate cannot be decoupled from the local cell-material interactions or individually probed. For example Matrigel (a commercial scaffold) is composed from proteins such as collagen and laminin, which have extensive roles in both mechanical support and biochemical signaling (Hughes et al., 2010). Removal of one of these molecules from a system will severely impact a range of cues, preventing the isolation and understanding of critical property parameters. In contrast, the use of synthetic polymer systems allows for a high degree of control over mechanical and physical cues, including modulus, mesh size and kinetics of degradation. However, without sufficient biological support the cell viability for encapsulation of cells within purely synthetic systems is low (Gunn et al., 2005; Caló and Khutoryanskiy, 2015).

Biosynthetic hydrogels provide both the tunable properties of a synthetic hydrogel, while incorporating critical biological molecules that support cell survival and growth. By incorporating only small amounts of proteins or peptides, it is possible to target specific cell-material interactions and understand the required microenvironment for developing neural networks within a 3D hydrogel. In prior research it was shown that a biosynthetic hydrogel fabricated from poly (vinyl alcohol) (PVA) modified with tyramine (PVA-Tyr) combined with sericin and gelatin (PVA-SG) demonstrated potential for soft tissue engineering (Lim et al., 2013). The tyramine functionalization allows for the formation of dityrosine crosslinks which are hydrolytically degradable due to an ester group in the tyramine linkage. PVA-Tyr is also capable of forming degradable bonds with unmodified proteins and peptides which have tyrosine residues, such as gelatin and sericin which provide cell adhesion and



protection functionalities, respectively (Lim, 2014; Aregueta-Robles, 2017; **Figure 1**). This system was subsequently tailored as a degradable construct for application as a living layer applied to neural interfacing electrodes (Aregueta-Robles et al., 2018). A range of hydrogel formulations investigating total hydrogel concentration, concentration of gelatin and sericin components and crosslinking conditions were characterized with respect to their mechanical properties, degradation behavior and biofunctionality. A 10 wt% formulation (8% PVA, 1% sericin, 1% gelatin) was shown to broadly match the mechanical properties of the CNS tissues and have a degradation profile appropriate for developing neural cultures. While it was demonstrated that PVA-SG supported the survival of clonal cells, including the development of neural-like networks from PC12s and Schwann cells (Aregueta-Robles et al., 2019), the ensuing encapsulation of primary neuroprogenitor cells was less successful. Primary cells were found to form small clusters but did not develop network behavior or the outgrowth of neural processes (Goding et al., 2017). It was hypothesized that the primary cells were unable to sufficiently interact with the biosynthetic hydrogel, and while cells produced both collagen and laminin, it was localized to the clusters. To successfully develop a primary

3D neural tissue analog it is necessary to understand the interactions of the cells both with neighboring cells and with the hydrogel carrier.

The aim of this study was to understand glial and neural cell communication both with each other and the biosynthetic hydrogel system. The goal was to use this knowledge to provide insight into critical material parameters that impact on cell survival, specifically in the initial period following hydrogel encapsulation. It is expected that greater insight into mechanisms of cell survival and differentiation in the short-term will inform improved material design for the establishment of long-term neural networks for 3D neuronal tissue models. PVA-SG hydrogel was used to encapsulate a complex primary ventral mesencephalic (VM) neural culture. Embryonic VM cells were used as they contain both glial and neural cell progenitors (Bronstein et al., 1995). Survival of encapsulated VM cells was evaluated across 10 days, assessing the role of key sensorial and adhesive cells (astrocytes), which are known to provide the essential intrinsic cues for local neuronal development. The cell-material interaction was focused on the astrocytic response of the VM culture and further evaluated by encapsulation of purified and matured astrocytes. Specifically, Yes-Associated

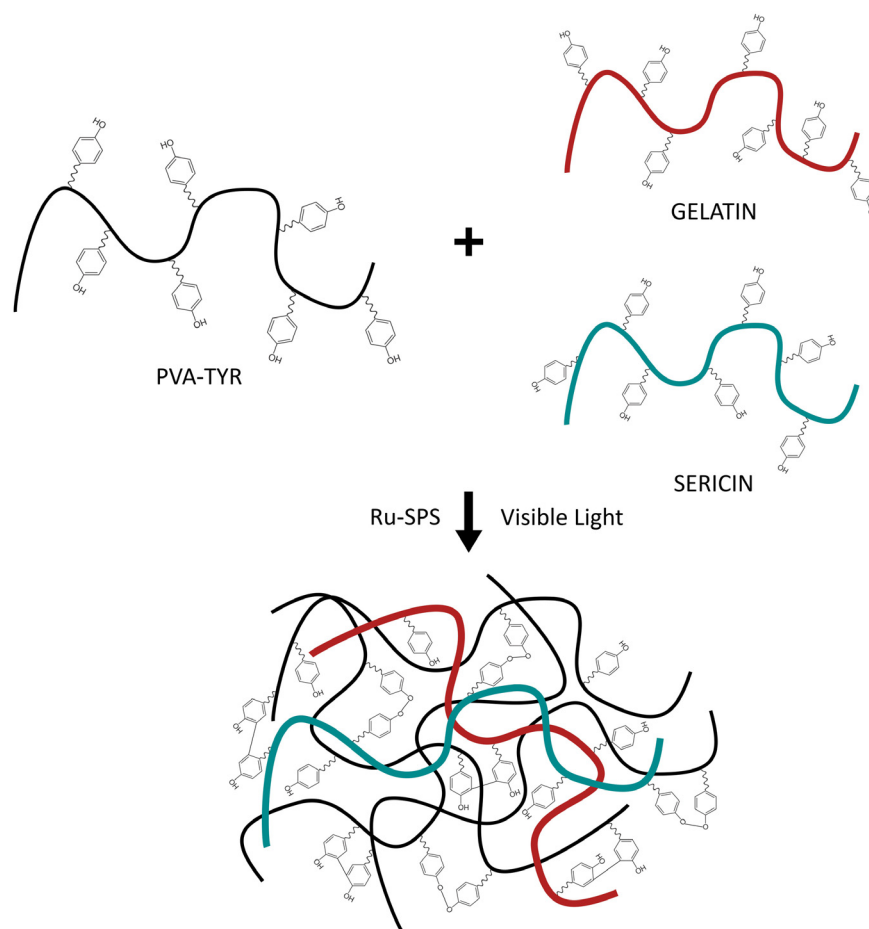


**FIGURE 1** | Schematic of the photopolymerization of PVA-SG hydrogels with visible light. Adapted with permission from Lim et al. (2013).

Protein (YAP), a dimensionality cell mechanosensor was used to elucidate local cell responses, together with cytoskeleton marker F-actin. These components signal cytoskeletal tension and impart critical information related to the mechanical sensing of the cells within the microenvironment. This spatial regulation perceived by the cells underpin their resulting proliferation or growth arrest. Understanding these cellular expressions are essential for 3D model development using materials as they are related to the spatial control that dictates cell-cell communication and function. Thus, these cellular expressions were further studied through quantifying the production of matrix metalloproteinase-2 (MMP-2) together with qPCR of the expression of the *p27<sup>Kip1</sup>* gene. MMP2 and *p27<sup>Kip1</sup>* are cellular factors that are responsible for cell spreading and migration in connection with YAP.

While these molecular signals produced by neuroglial cells have been extensively studied in 2D, their role in 3D cell-material interactions has not been elucidated. A few studies have suggested that YAP expression in 3D hydrogels could inform cell-material behavior and lead to more appropriate material design (Caliari et al., 2016). Herein, YAP expression in astrocytes in a 3D microenvironment has been studied for the first time, as a preliminary cellular mechanical approach, rather than a morphological one to understand neural outgrowth and inform material design. The results of this study propose that functionalization approaches for 3D material systems should focus on controllable hydrogel systems that promote tailoring of cell responses through provision of targeted mechanical and spatial cues.

## MATERIALS AND METHODS

### Polyvinyl Alcohol (PVA)-Tyramine (Tyr)/Sericin/Gelatin (PVA-SG) Hydrogel Fabrication

PVA-Tyr was synthesized as described previously (Aregueta-Robles et al., 2018). Hydrogels composed of PVA-Tyr functionalized with sericin and gelatin (PVA-SG) were then prepared by dissolving 8 wt% of PVA-Tyr polymer with 1 wt% sericin (Sigma S5201) and 1 wt% gelatin (Sigma G1890) in 1X Dulbecco's phosphate-buffered saline (DPBS, Sigma D8537) at 60°C to achieve a 10 wt% macromer solution. Upon complete dissolution, the macromer solution was allowed to cool down to room temperature (RT) and the photoinitiators tris (2,20-bipyridyl)dichlororuthenium(II) hexahydrate (Ru, Sigma 224758) and sodium persulfate (SPS, Sigma S6172) were added at a concentration of 1.2 mM and 12 mM, respectively. Subsequently, hydrogel solution was placed into circular silicone molds (10 mm diameter and 0.8 mm thickness) and covered with a glass cover slip. Hydrogels were polymerized by irradiating visible light (400–450 nm, Bluewave Dymax with a Schott GG400 long-pass filter, cut-on wavelength of 400 nm) for 3 min at an intensity of 15 mW/cm<sup>2</sup>. The final synthesized PVA-SG hydrogels were characterized as shown in **Supplementary Figure S1**.

PVA-SG hydrogels were fabricated under sterile conditions for *in vitro* cell studies.

## Physical Characterization

### Swelling Ratio and Mass Loss

Hydrogel physical characterization was performed as described by Aregueta-Robles et al. (2018). Immediately after photopolymerization, 3 samples per time point (0, 1, 3, 7, 10, 14, 21, 28 days) were weighed to determine their initial wet mass ( $m_i$ ). The samples for day 0 were lyophilized to obtain their dry mass ( $m_{d0}$ ), calculating the effective macromer as shown in Eq. 1:

$$\text{Effective Macromer \%} = \frac{m_{d0}}{m_i} \times 100\% \quad (1)$$

Subsequently, the other time point samples were placed in 12-well plates covered with 3 ml of DPBS and incubated at 37°C until the next time point for swelling analysis. Samples were blotted dry, to remove surface water and their swollen mass ( $m_s$ ) was measured. Samples were then lyophilized and weighted to obtain their final dry mass ( $m_d$ ). The mass swelling ratio ( $q$ ) was calculated using Eq. 2:

$$q = \frac{m_s}{m_d} \quad (2)$$

For the calculation of mass loss, the polymer percentage that left the hydrogel network, Eq. 3 was used:

$$\text{Mass Loss \%} = \frac{m_{d,i} - m_d}{m_{d,i}} \times 100 \quad (3)$$

Where the initial dry weight  $m_{d,i}$  of each sample was estimated using Eq. 4:

$$m_{d,i} = \frac{m_i \times \text{Effective Macromer \%}}{100} \quad (4)$$

### Mesh Size

The hydrogel mesh size was calculated as described in Kavanagh and Ross-Murphy (1998) and Kuijpers et al. (1999) together with the Flory and Erman model (Mark and Erman, 2007). The average mesh size was estimated using Eq. 5:

$$\varepsilon = \sqrt[3]{\frac{6RT}{\pi N_A G}} \quad (5)$$

where  $R$  is the gas constant,  $T$  is the absolute temperature,  $N_A$  the Avogadro's number and  $G$  is the shear modulus.

The shear modulus  $G$  was obtained using Eq. 6 (Landau and Lifshitz, 1970):

$$G = \frac{E}{2(1 + \nu)} \quad (6)$$

where the Young's modulus ( $E$ ) was calculated experimentally and the Poisson ratio of PVA-SG gels was assumed to be the same as for pure PVA gels reported in literature (Urayama et al., 1993). To confirm the mesh sizes calculated this way, a secondary method, outlined by Hickey and Peppas (Hickey and Peppas, 1995) is presented in **Supplementary Figure S2**.

## Mechanical Characterization

### AFM Surface Stiffness

Atomic force microscopy (AFM) was performed in contact mode on a Nanowizard IV AFM (JPK, Germany; now Bruker AXS,

CA, United States) using a colloidal modified E MLCT cantilever with low spring constant (0.01–0.1 N/m) (Bruker AXS, CA, United States) and a resonant frequency of 30 Hz. AFM was performed in DPBS buffer and measurements were acquired for each time point (Days 0, 1, 3, 7, 10, 14, 21, and 28). Images are  $512 \times 512$  pixels (unless otherwise specified) corresponding to  $10 \times 10 \mu\text{m}^2$  scans at a line frequency of 0.5–1 Hz with an aspect ratio of 1:1. For each sample 25 scans were taken and these were analyzed using JPKSPM Data processing software by applying a Hertz model fit.

### Compression Modulus

Uniaxial compression tests were performed using a Bose ElectroForce 3200 with a 2.5 N load cell at a crosshead speed of 0.5 mm/min as described by Aregueta-Robles et al. (2018). Hydrogel thickness and diameter were recorded prior to testing and samples were kept in DPBS during the measurements. The Young's modulus was obtained from the slope of the stress-strain curve in the linear range (10–15% strain) at each time point (Days 0, 1, 3, 7, 10, 14, 21, and 28). One measurement per sample was analyzed using three independent samples per time point. The results were processed using a Python 3 script developed in-house.

## Biological Characterization

### Cell Culture

#### *Ventral Mesencephalic (VM) Mixed Cell Population*

Primary cultures of ventral mesencephalic neurons (VM) were obtained from the mesencephalon of embryonic Sprague-Dawley rats according to methods previously described by Vallejo-Giraldo et al. (2018). Briefly, the ventral mesencephalon were dissected from embryonic (Day 14) rat brains and then mechanically dissociated with a pipette until the tissue was dispersed, retaining clump formation. Cells were grown in a humidified atmosphere of 5%  $\text{CO}_2$  at  $37^\circ\text{C}$  and culture in media [Dulbecco's modified Eagle's medium/F12, 33 mM D-glucose, 1% L-glutamine, 1% penicillin-streptomycin (PS), 1% fetal calf serum (FCS), supplemented with 2% B27].

#### *Primary Astrocyte Culture*

Primary astrocytes were obtained from hippocampal cultures obtained from P4 Sprague Dawley rat pups, adapted from previously described protocols (Czupalla et al., 2018; O'Sullivan et al., 2018). Pups were sacrificed with a lethal injection and decapitated using surgical scissors. The heads were placed in petri dishes containing ice-cold DPBS, and the brain was removed from the skull. At this point, the isolation of the hippocampus was done under a microscope using sterilized forceps. The meninges were removed, and then the two hemispheres of the brain were separated using a scalpel. The hippocampus of each hemisphere was identified as the slightly pink crescent moon shaped band, forceps and microscissors were used to remove unwanted tissue around the hippocampus. Tissue was mechanically homogenized with a pipette and the resulting cell suspension was plated into poly-lysine (PLL) (Sigma P4707) coated T75 flasks and cultured in humidified atmosphere of 5%  $\text{CO}_2$  at  $37^\circ\text{C}$  in media [Dulbecco's modified Eagle's medium/F12, 33 mM D-glucose, 1%

L-glutamine, 1% penicillin-streptomycin (PS), 1% fetal calf serum (FCS), supplemented with 2% B27]. After 10 days in culture, cells were passaged and when confluent shaken for 2 h at  $37^\circ\text{C}$  at 200 rpm as described (Healy et al., 2013; Schildge et al., 2013). An enriched astrocyte layer was obtained with high densities after 2 weeks. At this stage, the rat astrocyte purity was confirmed at  $> 97\%$  (Supplementary Figure S3).

### Cellular Encapsulation

Cellular encapsulation was achieved by agglomerating  $6.25 \times 10^6$  cells/ml into small clumps (as recommended by Aregueta-Robles et al., 2015). The clumps were directly incorporated into the PVA-SG solution prior to gelation, as described above in section "Polyvinyl Alcohol (PVA)-Tyramine (Tyr)/Sericin/Gelatin (PVA-SG) Hydrogel Fabrication." For astrocytes studies, cellular encapsulation of  $6.25 \times 10^6$  cells/ml of astrocytes were added to the PVA-SG solution as a single cell suspension, to reduce confounding factors such as cell-cell contacts. Once polymerization was completed, 1 ml of the culture medium was added to each well and incubated for 3 h after which the media was replaced with fresh media. From this point onward, half of the media volume was replaced with fresh media every 3 days. Encapsulation samples were placed in well chambers and cultured for 3, 7, and 10 days.

For 2D culture controls, tissue culture chambers were coated with PLL. They were then rinsed 3 times with DPBS and left to dry. 100,000 cells were plated on each chamber, and then 1 ml of the culture medium was added. Half of the volume was replaced with fresh media every 2 days for a period of 10 days. For the purpose of comparison between 2D tissue culture vs. 3D hydrogels, the amount of cells seeded on each of the samples was volumetrically normalized.

### Ethics Statement (Primary Cultures)

All experiments were performed in accordance with the UK guidelines and were approved by our institution (Imperial College London) veterinary committee for Schedule 1 tissue harvesting protocols.

### Immunofluorescent Labeling

Indirect double-immunofluorescent labeling was performed to visualize neurons and astrocyte cell populations as described previously (Vallejo-Giraldo et al., 2018; Aregueta-Robles et al., 2019) with detailed adaptations. VM cells encapsulated in PVA-SG hydrogels were fixed with 4% paraformaldehyde and 1% of sucrose for 20 min at room temperature. Once fixed, samples were washed with DPBS and permeabilized with buffered 0.5% Triton X-100 within a buffered isotonic solution (10.3 g sucrose, 0.292 g NaCl, 0.06 g  $\text{MgCl}_2$ , 0.476 g HEPES buffer, 0.5 ml Triton X-100, in 100 ml water, pH 7.2) at  $4^\circ\text{C}$  for 5 min. Non-specific binding sites were blocked with 1% bovine serum albumin (BSA) in DPBS at  $37^\circ\text{C}$  for 30 min and subsequently incubated for 24 h with a 1:100 concentration anti-gial fibrillary acidic protein (GFAP) antibody produced in mouse (Sigma) and 1:250 concentration anti- $\beta$ -Tubulin III antibody produced in rabbit (Sigma). Samples were washed 3 times with 0.05% Tween 20/DPBS and then incubated for 24 h in the secondary antibody Alexa Fluor® 488 goat anti-Mouse IgG/IgA/IgM (H + L)

(Molecular probes, 1:250) combined with the secondary antibody Alexa Fluor® 594 goat anti-Rabbit IgG (H + L) (Molecular probes, 1:250). Samples were washed 3 times with DPBS and counterstained with Hoechst 33342 (Molecular Probes, 1:2,000) for nuclear staining.

Indirect immunofluorescent labeling was performed to visualize YAP in primary astrocytes encapsulated in PVA-SG hydrogels following the processes detailed above. In this case the samples were incubated with a 1:200 concentration anti-YAP (Rb mAb to YAP, Cell Signaling) overnight. Samples were washed 3 times with 0.05% Tween 20/PBS and then incubated for 1 h in the secondary antibody Alexa Fluor® 594 goat anti-Rabbit IgG (H + L) (Molecular probes, 1:500) with green-conjugated phalloidin (Life Technologies, 1:100) prepared in 1% BSA in DPBS. After washing 3 times with DPBS, samples were counterstained with Hoechst 33342 (Molecular Probes, 1:2,000) for visualization of the nucleus.

### Microscopy and Image Analysis

Samples were imaged with a Leica SP8 inverted confocal microscope at a fixed scan size of 1,024 by 1,024 with image ratio of 1:1. Cell analysis was performed as described in Vallejo-Giraldo et al. (2018). At least 20 images at 63 × magnification were taken at random from each independent experiment, where Z-stack images were processed in Volocity® software to render a 3D construct of encapsulated cells. Cell density was analyzed by counting only labeled nuclei of astrocyte and neuron populations in an area of 247.8 μm × 247.8 μm. Neurite length was quantified by analyzing five random fields of view of three different technical replicas from three different samples using established stereological methods (Vallejo-Giraldo et al., 2018). The formula used was: neurite length =  $n \cdot T \cdot \pi / 2$ , where  $n$  is the number of times neurites intersect grid lines and  $T$  = distance between gridlines (taking magnification into account) as described in Kavanagh et al. (2006). Cell area and circularity of astrocytes were recorded from the green channel using the threshold function from the ImageJ software (National Institutes of Health, United States) to generate particles that were manually dispersed across the image. Likewise, YAP expression in astrocytes was recorded from the red channel using deconvolution methods to quantify YAP nuclear-to-cytosolic ratio. The percentage of a given classification (nucleus, nucleus and cytoplasm, and cytoplasm) with respect to the total cell count was calculated following methods described by Caliarì et al. (2016).

### Matrix Metalloproteinase-2 (MMP-2) Production by Gel Zymography

Primary encapsulated astrocyte supernatants were collected at each time point to detect MMP-2 production. 1 ml of the collected media was used for gelatin zymography analysis using the method described by Lachowski et al. (2019). Briefly, the zymography resolving gel solution was prepared using 4.6 ml distilled (DI) water, 2.7 ml 30% acrylamide (Sigma, A3699), 2.5 ml 1.5 M Tris (pH 8.8), 100 μl 10% SDS, 285 μl 2.8 mg/ml gelatin (Sigma, G2500), 6 μl TEMED (Sigma, T9281) and 100 μl 10% APS. The zymography loading gel was prepared using 3.4 ml DI water, 830 μl 30% acrylamide, 630 μl 1 M Tris (pH 6.8), 50 μl

10% SDS, 5 μl TEMED and 50 μl 10% APS. An MMP-2 standard (Sigma, PF037) was prepared at a concentration of 5 ng/ml and it was added to the non-reducing Laemmli buffer (Thermo Fisher Scientific, 84788). Supernatant samples were prepared adding non-reducing Laemmli buffer. Samples were then poured into the loading gel, and the zymography gels were run for 50 min at 200 V in Tris-Glycine SDS Running Buffer (10X) (Thermo Fisher Scientific, LC2675). The gels were then removed from the cassettes and washed (15 min × 4) with 2.5% (v/v) Triton X-100 in DI water. Subsequently, the gels were developed for 15 h at 37°C in the developing buffer (10 ml 1 M Tris (pH 7.5), 8 ml 5 M NaCl, 1 ml 1 M CaCl<sub>2</sub>, 1.6 ml 2.5% Triton X-100 and 179.4 ml DI water). Once developed, the gels were stained for 1 h in Coomassie blue staining solution (0.5 g Brilliant Blue (Sigma, 27816), 250 ml methanol, 100 ml acetic acid (Sigma, A6283) and 150 ml DI water). The gels were rinsed for 4 h with destaining solution containing 150 ml methanol, 5 ml formic acid (Sigma, F0507) and 350 ml DI water. Gels were then photographed with a UVP Biospectrum 500 Imaging System. Finally, the digested bands were analyzed using the ImageJ densitometry plugin.

For the MMP-2 production analysis, a 2D tissue culture control was used as reference for comparative analysis. Alternative 3D synthetic gels were not used given the implications of material composition on cell viability (being known poor survival; Gunn et al., 2005). Likewise, 3D Matrigel hydrogels were not used as the inherent composition of these gels promotes degradation of the matrix by metalloproteinases, imparting a complex interaction between cell signaling and matrix properties which could not be adequately decoupled.

### p27/<sup>Kip1</sup> qPCR

Total RNA from the encapsulated cultures at different time points was preserved in TRIzol™ Reagent (Invitrogen™, 15596026) followed by extraction using RNeasy Mini Kit (Qiagen, 74105). All RNA samples were treated with DNase to remove contaminating genomic DNA. RNA quality was assessed using Thermo Scientific NanoDrop™ One/One<sup>C</sup> followed by Agilent® 2100 Bioanalyzer™ (Agilent Technologies, CA) and samples with RNA Integrity Number (RIN) > 8 were used for downstream cDNA conversion with RT<sup>2</sup> first-strand kit (Qiagen GmbH, Germany) as per manufacturer's protocol.

p27/<sup>Kip1</sup> target gene was used for analysis with the gene sequence reported in Pellegata et al. (2006) (Forward 5'-CGGGGAGGAAGATGTCAA-3'; Reverse 5'-TGGACACTGCTCCGCTAAC-3'). The 18S ribosomal RNA (18sRNA) and glyceraldehyde-3-phosphate dehydrogenase (GAPDH) were used as reference housekeeping genes to normalize the expression of the target gene. The 18sRNA gene was designed using the Benchling software (Forward 5'-ACGGACCAGAGCGAAAGCATT-3'; Reverse 5'-GTCAATCCTGTCCGTGTCC-3') and the GAPDH gene was used from Zhang et al. (2014) (Forward 5'-CAACTCCCTCAAGATTGTGTCAGCAA-3'; Reverse 5'-GGCATGGACTGTGGTCATGA -3'). The qPCR reactions were carried out using Step One Plus (Applied Biosystems, Foster City, CA).  $N = 3$  experiments with  $n = 3$  samples per



time point were analyzed. The analysis was done using the delta-delta CT method.

## Statistical Analysis

All data presented here were confirmed using at least 3 replicates for each of the experimental groups. The results are expressed as the mean of the values  $\pm$  standard error of the mean. One-way ANOVA followed by a Bonferroni test were performed to determine the statistical significance ( $p < 0.05$ ), unless otherwise stated.

## RESULTS

### Physical Characterization

Ten percent PVA-SG hydrogels were found to maintain their circular shape over the 28 days of the study (**Supplementary Figure S4**). An apparent color change between Day 0 and Day 1 was observed due to the leaching of unreacted polymer and photoinitiator from the polymer mesh, a typical phenomenon of the Ru/SPS systems (Lim et al., 2013). After 1 day of incubation in DPBS at 37°C, the PVA-SG hydrogel mass swelling ratio (**Figure 2A**) was equal to  $12.92 \pm 1.4$ , slightly above the theoretical value of the mass swelling ratio for 10 wt% hydrogels. Mass swelling ratio increased at a steady rate, reaching a value of  $18.9 \pm 3.0$  at 28 days.

The hydrolytic degradation of the polymer chains of the hydrogels is shown in **Figure 2B**. A similar trend compared to the swelling profile (**Figure 2A**) was observed. The sol fraction (mass loss over the first 24 h) of PVA-SG hydrogels was  $21.2 \pm 4.6\%$ . A constant increase in mass loss was observed between Days 3 and 28 due to hydrolytic degradation of the hydrogels, with a total mass loss of  $11.8 \pm 3.0\%$  after the initial sol fraction mass loss. These observations correlated with a constant increase in hydrogel mesh size from  $10.5 \pm 0.9$  nm at day 1 to  $20.0 \pm 2.7$  nm at day 28 (**Figure 2C**).

### Mechanical Characterization

AFM micrographs of Day 0 and Day 28 of 10% PVA-SG hydrogels are presented in **Figure 3A**. An overall decrease in roughness was observed over time, with an initial value of  $40.11 \pm 0.55$  nm on Day 0 and a final value of  $7.97 \pm 0.11$  nm on Day 28. These changes in surface roughness support the hydrolytic degradation of the polymer chains of the hydrogels, corresponding to the macroscopic volume transition. The Young's modulus of the PVA-SG hydrogels was found to be  $18.40 \pm 0.79$  kPa at Day 0, and was observed to decrease over time, reaching a minimum value of  $2.96 \pm 0.14$  kPa by Day 28 (**Figure 3B**). These observations were confirmed with bulk compression testing of PVA-SG hydrogels (**Supplementary Figure S5**), which found Young's moduli in accordance with those obtained via AFM.

### Biological Characterization

#### Cell Viability

**Figure 4A** shows micrographs of neuron and astrocyte cell populations from the primary VM cultures encapsulated in the PVA-SG hydrogels over a period of 10 days. PVA-SG hydrogels

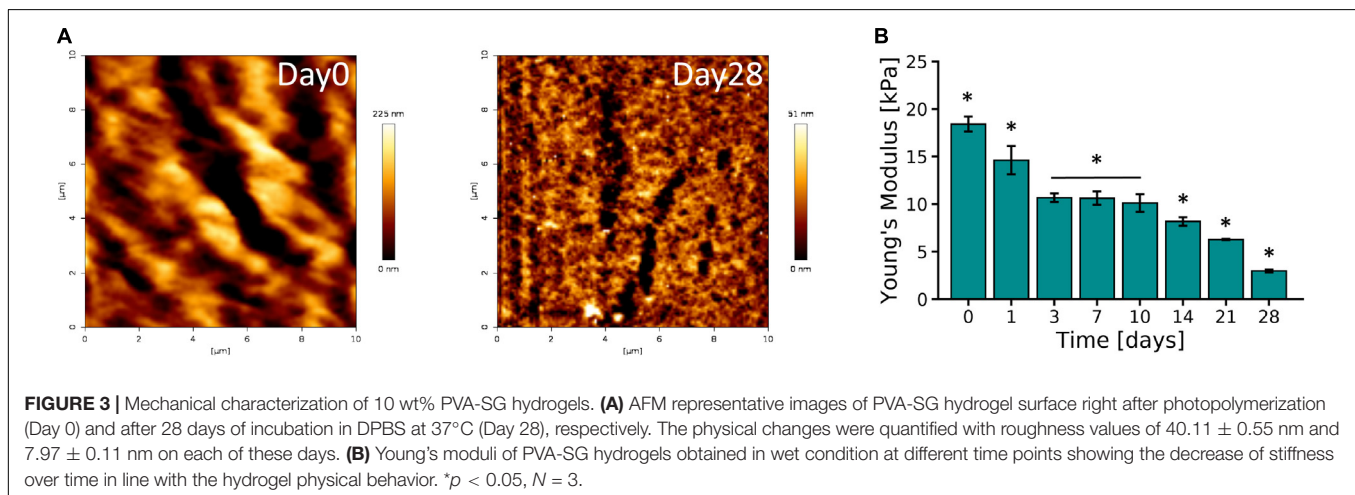
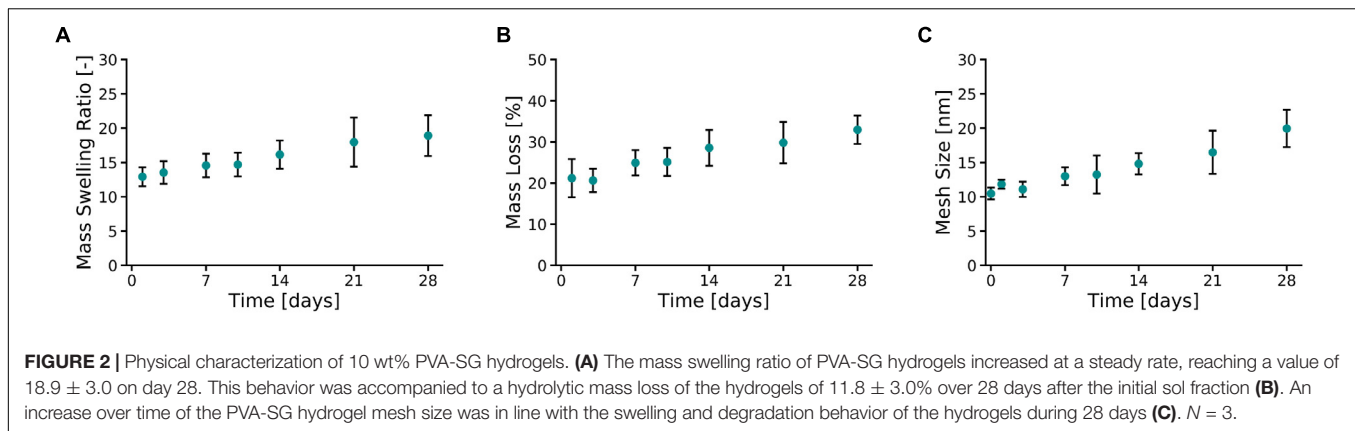
were observed to sustain neuronal presence with 86% on Day 3 and with a reduced neuron presence of 58 and 68% on Days 7 and 10, respectively. Conversely, the highest percentage of astrocyte presence (42%) was observed on Day 7 with a decrease by Day 10 to around 32% (**Figure 4B**). Neurite length, shown in **Figure 4C**, was found to correlate with the change in population of astrocytes, with the longest average neurite length being  $24.0 \pm 1.3$   $\mu\text{m}$  on Day 7. Neurite length significantly decreased to  $7.0 \pm 0.1$   $\mu\text{m}$  by Day 10, regressing as the astrocyte population concurrently reduced. The whole population, supporting the degenerative impact on neurons is shown in **Supplementary Figure S6**.

#### YAP Expression and Cell Factors

**Figure 5A** shows representative micrographs of primary astrocytes encapsulated in PVA-SG hydrogels and their expression of transcription factor YAP and F-actin over 10 days in culture. A high percentage (83.3%) of nuclear localization of YAP was observed on Day 3 (**Figure 5B**). By Days 7 and 10 respectively, a cytoplasmic-nuclear translocation was observed with 1:1 expression in both days. Analysis of F-actin suggests an increase in cell size, with cell area observed to increase from  $78.7 \pm 11.3$   $\mu\text{m}^2$  to  $150.0 \pm 20.6$   $\mu\text{m}^2$  from Days 3 to 10, respectively. This increase in cell size correlated with an increase in circularity of the astrocytes, from  $0.62 \pm 0.06$  to  $0.98 \pm 0.01$  (**Figure 5C**). **Figure 5D** shows the MMP-2 production of the encapsulated astrocytes in the PVA-SG hydrogels. All time points were found to have low MMP-2 production when compared to 2D tissue culture controls (TCP). The percentages of MMP-2 production of the astrocytes encapsulated in the hydrogels were within a range of  $2.7 \pm 2.3\%$  on day 3 to  $5.3 \pm 2.9\%$  on Day 10 when compared to MMP-2 production of 2D controls. These changes were then evaluated by the cell cycle regulatory function of p27/<sup>Kip1</sup> (Mao et al., 2015) using qPCR shown in **Figure 5E**. The expression of p27/<sup>Kip1</sup>, which is a member of cyclin-dependent kinases (CDKs) (Mao et al., 2015), was observed to be significantly upregulated by Day 7 and Day 10, with a twofold increase in expression compared to Day 3. This suggests the astrocytes have become quiescent.

## DISCUSSION

Hydrogels have been employed as 3D constructs which mimic the natural mechanical and structural properties of soft tissue (Khetan and Burdick, 2009; Goding et al., 2019; Syed et al., 2020). A biosynthetic PVA-SG hydrogel construct was chosen as the platform for this study, as it can be tailored to improve outcomes for neural cell encapsulation, as shown in prior research (Goding et al., 2017; Aregueta-Robles et al., 2018). The key objective of this study was to develop an understanding of neural cellular response to hydrogel encapsulation, to inform the design of future hydrogel constructs for neural tissue engineering applications, with the end goal of a hydrogel carrier which enables the development of complex neural networks such as those observed *in vivo*. As such, the use of complex, mixed neural populations is critical to this endeavor to adequately

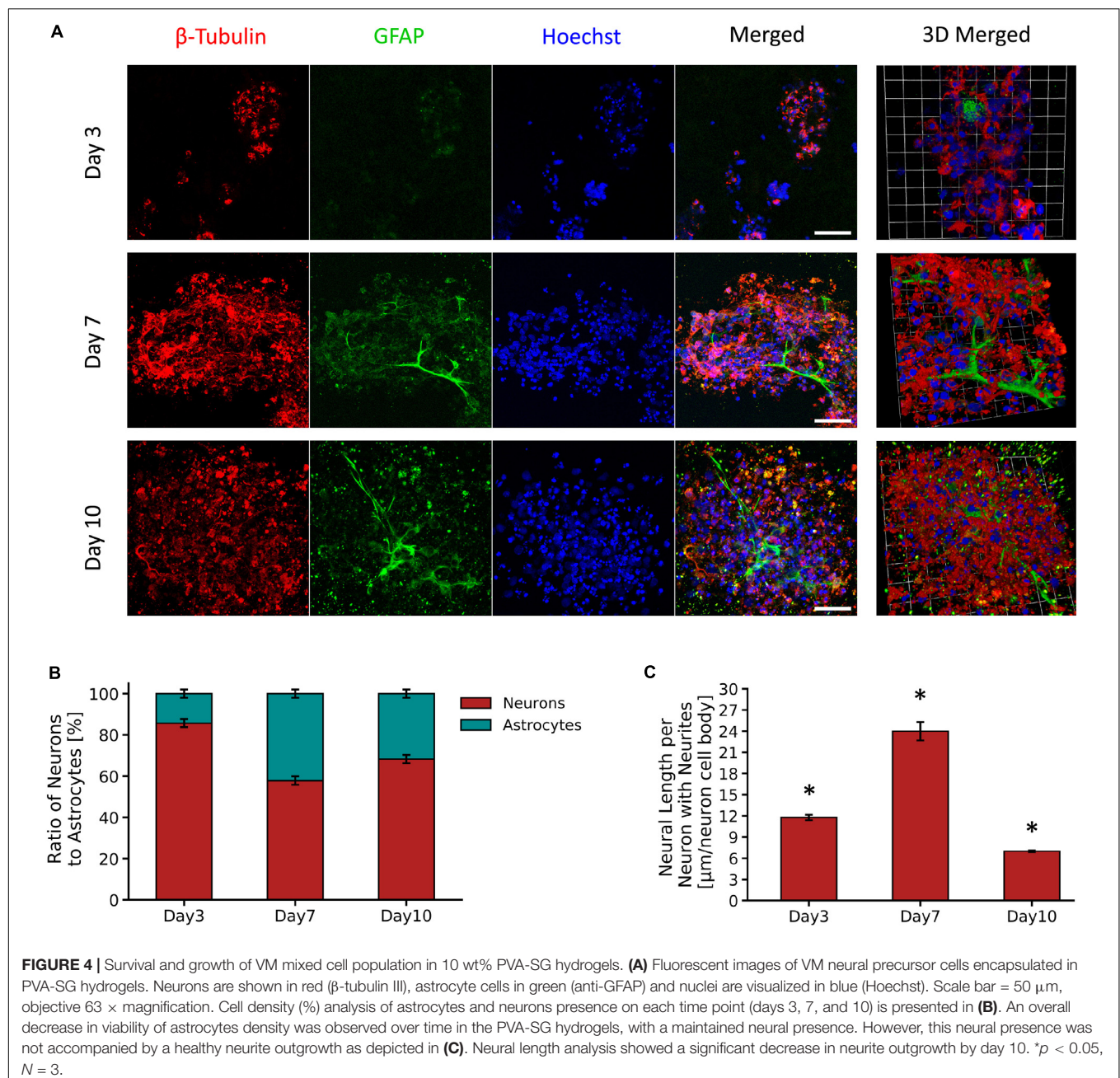


recapitulate the complexity of cellular cues present in native tissue. The most dominant example of these cues is the critical role which astrocytes play in the differentiation, viability, growth and homeostasis of neural populations. Therefore, understanding astrocyte response to encapsulation, and supporting the viability and normative function of an astrocyte subpopulation may provide a means to improve the outcomes of complex neural models within hydrogel carriers.

To explore the critical cellular cues provided by a 3D hydrogel construct, the physical properties of the 10% PVA-SG hydrogels were first evaluated by mass swelling, mass loss and mesh size analysis (**Figures 2A–C**). Observations of all these physical properties indicate the slow yet steady hydrolytic degradation of the PVA-SG construct over the 28 day period. This time scale is of significance in the context of the creation of neural networks and temporal regulation of cell migration and neurite outgrowth. In the context of neural interface development, this degradation timeframe also provides important wound healing information, as it is mimic the period across which the most pronounced host responses, namely gliosis, occur (Salatino et al., 2017). While the goal of this construct is to eventually degrade and be replaced with ECM components deposited by the encapsulated cell culture, it is important that the construct remains in place to support the encapsulated culture during

the wound healing processes which occur in the first month post implantation. As can be seen in **Figure 3B**, the mechanical stiffness of the construct is still within the ideal range for neural applications despite the progressing degradation of the polymer network (Guvendiren and Burdick, 2012). Of particular interest is the change in mesh size as the construct degrades. The initial mesh size of  $10.5 \pm 0.9$  nm is sufficient to allow the diffusion of smaller metabolites, however, may restrict the movement of larger molecules such as enzymes, growth factors and ECM components. Furthermore, small mesh sizes have been demonstrated to limit the capacity for cellular interaction and migration (Koshy et al., 2016; Barros et al., 2019). In fact, past studies have found that deposition of ECM components by encapsulated cells was localized to the immediate vicinity of the cell surface (Arequeta-Robles et al., 2015; Goding et al., 2017), correlating with the low mesh size measured for the encapsulating hydrogel.

Encapsulation of a primary mixed VM cell population within the PVA-SG hydrogel construct allowed for the examination of the behavior of key cellular populations, including astrocytes and neurons. The PVA-SG construct supported the viability of neurons over 10 days of culture, however, a decrease in astrocyte population was observed over time (**Figure 4B**). Neurite length was initially observed to increase up to  $24 \mu\text{m}$  by Day 7, however



subsequently decreased to 7  $\mu$ m by Day 10 (**Figure 4C**). It was hypothesized that this behavior was due to the declining viability of the astrocyte population which plays a vital role in supporting the development of neural networks. Although the PVA-SG hydrogels were associated with a sustained neural coverage over time, this did not translate into the development of an interconnected functional neural network. It is clear that the network development for VM derived neurons was not fully supported by the 3D PVA-SG hydrogels.

Critically, VM derived glial cells, and specifically the astrocytes have been demonstrated to promote neuronal survival and neurite outgrowth by releasing growth factors and providing

an ideal biochemical milieu for neuronal development *in vitro* (Fan et al., 2014; Vallejo-Giraldo et al., 2018; Fang et al., 2019). Astrocytes have been shown to modulate neuritogenesis and synaptogenesis, while also providing a neuroprotective effect against different neurotoxic agents (Hopkins et al., 2015; Becerra-Calixto and Cardona-Gómez, 2017). Thus, it was proposed that degeneration of the astrocyte population in the PVA-SG hindered the development of neurites and therefore prevented the development of a 3D neural network. Mechanistically, astrocytes, in their role as adhesive cells, have the ability to sense dimensional profiles, resulting in their mechano-activation. This generates cytosolic calcium signals that promote migration and



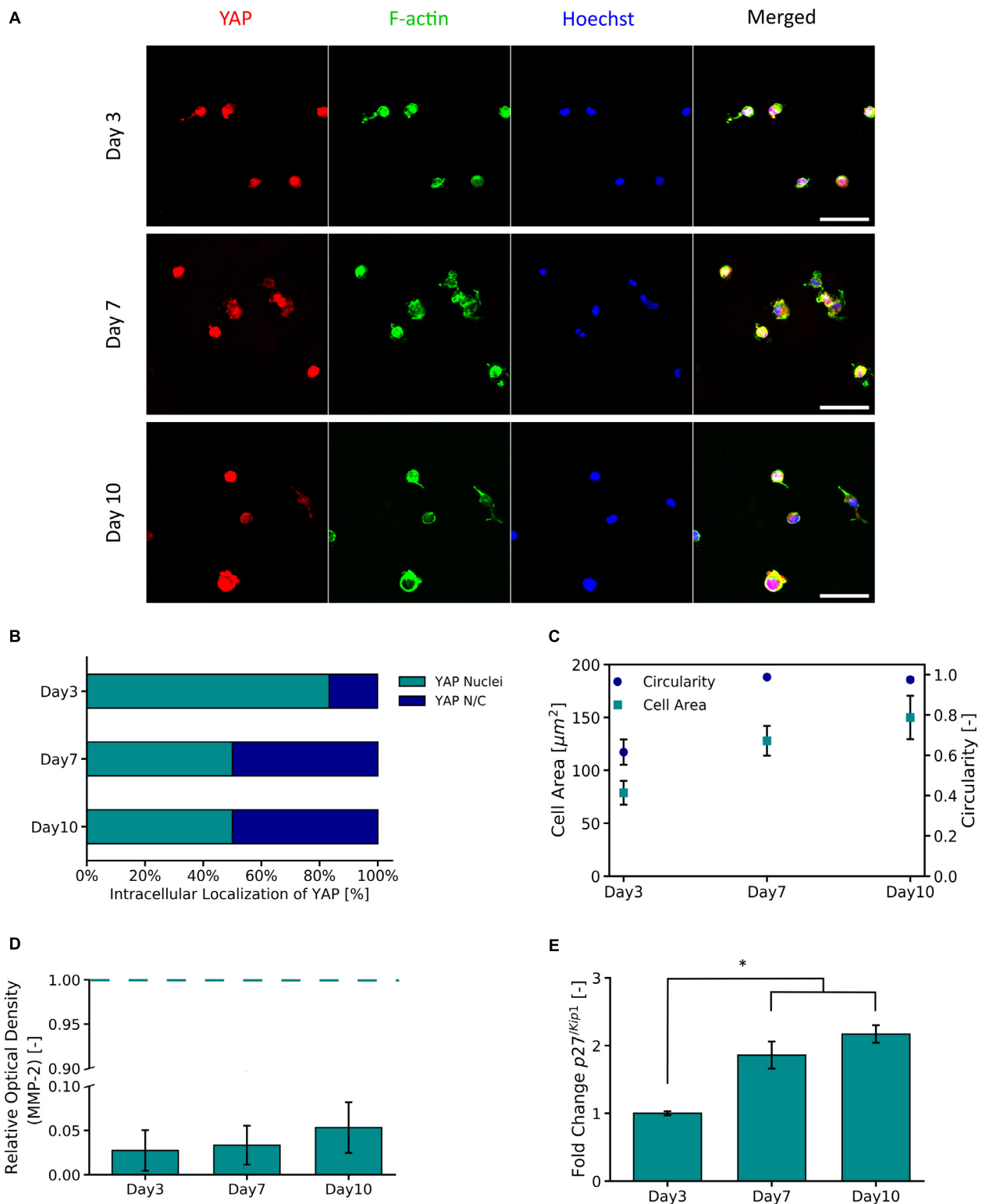


**FIGURE 5 |** YAP and F-Actin expression of primary astrocytes encapsulated in 10 wt% PVA-SG hydrogels. **(A)** Fluorescent images of primary astrocytes in PVA-SG hydrogels. YAP expression is visualized in red, F-Actin in green, and nuclei are shown in blue (Hoechst). Scale bar = 50  $\mu\text{m}$ , objective 63 $\times$  magnification. **(B)** YAP localization was evaluated during 10 days and showed a cytoplasmic-nuclear translocation over this time, expression that was correlated with the cell area and circularity of the astrocytes shown in **(C)**. The overtime cytoplasmic-nuclear translocation of YAP, correlated with the poor development of F-Actin and circular morphometric shapes of astrocytes encapsulated in the PVA-SG hydrogels. These unhealthy astrocytic shapes were confirmed with the low MMP-2 production of primary astrocytes encapsulated in the hydrogels shown in **(D)**. Together, the functional expression of  $p27^{Kip1}$  increased over time suggesting cell arrest and the poor migration and spreading of the astrocytes **(E)**. \* $p < 0.05$ ,  $N = 3$ .



development of neural networks, impacting on neural network dynamics (Huang et al., 2016; Oschmann et al., 2018). Hence it was hypothesized that despite being within the ideal stiffness range, the encapsulating hydrogel network does not support the natural biomechanical function of encapsulated astrocyte cell populations.

Having identified the importance of the astrocyte subpopulation, the encapsulation of purified astrocytes within the biosynthetic hydrogel was examined. This single cell component was used to probe the molecular mechanisms that prevent PVA-SG hydrogels from supporting primary 3D neural network development. The cell migration mechanisms were investigated, by quantifying YAP expression and its impact on cytoskeletal development, as well as the cell-division cycle of encapsulated astrocytes. YAP as transcriptional activator has emerged as an important mechanotransducer that couples physical cell development with cell-material interactions, an essential parameter to study cell spreading in 3D applications (Thomas et al., 2020). It has been shown that continued cell motility requires adaptive cytoskeletal remodeling, and this response is mediated by YAP (Mason et al., 2019). Furthermore, recent molecular biology studies have found that YAP promotes the proliferation of astrocytes through controlling distribution of the p27/*Kip1*, a gene which plays a critical role in the regulation of cell growth cycle (Huang et al., 2016; Xie et al., 2020). In **Figure 5B**, a high percentage (83.3%) of nuclear localization of YAP was observed on Day 3. However, by Days 7 and 10 a cytoplasmic-nuclear translocation was observed, indicating the inactivation of YAP in cells. Similar observations have been made in a study performed by Caliri et al. (2016) using 3D norbornene functionalized hyaluronic acid (HA) hydrogels. Hydrogels were fabricated with a similar initial stiffness to the PVA-SG but with two different rates of degradation. It was shown that MSCs encapsulated in slow non-degradable hydrogels displayed lower YAP/TAZ nuclear translocation compared to protease-degradable ones. Their findings demonstrated that in 3D systems YAP complex signaling is regulated by degradation, independently of the bulk hydrogel stiffness.

It has been reported that low nuclear activation of YAP results in limited spread of cells (Caliri et al., 2016). In the PVA-SG hydrogels, astrocytes were observed to initially increase in cell shape (circularity 0.62) supported by gelatin adhesion motifs. However, they displayed limited F-actin development over time, resulting in astrocytic morphometric shapes close to a circularity of 1 by Day 7 (**Figure 5C**). This result suggests that astrocytes were in an arrested growth phase due to space constraints of the encapsulating hydrogel mesh. Cell migration was studied by the evaluation of astrocyte MMP-2 production. Astrocytes as key players in neural homeostasis, are also the main source of MMPs within neural networks. These endogenous compounds drive different biological cascades to activate and/or to inhibit specific cellular receptor binding (Ogier et al., 2006). Particularly, MMP-2 has been shown to be key in astrocyte migration *in vitro* and *in vivo* (Hsu et al., 2006; Ogier et al., 2006). It has been shown that lowered nuclear YAP location is related to MMP activity (Tang et al., 2013). The expression of the MMP-2 over time was negligible, being  $2.7 \pm 2.3\%$  on

Day 3,  $3.3 \pm 2.2\%$  on Day 7 and  $5.3 \pm 2.9\%$  on Day 10, compared to 2D tissue controls (**Figure 5D**). The nature of the degradation of PVA-SG hydrogels is not dependent on MMP activity, but the experimental observations are in accordance with the concept that MMP-2 production and its migration effect can be correlated to cytoskeleton development (Ogier et al., 2006). The encapsulated astrocytes in the PVA-SG hydrogels showed limited F-actin development, and it is reasonable to conclude that coupled with low MMP-2 production, the astrocytes did not develop motile structures such the actin filaments (Ogier et al., 2006). Since cell migration is closely related to the cell cycle, the p27/*Kip1* gene from the cyclin-dependent kinase inhibitor (CDKIs) family was evaluated to corroborate the quiescent stage of the astrocytes. p27/*Kip1* is responsible for the regulation of cell spreading and migration in permissive environments, where a high expression of p27/*Kip1* is an indication of arrested cells at the G1 phase of the cell cycle (Sun et al., 2016). The gene analysis of p27/*Kip1* showed a significant twofold upregulation by Days 7 and 10, when compared to Day 3 (**Figure 5E**). These observations agree with other reports linking increased p27/*Kip1* expression with reduced YAP expression (Shen et al., 2020).

In these studies it was proposed that the restrictive nature of the PVA-SG hydrogel mesh network ( $10.5 \pm 0.9$  nm to  $20.0 \pm 2.7$  nm), despite having a low stiffness, induced an arrested quiescent state in the encapsulated astrocytes that promoted the cytoplasmic-nuclear translocation of YAP. This generated a cascade of events both in actin development and in the function of the cell cycle, ultimately leading to an inability to perform regular astrocytic function. These quiescent astrocytic populations would not support a permissive cellular milieu for neurons to form neural networks in 3D environments. One approach to overcome this effect could be moving away from fully dense hydrogel mesh networks and toward more permissive hydrogel structures. The controlled addition of natural fiber-forming polymers such as collagen can be used to create fibrillar mesh networks which provide adequate space for cell spreading and migration (Wolf et al., 2009; Tang-Schomer et al., 2014). However, to retain control of the hydrogel physicochemical properties, the balance between biological and synthetic components must be carefully designed. A common method for introducing interconnected networks in purely synthetic hydrogels is the incorporation of porogens such as gas-formation or soluble particles which are washed out after hydrogel formation. However, not all porogen techniques are compatible with cellular encapsulation protocols due to the use of potentially toxic components, or processes which negatively impact upon the viability of incorporated cells (Memic et al., 2019).

This study has demonstrated that appropriately tuned mechanical stiffness and incorporation of cell attachment motifs are not sufficient support the development of primary mixed neural cell cultures. The astrocyte subpopulation, which is critical in the development and continued viability of complex neural networks, was found to be critically dependent on the mechanospatial cues provided by the encapsulating construct. In the case of a fully dense PVA-SG hydrogel network, the mesh size of  $10.5 \pm 0.9$  nm to  $20.0 \pm 2.7$  nm was found

to negatively impact upon the cytoskeletal development of encapsulated astrocytes, ultimately leading to a quiescent astrocytic subpopulation incapable of supporting a developing neural network. This cellular response occurred despite the tailoring of mechanical properties and the incorporation of cell attachment motifs designed to encourage cell migration. The findings of this study suggest that the mechanospatial requirements of the astrocyte subpopulation needs to be accounted for in the design of tissue construct materials.

This research has demonstrated the role of YAP/actin polymerization together with  $p27^{Kip}$  gene as promising biomarkers in 3D environments to elucidate downstream effects in cell-material interaction. These findings, pave the way toward the understanding of complex 3D cell models for neural network formation in materials and further feedback this research with engineered functionalization approaches. The use of a physical process to widen the pores within a matrix or cell mediated degradable components could be employed to facilitate increased migration and the support of cells in 3D moving forward. Fibrillar structures may better replicate the natural structure of ECM and allow for the development of complex neural cell populations. The use of dynamic physical cues in biosynthetic hydrogels will be critical to enabling long term model neural constructs.

## CONCLUSION

These studies have demonstrated the importance of using systematic interrogation of both cellular and hydrogel components to understand the interactions between cells and materials in 3D. While primary VM cells were found to have poor growth and differentiation within the PVA-SG, it was identified that a critical cellular contributor to this result was the astrocyte population. A targeted study examining the molecular mechanisms associated with astrocyte interaction with the PVA-SG found that the constrictive mesh size of the hydrogel was the most likely factor inhibiting cell development. The arrested astrocyte growth resulted in the presentation of phenotypes that were not capable of supporting neural cells, and consequently degradation of neurites was observed over time. This study has demonstrated that appropriately tuned mechanical stiffness and incorporation of cell attachment motifs are not sufficient to support the development of primary mixed neural cell cultures. The astrocyte subpopulation was found to be critically dependent on the mechanospatial cues, and fully dense PVA-SG hydrogels can negatively impact upon the cytoskeletal

development of astrocytes. These results offer critical evidence of the interplay of the spatial-topology of the PVA-SG hydrogels on astrocyte behavior. They highlight the importance of focusing on cellular components, and in particular molecular mechanisms to motivate material design for the successful development of 3D neural tissue models.

## DATA AVAILABILITY STATEMENT

The raw data supporting the conclusions of this article will be made available by the authors, without undue reservation.

## AUTHOR CONTRIBUTIONS

CV-G, MG, JG, and RG designed the research and contributed to the manuscript. CV-G, MG, and OC performed the experiments. CV-G, MG, and JG analyzed the data. All authors have given approval to the final version of the manuscript.

## FUNDING

This work was funded by H2020 ERC-COG Living Bionics; Project No. 771985.

## ACKNOWLEDGMENTS

We acknowledge the members of Pantazis laboratory at Imperial College London, Drs. Dariusz Lachowski and Aregueta-Robles for their valuable support and discussions. We thank the Facility for Imaging by Light Microscopy (FILM) and the BME technical assistance of the Imperial College London. We thank Dr. Axel Moore for his help in the set-up of the compression measurements, and Dr. Richard Thorogate at London Centre for Nanotechnology (LCN), University College London for AFM help and guidance.

## SUPPLEMENTARY MATERIAL

The Supplementary Material for this article can be found online at: <https://www.frontiersin.org/articles/10.3389/fbioe.2020.601704/full#supplementary-material>

## REFERENCES

- Aregueta-Robles, U. A. (2017). *Engineering a Living Electrode: Growth of Neural Networks Within a 3D Hydrogel*.
- Aregueta-Robles, U. A., Lim, K. S., Martens, P. J., Lovell, N. H., Poole-Warren, L. A., and Green, R. (2015). Producing 3D neuronal networks in hydrogels for living bionic device interfaces. *Conf. Proc. IEEE Eng. Med. Biol. Soc.* 2015, 2600–2603. doi: 10.1109/embc.2015.7318924
- Aregueta-Robles, U. A., Martens, P. J., Poole-Warren, L. A., and Green, R. A. (2019). Tissue engineered hydrogels supporting 3D neural networks. *Acta Biomater.* 95, 269–284. doi: 10.1016/j.actbio.2018.11.044
- Aregueta-Robles, U. A., Woolley, A. J., Poole-Warren, L. A., Lovell, N. H., and Green, R. A. (2014). Organic electrode coatings for next-generation neural interfaces. *Front. Neuroeng.* 7:15. doi: 10.3389/fneng.2014.00015
- Aregueta-Robles, U. A., Martens, P. J., Poole-Warren, L. A., and Green, R. A. (2018). Tailoring 3D hydrogel systems for neuronal encapsulation in living electrodes. *J. Poly. Sci. Part B* 56, 273–287. doi: 10.1002/polb.24558
- Barros, D., Conde-Sousa, E., Gonçalves, A. M., Han, W. M., García, A. J., Amaral, I. F., et al. (2019). Engineering hydrogels with affinity-bound laminin as 3D neural stem cell culture systems. *Biomater. Sci.* 7, 5338–5349. doi: 10.1039/c9bm00348g

- Becerra-Calixto, A., and Cardona-Gómez, G. P. (2017). The role of astrocytes in neuroprotection after brain stroke: potential in cell therapy. *Front. Mol. Neurosci.* 10:88. doi: 10.3389/fnmol.2017.00088
- Bronstein, D., Perez-Otano, I., Sun, V., Sawin, S. M., Chan, J., Wu, G.-C., et al. (1995). Glia-dependent neurotoxicity and neuroprotection in mesencephalic cultures. *Brain Res.* 704, 112–116. doi: 10.1016/0006-8993(95)01189-7
- Calìari, S. R., Vega, S. L., Kwon, M., Soulas, E. M., and Burdick, J. A. (2016). Dimensionality and spreading influence MSC YAP/TAZ signaling in hydrogel environments. *Biomaterials* 103, 314–323. doi: 10.1016/j.biomaterials.2016.06.061
- Caló, E., and Khutoryanskiy, V. V. (2015). Biomedical applications of hydrogels: a review of patents and commercial products. *Eur. Polym. J.* 65, 252–267. doi: 10.1016/j.eurpolymj.2014.11.024
- Czupalla, C. J., Yousef, H., Wyss-Coray, T., and Butcher, E. C. (2018). Collagenase-based single cell isolation of primary murine brain endothelial cells using flow cytometry. *Bio-Protocol* 8:e3092. doi: 10.21769/BioProtoc.3092
- Edgar, J. M., Robinson, M., and Willerth, S. M. (2017). Fibrin hydrogels induce mixed dorsal/ventral spinal neuron identities during differentiation of human induced pluripotent stem cells. *Acta Biomater.* 51, 237–245. doi: 10.1016/j.actbio.2017.01.040
- Fan, C., Wang, H., Chen, D., Cheng, X., Xiong, K., Luo, X., et al. (2014). Effect of type-2 astrocytes on the viability of dorsal root ganglion neurons and length of neuronal processes. *Neural Regen. Res.* 9, 119–128. doi: 10.4103/1673-5374.125339
- Fang, A., Li, D., Hao, Z., Wang, L., Pan, B., Gao, L., et al. (2019). Effects of astrocyte on neuronal outgrowth in a layered 3D structure. *Biomed. Eng. Online* 18, 1–16.
- Gilmour, A., Poole-Warren, L., and Green, R. A. (2019). An improved in vitro model of cortical tissue. *Front. Neurosci.* 13:1349. doi: 10.3389/fnins.2019.01349
- Gilmour, A. D., Woolley, A. J., Poole-Warren, L. A., Thomson, C. E., and Green, R. A. (2016). A critical review of cell culture strategies for modelling intracortical brain implant material reactions. *Biomaterials* 91, 23–43. doi: 10.1016/j.biomaterials.2016.03.011
- Goding, J., Gilmour, A., Robles, U. A., Poole-Warren, L., Lovell, N., Martens, P., et al. (2017). A living electrode construct for incorporation of cells into bionic devices. *MRS Commun.* 7, 487–495. doi: 10.1557/mrc.2017.44
- Goding, J., Vallejo-Giraldo, C., Syed, O., and Green, R. (2019). Considerations for hydrogel applications to neural bioelectronics. *J. Mater. Chem. B* 7, 1625–1636. doi: 10.1039/c8tb02763c
- Gunn, J. W., Turner, S. D., and Mann, B. K. (2005). Adhesive and mechanical properties of hydrogels influence neurite extension. *J. Biomed. Mater. Res. Part A* 72, 91–97. doi: 10.1002/jbm.a.30203
- Guvendiren, M., and Burdick, J. A. (2012). Stiffening hydrogels to probe short-and long-term cellular responses to dynamic mechanics. *Nat. Commun.* 3:794.
- Healy, L. M., Sheridan, G. K., Pritchard, A. J., Rutkowska, A., Mullershausen, F., and Dev, K. K. (2013). Pathway specific modulation of S1P1 receptor signalling in rat and human astrocytes. *Br. J. Pharmacol.* 169, 1114–1129. doi: 10.1111/bph.12207
- Hickey, A. S., and Peppas, N. A. (1995). Mesh size and diffusive characteristics of semicrystalline poly (vinyl alcohol) membranes prepared by freezing/thawing techniques. *J. Memb. Sci.* 107, 229–237. doi: 10.1016/0376-7388(95)00119-0
- Hopkins, A. M., DeSimone, E., Chwalek, K., and Kaplan, D. L. (2015). 3D in vitro modeling of the central nervous system. *Prog. Neurobiol.* 125, 1–25. doi: 10.1016/j.pneurobio.2014.11.003
- Hsu, J.-Y. C., McKeon, R., Goussev, S., Werb, Z., Lee, J.-U., Trivedi, A., et al. (2006). Matrix metalloproteinase-2 facilitates wound healing events that promote functional recovery after spinal cord injury. *J. Neurosci.* 26, 9841–9850. doi: 10.1523/jneurosci.1993-06.2006
- Huang, Z., Hu, J., Pan, J., Wang, Y., Hu, G., Zhou, J., et al. (2016). YAP stabilizes SMAD1 and promotes BMP2-induced neocortical astrocytic differentiation. *Development* 143, 2398–2409. doi: 10.1242/dev.130658
- Hughes, C. S., Postovit, L. M., and Lajoie, G. A. (2010). Matrigel: a complex protein mixture required for optimal growth of cell culture. *Proteomics* 10, 1886–1890. doi: 10.1002/pmic.200900758
- Kaur, G., and Dufour, J. M. (2012). Cell lines: valuable tools or useless artifacts. *Spermatogenesis* 2, 1–5. doi: 10.4161/spmg.19885
- Kavanagh, E. T., Loughlin, J. P., Herbert, K. R., Dockery, P., Samali, A., Doyle, K. M., et al. (2006). Functionality of NGF-protected PC12 cells following exposure to 6-hydroxydopamine. *Biochem. Biophys. Res. Commun.* 351, 890–895. doi: 10.1016/j.bbrc.2006.10.104
- Kavanagh, G. M., and Ross-Murphy, S. B. (1998). Rheological characterisation of polymer gels. *Prog. Poly. Sci.* 23, 533–562. doi: 10.1016/S0079-6700(97)00047-6
- Khetan, S., and Burdick, J. (2009). Cellular encapsulation in 3D hydrogels for tissue engineering. *JoVE* e1590. doi: 10.3791/1590
- Koshy, S. T., Desai, R. M., Joly, P., Li, J., Bagrodia, R. K., Lewin, S. A., et al. (2016). Click-crosslinked injectable gelatin hydrogels. *Adv. Healthcare Mater.* 5, 541–547. doi: 10.1002/adhm.201500757
- Kuijpers, A., Engbers, G., Feijen, J., De Smedt, S., Meyvis, T., Demeester, J., et al. (1999). Characterization of the network structure of carbodiimide cross-linked gelatin gels. *Macromolecules* 32, 3325–3333. doi: 10.1021/ma981929v
- Lachowski, D., Cortes, E., Rice, A., Pinato, D., Rombouts, K., del Rio, et al. (2019). Matrix stiffness modulates the activity of MMP-9 and TIMP-1 in hepatic stellate cells to perpetuate fibrosis. *Sci. Rep.* 9:7299.
- Lam, D., Enright, H. A., Peters, S. K., Moya, M. L., Soscia, D. A., Cadena, J., et al. (2020). Optimizing cell encapsulation condition in ECM-Collagen I hydrogels to support 3D neuronal cultures. *J. Neurosci. Methods* 329, 108460. doi: 10.1016/j.jneumeth.2019.108460
- Landau, L. D., and Lifshitz, E. M. (1970). *Theory of Elasticity, vol. 7. Course of Theoretical Physics*, 2nd Edn. Oxford: Pergamon.
- Lim, K. (2014). *Fabrication and Characterisation of Degradable Biosynthetic Hydrogels for Cell Encapsulation: Development of a New Method for Protein Incorporation*.
- Lim, K. S., Alves, M. H., Poole-Warren, L. A., and Martens, P. J. (2013). Covalent incorporation of non-chemically modified gelatin into degradable PVA-tyramine hydrogels. *Biomaterials* 34, 7097–7105. doi: 10.1016/j.biomaterials.2013.06.005
- Lowry Curley, J., and Moore, M. J. (2017). 3D neural culture in dual hydrogel systems. *Methods Mol. Biol.* 1612, 225–237. doi: 10.1007/978-1-4939-7021-6\_17
- Mahoney, M. J., and Anseth, K. S. (2006). Three-dimensional growth and function of neural tissue in degradable polyethylene glycol hydrogels. *Biomaterials* 27, 2265–2274. doi: 10.1016/j.biomaterials.2005.11.007
- Mao, X., Zhang, D., Tao, T., Liu, X., Sun, X., Wang, Y., et al. (2015). O-GlcNAc glycosylation of p27kip1 promotes astrocyte migration and functional recovery after spinal cord contusion. *Exp. Cell Res.* 339, 197–205. doi: 10.1016/j.yexcr.2015.11.007
- Mark, J. E., and Erman, B. (2007). *Rubberlike Elasticity: A Molecular Primer*. Cambridge: Cambridge University Press.
- Mason, D. E., Collins, J. M., Dawahare, J. H., Nguyen, T. D., Lin, Y., Voytik-Harbin, S. L., et al. (2019). YAP and TAZ limit cytoskeletal and focal adhesion maturation to enable persistent cell motility. *J. Cell Biol.* 218, 1369–1389. doi: 10.1083/jcb.201806065
- Memici, A., Colombani, T., Eggermont, L. J., Rezaeeyazdi, M., Steingold, J., Rogers, Z. J., et al. (2019). Latest advances in cryogel technology for biomedical applications. *Adv. Therap.* 2:1800114. doi: 10.1002/adtp.201800114
- Ogier, C., Bernard, A., Chollet, A. M., Le Diguardier, T., Hanessian, S., Charton, G., et al. (2006). Matrix metalloproteinase-2 (MMP-2) regulates astrocyte motility in connection with the actin cytoskeleton and integrins. *Glia* 54, 272–284. doi: 10.1002/glia.20349
- Oschmann, F., Berry, H., Obermayer, K., and Lenk, K. (2018). From in silico astrocyte cell models to neuron-astrocyte network models: a review. *Brain Res. Bull.* 136, 76–84. doi: 10.1016/j.brainresbull.2017.01.027
- O'Sullivan, S. A., O'Sullivan, C., Healy, L. M., Dev, K. K., and Sheridan, G. K. (2018). Sphingosine 1-phosphate receptors regulate TLR4-induced CXCL5 release from astrocytes and microglia. *J. Neurochem.* 144, 736–747. doi: 10.1111/jnc.14313
- Pellegata, N. S., Quintanilla-Martinez, L., Siggelkow, H., Samson, E., Bink, K., Höfler, H., et al. (2006). Germ-line mutations in p27Kip1 cause a multiple endocrine neoplasia syndrome in rats and humans. *Proc. Natl. Acad. Sci. U.S.A.* 103, 15558–15563. doi: 10.1073/pnas.0603877103
- Salatino, J. W., Ludwig, K. A., Kozai, T. D., and Purcell, E. K. (2017). Glial responses to implanted electrodes in the brain. *Nat. Biomed. Eng.* 1, 862–877. doi: 10.1038/s41551-017-0154-1
- Satir, T. M., Nazir, F. H., Vizlin-Hodzie, D., Hardseus, E., Blennow, K., Wray, S., et al. (2020). Author correction: accelerated neuronal and synaptic maturation

- by brainphys medium increases A $\beta$  secretion and alters A $\beta$  peptide ratios from iPSC-derived cortical neurons. *Sci. Rep.* 10:3993. doi: 10.1038/s41598-020-61008-z
- Schildge, S., Bohrer, C., Beck, K., and Schachtrup, C. (2013). Isolation and culture of mouse cortical astrocytes. *J. Visual. Exp.* 50079. doi: 10.3791/50079
- Schutte, R. J., Xie, Y., Ng, N. N., Figueroa, P., Pham, A. T., and O'Dowd, D. K. (2018). Astrocyte-enriched feeder layers from cryopreserved cells support differentiation of spontaneously active networks of human iPSC-derived neurons. *J. Neurosci. Methods* 294, 91–101. doi: 10.1016/j.jneumeth.2017.07.019
- Serban, M. A., and Prestwich, G. D. (2008). Modular extracellular matrices: solutions for the puzzle. *Methods* 45, 93–98. doi: 10.1016/j.jmeth.2008.01.010
- Shen, X., Xu, X., Xie, C., Liu, H., Yang, D., Zhang, J., et al. (2020). YAP promotes the proliferation of neuroblastoma cells through decreasing the nuclear location of p27Kip1 mediated by Akt. *Cell Prolif.* 53:e12734.
- Sofroniew, M. V. (2015). Astrocyte barriers to neurotoxic inflammation. *Nat. Rev. Neurosci.* 16, 249–263. doi: 10.1038/nrn3898
- Sun, C., Wang, G., Wrighton, K. H., Lin, H., Songyang, Z., Feng, X.-H., et al. (2016). Regulation of p27Kip1 phosphorylation and G1 cell cycle progression by protein phosphatase PPM1G. *Am. J. Cancer Res.* 6:2207.
- Suri, S., and Schmidt, C. E. (2010). Cell-laden hydrogel constructs of hyaluronic acid, collagen, and laminin for neural tissue engineering. *Tissue Eng. Part A* 16, 1703–1716. doi: 10.1089/ten.tea.2009.0381
- Syed, O., Chapman, C., Vallejo-Giraldo, C., Genta, M., Goding, J., Kanelos, E., et al. (2020). “3D cell culture systems for the development of neural interfaces,” in *Neural Interface Engineering*, ed. L. Guo (Cham: Springer), 201–236. doi: 10.1007/978-3-030-41854-0\_8
- Tang, Y., Rowe, R. G., Botvinick, E. L., Kurup, A., Putnam, A. J., Seiki, M., et al. (2013). MT1-MMP-dependent control of skeletal stem cell commitment via a  $\beta$ 1-integrin/YAP/TAZ signaling axis. *Dev. Cell* 25, 402–416. doi: 10.1016/j.devcel.2013.04.011
- Tang-Schomer, M. D., White, J. D., Tien, L. W., Schmitt, L. I., Valentin, T. M., Graziano, D. J., et al. (2014). Bioengineered functional brain-like cortical tissue. *Proc. Natl. Acad. Sci. U.S.A.* 111, 13811–13816. doi: 10.1073/pnas.1324214111
- Thomas, D., Marsico, G., Isa, I. L. M., Thirumaran, A., Chen, X., Lukasz, B., et al. (2020). Temporal changes guided by mesenchymal stem cells on a 3D microgel platform enhances angiogenesis in vivo at a low-cell dose. *PNAS* 117, 19033–19044.
- Thomson, C., McCulloch, M., Sorenson, A., Barnett, S., Seed, B., Griffiths, I., et al. (2008). Myelinated, synapsing cultures of murine spinal cord—validation as an in vitro model of the central nervous system. *Eur. J. Neurosci.* 28, 1518–1535. doi: 10.1111/j.1460-9568.2008.06415.x
- Ulrich, A. B., and Pour, P. M. (2001). “Cell lines,” in *Brenner's Encyclopedia of Genetics*, 2nd Edn, eds S. Maloy and K. Hughes (San Diego, CA: Academic Press), 481–482.
- Urayama, K., Takigawa, T., and Masuda, T. (1993). Poisson's ratio of poly(vinyl alcohol) gels. *Macromolecules* 26, 3092–3096. doi: 10.1021/ma00064a016
- Vallejo-Giraldo, C., Krukiewicz, K., Calaresu, I., Zhu, J., Palma, M., Fernandez-Yague, M., et al. (2018). Attenuated glial reactivity on topographically functionalized poly (3, 4-Ethylenedioxythiophene): P-Toluene Sulfonate (PEDOT: PTS) neuroelectrodes fabricated by microimprint lithography. *Small* 14:1800863. doi: 10.1002/smll.201800863
- Wang, L., Wu, Y., Hu, T., Ma, P. X., and Guo, B. (2019). Aligned conductive core-shell biomimetic scaffolds based on nanofiber yarns/hydrogel for enhanced 3D neurite outgrowth alignment and elongation. *Acta Biomater.* 96, 175–187. doi: 10.1016/j.actbio.2019.06.035
- Wolf, K., Alexander, S., Schacht, V., Coussens, L. M., von Andrian, U. H., van Rheenen, J., et al. (2009). Collagen-based cell migration models in vitro and in vivo. *Semin. Cell Dev. Biol.* 20, 931–941. doi: 10.1016/j.semcdb.2009.08.005
- Xie, C., Shen, X., Xu, X., Liu, H., Li, F., Lu, S., et al. (2020). Astrocytic YAP promotes the formation of glia scars and neural regeneration after spinal cord injury. *J. Neurosci.* 40, 2644–2662. doi: 10.1523/jneurosci.2229-19.2020
- Zhang, L., Liu, S., Zhang, L., You, H., Huang, R., Sun, L., et al. (2014). Real-time qPCR identifies suitable reference genes for Borna disease virus-infected rat cortical neurons. *Int. J. Mol. Sci.* 15, 21825–21839. doi: 10.3390/ijms151221825

**Conflict of Interest:** The authors declare that the research was conducted in the absence of any commercial or financial relationships that could be construed as a potential conflict of interest.

Copyright © 2020 Vallejo-Giraldo, Genta, Cauvi, Goding and Green. This is an open-access article distributed under the terms of the Creative Commons Attribution License (CC BY). The use, distribution or reproduction in other forums is permitted, provided the original author(s) and the copyright owner(s) are credited and that the original publication in this journal is cited, in accordance with accepted academic practice. No use, distribution or reproduction is permitted which does not comply with these terms.





# Real-Time Fast Scan Cyclic Voltammetry Detection and Quantification of Exogenously Administered Melatonin in Mice Brain

Elisa Castagnola<sup>1</sup>, Elaine M. Robbins<sup>1,2</sup>, Kevin M. Woepfel<sup>1,3</sup>, Moriah McGuier<sup>4</sup>, Asiye Golabchi<sup>1,3</sup>, I. Mitch Taylor<sup>4</sup>, Adrian C. Michael<sup>2</sup> and Xinyan Tracy Cui<sup>1,3,5\*</sup>

<sup>1</sup> Department of Bioengineering, University of Pittsburgh, Pittsburgh, PA, United States, <sup>2</sup> Department of Chemistry, University of Pittsburgh, Pittsburgh, PA, United States, <sup>3</sup> Center for Neural Basis of Cognition, University of Pittsburgh, Pittsburgh, PA, United States, <sup>4</sup> Department of Chemistry, Saint Vincent College, Latrobe, PA, United States, <sup>5</sup> McGowan Institute for Regenerative Medicine, University of Pittsburgh, Pittsburgh, PA, United States

## OPEN ACCESS

### Edited by:

Jian Yang,  
Pennsylvania State University (PSU),  
United States

### Reviewed by:

Su-youne Chang,  
Mayo Clinic, United States  
Xuemei Wang,  
Southeast University, China

### \*Correspondence:

Xinyan Tracy Cui  
xic11@pitt.edu

### Specialty section:

This article was submitted to  
Biomaterials,  
a section of the journal  
Frontiers in Bioengineering and  
Biotechnology

**Received:** 02 September 2020

**Accepted:** 30 October 2020

**Published:** 24 November 2020

### Citation:

Castagnola E, Robbins EM, Woepfel KM, McGuier M, Golabchi A, Taylor IM, Michael AC and Cui XT (2020) Real-Time Fast Scan Cyclic Voltammetry Detection and Quantification of Exogenously Administered Melatonin in Mice Brain. *Front. Bioeng. Biotechnol.* 8:602216. doi: 10.3389/fbioe.2020.602216

Melatonin (MT) has been recently considered an excellent candidate for the treatment of sleep disorders, neural injuries, and neurological diseases. To better investigate the actions of MT in various brain functions, real-time detection of MT concentrations in specific brain regions is much desired. Previously, we have demonstrated detection of exogenously administered MT in anesthetized mouse brain using square wave voltammetry (SWV). Here, for the first time, we show successful detection of exogenous MT in the brain using fast scan cyclic voltammetry (FSCV) on electrochemically pre-activated carbon fiber microelectrodes (CFEs). *In vitro* evaluation showed the highest sensitivity (28.1 nA/ $\mu$ M) and lowest detection limit ( $20.2 \pm 4.8$  nM) ever reported for MT detection at carbon surface. Additionally, an extensive CFE stability and fouling assessment demonstrated that a prolonged CFE pre-conditioning stabilizes the background, *in vitro* and *in vivo*, and provides consistent CFE sensitivity over time even in the presence of a high MT concentration. Finally, the stable *in vivo* background, with minimized CFE fouling, allows us to achieve a drift-free FSCV detection of exogenous administered MT in mouse brain over a period of 3 min, which is significantly longer than the duration limit (usually < 90 s) for traditional *in vivo* FSCV acquisition. The MT concentration and dynamics measured by FSCV are in good agreement with SWV, while microdialysis further validated the concentration range. These results demonstrated reliable MT detection using FSCV that has the potential to monitor MT in the brain over long periods of time.

**Keywords:** fast scan cyclic voltammetry, melatonin, fouling, carbon fiber microelectrodes, brain, electrochemical impedance spectroscopy

## INTRODUCTION

Melatonin (MT), the pineal gland's major secretory product under dark conditions in all mammals, including humans (Farías et al., 2012), is well known for its role in circadian rhythms and modulation of the immune system (Maestroni et al., 1986; Cagnacci et al., 1992; Szczepanik, 2007; Salehi et al., 2019). MT is already recognized for the treatment of sleep disorder (Jan et al., 1994;

Buscemi et al., 2004; Xie et al., 2017). Furthermore, MT is a multitasking molecule (Reiter et al., 2010) with anti-inflammatory, antioxidant (Reiter et al., 2003; Hardeland, 2005; Reiter et al., 2016), neuroprotective (Túnez et al., 2004; Escribano et al., 2014), anti-nociceptive (Mukherjee et al., 2010; Wilhelmsen et al., 2011), and anticonvulsant properties (Fauteck et al., 1999; Banach et al., 2011; Aydin et al., 2015). As an antioxidant, MT prevents neurotoxicity, oxidative stress, and neuroinflammation in experimental models of Parkinson's (Antolín et al., 2002; Mayo et al., 2005) and Alzheimer's disease (Dragicevic et al., 2011; Rosales-Corral et al., 2012; Hossain et al., 2019; Luengo et al., 2019). In addition, MT's neuroprotective functions have shown therapeutic potentials for the treatment of amyotrophic lateral sclerosis (Zhang et al., 2013), Huntington's disease (Túnez et al., 2004; Escribano et al., 2014), and cerebral ischemia (Borlongan et al., 2000; Cuzzocrea et al., 2000), while its anti-inflammatory and anti-nociceptive actions can alleviate chronic pain both in experimental (Mukherjee et al., 2010; Wilhelmsen et al., 2011) and clinical (Korszun et al., 1999; Citera et al., 2000) studies. Due to its lipophilic character, MT can easily cross the blood–brain barrier and enter both glia and neurons, making it an excellent therapeutic choice for central nervous system (CNS) disorders (Miller et al., 2015; Golabchi et al., 2018; Salehi et al., 2019). MT's numerous physiological roles and potential therapeutic actions justify a strong need for real-time detection and monitoring of MT in the brain of laboratory animal models.

Previously, we have demonstrated detection of exogenously administered MT in anesthetized mouse brain using square wave voltammetry (SWV) (Castagnola et al., 2020). Fast scan cyclic voltammetry (FSCV) is an electroanalytical technique with higher temporal resolution (usually 100 ms) (Robinson et al., 2003; Swamy and Venton, 2007; Wood and Hashemi, 2013; Oh et al., 2016; Ou et al., 2019; Puthongkham and Venton, 2020) and, when used in combination with carbon fiber electrodes (CFEs), can achieve detection of sub-second fluctuations in neurotransmitter concentrations in real-time in the brain (Keithley et al., 2011; Wood and Hashemi, 2013; Nguyen and Venton, 2014; Mark DeWaele et al., 2017; Castagnola et al., 2018; Puthongkham and Venton, 2020). However, being primarily a background subtraction technique, FSCV measurements are limited to short time intervals (<90 s) due to the instability of the background currents, i.e., background drifting (Oh et al., 2016; Oh et al., 2016; Mark DeWaele et al., 2017; Meunier et al., 2019). This background drift can be attributed to a number of factors, comprising the changes occurring at the carbon surface itself—i.e., chemical reaction of electrode material, non-specific absorption of proteins, deposition of byproducts of electrochemical reactions (Harreither et al., 2016; Hensley et al., 2018; Puthongkham and Venton, 2020)—and changes in the surrounding chemical and biological neuro-environment—i.e., pH and local blood flow fluctuations (Mark DeWaele et al., 2017; Roberts and Sombers, 2018; Meunier et al., 2019). To predict the noise and extract the signal contribution from the drifting background, signal filtering (Mark DeWaele et al., 2017; Puthongkham and Venton, 2020), multivariate analyses (Hermans et al., 2008; Meunier et al., 2019), and waveform manipulations combined with mathematical

techniques (Oh et al., 2016; Meunier et al., 2019) have been investigated, but they require training sets (Johnson et al., 2016; Puthongkham and Venton, 2020) and/or data preprocessing (Puthongkham and Venton, 2020). On the other hand, different electrochemical procedures have been shown to restore the sensitivity of the carbon surface and preserve their current stability and sensitivity both *in vitro* and *in vivo* (Hafizi et al., 1990; Heien et al., 2003; Takmakov et al., 2010), suggesting a potential alternative to stabilize the FSCV current background. Additionally, different FSCV waveforms (Jackson et al., 1995; Ganesana et al., 2017; Hensley et al., 2018; Roberts and Sombers, 2018) have been investigated for different analytes, to identify the best holding/switching potentials and scan rate combination that maximizes sensitivity while minimize fouling (Heien et al., 2003; Cooper and Venton, 2009; Pyakurel et al., 2016; Cryan and Ross, 2019; Puthongkham and Venton, 2020). Specifically for MT, Ross' group (Hensley et al., 2018) has developed an optimized waveform that can minimize the electrode fouling due to MT oxidation byproduct deposition. Using this waveform, they demonstrated FSCV detection of MT in lymph node slices (Hensley et al., 2018).

To the best of our knowledge, real-time FSCV detection in the brain of living animals has not been previously reported. Here, we report a prolonged CFE electrochemical pre-conditioning protocol that stabilized the FSCV background for multiple minutes. Using the Ross' waveform at pre-electrochemically conditioned CFEs, we successfully demonstrated a *drift-free* FSCV detection of exogenous MT *in vivo* for 3 min. To demonstrate and support the reliability of this FSCV approach, we (1) performed an extensive evaluation of CFE stability and fouling in the presence of 5  $\mu$ M MT *in vitro*, (2) characterized *in vivo* FSCV signal baseline, and (3) evaluated the effects of biological tissue exposure on the impedance, capacitance, and sensitivity of the CFEs. Finally, we compared the *in vivo* MT concentrations measured by FSCV with those measured by SWV in our previous study (Castagnola et al., 2020) and used microdialysis from the tissue near the CFEs for further validation.

## MATERIALS AND METHODS

### Microelectrode Fabrication

#### CFE Fabrication and Pre-conditioning

Carbon fiber electrodes were fabricated as previously described in Taylor et al. (2012, 2015), and Castagnola et al. (2020). Briefly, borosilicate capillaries (0.4 mm ID, 0.6 mm OD; A-M systems Inc., Sequim, WA, United States), each containing a single carbon fiber (7  $\mu$ m diameter, T650; Cytec Carbon Fibers LLC., Piedmont, SC, United States), were pulled to a fine tip using a vertical puller (Narishige, Los Angeles, CA, United States). The tip was sealed with epoxy (Spurr Epoxy; Polysciences Inc., Warrington, PA, United States) and the exposed fiber was cut 400  $\mu$ m from the tip using a scalpel under an optical microscope (Szx12, Olympus). A mercury drop was injected into the barrel of the glass to create an electrical contact between the carbon fiber and a hookup wire (Nichrome; Goodfellow, Oakdale, PA, United States). CFEs were

soaked in isopropyl alcohol (Bath et al., 2000) (Fisher Chemical, United States) for 20 min prior to use. The entire procedure that involved handling mercury was performed under a chemical fume hood, with the user wearing gloves, eye protection, a lab coat, and mask. After use, all electrodes and other mercury-contaminated materials were disposed of according to protocols required by Environmental Health and Safety of the University of Pittsburgh, in compliance with U.S. Department of Labor Occupational Safety and Health Administration compliance guideline 1910.120.

Carbon fiber electrode surfaces were preconditioned by applying the Ross' FSCV waveform (0.2–1.3 V versus Ag/AgCl, 600 V/s) at 10 Hz overnight prior to the beginning of each experiment.

### Microdialysis Probes and Procedures

Concentric style microdialysis probes were fabricated as previously described (Nesbitt et al., 2015; Varner et al., 2016; Robbins et al., 2019). Briefly, the probes were constructed in-house using hollow fiber membranes (18 kDa molecular weight cutoff, Spectra/Por RC, Spectrum, Rancho Dominguez, CA, United States) with a 280  $\mu\text{m}$  OD, cut to a length of 1.5 mm. The inlet and outlet lines were made from fused silica capillary (75  $\mu\text{m}$  ID, 150  $\mu\text{m}$  OD, Polymicro Technologies, Phoenix, AZ, United States). Probes were perfused with artificial cerebrospinal fluid (aCSF; 142 mM NaCl, 1.2 mM  $\text{CaCl}_2$ , 2.7 mM KCl, 1.0 mM  $\text{MgCl}_2$ , 2.0 mM  $\text{NaH}_2\text{PO}_4$ , pH 7.4) at 2  $\mu\text{L}/\text{min}$  using a gastight syringe (1000 Series Gastight Hamilton<sup>TM</sup>, Reno, NV, United States) driven by a syringe pump [Harvard Apparatus Model 11 (55-1199), Holliston, MA, United States] starting prior to insertion into the brain and their functionality was verified by placing the probe membrane into a beaker of 5  $\mu\text{M}$  MT and detecting MT at the outlet. As aCSF does not have a carbonate buffer system, the pH was adjusted to pH 7.4, using NaOH and HCl (Sigma–Aldrich, MO, United States). Dialysate was analyzed for MT on a Shimadzu LCMS-2020 liquid chromatography mass spectrometer (LC-MS) using atmospheric pressure chemical ionization (APCI) by monitoring the  $[\text{M} + \text{H}]^+$  peak at 233.1  $m/z$ . MT was separated using a gradient of 10–90% solvent A to solvent B over 10 min, where solvent A was acetonitrile with 0.1% formic acid, and solvent B was water with 0.1% formic acid. Data were analyzed using Shimadzu Lab Solution software and in MATLAB (Mathworks). Dialysate was diluted with ultrapure water (Nanopure, Barnstead, Dubuque, IA, United States) before analysis to protect the instrument from damage due to the high salt content of the sample.

### In vitro FSCV Calibration

Fast scan cyclic voltammetry was performed with an EI 400 potentiostat (Ensmann Instruments; Bloomington, IN, United States) and the CV Tar Heels LabVIEW program (CV Tar Heels v4.3, University of North Carolina at Chapel Hill, Chapel Hill, NC, United States). The headstage gain was set to  $10^6$  V/A. Data were analyzed using HDCV software (UNC Chapel Hill). The electrode was scanned using the Ross waveform, corresponding to a triangular waveform with a positive holding potential of 0.2 V, a 1.3 V switching potential,

applied using a 600 V/s scan rate at 10 Hz (Hensley et al., 2018). MT was identified by inspection of the background-subtracted cyclic voltammograms. The MT oxidation peak occurred at 1.03 V (Figures 1A,F, 2B,D, 4C). Electrodes were calibrated using 0.1–5  $\mu\text{M}$  MT concentrations dissolved in aCSF. The different concentrations were diluted starting from a freshly prepared 1 mM MT solutions. Calibration was performed in flow cell equipped with a pneumatically actuated injection valve with 500  $\mu\text{L}$  sample loop (VICI AG International, Switzerland); flow through the system at 60 mL/h was driven with a syringe pump (Taylor et al., 2017).

Other analytes, such as DA and 5-HT that might interfere with MT detection, were tested using the same flow cell apparatus (Supplementary Section 1 and Supplementary Figures 1, 2 for more consideration about possible neurotransmitter/MT metabolite interferences).

### Electrochemical Characterization

Electrochemical impedance spectroscopy (EIS) measurements were used to investigate the electrode/solution interface prior to, during, and following implantation in the brain tissue, as previously described (Taylor et al., 2019; Castagnola et al., 2020). During the EIS measurements, a sine wave (10 mV RMS amplitude) was superimposed onto the open circuit potential while varying the frequency from 1 to  $10^5$  Hz. EIS was carried out using a potentiostat/galvanostat (Autolab, Metrohm, United States). The *in vitro* EIS was performed in aCSF in a three-electrode electrochemical cell set-up with a platinum counter electrode and an Ag/AgCl reference electrode. *In vivo*, a screw was used as counter electrode and the Ag/AgCl reference electrode was electrically connected via a salt bridge to the surface of the brain. Specifically, ca.  $1 \times 1 \text{ cm}^2$  square of Kimwipe (Kimtech<sup>TM</sup> Science Brand) was rolled and pulled through a pipet tip (volume 100–1250  $\mu\text{L}$ , SureOne, Fisher Scientific, MA). The pipet tip was filled with aCSF and the reference electrode (CHI111B, CH Instruments Inc., TX) inserted into the pipet tip. The wet exposed part of the kimwipe is placed in contact with the brain through a small pinhole craniotomy. Equivalent circuit modeling was performed using EIS Spectrum Analyzer 1.0. Model optimization was performed using a modified Levenburg–Marquardt algorithm with parametric weighting. A chi-square goodness of fit test was used to assess equivalent circuits describing the data. The variation of the FSCV current, defined here as the total current resulting from all faradaic and non-faradaic processes (i.e., background current) during the triangle voltage application, was recorded, *in vitro* and *in vivo*, using the EI 400 potentiostat and the CV Tar Heels LabVIEW program, and was evaluated by calculating (1) the charge storage capacity (CSC,  $\text{mC}/\text{cm}^2$ ) as  $\text{CSC} = \frac{|\int idt|}{\text{Area CFE}}$  in an entire CV cycle and (2) the capacitance (C, nF) as  $C = \frac{|\int idV|}{2 \cdot \text{scan rate} \cdot \text{potential window}}$ .

### In vivo Procedures

All procedures involving animals were approved by the Institutional Animal Care and Use Committee of the University of Pittsburgh. CFEs were acutely implanted in the visual cortex of male mice (C57BL/6J, 8–12 weeks, 22–35 g; Jackson Laboratory,

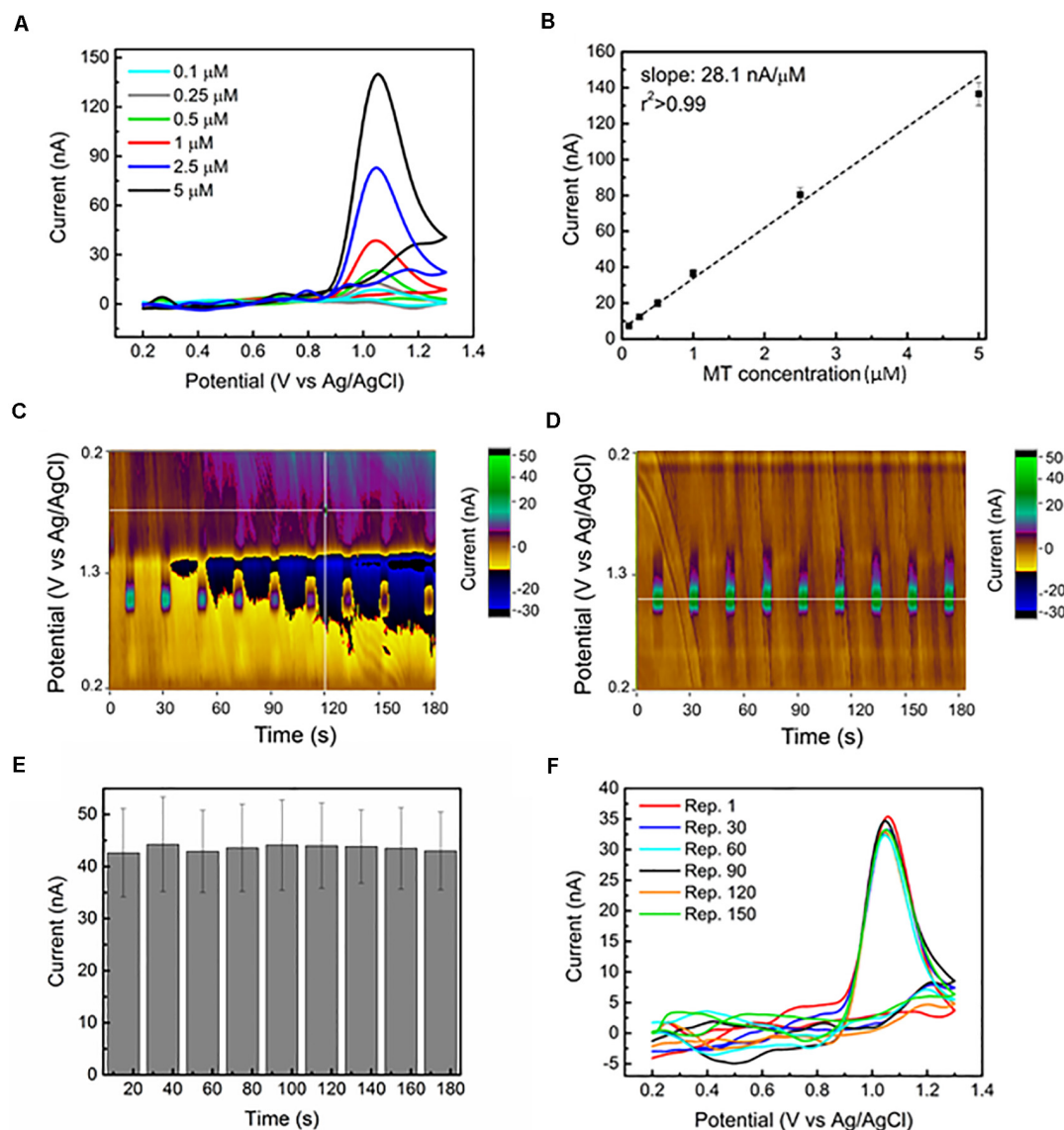


**FIGURE 1 |** Sensitive and stable MT detection via FSCV at CFEs in aCSF: **(A)** Representative background subtracted CVs, for 0.1, 0.25, 0.5, 1, 2.5, and 5  $\mu\text{M}$  bolus of MT, respectively, reveal a clear MT oxidation peak at 1.03 V. **(B)** *In vitro* FSCV MT calibration curve. The average ( $n = 6$ ) sensitivity (background subtracted peak current versus MT concentration) is linearly correlated. **(C)** Representative color plot for nine repetitions of 1  $\mu\text{M}$  MT bolus injections during a 3-min FSCV collection performed using a 15 min pre-conditioned CFE shows an unstable background, starting from 30 s. The changes in current (at the 1.03 V oxidation peak) following the injection of 1  $\mu\text{M}$  bolus of MT every 15 s are not clearly detectable because of the background drift. The electrochemical drift increased with time and after about 2 min, the current changes due to MT injections are no longer discernible. **(D)** Representative color plot for nine repetitions of 1  $\mu\text{M}$  MT bolus injections during a 3 min FSCV collection performed using an overnight preconditioned CFE show a stable background. The changes in current (at the 1.03 V oxidation peak) following the injection of 1  $\mu\text{M}$  bolus of MT every 15 s are clearly detected along the 3-min window. **(E)** Bar plot reporting the background-subtracted current amplitudes (average  $\pm$  SEM,  $n = 6$  CFEs) of the oxidation peak at 1.03 V collected for the nine repetitions along the 3 min from the overnight conditioned CFEs. The average current peak amplitudes (first:  $42.7 \pm 8.5$  nA, last  $43.0 \pm 7.5$  nA,  $n = 5$ ) are not significantly affected by time during the nine different injections [repeated measures ANOVA,  $F(7,42) = 0.235$ ,  $p > 0.05$ ]. **(F)** Background subtracted CV plots at different time points (from Repetition 1, corresponding to time zero, to Repetition 150, corresponding to 8 h of FSCV scanning) in response to 1  $\mu\text{M}$  bolus injections of MT every 3 min for more than 8 h. The reported plots are almost identical along this time, with a 0.74% variation in peak current amplitude.

Bar Harbor, ME, United States); this strain was selected for their low endogenous MT levels (Roseboom et al., 1998). Anesthesia was induced with 1.5–2% isoflurane mixed with oxygen flow at 1 L/min and maintained with 1.25–1.5%. Body temperature was maintained at 37°C with a thermostatic heating pad (Harvard

Apparatus, Holliston, MA, United States) and eye lubrication was maintained with lacrigel (Dechra Puralube Vet Ointment). The implantation procedures have been performed as previously reported (Castagnola et al., 2020). Briefly, the animal's head was fixed in a stereotaxic frame (Narishige International USA, Inc.).



In  $n = 12$  mice, a pinhole craniotomy was made over the visual cortex (1.0 mm anterior to lambda and 1.5 mm lateral from midline) with a high-speed drill (0.007 drill bit, Fine Science Tools, Inc., Foster City, CA, United States). An additional pinhole craniotomy was made to establish the connection to the reference electrode via a salt bridge. CFEs were lowered 0.8 mm below the brain surface.

Following insertion into the tissue, the CFE was subjected to the Ross FSCV waveform applied at 10 Hz for at least 30 min for stabilization. After the stabilization period, the animal received an intraperitoneal (i.p.) injection of 180 mg/kg MT ( $n = 5$ ) (99 + % Alfa Aesar, Haverhill, MA, United States) or a volume-matched injection of saline ( $n = 2$ ), followed by 3 min of FSCV recording. Similarly to our previous studies (Golabchi et al., 2018; Castagnola et al., 2020), 10  $\mu$ L dimethylsulfoxide (DMSO, 99% Alfa Aesar, Haverhill, MA, United States) was added in order to improve the solubility of the MT in 100  $\mu$ L saline vehicle. 10  $\mu$ L of DMSO was also added to the saline vehicle for the control group, in order to exclude the DMSO effect on the background stability.

In another  $n = 5$  mice, FSCV and microdialysis were performed simultaneously. In this case, the borosilicate glass tube of a CFE was glued to the stainless-steel housing of microdialysis probe. A larger craniotomy was performed to permit insertion of the devices. Then the microdialysis probes were perfused with aCSF at 2  $\mu$ L/min using a gastight syringe driven by a syringe pump (Harvard Apparatus, Holliston, MA, United States) for 1 h, while electrochemical stabilization of the CFE surface was performed. Immediately after, mice received a single 180 mg/kg, i.p. injection of MT, and FSCV measurements were performed and dialysate collected.

At the end of the *in vivo* measurement, the CFEs were removed from the brain with the help of the micromanipulator, washed with abundant DI water followed by post calibration. Then, the Ross' waveform was applied to the CFEs overnight ( $\geq 12$  h) at 600 V/s or, a more aggressive FSCV waveform ( $-0.5$  to  $1.9$  V versus Ag/AgCl and back at 400 V/s) was applied for 2 min, to remove the biological encapsulation and restore the CFE surface (see **Supplementary Section 3** and **Supplementary Figures 4, 9, 10**). In our previous study, we have demonstrated that this aggressive FSCV waveform ( $-0.5$  to  $1.9$  V versus Ag/AgCl and back at 400 V/s) was able to clean the CFEs from biological matter encapsulation after the extraction from the brain, preserving the CFE integrity (Castagnola et al., 2020). The post-calibration was repeated  $\geq 4$  h after the electrochemical cleaning procedure.

## Statistical Analyses

Statistical analyses were conducted using IBM SPSS software (v22, IBM Corp., Armonk, NY, United States) and Origin Pro 8.1 (OriginLab Corp., Northampton, MA, United States). One-way ANOVA with Bonferroni post-tests was used to compare changes in the sensitivity of CFEs to MT in presence of MT (continuous FSCV scanning) *in vitro*. One-way repeated measures ANOVA with Bonferroni post-tests was used to calculate the variations in MT sensitivity over time during consecutive MT injections *in vitro*, and the changes in CSC ( $\text{mC}/\text{cm}^2$ ) and capacitance ( $C$ , nF), as defined in Section "Electrochemical Characterization,"

over time *in vivo*. Two-way repeated measures ANOVA with Bonferroni post-tests was used to compare the EIS changes before, during, and following brain implant. Significance was determined at  $p < 0.05$ .

## RESULTS AND DISCUSSION

### *In vitro* FSCV Sensitivity and Selectivity

Melatonin oxidizes at carbon-based electrodes following a three-step reaction (Xiao-Ping et al., 2002; Vasantha and Chen, 2005; Hensley et al., 2018) involving the formation of a quinoneimine, which is both highly reactive and susceptible to electropolymerization, causing undesirable adsorption products to foul the electrode surface (Xiao-Ping et al., 2002; Vasantha and Chen, 2005; Hensley et al., 2018). To minimize the extent of MT fouling, the Ross' group optimized a FSCV waveform that combines a positive holding potential (0.2 V) and a faster scan rate (600 V/s) (Hensley et al., 2018). Furthermore, the use of a 1.3 V switching potential has shown to maximize the sensitivity of the primary oxidation peak (Hensley et al., 2018).

Using this waveform, we evaluated the sensitivity of our CFE in detecting MT *in vitro* with a range of MT concentration of 0.1–5  $\mu$ M in aCSF. The background subtracted CVs corresponding to this range of concentrations demonstrate clear oxidation peaks at 1.03 V, as reported in **Figure 1A**. The sensitivity is determined to be 28.1 nA/ $\mu$ M, based on the linear regression slope of the maximum faradaic current versus MT concentration plot. The average calibration plot ( $\pm$ SEM,  $n = 6$ ) follows a linear trend (**Figure 1B**), including linear regression fit ( $r^2 > 0.990$ ). Our sensitivity (28.1 nA/ $\mu$ M) is four times higher than what was reported in Hensley et al. (2018), which is likely due to the four times larger surface area of our CFEs. The lower detection limit (LOD), defined as three times the standard deviation of the noise, was estimated to be  $20.2 \pm 4.8$  nM ( $n = 7$ ), which is the lowest LOD value reported in literature using carbon-based materials and electrochemical detection methods for MT detection (Levent, 2012; Gomez et al., 2015; Apetrei and Apetrei, 2016; Neeraj Kumar, 2017). The selectivity of MT detection at CFEs using this FSCV waveform over other electroactive species, including ascorbic acid (AA), dopamine (DA), serotonin (5-HT) and their mixtures, and  $\text{H}_2\text{O}_2$  has been evaluated. The results have shown that MT can be distinguished among the most common electroactive neurotransmitters in the brain (data reported in **Supplementary Figures 1, 2** and **Supplementary Section 1**).

### *In vitro* FSCV Stability and Electrode Fouling

The stability of CFEs is important for monitoring MT variations over an extended duration of time *in vivo* (Mark DeWaele et al., 2017; Roberts and Sombers, 2018). As previously mentioned, one major limitation of traditional FSCV measurements is related to the instability of the background currents, i.e., background drift, that limits the FSCV data analysis to short time intervals ( $< 90$  s) (Mark DeWaele et al., 2017; Meunier et al., 2019).

Here, to evaluate the effect of a prolonged CFE pre-conditioning on the background stability and MT sensitivity over time, we applied the Ross' FSCV waveform (0.2–1.3 V versus Ag/AgCl, 600 V/s) at 10 Hz to CFE electrodes in aCSF overnight prior to the beginning of each experiment. This corresponds to cycling the CFEs for about 2 h at 60 Hz using the same waveform, longer than what previously reported (15 min at 60 Hz) (Takmakov et al., 2010; Meunier et al., 2020). This pre-conditioning procedure stabilized the current background *in vitro*, as can be observed in the representative color plots for nine repetitions of 1  $\mu$ M MT bolus injections during a 3-min collection in aCSF (**Figures 1C,D**). Using a 15 min conditioned CFE, the electrochemical drift started after 30 s, increased with time and, after about 2 min, the MT oxidation peak was no longer detectable because of the background instability (**Figure 1C**). In contrast, after the overnight pre-conditioning of the same CFE, we did not observe any background drift along the 3-min recording window (**Figure 1D**). The current amplitudes (average and SEM,  $n = 5$  CFEs) of the oxidation peak at 1.03 V collected for the 30 repetitions along 10 min are reported in the bar plot in **Figure 1E**. The averaged current peak amplitudes (first:  $42.7 \pm 8.6$  nA, last  $41.3 \pm 5.5$  nA,  $n = 5$ ) are not significantly affected by time during nine consecutive injections [repeated measures ANOVA,  $F(7,42) = 0.235$ ,  $p > 0.05$ ].

Electrochemical procedures have been used before sensing to pretreat carbon surface and activate the surface with functional groups that may improve detection (Engstrom and Strasser, 1984; Bowling et al., 1989; Cao et al., 2019), or during sensing to regenerate electrochemically active surfaces and restore the sensitivity of carbon microelectrodes affected by irreversible non-specific adsorption of biomolecules (Takmakov et al., 2010). In particular, oxidation of carbon surfaces using triangular waveforms with a switching potential higher than 1 V (i.e., 1.3 and 1.4 V versus Ag/AgCl) has been shown to preserve the current stability for DA detection both *in vitro* and *in vivo* (Hafizi et al., 1990; Heien et al., 2003; Takmakov et al., 2010) as a result of continuous carbon surface renewal (Takmakov et al., 2010). To our knowledge, the effect of a prolonged electrochemical preconditioning, in conjunction with continuous regeneration of the CFE surface, on FSCV background stability has not been reported.

The electrochemical pretreatments can have multiple effects on the electrode surface, and can (1) affect the concentration of physisorbed impurities on the carbon surface, i.e., electrode cleanliness (Bowling et al., 1989), (2) create surface oxygen-functional groups (Engstrom and Strasser, 1984; Bowling et al., 1989; Cao et al., 2019), (3) alter the carbon substrate structure due to the formation or removal of defects, in particular affecting the graphitic edge plane density (Poon et al., 1988; Bowling et al., 1989), and (4) modify the microscopic surface area (Poon et al., 1988; Bowling et al., 1989). The extent of these effects is likely to be dependent upon the number of electrochemical cycles or duration of the treatment. Here, we monitored the impedance and the FSCV current, i.e., background current during the triangle voltage application, during the electrochemical pre-conditioning. The impedance spectra and FSCV plots at different time points are reported in **Supplementary Figure 3**. We

observed a fast decrease in impedance and corresponding increase in FSCV current during the first 45 min. After that, these trends slowed down over time, and after 8 h of FSCV cycling at 10 Hz, both impedance and FSCV current maintained the stability for the following 16 h (under continuous cycling). The starting 45-min fast trend in impedance reduction and current increase is likely due to the separation of graphite planes (Maeda et al., 1985; Bowling et al., 1989), known to be the first step of the electrochemical activation (Bowling et al., 1989), with consequent fracturing of the graphite lattice and formation of edge plane defects. The formation of functional groups during the electrochemical conditioning has shown to further facilitate this phenomenon by creating strains in the lattice which causes edge planes to form and planes to delaminate (Bowling et al., 1989). The continuous FSCV cycling at 10 Hz with the 1.3 V switching potential likely increases the amount of oxygen groups at the surface and continues to favor this "activation process" until the maximum amount of defects is formed, at which point the carbon electrode surface reaches a stable state and we no longer observe impedance or FSCV current change upon cycling. SEM images of a pristine CFE, a CFE at which the Ross' waveform was applied overnight ( $\geq 12$  h) at 600 V/s and a CFE at which a more aggressive FSCV waveform (−0.5 to 1.9 V versus Ag/AgCl and back at 400 V/s) was applied for 2 min are reported in **Supplementary Figure 4**. The integrity of the CFE seems to be preserved after the electrochemical pretreatments.

To test the *in vitro* CFE stability to MT detection over time, we monitored the response of 1  $\mu$ M bolus injections of MT every 3 min for more than 8 h. The background subtracted CV plots at different time points (from Repetition 1, corresponding to time zero, to Repetition 150, corresponding to 8 h of FSCV scanning) are reported in **Figure 1F**. Despite variations in the current baseline, the MT oxidation peak was not affected over time, presenting a minimal 0.74% variation in current amplitude.

These results indicated the effectiveness of the prolonged CFE pre-conditioning on the background stabilization and the stability of the FSCV MT sensitivity over time. However, because the CFEs were exposed to MT only during the bolus MT injection (approximately 5 s), these experiments only partially represent the *in vivo* MT fouling situation. Thus, to estimate the CFE fouling in the presence of MT, CFEs were cycled using the Ross waveform for 1 h in aCSF containing a 5  $\mu$ M MT concentration. The results are reported in **Figure 2**. The CFE sensitivity to a bolus injection of 1  $\mu$ M MT and 5  $\mu$ M MT was tested before and after the FSCV cycling in MT and the peak amplitudes of MT oxidation were not significantly changed, both for the detection of 1  $\mu$ M MT (one-way ANOVA,  $p = 0.14$ ; Bonferroni post-tests n.s.) (**Figures 2A,B**) and 5  $\mu$ M MT (one-way ANOVA,  $p = 0.31$ ; Bonferroni post-tests n.s.) (**Figures 2C,D**). This result suggests that the optimized waveform is effective in preserving the electrode from fouling even in the presence of a high MT concentration. Additionally, the use of a 1.3 V switching potential, regenerating a fresh CFE surface by continuous etching of the carbon electrode (Takmakov et al., 2010; Keithley et al., 2011), may helped to mitigate the fouling.

We should note that we purposefully designed a highly aggressive *in vitro* fouling resistance test by challenging the CFE

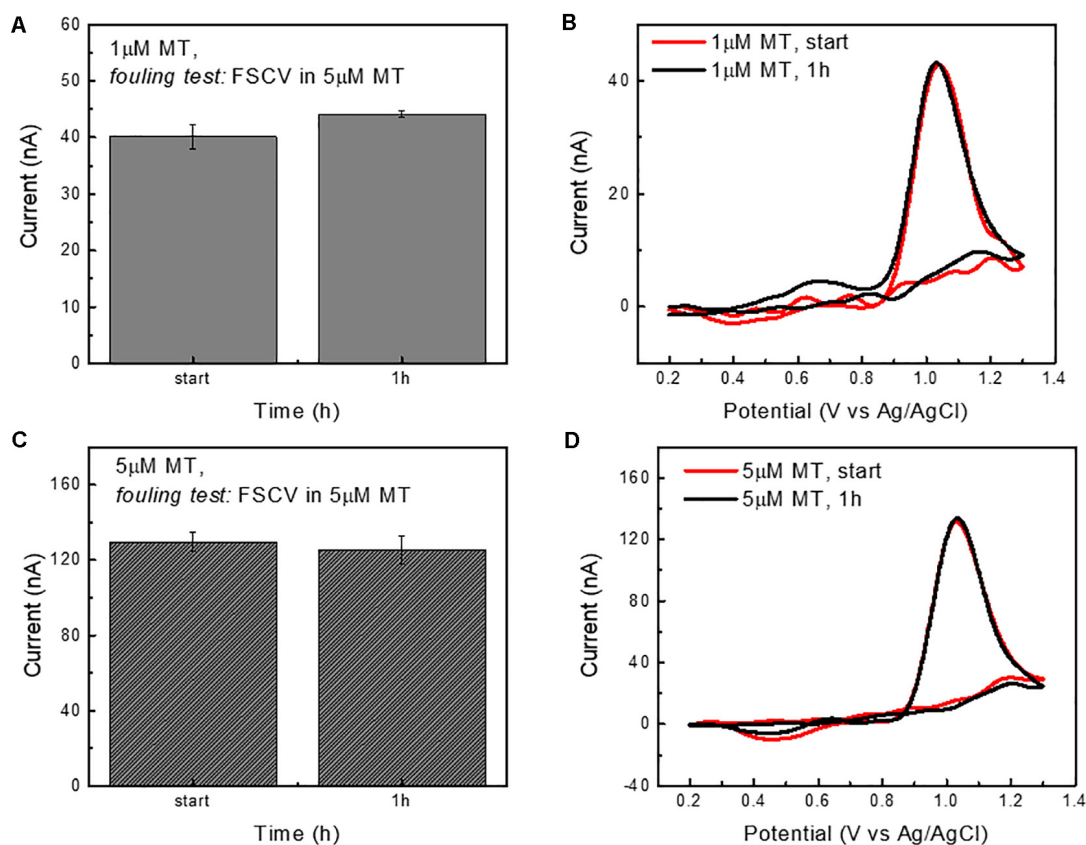


**FIGURE 2 |** CFE fouling test in the presence of MT (continuous FSCV scanning). **(A)** Bar plot reporting the current amplitudes (average  $\pm$  std,  $n = 5$  repetitions) of the oxidation peaks collected in response to 1  $\mu$ M bolus injections of MT at time zero and after 1 h of CFE FSCV continuous scanning in 5  $\mu$ M MT concentration in aCSF. The average current peak amplitudes ( $40.1 \pm 3.7$  and  $44.1 \pm 1.0$  nA) are not significantly different. **(B)** Representative background subtracted CVs in response to 1  $\mu$ M bolus injections of MT at the time 0 and after 1 h of CFE FSCV continuous scanning in 5  $\mu$ M MT concentration in aCSF. **(C)** Bar plot reporting the current amplitudes (average  $\pm$  std,  $n = 5$  repetitions) of the oxidation peak collected in response to 5  $\mu$ M bolus injections of MT at time zero and after 1 h of CFE FSCV continuous scanning in 5  $\mu$ M MT concentration in aCSF. The average current peak amplitudes (first:  $130 \pm 10$  and  $125.3 \pm 7.5$  nA after 1 h) are not significantly different. **(D)** Representative background subtracted CVs in response to 5  $\mu$ M bolus injections of MT at the time 0 and after 1 h of FSCV.

with high concentrations of MT. In our previous study, 5.5  $\mu$ M of MT corresponded to the peak concentration detected in the mouse brain after administration of high MT dose (180 mg/kg), which only lasted for a few minutes before MT being metabolized (Castagnola et al., 2020).

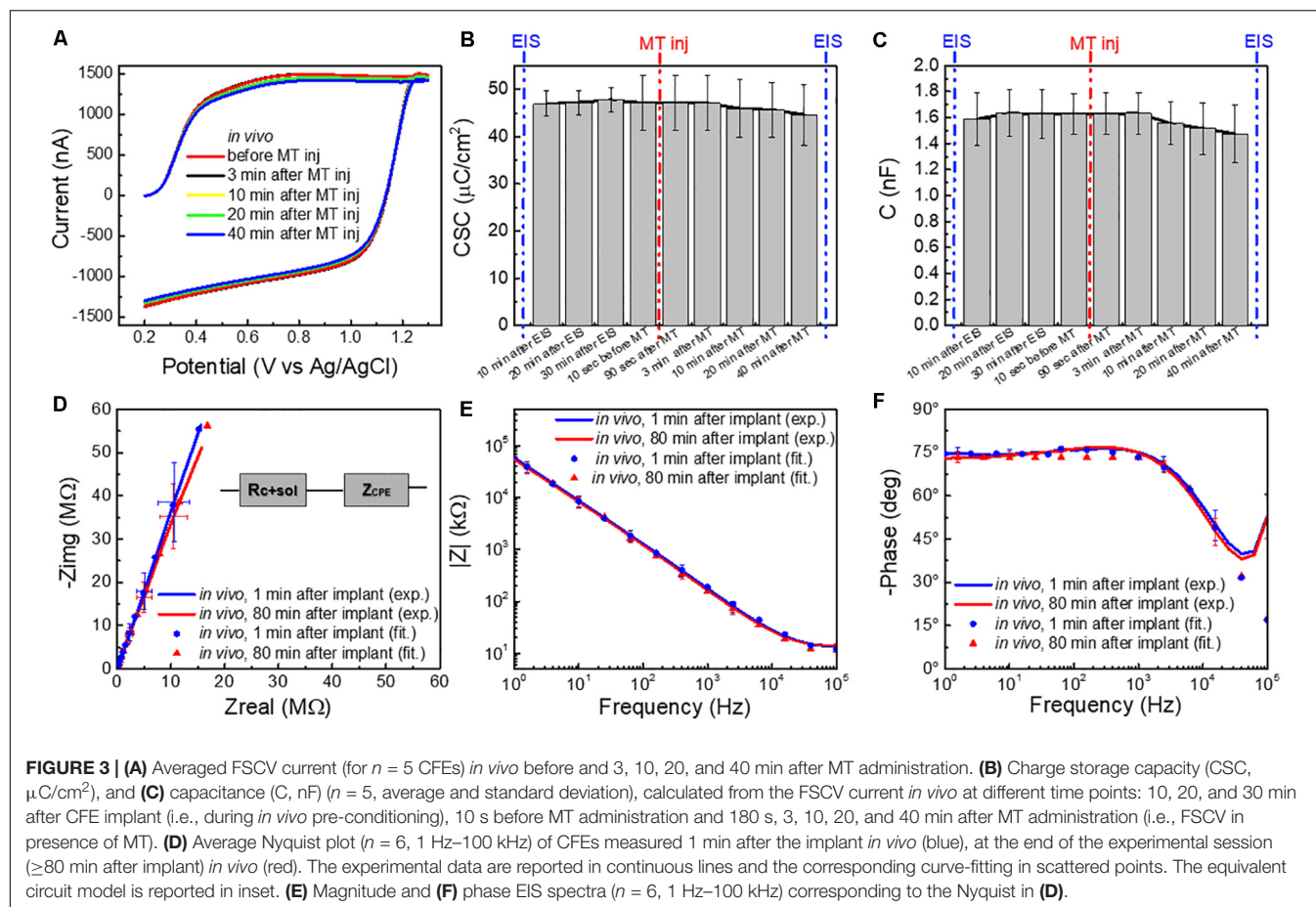
## Evaluation of CFE Fouling *in vivo* and Effect of Tissue Exposure on CFE Sensitivity

Recent works from the Sombers' group have suggested that the FSCV current can be used as a predictor of electrode fouling and sensitivity to multiple analytes *in situ* (Roberts et al., 2013; Meunier et al., 2017). Furthermore, EIS has been considered a valuable technique to probe electrode conditions and biofouling (Wilks et al., 2012; Alba et al., 2015), as well as predict electrochemical FSCV performance, using equivalent circuit models of the electrode/solution interface (Roberts et al., 2013; Meunier et al., 2020). Thus, to gain further insight about the extent of fouling *in vivo* and changes of electrode/tissue

interface, we monitored (1) the EIS of the CFEs *in vivo*, upon probe implantation and after the experimental sessions (composed of a 30–40 min of pre-conditioning with FSCV, MT injection and a 40 min post-injection FSCV, total of  $\sim 80$  min) and (2) the variation of the FSCV current *in vivo* before, during and after the MT injection (Figure 3). Additionally, to estimate the effects of tissue exposure on impedance, capacitance, and sensitivity of the CFEs, (1) EIS and FSCV current were measured before implantation and after explantation in aCSF and (2) the sensitivity of CFEs before and after tissue exposure *in vitro*. All EIS data were fitted to an equivalent circuit model (Supplementary Section 2 and Supplementary Figure 5) in order to better investigate the nature of impedance changes.

*In vivo*, little change in FSCV current, during and after the MT injection was observed (Figure 3A). The CSC ( $\text{mC}/\text{cm}^2$ ) (Figure 3B) and the capacitance ( $C$ , nF) (Figure 3C), calculated from the FSCV current, did not significantly change at different time points before and after the MT injection [repeated measures ANOVA,  $F(5,25) = 0.172$ ,  $p > 0.05$  for CSC;  $F(8,32) = 0.445$ ,  $p > 0.05$ , multiple comparisons Bonferroni post-tests n.s.].





Similarly, the impedance spectra (Figures 3D–F) did not significantly change during the experimental session of  $\geq 80$  min [two-way ANOVA with repeated measures:  $F(1,312) = 1.287$ ,  $p = 0.2576 > 0.05$ ].

Average Nyquist plots ( $n = 6$ ) of the experimental data and the corresponding curve-fitting of the most appropriate equivalent circuit model, i.e., a non-ideal Randles, are reported in Figures 3D–F and Supplementary Figure 6. More details about the model and the effect of tissue exposure are provided in Supplementary Section 2. Briefly, the non-ideal Randles equivalent circuit (Figure 3D inset) consists of a solution resistance ( $R_{\text{sol}+\text{carbon}}$ ) in series with a constant phase element ( $Z_{\text{CPE}}$ ). This is consistent with results reported in the literature for CFEs glue-sealed at the tip (Meunier et al., 2020). The constant phase element ( $Z_{\text{CPE}}$ ) is defined as:  $Z_{\text{CPE}} = 1/(j\omega)^n Y_0$ , where  $Y_0$  represents the double-layer capacitance and  $n$  is a constant related to the angle of rotation in the complex plane compared to the purely capacitive behavior ( $n = 1$  for a pure capacitor) (MacDonald, 1987; Nimbalkar et al., 2018; Meunier et al., 2020). The parameters obtained by fitting the experimental data to the model are reported in Table 1.

Immediately after CFEs were inserted in the brain, we observed (1) an increase in the real impedance, with a deviation from the ideal capacitor (Supplementary Figure 6), confirmed by the decrease of  $n$  values obtained from the fitting (Table 1)

and (2) an increase of the solution/CFE interface resistance  $R_{\text{sol}+\text{carbon}}$  (Table 1 and Supplementary Figure 7), most likely due to the more complex and resistive nature of the brain tissue compared to the aCSF, and may also be affected by the use of a different three-electrochemical system *in vivo* (Williams et al., 2007; Mercanzini et al., 2009; Meunier et al., 2020). It is important to note that the  $n$  values we measured from the *in vitro* EIS of CFEs are lower than what was reported in literature for similar CFEs (ca. 0.9) (Meunier et al., 2020). This is due to the effect of the overnight pre-conditioning, as the starting  $n$  value before pre-conditioning was 0.891. The higher  $Y_0$  *in vivo* is likely due to the higher ionic strength of the tissue in comparison with aCSF, which decreases the diffuse layer thickness and increases double-layer capacitance

**TABLE 1 |** Equivalent circuit model fit parameters.

	$R_{\text{sol}+\text{carbon}}$ (k $\Omega$ )	$Y_0$ (nS s $^n$ )	$n$
<i>In vitro</i> in aCSF, pre implant	5.3	3.4	0.853
<i>In vivo</i> time 0 (immediately after insertion in the brain)	9.2	3.7	0.829
<i>In vivo</i> time $\sim 80$ min (after conditioning and measurements)	9.0	3.8	0.815
<i>In vitro</i> in aCSF, post implant	6.9	3.6	0.833



(Bard et al., 1980; Meunier et al., 2020). During the *in vivo* measurements, all circuit parameters remain relatively steady. These results showed no significant evidence of CFE fouling during the duration of the *in vivo* experiments, consistent with the *in vitro* finding.

### *In vivo* MT Detection Using FSCV

Finally, we used FSCV to detect MT in the visual cortex of mouse brains in response to an i.p. injection of 180 mg/kg MT (Albertson et al., 1981; Sugden, 1983). In our recent SWV study, we demonstrated that the i.p. administration of this dosage creates fast changes in the MT concentration in the mouse brain (Castagnola et al., 2020). Similar MT dosages have shown to possess anticonvulsant effects and to reduce the seizure rank score in rat models of epilepsy (Albertson et al., 1981; Aydin et al., 2015). MT supplements in similar concentrations have also shown to ameliorate sleep deprivation-aggravated pain behavior and neuropathic pain in rats with chronic constriction nerve injury (Huang et al., 2014). MT administered intraperitoneally has specifically demonstrated to possess a strong antinociceptive and analgesic

effect (Sugden, 1983; Yu et al., 2000) and to potentiate sleep in mice and rats (Sugden, 1983; Wang et al., 2002).

Prior to the beginning of each *in vivo* experiment, CFEs were electrochemically pre-conditioned overnight in aCSF *in vitro*, as described in the previous section. After the implantation of CFEs in the visual cortex, the microelectrode surfaces were further stabilized by applying the same FSCV waveform at 10 Hz. Stable current backgrounds were observed after about 30–40 min of FSCV scanning.

The representative color plot for a 3-min FSCV background-subtracted current collection *in vivo* (**Supplementary Figure 11a**) and the average FSCV background ( $n = 10$ , black, **Supplementary Figure 11b**), collected before each MT recording session, show a stable background without observable current drift. Additionally, no changes were observed in the background subtracted CV after the injection of saline vehicle (**Figure 4A**). MT was administered i.p. at 180 mg/kg MT 10 s after the beginning of the FSCV acquisition. CFEs started to detect MT in the brain about 50 s following the i.p. injection (**Figure 4B**). The detection of MT using FSCV is clearly confirmed by the color plot current changes (**Figure 4B**) and

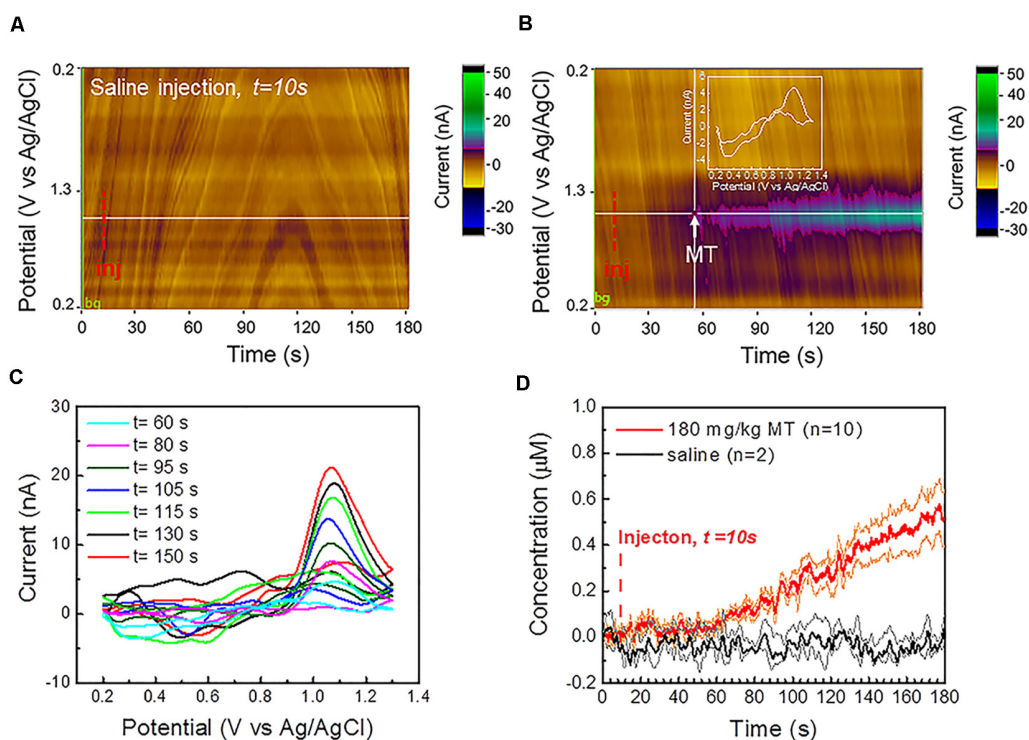


**FIGURE 4 |** *In vivo* MT FSCV detection: **(A)** Representative color plot for a 3 min FSCV data collection after saline control injection at 10 s *in vivo* shows a stable background without observable current drift. **(B)** Representative color plot for a 3-min FSCV data collection after MT injection at 10 s (i.p., 180 mg/kg). CFEs started to detect MT about 50 s after MT administration. **(C)** Representative *in vivo* background subtracted CV at different time points following i.p. injection reveals a clear MT oxidation potential peak, that increase during the recording period. **(D)** Average *in vivo* MT concentration ( $\pm$ SEM) over time, detected at CFEs using FSCV before and after the i.p. administration (at 10 s) of 180 mg/kg MT (red,  $n = 10$ ) and saline vehicle ( $n = 2$ , black), respectively. The orange and green lines correspond to the min and max concentration trends, calculated as mean  $\pm$  SEM (i.e., mean  $\pm$  standard deviation divided by the square root of the sample size) for experimental and control groups, respectively. CFEs started to detect an increase in MT concentration about 50 s following the i.p. injection and reach the concentration of 0.51  $\mu$ M (0.40  $\mu$ M min, 0.62  $\mu$ M max) 170 s following MT administration. No change has been observed in the background-subtracted FSCV after injection of saline vehicle. 10  $\mu$ L DMSO was added in order to improve the solubility of the MT in 100  $\mu$ L saline vehicle, as well as in the saline vehicle for the control group, in order to exclude the DMSO effect on background stability.

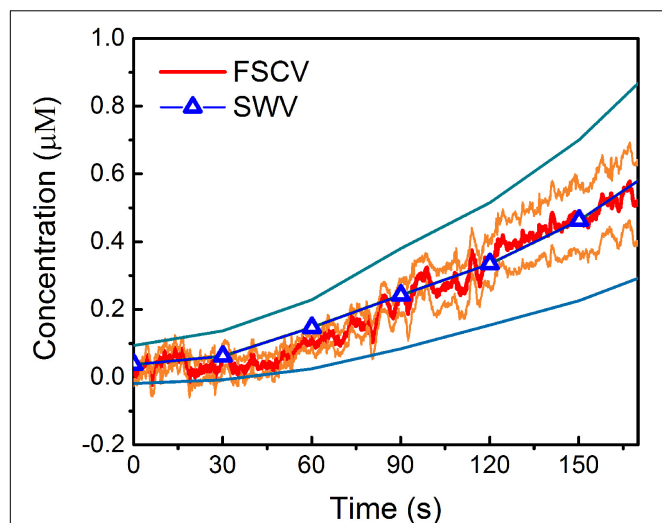


**FIGURE 5 |** Comparison of *in vivo* MT detection using FSCV and SWV: Average *in vivo* MT concentration ( $\pm$ SEM), over time, detected at CFEs using FSCV (red) and SWV (blue) after the i.p. administration of 180 mg/kg MT. In these plots,  $t = 0$  is the time of injection for both SWV and FSCV measurements. The orange and light-blue lines correspond to the min and max concentration trends, calculated as mean  $\pm$  SEM (i.e., mean  $\pm$  standard deviation divided by the square root of the sample size) for FSCV and SWV, respectively.

by the background subtracted CVs, showing an increase of the current amplitude of the characteristic MT peak at 1.03 V over time, as seen in **Figure 4C**.

Our previous SWV studies (Taylor et al., 2019; Castagnola et al., 2020) have concluded that there is a drastic decrease in CFE sensitivity after it is explanted from the brain tissue and this is mainly attributed to the encapsulation of the CFE by biological matter pulled out during the explantation process itself. For this reason, we used the pre-calibration curve of electrode sensitivity to determine the *in vivo* MT concentrations. Measured MT concentration ( $\pm$ SEM) was plotted over time before and after the MT injection ( $n = 10$ , red, **Figure 4D**) and showed a linear increase after 50 s and reached  $0.51 \mu\text{M}$  ( $0.40 \mu\text{M}$  min,  $0.62 \mu\text{M}$  max) after 170 s. In comparison, the average baseline (background-subtracted FSCV) after injection of saline vehicle ( $n = 2$ , black, **Figure 4D**) remained flat.

In summary, the CFE electrochemical pre-conditioning enabled a stable FSCV background over a recording session of 3 min, more than twice the duration limit (usually  $< 90$  s) reported in literature for FSCV measurements before the background drifting occurs, which has prevented accurate analysis of chemical fluctuations in the brain (Mark DeWaele et al., 2017; Meunier et al., 2019). This allowed us to obtain stable FSCV detection of MT *in vivo* for 3 min.

## Comparison With SWV and Microdialysis

Remarkably, when comparing the *in vivo* MT concentrations detected using FSCV to those obtained in our previous SWV study (Castagnola et al., 2020), during the 170 s post i.p. injection of 180 mg/kg MT, we observed a very similar trend

(**Figure 5**). The averaged detected concentrations at 170 s after MT administration were  $0.55 \mu\text{M}$  ( $0.40 \mu\text{M}$  min,  $0.64 \mu\text{M}$  max) for FSCV and  $0.53 \mu\text{M}$  ( $0.32 \mu\text{M}$  min,  $0.82 \mu\text{M}$  max) for SWV. It is worth noting that FSCV provides 240 times greater temporal resolution (0.1 versus 24 s) and 200 times higher sensitivity ( $28.1$  versus  $0.14 \text{ nA}/\mu\text{M}$ ) than SWV.

To provide a further validation of our electrochemical MT quantification, we compared the electrochemical results with microdialysis, by simultaneously performing microdialysis and FSCV experiments in the same location of same mice ( $n = 5$ ). The dialysate, collected for 40 min before and after i.p. injection, was analyzed using LC-MS, i.e., injected onto an LC-MS and compared to a calibration curve. First of all, no MT peak was observed in baseline dialysate collected before the MT administration (**Supplementary Figure 12**). This is in agreement with the known low endogenous MT background in C57BL/6J mice (Roseboom et al., 1998). After MT injection, we obtained an average concentration of  $4.3 \mu\text{M}$  ( $n = 5$ ,  $3.34$  min and  $6.69$  max) from the dialysate collected for 40 min, which is on the same order of magnitude of the MT concentration detected with the SWV measurement [maximum detected concentration was  $5.5 \mu\text{M}$  ( $4.4 \mu\text{M}$  min,  $6.5 \mu\text{M}$  max) after 17.9 minutes following the MT administration] (Castagnola et al., 2020). It is worth pointing out that one cannot expect a perfect match between microdialysis and electrochemical results. Our electrochemical detections use pre-calibration, which may provide an underestimation of the MT *in vivo* concentration. On the other hand, the microdialysis result is an underestimation due to the impact of the microdialysis probes on the brain tissues and the corresponding recovery factor (Yang et al., 2000; Watson et al., 2006; Jaquins-Gerstl and Michael, 2015). Furthermore, there are clear differences in temporal resolution between the microdialysis (averaged over 40 min) and electrochemical methods (measured at subseconds for FSCV and seconds for SWV) (Watson et al., 2006; Jaquins-Gerstl and Michael, 2015; Puthongkham and Venton, 2020). Nevertheless, having the estimated MT concentrations in the same range supports the reliability of FSCV and SWV to measure MT in real time in mouse brain.

## CONCLUSION

In this study, we established a prolonged CFE electrochemical pre-conditioning protocol to enable stable FSCV background and demonstrated that pre-conditioning CFE with the Ross's FSCV waveform overnight resulted in a stable sensitivity in response to  $1 \mu\text{M}$  bolus injections of MT over a period of 8 h, or in the prolonged presence of a high MT concentration of  $5 \mu\text{M}$ . Using the FSCV current and EIS as a predictor of the electrode/solution interface variations, we estimated the extent of fouling *in vivo*, and the effects of the tissue exposure on the impedance, capacitance, and sensitivity of the CFEs. We found no significant evidence of CFE fouling during the duration of the *in vivo* experiments, confirming the result obtained *in vitro*. Remarkably, *in vivo* measurements demonstrated a drift-free FSCV detection of exogenous MT in mouse brain for 3 min,

004 more than twice the duration limit (usually < 90 s) reported in literature before FSCV background drifting occurs (Mark DeWaele et al., 2017; Meunier et al., 2019). The *in vivo* MT concentrations measured by FSCV are consistent with those measured by SWV upon the same MT injection regime (Castagnola et al., 2020), which is also supported by microdialysis. These results support the ability and reliability of FSCV to measure exogenously delivered MT *in real time* over several minutes *in vivo*.

## DATA AVAILABILITY STATEMENT

The raw data supporting the conclusions of this article will be made available by the authors, without undue reservation.

## ETHICS STATEMENT

All procedures involving animals were approved by the Institutional Animal Care and Use Committee of the University of Pittsburgh.

## AUTHOR CONTRIBUTIONS

EC led *in vitro* and *in vivo* experiments, performed *in vitro* and *in vivo* fouling experiments and data analysis, and wrote the manuscript. ER fabricated microdialysis probes and led

microdialysis experiments and analysis. KW performed parts of the surgeries and SEM imaging. AG performed parts of the surgeries. MM performed impedance measurements and *in vitro* calibrations and helped with CFEs fabrication. IT fabricated the CFEs, supervised the *in vitro* and fouling experiments, and edited the manuscript. AM supervised the microdialysis experiments and edited the manuscript. XTC supervised the project, guided the data analysis, and edited the manuscript. All authors contributed to the article and approved the submitted version.

## FUNDING

This work was supported by NIH (Grants R01NS062019, R01NS089688, R21DA043817, and R21 DA049592).

## ACKNOWLEDGMENTS

We thank Neha Chodapaneeedi and Julian Metro for helping with CFE fabrication and characterization.

## SUPPLEMENTARY MATERIAL

The Supplementary Material for this article can be found online at: <https://www.frontiersin.org/articles/10.3389/fbioe.2020.602216/full#supplementary-material>

## REFERENCES

- Alba, N. A., Du, Z. J., Catt, K. A., Kozai, T. D., and Cui, X. T. (2015). In vivo electrochemical analysis of a PEDOT/MWCNT neural electrode coating. *Biosensors* 5, 618–646. doi: 10.3390/bios5040618
- Albertson, T. E., Peterson, S., Stark, L., Lakin, M., and Winters, W. (1981). The anticonvulsant properties of melatonin on kindled seizures in rats. *Neuropharmacology* 20, 61–66. doi: 10.1016/0028-3908(81)90043-5
- Antolín, I., Mayo, J. C., Sainz, R. M., del Brío, M. de L., Herrera, F., Martín, V., et al. (2002). Protective effect of melatonin in a chronic experimental model of Parkinson's disease. *Brain Res.* 943, 163–173. doi: 10.1016/S0006-8993(02)02551-9
- Apetrei, I. M., and Apetrei, C. (2016). Voltammetric determination of melatonin using a graphene-based sensor in pharmaceutical products. *Int. J. Nanomed.* 11, 1859–1866. doi: 10.2147/ijn.s104941
- Aydin, L., Gundogan, N. U., and Yazici, C. (2015). Anticonvulsant efficacy of melatonin in an experimental model of hyperthermic febrile seizures. *Epilepsy Res.* 118, 49–54. doi: 10.1016/j.eplepsyres.2015.11.004
- Banach, M., Gurdziel, E., Jędrych, M., and Borowicz, K. K. (2011). Melatonin in experimental seizures and epilepsy. *Pharmacol. Rep.* 63, 1–11. doi: 10.1016/S1734-1140(11)70393-0
- Bard, A., Faulkner, L., Leddy, J., and Zoski, C. (1980). *Electrochemical Methods: Fundamentals and Applications*. New York, NY: Wiley.
- Bath, B. D., Michael, D. J., Joseph, J. D., Runnels, P. L., and Wightman, R. M. (2000). Subsecond Adsorption and Desorption of Dopamine at Carbon-Fiber Microelectrodes. *Anal. Chem.* 72, 5994–6002. doi: 10.1021/ac000849y
- Borlongan, C. V., Yamamoto, M., Takei, N., Kumazaki, M., Ungsuparkorn, C., Hida, H., et al. (2000). Glial cell survival is enhanced during melatonin-induced neuroprotection against cerebral ischemia. *FASEB J.* 14, 1307–1317. doi: 10.1096/fj.14.10.1307
- Bowling, R., Packard, R. T., and McCreery, R. L. (1989). Mechanism of electrochemical activation of carbon electrodes: role of graphite lattice defects. *Langmuir* 5, 683–688. doi: 10.1021/la00087a022
- Buscemi, N., Vandermeer, B., Pandya, R., Hooton, N., Tjosvold, L., Hartling, L., et al. (2004). Melatonin for treatment of sleep disorders. *Evid. Rep. Technol. Assess.* 108, 1–7.
- Cagnacci, A., Elliott, J., and Yen, S. (1992). Melatonin: a major regulator of the circadian rhythm of core temperature in humans. *J. Clin. Endocrinol. Metab.* 75, 447–452. doi: 10.1210/jc.75.2.447
- Cao, Q., Puthongkham, P., and Venton, B. J. (2019). New insights into optimizing chemical and 3D surface structures of carbon electrodes for neurotransmitter detection. *Analytic. Methods* 11, 247–261. doi: 10.1039/c8ay02472c
- Castagnola, E., Vahidi, N. W., Nimbalkar, S., Rudraraju, S., Thielk, M., Zucchini, E., et al. (2018). In vivo dopamine detection and single unit recordings using intracortical glassy carbon microelectrode arrays. *MRS Advances* 3:1629. doi: 10.1557/adv.2018.98
- Castagnola, E., Woeppel, K., Golabchi, A., McGuier, M., Chodapaneeedi, N., Metro, J., et al. (2020). Electrochemical detection of exogenously administered melatonin in the brain. *Analyst* 145, 2612–2620. doi: 10.1039/d0an00051e
- Citera, G., Arias, M., Maldonado-Cocco, J., La, M., Roseff, M., Brusco, L., et al. (2000). The effect of melatonin in patients with fibromyalgia: a pilot study. *Clin. Rheumatol.* 19, 9–13. doi: 10.1007/s100670050003
- Cooper, S. E., and Venton, B. J. (2009). Fast-scan cyclic voltammetry for the detection of tyramine and octopamine. *Analytic. Bioanalytic. Chem.* 394, 329–336. doi: 10.1007/s00216-009-2616-0
- Cryan, M. T., and Ross, A. E. (2019). Scalene Waveform for Codetection of Guanosine and Adenosine Using Fast-Scan Cyclic Voltammetry. *Analytic. Chem.* 91, 5987–5993. doi: 10.1021/acs.analchem.9b00450
- Cuzzocrea, S., Costantino, G., Gitto, E., Mazzon, E., Fula, F., Serrano, I., et al. (2000). Protective effects of melatonin in ischemic brain injury. *J. Pineal Res.* 29, 217–227.
- Dragicevic, N., Copes, N., O'Neal-Moffitt, G., Jin, J., Buzzeo, R., Mamcarz, M., et al. (2011). Melatonin treatment restores mitochondrial function in Alzheimer's mice: a mitochondrial protective role of melatonin membrane receptor signaling. *J. Pineal Res.* 51, 75–86. doi: 10.1111/j.1600-079x.2011.00864.x



- Engstrom, R. C., and Strasser, V. A. (1984). Characterization of electrochemically pretreated glassy carbon electrodes. *Analytic. Chem.* 56, 136–141. doi: 10.1021/ac00266a005
- Escribano, B. M., Colin-Gonzalez, A. L., Santamaría, A., and Túnez, I. (2014). The role of melatonin in multiple sclerosis, Huntington's disease and cerebral ischemia. *CNS Neurol. Disord. Drug Targets* 13, 1096–1119. doi: 10.2174/1871527313666140806160400
- Fariás, J. G., Zepeda, A. B., and Calaf, G. M. (2012). Melatonin protects the heart, lungs and kidneys from oxidative stress under intermittent hypobaric hypoxia in rats. *Biol. Res.* 45, 81–85. doi: 10.4067/s0716-97602012000100011
- Fauteck, J.-D., Schmidt, H., Lerchl, A., Kurlemann, G., and Wittkowski, W. (1999). Melatonin in epilepsy: first results of replacement therapy and first clinical results. *Neurosignals* 8, 105–110. doi: 10.1159/000014577
- Ganesana, M., Lee, S. T., Wang, Y., and Venton, B. J. (2017). Analytical techniques in neuroscience: recent advances in imaging, separation, and electrochemical methods. *Analytic. Chem.* 89, 314–341. doi: 10.1021/acs.analchem.6b04278
- Golabchi, A., Wu, B., Li, X., Carlisle, D. L., Kozai, T. D., Friedlander, R. M., et al. (2018). Melatonin improves quality and longevity of chronic neural recording. *Biomaterials* 180, 225–239. doi: 10.1016/j.biomaterials.2018.07.026
- Gomez, F. J. V., Martín, A., Silva, M. F., and Escarpa, A. (2015). Screen-printed electrodes modified with carbon nanotubes or graphene for simultaneous determination of melatonin and serotonin. *Microchim. Acta* 182, 1925–1931. doi: 10.1007/s00604-015-1520-x
- Hafizi, S., Kruk, Z. L., and Stamford, J. A. (1990). Fast cyclic voltammetry: improved sensitivity to dopamine with extended oxidation scan limits. *J. Neurosci. Methods* 33, 41–49. doi: 10.1016/0165-0270(90)90080-y
- Hardeland, R. (2005). Antioxidative protection by melatonin. *Endocrine* 27, 119–130.
- Harreither, W., Trouillon, R., Poulin, P., Neri, W., Ewing, A. G., and Safina, G. (2016). Cysteine residues reduce the severity of dopamine electrochemical fouling. *Electrochim. Acta* 210, 622–629. doi: 10.1016/j.electacta.2016.05.124
- Heien, M. L., Phillips, P. E., Stuber, G. D., Seipel, A. T., and Wightman, R. M. (2003). Overoxidation of carbon-fiber microelectrodes enhances dopamine adsorption and increases sensitivity. *Analyst* 128, 1413–1419. doi: 10.1039/b307024g
- Hensley, A. L., Colley, A. R., and Ross, A. E. (2018). Real-Time Detection of Melatonin Using Fast-Scan Cyclic Voltammetry. *Analytic. Chem.* 90, 8642–8650. doi: 10.1021/acs.analchem.8b01976
- Hermans, A., Keithley, R. B., Kita, J. M., Sombers, L. A., and Wightman, R. M. (2008). Dopamine detection with fast-scan cyclic voltammetry used with analog background subtraction. *Analytic. Chem.* 80, 4040–4048. doi: 10.1021/ac800108j
- Hossain, M. F., Uddin, M. S., Uddin, G. S., Sumsuzzman, D. M., Islam, M. S., Barreto, G. E., et al. (2019). Melatonin in Alzheimer's disease: a latent endogenous regulator of neurogenesis to mitigate Alzheimer's neuropathology. *Molecular Neurobiol.* 56, 8255–8276. doi: 10.1007/s12035-019-01660-3
- Huang, C.-T., Chiang, R. P.-Y., Chen, C.-L., and Tsai, Y.-J. (2014). Sleep deprivation aggravates median nerve injury-induced neuropathic pain and enhances microglial activation by suppressing melatonin secretion. *Sleep* 37, 1513–1523. doi: 10.5665/sleep.4002
- Jackson, B. P., Dietz, S. M., and Wightman, R. M. (1995). Fast-scan cyclic voltammetry of 5-hydroxytryptamine. *Analytic. Chem.* 67, 1115–1120.
- Jan, J. E., Espezel, H., and Appleton, R. (1994). The treatment of sleep disorders with melatonin. *Dev. Med. Child Neurol.* 36, 97–107.
- Jaquins-Gerstl, A., and Michael, A. C. (2015). A review of the effects of FSCV and microdialysis measurements on dopamine release in the surrounding tissue. *Analyst* 140, 3696–3708. doi: 10.1039/c4an02065k
- Johnson, J. A., Rodeberg, N. T., and Wightman, R. M. (2016). Failure of standard training sets in the analysis of fast-scan cyclic voltammetry data. *ACS Chem. Neurosci.* 7, 349–359. doi: 10.1021/acschemneuro.5b00302
- Keithley, R. B., Takmakov, P., Bucher, E. S., Belle, A. M., Owesson-White, C. A., Park, J., et al. (2011). Higher Sensitivity Dopamine Measurements with Faster-Scan Cyclic Voltammetry. *Anal. Chem.* 83, 3563–3571. doi: 10.1021/ac200143v
- Korszun, A., Sackett-Lundeen, L., Papadopoulos, E., Brucksch, C., Masterson, L., Engelberg, N., et al. (1999). Melatonin levels in women with fibromyalgia and chronic fatigue syndrome. *J. Rheumatol.* 26, 2675–2680.
- Levent, A. (2012). Electrochemical determination of melatonin hormone using a boron-doped diamond electrode. *Diamond Related Mater.* 21, 114–119. doi: 10.1016/j.diamond.2011.10.018
- Luengo, E., Buendia, I., Fernández-Mendivil, C., Trigo-Alonso, P., Negro, P., Michalska, P., et al. (2019). Pharmacological doses of melatonin impede cognitive decline in tau-related Alzheimer models, once tauopathy is initiated, by restoring the autophagic flux. *J. Pineal Res.* 67:e12578. doi: 10.1111/jpi.12578
- MacDonald, J. R. (1987). *Impedance Spectroscopy—Emphasizing Solid Materials and Systems*. Hoboken, NJ: John Wiley and Sons, 1–346.
- Maeda, Y., Okemoto, Y., and Inagaki, M. (1985). Electrochemical formation of graphite-sulfuric acid intercalation compounds on carbon fibers. *J. Electrochem. Soc.* 132:2369. doi: 10.1149/1.2113579
- Maestroni, G. J., Conti, A., and Pierpaoli, W. (1986). Role of the pineal gland in immunity: circadian synthesis and release of melatonin modulates the antibody response and antagonizes the immunosuppressive effect of corticosterone. *J. Neuroimmunol.* 13, 19–30.
- Mark DeWaele, Y. O., Park, C., Kang, Y. M., Shin, H., Blaha, C. D., Bennet, K. E., et al. (2017). A baseline drift detrending technique for fast scan cyclic voltammetry. *Analyst* 142, 4317–4321. doi: 10.1039/c7an01465a
- Mayo, J. C., Sainz, R. M., Tan, D.-X., Antolín, I., Rodríguez, C., and Reiter, R. J. (2005). Melatonin and Parkinson's disease. *Endocrine* 27, 169–178.
- Mercanzini, A., Colin, P., Bensadoun, J.-C., Bertsch, A., and Renaud, P. (2009). In vivo electrical impedance spectroscopy of tissue reaction to microelectrode arrays. *IEEE Trans. Biomed. Eng.* 56, 1909–1918. doi: 10.1109/tbme.2009.2018457
- Meunier, C. J., Denison, J. D., McCarty, G. S., and Sombers, L. A. (2020). Interpreting Dynamic Interfacial Changes at Carbon Fiber Microelectrodes Using Electrochemical Impedance Spectroscopy. *Langmuir* 36, 4214–4223. doi: 10.1021/acs.langmuir.9b03941
- Meunier, C. J., McCarty, G. S., and Sombers, L. A. (2019). Drift Subtraction for Fast-Scan Cyclic Voltammetry Using DoubleWaveform Partial-Least-Squares Regression. *Anal. Chem.* 91, 7319–7327. doi: 10.1021/acs.analchem.9b01083
- Meunier, C. J., Roberts, J. G., McCarty, G. S., and Sombers, L. A. (2017). Background Signal as an in Situ Predictor of Dopamine Oxidation Potential: Improving Interpretation of Fast-Scan Cyclic Voltammetry Data. *ACS Chem. Neurosci.* 8, 411–419. doi: 10.1021/acschemneuro.6b00325
- Miller, E., Morel, A., Saso, L., and Saluk, J. (2015). Melatonin redox activity. Its potential clinical applications in neurodegenerative disorders. *Curr. Topics Med. Chem.* 15, 163–169. doi: 10.2174/1568026615666141209160556
- Mukherjee, D., Roy, S. G., Bandyopadhyay, A., Chattopadhyay, A., Basu, A., Mitra, E., et al. (2010). Melatonin protects against isoproterenol-induced myocardial injury in the rat: antioxidative mechanisms. *J. Pineal Res.* 48, 251–262. doi: 10.1111/j.1600-079x.2010.00749.x
- Neeraj Kumar, R. N. G. (2017). Electrochemical Behavior of Melatonin and its Sensing in Pharmaceutical Formulations and in Human Urine. *Curr. Pharm. Analysis* 13, 85–90. doi: 10.2174/1573412912666160422154459
- Nesbitt, K. M., Varner, E. L., Jaquins-Gerstl, A., and Michael, A. C. (2015). Microdialysis in the rat striatum: effects of 24 h dexamethasone retrodialysis on evoked dopamine release and penetration injury. *ACS Chem. Neurosci.* 6, 163–173. doi: 10.1021/cn500257x
- Nguyen, M. D., and Venton, B. J. (2014). Fast-scan Cyclic Voltammetry for the Characterization of Rapid Adenosine Release. *Comput. Struct. Biotechnol. J.* 29, 47–54. doi: 10.1016/j.csbj.2014.12.006
- Nimbalkar, S., Castagnola, E., Balasubramani, A., Scarpellini, A., Samejima, S., Khorasani, A., et al. (2018). Ultra-capacitive carbon neural probe allows simultaneous long-term electrical stimulations and high-resolution neurotransmitter detection. *Sci. Rep.* 8, 1–14.
- Oh, Y., Park, C., Kim, D. H., Shin, H., Kang, Y. M., DeWaele, M., et al. (2016). Monitoring in vivo changes in tonic extracellular dopamine level by charge-balancing multiple waveform fast-scan cyclic voltammetry. *Analytical Chem.* 88, 10962–10970. doi: 10.1021/acs.analchem.6b02605
- Ou, Y., Buchanan, A. M., Witt, C. E., and Hashemi, P. (2019). Frontiers in electrochemical sensors for neurotransmitter detection: towards measuring neurotransmitters as chemical diagnostics for brain disorders. *Analytic. Methods* 11, 2738–2755. doi: 10.1039/c9ay00055k
- Poon, M., McCreery, R. L., and Engstrom, R. (1988). Laser activation of carbon electrodes. Relationship between laser-induced surface effects and electron



- transfer activation. *Analytic. Chem.* 60, 1725–1730. doi: 10.1021/ac00168a018
- Puthongkham, P., and Venton, B. J. (2020). Recent Advances in Fast-Scan Cyclic Voltammetry. *Analyst* 145, 1087–1102. doi: 10.1039/c9an01925a
- Pyakurel, P., Privman Champaloux, E., and Venton, B. J. (2016). Fast-scan cyclic voltammetry (FSCV) detection of endogenous octopamine in *Drosophila melanogaster* ventral nerve cord. *ACS Chem. Neurosci.* 7, 1112–1119. doi: 10.1021/acscchemneuro.6b00070
- Reiter, R. J., Mayo, J. C., Tan, D. X., Sainz, R. M., Alatorre-Jimenez, M., and Qin, L. (2016). Melatonin as an antioxidant: under promises but over delivers. *J. Pineal Res.* 61, 253–278. doi: 10.1111/jpi.12360
- Reiter, R. J., Tan, D.-X., and Fuentes-Broto, L. (2010). Melatonin: a multitasking molecule. *Prog. Brain Res.* 181, 127–151. doi: 10.1016/s0079-6123(08)81008-4
- Reiter, R. J., Tan, D.-X., Mayo, J. C., Sainz, R. M., Leon, J., and Czarnocki, Z. (2003). Melatonin as an antioxidant: biochemical mechanisms and pathophysiological implications in humans. *Acta Biochim. Polonica* 50, 1129–1146. doi: 10.18388/abp.2003.3637
- Robbins, E. M., Jaquins-Gerstl, A., Fine, D. F., Leong, C. L., Dixon, C. E., Wagner, A. K., et al. (2019). Extended (10-Day) Real-Time Monitoring by Dexamethasone-Enhanced Microdialysis in the Injured Rat Cortex. *ACS Chem. Neurosci.* 10, 3521–3531. doi: 10.1021/acscchemneuro.9b00145
- Roberts, J. G., and Sombers, L. A. (2018). Fast-scan cyclic voltammetry: chemical sensing in the brain and beyond. *Anal. Chem.* 90, 490–504. doi: 10.1021/acs.analchem.7b04732
- Roberts, J. G., Toups, J. V., Eyualet, E., McCarty, G. S., and Sombers, L. A. (2013). In situ electrode calibration strategy for voltammetric measurements in vivo. *Analytic. Chem.* 85, 11568–11575. doi: 10.1021/ac402884n
- Robinson, D. L., Venton, B. J., Heien, M. L., and Wightman, R. M. (2003). Detecting subsecond dopamine release with fast-scan cyclic voltammetry in vivo. *Clinic. Chem.* 49, 1763–1773. doi: 10.1373/49.10.1763
- Rosales-Corral, S. A., Acuña-Castroviejo, D., Coto-Montes, A., Boga, J. A., Manchester, L. C., Fuentes-Broto, L., et al. (2012). Alzheimer's disease: pathological mechanisms and the beneficial role of melatonin. *J. Pineal Res.* 52, 167–202. doi: 10.1111/j.1600-079x.2011.00937.x
- Roseboom, P. H., Namboodiri, M. A., Zimonjic, D. B., Popescu, N. C., Rodriguez, I. R., Gastel, J. A., et al. (1998). Natural melatonin knockdown in C57BL/6J mice: rare mechanism truncates serotonin N-acetyltransferase. *Mol. Brain Res.* 63, 189–197. doi: 10.1016/s0169-328x(98)00273-3
- Salehi, B., Sharopov, F., Fokou, P. V. T., Kobylinska, A., Jonge, L. D., Tadio, K., et al. (2019). Melatonin in medicinal and food plants: Occurrence, bioavailability, and health potential for humans. *Cells* 8:681. doi: 10.3390/cells8070681
- Sugden, D. (1983). Psychopharmacological effects of melatonin in mouse and rat. *J. Pharmacol. Experim. Therap.* 227, 587–591.
- Swamy, B. K., and Venton, B. J. (2007). Carbon nanotube-modified microelectrodes for simultaneous detection of dopamine and serotonin in vivo. *Analyst* 132, 876–884. doi: 10.1039/b705552h
- Szczepanik, M. (2007). Melatonin and its influence on immune system. *J. Physiol. Pharmacol.* 58, 115–124.
- Takmakov, P., Zachek, M. K., Keithley, R. B., Walsh, P. L., Donley, C., McCarty, G. S., et al. (2010). Carbon microelectrodes with a renewable surface. *Anal. Chem.* 82, 2020–2028. doi: 10.1021/ac902753x
- Taylor, I. M., Jaquins-Gerstl, A., Sesack, S. R., and Michael, A. C. (2012). Domain-dependent effects of DAT inhibition in the rat dorsal striatum. *J. Neurochem.* 122, 283–294. doi: 10.1111/j.1471-4159.2012.07774.x
- Taylor, I. M., Nesbitt, K. M., Walters, S. H., Varner, E. L., Shu, Z., Bartlow, K. M., et al. (2015). Kinetic diversity of dopamine transmission in the dorsal striatum. *J. Neurochem.* 133, 522–531. doi: 10.1111/jnc.13059
- Taylor, I. M., Patel, N. A., Freedman, N. C., Castagnola, E., and Cui, X. T. (2019). Direct in vivo electrochemical detection of resting dopamine using Poly (3, 4-ethylenedioxythiophene)/Carbon Nanotube functionalized microelectrodes. *Anal. Chem.* 91, 12917–12927. doi: 10.1021/acs.analchem.9b02904
- Taylor, I. M., Robbins, E. M., Catt, K. A., Cody, P. A., Happe, C. L., and Cui, X. T. (2017). Enhanced dopamine detection sensitivity by PEDOT/graphene oxide coating on in vivo carbon fiber electrodes. *Biosens. Bioelectron.* 89, 400–410. doi: 10.1016/j.bios.2016.05.084
- Túnez, I., Montilla, P., Del Carmen, Munoz, M., Feijóo, M., and Salcedo, M. (2004). Protective effect of melatonin on 3-nitropropionic acid-induced oxidative stress in synaptosomes in an animal model of Huntington's disease. *J. Pineal Res.* 37, 252–256. doi: 10.1111/j.1600-079x.2004.00163.x
- Varner, E. L., Jaquins-Gerstl, A., and Michael, A. C. (2016). Enhanced intracranial microdialysis by reduction of traumatic penetration injury at the probe track. *ACS Chem. Neurosci.* 7, 728–736. doi: 10.1021/acscchemneuro.5b00331
- Vasantha, V. S., and Chen, S. M. (2005). Effect of Reaction Conditions on Electropolymerization of Melatonin on Bare Electrodes and PEDOT-Modified Electrodes. *J. Electrochem. Soc.* 152, D151–D159.
- Wang, F., Li, J.-C., Wu, C.-F., Yang, J.-Y., Xu, F., and Peng, F. (2002). Hypnotic activity of melatonin: involvement of semicarbazide hydrochloride, blocker of synthetic enzyme for GABA. *Acta Pharmacol. Sin.* 23, 860–864.
- Watson, C. J., Venton, B. J., and Kennedy, R. T. (2006). *In Vivo Measurements of Neurotransmitters by Microdialysis Sampling*. Washington, DC: ACS Publications.
- Wilhelmsen, M., Amirian, I., Reiter, R. J., Rosenberg, J., and Gögenur, I. (2011). Analgesic effects of melatonin: a review of current evidence from experimental and clinical studies. *J. Pineal Res.* 51, 270–277. doi: 10.1111/j.1600-079x.2011.00895.x
- Wilks, S. J., Richner, T. J., Brodnick, S. K., Kipke, D. R., Williams, J. C., and Otto, K. J. (2012). Voltage biasing, cyclic voltammetry, & electrical impedance spectroscopy for neural interfaces. *JoVE* 60:e3566.
- Williams, J. C., Hippensteel, J. A., Dilgen, J., Shain, W., and Kipke, D. R. (2007). Complex impedance spectroscopy for monitoring tissue responses to inserted neural implants. *J. Neural Eng.* 4:410. doi: 10.1088/1741-2560/4/4/007
- Wood, K. M., and Hashemi, P. (2013). Fast-scan cyclic voltammetry analysis of dynamic serotonin responses to acute escitalopram. *ACS Chem. Neurosci.* 4, 715–720. doi: 10.1021/cn4000378
- Xiao-Ping, W., Lan, Z., Wen-Rong, L., Duan, J.-P., Chen, H.-Q., and Chen, G.-N. (2002). Study on the Electrochemical Behavior of Melatonin with an Activated Electrode. *Electroanalysis* 14, 1654–1660. doi: 10.1002/elan.200290007
- Xie, Z., Chen, F., Li, W. A., Geng, X., Li, C., Meng, X., et al. (2017). A review of sleep disorders and melatonin. *Neurol. Res.* 39, 559–565.
- Yang, H., Peters, J. L., Allen, C., Chern, S.-S., Coalson, R. D., and Michael, A. C. (2000). A theoretical description of microdialysis with mass transport coupled to chemical events. *Anal. Chem.* 72, 2042–2049. doi: 10.1021/ac991186r
- Yu, C.-X., Zhu, C.-B., Xu, S.-F., Cao, X.-D., and Wu, G.-C. (2000). The analgesic effects of peripheral and central administration of melatonin in rats. *Eur. J. Pharmacol.* 403, 49–53. doi: 10.1016/s0014-2999(00)00421-0
- Zhang, Y., Cook, A., Kim, J., Baranov, S. V., Jiang, J., Smith, K., et al. (2013). Melatonin inhibits the caspase-1/cytochrome c/caspase-3 cell death pathway, inhibits MT1 receptor loss and delays disease progression in a mouse model of amyotrophic lateral sclerosis. *Neurobiol. Dis.* 55, 26–35. doi: 10.1016/j.nbd.2013.03.008

**Conflict of Interest:** The authors declare that the research was conducted in the absence of any commercial or financial relationships that could be construed as a potential conflict of interest.

Copyright © 2020 Castagnola, Robbins, Woepel, McGuier, Golabchi, Taylor, Michael and Cui. This is an open-access article distributed under the terms of the Creative Commons Attribution License (CC BY). The use, distribution or reproduction in other forums is permitted, provided the original author(s) and the copyright owner(s) are credited and that the original publication in this journal is cited, in accordance with accepted academic practice. No use, distribution or reproduction is permitted which does not comply with these terms.



# Colorimetric Nanoplasmonics to Spot Hyperglycemia From Saliva

Paolo Donati<sup>†</sup>, Tania Pomili<sup>†</sup>, Luca Boselli<sup>\*</sup> and Pier P. Pompa<sup>\*</sup>

*Nanobiointeractions and Nanodiagnostics, Istituto Italiano di Tecnologia, Genova, Italy*

## OPEN ACCESS

### Edited by:

Christian Bergaud,  
Laboratoire d'Analyse et  
d'Architecture des Systèmes (LAAS),  
France

### Reviewed by:

Wendell Karlos Tomazelli Coltro,  
Universidade Federal de Goiás, Brazil  
Manas Ranjan Gartia,  
Louisiana State University,  
United States

### \*Correspondence:

Luca Boselli  
luca.boselli@iit.it  
Pier P. Pompa  
pierpaolo.pompa@iit.it

<sup>†</sup>These authors have contributed  
equally to this work

### Specialty section:

This article was submitted to  
Nanobiotechnology,  
a section of the journal  
Frontiers in Bioengineering and  
Biotechnology

**Received:** 31 August 2020

**Accepted:** 16 November 2020

**Published:** 07 December 2020

### Citation:

Donati P, Pomili T, Boselli L and  
Pompa PP (2020) Colorimetric  
Nanoplasmonics to Spot  
Hyperglycemia From Saliva.  
Front. Bioeng. Biotechnol. 8:601216.  
doi: 10.3389/fbioe.2020.601216

Early diagnostics and point-of-care (POC) devices can save people's lives or drastically improve their quality. In particular, millions of diabetic patients worldwide benefit from POC devices for frequent self-monitoring of blood glucose. Yet, this still involves invasive sampling processes, which are quite discomforting for frequent measurements, or implantable devices dedicated to selected chronic patients, thus precluding large-scale monitoring of the globally increasing diabetic disorders. Here, we report a non-invasive colorimetric sensing platform to identify hyperglycemia from saliva. We designed plasmonic multibranched gold nanostructures, able to rapidly change their shape and color (naked-eye detection) in the presence of hyperglycemic conditions. This "reshaping approach" provides a fast visual response and high sensitivity, overcoming common detection issues related to signal (color intensity) losses and bio-matrix interferences. Notably, optimal performances of the assay were achieved in real biological samples, where the biomolecular environment was found to play a key role. Finally, we developed a dipstick prototype as a rapid home-testing kit.

**Keywords:** plasmonics, colorimetric sensors, hyperglycemia, gold nanoparticles, reshaping

## INTRODUCTION

Point of care (POC) devices for self-monitoring of blood glucose are a life-changing technology and nowadays a norm for diabetes control. However, commercially available devices generally employ a relatively expensive hardware (reading system) and require a quite invasive sampling process (finger-pricks) involving a certain physical discomfort, especially for patients necessitating frequent measurements. It is worth mentioning that repeated finger-prick sampling also presents some risk, due to possible exposure to blood-borne pathogens and infections (Thompson and Perz, 2009). For these reasons, small implantable sensors have recently entered the clinical use for chronic patients, and different non-invasive approaches, such as near-infrared transcutaneous spectroscopy (Yadav et al., 2015), breath acetone measurements (Saasa et al., 2018), and other optical and electrical/electrochemical sensing techniques, are currently under investigation in the field (Bharathi and Nogami, 2001; Luo et al., 2004; Wu et al., 2007; Jv et al., 2010; Jiang et al., 2010; Xiong et al., 2015; Xu et al., 2017; Cao et al., 2019; Shokrehodaei and Quinones, 2020).

An interesting alternative currently attracting tremendous interest in the diagnostic community is the use of saliva as biological source (Kaufman and Lamster, 2000; Zhang et al., 2016; Kim et al., 2019; To et al., 2020). Saliva holds a huge variety of well-known disease-related biomarkers, including glucose, representing an ideal medium for the development of non-invasive tools for self-monitoring of hyperglycemia (Elkington et al., 2014; Zhang W. et al., 2015; Zhang et al., 2016). Several studies showed good correlation between the glucose amount present in saliva and in blood (Gupta et al., 2017). However, salivary glucose was found to be ca. 100 times less

concentrated (Zhang W. et al., 2015). This requires the new salivary POCs to gain a breakthrough in terms of sensitivity, while maintaining rapidity, accuracy, and clear readout. A few examples in this context have been recently reported (Elkington et al., 2014), including pioneering works on wearable devices (de Castro et al., 2019; Arakawa et al., 2020), yet many opportunities in this field remain unexplored.

In this framework, for example, gold nanoparticles (GNPs) present enormous potential for the development of a new generation of highly sensitive sensors (Liu and Lu, 2003; Luo et al., 2004; Pingarrón et al., 2008; Sperling et al., 2008; Zhang et al., 2012; Valentini and Pompa, 2013, 2016; Howes et al., 2014; Chen et al., 2016; Valentini et al., 2017; Qin et al., 2018; Quesada-González and Merkoçi, 2018; Donati et al., 2019; Hao et al., 2019; Loynachan et al., 2019; Quesada-González et al., 2019), due to their unique size-, shape-, and dispersion-state-dependent plasmonic properties, which can be exploited for the realization of “naked-eye detection” assays (Baron et al., 2005; Wang et al., 2006; Song et al., 2011; Liu et al., 2012; Zhao et al., 2016; Donati et al., 2019; Lu et al., 2019; Xu et al., 2019). Common colorimetric approaches involve target-mediated GNP aggregation/assembly strategies or growth/etching processes (Valentini et al., 2013; Rao et al., 2019). The “aggregation approach” can be very fast and sensitive, but it often requires precise NP functionalization to ensure selectivity. In addition, in biological media, the “biomolecular corona” can potentially mask the prepared functionality, often promoting non-specific interactions (i.e., NP uncontrolled aggregation) (Monopoli et al., 2012; Del Pino et al., 2014; Castagnola et al., 2017). Generally, the “growth approach” also presents some drawbacks in complex media, since the surrounding proteins and metabolites could interact with the reagents involved, while protein adsorption onto the GNPs can interfere in the nanostructure growth (i.e., inhibiting the process or even acting as shape directing agents) (Chakraborty et al., 2018; Chakraborty and Parak, 2019). Nevertheless, some very interesting examples are reported in the literature (Rodríguez-Lorenzo et al., 2012). A more promising strategy is the “etching approach” involving, in the case of glucose sensors, the glucose oxidase (GOx) enzyme. GOx is able to react specifically with glucose in complex media producing  $H_2O_2$  that, via Fenton or Fenton-like reactions, transforms in the free radical form able to rapidly oxidize (and partially dissolve) the GNPs (Rao et al., 2019). A colorimetric assay for blood glucose determination using this mechanism was explored on gold nanorods and the color change was obtained following the particle corrosion and shortening in presence of glucose (Liu et al., 2013).

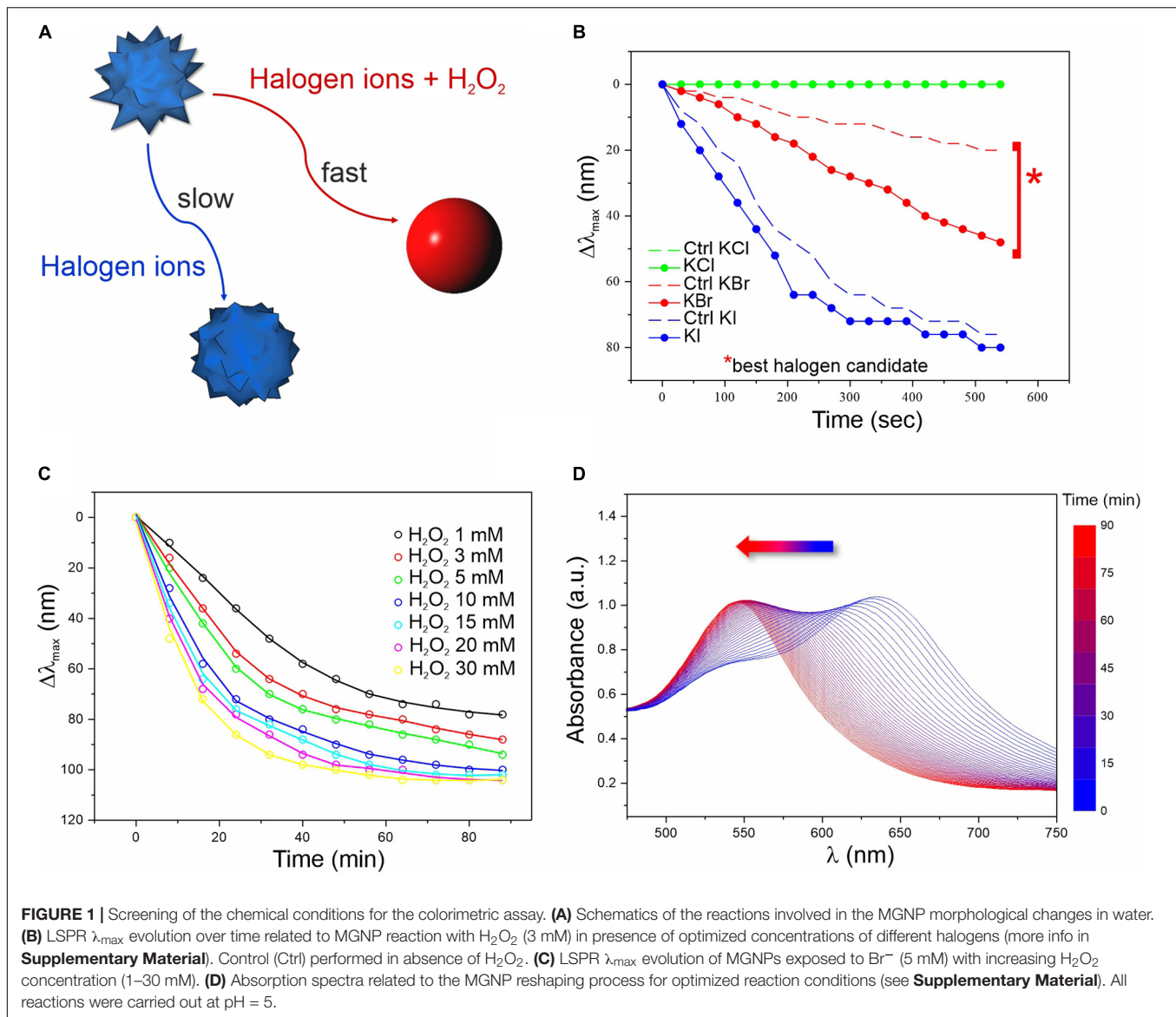
Here, to gain the high sensitivity necessary for rapid glucose detection at salivary concentration, we developed a novel strategy combining multibranched (spiky) GNPs, GOx, and bromine ( $Br^-$ ) mediated particle reshaping, which allows for a rapid color change without any optical density (OD) loss, typically related to NP dissolution. Furthermore, we transferred our sensing technology onto a substrate, obtaining a rapid and highly sensitive colorimetric home-testing prototype for self-monitoring of salivary glucose levels.

## RESULTS

For simplicity, basic chemical aspects and optimizations of the sensing platform were preliminarily explored in water solvent and in absence of enzyme (**Figure 1**). A synthetic procedure for highly responsive multibranched GNPs (MGNPs) was optimized for the current strategy, slightly modifying a previously reported method (Maiorano et al., 2011). The prepared colloidal suspensions were fully characterized (see **Supplementary Material** and **Supplementary Figures S1, S2**). The MGNPs were monodisperse, presenting an average size of about 60 nm. The selected stabilizing agent (Hepes) guaranteed high NP reactivity and colloidal stability. Concerning the particle shape, the tips represented the more sensitive units (where the lowest energy plasmon mode is mainly localized) (Rodríguez-Lorenzo et al., 2009), therefore the nanostructures were tuned to obtain multiple short tips (average length of c.a. 8 nm) to gain clear color distinction with minimal morphological changes (i.e., through preferential tips gold oxidation). Since the spiky structure is responsible of the MGNPs blue color, the NPs gradually change to the characteristic red color when becoming spherical (Kumar et al., 2007; Rodríguez-Lorenzo et al., 2011; Potenza et al., 2017).

We first evaluated the MGNP responses to different pH values (**Supplementary Figure S3**) and halogens (**Figure 1B**) in presence or absence (negative control) of  $H_2O_2$ . At certain conditions,  $H_2O_2$  can itself oxidize GNP surface atoms, leading to etching and morphological changes. However, this process has low efficiency and normally occurs on a much larger timescale (several hours) compared to our aimed few-minute response (Tsung et al., 2006). Therefore, we evaluated the effect of three different halogens ( $I^-$ ,  $Br^-$ , and  $Cl^-$ ) potentially able, in acidic conditions, to boost the oxidation process and promote a quick color change (Yuan et al., 2015; Zhang Z. et al., 2015; Zhu et al., 2015; Cheng et al., 2019).

As expected, in presence of  $H_2O_2$  and  $Br^-$  (2:1 molar ratio), MGNPs presented faster LSPR blue-shift when lowering the pH (see **Supplementary Figure S3**). Nevertheless, all tested conditions showed a remarkable  $\lambda_{max}$  shift within 10 min, and pH = 5 was selected as the optimal condition for the enzyme activity as well as NP stability (**Supplementary Figure S3B**). Concerning the halogen ions tested, bromine resulted the best candidate, promoting a fast (within 10 min) and wide LSPR shift in presence of a relatively low  $H_2O_2$  concentration (together with a relatively small shift for the control), while iodine ions led to drastic blue-shift, independently of  $H_2O_2$  (**Figure 1B**). No interesting effects were observed using chlorine ions for this platform. In presence of  $Br^-$  at established concentration, increasing the amount of  $H_2O_2$  led to faster morphological changes (**Figure 1C** and **Supplementary Figure S4**), but at high concentrations ( $\geq 10$  mM) harsher etching involved also some OD loss (see **Supplementary Figure S5**). However, within the concentration range of interest (1–3 mM), irreversible corrosion of the nanostructure was avoided (or very limited) even on the long-term (see the plateau in **Figures 1C,D**), while keeping relatively fast spectral changes. When carefully dosing the MGNPs/ $Br^-$ / $H_2O_2$  stoichiometry, we could achieve



a final absorbance as intense as the starting one (**Figure 1D**), and an almost linear LSPR evolution pathway with minor intensity differences. However, in water, the presented platform has significant limitations, due to some uncontrolled etching occurring in the control, with relatively small variations in the reagents molar ratio.

Adapting this platform to real working conditions in saliva, employing glucose spikes, GOx enzyme, and a large excess of  $\text{Br}^-$  (see scheme in **Figure 2A**) resulted in a strikingly better performance than the previous one. The system was so stable that we could employ much larger  $\text{Br}^-$  concentration than in water, without affecting the control. Proteins and metabolites present in saliva can rapidly coat the MGNPs forming the so-called biomolecular corona, which can act as an organic shield protecting and stabilizing the surface atoms (see **Supplementary Figure S6**). In particular, proteins (i.e., mucin) promote higher colloidal stability limiting the surface availability by steric

hindrance, while salivary thiols (i.e., cysteine, glutathione and others) can act as surface ligands (Yang et al., 2007; Boselli et al., 2017). These factors together firmly preserve the MGNP shape even in presence of a large excess of  $\text{Br}^-$  that otherwise would lead to uncontrolled fast etching and immediate color change even in absence of glucose. Indeed, the saliva medium allowed for a significant extension of the dynamic range of the assay along with a faster response, meaning that resolution and sensitivity were also strongly improved (see **Figure 2B**). Analyzing the physiological control (no added glucose), no significant spectral changes were observed, indicating a better resolution of the nanosensor in saliva compared to non-biological media (see **Figures 1B, 2A,B**). This is a key point since it excludes the possibility of false positives, due to spontaneous color changes of the MGNPs in the test timeframe (10–20 min); furthermore, it guarantees a faster naked-eye recognizable color distinction, due exclusively to the glucose present in saliva. The presence



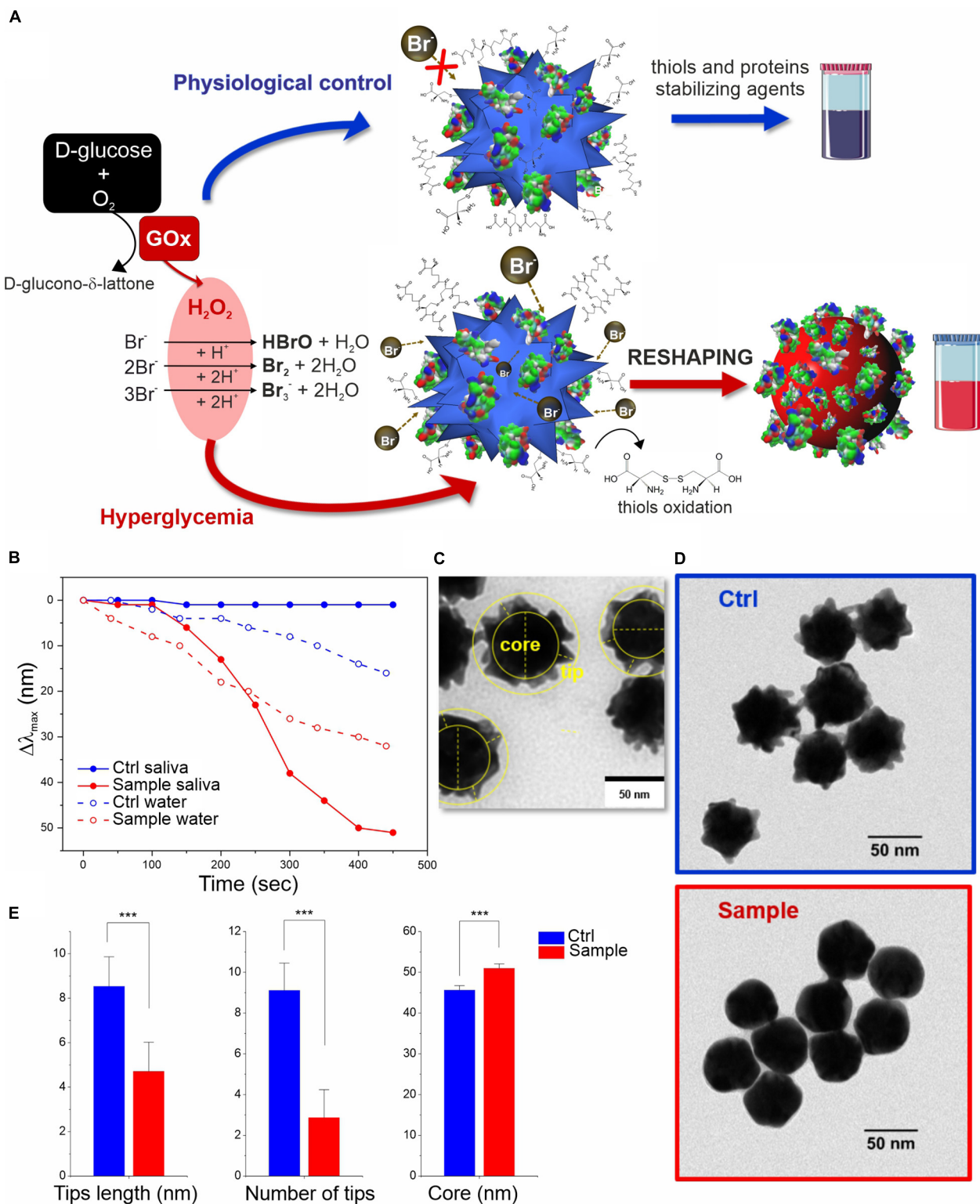


**FIGURE 2 |** *In vitro* colorimetric assay using MGNPs suspended in saliva: **(A)** schematics of the mechanisms involved; **(B)** LSPR  $\Delta\lambda_{\max}$  evolution over time related to the reshaping in saliva and in water (the two model platforms performance are compared at their own Br<sup>-</sup> optimized conditions while involving the same particles number, and H<sub>2</sub>O<sub>2</sub> final concentration, 2 mM). TEM micrographs related to the MGNPs before **(C)** and after **(D)** the assay with non-supplemented saliva (blue) and with glucose supplement to simulate hyperglycemia condition (red). **(E)** Statistical TEM analysis measuring tips (numbers and lengths) and “core” dimensional variation between control and sample nanostructures ( $p < 0.001$  in all cases). Statistical significance was determined by Mann-Whitney test ( $***p < 0.001$ ). See experimental details in **Supplementary Material**.

of non-physiological glucose concentrations in saliva ( $\geq 2$  mM), reproducing hyperglycemia conditions, indeed promoted a fast spectral change with a large blue-shift of the LSPR  $\lambda_{max}$ , and no significant OD loss (**Supplementary Figure S7**).

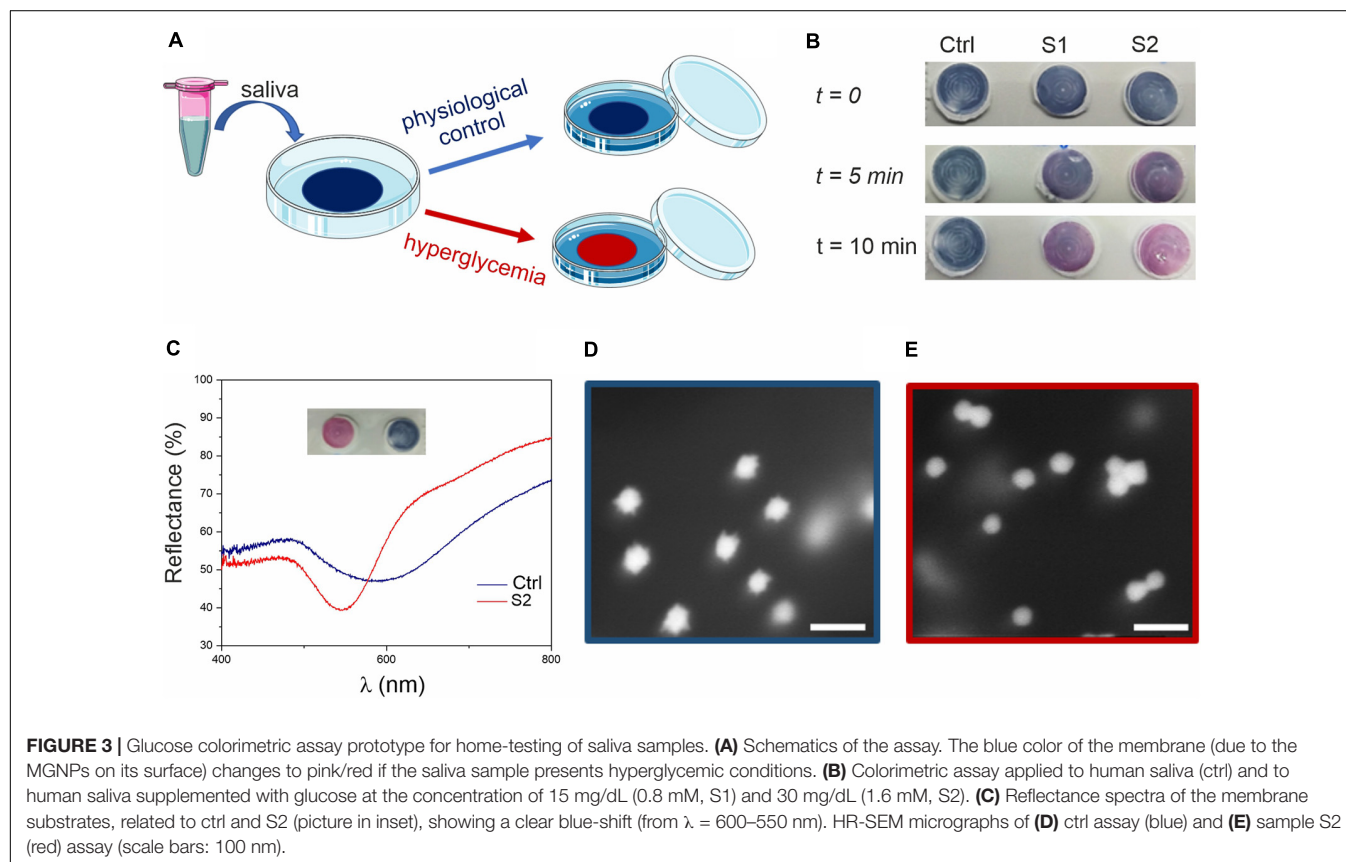
The molecular mechanism underlying the sensing strategy can be divided in two phases, one involving the oxidant species production and a second in which such species trigger a series of reactions, leading to MGNP morphological changes. The first part is quite well-known, at least in its separate steps: the glucose/GOx-generated  $H_2O_2$  reacts with the  $Br^-$  present in stoichiometric excess (even if part of it might be sequestered by saliva components), producing  $Br_2$ ,  $Br_3^-$  and  $HBrO$  (the latter eventually converting to  $Br_2$ ) (Yuan et al., 2015; Zhu et al., 2015).

In the second phase, the bromine oxidant species can interact with MGNPs through multiple pathways: beyond direct gold surface oxidation, the reaction mechanism responsible for the reshaping process is likely to involve the biomolecular corona (including salivary proteins and thiols). It may be envisaged that the surface atoms of the MGNP tips are less protected by the protein layer, thus being more prone to oxidation than the particle core. The structural changes are also promoted by oxidation of the salivary thiol ligands by  $Br_2$  (Wu et al., 1996), leading to an unanchored surface (with high tension) that can immediately start rearranging. This reshaping process is probably additionally boosted by the  $Br^-$  excess coordination (Jang et al., 2012). Furthermore, a series of gold oxidation/reduction reactions (promoted by  $Br_2$  and R-SH

species, respectively) can also promote gold atoms migration from surface convexity to the concavity (from higher to lower surface potential), leading to the more thermodynamically stable spherical shape (Xia et al., 2009). In this case, R-SH species would play a double role, protecting the shape in absence of glucose but also supporting the reshaping (instead of the etching) in presence of hyperglycemic conditions.

The reshaping process in saliva was also analyzed by TEM (**Figures 2C–E** and **Supplementary Figure S8**), confirming no significant differences in the morphology of MGNP control (in absence of glucose supplement) with respect to primary particles, while an evident smoothening of the nanostructure surface was observed in hyperglycemic conditions, obtaining quasi-spherical GNP shape. Furthermore, statistical geometrical measurements (**Figure 2E**) showed a final size distribution compatible with a redistribution of the MGNP gold atoms onto the surface concavities, with a negligible loss of the metal atoms. The “core size” increase of the nanostructure, indeed, can be considered as another evidence in favor of gold atoms rearrangement process and particle reshaping, against irreversible “MGNPs dissolution” (see **Figures 2C,E**). The described results demonstrated that we were able to achieve sensitive glucose detection without losing the optical signal (color intensity), which is a significant technological advancement, especially aiming at “naked-eye” detection.

In order to realize a portable home-testing device prototype, the sensing platform was transferred onto a solid substrate.



Among the different materials tested (including cellulose acetate, nitrocellulose, PVDF), a porous nylon membrane was selected, presenting well structured (ordered) surface and a good balance between wettability and hydrophobicity (see **Supplementary Figure S9**), enabling stable adsorption of MGNPs. By placing the membrane in a syringe filter holder, we could homogeneously immobilize a reproducible particle amount in a few seconds by simple injection. Additionally, few microlitres of the enzyme were also deposited to have all the reagents, otherwise suffering for long-term stability, dried on the substrate, and ready for the analysis (see **Supplementary Material**).

The use of a solid substrate, led to a significant improvement of the reagents stability. While colloidal dispersions of MGNPs in water lose their morphological and plasmonic properties overtime, the on-substrate assay showed excellent stability up to 6 months, meaning that also the enzyme functionality was maintained (see **Supplementary Figure S10**). An additional advantage is that, even after glucose testing, the “test strip” could be stored, keeping the outcome unaltered for  $\geq 6$  months.

Saliva samples were tested with this dipstick-like colorimetric assay prototype as depicted in the schematics reported in **Figure 3A**. A small amount (20  $\mu\text{L}$ ) of glucose supplemented saliva (with glucose above physiological concentrations) was sufficient to trigger a rapid color change from blue to red (**Figure 3B**) within 5–15 min, depending on the glucose

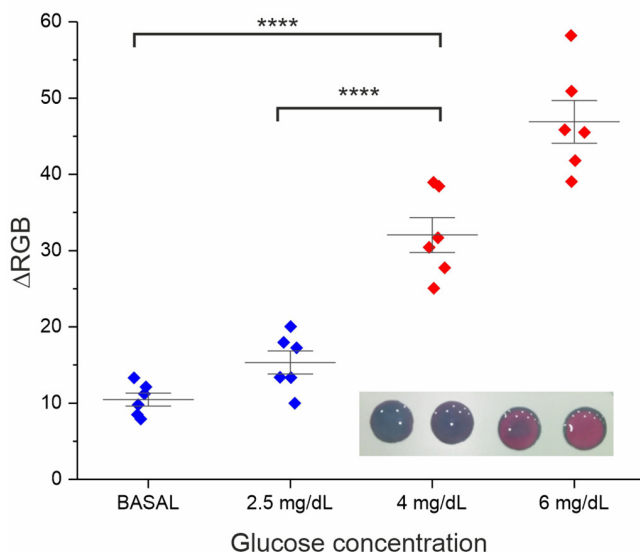
concentration. Further controls related to the assay are reported in **Supplementary Figure S11**.

After assessing hyperglycemic saliva and non-supplemented saliva (control), the substrates were analyzed by using reflectance spectroscopy (**Figure 3C**) and scanning electron microscopy (SEM, **Figures 3D,E**). From the reflectance spectra, glucose supplemented saliva appeared to be ca. 50 nm blue-shifted compared to the control (consistent with the data observed in suspension), with the curves minima corresponding to the particles LSPR. From SEM imaging, we could observe the nanostructure morphology directly on the membrane, confirming the reshaping process also on the substrate, with spherical GNPs on the test membrane after exposure to hyperglycemic saliva.

The assay prototype was finally optimized for analysis on real samples, considering that physiological glucose concentration in saliva is commonly  $<2$  mg/dL ( $<130$  mg/dL in human serum) while it is  $\geq 4$  mg/dL for hyperglycemic condition ( $\geq 160$ –200 mg/dL in human serum) (Abikshyeet et al., 2012). It is important to stress that the correlation between hematic and salivary glucose is not based on a constant ratio over the whole range of concentrations (Abikshyeet et al., 2012).

For this reason, aiming at an ON/OFF response as an alarm bell for healthcare, we set our threshold about  $\geq 4 \pm 0.5$  mg/dL. For salivary glucose concentrations above this range values, the assay must produce an evident color change.

A



B

Donors (n)	Glucose concentration (mg/dL)	Assay's colour (ON/OFF)
1	2.6	●
2	5.0	●
3	5.4	●
4	7.4	●
5	3.1	●
6	2.7	●
7	4.4	●
8	4.3	●
9	2.4	●
10	4.0	●
11	1.6	●
12	3.0	●
13	1.5	●
14	1.5	●
15	1.5	●
16	1.8	●
17	1.5	●
18	2.2	●
19	1.8	●
20	1.7	●

**FIGURE 4 |** Assay performance analysis in real saliva samples. **(A)** Validation of the RGB-based readout. Six saliva samples were involved in this study (the average of two experimental replicates is reported). Besides the basal glucose concentration, all samples were normalized through glucose spike at 2.5, 4, and 6 mg/dL, the RGB coordinates values were measured at  $t = 0$  and 15 min with a smartphone app (ColorGrab), and the  $\Delta\text{RGB}$  was calculated. Statistical significance was determined using a one-way ANOVA and Tukey's multiple comparison test ( $****P < 0.0001$ ). A representative image of the assay at the four different concentrations is reported in the inset. **(B)** Assay results for clinical saliva samples from both diabetic subjects (donors 1–12) and healthy subjects (donor 13–20). The “ON” outcome (red dots) refers to  $\Delta\text{RGB} \geq 30 \pm 10$ .

To numerically estimate the colorimetric changes of our device and perform statistical data analysis, RGB coordinates of the substrate were acquired using a smartphone app (see **Supplementary Material**).

A proof-of-concept experiment was performed measuring multiple saliva samples from different healthy donors with the addition of increasing concentrations of glucose from basal physiological values ( $<2$  mg/dL) to hyperglycemic ones (4 and 6 mg/dL). A significant difference in the color variation was observed between physiological and hyperglycemic conditions by both naked-eye and RGB analysis, identifying our colorimetric threshold as  $\Delta\text{RGB} \geq 30 \pm 10$  (see **Figure 4**).

$\Delta\text{RGB}$  values were also employed to measure the limit of detection (LOD). In this context, the assay performances were very good and reproducible using different independently produced devices to analyze the same saliva sample from a donor, reaching a LOD of 0.4 mg/dL (see **Supplementary Figure S12**), in line with the best performing glucose colorimetric sensors reported (Gabriel et al., 2016; de Castro et al., 2019). However, some variability on the LOD values was expected when analyzing saliva samples from multiple different donors (presenting some difference in the composition), resulting in a more representative average value of 1.4 mg/dL (see **Supplementary Material**). Such LOD value is still appropriate for our ON/OFF detection, allowing to cope with the intrinsic biological variability or real clinical samples.

Further validation of the assay prototype was performed through a small clinical study involving twenty different saliva samples, 12 from diabetic subjects and 8 from healthy subjects (see **Figure 4B**). The analysis was carried out using in parallel a commercial high-sensitive glucose kit (as standard reference technique) and our device. We observed good reliability of our rapid test (95%) from this screening, attesting concrete potential for future applications.

## DISCUSSION

The nanoscale architecture of MGNPs and their sensitive plasmonic features were exploited for the development of a novel colorimetric assay for hyperglycemia, demonstrated to be effective in real saliva samples. Interestingly, the sensing platform, when operating in salivary medium, showed improved solidity and better dynamic range than in water, suggesting a proactive role of the biomolecular corona both in stabilizing the nanosensor and in promoting the reshaping process (instead of etching). The technological transfer from solution to the solid substrate finally led to the realization of a dipstick-like prototype for non-invasive self-monitoring of glycemia. The assay was finally validated as a rapid test (15 min) on various

clinical samples, showing good reliability and, with further technological development, great potential for future home-testing applications. Overall, it is important to stress that the designed sensing platform could be easily adapted for the monitoring of several other pathologies, directly involving different oxidase enzymes.

## DATA AVAILABILITY STATEMENT

The raw data supporting the conclusions of this article will be made available by the authors upon reasonable request.

## ETHICS STATEMENT

The studies involving human participants were reviewed and approved by the Comitato Etico Regionale della Liguria. The patients/participants provided their written informed consent to participate in this study.

## AUTHOR CONTRIBUTIONS

All the authors contributed to the development of the ideas behind the work, experimental design, and manuscript writing.

## FUNDING

This work was partially supported by the AICube SRL. The funder AICube SRL was not involved in the study design, collection, analysis, interpretation of data, the writing of this article or the decision to submit it for publication.

## ACKNOWLEDGMENTS

We acknowledge Simone Lauciello and Luca Leoncino for SEM and TEM imaging, Gabriele Maiorano for help with the nanoparticle synthesis, and Mariangela Rondanelli, Clara Gasparri, and Letizia Oberto for the collection of diabetic subject's saliva samples.

## SUPPLEMENTARY MATERIAL

The Supplementary Material for this article can be found online at: <https://www.frontiersin.org/articles/10.3389/fbioe.2020.601216/full#supplementary-material>

## REFERENCES

- Abikshyeet, P., Ramesh, V., and Oza, N. (2012). Glucose estimation in the salivary secretion of diabetes mellitus patients. *Diabetes Metab. Syndr. Obes. Targets Ther.* 5:149. doi: 10.2147/dmso.s32112
- Arakawa, T., Tomoto, K., Nitta, H., Toma, K., Takeuchi, S., Sekita, T., et al. (2020). A wearable cellulose acetate-coated mouthguard biosensor for in vivo salivary glucose measurement. *Anal. Chem.* 92, 12201–12207. doi: 10.1021/acs.analchem.0c01201
- Baron, R., Zayats, M., and Willner, I. (2005). Dopamine-, L-DOPA-, Adrenaline-, and Noradrenaline-induced growth of Au nanoparticles: assays for the detection of neurotransmitters and of tyrosinase activity. *Anal. Chem.* 77, 1566–1571. doi: 10.1021/ac048691v



- Bharathi, S., and Nogami, M. (2001). A glucose biosensor based on electrodeposited biocomposites of gold nanoparticles and glucose oxidase enzyme. *Analyst* 126, 1919–1922.
- Boselli, L., Polo, E., Castagnola, V., and Dawson, K. A. (2017). Regimes of biomolecular ultrasmall nanoparticle interactions. *Angew. Chem. Intern. Edn.* 56, 4215–4218. doi: 10.1002/anie.201700343
- Cao, L., Wang, P., Chen, L., Wu, Y., and Di, J. (2019). A photoelectrochemical glucose sensor based on gold nanoparticles as a mimic enzyme of glucose oxidase. *RSC Adv.* 9, 15307–15313. doi: 10.1039/c9ra02088h
- Castagnola, V., Cookman, J., De Araujo, J., Polo, E., Cai, Q., Silveira, C., et al. (2017). Towards a classification strategy for complex nanostructures. *Nanoscale Horiz.* 2, 187–198. doi: 10.1039/c6nh00219f
- Chakraborty, I., Feliu, N., Roy, S., Dawson, K., and Parak, W. J. (2018). Protein-mediated shape control of silver nanoparticles. *Bioconjug. Chem.* 29, 1261–1265. doi: 10.1021/acs.bioconjug.8b00034
- Chakraborty, I., and Parak, W. J. (2019). Protein-induced shape control of noble metal nanoparticles. *Adv. Mater. Interf.* 6, 1801407. doi: 10.1002/admi.201801407
- Chen, G., Roy, I., Yang, C., and Prasad, P. N. (2016). Nanochemistry and nanomedicine for nanoparticle-based diagnostics and therapy. *Chem. Rev.* 116, 2826–2885. doi: 10.1021/acs.chemrev.5b00148
- Cheng, X., Huang, Y., Yuan, C., Dai, K., Jiang, H., and Ma, J. (2019). Colorimetric detection of  $\alpha$ -glucosidase activity based on the etching of gold nanorods and its application to screen anti-diabetic drugs. *Sens. Actuat. B Chem.* 282, 838–843. doi: 10.1016/j.snb.2018.11.097
- de Castro, L. F., de Freitas, S. V., Duarte, L. C., de Souza, J. A. C., Paixão, T. R., and Coltro, W. K. (2019). Salivary diagnostics on paper microfluidic devices and their use as wearable sensors for glucose monitoring. *Anal. Bioanal. Chem.* 411, 4919–4928. doi: 10.1007/s00216-019-01788-0
- Del Pino, P., Pelaz, B., Zhang, Q., Maffre, P., Nienhaus, G. U., and Parak, W. J. (2014). Protein corona formation around nanoparticles—from the past to the future. *Mater. Horiz.* 1, 301–313. doi: 10.1039/c3mh00106g
- Donati, P., Moglianetti, M., Veronesi, M., Prato, M., Tatulli, G., Bandiera, T., et al. (2019). Nanocatalyst/nanoplasmon-enabled detection of organic mercury: a one-minute visual test. *Angew. Chem. Intern. Edn.* 58, 10285–10289. doi: 10.1002/anie.201905669
- Elkington, D., Belcher, W., Dastoor, P., and Zhou, X. (2014). Detection of salivary-range glucose concentrations using organic thin-film transistors. *Appl. Phys. Lett.* 105, 043303. doi: 10.1063/1.4892012
- Gabriel, E. F., Garcia, P. T., Cardoso, T. M., Lopes, F. M., Martins, F. T., and Coltro, W. K. (2016). Highly sensitive colorimetric detection of glucose and uric acid in biological fluids using chitosan-modified paper microfluidic devices. *J. Anal. Chem.* 141, 4749–4756. doi: 10.1039/c6an00430j
- Gupta, S., Nayak, M. T., Sunitha, J., Dawar, G., Sinha, N., and Rallan, N. S. (2017). Correlation of salivary glucose level with blood glucose level in diabetes mellitus. *J. Oral Maxillofac. Pathol.* 21, 334. doi: 10.4103/jomfp.jomfp\_222\_15
- Hao, Z., Pan, Y., Shao, W., Lin, Q., and Zhao, X. (2019). Graphene-based fully integrated portable nanosensing system for on-line detection of cytokine biomarkers in saliva. *Biosens. Bioelectron.* 134, 16–23. doi: 10.1016/j.bios.2019.03.053
- Howes, P. D., Chandrawati, R., and Stevens, M. M. (2014). Colloidal nanoparticles as advanced biological sensors. *Science* 346, 1247390. doi: 10.1126/science.1247390
- Jang, E., Lim, E.-K., Choi, J., Park, J., Huh, Y.-J., Suh, J.-S., et al. (2012). Br-assisted ostwald ripening of Au nanoparticles under H<sub>2</sub>O<sub>2</sub> redox. *Cryst. Growth Design* 12, 37–39. doi: 10.1021/cg201243n
- Jiang, Y., Zhao, H., Lin, Y., Zhu, N., Ma, Y., and Mao, L. (2010). Colorimetric detection of glucose in rat brain using gold nanoparticles. *Angew. Chem. Intern. Edn.* 49, 4800–4804. doi: 10.1002/anie.201001057
- Jv, Y., Li, B., and Cao, R. (2010). Positively-charged gold nanoparticles as peroxidase mimic and their application in hydrogen peroxide and glucose detection. *Chem. Commun.* 46, 8017–8019. doi: 10.1039/c0cc02698k
- Kaufman, E., and Lamster, I. B. (2000). Analysis of saliva for periodontal diagnosis: a review. *J. Clin. Periodontol.* 27, 453–465. doi: 10.1034/j.1600-051x.2000.027007453.x
- Kim, J., Campbell, A. S., de Ávila, B. E.-F., and Wang, J. (2019). Wearable biosensors for healthcare monitoring. *Nat. Biotechnol.* 37, 389–406. doi: 10.1038/s41587-019-0045-y
- Kumar, P. S., Pastoriza-Santos, I., Rodríguez-González, B., De Abajo, F. J. G., and Liz-Marzán, L. M. (2007). High-yield synthesis and optical response of gold nanostars. *Nanotechnology* 19, 015606. doi: 10.1088/0957-4484/19/01/015606
- Liu, D., Chen, W., Tian, Y., He, S., Zheng, W., Sun, J., et al. (2012). A highly sensitive gold-nanoparticle-based assay for acetylcholinesterase in cerebrospinal fluid of transgenic mice with Alzheimer's disease. *Adv. Healthc. Mater.* 1, 90–95. doi: 10.1002/adhm.201100002
- Liu, J., and Lu, Y. (2003). A colorimetric lead biosensor using DNAzyme-directed assembly of gold nanoparticles. *J. Am. Chem. Soc.* 125, 6642–6643. doi: 10.1021/ja034775u
- Liu, X., Zhang, S., Tan, P., Zhou, J., Huang, Y., Nie, Z., et al. (2013). A plasmonic blood glucose monitor based on enzymatic etching of gold nanorods. *Chem. Commun.* 49, 1856–1858. doi: 10.1039/c3cc38476d
- Loynachan, C. N., Soleimany, A. P., Dudani, J. S., Lin, Y., Najer, A., Bekdemir, A., et al. (2019). Renal clearable catalytic gold nanoclusters for in vivo disease monitoring. *Nat. Nanotechnol.* 14, 883–890. doi: 10.1038/s41565-019-0527-6
- Lu, M., Su, L., Luo, Y., Ma, X., Duan, Z., Zhu, D., et al. (2019). Gold nanoparticle etching induced by an enzymatic-like reaction for the colorimetric detection of hydrogen peroxide and glucose. *Analyt. Methods* 11, 4829–4834. doi: 10.1039/c9ay01599j
- Luo, X.-L., Xu, J.-J., Du, Y., and Chen, H.-Y. (2004). A glucose biosensor based on chitosan-glucose oxidase-gold nanoparticles biocomposite formed by one-step electrodeposition. *Analyt. Biochem.* 334, 284–289. doi: 10.1016/j.ab.2004.07.005
- Maiorano, G., Rizzello, L., Malvindi, M. A., Shankar, S. S., Martiradonna, L., Falqui, A., et al. (2011). Monodispersed and size-controlled multibranched gold nanoparticles with nanoscale tuning of surface morphology. *Nanoscale* 3, 2227–2232. doi: 10.1039/c1nr10107b
- Monopoli, M. P., Åberg, C., Salvati, A., and Dawson, K. A. (2012). Biomolecular coronas provide the biological identity of nanosized materials. *Nat. Nanotechnol.* 7, 779. doi: 10.1038/nnano.2012.207
- Pingarrón, J. M., Yanez-Sedeno, P., and González-Cortés, A. (2008). Gold nanoparticle-based electrochemical biosensors. *Electrochim. Acta* 53, 5848–5866. doi: 10.1016/j.electacta.2008.03.005
- Potenza, M., Krpetić, Ž., Sanvito, T., Cai, Q., Monopoli, M., and de Araújo, J. (2017). Detecting the shape of anisotropic gold nanoparticles in dispersion with single particle extinction and scattering. *Nanoscale* 9, 2778–2784. doi: 10.1039/c6nr08977a
- Qin, L., Zeng, G., Lai, C., Huang, D., Xu, P., Zhang, C., et al. (2018). “Gold rush” in modern science: fabrication strategies and typical advanced applications of gold nanoparticles in sensing. *Coordinat. Chem. Rev.* 359, 1–31. doi: 10.1016/j.ccr.2018.01.006
- Quesada-González, D., and Merkoçi, A. (2018). Nanomaterial-based devices for point-of-care diagnostic applications. *Chem. Soc. Rev.* 47, 4697–4709. doi: 10.1039/c7cs00837f
- Quesada-González, D., Stefani, C., González, I., de la Escosura-Muñiz, A., Domingo, N., Mutjé, P., et al. (2019). Signal enhancement on gold nanoparticle-based lateral flow tests using cellulose nanofibers. *Biosens. Bioelectron.* 141, 111407. doi: 10.1016/j.bios.2019.111407
- Rao, H., Xue, X., Wang, H., and Xue, Z. (2019). Gold nanorod etching-based multicolorimetric sensors: strategies and applications. *J. Mater. Chem. C* 7, 4610–4621. doi: 10.1039/c9tc00757a
- Rodríguez-Lorenzo, L., Alvarez-Puebla, R. A., Pastoriza-Santos, I., Mazzucco, S., Stéphan, O., Kociak, M., et al. (2009). Zeptomol detection through controlled ultrasensitive surface-enhanced Raman scattering. *J. Am. Chem. Soc.* 131, 4616–4618. doi: 10.1021/ja809418t
- Rodríguez-Lorenzo, L., de La Rica, R., Álvarez-Puebla, R. A., Liz-Marzán, L. M., and Stevens, M. M. (2012). Plasmonic nanosensors with inverse sensitivity by means of enzyme-guided crystal growth. *Nat. Mater.* 11, 604–607. doi: 10.1038/nmat3337
- Rodríguez-Lorenzo, L., Romo-Herrera, J. M., Pérez-Juste, J., Alvarez-Puebla, R. A., and Liz-Marzán, L. M. (2011). Reshaping and LSPR tuning of Au nanostars in the presence of CTAB. *J. Mater. Chem.* 21, 11544–11549. doi: 10.1039/c1jm10603a
- Saasa, V., Malwela, T., Beukes, M., Mokgotho, M., Liu, C.-P., and Mwakikunga, B. (2018). Sensing technologies for detection of acetone in human breath for diabetes diagnosis and monitoring. *Diagnostics* 8, 12. doi: 10.3390/diagnostics8010012

- Shokrehkhodaei, M., and Quinones, S. (2020). Review of non-invasive glucose sensing techniques: optical, electrical and breath acetone. *Sensors* 20:1251. doi: 10.3390/s20051251
- Song, Y., Wei, W., and Qu, X. (2011). Colorimetric biosensing using smart materials. *Adv. Mater.* 23, 4215–4236. doi: 10.1002/adma.201101853
- Sperling, R. A., Gil, P. R., Zhang, F., Zanella, M., and Parak, W. J. (2008). Biological applications of gold nanoparticles. *Adv. Mater. Interf.* 37, 1896–1908.
- Thompson, N. D., and Perz, J. F. (2009). Eliminating the blood: ongoing outbreaks of hepatitis B virus infection and the need for innovative glucose monitoring technologies. *J. Diabetes Sci. Technol.* 3, 283–288. doi: 10.1177/193229680900300208
- To, K. K.-W., Tsang, O. T.-Y., Leung, W.-S., Tam, A. R., Wu, T.-C., Lung, D. C., et al. (2020). Temporal profiles of viral load in posterior oropharyngeal saliva samples and serum antibody responses during infection by SARS-CoV-2: an observational cohort study. *Lancet Infect. Dis.* 20, 565–574. doi: 10.1016/s1473-3099(20)30196-1
- Tsung, C.-K., Kou, X., Shi, Q., Zhang, J., Yeung, M. H., Wang, J., et al. (2006). Selective shortening of single-crystalline gold nanorods by mild oxidation. *J. Am. Chem. Soc.* 128, 5352–5353. doi: 10.1021/ja060447t
- Valentini, P., Fiammengio, R., Sabella, S., Gariboldi, M., Maiorano, G., Cingolani, R., et al. (2013). Gold-nanoparticle-based colorimetric discrimination of cancer-related point mutations with picomolar sensitivity. *ACS Nano* 7, 5530–5538. doi: 10.1021/nn401757w
- Valentini, P., Galimberti, A., Mezzasalma, V., De Mattia, F., Casiraghi, M., Labra, M., et al. (2017). DNA barcoding meets nanotechnology: development of a universal colorimetric test for food authentication. *Angew. Chem. Intern. Edn.* 56, 8094–8098. doi: 10.1002/anie.201702120
- Valentini, P., and Pompa, P. P. (2013). Gold nanoparticles for naked-eye DNA detection: smart designs for sensitive assays. *RSC Adv.* 3, 19181–19190. doi: 10.1039/c3ra43729a
- Valentini, P., and Pompa, P. P. (2016). A universal polymerase chain reaction developer. *Angew. Chem. Intern. Edn.* 55, 2157–2160. doi: 10.1002/anie.201511010
- Wang, Z., Lévy, R., Fernig, D. G., and Brust, M. (2006). Kinase-catalyzed modification of gold nanoparticles: a new approach to colorimetric kinase activity screening. *J. Am. Chem. Soc.* 128, 2214–2215. doi: 10.1021/ja058135y
- Wu, B.-Y., Hou, S.-H., Yin, F., Li, J., Zhao, Z.-X., Huang, J.-D., et al. (2007). Amperometric glucose biosensor based on layer-by-layer assembly of multilayer films composed of chitosan, gold nanoparticles and glucose oxidase modified Pt electrode. *Biosens. Bioelectron.* 22, 838–844. doi: 10.1016/j.bios.2006.03.009
- Wu, X., Rieke, R. D., and Zhu, L. (1996). Preparation of disulfides by the oxidation of thiols using bromine. *Synthet. Commun.* 26, 191–196. doi: 10.1080/00397919608003879
- Xia, Y., Xiong, Y., Lim, B., and Skrabalak, S. E. (2009). Shape-controlled synthesis of metal nanocrystals: simple chemistry meets complex physics? *Angew. Chem. Intern. Edn.* 48, 60–103. doi: 10.1002/anie.200802248
- Xiong, Y., Zhang, Y., Rong, P., Yang, J., Wang, W., and Liu, D. (2015). A high-throughput colorimetric assay for glucose detection based on glucose oxidase-catalyzed enlargement of gold nanoparticles. *Nanoscale* 7, 15584–15588. doi: 10.1039/c5nr03758a
- Xu, M., Song, Y., Ye, Y., Gong, C., Shen, Y., Wang, L., et al. (2017). A novel flexible electrochemical glucose sensor based on gold nanoparticles/polyaniline arrays/carbon cloth electrode. *Sens. Actuat. B Chem.* 252, 1187–1193. doi: 10.1016/j.snb.2017.07.147
- Xu, S., Jiang, L., Liu, Y., Liu, P., Wang, W., and Luo, X. (2019). A morphology-based ultrasensitive multicolor colorimetric assay for detection of blood glucose by enzymatic etching of plasmonic gold nanobipyramids. *Analyt. Chim. Acta* 1071, 53–58. doi: 10.1016/j.aca.2019.04.053
- Yadav, J., Rani, A., Singh, V., and Murari, B. M. (2015). Prospects and limitations of non-invasive blood glucose monitoring using near-infrared spectroscopy. *Biomed. Signal. Process. Control* 18, 214–227. doi: 10.1016/j.bspc.2015.01.005
- Yang, W., Gooding, J. J., He, Z., Li, Q., and Chen, G. (2007). Fast colorimetric detection of copper ions using L-cysteine functionalized gold nanoparticles. *J. Nanosci. Nanotechnol.* 7, 712–716. doi: 10.1166/jnn.2007.116
- Yuan, H., Janssen, K. P., Franklin, T., Lu, G., Su, L., Gu, X., et al. (2015). Reshaping anisotropic gold nanoparticles through oxidative etching: the role of the surfactant and nanoparticle surface curvature. *RSC Adv.* 5, 6829–6833. doi: 10.1039/c4ra14237c
- Zhang, C.-Z., Cheng, X.-Q., Li, J.-Y., Zhang, P., Yi, P., Xu, X., et al. (2016). Saliva in the diagnosis of diseases. *Intern. J. Oral Sci.* 8, 133–137.
- Zhang, M., Liu, Y.-Q., and Ye, B.-C. (2012). Colorimetric assay for parallel detection of Cd<sup>2+</sup>, Ni<sup>2+</sup> and Co<sup>2+</sup> using peptide-modified gold nanoparticles. *Analyst* 137, 601–607. doi: 10.1039/c1an15909g
- Zhang, W., Du, Y., and Wang, M. L. (2015). Noninvasive glucose monitoring using saliva nano-biosensor. *Sens. Biosens. Res.* 4, 23–29. doi: 10.1016/j.sbsr.2015.02.002
- Zhang, Z., Chen, Z., Wang, S., Cheng, F., and Chen, L. (2015). Iodine-mediated etching of gold nanorods for plasmonic ELISA based on colorimetric detection of alkaline phosphatase. *ACS Appl. Mater. Interf.* 7, 27639–27645. doi: 10.1021/acsami.5b07344
- Zhao, Q., Huang, H., Zhang, L., Wang, L., Zeng, Y., Xia, X., et al. (2016). Strategy to fabricate naked-eye readout ultrasensitive plasmonic nanosensor based on enzyme mimetic gold nanoclusters. *Analyt. Chem.* 88, 1412–1418. doi: 10.1021/acs.analchem.5b04089
- Zhu, Q., Wu, J., Zhao, J., and Ni, W. (2015). Role of bromide in hydrogen peroxide oxidation of CTAB-stabilized gold nanorods in aqueous solutions. *Langmuir* 31, 4072–4077. doi: 10.1021/acs.langmuir.5b00137

**Conflict of Interest:** The authors declare that the research was conducted in the absence of any commercial or financial relationships that could be construed as a potential conflict of interest.

Copyright © 2020 Donati, Pomili, Boselli and Pompa. This is an open-access article distributed under the terms of the Creative Commons Attribution License (CC BY). The use, distribution or reproduction in other forums is permitted, provided the original author(s) and the copyright owner(s) are credited and that the original publication in this journal is cited, in accordance with accepted academic practice. No use, distribution or reproduction is permitted which does not comply with these terms.



# Dexamethasone-Enhanced Microdialysis and Penetration Injury

Andrea Jaquins-Gerstl\* and Adrian C. Michael

Department of Chemistry, University of Pittsburgh, Pittsburgh, PA, United States

## OPEN ACCESS

### Edited by:

Valentina Castagnola,  
Italian Institute of Technology (IIT), Italy

### Reviewed by:

Yawen Li,  
Lawrence Technological University,  
United States  
Carmen Alvarez-Lorenzo,  
University of Santiago  
de Compostela, Spain

### \*Correspondence:

Andrea Jaquins-Gerstl  
asj19@pitt.edu

### Specialty section:

This article was submitted to  
Biomaterials,  
a section of the journal  
Frontiers in Bioengineering and  
Biotechnology

**Received:** 02 September 2020

**Accepted:** 11 November 2020

**Published:** 08 December 2020

### Citation:

Jaquins-Gerstl A and Michael AC  
(2020) Dexamethasone-Enhanced  
Microdialysis and Penetration Injury.  
Front. Bioeng. Biotechnol. 8:602266.  
doi: 10.3389/fbioe.2020.602266

Microdialysis probes, electrochemical microsensors, and neural prosthetics are often used for *in vivo* monitoring, but these are invasive devices that are implanted directly into brain tissue. Although the selectivity, sensitivity, and temporal resolution of these devices have been characterized in detail, less attention has been paid to the impact of the trauma they inflict on the tissue or the effect of any such trauma on the outcome of the measurements they are used to perform. Factors affecting brain tissue reaction to the implanted devices include: the mechanical trauma during insertion, the foreign body response, implantation method, and physical properties of the device (size, shape, and surface characteristics). Modulation of the immune response is an important step toward making these devices with reliable long-term performance. Local release of anti-inflammatory agents such as dexamethasone (DEX) are often used to mitigate the foreign body response. In this article microdialysis is used to locally deliver DEX to the surrounding brain tissue. This work discusses the immune response resulting from microdialysis probe implantation. We briefly review the principles of microdialysis and the applications of DEX with microdialysis in (i) neuronal devices, (ii) dopamine and fast scan cyclic voltammetry, (iii) the attenuation of microglial cells, (iv) macrophage polarization states, and (v) spreading depolarizations. The difficulties and complexities in these applications are herein discussed.

**Keywords:** microdialysis, dexamethasone, penetration injury, brain, mitigate

## INTRODUCTION

Microdialysis is a powerful technique for near real-time intracranial chemical monitoring in both animal models and human patients (Roberts and Anderson, 1979; Ungerstedt, 1984, 1991; Benveniste et al., 1987, 1989; Benveniste, 1989; Santiago and Westerink, 1990; Carneheim and Stahle, 1991; Parsons et al., 1991; Dykstra et al., 1992; Stenken, 1999; Hutchinson et al., 2000; Chefer et al., 2001; Stenken et al., 2001, 2010; Bosche et al., 2003, 2010; Schuck et al., 2004; Ungerstedt and Rostami, 2004; Parkin et al., 2005; Shou et al., 2006; Mitala et al., 2008; Hashemi et al., 2009; Jaquins-Gerstl et al., 2011; Wang and Michael, 2012; Zhang et al., 2013; Nesbitt et al., 2015; Dreier et al., 2016). A key advantage of microdialysis is its broad scope: it has been used to monitor neurotransmitters, peptides, amino acids, metabolites, and hormones, etc. This is possible because the only requirement is that the molecule of interest be smaller than the molecular weight cutoff of the chosen membrane material. As probes are perfused with, typically, an artificial cerebrospinal fluid solution (aCSF), small molecules enter the probe by passive diffusion and are swept to the probe outlet. The outlet is either interfaced directly to an analytical system, such as liquid chromatography, capillary electrophoresis, or mass spectrometry for on-line analysis, or discrete

dialysate samples are collected and stored for later off-line analysis. Because microdialysis is highly compatible with awake-behaving animals, numerous studies have examined the relationships between chemical events in the extracellular space of the brain and animal behaviors (Becker and Cha, 1989; Robinson and Justice, 1991; Castner et al., 1993; Borjigin and Liu, 2008). Microdialysis also finds use in anesthetized or sedated patients receiving intensive care, after traumatic brain injury for example (Globus et al., 1995; Strong et al., 2002, 2005, 2007; Ungerstedt and Rostami, 2004; Westerink and Cremers, 2007; Haddad and Arabi, 2012; Sanchez et al., 2013; Rogers et al., 2017; Booth et al., 2018; Pagkalos et al., 2018; Gowers et al., 2019).

Slow temporal resolution is often mentioned as a limitation of microdialysis. It is important, however, to consider the factors that limit temporal resolution. Often, extended sample collection times are necessary to assure that a detectable quantity of target analyte is available. Thus, over time, various workers have improved the temporal resolution of microdialysis by developing refined analytical methods with lower detection limits. For example, the Kennedy group has developed numerous rapid dialysate analyses by on-line capillary liquid chromatography or on-line capillary electrophoresis (Watson et al., 2006; Li et al., 2009; Perry et al., 2009; Wang et al., 2010; Lee et al., 2013; Kennedy et al., 2018; Ngernsutivorakul et al., 2018). The Andrews and Weber groups have used capillary liquid chromatography to analyze dopamine and serotonin in brain dialysates with minute and sub-minute temporal resolution (Liu et al., 2010; Yang et al., 2013; Zhang et al., 2013; Gu et al., 2015; Wilson and Michael, 2017).

Past observations from our laboratory have suggested, further, that an additional limitation of the temporal resolution of microdialysis-based monitoring stems from the so-called penetration trauma of the tissue surrounding the track of the microdialysis probe itself. Early experiments in the Michael lab attempted to monitor electrically evoked dopamine release in the rat striatum using a dopamine-sensitive microelectrode interfaced to the outlet line of a microdialysis probe (Lu et al., 1998; Yang and Michael, 2007; Nesbitt et al., 2013; Varner et al., 2016). *In vitro* characterization of the probe-microelectrode combination suggested a temporal resolution near 30 s, sufficiently rapid to monitor evoked dopamine responses recorded at microelectrodes implanted directly in brain tissue. However, evoked responses were not observable at the probe outlet without the aid of a dopamine uptake inhibitor, nomifensine (Borland et al., 2005). Eventually, we performed experiments with microelectrodes implanted side-by-side with microdialysis probes: without the aid of the uptake inhibitor there was, unexpectedly, no evoked response in the tissue surrounding the probe. Thus, our failure to detect evoked dopamine release at the probe outlet was not a matter of temporal resolution but rather was a matter of tissue disruption: there was no evoked response taking place in the surrounding tissue (Borland et al., 2005). This finding raised our initial concerns that the tissue surrounding the probe was in an abnormal, most likely traumatized, state and prompted our subsequent focus on the issue of penetration trauma and, eventually, strategies to mitigate it. These strategies are the focus of this review article.

A key, and somewhat unique, strategy available to the mitigation of penetration trauma induced by the implantation of microdialysis probes is so-called “retrodialysis” (Stenken, 1999; Shippenberg and Thompson, 2001; Cano-Cebrian et al., 2005). Retrodialysis is the term coined for the delivery of substances to brain tissues via the microdialysis probe itself. The focus of this review is our experience with dexamethasone (DEX)-enhanced microdialysis, which involves the retrodialysis of DEX to the probe track (Schuck et al., 2004; Nesbitt, 2015; Nesbitt et al., 2015; Kozai et al., 2016). DEX is a very well-known anti-inflammatory agent that has proven, thus far, highly effective at mitigating probe-induced penetration trauma during intracranial microdialysis in both the rat striatum and the rat cortex.

Dexamethasone-enhanced microdialysis offers key and specific benefits. First, it has facilitated the detection of evoked dopamine release at the probe outlet, resolving the technical difficulty described above. Second, we have found that DEX-enhanced microdialysis offers stabilized monitoring performance in brain tissue for at least 10 days following probe insertion. We hope that this improvement in longitudinal monitoring capability will be a benefit especially to patients who require neuromonitoring after traumatic brain injury.

Of course, DEX is not just an anti-inflammatory agent: it is steroid with its own potential neurochemical effects, raising the possibility that it might alter the outcome of neurochemical investigations. This, of course, must be acknowledged and addressed. As will be discussed later in this review, we have found that it is not necessary to deliver DEX continuously throughout an extended period of microdialysis monitoring. Preliminary evidence suggests that DEX retrodialysis is mainly needed at the time of probe insertion and that its benefits last beyond the termination of retrodialysis (Nesbitt, 2015; Nesbitt et al., 2015; Kozai et al., 2016; Varner et al., 2016). This is a matter that potential adopters of DEX-enhanced microdialysis will need to evaluate in the future in the context of their own particular intended applications.

## PRINCIPLES OF MICRODIALYSIS

The underlying process driving microdialysis sampling is the passive diffusion of substances across a semi-permeable hollow-fiber dialysis membrane (Stenken et al., 1997, 2001, 2010; Stenken, 1999; Chefer et al., 2001; Bungay et al., 2007; Chaurasia et al., 2007; Huang et al., 2008; Darvesh et al., 2011). Various polymeric materials, with molecular weight cutoff values between 10 and 100 kDa, are available for probe construction (Stenken, 1999; Chefer et al., 2001; Bungay et al., 2007; Darvesh et al., 2011; Hammarlund-Udenaes, 2017). The overall sampling efficiency, however, is influenced by the membrane and the tortuosity and volume fraction of the brain tissue, the tendency of analyte molecules to stick to the membrane or connecting tubing, the stability of the analyte molecule, etc. (Torto et al., 1999). The probes are commonly between 200 and 500  $\mu\text{m}$  in external diameter and several millimeters in length, chosen to match the target brain structure. The dialysate concentration of a target analyte is proportional, but not quantitatively equal,



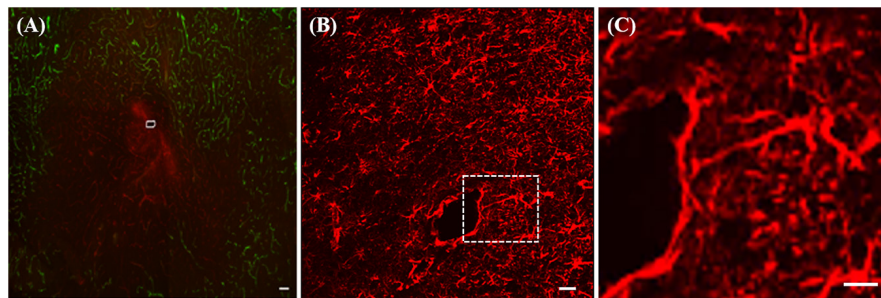


**FIGURE 1 | (A)** Fluorescence image of ischemia (green-blood vessels) and a PECAM (red) halo at a microdialysis probe track (white marking) in rat striatum. **(B)** GFAP immunoreactivity after 24-h probe implant, **(C)** enlargement of the area in the white box in B showing a glial cell extending a process ~300 μm toward the track. All scale bars = 100 μm. Adopted from references (Mitala et al., 2008; Jacquins-Gerstl and Michael, 2009).

to its concentration in the surrounding extracellular space (Ungerstedt, 1991). The analyte concentration at the probe outlet ( $C_{OUT}$ ) reflects two contributions, one derived from the external medium ( $C_{EXT}$ ), and one derived from the probe inlet ( $C_{IN}$ ) if analyte retrodialysis is ongoing. The relationship between these quantities is:

$$C_{OUT} = (1 - E) C_{IN} + R C_{EXT,\infty} \quad (1)$$

where  $E$  is the extraction fraction and  $R$  is the so-called relative recovery: the term  $C_{EXT,\infty}$  denotes the concentration of analyte in the external medium sufficiently far from the probe so as not to be disturbed by the probe *per se*. “Conventional microdialysis” refers to the case that  $C_{IN} = 0$ . A common rearrangement of Eq. 1 leads to the concentration differences plot:

$$C_{IN} - C_{OUT} = E C_{IN} - R C_{EXT,\infty} \quad (2)$$

Equation 2 shows that a plot of  $C_{IN} - C_{OUT}$  (the concentration differences) against  $C_{IN}$  is expected to be a straight line, with a slope of  $E$  and an x-intercept of  $R C_{EXT,\infty}$ . While such a plot provides the value of the extraction fraction, the relative recovery cannot generally be measured without independent knowledge of the external concentration. Thus, while *in vitro* probe calibration is straightforward, generally the value of  $R$  is an uncertain quantity during *in vivo* measurements. It is now generally recognized that  $R$  values determined during *in vitro* calibration are not reliably applicable to *in vivo* conditions: investigators need to keep this in mind. Our preference, and recommendation, is to report “dialysate concentrations” of analytes of interest, without attempting to convert to *in vivo* concentrations. A number of mathematical models have been developed in an effort to theoretically predict *in vivo*  $R$  values (Amberg and Lindefors, 1989; Benveniste, 1989; Lindefors et al., 1989; Bungay et al., 1990, 2003, 2007) but such work is beyond the scope of this review.

## INFLAMMATION

### Penetration Trauma

The average spacing of the microvessels in brain tissues is around 50 μm and a number of larger blood vessels are also

present. Inevitably, therefore, insertion of microdialysis probes and other neural devices such as microelectrode arrays with dimensions greater than 50 μm induces penetration trauma (Benveniste and Diemer, 1987; Zhou et al., 2001). In one of our first studies using immunohistochemistry we labeled blood vessels with dye-laden polystyrene nanobeads (100 nm in diameter) delivered to the brain by transcardial perfusion and the antibody platelet endothelial cell adhesion molecule (PECAM), a histochemical marker for endothelial cells. In healthy tissue the blood vessels were double-labeled with nanobeads and PECAM. However, tissue near the microdialysis probe tracks exhibited ischemia (diminished blood flow), in the form of PECAM immunoreactivity and blood vessels devoid of nanobeads, **Figure 1A** (Mitala et al., 2008). Probe tracks were surrounded by endothelial cell debris, which appeared as a diffuse halo of PECAM immunoreactivity and there was a large region that was devoid of the nanobeads indicating a lack of blood flow (Jaquins-Gerstl and Michael, 2009).

Moreover, the penetration trauma triggers a tissue response: sometimes called a foreign body response or a wound-healing response. The tissue response, left unattended, leads to gliosis of the probe track. Within a few days of insertion, microdialysis probes are surrounded by a layer of activated glial cells that do not exhibit the same neurochemical responsiveness of normal, healthy brain tissue, **Figures 1B,C** (Jaquins-Gerstl et al., 2011). Microdialysis probe tracks are surrounded by glia exhibiting marked hyperplasia and hypertrophy, **Figure 1B**. A closer view, **Figure 1C**, shows that the track is encircled around most of its circumference (~75%) by a barrier of GFAP immunoreactive elements, revealing that glial encapsulation and isolation of the probe is underway 24 h after implantation. The field of view in **Figure 1C** prominently displays a glial cell extending a process in excess of 300 μm in a linear fashion from the cell body toward the probe track.

We are not the first to report the penetration injury associated with microdialysis probes. Drew’s work examined the tissue surrounding microdialysis probes implanted in the striatum by light microscopy and revealed tissue damage 1.4 mm and neuronal loss 400 μm from the probe track (Clapp-Lilly et al., 1999). Drew also used hibernation as a model of neuroprotection by placing microdialysis probes into the striatum of the

Arctic ground squirrel. Activated microglia and astrocytes were dramatically attenuated around the probe tracks in hibernating animals compared to euthermic controls (Zhou et al., 2001). Not only does the large size of the microdialysis probe cause damage, but the tissue response to the probe also contributes to the severity of the injury.

Implantation results in activation of biochemical and cellular mechanisms to heal the injury. The initial response is initiated as soon as a device is implanted. It may last from minutes to weeks depending on the injury (Szarowski et al., 2003). A host of immune processes are set into motion which have been well-documented in current literature. Following penetration injury from the microdialysis probe, the blood brain barrier is compromised due to vascular damage, and blood-borne macrophages enter the brain and become indistinguishable from resident microglia. Microglia/macrophages then transform morphologically and functionally into an active state, home toward the site of injury, and are involved in phagocytosis and debris clearance (Stence et al., 2001; Kozai et al., 2012, 2015, 2016, 2017; Bettinger et al., 2020). In addition, microglia and blood-borne macrophages can release reactive oxygen species, which can damage healthy bystander cells such as neurons.

From our own studies we know that microdialysis probe implantation causes inflammation: it restricts blood flow (ischemia), activates macrophages, reduces neurons, diminished dopamine terminal, and axons and triggers gliosis, shown in **Figure 2** (Jaquins-Gerstl and Michael, 2009; Nesbitt et al., 2013). Therefore, the tissue sampled by microdialysis is not in its normal state. Even though the injury associated with microdialysis probe implantation is significant, it is important to note that overall brain function and animal behavior does not change (Jaquins-Gerstl and Michael, 2009; Nesbitt et al., 2013). Efforts to reduce the tissue response associated with neural device implantation have been made and are further discussed in this manuscript.

## Strategies to Reduce Inflammation

Inflammation is a complex reaction involving protein adsorption, leukocyte migration, localization and activation, and secretion of inflammatory mediators (Ghirnikar et al., 1998; Lefkowitz and Lefkowitz, 2001; Zhong and Bellamkonda, 2005; Klueh et al., 2007; Anderson et al., 2008; Winslow and Tresco, 2010; Chao et al., 2012). The degree of intensity of this response is largely influenced by the extent of tissue injury, implantation site, implant shape and size, and chemical and physical properties of the membrane material (Bridges and García, 2008). Strategies to mediate inflammation are a subject of much interest. It is thought that preventing non-specific protein adsorption and subsequent immune cell adhesion onto the biomaterial surface (Wisniewski and Reichert, 2000; Wisniewski et al., 2000; Bridges and García, 2008; Helmy et al., 2009) can reduce leukocyte recruitment and tissue fibrosis (Gerritsen et al., 1999; Gifford et al., 2006). Although this has proven successful *in vitro*, implementing these *in vivo* have not translated into decreasing the inflammatory responses (Wisniewski et al., 2001; Polikov et al., 2005).

A more direct and active approach regulating the tissue response has been through the delivery of anti-inflammatory agents (Nakase et al., 2002; Zhong and Bellamkonda, 2005, 2007;

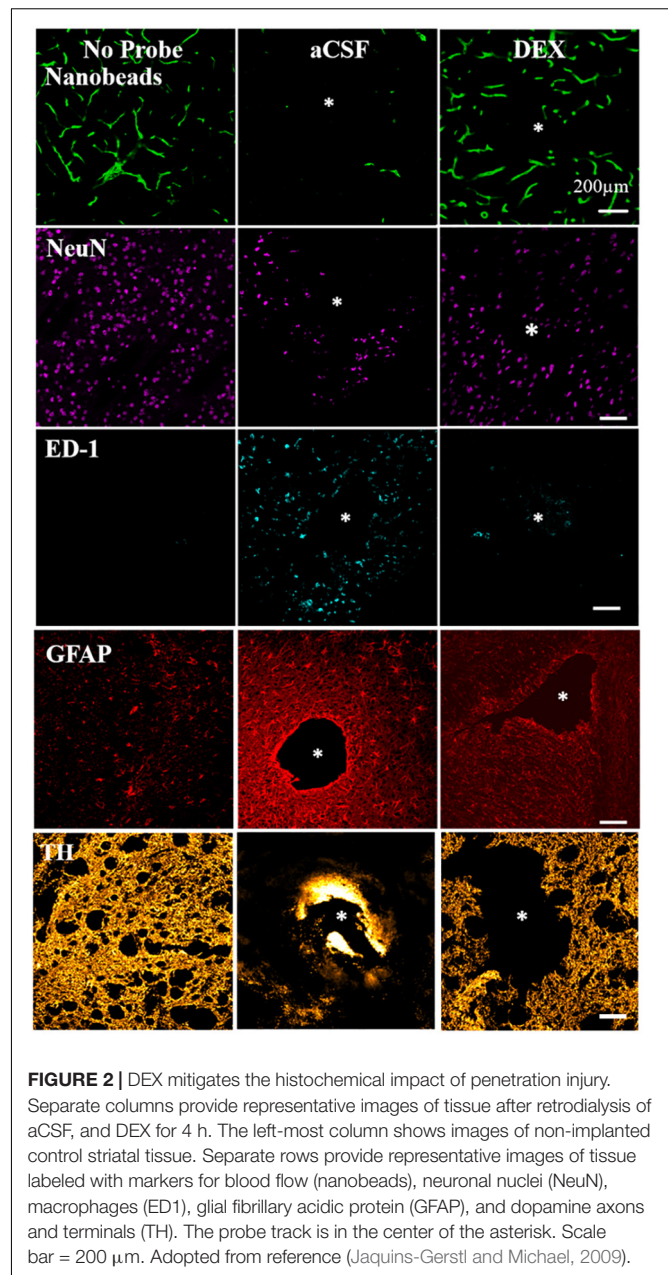
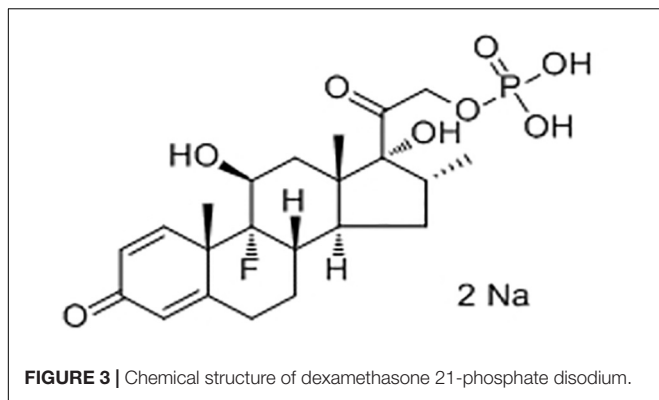


**FIGURE 2 |** DEX mitigates the histochemical impact of penetration injury. Separate columns provide representative images of tissue after retrodialysis of aCSF, and DEX for 4 h. The left-most column shows images of non-implanted control striatal tissue. Separate rows provide representative images of tissue labeled with markers for blood flow (nanobeads), neuronal nuclei (NeuN), macrophages (ED1), glial fibrillary acidic protein (GFAP), and dopamine axons and terminals (TH). The probe track is in the center of the asterisk. Scale bar = 200  $\mu$ m. Adopted from reference (Jaquins-Gerstl and Michael, 2009).

Kim et al., 2007; Klueh et al., 2007; Nichols et al., 2012; Wang et al., 2012; Zachman et al., 2012; Koh et al., 2013). One such anti-inflammatory agent used in this area is glucocorticoid steroids. Glucocorticoid steroids are a class of steroids that bind to the glucocorticoid receptor which regulates inflammation; they have been used extensively to treat inflammatory conditions (Chao et al., 2012; Webber et al., 2012).

Dexamethasone is a potent synthetic glucocorticoid associated with diminished migration and activation of immune cells, upregulation of anti-inflammatory cytokines, and decreased collagen production at the implant site (Schmidt et al., 1999; Hickey et al., 2002; Norton et al., 2005; Klueh et al., 2007; Chao et al., 2012). Once DEX crosses the cell membrane it



binds to specific cytoplasmic receptors such as the glucocorticoid receptors and then moves into the nucleus (Patacsil et al., 2016). This ability to cross cell membranes results in interference of leukocyte infiltration at the inflammation site along with inhibiting other inflammatory mediators.

Like many glucocorticoids, DEX has limited solubility. To overcome this problem, manufacturers have formulated DEX as water soluble hemisuccinate or phosphate ester pro-drugs. DEX 21-phosphate disodium (**Figure 3**), a phosphate ester pro-drug of DEX, is converted to active steroid DEX in blood rapidly and completely. DEX is used to treat many different inflammatory conditions such as allergic reactions, skin conditions, ulcerative colitis, arthritis, lupus, psoriasis, and breathing disorders. Most recently, it was used to treat patients hospitalized with COVID-19 (Lammers et al., 2020; Stauffer et al., 2020).

## APPLICATIONS

Dexamethasone has a wide variety of uses in the medical and science field and is widely prescribed. This section discusses applications of DEX used in science as an anti-inflammatory drug, see **Table 1** for a summary.

### DEX and Neuronal Devices

Several studies have examined the use of DEX with regard to neural prosthetics. In 2003, Shain et al. (2003) published a study using DEX to reduce gliosis near implanted silicone devices in the brain. Peripheral injections of DEX were made by subcutaneous injection. DEX was dissolved in ethanol (0.2 mg/mL) and delivered to produce a dose of 200 mg/kg. This study revealed that DEX reduced gliosis near the implanted device. However, the effects of the drug on the major inflammatory cells at the interface, which were macrophages, were not investigated.

Later in 2005, Spataro et al. (2005) injected DEX (200 mg/kg) for 1 or 6 days subcutaneously and showed the tissue reaction around neural implants was reduced. DEX treatment greatly attenuated astroglia responses. Cohorts with 6-day treatment showed this was more effective than a single injection regime.

Others have used DEX (100 µg) incorporated into a nitrocellulose coating deposited on electrodes for local drug delivery (Zhong and Bellamkonda, 2007). The local delivery of

DEX reduced inflammation at 1-week post implantation but not at 4 weeks (Zhong and Bellamkonda, 2007), possibly because the amount of drug incorporated into the coating was not high enough for long-term release at a sufficient dosage.

Dexamethasone has been used to down regulate nitric oxide production which protects neurons (Zha et al., 2011), (Hempen et al., 2002), inhibits astrocyte proliferation and inhibited proliferation of NG2 cells (Kim and Martin, 2006). Because DEX can have serious side effects other studies have incorporated DEX into different probe coatings; poly(ethyl-vinyl) acetate, nitrocellulose, carbon nanotubes, and poly (lactic-co-glycolic acid) nanoparticles within alginate hydrogel matrices (Hempen et al., 2002; Kim and Martin, 2006; Zhong and Bellamkonda, 2007; Mercanzini et al., 2010; Luo et al., 2011). Benefits common to all the studies included decreased astrocytic response, reduced microglial/macrophage activity, mitigated neuronal loss, and minimized chondroitin sulfate proteoglycan expression.

### Dopamine Microdialysis and Detection With Fast Scan Cyclic Voltammetry

Dopamine (DA) is one of the analytes commonly sampled with microdialysis. DA is an important neurotransmitter with numerous roles in normal brain function and it is also involved in a variety of disorders including substance abuse, schizophrenia, and Parkinson's disease (Lotharius and Brundin, 2002; Phillips et al., 2003; Schultz, 2007; Brisch et al., 2014). Microdialysis coupled to fast scan cyclic voltammetry (FSCV) is a method commonly used in our lab and many others for studying DA *in vivo* (Garris and Wightman, 1995; Robinson et al., 2003; Michael and Borland, 2006).

Previous studies from our lab demonstrate that the penetration trauma associated with microdialysis profoundly changes DAergic activity near the probe site. We placed voltammetric microelectrodes in the tissue adjacent to the probes. We compared DA as measured with microelectrodes placed 1 mm from the probes, 235 µm from the probes, and immediately adjacent to the probes, called a dialytrode. These recording locations produce dramatically different results, revealing a previously unrecognized 1000-fold gradient of DA activity across the traumatized tissue layer. DA levels measured 1 mm from the probe were in the micromolar range, whereas DA levels 235 µm from the probes were in the nanomolar range and the DA response at the dialytrode was completely abolished (Borland et al., 2005; Yang and Michael, 2007). Only after the administration of a dopamine uptake inhibitor nomifensine, (20 mg/kg i.p.) was DA detectable at the dialytrode. We questioned "why does penetration trauma of the microdialysis probe have an extreme impact on *in vivo* measurements of DA?"

One of our group's objectives was to reduce, if not eliminate, the penetration injury and its deleterious effects on neurochemical monitoring. Motivated by the findings of Shain and others (Turner et al., 1999; Shain et al., 2003), we investigated the retrodialysis of DEX in the rat striatum. We showed that combining a 5-day post-implantation wait period with continuous retrodialysis of a low-micromolar concentration of DEX vastly reduces both the voltammetric and histological



**TABLE 1** | Summary of DEX applications.

Author (year)	Dose	Treatment	Device type	Indwelling period	Comments
Shain et al., 2003	200 mg/kg	Peripheral injection once	Neural prosthetic	1 day, 1 and 6 weeks	Reduced gliosis near the implanted
Spataro et al., 2005	200 mg/kg	Subcutaneous injections daily and single	Neural prosthetic	1 and 6 weeks	Attenuated astroglia while microglia and vascular responses increased
Zhong and Bellamkonda, 2007	Nitrocellulose-DEX (100 $\mu$ g) coating, thickness = 1.72 $\mu$ m	Coating, continuous	Neural prosthetic	1 and 4 weeks	Attenuate the inflammatory response and reduce neuronal loss
Keeler et al., 2015a	20 $\mu$ g/ml DEX	Infusions performed in 1-h increments for 6 h, in subcutaneous space near the spine	Microdialysis probe	7 days	Delayed infusion resulted in an increased percentage of CD68 <sup>+</sup> , CD163 <sup>+</sup> , and an up regulation in IL-6, decrease in CCL2 concentrations, macrophages shift to a M(DEX) activation state
Keeler et al., 2015b	20 $\mu$ g/ml DEX	Infusions performed in 1-h increments for 6 h, dorsal subcutaneous space	Microdialysis probe	3 days	Decreases in both IL-6 and CCL2 in non-delayed DEX, increase in IL-6 in delayed DEX, macrophages shift to a M(DEX) activation state
Nesbitt, 2015	10 $\mu$ M for 24 h then 2 $\mu$ M DEX (less than 20 nanomoles)	Retrodialysis in striatum	Microdialysis probe	4 and 24 h	Stabilizes evoked dopamine responses and protects DA terminals
Kozai et al., 2016	10 $\mu$ M DEX	Retrodialysis in cortex	Microdialysis probe	6 h	Significantly reduces microglial activation, T-stage morphology, and directionality polarization
Varner et al., 2016	10 $\mu$ M for 24 h then 2 $\mu$ M DEX (less than 20 nanomoles)	Retrodialysis in striatum	Microdialysis probe	5 days	Reinstated evoked dopamine activity, suppresses activation of microglia
Varner et al., 2017	10 $\mu$ M for 24 h then 2 $\mu$ M DEX (less than 20 nanomoles)	Retrodialysis in prefrontal cortex	Microdialysis probe	2 h, 5 and 10 days	Improved the detection of spreading depolarizations, induced transients and increased amplitudes of K <sup>+</sup> spikes
Robbins et al., 2019	10 $\mu$ M for 24 h then 2 $\mu$ M DEX	Retrodialysis in prefrontal cortex with/out CCI	Microdialysis probe	10–12 days	Facilitates the monitoring of spontaneous spreading depolarizations

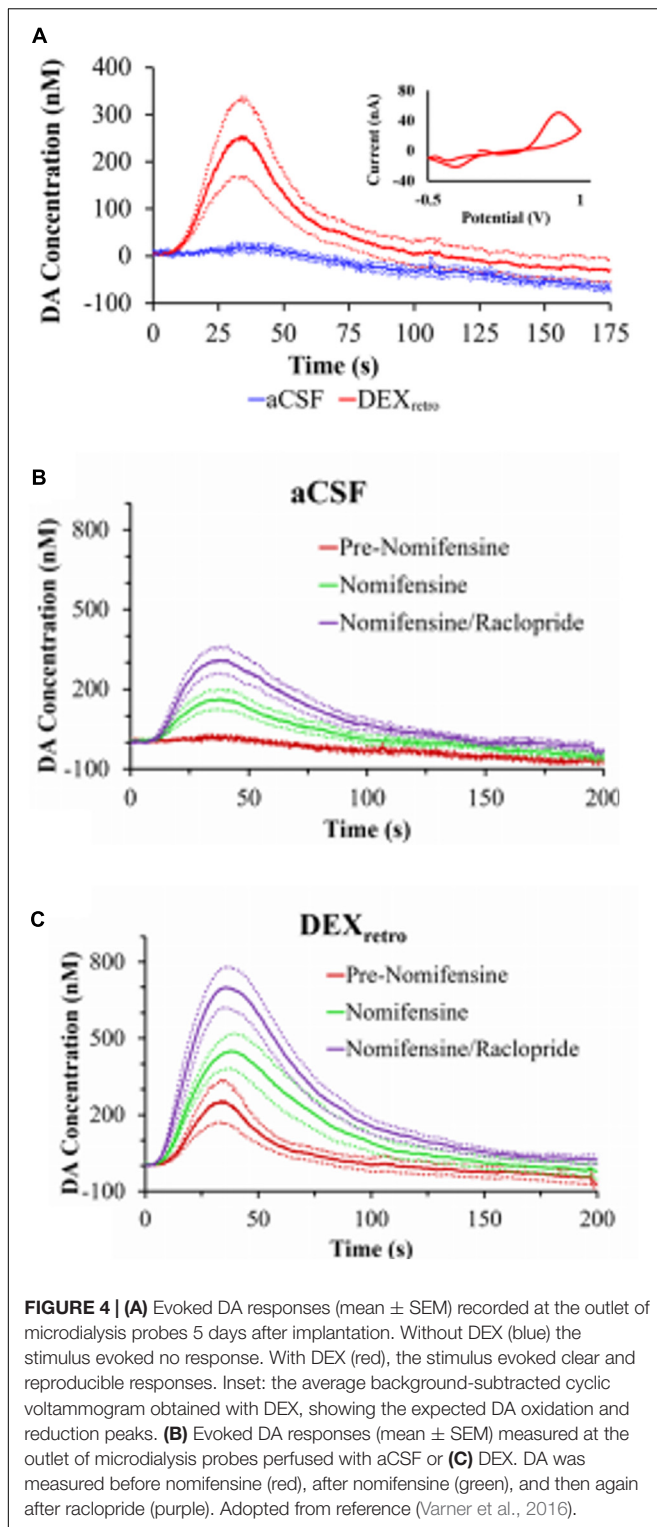
signs of the penetration injury, **Figure 4** (Varner et al., 2016). DA measurements were taken at the outlet of the probe. At 5-days after probe implantation, retrodialysis of DEX: (1) reinstates normal evoked DA release activity in the tissue adjacent to the probe, (2) facilitates robust detection of evoked DA release, (3) establishes quantitative agreement between evoked DA measured simultaneously at the probe outlet and in the tissue next to the probe, (4) reinstates normal immunoreactivity for tyrosine hydroxylase and the dopamine transporter near the probe, and (5) prevents glial scarring at the probe track (Varner et al., 2016). Our findings support that the beneficial effects of DEX in this application may be attributed to its actions as an anti-inflammatory agent.

We also used voltammetry next to microdialysis probes to record electrically evoked DA release during the retrodialysis of DEX (Nesbitt et al., 2013). In this study a carbon fiber voltammetric electrode was inserted into the striatum of an anesthetized rat and a stimulating electrode was lowered into the medial forebrain bundle (MFB), **Figure 5** (Nesbitt et al., 2013). Electrically evoked release was recorded by FSCV during

electrical stimulation of the MFB. The final position of the probe was such that the distance between the tip of the microelectrode and the surface of the probe was 70  $\mu$ m and the distance between the top of the electrode and the probe was 100  $\mu$ m. This investigation focused on acute implants only 4 h in duration. We observed that microdialysis probes disrupt evoked DA release. If microdialysis probes were perfused with no DEX, all the electrically evoked DA responses were abolished (Nesbitt et al., 2013). DA was not detected during any of the electrical stimuli applied after implanting the probe. Next, a dose of nomifensine (20 mg/kg i.p.) was given to the rats which caused stimulated DA release. In the case of microdialysis probes perfused with DEX, implanting the probe next to the microelectrode diminished, but did not abolish, electrically evoked DA release. Again, these results confirm that DEX preserved DA activity in the tissue next to the microdialysis probes.

Immunohistochemistry was performed on brain tissue containing the probe using markers for ischemia, neuronal nuclei, macrophages, and DA axons and terminals (tyrosine hydroxylase). Probes perfused with no DEX caused profound





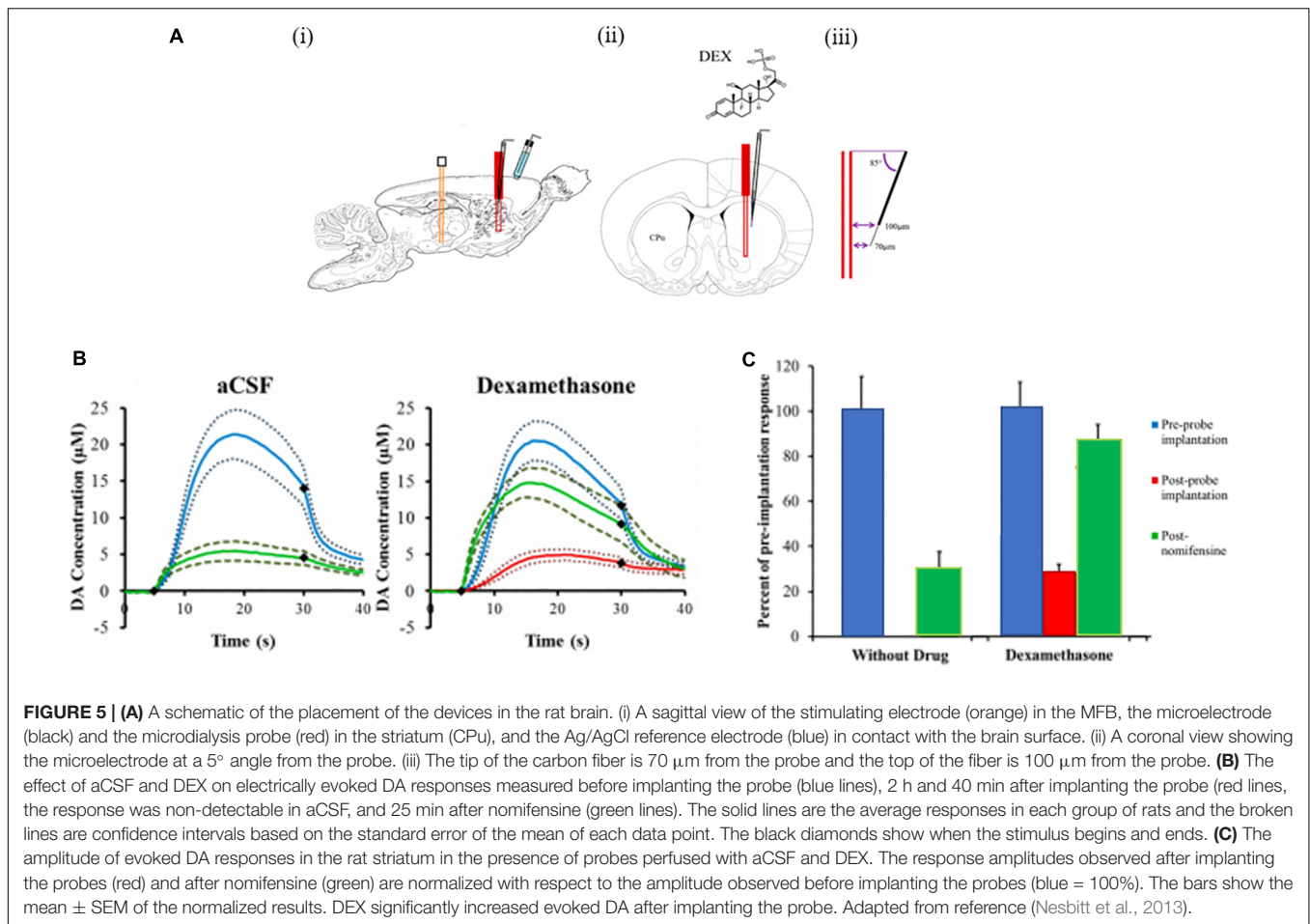
ischemia, a loss of striatal neurons near the probes, activation of macrophages and a loss of tyrosine hydroxylase meaning profoundly disrupted DA axons and terminals (Nesbitt, 2015). Tissue with DEX perfusion showed a decrease in ischemia, neurons near the probe and few activated macrophages,

indicating that DEX protected the brain tissue near the probe. Tyrosine hydroxylase was preserved in tissue surrounding the probe with DEX. We conclude that retrodialysis of DEX mitigates penetration injury during brain microdialysis (Nesbitt, 2015).

Using a longer time frame, 4 and 24 h, we implanted microdialysis probes in the rat striatum. We used with and without DEX in the perfusion fluid and measured evoked DA release at the outlet of the probes with FSCV. Responses at the probe outlet were below the detection limits of FSCV unless animals were treated with nomifensine, which increases the microdialysis recovery of evoked dopamine transients (Church et al., 1987; Pontieri et al., 1995). When probes were perfused without DEX, post-nomifensine responses at the probe outlet exhibited a significant decline in amplitude between 4- and 24-h post-implantation. However, DEX abolished this instability, both in animals treated first with nomifensine and then with raclopride, a  $D_2$  dopamine receptor antagonist. This study demonstrated that DEX stabilizes, but does not alter, evoked DA responses at the outlet of microdialysis probes.

## Dexamethasone and Macrophage Polarization States

Understanding the biochemistry that occurs at the site of an implanted biomaterial is important in a wide range of clinical contexts. Julie Stenken's group from the University of Arkansas has used microdialysis sampling with DEX to understand the inflammatory response caused by macrophages. Although DEX has widely been used as a releasing agent in biomaterials, Stenken and others have identified DEX as a modulator which produces a phenotype that has characteristics of the M2c macrophage (Van Coillie et al., 1999; Martinez, 2011; Keeler et al., 2015b). Macrophages play roles in opposing processes such as inflammation vs anti-inflammation and tissue destruction vs tissue remodeling. Macrophages are driven by micro-environmental chemical signals present within the extracellular matrix which result in different macrophage polarization states (Gordon and Taylor, 2005; Mantovani et al., 2013; Keeler et al., 2015b). While different materials have been used to elicit a desired macrophage activation state, it is unknown whether modulators can be used to shift the macrophage activation state. Stenken et al. was the first to use modulators to attempt regulating the macrophage activation state at an implant site. The primary hypothesis was that by producing a predominantly M2c activation state, improved healing would be seen at the implant site (Keeler et al., 2015b). In this study, DEX was delivered through the microdialysis probe to alter the activation state of macrophages in awake Sprague-Dawley rats. Two probes were implanted in the subcutaneous space on either side of the spine with  $\sim 1$ -inch separation between the probes. The delivery of DEX (20  $\mu$ g/ml) resulted in an increase in the percentage of M2c macrophages seen in the tissue surrounding the microdialysis probe. Remarkably, differences were seen when DEX was delivered immediately following probe implantation as compared to a delayed delivery. In tissue where DEX was immediately delivered, fewer macrophages were present compared to the delayed delivery.



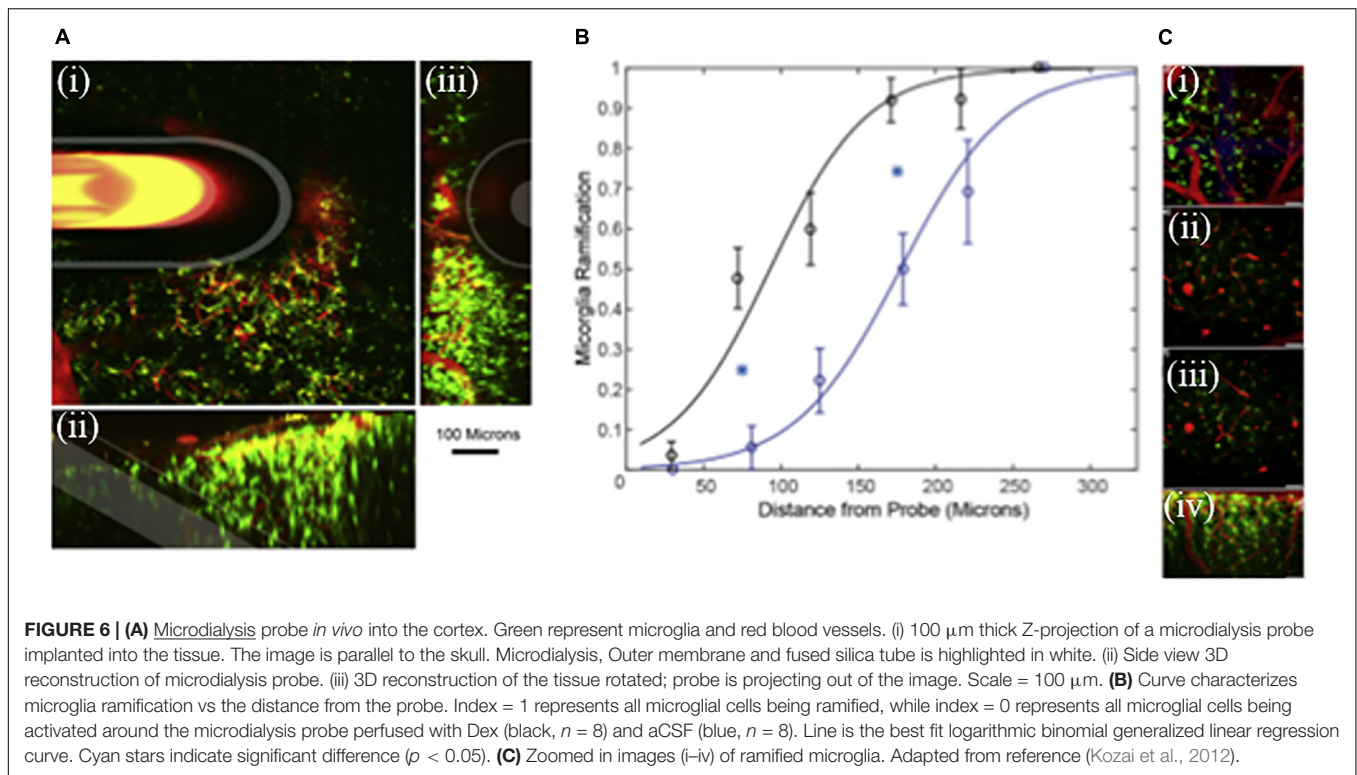
The gene expression profiles of the chemokine CCL2 and the inflammatory cytokine IL-6 were also examined; these too were different. CCL2 is known to be one of the primary chemokines responsible for the migration and infiltration of monocytes to a wound site. Once at the wound site, monocytes differentiate to macrophages. While both CCL2 and IL-6 were significantly down-regulated in the tissue from immediate DEX delivery, IL-6 was seen to be significantly up-regulated in response to a delayed DEX infusion. These results showed that it is possible to use modulators to shift macrophages *in vivo* to a desired activation state at an implant site while also characterizing a predominantly M2c environment (Keeler et al., 2015b).

The time course required for altering macrophages was also examined by Stenken et al. by delivering DEX through an implanted microdialysis probe in the subcutaneous space of male rats (Keeler et al., 2015a,b). They investigated a 3-day post-implantation time period for initiating DEX infusion. They sought to determine if the start of DEX infusion is delayed, allowing the initial inflammatory response to begin, would be more optimal in terms of converting macrophages to an M(Dex) state. The resulting foreign body response to the implanted microdialysis probes was examined by immunohistochemical and molecular means at the gene and protein level. The delayed delivery of DEX resulted in an upregulation of IL-6 gene

transcripts as well as a moderate decrease in CCL2 concentrations (Keeler et al., 2015a,b). The delayed DEX treatment resulted in an increase in cellular density in the tissue surrounding the microdialysis probe. More importantly the delayed delivery of DEX shifted the macrophages to an M(Dex) activation state. Most studies involved in the use of modulators to shift the activation state of macrophages has primarily been *in vitro*. Stenken's work is cutting edge as it demonstrates the use of microdialysis sampling to deliver DEX to alter macrophage polarization *in vivo*, which improves tissue remodeling.

## DEX Retrodialysis Attenuates Microglial Activity

Microglia play a critical role in living brain tissue. They perform a wide range of tasks while in the native ramified state; they are constantly scavenging the CNS for plaques, damaged neurons, and synapses. They are also involved in experience-dependent synaptic maintenance (Wake et al., 2009; Tremblay et al., 2010), debris clearing (Nimmerjahn et al., 2005), and surveillance against injury and invasion (Nimmerjahn et al., 2005). Microglial cells are extremely sensitive to even small pathological changes in the CNS and are also extremely plastic. They adopt a specific form in response to the local conditions and chemical signals



they have detected (Nimmerjahn et al., 2005). When a brain insult is detected by microglial cells, they enter an ameboid form called a transition stage (*T*-stage); this process is generally referred to as “microglial activation.” During this stage, the resting microglia retract their processes, which become fewer and much thicker, increase the size of their cell bodies, change the expression of various enzymes and receptors, and begin to produce immune response molecules. Acutely, following probe insertion, nearby microglia activate and encapsulate the implant with their processes and lamellipodia sheath (Kozai et al., 2012).

We wanted to understand how DEX affects microglia morphology/motility in real time by characterizing the dynamic microglia response to penetration trauma of microdialysis probes. We employed *in vivo* two-photon microscopy to quantify the acute microglial response to microdialysis probes in the brain with or without retrodialysis of DEX. We examined the cellular microglial response to microdialysis probe insertion up to 6 h; morphological changes and activation characteristics of microglia around the implants were observed and quantified, **Figure 6** (Kozai et al., 2016). We found that implantation of the microdialysis probe with DEX reduced microglial activation. In tissue without DEX (aCSF perfused) the activation state of the microglia were delayed and were significant. DEX had a significant effect on the radius of microglia activation, morphology, *T*-stage activation, and microglia directionality index. The temporal dynamics of microglial response also showed distinct differences between the control and DEX treated tissue. While many microglia appeared non-polarized with unusually thicker processes in the DEX treated tissue at 6 h, some polarized toward nearby blood brain barrier. In this study the local

administration of DEX rendered it a great candidate to reduce the effects of penetration injury by neural probes (Kozai et al., 2016).

## Spreading Depolarizations and Microdialysis

One application of clinical microdialysis is monitoring brain injured patients in the intensive care unit to identify chemical markers of secondary brain injuries. Our group and others have focused on a phenomenon of secondary injury called spreading depolarization (SD). Incidences of SDs are significantly correlated with poor patient outcomes, including death, vegetative state, and severe disability (Hartings et al., 2009, 2011a,b; Lauritzen et al., 2011). SD is characterized by a wave of near-complete depolarization of neurons and glia resulting in a temporary disruption of the ion homeostasis and silencing of electrical activity (Guiou et al., 2005; Fabricius et al., 2006; Dreier et al., 2006a,b, 2009; Strong et al., 2007; Dreier, 2011; Seule et al., 2015; Rogers et al., 2017). Excess  $\text{K}^+$  released into the extracellular space during SDs can diffuse to and depolarize neighboring cells, thus creating a wave that propagates across the cortex at a rate of 2–5 mm/min. The brain tissue depends on the vasculature to deliver glucose and oxygen to meet these energy demands. The swelling and restricted blood flow commonly observed after a TBI can hinder this process. Clusters of SDs impose particularly severe energy demands on the injured brain and can result in long-lasting declines in basal glucose (Fabricius et al., 2006; Dreier et al., 2006a; Feuerstein et al., 2010; Nakamura et al., 2010; Lauritzen et al., 2011; Hartings et al., 2011a,b).

The importance of SD monitoring during neurointensive care has been widely recognized and numerous animal studies

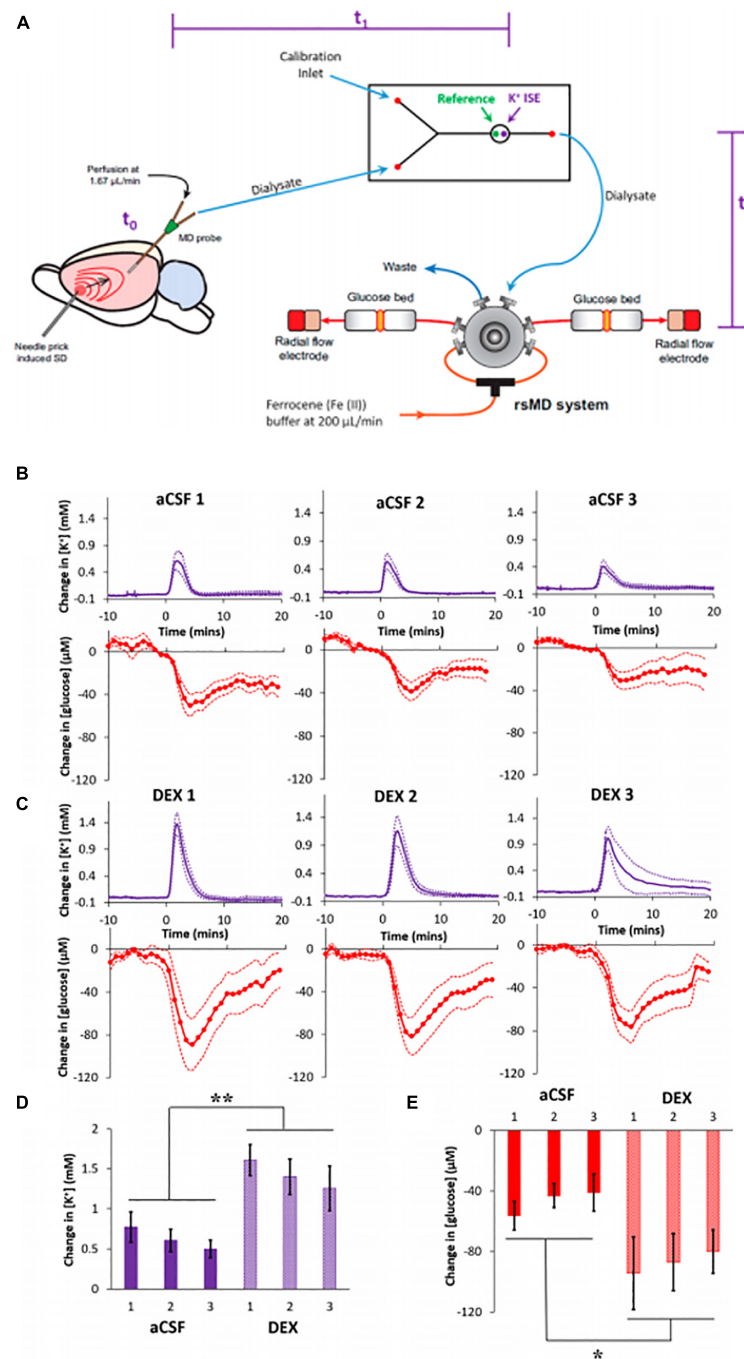


**FIGURE 7 | (A)** Experimental design of the rsMD. SD was induced by needle pricks in the cortex. The SD arrives at the microdialysis probe at  $t_0$ ; intervals between the needle pricks and  $t_0$  were typically less than 1 min. Next, the sample travels to the  $\text{K}^+$  ISE in approximately 4 min,  $t_1$ . Finally, the sample travels to the glucose detector in approximately 7 min,  $t_2$ . **(B)** Cortical responses to three needle pricks recorded 2 h after probe insertion with aCSF or **(C)** DEX (mean  $\pm$  SEM). Maximum changes in **(D)**  $\text{K}^+$  and **(E)** glucose were analyzed with two-way ANOVAs with group (aCSF, DEX) and needle prick (1, 2, 3; repeated measures) as the factors. The needle prick and interactions were not significant, but group was significant for both  $\text{K}^+$  [ $F(1,14) = 13.422$ ] and glucose [ $F(1,14) = 6.253$ ]. \*\* $p < 0.005$  and \* $p < 0.05$ . Adapted from reference (Varner et al., 2017).

have been dedicated to improving SD monitoring (Dreier, 2011; Ayata and Lauritzen, 2015; Dreier et al., 2016; Osier and Dixon, 2016). Methods for SD monitoring include electrocorticograph (ECoG), blood flow analysis, and microdialysis. The Boutelle lab

has developed a rapid sampling microdialysis (rsMD) system (**Figure 7**) that monitors SD-associated changes in glucose and lactate at the patient's bedside (Jones et al., 2002). Combining the rsMD system with an online  $\text{K}^+$  ion-selective electrode and



ECoG provides a multimodal analysis system that can detect episodes of SDs in the days following the patient's primary injury (Rogers et al., 2013, 2017; Papadimitriou et al., 2016).

Our group reported that DEX conferred profound benefits to the microdialysis monitoring of SDs induced glucose and  $K^+$  transients in the rat cortex, **Figure 7** (Varner et al., 2017). We inserted microdialysis probes, with and without retrodialysis of DEX, and monitored SD-induced glucose and  $K^+$  transients 2 h, 5 days, or 10 days later (Varner et al., 2017). SDs were induced by needle pricks and were performed at 30-min intervals. Retrodialysis of DEX improved the detection of SD-induced transients at all three time points. DEX increased the amplitudes of the SD-induced  $K^+$  spikes and glucose dips by 127% and 86% (averages of the three responses), respectively, compared to those observed without DEX. In the presence of DEX, the amplitudes of the  $K^+$  spikes were significantly larger at 2 h compared to 5 and 10 days. In contrast, there were no significant differences between the amplitudes of the glucose dips at the three time points. In the presence of DEX, the fraction of  $K^+$  spikes accompanied by quantifiable glucose dips was relatively constant across the three time points. In the absence of DEX, glucose dips were essentially non-detectable 5 days after probe insertion.

In our 10-day studies, DEX retrodialysis was performed only during the first 5 days, confirming that continuous DEX delivery for the entire 10-day time window is not required. After retrodialysis of DEX, histochemical inspection of probe tracks found no signs of ischemia or gliosis 10 days after insertion (Varner et al., 2017). Our findings confirmed that DEX enhances the performance of microdialysis for monitoring SD-induced glucose and  $K^+$  transients in the rat cortex for at least 10 days after probe insertion.

Our most recent study was to investigate whether the microdialysis with DEX is translatable to the monitoring of spontaneous SD in rats after controlled cortical impact (CCI), a widely studied rodent model of TBI (Dixon et al., 1987; Wagner et al., 2005; Xiong et al., 2013). Microdialysis probes were placed 1 or 3 mm away from the CCI site expecting that the secondary injury would spread over time into the penumbra (Robbins et al., 2019). But this did not happen. There was no difference between 1 and 3 mm location of the probes. We recorded  $K^+$  and glucose in dialysates from 10 rats for 10–12 days following CCI and microdialysis probe insertion (Robbins et al., 2019). Overall, recordings from  $n = 8$  rats exhibited 185 spontaneous SDs, hallmarked by a transient rise, and fall in dialysate  $K^+$ , over the course of 5–7 min. Of the SDs observed while we were also monitoring glucose ( $n = 126$ ), some were accompanied by negative glucose transients ( $n = 89$ ), no obvious change in glucose ( $n = 25$ ), or transient increases in glucose ( $n = 12$ ). Some rats ( $n = 2$ ) exhibited no SDs, which seems to be consistent with clinical reports that SDs are detected in some but not all TBI patients who undergo neuromonitoring (Hartings et al., 2011a,b; Dreier et al., 2016).

We also observed a second post-CCI phenomenon consisting of a slow, progressive decline of dialysate glucose from basal concentrations to levels below the detection limit (Robbins et al., 2019). Once this occurred, glucose concentrations did not return to detectable levels. We found a high degree of animal-to-animal

variability in the outcome of chemical monitoring after CCI. Individual animals varied widely in the number and frequency of SDs and the onset and duration of progressive glucose decline. We attribute this to the varied extent of the injury induced by CCI. Despite the animal-to-animal variability, this study yielded several consistent observations. Most rats (8 of 10) exhibited spontaneous SDs, either isolated or in clusters. Spontaneous SDs occurred before, during, and after the glucose decline.

Probe tracks were examined by immunohistochemistry and showed no presence of a glial barrier, absence of blood flow, or profound losses of neurons: these observations indicate the anti-inflammatory efficacy of DEX in the presence of CCI. This study adds to a mounting body of evidence that DEX-enhanced microdialysis facilitates extended intracranial microdialysis in the rat brain over the course of at least 10 days.

## OUTLOOK

The development of long-term microdialysis is an inspiring yet greatly challenging process. The foreign bodies response toward the penetration trauma associated with the implant is a critical barrier to overcome even with the use of an anti-inflammatory drug such as DEX. We have shown studies where DEX-enhanced microdialysis was used to stabilize the surrounding tissue allowing for better detection of (a) DA, (b) attenuated microglia, (c) reduce gliosis, and (d) enhances the detection of  $K^+$  and glucose transients induced by spreading depolarization. DEX improves and stabilizes the tissue surrounding the probe and promotes longevity of the probe.

Current and cutting-edge research is being performed in clinical studies using DEX and microdialysis with the eventual goal of better patient outcomes. There are many types of cells involved in the bodies' response to the microdialysis implant, although DEX is very successful at damping the immune response. Many questions still arise. To what extent does macrophages traffic across the blood brain barrier following chronic implantation? What is the extent of changes to the local vasculature and the intact blood brain barrier? Are there better strategies for reducing the foreign body response? Are there better suited drugs or probe coating which could be used with microdialysis? Understanding the penetration injury associated with probe implantation and providing protective strategies promotes long-term sampling by microdialysis and plays a lasting role in understanding the neurochemistry of the brain. The future of long term microdialysis is unlimited.

## AUTHOR CONTRIBUTIONS

AJ-G and AM conceived the overall topics of discussion. AJ-G wrote the sections. Both authors read and approved the final manuscript.

## FUNDING

Salary support was provided by the authors through the NIH grants R01NS102725.

## REFERENCES

- Amberg, G., and Lindefors, N. (1989). Intracerebral microdialysis: II. Mathematical studies of diffusion kinetics. *J. Pharmacol. Methods* 22, 157–183. doi: 10.1016/0160-5402(89)90012-0
- Anderson, J. M., Rodriguez, A., and Chang, D. T. (2008). *Foreign Body Reaction to Biomaterials. In Seminars in Immunology*. Amsterdam: Elsevier, 86–100. doi: 10.1016/j.smim.2007.11.004
- Ayata, C., and Lauritzen, M. J. P. R. (2015). Spreading depression, spreading depolarizations, and the cerebral vasculature. *Cen. Ayata Martin Lauritzen* 95, 953–993. doi: 10.1152/physrev.00027.2014
- Becker, J. B., and Cha, J. H. (1989). Estrous cycle-dependent variation in amphetamine-induced behaviors and striatal dopamine release assessed with microdialysis. *Behav. Brain Res.* 35, 117–125. doi: 10.1016/S0166-4328(89)80112-3
- Benveniste, H. (1989). Brain microdialysis. *J. Neurochem.* 52, 1667–1679. doi: 10.1111/j.1471-4159.1989.tb07243.x
- Benveniste, H., and Diemer, N. H. (1987). Cellular reactions to implantation of a microdialysis tube in the rat hippocampus. *Acta Neuropathol.* 74, 234–238. doi: 10.1007/BF00688186
- Benveniste, H., Dreier, J., Schousboe, A., and Diemer, N. H. (1987). Regional cerebral glucose phosphorylation and blood-flow after insertion of a microdialysis fiber through the dorsal hippocampus in therat. *J. Neurochem.* 49, 729–734. doi: 10.1111/j.1471-4159.1987.tb00954.x
- Benveniste, H., Hansen, A. J., and Ottosen, N. S. (1989). Determination of brain interstitial concentrations by microdialysis. *J. Neurochem.* 52, 1741–1750. doi: 10.1111/j.1471-4159.1989.tb07252.x
- Bettinger, C. J., Ecker, M., Kozai, T. D. Y., Malliaras, G. G., Meng, E., Voit, W., et al. (2020). Recent advances in neural interfaces—Materials chemistry to clinical translation. *MRS Bull.* 45, 655–668. doi: 10.1557/mrs.2020.195
- Booth, M. A., Gowers, S. A., Leong, C. L., Rogers, M. L., Samper, I. C., Wickham, A. P., et al. (2018). Chemical monitoring in clinical settings: recent developments toward real-time chemical monitoring of patients. *Anal. Chem.* 90, 2–18. doi: 10.1021/acs.analchem.7b04224
- Borjigin, J., and Liu, T. (2008). Application of long-term microdialysis in circadian rhythm research. *Pharmacol. Biochem. Behav.* 90, 148–155. doi: 10.1016/j.pbb.2007.10.010
- Borland, L. M., Shi, G., Yang, H., and Michael, A. C. (2005). Voltammetric study of extracellular dopamine near microdialysis probes acutely implanted in the striatum of the anesthetized rat. *J. Neurosci. Methods* 146, 149–158. doi: 10.1016/j.jneumeth.2005.02.002
- Bosche, B., Dohmen, C., Graf, R., Neveling, M., Staub, F., Kracht, L., et al. (2003). Extracellular concentrations of non-transmitter amino acids in peri-infarct tissue of patients predict malignant middle cerebral artery infarction. *Clin. Trial* 34, 2908–2913. doi: 10.1161/01.STR.0000100158.51986.EB
- Bosche, B., Graf, R., Ernestus, R. I., Dohmen, C., Reithmeier, T., Brinker, G., et al. (2010). Recurrent spreading depolarizations after subarachnoid hemorrhage decreases oxygen availability in human cerebral cortex. *Ann. Neurol.* 67, 607–617. doi: 10.1002/ana.21943
- Bridges, A. W., and García, A. (2008). Anti-inflammatory polymeric coatings for implantable biomaterials and devices. *J. Diabetes Sci. Technol.* 2, 984–994. doi: 10.1177/193229680800200628
- Brisch, R., Saniotis, A., Wolf, R., Bielau, H., Bernstein, H. G., Steiner, J., et al. (2014). The role of dopamine in schizophrenia from a neurobiological and evolutionary perspective: old fashioned, but still in vogue. *Front. Psychiatry* 5:47. doi: 10.3389/fpsy.2014.00047
- Bungay, P. M., Morrison, P. F., and Dedrick, R. L. (1990). Steady-state theory for quantitative microdialysis of solutes and water in vivo and in vitro. *Life Sci.* 46, 105–119. doi: 10.1016/0024-3205(90)90043-Q
- Bungay, P. M., Morrison, P. F., Dedrick, R. L., Chefer, V. I., and Zapata, A. (2007). “Principles of quantitative microdialysis,” in *Handbook of Microdialysis: Methods, Applications, and Perspectives*, eds B. H. C. Westerink and T. Cremers (Amsterdam: Elsevier), 131–167. doi: 10.1016/S1569-7339(06)16008-7
- Bungay, P. M., Newton-Vinson, P., Isele, W., Garris, P. A., and Justice, J. B. (2003). Microdialysis of dopamine interpreted with quantitative model incorporating probe implantation trauma. *J. Neurochem.* 86, 932–946. doi: 10.1046/j.1471-4159.2003.01904.x
- Cano-Cebrian, M. J., Zornoza, T., Polache, A., and Granero, L. (2005). Quantitative in vivo microdialysis in pharmacokinetic studies: some reminders. *Curr. Drug Metab.* 6, 83–90. doi: 10.2174/1389200053586109
- Carneheim, C., and Stahle, L. (1991). Microdialysis of lipophilic compounds: a methodological study. *Pharmacol. Toxicol.* 69, 378–380. doi: 10.1111/j.1600-0773.1991.tb01315.x
- Castner, S. A., Xiao, L., and Becker, J. B. (1993). Sex differences in striatal dopamine: in vivo microdialysis and behavioral studies. *Brain Res.* 610, 127–134. doi: 10.1016/0006-8993(93)91225-H
- Chao, J., Viets, Z., Donham, P., Wood, J. G., and Gonzalez, N. C. (2012). Dexamethasone blocks the systemic inflammation of alveolar hypoxia at several sites in the inflammatory cascade. *Am. J. Physiol. Heart Circulat. Physiol.* 303, H168–H177. doi: 10.1152/ajpheart.00106.2012
- Chaurasia, C. S., Müller, M., Bashaw, E. D., Benfeldt, E., Bolinder, J., Bullock, R., et al. (2007). AAPS-FDA workshop white paper: microdialysis principles, application and regulatory perspectives. *Pharm. Res.* 24, 1014–1025. doi: 10.1007/s11095-006-9206-z
- Chefer, V. I., Thompson, A. C., Zapata, A., and Shippenberg, T. S. (2001). *Overview of Brain Microdialysis: Current Protocols in Neuroscience*. Hoboken, NJ: John Wiley & Sons, Inc.
- Church, W. H., Justice, J. B. Jr., and Byrd, L. D. (1987). Extracellular dopamine in rat striatum following uptake inhibition by cocaine, nomifensine and benztropine. *Eur. J. Pharmacol.* 139, 345–348. doi: 10.1016/0014-2999(87)90592-9
- Clapp-Lilly, K. L., Roberts, R. C., Duffy, L. K., Irons, K. P., Hu, Y., and Drew, K. L. (1999). An ultrastructural analysis of tissue surrounding a microdialysis probe. *J. Neurosci. Methods* 90, 129–142. doi: 10.1016/S0165-0270(99)00064-3
- Darvesh, A. S., Carroll, R. T., Geldenhuys, W. J., Gudelsky, G. A., Klein, J., Meshul, C. K., et al. (2011). In vivo brain microdialysis: advances in neuropsychopharmacology and drug discovery. *Exp. Opin. Drug Discov.* 6, 109–127. doi: 10.1517/17460441.2011.547189
- Dixon, C. E., Lyeth, B. G., Povlishock, J. T., Findling, R. L., Hamm, R. J., Marmarou, A., et al. (1987). A fluid percussion model of experimental brain injury in the rat. *J. Neurosurg.* 67, 110–119. doi: 10.3171/jns.1987.67.1.0110
- Dreier, J. P. (2011). The role of spreading depression, spreading depolarization and spreading ischemia in neurological disease. *Nat. Med.* 17, 439–447. doi: 10.1038/nm.2333
- Dreier, J. P., Bhatia, R., Major, S., Drenckhahn, C., Lehmann, T. N., Sarrafzadeh, A., et al. (2006a). Delayed ischaemic neurological deficits after subarachnoid haemorrhage are associated with clusters of spreading depolarizations. *Brain* 129, 3224–3237.
- Dreier, J. P., Fabricius, M., Ayata, C., Sakowitz, O. W., Shuttleworth, C. W., Dohmen, C., et al. (2016). Recording, analysis, and interpretation of spreading depolarizations in neurointensive care: review and recommendations of the COSBID research group. *J. Cereb. Blood Flow Metab.* 37, 1595–1625.
- Dreier, J. P., Major, S., Manning, A., Woitzik, J., Drenckhahn, C., Steinbrink, J., et al. (2009). Cortical spreading ischaemia is a novel process involved in ischaemic damage in patients with aneurysmal subarachnoid haemorrhage. *Brain* 132, 1866–1881. doi: 10.1093/brain/awp102
- Dreier, J. P., Woitzik, J., Fabricius, M., Bhatia, R., Major, S., Drenckhahn, C., et al. (2006b). Delayed ischaemic neurological deficits after subarachnoid haemorrhage are associated with clusters of spreading depolarizations. *Brain* 129, 3224–3237. doi: 10.1093/brain/awp102
- Dykstra, K. H., Hsiao, J. K., Morrison, P. F., Bungay, P. M., Mefford, I. N., Scully, M. M., et al. (1992). Quantitative examination of tissue concentration profiles associated with microdialysis. *J. Neurochem.* 58, 931–940. doi: 10.1111/j.1471-4159.1992.tb09346.x
- Fabricius, M., Fuhr, S., Bhatia, R., Boutelle, M., Hashemi, P., Strong, A. J., et al. (2006). Cortical spreading depression and peri-infarct depolarization in acutely injured human cerebral cortex. *Brain* 129, 778–790. doi: 10.1093/brain/awh716
- Feuerstein, D., Manning, A., Hashemi, P., Bhatia, R., Fabricius, M., Tolia, C., et al. (2010). Dynamic metabolic response to multiple spreading depolarizations in patients with acute brain injury: an online microdialysis study. *J. Cereb. Blood Flow Metab.* 30, 1343–1355. doi: 10.1038/jcbfm.2010.17
- Garris, P. A., and Wightman, R. M. (1995). *Regional differences in dopamine release, uptake, and diffusion measured by fast-scan cyclic voltammetry. In Voltammetric methods in brain systems*. New York, NY: Springer, 179–220. doi: 10.1385/0-89603-312-0:179

- Gerritsen, M., Jansen, J., and Lutterman, J. (1999). Performance of subcutaneously implanted glucose sensors for continuous monitoring. *Neth. J. Med* 54, 167–179. doi: 10.1016/S0300-2977(99)00006-6
- Ghirnikar, R. S., Lee, Y. L., and Eng, L. F. (1998). Inflammation in traumatic brain injury: role of cytokines and chemokines. *Neurochem. Res.* 23, 329–340. doi: 10.1023/A:102245332560
- Gifford, R., Kehoe, J. J., Barnes, S. L., Kornilayev, B. A., Alterman, M. A., and Wilson, G. S. J. B. (2006). Protein interactions with subcutaneously implanted biosensors. *Biomaterials* 27, 2587–2598. doi: 10.1016/j.biomaterials.2005.11.033
- Globus, M. Y., Alonso, O., Dietrich, W. D., Busto, R., and Ginsberg, M. D. (1995). Glutamate release and free radical production following brain injury: effects of posttraumatic hypothermia. *J. Neurochem.* 65, 1704–1711. doi: 10.1046/j.1471-4159.1995.65041704.x
- Gordon, S., and Taylor, P. R. (2005). Monocyte and macrophage heterogeneity. *Nat. Rev. Immunol.* 5:953. doi: 10.1038/nri1733
- Gowers, S. A., Rogers, M. L., Booth, M. A., Leong, C. L., Samper, I. C., Phairatana, T., et al. (2019). Clinical translation of microfluidic sensor devices: focus on calibration and analytical robustness. *Lab. Chip* 19, 2537–2548. doi: 10.1039/C9LC00400A
- Gu, H., Varner, E. L., Groskreutz, S. R., Michael, A. C., and Weber, S. G. (2015). In vivo monitoring of dopamine by microdialysis with 1 min temporal resolution using online capillary liquid chromatography with electrochemical detection. *Anal. Chem.* 87, 6088–6094. doi: 10.1021/acs.analchem.5b00633
- Guiou, M., Sheth, S., Nemoto, M., Walker, M., Pouratian, N., Ba, A., et al. (2005). Cortical spreading depression produces long-term disruption of activity-related changes in cerebral blood volume and neurovascular coupling. *J. Biomed. Opt.* 10:0110044–0110047. doi: 10.1117/1.1852556
- Haddad, S. H., and Arabi, Y. M. (2012). Critical care management of severe traumatic brain injury in adults. *Scand. J. Trauma Resuscit. Emerg. Med.* 20:12. doi: 10.1186/1757-7241-20-12
- Hammarlund-Udenaes, M. (2017). Microdialysis as an important technique in systems pharmacology—a historical and methodological review. *AAPS J* 19, 1294–1303. doi: 10.1208/s12248-017-0108-2
- Hartings, J. A., Bullock, M. R., Okonkwo, D. O., Murray, L. S., Murray, G. D., Fabricius, M., et al. (2011a). Spreading depolarisations and outcome after traumatic brain injury: a prospective observational study. *Lancet Neurol.* 10, 1058–1064. doi: 10.1016/S1474-4422(11)70243-5
- Hartings, J. A., Strong, A. J., Fabricius, M., Manning, A., Bhatia, R., Dreier, J. P., et al. (2009). Spreading depolarizations and late secondary insults after traumatic brain injury. *J. Neurotrauma* 26, 1857–1866. doi: 10.1089/neu.2009.0961
- Hartings, J. A., Watanabe, T., Bullock, M. R., Okonkwo, D. O., Fabricius, M., Woitzik, J., et al. (2011b). Spreading depolarizations have prolonged direct current shifts and are associated with poor outcome in brain trauma. *Brain* 134(Pt. 5), 1529–1540. doi: 10.1093/brain/awr048
- Hashemi, P., Bhatia, R., Nakamura, H., Dreier, J. P., Graf, R., Strong, A. J., et al. (2009). Persisting depletion of brain glucose following cortical spreading depression, despite apparent hyperaemia: evidence for risk of an adverse effect of Leao's spreading depression. *J. Cereb. Blood Flow Metab.* 29, 166–175. doi: 10.1038/jcbfm.2008.108
- Helmy, A., Carpenter, K. L., Skepper, J. N., Kirkpatrick, P. J., Pickard, J. D., and Hutchinson, P. J. (2009). Microdialysis of cytokines: methodological considerations, scanning electron microscopy, and determination of relative recovery. *J. Neurotrauma* 26, 549–561. doi: 10.1089/neu.2008.0719
- Hempen, C., Weiss, E., and Hess, C. F. (2002). Dexamethasone treatment in patients with brain metastases and primary brain tumors: do the benefits outweigh the side-effects? *Support Care Cancer* 10, 322–328. doi: 10.1007/s00520-001-0333-0
- Hickey, T., Kreutzer, D., Burgess, D., and Moussy, F. (2002). In vivo evaluation of a dexamethasone/PLGA microsphere system designed to suppress the inflammatory tissue response to implantable medical devices. *J. Biomed. Mater. Res.* 61, 180–187. doi: 10.1002/jbm.10016
- Huang, C.-M., Nakatsuiji, T., Liu, Y.-T., and Shi, Y. J. R. (2008). In vivo tumor secretion probing via ultrafiltration and tissue chamber: implication for anti-cancer drugs targeting secretome. *Recent Pat. Anticancer Drug Discov.* 3, 48–54. doi: 10.2174/157489208783478694
- Hutchinson, P. J., O'Connell, M. T., Al-Rawi, P. G., Maskell, L. B., Kett-White, R., Gupta, A. K., et al. (2000). Clinical cerebral microdialysis: a methodological study. *J. Neurosurg.* 93, 37–43. doi: 10.3171/jns.2000.93.1.0037
- Jaquins-Gerstl, A., and Michael, A. C. (2009). Comparison of the brain penetration injury associated with microdialysis and voltammetry. *J. Neurosci. Methods* 183, 127–135. doi: 10.1016/j.jneumeth.2009.06.023
- Jaquins-Gerstl, A., Shu, Z., Zhang, J., Liu, Y., Weber, S. G., and Michael, A. C. (2011). Effect of dexamethasone on gliosis, ischemia, and dopamine extraction during microdialysis sampling in brain tissue. *Anal. Chem.* 83, 7662–7667. doi: 10.1021/ac200782h
- Jones, D., Parkin, M., Langemann, H., Landolt, H., and Hopwood, S. (2002). On-line monitoring in neurointensive care: enzyme-based electrochemical assay for simultaneous, continuous monitoring of glucose and lactate from critical care patients. *J. Electroanal. Chem.* 538, 243–252. doi: 10.1016/S0022-0728(02)00839-2
- Keeler, G. D., Durdik, J. M., and Stenken, J. A. (2015a). Effects of delayed delivery of dexamethasone-21-phosphate via subcutaneous microdialysis implants on macrophage activation in rats. *Acta Biomater.* 23, 27–37. doi: 10.1016/j.actbio.2015.05.011
- Keeler, G. D., Durdik, J. M., and Stenken, J. A. (2015b). Localized delivery of dexamethasone-21-phosphate via microdialysis implants in rat induces M (GC) macrophage polarization and alters CCL2 concentrations. *Acta Biomater.* 12, 11–20. doi: 10.1016/j.actbio.2014.10.022
- Kennedy, R. T., Yoon, H. J., Ngernsativorakul, T., and Lee, W. H. (2018). *Microfabrication of a Microdialysis Probe With Nanoporous Membrane*. U.S. Patent No WO2017100028. Washington, DC: U.S. Patent and Trademark Office.
- Kim, D. H., and Martin, D. C. J. B. (2006). Sustained release of dexamethasone from hydrophilic matrices using PLGA nanoparticles for neural drug delivery. *Biomaterials* 27, 3031–3037. doi: 10.1016/j.biomaterials.2005.12.021
- Kim, D. H., Smith, J. T., Chilkoti, A., and Reichert, W. M. J. B. (2007). The effect of covalently immobilized rhIL-1ra-ELP fusion protein on the inflammatory profile of LPS-stimulated human monocytes. *Biomaterials* 28, 3369–3377. doi: 10.1016/j.biomaterials.2007.04.010
- Klueh, U., Kaur, M., Montrose, D. C., and Kreutzer, D. L. (2007). Inflammation and glucose sensors: use of dexamethasone to extend glucose sensor function and life span in vivo. *J. Diabetes Sci. Technol.* 1, 496–504. doi: 10.1177/193229680700100407
- Koh, A., Lu, Y., and Schoenfisch, M. H. J. A. C. (2013). Fabrication of nitric oxide-releasing porous polyurethane membranes-coated needle-type implantable glucose biosensors. *Anal. Chem.* 85, 10488–10494. doi: 10.1021/ac402312b
- Kozai, T. D., Jaquins-Gerstl, A. S., Vazquez, A. L., Michael, A. C., and Cui, X. T. (2015). Brain tissue responses to neural implants impact signal sensitivity and intervention strategies. *ACS Chem. Neurosci.* 6, 48–67. doi: 10.1021/cn500256e
- Kozai, T. D. Y., Jaquins-Gerstl, A. S., Vazquez, A. L., Michael, A. C., and Cui, X. T. (2016). Dexamethasone retrodialysis attenuates microglial response to implanted probes in vivo. *Biomaterials* 87, 157–169. doi: 10.1016/j.biomaterials.2016.02.013
- Kozai, T. D. Y., Kipke, D. R., and Subbaroyan, J. (2017). *Probe Insertion Device for Implanting a Probe Into Tissue*. U.S. Patent No US9814489B2. Washington, DC: U.S. Patent and Trademark Office.
- Kozai, T. D. Y., Vazquez, A. L., Weaver, C. L., Kim, S.-G., and Cui, X. T. (2012). In vivo two-photon microscopy reveals immediate microglial reaction to implantation of microelectrode through extension of processes. *J. Neural. Eng.* 9:066001. doi: 10.1088/1741-2560/9/6/066001
- Lammers, T., Sofias, A. M., van der Meel, R., Schiffelers, R., Storm, G., Tacke, F., et al. (2020). Dexamethasone nanomedicines for COVID-19. *Nat. Nanotechnol.* 15, 622–624. doi: 10.1038/s41565-020-0752-z
- Lauritzen, M., Dreier, J. P., Fabricius, M., Hartings, J. A., Graf, R., and Strong, A. J. (2011). Clinical relevance of cortical spreading depression in neurological disorders: migraine, malignant stroke, subarachnoid and intracranial hemorrhage, and traumatic brain injury. *J. Cereb. Blood Flow Metab.* 31, 17–35. doi: 10.1038/jcbfm.2010.191
- Lee, W. H., Slaney, T. R., Hower, R. W., and Kennedy, R. T. (2013). Microfabricated sampling probes for in vivo monitoring of neurotransmitters. *Anal. Chem.* 85, 3828–3831. doi: 10.1021/ac400579x



- Lefkowitz, D. L., and Lefkowitz, S. S. J. I. (2001). Macrophage-neutrophil interaction: a paradigm for chronic inflammation revisited. *Immunol. Cell Biol.* 79, 502–506. doi: 10.1046/j.1440-1711.2001.01020.x
- Li, Q., Zubietta, J. K., and Kennedy, R. T. (2009). Practical aspects of in vivo detection of neuropeptides by microdialysis coupled off-line to capillary LC with multistage MS. *Anal. Chem.* 81, 2242–2250. doi: 10.1021/ac802391b
- Lindfors, N., Brodin, E., and Ungerstedt, U. (1989). Amphetamine facilitates the in vivo release of neurokinin A in the nucleus accumbens of the rat. *Eur. J. Pharmacol.* 160, 417–420. doi: 10.1016/0014-2999(89)90100-3
- Liu, Y., Zhang, J., Xu, X., Zhao, M., Andrews, A. M., and Weber, S. G. (2010). Capillary ultrahigh performance liquid chromatography with elevated temperature for sub-one minute separations of basal serotonin in submicroliter brain microdialysate samples. *Anal. Chem.* 82, 9611–9616. doi: 10.1021/ac102200q
- Lotharius, J., and Brundin, P. J. N. R. N. (2002). Pathogenesis of Parkinson's disease: dopamine, vesicles and  $\alpha$ -synuclein. *Nat. Rev. Neurosci.* 3, 932. doi: 10.1038/nrn983
- Lu, Y., Peters, J. L., and Michael, A. C. (1998). Direct comparison of the response of voltammetry and microdialysis to electrically evoked release of striatal dopamine. *J. Neurochem.* 70, 584–593. doi: 10.1046/j.1471-4159.1998.70020584.x
- Luo, X., Matrangola, C., Tan, S., Alba, N., and Cui, X. T. J. B. (2011). Carbon nanotube nanoreservoir for controlled release of anti-inflammatory dexamethasone. *Biomaterials* 32, 6316–6323. doi: 10.1016/j.biomaterials.2011.05.020
- Mantovani, A., Biswas, S. K., Galdiero, M. R., Sica, A., and Locati, M. (2013). Macrophage plasticity and polarization in tissue repair and remodelling. *J. Pathol.* 229, 176–185. doi: 10.1002/path.4133
- Martinez, F. O. (2011). Regulators of macrophage activation. *Eur. J. Immunol.* 41, 1531–1534. doi: 10.1002/eji.201141670
- Mercanzini, A., Reddy, S. T., Velluto, D., Colin, P., Maillard, A., Bensadoun, J.-C., et al. (2010). Controlled release nanoparticle-embedded coatings reduce the tissue reaction to neuroprostheses. *J. Control. Rel.* 145, 196–202. doi: 10.1016/j.jconrel.2010.04.025
- Michael, A. C., and Borland, L. (2006). *Electrochemical Methods for Neuroscience*. Boca Raton, FL: CRC press. doi: 10.1201/9781420005868
- Mitala, C. M., Wang, Y., Borland, L. M., Jung, M., Shand, S., Watkins, S., et al. (2008). Impact of microdialysis probes on vasculature and dopamine in the rat striatum: a combined fluorescence and voltammetric study. *J. Neurosci. Methods* 174, 177–185. doi: 10.1016/j.jneumeth.2008.06.034
- Nakamura, H., Strong, A. J., Dohmen, C., Sakowitz, O. W., Vollmar, S., Sue, M., et al. (2010). Spreading depolarizations cycle around and enlarge focal ischaemic brain lesions. *Brain* 133, 1994–2006. doi: 10.1093/brain/awq117
- Nakase, H., Okazaki, K., Tabata, Y., Ozeki, M., Watanabe, N., Ohana, M., et al. (2002). New cytokine delivery system using gelatin microspheres containing interleukin-10 for experimental inflammatory bowel disease. *J. Pharmacol. Exp. Ther.* 301, 59–65. doi: 10.1124/jpet.301.1.59
- Nesbitt, K. M. (2015). *Retrodialysis of Pharmacological Agents Mitigates Tissue Damage during Brain Microdialysis and Preserves Dopamine Activity in Surrounding Tissue*. Pittsburgh, PA: University of Pittsburgh.
- Nesbitt, K. M., Jaquins-Gerstl, A., Skoda, E. M., Wipf, P., and Michael, A. C. (2013). Pharmacological Mitigation of Tissue Damage during Brain Microdialysis. *Anal. Chem.* 85, 8173–8179. doi: 10.1021/ac401201x
- Nesbitt, K. M., Varner, E. L., Jaquins-Gerstl, A., and Michael, A. C. (2015). Microdialysis in the rat striatum: effects of 24 h dexamethasone retrodialysis on evoked dopamine release and penetration injury. *ACS Chem. Neurosci.* 6, 163–173. doi: 10.1021/cn500257x
- Ngernsuvivorakul, T., Steyer, D. J., Valenta, A. C., and Kennedy, R. T. (2018). In vivo chemical monitoring at high spatiotemporal resolution using microfabricated sampling probes and droplet-based microfluidics coupled to mass spectrometry. *Anal. Chem.* 90, 10943–10950. doi: 10.1021/acs.analchem.8b02468
- Nichols, S. P., Koh, A., Brown, N. L., Rose, M. B., Sun, B., Slomberg, D. L., et al. (2012). The effect of nitric oxide surface flux on the foreign body response to subcutaneous implants. *Biomaterials* 33, 6305–6312. doi: 10.1016/j.biomaterials.2012.05.053
- Nimmerjahn, A., Kirchhoff, F., and Helmchen, F. J. S. (2005). Resting microglial cells are highly dynamic surveillants of brain parenchyma in vivo. *Science* 308, 1314–1318. doi: 10.1126/science.1110647
- Norton, L., Tegnell, E., Toporek, S., and Reichert, W. J. B. (2005). In vitro characterization of vascular endothelial growth factor and dexamethasone releasing hydrogels for implantable probe coatings. *Biomaterials* 26, 3285–3297. doi: 10.1016/j.biomaterials.2004.07.069
- Osier, N. D., and Dixon, C. E. (2016). The controlled cortical impact model: applications, considerations for researchers, and future directions. *Front. Neurol.* 7:134. doi: 10.3389/fneur.2016.00134
- Pagkalos, I., Rogers, M. L., Boutelle, M. G., and Drakakis, E. M. J. C. (2018). A high-performance application specific integrated circuit for electrical and neurochemical traumatic brain injury monitoring. *Chemphyschem* 19, 1215–1225. doi: 10.1002/cphc.201701119
- Papadimitriou, K. I., Wang, C., Rogers, M. L., Gowers, S. A., Leong, C. L., Boutelle, M. G., et al. (2016). High-performance bioinstrumentation for real-time neuroelectrochemical traumatic brain injury monitoring. *Front. Hum. Neurosci.* 10:212. doi: 10.3389/fnhum.2016.00212
- Parkin, M., Hopwood, S., Jones, D. A., Hashemi, P., Landolt, H., Fabricius, M., et al. (2005). Dynamic changes in brain glucose and lactate in pericontusional areas of the human cerebral cortex, monitored with rapid sampling on-line microdialysis: relationship with depolarisation-like events. *J. Cereb. Blood Flow Metab.* 25, 402–413. doi: 10.1038/sj.jcbfm.9600051
- Parsons, L., Smith, A., and Justice, J. (1991). The in vivo microdialysis recovery of dopamine is altered independently of basal level by 6-hydroxydopamine lesions to the nucleus accumbens. *J. Neurosci. Methods* 40, 139–147. doi: 10.1016/0165-0270(91)90063-6
- Patacsil, J. A., McAuliffe, M. S., Feyh, L. S., and Sigmon, L. L. (2016). Local anesthetic adjuvants providing the longest duration of analgesia for single-injection peripheral nerve blocks in orthopedic surgery: a literature review. *Aana J.* 84, 95–103.
- Perry, M., Li, Q., and Kennedy, R. T. (2009). Review of recent advances in analytical techniques for the determination of neurotransmitters. *Anal. Chim. Acta* 653, 1–22. doi: 10.1016/j.aca.2009.08.038
- Phillips, P. E., Stuber, G. D., Heien, M. L., Wightman, R. M., and Carelli, R. M. J. N. (2003). Subsecond dopamine release promotes cocaine seeking. *Nature* 422:614. doi: 10.1038/nature01476
- Polikov, V. S., Tresco, P. A., and Reichert, W. M. (2005). Response of brain tissue to chronically implanted neural electrodes. *J. Neurosci. Methods* 148, 1–18. doi: 10.1016/j.jneumeth.2005.08.015
- Pontieri, F. E., Tanda, G., and Di Chiara, G. (1995). Intravenous cocaine, morphine, and amphetamine preferentially increase extracellular dopamine in the “shell” as compared with the “core” of the rat nucleus accumbens. *Proc. Natl. Acad. Sci. U.S.A.* 92, 12304–12308. doi: 10.1073/pnas.92.26.12304
- Robbins, E. M., Jaquins-Gerstl, A., Fine, D. F., Leong, C. L., Dixon, C. E., Wagner, A. K., et al. (2019). Extended (10-Day) real-time monitoring by dexamethasone-enhanced microdialysis in the injured rat cortex. *ACS Chem. Neurosci.* 10, 3521–3531. doi: 10.1021/acschemneuro.9b00145
- Roberts, P. J., and Anderson, S. D. (1979). Stimulatory effect of L-glutamate and related amino acids on [3H]dopamine release from rat striatum: an in vitro model for glutamate actions. *J. Neurochem.* 32, 1539–1545. doi: 10.1111/j.1471-4159.1979.tb11096.x
- Robinson, D. L., Venton, B. J., Heien, M. L., and Wightman, R. M. (2003). Detecting subsecond dopamine release with fast-scan cyclic voltammetry in vivo. *Clin. Chem.* 49, 1763–1773. doi: 10.1373/49.10.1763
- Robinson, T. E., and Justice, J. B. (eds) (1991). *Techniques in the Behavioral and Neural Sciences*. Amsterdam: Elsevier.
- Rogers, M. L., Feuerstein, D., Leong, C. L., Takagaki, M., Niu, X., Graf, R., et al. (2013). Continuous online microdialysis using microfluidic sensors: dynamic neurometabolic changes during spreading depolarization. *ACS Chem. Neurosci.* 4, 799–807. doi: 10.1021/cn400047x
- Rogers, M. L., Leong, C. L., Gowers, S. A., Samper, I. C., Jewell, S. L., Khan, A., et al. (2017). Simultaneous monitoring of potassium, glucose and lactate during spreading depolarization in the injured human brain—proof of principle of a novel real-time neurochemical analysis system, continuous online microdialysis. *J. Cereb. Blood Flow Metab.* 37, 1883–1895. doi: 10.1177/0271678X16674486
- Sanchez, J. J., Bidot, C. J., O'Phelan, K., Gajavelli, S., Yokobori, S., Olvey, S., et al. (2013). Neuromonitoring with microdialysis in severe traumatic brain injury patients. *Acta Neurochir. Suppl.* 118, 223–227. doi: 10.1007/978-3-7091-1434-6\_42



- Santiago, M., and Westerink, B. H. (1990). Characterization of the in vivo release of dopamine as recorded by different types of intracerebral microdialysis probes. *Naunyn Schmiedebergs Arch. Pharmacol.* 342, 407–414. doi: 10.1007/BF00169457
- Schmidt, M. H., Pauels, G., Lügering, N., Lügering, A., Domschke, W., and Kucharzik, T. J. (1999). Glucocorticoids induce apoptosis in human monocytes: potential role of IL-1 $\beta$ . *J. Immunol.* 163, 3484–3490.
- Schuck, V. J., Rinas, L., and Derendorf, H. (2004). In vitro microdialysis sampling of docetaxel. *J. Pharm. Biomed. Anal.* 36, 807–813. doi: 10.1016/j.jpba.2004.07.007
- Schultz, W. (2007). Multiple dopamine functions at different time courses. *Annu. Rev. Neurosci.* 30, 259–288. doi: 10.1146/annurev.neuro.28.061604.135722
- Seule, M., Keller, E., Unterberg, A., and Sakowitz, O. (2015). The hemodynamic response of spreading depolarization observed by near infrared spectroscopy after aneurysmal subarachnoid hemorrhage. *Neurocrit. Care* 23, 108–112. doi: 10.1007/s12028-015-0111-3
- Shain, W., Spataro, L., Dilgen, J., Haverstick, K., Retterer, S., Isaacson, M., et al. (2003). Controlling cellular reactive responses around neural prosthetic devices using peripheral and local intervention strategies. *IEEE Trans. Neural Syst. Rehabil. Eng.* 11, 186–188. doi: 10.1109/TNSRE.2003.814800
- Shippenberg, T. S., and Thompson, A. C. (2001). Overview of microdialysis. *Curr. Protoc. Neurosci.* 7:7.1. doi: 10.1002/0471142301.ns0701s00
- Shou, M., Ferrario, C. R., Schultz, K. N., Robinson, T. E., and Kennedy, R. T. (2006). Monitoring dopamine in vivo by microdialysis sampling and on-line CE-laser-induced fluorescence. *Anal. Chem.* 78, 6717–6725. doi: 10.1021/ac0608218
- Spataro, L., Dilgen, J., Retterer, S., Spence, A., Isaacson, M., Turner, J., et al. (2005). Dexamethasone treatment reduces astroglia responses to inserted neuroprosthetic devices in rat neocortex. *Exp. Neurol.* 194, 289–300. doi: 10.1016/j.expneurol.2004.08.037
- Stauffer, W. M., Alpern, J. D., and Walker, P. F. (2020). COVID-19 and dexamethasone: a potential strategy to avoid steroid-related stronglylides hyperinfection. *JAMA* 324, 623–624. doi: 10.1001/jama.2020.13170
- Stence, N., Waite, M., and Dailey, M. E. (2001). Dynamics of microglial activation: a confocal time-lapse analysis in hippocampal slices. *Glia* 33, 256–266. doi: 10.1002/1098-1136(200103)33:3<256::AID-GLIA1024>3.0.CO;2-J
- Stenzen, J. A. (1999). Methods and issues in microdialysis calibration. *Anal. Chim. Acta* 379, 337–358. doi: 10.1016/S0003-2670(98)00598-4
- Stenzen, J. A., Chen, R., and Yuan, X. (2001). Influence of geometry and equilibrium chemistry on relative recovery during enhanced microdialysis. *Anal. Chim. Acta* 436, 21–29. doi: 10.1016/S0003-2670(01)00885-6
- Stenzen, J. A., Church, M. K., Gill, C. A., and Clough, G. F. (2010). How minimally invasive is microdialysis sampling? A cautionary note for cytokine collection in human skin and other clinical studies. *AAPS J.* 12, 73–78. doi: 10.1208/s12248-009-9163-7
- Stenzen, J. A., Lunte, C. E., Southard, M. Z., and Stahle, L. (1997). Factors that influence microdialysis recovery. *Comparison of experimental and theoretical microdialysis recoveries in rat liver. J. Pharm. Sci.* 86, 958–966. doi: 10.1021/js960269+
- Strong, A. J., Boutelle, M. G., Vespa, P. M., Bullock, M. R., Bhatia, R., and Hashemi, P. (2005). Treatment of critical care patients with substantial acute ischemic or traumatic brain injury. *Crit. Care Med.* 33, 2147–2149. doi: 10.1097/01.CCM.0000179029.95415.51
- Strong, A. J., Fabricius, M., Boutelle, M. G., Hibbins, S. J., Hopwood, S. E., Jones, R., et al. (2002). Spreading and synchronous depressions of cortical activity in acutely injured human brain. *Stroke* 33, 2738–2743. doi: 10.1161/01.STR.0000043073.69602.09
- Strong, A. J., Hartings, J. A., and Dreier, J. P. (2007). Cortical spreading depression: an adverse but treatable factor in intensive care? *Curr. Opin. Crit. Care* 13, 126–133. doi: 10.1097/MCC.0b013e32807faffb
- Szarowski, D. H., Andersen, M. D., Retterer, S., Spence, A. J., Isaacson, M., Craighead, H. G., et al. (2003). Brain responses to micro-machined silicon devices. *Brain Res.* 983, 23–35. doi: 10.1016/S0006-8993(03)00323-3
- Torto, N., Gorton, L., Laurell, T., and Marko-Varga, G. (1999). Technical issues of in vitro microdialysis sampling in bioprocess monitoring. *Trends Anal. Chem.* 18, 252–260. doi: 10.1016/S0165-9936(98)00115-0
- Tremblay, M. É., Lowery, R. L., and Majewska, A. K. (2010). Microglial interactions with synapses are modulated by visual experience. *PLoS Biol.* 8:e1000527. doi: 10.1371/journal.pbio.1000527
- Turner, J. N., Shain, W., Szarowski, D. H., Andersen, M., Martins, S., Isaacson, M., et al. (1999). Cerebral astrocyte response to micromachined silicon implants. *Exp. Neurol.* 156, 33–49. doi: 10.1006/exnr.1998.6983
- Ungerstedt, U. (1984). “Measurement of neurotransmitter release by intracranial dialysis,” in *In Measurement of Neurotransmitter Release In Vivo*, ed. C. A. Marsden (New York, NY: John Wiley & Sons), 81–105.
- Ungerstedt, U. (1991). Microdialysis—principles and applications for studies in animals and man. *J. Intern. Med.* 230, 365–373. doi: 10.1111/j.1365-2796.1991.tb00459.x
- Ungerstedt, U., and Rostami, E. (2004). Microdialysis in neurointensive care. *Curr. Pharm. Des.* 10, 2145–2152. doi: 10.2174/1381612043384105
- Van Coillie, E., Van Damme, J., and Opdenakker, G. J. C. (1999). The MCP/eotaxin subfamily of CC chemokines. *Cytokine Growth Factor Rev.* 10, 61–86. doi: 10.1016/S1359-6101(99)00005-2
- Varner, E. L., Jacquins-Gerstl, A., and Michael, A. C. (2016). Enhanced intracranial microdialysis by reduction of traumatic penetration injury at the probe track. *ACS Chem. Neurosci.* 7, 728–736. doi: 10.1021/acscchemneuro.5b00331
- Varner, E. L., Leong, C. L., Jacquins-Gerstl, A., Nesbitt, K. M., Boutelle, M. G., and Michael, A. C. (2017). Enhancing continuous online microdialysis using dexamethasone: measurement of dynamic neurometabolic changes during spreading depolarization. *ACS Chem. Neurosci.* 8, 1779–1788. doi: 10.1021/acscchemneuro.7b00148
- Wagner, A. K., Sokoloski, J. E., Ren, D., Chen, X., Khan, A. S., Zafonte, R. D., et al. (2005). Controlled cortical impact injury affects dopaminergic transmission in the rat striatum. *J. Neurochem.* 95, 457–465. doi: 10.1111/j.1471-4159.2005.03382.x
- Wake, H., Moorhouse, A. J., Jinno, S., Kohsaka, S., and Nabekura, J. J. (2009). Resting microglia directly monitor the functional state of synapses in vivo and determine the fate of ischemic terminals. *J. Neurosci.* 29, 3974–3980. doi: 10.1523/JNEUROSCI.4363-08.2009
- Wang, M., Slaney, T., Mabrouk, O., and Kennedy, R. T. (2010). Collection of nanoliter microdialysate fractions in plugs for off-line in vivo chemical monitoring with up to 28 channels; temporal resolution. *J. Neurosci. Methods* 190, 39–48. doi: 10.1016/j.jneumeth.2010.04.023
- Wang, Y., Ma, Y. Y., Song, X. L., Cai, H. Y., Chen, J. C., Song, L. N., et al. (2012). Upregulations of glucocorticoid-induced leucine zipper by hypoxia and glucocorticoid inhibit proinflammatory cytokines under hypoxic conditions in macrophages. *J. Immunol.* 188:222. doi: 10.4049/jimmunol.1002958
- Wang, Y., and Michael, A. C. (2012). Microdialysis probes alter presynaptic regulation of dopamine terminals in rat striatum. *J. Neurosci. Methods* 208, 34–39. doi: 10.1016/j.jneumeth.2012.04.009
- Watson, C. J., Venton, B. J., and Kennedy, R. T. (2006). In vivo measurements of neurotransmitters by microdialysis sampling. *Anal. Chem.* 78, 1391–1399. doi: 10.1021/ac0693722
- Webber, M. J., Matson, J. B., Tamboli, V. K., and Stupp, S. I. (2012). Controlled release of dexamethasone from peptide nanofiber gels to modulate inflammatory response. *Biomaterials* 33, 6823–6832. doi: 10.1016/j.biomaterials.2012.06.003
- Westerink, B. H., and Cremers, T. I. (2007). *Handbook of Microdialysis: Methods, Applications and Perspectives*. Cambridge, MA: Academic Press.
- Wilson, G. S., and Michael, A. C. (2017). *Compendium Of In Vivo Monitoring In Real-time Molecular Neuroscience-Volume 2: Microdialysis And Sensing Of Neural Tissues*. Singapore: World Scientific Publishing Company. doi: 10.1142/10462
- Winslow, B. D., and Tresco, P. A. (2010). Quantitative analysis of the tissue response to chronically implanted microwire electrodes in rat cortex. *Biomaterials* 31, 1558–1567. doi: 10.1016/j.biomaterials.2009.11.049
- Wisniewski, N., Klitzman, B., Miller, B., and Reichert, W. M. (2001). Decreased analyte transport through implanted membranes: differentiation of biofouling from tissue effects. *J. Biomed. Mater. Res.* 57, 513–521. doi: 10.1002/1097-4636(20011215)57:4<513::AID-JBM1197>3.0.CO;2-E
- Wisniewski, N., Moussy, F., and Reichert, W. J. (2000). Characterization of implantable biosensor membrane biofouling. *Fresen. J. Anal. Chem.* 366, 611–621. doi: 10.1007/s002160051556
- Wisniewski, N., and Reichert, M. J. C. (2000). Methods for reducing biosensor membrane biofouling. *Coll. Surf. B Biointerface* 18, 197–219. doi: 10.1016/S0927-7765(99)00148-4

- Xiong, Y., Mahmood, A., and Chopp, M. (2013). Animal models of traumatic brain injury. *Nat. Rev. Neurosci.* 14, 128–142. doi: 10.1038/nrn3407
- Yang, H., and Michael, A. C. (2007). “In vivo fast-scan cyclic voltammetry of dopamine near microdialysis probes,” in *Electrochemical Methods for Neuroscience*, eds A. C. Michael and L. M. Borland (Boca Raton, FL: CRC Press). doi: 10.1201/9781420005868.ch22
- Yang, H., Thompson, A. B., McIntosh, B. J., Altieri, S. C., and Andrews, A. M. (2013). Physiologically relevant changes in serotonin resolved by fast microdialysis. *ACS Chem. Neurosci.* 4, 790–798. doi: 10.1021/cn400072f
- Zachman, A. L., Crowder, S. W., Ortiz, O., Zienkiewicz, K. J., Bronikowski, C. M., Yu, S. S., et al. (2012). Pro-angiogenic and anti-inflammatory regulation by functional peptides loaded in polymeric implants for soft tissue regeneration. *Tissue Eng. Part A* 19, 437–447. doi: 10.1089/ten.tea.2012.0158
- Zha, Q., Wang, Y., Fan, Y., and Zhu, M. Y. (2011). Dexamethasone-induced up-regulation of the human norepinephrine transporter involves the glucocorticoid receptor and increased binding of C/EBP- $\beta$  to the proximal promoter of norepinephrine transporter. *J. Neurochem.* 119, 654–663. doi: 10.1111/j.1471-4159.2011.07448.x
- Zhang, J., Jacquins-Gerstl, A., Nesbitt, K. M., Rutan, S. C., Michael, A. C., and Weber, S. G. (2013). In vivo monitoring of serotonin in the striatum of freely moving rats with one minute temporal resolution by online microdialysis-capillary high-performance liquid chromatography at elevated temperature and pressure. *Anal. Chem.* 85, 9889–9897. doi: 10.1021/ac4023605
- Zhong, Y., and Bellamkonda, R. V. (2005). Controlled release of anti-inflammatory agent alpha-MSH from neural implants. *J. Control. Rel.* 106, 309–318. doi: 10.1016/j.jconrel.2005.05.012
- Zhong, Y., and Bellamkonda, R. V. (2007). Dexamethasone-coated neural probes elicit attenuated inflammatory response and neuronal loss compared to uncoated neural probes. *Brain Res.* 1148, 15–27. doi: 10.1016/j.brainres.2007.02.024
- Zhou, F., Zhu, X., Castellani, R. J., Stimmelmayer, R., Perry, G., Smith, M. A., et al. (2001). Hibernation, a model of neuroprotection. *Am. J. Pathol.* 158, 2145–2151. doi: 10.1016/S0002-9440(10)64686-X

**Conflict of Interest:** The authors declare that the research was conducted in the absence of any commercial or financial relationships that could be construed as a potential conflict of interest.

Copyright © 2020 Jacquins-Gerstl and Michael. This is an open-access article distributed under the terms of the Creative Commons Attribution License (CC BY). The use, distribution or reproduction in other forums is permitted, provided the original author(s) and the copyright owner(s) are credited and that the original publication in this journal is cited, in accordance with accepted academic practice. No use, distribution or reproduction is permitted which does not comply with these terms.



# Disentangling Biomolecular Corona Interactions With Cell Receptors and Implications for Targeting of Nanomedicines

Aldy Aliyandi<sup>1</sup>, Inge S. Zuhorn<sup>2\*</sup> and Anna Salvati<sup>1\*</sup>

<sup>1</sup> Department of Nanomedicine & Drug Targeting, Groningen Research Institute of Pharmacy, University of Groningen, Groningen, Netherlands, <sup>2</sup> Department of Biomedical Engineering, University of Groningen, University Medical Center Groningen, Groningen, Netherlands

## OPEN ACCESS

### Edited by:

Valentina Castagnola,  
Italian Institute of Technology (IIT), Italy

### Reviewed by:

Giulio Caracciolo,  
Sapienza University of Rome, Italy  
Michihiro Nakamura,  
Yamaguchi University, Japan

### \*Correspondence:

Inge S. Zuhorn  
i.zuhorn@umcg.nl  
Anna Salvati  
a.salvati@rug.nl

### Specialty section:

This article was submitted to  
Biomaterials,  
a section of the journal  
Frontiers in Bioengineering and  
Biotechnology

**Received:** 27 August 2020

**Accepted:** 17 November 2020

**Published:** 10 December 2020

### Citation:

Aliyandi A, Zuhorn IS and  
Salvati A (2020) Disentangling  
Biomolecular Corona Interactions  
With Cell Receptors and Implications  
for Targeting of Nanomedicines.  
Front. Bioeng. Biotechnol. 8:599454.  
doi: 10.3389/fbioe.2020.599454

Nanoparticles are promising tools for nanomedicine in a wide array of therapeutic and diagnostic applications. Yet, despite the advances in the biomedical applications of nanomaterials, relatively few nanomedicines made it to the clinics. The formation of the biomolecular corona on the surface of nanoparticles has been known as one of the challenges toward successful targeting of nanomedicines. This adsorbed protein layer can mask targeting moieties and creates a new biological identity that critically affects the subsequent biological interactions of nanomedicines with cells. Extensive studies have been directed toward understanding the characteristics of this layer of biomolecules and its implications for nanomedicine outcomes at cell and organism levels, yet several aspects are still poorly understood. One aspect that still requires further insights is how the biomolecular corona interacts with and is “read” by the cellular machinery. Within this context, this review is focused on the current understanding of the interactions of the biomolecular corona with cell receptors. First, we address the importance and the role of receptors in the uptake of nanoparticles. Second, we discuss the recent advances and techniques in characterizing and identifying biomolecular corona-receptor interactions. Additionally, we present how we can exploit the knowledge of corona-cell receptor interactions to discover novel receptors for targeting of nanocarriers. Finally, we conclude this review with an outlook on possible future perspectives in the field. A better understanding of the first interactions of nanomaterials with cells, and -in particular -the receptors interacting with the biomolecular corona and involved in nanoparticle uptake, will help for the successful design of nanomedicines for targeted delivery.

**Keywords:** nanoparticles, biomolecular corona, cell receptors, uptake, targeting, corona-receptor interactions

## INTRODUCTION

Over the past decades, nano-sized materials have emerged as powerful tools in many application fields, including nanomedicine, where they are used for therapeutic and diagnostic purposes (Peer et al., 2007; Cheng et al., 2015; D’Mello et al., 2017; Shi et al., 2017; Wolfram and Ferrari, 2019). In particular, nanomedicines have been widely exploited for their potential to deliver cancer therapeutics (Peer et al., 2007; Shi et al., 2017; Wolfram and Ferrari, 2019). Thanks to

their size, nano-sized drug carriers can be used to passively target tumor tissue via the so-called enhanced permeation and retention (EPR) effect (Matsumura and Maeda, 1986; Jain, 1987; Danhier et al., 2010; Chauhan and Jain, 2013). Alternatively, they can also be used for active targeting by functionalizing their surface with targeting moieties to reach the tumor. However, the efficacy of EPR and targeting efficiency of nanoparticles are currently under scrutiny, as many nanomedicines designed for either passive or active targeting have resulted in various levels of success and only relatively few of them, primarily passively targeted, made it to the market (Venditto and Szoka, 2013; Danhier, 2016; Lammers et al., 2016; Torrice, 2016; Wilhelm et al., 2016; Sindhwani et al., 2020). It is recognized that a better understanding of how these objects behave at cellular and molecular levels is crucial to improve their clinical success (Iversen et al., 2011; Time to deliver, 2014).

Nanoparticles exhibit unique characteristics that are very different from their bulk counterparts due to specific physicochemical features. For instance, nanoparticles have a large surface area to volume ratio and high surface free energy that makes them extremely reactive. Consequently, pristine nanoparticles will not keep a bare surface upon exposure to a biological environment. In fact, unless they are specifically designed to avoid it, once nanoparticles are in contact with a biological fluid, proteins and other biomolecules will adsorb on the nanoparticle surface forming the so-called “biomolecular corona” (Cedervall et al., 2007a; Mahmoudi et al., 2011; Monopoli et al., 2012; Schöttler et al., 2016b). The formation of this layer is known to have profound effects on the biological outcomes of nanoparticles, including the subsequent interactions with cells (Zuhorn et al., 2002), toxicity (Kim et al., 2014), biodistribution, immune response (Dobrovolskaia et al., 2016), and targeting capability (Salvati et al., 2013; Hadjidemetriou et al., 2015).

In recent years, the complexity and crucial role of the biomolecular corona on the fate of nanoparticles and its impact on targeting efficacy have drawn a massive interest (Ge et al., 2015; Caracciolo et al., 2017; Barui et al., 2019; Liu et al., 2020; Nienhaus et al., 2020). Indeed, extensive research is focused on understanding the many important aspects that can affect nanoparticle targeting efficacy, including for instance nanoparticle physico-chemical properties such as size, shape, charge, elasticity and complex details of how the targeting ligands are exposed and oriented on the nanoparticle surface (Alexis et al., 2008; Decuzzi et al., 2010; Sahay et al., 2010; Albanese et al., 2012; Mahon et al., 2012; Toy et al., 2014; Sykes et al., 2014; Anselmo et al., 2015; Cheng et al., 2015; Hoshyar et al., 2016; Li et al., 2020). All these factors are also known to affect corona composition, together with other details of the environment and exposure conditions, such as for instance the amount and type of serum, the temperature, and the presence of flow and shear stress (Lundqvist et al., 2008; Petros and Desimone, 2010; Tenzer et al., 2011; Vilanova et al., 2016; Shi et al., 2017; Nienhaus et al., 2020). Importantly, it has also emerged that the adsorbed corona layer can be recognized by cell receptors at the cell membrane and that this initial recognition is another crucial step that affects the overall fate of nanoparticles (Lara et al., 2017, 2018; Francia et al., 2019), including their interactions with certain cell types, intracellular trafficking, and

ability to cross biological barriers. However, several aspects of how the biomolecular corona interacts with and is “read” by cells are still poorly understood (Sahay et al., 2010; Duncan and Richardson, 2012). A better understanding of these interactions can help in improving the current design of nanomedicines and achieve targeting.

Within this context, in this review, we will summarize the current understanding of the role of cell receptors on nanoparticle-cell interactions, and in particular how the biomolecular corona interacts with and is recognized by cell receptors. Next, available methods to characterize biomolecular corona-receptor interactions and identify corona proteins associated with increased or decreased nanoparticle uptake will also be discussed and compared. Furthermore, we will discuss how the corona can be exploited for targeting, but also as a tool to identify (novel) receptors for efficient and targeted uptake of nanomedicines. Finally, future perspectives on how to apply this knowledge for better design of targeted nanocarriers are proposed.

## THE ROLE OF RECEPTORS IN NANOPARTICLE UPTAKE

The interaction of nanoparticles with the cell membrane is the first step prior to their internalization. In active targeting, nanoparticles are modified with surface ligands in order to control these first interactions and achieve binding to specific cell receptors. However, even after successful binding to the targeted receptors, other aspects can affect targeting and limit nanomedicine efficacy. The subsequent uptake efficiency and uptake kinetics, as well as the eventual fate of nanoparticles inside cells and details of intracellular distribution kinetics can all be strongly determined by which receptors they initially bind (Zuhorn et al., 2007; Georgieva et al., 2011). In most cases, following endocytosis, nanoparticles typically end up in the lysosomes, and strategies for endosomal escape are being developed in order to allow access to the cytosol and targeting of other intracellular compartments (Rejman et al., 2004; Iversen et al., 2011; Varkouhi et al., 2011; Rehman et al., 2013). At the same time, different intracellular fates can be observed depending on the interactions with different receptors. For instance, in the blood-brain barrier, some receptors, such as insulin receptor, transferrin receptor, and low-density lipoprotein (LDL) receptor, are known to facilitate nanoparticle transport across the cell to reach the underlying tissue (transcytosis) (Georgieva et al., 2014; Pulgar, 2019), while other receptors facilitate nanoparticles to end up in lysosomes, where the drug they deliver may be released and—if not resistant to the lysosomal environment—degraded. Additionally, different receptors may activate uptake via different endocytic mechanisms and the uptake mechanism may affect nanoparticle intracellular fate, as well as uptake efficiency and kinetics (Rejman et al., 2004; Rehman et al., 2011). For instance, stimulation of caveolae-mediated endocytosis is thought to promote transcytosis in peripheral blood vessels as well as in the blood-brain barrier (Andreone et al., 2017; Villaseñor et al., 2019). Therefore, it is of importance to ensure



that nanoparticles bind to the right receptors, so that they end up not only in the right cells, but also in the right cell compartments, and with uptake efficiency and uptake kinetics which are optimal for specific applications (see **Figure 1** for illustration).

## THE ROLE OF THE BIOMOLECULAR CORONA IN NANOPARTICLE UPTAKE

In order to reach their receptors *in vivo*, nanoparticles will be first exposed to a complex biological fluid, such as for instance serum. In this environment, various proteins and other biomolecules will adsorb on the nanoparticle surface forming a biomolecular corona. This layer will then replace the synthetic identity of bare nanoparticles and in some cases it can mask the ligands of functionalized nanoparticles, which may result in the loss of targeting (Salvati et al., 2013; Hadjide metriou et al., 2015). Additionally, some proteins with high binding affinity can strongly adsorb to the nanoparticle surface for a long period of time, creating a layer called the hard corona. In contrast to the soft corona, where proteins can be easily replaced by other proteins following dynamic changes of the surrounding environment, the hard corona is highly resistant toward such changes. Overall, this complex and dynamic layer confers nanoparticles a new biological identity. The eventual interactions between nanoparticles and cell receptors, thus receptor recognition and nanoparticle uptake, can all be affected by the presence of this layer. Strategies have been developed to prevent the formation of the biomolecular corona and maintain targeting efficiency, for instance, by creating a stealth layer using polyethylene glycol (PEG) and other special polymers or by introducing zwitterionic modifications on the nanoparticle surface (Veronese and Pasut, 2005; Yuan et al., 2012; García et al., 2014; Moyano et al., 2014; Pozzi et al., 2014; Alberg et al., 2020). However, it has been shown that in the case of PEGylated surfaces, nanoparticles still could adsorb proteins (Schöttler et al., 2016a).

Given the crucial role of the biomolecular corona and cell receptors in mediating nanoparticle uptake and determining their intracellular fate, it is of great importance to study in more detail the interactions between the biomolecular corona and cell receptors. Several studies have demonstrated that, indeed, the biomolecular corona itself can be recognized by cell receptors. For instance, in 2002, a study suggested that adsorption of apolipoprotein E (ApoE) from the blood to polysorbate 80-coated nanoparticles was responsible for the transport of the nanoparticles across the blood-brain barrier (BBB) (Kreuter et al., 2002). Deng et al. (2011) demonstrated that negatively charged poly(acrylic acid)-conjugated gold nanoparticles adsorbed and induced unfolding of fibrinogen from human plasma, which triggered interaction with the Mac-1 receptor and resulted in the release of inflammatory cytokines. Another study also showed that ionizable lipid nanoparticles could naturally adsorb apolipoprotein-E (ApoE), leading to enhanced uptake into hepatocyte via several receptors that contain ApoE binding ligands (Akinc et al., 2010; Williams and Chen, 2010). Similarly, lipid nanoparticles made of 1,2-dioleoyl-3-trimethylammonium propane (DOTAP) and DNA preferentially adsorbed high

amount of vitronectin from human plasma that promoted uptake into cancer cells overexpressing vitronectin receptors integrin  $\alpha v \beta 3$  (Caracciolo et al., 2013). Next to lipid nanoparticles, inorganic nanoparticles have also been shown to interact with distinct receptors once a biomolecular corona formed on their surface. For instance, in the presence of human serum, silica nanoparticles were shown to enter cells via interaction with the LDL receptor and/or Fc-gamma receptor I (Fc $\gamma$ RI) due to the abundance of LDL and immunoglobulin G (IgG) on the biomolecular corona (Lara et al., 2017; Francia et al., 2019). Not only single corona proteins, but also complex biomolecular surface layer motifs were observed to mediate cellular uptake via interaction with scavenger receptors (Lara et al., 2018).

## METHODS TO ELUCIDATE NANOPARTICLE BIOMOLECULAR CORONA-RECEPTOR INTERACTIONS

In order to gain a better understanding of how the biomolecular corona is recognized by cells and identify the cell receptors interacting with the corona, several strategies have been used in the recent years. Different methods have been developed to recover corona-coated nanoparticles, typically using centrifugation, size exclusion chromatography, magnetic extraction (for magnetic nanoparticles) or other similar approaches (Cedervall et al., 2007b; Docter et al., 2014; Bonvin et al., 2017; Francia et al., 2020). While in most cases it is only the hard corona to be recovered and characterized, more recently new methods based on field flow fractionation, *in situ* click chemistry and photo-affinity based chemoproteomics have been developed to characterize nanoparticles with both their hard and soft corona (Weber et al., 2018; Mohammad-Beigi et al., 2020; Pattipeiluhu et al., 2020). Overall, it will be important for the field to address current limitations in isolating the protein corona in different laboratories and/or by using different methods (Monopoli et al., 2013; Pisani et al., 2017). In order to overcome such limitations, best practice experimental approaches should be established for each stage of biomolecular corona studies, as for instance recently proposed at a broader level for experimental studies focused on the biological interactions of nanoparticles (Faria et al., 2018). Thus, following corona isolation, mass spectrometry is typically used to identify the protein corona composition and other methods, such as correlation analysis and corona fingerprinting, have been coupled to corona proteomics to discover which of the identified corona components correlate with higher or lower uptake by cells. However, identification of corona proteins *per se* is not enough, because not every protein in the corona may interact with cell receptors, for instance if it is not exposed on the nanoparticle surface in the correct orientation. Therefore, mapping of which protein epitopes on the biomolecular corona are accessible for cell receptors is another crucial step to identify potential interactions with cell receptors. Similarly, not all properly exposed proteins may be able to interact with cell receptors, for instance because of competition with other proteins with stronger affinity for the same receptors; thus, it is important to know which ones actually play a role.

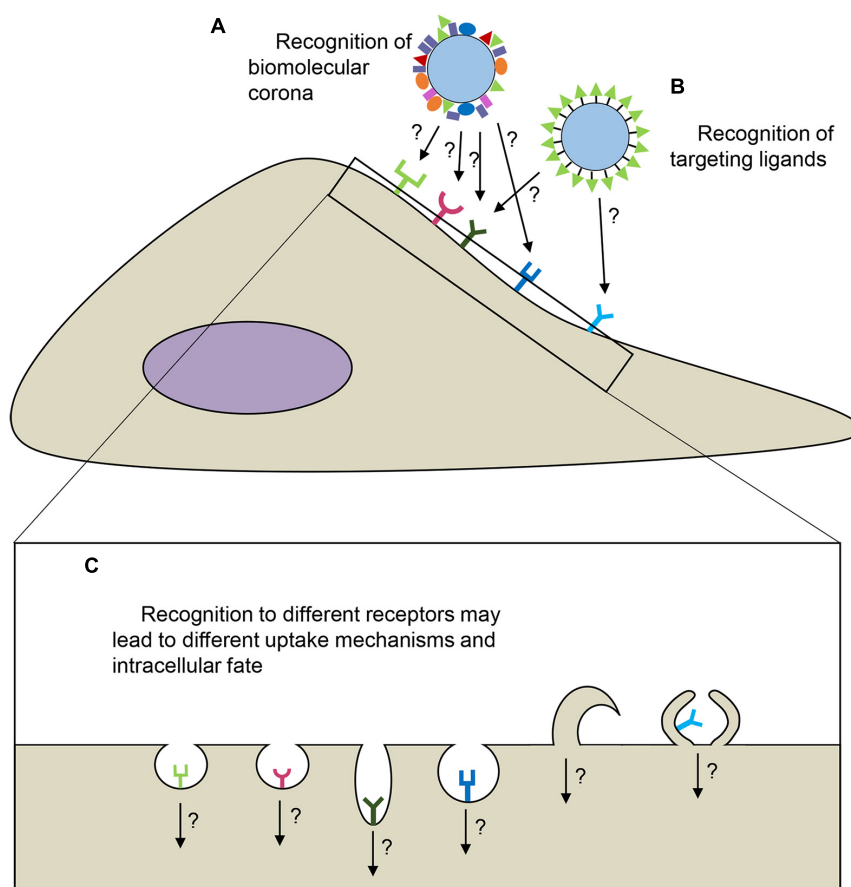


**FIGURE 1 |** Interactions of nanoparticles with cell receptors. Recognition can be achieved via the biomolecular corona (**A**) and/or targeting ligands (**B**) (Allen, 2002; Lara et al., 2017; Francia et al., 2019; Villaverde and Baeza, 2019). Depending on which receptors nanoparticles interact with, uptake mechanisms may differ (here illustrated by different shapes of the membrane invaginations and membrane protrusions), which could affect the intracellular fate of nanoparticles (**C**).

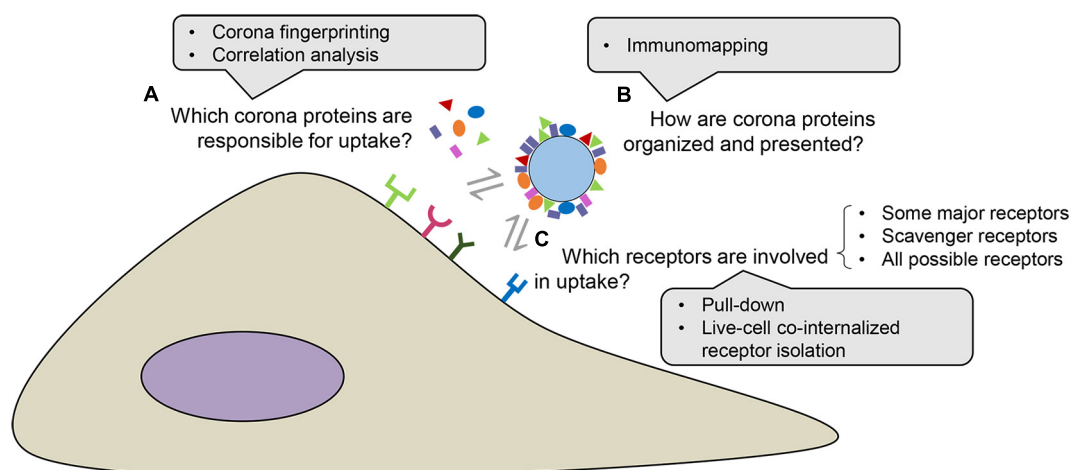
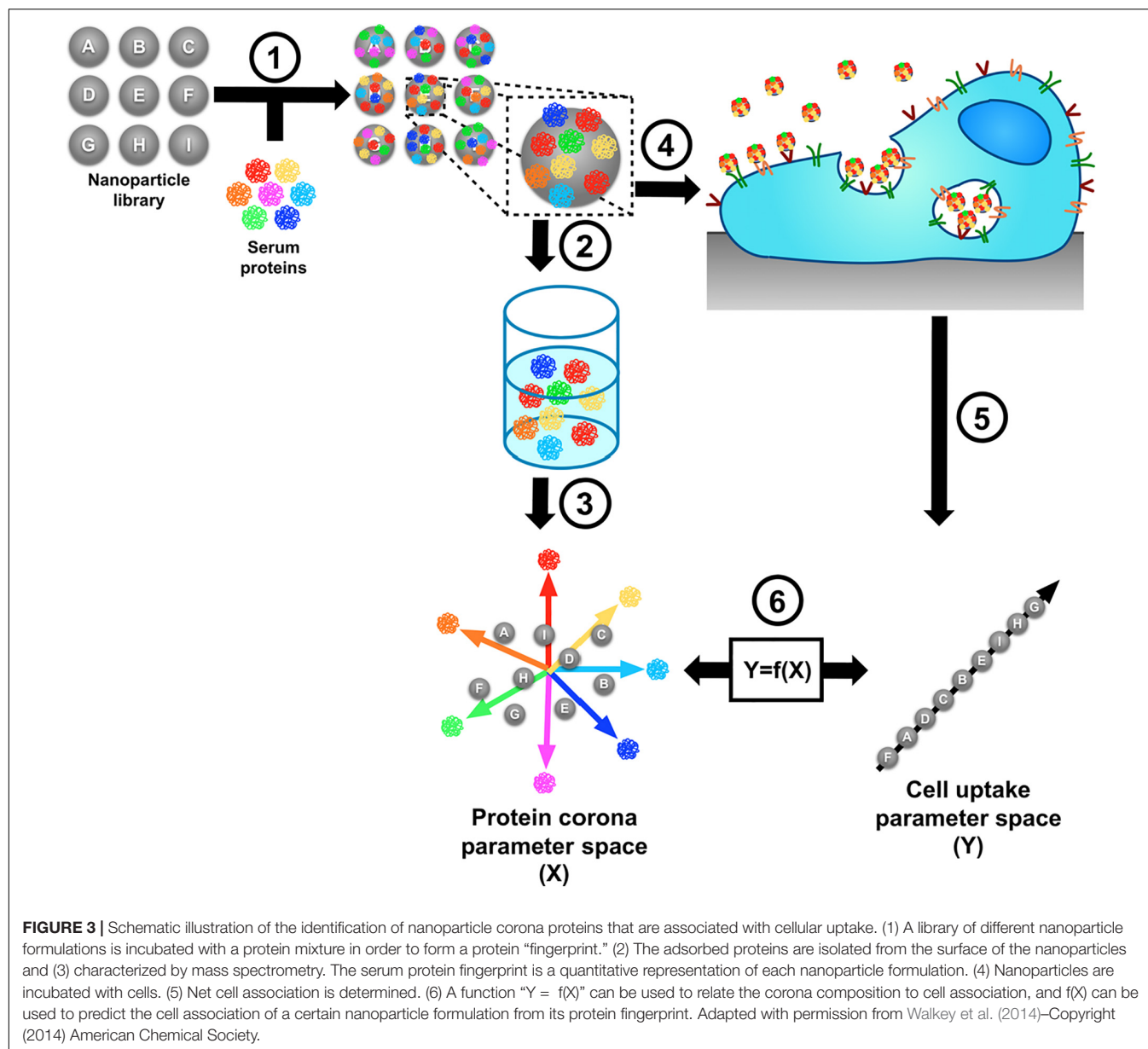


**FIGURE 2 |** Methods to elucidate nanoparticle protein corona-receptor interactions. First, corona proteins involved in nanoparticle uptake can be identified by associating the corona composition and nanoparticle uptake efficiency, for instance by using corona fingerprinting or correlation analysis (**A**) (Walkey et al., 2014; Liu et al., 2015; Ritz et al., 2015). The distribution of corona proteins and how their epitopes are presented can be determined by immunomapping-based techniques (**B**) (Kelly et al., 2015). Finally, receptors involved in the uptake of nanoparticle-corona complexes can be deduced from the corona composition or can be directly identified using pull-down or live-cell co-internalized receptor isolation approaches (**C**) (Bewersdorff et al., 2017; Ito et al., 2020; Aliyandi et al., unpublished).



All of these aspects are discussed in more detail in the following sections (see **Figure 2** for a simplified illustrative overview).

## Associating Corona Composition With Nanoparticle Uptake

Identification of all corona components, for instance by proteomics, is the very first step toward understanding nanoparticle corona interactions with cell receptors. Then, the next step is to identify which actual components of the biomolecular corona are responsible for regulating nanoparticle uptake (**Figure 2A**). Dissecting the biomolecular corona could be extremely challenging, given the high complexity of this layer. However, in recent years, a straightforward approach has been developed to make this possible. The idea was based on using a

library consisting of nanoparticles with various physicochemical properties to tune the corona composition and then associating the abundance of certain corona proteins with the nanoparticle cellular uptake efficiency. One way to do it is by applying quantitative structure–activity relationship (QSAR) models to predict nanoparticle–cell association as introduced by Walkey et al. (2014). To this end, a combination of biophysical, biological, and bioinformatic methods is required, as illustrated in **Figure 3**. The study showed that, by using a library containing more than 100 nanoparticle formulations and measuring their uptake by cells, this approach enabled the identification of 39 proteins classified as promoters, e.g.,  $\alpha$ -1 microglobulin and hyaluronan-binding protein 2, and of 25 inhibitors of cell association, e.g. complement C3. Similarly, Palchetti et al. (2016) used this approach to predict cell association of 16 lipid nanoparticles.

Interestingly, they showed that only 8 protein corona fingerprints were shown to be the most important stimulators of nanoparticle uptake in HeLa cells. In another study, similar approaches were used to identify liposomal formulations with a corona fingerprint that allowed increased uptake in pancreatic adenocarcinoma cells (Palchetti et al., 2019). Similarly, Liu et al. (2015) showed that by using a combination of linear and non-linear QSARs to analyze cell association of more than 80 gold nanoparticle formulations, some proteins, such as apolipoprotein B-100,  $\alpha$ -1 antitrypsin, and plasminogen, were found to be significant protein corona fingerprints correlating with high nanoparticle-cell association. A combination of linear and non-linear QSAR has also been used to correlate the protein corona of 17 different liposomal formulations to the cellular uptake and cell viability of PC3 and HeLa cells (Bigdeli et al., 2016). For each formulation, a total of 12 different biological endpoints were measured and QSAR analysis was used to correlate the biological responses with both the liposome physicochemical properties and the protein corona fingerprints. The use of multiple cellular responses showed that different descriptors seem to be involved into different biological processes. Along these lines, a more complex correlation analysis involving three variables was also applied as another means of predicting nanoparticle-cell association (Yin et al., 2019): by adding the inflammatory response as another variable next to biomolecular corona composition and cellular uptake, Yin et al. (2019) revealed a strong statistical correlation between the fractions of certain proteins bound to nanoparticles, the association after inhalation of these nanoparticles to immune cells in the lungs, and the total protein content in bronchoalveolar lavage fluid. A similar correlation analysis between corona composition and cellular uptake was performed by Ritz et al. (2015). By correlating the corona composition of six different polystyrene nanoparticles with their cellular uptake, the authors could discover that apolipoprotein H significantly increased nanoparticle uptake when adsorbed on the nanoparticle surface, while apolipoprotein A4 and C3 significantly decreased uptake. By using this approach, corona proteins that can either promote or hamper nanoparticle uptake can be identified and may be used to achieve targeting or to reduce clearance (Yang et al., 2020).

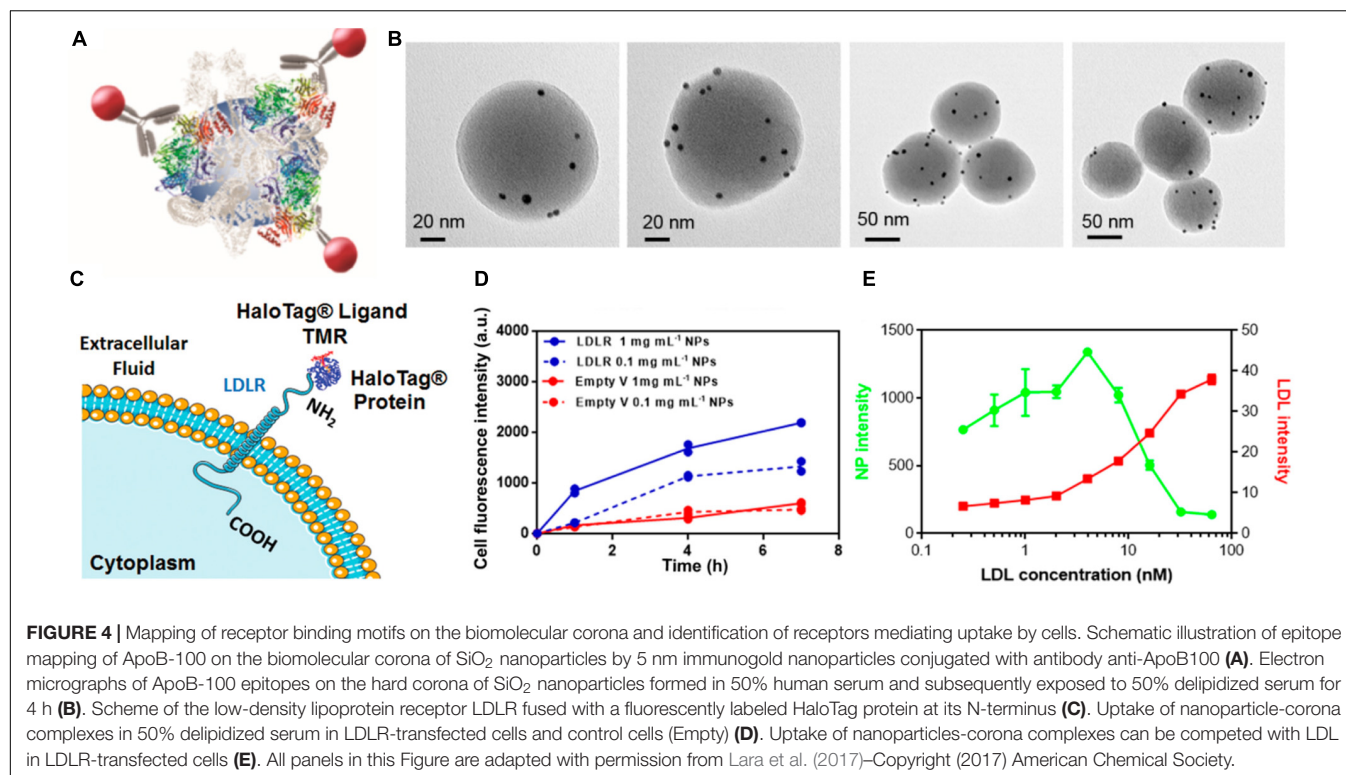
All these studies have highlighted the possibility to identify in a single analysis various corona proteins that were responsible for regulating uptake. However, correlation analysis, by nature, is closely associated with coincidence since it does not necessarily reflect causation. Therefore, further validation to confirm the involvement of those proteins in the uptake is needed, and this step could be laborious if the preceding screening generated too many candidates. The need of having a large nanoparticle library could also be a limitation of this approach. Without having different formulations of nanoparticles, correlation analysis would be more difficult to be performed, since a large library allows to narrow down the number of the resulting protein candidates. Despite these limitations, this approach allowed for the identification of corona proteins that play a role in nanoparticle uptake. Additionally, some independent studies with different types of nanoparticles and cells showed that similar proteins were found to be associated with uptake, and this cross-study validation further corroborates a (strong) relation

of these proteins with uptake (Ritz et al., 2015; Yang et al., 2020).

## Mapping of Receptor Binding Motifs and Epitopes Exposed on the Biomolecular Corona

The approaches described in the previous section allow to get an idea on which proteins in the corona might have an important role in nanoparticle uptake. However, it is likely that not all of the correlated proteins are properly exposed and accessible by cell receptors. Therefore, the next important step is to discriminate whether proteins are correctly presented to interact with their receptors (**Figure 2B**). This is of particular importance since different nanoparticles may expose the same corona proteins differently. Kelly et al. (2015) demonstrated that by using a combination of electron microscopy and differential centrifugal sedimentation (DCS), it is possible to map the spatial location of the proteins exposed on the biomolecular corona as well as their functional motifs and binding sites. The authors used immunogold-labeled monoclonal antibodies against transferrin and IgG to recognize multiple epitopes at once on human plasma-coated polystyrene nanoparticles of 220 nm. By using differential centrifugal sedimentation (DCS), the immunolabeling as well as the corresponding shift in nanoparticle diameter could be measured. Importantly, the results also indicated that transferrin and IgG were randomly organized in various locations on the nanoparticle surface. The same approaches were applied by Lara et al. (2017) to map apolipoprotein B-100 in the biomolecular corona formed on 100 nm silica nanoparticles in human plasma (see **Figures 4A,B**). Similarly, using immunometric mapping on graphene nanoflakes, Castagnola et al. (2018) found that their corona was rich in apolipoprotein A-I presentation, and, more importantly, they were able to map specific functional epitopes known to mediate the binding of high-density lipoproteins to receptors that are abundant in the liver. Next to this, other techniques have also been used to characterize receptor recognition motifs. Lo Giudice et al. (2016) used a flow cytometry-based method to map the availability of recognition fragments of transferrin and IgG on the biomolecular corona of polystyrene nanoparticles. Since a single laser on a flow cytometer can be used for multicolor experiments, this system also allows for mapping of different epitopes on multi-component biomolecular corona systems. Herda et al. (2017) reported a similar method using immuno-labeled quantum dots and fluorescence measurements to map the available epitopes on transferrin-modified silica nanoparticles. Gianneli et al. (2018) developed a fast and label-free screening methodology using a quartz crystal microbalance (QCM) to detect and quantify the accessible functional epitopes of transferrin-coated nanoparticles. Obviating the need to modify the nanoparticle surface with e.g., antibodies will prevent possible perturbations of the biomolecular corona. Similarly, in another work, QCM was also used to screen for nanoparticle binding to cells directly grown on the sensor surface (Gianneli et al., 2017). Another interesting approach to identify all epitopes exposed on the corona was reported by O'Connell et al. (2015), who





utilized a high content human protein microarray containing 9,483 full-length human proteins to determine the so-called “nanoparticle interactome.” The microarray was exposed to nanoparticles in human plasma and in this way potential proteins interacting with the nanoparticles (via their corona) were identified (O’Connell et al., 2015).

Next to epitope presentation, the molecular structure of corona proteins and their spatial arrangement on the nanoparticle surface should also be characterized. For instance, in a recent study, Duan et al. (2019) used limited proteolysis coupled with LC-MS/MS to characterize the orientation and unfolding of adsorbed proteins such as transferrin and catalase on polystyrene and iron oxide. Miclăuş et al. (2014) instead exploited localized surface plasmon resonance to detect differences in soft and hard corona kinetics at the edges or at the facets of silver nanocubes. All these studies were performed using non-porous nanoparticles, where adsorption of proteins is not complicated by protein penetration through the surface as it could happen on porous nanoparticles. In a recent study, instead, the penetration depth of several proteins within mesoporous silica nanoparticles could be clearly visualized using a combination of stochastic optical reconstruction microscopy (STORM) and a mathematical model (Clemments et al., 2017). This study showed that the penetration depth depends on the type of corona proteins and the size of the pores. The presence of photo-switchable fluorophores that stochastically turned on and off allowed for epitope mapping with a high localization accuracy. Similarly, Feiner-Gracia et al. (2017) demonstrated that these techniques could be used to reveal the heterogeneity of the biomolecular corona formation within a mesoporous silica nanoparticle

population, and how this evolved over time depending on the nanoparticle properties.

## Identification of Cellular Receptors That Interact With the Biomolecular Corona

While the above approaches allow to more accurately identify which corona components play a role in nanoparticle uptake, the next important aspect to unravel is which cell receptors are involved (Figure 2C). Thus, following the identification of all possible interacting receptors based on corona composition and/or epitope mapping, it is important to verify which of them can actually recognize and bind to the corona and if such recognition and the interaction with those receptors also lead to nanoparticle internalization. For instance, Caracciolo et al. (2013) showed that abundant adsorption of vitronectin from human plasma on lipid nanoparticles promoted nanoparticle uptake into cancer cells overexpressing integrin  $\alpha v \beta 3$ , suggesting the involvement of this receptor in the uptake. Epitope mapping can also be used to predict the involvement of certain receptors. In the study by Lara et al. (2017) discussed above, epitope mapping showed exposure of apolipoprotein B-100 and the Fc region of IgG in the biomolecular corona of 100 nm silica (Figures 4A,B). Then, the authors also showed that in cells overexpressing their receptors, i.e., the LDL receptor and Fc-gamma receptor I, respectively, nanoparticle uptake was enhanced (see Figures 4C,D for LDL receptor), while adding LDL reduced it (Figure 4E). These results suggested that nanoparticle uptake was mediated by recognition of the biomolecular corona by these specific receptors. These studies also showed that the

biomolecular corona can be recognized by multiple receptors in the same cells. Interactions with multiple receptors may lead to uptake via multiple pathways. In line with this, Francia et al. (2019) showed that 50 nm SiO<sub>2</sub> nanoparticles coated with a different corona (in low or high amounts of human serum) interacted with different receptors and consecutively were internalized by cells using different pathways. Thus, the interaction of the corona with specific cell receptors can also affect the mechanisms cells use for nanoparticle internalization.

Given the wide variety of proteins constituting the biomolecular corona, it has also emerged that more complex motifs can be formed in this layer. Unlike individual corona proteins that can interact with their corresponding receptors, these complex structures can form a unique pattern and such patterns may be recognized by unrelated receptors, as it was observed in a recent study for scavenger receptors (Lara et al., 2018). Scavenger receptors belong to a supergroup consisting of a broad range of structurally unrelated receptors that recognize a large array of ligands, including modified LDL, apoptotic cells, unfolded proteins, endogenous proteins that have been in some way altered, and various pathogens (Zani et al., 2015). Nanoparticle-scavenger receptor interactions were already reported in earlier studies where denaturation of albumin following adsorption to nanoparticles directed the albumin-nanoparticle complexes to bind to scavenger receptors (Schnitzer and Bravo, 1993; Fleischer and Payne, 2014). Similarly, in their study, Lara et al. (2018) overexpressed the macrophage receptor with collagenous structure (MARCO) in HEK-293T (wild-type HEK293T having undetectable levels of this receptor) and showed that MARCO-expressing cells internalized a higher amount of human serum-coated 100 nm SiO<sub>2</sub> compared to wild-type cells, suggesting interactions of the biomolecular corona with MARCO. Interestingly, the interaction with MARCO could not be competed out by the most known ligands of this receptor (even up to considerable excess), suggesting a different mode of binding of the SiO<sub>2</sub> nanoparticles to this receptor. Apart from MARCO, another scavenger receptor, SR-B1, was also shown to be involved in the uptake of protein corona-coated graphene nanoflakes in HEK-293T cells overexpressing this receptor (Alnasser et al., 2019).

The above studies have demonstrated that the biomolecular corona can be recognized by multiple receptors. Thus, in order to gain a better understanding of nanoparticle outcomes on cells, it is essential to identify all the receptors interacting with the corona and to discriminate, among them, those that mediate nanoparticle uptake. This is even more important in the case of targeted nanomedicines, which may interact (themselves or via their corona) with receptors other than the targeted one, thus affecting their targeting and efficacy. Other methods are required in order to be able to identify such receptors.

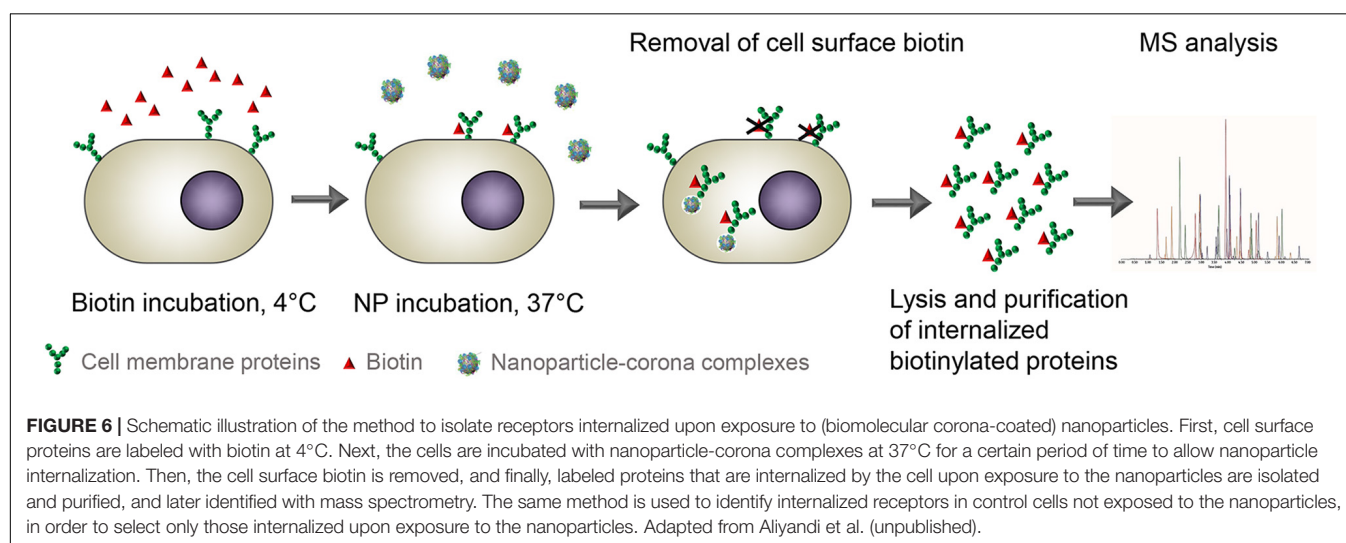
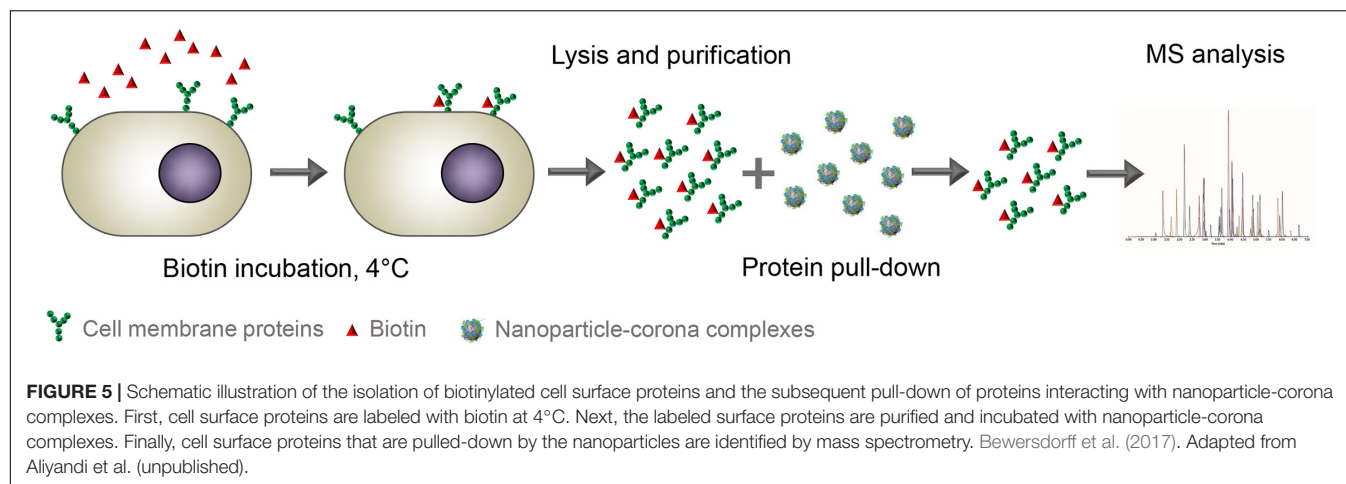
## Identification of Cellular Receptors That Mediate Uptake of Nanoparticle-Corona Complexes by Cells

The studies discussed in the previous sections showed, together with many other similar works, that the mere presence of

a protein in the corona forming on nanoparticles does not guarantee specific recognition by cell receptors. Therefore, without having information on the epitopes which are properly exposed on the nanoparticle surface, including novel epitopes formed upon conformational changes upon adsorption or via complex motifs created on the corona, it is difficult to identify possible receptors. Identification of the receptors involved in corona recognition and nanoparticle uptake in specific cell types can also allow the development of novel targeting strategies (Figure 2C). Recently, some new methods have been developed to make such identification possible. By combining biotinylation of the cell surface, corona proteomics, and mass spectrometry, all possible interaction partners of the biomolecular corona can be identified. Below we discuss two approaches based on the aforementioned techniques that have been recently used to unravel cell receptors interacting with the biomolecular corona.

### Pull-Down Receptor Identification Approach

In a recent study, Bewersdorff et al. (2017) used a pull-down approach in order to identify the cellular binding partners of serum-coated sulfated dendritic polyglycerol (dPGS) nanoparticles. They determined the corona composition and cellular uptake of nanoparticles by THP-1 cells, and at the same time, they identified the possible cellular interaction partners of the nanoparticles with the THP-1 cells using a pull-down approach (see Figure 5 for simplified schematic protocol). Briefly, cell surface proteins were first labeled with biotin at 4°C to prevent their internalization. Then, the biotinylated surface proteins were purified from the rest of the cell components to obtain a purified cell surface protein fraction. Different methods based on cell surface biotinylation have been developed and optimized to purify and isolate cell surface proteins for cell membrane proteomic studies, including studies aiming at identifying potential novel targets for cancer therapy (Jang and Hanash, 2003; Elia, 2008; Elschenbroich et al., 2010; Kuhlmann et al., 2018). For instance, similar approaches were used to identify receptors overexpressed on osteosarcoma cells which could be used for targeting (Posthumadeboer et al., 2013). Bewersdorff et al., instead, used cell surface biotinylation to isolate cell surface proteins and incubate the isolated fraction with serum corona-coated nanoparticles. Thus, the cell surface proteins interacting with the corona-coated nanoparticles were pulled-down and were identified by mass spectrometry. In this way, 22 cell surface proteins were identified on dPGS nanoparticles, among which some were shown to be receptors for specific corona proteins. For example, integrin beta-2 and transferrin receptor 1 (TFR1) were identified in the pull-down, and their corresponding ligands (serotransferrin and vitronectin, respectively) were also detected in the corona. Recently, the same approach was used to identify nanoparticle receptors in brain and liver endothelial cells using 200 nm silica (Aliyandi et al., unpublished). Interestingly, in the two endothelial cell types, different amounts and types of cell surface receptors were involved in the interaction with the same human plasma corona-coated nanoparticles. Moreover, the pull down also allowed for strong enrichment of cell surface receptors on the nanoparticle



corona, while in some cases these receptors were not even identified by mass spectrometry in the cell surface fraction.

Thus, the unbiased screening offered by this approach can be used not only to identify potential interacting receptors, but also to identify previously unknown receptors, and therefore increases the chances to discover novel drug carrier targets. However, the receptors identified with this approach may also include false-positive hits, for instance due to damage of the isolated proteins during extraction, changes in protein conformation, or also because of wrong orientation, leading to interactions of the biomolecular corona with the cytosolic domains of the isolated receptors. In addition, the relatively high number of receptors detected using this method could be a challenge for selecting receptor candidates for further validation, and it is also likely that not all of them may promote internalization upon interaction with the biomolecular corona. Thus, other steps are required to narrow down the receptor numbers and to determine which, among all identified receptors, allows efficient nanoparticle uptake. For example, this can be achieved by using the pull-down approach with nanoparticles showing minimal uptake in the same cells and by excluding the receptors

identified, likely to be involved in non-specific binding that does not trigger uptake.

### Live-Cell Internalized Receptor Identification Approach

Next to the pull-down approach using isolated cell membrane fractions, another method has been recently applied to study interactions between nanoparticle-corona complexes and cell surface receptors directly on live cells (Aliyandi et al., unpublished). Cell surface biotinylation on live cells is commonly used to study mechanisms of endocytosis in cells (Leser et al., 1996; Meulendyke et al., 2005; Bitsikas et al., 2014; Ito et al., 2014). For instance, similar approaches were used to determine the cell-surface expression and endocytic rate of proteins in primary astrocytes, to study endocytosis and recycling of membrane proteins, and also to compare the endocytic flux of different uptake mechanisms (Cihil and Swiatecka-Urban, 2013; Bitsikas et al., 2014; Tham and Moukhles, 2017). Cell surface biotinylation has also been performed on brain tissue slices to measure plasma membrane protein trafficking in neurons (Gabriel et al., 2014). Similar methods have also been used directly *in vivo*

in mice to study differences in cell surface proteins in the vascular cells of different organs and how these change upon infection by *Staphylococcus aureus* (Toledo et al., 2019). In recent work, instead, the method was used to identify all cell receptors involved in nanoparticle uptake and bypass some of the discussed limitations of the pull-down approach (Aliyandi et al., unpublished). In summary (see **Figure 6** for simplified schematic protocol), cell surface proteins are first labeled in the same way as in the pull-down approach, but now using reversible biotinylation. Then, the live biotinylated cells are incubated with nanoparticle-corona complexes to allow cellular uptake. Finally, the biotinylated receptors that are internalized upon exposure to nanoparticles are isolated, purified, and identified by mass spectrometry. The identified receptors are compared to those obtained with the same methods in cells not exposed to nanoparticles, in order to select the internalized receptors that are identified only upon exposure to nanoparticles. The advantage of this method is that it allows to exclude contaminations caused by non-specific binding or receptor interactions that do not lead to nanoparticle uptake. Additionally, since interactions occur on live cells (thus with native receptors), complications resulting from conformational changes or binding to incorrect domains are, as well, excluded. In another recent study, Ito et al. (2020) used a similar approach to identify receptors involved in endocytosis, but without using nanoparticles. They showed that 34 out of 125 cell surface proteins were selectively internalized into brain microvascular endothelial cells, but not into human umbilical vein endothelial cells (HUVEC), suggesting the potential of these proteins as receptors to target drug carriers to the blood-brain barrier.

In contrast to the pull-down approach, the number of receptors identified using this method is lower, thanks to the minimal presence of receptors involved in non-specific binding and other false-positive hits generated with extracted receptors. Nevertheless, also with this method validation is required to confirm the involvement of the identified receptors in nanoparticle uptake. Interestingly, among many receptors that were identified with this approach, there were some for which ligands are not (yet) known, thus it is important to clarify their role in uptake. Importantly, the method may allow to discover receptors with a potential application as novel drug carrier targets. Despite all these benefits, it is also important to mention that the isolation process in this approach depends on the presence of the receptors inside the cells. Therefore, receptors that are quickly recycled back to the cell membrane might not be isolated. Applying this method after short nanoparticle incubation times may help to overcome this limitation.

## CONCLUSION AND FUTURE PERSPECTIVES

To achieve ideal nanomedicine design with better targeting efficiency, it is of great importance to first understand the

interactions between nano-sized materials and living organisms at the cellular and molecular levels. In the presence of a biological fluid, nanoparticles are covered by a biomolecular corona which could potentially determine many of those interactions. It is now widely acknowledged that many key processes are driven by initial recognition of this adsorbed layer by cell receptors. Thus, the corona can affect receptor-mediated outcomes such as nanoparticle targeting, biodistribution, ability to cross biological barriers, and intracellular trafficking. The latest findings on the interactions between the biomolecular corona and cell receptors discussed in this review provide a deeper understanding of the complexity of this very first step in nanoparticle-cell interactions and its implications for the following outcomes at cell level. All these recent works showed that a combination of the knowledge of biomolecular corona composition, how these components are organized and presented, and which and how many receptors interact with this adsorbed layer are all critical aspects to be considered when designing targeted drug carriers. Thus, with the benefits and limitations offered by the discussed methods, better insights could be achieved by, for instance, combining some of them on the same system. At the same time, the biomolecular corona itself can be used as a tool to discover potential ligands as well as receptors involved in nanoparticle uptake in specific cell types to be used for novel targeting strategies (Walkey et al., 2014; Liu et al., 2015; Ritz et al., 2015; Yin et al., 2019; Yang et al., 2020). Indeed, many more aspects are yet still to be disentangled, for instance, how other physiological factors such as flow and shear stress (in blood) influence not only the biomolecular corona composition, but also the resulting interactions with cell receptors. To this end, systematic and reproducible tools must be developed that include a more physiological platform to mimic *in vivo* conditions, while allowing a comprehensive characterization of the biomolecular corona, and investigation of the corresponding biological interactions. We believe that further developments in this direction will help to provide valuable insights and opportunities for accelerating the bench-to bed translation of nanomedicine.

## AUTHOR CONTRIBUTIONS

AA wrote the manuscript together with AS and IZ and compiled the figures. AS and IZ aided in the idea conception, development, and literature research. All authors contributed to the article and approved the submitted version.

## FUNDING

This work was partially supported by the European Research Council (ERC) under the European Union's Horizon 2020 Research and Innovation Programme under grant agreement no. 637614 (NanoPaths).



## REFERENCES

- Akinc, A., Querbes, W., De, S., Qin, J., Frank-Kamenetsky, M., Jayaprakash, K. N., et al. (2010). Targeted delivery of RNAi therapeutics with endogenous and exogenous ligand-based mechanisms. *Mol. Ther.* 18, 1357–1364. doi: 10.1038/mt.2010.85
- Albanese, A., Tang, P. S., and Chan, W. C. W. (2012). The effect of nanoparticle size, shape, and surface chemistry on biological systems. *Annu. Rev. Biomed. Eng.* 14, 1–16. doi: 10.1146/annurev-bioeng-071811-150124
- Alberg, I., Kramer, S., Schinnerer, M., Hu, Q., Seidl, C., Leps, C., et al. (2020). Polymeric nanoparticles with neglectable protein corona. *Small* 16, 1907574. doi: 10.1002/sml.201907574
- Alexis, F., Pridgen, E., Molnar, L. K., and Farokhzad, O. C. (2008). Factors affecting the clearance and biodistribution of polymeric nanoparticles. *Mol. Pharm.* 5, 505–515. doi: 10.1021/mp800051m
- Allen, T. M. (2002). Ligand-targeted therapeutics in anticancer therapy. *Nat. Rev. Cancer* 2, 750–763. doi: 10.1038/nrc903
- Alnasser, F., Castagnola, V., Boselli, L., Esquivel-Gaon, M., Efeoglu, E., McIntyre, J., et al. (2019). Graphene nanoflake uptake mediated by scavenger receptors. *Nano Lett.* 19, 1260–1268. doi: 10.1021/acs.nanolett.8b04820
- Andreone, B. J., Chow, B. W., Tata, A., Lacoste, B., Ben-Zvi, A., Bullock, K., et al. (2017). Blood-brain barrier permeability is regulated by lipid transport-dependent suppression of caveolae-mediated transcytosis. *Neuron* 94, 581.e5–594.e5. doi: 10.1016/j.neuron.2017.03.043
- Anselmo, A. C., Zhang, M., Kumar, S., Vogus, D. R., Menegatti, S., Helgeson, M. E., et al. (2015). Elasticity of nanoparticles influences their blood circulation, phagocytosis, endocytosis, and targeting. *ACS Nano* 9, 3169–3177. doi: 10.1021/acsnano.5b00147
- Barui, A. K., Oh, J. Y., Jana, B., Kim, C., and Ryu, J. (2019). Cancer-targeted nanomedicine: overcoming the barrier of the protein corona. *Adv. Ther.* 3:1900124. doi: 10.1002/adtp.201900124
- Bewersdorff, T., Vonnemann, J., Kanik, A., Haag, R., and Haase, A. (2017). The influence of surface charge on serum protein interaction and cellular uptake: studies with dendritic polyglycerols and dendritic polyglycerol-coated gold nanoparticles. *Int. J. Nanomed.* 12, 2001–2019. doi: 10.2147/IJN.S124295
- Bigdeli, A., Palchetti, S., Pozzi, D., Hormozi-Nezhad, M. R., Baldelli Bombelli, F., Caracciolo, G., et al. (2016). Exploring cellular interactions of liposomes using protein corona fingerprints and physicochemical properties. *ACS Nano* 10, 3723–3737. doi: 10.1021/acsnano.6b00261
- Bitsikas, V., Corrêa, I. R., and Nichols, B. J. (2014). Clathrin-independent pathways do not contribute significantly to endocytic flux. *eLife* 2014, 1–26. doi: 10.7554/eLife.03970
- Bonvin, D., Chiappe, D., Moniatte, M., Hofmann, H., and Mionić Ebersold, M. (2017). Methods of protein corona isolation for magnetic nanoparticles. *Analyst* 142, 3805–3815. doi: 10.1039/c7an00646b
- Caracciolo, G., Cardarelli, F., Pozzi, D., Salomone, F., Maccari, G., Bardi, G., et al. (2013). Selective targeting capability acquired with a protein corona adsorbed on the surface of 1,2-Dioleoyl-3-trimethylammonium Propane/DNA Nanoparticles. *ACS Appl. Mater. Interfaces* 5, 13171–13179. doi: 10.1021/am404171h
- Caracciolo, G., Farokhzad, O. C., and Mahmoudi, M. (2017). Biological identity of nanoparticles in vivo: clinical implications of the protein corona. *Trends Biotechnol.* 35, 257–264. doi: 10.1016/j.tibtech.2016.08.011
- Castagnola, V., Zhao, W., Boselli, L., Lo Giudice, M. C., Meder, F., Polo, E., et al. (2018). Biological recognition of graphene nanoflakes. *Nat. Commun.* 9:1577. doi: 10.1038/s41467-018-04009-x
- Cedervall, T., Lynch, I., Lindman, S., Berggård, T., Thulin, E., Nilsson, H., et al. (2007a). Understanding the nanoparticle-protein corona using methods to quantify exchange rates and affinities of proteins for nanoparticles. *Proc. Natl. Acad. Sci. U.S.A.* 104, 2050–2055. doi: 10.1073/pnas.0608582104
- Cedervall, T., Lynch, I., Lindman, S., Berggård, T., Thulin, E., Nilsson, H., et al. (2007b). Understanding the nanoparticle-protein corona using methods to quantify exchange rates and affinities of proteins for nanoparticles. *Proc. Natl. Acad. Sci. U. S. A.* 104, 2050–2055.
- Chauhan, V. P., and Jain, R. K. (2013). Strategies for advancing cancer nanomedicine. *Nat. Mater.* 12, 958–962. doi: 10.1038/nmat3792
- Cheng, C. J., Tietjen, G. T., Saucier-Sawyer, J. K., and Saltzman, W. M. (2015). A holistic approach to targeting disease with polymeric nanoparticles. *Nat. Rev. Drug Discov.* 14, 239–247. doi: 10.1038/nrd4503
- Cihil, K. M., and Swiatecka-Urban, A. (2013). The cell-based L-glutathione protection assays to study endocytosis and recycling of plasma membrane proteins. *J. Vis. Exp.* 82:50867. doi: 10.3791/50867
- Clemments, A. M., Botella, P., and Landry, C. C. (2017). Spatial Mapping of Protein Adsorption on Mesoporous Silica Nanoparticles by Stochastic Optical Reconstruction Microscopy. *J. Am. Chem. Soc.* 139, 3978–3981. doi: 10.1021/jacs.7b01118
- Danhier, F. (2016). To exploit the tumor microenvironment: Since the EPR effect fails in the clinic, what is the future of nanomedicine? *J. Control. Release* 244, 108–121. doi: 10.1016/j.jconrel.2016.11.015
- Danhier, F., Feron, O., and Préat, V. (2010). To exploit the tumor microenvironment: Passive and active tumor targeting of nanocarriers for anti-cancer drug delivery. *J. Control. Release* 148, 135–146. doi: 10.1016/j.jconrel.2010.08.027
- Decuzzi, P., Godin, B., Tanaka, T., Lee, S. Y., Chiappini, C., Liu, X., et al. (2010). Size and shape effects in the biodistribution of intravascularly injected particles. *J. Control. Release* 141, 320–327. doi: 10.1016/j.jconrel.2009.10.014
- Deng, Z. J., Liang, M., Monteiro, M., Toth, I., and Minchin, R. F. (2011). Nanoparticle-induced unfolding of fibrinogen promotes Mac-1 receptor activation and inflammation. *Nat. Nanotechnol.* 6, 39–44. doi: 10.1038/nnano.2010.250
- D'Mello, S. R., Cruz, C. N., Chen, M. L., Kapoor, M., Lee, S. L., and Tyner, K. M. (2017). The evolving landscape of drug products containing nanomaterials in the United States. *Nat. Nanotechnol.* 12, 523–529. doi: 10.1038/nnano.2017.67
- Dobrovolskaia, M. A., Shurin, M., and Shvedova, A. A. (2016). Current understanding of interactions between nanoparticles and the immune system. *Toxicol. Appl. Pharmacol.* 299, 78–89. doi: 10.1016/j.taap.2015.12.022
- Docter, D., Distler, U., Storck, W., Kuharev, J., Wünsch, D., Hahlbrock, A., et al. (2014). Quantitative profiling of the protein coronas that form around nanoparticles. *Nat. Protoc.* 9, 2030–2044. doi: 10.1038/nprot.2014.139
- Duan, Y., Liu, Y., Coreas, R., and Zhong, W. (2019). Mapping molecular structure of protein locating on nanoparticles with limited proteolysis. *Anal. Chem.* 91, 4204–4212. doi: 10.1021/acs.analchem.9b00482
- Duncan, R., and Richardson, S. C. W. (2012). Endocytosis and intracellular trafficking as gateways for nanomedicine delivery: Opportunities and challenges. *Mol. Pharm.* 9, 2380–2402. doi: 10.1021/mp300293n
- Elia, G. (2008). Biotinylation reagents for the study of cell surface proteins. *Proteomics* 8, 4012–4024. doi: 10.1002/pmic.200800097
- Elschenbroich, S., Kim, Y., Medin, J. A., and Kislinger, T. (2010). Isolation of cell surface proteins for mass spectrometry-based proteomics. *Expert Rev. Proteomics* 7, 141–154. doi: 10.1586/ep.09.97
- Faria, M., Björnmal, M., Thurecht, K. J., Kent, S. J., Parton, R. G., Kavallaris, M., et al. (2018). Minimum information reporting in bio-nano experimental literature. *Nat. Nanotechnol.* 13, 777–785. doi: 10.1038/s41565-018-0246-4
- Feiner-Gracia, N., Beck, M., Pujals, S., Tosi, S., Mandal, T., Buske, C., et al. (2017). Super-resolution microscopy unveils dynamic heterogeneities in nanoparticle protein corona. *Small* 13:1701631. doi: 10.1002/sml.201701631
- Fleischer, C. C., and Payne, C. K. (2014). Secondary structure of corona proteins determines the cell surface receptors used by nanoparticles. *J. Phys. Chem. B* 118, 14017–14026. doi: 10.1021/jp502624n
- Francia, V., Schiffelers, R. M., Cullis, P. R., and Witzigmann, D. (2020). The biomolecular corona of lipid nanoparticles for gene therapy. *Bioconjug. Chem.* 31, 2046–2059. doi: 10.1021/acs.bioconjchem.0c00366
- Francia, V., Yang, K., Deville, S., Reker-Smit, C., Nelissen, I., and Salvati, A. (2019). Corona composition can affect the mechanisms cells use to internalize nanoparticles. *ACS Nano* 13, 11107–11121. doi: 10.1021/acsnano.9b03824
- Gabriel, L. R., Wu, S., and Melikian, H. E. (2014). Brain slice biotinylation: an ex vivo approach to measure region-specific plasma membrane protein trafficking in adult neurons. *J. Vis. Exp.* 86:e51240. doi: 10.3791/51240

- García, K. P., Zarschler, K., Barbaro, L., Barreto, J. A., O'Malley, W., Spiccia, L., et al. (2014). Zwitterionic-coated "stealth" nanoparticles for biomedical applications: recent advances in countering biomolecular corona formation and uptake by the mononuclear phagocyte system. *Small* 10, 2516–2529. doi: 10.1002/sml.201303540
- Ge, C., Tian, J., Zhao, Y., Chen, C., Zhou, R., and Chai, Z. (2015). Towards understanding of nanoparticle–protein corona. *Arch. Toxicol.* 89, 519–539. doi: 10.1007/s00204-015-1458-0
- Georgieva, J. V., Hoekstra, D., and Zuhorn, I. S. (2014). Smuggling drugs into the brain: An overview of ligands targeting transcytosis for drug delivery across the blood–brain barrier. *Pharmaceutics* 6, 557–583. doi: 10.3390/pharmaceutics6040557
- Georgieva, J. V., Kalicharan, D., Couraud, P.-O., Romero, I. A., Weksler, B., Hoekstra, D., et al. (2011). Surface characteristics of nanoparticles determine their intracellular fate in and processing by human blood–brain barrier endothelial cells in vitro. *Mol. Ther.* 19, 318–325. doi: 10.1038/mt.2010.236
- Gianneli, M., Polo, E., Lopez, H., Castagnola, V., Aastrup, T., and Dawson, K. A. (2018). Label-free in-flow detection of receptor recognition motifs on the biomolecular corona of nanoparticles. *Nanoscale* 10, 5474–5481. doi: 10.1039/C7NR07887K
- Gianneli, M., Yan, Y., Polo, E., Peiris, D., Aastrup, T., and Dawson, K. A. (2017). Novel QCM-based method to predict in vivo behaviour of nanoparticles. *Procedia Technol.* 27, 197–200. doi: 10.1016/j.protcy.2017.04.084
- Hadjidemetriou, M., Al-Ahmady, Z., Mazza, M., Collins, R. F., Dawson, K., and Kostarelos, K. (2015). In vivo biomolecule corona around blood-circulating, clinically used and antibody-targeted lipid bilayer nanoscale vesicles. *ACS Nano* 9, 8142–8156. doi: 10.1021/acs.nano.5b03300
- Herda, L. M., Hristov, D. R., Lo Giudice, M. C., Polo, E., and Dawson, K. A. (2017). Mapping of molecular structure of the nanoscale surface in bionanoparticles. *J. Am. Chem. Soc.* 139, 111–114. doi: 10.1021/jacs.6b12297
- Hoshyar, N., Gray, S., Han, H., and Bao, G. (2016). The effect of nanoparticle size on in vivo pharmacokinetics and cellular interaction. *Nanomedicine* 11, 673–692. doi: 10.2217/nnm.16.5
- Ito, S., Ohtsuki, S., Murata, S., Katsukura, Y., Suzuki, H., Funaki, M., et al. (2014). Involvement of insulin-degrading enzyme in insulin- and atrial natriuretic peptide-sensitive internalization of amyloid- $\beta$  peptide in mouse brain capillary endothelial cells. *J. Alzheimer's Dis.* 38, 185–200. doi: 10.3233/JAD-122077
- Ito, S., Oishi, M., Ogata, S., Uemura, T., Couraud, P. O., Masuda, T., et al. (2020). Identification of cell-surface proteins endocytosed by human brain microvascular endothelial cells in vitro. *Pharmaceutics* 12, 1–19. doi: 10.3390/pharmaceutics12060579
- Iversen, T. G., Skotland, T., and Sandvig, K. (2011). Endocytosis and intracellular transport of nanoparticles: Present knowledge and need for future studies. *Nano Today* 6, 176–185. doi: 10.1016/j.nantod.2011.02.003
- Jain, R. K. (1987). Transport of molecules in the tumor interstitium: a review. *Cancer Res.* 47, 3039–3051.
- Jang, J. H., and Hanash, S. (2003). Profiling of the cell surface proteome. *Proteomics* 3, 1947–1954. doi: 10.1002/pmic.200300563
- Kelly, P. M., Åberg, C., Polo, E., O'Connell, A., Cookman, J., Fallon, J., et al. (2015). Mapping protein binding sites on the biomolecular corona of nanoparticles. *Nat. Nanotechnol.* 10, 472–479. doi: 10.1038/nnano.2015.47
- Kim, J. A., Salvati, A., Åberg, C., and Dawson, K. A. (2014). Suppression of nanoparticle cytotoxicity approaching in vivo serum concentrations: Limitations of in vitro testing for nanosafety. *Nanoscale* 6, 14180–14184. doi: 10.1039/c4nr04970e
- Kreuter, J., Shamenkov, D., Petrov, V., Ramge, P., Cychutek, K., Koch-Brandt, C., et al. (2002). Apolipoprotein-mediated transport of nanoparticle-bound drugs across the blood–brain barrier. *J. Drug Target.* 10, 317–325. doi: 10.1080/10611860290031877
- Kuhlmann, L., Cummins, E., Samudio, I., and Kislinger, T. (2018). Cell-surface proteomics for the identification of novel therapeutic targets in cancer. *Expert Rev. Prot.* 15, 259–275. doi: 10.1080/14789450.2018.1429924
- Lammers, T., Kiessling, F., Ashford, M., Hennink, W., Crommelin, D., and Strom, G. (2016). Cancer nanomedicine: Is targeting our target? *Nat. Rev. Mater.* 1:16069. doi: 10.1038/natrevmats.2016.69
- Lara, S., Alnasser, F., Polo, E., Garry, D., Lo Giudice, M. C., Hristov, D. R., et al. (2017). Identification of receptor binding to the biomolecular corona of nanoparticles. *ACS Nano* 11, 1884–1893. doi: 10.1021/acs.nano.6b07933
- Lara, S., Perez-Potti, A., Herda, L. M., Adumeau, L., Dawson, K. A., and Yan, Y. (2018). Differential recognition of nanoparticle protein corona and modified low-density lipoprotein by macrophage receptor with collagenous structure. *ACS Nano* 12, 4930–4937. doi: 10.1021/acs.nano.8b02014
- Leser, G. P., Ector, K. J., and Lamb, R. A. (1996). The paramyxovirus simian virus 5 hemagglutinin-neuraminidase glycoprotein, but not the fusion glycoprotein, is internalized via coated pits and enters the endocytic pathway. *Mol. Biol. Cell* 7, 155–172. doi: 10.1091/mbc.7.1.155
- Li, Z., Xiao, C., Yong, T., Li, Z., Gan, L., and Yang, X. (2020). Influence of nanomedicine mechanical properties on tumor targeting delivery. *Chem. Soc. Rev.* 49, 2273–2290. doi: 10.1039/c9cs00575g
- Liu, N., Tang, M., and Ding, J. (2020). The interaction between nanoparticles–protein corona complex and cells and its toxic effect on cells. *Chemosphere* 245:125624. doi: 10.1016/j.chemosphere.2019.125624
- Liu, R., Jiang, W., Walkey, C. D., Chan, W. C. W., and Cohen, Y. (2015). Prediction of nanoparticles–cell association based on corona proteins and physicochemical properties. *Nanoscale* 7, 9664–9675. doi: 10.1039/C5NR01537E
- Lo Giudice, M. C., Herda, L. M., Polo, E., and Dawson, K. A. (2016). In situ characterization of nanoparticle biomolecular interactions in complex biological media by flow cytometry. *Nat. Commun.* 7:13475. doi: 10.1038/ncomms13475
- Lundqvist, M., Stigler, J., Elia, G., Lynch, I., Cedervall, T., and Dawson, K. A. (2008). Nanoparticle size and surface properties determine the protein corona with possible implications for biological impacts. *Proc. Natl. Acad. Sci. U.S.A.* 105, 14265–14270. doi: 10.1073/pnas.0805135105
- Mahmoudi, M., Lynch, I., Ejtehadi, M. R., Monopoli, M. P., Bombelli, F. B., and Laurent, S. (2011). Protein–nanoparticle interactions: opportunities and challenges. *Chem. Rev.* 111, 5610–5637. doi: 10.1021/cr100440g
- Mahon, E., Salvati, A., Baldelli Bombelli, F., Lynch, I., and Dawson, K. A. (2012). Designing the nanoparticle–biomolecule interface for "targeting and therapeutic delivery." *J. Control. Release* 161, 164–174. doi: 10.1016/j.jconrel.2012.04.009
- Matsumura, Y., and Maeda, H. (1986). A new concept for macromolecular therapeutics in cancer chemotherapy: mechanism of tumor tropic accumulation of proteins and the antitumor agent smancs. *Cancer Res.* 46, 6387–6392.
- Meulendyke, K. A., Wurth, M. A., McCann, R. O., and Dutch, R. E. (2005). Endocytosis plays a critical role in proteolytic processing of the hendra virus fusion protein. *J. Virol.* 79, 12643–12649. doi: 10.1128/jvi.79.20.12643-12649.2005
- Miclăuş, T., Bochenkov, V. E., Ogaki, R., Howard, K. A., and Sutherland, D. S. (2014). Spatial mapping and quantification of soft and hard protein coronas at silver nanocubes. *Nano Lett.* 14, 2086–2093. doi: 10.1021/nl500277c
- Mohammad-Beigi, H., Hayashi, Y., Zeuthen, C. M., Eskandari, H., Scavenius, C., Juul-Madsen, K., et al. (2020). Mapping and identification of soft corona proteins at nanoparticles and their impact on cellular association. *Nat. Commun.* 11:4535. doi: 10.1038/s41467-020-18237-7
- Monopoli, M. P., Åberg, C., Salvati, A., and Dawson, K. A. (2012). Biomolecular coronas provide the biological identity of nanosized materials. *Nat. Nanotechnol.* 7, 779–786. doi: 10.1038/nnano.2012.207
- Monopoli, M. P., Wan, S., Bombelli, F. B., Mahon, E., and Dawson, K. A. (2013). Comparisons of nanoparticle protein corona complexes isolated with different methods. *Nano Life* 03:1343004. doi: 10.1142/S1793984413430046
- Moyano, D. F., Saha, K., Prakash, G., Yan, B., Kong, H., Yazdani, M., et al. (2014). Fabrication of corona-free nanoparticles with tunable hydrophobicity. *ACS Nano* 8, 6748–6755. doi: 10.1021/nn5006478
- Nienhaus, K., Wang, H., and Nienhaus, G. U. (2020). Nanoparticles for biomedical applications: exploring and exploiting molecular interactions at the nano-bio interface. *Mater. Today Adv.* 5:100036. doi: 10.1016/j.mtadv.2019.100036
- Time to deliver (2014). Time to deliver. *Nat. Biotechnol.* 32:961. doi: 10.1038/nbt.3045
- O'Connell, D. J., Bombelli, F. B., Pitek, A. S., Monopoli, M. P., Cahill, D. J., and Dawson, K. A. (2015). Characterization of the bionano interface and

- mapping extrinsic interactions of the corona of nanomaterials. *Nanoscale* 7, 15268–15276. doi: 10.1039/c5nr01970b
- Palchetti, S., Caputo, D., Digiaco, L., Capriotti, A., Coppola, R., Pozzi, D., et al. (2019). Protein corona fingerprints of liposomes: new opportunities for targeted drug delivery and early detection in pancreatic cancer. *Pharmaceutics* 11:31. doi: 10.3390/pharmaceutics11010031
- Palchetti, S., Digiaco, L., Pozzi, D., Peruzzi, G., Micarelli, E., Mahmoudi, M., et al. (2016). Nanoparticles-cell association predicted by protein corona fingerprints. *Nanoscale* 8, 12755–12763. doi: 10.1039/c6nr03898k
- Pattipeiluhu, R., Crielard, S., Klein-Schiphorst, I., Florea, B. I., Kros, A., and Campbell, F. (2020). Unbiased identification of the liposome protein corona using photoaffinity-based chemoproteomics. *ACS Cent. Sci.* 6, 535–545. doi: 10.1021/acscentsci.9b01222
- Peer, D., Karp, J. M., Hong, S., Farokhzad, O. C., Margalit, R., and Langer, R. (2007). Nanocarriers as an emerging platform for cancer therapy. *Nat. Nanotechnol.* 2, 751–760. doi: 10.1038/nnano.2007.387
- Petros, R. A., and Desimone, J. M. (2010). Strategies in the design of nanoparticles for therapeutic applications. *Nat. Rev. Drug Discov.* 9, 615–627. doi: 10.1038/nrd2591
- Pisani, C., Gaillard, J. C., Dorandeu, C., Charnay, C., Guari, Y., Chopineau, J., et al. (2017). Experimental separation steps influence the protein content of corona around mesoporous silica nanoparticles. *Nanoscale* 9, 5769–5772. doi: 10.1039/c7nr01654a
- Posthumadeboer, J., Piersma, S. R., Pham, T. V., Van Egmond, P. W., Knol, J. C., Cleton-Jansen, A. M., et al. (2013). Surface proteomic analysis of osteosarcoma identifies EPHA2 as receptor for targeted drug delivery. *Br. J. Cancer* 109, 2142–2154. doi: 10.1038/bjc.2013.578
- Pozzi, D., Colapicchioni, V., Caracciolo, G., Piovesana, S., Capriotti, A. L., Palchetti, S., et al. (2014). Effect of poly(ethylene glycol) (PEG) chain length on the bio-nano- interactions between PEGylated lipid nanoparticles and biological fluids: From nanostructure to uptake in cancer cells. *Nanoscale* 6, 2782–2792. doi: 10.1039/c3nr05559k
- Pulgar, V. M. (2019). Transcytosis to cross the blood brain barrier, new advancements and challenges. *Front. Neurosci.* 13:1019. doi: 10.3389/fnins.2018.01019
- Rehman, Z. U., Hoekstra, D., and Zuhorn, I. S. (2011). Protein kinase A inhibition modulates the intracellular routing of gene delivery vehicles in HeLa cells, leading to productive transfection. *J. Control. Release* 156, 76–84. doi: 10.1016/j.jconrel.2011.07.015
- Rehman, Z. U., Hoekstra, D., and Zuhorn, I. S. (2013). Mechanism of polyplex- and lipoplex-mediated delivery of nucleic acids: Real-time visualization of transient membrane destabilization without endosomal lysis. *ACS Nano* 7, 3767–3777. doi: 10.1021/nn3049494
- Rejman, J., Oberle, V., Zuhorn, I. S., and Hoekstra, D. (2004). Size-dependent internalization of particles via the pathways of clathrin- and caveolae-mediated endocytosis. *Biochem. J.* 377, 159–169. doi: 10.1042/bj20031253
- Ritz, S., Schöttler, S., Kotman, N., Baier, G., Musyanovych, A., Kuharev, J., et al. (2015). Protein Corona of Nanoparticles: Distinct Proteins Regulate the Cellular Uptake. *Biomacromolecules* 16, 1311–1321. doi: 10.1021/acs.biomac.5b01018
- Sahay, G., Alakhova, D. Y., and Kabanov, A. V. (2010). Endocytosis of nanomedicines. *J. Control. Release* 145, 182–195. doi: 10.1016/j.jconrel.2010.01.036
- Salvati, A., Pitek, A. S., Monopoli, M. P., Prapainop, K., Bombelli, F. B., Hristov, D. R., et al. (2013). Transferrin-functionalized nanoparticles lose their targeting capabilities when a biomolecule corona adsorbs on the surface. *Nat. Nanotechnol.* 8, 137–143. doi: 10.1038/nnano.2012.237
- Schnitzer, J. E., and Bravo, J. (1993). High affinity binding, endocytosis, and degradation of conformationally modified albumins. *Potential role of gp30 and gp18 as novel scavenger receptors. J. Biol. Chem.* 268, 7562–7570.
- Schöttler, S., Becker, G., Winzen, S., Steinbach, T., Mohr, K., Landfester, K., et al. (2016a). Protein adsorption is required for stealth effect of poly(ethylene glycol)- and poly(phosphoester)-coated nanocarriers. *Nat. Nanotechnol.* 11, 372–377. doi: 10.1038/nnano.2015.330
- Schöttler, S., Landfester, K., and Mailänder, V. (2016b). Controlling the stealth effect of nanocarriers through understanding the protein corona. *Angew. Chemie Int. Ed.* 55, 8806–8815. doi: 10.1002/anie.201602233
- Shi, J., Kantoff, P. W., Wooster, R., and Farokhzad, O. C. (2017). Cancer nanomedicine: Progress, challenges and opportunities. *Nat. Rev. Cancer* 17, 20–37. doi: 10.1038/nrc.2016.108
- Sindhwan, S., Syed, A. M., Ngai, J., Kingston, B. R., Maiorino, L., Rothschild, J., et al. (2020). The entry of nanoparticles into solid tumours. *Nat. Mater.* 19, 566–575. doi: 10.1038/s41563-019-0566-2
- Sykes, E. A., Chen, J., Zheng, G., and Chan, W. C. W. (2014). Investigating the impact of nanoparticle size on active and passive tumor targeting efficiency. *ACS Nano* 8, 5696–5706. doi: 10.1021/nn500299p
- Tenzer, S., Docter, D., Rosfa, S., Wlodarski, A., Kuharev, J., Reik, A., et al. (2011). Nanoparticle size is a critical physicochemical determinant of the human blood plasma corona: A comprehensive quantitative proteomic analysis. *ACS Nano* 5, 7155–7167. doi: 10.1021/nn201950e
- Tham, D. K. L., and Moukhes, H. (2017). Determining cell-surface expression and endocytic rate of proteins in primary astrocyte cultures using biotinylation. *J. Vis. Exp.* 2017:e55974. doi: 10.3791/55974
- Toledo, A. G., Golden, G., Campos, A. R., Cuello, H., Sorrentino, J., Lewis, N., et al. (2019). Proteomic atlas of organ vasculopathies triggered by *Staphylococcus aureus* sepsis. *Nat. Commun.* 10:4656. doi: 10.1038/s41467-019-12672-x
- Torriche, M. (2016). Does nanomedicine have a delivery problem? *ACS Cent. Sci.* 2, 434–437. doi: 10.1021/acscentsci.6b00190
- Toy, R., Peiris, P. M., Ghaghada, K. B., and Karathanasis, E. (2014). Shaping cancer nanomedicine: The effect of particle shape on the in vivo journey of nanoparticles. *Nanomedicine* 9, 121–134. doi: 10.2217/nmm.13.191
- Varkouhi, A. K., Scholte, M., Storm, G., and Haisma, H. J. (2011). Endosomal escape pathways for delivery of biologicals. *J. Control. Release* 151, 220–228. doi: 10.1016/j.jconrel.2010.11.004
- Venditto, V. J., and Szoka, F. C. (2013). Cancer nanomedicines: so many papers and so few drugs! *Adv. Drug Deliv. Rev.* 65, 80–88. doi: 10.1016/j.addr.2012.09.038
- Veronese, F. M., and Pasut, G. (2005). PEGylation, successful approach to drug delivery. *Drug Discov. Today* 10, 1451–1458. doi: 10.1016/S1359-6446(05)03575-0
- Vilanova, O., Mittag, J. J., Kelly, P. M., Milani, S., Dawson, K. A., Rädler, J. O., et al. (2016). Understanding the kinetics of protein-nanoparticle corona formation. *ACS Nano* 10, 10842–10850. doi: 10.1021/acsnano.6b04858
- Villaseñor, R., Lampe, J., Schwaninger, M., and Collin, L. (2019). Intracellular transport and regulation of transcytosis across the blood–brain barrier. *Cell. Mol. Life Sci.* 76, 1081–1092. doi: 10.1007/s00018-018-2982-x
- Villaverde, G., and Baeza, A. (2019). Targeting strategies for improving the efficacy of nanomedicine in oncology. *Beilstein J. Nanotechnol.* 10, 168–181. doi: 10.3762/bjnano.10.16
- Walkey, C. D., Olsen, J. B., Song, F., Liu, R., Guo, H., Olsen, D. W. H., et al. (2014). Protein corona fingerprinting predicts the cellular interaction of gold and silver nanoparticles. *ACS Nano* 8, 2439–2455. doi: 10.1021/nn406018q
- Weber, C., Simon, J., Mailänder, V., Morsbach, S., and Landfester, K. (2018). Preservation of the soft protein corona in distinct flow allows identification of weakly bound proteins. *Acta Biomater.* 76, 217–224. doi: 10.1016/j.actbio.2018.05.057
- Wilhelm, S., Tavares, A. J., Dai, Q., Ohta, S., Audet, J., Dvorak, H. F., et al. (2016). Analysis of nanoparticle delivery to tumours. *Nat. Rev. Mater.* 1, 1–12. doi: 10.1038/natrevmats.2016.14
- Williams, K. J., and Chen, K. (2010). Recent insights into factors affecting remnant lipoprotein uptake. *Curr. Opin. Lipidol.* 21, 218–228. doi: 10.1097/MOL.0b013e328338cab
- Wolfram, J., and Ferrari, M. (2019). Clinical cancer nanomedicine. *Nano Today* 25, 85–98. doi: 10.1016/j.nantod.2019.02.005
- Yang, K., Mesquita, B., Horvatovich, P., and Salvati, A. (2020). Tuning liposome composition to modulate corona formation in human serum and cellular uptake. *Acta Biomater.* 106, 314–327. doi: 10.1016/j.actbio.2020.02.018
- Yin, B., Chan, C. K. W., Liu, S., Hong, H., Wong, S. H. D., Lee, L. K. C., et al. (2019). Intrapulmonary cellular-level distribution of inhaled nanoparticles with defined functional groups and its correlations with protein corona and inflammatory response. *ACS Nano* 13, 14048–14069. doi: 10.1021/acsnano.9b06424
- Yuan, Y.-Y., Mao, C.-Q., Du, X.-J., Du, J.-Z., Wang, F., and Wang, J. (2012). Surface charge switchable nanoparticles based on zwitterionic polymer for enhanced drug delivery to tumor. *Adv. Mater.* 24, 5476–5480. doi: 10.1002/adma.201202296

- Zani, I., Stephen, S., Mughal, N., Russell, D., Homer-Vanniasinkam, S., Wheatcroft, S., et al. (2015). Scavenger receptor structure and function in health and disease. *Cells* 4, 178–201. doi: 10.3390/cells4020178
- Zuhorn, I. S., Kalicharan, D., Robillard, G. T., and Hoekstra, D. (2007). Adhesion receptors mediate efficient non-viral gene delivery. *Mol. Ther.* 15, 946–953. doi: 10.1038/mt.sj.6300139
- Zuhorn, I. S., Visser, W. H., Bakowsky, U., Engberts, J. B. F. N., and Hoekstra, D. (2002). Interference of serum with lipoplex-cell interaction: modulation of intracellular processing. *Biochim. Biophys. Acta Biomembr.* 1560, 25–36. doi: 10.1016/S0005-2736(01)00448-5

**Conflict of Interest:** The authors declare that the research was conducted in the absence of any commercial or financial relationships that could be construed as a potential conflict of interest.

Copyright © 2020 Aliyandi, Zuhorn and Salvati. This is an open-access article distributed under the terms of the Creative Commons Attribution License (CC BY). The use, distribution or reproduction in other forums is permitted, provided the original author(s) and the copyright owner(s) are credited and that the original publication in this journal is cited, in accordance with accepted academic practice. No use, distribution or reproduction is permitted which does not comply with these terms.





# Methods to Scale Down Graphene Oxide Size and Size Implication in Anti-cancer Applications

Immacolata Tufano<sup>1,2</sup>, Raffaele Vecchione<sup>1\*</sup> and Paolo Antonio Netti<sup>1,2,3</sup>

<sup>1</sup> Center for Advanced Biomaterials for HealthCare@CRIB, Istituto Italiano di Tecnologia, Naples, Italy, <sup>2</sup> Department of Chemical, Materials and Industrial Production Engineering, University of Naples Federico II, Naples, Italy, <sup>3</sup> Interdisciplinary Research Center of Biomaterials, University of Naples Federico II, Naples, Italy

## OPEN ACCESS

### Edited by:

Davide Ricci,  
University of Genoa, Italy

### Reviewed by:

Consolato Sergi,  
University of Alberta Hospital, Canada  
Emanuel Axente,  
National Institute for Laser Plasma  
and Radiation Physics, Romania

### \*Correspondence:

Raffaele Vecchione  
raffaele.vecchione@iit.it

### Specialty section:

This article was submitted to  
Biomaterials,  
a section of the journal  
Frontiers in Bioengineering and  
Biotechnology

**Received:** 01 October 2020

**Accepted:** 10 November 2020

**Published:** 23 December 2020

### Citation:

Tufano I, Vecchione R and  
Netti PA (2020) Methods to Scale  
Down Graphene Oxide Size and Size  
Implication in Anti-cancer  
Applications.  
Front. Bioeng. Biotechnol. 8:613280.  
doi: 10.3389/fbioe.2020.613280

Despite considerable progress in the comprehension of the mechanisms involved in the origin and development of cancer, with improved diagnosis and treatment, this disease remains a major public health challenge with a considerable impact on the social and economic system, as well as on the individual. One way to improve effectiveness and reduce side effects is to consider responsive stimuli delivery systems that provide tailor-made release profiles with excellent spatial and temporal control. 2D nanomaterials possess special physicochemical properties (e.g., light, ultrasonic and magnetic responses) and biological behaviors such as endocytosis, biodistribution, biodegradation, and excretory pathways, which lead to their use in various biomedical applications. In particular, among 2D nanomaterials, graphene and its derivatives, namely graphene oxide (GO) nanomaterials, have attracted enormous attention in cancer diagnosis and therapy because they combine, in a unique material, extremely small size, NIR absorption, delocalized electrons, extremely high surface area, and versatile surface functionality. Taking into account the fundamental role played by GO size, in this review, we summarize the main methods employed to reduce and homogenize in nanometric scale the lateral dimensions of graphene oxide produced by chemical exfoliation of graphite, as well as post-synthesis separation techniques to uniform the size. We also discuss the implication of the small size in cancer treatment by exploiting GO nanocarriers as an effective theranostic tool.

**Keywords:** nanomedicine, 2D nanomaterials, graphene oxide, anticancer treatment, theranostic tool, photoacoustics

## INTRODUCTION

In accordance with the latest report of the International Agency for Research on Cancer, the incidence of cancer is increasing worldwide (Bray et al., 2018). Diagnosis has progressively increased from 14.8 million in 2014 to 18.1 million in 2018 (of which 23.4% in Europe) and 29.5 million are expected in 2040. Global cancer mortality has increased from 8.2 million in 2014 to 9.6 million in 2018. Patients surviving five years after diagnosis are currently 43.8 million. Despite considerable progress in diagnosis and treatment, this remains one of the most critical diseases with an enormous impact on the social and economic system (Torre et al., 2015). Current cancer treatment requires surgical resection (for solid tumors), followed by radiation

therapy, chemotherapy, or immunotherapy to kill the remaining cancer cells. The term cancer is used to define a series of critical diseases associated with replication and uncontrolled cellular spread. The abnormal proliferation of cells develops a tumor malformation characterized by a heterogeneous and complex microenvironment, which includes blood vessels, immune cells, and signaling molecules. This dynamic microenvironment strongly influences the growth and evolution of the tumor and the success of therapies. The impressive progress achieved in recent decades on the etiology of cancer has not even translated into tangible progress in therapy (Srinivasan et al., 2016). It is well known that most conventional chemotherapeutic drugs show unfavorable chemical-physical and pharmacological properties such as low aqueous solubility, irritating nature, lack of stability, rapid metabolism, and non-selective drug distribution (Iwamoto, 2013). These properties cause several adverse effects, including less therapeutic activity, dose-limiting side effects, low bioavailability of the anticancer drug at the site of action as well as high organ toxicity limiting the maximum tolerated dose and patient quality of life. Besides, resistance to many of the most active cytotoxic agents used in cancer therapy can occur in many tumors. Some tumors, initially responsive, recur and become resistant not only to the initial therapeutic agents but also to other drugs not used for treatment (Tomida and Tsuruo, 2002). This phenomenon is known as multidrug resistance (MDR) and is one of the main causes of failure in chemotherapeutic treatments. Therefore, it is necessary to develop highly efficient therapeutic systems able to overcome biological barriers, selectively distinguish cancerous tissues from healthy ones and react “intelligently” to the heterogeneous and complex tumor microenvironment for the on-demand release of therapeutic agents in the optimal dosage range (Sun et al., 2014). As early as 2006, the National Cancer Institute recognized nanotechnology as the science that can effectively change the basis for the diagnosis, treatment, and prevention of cancer, allowing the study and treatment of this disease at a molecular scale, in real-time and during the early stages of the process. Although particles between 10 and 100 nm are known since ancient times as components of pigments and dyes, the concept of nanotechnology as a potential manipulation of matter on the atomic scale is quite recent (Thrall, 2004). The application of nanotechnology to disease treatment, diagnosis, monitoring, and control of biological systems is referred to as “Nanomedicine.” The success of nanotechnology in the healthcare field is due to the possibility of working at the same scale as many biological processes, cellular mechanisms, and organic molecules (Liu et al., 2007). The traditional application of nanotechnology in cancer therapy is to improve pharmacokinetics and reduce the side effects of chemotherapy through nanocarriers that target selectively and deliver anti-cancer drugs to tumor tissues. The nanocarriers used for drug delivery are manufactured from both soft (organic and polymeric) and hard (inorganic) materials assembled in different architectures such as polymeric micelles, nanoparticles, liposomes, and dendrimers, which share the dimensional characteristic of the nanometric scale. The active cargo can be easily encapsulated or covalently bonded with the nanocarriers exploiting the chemical-physical

properties of the materials that compose them (Fleige et al., 2012). The nanostructured transport systems are originally designed to increase cellular uptake and accumulation due to their nanometric size. One of the unique features of almost all solid tumors is “leaky” tumor vascularization and compromised lymphatic drainage. As previously described, a growing tumor mass generates a network of abnormal blood vessels (angiogenesis) for increasing oxygen and nutrients supply. This feature, combined with the poor lymphatic clearance typical of tumor masses, allows particles between 10 and 100 nm in size to passively penetrate through the pores of blood vessel walls and accumulate preferentially in tumor sites rather than in other healthy tissues. This effect, known as enhanced permeability and retention, (EPR) has shown promising results compared to standard therapies in terms of reduced toxicity in healthy tissues and increased drug concentration at the target site. Over the past 20 years, a variety of nano-carriers such as liposomes, micelles, albumin nanoparticles and polymeric conjugates have been approved for the treatment of various tumors (Ventola, 2017). However, the nanocarrier exploiting the EPR effect must necessarily have a long circulation time in the blood to arrive at the target area. One of the approaches commonly used to increase the efficiency of drug transport to cells and cancerous tissues is to modify the surface of nanocarriers with water-soluble polymers such as polyethylene glycol (PEG). Because of their hydrophilic nature, PEG chains create a hydrated cloud that protects the surface from aggregation, opsonization, and phagocytosis, increasing blood circulation time (Suk et al., 2016). Doxil<sup>®</sup>, PEG-coated liposomal doxorubicin was approved by the US FDA in 1995 and is used for the treatment of breast cancer through the accumulation of passive cancer. However, the passive targeting of drug carrier systems through the EPR effect has some limitations. First, the EPR effect is highly biologically dependent on the degree of vascularization and angiogenesis of the tumor. Also, the high interstitial pressure in the central area of the tumor not only inhibits the delivery of the drug by convection but also compresses new blood vessels. As a result, blood is led away from the center of the tumor to the periphery (Attia et al., 2019). An ideal nanocarrier should simultaneously show a high accumulation in the tumor and cellular internalization after achieving tumor tissue. However, the EPR effect does not enhance the uptake of nanoparticles into the cells. For this reason, next-generation therapeutic nanoparticles have an active targeting mechanism. Active targeting is usually performed by binding a variety of specific ligands to the surface of the nanocarrier that can recognize specific surface molecules that are overexpressed by tumor cells but not present in normal cells. Through this mechanism, it is possible to increase the affinity of the nanocarrier for the surface of cancer cells or tumor tissue and thus significantly increase the amount of drug delivered to the target cell compared to the free drug or passive targeting nanosystems (Qiao et al., 2019). The stochastic nature of ligand-receptor interactions in active targeting and the lack of cell, tissue, and organ specificity of the laws governing the spread of the nanocarrier within the body in passive targeting, result in these processes being poorly applied in the clinic and suggest the need for more efficient delivery strategies (Mura et al., 2013).

One way to improve effectiveness and reduce side effects is to consider responsive stimuli delivery systems that provide tailor-made release profiles with excellent spatial and temporal control. Compared to traditional nanocarriers, responsive stimuli delivery systems are designed to improve solubility, bioavailability and to prolong the blood circulation time, besides, they can be chemically optimized to achieve selective drug release at desired action sites, which can enable them to bypass physiological or pathological barriers and achieve higher therapeutic efficacy (Vijayakameswara Rao et al., 2018). Commonly this approach has been realized with biocompatible materials properly engineered to undergo a specific protonation, a hydrolytic rupture, a conformational change in response to a specific stimulus. The investigated stimuli include endogenous stimuli (e.g., reactive oxygen species (ROS), redox, pH, and enzymes) and exogenous stimuli (e.g., light, temperature, magnetic field, and ultrasound). Another aspect to consider in designing an effective therapy plan is the real-time monitoring of the therapy. With conventional treatments, diagnosis, therapy, and evaluation of the effect of the therapy are independent processes. This prolongs healing times and increases the suffering of cancer patients, especially when considering that contrast agents used in classical imaging techniques are not free of side effects. To overcome these obstacles, a promising clinical application consists of systems able to combine drug and diagnostic agents on the same nanocarriers to detect disease status and also provide therapeutic agents to target sites with real-time monitoring of pharmacokinetics, distribution and accumulation of drugs in tumors, leading to effective tumor inhibition as soon as possible (Zhao et al., 2018). Nano-systems that can integrate imaging and therapy are referred to as nano-theranostics. If the materials selected for nano-theranostic systems are responsive to electromagnetic, sound, or thermal fields, it is also possible to combine chemotherapy and imaging with other treatments. One of the most studied topics in recent years is the combination of chemotherapy with photothermal therapy (PTT) since photothermal therapy is a minimally invasive and potentially effective treatment. Photothermal therapy is a physical-chemical therapy for the treatment of cancer that employs optical radiation in the near-infrared (NIR) wavelength range (700–2000 nm). When a laser is focused on a tissue, the photons are absorbed by the intercellular and intracellular areas and the energy of the photons is converted into heat. As a result, the temperature of the tissues increases, leading to the death of cells and tissues (Lo, 2017). The local increase in temperature due to radiation not only causes the ablation of tumors but improves the permeability of the cell membrane, making the accumulation of nanoparticles in tumor cells more effectively and hinders the repair of DNA damage caused by anticancer drugs in tumor cells, increasing the effects of chemotherapy agents (Park et al., 2010). In addition, NIR radiation used, also known as “optical window” or “therapeutic window,” is the wavelength range that has the greatest depth of penetration into tissues. The most widely accepted NIR photothermal agents include fluorescent dyes, two-dimensional inorganic materials (e.g., carbon nanotubes, graphene oxide, and gold materials), and polydopamine (Sakudo, 2016). Ultra-thin two-dimensional (2D) nanomaterials are a

large class of nanomaterials with sheetlike structures, lateral dimensions greater than 100 nm, and thickness less than 5 nm (Tan et al., 2017). This class of materials is in continuous evolution and includes nanomaterials of different chemical compositions and crystalline structures. Generally speaking, ultra-thin 2D nanomaterials are distinguished as layered and non-layered 2D nanomaterials. In layered nanomaterials, the atoms in each layer are connected by strong chemical bonds, while the layers stack together to form bulk crystals through weak van der Waals interactions. In contrast, non-layered nanomaterials crystallize in three dimensions through atomic or chemical bonds to form bulk crystals. The study of 2D nanomaterials was first reported when Novoselov et al. (2004) succeeded in exfoliating graphene from graphite (Novoselov et al., 2004), and since then research on ultra-thin two-dimensional nanomaterials has grown exponentially in the fields of condensed matter physics, materials science, chemistry, and nanotechnology. The unique characteristics of 2D nanomaterials have raised important and exciting questions about their interactions with biological systems. Being the thinnest materials, 2D nanomaterials have the highest specific surface areas among all known materials, which means that they can efficiently load and deliver therapeutic agents. Also, the planar nanostructure gives these nanomaterials special physicochemical properties (e.g., light, ultrasonic and magnetic responses) and biological behaviors such as endocytosis, biodistribution, biodegradation, and excretory pathways, which lead to their use in various biomedical applications (Chimene et al., 2015; Hu et al., 2019). Among 2D nanomaterials, graphene, and its derivatives have attracted enormous attention in cancer diagnosis and therapy because they combine, in a unique material, extremely small size, NIR absorption, delocalized electrons, extremely high surface area, and versatile surface functionality. Graphene is an allotropic form of carbon defined as a single layer (monolayer) of carbon atoms  $sp^2$ -bonded, which are densely packed in a hexagonal honeycomb lattice (Suryanto, 2017). Since its recent discovery, this material has attracted enormous attention for its unique and, sometimes surprising, properties. Graphene is the thinnest and lightest compound known, it has a maximum tensile strength that is hundreds of times higher than steel; the electronic mobility exhibited by graphene even at room temperature, makes it an excellent heat conductor and also the best conductor of electricity and it has a great ability of optical transmittance (Rajakumar et al., 2020). In the original study of Novoselov et al. (2004) single or a few layers of pristine graphene were obtained with the “scotch tape” method of mechanical exfoliation of the graphite using adhesive tape. However, this method is not scalable, and therefore other approaches have been proposed, including chemical vapor deposition (Obraztsov, 2009), arc discharge (Subrahmanyam et al., 2009), and epitaxial growth on SiC (Camara et al., 2008). To date, the most widely used method when large scale graphene production is required is the wet chemical exfoliation of graphite (Eigler et al., 2013). This method involves the liquid-phase exfoliation of graphite which is composed of layers of graphene assembled parallel to each other and linked together by Van der Waals interactions. To break the interactions that hold together the graphene layers in the

graphite, intense oxidation of the aromatic system is necessary. The oxidation generates an intermediate, known as graphite oxide with a high density of oxygenated functional groups and which is then transformed into reduced graphene oxide by chemical or electrochemical reduction. Graphite oxide, obtained from the oxidation of graphite, can be exfoliated in solution to form graphene oxide (monolayer) (GO), or partially exfoliated to form few-layers graphene oxide (Bianco et al., 2013). GO, initially considered as an intermediate of one of the graphene production processes, has become a material that can be considered both for fundamental research and for its potential applications. The simple, scalable, and economical production process, coupled with the peculiar chemical-physical characteristics, make GO one of the most promising nanomaterials in several fields and, notably, in the cross-section of nanotechnology and biotechnology. GO is a single or a few-layer material with a high oxygen content, typically characterized by atomic C/O ratios below 3.0 and generally closer to 2.0. Unlike the perfectly ordered crystalline structure of graphene, GO has a two-dimensional structure in which crystalline regions and regions with amorphous defects of  $sp^3$  (Srinivasan et al., 2016) hybridized carbons and functional groups containing oxygen, coexist (He et al., 1998; **Figure 1**). The different oxygenated functions located on one or both sides of the GO sheet, make this material soluble and processable in water and many organic solvents and make the surface of GO very versatile for functionalization or chemical changes to finely modify its properties or to increase biocompatibility (Singh et al., 2018).

The aromatic structure instead allows non-covalent interaction with  $\pi$  conjugated molecules and confers to the GO the ability to absorb light in the range of NIR (700–900 nm). This property is particularly interesting when considering cellular hyperthermia in the treatment of tumors as a minimally invasive alternative to surgery (Gonçalves et al., 2013). Furthermore, functionalized graphene oxide and nanocomposites based on GO have interesting optical and magnetic properties and can be employed as contrast agents for various biological imaging modalities including fluorescence imaging, photoacoustic imaging, and magnetic resonance imaging (Yang et al., 2013). The era of GO in cancer therapy started in 2008 with pioneering Dai's group study. They demonstrated that polyethylene glycol-functionalized nanographene oxide (NGO-PEG) was able to efficiently complex water-insoluble aromatic drug molecules via non-covalent Van der Waals interactions. This new nanocarrier showed *in vitro* cellular uptake and killing potential for some cancer cell lines (Liu et al., 2008). Subsequently, GO was conjugated with biopolymers (Mirzaie et al., 2019), biomolecules (Li R. et al., 2020), metals (Kordi et al., 2019; Cobos et al., 2020), and metal oxides (Luo Y. et al., 2019; Pramanik et al., 2019) to create intelligent nanoplatforms able to respond at every stage of the cancer treatment process, from targeting to imaging and therapy. Recently Burnett et al. (2020) considered, for the first time, GO not as a platform for drug transport or photothermal therapy, but as the therapy itself on human osteosarcoma cancer cells. The authors aimed to evaluate the toxicity of GO on osteosarcoma *in vitro* by determining the production of reactive oxygen species (ROS) and the rate of apoptosis in normal

osteoblast cell line and human osteosarcoma cell lines. In the latter case, they used the CRISPR-Cas9 technique, a molecular scissor, to remove the insulin growth factor 1 (IGF<sub>1</sub>) and its binding protein (IGFBP<sub>3</sub>) involved in the tumorigenesis. Their results showed a significantly higher rate of apoptosis and ROS generation in the osteosarcoma cells than in normal osteoblasts, especially in cells in which IGF<sub>1</sub> and IGFBP<sub>3</sub> were knocked out. Although it seems that GO applications in the field of cancer therapy are only limited by the creativity of scientists, to date, no biomedical nano-material based on GO has been successfully translated into clinical use in patients. This is partly due to the relatively recent application of GO in the biomedical field, but, above all, it depends on the fact that data on the biocompatibility and cytotoxic potential of graphite oxide are controversial and not yet complete. In a systematic study on the toxicity of GO *in vitro*, Chang et al. (2011) investigate the effect of GO on the morphology, viability, mortality, and membrane integrity of human lung carcinoma epithelial cell line. Their results suggest that GO has no obvious toxicity on cell lines even at high doses, but GO causes dose-dependent oxidative stress which induces a slight decrease in cell viability at the dose of 200  $\mu\text{g/mL}$  (Chang et al., 2011). The overproduction of oxygen reactive species (ROS) is a known and typical toxicological mechanism of nanoparticles also of a different nature than carbon nanoparticles and has been confirmed for GO also on other cell lines, e.g., on murine lung epithelial cell lines, without any influence on viability and cell proliferation even at relatively high doses (Bengtson et al., 2016). Wang K. et al. (2011) demonstrated instead a dose-dependent toxicity of GO both *in vitro* and *in vivo*. In particular, human fibroblast cells internalize graphene oxide nanosheets predominantly in the cytoplasm, and even at 50  $\mu\text{g/mL}$  doses cause apparent toxicity in terms of decreased cell survival rate, cell-floating activation and cell apoptosis. Similar serious results were found after intravenous administration in mice. GO remains in the bloodstream for a long time and mainly accumulates in the lungs, liver, and spleen. The lungs are the most affected organs and the formation of epithelioid granulomas and interstitial inflammation is observed as the dose of GO increases (Wang K. et al., 2011). Radiotracking techniques to determine the distribution of GO in mice confirm the high absorption and long-term retention of GO in the lungs, kidneys, and spleen, with less accumulation in the brain, heart, and bones. In addition, GO showed good compatibility with red blood cells (Zhang X. et al., 2011). Liu Y. et al. (2013) also highlighted the mutagenic potential of GO *in vitro* and *in vivo*. At molecular level, GO interacts with genomic DNA and interferes with DNA replication, this interaction is very rapid and reaches its maximum effect after two hours of treatment with GO at a concentration of 600  $\mu\text{g/mL}$ . The authors attribute this mutagenic effect to the structural similarity between the highly planar graphene oxide nanosheets and planar aromatic DNA intercalators such as ethidium bromide or proflavine. Exactly like the DNA intercalators, GO could insert between the double helix base pairs and interfere with the flow of genetic information. To overcome this limitation, GO is usually covalently functionalized with hydrophilic polymers as polyethylene glycol. GO Pegylation can profoundly change



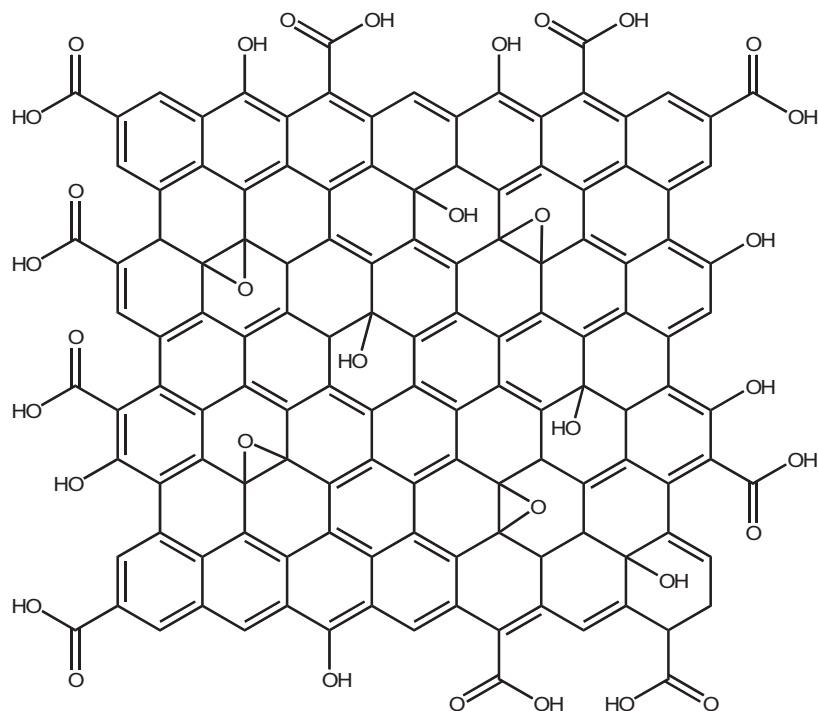


**FIGURE 1** | Chemical structure of Graphene Oxide based on the Lerf-Klinowski model.

GO cytotoxicity by attenuating the hydrophobic interactions between graphene or GO with cells and tissues (Zhang et al., 2012). One of the main causes of the controversy about the cytotoxicity of GO is undoubtedly the inhomogeneity of the material. GO is a heterogeneous material consisting of sheets with different sizes, number of layers, degree of oxidation, and chemical surface. Moreover, most of the synthetic methods used for the production of GO, although simple, low cost, and scalable, lack reproducibility as they require a long and tedious work-up that can heavily affect the chemical-physical characteristics of the material obtained. The first problem to be addressed in the design of GO-based theranostic nanoplatforms is to obtain a starting material with suitable and homogeneous dimensions. GO has size-dependent properties. First, the colloidal stability of GO sheets in aqueous solution and biological media is size-dependent. Nanometer-scale GO sheets form more stable colloidal dispersions due to the high density of charge resulting from the ionized -COOH groups at their edges (Kim et al., 2010). It is well known that the chemical-physical properties of materials, particularly their size, may regulate the cellular response to them. The size of the material impacts cellular uptake, renal clearance, transport to blood or brain barriers, and even partly the biological or toxicological effects induced by the material (Salatin et al., 2015). Graphene materials have sizes ranging from 10 nm, the size of some proteins, to more than 20  $\mu\text{m}$ , larger than many cells. Large sheets can therefore adhere to the plasma membrane and spread into the cells, while small sheets can be internalized via one or more receptor-mediated endocytosis mechanisms (Sanchez et al., 2012). The mechanism

of nanoparticle internalization in cells also depends on the type of cell. Yue et al. (2012) exploited the intrinsic photoluminescence of GO in NIR to study the internalization of GO samples with lateral dimensions of 350 nm and 2  $\mu\text{m}$  respectively in phagocytes (e.g., Macrophages) and non-phagocytes (e.g., Endothelial cells and cancer cells) cells. Their results showed that GO internalization in all non-phagocytes cells is negligible, which is possibly due to strong electrostatic repulsions between GO and cell surface (negatively charged). In comparison to the small GO signal in non-phagocytic cells, apparent fluorescence increases are observed in phagocytic cells, indicating a high macrophage uptake potential (Yue et al., 2012). Moreover, the saturated absorption of the two GO sheets with different sizes is similar, which means that GO, unlike traditional spherical or cylindrical particles, is internalized by macrophages in a way that is independent of size (Mendes et al., 2015). In contrast, the inflammatory response in cells and animals is strongly dependent on size and GO samples between 750 and 1300 nm induce increased production of inflammatory cytokines both *in vitro* and *in vivo* compared to GO samples between 50 and 350 nm (Ma et al., 2015). As we pointed out earlier, the tumor microenvironment allows the passive accumulation of nanoparticles via the enhanced permeability and retention (EPR) effect, which essentially relies on the size of the nanoparticles. Using single proton emission computed tomography (SPECT) imaging with (Deb et al., 2018).  $^{125}\text{I}$ -radiolabeling, Cai et al. discovered that sub-50 nm is the favored size range for successful PEGylated GO tumor accumulation *in vivo* through the EPR effect (Cao et al., 2016). In particular (Deb et al., 2018), I

Pegylated nano GO sheets with size less than 50 nm injected intravenously in nude mice with 4T1 tumors, displayed intense and uniform radioactive signals of the whole tumor region within 6 h after injection. The signal remained stable after 24 and 48 h and could be observed even after 96 h for the EPR effect. In contrast, the signal emitted by GO-sheets larger than 50 nm is very low even 1 h after injection and decreases rapidly, getting negligible after 6 h after injection. In addition, the distribution pattern of the two materials in healthy tissue is very similar, the liver was the organ with the greatest accumulation of both, although GO with size below 50 nm was eliminated faster than the one with a larger size. The emission of photoluminescence is also size-dependent and is attributed both to the increase in the energy gap due to the rise in oxygenated functional groups and to the nanostructure's electronic structure (Hens et al., 2012). In nanomedicine applications, therefore, the synthesis of GO with precise dimensions and narrow size distribution is crucial. Unfortunately, GO sheets are often prepared by chemical exfoliation of graphite and the lateral dimensions of the GO prepared by this convenient method are very polydisperse in the range from tens of nanometers to a hundreds of micrometers. Therefore, it is important to design methods during or post-synthesis to satisfy the above requirements. In this review, we highlight how the size of GO sheets can be controlled and optimized in the nanometric range that is appropriate for biological applications. Although graphene materials with dimensions below 10 nm are successfully obtained by bottom-up approaches from small molecules by microwave irradiation, hydrothermal, and pyrolysis method (Gayen et al., 2019), we focus much of the review on the size control strategies for GO obtained with the simpler and more cost effective top-down graphite oxidation methodologies. First, the general methods of GO synthesis are presented. In the following sections, we describe different strategies to control the size of GO nanoparticles that we distinguish as direct controllable synthesis and post-synthesis separation. In the last section, we will emphasize the applications of nano-graphene oxide (nGO) based platforms in cancer therapy. Nanocomposites in which GO is used in combination with inorganic particles (gold, iron oxide nanoparticles) are not described in this review.

## SYNTHETIC APPROACHES

Graphite, the precursor of GO, has a highly ordered crystalline structure composed of layers of  $sp^2$  hybridized carbon atoms connected within each layer by covalent and metallic bonds and by weak Van der Waals interactions between the layers. As a consequence, graphite is anisotropic, being a good electrical and thermal conductor in-plane and a weak electrical and thermal conductor perpendicular to the plane. The carbon layers in graphite are known as graphene layers (Chung, 2002). Anisotropy allows graphite to undergo chemical reactions called intercalation reactions in which the reagents are inserted between the graphene layers of graphite to form graphite intercalation compounds (GICs) that are electrically more conductive than graphite and then develop into other compounds like graphite oxide. Because

of the considerable thermodynamic stability of graphite, the conversion of graphite to graphite oxide requires very drastic reaction conditions involving concentrated acidic media and strong oxidizing agents. The recipes for graphite oxidation still used today, although with some modifications, are almost all based on three main methods: Brodie's method of 1855 (Brodie, 1858), Staudenmaier's method of 1889 (Staudenmaier, 1899), and the Hummers method of Hummers and Offeman (1958). Brodie's method consists of heating graphite at 60°C for 3–4 days in a mixture of potassium chlorate, an oxidizing agent, in fuming nitric acid. The oxidation step must be repeated for 4–7 cycles and before each step, the partially oxidized product must be isolated, washed, and dried. Staudenmaier works on Brodie's method to speed up the reaction and increase yield. He discovered that by replacing fuming nitric acid with a mixture of concentrated sulfuric acid: fuming nitric acid 3:1 and slowly adding potassium chlorate in multiple portions, the reaction continues in a single vessel. However, this reaction requires 4 days to complete. More than 100 years after Brodie's discovery, Hummers and Offemann proposed a new, faster, and safer method for graphite oxidation. This method involves three reaction steps at controlled temperatures. At low temperature (below 5°C) it occurs the slow addition of an excess of potassium permanganate (three eq.) to a suspension of graphite and sodium nitrite in concentrated sulfuric acid. The reaction continues for 30 min at mid-temperature ( $\sim 35^\circ\text{C}$ ) and the mixture becomes more homogenous. After this time, warm water is added to the mixture causing heat generation, the temperature reaches 98°C and the reaction is maintained at this temperature for 15 min by an exothermal heat, then the reaction is quenched with a hydrogen peroxide solution to reduce the residual permanganate and manganese dioxide to soluble colorless manganese sulfate. The formation of a bright yellow pasty mixture is evidence of the successful conversion of pristine graphite in GO. The oxidation products obtained with the three methods differ slightly in chemical composition and degree of oxidation. In general, GO obtained with the Hummer method has a higher degree of oxidation as revealed by the lower carbon to oxygen ratio (GO-Hummers 1.12 < GO-Staudenmaier 1.77 < GO-Brodie 2.52) and by the higher spatial distance between the layers observed in the XRD patterns (GO-Hummers 0.8133 nm > GO-Staudenmaier 0.7226 nm > GO-Brodie 0.7084 nm) (Shamaila et al., 2016). Although the methods using  $\text{KClO}_3$  and  $\text{HNO}_3$  suffer from long reaction times and the evolution of acid fog resulting from fuming nitric acid, and the highly explosive  $\text{ClO}_2$  gas generated when chlorate is mixed with strong acids, they remain the most powerful and well-known oxidative methods for producing GO on a preparative scale (Brisebois and Sijaj, 2020). Instead, the fastest, easiest, and safest Hummer method is the most widely used approach to obtain graphite oxide on a large scale. Because of its satisfactory characteristics, this method has been widely used to investigate the mechanism of GO formation, as well as widely revisited and modified. One of the most popular modifications of the Hummers method was proposed by Marcano et al. (2010) The Marcano method, known as the improved Hummers method, involves using a quantity of oxidizing agent ( $\text{KMnO}_4$ ) twice as much as the Hummers

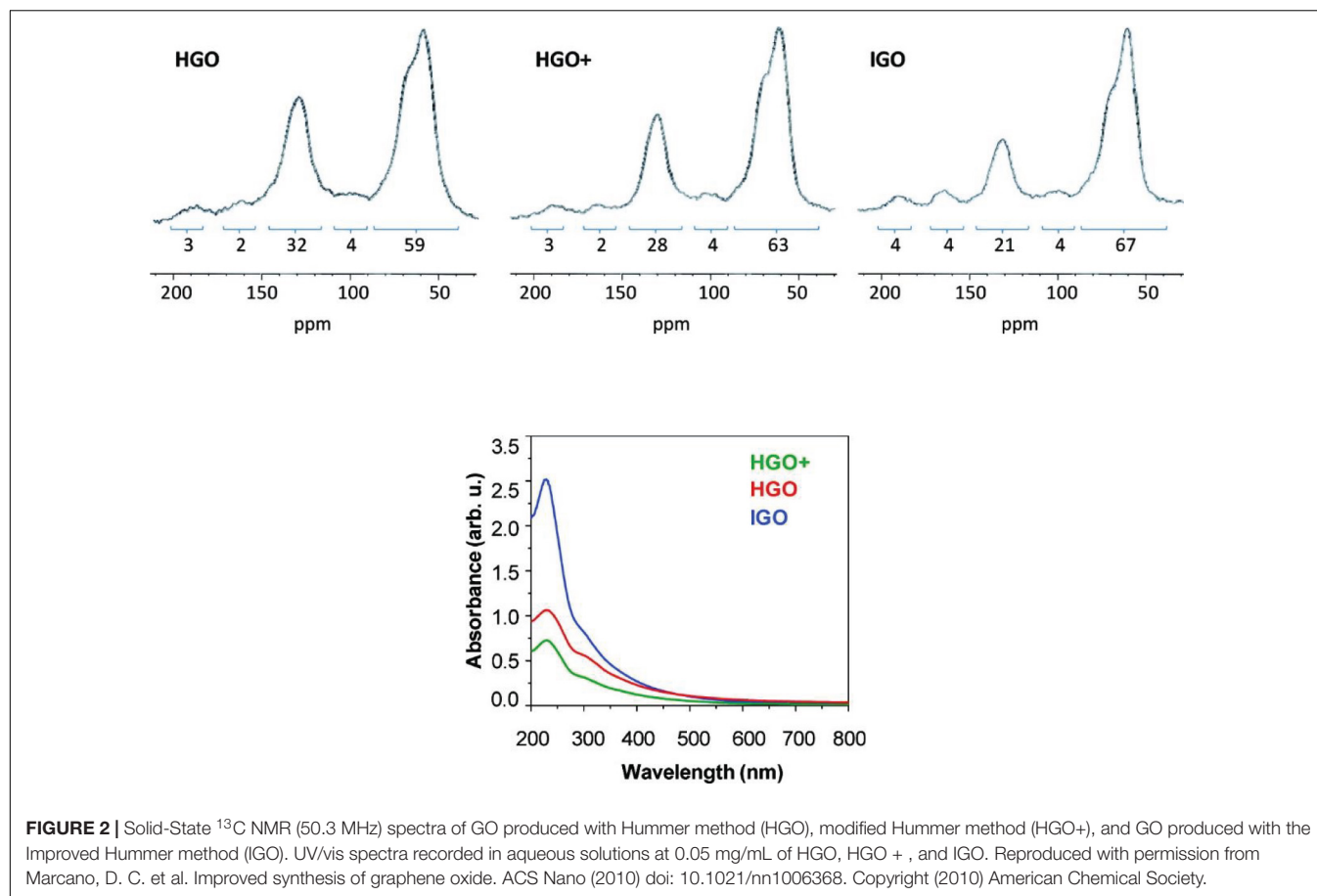
method, and the replacement of sodium nitrate with phosphoric acid ( $\text{H}_3\text{PO}_4$ ). The use of a higher amount of oxidizer results in a product with a higher degree of oxidation, as evidenced by the high ratio of alcohol/epoxide ( $\sim 60$  ppm) signals and graphitic  $\text{sp}^2$  carbon signal (130 ppm) in Solid-State  $^{13}\text{C}$  NMR spectra (Figure 2) of GO produced with the improved Hummer method (IGO) compared to NMR spectra of GO produced with Hummer method (HGO) and modified Hummer method (HGO+) with additional  $\text{KMnO}_4$ . The use of phosphoric acid, instead, allows obtaining a product with a more regular structure and with a greater number of isolated aromatic rings preserved, as evidenced by the overall absorption in the UV/Vis spectra of the three samples (Figure 2).

Also, the elimination of nitrate from the synthetic procedure avoids the evolution of  $\text{NO}_2$  and  $\text{N}_2\text{O}_4$  toxic gases. Chen et al. compared GO samples obtained from the same graphite source with the Hummer method without or with the use of  $\text{NaNO}_3$ , demonstrating that the exclusion of sodium nitrate from the reaction formula does not affect the chemical-physical properties (dispersibility, chemical structures, thicknesses, and lateral dimensions) of the product and the overall yield (Chen et al., 2013a). The authors provide a convenient method for the purification of wastewater collected from the GO purification process. The pollutant  $\text{Mn}^{2+}$  ions from wastewater can be easily converted into a precipitate of  $\text{Mn}_3\text{O}_4$  by adding  $\text{KOH}$ . The post-treatment of waste from nanomaterial production processes is a low considered issue, but essential for commercialization. Another version of the modified Hummers method without sodium nitrate consists of pre-oxidization of graphite flakes with a mixture of sulfuric acid, phosphorus pentoxide  $\text{P}_2\text{O}_5$ , and persulfate ions ( $\text{S}_2\text{O}_8^{2-}$ ) for 5 h at  $80^\circ\text{C}$  (Batalha et al., 2016). The oxidative pre-treatment increases the distance between the graphite layers in the graphite and renders it more available for the subsequent oxidation process. This two-step method results in GO samples with higher oxygen content. The increased interest in the properties of this material encouraged researchers to look for more rapid, cost-effective, green (free of toxic gases and polluting heavy metals), and safe (no risk of explosion) synthesis methods. In this scenario, oxidizers other than potassium permanganate were considered. For example, benzoyl peroxide (BPO) heated to  $110^\circ\text{C}$  in an open vessel with graphite powder oxidizes the pristine graphite in 10 min under acid and metal-free conditions (Shen et al., 2009). Although this method is highly efficient, the high instability of benzoyl peroxide and the structural damage in the oxidation product due to the high operating temperature render this procedure not applicable on a large scale. Peng et al. (2015) proposed a completely new method for GO synthesis using potassium ferrate ( $\text{K}_2\text{FeO}_4$ ) as oxidant.  $\text{K}_2\text{FeO}_4$  has a higher oxidation efficiency than  $\text{KMnO}_4$  in an acid environment, it can be handled without risk of explosion at temperatures as high as  $100^\circ\text{C}$  and it does not generate toxic or polluting by-products. In this approach, highly water-soluble GO is obtained after only 1 h stirring of a mixture of concentrated sulfuric acid,  $\text{K}_2\text{FeO}_4$ , and graphite flake at room temperature. The GO sheets prepared with  $\text{K}_2\text{FeO}_4$  have a single layer morphology [ $\sim 0.9$  nm thickness as measured by Atomic Force Microscopy (AFM)] with an average numerical

width of  $\sim 10$   $\mu\text{m}$  (from Scanning Electron Microscopy (SEM) images) and a degree of oxidation nearly equal to that of the GO produced using  $\text{KMnO}_4$ . The authors claim that the high oxidation and exfoliation state is due to the synergy between  $\text{FeO}_4^{2-}$  ions and atomic oxygen  $[\text{O}]$  produced *in situ*. Since the reaction process is extremely simple and requires no energy transfer (neither heating nor cooling), it is straightforward to scale up. Besides, the work-up of this method allows to recover the sulfuric acid used for centrifugation and to reuse it for at least another 10 times without affecting the reaction time and the quality of the product. This eco-friendly, safe, highly efficient, scalable, and low-cost approach is unfortunately difficult to reproduce because the strong oxidizing power of ferrate (VI) is directly related to its instability, particularly in acidic environments (Sofer et al., 2016). In high-acid aqueous solutions, potassium ferrate (VI) decomposes in a few seconds via an autocatalytic process, which limits its applications in chemical synthesis. Moreover, it is not widely commercially available and its synthesis involves the use of chlorine gas which is highly toxic. Among the modern approaches, particular attention is focused on the production of GO by electrochemical exfoliation which is simple, environmentally friendly, and substrate-free. Typically, GO flakes are generated taking advantage of the electrical conductivity of graphite (e.g., foil, rod or flakes, flexible paper) in aqueous electrolytes ( $\text{H}_2\text{SO}_4$  or  $\text{H}_3\text{PO}_4$ ). A typical apparatus for electrochemical exfoliation of graphite consists of an electrochemical cell with two electrodes of graphite in an aqueous solution of electrolytes (Liu J. et al., 2013). At first, a static potential of 1 V is applied to the two electrodes to wet the electrode surface and facilitate the accumulation of charges around the anode. The applied potential is then increased to +7 V and maintained for 5–10 min. At this potential value, the anions in the electrolytic solution are guided to intercalate between the galleries of the graphene layers. By alternating the potential between +7 and -7 V it is possible to obtain exfoliation of both electrodes. After only a few minutes of electrolysis, a change in color of the aqueous electrolyte from transparent to dark is observed, which indicates the formation of GO. Similar to chemical oxidation, various sources of graphite or metals such as platinum and titanium can be used as electrodes and a variety of electrolytes including inorganic aqueous solutions, surfactants, molten salts, and ionic liquids. The electrochemical exfoliation of graphite is a tunable process because the chemical and chemical-physical properties of the oxidation product (morphology and degree of oxidation) can be easily adapted by adjusting the experimental set-up (type and geometry of the electrodes, solution, electrolytic, applied voltage, time and temperature). An extensive review of electrochemical methods for GO synthesis has been provided very recently by Fang et al. (2019).

## MECHANISM OF GRAPHENE OXIDE FORMATION AND BREAKAGE

Knowing the formation mechanism of GO is a key step in the development of new materials with the desired properties. However, despite the remarkable progress in understanding the

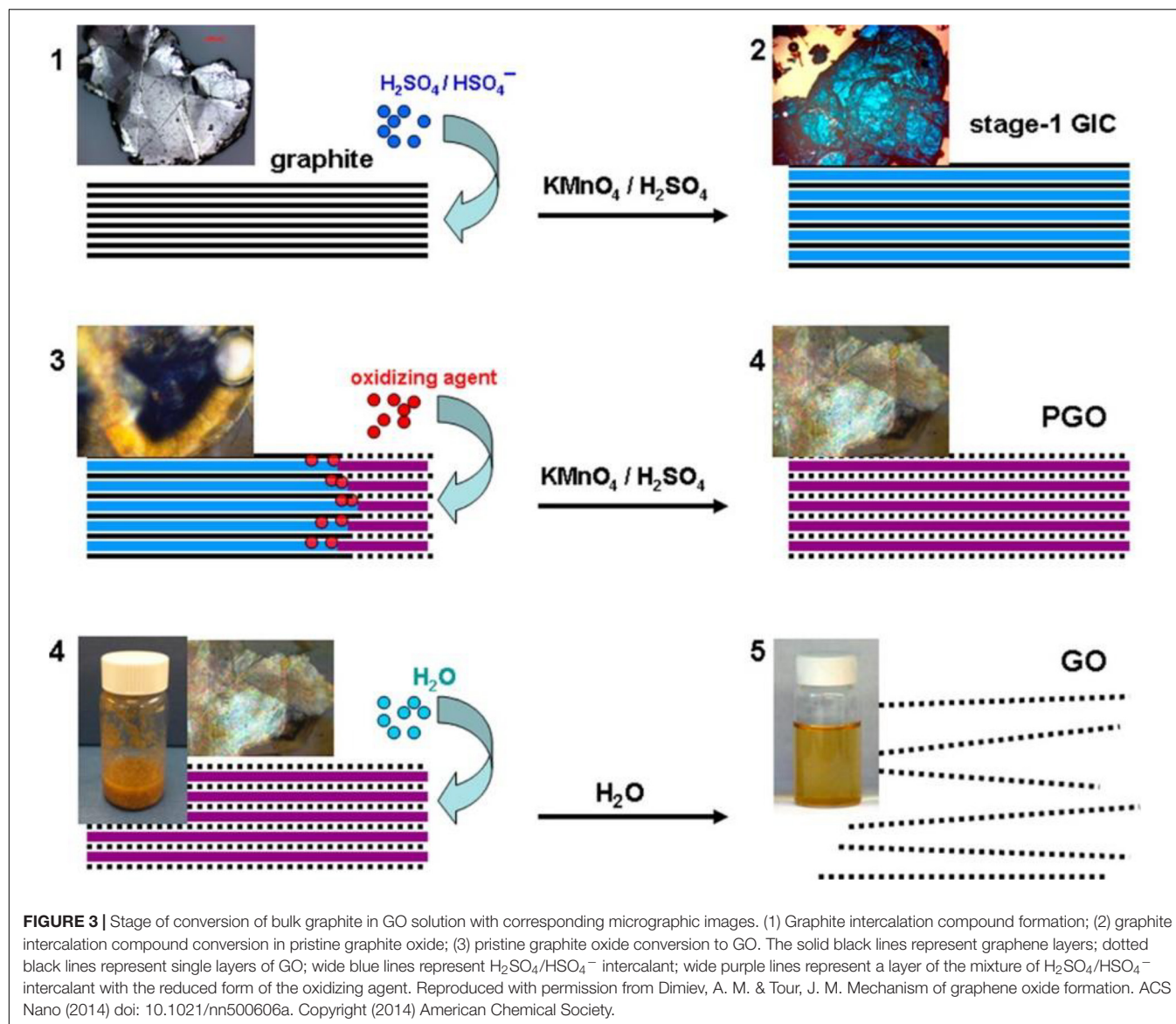


chemistry and structure of GO, the mechanism of its formation received little attention from the scientific community. The majority of the studies reported are theoretical and focus on the introduction of oxygen atoms into the graphene lattice with the formation of C-O bonds (Gao et al., 2011; Li C. et al., 2020). In an elegant work of Dimiev and Tour (2014), Dimiev and Tour have illuminated the steps that occur during the oxidation of graphite with potassium permanganate into concentrated sulfuric acid both within the solid graphite (between the graphene layers) and at the solid/liquid interface. Starting from the assumption that the characterization of the final graphite oxide obtained with the Hummer method, washed with water and dried is not very informative in mechanistic terms, the intermediate products that are formed in the various step of additions of permanganate have been isolated. The characterization, through optical microscopy and Raman spectrometry, of the obtained intermediates has permitted to identify of three distinct independent steps in the chemical oxidation of graphite with strong oxidants in concentrated mineral acids. The first step is the classic graphite intercalation reaction in which  $\text{H}_2\text{SO}_4$  molecules and  $\text{HSO}_4^-$  ions intercalate between graphite galleries without creating an orderly structure. The intercalation compound is formed after a few minutes that the graphite is exposed to the acid medium and imparts an intense blue color to the graphite. The intercalation is a necessary step for successful oxidation because it increases

the distance between the graphene layers in the graphite making the tunnels between the layers accessible to the oxidizing agent. The second step is the conversion of GIC into the oxidized form of graphite called pristine GO. In this step, the oxidizing agent molecules are inserted into the pre-occupied graphite galleries. Optical microscopies of the graphite flakes isolated at this stage clearly show that the conversion from intercalation compound (blue color at the center of the flake) to pristine GO (pearly white color at the edges) propagates from the edges of the flakes to the center (Figure 3). Theoretically, in the conversion from the intercalation product to the oxidation product, the oxidant molecules should replace or intercalate with the acid molecules present in the graphite interlayers. The experimental data show, instead, that the speed of the oxidation reaction is greater than the rate of diffusion, in other words, before the oxidizing agent diffuses between the graphite layers, it reacts rapidly with the nearby carbon atoms. So the pristine graphite oxide formation is the step that determines the rate of the entire GO formation process.

The final step is the conversion of pristine graphite oxide to GO by reaction with water during quenching and washing procedures. At this stage the graphite oxide, if sufficiently oxidized, delaminates spontaneously into single atomic layer sheets. To obtain exfoliation hydrogen bonds and electrostatic interactions between water and GO must overcome the

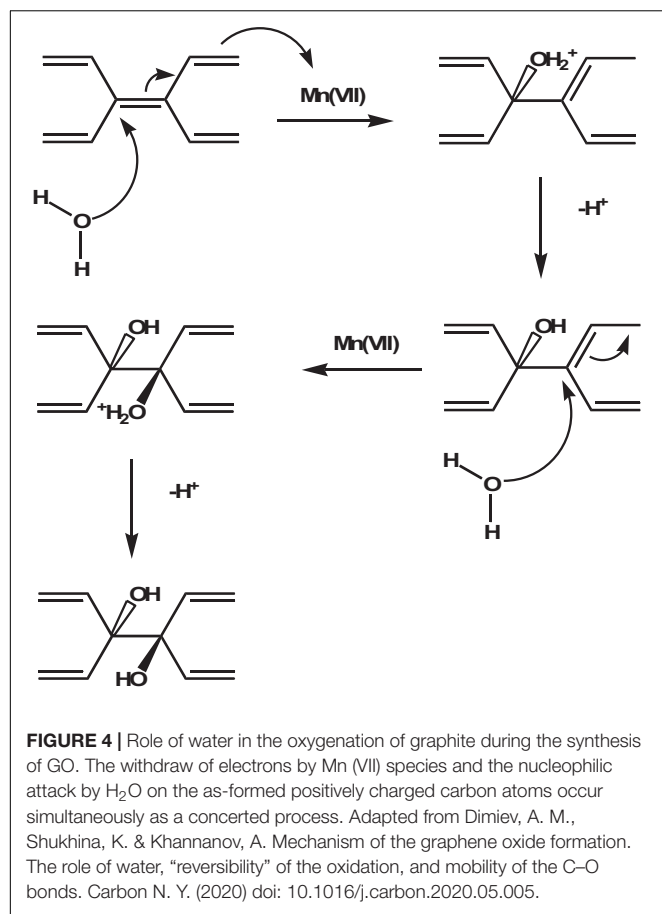




electrostatic interaction between graphene layers and intercalants (within each layer) and water molecules must be able to hydrolyze covalent sulfates that cross-link neighboring layers. Very recently the same authors have corrected the mechanism by reconsidering the role of water in the formation of GO. To investigate the nature of the effective oxidizing species attacking graphite layers, they found that the rate of oxidation reaction increases by a factor of 12 when the reaction is carried out in slightly diluted sulfuric acid (92%-88%) rather than in commercially available  $\text{H}_2\text{SO}_4$  at a concentration of 95%-98% (Dimiev et al., 2020). This observation opens an important perspective on the reaction mechanism. Following the same procedure of isolation and characterization of intermediates, the authors conclude that the species attacking the carbon atoms in the Hummers method are water molecules and not oxidant molecules. However, manganese species (VII) cannot be completely omitted from the reaction equation because they are consumed during the reaction and because once the

first equivalent of permanganate is consumed, the reaction does not go on unless another one is added. The authors claim that the reaction occurs directly between the  $\text{H}_2\text{SO}_4$ -graphite intercalation compound and water according to a mechanism very similar to the hydration of aromatic hydrocarbons in acid media (Figure 4) where water nucleophilically attacks the carbon atoms of graphite and the Mn (VII) species accept the electrons that are released, reducing to Mn (IV).

Since the formation of GO is a process controlled by the rate at which oxidizing molecules or water molecules diffuse between the graphite layers, smaller graphite flakes oxidize faster than larger ones. In addition, since no any graphite flake is equal to another, it is not surprising that GO is a material with a wide size distribution ranging from a few nanometers to hundreds of micrometers. However, it is possible to select GO sheets of appropriate size through post-synthesis methods or reduce the sheet size by adjusting the parameters of the chemical reaction



or by using mechanical promoters. The structural characteristics of the obtained nGO and the breaking mechanism are very dependent on the method used for breaking. In general, when acting on the chemical reaction (by varying the amount of oxidants, the time or temperature of the reaction) GO nanosheets with a higher oxygen content are obtained (Zhang et al., 2013), while when using physical methods to promote breakage (ultrasonication) nanosheet with a higher C/O ratio is obtained (Gonçalves et al., 2014). These experimental observations reflect a different breaking mechanism. As it is known, crystalline and amorphous regions coexist in the structure of GO. The breakage of GO into sheets with lower lateral size occurs through the formation and propagation of cracks over defects zones, in particular regions with the  $sp^3$  bond like -C-OH and O-C-O. When GO is fragmented by increasing the amount of oxidants or prolonging the reaction time, the reaction mechanism is similar to that of oxidizing olefins with  $KMnO_4$  in an aqueous solution and has been demonstrated experimentally following the gradual opening of carbon nanotubes as the exposure time of the system in the oxidizing medium increases (Kosynkin et al., 2009). This mechanism involves the formation of a manganate ester in the rate-determining stage of the reaction. The ester further oxidizes to dione in the dehydrating medium and distorts the nearby double bonds making them more available to the next permanganate attack. The ketones can be further converted,

through their O-protonated forms, to the carboxylic acids that will line the edges of the nanosheet (Figure 5).

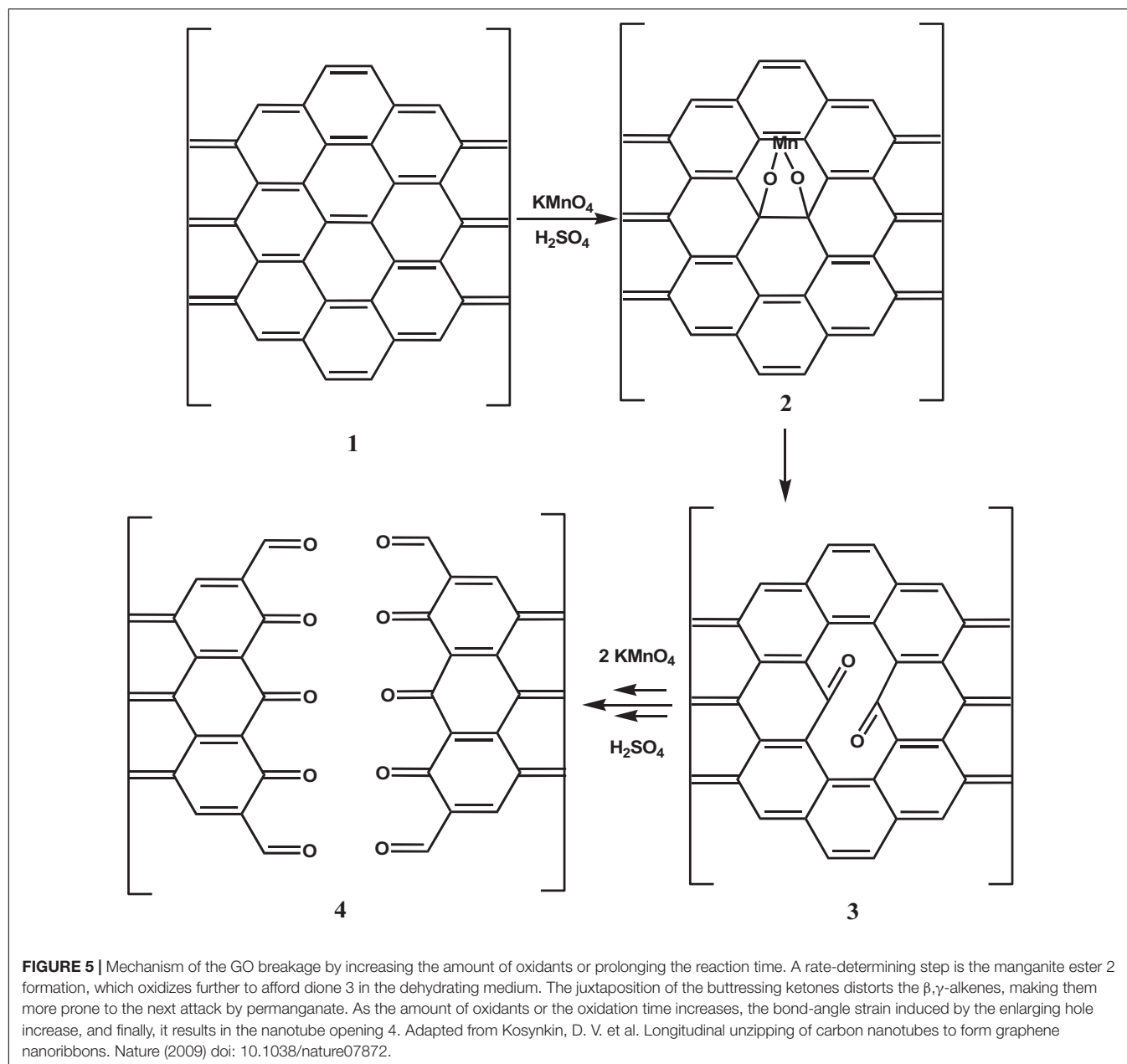
When the breaking of GO occurs by applying an external energy source, the mechanism involves the breaking of chemical bonds. The breaking starts from defects zones, in particular regions with the  $sp^3$  bonds like -C-OH and O-C-O, as previously said. After propagation of cracks, smaller sheets are obtained (Figure 6). If the process continues a smaller, but also more hydrophobic material will form. The use of ultrasound generates a local increase in temperature and pressure that promotes the decomposition of water molecules in the medium into hydroxyl radicals.  $\cdot OH$  radicals have the potential to reduce carboxylic and carbonyl groups by restructuring the aromatic carbon network and forming a more hydrophobic material (Gonçalves et al., 2014). This mechanism is defined as confined hot spot atomic reduction of GO.

## STRATEGIES FOR SIZE-CONTROL OF GRAPHENE OXIDE SHEETS

The main methods for controlling the size of nGO sheets are summarized in Table 1. Generally, they can be categorized as direct controllable synthesis and post-synthesis separation.

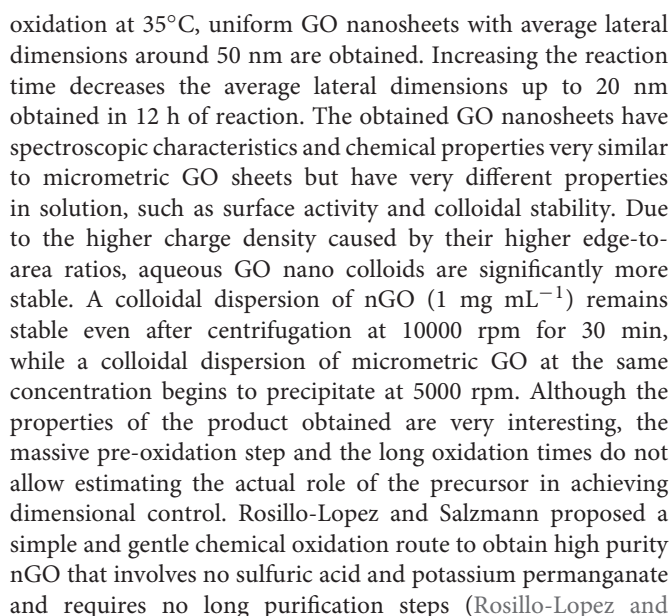
### Direct Controllable Synthesis Different Precursors

As source of GO production, graphite is intercalated with the acid medium, converted into its oxidized form by oxidants, and finally exfoliated by reaction with water. Graphite can be divided into natural graphite, organic matter rich in carbon, and artificial graphite, a synthetic matter obtained by heating of petroleum coke, coal-tar pitch, or oil. The particles are polycrystalline in both cases and composed of various single-crystalline domains (depending on the size of the domains, graphite is distinguished in micro- and macro-crystalline graphite). However, these domains are typically oriented in the same direction in natural graphite and randomly oriented in synthetic graphite (Asenbauer et al., 2020). The raw material characteristics play an important role in the properties of the oxidation material. For instance, natural graphite has a more orderly, but also wider crystalline structure, which facilitates the intercalation of oxidants between the graphene layers and the GO from natural graphite has a yield of exfoliation in water that is almost twice as high as the GO from artificial graphite (Botas et al., 2013). The size of graphite precursors, on the other hand, affects both the efficiency of the oxidation process and the lateral dimensions of GO sheets. McAllister et al. (2007) discovered that graphite flakes with a size of around 45  $\mu m$  are completely intercalated and rapidly oxidized, while larger flakes ( $\sim 400 \mu m$ ) do not intercalate completely and require more time to oxidize. Chen et al. (2016) fractionated graphite powders in three portions at increasing-size using standard sieves and oxidized them with an optimized Hummers method in which the volume of sulfuric acid used was increased as the size of the powders increased. The GO sheets obtained by this process are mostly single-layer and have an extremely narrow size distribution that



is highly dependent on the size of their graphite precursors (Chen et al., 2016). Therefore, the selection of the starting material is an important factor in predicting the size of the product obtained after oxidation. Concerning the initial size of graphite flakes used for synthesis size reduction control can be obtained by the same chemical exfoliation method, but with different precursors. Graphite nanofibers are materials produced by the decomposition at temperatures between 450 and 750°C of gases containing carbon and their mixtures on appropriate metal or metal alloy surfaces. These structures consist of very small graphite plates stacked in a particular conformation (parallel, perpendicular, or cornered to the fiber axis) and are widely used in hydrogen storage applications (Chambers et al.,

1998). The controlled oxidation of graphite nanofibers yields GO nanosheets with lateral dimensions below 100 nm and high colloidal stability. The graphite nanofibers used in this work have a highly crystalline structure in which the graphene sheets are coin-stacked along the  $\langle 001 \rangle$  fiber growth direction. The average diameter of nanofibers is about 130 nm, and the length is up to a few micrometers (Luo et al., 2010). In a typical experiment, the nanofibers are first subjected to a pre-oxidative treatment with  $K_2S_2O_8$  and  $P_2O_5$  in concentrated sulfuric acid for 4.5 h at 80°C, then naturally cooled, washed with water, and filtered. After pre-oxidation, the graphite nanofibers are oxidized using the modified Hummers method and then purified using an acid: acetone washing procedure. After 2 h of



Salzmann, 2016). Their synthetic methodology involves the use of Arc-discharge (ADC) material consisting of single-wall carbon nanotubes (SWCNT), multi-wall carbon nanotubes (MWCNT), and graphitic carbon obtained through the arc-discharge technique which consists in the application of a direct current between two graphite electrodes placed in an atmosphere of inert gas. Due to the high temperature between the electrodes the graphite at the anode sublimates and at the cathode a dark deposit containing the ADC material is formed (Rakhi, 2018). The carbon nanostructures obtained with this technique are highly flexible and have many small defects. The material is simply refluxed in a 1:1 solution of distilled water: nitric acid 6M for 20 h, then diluted with water and filtered. Neutralizing the dark brown filtrate obtained by carefully adding NaOH pellets, the precipitation of sodium-containing nGO is observed. The solid is vacuum filtered, purified by dialysis, and freeze-dried to obtain a dark brown nGO solid with a 21% yield. AFM and transmission electron microscopy (TEM) images show that the obtained flakes have a double-triple-layer morphology with an average lateral size between 20



**TABLE 1 |** List of methods for controlling the size of nGO sheets.

	General Method	Specific strategy	Feature size	References
Direct Controllable Synthesis	Different Precursors	<b>Graphite Nanofibers:</b> very small graphite plates (diameter about 130 nm and length up 5 $\mu\text{m}$ ) stacked in particular conformation	100-50 nm	Luo et al., 2010
		<b>Arc-discharge Material:</b> carbon material highly flexible and defective obtained by electrical breakdown	20-40 nm	Rosillo-Lopez and Salzmman, 2016
		<b>Aphanatic Graphite:</b> kind of graphite with disorder structure obtained by thermal decomposition of deep metamorphic	4.5 nm	Shen et al., 2020
	Reaction Parameters	<b>Time and Oxidant Amounts:</b> increase in the amount of oxidizing agent and timescale of oxidation in the same batch	50-20 nm	Zhang L. et al., 2009, Zhang et al., 2013
		<b>More Oxidation Cycles:</b> for each cycle the obtained product was isolated, purified and re-oxidized	10-5 nm	Fan et al., 2015
	Physical Promoters	<b>Ultra Sonication:</b> application of sound energy in a water bath or through probes to break GO sheets in low temperature conditions	100-500 nm	Farazas et al., 2018; Méndez-Romero et al., 2020
Post-synthesis Separation	Centrifugation	<b>Ball Milling:</b> graphite with or without solvents or oxidants was mechano-chemical oxidized in a rotating cylindrical jar filled with loose grinding balls.	depending on conditions from $\mu\text{m}$ to 30-50 nm	Posudievsky et al., 2012; Mahmoud et al., 2018; Luo D. et al., 2019
		<b>Differential Centrifugation Method:</b> GO sheets to be separated was divided in several fractions according to their size by varying the centrifugal force applied	250-900 nm	Chen et al., 2013b; Huang and Yuan, 2016
		<b>Density Gradient Centrifugation:</b> GO to be separated was placed on the surface of a vertical column of liquid with increased density from top to bottom and centrifuged. The particles migrated through the solvent gradient and settled where their buoyancy density equaled that of the gradient	40-500 nm	Sun et al., 2010; Li et al., 2013; Bidram et al., 2016
	Flocculation by Solvent	<b>Protonation in Organic Solvents:</b> large GO sheets precipitated selectively in organic solvents by protonation of carboxyl groups on the edges	500-100 $\mu\text{m}$	Zhang et al., 2015
		<b>pH Assisted Precipitation:</b> nGO sheets were recovered from the strongly acidic precipitate obtained from the work-up of the classic oxidation reaction by increasing pH value to 1.7 with 1M NaOH	90 nm	Hu et al., 2015

and 40 nm. The XPS survey spectra of GO flakes show that the final material contains only carbon and oxygen and the nitrogen impurities coming from the method are completely absent. The high purity of the obtained product combined with the simple procedure and the absence of harmful by-products makes this procedure very competitive, even if the yield is low and, during the reaction, there is the development of nitrogen oxide fumes ( $\text{NO}_x$ ). The authors, through thermal annealing investigations of nan-GO under high vacuum, also hypothesized the formation of a cyclic carboxylic anhydride during the thermal annealing of their GO. The anhydrides of the carboxylic acids are highly reactive chemical species that may constitute sites for the subsequent chemical functionalization with purpose-specific nucleophiles. Very recently graphene oxide quantum dots with an average lateral size of about 4.5 nm and an average thickness of  $\sim 3$  nm have been successfully synthesized using the Hummers method with sodium nitrite starting from aphanatic graphite (Shen et al., 2020). Aphanatic graphite is a kind of graphite ore that is composed of carbonaceous material by thermal decomposition of deep metamorphic products (such as from coal deterioration). It has lower thermal conductivity, lubrication, and oxidation resistance than fully crystalline graphite and therefore is much lower in price than flake graphite. Furthermore, unlike graphite flakes which have a layered structure with a length of each layer of about 35  $\mu\text{m}$ , the aphanatic graphite has a particle structure with an average particle diameter of about 5  $\mu\text{m}$ . Within each graphite aphanatic particle, there are small graphite nanocrystals not completely exfoliated during the formation period with dimensions less than 10 nm (**Figure 7A**). These defective characteristics allow the synthesis of graphene quantum dots by oxidation.

As explained above, in fact, the oxidation process of graphite under the conditions of the Hummers method is diffusion-controlled. With the same oxidant, the smaller and less crystalline graphite flakes are oxidized faster and more homogeneously than the large and highly crystalline flakes because the resistance to diffusion between the layers is lower (**Figure 7B**).

## Reaction Parameters

Graphene oxide is obtained by the oxidation of graphite flakes in strong mineral acids with potent oxidizing agents. As pointed out above the degree of oxidation, i.e., the O/C ratio, affects structural properties such as the degree of exfoliation, the content of defects, the number of functional groups, and also the size of the sheets. More precisely, the degree of oxidation is linearly correlated with the size of the flakes, therefore, increase the kinetics of oxidation by changing the reaction parameters of the classical method (stoichiometric amount of reagents, temperature, and reaction time), it is achievable GO flakes with smaller lateral dimensions than the starting graphite. The effect of the oxidation time and the amount of oxidants in the dimensional control of GO sheets obtained with the Hummer method was first studied in 2009. In this experiment, the graphite flakes are oxidized using the Hummer method with  $\text{KMnO}_4$  and  $\text{NaNO}_3$  in  $\text{H}_2\text{SO}_4$ . In the first reaction step, 4.5 eq. of  $\text{KMnO}_4$  are added to the mixture of graphite, sulfuric acid, and sodium nitrate, and the reaction is continued for 5 days at room temperature. A further

2.25 eq. of  $\text{KMnO}_4$  are then added to the resulting mixture and stirring is continued at room temperature for 5 days. The step of adding the 2.25 eq. of oxidizer and stirring for 5 days is repeated twice more and, at each step, the reaction products are isolated, purified, and characterized (Zhang L. et al., 2009). The single-layer GO sheets obtained with this extensive procedure exhibit a regular decrease in average lateral size as oxidants and reaction time increase. Using a similar procedure, Zhang et al. (2013) prepared GO nanosheets with a lateral size of less than 50 nm after three cycles of oxidation with  $\text{KMnO}_4$  of pre-oxidized graphite with  $\text{P}_2\text{O}_5$  and  $\text{K}_2\text{S}_2\text{O}_8$ . The TEM images of GO nanosheets obtained after three oxidation cycles show single layer sheets with rough edges and uniform lateral dimensions below 50 nm. The colloidal solutions of the nanosheets are stable in a wide range of pH values from 10 to 4, as evidenced by the value of their zeta potential which remains always below -30 mV. GO colloids are only stable when the zeta potential was below -30 mV. The colloidal stability in aqueous solution at different pH values is due to the higher degree of oxidation. FT-IR and XPS analyses indicate a higher content of oxygenated groups compared to GO samples obtained with lower oxidation steps. Moreover, GO nanosheets obtained after three oxidation steps emit a strong fluorescence at 520 nm when excited at 400 nm, which is almost six times stronger than nanosheets obtained after one or two oxidation cycles at the same concentration. The nanometer size, colloidal stability, and fluorescence emission are the characteristics required for biological applications of GO. The authors have also analyzed the cellular uptake and cytotoxicity of these materials on cells, finding that these events are similarly size-dependent. It is interesting to note that Fan et al. (2015) report the synthesis of photo-luminescent graphene oxide quantum dots of circular shape and diameter less than 10 nm by processing the purified GO obtained with the modified Hummer method to a further oxidation procedure with the same method. Tuning the reaction parameters is not a cost-effective solution for large-scale GO synthesis because it is time-consuming and it requires a large excess of acids and oxidizing agents.

## Physical Promoters

### Ultrasonication

The application of ultrasound and mechanical shaking are the most commonly reported procedures to perform the exfoliation of pristine graphite oxide in water in the final step of chemical oxidation. Sonication is only necessary for GO samples that are not fully oxidized, made from graphite samples with large particle size, but if the as-prepared GO is sufficiently oxidized it should spontaneously delaminate into single-layer sheets by simple stirring in water (Dimiev and Eigler, 2016). However, the sonication of aqueous GO dispersions is an efficient method to control the size of the flakes. Sonication is a process in which sound energy is applied to agitate particles in a medium. It is usually performed in a water bath in which samples are placed or through probes immersed directly in the sample to be sonicated. During sonication, vacuum bubbles are formed in the liquid. When the vacuum bubbles reach a certain size they collapse violently creating a high-pressure acoustic wave. The implosion of the bubble results in shear forces from cavitation

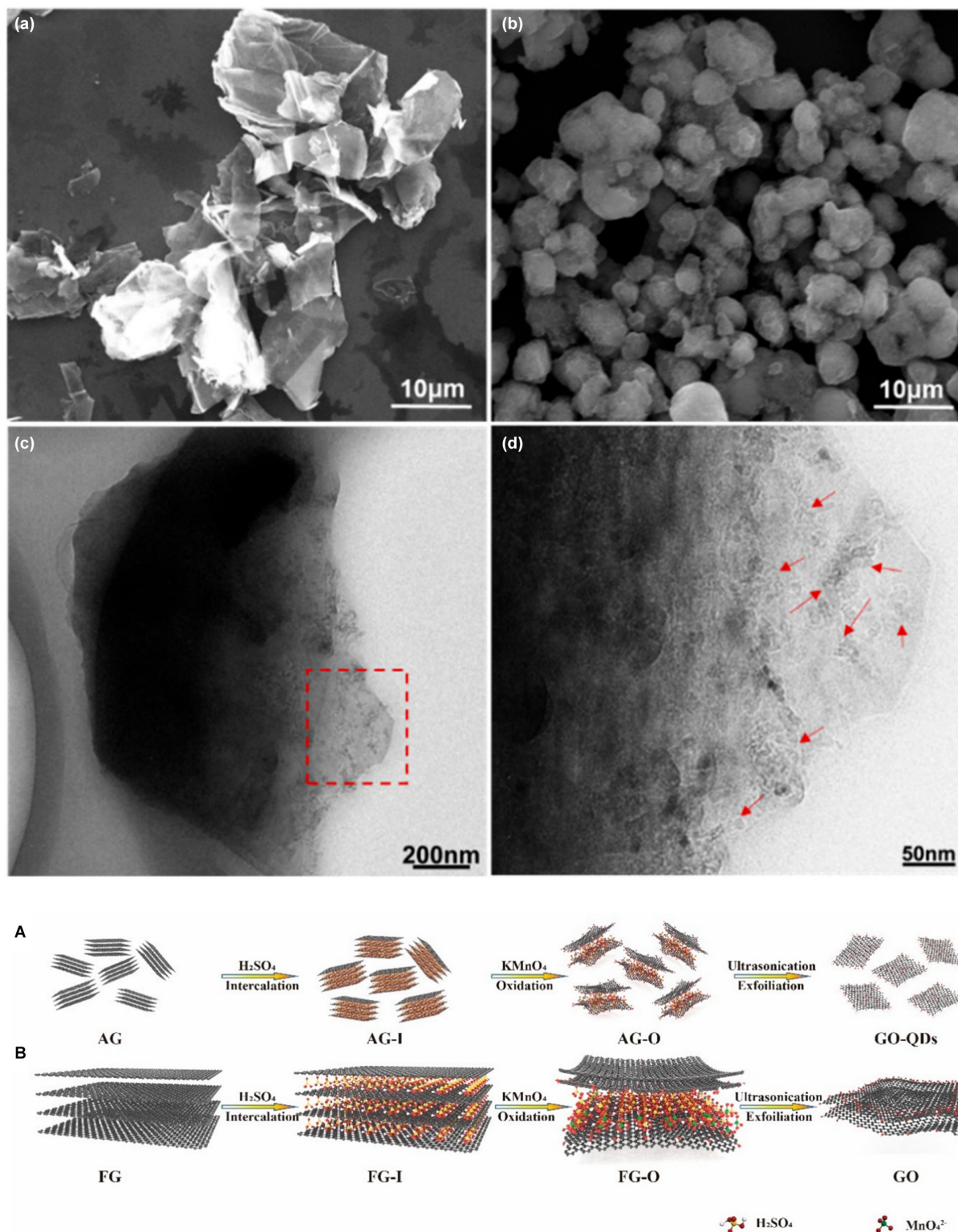


**FIGURE 7 |** (a) SEM image of natural graphite, (b–d) SEM and TEM images of aphanitic graphite, the red arrows indicate the small graphite nanocrystal. Schematic comparison between the exfoliation mechanism of aphanitic graphite (A) and natural graphite (B) with the same amount of intercalator and oxidizer. Adapted from Shen, S. et al. Graphene quantum dots with high yield and high quality synthesized from low-cost precursor of aphanitic graphite. *Nanomaterials* (2020) doi: 10.3390/nano10020375.

and stress waves, extreme temperature and pressure, fast cooling times, and high-speed liquid jets (Han et al., 2014). These intense local forces break the GO sheets according to the mechanism described above. Qi et al. (2014) reported a facile sonochemical method for the preparation of size-specified GO sheets started from large GO sheets with a wide dimensional distribution from a few hundred nanometers up to about 5000  $\mu\text{m}$ , obtained via a mild Hummers method performed at low temperature (35°C) for two h. The obtained GO flakes are dispersed in water at a concentration of 0.5 mg/mL and subjected to bath ultrasonication for a selected time (3, 6, 9 h). The temperature of the water in the ultrasonic bath must be kept below 35°C to avoid the reduction of GO (Qi et al., 2014). The lateral size of the resulting GO samples shows a Gaussian distribution with the maximum decreasing regularly with increasing ultrasound time. Moreover, the SEM images of the samples show that at the early stage of ultrasonication, the sheet size decrease sharply and then the decrease slows down with the increase of ultrasonication time. Another interesting phenomenon observed during the ultrasonic process is that the color of the solution becomes more intense as the ultrasonic process increases, indicating that this process does not affect only the lateral dimension of the sheets but also the chemistry. An accurate characterization of the obtained materials has allowed establishing, for the first time, that ultrasounds are effective in exfoliating GO sheets, but also in increasing the degree of oxidation of samples not completely oxidized through mechanical shear forces created by the collapse of cavitation bubbles. The effect of sonication in reducing the lateral size of GO sheets has also been demonstrated with the GO obtained with the Marciano method (Farazas et al., 2018). As we have stressed previously when considering the reduction of GO size by ultrasonication, the possible chemical reduction must be taken into account. The product that is obtained is a reduced graphene oxide, rGO, in which  $\text{sp}^2$  domains restored by reduction and residual oxygenated functional groups coexist. Méndez-Romero et al. have recently reported a simple but highly effective approach to prepare GO around 100 nm in lateral dimension and high concentration by ultrasound in low-temperature conditions, without alteration of electronic properties and excellent solubility in water (Méndez-Romero et al., 2020). Their procedure consists of sonicating an aqueous dispersion of GO ( $3\text{mg mL}^{-1}$ ) with an ultrasonic probe operating at a 40% amplitude while keeping the temperature strictly controlled at 18°C for 4 h. The dynamic light scattering (DLS) analysis of the samples taken at regular time intervals (every 30 min for a total of 4 h) shows that the lateral size of the flakes decreases significantly in the first 2 h of the process from 500 nm to about 100 nm, reached 100 nm, the size decreases more slowly as the time of sonication increases. As described above, when the reduction of the lateral dimensions of the GO is achieved by applying an external energy source, the breaking mechanism begins at the defective sites ( $\text{sp}^3$  hybridized carbon atoms) and then proceeds through the formation of hot spots that result in a further decrease in size, but also in the degree of oxidation. If, however, the temperature of the experiment is carefully controlled, it is possible stopping the reduction in size at an intermediate step and avoiding a decrease in the O/C ratio. The plot in **Figure 8** shows the progression in

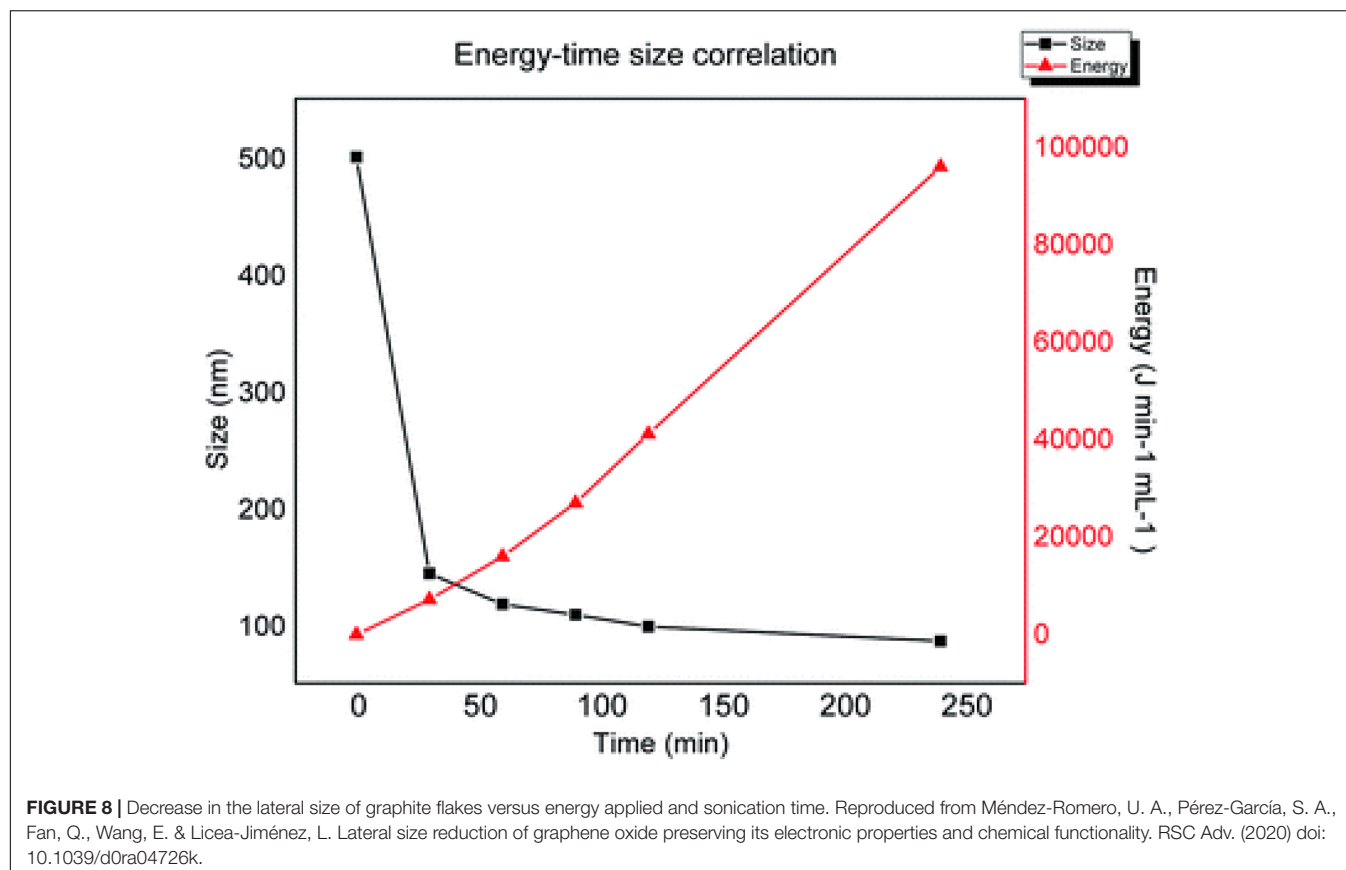
size reduction depending on the energy during the time of the experiment. At the initial stage, a small energy increase induced strong decrease in a short time because there are many defective sites. At the plateau, the defective sites are now depleted and the further increase in energy does not cause a strong decrease in size because the controlled temperature does not allow the formation of hot spots.

Raman and XPS analyses allowed establishing that the sonication at a low temperature preserves the C/O ratio and consequently the chemical stability, the bandgap, the electronic energy levels, and the functionality. Reducing the lateral dimensions of GO by application of acoustic waves is, therefore, an effective approach, but must be used carefully to avoid structural damage to the product caused by the reduction due to local heat generation or by the inclusion of impurities released by the deterioration of immersion probes under operating conditions.

### Ball mill

The reduction of particle size using a mechanical force is termed mechanical milling (Ullah et al., 2014). The method was developed in 1970 by John Benjamin to synthesize oxide dispersion strengthened capable of withstanding high temperature and pressure (Benjamin, 1970). The process consists of inserting the powder to be ground, eventually together with solvents or surfactants, into a rotating cylindrical grinding jar (ball mill) filled with loose grinding balls (Piras et al., 2019). The rotation of the balls in the jar creates impact forces and shear forces that act in combination to reduce the size of the powder. The mechanical stress produced in a ball mill can therefore be used as a pre-treatment of graphite flakes. Luo D. et al. (2019) prepared GO from large micron-size graphite flake subjected to ball milling. The shiny silver flakes become a fine black powder after ball milling and are quickly dispersed in a lower amount of sulfuric acid than commonly used in the Hummers method indicating the formation of a graphite intercalation compound. The fine powder is more active, and the defects generated by the ball milling process also serve as weak points for intercalation. The oxidation reaction is then conducted by adding the oxidizing agent and keeping the temperature below 5°C by adding dry ice pellets directly into the reaction vessel. The authors declare that the addition of dry ice is the key passage of their method because it can provide enough cooling to avoid the decomposition of the  $\text{Mn}_2\text{O}_7$  surface, the explosive compound formed by the reaction of  $\text{KMnO}_4$  in  $\text{H}_2\text{SO}_4$ . After quenching, hydrolysis, and purification, a dark yellow GO solution is obtained which disperses easily in water by ultrasonication and which has the usual spectroscopic features of GO obtained by conventional methods. The majority of GO sheets, observed with electron microscopy, have a single layer with a narrow dimensional distribution around 300 nm. However, comminution using ball mills not only reduces the particle size but the high rotation speed and the collisions of the jars and balls also provide sufficient kinetic energy for the breakdown of the bonds in the aromatic graphite structure. This process introduces functional groups on the edges, surfaces, and basal planes of graphene materials during the milling process (Bharath et al., 2015).





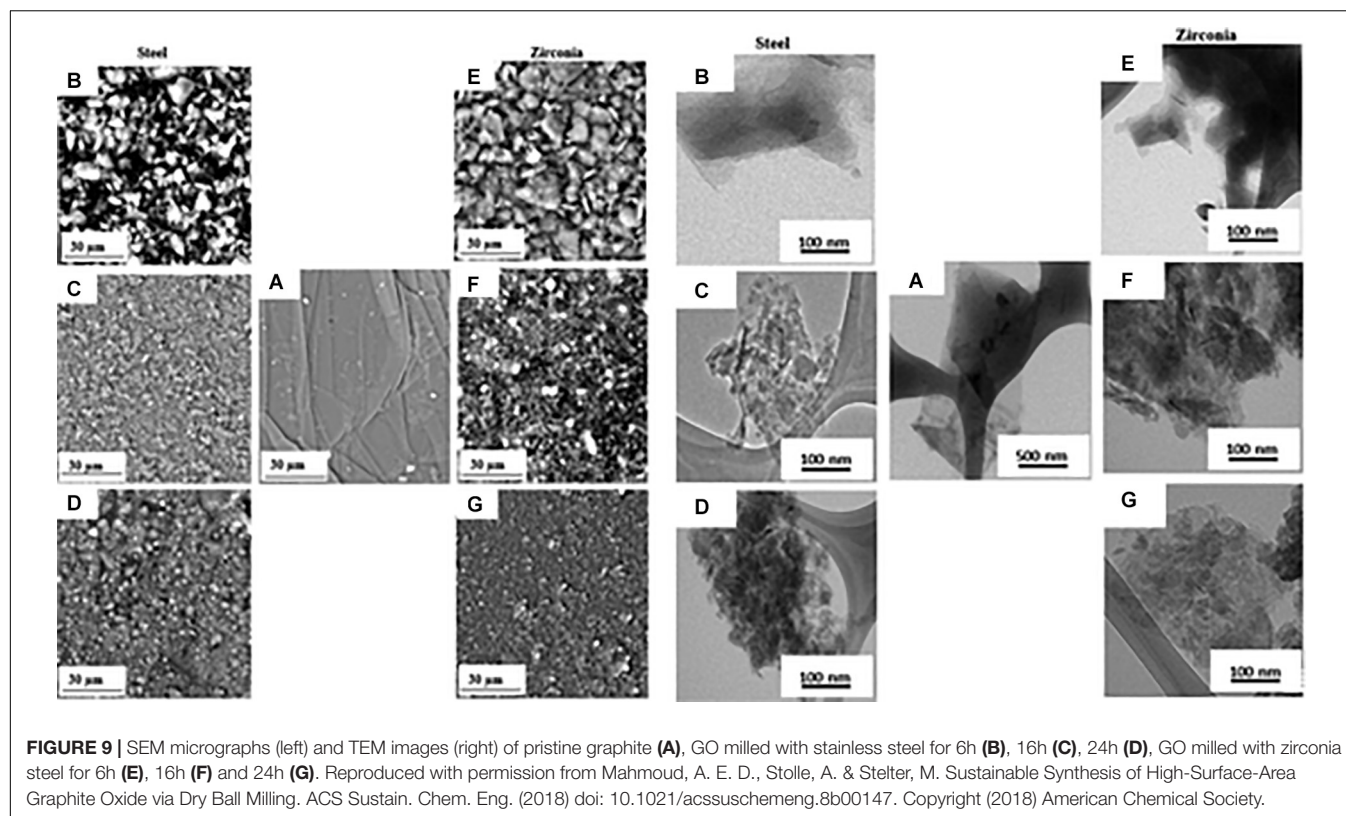
Therefore, mechanochemical ball milling can be employed for the production of GO without the need for additional oxidants other than air. Mahmoud et al. (2018) developed a one-step, dry production route to synthesize GO. The authors utilize graphite flakes of 300 mesh and evaluate the effect of two different milling materials (steel and zirconia) and the milling time (6 h, 16 h, and 24 h) on the characteristics of the GO produced (Mahmoud et al., 2018). SEM and TEM micrographs display a change in sample morphology after ball milling. The samples exhibit irregular and stacked layered structure with a reduction in lateral dimensions that increases with increasing milling time, independently of the milling material (Figure 9).

Thermal and Raman analyses show that the GO produced by ball milling has a structure with fewer defects than the GO synthesized by chemical route without contamination of other chemical elements. However, the degree of oxidation obtained with this technique is lower than that of GO obtained by chemical exfoliation of graphite, as evidenced by the red-shift of the absorbance peak in UV-vis spectra. The C/O ratio in GO samples obtained with ball mill decreases with increasing milling time as shown by the XPS spectra but remains lower than the chemically obtained GO samples. This trend is independent of the material used for the jar and milling balls, although the rate of C/O decrease in the material as the milling time increases is more pronounced for stainless steel ball (due to their higher density) than for zirconia materials. One opportunity to increase the degree of oxidation of the GO obtained with

this technique could be to mill the graphite together with a chemical oxidant. Dry mechanochemical oxidation of graphite with various solid oxidizers ( $\text{KMnO}_4$ ,  $(\text{NH}_4)_2\text{S}_2\text{O}_8$ ) was reported by Posudievsky et al. (2012) obtaining a degree of oxidation comparable to that of dry methods in which air is used as an oxidizer. In this approach potassium permanganate, in the absence of acid, cannot form an oxidant as strong as manganese anhydride as it is used in the case of graphite oxidation with the Hummers method. Subsequently, the same authors conducted a comparative study of graphite oxidation by potassium permanganate in the absence and the presence of a small, stoichiometrically necessary, amount of sulfuric acid (87%) under identical conditions of the mechanochemical treatment (Posudievsky et al., 2013). The mechano-chemical treatment of the mixture of graphite and the oxidizing solid  $\text{KMnO}_4$  in the presence of a small amount of sulfuric acid allows preparing the graphite oxide with a high degree of oxidation and with lateral dimensions between 30 and 50 nm. The obtained GO nanosheets have an exceptional dispersibility in aqueous solution up to the concentration of  $4.6 \text{ mg mL}^{-1}$  without the use of sonication.

## Post-synthesis Separation Centrifugation

Centrifugation is one of the most widely used techniques for separating mixtures by size and density. This technique relies on the different sedimentation rate of a material as a function



of its size, shape, and buoyant density, but also of the density and viscosity of the centrifugal medium and the rotor speed. The rotor spin results in a centrifugal force that pushes the sample particles downwards. The sedimentation rate of each particle in the sample is dependent on the physical properties of the particles, the viscosity of the medium, and the centrifugal force applied. For equal centrifugal force and viscosity of the medium, the sedimentation rate of a particle is related to its size (molecular weight) and the difference between the density of the particles and the density of the solution. Therefore, particles of different size, or density, sediment at different speeds and separate. Recently, because of its high performance, scalable production capacity, and lack of nanoparticle aggregation, direct dimensional separation in the liquid phase by centrifugation has proven to be an effective process for the separation of gold particles, carbon nanotubes, and graphene materials (Green and Hersam, 2009; Hároz et al., 2010; Qiu and Mao, 2011). There are two basic types of centrifugal separation, differential pelleting and density gradient. In the differential centrifugation method, the materials to be separated are divided into several fractions according to their size by varying the centrifugal forces applied. The centrifuge tube is loaded with a uniform mixture of the sample solution and centrifuged at low speed. At the end of the cycle, two fractions are obtained: a pellet containing the largest sedimented material and a supernatant solution of non-sedimented material. The two fractions are extracted by decanting the supernatant solution from the pellet. The smaller material in the supernatant is further differentiated according to its size by gradually increasing the

speed of each cycle. Alternatively, the starting solution can be centrifuged at high speed by separating the small particles in the supernatant from the large particles in the sediment, and then the precipitate can be dimensionally differentiated by reducing the centrifugal forces applied. This separation method is applied to GO flakes prepared with the modified Hummers method (Chen et al., 2013b). The aqueous suspension of GO ( $0.1 \text{ mg mL}^{-1}$ ) obtained by ultrasonication and centrifugation from Hummers methods was processed by successive steps of centrifugation at decreasing speed. In each centrifuge cycle, the average size of the GO nanosheets in the supernatant decreases because the larger flakes sediment at a higher speed as opposed to the applied acceleration. AFM images of the three aqueous suspensions separated by this method, reveal flakes with a quite uniform lateral size distribution, and different average lateral size from 260 nm, for the supernatant obtained at high centrifugation rates, to 977 nm, for the one obtained at lower rates. When considering the dimensional separation of GO by centrifugation, it must always be considered that the theory of sedimentation, based on the assumption of spherical and homogeneous sediment particles (Stokes law) may have limitations when applied to an inhomogeneous and two-dimensional material. Huang and Yuan (2016) carefully characterized aqueous suspensions of GO separated by differential gradient centrifugation, demonstrating that the sedimentation process of GO in aqueous solution does not depend only on the lateral dimensions, but especially on the degree of oxidation and the interlayer distance between the graphene layers in GO. In particular, a high degree of oxidation

and a larger *d*-spacing increase the hydration level of the sheets and they sediment more slowly due to the higher viscous resistance (Huang and Yuan, 2016). Another separation method is density gradient centrifugation in which the components of a sample are placed on the surface of a vertical column of liquid with increasing density from top to bottom and then centrifuged. The two main types of density gradient centrifugation are rate-zonal separation and isopycnic separation. In the isopycnic technique, the sample has a density between the lowest and the highest density of the column gradient. The particles migrate through the solvent gradient, during centrifugation, until they reach the point where their buoyancy density is equal to that of the gradient. This is known as the isopycnic point or isodense position. This separation method based on balancing the density of the colloidal material with that of a support medium was applied to separate carbon nanotubes by diameter/chirality/wall thickness (Arnold et al., 2005; Arnold et al., 2006; Wei et al., 2008; Green et al., 2009) and to separate GO sheets by the number of layers using a density gradient formed by aqueous solutions of non-ionic gradient medium, iodixanol. GO-iodixanol complexes have buoyancy densities that vary with the thickness of the encapsulated GO sheets and can be separated regardless of their lateral size (Li et al., 2013). In rate zonal centrifugation, instead, the gradient has a lower density throughout the tube to ensure that the distance a particle travels through the gradient depends exclusively on the diameter of the particle. Larger particles will be able to travel to the lower layer because they are more massive. The higher mass allows particles to travel through layers with a higher viscosity, while the smaller particles will stay at the top because they do not have the mass to travel through the more viscous layers. In this way, the particles that sediment faster are not contaminated by the slower particles as in differential centrifugation. The first-rate zonal separation of GO nano-sheets was reported in Sun et al. (2008). In this paper, the authors explore cellular imaging and drug delivery properties of nGO sheets prepared by the modified Hummer method from expanded graphite and functionalized with PEG to enhance solubility and stability in salts and cell solutions. The mixture containing functionalized GO sheets is then subjected to 2.5 h of centrifugation at  $\sim 30000\text{ g}$  in an iodixanol gradient obtaining multiple layers of different size PEG- GO sheets along with the centrifuge tube. AFM images of the fractions collected layer by layer show that the flake size increases monotonically along the centrifuge tube and in each fraction, most of the flakes have a uniform lateral size. This method was subsequently optimized and applied to pure GO (Bidram et al., 2016). Using a simple sucrose gradient, Sun et al. (2010) demonstrated that by adjusting the separation parameters, including centrifugation time and density gradient profile it is possible to obtain GO sheets with targeted size and degree of oxidation. In their method, a freshly prepared GO suspension was layered on top of the density gradient (20–66% gradient) and centrifuged at 50K rpm for 15 min. After centrifugation, GO sheets were separated into different zones along the centrifuge tube, AFM characterization indicated that sampling along the centrifuge tube yielded GO sheets of increasing size from 40 (upper fractions) to 450 nm (down fractions) while TEM characterization showed a single

layer structure for GO sheets found at the top of centrifuge tube and a multilayer structure for those at the bottom of tube. These results are coherent with the sedimentation behavior of GO sheets, the thick and heavy multilayered structures sediment faster than single layered ones, allowing single layered fractions to separate according to size. Reducing the centrifugation time from 15 to 5 min results in fractions separated in terms of degree of oxidation. This result was confirmed by using various characterization techniques (Figure 10). Calling f5, 10, 15, 20, 30 the fractions collected from top to bottom in the centrifuge tube, Figure 10A shows absorption measurements in the UV-vis range after curves normalization to the absorbance peak relative to a  $\pi$ -electron plasmon excitation of graphitic carbon at 230 nm. GO sheets in upper fractions had much lower absorbance in the visible range, 400–800 nm, while the visible absorbance of lower fractions increased significantly. “Pristine” graphene made by intercalation and exfoliation without oxidation showed a ratio of absorbance intensity at 400 nm to that at 800 nm ( $\text{Abs}_{400\text{ nm}}/\text{Abs}_{800\text{ nm}}$ ) near to 1.5:1 (Li et al., 2008), while fully oxidized GO showed a ratio near to 4.5:1. Similar results are obtained in the separated fractions with the density gradient ultracentrifugal rate separation method (Figure 10B), indicating that GO sheets were separated in terms of degree of oxidation, with less functionalized graphene sheets being distributed in higher fraction numbers. This was further confirmed by the red shift of the UV absorption peak from ca. 230 nm for f5 to 260 nm for f30 (Figure 10C) such a red shift has previously been reported when the degree of reduction of GO is increased (Wang et al., 2008). The C-O peak (at ca. 286.5 eV) in XPS spectrum of f30 fraction (Figure 10D) is much weaker than that in the f10 fraction (Figure 10E) indicating a lower number of oxygenated functional groups present in the lower fractions and therefore a low degree of oxidation. The high fluorescence intensity of the f5 fraction (Figure 10F) is very interesting for drug delivery and cellular imaging applications. Fluorescence is consistent with the presence of GO sheets with extremely small size and a high degree of oxidation.

### Flocculation by Solvent

The colloidal stability of GO sheets in aqueous solution resulted from the competition between the dispersive electrostatic repulsive interactions between the sheets, arising from the ionized carboxyl groups on the edges, and the attractive Van der Waals face-to-face interactions that promote aggregation. The increased colloidal stability of GO in aqueous solution is due to a combination of increased electrostatic repulsion, decreased overlap areas, and decreased probability of overlapping. Therefore, in an aqueous medium with the same pH value, GO sheets with smaller size could have a higher solubility than larger sheets because they exhibit a high edge to area ratio and a higher density of ionized carboxylic groups. In addition, the solubility of GO sheets in water is a function of the pH of the dispersion, as the pH of the medium decreases, the carboxyl groups on the edges become protonated, the repulsion forces decrease, the Van der Waals attraction forces prevail and the colloids precipitate. Wang X. et al. (2011) used this pH dependence to selectively precipitate large quantities of GO sheets mostly

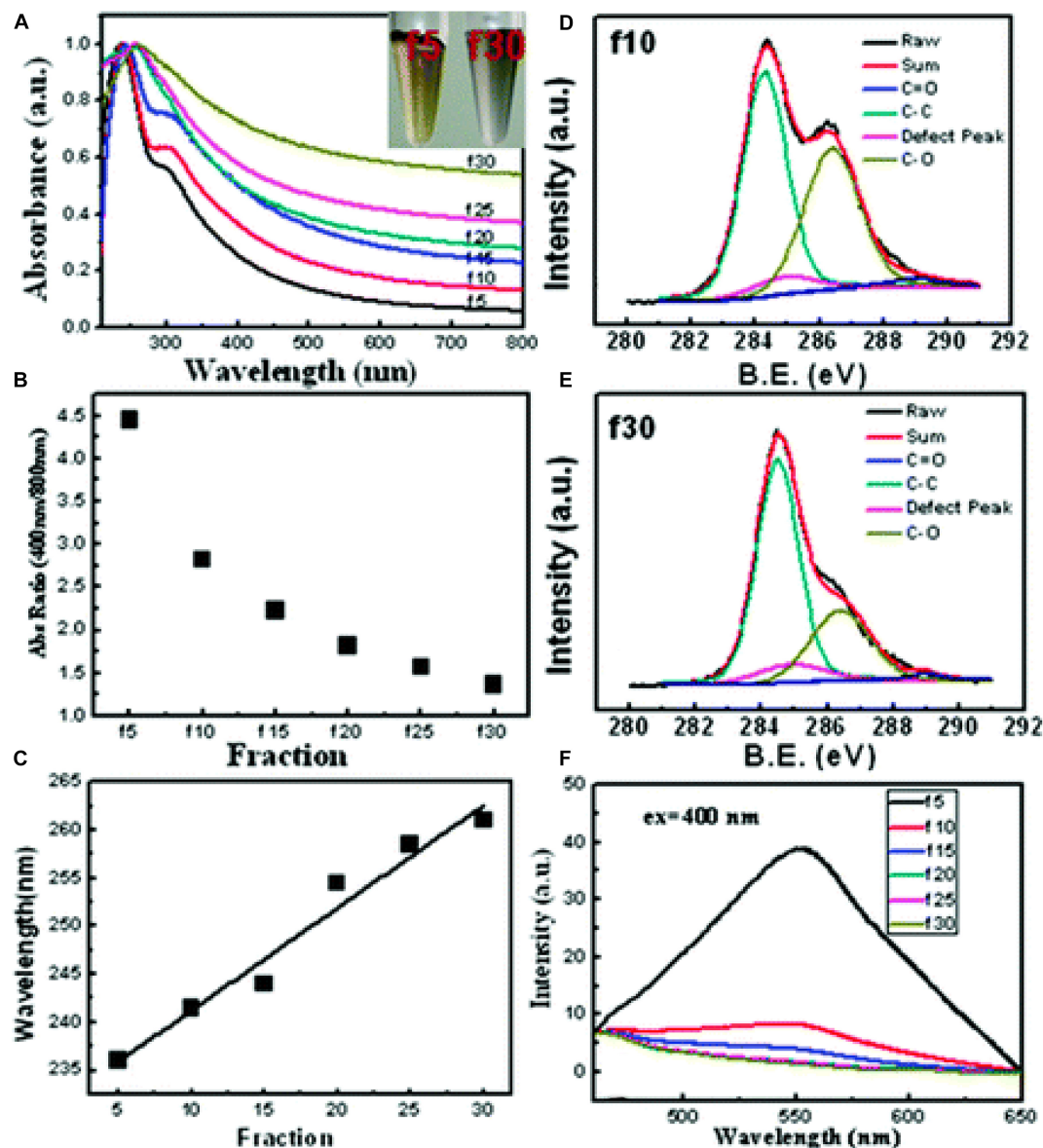


**FIGURE 10 | (A)** UV-vis absorption spectra of GO in different fractions from the density gradient ultracentrifugal rate separation in 20%-66% (w/v) sucrose gradient for 5 min. Inset: photograph of GO (f15 (left) and f30 (right)) after dilution. **(B)** Ratio of absorption at 400 nm to that at 800 nm of GO in different fractions from density gradient ultracentrifugal rate separation in 20%-66% (w/v) sucrose gradient for 5 min. **(C)** Variation in the wavelength of the absorption maximum of GO in different fractions from density gradient ultracentrifugal rate separation in 20%-66% (w/v) sucrose gradient for 5 min. **(D,E)** XPS spectra of f10 and f30 GO fractions from density gradient ultracentrifugal rate separation in 20%-66% (w/v) sucrose gradient for 5 min. **(F)** Fluorescence ( $\lambda_{\text{ex}} = 400 \text{ nm}$ ) spectra of GO in different fractions from density gradient ultracentrifugal rate separation in 20%-66% (w/v) sucrose gradient for 5 min. Reproduced with permission from Sun, X., Luo, D., Liu, J. & Evans, D. G. Monodisperse chemically modified graphene obtained by density gradient ultracentrifugal rate separation. *ACS Nano* (2010) doi: 10.1021/nn1000386. Copyright (2010) American Chemical Society.

larger than  $40 \mu\text{m}^2$  and narrow size distribution raising the pH of the aqueous dispersion to 4 with HCl 1M. Instead, Zhang et al. (2015) use the protonation in organic solvents (ethanol, tetrahydrofuran) of carboxyl groups on the edges of GO sheets to selectively precipitate large GO sheets according to their size. Starting from the consideration that GO sheets with smaller lateral dimensions have greater colloidal stability, Hu et al. (2015) reconsidered the general work-up procedure of classical

GO synthesis. Usually, after quenching with distilled water containing a small amount of  $\text{H}_2\text{O}_2$ , the reaction product is filtered and the precipitate further purified. The authors have proven instead that the strongly acidic filtrate (pH  $\sim 1$ ) recovered from filtration contains unprecipitated nGO. The nGO present in the filtrate undergoes fast aggregation and forms stable floccules by gradual addition at room temperature of a 1M KOH or NaOH solution until the pH value increases to  $\sim 1.7$  (Hu et al.,



2015). The sediment, isolated and characterized, contained nGO flakes with a multi-layer structure [thickness of about 3.5 nm (4-5 layers)] and narrow size distribution with an average size of less than 90 nm.

## NANO GRAPHENE OXIDE IN CANCER THERAPY

The intrinsic properties of nGO make this material very interesting in the field of biomedicine. The oxygen atoms chemically bonded to the carbon lattice by treatment with strong oxidizing agents in an acidic environment are defects introduced in the ideal graphite plane, but they provide the GO with unique properties such as hydrophilicity, i.e., the ability to dissolve and to form stable colloidal solutions in water and some low molecular weight alcohols. The oxygenated groups present on the surface of the GO and the nanometric dimensions are not enough to balance the screening of the electrostatic charges when the nGO is in biological media, consequently, the nGO tends to aggregate in physiological solutions with salts and proteins (Muñoz et al., 2019). The surface functionalization of GO increases solubility under physiological conditions and opens the scenario to a wide range of biomedical applications. In general, the chemical functionalization of the GO may be of covalent or non-covalent type. Covalent functionalization involves the conversion of the functional groups present on the GO and/or the chemical bond between the functional groups and external species such as small molecules, polymers, and inorganic particles. Non-covalent functionalization, on the other hand, exploits the large, atomically flat surface of GO as an anchor for other chemical species through secondary interactions such as Van der Waals forces and  $\pi$ - $\pi$  interactions (Lonkar et al., 2015).

## Drug Delivery Application in Cancer Therapy

Graphene oxide can be used as an efficient nanocarrier for the loading and transport of water-insoluble aromatic molecules using non-covalent interactions. Approximately 50% of GO carbon atoms are  $sp^2$  carbons and therefore can interact with conjugated  $\pi$  molecules. After the pioneering study by Dai and collaborators Liu et al. (2008), many other research groups have confirmed the excellent drug loading ability of the nGO. In this context Zhang et al. (2010) first demonstrated the ability of nGO to load simultaneously two drugs [doxorubicin (DOX) and camptotecin (CPT)] with synergistic action and a loading efficacy comparable to the loading of a single drug. This approach is very advantageous because it allows to the reduction of multi-drug resistance to anticancer drugs, the phenomenon that occurs when cancer cells develop resistance to anticancer drugs with different structures and mechanisms of action (Szakács et al., 2006). In this work, the nGO is covalently modified with folic acid molecules for selective targeting of folate receptors overexpressed by cancer cells, and two aromatic anticancer drugs were loaded on both sides of the graphene sheets through  $\pi$ - $\pi$  stacking and hydrophobic non-covalent interactions (Figure 11A). The amount of drug-loaded was estimated by UV/Vis spectroscopy.

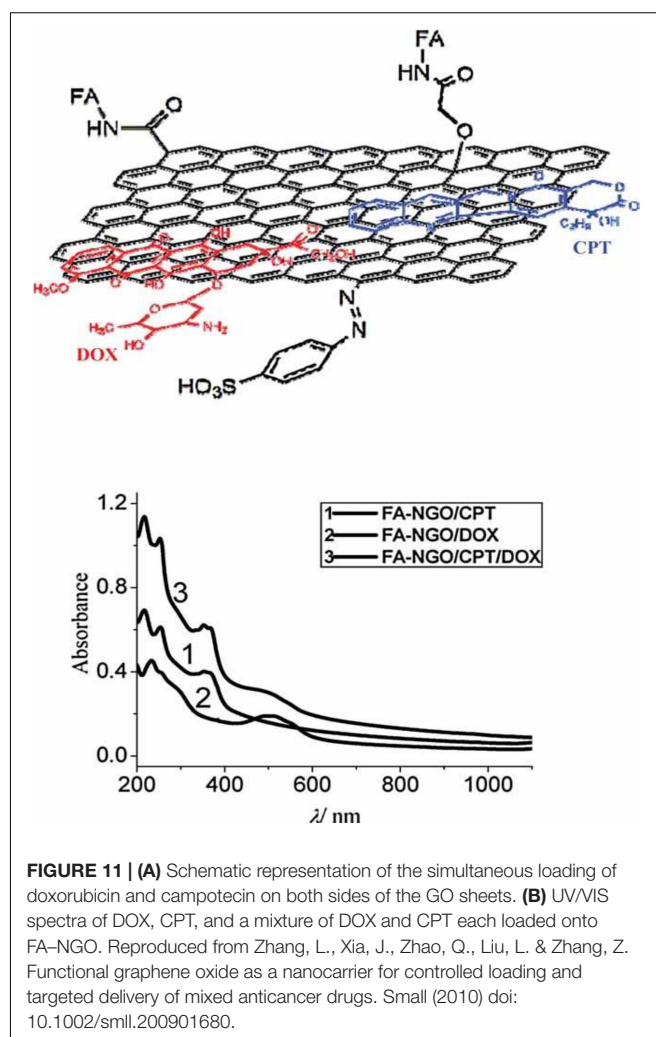


**FIGURE 11 | (A)** Schematic representation of the simultaneous loading of doxorubicin and camptotecin on both sides of the GO sheets. **(B)** UV/VIS spectra of DOX, CPT, and a mixture of DOX and CPT each loaded onto FA-NGO. Reproduced from Zhang, L., Xia, J., Zhao, Q., Liu, L. & Zhang, Z. Functional graphene oxide as a nanocarrier for controlled loading and targeted delivery of mixed anticancer drugs. Small (2010) doi: 10.1002/sml.200901680.

The simultaneous presence of absorption peaks at  $\sim 490$  nm (characteristic of DOX) and  $\sim 365$  nm (characteristic of CPT) suggested that both DOX and CPT were loaded onto the nGO-folic acid platform (Figure 11B). This system displayed therapeutic efficacy in killing cells from the human breast cancer cell line (MCF-7).

The strategy of overcoming MDR by loading multiple drugs with different actions on the same nanocarrier is frequently used and the nGO is one of the most flexible systems for this purpose. The planar carbon atoms structure allows combining, through non-covalent interactions, multiple hydrophobic drugs with high loading efficiency. Deb et al. (2018) studied the synergistic effect against breast cancer of two anti-cancer drugs, camptothecin (CPT) and 3,3'-diindolylmethane (DIM), co-loaded on a nano biocomposite (GO-CS-FA-CPT-DIM) of GO functionalized with chitosan (CT) and decorated with folic acid (FA), as a targeting moiety (Deb et al., 2018). The *in vitro* tests showed that the anticancer activity of GO-CS-FA-CPT-DIM was higher in comparison to the free CPT probably because of the different mechanisms of action employed by CPT and DIM. In addition, *in vivo* tests revealed a reduction in common side

effects of CPT when administered free, such as gastrointestinal diseases, disruption of renal function, cumulative hematological toxicity, and liver inflammations. Another combination of chemotherapy drugs with synergistic effect loaded on GO was contemporaneously tested by Tiwari et al. (2019). They loaded two widely used anticancer chemotherapy drugs, quercetin, and gefitinib on a GO larger than 100 nm grafted with polyvinylpyrrolidone (PVD), a highly hydrophilic and biologically compatible polymer, and investigated the loading and cancer cells cytotoxicity of two individual drug systems and combined system in ovarian cancer cells PA-1 compared to ovarian epithelial cells IOSE-364. They founded that the release rate of the two drugs combined on the GO nanocarrier coated with PVP in phosphate-buffered saline (PBS) solution was higher than that of individual drugs on the same system. They attributed the better release rate to intermolecular interactions, such as  $\pi$ - $\pi$  stacking, and to the strong inter- and intra-molecular hydrogen bonds between the electronegative atoms present in the structure of the drug molecules and the carrier. In addition, their results showed that both the systems with single drugs and the system with combined drugs had no significant cytotoxic effects on the IOSE cells, while high toxicity was detected on ovarian cancer cells PA-1, and the combined system showed the highest toxicity at the same concentration. Bullo et al. (2019) designed an anticancer nanocomposite of nGO coated with polyethylene glycol and loaded with two anticancer drugs; protocatechuic acid (PCA) and chlorogenic acid (CA). The DLS measurements showed that the final nanocomposite had a narrow distribution, in the range of 10–40 nm with a median value of 8 nm. This nano-formulation showed strong anticancer activity against liver cancer, HepG2, and colon cancer, HT29 cells compared to free drugs. Covalent functionalization includes a variety of reactions as esterification, amidation, click chemistry, nitrene chemistry, and radical addition (Layek and Nandi, 2013) and is widely used for drug loading, coating the nGO with biocompatible polymers, or bonding targeting motives. According to widely agreed Lerf and Klinowski's model, GO sheets have chemically reactive oxygenated functions, such as carboxylic acid groups at the edges and epoxy and hydroxylic groups on the basal planes (He et al., 1998). Although there are examples of functionalization of the hydroxyl and epoxy groups located in the basal plane of the GO (Layek et al., 2010; Sydlik and Swager, 2013), the chemistry of GO is dominated by the chemistry of the carboxylic and carbonylic functional groups located at the edges. Most approaches exploit the protocols of carboxylic acid conversion reactions into esters or amides (Zhang X. et al., 2009; Yu et al., 2010). The introduction of substituted amines is one of the most common covalent functionalization methods and the final products are designed for various applications. An example of the use of GO functionalized amine (GO-NH<sub>2</sub>) for biological applications is provided by the work of Singh et al. (2012). They synthesized GO-NH<sub>2</sub> by activation of GO carboxylic acid groups with thionyl chloride in dimethylformamide and subsequent reaction with sodium azide and demonstrated that it was a safer alternative for biomedical applications, compared to oxygenated derivatives. It is known that GO, when administered intravenously in mice, has the potential to cause a strong aggregation response in

platelets on a scale comparable to that caused by thrombin, one of the most powerful physiological platelet agonists, and triggers extensive pulmonary thromboembolism, consistent with the prothrombotic nature of this material (Singh et al., 2011). *In vivo* and *in vitro* tests showed that modified amine GO, being positively charged, was more biocompatible than GO, had no stimulating action toward platelets and does not induce pulmonary thromboembolism in mice. Wojtoniszak et al. (2013) covalently bonded GO with methotrexate (MTX), a folic acid analog used as a chemotherapeutic agent via amide binding. Wu et al. (2014) used the same chemical route to functionalize a nano-size GO with hyaluronic acid (HA), a naturally occurring polysaccharide with excellent physicochemical properties, such as biodegradability, biocompatibility, and non-immunogenicity. The obtained nGO-HA system showed a high loading capacity of the anti-tumor drug DOX and high cytotoxicity to cervical cancer cells. The *in vivo* toxicity studies showed very low cytotoxicity, good blood compatibility, and no evident toxic effects in mice. GO-HA/DOX could selectively accumulate in the malignant tumor issues by receptor-mediated endocytosis and inhibit tumor growth. As discussed extensively earlier, one way to increase nanocarrier accumulation at the tumor site is to bond ligand at the nanocarrier surface to selectively recognize specific molecules that are over-expressed by tumor cells and tissues, but are not present in healthy cells and tissues. Li J. et al. (2018) presented a dual-targeting platform of GO with high stability and drug loading capacity for the inhibition of pulmonary metastasis of breast cancer. This platform was based on a GO modified with folic acid and heparin via a polyethyleneimine linker. Heparin with a quantity of hydrophilic carboxylic and sulphonated groups maintained the GO surface negatively charged, thus avoiding rapid elimination from circulation and acting as a potential targeting material because it could bind competitively to the receptor for advanced glycation end products-mediated expression of malignant cells. The *in vivo* assays indicated that this dual targeting system could not only inhibit the *in situ* tissue growth, but also suppress the pulmonary metastasis. Pham et al. obtained a GO with lateral size less than 100 nm by ultrasonication of the graphite oxide flakes obtained by the Hummer's method and chemically functionalized it with alendronate (AL), a second-generation bisphosphonate approved by FDA to treat tumor-associated hypercalcemia and several bone-related diseases for the treatment of bone metastasis in advanced breast cancer (Pham et al., 2019). The *in vivo* tests showed that the alendronate functionalization was able to increase NGO accumulation in the skeletal system and enhanced *in vivo* retention times after intravenous administration. In addition, the nanosheets preferentially accumulated in bone bearing tumors and not in healthy bones due to the tumor microenvironment. Bone surfaces are normally covered by cells and organic matrix, which might reduce AL binding, whereas bone remodeling during osteolytic lesion development leads to the digestion of bone organic matrix and cell detachment. GO has also been explored to implement drug delivery systems able to respond intelligently to the tumor microenvironment. As is well known, the extracellular pH of tumor tissue is often acidic due to acid metabolites caused by anaerobic glycolysis

in hypoxia. This pH difference can be utilized to achieve a targeted release of the drug. For this purpose, Depan et al. (2011) synthesized a novel drug carrier based on GO by attaching DOX to GO via strong  $\pi$ - $\pi$  stacking interaction, followed by encapsulation of GO with folic acid conjugated chitosan. The hydrophilicity and cationic nature of chitosan enhanced the stability of the nanocarrier system in the aqueous medium. The loading and release of DOX are strongly pH-dependent and compared to pH 7.4, the nano-hybrid system exhibited higher drug release at pH 5.3, which is ascribed due to the reduced interaction between DOX and drug carrier. Zhou T. et al. (2014) exploited citraconic anhydride-functionalized poly(allylamine) (PAH-Cit), a common charge-reversal polyelectrolyte, which can be readily converted back to cationic poly(allylamine) by amide hydrolysis upon exposure to mild acidic environments, such as those found within late endosomes and lysosomes. They synthesized the charge-reversal polyelectrolyte and loaded it onto GO sheets by electrostatic interaction, then bonded the DOX to anionic PAH-Cit by covalent linkage of carboxyl group with amino group. The release mechanism of the drug involved the conversion of PAH-Cit into cationic poly(allylamine) as a result of endocytosis and exposure to acidic endosome or lysosome environments. Lv et al. (2016) developed a multifunctional GO as a drug carrier targeting to hepatocarcinoma cells. They first modified the GO surface with polyethyleneimine (PEI), then they derivatized the PEI-NH<sub>2</sub> groups with fluorescein isothiocyanate (FI), as imaging dye, and polyethylene glycol (PEG)-linked lactobionic acid (LA), as targeting ligand, and acetylated the remaining terminal amines of the PEI. The formed carrier, loaded with DOX through  $\pi$ - $\pi$  stacking interactions was water soluble and displayed a pH-responsive DOX release behavior with a faster DOX release rate at pH 5.8 than that of the physiological pH. Another important feature of this carrier was its good cell viability and the ability to specifically target hepatocarcinoma cells overexpressing asialoglycoprotein receptors. An analogous pH responsive drug delivery system based on GO functionalized with carboxymethyl chitosan (CMC), fluorescein isothiocyanate and lactobionic acid (LA) was developed by Pan et al. (2016). A nGO with lateral size of 40 nm was double-functionalized with 2-(4-hydroxyphenyl)imidazo[4,5-f] [1,10]phenanthroline (p-HPIP), an excellent intercalating ligand in DNA-binding, polyethyleneimine (PEI), to improve the stability of NGO-based nanosystem under water/physiological conditions and transferrin (Tf) as a surface decorator by Zhou et al. (2016); **Figure 12A**. This nano-system (Tf-NGO@HPIP) was internalized through receptor-mediated endocytosis and triggered pH-dependent drug release in acidic environments and in presence of cellular enzymes. Moreover, it showed enhanced cytotoxicity toward cancer cells by triggering cell apoptosis through the overproduction of intracellular superoxides (**Figure 12B**).

Another research group, instead, exploited the high concentration of glutathione (GSH) present in the cytosol of tumor cells to trigger the release of the drug from a nanocarrier consisting of GO coated with a newly synthesized PEG cross-linked via disulfide bonds and loaded with DOX hydrochloride (Wen et al., 2012). The PEG coating improved

the stability and circulation time of the nanocarrier, while the presence of disulfide bonds allowed the rapid release of the drug through the exchange reaction of thiol ligands by cellular GSH. In the presence of high GSH concentration, PEG-coated NGO was internalized via endocytosis thereby initiating rapid disulfide cleavage of a stabilizing PEG shell, which initiates the rapid release of encapsulated payload (**Figure 13**). The confocal laser scanning microscopy and flow cytometric analyses demonstrated the pharmacological efficacy of the intracellular release of doxorubicin hydrochloride from functionalized nanocarrier in the presence of elevated GSH concentrations.

Zhao et al. (2014) oxidized for 36 h a graphite pre-treated with P<sub>2</sub>O<sub>5</sub> and K<sub>2</sub>S<sub>2</sub>O<sub>8</sub> to obtain nGO with nearly spherical shaped and monodisperse size of  $43.36 \pm 8.42$  nm. To increase the half-life and bypass recognition and clearance by the reticuloendothelial system (RES), the GO nano-spheres were coated with a PEG synthesized to be responsive to the tumor reducing environment. This strategy involved the PEGylation of alginate (ALG), to obtain ALG-PEG, and then a conjugation of cytamine (Cy) to ALG-PEG by the amidation between the -NH<sub>2</sub> group of Cy and the -COOH groups of ALG. The Cy-ALG-PEG polymer was grafted onto the surface of the nGO via a reduction-sensitive disulfide bond, so the nanocarrier was responsive to cleave the disulfide bond to detach the Cy-ALG-PEG polymer moieties in reducing condition. The near-spherical shape and nanometric dimensions of the carrier also allow for high DOX loading capacity and excellent encapsulation efficiency. The same research group also investigated the functionalization of GO to obtain systems responsive to more than one stimulus (Zhao et al., 2015) through a PEGylate GO functionalized with cytamine. The authors studied the release of DOX *in vitro* simulating pH and glutathione concentration levels under physiological conditions (pH 7.4 and [GSH] 10  $\mu$ M) and in the tumor microenvironment (pH 5.0-5.5 and [GSH] up to 10 mM) and founded that the initial DOX release was 6-fold faster at pH 5.0 in the presence of 10 mM than at pH 7.4 in the presence of 10  $\mu$ M GSH. As the simultaneous loading of several drugs with different mechanisms of action on the same nanocarrier, obtaining a nanocarrier sensitive to double/multiple endogenous stimuli is also a way to increase therapeutic efficacy. Recently, Zhang J. et al. (2019) designed and constructed a dual-sensitive cancer combination treatment system utilizing GO to load proapoptotic peptide (KLA) and anticancer drugs. The proapoptotic peptide is an amino acid sequence of lysine (K), leucine (L), and alanine (A), (KLAKLAK)<sub>2</sub>, that can induce mitochondrial-dependent apoptosis while remaining relatively non-toxic extracellularly. The GO was firstly modified with (3-mercaptopropyl)-trimethoxysilane to obtain GO-SH, then converted in GO-SSNH<sub>2</sub> by reaction with S-(2-aminoethylthio)-2-thiopyridine hydrochloride and finally, alkyne-modified disulfide-functionalized GO (GO-SS-alkyne) was obtained by reaction with propargyl bromide. The proapoptotic peptide was synthesized by employing a standard Fmoc chemistry through the solid-phase peptide synthesis and terminated with azide group (-N<sub>3</sub>) and connect onto GO-SS-alkyne by azide-alkyne click chemistry reaction. Then, the aromatic anticancer drug DOX was loaded on GO by  $\pi$ - $\pi$



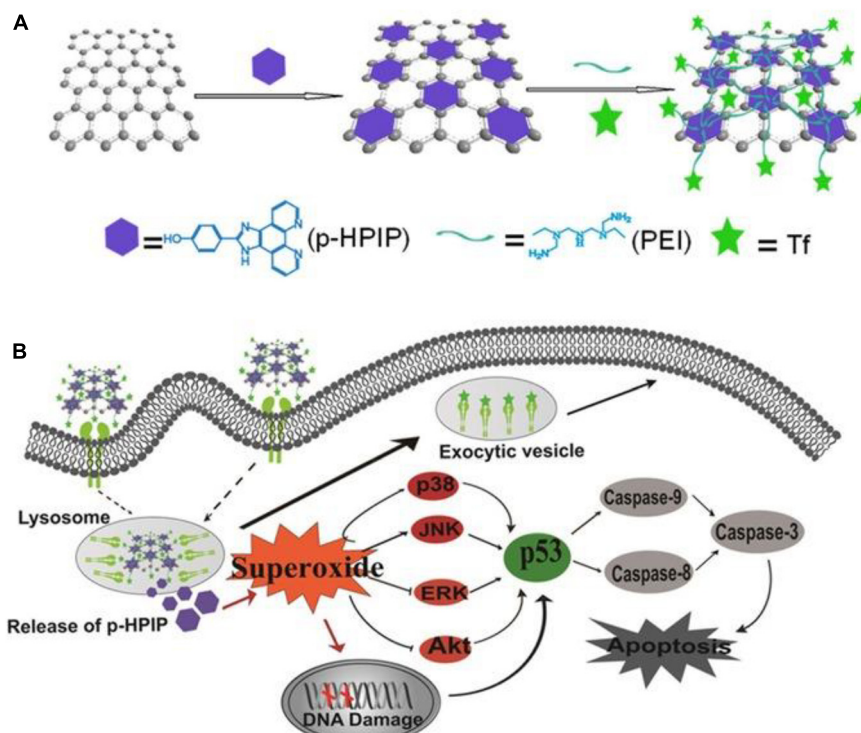


**FIGURE 12 | (A)** Synthetic scheme for the double functionalization of the nGO. **(B)** Schematic illustration of the activation intracellular apoptotic signaling pathways by Tf-NGO@HPIP. Reproduced from Zhou, B., Huang, Y., Yang, F., Zheng, W. & Chen, T. Dual-Functional Nanographene Oxide as Cancer-Targeted Drug-Delivery System to Selectively Induce Cancer-Cell Apoptosis. *Chem. - An Asian J.* (2016) doi: 10.1002/asia.201501277.

conjugation and hydrogen bonding interactions and bovine serum albumin (BSA) was used to coat the GO carrier to enhance the stability of the system and the hydrophilicity of the GO carrier after drug loading (**Figure 14A**). The action mechanism of the double sensitive nanocarrier is schematically illustrated in **Figure 14B**. After accumulation in the tumor tissues by the EPR effect, the nanocomposite penetrated the cell membrane and was uptaken by the tumor cells (a), the low pH triggered the release of DOX in the endosomes (b,c), while the high concentration of GSH induced the cleavage of the KLA from the surface of the GO by the scission of the disulphide bonds (d). The free peptide and the Dox showed a synergistic therapeutic effect (e).

## Theranostic Application in Cancer Therapy

As described above, GO exhibits size-dependent photoluminescence. The photoluminescence of GO is due to the functionalization of the carbon lattice, which induces the opening of the energy gap. When the absorption of an incident photon occurs, an electron is promoted to a higher energy level orbital, leaving a positively charged hole below (**Figure 15**). This electron-hole pair, created for the absorption of a photon is called an exciton.

The creation of an exciton is followed by the non-radiative decay of the electron at the lower energy empty

molecular orbital (LUMO) and the hole at the higher energy occupied orbital (HOMO). This process is then followed by radiative recombination of the exciton that generates the emission of a photon with lower energy than the incident photon. The efficiency of this process is described by the quantum fluorescence yield, i.e., the ratio between absorbed and emitted photons, which, for the GO, is reported to be 0.02-0.5% due to the electron-hole recombination through non-radiative processes. Among the non-radiative processes involved, conversion to thermal energy is used for photothermal therapy of GO. Photothermal therapy uses an optical absorbing agent to generate heat as a result of light radiation, producing a temperature increase that kills the cancer cells (Yang et al., 2013). Electromagnetic radiation with a wavelength between 650 and 900 nm (NIR) is very interesting for medical applications because in this window absorption by the skin and tissues is minimal and penetration is intense (Weissleder, 2001). The results of GO as a photothermal agent for tumor ablation are presented for the first time in Yang et al. (2010). In this study, single or double-layer GO nano-sheets with lateral dimensions between 10 and 50 nm coated with amine-terminated six-arm branched PEG (NGS-PEG) were used. To verify the potential in photothermal therapy, an aqueous dispersion of NGS-PEG at a concentration of 0.5 mg/mL was irradiated with a NIR laser at 808 nm with a power density of  $2\text{ W cm}^{-2}$ , using water as a control. In contrast to the water sample, the NGS-PEG solution showed a rapid increase in



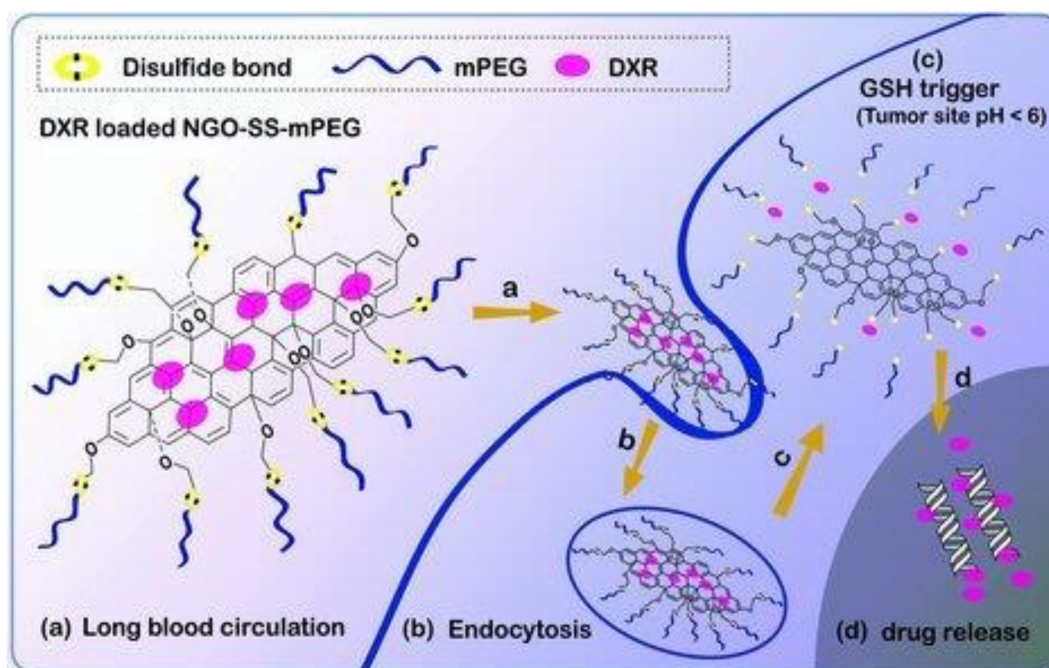


**FIGURE 13 |** Schematic diagram illustrating the fate of redox-sensitive GO-based nanocarrier. When PEG-coated nGO (a) with disulfide bridges is endocytosed in tumor cells by EPR effect (b), the high concentration of GSH at the tumor site triggers PEG detachment (c) and the rapid release of the loaded drug (d). Reproduced from Wen, H. et al. Engineered redox-responsive PEG detachment mechanism in PEGylated nano-graphene oxide for intracellular drug delivery. *Small* (2012) doi: 10.1002/smll.201101613.

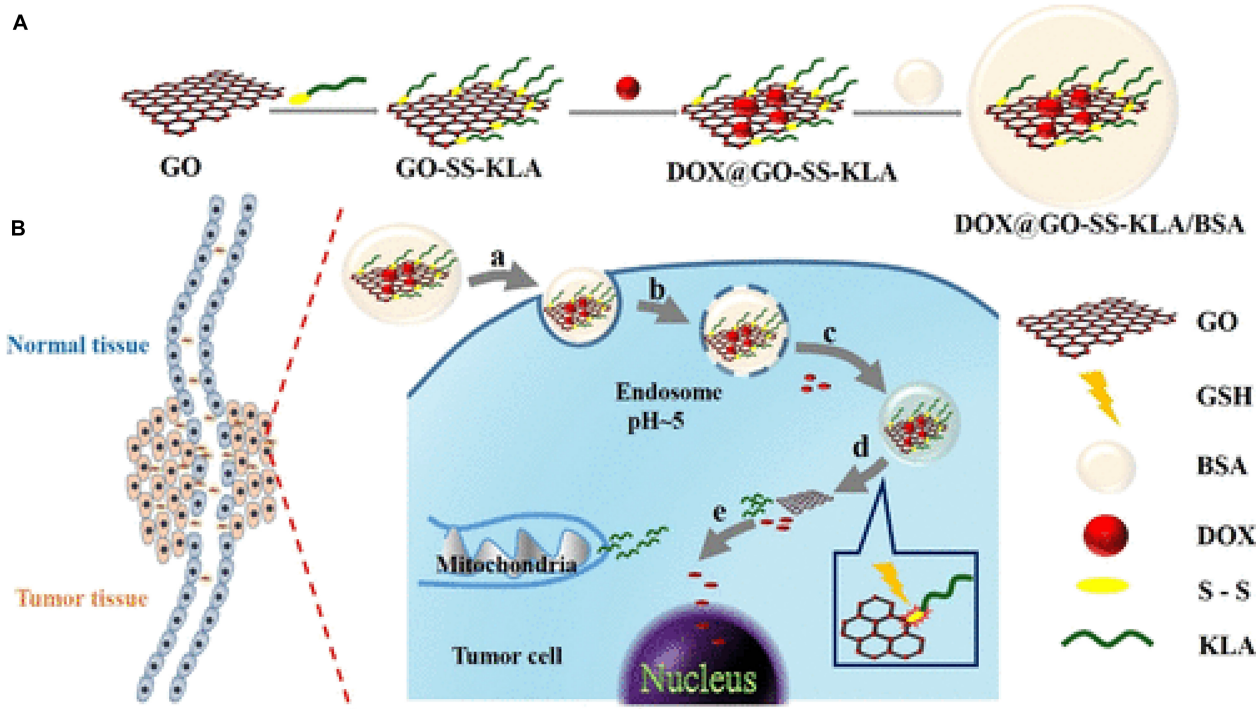


**FIGURE 14 | (A)** Synthetic route for GO - proapoptotic peptide- DOX double sensitive nanocarrier. **(B)** action mechanism after nanocarrier accumulation in tumor tissue by the EPR effect. Reproduced with permission from Zhang, J. et al. Dual-Sensitive Graphene Oxide Loaded with Proapoptotic Peptides and Anticancer Drugs for Cancer Synergetic Therapy. *Langmuir* (2019) doi: 10.1021/acs.langmuir.9b00611. Copyright (2019) American Chemical Society.

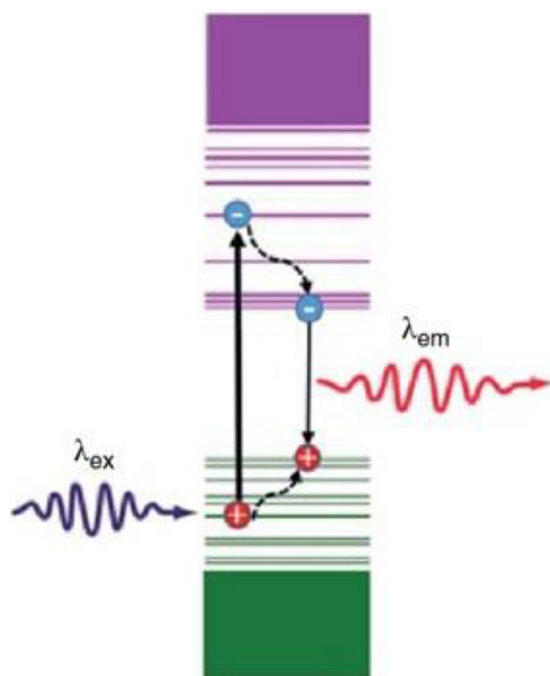


**FIGURE 15** | Illustration of photoluminescence mechanism of GO.

T. The *in vivo* behavior of the PEGylated nGO sheet labeled with a fluorescent dye was studied in tumor-bearing mice using *in vivo* fluorescence imaging. Polyethylene glycol-conjugated nanofold showed high passive tumor accumulation due to the EPR effect in several different tumor models and low retention in the reticuloendothelial systems. Fluorescence measures showed that the system was widely distributed throughout the body 30 min after injection, but tended to accumulate in the tumor over time, particularly 24h after injection there was an accumulation in the tumor with relatively low signals in other parts of the body. The dye or PEGylated dye at the same concentration, used as a control, was eliminated after a few hours (renal clearance). In the same study, to explore the effects of photothermal therapy *in vivo* a NIR (808 nm) laser at a power density of  $2 \text{ W cm}^{-2}$  was used to ablate tumors bearing the functional nanosheets. The superficial temperature of tumors in mice injected with NGS reaches about  $50^\circ\text{C}$  after laser irradiation, while the T of the control increases by about  $2^\circ\text{C}$ . All tumors on mice treated with NGS disappeared one day after treatment, leaving black scar tissue that went away one week after treatment (**Figure 16**), no reappearance of the tumor was observed in the 40 days following treatment. In contrast, the three control groups all exhibited rapid tumor growth, indicating that NIR radiation alone did not affect tumor growth. Moreover, mice in the control groups showed an average life span of about 16 days, while mice injected with NGS survived over 40 days.

Kurapati and Raichur (2013) synthesized GO-poly(allylamine hydrochloride) (PAH) composite capsules using dextran sulfate (DS) doped calcium carbonate [ $\text{CaCO}_3$  (DS)] as a sacrificial template and studied the capsule breaking mechanism and the releasing of encapsulated anticancer drug DOX upon NIR-laser

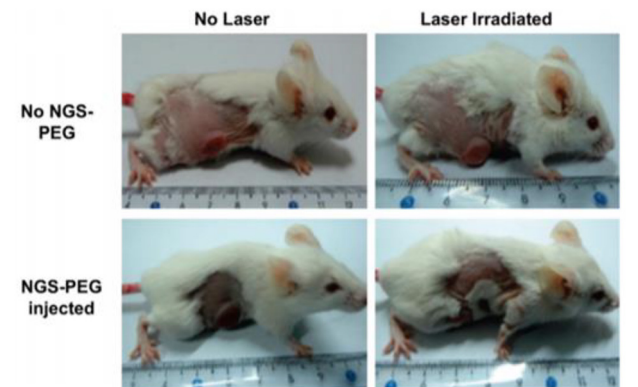


**FIGURE 16** | representative photos of tumor ablation in mice after photothermal treatment. Reproduced with permission from Yang, K. et al. Graphene in mice: Ultrahigh *in vivo* tumor uptake and efficient photothermal therapy. *Nano Lett.* (2010) doi: 10.1021/nl100996u. Copyright (2010) American Chemical Society.

(1064 nm) irradiation for different periods and power of the laser. The optical microscopy and low and high magnification transmission electron microscopy images showed that the breakage of the capsules by irradiation with NIR light began with a small hole and then extended as exposure time and laser power increased. This kind of breaking is known in the literature as a “point-wise opening” and has been reported for gold nanoparticles (Bédard et al., 2008). As reported earlier, NIR-laser irradiation of GO resulted in the generation of excitons, which decay into heat and produced strong heating of the surrounding environment. GO has superior thermal conductivity, specific heat capacity, and NIR-absorption compared to gold nanoparticles, and upon irradiation of the NIR-laser (30 mW) for 45 s, the capsule suspension temperature was increased from  $25^\circ\text{C}$  to  $40^\circ\text{C}$  due to local heating. Similarly, the amount of DOX released increased, in comparison to the control, as the breakage of the capsules is enlarged with an increase in the laser exposure time. Jung et al. (2014) reported a nGO -hyaluronic acid composite with spherical morphology and lateral size of  $\sim 250 \text{ nm}$  for photothermal ablation therapy of melanoma skin cancer using a near-infrared (NIR) laser. Hyaluronic acid is a widely used transdermal carrier of chemical drugs and biopharmaceuticals. In this work, transdermal delivery of NGO-HA through the normal and cancerous skin was investigated by confocal laser scanning microscopy after labeling the system with a fluorescent dye, Hilyte647. Confocal laser scanning microscopy revealed a negligible (**Figure 17**) NGO-HA transdermally deliver in healthy tissue and deep penetration into the tumor tissues. The red fluorescence of Hilyte647-labeled NGO-HA was observed in every tissue site including stratum corneum, epidermis, dermis, and tumor tissue, and could be detected from the top and even from the bottom of the dissected 5mm long tumor tissues (**Figure 17D**). This high penetration resulted both from increased permeability and retention of the tumor mass under the skin and from targeting due to over-expressed hyaluronic acid receptors in the tumor tissue. The same PEG-coated GO nano-system shows

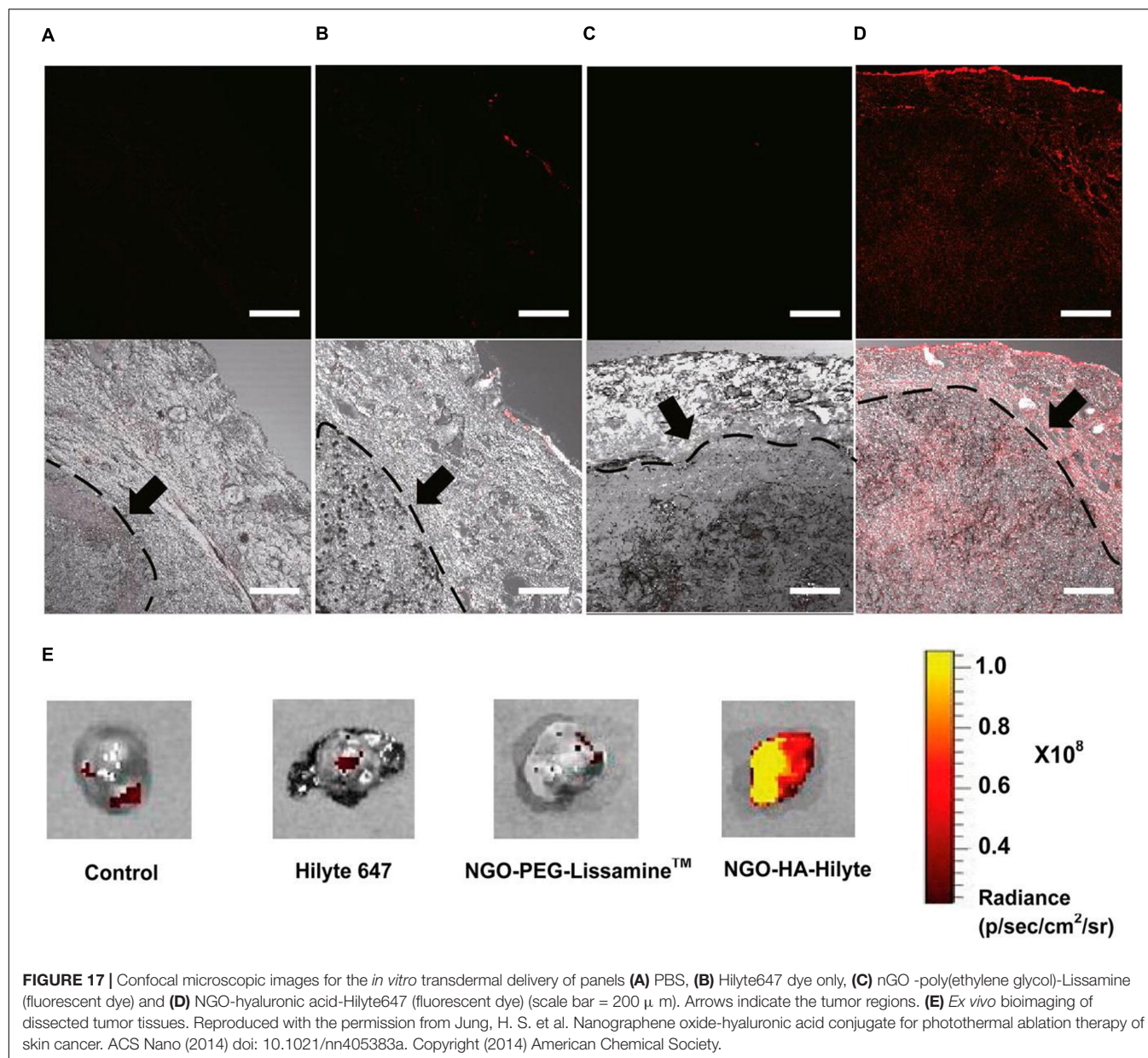
lower penetration (**Figure 17E**). The NIR irradiation (808 nm, 2 W/cm<sup>2</sup>) for 10 min resulted in complete ablation of tumor tissues with no recurrence of tumorigenesis.

The photothermal effect of GO nanoparticles was also investigated by two-photon excitation induced by an ultrafast pulsed laser. Two-photon microscopy with a NIR laser is a hopeful technique for premature detection and therapy of cancer due to the lower background signal, penetration into deep tissue (due to low Rayleigh diffusion and low tissue absorption of NIR light), reduced photobleaching, and reduced phototoxicity. GO nanoparticles with dimensions around 30 nm were prepared and functionalized with transferrin, an efficient ligand for targeting cancer cells that overregulate transferrin receptors, and PEGylate to prolong their circulation in the blood (Li et al., 2012). The two-photon luminescence spectrum of the sample irradiated with a Titanium: Sapphire femtosecond laser, in the range between 400 and 650 nm, had a maximum at 590 nm. The logarithmic scale graph of photoluminescence intensity versus incident power fits a straight line with a slope close to 2, indicating that photoluminescence is due to the excitation of two photons. The photothermal effect was estimated *in vitro* in gastric cancer cells (AGS). After irradiation with a laser power of about 4 mW, the integrity of the cell membrane of the cells incubated with GO became compromised, while an order of magnitude higher laser power was required to induce cell damage or death in the control cells. Also, when the incubated GO cells were raster-scanned at 4 mW, the formation of bubbles (black dots) was instantly noticeable, the addition of ethidium bromide after a couple of minutes revealed staining on most cells. Increasing the laser power to 8 mW it resulted in a more intense perforation of the cell membrane, confined only to the area exposed to laser radiation. The authors attributed the strong micro bubbling observed to the instantaneous heat production by GO particles as a result of laser radiation. The irradiation of an ultrafast pulsed laser can generate a large number of hot carriers with electrons in the conduction bands and holes in the valence bands. The temperature of the hot carriers can increase by a few thousand degrees in about 50 femtoseconds from the absorption of two photons. These hot carriers then recombine releasing energy through photoluminescence emission and through collisions with the GO lattice that causes an increase in temperature. The temperature increase caused by laser excitation should be able to *in situ* reduced GO by producing CO<sub>2</sub>, which increases the formation of bubbles. The collapse of the microbubbles can produce high-pressure shock waves that mechanically disrupt cell membranes and cause instant cell death (necrosis). nGO platforms are widely explored for combined anticancer therapies. Achieving the combination of chemotherapy and photothermal therapy is an important goal for next-generation cancer treatments as it allows a higher death rate of cancer cells with a lower dose of the drug, minimizing side effects and multi-drug resistance. Zhang W. et al. (2011) studied the combined effect of photothermal therapy and chemotherapy of nGO coated with polyethylene glycol *in vitro* and *in vivo* demonstrating that at a fixed laser frequency and concentration of the drug-loaded on the carrier, combined therapy had a superior efficiency in the complete ablation of tumors compared to individual treatments.

Qin et al. (2013) explored the chemo-photothermal therapy synergic effect of nGO coated with polyvinylpyrrolidone and functionalized with folic acid. The system showed an ultrahigh loading ratio of DOX, and extraordinary photothermal energy conversion efficiency when irradiated with 2W/cm<sup>2</sup> NIR laser at 808 nm. In elegant work, Zhang H. et al. (2019) presented a multifunctional nanosystem based on GO for synergistic multistage tumor-targeting and combined chemo-photothermal therapy. First the authors synthesized a prodrug consisting of hyaluronic acid and methotrexate (MTX) via an esterification reaction. MTX is a chemotherapy agent structurally similar to folic acid and able to achieve effective cell internalization through specific interactions with FA receptors over-expressed by various tumor cells. The MTX-HA prodrug was grafted to carboxyl-functionalized GO (GO-COOH) through a relatively stable adipicdihydrazide (ADH) cross-linker via an amidation reaction (**Figure 18A**) that ensures nanosystem stability during blood circulation after intravenous injection. As described in **Figure 18B** the accumulation in tumor tissue and within cancer cells was achieved through the MTX-HA dual active targeting mechanism. After cell internalization, the ester bond between MTX and HA was cleaved in acidic endo/lysosomes inside tumor cells (pH 4.5-5.5) (Li Y. et al., 2018) to achieve MTX release, and simultaneously the high local heat-induced by NIR radiation on the GO platform leads to highly efficient cell death via the combination of chemotherapy and PTT therapy.

The intrinsic photoluminescence of nanosized GO and the unique photostability make this material also applicable in the field of biomedical imaging. Contrast agent-based imaging techniques are used for the early detection of tumors, for understanding the distribution of the nanocarrier in tumors and other organs, for evaluating the therapeutic efficacy, and for post-treatment monitoring (Stankovich et al., 2007). Sun et al. (2008) proposed GO nanosheets with lateral dimensions below 10 nm, obtained by a density gradient ultracentrifugation method used for live cell imaging in the near-infrared (NIR). In this work, nGO was coated with polyethylene glycol and covalently conjugated with a specific Rituxan B-cell antibody (anti-CD20) for selective targeting of B-cell lymphoma cells (nGO-PEG-Rituxan). NIR fluorescence images showed that the nGO-PEG-Rituxan conjugate was effectively internalized and exhibited luminescence in the visible and NIR regions, although the quantum fluorescence yield was difficult to quantify due to the inhomogeneous species in the sample. The system was also assessed as an anticancer nanocarrier, by loading DOX through non-covalent interactions  $\pi$ -stacking, demonstrating a high loading capacity and selective inhibition of cell growth. Kalluru et al. (2016) functionalized a GO with lateral size less than 100 nm with NH<sub>2</sub>-PEG-folate moiety via carbodiimide crosslinker chemistry to form GO-PEG-folate to ensure the targeting ability of the folate moieties to the folate receptors on cancer cells. This system exhibited wavelength-dependent single-photon excitation-induced photoluminescence in the short NIR and visible region and acted as a single-photon excitation induced *in vitro* fluorescent cellular marker. Moreover, the authors demonstrated, for the first time, that nGO-PEG-folate can induce singlet (Bray et al., 2018) O<sub>2</sub>





generation upon NIR light excitation. This finding is particularly relevant in the field of cancer therapy because it allows considering GO not only as a photothermal agent but also as a photodynamic agent. Photodynamic therapy (PDT) is Food and Drug Administration (FDA) approved treatment for a variety of oncological, cardiovascular, dermatological, and ophthalmic diseases. PDT utilizes molecule or nanoparticle, named photosensitizer, to convert oxygen from the triplet ground state to the singlet state. This highly reactive oxygen species react with cellular components such as DNA or proteins and do irreversible damage to their structure or function causing apoptosis (Aioub et al., 2018). Until this study, GO was considered as a platform for the loading and delivery of photosensitizer for PDT, which, in most cases, are hydrophobic

in nature (Zhou et al., 2012; Zhou L. et al., 2014). In this work, the generation of  $^1\text{O}_2$  by the photo-excitation of GO-PEG-folate was investigated with fluorescence lifetime spectroscopy upon excitation using 808 nm and 980 nm light excitation, a  $^1\text{O}_2$  phosphorescence emission at  $\sim 1265$  nm was detected only upon 980 nm excitation. The photodynamic effect was demonstrated *in vitro* on GO-PEG-folate internalized B16F0 melanoma cancer cells, after photo-irradiation using 808 and 980 nm lasers high intracellular ROS levels and a high percentage of cellular deaths were observed. The percentage of cellular deaths by 980 nm light irradiation was about 1.9 times higher than the cellular deaths observed using 808 nm light, as GO-PEG-folate can sensitize generation of  $^1\text{O}_2$  only upon 980 nm light, the cellular deaths observed at 808 nm excitation was



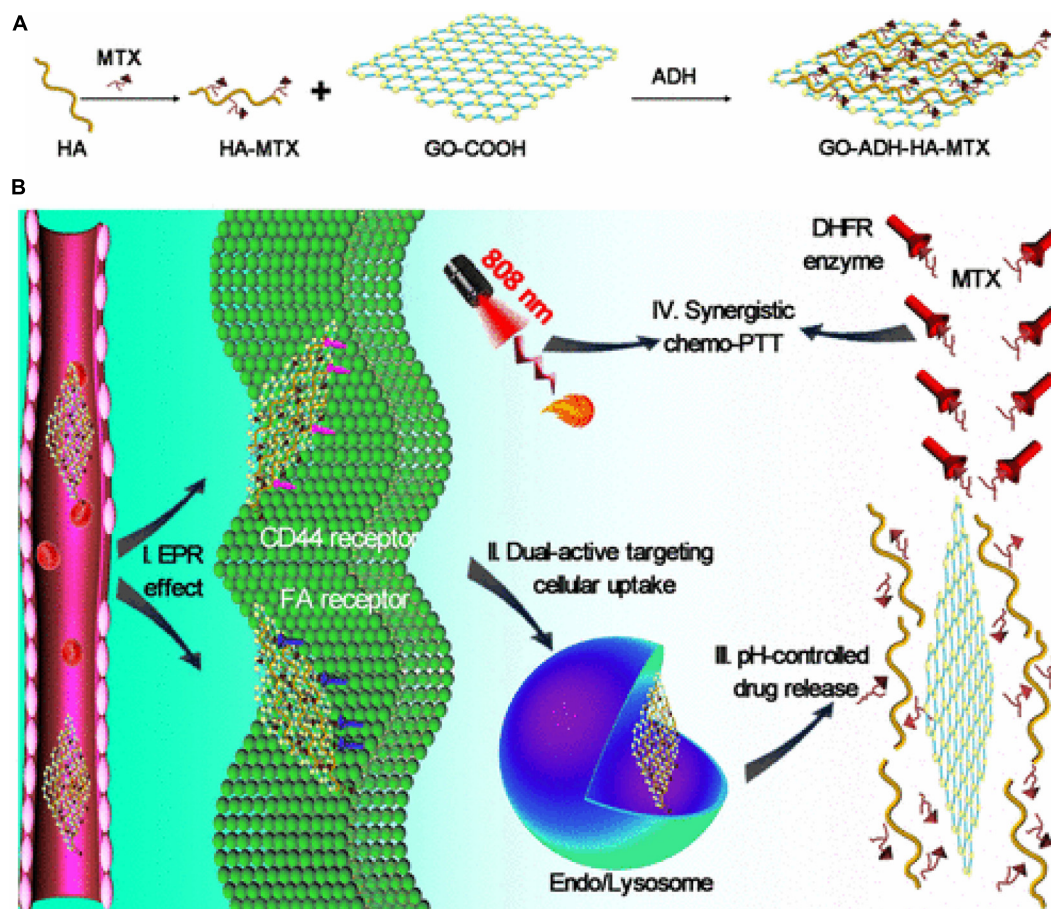


**FIGURE 18 | (A)** synthetic route for GO-ADH-HA-MTX nanosystems; **(B)** schematic illustration of GO-ADH-HA-MTX nanosystems for combination therapy of chemotherapy and PTT through dual-active targeting delivery: (i) accumulation of nanosystems within tumor sites through EPR effect; (ii) improved tumor cellular internalization of nanosystems through dual active targeting mechanisms by specific recognition for HA or MTX; (iii) controlled release of MTX from nanosystems through acid-induced cleavage of ester linkage; (iv) combination therapy of chemotherapy and PTT. Reproduced with permission from Zhang, H. et al. Multifunctional Nanosystem Based on Graphene Oxide for Synergistic Multistage Tumor-Targeting and Combined Chemo-Photothermal Therapy. *Mol. Pharm.* (2019) doi: 10.1021/acs.molpharmaceut.8b01335. Copyright (2019) American Chemical Society.

probably due to the PTT and PDT combination. The autofluorescence of biological tissue may interfere with the intrinsic visible fluorescence of nGO limiting the application of this material in classical imaging techniques (Yang et al., 2013). However, materials with a photothermal effect usually can be used as contrast agents for photoacoustic imaging, (PAI) an innovative, hybrid, non-invasive imaging method that combines the advantages of optical and ultrasound methods (Yang et al., 2007) is based on the detection of ultrasound waves produced by the photothermal expansion of light-absorbing tissues or contrast probes under pulsed laser irradiation and has attracted broad attention as an exciting non-invasive imaging method for tumor imaging and monitoring of tumor angiogenesis because it allows an unprecedented sensitivity (Cook et al., 2013) and it is not affected by the autofluorescence in biological tissues commonly experienced by fluorescence imaging. The majority of GO PAI imaging studies exploit the large surface area of carbon atoms and the variety of oxygenated functional

groups to covalently or non-covalently bind organic or inorganic contrast agents and thus increase NIR absorption and PAI signal (Wang et al., 2013; Yan et al., 2015; Rong et al., 2016). Very recently Jun et al. (2020) presented the results of a derivative of GO as a theranostic agent for photoacoustic imaging-driven tumor-targeted photothermal therapy. The GO nanosheets used in this work were functionalized with folic acid, (FA), conjugated chitosan, (CS), through physical adsorption via hydrogen bonding and electrostatic interaction. The resulting derivate presented a lateral dimension of around 400 nm, showed the ability to target folate receptors, low toxicity, even at high concentrations, and was proved to be an excellent photothermal agent able to destroy more than 80% of cancer cells under laser irradiation. The ability of FA-CS-GO to function as a new PAI contrast agent was demonstrated *in vivo* performing PAI imaging before and after FA-CS-GO injection via tail vein in mouse tumor-bearing. Before injection, only major blood vessels (with hemoglobin as an endogenous contrast agent) in the tumor

area are observed. After 24 h from the injection of FA-CS-GO, instead, the PA signals in the tumor area are higher and an outline tumor microstructure was observed, suggesting the gradual accumulation of FA-CS-GO in the tumor area due to the receptor-mediated endocytosis.

## CONCLUSION

Nanotechnology has been recognized in 2006 by the National Cancer Institute as the science that can effectively change the basis for the diagnosis, treatment, and prevention of cancer, allowing the study and treatment of this disease at a molecular scale, in real-time and during the early stages of the process. 2D nanomaterials possess special physicochemical properties (e.g., light, ultrasonic and magnetic responses) and biological behaviors such as endocytosis, biodistribution, biodegradation, and excretory pathways, which lead to their use in various biomedical applications. In particular, among 2D nanomaterials, graphene and its derivatives have attracted enormous attention in cancer diagnosis and therapy because they combine, in a unique material, extremely small size, NIR absorption, delocalized electrons, extremely high surface area, and versatile surface functionality. GO, initially considered as an intermediate of one of the graphene production processes, has become a material that can be considered both for fundamental research and for its potential applications. GO is one of the most explored materials in nanomedicine due to its extraordinary intrinsic properties. The GO has a high surface area that can be exploited for the loading of drugs and biomolecules, forms stable colloidal dispersions in water and its structure contains a variety of oxygenated functional groups useful for the covalent modification. Furthermore, GO has interesting optical properties useful for phototherapy and biomedical imaging. Known since the beginning of the last century, the oxidation of graphite with strong oxidants in concentrated acid media remains the most commonly used method to produce GO on a large scale. However, the lateral dimensions of GO prepared by this convenient method have a very polydisperse distribution in the range of tens of nanometers to hundreds of micrometers.

Obtaining GO sheets with narrow size distribution in the nanometer range is very desirable especially for the nascent biomedical applications of GO. As is known, the physicochemical properties of the material, in particular the lateral dimensions, influence both the optical properties and the absorption and cellular response. Therefore, size is one of the first factors to check when considering GO as a therapeutic platform. Considering the importance of reducing the lateral size of GO nanosheet below 50 nm, in this review, we summarize the main methods employed to reduce and homogenize in nanometric scale the lateral dimensions of GO produced by chemical exfoliation of graphite. For this purpose, a variety of methods have been developed which can generally be distinguished in direct controllable synthesis and post-synthesis separation. The direct controllable synthesis approach involves intervention during the chemical oxidation process by using different precursors, or by tuning the reaction parameters (amount of oxidants, time, and temperature) or by employing physical promoters which mechanically break pristine graphite or GO sheets obtained. The post-synthesis separation involves instead the GO bulk fractionation through centrifugation or selective precipitation in organic solvents, or different pH aqueous solution. nGO platforms are widely explored for combined anticancer therapies. Indeed, together with the ability to accumulate a large amount of drug, for high surface development, they can be photo-stimulated producing heat and CO<sub>2</sub>, which both induce cell death. Moreover, they can be detected for their photo-luminescence properties providing the possibility to have a theranostic tool. All these features represent an important goal for next-generation cancer treatments as they allow a controlled and higher death rate of cancer cells with a lower dose of the drug, minimizing side effects and multi-drug resistance.

## AUTHOR CONTRIBUTIONS

IT and RV wrote the manuscript. RV and PN revised the manuscript. All authors did the conceptualization contributed to the article and approved the submitted version.

## REFERENCES

- Aioub, M., Austin, L. A., and El-Sayed, M. A. (2018). Gold nanoparticles for cancer diagnostics, spectroscopic imaging, drug delivery, and plasmonic photothermal therapy. *Inorgan. Framework. Smart Nanomed.* 2018, 41–91. doi: 10.1016/b978-0-12-813661-4.00002-x
- Arnold, M. S., Green, A. A., Hulvat, J. F., Stupp, S. I., and Hersam, M. C. (2006). Sorting carbon nanotubes by electronic structure using density differentiation. *Nat. Nanotechnol.* 1, 60–65. doi: 10.1038/nnano.2006.52
- Arnold, M. S., Stupp, S. I., and Hersam, M. C. (2005). Enrichment of single-walled carbon nanotubes by diameter in density gradients. *Nano Lett.* 5, 713–8. doi: 10.1021/nl050133o
- Asenbauer, J., Eisenmann, T., Kuenzel, M., Kazzazi, A., Chen, Z., and Bresser, D. (2020). The success story of graphite as a lithium-ion anode material – fundamentals, remaining challenges, and recent developments including silicon (oxide) composites. *Sustain. Ener. Fuels* 4, 5387–5416. doi: 10.1039/d0se00175a
- Attia, M. F., Anton, N., Wallyn, J., Omran, Z., and Vandamme, T. F. (2019). An overview of active and passive targeting strategies to improve the nanocarriers efficiency to tumour sites. *J. Pharm. Pharmacol.* 71, 1185–1198. doi: 10.1111/jphp.13098
- Batalha, W., Gargarella, P., and Kiminami, C. S. (2016). Novo Protocolo De Obtenção De Óxido De Grafite. 22º CBECiMat - Congr Bras Eng e Ciência dos Mater Natal. *RN Bras.* 2016, 139–151.
- Bédard, M. F., Braun, D., Sukhorukov, G. B., and Skirtach, A. G. (2008). Toward self-assembly of nanoparticles on polymeric microshells: Near-IR release and permeability. *ACS Nano.* 2, 1807–16. doi: 10.1021/nn8002168
- Bengtson, S., Kling, K., Madsen, A. M., Noergaard, A. W., Jacobsen, N. R., Clausen, P. A., et al. (2016). No cytotoxicity or genotoxicity of graphene and graphene oxide in murine lung epithelial FE1 cells in vitro. *Environ. Mol. Mutagen* 57, 469–82. doi: 10.1002/em.22017
- Benjamin, J. S. (1970). Dispersion strengthened superalloys by mechanical alloying. *Metall. Trans.* 1, 943–2951.
- Bharath, G., Madhu, R., Chen, S. M., Veeramani, V., and Mangalaraj, D. (2015). Solvent-free mechanochemical synthesis of graphene oxide and Fe<sub>3</sub>O<sub>4</sub>-reduced graphene oxide nanocomposites for sensitive detection of nitrite. *J. Mater. Chem.* 5, 13392–13401.

- Bianco, A., Cheng, H. M., Enoki, T., Gogotsi, Y., Hurt, R. H., Koratkar, N., et al. (2013). All in the graphene family - A recommended nomenclature for two-dimensional carbon materials. *Carbon*. 65, 1–6. doi: 10.1016/j.carbon.2013.08.038
- Bidram, E., Sulistio, A., Amini, A., Fu, Q., Qiao, G. G., Stewart, A., et al. (2016). Fractionation of graphene oxide single nano-sheets in water-glycerol solutions using gradient centrifugation. *Carbon N Y* 103, 363–371. doi: 10.1016/j.carbon.2016.02.095
- Botas, C., Pérez-Mas, A. M., Álvarez, P., Santamaría, R., Granda, M., Blanco, C., et al. (2013). Optimization of the size and yield of graphene oxide sheets in the exfoliation step. *Carbon* 63, 576–578. doi: 10.1016/j.carbon.2013.06.096
- Bray, F., Ferlay, J., Soerjomataram, I., Siegel, R. L., Torre, L. A., and Jemal, A. (2018). Global cancer statistics 2018: GLOBOCAN estimates of incidence and mortality worldwide for 36 cancers in 185 countries. *CA Cancer J. Clin.* 68, 394–424. doi: 10.3322/caac.21492
- Brisebois, P. P., and Sij, M. (2020). Harvesting graphene oxide-years 1859 to 2019: A review of its structure, synthesis, properties and exfoliation. *J. Mater. Chem. C* 5:8.
- Brodie, B. C. (1858). on the atomic weight of graphit. *Roy. Soc. Lon.* 1858, 249–259.
- Bullo, S., Buskaran, K., Baby, R., Dorniani, D., Fakurazi, S., and Hussein, M. Z. (2019). Dual Drugs Anticancer Nanoformulation using Graphene Oxide-PEG as Nanocarrier for Protocatechuic Acid and Chlorogenic Acid. *Pharm. Res.* 36:91.
- Burnett, M., Abuetabh, Y., Wronski, A., Shen, F., Persad, S., Leng, R., et al. (2020). Graphene oxide nanoparticles induce apoptosis in wild-type and CRISPR/Cas9-IGF1R/IGFBP3 knocked-out osteosarcoma cells. *J. Cancer*. 11, 5007–5023. doi: 10.7150/jca.46464
- Camara, N., Rius, G., Huntzinger, J. R., Tiberj, A., Mestres, N., Godignon, P., et al. (2008). Selective epitaxial growth of graphene on SiC. *Appl. Phys. Lett.* 93:123503.
- Cao, T., You, P., Zhou, X., Luo, J., Xu, X., Zhou, Z., et al. (2016). Visualization of size-dependent tumour retention of PEGylated nanographene oxide: Via SPECT imaging. *J. Mater. Chem. B* 4:39.
- Chambers, A., Park, C., Baker, R. T. K., and Rodriguez, N. M. (1998). Hydrogen storage in graphite nanofibers. *J. Phys. Chem. B* 20, 714–21. doi: 10.1021/la0349875
- Chang, Y., Yang, S. T., Liu, J. H., Dong, E., Wang, Y., and Cao, A. (2011). In vitro toxicity evaluation of graphene oxide on A549 cells. *Toxicol. Lett.* 200, 201–10. doi: 10.1016/j.toxlet.2010.11.016
- Chen, J., Chi, F., Huang, L., Zhang, M., Yao, B., Li, Y., et al. (2016). Synthesis of graphene oxide sheets with controlled sizes from sieved graphite flakes. *Carbon N Y* 110, 34–40. doi: 10.1016/j.carbon.2016.08.096
- Chen, J., Yao, B., Li, C., and Shi, G. (2013a). An improved Hummers method for eco-friendly synthesis of graphene oxide. *Carbon N Y* 64, 225–229. doi: 10.1016/j.carbon.2013.07.055
- Chen, J., Zhang, X., Zheng, X., Liu, C., Cui, X., and Zheng, W. (2013b). Size distribution-controlled preparation of graphene oxide nanosheets with different C/O ratios. *Mater. Chem. Phys.* 139, 8–11. doi: 10.1016/j.matchemphys.2012.12.025
- Chimene, D., Alge, D. L., and Gaharwar, A. K. (2015). Two-Dimensional Nanomaterials for Biomedical Applications: Emerging Trends and Future Prospects. *Adv. Mater.* 27, 7261–84. doi: 10.1002/adma.201502422
- Chung, D. D. L. (2002). Review: Graphite. *J. Mater. Sci.* 37, 1475–1489.
- Cobos, M., De-La-pinta, I., Quindós, G., Fernández, M. D., and Fernández, M. J. (2020). Graphene oxide-silver nanoparticle nanohybrids: Synthesis, characterization, and antimicrobial properties. *Nanomaterials* 10:376. doi: 10.3390/nano10020376
- Cook, J. R., Frey, W., and Emelianov, S. (2013). Quantitative photoacoustic imaging of nanoparticles in cells and tissues. *ACS Nano*. 7, 1272–1280. doi: 10.1021/nn304739s
- Deb, A., Andrews, N. G., and Raghavan, V. (2018). Natural polymer functionalized graphene oxide for co-delivery of anticancer drugs: In-vitro and in-vivo. *Int. J. Biol. Macromol.* 113, 515–525. doi: 10.1016/j.ijbiomac.2018.02.153
- Depan, D., Shah, J., and Misra, R. D. K. (2011). Controlled release of drug from folate-decorated and graphene mediated drug delivery system: Synthesis, loading efficiency, and drug release response. *Mater. Sci. Eng. C* 31, 305–1312.
- Dimiev, A. M., and Eigler, S. (2016). Graphene Oxide: Fundamentals and Applications. *Graphene Oxide* 2016:464.
- Dimiev, A. M., and Tour, J. M. (2014). Mechanism of graphene oxide formation. *ACS Nano*. 8, 3060–8. doi: 10.1021/nn500606a
- Dimiev, A. M., Shukhina, K., and Khannanov, A. (2020). Mechanism of the graphene oxide formation. The role of water, “reversibility” of the oxidation, and mobility of the C–O bonds. *Carbon N Y* 2020:166.
- Eigler, S., Enzelberger-Heim, M., Grimm, S., Hofmann, P., Kroener, W., Geworski, A., et al. (2013). Wet chemical synthesis of graphene. *Adv. Mater.* 25, 3583–7.
- Fan, T., Zeng, W., Tang, W., Yuan, C., Tong, S., Cai, K., et al. (2015). Controllable size-selective method to prepare graphene quantum dots from graphene oxide. *Nanosci. Res. Lett.* 10:55.
- Fang, S., Lin, Y., and Hu, Y. H. (2019). Recent advances in green, safe, and fast production of graphene oxide via electrochemical approaches. *ACS Sust. Chem. Engin.* 7:15.
- Farazas, A., Mavropoulos, A., Christofilos, D., Tsiaoussis, I., and Tsipas, D. (2018). Ultrasound assisted green synthesis and characterization of graphene oxide. *Int. J. Nanosci. Nanotechnol.* 14, 11–17.
- Feige, E., Quadir, M. A., and Haag, R. (2012). Stimuli-responsive polymeric nanocarriers for the controlled transport of active compounds: concepts and applications. *Adv. Drug Deliv. Rev.* 64, 866–884. doi: 10.1016/j.addr.2012.01.020
- Gao, X., Jiang, D. E., Zhao, Y., Nagase, S., Zhang, S., and Chen, Z. (2011). Theoretical insights into the structures of graphene oxide and its chemical conversions between graphene. *J. Comput. Theor. Nanosci.* 8, 2406–2422. doi: 10.1166/jctn.2011.1972
- Gayen, B., Palchoudhury, S., and Chowdhury, J. (2019). Carbon dots: A mystic star in the world of nanoscience. *J. Nanomater.* 2019:3451307.
- Gonçalves, G., Vila, M., Bdkin, I., De Andrés, A., Emami, N., Ferreira, R. A. S., et al. (2014). Breakdown into nanoscale of graphene oxide: Confined hot spot atomic reduction and fragmentation. *Sci. Rep.* 4:6735.
- Gonçalves, G., Vila, M., Portolés, M. T., Vallet-Regi, M., Gracio, J., and Marques, P. A. A. P. (2013). Nano-graphene oxide: A potential multifunctional platform for cancer therapy. *Adv. Healthc. Mater.* 2, 1072–90. doi: 10.1002/adhm.201300023
- Green, A. A., and Hersam, M. C. (2009). Solution phase production of graphene with controlled thickness via density differentiation. *Nano. Lett.* 9, 4031–4036. doi: 10.1021/nl902200b
- Green, A. A., Duch, M. C., and Hersam, M. C. (2009). Isolation of single-walled carbon nanotube enantiomers by density differentiation. *Nano. Res.* 2, 69–77. doi: 10.1007/s12274-009-9006-y
- Han, J. T., Jang, J. I., Kim, H., Hwang, J. Y., Yoo, H. K., and Woo, J. S. (2014). Extremely efficient liquid exfoliation and dispersion of layered materials by unusual acoustic cavitation. *Sci. Rep.* 4:5133.
- Hároz, E. H., Rice, W. D., Lu, B. Y., Ghosh, S., Hauge, R. H., Weisman, R. B., et al. (2010). Enrichment of armchair carbon nanotubes via density gradient ultracentrifugation: Raman spectroscopy evidence. *ACS Nano*. 4, 1955–62. doi: 10.1021/nn901908n
- He, H., Klinowski, J., Forster, M., and Lerf, A. (1998). A new structural model for graphite oxide. *Chem. Phys. Lett.* 287, 53–56. doi: 10.1016/s0009-2614(98)00144-4
- Hens, S. C., Lawrence, W. G., Kumbhar, A. S., and Shenderova, O. (2012). Photoluminescent nanostructures from graphite oxidation. *J. Phys. Chem. C* 116, 20015–20022. doi: 10.1021/jp303061e
- Hu, T., Mei, X., Wang, Y., Weng, X., Liang, R., and Wei, M. (2019). Two-dimensional nanomaterials: fascinating materials in biomedical field. *Sci. Bull.* 64, 1707–1727. doi: 10.1016/j.scib.2019.09.021
- Hu, X., Yu, Y., Wang, Y., Zhou, J., and Song, L. (2015). Separating nano graphene oxide from the residual strong-acid filtrate of the modified Hummers method with alkaline solution. *Appl. Surf. Sci.* 329, 83–86. doi: 10.1016/j.apsusc.2014.12.110
- Huang, J. J., and Yuan, Y. J. (2016). A sedimentation study of graphene oxide in aqueous solution using gradient differential centrifugation. *Phys. Chem. Chem. Phys.* 18, 12312–12322. doi: 10.1039/c6cp00167j
- Hummers, W. S., and Offeman, R. E. (1958). Preparation of Graphitic Oxide. *J. Am. Chem. Soc.* 80:139.
- Iwamoto, T. (2013). Clinical application of drug delivery systems in cancer chemotherapy: review of the efficacy and side effects of approved drugs. *Biol. Pharm. Bull.* 36, 715–718. doi: 10.1248/bpb.b12-01102



- Jun, S. W., Manivasagan, P., Kwon, J., Nguyen, V. T., Mondal, S., Ly, C. D., et al. (2020). Folic acid-conjugated chitosan-functionalized graphene oxide for highly efficient photoacoustic imaging-guided tumor-targeted photothermal therapy. *Int. J. Biol. Macromol.* 155, 961–971. doi: 10.1016/j.ijbiomac.2019.11.055
- Jung, H. S., Kong, W. H., Sung, D. K., Lee, M. Y., Beack, S. E., and Keum, D. H. (2014). Nanographene oxide-hyaluronic acid conjugate for photothermal ablation therapy of skin cancer. *ACS Nano* 8, 260–8. doi: 10.1021/nn405383a
- Kalluru, P., Vankayala, R., Chiang, C. S., and Hwang, K. C. (2016). Nano-graphene oxide-mediated In vivo fluorescence imaging and bimodal photodynamic and photothermal destruction of tumors. *Biomaterials* 95, 1–10. doi: 10.1016/j.biomaterials.2016.04.006
- Kim, J., Cote, L. J., Kim, F., Yuan, W., Shull, K. R., and Huang, J. (2010). Graphene oxide sheets at interfaces. *J. Am. Chem. Soc.* 132, 8180–6.
- Kordi, F., Khorsand Zak, A., Darroudi, M., and Hazrati Saedabadi, M. (2019). Synthesis and characterizations of Ag-decorated graphene oxide nanosheets and their cytotoxicity studies. *Chem. Pap.* 73, 1945–1952. doi: 10.1007/s11696-019-00747-4
- Kosynkin, D. V., Higginbotham, A. L., Sinitskii, A., Lomeda, J. R., Dimiev, A., Price, B. K., et al. (2009). Longitudinal unzipping of carbon nanotubes to form graphene nanoribbons. *Nature* 458, 872–6. doi: 10.1038/nature07872
- Kurapati, R., and Raichur, A. M. (2013). Near-infrared light-responsive graphene oxide composite multilayer capsules: A novel route for remote controlled drug delivery. *Chem. Commun.* 49, 734–736. doi: 10.1039/c2cc38417e
- Layek, R. K., and Nandi, A. K. (2013). A review on synthesis and properties of polymer functionalized graphene. *Polymer* 54, 5087–5103. doi: 10.1016/j.polymer.2013.06.027
- Layek, R. K., Samanta, S., Chatterjee, D. P., and Nandi, A. K. (2010). Physical and mechanical properties of poly(methyl methacrylate) -functionalized graphene/poly(vinylidene fluoride) nanocomposites: Piezoelectric  $\beta$  polymorph formation. *Polymer* 42, 8425–8434.
- Li, C., Chen, X., Shen, L., and Bao, N. (2020). Revisiting the Oxidation of Graphite: Reaction Mechanism, Chemical Stability, and Structure Self-Regulation. *ACS Omega* 5, 3397–3404. doi: 10.1021/acsomega.9b03633
- Li, J. L., Bao, H. C., Hou, X. L., Sun, L., Wang, X. G., and Gu, M. (2012). Graphene oxide nanoparticles as a nonbleaching optical probe for two-photon luminescence imaging and cell therapy. *Angew. Chem. Int. Ed.* 51, 1830–4. doi: 10.1002/anie.201106102
- Li, J., Liang, X., Zhang, J., Yin, Y., Zuo, T., Wang, Y., et al. (2018). Inhibiting pulmonary metastasis of breast cancer based on dual-targeting graphene oxide with high stability and drug loading capacity. *Nanomed. Nanotechnol. Biol. Med.* 4:14.
- Li, R., Gao, R., Wang, Y., Liu, Z., Xu, H., Duan, A., et al. (2020). Gastrin releasing peptide receptor targeted nano-graphene oxide for near-infrared fluorescence imaging of oral squamous cell carcinoma. *Sci. Rep.* 10:2020.
- Li, S., Zhu, F., Meng, F., Li, H., Wang, L., Zhao, J., et al. (2013). Separation of graphene oxide by density gradient centrifugation and study on their morphology-dependent electrochemical properties. *J. Electroanal. Chem.* 703, 135–145. doi: 10.1016/j.jelechem.2013.05.020
- Li, X., Zhang, G., Bai, X., Sun, X., Wang, X., Wang, E., et al. (2008). Highly conducting graphene sheets and Langmuir-Blodgett films. *Nat. Nanotechnol.* 3, 538–542. doi: 10.1038/nnano.2008.210
- Li, Y., Zhang, H., Chen, Y., Ma, J., Lin, J., Zhang, Y., et al. (2018). Integration of phospholipid-hyaluronic acid-methotrexate nanocarrier assembly and amphiphilic drug-drug conjugate for synergistic targeted delivery and combinational tumor therapy. *Biomater. Sci.* 6, 1818–1833. doi: 10.1039/c8bm00009c
- Liu, J., Yang, H., Zhen, S. G., Poh, C. K., Chaurasia, A., Luo, J., et al. (2013). A green approach to the synthesis of high-quality graphene oxide flakes via electrochemical exfoliation of pencil core. *RSC Adv.* 3:29.
- Liu, Y., Luo, Y., Wu, J., Wang, Y., Yang, X., Yang, R., et al. (2013). Graphene oxide can induce in vitro and in vivo mutagenesis. *Sci. Rep.* 3:3469.
- Liu, Y., Miyoshi, H., and Nakamura, M. (2007). Nanomedicine for drug delivery and imaging: a promising avenue for cancer therapy and diagnosis using targeted functional nanoparticles. *Int. J. Cancer* 120, 2527–2537. doi: 10.1002/ijc.22709
- Liu, Z., Robinson, J. T., Sun, X., and Dai, H. (2008). PEGylated nanographene oxide for delivery of water-insoluble cancer drugs. *J. Am. Chem. Soc.* 130, 10876–7. doi: 10.1021/ja803688x
- Lo, K. K. W. (2017). *Inorganic and Organometallic Transition Metal Complexes with Biological Molecules and Living Cells*. London: Academic Press.
- Lonkar, S. P., Deshmukh, Y. S., and Abdala, A. A. (2015). Recent advances in chemical modifications of graphene. *Nano Res.* 8, 1039–1074. doi: 10.1007/s12274-014-0622-9
- Luo, D., Zhang, F., Ren, Z., Ren, W., Yu, L., Jiang, L., et al. (2019). An improved method to synthesize nanoscale graphene oxide using much less acid. *Mater. Tod. Phys.* 9:100097. doi: 10.1016/j.mtphys.2019.100097
- Luo, J., Cote, L. J., Tung, V. C., Tan, A. T. L., Goins, P. E., Wu, J., et al. (2010). Graphene oxide nanocolloids. *J. Am. Chem. Soc.* 13, 17667–9.
- Luo, Y., Tang, Y., Liu, T., Chen, Q., Zhou, X., Wang, N., et al. (2019). Engineering graphene oxide with ultrasmall SPIONs and smart drug release for cancer theranostics. *Chem. Commun.* 55, 1963–1966. doi: 10.1039/c8cc09185d
- Lv, Y., Tao, L., Annie Bligh, S. W., Yang, H., Pan, Q., and Zhu, L. (2016). Targeted delivery and controlled release of doxorubicin into cancer cells using a multifunctional graphene oxide. *Mater. Sci. Eng. C* 59, 652–660. doi: 10.1016/j.msec.2015.10.065
- Ma, J., Liu, R., Wang, X., Liu, Q., Chen, Y., Valle, R. P., et al. (2015). Crucial Role of Lateral Size for Graphene Oxide in Activating Macrophages and Stimulating Pro-inflammatory Responses in Cells and Animals. *ACS Nano* 9, 10498–515. doi: 10.1021/acsnano.5b04751
- Mahmoud, A. E. D., Stolle, A., and Stelter, M. (2018). Sustainable Synthesis of High-Surface-Area Graphite Oxide via Dry Ball Milling. *ACS Sustain. Chem. Eng.* 6, 6358–6369. doi: 10.1021/acssuschemeng.8b00147
- Marcano, D. C., Kosynkin, D. V., Berlin, J. M., Sinitskii, A., Sun, Z., Slesarev, A., et al. (2010). Improved synthesis of graphene oxide. *ACS* 4, 4806–14.
- McAllister, M. J., Li, J. L., Adamson, D. H., Schniepp, H. C., Abdala, A. A., Liu, J., et al. (2007). Single sheet functionalized graphene by oxidation and thermal expansion of graphite. *Chem. Mater.* 19, 4396–4404. doi: 10.1021/cm0630800
- Mendes, R. G., Koch, B., Bachmatiuk, A., Ma, X., Sanchez, S., Damm, C., et al. (2015). A size dependent evaluation of the cytotoxicity and uptake of nanographene oxide. *J. Mater. Chem. B* 3, 2522–2529. doi: 10.1039/c5tb00180c
- Méndez-Romero, U. A., Pérez-García, S. A., Fan, Q., Wang, E., and Licea-Jiménez, L. (2020). Lateral size reduction of graphene oxide preserving its electronic properties and chemical functionality. *RSC Adv.* 10, 29432–29440. doi: 10.1039/d0ra04726k
- Mirzaie, Z., Reisi-Vanani, A., and Barati, M. (2019). Polyvinyl alcohol-sodium alginate blend, composited with 3D-graphene oxide as a controlled release system for curcumin. *J. Drug Deliv. Sci. Technol.* 2019, 380–387. doi: 10.1016/j.jddst.2019.02.005
- Muñoz, R., Singh, D. P., Kumar, R., and Matsuda, A. (2019). Graphene Oxide for Drug Delivery and Cancer Therapy. *Nanostruct. Poly. Compos. Biomed. Appl.* 2019, 447–488. doi: 10.1016/b978-0-12-816771-7.00023-5
- Mura, S., Nicolas, J., and Couvreur, P. (2013). Stimuli-responsive nanocarriers for drug delivery. *Nat. Mater.* 12, 991–1003.
- Novoselov, K. S., Geim, A. K., Morozov, S. V., Jiang, D., Zhang, Y., Dubonos, S. V., et al. (2004). Electric field in atomically thin carbon films. *Science* 80, 306, 666–9. doi: 10.1126/science.1102896
- Obraztsov, A. N. (2009). Making graphene on a large scale. *Nat. Nanotechnol.* 4, 212–3. doi: 10.1038/nnano.2009.67
- Pan, Q., Lv, Y., Williams, G. R., Tao, L., Yang, H., Li, H., et al. (2016). Lactobionic acid and carboxymethyl chitosan functionalized graphene oxide nanocomposites as targeted anticancer drug delivery systems. *Carbohydr. Polym.* 151, 812–820. doi: 10.1016/j.carbpol.2016.06.024
- Park, J. H., Von Maltzahn, G., Ong, L. L., Centrone, A., Hatton, T. A., Ruoslahti, E., et al. (2010). Cooperative nanoparticles for tumor detection and photothermally triggered drug delivery. *Adv. Mater.* 22, 880–5. doi: 10.1002/adma.200902895
- Peng, L., Xu, Z., Liu, Z., Wei, Y., Sun, H., and Li, Z. (2015). An iron-based green approach to 1-h production of single-layer graphene oxide. *Nat. Commun.* 6:5716.
- Pham, T. T., Nguyen, H. T., Phung, C. D., Pathak, S., Regmi, S., Ha, D. H., et al. (2019). Targeted delivery of doxorubicin for the treatment of bone metastasis from breast cancer using alendronate-functionalized graphene oxide nanosheets. *J. Ind. Eng. Chem.* 76, 310–317. doi: 10.1016/j.jiec.2019.03.055



- Piras, C. C., Fernández-Prieto, S., and De Borggraeve, W. M. (2019). Ball milling: A green technology for the preparation and functionalisation of nanocellulose derivatives. *Nanosci. Adv.* 1, 937–947. doi: 10.1039/c8na00238j
- Posudievsky, O. Y., Khazieva, O. A., Koshechko, V. G., and Pokhodenko, V. D. (2012). Preparation of graphene oxide by solvent-free mechanochemical oxidation of graphite. *J. Mater. Chem.* 25, 12465–12467. doi: 10.1039/c2jm16073k
- Posudievsky, O. Y., Kozarenko, O. A., Khazieva, O. A., Koshechko, V. G., and Pokhodenko, V. D. (2013). Ultrasound-free preparation of graphene oxide from mechanochemically oxidized graphite. *J. Mater. Chem. A* 1, 6658–6663. doi: 10.1039/c3ta10542c
- Pramanik, N., Ranganathan, S., Rao, S., Suneet, K., Jain, S., Rangarajan, A., et al. (2019). A Composite of Hyaluronic Acid-Modified Graphene Oxide and Iron Oxide Nanoparticles for Targeted Drug Delivery and Magnetothermal Therapy. *ACS Omega* 45, 9284–9293. doi: 10.1021/acsomega.9b00870
- Qi, X., Zhou, T., Deng, S., Zong, G., Yao, X., and Fu, Q. (2014). Size-specified graphene oxide sheets: Ultrasonication assisted preparation and characterization. *J. Mater. Sci.* 4:49.
- Qiao, Y., Wan, J., Zhou, L., Ma, W., Yang, Y., Luo, W., et al. (2019). Stimuli-responsive nanotherapeutics for precision drug delivery and cancer therapy. *Wiley Interdisc. Rev. Nanomed. Nanobiotechnol.* 11:e1527. doi: 10.1002/wnan.1527
- Qin, X. C., Guo, Z. Y., Liu, Z. M., Zhang, W., Wan, M. M., and Yang, B. W. (2013). Folic acid-conjugated graphene oxide for cancer targeted chemo-photothermal therapy. *J. Photochem. Photobiol. B Biol.* 120, 156–62. doi: 10.1016/j.jphotobiol.2012.12.005
- Qiu, P., and Mao, C. (2011). Viscosity gradient as a novel mechanism for the centrifugation-based separation of nanoparticles. *Adv. Mater.* 23, 4880–5. doi: 10.1002/adma.201102636
- Rajakumar, G., Zhang, X. H., Gomathi, T., Wang, S. F., Ansari, M. A., Mydhili, G., et al. (2020). Current use of carbon-based materials for biomedical applications-A prospective and review. *Processes* 8:355. doi: 10.3390/pr8030355
- Rakhi, R. B. (2018). *Preparation and properties of manipulated carbon nanotube composites and applications*. In: *Nanocarbon and its Composites: Preparation*. Netherlands: Elsevier.
- Rong, P., Wu, J., Liu, Z., Ma, X., Yu, L., Zhou, K., et al. (2016). Fluorescence dye loaded nano-graphene for multimodal imaging guided photothermal therapy. *RSC Adv.* 6, 1894–1901. doi: 10.1039/c5ra24752g
- Rosillo-Lopez, M., and Salzmänn, C. G. (2016). A simple and mild chemical oxidation route to high-purity nano-graphene oxide. *Carbon N Y* 106, 56–63. doi: 10.1016/j.carbon.2016.05.022
- Sakudo, A. (2016). Near-infrared spectroscopy for medical applications: Current status and future perspectives. *Clin. Chim. Acta.* 455, 181–8. doi: 10.1016/j.cca.2016.02.009
- Salatin, S., Maleki Dizaj, S., and Yari Khosroushahi, A. (2015). Effect of the surface modification, size, and shape on cellular uptake of nanoparticles. *Cell Biol. Int.* 39, 881–90. doi: 10.1002/cbin.10459
- Sanchez, V. C., Jachak, A., Hurt, R. H., and Kane, A. B. (2012). Biological interactions of graphene-family nanomaterials: An interdisciplinary review. *Chem. Res. Toxicol.* 13, 15–34. doi: 10.1021/tx200339h
- Shamaila, S., Sajjad, A. K. L., and Iqbal, A. (2016). Modifications in development of graphene oxide synthetic routes. *Chem. Engin. J.* 294, 458–477. doi: 10.1016/j.cej.2016.02.109
- Shen, J., Hu, Y., Shi, M., Lu, X., Qin, C., Li, C., et al. (2009). Fast and facile preparation of graphene oxide and reduced graphene oxide nanoplatelets. *Chem. Mater.* 15:21.
- Shen, S., Wang, J., Wu, Z., Du, Z., Tang, Z., and Yang, J. (2020). Graphene quantum dots with high yield and high quality synthesized from low cost precursor of aphanitic graphite. *Nanomaterials* 10:375. doi: 10.3390/nano10020375
- Singh, D. P., Herrera, C. E., Singh, B., Singh, S., Singh, R. K., and Kumar, R. (2018). Graphene oxide: An efficient material and recent approach for biotechnological and biomedical applications. *Mater. Sci. Engin. C* 86, 173–197. doi: 10.1016/j.msec.2018.01.004
- Singh, S. K., Singh, M. K., Kulkarni, P. P., Sonkar, V. K., Grácio, J. J. A., and Dash, D. (2012). Amine-modified graphene: Thrombo-protective safer alternative to graphene oxide for biomedical applications. *ACS Nano* 3:1966. doi: 10.1021/nn5000578
- Singh, S. K., Singh, M. K., Nayak, M. K., Kumari, S., Shrivastava, S., Grácio, J. J. A., et al. (2011). Thrombus inducing property of atomically thin graphene oxide sheets. *ACS Nano* 5, 4987–96. doi: 10.1021/nn201092p
- Sofer, Z., Luxa, J., and Jankovský, O. (2016). Sedmidubský D, Bystroň T, Pumera M. Synthesis of Graphene Oxide by Oxidation of Graphite with Ferrate(VI) Compounds: Myth or Reality? *Angew. Chem. Int. Ed.* 55, 11965–9. doi: 10.1002/anie.201603496
- Srinivasan, M., Rajabi, M., and Mousa, S. A. (2016). Nanobiomaterials in cancer therapy. *Nanobiomater. Cancer Ther.* 7, 57–89. doi: 10.1016/b978-0-323-42863-7.00003-7
- Stankovich, S., Dikin, D. A., Piner, R. D., Kohlhaas, K. A., Kleinhammes, A., Jia, Y., et al. (2007). Synthesis of graphene-based nanosheets via chemical reduction of exfoliated graphite oxide. *Carbon N Y* 45, 1558–1565. doi: 10.1016/j.carbon.2007.02.034
- Staudenmaier, L. (1899). Procedure for the preparation of graphitic acid. *Ber. Dtsch. Chem. Ges.* 32:1394.
- Subrahmanyam, K. S., Panchakarla, L. S., Govindaraj, A., and Rao, C. N. R. (2009). Simple method of preparing graphene flakes by an arc-discharge method. *J. Phys. Chem. C* 113, 4257–4259. doi: 10.1021/jp900791y
- Suk, J. S., Xu, Q., Kim, N., Hanes, J., and Ensign, L. M. (2016). PEGylation as a strategy for improving nanoparticle-based drug and gene delivery. *Adv. Drug Deliv. Rev.* 99, 28–51. doi: 10.1016/j.addr.2015.09.012
- Sun, T., Zhang, Y. S., Pang, B., Hyun, D. C., Yang, M., and Xia, Y. (2014). Engineered nanoparticles for drug delivery in cancer therapy. *Angew Chem. Int. Ed.* 53, 12320–12364.
- Sun, X., Liu, Z., Welscher, K., Robinson, J. T., Goodwin, A., Zaric, S., et al. (2008). Nano-graphene oxide for cellular imaging and drug delivery. *Nano. Res.* 1, 203–212. doi: 10.1007/s12274-008-8021-8
- Sun, X., Luo, D., Liu, J., and Evans, D. G. (2010). Monodisperse chemically modified graphene obtained by density gradient ultracentrifugal rate separation. *ACS Nano* 6, 3381–3389. doi: 10.1021/nn1000386
- Suryanto. (2017). *Nanotechnologies-Vocabulary-Part 13: Graphene and Related Two-Dimensional (2D) Materials*. Geneva: ISO.
- Sydlik, S. A., and Swager, T. M. (2013). Functional graphenic materials via a Johnson-Claissen rearrangement. *Adv. Funct. Mater.* 23, 1873–1882. doi: 10.1002/adfm.201201954
- Szakács, G., Paterson, J. K., Ludwig, J. A., Booth-Genthe, C., and Gottesman, M. M. (2006). Targeting multidrug resistance in cancer. *Nat. Rev. Drug Discov.* 5, 219–34.
- Tan, C., Cao, X., Wu, X. J., He, Q., Yang, J., Zhang, X., et al. (2017). Recent Advances in Ultrathin Two-Dimensional Nanomaterials. *Chem. Rev.* 117, 6225–6331. doi: 10.1021/acs.chemrev.6b00558
- Thrall, J. H. (2004). Nanotechnology and medicine. *Radiology* 230, 315–318.
- Tiwari, H., Karki, N., Pal, M., Basak, S., Verma, R. K., Bal, R., et al. (2019). Functionalized graphene oxide as a nanocarrier for dual drug delivery applications: The synergistic effect of quercetin and gefitinib against ovarian cancer cells. *Coll. Surf. B Biointerf.* 178, 452–459. doi: 10.1016/j.colsurfb.2019.03.037
- Tomida, A., and Tsuruo, T. (2002). Drug resistance pathways as targets. *Anticancer Drug Dev.* 2002, 77–90. doi: 10.1016/b978-012072651-6/50006-1
- Torre, L. A., Bray, F., Siegel, R. L., Ferlay, J., Lortet-Tieulent, J., and Jemal, A. (2015). Global cancer statistics, 2012. *CA Cancer J. Clin.* 65, 87–108. doi: 10.3322/caac.21262
- Ullah, M., Ali, M., and Hamid, S. (2014). Structure-controlled Nanomaterial Synthesis using Surfactant-assisted Ball Milling- A Review. *Curr. Nanosci.* 10, 344–354. doi: 10.2174/15734137113096660114
- Ventola, C. L. (2017). Progress in nanomedicine: approved and investigational nanodrugs. *Pharm. Ther.* 42:742.
- Vijayakameswara Rao, N., Ko, H., Lee, J., and Park, J. H. (2018). Recent progress and advances in stimuli-responsive polymers for cancer therapy. *Front. Bioengin. Biotechnol.* 6:110.
- Wang, K., Ruan, J., Song, H., Zhang, J., Wo, Y., Guo, S., et al. (2011). Biocompatibility of Graphene Oxide. *Nanoscale Res. Lett.* 6:8.
- Wang, W. L., Meng, S., and Kaxiras, E. (2008). Graphene NanoFlakes with large spin. *Nano. Lett.* 8, 766–766. doi: 10.1021/nl073364z
- Wang, X., Bai, H., and Shi, G. (2011). Size fractionation of graphene oxide sheets by pH-assisted selective sedimentation. *J. Am. Chem. Soc.* 133, 6338–42. doi: 10.1021/ja200218y

- Wang, Y. W., Fu, Y. Y., Peng, Q., Guo, S. S., Liu, G., and Li, J. (2013). Dye-enhanced graphene oxide for photothermal therapy and photoacoustic imaging. *J. Mater. Chem. B* 1:42.
- Wei, L., Lee, C. W., Li, L. J., Sudibya, H. G., Wang, B., and Chen, L. Q. (2008). Assessment of (n,m) selectively enriched small diameter single-walled carbon nanotubes by density differentiation from cobalt-incorporated MCM-41 for macroelectronics. *Chem. Mater.* 20:24.
- Weissleder, R. (2001). A clearer vision for in vivo imaging. *Nat. Biotechnol.* 19, 316–7. doi: 10.1038/86684
- Wen, H., Dong, C., Dong, H., Shen, A., Xia, W., Cai, X., et al. (2012). Engineered redox-responsive PEG detachment mechanism in PEGylated nano-graphene oxide for intracellular drug delivery. *Small* 8, 760–9. doi: 10.1002/sml.201101613
- Wojtoniszak, M., Urbas, K., Peruzińska, M., Kurzawski, M., Drożdżik, M., and Mijowska, E. (2013). Covalent conjugation of graphene oxide with methotrexate and its antitumor activity. *Chem. Phys. Lett.* 151, 568–569.
- Wu, H., Shi, H., Wang, Y., Jia, X., Tang, C., Zhang, J., et al. (2014). Hyaluronic acid conjugated graphene oxide for targeted drug delivery. *Carbon N Y* 69, 379–389. doi: 10.1016/j.carbon.2013.12.039
- Yan, X., Hu, H., Lin, J., Jin, A. J., Niu, G., Zhang, S., et al. (2015). Optical and photoacoustic dual-modality imaging guided synergistic photodynamic/photothermal therapies. *Nanoscale* 6:7.
- Yang, K., Feng, L., Shi, X., and Liu, Z. (2013). Nano-graphene in biomedicine: Theranostic applications. *Chem. Soc. Rev.* 42, 530–47. doi: 10.1039/c2cs35342c
- Yang, K., Zhang, S., Zhang, G., Sun, X., Lee, S. T., and Liu, Z. (2010). Graphene in mice: Ultrahigh in vivo tumor uptake and efficient photothermal therapy. *Nano Lett.* 10, 3318–23. doi: 10.1021/nl100996u
- Yang, X., Skrabalak, S. E., Li, Z. Y., Xia, Y., and Wang, L. V. (2007). Photoacoustic tomography of a rat cerebral cortex in vivo with Au nanocages as an optical contrast agent. *Nano Lett.* 7, 3798–802. doi: 10.1021/nl072349r
- Yu, D., Yang, Y., Durstock, M., Baek, J. B., and Dai, L. (2010). Soluble P3HT-grafted graphene for efficient bilayer-heterojunction photovoltaic devices. *ACS Nano* 4, 5633–40. doi: 10.1021/nn101671t
- Yue, H., Wei, W., Yue, Z., Wang, B., Luo, N., Gao, Y., et al. (2012). The role of the lateral dimension of graphene oxide in the regulation of cellular responses. *Biomaterials* 33, 013–21.
- Zhang, H., Li, Y., Pan, Z., Chen, Y., Fan, Z., Tian, H., et al. (2019). Multifunctional Nanosystem Based on Graphene Oxide for Synergistic Multistage Tumor-Targeting and Combined Chemo-Photothermal Therapy. *Mol. Pharm.* 5, 1982–1998. doi: 10.1021/acs.molpharmaceut.8b01335
- Zhang, H., Peng, C., Yang, J., Lv, M., Liu, R., He, D., et al. (2013). Uniform ultrasmall graphene oxide nanosheets with low cytotoxicity and high cellular uptake. *ACS Appl. Mater. Interf.* 13, 1761–7. doi: 10.1021/am303005j
- Zhang, J., Chen, L., Shen, B., Chen, L., Mo, J., and Feng, J. (2019). Dual-Sensitive Graphene Oxide Loaded with Proapoptotic Peptides and Anticancer Drugs for Cancer Synergistic Therapy. *Langmuir* 65, 6120–6128. doi: 10.1021/acs.langmuir.9b00611
- Zhang, L., Liang, J., Huang, Y., Ma, Y., Wang, Y., and Chen, Y. (2009). Size-controlled synthesis of graphene oxide sheets on a large scale using chemical exfoliation. *Carbon* 47, 3365–3368. doi: 10.1016/j.carbon.2009.07.045
- Zhang, L., Xia, J., Zhao, Q., Liu, L., and Zhang, Z. (2010). Functional graphene oxide as a nanocarrier for controlled loading and targeted delivery of mixed anticancer drugs. *Small* 6, 537–44. doi: 10.1002/sml.200901680
- Zhang, W., Guo, Z., Huang, D., Liu, Z., Guo, X., and Zhong, H. (2011). Synergistic effect of chemo-photothermal therapy using PEGylated graphene oxide. *Biomaterials* 32, 8555–61. doi: 10.1016/j.biomaterials.2011.07.071
- Zhang, W., Zou, X., Li, H., Hou, J., Zhao, J., Lan, J., et al. (2015). Size fractionation of graphene oxide sheets by the polar solvent-selective natural deposition method. *RSC Adv.* 5, 146–152. doi: 10.1039/c4ra08516g
- Zhang, X., Huang, Y., Wang, Y., Ma, Y., Liu, Z., and Chen, Y. (2009). Synthesis and characterization of a graphene-C60 hybrid material. *Carbon* 47, 334–337. doi: 10.1016/j.carbon.2008.10.018
- Zhang, X., Yin, J., Peng, C., Hu, W., Zhu, Z., Li, W., et al. (2011). Distribution and biocompatibility studies of graphene oxide in mice after intravenous administration. *Carbon N Y* 49, 986–995. doi: 10.1016/j.carbon.2010.11.005
- Zhang, Y., Nayak, T. R., Hong, H., and Cai, W. (2012). Graphene: A versatile nanoplatform for biomedical applications. *Nanoscale* 4, 3833–3842. doi: 10.1039/c2nr31040f
- Zhao, C. Y., Cheng, R., Yang, Z., and Tian, Z. M. (2018). Nanotechnology for cancer therapy based on chemotherapy. *Molecules* 23:826. doi: 10.3390/molecules23040826
- Zhao, X., Liu, L., Li, X., Zeng, J., Jia, X., and Liu, P. (2014). Biocompatible graphene oxide nanoparticle-based drug delivery platform for tumor microenvironment-responsive triggered release of doxorubicin. *Langmuir* 30, 10419–29. doi: 10.1021/la502952f
- Zhao, X., Yang, L., Li, X., Jia, X., Liu, L., and Zeng, J. (2015). Functionalized graphene oxide nanoparticles for cancer cell-specific delivery of antitumor drug. *Bioconjug. Chem.* 26, 128–36. doi: 10.1021/bc5005137
- Zhou, B., Huang, Y., Yang, F., Zheng, W., and Chen, T. (2016). Dual-Functional Nanographene Oxide as Cancer-Targeted Drug-Delivery System to Selectively Induce Cancer-Cell Apoptosis. *Chem. Asian J.* 11, 1008–19. doi: 10.1002/asia.201501277
- Zhou, L., Jiang, H., Wei, S., Ge, X., Zhou, J., and Shen, J. (2012). High-efficiency loading of hypocrelin B on graphene oxide for photodynamic therapy. *Carbon N Y* 50, 5594–5604. doi: 10.1016/j.carbon.2012.08.013
- Zhou, L., Zhou, L., Wei, S., Ge, X., Zhou, J., Jiang, H., et al. (2014). Combination of chemotherapy and photodynamic therapy using graphene oxide as drug delivery system. *J. Photochem. Photobiol. B Biol.* 135, 7–16. doi: 10.1016/j.jphotobiol.2014.04.010
- Zhou, T., Zhou, X., and Xing, D. (2014). Controlled release of doxorubicin from graphene oxide based charge-reversal nanocarrier. *Biomaterials* 13:35.

**Conflict of Interest:** The authors declare that the research was conducted in the absence of any commercial or financial relationships that could be construed as a potential conflict of interest.

Copyright © 2020 Tufano, Vecchione and Netti. This is an open-access article distributed under the terms of the Creative Commons Attribution License (CC BY). The use, distribution or reproduction in other forums is permitted, provided the original author(s) and the copyright owner(s) are credited and that the original publication in this journal is cited, in accordance with accepted academic practice. No use, distribution or reproduction is permitted which does not comply with these terms.



# A Review: Electrode and Packaging Materials for Neurophysiology Recording Implants

Weiyang Yang, Yan Gong and Wen Li\*

Microtechnology Lab, Department of Electrical and Computer Engineering, Michigan State University, East Lansing, MI, United States

## OPEN ACCESS

### Edited by:

Elisa Castagnola,  
University of Pittsburgh, United States

### Reviewed by:

Juan Aceros,  
University of North Florida,  
United States  
Lan Yin,  
Tsinghua University, China  
Davide Polese,  
Istituto per la Microelettronica e  
Microsistemi, Italy

### \*Correspondence:

Wen Li  
wenli@msu.edu

### Specialty section:

This article was submitted to  
Biomaterials,  
a section of the journal  
Frontiers in Bioengineering and  
Biotechnology

**Received:** 29 October 2020

**Accepted:** 10 December 2020

**Published:** 14 January 2021

### Citation:

Yang W, Gong Y and Li W (2021) A  
Review: Electrode and Packaging  
Materials for Neurophysiology  
Recording Implants.  
Front. Bioeng. Biotechnol. 8:622923.  
doi: 10.3389/fbioe.2020.622923

To date, a wide variety of neural tissue implants have been developed for neurophysiology recording from living tissues. An ideal neural implant should minimize the damage to the tissue and perform reliably and accurately for long periods of time. Therefore, the materials utilized to fabricate the neural recording implants become a critical factor. The materials of these devices could be classified into two broad categories: electrode materials as well as packaging and substrate materials. In this review, inorganic (metals and semiconductors), organic (conducting polymers), and carbon-based (graphene and carbon nanostructures) electrode materials are reviewed individually in terms of various neural recording devices that are reported in recent years. Properties of these materials, including electrical properties, mechanical properties, stability, biodegradability/bioresorbability, biocompatibility, and optical properties, and their critical importance to neural recording quality and device capabilities, are discussed. For the packaging and substrate materials, different material properties are desired for the chronic implantation of devices in the complex environment of the body, such as biocompatibility and moisture and gas hermeticity. This review summarizes common solid and soft packaging materials used in a variety of neural interface electrode designs, as well as their packaging performances. Besides, several biopolymers typically applied over the electrode package to reinforce the mechanical rigidity of devices during insertion, or to reduce the immune response and inflammation at the device-tissue interfaces are highlighted. Finally, a benchmark analysis of the discussed materials and an outlook of the future research trends are concluded.

**Keywords:** neurophysiology, implantable, microelectrodes, organic, inorganic, packaging, materials

## INTRODUCTION

Neurological disorders and diseases in the central and peripheral nervous systems, such as Parkinson's disease, Alzheimer's disease, and epilepsy, are affecting hundreds of millions of people worldwide (Siuly and Zhang, 2016; Feigin et al., 2019; Wijeratne et al., 2020). Neurophysiology recording electrodes act as a seamless interface between the nervous system and the outside world and help diagnose these neurological diseases. Several types of neural signals could be measured from the brain using electrodes (Hashemi Noshahr et al., 2020), including electroencephalogram (EEG) (10–400  $\mu$ Vpp; 1 mHz–200 Hz) (Acharya et al., 2019), electrocorticogram (ECoG) (10–1,000  $\mu$ Vpp; 1 mHz–200 Hz) (Thukral et al., 2018; Kanth and Ray, 2020), in addition to local

field potentials (LFPs) (0.5–5 mVpp; 1 mHz–200 Hz) and action potential spikes (50–500  $\mu$ Vpp for extracellular; 10–70 mVpp for intracellular; 100 Hz–10 kHz) (Herreras, 2016; Chen et al., 2017a). EEG is noninvasive but suffers from low spatial resolution and poor signal-to-noise ratio (SNR) because of signal attenuation through the scalp and skull. Mechanical disturbances and electromyographic activities also incur the artifacts that further influence the spatial and temporal resolutions of EEG recording (Jiang et al., 2019). Unlike EEG, ECoG directly measures the signals from the cerebral cortex via neurophysiological implants without any internal and external source noises due to the scalp and skull, leading to lower tissue interference, greater precision, higher sensitivity, and reduced noise interference. Although some special ECoG arrays, such as “NeuroGrid,” have been proved to be capable of recording spike activity and LFPs (Khodagholy et al., 2015), almost ECoG can only gather the electrophysiological signals from the superficial surface of the cerebral cortex and is incapable of capturing spikes from individual neurons. Therefore, penetrating electrodes suitable for recording LFPs and action potentials with high spatiotemporal resolution have been widely used in the neuroscience community (Hong and Lieber, 2019). Despite recent advances in electrode technologies, all existing electrode implants are still suffering from poor long-term stability and crosstalk, due to long-standing challenges such as material biocompatibility, hermetic packaging, the relatively large physical dimensions of the devices, as well as mechanical mismatch between the brain tissue and the implant (Fattahi et al., 2014). Similarly to the central nervous system, for the peripheral nervous systems, surgically implanted neural electrodes could be categorized into regenerative electrodes, intra-fascicular electrodes, inter-fascicular electrodes, and extra-neural electrodes (Russell et al., 2019). These electrodes have more strict requirements for some material properties, such as flexibility and biocompatibility (Russell et al., 2019). Indeed, careful selection and design of electrode and packaging/substrate materials are significantly essential to improve the recording quality and long-term stability of the electrode implants. Therefore, to thoroughly study the electrical activity of neuronal circuits underlying various disorders, developing innovative neural recording devices have been long-standing interests of many scientists, intending to achieve the best combination of excellent electrical properties, high spatiotemporal precision, prominent biocompatibility, outstanding long-term stability, and safety of the electrode devices.

To date, many research efforts have been devoted to the design and fabrication of implantable neural recording electrodes with different materials on various substrates. The materials of these devices could be classified into two broad categories: electrode materials as well as packaging and substrate materials. While silicon-based materials, as well as common metallic materials (e.g., platinum or iridium) and their derivatives (e.g., platinum black and iridium oxide), are widely used in electrode manufacturing, they are still antagonistic to the soft, ionic, wet, and dynamic nature of the biological tissue, with their hard, electronic, dry, and static nature. Non-conventional conducting materials that were not initially developed for neural

implants have been receiving much attention and applied for neurophysiological recording in recent years because of their favorable properties and manufacturing advantages. Examples of these emerging electrode materials include graphene (Park et al., 2016; Kostarelos et al., 2017), indium tin oxide (ITO) (Aydin and Sezgintürk, 2017), carbon-polymer hybrid nanostructures (Guo et al., 2017; Saunier et al., 2020). In the search for suitable packaging and substrate materials, various types of glass and ceramic materials, such as alumina (Shen and Maharbiz, 2019), silicon nitride (Zhao et al., 2019), silicon carbide (SiC) (Lei et al., 2016), and silica (Cheng et al., 2013b), have greatly expanded the options for researchers. With the advancement of material synthesis technology, polymers have played an important role in medical device packaging. With their stable and unique physical properties, many polymeric materials, including SU-8 (Altuna et al., 2010), polyimide (Bakonyi et al., 2013), Parylene (Ceyssens and Puers, 2015), polydimethylsiloxane (PDMS), and liquid crystal polymers (LCPs) (Hwang et al., 2013), have been widely used as packaging materials for neural recording electrodes. The design consideration of neural stimulation electrodes is similar to that of neural recording electrodes, concerning biocompatibility, mechanical properties, electrical properties, and stability (Shepherd et al., 2018). For example, platinum black and Ir/IrOx are also widely used as stimulating electrodes (Zhang et al., 2015; Chen et al., 2019). Large charge storage capacity is specifically required for stimulating electrodes to achieve better stimulating performance (Hudak et al., 2017). Neural stimulators also have the same strict requirements on hermeticity, long-term stability, and biocompatibility of device package (Vanhoestenbergh and Donaldson, 2013; Donaldson and Brindley, 2016). Many materials that have been utilized in neural stimulating probes include but are not limited to: ceramics, glass, epoxy, silicone, and so on (Amanat et al., 2010; Vanhoestenbergh and Donaldson, 2013; Shepherd et al., 2018).

To draw a clear picture and guide the material design for future device development, this article reviews the current materials for the fabrication and packaging of neural recording implants that were reported in the literature in the most recent years. In the following sections, Section Key Challenges of Neural Implants discusses several important material properties, including electrical properties, mechanical properties, stability, biodegradability/bioresorbability, biocompatibility, and optical properties, as well as the critical impact of these properties on the performance of electrode implants. Section Key Material Characteristics provides a detailed discussion of various electrode materials in three different categories: inorganic materials (e.g., metals and semiconductors), organic materials [e.g., poly(3,4-ethylene dioxythiophene):poly(styrene sulfonate) (PEDOT:PSS) and poly(pyrrole) (PPy)], and carbon-based materials (e.g., graphene and carbon nanostructures). Approaches to improve the recording performance of the electrode materials are also reviewed. Next, Section Electrode Materials categorizes and introduces various solid and soft packaging materials, respectively. Also highlighted are the biopolymers for coating and surface functionalization to temporarily enhance the mechanical rigidity of the implants during insertion or to suppress the immune response and inflammation at device-tissue interfaces.



Finally, the conclusion and outlook in Section Packaging and Substrate Materials provides an insightful overview of the discussed electrode and packaging materials and put forward the future and potential research trends in the related fields.

## KEY CHALLENGES OF NEURAL IMPLANTS

### Tissue Responses

Before selecting candidate materials for neural electrode implants, it is essential to understand the biological response to foreign objects, e.g., neural implants. The inflammatory response is usually caused by tissue injured during the implantation surgery or the existence of the implants in the body. Inflammation achieves the purpose of containing, neutralizing, diluting, or isolating the harmful substances through a series of complex physiological reactions (Anderson, 2001). These inflammatory reactions will significantly affect the functionality and stability of implanted devices. First, acute inflammation will occur in the first few days of implantation. A large amount of blood will flow to the damaged tissue through the dilated blood vessels, and then a blood clot will be formed to close the wound (Anderson, 2001). Then the tissue fluid containing water, salt, and protein will form edema (Anderson, 1988). At this stage, the implants have to overcome the contamination of blood and tissue fluids that may cover the implants and cause device malfunction. Similarly, the extrusion and tissue deformation that may be caused by edema also require a certain strength of the inserted implant. This means that the electrode, package, or substrate materials must have a certain mechanical strength. The tissue environment is moist and chemically rich, which is not an ideal environment for implants (Shen and Maharbiz, 2020). Moreover, the immune response will release reactive oxidative species (ROS), which attack and degrade the implants (Patrick et al., 2011; Takmakov et al., 2015). With the continual presence of the implant, the inflammatory response will be transformed into chronic inflammation. A major feature in this phase is the regeneration of damaged epithelium and vascular tissue (Wahl et al., 1989; Fong et al., 1990; Pierce et al., 1991), which may encapsulate the implants and consequently degrade the recording stability and accuracy of the electrodes. The immune response of the tissue does not stop at this phase, so the implant still faces the attack of ROS. Once a foreign object is implanted into the body, a sequence of events (e.g., inflammation and foreign body response) occurs in the surrounding tissue and ultimately ends at the formation of foreign body giant cells at biotic-abiotic interfaces (Anderson et al., 2008). The intensity of the response is directly related to the properties of the implant (Anderson, 2001), such as size, shape, topography, and chemical and physical properties of the selected material. As the final stage of the inflammatory response, tissues try to wrap the implants with a vascular, collagenous fibrous capsule with a thickness of 50–200  $\mu\text{m}$  to isolate foreign objects (Ratner and Bryant, 2004). This fibrous wall will undoubtedly affect the electrical coupling between the implant and the targeted neurons, which may cause signal degradation and ultimately implant failure. The temporal variations of tissue

responses and stages of foreign body reaction are shown in Figures 1A,B.

### Surgical Challenges

Before the neurophysiology recording implants are surgically implanted into the body (Morales and Clément, 2018), sterilization is a significant and indispensable step to reduce the microbial contaminants (e.g., viruses) by six orders of magnitude (Stieglitz, 2010), and thereby reduce the intensity of inflammation. Various sterilization methods have been explored to suitably match various neurophysiology recording implants (Stieglitz, 2010). Nowadays, there are a great number of sterilization methods compliant with biomedical device regulation (Booth, 1998), including chemical sterilization (ethanol 70%), dry heating (160–190°C), autoclaving (120–135°C), ethylene oxide gas, hydrogen peroxide gas plasma, peracetic acid and UV radiation. Relatively required high temperatures in dry heat and autoclaving sterilization will accelerate the oxidation and corrosion speed of the electrode materials, and hence can destroy the functionality of the whole implants, especially for easily-oxidized materials, such as silver thin films and silver nanowires (Elechiguerra et al., 2005; Chu et al., 2019). For packaging materials, high temperature and liquid uptake are the main concerns during these sterilization procedures (Lecomte et al., 2018; Shen and Maharbiz, 2020). In particular for biodegradable packaging materials, dry heat and autoclaving sterilization may cause partial denaturation to collagen (Wiegand et al., 2009), morphology change to silk (Yucel et al., 2014), and melting and degradation to [poly(lactic-co-glycolic acid) PLGA] (Athanasίου et al., 1996). The sterilization process has less impact on synthetic polymer packaging materials than biodegradable materials, but it is still worthy of note. For instance, significant delamination of Parylene C encapsulation has been revealed after the steam sterilization process because of the insufficient adhesion strength between Parylene C and encapsulated device (Schander et al., 2016). In addition, because its glass transition temperature is around 90°C, high-temperature may cause degradation in the mechanical and optical properties of Parylene C. Ceramic materials have relatively broad options of sterilization methods due to their low water-vapor permeability and high-temperature resistance (Shen and Maharbiz, 2020). While ethylene oxide sterilization can be operated at relatively low temperatures, the permeability of polymers can allow liquid stored in the buck material and a degassing step is required (Shen and Maharbiz, 2020). In addition, ethylene oxide is a central nervous inhibitor, stimulant and protoplasmic toxin (Mendes et al., 2007). Improper exposure of neural implants to ethylene oxide can cause acute poisoning and chronic effects, such as severe headache, loss of consciousness, neurasthenic syndrome and dysfunction of the vegetative nerve with long-term light exposure (Golberg, 2018). Unlike ethylene oxide gas, hydrogen peroxide gas plasma has the benefit of non-toxic final decomposition products (McEvoy and Rowan, 2019). However, because of the oxidation reaction during the sterilization of hydrogen peroxide gas plasma (McEvoy and Rowan, 2019), selecting electrical

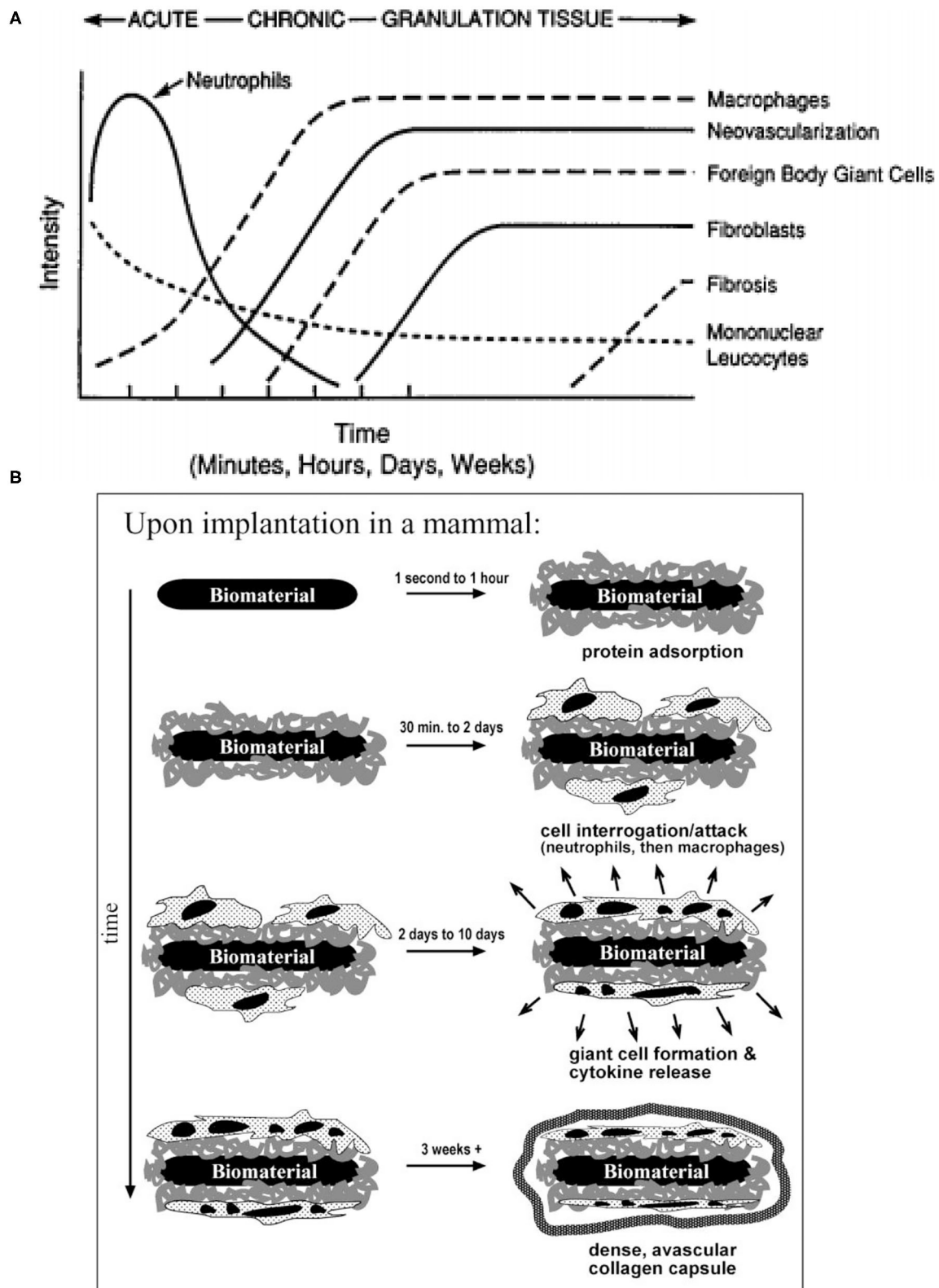


**FIGURE 1 |** Temporal variations and stages of tissue responses to neural implants. **(A)** The temporal variations in the acute inflammatory response, chronic inflammatory response, granulation tissue development, and foreign body reaction to implanted biomaterials (reprinted with permission from Anderson, 2001). **(B)** The different stages of foreign body reaction to an implanted neural implant (reprinted with permission from Ratner and Bryant, 2004).

materials should be more careful to avoid damages due to excessive oxidation.

## KEY MATERIAL CHARACTERISTICS

### Electrical Properties

For electrophysiology recording, the electrode/electrolyte boundary is comprised of electrochemical reactions (Faradic) and double-layer charging (capacitive) (Eles et al., 2018; Ferro and Melosh, 2018). Electrochemical impedance (typically at 1 kHz) is a critical factor in benchmarking the performance of the recording electrodes (Szostak et al., 2017). The targeted impedance range of microelectrodes is from  $\sim 0.1$  to  $2\text{ M}\Omega$  with the proper recording system utilization (Neto et al., 2018). Although some studies indicate the impedance does not have a major impact on the signal quality (Arcot Desai et al., 2010), most studies state that electrochemical impedance greatly affects the signal recording quality (Chung et al., 2015; Kozai et al., 2015; Zhao et al., 2016). The design of electrodes present tradeoffs in dimensions, electrochemical impedance, and background noise of recording. Miniaturized electrodes with diameters of 4 to  $100\text{ }\mu\text{m}$  allow for single-unit recording with high spatial resolution and minimal invasiveness, but at the expense of increased electrochemical impedance that could cause signal quality reduction and background Johnson noise increase. In particular, Johnson noise, also known as thermal noise, is proportional to the square root of the impedance of electrodes (Fang et al., 2015; Wang et al., 2018), as given by the following general equation:

$$V_{\text{noise}} = \sqrt{4kT\text{Re}\{Z\}\Delta F}$$

Where  $k$  is Boltzmann's constant,  $T$  is the temperature value,  $\text{Re}\{Z\}$  is the resistive component of the electrode impedance, and  $\Delta F$  is the frequency band (Stenger and McKenna, 1994). The most common solution to this challenge is to increase the effective surface area of microelectrodes by surface modification with electrically conducting polymers, nanomaterials, or nanostructures (Baranauskas et al., 2011; Xie et al., 2012), which will effectively reduce the impedance while keeping device dimensions at a cellular scale to achieve high recording resolution, as shown in **Figure 2A**. Conducting polymers (CPs), such as PPy and poly (3,4-ethylenedioxythiophene) (PEDOT), has also shown promise in improving ionic-to-electronic charges transfer at the interface between the tissue and the recording site (Bobacka et al., 2000; Cui et al., 2001), therefore increased charge capacity of microelectrodes. Insulation layer as a part of the recording system, once it has been damaged due to material degradation or insulation delamination (Beygi et al., 2019), the electrical properties of the entire system will also change. The delamination changes electrode electrical properties by expanding the geometric area of the exposed conductor, in turn, this averages the recorded potentials across an electrode surface area and attenuates the neural signal (Wellman et al., 2018). Besides, an increase in the surface area will cause abnormal impedance change of the electrode during long-term

implantation (Gong et al., 2020), which will further deteriorate the recording quality (Prasad et al., 2012).

### Biocompatibility

The biocompatibility of a recording electrode implant depends on various factors, including electrode materials, device geometry, and surrounding environments. From the material standpoint, biocompatibility can be defined as the "ability of a material to perform an appropriate host response in a specific application" (Williams, 1986). An ideal biomaterial for neural recording implants should be non-cytotoxic *in vivo* and release no substances or substances at only low, non-toxic concentrations. The tissue should produce minimal glial encapsulation surrounding the implant and only mild foreign body reaction without evidence of necrosis or implant rejection (Navarro et al., 2005; Márton et al., 2020), as shown in **Figure 2B**. Evaluation of material/device biocompatibility is critical and may include the tests of cytotoxicity, acute/chronic systemic toxicity, sub-acute/sub-chronic toxicity, sensitization, irritation, genotoxicity, hemocompatibility, toxicokinetic studies, and immunotoxicology (Feron et al., 2018). Since the same material may respond differently to different biological environments, the International Organization of Standard (ISO) enacts various test and evaluation protocols to evaluate the materials' biocompatibility, considering various body contact types, contact time, environments of intended use (*in vitro*, *ex vivo*, or *in vivo*), and test methods as mentioned in Hanson et al. (1996) and Frederick (2007).

### Stability

Material stability is another important consideration of neural recording implants (Tang et al., 2008; Lago and Cester, 2017; Li et al., 2018a; Chiang et al., 2020). The fabrication imperfection of the electrode or the packaging materials, such as unavoidable pinholes and defects, could cause the oxidation and delamination of the materials, and hence, shorten the longevity of the implants in liquid environments with a high concentration of ions, such as cerebrospinal fluid (Porrizzo et al., 2014; Chen et al., 2017b). The heterogeneous junction where an electrode interfaces with an adhesion-promoting layer (e.g., Ti or Cr) or the heterogeneous alloys is also a potential risk of electrode reliability. The two different metals can form a short circuit galvanic cell in the tissue fluid that accelerates the corrosion of one of the metals and weakens the metal-to-metal bonding strength (McFadden, 1969). Therefore, higher atomic weight transition metals with high corrosion resistance, such as platinum and iridium, were selected as the primary electrode materials (Cogan et al., 2005; Rodger et al., 2008; Patrick et al., 2011). Homogenous alloys with multiple metal elements can also improve corrosion resistance (Wellman et al., 2018). Surface modification of electrodes with electrodeposited CPs is another method to slow down metal corrosion and improve device stability (Pranti et al., 2017; Dijk et al., 2020). For example, electrodeposited PEDOT is quite chemically stable in the damp, oxygen-rich environments because PEDOT can be further polymerized by the oxygen and protect the metal electrodes from direct exposure to reactive, oxygenated





solution (Halliwell, 1992), and therefore, prevent the metals from corrosion (De Vittorio et al., 2014; Yang et al., 2019a). However, further polymerization could cause the increased electrochemical impedance of the whole electrodes due to cracking or delamination of the PEDOT layer (Kozai et al., 2014; Wellman et al., 2018).

Biofouling also contributes to the instability of the neurophysiological recording implants. Biofouling leads to the encapsulation of protein and glial cells on electrodes, especially on those with high electrochemical surface areas, and therefore, restricts ionic diffusion at the electrode-electrolyte interface (Seymour and Kipke, 2007; Du et al.,



2015). In addition, the tissue response persistently promotes the degradation of electrode materials and insulation. To minimize electrode biofouling, significant efforts have been made on surface modification or functionalization to alter the chemical terminations, morphology, and wettability of the electrode surface (Wellman et al., 2018). Several hydrogel and polymer coatings, such as polyethylene glycol (PEG) and PEG methacrylate (PEGMA), have been utilized to improve the hydrophilicity of the electrode surface (Justin and Guiseppi-Elie, 2010; Heo et al., 2012; Cheng et al., 2013a). With large amounts of water in their structures, these materials are highly hydrated to increase the energetic penalty of removing water for protein and microorganism attachment. Engineered antifouling electrode materials, such as  $sp^3$  carbon-enriched, boron-doped polycrystalline diamond (BDD), also show the advantages of improved biocompatibility and reduced biofouling compared to conventional electrode materials (Meijs et al., 2016; Fan et al., 2020), as shown in **Figure 2C**. Moreover, nanostructured surfaces with low friction and low surface energies can effectively decrease cell attachment onto the implant surface, and hence, reduce the possibility of biofouling formation (Chapman et al., 2017; Boehler et al., 2020).

### Biodegradability/Bioresorbability

In contrast to stability, biodegradability is another prevailing topic that has been extensively studied in neural implants (Thukral et al., 2018). Unlike the aim of the stability to keep the implant devices *in vivo* for long-term detection, biodegradability requires the implants to be biodegradable and bioresorbable after a certain period (days to weeks) in order to avoid secondary damage to surrounding tissues during implant removal (Won et al., 2018). Some inorganic materials, including metals [e.g., gold nanoparticles (GNPs)], semiconductors [e.g., silicon nanomembranes (Si NMs)], and dielectrics [e.g., silicon dioxide ( $SiO_2$ )], have shown outstanding degradation behavior (Kang et al., 2016; Lu et al., 2018). Combining those materials with biodegradable organic materials enables high-performance and less-invasive implantable devices (Li et al., 2018b). Despite studies on biodegradable bulk materials, recently, special attention has been paid to engineering multi-functional thin-film materials that combine degradability with other desired properties (electrical, optical, mechanical) and can be dissolved in the phosphate-buffered saline (PBS) in 30 days (Wu et al., 2014; Xue et al., 2018; Xu et al., 2019), as shown in **Figure 2D**. However, the biodegradation performance of most thin-film degradable materials has only been tested in de-ionized (DI) water or saline solution (0.9% NaCl) (Lewitus et al., 2010, 2011). Since the *in vivo* environments are much more complicated than the *in vitro* environments due to the presence of biological molecules, such as proteins and cells, *in vivo* evaluation of these materials must be conducted to understand better their degradation rate and safety in living tissues (Lecomte et al., 2017; Lee et al., 2017b).

### Mechanical Properties

Mechanical properties of the neural implants are extremely important for *in vivo* applications. The Young's moduli of traditional solid materials (silicon, glass, and metal) range from

50 to 200 GPa, orders of magnitude higher than those of the nervous tissues that are typically 3.15–10 kPa (Patil and Thakor, 2016). The mechanical property mismatch between the soft tissue and the stiff implants induces reoccurring electrode movement from the target neurons in response to natural body motions (Gilletti and Muthuswamy, 2006), resulting in unreliable recording from the same neurons for an extended period. In the long term, the presence of stiff implants elicits the effect of tissue staining at the implant site due to inflammatory response, and consequently neuronal degeneration and glial scar formation near the electrodes that prohibit the transformation of neural signals (Fang et al., 2015; Lacour et al., 2016; Ferro and Melosh, 2018; Wang et al., 2018). Moreover, the stress induced by the micromotions of surrounding tissues can cause mechanical damage to the implants, such as cracks or delamination of the electrode materials, and then permanent device failure (Cogan et al., 2004; Marin and Fernández, 2010; Patil and Thakor, 2016). Compared to solid materials, soft materials, such as silicone, Parylene C (PA), SU-8, and polyimide (PI), with Young's moduli of 1–10 GPa, are more compliant with the soft tissue to form a conformal contact (Wang et al., 2012; Minev et al., 2015; Patil and Thakor, 2016), as shown in **Figure 2E**. PDMS can achieve even lower Young's modulus of 1 MPa, becoming one of the softest prevailing packaging and substrate materials for neural implants (Sun et al., 2004).

Besides the above materials with consistent mechanical properties, shape-memory materials can be deformed from the initial shape under external stimuli, such as temperature, humidity, etc. (Lee et al., 2016a). Before and during implantation, devices made of shape-memory materials are stiff enough to penetrate the target tissue (Beattie et al., 2000; Christensen et al., 2014). Once adapted to the physiological conditions, the implanted devices can be programmed to snake around and climb nerves (Moore, 2019). For example, Zhao et al. reported a 16-electrode microwire electrode arrays made of a shape memory metallic alloy (Zhao et al., 2018), nitinol, which an equiatomic alloy of nickel and titanium exhibiting shape memory effect due to thermally-induced phase transition (Lendlein and Kelch, 2002). The device can conform to the brain vasculature with minimized damage to the blood vessels during implantation. Shape-memory polymers (SMPs), such as thiol-ene/acrylate-based SMPs (Ecker et al., 2017; Black et al., 2018a), provide good elasticity and the diminished rigidity and mechanical mismatch with the soft tissue, suitable for use in manufacturing surgical devices and medical implants. The shape-memory effect of these materials is induced by the cross-links of polymeric chains and the corresponding external stress at the transition temperature (Lee et al., 2016a).

### Optical Transparency

Optical transparency of an electrode implant allows one to combine electrophysiological recording with other modalities, such as high-resolution optical imaging and optogenetics (Won et al., 2018). To date, high-resolution, systematic electrophysiological recording on optically scanned tissue surfaces of the brain has not been implemented, because conventional opaque electrode materials do not satisfy the

optical qualification of high-resolution imaging (Fekete and Pongrácz, 2017). Optogenetics applications also require high transmittance of the materials over a broad spectrum or under the specifically targeted wavelength for activating or inhibiting the genetically modified neurons with the minimum optical propagation loss (Thukral et al., 2018). With a unique combination of electrical conductivity, broadband transparency, and biocompatibility, several transparent conducting materials, such as ITO (**Figure 2F**), graphene, and PEDOT:PSS, have been explored as electrode materials (Park et al., 2018). These materials also provide sufficiently wide bandgaps to limit photoelectrochemical (PEC) artifacts that arise from photo illumination of electrodes during opto-stimulation and two-photon imaging (Castagnola et al., 2017; Kostarelos et al., 2017; Yang et al., 2017). In addition, Au nanomesh electrodes (Seo et al., 2017) or PEDOT:PSS-coated Au (Qiang et al., 2018) microelectrodes have been proven to achieve low electrochemical impedance and some degree of optical transparency, capable of electrophysiological recording in the brain. To realize fully transparent neural recording implants, polymers, such as polyethylene terephthalate (PET), PA, and PDMS, usually act as transparent substrate and encapsulation of the electrodes (Kim et al., 2017; Ren et al., 2018).

## ELECTRODE MATERIALS

### Inorganic Materials

Recently, much attention has been devoted to investigating innovative electrode materials to improve electrical, mechanical, and optical properties, as well as stability, biocompatibility, or biodegradability of recording electrodes (Fattahi et al., 2014). This section classifies the electrode materials into inorganic, organic, and carbon-based materials, and discusses the advantages, disadvantages, and applications of each specific material in detail.

#### Metals

Metals are the most prevailing and common electrode materials for neural recording for nearly 50 years (Kim et al., 2018). Widely used metal electrode materials, such as Au, platinum (Pt), iridium (Ir), tungsten (W), and tantalum (Ta), offer a great number of desirable properties, including chemical inertness, high electrical conductivity, and excellent biocompatibility in biological environments (Barrese et al., 2016; Won et al., 2018; Burton et al., 2020). Au/Pt and Ir/Pt have been used as the electrode materials for “Utah array” and “Michigan Probe,” two of the most popular neural interface electrodes (House et al., 2006; Kim et al., 2010a). However, these materials suffer from limited electrochemical conductivity and injection charge density, especially when the electrode is shrunk to a micrometer scale for better spatial resolution (Lee et al., 2016a).

To address the impedance-size trade-off in microelectrodes, three dimensional (3D) nanostructured Au microelectrodes have been developed wherein nanoporous structures were created on the microelectrode surface to achieve larger surface area and therefore lower impedance (Fairfield, 2018). The nanotopography of such nanoporous structures also improves

*in vivo* stability of electrode implants by reducing the incidence of glial scar encapsulation while maintaining high neuronal coverage. Surface modification with Au nanorods, nanoflakes, or nanopillars is another option to increase the effective recording area without change the overall electrode dimensions (Zhou et al., 2009; Kim et al., 2010b; Nick et al., 2014). For example, Nick et al. fabricated Au nanopillars on the microelectrodes, showing a reduction of 1 kHz impedance by up to 89.5 times and dramatic impedance decrease over 1 Hz to 100 kHz (Nick et al., 2014). With a determined diameter, a larger high-aspect ratio of the nanopillars results in lower impedance of the electrode. Similarly, Zhou et al. integrated an Au-nanorod array on flexible thin-film microelectrodes using locally patterned anodized porous alumina as a template (Zhou et al., 2009). The interface impedance of this 3D electrode was 25 times smaller than that of conventional two dimensional (2D) planar microelectrodes under the same dimensions. Moreover, 3D electrodes modified with Au nanoflakes have also been reported by Kim et al., demonstrating a maximum impedance reduction factor of 57.9 with an electrode diameter of 5  $\mu\text{m}$  (Kim et al., 2010b).

An alternative nanostructure for electrode surface modification is Pt black, a nanoparticulate-like Pt formed from electroplating. Zhang et al. show that, with Pt black, the 1 kHz impedance of a 100  $\mu\text{m}$  diameter electrode wire decreased from 16.6 to 3.5  $\text{k}\Omega$  and the charge injection limit increased from 0.286 to 1.906  $\text{mC}/\text{cm}^2$  (Zhang et al., 2015). Furthermore, alloys with two or more than two metals have been investigated for nanoparticle synthesis to improve the stability of metallic nanoparticles. One example is the bimetallic Au/Pt alloy nanoparticle modified Au microelectrode, which exhibits an average 1 kHz impedance of 0.23  $\text{M}\Omega$  with a recording site of 20  $\mu\text{m}$  diameter (Zhao et al., 2016), as shown in **Figure 3A**.

Ir/IrOx (iridium oxide) is another prevailing electrode material and often used in the format of either a bulky wire or a thin film coating (Zeng et al., 2017; Black et al., 2018b; Chen et al., 2019; Ghazavi et al., 2020). Ir wires are very stiff and highly resistant to corrosion (Loeb et al., 1995), whereas IrOx thin films are unstable and prone to degradation as electrode dimensions decrease and charge densities increase (Cogan et al., 2004). However, untreated Ir electrodes suffer from limited charge injection capacity. Ir alloys, such as PtIr, exhibit significantly improved mechanical and electrochemical properties (Wellman et al., 2018). Cassar et al. electrodeposited a PtIr coating (EPIC) on the tip of 75  $\mu\text{m}$ -diameter microwire electrodes, resulting in reduced electrochemical impedance from  $534 \pm 57 \text{ k}\Omega$  to  $80 \pm 18 \text{ k}\Omega$  and improved SNR (Cassar et al., 2019).

### Semiconductors

Semiconductors can be readily configured into various electronic elements (e.g., sensors, transistors, switches, etc.) with desired properties (e.g., signal transduction, amplification, multiplexing, etc.) to achieve a complex, integrated biointerface system (Maiolo et al., 2019; Zhang et al., 2020). Organic semiconductors provide unique advantages of mechanical compliance, biodegradability, and stretchability. Contrastly inorganic semiconductors are more rigid but provide faster response, higher sensitivity,

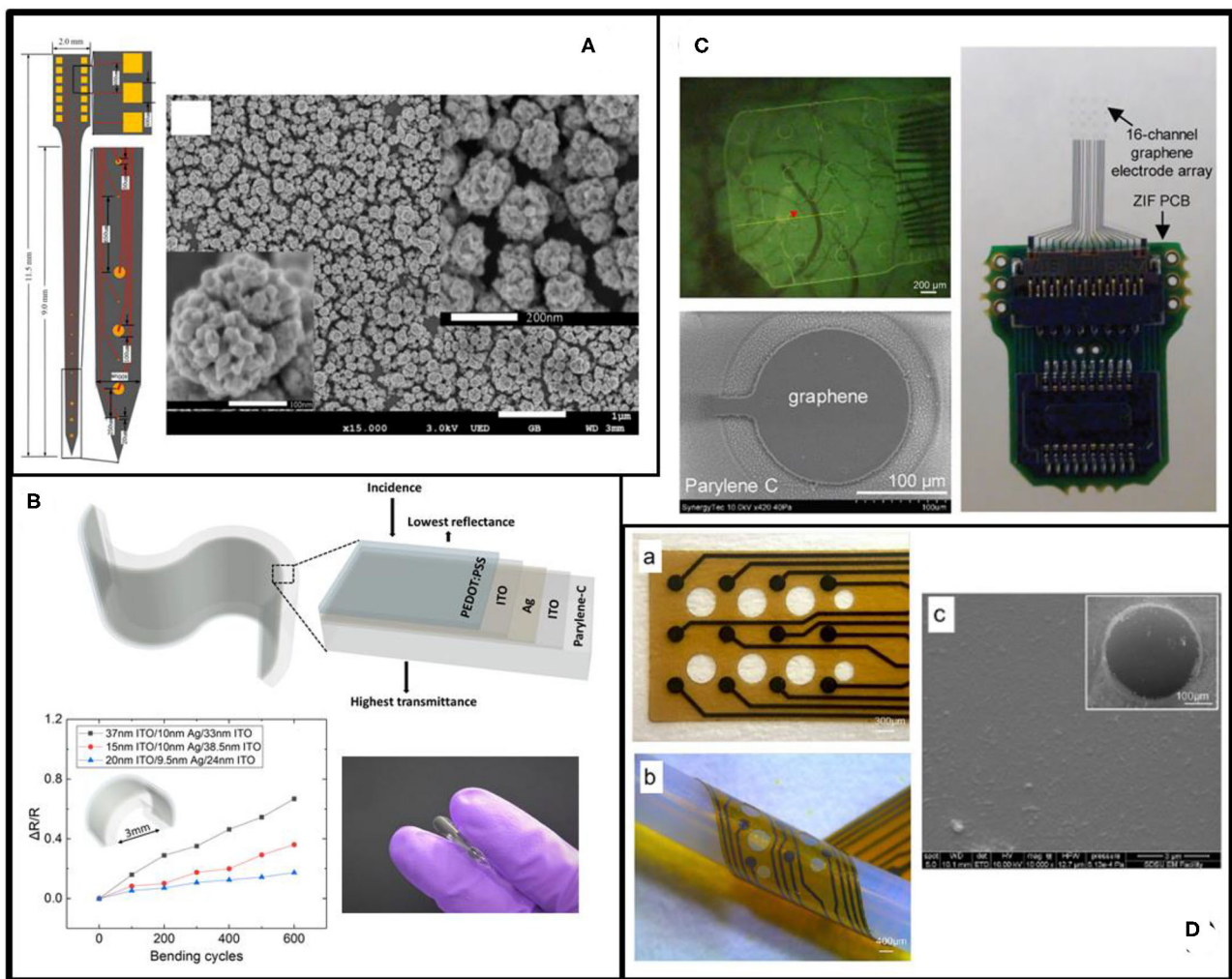


**FIGURE 3 |** Examples of electrode materials. **(A)** The electrodes of the neurophysiological implants (left) are made of Au/Pt alloy as indicated in the SEM image (right) (reprinted with permission from Zhao et al., 2016). **(B)** Flexible PEDOT:PSS-ITO-Ag-ITO thin films on Parylene C substrate (upper) for ECoG array to overcome the brittleness of a single layer of ITO. The lower left and lower right figures show the good bendability and flexibility of ITO-Ag-ITO structure, respectively (reprinted with permission from Yang et al., 2019b). **(C)** Transparent graphene as the electrode material (lower left) on the  $\mu$ ECoG array (right) for the neurophysiology signal recording and imaging (upper left) (reprinted with permission from Park et al., 2018). **(D)** Thin-film glassy carbon recording electrodes on flexible polyimide (left). The SEM image (right) shows the surface morphology of the glassy carbon (reprinted with permission from Vomero et al., 2017).

better accuracy, and lower power consumption of biological sensing than organic semiconductors because of high charge carrier mobilities in inorganic materials (Jiang and Tian, 2018). Moreover, advancement in modern semiconductor technologies allows precise batch fabrication of high-performance inorganic semiconductor devices in various architectures at submicron or even nanometer scale, matching the size of subcellular and molecular targets.

Silicon (Si) is the most commonly used semiconducting material in neurophysiological implants. The well-developed microfabrication and photolithography techniques for complementary metal-oxide-semiconductor (CMOS) integrated circuits enable the design and fabrication of high density, high-channel-count multielectrode arrays, capable of mapping activity

from large-scale neural networks with high spatiotemporal resolution (Hong and Lieber, 2019). As the current state of the art, the Neuropixel Si probe developed by Jun et al. integrates 960 recording sites (384 configurable recording channels) on a  $70 \times 20 \mu\text{m}$  shank, weighs only  $\sim 0.3 \text{ g}$ , and provides on-chip signal amplification and digitization (Jun et al., 2017). Each probe enables stable and chronic recordings from more than 100 neurons for over 150 days while remaining low noise (Jun et al., 2017).

With high sensitivity to changes in electrical potentials and surface charges, Si-based nanostructure materials are also used to make low impedance microelectrode interface for neurophysiology recording (Fairfield, 2018; Jiang and Tian, 2018). For example, Si nanowires have been utilized as low



impedance nanoelectrodes to intracellularly record action potential from cultured neurons at high precision (Robinson et al., 2012; Liu et al., 2017a). Besides, a forest of randomly oriented gold coated-Si nanowires has been proved to achieve the non-invasive extracellular recording of astrocytes by mimicking the properties of astrocytes *in vivo* (Saracino et al., 2020). Compared to bulky materials, improved stretchability and bendability can be achieved with Si nanowires. Similarly, an amorphous atomic structured Si material has been proposed to create mesostructures with fibrils and voids, with an average Young's modulus of 2–3 orders smaller than that of the single-crystalline Si (Jun et al., 2017). As key building blocks, nanowires can also be integrated with microporous gel-based scaffolds, yielding highly sensitive and flexible 3D neural probes for mapping the propagation of the action potential (Dai et al., 2016). These 3D electrodes offer excellent spatial resolution and stability with little immune response to chronic implantation. In addition, Si nanowires can be configured into field-effect transistors (FETs), capable of sensing neurophysiological signals at a faster switching speed. Unlike faradaic measurement of neural signals through electrodes, the charge carrier density of FETs can be modulated as a function of LFP in surrounding tissues, allowing spikes tracking along neurites and neural networks with single-cell resolution and reasonably high sensitivity (Hutzler et al., 2006; Patolsky et al., 2006; Veliev et al., 2017). Recently, Yu et al. reported a flexible and bioresorbable neural electrode array based on Si NMs (Yu et al., 2016). With biodegradable SiO<sub>2</sub> insulation and PLGA substrate, the whole device was able to degrade in PBS (pH = 10) within 15 days.

ITO is a well-known n-type semiconductor material that is often utilized in transparent microelectrodes. ITO has high conductivity, excellent transparency over the entire visible spectrum due to a large bandgap of around 4 eV, as well as confirmed biocompatibility (Falco et al., 2016). ITO can be grown on either solid or flexible substrates using well-developed physical vapor deposition techniques (e.g., sputtering). However, similar to metals, ITO electrodes suffer from increased electrochemical impedance when the electrode sizes decrease, leading to undesirable electrochemical reactions with the brain tissue and poor recording quality due to increased thermal noise and ion-based electric fluctuations of surrounding media (Yang et al., 2017). In addition, ITO is relatively brittle, making it unsuitable for use in large patterns (e.g., pads or interconnection wires) on flexible substrates (Kwon et al., 2013). Surface modification of ITO with conductive thin film coatings (e.g., PEDOT:PSS, Ag, Au) has been explored to address these shortcomings. Recently, Yang et al. reported an ultra-flexible, conductive, and transparent thin film using a PEDOT:PSS/ITO/Ag/ITO multilayer structure on PA, as shown in **Figure 3B**. The electrode showed at least 10× reduction in electrochemical impedance, ~7% transmittance improvement, and stability after over 600 cycles of mechanical bending (Yang et al., 2019b). Other semiconducting materials, such as germanium (Ge), silicon germanium alloy (SiGe), indium-doped zinc oxide (IZO), indium-gallium-zinc oxide (a-IGZO), and zinc oxide (ZnO), has also been investigated as recording electrode materials because of their desired electrical, mechanical, optical,

biocompatible, and stable/biodegradable properties (Gao et al., 2012; Dagdeviren et al., 2013; Lee et al., 2015; Gutierrez-Heredia et al., 2017; Mao et al., 2018; Huerta et al., 2019).

## Organic Materials

Given the same device dimensions, organic materials offer lower Young's moduli than inorganic materials, reducing potential adverse outcomes including inflammation response, glial scar encapsulation, unstable neural recording, and mechanical failure of implants (Lago and Cester, 2017). Organic materials also provide significant advantages of easily modifiable surface structures, mixed ionic and electronic charge transport, less biofouling/surface oxides, and the wide option of biocompatible materials (Feron et al., 2018).

## Conducting Polymer (CP)

CPs, as organic polymers, consist of monomeric compounds linked in chains of alternating single and double bonds, and doped with a stabilizing counter-ion. CPs have the mechanical properties matched with those of biological tissues. Because conjugated polymers have narrower band gaps, electrons can move easily between the conducting band and valence band. CPs can transduce ionic currents to electronic currents through redox reaction in bulk and volumetric charging, resulting in low impedance and high charge storage capacity (Green and Abidian, 2015; Rivnay et al., 2016). Due to the diversity and adaptability of synthetic processes, the ionic-electronic transport and biochemical surface characteristics are tunable for improving the performance and stability/biodegradation of CPs (Rivnay et al., 2017). Furthermore, dopants, such as small cations/anions (Na<sup>+</sup>, Cl<sup>-</sup>, and ClO<sub>4</sub><sup>-</sup>) and large polymeric species (polystyrene sulfonate and polyvinyl sulfonate), can be utilized to improve the electrical conductivity of organic materials by adding electrons to the conduction band (n-doping) or removing electrons from the valence band (p-doping) (Le et al., 2017).

PEDOT:PSS is a prevailing class of CPs for neural interfacing applications. PEDOT:PSS possesses many desirable properties, including high biostability, outstanding biocompatibility, and excellent electrochemical properties. Studies show that, with the same electrode area, the electrochemical impedance of microelectrodes is an order of magnitude lower than that of Pt microelectrodes (Ganji et al., 2017). Khodagholy et al. proposed a PEDOT:PSS-based, high-density NeuroGrid that consists of patterned PEDOT:PSS electrodes with the neuron-size density, capable of simultaneously recording LFPs and action potentials in anesthetized and awake human subjects (Khodagholy et al., 2015, 2016). The enhancement in electrochemical conductivity of PEDOT:PSS-coated electrodes can be attributed to the increased surface roughness of the electrode, as confirmed by Yang et al. (2017, 2019a). Their studies show that the average surface roughness (Ra) of the PEDOT:PSS coated electrode increased from 0.85 nm to 3.33 nm, resulting in dramatically improved charge storage capacity and impedance by several orders of magnitude. Similarly, Pranti et al. reported that electropolymerization of 1 μm thick PEDOT:PSS on chronic Au microelectrodes increased the electrode surface area, and the corresponding electrochemical impedance was reduced by



~99% (Pranti et al., 2018). Besides planar films, ordered PEDOT nanostructures can be self-assembled on the electrode surface with surfactant molecules as a template to further reduce the electrode impedance (Yang et al., 2005). Abidian et al. also reported that PEDOT-based nanotubes enable ~8 times lower impedance and much higher charge capacity density than planar PEDOT films, mostly due to the increased surface area (Abidian et al., 2010). PEDOT:PSS can be applied by spin-coating or ink-jet printing in a low-cost and rapid fashion, but at the expense of poor adhesion with underlying electrode materials. Electrodeposition techniques, such as electroplating, can improve the bonding strength at the PEDOT-electrode interface, preventing potential risk of PEDOT delamination in the biological environment (Abidian et al., 2010). A recent study by Boehlet et al. also demonstrates that pre-treating the smooth Pt electrode with porous Pt structures before the PEDOT deposition can enhance the adhesion between PEDOT and Pt. The PEDOT film deposited on the porous Pt substrate shows no delamination after more than 100 days in accelerated aging tests in PBS (Boehler et al., 2017).

Besides PEDOT, several other CPs, such as PPy, poly(aniline) (PANi), poly(thiophene) (PT), and some of their derivatives (Juarez-Hernandez et al., 2016; Kojabad et al., 2019; Nagane et al., 2020) are also alternative candidates. PPy has outstanding water solubility (Kojabad et al., 2019), 40–200 S/cm conductivity (Guimard et al., 2007), low Young's moduli of 0.35 psi for thin films (15–35  $\mu\text{m}$  thick) (Diaz and Hall, 1983), and 430–800 MPa for nanocomposites (Sevil and Zuhail, 2010). PPy can be electrodeposited *in situ* on the electrode surface with different dopants. PANi has an electrical conductivity of 5 S/cm (Guimard et al., 2007) and is primarily used as a coating material on electrodes instead of a standalone electrode material due to its relatively small Young's modulus (2–4 GPa) (Passeri et al., 2011). Nanostructured PANi can be synthesized by chemical oxidative or electrochemical polymerization in an aqueous solution that contains a variety of surfactants to precisely tailor the structure of the film at small length scales for increased effective surface area (Yang et al., 2005; Juarez-Hernandez et al., 2016). Functionalized PT copolymer, with precisely tunable electrical, optical, mechanical, and adhesive properties, is also applicable for neural recording electrodes (Nagane et al., 2020). For PT, the maximum conductivity is 10–100 S/cm, and Young's modulus of thin films is ~3 GPa (Wang and Feng, 2002).

## Carbon-Based Materials

Carbon-based materials, such as graphene, carbon nanofibers, carbon nanotubes, are another promising class of electrode materials. Carbon-based materials have high biocompatibility and valuable mechanical properties, such as high tensile strength, and can be prepared by various approaches, including chemical vapor deposition (CVD), electrospinning, and exfoliation.

### Graphene

Graphene, a 2D single-layer sheet of carbon atoms in a hexagonal arrangement, has a great number of outstanding properties: ~90% optical transmittance (Park et al., 2014), 76  $\Omega/\text{sheet}$  resistance (for a 4-layer structure), 200,000  $\text{cm}^2/\text{VS}$  electron

mobility (Bolotin et al., 2008), and  $\sim 5 \times 10^3$  W/mK thermal conductivity (Balandin et al., 2008; Wang et al., 2017; Armano and Agnello, 2019). The remarkable biocompatibility makes graphene an appropriate choice for neural interface applications (Park et al., 2016; Liu et al., 2017b; Thunemann et al., 2018). Moreover, the outstanding transparency of the graphene microelectrode enables simultaneous neurophysiological recording, light stimulation, and optical imaging of living tissues (Park et al., 2014). Despite many benefits, graphene has a large Young's modulus (~1.0 TPa) (Shin et al., 2012; Patil and Thakor, 2016) and a large impedance at the graphene-electrolyte interface, possibly due to the intrinsic hydrophobicity of graphene (Chen et al., 2013). The comparatively low double-layer capacitance of single- or few-layered graphene could cause considerable thermal noise and low SNR of neural recording. Therefore, it is critical to reduce the mechanical mismatch between graphene electrodes and surrounding tissues as well as to improve the electrical properties of hydrophobic graphene. Small area graphene can be prepared using mechanical exfoliation, which is tedious and time-consuming. CVD allows growing high-quality graphene over large areas at either high temperatures of over 1,000°C or on specific substrates in a specific gas mixture, but is incompatible with polymer materials (Kireev et al., 2016). Significant efforts have been made in recent years to transfer CVD graphene from rigid substrates onto soft substrates. For example, Park et al. transferred and stacked four graphene monolayers sequentially onto a flexible PA film (Park et al., 2014) as the electrode material. Later, the same group reported a transparent carbon-layered 16-channel array and succeeded in simultaneous *in vivo* recording of light-evoked neural signals in conjunction with fluorescence imaging (Park et al., 2018), as shown in **Figure 3C**. The photoelectrochemical effect (also known as Becquerel effect) of graphene is neglectable due to its metal-like zero band nature and relatively high work function (4.5 eV) (Park et al., 2016, 2018). Similarly, Chen et al. transferred graphene onto SU-8 and demonstrated that introducing hydroxyl groups on the graphene surface by a mild stream plasma treatment can effectively increase the water contact angle from  $91.1^\circ \pm 5.6^\circ$  to  $41^\circ \pm 4.7^\circ$  (Chen et al., 2013). The increase in graphene hydrophilicity leads to impedance reduction from 7,216 to 5,424  $\Omega/\text{mm}^2$  and SNR improvement from  $20.3 \pm 3.3$  dB to  $27.8 \pm 4.0$  dB. Besides electrode configurations, Kireev et al. developed graphene-based FETs on flexible polyimide-on-steel and found that the device did not show significant loss in recording capability after up to 1,000 cycles of mechanical bending (Kireev et al., 2016).

### Carbon Nanostructures

3D carbon nanostructures, such as carbon fibers (CFs) and carbon nanotubes (CNTs), can be utilized as a standalone electrode or as a surface coating to improve the surface area and electrochemical impedance (Kozai et al., 2012; Fattahi et al., 2014; Patel et al., 2016, 2017; Fairfield, 2018). Standalone carbon fiber microelectrodes (CFMEs) are typically constructed by insulating carbon nanofibers with pulled glass pipettes (Hejazi et al., 2020) or PA (Guitchounts et al., 2013; Patel et al., 2015; Deku et al., 2018; Gillis et al., 2018; Massey et al., 2019) followed by opening

the electrode tip with chemical etching, plasma removal, or laser cutting. Recently Patel et al. assembled 16 CFMEs to form a multichannel CFME array, capable of chronic recording of single unit activity for one month (Patel et al., 2015). Such CFMEs electrodes can be functionalized with electrodeposited PEDOT (Patel et al., 2015; Massey et al., 2019) or IrOx (Deku et al., 2018; Gillis et al., 2018) to further improve their impedance and charge capacity density. An alternative method to fabricate CF electrodes is thermal drawing (Guo et al., 2017), by which carbon nanofiber (CNF) composites were unidirectionally aligned in cyclic olefin copolymer (COC) as a recording electrode. The as-fabricated fiber had overall dimensions of  $<100 \times 100 \mu\text{m}^2$ , including a single recording site of CNF composite with a size ranging from  $18 \times 11.3 \mu\text{m}^2$  to  $35.2 \times 20.1 \mu\text{m}^2$ , and dramatically reduced impedance magnitude by 2 orders compared to the conventional polymer electrodes (Guo et al., 2017). Alternatively, Yu et al. demonstrated *in situ* growth of vertically aligned carbon nanofibers on pre-patterned Ni catalyst using direct current catalytic plasma-enhanced CVD. The array consists of 40 electrodes in one line with  $15 \mu\text{m}$  spacing along a complete length of  $600 \mu\text{m}$ . The conical shape of the CNFs facilitates the penetration of electrodes into the interior of tissues or individual cells to improve electrical coupling (Yu et al., 2012). Besides purer CNFs, Saunier et al. reported a composite PEDOT:CNF material combining PEDOT with CNFs through electrochemical deposition. The PEDOT:CNF modified microelectrode demonstrates low specific impedance of  $1.28 \text{ M}\Omega \mu\text{m}^2$  at  $1 \text{ kHz}$  and unrivaled charge injection limit of  $10.03 \text{ mC/cm}^2$ , suitable for multifunctional electrophysiological recording and neurotransmitter sensing. Moreover, CNF has magnetic susceptibility close to water and tissues, making it compatible with high field functional magnetic resonance imaging (fMRI) to enable high-resolution electrophysiological measurements and anatomical studies of large-scale neural networks without electrode interference with MRI images (Lu et al., 2019).

Unlike the CNFs, CNTs have smaller sizes with higher density and can be divided into single-walled carbon nanotubes (SWCNTs) and multi-walled carbon nanotubes (MWCNTs) (Fattahi et al., 2014). SWCNT is a single graphite sheet wrapped into a cylindrical tube, while the MWCNTs nest several SWCNTs together concentrically, looking like rings of a tree trunk (Zhang et al., 2011). Perfect SWCNTs have outstanding mechanical properties and electrical properties, quite similar to the perfect MWNTs due to the weak coupling of nanotubes in MWNTs (Eatemadi et al., 2014). Additionally, the rolling direction of the SWCNTs decides the properties that are more like metals or semiconductors (Saifuddin et al., 2013). For use in neural electrode implants, CNTs can be electrochemically coated on the conventional tungsten and stainless steel wires under ambient environments at low temperatures to improve the impedance and charge transfer properties of the electrodes (Keefer et al., 2008). Furthermore, the tungsten wires can be etched electrochemically to obtain pure carbon nanotube probes as intracellular recording electrodes (Yoon et al., 2013). Besides electrochemical deposition, CVD methods can synthesize CNTs directly on the tip of quartz-insulated platinum/tungsten electrodes (Ansaldi et al., 2011).

Compared to electrochemically deposited CNTs, the chemical vapor deposited CNTs show remarkable mechanical toughness and stability over time. The CVD-CNT-coated microelectrodes can retain unaltered impedance values after 1 year storage or after being subjected to a million current pulses at charge injection limit. CNT can also be integrated with flexible polymer substrates to implement flexible CNT electrodes. For example, Lin et al. embedded pre-patterned CNT structures into a PA film to create a flexible CNT electrode array with significantly reduced mechanical rigidity and low impedance for the high-quality recording of spontaneous spikes from the crayfish nerve cord (Lin et al., 2009). Similar to graphene, studies show that the electrical properties of the CNT-based electrodes can be improved by tuning the hydrophilicity of CNTs. For example, plasma/UVO<sub>3</sub> treatment of  $<10\text{s}$  can alter the surface wettability of CNT from superhydrophobicity to superhydrophilicity, mainly due to the formation of -OH terminations (Chen et al., 2010; Su et al., 2010; Pan et al., 2016). Amino-functionalization of the MWCNTs surface with a 2 wt% 1,4-diaminobutane solution can also improve the hydrophilicity of the surface, lasting for at least 6 months in the air (Yen et al., 2011). While widely used in neural electrode implants, the cytotoxicity of these nanostructures is still a big concern, since the nanomaterials can penetrate through the blood-brain barrier (BBB) and cause irreversible cell death and damage to the brain (Tang et al., 2008; Furtado et al., 2018).

### Glassy Carbon

Glassy carbon (GC) offers a wide range of mechanical, electrical, and electrochemical properties, which can be specifically tailored with different pyrolysis temperatures under different fabrication conditions to match the properties of the target tissue (Cassar et al., 2019). Because flexible polymer substrates are unable to tolerate high pyrolysis temperatures, pattern transfer techniques are often used to fabricate GC based, flexible ECoG microelectrode arrays on polyimide substrates (Vomero et al., 2016; Castagnola et al., 2018), as shown in **Figure 3D**. Furthermore, coating GC based microelectrodes with CPs, such as PEDOT:PSS, helps to reduce the impedance magnitude of a  $60 \mu\text{m}$ -diameter electrode by at least 2 orders (Vomero et al., 2016). Most recently, Chen et al. designed and fabricated a cone-shaped glassy carbon neural electrode array using 3D printing and chemical pyrolysis technologies (Chen et al., 2020). The electrode had a  $0.78 \text{ mm}^2$  recording area exposed at the tip, and the corresponding impedance, capacitance, and SNR are  $7.1 \text{ k}\Omega$ ,  $9.18 \text{ mF/cm}^2$  and  $50.73 \pm 6.11$ , respectively (Chen et al., 2020).

### Diamond

In recent years, diamond has emerged as a promising electrode material for neurophysiological recording and neurotransmitter sensing. Boron-doped polycrystalline diamond (BDD) offers unique properties, including wide aqueous potential window, chemical inertness, capability for surface modification, tunable electrical conductivity, and biocompatibility (Alcaide et al., 2016; Hébert et al., 2016; McDonald et al., 2017; Yang and Narayan, 2019). Despite the many benefits of this material, the mechanical property mismatch between BDD (Young's modulus of  $\sim 10^3 \text{ GPa}$ )

(Wild and Wörner, 2004) and soft tissues is a major obstacle that impedes the development of BDD into fully implantable electrochemical devices. Compared to other semiconducting materials, diamond processing and patterning are more difficult due to its extreme mechanical hardness, lack of ductility, and weldability (Garrett et al., 2016). Therefore, attempts have been made to develop new material synthesis and processing methods to fabricate diamond-based electrodes with improved flexibility. For example, Fan et al. demonstrated a wafer-scale fabrication method to transfer large-scale, pre-patterned BDD microelectrode arrays from a solid silicon substrate onto a flexible PA substrate (Fan et al., 2017, 2020). The electrodes made of the BDD growth side exhibited a rougher topology, a higher  $sp^3$  content, and a large grain size than the nucleation side, enabling a wide working potential window, a low background noise, a resistance to chemical fouling, and a reduced electrochemical impedance (Fan et al., 2020).

## PACKAGING AND SUBSTRATE MATERIALS

### Comprehensive Consideration of Packaging/Substrate Materials

For all implantable devices, the biocompatibility of packaging and substrate materials is a prerequisite that must be met (Madou, 2018), not only for the device's long-term stability but also for the user's safety (Onuki et al., 2008). The Implant-induced inflammatory response is complicated and inevitable since the chemical aggressive reaction produced by the inflammatory response is the body's natural self-protection mechanism. Although the impact of the inflammatory response on the performance and lifetime of the implant package needs further characterization by researchers, the aggressive environment caused by inflammation sets a high bar for hermetic seal and chemical stability of the packaging material.

The next factor to be considered is the hermeticity of packaging materials. There are two basic packaging strategies: hermeticity and non-hermeticity packaging. The choice of a specific packaging strategy depends on the required implant's stability (long-term or short-term) and the inner design (Alt et al., 2016). Due to the complex and aggressive environment *in vivo*, hermeticity is a key criterion for packaging materials of implantable electrodes. Ideally, the packaging should effectively isolate the internal electronics from the human body environment (Joung, 2013), trap the outgassing of the inner materials, and dissipate the electrically-induced heat to the surroundings. The hermeticity of the packaging material directly affects the life expectancy of the implants (Jiang and Zhou, 2009), and can be characterized using permeability. In general, helium permeability is quantified by the amount of helium through a certain thickness of common materials in a certain period (Greenhouse, 1999; Joung, 2013). The helium leak test was recognized as an industry standard (Costello et al., 2012) and can be simply converted into the leak rate of another gas of interest, such as  $H_2O$  (Jeong et al., 2016). However, the helium leak test can be misleading in the case of a polymer

package (Vanhoestenbergh and Donaldson, 2011). Therefore, many researchers started to choose moisture permeability as the standard for quantifying the hermeticity of the packaging (Sim et al., 2017; Bettinger et al., 2020; Patil et al., 2020; Song et al., 2020). In theory, all materials will leak to some extent (Ely, 2000) but with different permeabilities. As shown in Figure 4, the permeability of metal is the lowest, which means even a thin ( $10^{-4}$  cm) metal can prevent moisture permeation (with a permeability of  $<10^{-25} \frac{cm^3_{STP} \cdot cm}{cm^2 \cdot sec \cdot cmHg}$ ) for a very long time (10 years), while the sealing performance of soft polymers, such as silicone, is not good among common packaging materials (Song et al., 2020). As such, thin-film polymers may not be a favorable candidate for impermeable barriers in chronically implanted devices (Jiang and Zhou, 2009). Thicker polymer protective encapsulation or composite materials combining polymers with other materials of better permeability (e.g., metal, ceramics, glass, etc.) should be considered (Jiang and Zhou, 2009).

Other considerations for packaging and substrate materials are based on intended applications and implantation sites. For example, packaging materials for ECoG recording electrodes have a high demand for flexibility and stretchability but low constraint in hermeticity. Therefore, polymers (e.g., silicone and polyetheretherketone), even with relatively high water vapor permeability, are still widely used as packaging and substrate materials in many ECoG implants (Henle et al., 2011b; Mestais et al., 2014; Woods et al., 2018). For recording from deep brain regions, good mechanical strength is required to allow device insertion to the target location with minimal disturbance to the surroundings (Connolly et al., 2015). Therefore, extra attention should be made to the buckling force and the dimensions of the electrode implants, such as silicon probes, to ensure sufficient mechanical strength and toughness for device implantation (Hetke et al., 2002). Packaging of such rigid implants usually involves solid materials, such as  $SiO_2$  (Cheng et al., 2013b; Lee et al., 2013b) and  $Si_3N_4$  (Oh et al., 2003; Zhao et al., 2019).

There are many more factors that limit the choice of materials, including but not limited to, low coefficient of friction of the material to avoid wear debris (Patel and Gohil, 2012), compatibility with wireless communication (Joung, 2013), thermal conductivity, and matched thermal expansion coefficient (Jiang and Zhou, 2009). In general, a major challenge in designing and fabricating a chronically stable neural interface is producing a conformal, dense barrier layer for encapsulation (Joshi-Imre et al., 2019) without releasing toxicity to the tissues (Shen and Maharbiz, 2020). This is particularly difficult when a neural implant has complicated topography (e.g., 3D structure) (Joshi-Imre et al., 2019). While looking for suitable materials, it is also critical to identify various causes of packaging failures under the complex biological environment (Anderson, 2001), which can be attributed to a combination of factors including packaging delamination, inflammatory response, and package damage related to the defects from manufacturing (Joshi-Imre et al., 2019; Gong et al., 2020). No material is perfect, wisely choosing material based on different devices and making good use of the advantages of different materials is a challenge that every engineer must face when designing biomedical implants.



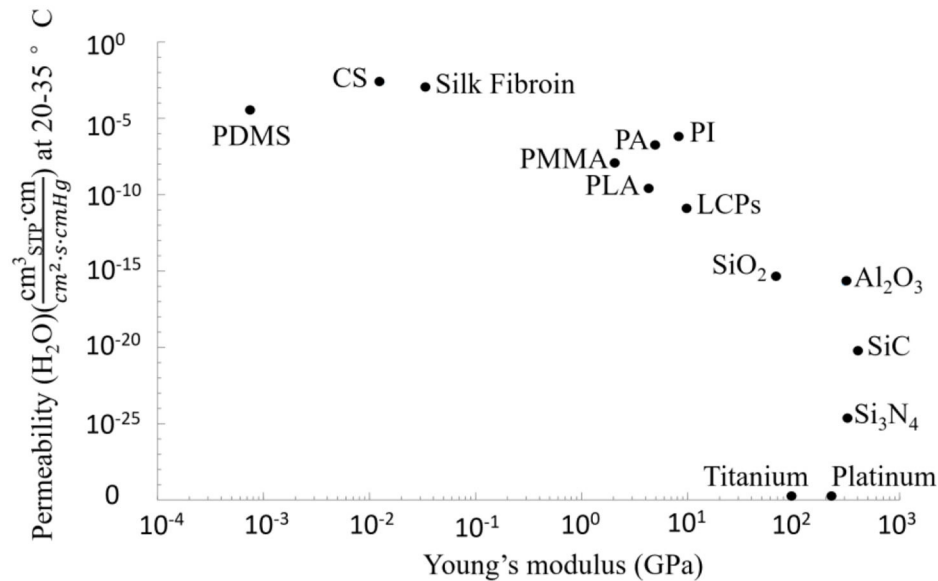


**FIGURE 4** | Logarithmic plot of Young's moduli and moisture permeability (H<sub>2</sub>O) for various packaging materials. Data points are representative values available from Table 2.

"The design of biocompatible materials for device packaging is arguably as much of a challenge as the design of the device itself." (Wasikiewicz et al., 2013).

## Solid Packaging Materials

In this article, solid packaging materials generally refer to materials whose Young's moduli are higher than cortical bone (15–30 GPa). Most of these materials are inorganic materials represented by metals, ceramics, and glass. Compared to polymers, inorganic solid materials have low gas and moisture permeability, and therefore, have been widely used as substrates and packaging materials in many implantable systems (Loeb et al., 2000; Strojnik and Peckham, 2000; Forde and Ridgely, 2006). Moreover, because of their rigid physical properties, these materials can provide extra mechanical support for device insertion into tissue. However, most inorganic packaging materials cannot fulfill flexibility and mechanical robustness simultaneously. Among all the solid packaging materials, ceramics and glass are very mature packaging materials because of their excellent chemical stability and good hermeticity. Although metal and silicon are not mainstream packaging materials, they still have many favorable characteristics. This section will review and discuss the use of these materials in neural recording devices.

As one of the oldest materials, metal has been utilized in implantable devices for a very long time. Some metal materials, such as titanium, platinum, some alloys, and stainless steel, have good biocompatibility, *in vivo* stability, and very low permeability (Scholten and Meng, 2015). Although few neural recording implants directly use metal as a packaging layer, many applications combined metal thin film with ceramic or polymers to form a hybrid package for implants, such as in

a miniaturized inductively-powered neural implant (Khalifa et al., 2017). The advantage of metal lies in its excellent mechanical strength, making it less fragile than ceramic and glass (Scholten and Meng, 2015). However, the application of metal materials to packaging has several problems. First, most metals have good conductivity, which may cause short circuits in internal electronic components. Second, metal corrosion in ionic biological environments is still a challenge (Subramanian et al., 2011). Passive electrochemical corrosion, crevice corrosion, and active electrochemical corrosion can severely affect the stability of metals. Changes in local pH values due to water electrolysis or active electrochemical reactions are also a major threat to metal (Jiang and Zhou, 2009). Third, the bonding strength at the metal-glass interface can be weakened after temperature cycling (Jiang and Zhou, 2009). Moreover, the opacity of metal packages to electromagnetic (EM) field provides EM shielding for internal electronics but restricts their use in wireless implantable devices.

Compared to polymers, many ceramics are gas/water-impermeable, chemically stable, biocompatible, electrically insulating, and physically hard (Vlasov and Karabanova, 1993; Piconi and Maccauro, 1999). However, it is difficult to machine ceramic and glass materials using conventional microfabrication techniques. As such, how to ensure the hermetic seal while allowing the electrode to pass through the ceramic encapsulation must be taken into design consideration (Stieglitz, 2010). In some early devices (Cameron et al., 1997; Loeb et al., 2000), glass-to-metal bonding was used, and various processing methods were investigated based on the type of packaging glass and the metal materials. Two typical bonding techniques are compression bonding and reactive bonding. The compression bonding utilizes different coefficients of thermal expansion of the materials to make the materials tightly squeezed together,



while reactive bonding uses chemicals as bonding media. In the later development, ceramic-to-metal bonding techniques were developed and can be categorized into feedthrough (Forde and Ridgely, 2006), active brazing (Agathopoulos et al., 1997), non-active brazing (Messler, 2004), and diffusion bonding (Savage, 2013). With these bonding technologies, the electrode can pass through the ceramic encapsulation layer without affecting hermeticity. For example, Borton's group (Borton et al., 2013) integrated a 104 channel recording with a wireless neural interface using hermetic feedthrough assembly, which contains an array of 104 Pt Ir feedthrough pins embedded in groups of 8 metal-ceramic seals.

With the continuous advancement of hermetic bonding and sealing methods, various packaging materials are also emerging, such as SiO<sub>2</sub> (Cheng et al., 2013b; Lee et al., 2013b; Song et al., 2019b; Chiang et al., 2020), Si<sub>3</sub>N<sub>4</sub> (Oh et al., 2003; Zhao et al., 2019), SiC (Lei et al., 2016; Saddow et al., 2016), alumina (Al<sub>2</sub>O<sub>3</sub>) (Stieglitz, 2010; Shen and Maharbiz, 2019), aluminum nitride (AlN) (Murphy, 2008; Besleaga et al., 2017), and so on. Among these materials, SiO<sub>2</sub> and Si<sub>3</sub>N<sub>4</sub> have good chemical stability and unique optical properties. Particularly, SiO<sub>2</sub>, with internal transmittance is higher than 90% between 470 and 800 nm (Wang et al., 2011), has been utilized in the packaging of implantable devices that requires a certain degree of light transmission (Kino et al., 2018). For example, Song et al. reported a scalable approach for flexible biocompatible electronic systems, where thin microscale device components are integrated on a flexible polymer substrate to form an interconnected array for multimodal, high-performance biointerfaces (Song et al., 2019a). A thin SiO<sub>2</sub> layer of 900 nm thermally grown on the surfaces of the silicon wafer served as an encapsulation layer. The SiO<sub>2</sub> packaging at this thickness can provide a long-lived, flexible biofluid barrier for flexible devices. As an alternative, Al<sub>2</sub>O<sub>3</sub> is not only chemically inert but also transparent at ultrasonic frequencies (Shen and Maharbiz, 2019), capable of packaging acoustic-based wireless medical devices wherein ultrasonic waves are used for efficient energy transfer and communication (Denisov and Yeatman, 2010; Seo et al., 2013). In recent years, SiC has become a hot topic in the packaging field because of its good biocompatibility and chemical inertia. SiC can be deposited at temperatures of lower than 400°C through plasma-enhanced CVD (PECVD) or low-pressure chemical vapor deposition (LPCVD) (Cogan et al., 2003; Hsu et al., 2007; Phan et al., 2019), making it compatible with the fabrication processes of many devices and materials. SiC package also provides less degradation rate in saline and better stability compared to Si<sub>3</sub>N<sub>4</sub> and low-temperature SiO<sub>2</sub> package (Lei et al., 2016). As evident in Kim et al.'s study (Kim et al., 2009), a multi-level hybrid packaging method based on PECVD deposited a-SiC<sub>x</sub>:H exhibited superior biocompatibility and reliability after accelerated lifetime testing. Furthermore, thin SiC films can become very flexible, suitable for use in packaging flexible implantable devices, such as ECoG arrays (Diaz-Botia et al., 2017).

Despite many advantages, the drawbacks of ceramic and glass materials cannot be ignored. First, even though most ceramics have good chemical stability, degradation of ceramics will still occur when the materials are soaked in

ionic liquid environments, for example, Al<sub>2</sub>O<sub>3</sub> dissolution in water. Second, there is a lack of viable etching techniques for ceramic and glass. Although many methods have been developed, the construction of ceramic and glass structures is still relatively complicated, making the package miniaturization difficult and incompatible with device fabrication technologies (Scholten and Meng, 2015). Third, the fabrication process of ceramic and glass package must be controlled precisely since even a small deposition variation can result in significant changes in package stability (Shen and Maharbiz, 2020).

## Soft Packaging Materials

Herein soft packaging materials generally refer to materials whose Young's moduli are between 10<sup>5</sup> Pa (for soft tissue) and 10<sup>10</sup> Pa (for hard tissue). It must be pointed out that the dividing line between flexible and solid packaging materials is changeable, solid packaging materials can also become flexible under certain conditions, such as small sizes, thin-film configurations, special structures, etc. (Viana et al., 2010). Compared to solid materials, soft polymeric materials dominate the choice of packaging materials for miniaturized neural implants because they offer many advantages, including high conformability, mechanical flexibility, small form factor, low price, and ease of use. Polymers can be cast, photopatterned, or dry etched at low temperatures, reducing the complexity of etching steps and infrastructure needs (Kim and Meng, 2015). Polymers also play an important role in the mechanical shielding of wire connectors to prevent accidental circuit breaks and provide a certain degree of mechanical buffering that avoids damaging the soft tissue by internal hard materials (Wasikiewicz et al., 2013). Many polymers have been developed and used to package neural implants, such as PI, PA, PDMS, polymethylmethacrylate (PMMA), liquid crystal polymers (LCPs), polycarbonate (PC), polystyrene (PS), SU-8, and so on. Due to their relatively high gas permeability (low hermeticity), thick polymer encapsulation must be used in chronic implants to protect the internal devices from being damaged (Jiang and Zhou, 2009; Wasikiewicz et al., 2013), at the expense of increased volume of the device and unstable thermal properties of the polymer (Barrese et al., 2013; Takmakov et al., 2015; Caldwell et al., 2020).

Among the emerging polymer packaging materials, PDMS is the most widely used coating material (Wasikiewicz et al., 2013) and the most established polymer for neural implants (Yoda, 1998; Colas and Curtis, 2004; Mata et al., 2005; Lacour et al., 2010; Rogers et al., 2010; Alt et al., 2016). PDMS offers good insulation, vibration absorption, good adaptability to tissue's deformation due to excellent elasticity (Wu et al., 1999; Kim et al., 2011; Mineev et al., 2015; Alt et al., 2016), diffusional resistance to contamination solutes (Wu et al., 1999), good optical transparency (Jeong et al., 2015), hardly observed degradation (Alt et al., 2016), lower foreign body response (Bae et al., 2014), as well as low cost and availability. The most notable quality of PDMS is its superior, FDA-approved biocompatibility (Henle et al., 2011a; Bae et al., 2014) for chronic implants (USP class VI). It is one of the few packaging materials that

have been tested for long-term implantation (Brindley et al., 1986; Schiavone et al., 2018). However, the high permeability of PDMS coating remains unsolved. A thin coating of PDMS cannot provide effective protection and may cause a delamination problem (Kinloch, 2012). Although a thick PDMS coating of 100–300  $\mu\text{m}$  has significantly reduced permeability (Ordonez et al., 2012), the bulky material greatly restricts the miniaturization of the device, and thus, the utilization of PDMS in ultra-small implants. To address this challenge, attempts have been made by combining PDMS with other flexible materials such as PA (Henle et al., 2011a), PET (Shur et al., 2020) or PI (Ordonez et al., 2013) to form a composite packaging layer with improved hermeticity.

As an alternative polymer packaging material for long-term implants, Parylene consists of various chemical variants, including PA, Parylene D, Parylene HT, Parylene N, among which PA is one of the most prevailing packaging materials for neural implants (Ceyssens and Puers, 2015). It is also worth noting that Parylene HT is becoming more and more popular due to its improved packaging performance (Kumar, 2010). Currently, the commercial market of Parylene is dominated by two companies, Specialty Coating System (SCS) and Kisco Conformal Coating LLC (Kim and Meng, 2015). PA can be conformally deposited by CVD at room temperature and structured by oxygen plasma dry etching or laser. Those low fabrication requirements make PA compatible with many materials (Fan et al., 2020) and device designs. As a packaging material, PA has excellent biocompatibility (USP class VI), chemical inertness (De la Oliva et al., 2018), low conductivity, low intrinsic stress (Zöpfl et al., 2009), low pin-hole density, and conformal coating (Rodger et al., 2008). PA is also optically transparent with the transmission of 65–80 % over a spectrum range of 470 to 850 nm (Kwon et al., 2013; Alt et al., 2016; Bi et al., 2016), applicable for packaging many optical devices (Ledochowitsch et al., 2011; Park et al., 2014). However, PA has a low glass transition temperature ( $T_g = 90^\circ\text{C}$ ) (Kahouli et al., 2012), which limits subsequent fabrication methods. Although PA can effectively isolate external erosion for a certain period, long-term *in vivo* and reactive accelerated aging (RAA) studies show that the insulation properties of PA can degrade over time due to moisture absorption in liquid environments (Ordonez et al., 2012; Gong et al., 2020). A more in-depth understanding of PA's degradation mechanism will be critical for further improvement in the packaging performance of PA (Caldwell et al., 2020).

As a material with a long and rich history, the first discovery of PI can be traced back to 1908. Today, PI is already a very mature material and widely available in various forms (Liang et al., 1992; Rousche et al., 2001; Hassler et al., 2011; Bakonyi et al., 2013; Kim et al., 2013). PI has a great potential for a variety of applications in neural implants (Mian et al., 2005; Rubehn and Stieglitz, 2010; Viventi et al., 2011; Schaubroeck et al., 2017; Kampasi et al., 2020), such as multi-level interconnects, multi-chip module packaging, and flexible circuitry (Frazier, 1995). Compared with PA, PI provides better high-temperature stability (up to  $400^\circ\text{C}$ ), higher glass transition temperature (Kim and Meng, 2015), better dielectric properties (Frazier,

1995), and lower moisture absorption. Especially for mechanical properties, PI has a tensile strength of 390 MPa, almost 6 times higher than that of PA, and Young's modulus of 8.37 GPa, 2.6 times higher (Stieglitz et al., 2000; Hassler et al., 2011). Consequently, PI enables much better durability under repetitive bending at the same thickness. Another advantage of PI is that its thermal expansion coefficient matches with Si so that thermally-induced mechanical stress can be negligible (Ceyssens and Puers, 2015). However, although PI has been proven to have considerably good biocompatibility, it is not FDA certified for human implantation. The poor adhesion of PI with certain materials, such as copper, is another major challenge (Kim and Meng, 2015; Bang, 2016). Moreover, studies show that the insulation lifetime of PI is quite limited in the saline environment, which may limit the use of PI in long-term implants. It is of note that significant shrinkage (20–50%) occurs during the PI curing process (Bagolini et al., 2002; Ma et al., 2009), which should always be considered in device design and manufacturing.

There are other polymer candidates in addition to the above materials. For example, PMMA exhibits higher impact resistance and lower electronic fluctuation (Joung, 2013; Kim et al., 2015) than PDMS and is expected as a possible replacement for PDMS in the future. SU-8 is a negative photoresist, epoxy-based polymer, which allows convenient, rapid, and cost-effective microfabrication processing (Márton et al., 2020). Despite the debate of the biocompatibility of SU-8 (Márton et al., 2020), SU-8 is still used as a packaging layer for many neural implants (Hong et al., 2018; Lee et al., 2019). For example, Hong et al. reported a SU-8 encapsulated, syringe-injectable mesh electronics, which enables multiplexed and chronically stable recording from diverse retinal ganglion cell (RGC) types in mice. LCPs have been explored as a stable and biocompatible material for both flexible substrates and packaging materials under *in vivo* conditions (Hwang et al., 2013). Besides their good chemical stability and high interfacial adhesion (Hwang et al., 2013), LCPs have lower permeability ( $2.19 \times 10^{-11} \text{ atm cm}^2/\text{s}$ ) than other polymer packaging materials (Au et al., 2019). Due to the surface alignment of the LCP when exposed to shear flow during fabrication, LCP has an anisotropic molecular structure and a crystalline surface with an amorphous core, resulting in relatively better mechanical and moisture barrier properties (Au et al., 2019). Although LCP has many attractive advantages, the long-term reliability of the LCP package still needs to gain widespread acceptance (Jeong et al., 2016). Moreover, due to its anisotropic structure, a small mistake in fabrication may cause tear-out, internal cracking, and other problems on the LCP surface, which makes further processing very challenging (Au et al., 2019).

## Biodegradable Encapsulation and Stiffener Material

A biopolymer usually is produced by microbial systems, extracted from plants, or chemically synthesized by biological components (Rebelo et al., 2017). Compared with synthetic polymers, the biggest advantage of biopolymers lies in their

degradability and renewability (Cziple and Marques, 2008; Niaounakis, 2015). Generally speaking, the encapsulation and substrate material of chronic neural implants should remain stable in the host body. This requirement seems to contradict the degradability of biopolymers. However, it must be noted that some applications only require stable biotic-abiotic interfaces for a certain period of time (Muskovich and Bettinger, 2012; Lu et al., 2020). In the area of biodegradable encapsulation, Choi et al. (2020) demonstrated a bioresorbable polyanhydride-based polymer (PBTPA). The result shows PBTPA film has good biocompatibility, low swelling during dissolution in water, mechanical properties supporting robust operation in flexible devices, and good processability potential. By controlling the monomer composition and thickness, PBTPA can provide a strong water-barrier at timescales from hours to weeks. Moreover, the use of partial bioresorbable LED circuits illustrated its potential application in the optogenetics area. In addition to biodegradable polymers, Si membranes have also been explored as a water barrier layer for biodegradable encapsulation of neural interfaces. For example, John A. Rogers' group (Lee et al., 2017b) presented the use of silicon nanomembranes as bioresorbable water barriers in temporary electronic implants and environmental monitors.

Other major applications of the biopolymers include surface functionalization of the package surface to effectively reduce the immune response or temporary stiffening sheaths to escort a flexible implant into a designated position (Chung et al., 2019). At present, poly lactic acid (PLA), silk, and PEG are commonly used. Made from natural starch, such as corn, rice, and potatoes (Rebelo et al., 2017), PLA has relatively good mechanical properties and absorbability, and therefore are typically used in orthopedic devices, such as stents or scaffolds. The application of PLA does not stop at orthopedic study, as it can also be configured as a foam with oriented inner channels for repairing chronic spinal cord injuries (Cai et al., 2007). As an ancient material, the core silk fibroin fibers in raw silk have strong mechanical resistance. Silk fibroin and its other variants can be used in various soft tissues, such as ligaments (Altman et al., 2003), bladder (Franck et al., 2013), and musculoskeletal (Meinel and Kaplan, 2012). Recently, silk fibroin has been explored as the substrate material for optical or wirelessly powered neural implants (Hwang et al., 2012; Tao et al., 2015; Perotto et al., 2017). In the study of a flexible fish-bone-shaped neural probe (Wu et al., 2011), a silk sheath was utilized to reinforce the PI probe and provide temporary mechanical strength during probe implantation. Alternatively, PEG-based hydrogels hold tremendous promise as coatings to enhance the biocompatibility of neural prosthesis (Rao et al., 2011). For example, Kato et al. (2006) reported a multichannel flexible neural probe, in which the bioactive components of nerve growth factor (NGF) and PEG were mixed in the packaging material to repair the damaged neurons. PEG, another biodegradable polymer, has been utilized as a temporary stiffening sheath covering flexible electrode implants (Felix et al., 2013) or a stiffening filler in microfluidic channels of a flexible probe to improve the stiffness without increasing volumetric structure (Takeuchi et al., 2005). More comprehensive reviews

of coating and stiffening materials are given in Kuo et al. (2013) and Wang et al. (2020).

## CONCLUSION AND OUTLOOK

Investigation of the novel electrode and packaging/substrate materials is, at present, one of the most prevailing topics in developing advanced neural recording electrodes, as evident by continuous growth in literature. While electrodes are the most significant element that directly influences the quality of neurophysiology recording, electrode packaging is equally important that help assist in device implantation as well as maintain device functionality and long-term stability. With recent advancements in material science and engineering, implantable electrode interfaces capable of recording neural activity with high spatiotemporal resolution can now be achieved. This article reviewed typical electrode and packaging materials associated with the state-of-the-art electrode devices, as guidance for future device development. **Tables 1, 2** summarize the main properties of the selected electrode materials and packaging materials, respectively. In particular, **Table 1** lists the properties of various electrode materials discussed in this review, including their electrical properties, biocompatibility, stability, biodegradability and bioresorbability, mechanical flexibility and bendability, Young's modulus and broad-band optical transmission, as detailed in sections Key Material Characteristics and Electrode Materials. **Table 2** discusses the water vapor permeability, Young's modulus, optical transparency from 470 to 800 nm, and stability of the representative packaging materials introduced in this article. Of these materials, synthetic polymers have the most balanced performance and can maintain good packaging performance for a relatively long time.

With the trend of further miniaturization in large-scale, high-density recording electrodes, many challenges still remain unsolved, mostly related to chronic stability, high fidelity of recording, and minimal foreign-body immune responses. For moving forward, one research area that has received much recent attention is to design and develop composite materials that combine the unique advantages of different existing materials while eliminating their major drawbacks. The use of composite materials in electrode structuring has the potential to bring disruptive changes to single material designs. For example, Yang et al. designed a PEDOT:PSS-ITO-Ag-ITO on PA assembly that greatly enhanced the transparency and electrochemical conductivity while overcoming the brittleness of ITO and the oxidation of Ag thin films. Pal et al. (2016) demonstrate a flexible bio-sensor that combines PEDOT:PSS sensing elements on a fully biodegradable and flexible silk protein fibroin support to achieve excellent electrochemical activity and stability over days. Composite electrode materials can be prepared by *in situ* electrodeposition or multilayered assembly of inorganic and/or organic conducting materials on planar substrates to achieve the desired electrochemical, biological, optical, and mechanical properties. Recently, with their tunable composites, configurations, and density, 3D nanostructured materials represent novel electrode materials to

**TABLE 1** | Summary of various electrode materials with key properties.

Electrode materials		Electrical properties (impedance @1 kHz)	Biocompatibility	Stability	Biodegradability/ Bioresorbability	Mechanical flexibility/ be-ndability	Young's modulus	Optical Transmission (400–700 nm)	References
GNPs	Nanopillars	13.1 ± 2.7 kΩ-1172.3 ± 241.6 kΩ (0–22.5 μm height)		14 days <i>in vitro</i>					
	Nanorods	1.847 kΩ (10,000 μm <sup>2</sup> area)	Cytotoxic (depend on the size of GNPs)	20 times (agarose gel insertion)	Biodegradable	Bendable	1–10 GPa	Opaque	Zhou et al., 2009; Kim et al., 2010b; Nick et al., 2014; Lee et al., 2016b
	Nanoflakes	11.9 ± 1.47 kΩ-249 ± 28.1 kΩ (5–50 μm diameter)		A month					
Pt black		3.5 kΩ (4 mm length, ~100 μm diameter)	Biocompatible	3 days <i>in vivo</i>	N/A	Bendable	N/A	Opaque	Zhang et al., 2015; Lee et al., 2017a; Zátönyi et al., 2018
Au/Pt alloy		0.23 MΩ (20 nm diameter)	Biocompatible	7 times (ultrasonic treatments)	N/A	N/A	113.8 GPa	Opaque	Zhao et al., 2016
Ir/Pt alloy		80 ± 18 kΩ (13 mm length, 75 μm diameter)	Biocompatible	12 weeks <i>in vivo</i>	N/A	Bendable	185.5–189.6 GPa	Opaque	Cassar et al., 2019
Si nanowires		~20 MΩ (100 nm–200 nm tip diameter)	Biocompatible	8 days (rodent neurons) 6 weeks (hiPSC-derived neurons)	Biodegradable	N/A	60–240 GPa	Transparent	Sohn et al., 2010; Marcon and Boukherroub, 2014; Liu et al., 2017a
Si NMs		~50 kΩ~250 kΩ (200 <sup>2</sup> -500 <sup>2</sup> μm <sup>2</sup> )	Biocompatible	A month <i>in vivo</i>	Bioresorbable	Flexible	3.25–180 GPa (2 nm–25 nm thickness)	Transparent	Yu et al., 2016; Bai et al., 2019
ITO/PEDOT:PSS		~ 40 kΩ~100 kΩ (10–80 μm diameter)	Biocompatible	4 weeks <i>in vitro</i>	N/A	Flexible	~77 GPa (on glass)	Transparent (> 80 %)	Li and Chang, 2014; Yang et al., 2017
PEDOT:PSS/nanostructured Pt		9.2 kΩ (500 μm diameter)	Biocompatible	1,500 CV cycles	N/A	Flexible	N/A	Opaque	Boehler et al., 2017
PPy nanotubes/GNP		~5 kΩ (300 μm diameter)	Biocompatible	Stable	Biodegradable	Flexible/benda-ble	N/A	N/A	Kojabad et al., 2019
Diamond		~ 207.9 kΩ (0.0079 mm <sup>2</sup> area)	Biocompatible	Stable	N/A	Flexible (on Parylene C)	~10 <sup>3</sup> GPa	Opaque	Fan et al., 2020
Graphene		243.5 ± 15.9 kΩ (~200 μm diameter)	Biocompatible	70 days <i>in vivo</i>	N/A	Flexible	~1 TPa	Transparent (>90%)	Lee et al., 2013a; Park et al., 2014
CNFs		~1 MΩ (2 cm length, 25.7 × 16.6 μm <sup>2</sup> )	Biocompatible	4 weeks <i>in vivo</i>	Unbiodegradable	Flexible	6–207 GPa	N/A	Lawrence et al., 2008; Guo et al., 2017; Farzamfar et al., 2019
CNTs		~64.5 Ω mm <sup>-2</sup>	Biocompatible	Stable	Unbiodegradable	Flexible	530–700 GPa	Transparent (~60%)	Lawrence et al., 2008; Su et al., 2010; Deng et al., 2011
Glassy carbon		11.0 ± 5.4 kΩ (300 μm diameter)	Biocompatible (12 days)	Stable	N/A	Flexible	20 GPa	Opaque	Vomero et al., 2016, 2017



**TABLE 2 |** Summary of various packaging materials with key properties.

	Permeability (H <sub>2</sub> O) ( $\frac{\text{cm}^3_{\text{STP}} \cdot \text{cm}}{\text{cm}^2 \cdot \text{s} \cdot \text{cmHg}}$ ) at 20–35°C	Young's modulus (GPa)	Transparency From wavelengths 470 nm–800 nm (@wavelength) (thickness)	Stability <i>in vivo</i> or in solution		References
				Time	Method	
Titanium (thin film)	≈0	90	~55% (5 nm)	16 years	<i>In vivo</i>	Scarano et al., 2005; Greenhouse et al., 2011; Nakai et al., 2011; Axelevitch et al., 2012
platinum	≈0	213	~35% (20 nm)	3.25 years	<i>In vivo</i>	Farraro and Mclellan, 1977; Oh et al., 1993; Griffith and Humphrey, 2006; Greenhouse et al., 2011
SiO <sub>2</sub>	4.63 E-16	66	91–88% (1 mm)	~60 year (Converted to 37°C)	PBS Soak (95°C)	Jaccodine and Schlegel, 1966; Fahlteich et al., 2011; Wang et al., 2011; Song et al., 2019a
Si <sub>3</sub> N <sub>4</sub>	2.06 E-25	319.4	15% (@450 nm)–60%(@800 nm) (1 mm)	383 days	<i>In vivo</i>	Bruis et al., 2001; Su et al., 2004; Wise et al., 2004; Andringa et al., 2015
SiC	6.18 E-21	410	90% (@450 nm) (300 nm)	> 6 weeks	<i>In vivo</i>	Anma et al., 2001; Chawla et al., 2004; Zambov et al., 2006; Vomero et al., 2018
Al <sub>2</sub> O <sub>3</sub>	1.73 E-16	303	85% (@450 nm)–0% (700 nm) (1 mm)	>5 months	PBS Soak (37°C)	Vekinis et al., 1990; Jiang et al., 2008; Fahlteich et al., 2011; Peled et al., 2014
PI	6.35 E-7	8.45	80% (25 μm)	1,091 days	<i>In vivo</i>	Hubbell Jr. et al., 1975; Rubehn and Stieglitz, 2010; Barrese et al., 2013
PA	1.9 E-7	4.75	95% (20 μm)	1,200 days	<i>In vivo</i>	Hubbell Jr. et al., 1975; Shih et al., 2003; He et al., 2009; Barrese et al., 2013
PDMS	4 E-5	7.5E-4	93.39%	>18 weeks	<i>In vivo</i>	Armani et al., 1999; Metz et al., 2005; Henle et al., 2011b; Ko et al., 2017
PMMA	11.4 E-9	2	94%	3–6 months	<i>In vivo</i>	Kim et al., 2004; Jackson et al., 2010; Landi et al., 2013; Keller and Kouzes, 2017
LCPs	1.14 E-11	10	50% (@650 nm)– 90% (@850 nm)	2.5 years	<i>In vivo</i>	Mehta and Isayev, 1991; Flodberg et al., 2000; Jeong et al., 2016
CS membrane	2.4 E-3	0.013	70% (@450 nm)–83%(800 nm) (0.5 μm)	120 days	<i>In vivo</i>	Kweon et al., 2001; Gu et al., 2013; Li et al., 2014; Meyer et al., 2016
Silk fibroin film	1.2 E-3	0.034	90%	2 weeks	<i>In vivo</i>	Kweon et al., 2001; Hopkins et al., 2013; Cho et al., 2014
PLA	2.4 E-10	4.2–5.7	92–94%	4 months	<i>In vivo</i>	Solarski et al., 2005; Bang and Kim, 2012; Tyler et al., 2016; Arrieta et al., 2017

further improve the electrochemical impedance and the capacity of the injection charge density, two important factors that determine the SNRs and recording quality of the electrodes. While promising, the *in vivo* evaluation of these composite materials is incomplete, preventing their applications in chronic neural interfaces.

Surface modification combining the traditional materials (such as PA, PI, Ceramic) with biopolymers or nanomaterials also greatly expands the potential application scenarios of packaging

materials. As an important technology, surface functionalization can be achieved by fabricating nanofibers from synthetic polymers and biopolymers with different bioactive molecules to improve their applicability (Sofi et al., 2019). Common techniques include but not limited to electrospinning (Barakat et al., 2010), plasma treatment (Grace and Gerenser, 2003), wet chemical treatment (Nam et al., 1999), surface grafting (Liu et al., 2004), etc. These surface functionalization techniques can modify the packaging material with varying mechanical

stiffnesses and improved biocompatibility according to specific needs (Ghasemi-Mobarakeh et al., 2009; Sofi et al., 2019). However, the long-term stability, scalability, and compatibility of these surface functionalization techniques with other electrode fabrication/packaging techniques remain unclear and deserve further investigation.

Besides improving existing materials, new electrode materials (e.g., diamond and MXenes) and structure/packaging materials (e.g., self-healing polymer and shape memory polymer) that were not originally used in neural interfaces are being explored (Driscoll et al., 2018, 2020). For example, Driscoll et al. purposed flexible  $\text{Ti}_3\text{C}_2$  MXene microelectrode arrays for *in vivo* micro-ECoG recording with the benefits of significantly high volumetric capacitance, electrical conductivity, surface functionality, and sensitivity (Driscoll et al., 2020). As an emerging packaging material, the self-healing materials, such as a self-healing PDMS-based elastomer, have been explored to build self-healing, flexible electrodes (Dhler et al., 2020), which has a potential application in neural implants. Most recently, Bashandeh et al. reported

an SMP material as a precursor to form different 3D kirigami microstructures (Bashandeh et al., 2020). While significant progress has been made, comprehensive evaluation of their functionality, long-term stability and biocompatibility is needed to fully realize the true potential of these new materials for use in neural recording interfaces.

## AUTHOR CONTRIBUTIONS

WY and YG wrote the manuscript. WL revised the manuscript. All authors contributed to the article and approved the submitted version.

## FUNDING

This work was supported by National Science Foundation under the Award Number ECCS-2024270 and Michigan State University for financial support.

## REFERENCES

- Abidian, M. R., Corey, J. M., Kipke, D. R., and Martin, D. C. (2010). Conducting-polymer nanotubes improve electrical properties, mechanical adhesion, neural attachment, and neurite outgrowth of neural electrodes. *Small* 6, 421–429. doi: 10.1002/smll.200901868
- Acharya, U. R., Hagiwara, Y., Deshpande, S. N., Suren, S., Koh, J. E. W., Oh, S. L., et al. (2019). Characterization of focal EEG signals: a review. *Futur. Gener. Comput. Syst.* 91, 290–299. doi: 10.1016/j.future.2018.08.044
- Agathopoulos, S., Moretto, P., and Peteves, S. D. (1997). *Brazing of zirconia to Ti and Ti6Al4V*. Westerville, OH: American Ceramic Society.
- Alcaide, M., Taylor, A., Fjorback, M., Zachar, V., and Pennisi, C. P. (2016). Boron-doped nanocrystalline diamond electrodes for neural interfaces: *in vivo* biocompatibility evaluation. *Front. Neurosci.* 10:87. doi: 10.3389/fnins.2016.00087
- Alt, M. T., Fiedler, E., Rudmann, L., Ordonez, J. S., Ruther, P., and Stieglitz, T. (2016). Let there be light—optoprobes for neural implants. *Proc. IEEE* 105, 101–138. doi: 10.1109/JPROC.2016.2577518
- Altman, G. H., Diaz, F., Jakuba, C., Calabro, T., Horan, R. L., Chen, J., et al. (2003). Silk-based biomaterials. *Biomaterials* 24, 401–416. doi: 10.1016/S0142-9612(02)00353-8
- Altuna, A., Gabriel, G., de la Prida, L. M., Tijero, M., Guimerá, A., Berganzo, J., et al. (2010). SU-8-based microneedles for *in vitro* neural applications. *J. Micromech. Microeng.* 20:064014. doi: 10.1088/0960-1317/20/6/064014
- Amanat, N., James, N. L., and McKenzie, D. R. (2010). Welding methods for joining thermoplastic polymers for the hermetic enclosure of medical devices. *Med. Eng. Phys.* 32, 690–699. doi: 10.1016/j.medengphys.2010.04.011
- Anderson, J. M. (1988). Inflammatory response to implants. *ASAIO J.* 34, 101–107. doi: 10.1097/00002480-198804000-00005
- Anderson, J. M. (2001). Biological responses to materials. *Annu. Rev. Mater. Res.* 31, 81–110. doi: 10.1146/annurev.matsci.31.1.81
- Anderson, J. M., Rodriguez, A., and Chang, D. T. (2008). Foreign body reaction to biomaterials. *Semin. Immunol.* 20, 86–100. doi: 10.1016/j.smim.2007.11.004
- Andringa, A. M., Perrotta, A., de Peuter, K., Knoops, H. C., Kessels, W. M., and Creatore, M. (2015). Low-temperature plasma-assisted atomic layer deposition of silicon nitride moisture permeation barrier layers. *ACS Appl. Mater. Interfaces* 7, 22525–22532. doi: 10.1021/acsami.5b06801
- Anma, H., Yoshimoto, Y., Warashina, M., and Hatanaka, Y. (2001). Low temperature deposition of SiC thin films on polymer surface by plasma CVD. *Appl. Surf. Sci.* 175, 484–489. doi: 10.1016/S0169-4332(01)00127-1
- Ansaldo, A., Castagnola, E., Maggolini, E., Fadiga, L., and Ricci, D. (2011). Superior electrochemical performance of carbon nanotubes directly grown on sharp microelectrodes. *ACS Nano* 5, 2206–2214. doi: 10.1021/nn103445d
- Arcot Desai, S., Rolston, J. D., Guo, L., and Potter, S. M. (2010). Improving impedance of implantable microwire multi-electrode arrays by ultrasonic electroplating of durable platinum black. *Front. Neuroeng.* 3:5. doi: 10.3389/fneng.2010.00005
- Armani, D., Liu, C., and Aluru, N. (1999). “Re-configurable fluid circuits by PDMS elastomer micromachining,” in *Technical Digest. IEEE International MEMS 99 Conference. Twelfth IEEE International Conference on Micro Electro Mechanical Systems (Cat. No. 99CH36291)* (IEEE), 222–227. doi: 10.1109/MEMSYS.1999.746817
- Armano, A., and Agnello, S. (2019). Two-dimensional carbon: a review of synthesis methods, and electronic, optical, and vibrational properties of single-layer graphene. *C. J. Carbon Res.* 5:67. doi: 10.3390/c5040067
- Arrieta, M. P., Samper, M. D., Aldas, M., and López, J. (2017). On the use of PLA-PHB blends for sustainable food packaging applications. *Materials* 10:1008. doi: 10.3390/ma10091008
- Athanasios, K. A., Niederauer, G. G., and Agrawal, C. M. (1996). Sterilization, toxicity, biocompatibility and clinical applications of polylactic acid/polyglycolic acid copolymers. *Biomaterials* 17, 93–102. doi: 10.1016/0142-9612(96)85754-1
- Au, S. L. C., Chen, F. Y. B., Budgett, D. M., Malpas, S. C., Guild, S. J., and McCormick, D. (2019). Injection molded liquid crystal polymer package for chronic active implantable devices with application to an optogenetic stimulator. *IEEE Trans. Biomed. Eng.* 67, 1357–1365. doi: 10.1109/TBME.2019.2936577
- Axelevitch, A., Gorenstein, B., and Golan, G. (2012). Investigation of optical transmission in thin metal films. *Phys. Proc.* 32, 1–13. doi: 10.1016/j.phpro.2012.03.510
- Aydin, E. B., and Sezgin, M. K. (2017). Indium tin oxide (ITO): a promising material in biosensing technology. *TrAC Trends Anal. Chem.* 97, 309–315. doi: 10.1016/j.trac.2017.09.021
- Bae, W. J., Kim, K. S., Kim, S. J., Cho, H. J., Hong, S. H., Lee, J. Y., et al. (2014). AB222 comparison of biocompatibility between PDMS and PMMA as packaging materials for the intravesical implantable device: changes of macrophage and macrophage migratory inhibitory factor. *Transl. Androl. Urol.* 3(Suppl. 1):AB22. doi: 10.3978/j.issn.2223-4683.2014.s222
- Bagolini, A., Pakula, L., Scholtes, T. L. M., Pham, H. T. M., French, P. J., and Sarro, P. M. (2002). Polyimide sacrificial layer and novel materials for post-processing surface micromachining. *J. Micromech. Microeng.* 12:385. doi: 10.1088/0960-1317/12/4/306

- Bai, W., Shin, J., Fu, R., Kandela, I., Lu, D., Ni, X., et al. (2019). Bioresorbable photonic devices for the spectroscopic characterization of physiological status and neural activity. *Nat. Biomed. Eng.* 3, 644–654. doi: 10.1038/s41551-019-0435-y
- Bakonyi, P., Kumar, G., Nemestóthy, N., Lin, C. Y., and Béla-Bakó, K. (2013). Biohydrogen purification using a commercial polyimide membrane module: studying the effects of some process variables. *Int. J. Hydrogen Energy* 38, 15092–15099. doi: 10.1016/j.ijhydene.2013.09.133
- Balandin, A. A., Ghosh, S., Bao, W., Calizo, I., Teweldebrhan, D., Miao, F., et al. (2008). Superior thermal conductivity of single-layer graphene. *Nano Lett.* 8, 902–907. doi: 10.1021/nl0731872
- Bang, G., and Kim, S. W. (2012). Biodegradable poly (lactic acid)-based hybrid coating materials for food packaging films with gas barrier properties. *J. Ind. Eng. Chem.* 18, 1063–1068. doi: 10.1016/j.jiec.2011.12.004
- Bang, S. H. (2016). Improvement of NiMoNb to polyimide adhesion by inductively coupled nitrogen plasma treatment. *Appl. Surf. Sci.* 360, 553–558. doi: 10.1016/j.apsusc.2015.10.202
- Barakat, N. A., Abadir, M. F., Sheikh, F. A., Kanjwal, M. A., Park, S. J., and Kim, H. Y. (2010). Polymeric nanofibers containing solid nanoparticles prepared by electrospinning and their applications. *Chem. Eng. J.* 156, 487–495. doi: 10.1016/j.cej.2009.11.018
- Baranauskas, G., Maggolini, E., Castagnola, E., Ansaldo, A., Mazzoni, A., Angotzi, G. N., et al. (2011). Carbon nanotube composite coating of neural microelectrodes preferentially improves the multiunit signal-to-noise ratio. *J. Neural Eng.* 8:06013. doi: 10.1088/1741-2560/8/6/06013
- Barrese, J. C., Aceros, J., and Donoghue, J. P. (2016). Scanning electron microscopy of chronically implanted intracortical microelectrode arrays in non-human primates. *J. Neural Eng.* 13:26003. doi: 10.1088/1741-2560/13/2/026003
- Barrese, J. C., Rao, N., Paroo, K., Triebwasser, C., Vargas-Irwin, C., Franquemont, L., et al. (2013). Failure mode analysis of silicon-based intracortical microelectrode arrays in non-human primates. *J. Neural Eng.* 10:06014. doi: 10.1088/1741-2560/10/6/06014
- Bashandeh, K., Lee, J., Wu, Q., Li, Y., Wang, X., Shi, Y., et al. (2020). Mechanics and deformation of shape memory polymer kirigami microstructures. *Extreme Mech. Lett.* 39:100831. doi: 10.1016/j.eml.2020.100831
- Beattie, M. S., Farooqui, A. A., and Bresnahan, J. C. (2000). Review of current evidence for apoptosis after spinal cord injury. *J. Neurotrauma* 17, 915–925. doi: 10.1089/neu.2000.17.915
- Besleaga, C., Dumitru, V., Trinca, L. M., Popa, A.-C., Negri, C.-C., Kołodziejczyk, Ł., et al. (2017). Mechanical, corrosion and biological properties of room-temperature sputtered aluminum nitride films with dissimilar nanostructure. *Nanomaterials* 7:394. doi: 10.3390/nano7110394
- Bettinger, C. J., Ecker, M., Kozai, T. D. Y., Malliaras, G. G., Meng, E., and Voit, W. (2020). Recent advances in neural interfaces—materials chemistry to clinical translation. *MRS Bull.* 45, 655–668. doi: 10.1557/mrs.2020.195
- Beygi, M., Bentley, J. T., Frewin, C. L., Kuliasha, C. A., Takshi, A., Bernardin, E. K., et al. (2019). Fabrication of a monolithic implantable neural interface from cubic silicon carbide. *Micromachines* 10:430. doi: 10.3390/mi10070430
- Bi, X., Xie, T., Fan, B., Khan, W., Guo, Y., and Li, W. (2016). A flexible, micro-lens-coupled LED stimulator for optical neuromodulation. *IEEE Trans. Biomed. Circuits Syst.* 10, 972–978. doi: 10.1109/TBCAS.2016.2599406
- Black, B. J., Ecker, M., Stiller, A., Rihani, R., Danda, V. R., Reed, L., et al. (2018a). *In vitro* compatibility testing of thiol-ene/acrylate-based shape memory polymers for use in implantable neural interfaces. *J. Biomed. Mater. Res. A* 106, 2891–2898. doi: 10.1002/jbm.a.36478
- Black, B. J., Kanneganti, A., Joshi-Imre, A., Rihani, R., Chakraborty, B., Abbott, J., et al. (2018b). Chronic recording and electrochemical performance of Utah microelectrode arrays implanted in rat motor cortex. *J. Neurophysiol.* 120, 2083–2090. doi: 10.1152/jn.00181.2018
- Bobacka, J., Lewenstam, A., and Ivaska, A. (2000). Electrochemical impedance spectroscopy of oxidized poly (3, 4-ethylenedioxythiophene) film electrodes in aqueous solutions. *J. Electroanal. Chem.* 489, 17–27. doi: 10.1016/S0022-0728(00)00206-0
- Boehler, C., Oberueber, F., Schlabach, S., Stieglitz, T., and Asplund, M. (2017). Long-term stable adhesion for conducting polymers in biomedical applications: IrOx and nanostructured platinum solve the chronic challenge. *ACS Appl. Mater. Interfaces* 9, 189–197. doi: 10.1021/acsami.6b13468
- Boehler, C., Vieira, D. M., Egert, U., and Asplund, M. (2020). NanoPt—a nanostructured electrode coating for neural recording and microstimulation. *ACS Appl. Mater. Interfaces* 12, 14855–14865. doi: 10.1021/acsami.9b22798
- Bolotin, K. I., Sikes, K. J., Jiang, Z., Klima, M., Fudenberg, G., Hone, J., et al. (2008). Ultrahigh electron mobility in suspended graphene. *Solid State Commun.* 146, 351–355. doi: 10.1016/j.ssc.2008.02.024
- Booth, A. (1998). *Sterilization of Medical Devices*. Boca Raton, FL: CRC Press.
- Borton, D. A., Yin, M., Aceros, J., and Nurmikko, A. (2013). An implantable wireless neural interface for recording cortical circuit dynamics in moving primates. *J. Neural Eng.* 10:026010. doi: 10.1088/1741-2560/10/2/026010
- Brindley, G. S., Polkey, C. E., Rushton, D. N., and Cardozo, L. (1986). Sacral anterior root stimulators for bladder control in paraplegia: the first 50 cases. *J. Neurol. Neurosurg. Psychiatry* 49, 1104–1114. doi: 10.1136/jnnp.49.10.1104
- Bruls, R. J., Hintzen, H. T., De With, G., and Metselaar, R. (2001). The temperature dependence of the Young's modulus of MgSiN<sub>2</sub>, AlN and Si<sub>3</sub>N<sub>4</sub>. *J. Eur. Ceramic Soc.* 21, 263–268. doi: 10.1016/S0955-2219(00)00210-7
- Burton, A., Obaid, S. N., Vázquez-Guardado, A., Schmit, M. B., Stuart, T., Cai, L., et al. (2020). Wireless, battery-free subdermally implantable photometry systems for chronic recording of neural dynamics. *Proc. Natl. Acad. Sci. U.S.A.* 117, 2835–2845. doi: 10.1073/pnas.1920073117
- Cai, J., Ziemba, K. S., Smith, G. M., and Jin, Y. (2007). Evaluation of cellular organization and axonal regeneration through linear PLA foam implants in acute and chronic spinal cord injury. *J. Biomed. Mater. Res. A* 83, 512–520. doi: 10.1002/jbm.a.31296
- Caldwell, R., Street, M. G., Sharma, R., Takmakov, P., Baker, B., and Rieth, L. (2020). Characterization of parylene-C degradation mechanisms: *in vitro* reactive accelerated aging model compared to multiyear *in vivo* implantation. *Biomaterials* 232:119731. doi: 10.1016/j.biomaterials.2019.119731
- Cameron, T., Loeb, G. E., Peck, R. A., Schulman, J. H., Strojnik, P., and Troyk, P. R. (1997). Micromodular implants to provide electrical stimulation of paralyzed muscles and limbs. *IEEE Trans. Biomed. Eng.* 44, 781–790. doi: 10.1109/10.623047
- Cassar, I. R., Yu, C., Sambangi, J., Lee, C. D., Whalen, J. J. III., Petrossians, A., et al. (2019). Electrodeposited platinum-iridium coating improves *in vivo* recording performance of chronically implanted microelectrode arrays. *Biomaterials* 205, 120–132. doi: 10.1016/j.biomaterials.2019.03.017
- Castagnola, E., Marrani, M., Maggolini, E., Maita, F., Pazzini, L., Polese, D., et al. (2017). Recording high frequency neural signals using conformable and low-impedance ECoG electrodes arrays coated with PEDOT-PSS-PEG. *Adv. Sci. Technol.* 102, 77–85. doi: 10.4028/www.scientific.net/AST.102.77
- Castagnola, E., Vahidi, N. W., Nimbalkar, S., Rudraraju, S., Thielk, M., Zucchini, E., et al. (2018). *In vivo* dopamine detection and single unit recordings using intracortical glassy carbon microelectrode arrays. *MRS Adv.* 3, 1629–1634. doi: 10.1557/adv.2018.98
- Ceyssens, F., and Puers, R. (2015). Insulation lifetime improvement of polyimide thin film neural implants. *J. Neural Eng.* 12:54001. doi: 10.1088/1741-2560/12/5/054001
- Chapman, C. A. R., Wang, L., Chen, H., Garrison, J., Lein, P. J., and Seker, E. (2017). Nanoporous gold biointerfaces: modifying nanostructure to control neural cell coverage and enhance electrophysiological recording performance. *Adv. Funct. Mater.* 27:1604631. doi: 10.1002/adfm.201604631
- Chawla, N., Ganesh, V. V., and Wunsch, B. (2004). Three-dimensional (3D) microstructure visualization and finite element modeling of the mechanical behavior of SiC particle reinforced aluminum composites. *Scr. Mater.* 51, 161–165. doi: 10.1016/j.scriptamat.2004.03.043
- Chen, B., Zhang, B., Chen, C., Hu, J., Qi, J., He, T., et al. (2020). Penetrating glassy carbon neural electrode arrays for brain-machine interfaces. *Biomed. Microdevices* 22:43. doi: 10.1007/s10544-020-00498-0
- Chen, C., Ruan, S., Bai, X., Lin, C., Xie, C., and Lee, I.-S. (2019). Patterned iridium oxide film as neural electrode interface: biocompatibility and improved neurite outgrowth with electrical stimulation. *Mater. Sci. Eng. C* 103:109865. doi: 10.1016/j.msec.2019.109865
- Chen, C.-H., Lin, C.-T., Hsu, W.-L., Chang, Y.-C., Yeh, S.-R., Li, L.-J., et al. (2013). A flexible hydrophilic-modified graphene microprobe for neural and cardiac recording. *Nanomedicine* 9, 600–604. doi: 10.1016/j.nano.2012.12.004
- Chen, C.-H., Su, H.-C., Chuang, S.-C., Yen, S.-J., Chen, Y.-C., Lee, Y.-T., et al. (2010). Hydrophilic modification of neural microelectrode

- arrays based on multi-walled carbon nanotubes. *Nanotechnology* 21:485501. doi: 10.1088/0957-4484/21/48/485501
- Chen, L., Ilham, S. J., Guo, T., Emadi, S., and Feng, B. (2017a). *In vitro* multichannel single-unit recordings of action potentials from the mouse sciatic nerve. *Bioméd. Phys. Eng. Express* 3:45020. doi: 10.1088/2057-1976/aa7efa
- Chen, R., Canales, A., and Anikeeva, P. (2017b). Neural recording and modulation technologies. *Nat. Rev. Mater.* 2:16093. doi: 10.1038/natrevmats.2016.93
- Cheng, J., Zhu, G., Wu, L., Du, X., Zhang, H., Wolfrum, B., et al. (2013a). Photopatterning of self-assembled poly (ethylene) glycol monolayer for neuronal network fabrication. *J. Neurosci. Methods* 213, 196–203. doi: 10.1016/j.jneumeth.2012.12.020
- Cheng, M.-Y., Je, M., Tan, K. L., Tan, E. L., Lim, R., Yao, L., et al. (2013b). A low-profile three-dimensional neural probe array using a silicon lead transfer structure. *J. Micromech. Microeng.* 23:95013. doi: 10.1088/0960-1317/23/9/095013
- Chiang, C.-H., Won, S. M., Orsborn, A. L., Yu, K. J., Trumpis, M., Bent, B., et al. (2020). Development of a neural interface for high-definition, long-term recording in rodents and nonhuman primates. *Sci. Transl. Med.* 12:eay4682. doi: 10.1126/scitranslmed.aay4682
- Cho, S. Y., Lee, M. E., Choi, Y., and Jin, H. J. (2014). Cellulose nanofiber-reinforced silk fibroin composite film with high transparency. *Fibers Polymers* 15, 215–219. doi: 10.1007/s12221-014-0215-y
- Choi, Y. S., Koo, J., Lee, Y. J., Lee, G., Avila, R., Ying, H., et al. (2020). Biodegradable polyanhydrides as encapsulation layers for transient electronics. *Adv. Funct. Mater.* 30:2000941. doi: 10.1002/adfm.202000941
- Christensen, M. B., Pearce, S. M., Ledbetter, N. M., Warren, D. J., Clark, G. A., and Tresco, P. A. (2014). The foreign body response to the Utah slant electrode array in the rat sciatic nerve. *Acta Biomater.* 10, 4650–4660. doi: 10.1016/j.actbio.2014.07.010
- Chu, X., Wang, K., Tao, J., Li, S., Ji, S., and Ye, C. (2019). Tackling the stability issues of silver nanowire transparent conductive films through FeCl<sub>3</sub> dilute solution treatment. *Nanomaterials* 9:533. doi: 10.3390/nano9040533
- Chung, T., Wang, J. Q., Wang, J., Cao, B., Li, Y., and Pang, S. W. (2015). Electrode modifications to lower electrode impedance and improve neural signal recording sensitivity. *J. Neural Eng.* 12:56018. doi: 10.1088/1741-2560/12/5/056018
- Chung, J. E., Joo, H. R., Smyth, C. N., Fan, J. L., Geaghan-Breiner, C., Liang, H., et al. (2019). Chronic implantation of multiple flexible polymer electrode arrays. *J. Vis. Exp.* 4:e59957. doi: 10.3791/59957
- Cogan, S. F., Edell, D. J., Guzelian, A. A., Ping Liu, Y., and Edell, R. (2003). Plasma-enhanced chemical vapor deposited silicon carbide as an implantable dielectric coating. *J. Biomed. Mater. Res. A* 67, 856–867. doi: 10.1002/jbma.a.10152
- Cogan, S. F., Guzelian, A. A., Agnew, W. F., Yuen, T. G. H., and McCreery, D. B. (2004). Over-pulsing degrades activated iridium oxide films used for intracortical neural stimulation. *J. Neurosci. Methods* 137, 141–150. doi: 10.1016/j.jneumeth.2004.02.019
- Cogan, S. F., Troyk, P. R., Ehrlich, J., and Plante, T. D. (2005). *In vitro* comparison of the charge-injection limits of activated iridium oxide (AIROF) and platinum-iridium microelectrodes. *IEEE Trans. Biomed. Eng.* 52, 1612–1614. doi: 10.1109/TBME.2005.851503
- Colas, A., and Curtis, J. (2004). Silicone biomaterials: history and chemistry. *Biomater. Sci.* 2, 80–85.
- Connolly, A. T., Vetter, R. J., Hetke, J. F., Teplitzky, B. A., Kipke, D. R., Pellinen, D. S., et al. (2015). A novel lead design for modulation and sensing of deep brain structures. *IEEE Trans. Biomed. Eng.* 63, 148–157. doi: 10.1109/TBME.2015.2492921
- Costello, S., Desmulliez, M. P., and McCracken, S. (2012). Review of test methods used for the measurement of hermeticity in packages containing small cavities. *IEEE Trans. Compon. Packaging Manuf. Technol.* 2, 430–438. doi: 10.1109/TCPMT.2011.2176122
- Cui, X., Lee, V. A., Raphael, Y., Wiler, J. A., Hetke, J. F., Anderson, D. J., et al. (2001). Surface modification of neural recording electrodes with conducting polymer/biomolecule blends. *J. Biomed. Mater. Res.* 56, 261–272. doi: 10.1002/1097-4636(200108)56:2<261::AID-JBM1094>3.0.CO;2-I
- Cziple, F. A., and Marques, A. J. V. (2008). *Biopolymers Versus Synthetic Polymers*. Resita: Eftimie Murgu University.
- Dagdeviren, C., Hwang, S., Su, Y., Kim, S., Cheng, H., Gur, O., et al. (2013). Transient, biocompatible electronics and energy harvesters based on ZnO. *Small* 9, 3398–3404. doi: 10.1002/sml.201300146
- Dai, X., Zhou, W., Gao, T., Liu, J., and Lieber, C. M. (2016). Three-dimensional mapping and regulation of action potential propagation in nanoelectronics-innervated tissues. *Nat. Nanotechnol.* 11, 776–782. doi: 10.1038/nnano.2016.96
- De la Oliva, N., Mueller, M., Stieglitz, T., Navarro, X., and Del Valle, J. (2018). On the use of Parylene C polymer as substrate for peripheral nerve electrodes. *Sci. Rep.* 8:5965. doi: 10.1038/s41598-018-24502-z
- De Vittorio, M., Martiradonna, L., and Assad, J. (eds.). (2014). *Nanotechnology and Neuroscience: Nano-Electronic, Photonic and Mechanical Neuronal Interfacing*. New York, NY: Springer.
- Deku, F., Joshi-Imre, A., Mertiri, A., Gardner, T. J., and Cogan, S. F. (2018). Electrodeposited iridium oxide on carbon fiber ultramicroelectrodes for neural recording and stimulation. *J. Electrochem. Soc.* 165:D375. doi: 10.1149/2.0401809jes
- Deng, L., Eichhorn, S. J., Kao, C.-C., and Young, R. J. (2011). The effective Young's modulus of carbon nanotubes in composites. *ACS Appl. Mater. Interfaces* 3, 433–440. doi: 10.1021/am1010145
- Denisov, A., and Yeatman, E. (2010). “Ultrasonic vs. inductive power delivery for miniature biomedical implants,” in *2010 International Conference on Body Sensor Networks* (Singapore: IEEE), 84–89.
- Dhler, D., Kang, J., Cooper, C. B., Tok, J. B. H., Rupp, H., Binder, W. H., et al. (2020). Tuning the self-healing response of poly (dimethylsiloxane)-based elastomers. *ACS Appl. Polymer Mater.* 2, 4127–4139. doi: 10.1021/acsapm.0c00755
- Diaz, A. F., and Hall, B. (1983). Mechanical properties of electrochemically prepared polypyrrole films. *IBM J. Res. Dev.* 27, 342–347. doi: 10.1147/rd.274.0342
- Diaz-Botia, C. A., Luna, L. E., Neely, R. M., Chamanzar, M., Carraro, C., Carmena, J. M., et al. (2017). A silicon carbide array for electrocorticography and peripheral nerve recording. *J. Neural Eng.* 14:56006. doi: 10.1088/1741-2552/aa7698
- Dijk, G., Rutz, A. L., and Malliaras, G. G. (2020). Stability of PEDOT: PSS-coated gold electrodes in cell culture conditions. *Adv. Mater. Technol.* 5:1900662. doi: 10.1002/admt.201900662
- Donaldson, N., and Brindley, G. S. (2016). “The historical foundations of bionics,” in *Neurobionics Biomedical Engineering Neural Prostheses* (Hoboken, NJ: John Wiley Sons, Inc.).
- Driscoll, N., Maleski, K., Richardson, A. G., Murphy, B., Anasori, B., Lucas, T. H., et al. (2020). Fabrication of Ti<sub>3</sub>C<sub>2</sub> MXene microelectrode arrays for *in vivo* neural recording. *J. Vis. Exp.* 12:e60741. doi: 10.3791/60741
- Driscoll, N., Richardson, A. G., Maleski, K., Anasori, B., Adelewe, O., Lelyukh, P., et al. (2018). Two-dimensional Ti<sub>3</sub>C<sub>2</sub> MXene for high-resolution neural interfaces. *ACS Nano* 12, 10419–10429. doi: 10.1021/acsnano.8b06014
- Du, Z. J., Luo, X., Weaver, C. L., and Cui, X. T. (2015). Poly (3, 4-ethylenedioxythiophene)-ionic liquid coating improves neural recording and stimulation functionality of MEAs. *J. Mater. Chem. C* 3, 6515–6524. doi: 10.1039/C5TC00145E
- Eatemadi, A., Daraee, H., Karimkhanloo, H., Kouhi, M., Zarghami, N., Akbarzadeh, A., et al. (2014). Carbon nanotubes: properties, synthesis, purification, and medical applications. *Nanoscale Res. Lett.* 9:393. doi: 10.1186/1556-276X-9-393
- Ecker, M., Danda, V., Shoffstall, A. J., Mahmood, S. F., Joshi-Imre, A., Frewin, C. L., et al. (2017). Sterilization of thiol-ene/acrylate based shape memory polymers for biomedical applications. *Macromol. Mater. Eng.* 302:1600331. doi: 10.1002/mame.201600331
- Elechiguerra, J. L., Larios-Lopez, L., Liu, C., Garcia-Gutierrez, D., Camacho-Bragado, A., and Yacaman, M. J. (2005). Corrosion at the nanoscale: the case of silver nanowires and nanoparticles. *Chem. Mater.* 17, 6042–6052. doi: 10.1021/cm051532n
- Eles, J. R., Vazquez, A. L., Kozai, T. D. Y., and Cui, X. T. (2018). *In vivo* imaging of neuronal calcium during electrode implantation: spatial and temporal mapping of damage and recovery. *Biomaterials* 174, 79–94. doi: 10.1016/j.biomaterials.2018.04.043
- Ely, K. (2000). Issues in hermetic sealing of medical products. *Med. Device Diagnostic Ind.* 22, 186–195.



- Fahlteich, J., Schönberger, W., Fahland, M., and Schiller, N. (2011). Characterization of reactively sputtered permeation barrier materials on polymer substrates. *Surf. Coat. Technol.* 205, S141–S144. doi: 10.1016/j.surfcoat.2011.01.045
- Fairfield, J. A. (2018). Nanostructured materials for neural electrical interfaces. *Adv. Funct. Mater.* 28:1701145. doi: 10.1002/adfm.201701145
- Falco, A., Matarese, B., Feyen, P., Benfenati, F., Lugli, P., and de Mello, J. C. (2016). Investigation of the stability and biocompatibility of commonly used electrode materials in organic neurooptoelectronics. *IEEE Trans. Nanotechnol.* 15, 746–753. doi: 10.1109/TNANO.2016.2536946
- Fan, B., Rusinek, C. A., Thompson, C. H., Setien, M., Guo, Y., Rechenberg, R., et al. (2020). Flexible, diamond-based microelectrodes fabricated using the diamond growth side for neural sensing. *Microsyst. Nanoeng.* 6:42. doi: 10.1038/s41378-020-0155-1
- Fan, B., Zhu, Y., Rechenberg, R., Rusinek, C. A., Becker, M. F., and Li, W. (2017). Large-scale, all polycrystalline diamond structures transferred onto flexible Parylene-C films for neurotransmitter sensing. *Lab Chip* 17, 3159–3167. doi: 10.1039/C7LC00229G
- Fang, Y., Li, X., and Fang, Y. (2015). Organic bioelectronics for neural interfaces. *J. Mater. Chem. C* 3, 6424–6430. doi: 10.1039/C5TC00569H
- Farraro, R., and McLellan, R. B. (1977). Temperature dependence of the Young's modulus and shear modulus of pure nickel, platinum, and molybdenum. *Metall. Trans. A* 8, 1563–1565. doi: 10.1007/BF02644859
- Farzamfar, S., Salehi, M., Tavangar, S. M., Verdi, J., Mansouri, K., Ai, A., et al. (2019). A novel polycaprolactone/carbon nanofiber composite as a conductive neural guidance channel: an *in vitro* and *in vivo* study. *Prog. Biomater.* 8, 239–248. doi: 10.1007/s40204-019-00121-3
- Fattahi, P., Yang, G., Kim, G., and Abidian, M. R. (2014). A review of organic and inorganic biomaterials for neural interfaces. *Adv. Mater.* 26, 1846–1885. doi: 10.1002/adma.201304496
- Feigin, V. L., Nichols, E., Alam, T., Bannick, M. S., Beghi, E., Blake, N., et al. (2019). Global, regional, and national burden of neurological disorders, 1990–2016: a systematic analysis for the global burden of disease study 2016. *Lancet Neurol.* 18, 459–480. doi: 10.1016/S1474-4422(18)30499-X
- Fekete, Z., and Pongrácz, A. (2017). Multifunctional soft implants to monitor and control neural activity in the central and peripheral nervous system: a review. *Sens. Actuat. B Chem.* 243, 1214–1223. doi: 10.1016/j.snb.2016.12.096
- Felix, S. H., Shah, K. G., Tolosa, V. M., Sheth, H. J., Tooker, A. C., Delima, T. L., et al. (2013). Insertion of flexible neural probes using rigid stiffeners attached with biodissolvable adhesive. *J. Visual. Exp.* 2013:e50609. doi: 10.3791/50609
- Feron, K., Lim, R., Sherwood, C., Keynes, A., Brichta, A., and Dastoor, P. C. (2018). Organic bioelectronics: materials and biocompatibility. *Int. J. Mol. Sci.* 19:2382. doi: 10.3390/ijms19082382
- Ferro, M. D., and Melosh, N. A. (2018). Electronic and ionic materials for neurointerfaces. *Adv. Funct. Mater.* 28:1704335. doi: 10.1002/adfm.201704335
- Flodberg, G., Hellman, A., Hedenqvist, M. S., Sadiku, E. R., and Gedde, U. W. (2000). Barrier properties of blends based on liquid crystalline polymers and polyethylene. *Polymer Eng. Sci.* 40, 1969–1978. doi: 10.1002/pen.11328
- Fong, Y., Moldawer, L. L., Shires, G. T., and Lowry, S. F. (1990). The biologic characteristics of cytokines and their implication in surgical injury. *Surg. Gynecol. Obstet.* 170, 363–378.
- Forde, M., and Ridgely, P. (2006). “Implantable cardiac pacemakers,” in *Medical Devices and Systems Biomed Engineering Handbook*, 3rd Edn (Boca Raton, FL: CRC Press; Taylor Fr. Group).
- Franck, D., Gil, E. S., Adam, R. M., Kaplan, D. L., Chung, Y. G., Estrada, C. R. Jr., et al. (2013). Evaluation of silk biomaterials in combination with extracellular matrix coatings for bladder tissue engineering with primary and pluripotent cells. *PLoS ONE* 8:e56237. doi: 10.1371/journal.pone.0056237
- Frazier, A. B. (1995). Recent applications of polyimide to micromachining technology. *IEEE Trans. Ind. Electron.* 42, 442–448. doi: 10.1109/41.464605
- Frederick, S. (2007). *Biocompatibility of Materials in Medical Devices*. Wiley Encyclopedia of Chemical Biology. Hoboken, NJ: Wiley.
- Furtado, D., Björnmalm, M., Ayton, S., Bush, A. I., Kempe, K., and Caruso, F. (2018). Overcoming the blood–brain barrier: the role of nanomaterials in treating neurological diseases. *Adv. Mater.* 30:1801362. doi: 10.1002/adma.201801362
- Ganji, M., Elthakeb, A. T., Tanaka, A., Gilja, V., Halgren, E., and Dayeh, S. A. (2017). Scaling effects on the electrochemical performance of poly (3, 4-ethylenedioxythiophene (PEDOT), Au, and Pt for electrocorticography recording. *Adv. Funct. Mater.* 27:1703018. doi: 10.1002/adfm.201703018
- Gao, R., Strehle, S., Tian, B., Cohen-Karni, T., Xie, P., Duan, X., et al. (2012). Outside looking in: nanotube transistor intracellular sensors. *Nano Lett.* 12, 3329–3333. doi: 10.1021/nl301623p
- Garrett, D. J., Tong, W., Simpson, D. A., and Meffin, H. (2016). Diamond for neural interfacing: a review. *Carbon* 102, 437–454. doi: 10.1016/j.carbon.2016.02.059
- Ghasemi-Mobarakeh, L., Prabhakaran, M. P., Morshed, M., Nasr-Esfahani, M. H., and Ramakrishna, S. (2009). Electrical stimulation of nerve cells using conductive nanofibrous scaffolds for nerve tissue engineering. *Tissue Eng. A* 15, 3605–3619. doi: 10.1089/ten.tea.2008.0689
- Ghazavi, A., Maeng, J., Black, M., Salvi, S., and Cogan, S. F. (2020). Electrochemical characteristics of ultramicro-dimensioned SIROF electrodes for neural stimulation and recording. *J. Neural Eng.* 17:016022. doi: 10.1088/1741-2552/ab52ab
- Gilletti, A., and Muthuswamy, J. (2006). Brain micromotion around implants in the rodent somatosensory cortex. *J. Neural Eng.* 3, 189–195. doi: 10.1088/1741-2560/3/3/001
- Gillis, W. F., Lissandrello, C. A., Shen, J., Pearre, B. W., Mertiri, A., Deku, F., et al. (2018). Carbon fiber on polyimide ultra-microelectrodes. *J. Neural Eng.* 15:016010. doi: 10.1088/1741-2552/aa8c88
- Golberg, L. (2018). *Hazard Assessment of Ethylene Oxide*. Boca Raton, FL: CRC Press.
- Gong, Y., Liu, W., Wang, R., Brauer, M. H., Zheng, K., and Li, W. (2020). Stability performance analysis of various packaging materials and coating strategies for chronic neural implants under accelerated, reactive aging tests. *Micromachines* 11:810. doi: 10.3390/mi11090810
- Grace, J. M., and Gerenser, L. J. (2003). Plasma treatment of polymers. *J. Disper. Sci. Technol.* 24, 305–341. doi: 10.1081/DIS-120021793
- Green, R., and Abidian, M. R. (2015). Conducting polymers for neural prosthetic and neural interface applications. *Adv. Mater.* 27, 7620–7637. doi: 10.1002/adma.201501810
- Greenhouse, H. (1999). *Hermeticity of Electronic Packages*. Norwich; New York, NY: Noyes Publication; William Andrew Publishing LLC.
- Greenhouse, H., Lowry, R. K., and Romenesko, B. (2011). *Hermeticity of Electronic Packages*. William Andrew.
- Griffith, R. W., and Humphrey, D. R. (2006). Long-term gliosis around chronically implanted platinum electrodes in the Rhesus macaque motor cortex. *Neurosci. Lett.* 406, 81–86. doi: 10.1016/j.neulet.2006.07.018
- Gu, Z., Xie, H., Huang, C., Li, L., and Yu, X. (2013). Preparation of chitosan/silk fibroin blending membrane fixed with alginate dialdehyde for wound dressing. *Int. J. Biol. Macromol.* 58, 121–126. doi: 10.1016/j.ijbiomac.2013.03.059
- Guimard, N. K., Gomez, N., and Schmidt, C. E. (2007). Conducting polymers in biomedical engineering. *Prog. Polym. Sci.* 32, 876–921. doi: 10.1016/j.progpolymsci.2007.05.012
- Guithounts, G., Markowitz, J. E., Liberti, W. A., and Gardner, T. J. (2013). A carbon-fiber electrode array for long-term neural recording. *J. Neural Eng.* 10:046016. doi: 10.1088/1741-2560/10/4/046016
- Guo, Y., Jiang, S., Grena, B. J. B., Kimbrough, I. F., Thompson, E. G., Fink, Y., et al. (2017). Polymer composite with carbon nanofibers aligned during thermal drawing as a microelectrode for chronic neural interfaces. *ACS Nano* 11, 6574–6585. doi: 10.1021/acsnano.6b07550
- Gutierrez-Heredia, G., Rodriguez-Lopez, O., Garcia-Sandoval, A., and Voit, W. E. (2017). Highly stable indium-gallium-zinc-oxide thin-film transistors on deformable softening polymer substrates. *Adv. Electron. Mater.* 3:1700221. doi: 10.1002/aelm.201700221
- Halliwell, B. (1992). Reactive oxygen species and the central nervous system. *J. Neurochem.* 59, 1609–1623. doi: 10.1111/j.1471-4159.1992.tb10990.x
- Hanson, S., Lalor, P. A., Niemi, S. M., Northup, S. J., Ratner, B. D., et al. (1996). “Testing biomaterials,” in *Biomaterials Science*, eds B. D. Ratner, A. S. Hoffman, F. J. Schoen, and J. E. Lemons (New York, NY: Elsevier), 215–242.
- Hashemi Noshahr, F., Nabavi, M., and Sawan, M. (2020). Multi-channel neural recording implants: a review. *Sensors* 20:904. doi: 10.3390/s20030904
- Hassler, C., Boretius, T., and Stieglitz, T. (2011). Polymers for neural implants. *J. Polym. Sci. B Polym. Phys.* 49, 18–33. doi: 10.1002/polb.22169

- He, X., Zhang, F., and Zhang, X. (2009). Effects of parylene C layer on high power light emitting diodes. *Appl. Surf. Sci.* 256, 6–11. doi: 10.1016/j.apsusc.2009.03.085
- Hébert, C., Cottance, M., Degardin, J., Scorsone, E., Rousseau, L., Lissorgues, G., et al. (2016). Monitoring the evolution of boron doped porous diamond electrode on flexible retinal implant by OCT and *in vivo* impedance spectroscopy. *Mater. Sci. Eng. C* 69, 77–84. doi: 10.1016/j.msec.2016.06.032
- Hejazi, M. A., Tong, W., Stacey, A., Sun, S. H., Yunzab, M., Almasi, A., et al. (2020). High fidelity bidirectional neural interfacing with carbon fiber microelectrodes coated with boron-doped carbon nanowalls: an acute study. *Adv. Funct. Mater.* 2006101. doi: 10.1002/adfm.202006101
- Henle, C., Hassler, C., Kohler, F., Schuettler, M., and Stieglitz, T. (2011a). “Mechanical characterization of neural electrodes based on PDMS-parylene C-PDMS sandwiched system,” in *2011 Annual International Conference of the IEEE Engineering in Medicine and Biology Society* (Boston, MA: IEEE).
- Henle, C., Raab, M., Cordeiro, J. G., Doostkam, S., Schulze-Bonhage, A., Stieglitz, T., et al. (2011b). First long term *in vivo* study on subdurally implanted micro-ECOG electrodes, manufactured with a novel laser technology. *Biomed. Microdevices* 13, 59–68. doi: 10.1007/s10544-010-9471-9
- Heo, D. N., Yang, D. H., Lee, J. B., Bae, M. S., Park, H. N., and Kwon, I. K. (2012). “Cell fouling resistance of PEG-grafted polyimide film for neural implant applications,” in *Third International Conference on Smart Materials and Nanotechnology in Engineering* (Shenzhen: International Society for Optics and Photonics).
- Herreras, O. (2016). Local field potentials: myths and misunderstandings. *Front. Neural Circuits* 10:101. doi: 10.3389/fncir.2016.00101
- Hetke, J. F., Anderson, D. J., Finn, W. E., and LoPresti, P. G. (2002). “Silicon microelectrodes for extracellular recording,” in *Handbook Neuroprosthetic Methods*, eds W. E. Finn and P. G. LoPresti (Boca Raton, FL: CRC Press), 163–191.
- Hong, G., Fu, T. M., Qiao, M., Viveros, R. D., Yang, X., Zhou, T., et al. (2018). A method for single-neuron chronic recording from the retina in awake mice. *Science* 360, 1447–1451. doi: 10.1126/science.aas9160
- Hong, G., and Lieber, C. M. (2019). Novel electrode technologies for neural recordings. *Nat. Rev. Neurosci.* 20, 330–345. doi: 10.1038/s41583-019-0140-6
- Hopkins, A. M., De Laporte, L., Tortelli, F., Spedden, E., Staii, C., Atherton, T. J., et al. (2013). Silk hydrogels as soft substrates for neural tissue engineering. *Adv. Funct. Mater.* 23, 5140–5149. doi: 10.1002/adfm.201300435
- House, P. A., MacDonald, J. D., Tresco, P. A., and Normann, R. A. (2006). Acute microelectrode array implantation into human neocortex: preliminary technique and histological considerations. *Neurosurg. Focus* 20:E4. doi: 10.3171/foc.2006.20.5.5
- Hsu, J.-M., Tathireddy, P., Rieth, L., Normann, A. R., and Solzbacher, F. (2007). Characterization of a-SiC<sub>x</sub>: H thin films as an encapsulation material for integrated silicon based neural interface devices. *Thin Solid Films* 516, 34–41. doi: 10.1016/j.tsf.2007.04.050
- Hubbell Jr., W. H., Brandt, H., and Munir, Z. A. (1975). Transient and steady-state water vapor permeation through polymer films. *J. Polymer Sci. Polymer Phys. Edn.* 13, 493–507. doi: 10.1002/pol.1975.180130304
- Hudak, E. M., Kumsa, D. W., Martin, H. B., and Mortimer, J. T. (2017). Electron transfer processes occurring on platinum neural stimulating electrodes: calculated charge-storage capacities are inaccessible during applied stimulation. *J. Neural Eng.* 14:46012. doi: 10.1088/1741-2552/aa6945
- Huerta, F. L., García, R. M. W., González, L. G., May, A. L. H., Arriaga, W. C., Vega, R., et al. (2019). “Biocompatibility and surface properties of hydrogenated amorphous silicon-germanium thin films prepared by LF-PECVD,” in *IOP Conference Series: Materials Science and Engineering* (Beijing: IOP Publishing).
- Hutzler, M., Lambacher, A., Eversmann, B., Jenkner, M., Thewes, R., and Fromherz, P. (2006). High-resolution multitransistor array recording of electrical field potentials in cultured brain slices. *J. Neurophysiol.* 96, 1638–1645. doi: 10.1152/jn.00347.2006
- Hwang, G. T., Im, D., Lee, S. E., Lee, J., Koo, M., Park, S. Y., et al. (2013). *In vivo* silicon-based flexible radio frequency integrated circuits monolithically encapsulated with biocompatible liquid crystal polymers. *ACS Nano* 7, 4545–4553. doi: 10.1021/nn401246y
- Hwang, S.-W., Tao, H., Kim, D.-H., Cheng, H., Song, J.-K., Rill, E., et al. (2012). A physically transient form of silicon electronics. *Science* 337, 1640–1644. doi: 10.1126/science.1226325
- Jaccodine, R. J., and Schlegel, W. A. (1966). Measurement of strains at Si-SiO<sub>2</sub> interface. *J. Appl. Phys.* 37, 2429–2434. doi: 10.1063/1.1708831
- Jackson, N., Sridharan, A., Anand, S., Baker, M., Okandan, M., and Muthuswamy, J. (2010). Long-term neural recordings using MEMS based moveable microelectrodes in the brain. *Front. Neuroeng.* 3:10. doi: 10.3389/fneng.2010.00010
- Jeong, J., Bae, S. H., Seo, J. M., Chung, H., and Kim, S. J. (2016). Long-term evaluation of a liquid crystal polymer (LCP)-based retinal prosthesis. *J. Neural Eng.* 13:025004. doi: 10.1088/1741-2560/13/2/025004
- Jeong, J.-W., McCall, J. G., Shin, G., Zhang, Y., Al-Hasani, R., Kim, M., et al. (2015). Wireless optofluidic systems for programmable *in vivo* pharmacology and optogenetics. *Cell* 162, 662–674. doi: 10.1016/j.cell.2015.06.058
- Jiang, D., Hulbert, D. M., Anselmi-Tamburini, U., Ng, T., Land, D., and Mukherjee, A. K. (2008). Optically transparent polycrystalline Al<sub>2</sub>O<sub>3</sub> produced by spark plasma sintering. *J. Am. Ceramic Soc.* 91, 151–154. doi: 10.1111/j.1551-2916.2007.02086.x
- Jiang, G., and Zhou, D. D. (2009). “Technology advances and challenges in hermetic packaging for implantable medical devices,” in *Implantable Neural Prostheses* 2, eds D. Zhou and E. Greenbaum (New York, NY: Springer), 27–61.
- Jiang, X., Bian, G.-B., and Tian, Z. (2019). Removal of artifacts from EEG signals: a review. *Sensors* 19:987. doi: 10.3390/s19050987
- Jiang, Y., and Tian, B. (2018). Inorganic semiconductor biointerfaces. *Nat. Rev. Mater.* 3, 473–490. doi: 10.1038/s41578-018-0062-3
- Joshi-Imre, A., Black, B. J., Abbott, J., Kanneganti, A., Rihani, R., Chakraborty, B., et al. (2019). Chronic recording and electrochemical performance of amorphous silicon carbide-coated Utah electrode arrays implanted in rat motor cortex. *J. Neural Eng.* 16:046006. doi: 10.1088/1741-2552/ab1bc8
- Joung, Y.-H. (2013). Development of implantable medical devices: from an engineering perspective. *Int. Neurol.* 17:98. doi: 10.5213/inj.2013.17.3.98
- Juarez-Hernandez, L. J., Cornella, N., Pasquardini, L., Battistoni, S., Vidalino, L., Vanzetti, L., et al. (2016). Bio-hybrid interfaces to study neuromorphic functionalities: new multidisciplinary evidences of cell viability on poly (aniline)(PANI), a semiconductor polymer with memristive properties. *Biophys. Chem.* 208, 40–47. doi: 10.1016/j.bpc.2015.07.008
- Jun, J. J., Steinmetz, N. A., Siegle, J. H., Denman, D. J., Bauza, M., Barbarits, B., et al. (2017). Fully integrated silicon probes for high-density recording of neural activity. *Nature* 551, 232–236. doi: 10.1038/nature24636
- Justin, G., and Guiseppe-Elie, A. (2010). Electroconductive blends of poly (HEMA-co-PEGMA-co-HMMA-co-SPMA) and poly (Py-co-PyBA): *in vitro* biocompatibility. *J. Bioact. Compat. Polym.* 25, 121–140. doi: 10.1177/0883911509350660
- Kahouli, A., Sylvestre, A., Jomni, F., Yangui, B., and Legrand, J. (2012). Ac-conductivity and dielectric relaxations above glass transition temperature for parylene-C thin films. *Appl. Phys. A* 106, 909–913. doi: 10.1007/s00339-011-6706-4
- Kampasi, K., Alameda, J., Sahota, S., Hernandez, J., Patra, S., and Haque, R. (2020). “Design and microfabrication strategies for thin-film, flexible optical neural implant,” in *2020 42nd Annual International Conference of the IEEE Engineering in Medicine & Biology Society (EMBC)*.
- Kang, S.-K., Murphy, R. K. J., Hwang, S.-W., Lee, S. M., Harburg, D. V., Krueger, N. A., et al. (2016). Bioresorbable silicon electronic sensors for the brain. *Nature* 530, 71–76. doi: 10.1038/nature16492
- Kanth, S. T., and Ray, S. (2020). Electroencephalogram (EEG) is highly informative in primate visual cortex. *J. Neurosci.* 40, 2430–2444. doi: 10.1523/JNEUROSCI.1368-19.2020
- Kato, Y., Saito, I., Hoshino, T., Suzuki, T., and Mabuchi, K. (2006). “Preliminary study of multichannel flexible neural probes coated with hybrid biodegradable polymer,” in *2006 International Conference of the IEEE Engineering in Medicine and Biology Society* (New York, NY).
- Keefer, E. W., Botterman, B. R., Romero, M. I., Rossi, A. F., and Gross, G. W. (2008). Carbon nanotube coating improves neuronal recordings. *Nat. Nanotechnol.* 3, 434–439. doi: 10.1038/nnano.2008.174
- Keller, P. E., and Kouzes, R. T. (2017). *Water Vapor Permeation in Plastics* (No. PNNL-26070). Richland, WA: Pacific Northwest National Lab (PNNL).

- Khalifa, A., Karimi, Y., Stanačević, M., and Etienne-Cummings, R. (2017). "Novel integration and packaging concepts of highly miniaturized inductively powered neural implants," in *2017 39th Annual International Conference of the IEEE Engineering in Medicine and Biology Society* (Jeju Island: EMBC).
- Khodagholy, D., Gelinas, J. N., Thesen, T., Doyle, W., Devinsky, O., Malliaras, G. G., et al. (2015). NeuroGrid: recording action potentials from the surface of the brain. *Nat. Neurosci.* 18, 310–315. doi: 10.1038/nn.3905
- Khodagholy, D., Gelinas, J. N., Zhao, Z., Yeh, M., Long, M., Greenlee, J. D., et al. (2016). Organic electronics for high-resolution electrocorticography of the human brain. *Sci. Adv.* 2:e1601027. doi: 10.1126/sciadv.1601027
- Kim, B. J., and Meng, E. (2015). Review of polymer MEMS micromachining. *J. Micromech. Microeng.* 26:13001. doi: 10.1088/0960-1317/26/1/013001
- Kim, D.-H., Viventi, J., Amsden, J. J., Xiao, J., Vigeland, L., Kim, Y.-S., et al. (2010a). Dissolvable films of silk fibroin for ultrathin conformal bio-integrated electronics. *Nat. Mater.* 9, 511–517. doi: 10.1038/nmat2745
- Kim, D. H., Lu, N., Ma, R., Kim, Y. S., Kim, R. H., Wang, S., et al. (2011). Epidermal electronics. *Science* 333, 838–843. doi: 10.1126/science.1206157
- Kim, G. H., Kim, K., Lee, E., An, T., Choi, W., Lim, G., et al. (2018). Recent progress on microelectrodes in neural interfaces. *Materials* 11:1995. doi: 10.3390/ma11101995
- Kim, J.-H., Kang, G., Nam, Y., and Choi, Y.-K. (2010b). Surface-modified microelectrode array with flake nanostructure for neural recording and stimulation. *Nanotechnology* 21:85303. doi: 10.1088/0957-4484/21/8/085303
- Kim, J.-M., Im, C., and Lee, W. R. (2017). Plateau-shaped flexible polymer microelectrode array for neural recording. *Polymers* 9:690. doi: 10.3390/polym9120690
- Kim, S., Bhandari, R., Klein, M., Negi, S., Rieth, L., Tathireddy, P., et al. (2009). Integrated wireless neural interface based on the Utah electrode array. *Biomed. Microdevices* 11, 453–466. doi: 10.1007/s10544-008-9251-y
- Kim, S. B., Kim, Y. J., Yoon, T. L., Park, S. A., Cho, I. H., Kim, E. J., et al. (2004). The characteristics of a hydroxyapatite–chitosan–PMMA bone cement. *Biomaterials* 25, 5715–5723. doi: 10.1016/j.biomaterials.2004.01.022
- Kim, S. J., Choi, B., Kim, K. S., Bae, W. J., Hong, S. H., Lee, J. Y., et al. (2015). The potential role of polymethyl methacrylate as a new packaging material for the implantable medical device in the bladder. *Biomed Res. Int.* 2015:852456. doi: 10.1155/2015/852456
- Kim, T. I., McCall, J. G., Jung, Y. H., Huang, X., Siuda, E. R., Li, Y., et al. (2013). Injectable, cellular-scale optoelectronics with applications for wireless optogenetics. *Science* 340, 211–216. doi: 10.1126/science.1232437
- Kinloch, A. J. (2012). *Adhesion and Adhesives: Science and Technology*. Dordrecht: Springer Science & Business Media.
- Kino, H., Fukushima, T., and Tanaka, T. (2018). Study of Al-doped ZnO transparent stimulus electrode for fully implantable retinal prosthesis with three-dimensionally stacked retinal prosthesis chip. *Sensors Mater.* 30, 225–234. doi: 10.18494/SAM.2018.1741
- Kireev, D., Zadorozhnyi, I., Qiu, T., Sarik, D., Brings, F., Wu, T., et al. (2016). "Graphene field-effect transistors for *in vitro* and *ex vivo* recordings," in *IEEE Transactions on Nanotechnology*, Vol. 16 (IEEE), 140–147.
- Ko, E. H., Kim, H. J., Lee, S. M., Kim, T. W., and Kim, H. K. (2017). Stretchable Ag electrodes with mechanically tunable optical transmittance on wavy-patterned PDMS substrates. *Sci. Rep.* 7:46739. doi: 10.1038/srep46739
- Kojabad, Z. D., Shojaosadati, S. A., Firoozabadi, S. M., and Hamed, S. (2019). Polypyrrole nanotube modified by gold nanoparticles for improving the neural microelectrodes. *J. Solid State Electrochem.* 23, 1533–1539. doi: 10.1007/s10008-019-04245-1
- Kostarelos, K., Vincent, M., Hebert, C., and Garrido, J. A. (2017). Graphene in the design and engineering of next-generation neural interfaces. *Adv. Mater.* 29:1700909. doi: 10.1002/adma.201700909
- Kozai, T. D. Y., Alba, N. A., Zhang, H., Kotov, N. A., Gaunt, R. A., and Cui, X. T. (2014). "Nanostructured coatings for improved charge delivery to neurons," in *Nanotechnology and Neuroscience: Nano-Electronic, Photonic and Mechanical Neuronal Interfacing*, eds M. De Vittorio, L. Martiradonna, and J. Assad (New York, NY: Springer), 71–134.
- Kozai, T. D. Y., Du, Z., Gugel, Z. V., Smith, M. A., Chase, S. M., Bodily, L. M., et al. (2015). Comprehensive chronic laminar single-unit, multi-unit, and local field potential recording performance with planar single shank electrode arrays. *J. Neurosci. Methods* 242, 15–40. doi: 10.1016/j.jneumeth.2014.12.010
- Kozai, T. D. Y., Langhals, N. B., Patel, P. R., Deng, X., Zhang, H., Smith, K. L., et al. (2012). Ultrasmall implantable composite microelectrodes with bioactive surfaces for chronic neural interfaces. *Nat. Mater.* 11, 1065–1073. doi: 10.1038/nmat3468
- Kumar, R. (2010). Parylene HT®: a high temperature vapor phase polymer for electronics applications. *Addit. Pap. Present.* 2010, 108–113. doi: 10.4071/HITEC-RKumar-TP13
- Kuo, J. T., Kim, B. J., Hara, S. A., Lee, C. D., Gutierrez, C. A., Hoang, T. Q., et al. (2013). Novel flexible parylene neural probe with 3D sheath structure for enhancing tissue integration. *Lab Chip* 13, 554–561. doi: 10.1039/C2LC40935F
- Kweon, H., Ha, H. C., Um, I. C., and Park, Y. H. (2001). Physical properties of silk fibroin/chitosan blend films. *J. Appl. Polym. Sci.* 80, 928–934. doi: 10.1002/app.1172
- Kwon, K. Y., Sirowatka, B., Weber, A., and Li, W. (2013). Opto-μECoG array: a hybrid neural interface with transparent μECoG electrode array and integrated LEDs for optogenetics. *IEEE Trans. Biomed. Circuits Syst.* 7, 593–600. doi: 10.1109/TBCAS.2013.2282318
- Lacour, S. P., Benmerah, S., Tarte, E., FitzGerald, J., Serra, J., McMahon, S., et al. (2010). Flexible and stretchable micro-electrodes for *in vitro* and *in vivo* neural interfaces. *Med. Biol. Eng. Comp.* 48, 945–954. doi: 10.1007/s11517-010-0644-8
- Lacour, S. P., Courtine, G., and Guck, J. (2016). Materials and technologies for soft implantable neuroprostheses. *Nat. Rev. Mater.* 1:16063. doi: 10.1038/natrevmats.2016.63
- Lago, N., and Cester, A. (2017). Flexible and organic neural interfaces: a review. *Appl. Sci.* 7:1292. doi: 10.3390/app7121292
- Landi, G., Henninger, M., del Mauro, A. D. G., Borriello, C., Di Luccio, T., and Neitzert, H. C. (2013). Investigation of the optical characteristics of a combination of InP/ZnS-quantum dots with MWCNTs in a PMMA matrix. *Optic. Mater.* 35, 2490–2495. doi: 10.1016/j.optmat.2013.07.007
- Lawrence, J. G., Berhan, L. M., and Nadarajah, A. (2008). Elastic properties and morphology of individual carbon nanofibers. *ACS Nano* 2, 1230–1236. doi: 10.1021/nn7004427
- Le, T.-H., Kim, Y., and Yoon, H. (2017). Electrical and electrochemical properties of conducting polymers. *Polymers* 9:150. doi: 10.3390/polym9040150
- Lecomte, A., Degache, A., Descamps, E., Dahan, L., and Bergaud, C. (2017). *In vitro* and *in vivo* biostability assessment of chronically-implanted Parylene C neural sensors. *Sens. Actuat. B Chem.* 251, 1001–1008. doi: 10.1016/j.snb.2017.05.057
- Lecomte, A., Descamps, E., and Bergaud, C. (2018). A review on mechanical considerations for chronically-implanted neural probes. *J. Neural Eng.* 15:031001. doi: 10.1088/1741-2552/aa8b4f
- Ledochowitsch, P., Olivero, E., Blanche, T., and Maharbiz, M. M. (2011). "A transparent μECoG array for simultaneous recording and optogenetic stimulation," in *2011 Annual International Conference of the IEEE Engineering in Medicine and Biology Society* (Boston, MA: IEEE), 2937–2940.
- Lee, J., Ozden, I., Song, Y.-K., and Nurmikko, A. V. (2015). Transparent intracortical microprobe array for simultaneous spatiotemporal optical stimulation and multichannel electrical recording. *Nat. Methods* 12, 1157–1162. doi: 10.1038/nmeth.3620
- Lee, J. H., Kim, H., Kim, J. H., and Lee, S.-H. (2016a). Soft implantable microelectrodes for future medicine: prosthetics, neural signal recording and neuromodulation. *Lab Chip* 16, 959–976. doi: 10.1039/C5LC00842E
- Lee, J. M., Hong, G., Lin, D., Schuhmann Jr, T. G., Sullivan, A. T., Viveros, R. D., et al. (2019). Nanoenabled direct contact interfacing of syringe-injectable mesh electronics. *Nano Lett.* 19, 5818–5826. doi: 10.1021/acs.nanolett.9b03019
- Lee, S., Kanno, S., Kino, H., and Tanaka, T. (2013b). Study of insertion characteristics of Si neural probe with sharpened tip for minimally invasive insertion to brain. *JPN. J. Appl. Phys.* 52:04CL04. doi: 10.7567/JJAP.52.04CL04
- Lee, S. K., Kim, H., and Shim, B. S. (2013a). Graphene: an emerging material for biological tissue engineering. *Carbon Lett.* 14, 63–75. doi: 10.5714/CL.2013.14.2.063
- Lee, U., Yoo, C.-J., Kim, Y.-J., and Yoo, Y.-M. (2016b). Cytotoxicity of gold nanoparticles in human neural precursor cells and rat cerebral cortex. *J. Biosci. Bioeng.* 121, 341–344. doi: 10.1016/j.jbiosc.2015.07.004
- Lee, Y. J., Kim, H., Kang, J. Y., Do, S. H., and Lee, S. H. (2017a). Biofunctionalization of nerve interface via biocompatible polymer-roughened Pt black on cuff electrode for chronic recording. *Adv. Healthc. Mater.* 6:1601022. doi: 10.1002/adhm.201601022



- Lee, Y. K., Yu, K. J., Song, E., Barati Farimani, A., Vitale, F., Xie, Z., et al. (2017b). Dissolution of monocrystalline silicon nanomembranes and their use as encapsulation layers and electrical interfaces in water-soluble electronics. *ACS Nano* 11, 12562–12572. doi: 10.1021/acsnano.7b06697
- Lei, X., Kane, S., Cogan, S., Lorach, H., Galambos, L., Huie, P., et al. (2016). SiC protective coating for photovoltaic retinal prosthesis. *J. Neural Eng.* 13:46016. doi: 10.1088/1741-2560/13/4/046016
- Lendlein, A., and Kelch, S. (2002). Shape-memory polymers. *Angew. Chemie Int. Ed.* 41, 2034–2057. doi: 10.1002/1521-3773(20020617)41:12<;AID-ANIE2034>;3.0.CO;2-M
- Lewitus, D., Smith, K. L., Shain, W., and Kohn, J. (2011). Ultrafast resorbing polymers for use as carriers for cortical neural probes. *Acta Biomater.* 7, 2483–2491. doi: 10.1016/j.actbio.2011.02.027
- Lewitus, D., Vogelstein, R. J., Zhen, G., Choi, Y.-S., Kohn, J., Harshbarger, S., et al. (2010). Designing tyrosine-derived polycarbonate polymers for biodegradable regenerative type neural interface capable of neural recording. *IEEE Trans. Neural Syst. Rehabil. Eng.* 19, 204–212. doi: 10.1109/TNSRE.2010.2098047
- Li, J., Song, E., Chiang, C.-H., Yu, K. J., Koo, J., Du, H., et al. (2018a). Conductively coupled flexible silicon electronic systems for chronic neural electrophysiology. *Proc. Natl. Acad. Sci. U.S.A.* 115, E9542–E9549. doi: 10.1073/pnas.1813187115
- Li, R., Wang, L., Kong, D., and Yin, L. (2018b). Recent progress on biodegradable materials and transient electronics. *Bioact. Mater.* 3, 322–333. doi: 10.1016/j.bioactmat.2017.12.001
- Li, T.-C., and Chang, R.-C. (2014). Improving the performance of ITO thin films by coating PEDOT: PSS. *Int. J. Precis. Eng. Manuf. Technol.* 1, 329–334. doi: 10.1007/s40684-014-0041-0
- Li, W., Long, Y., Liu, Y., Long, K., Liu, S., Wang, Z., et al. (2014). Fabrication and characterization of chitosan–collagen crosslinked membranes for corneal tissue engineering. *J. Biomater. Sci. Polymer Edn.* 25, 1962–1972. doi: 10.1080/09205063.2014.965996
- Liang, K., Grebowicz, J., Valles, E., Karasz, F. E., and MacKnight, W. J. (1992). Thermal and rheological properties of miscible polyethersulfone/polyimide blends. *J. Polym. Sci. B Polym. Phys.* 30, 465–476. doi: 10.1002/polb.1992.090300506
- Lin, C.-M., Lee, Y.-T., Yeh, S.-R., and Fang, W. (2009). Flexible carbon nanotubes electrode for neural recording. *Biosens. Bioelectron.* 24, 2791–2797. doi: 10.1016/j.bios.2009.02.005
- Liu, X., Lu, Y., Iseri, E., Ren, C., Liu, H., Komiyama, T., et al. (2017b). “Transparent artifact-free graphene electrodes for compact closed-loop optogenetics systems,” in *2017 IEEE International Electron Devices Meeting (IEDM)* (San Francisco, CA).
- Liu, R., Chen, R., Elthakeb, A. T., Lee, S. H., Hinckley, S., Khraiche, M. L., et al. (2017a). High density individually addressable nanowire arrays record intracellular activity from primary rodent and human stem cell derived neurons. *Nano Lett.* 17, 2757–2764. doi: 10.1021/acs.nanolett.6b04752
- Liu, Z. M., Xu, Z. K., Wang, J. Q., Wu, J., and Fu, J. J. (2004). Surface modification of polypropylene microfiltration membranes by graft polymerization of N-vinyl-2-pyrrolidone. *Eur. Polymer J.* 40, 2077–2087. doi: 10.1016/j.eurpolymj.2004.05.020
- Loeb, G. E., Richmond, F. J. R., Chapin, J. K., Moxon, K. A., and Gaal, G. (2000). “BION implants for therapeutic and functional electrical stimulation,” in *Neural Prostheses for Restoration of Sensory and Motor Function*, eds J. K. Chapin and K. A. Moxon (Boca Raton, FL: CRC Press).
- Loeb, G. E., Peck, R. A., and Martyniuk, J. (1995). Toward the ultimate metal microelectrode. *J. Neurosci. Methods* 63, 175–183. doi: 10.1016/0165-0270(95)00107-7
- Lu, D., Yan, Y., Avila, R., Kandela, I., Stepien, I., Seo, M. H., et al. (2020). Bioresorbable, wireless, passive sensors as temporary implants for monitoring regional body temperature. *Adv. Healthcare Mater.* 9:2000942. doi: 10.1002/adhm.202000942
- Lu, L., Fu, X., Liew, Y., Zhang, Y., Zhao, S., Xu, Z., et al. (2019). Soft and MRI compatible neural electrodes from carbon nanotube fibers. *Nano Lett.* 19, 1577–1586. doi: 10.1021/acs.nanolett.8b04456
- Lu, L., Yang, Z., Meacham, K., Cvetkovic, C., Corbin, E. A., Vázquez-Guardado, A., et al. (2018). Biodegradable monocrystalline silicon photovoltaic microcells as power supplies for transient biomedical implants. *Adv. Energy Mater.* 8:1703035. doi: 10.1002/aenm.201703035
- Ma, S., Li, Y., Sun, X., Yu, X., and Jin, Y. (2009). “Study of polyimide as sacrificial layer with O<sub>2</sub> plasma releasing for its application in MEMS capacitive FPA fabrication,” in *2009 International Conference on Electronic Packaging Technology & High Density Packaging* (Beijing: IEEE).
- Madou, M. J. (2018). *Fundamentals of Microfabrication and Nanotechnology, Three-Volume Set*. Boca Raton, FL: CRC Press.
- Maiolo, L., Polese, D., and Convertino, A. (2019). The rise of flexible electronics in neuroscience, from materials selection to *in vitro* and *in vivo* applications. *Adv. Phys. X* 4:1664319. doi: 10.1080/23746149.2019.1664319
- Mao, D., Morley, J., Zhang, Z., Donnelly, M., and Xu, G. (2018). High-yield passive Si photodiode array towards optical neural recording. *IEEE Electron Device Lett.* 39, 524–527. doi: 10.1109/LED.2018.2802451
- Marcon, L., and Boukherroub, R. (2014). “Biocompatibility of semiconducting silicon nanowires,” in *Semiconducting Silicon Nanowires for Biomedical Applications* ed. J. L. Coffey (New York, NY: Elsevier), 62–85.
- Marin, C., and Fernández, E. (2010). Biocompatibility of intracortical microelectrodes: current status and future prospects. *Front. Neuroeng.* 3:8. doi: 10.3389/fneng.2010.00008
- Márton, G., Tóth, E. Z., Wittner, L., Fiáth, R., Pinke, D., Orbán, G., et al. (2020). The neural tissue around SU-8 implants: a quantitative *in vivo* biocompatibility study. *Mater. Sci. Eng. C* 112:110870. doi: 10.1016/j.msec.2020.110870
- Massey, T. L., Santacruz, S. R., Hou, J. F., Pister, K. S. J., Carmena, J. M., and Maharbiz, M. M. (2019). A high-density carbon fiber neural recording array technology. *J. Neural Eng.* 16:16024. doi: 10.1088/1741-2552/aae8d9
- Mata, A., Fleischman, A. J., and Roy, S. (2005). Characterization of polydimethylsiloxane (PDMS) properties for biomedical micro/nanosystems. *Biomed. Microdevices* 7, 281–293. doi: 10.1007/s10544-005-6070-2
- McDonald, M., Monaco, A., Vahidpour, F., Haenen, K., Giugliano, M., and Nesladek, M. (2017). Diamond microelectrode arrays for *in vitro* neuronal recordings. *MRS Commun.* 7, 683–690. doi: 10.1557/mrc.2017.62
- McEvoy, B., and Rowan, N. J. (2019). Terminal sterilization of medical devices using vaporized hydrogen peroxide: a review of current methods and emerging opportunities. *J. Appl. Microbiol.* 127, 1403–1420. doi: 10.1111/jam.14412
- McFadden, J. T. (1969). Metallurgical principles in neurosurgery. *J. Neurosurg.* 31, 373–385. doi: 10.3171/jns.1969.31.4.0373
- Mehta, A., and Isayev, A. I. (1991). Rheology, morphology, and mechanical characteristics of poly (etherether ketone)-liquid crystal polymer blends. *Polymer Eng. Sci.* 31, 971–980. doi: 10.1002/pen.760311307
- Meijs, S., Alcaide, M., Sørensen, C., McDonald, M., Sørensen, S., Rechendorff, K., et al. (2016). Biofouling resistance of boron-doped diamond neural stimulation electrodes is superior to titanium nitride electrodes *in vivo*. *J. Neural Eng.* 13:56011. doi: 10.1088/1741-2560/13/5/056011
- Meinel, L., and Kaplan, D. L. (2012). Silk constructs for delivery of musculoskeletal therapeutics. *Adv. Drug Deliv. Rev.* 64, 1111–1122. doi: 10.1016/j.addr.2012.03.016
- Mendes, G. C. C., Brandao, T. R. S., and Silva, C. L. M. (2007). Ethylene oxide sterilization of medical devices: a review. *Am. J. Infect. Control* 35, 574–581. doi: 10.1016/j.ajic.2006.10.014
- Messler, R. W. (2004). *Joining of Materials and Structures: from Pragmatic Process to Enabling Technology*. Oxford: Butterworth-Heinemann.
- Mestais, C. S., Charvet, G., Sauter-Starace, F., Foerster, M., Ratel, D., and Benabid, A. L. (2014). WIMAGINE: wireless 64-channel ECoG recording implant for long term clinical applications. *IEEE Trans. Neural Syst. Rehabil. Eng.* 23, 10–21. doi: 10.1109/TNSRE.2014.2333541
- Metz, S. J., van de Ven, W. J. C., Potreck, J., Mulder, M. H. V., and Wessling, M. (2005). Transport of water vapor and inert gas mixtures through highly selective and highly permeable polymer membranes. *J. Memb. Sci.* 251, 29–41. doi: 10.1016/j.memsci.2004.08.036
- Meyer, C., Stenberg, L., Gonzalez-Perez, F., Wrobel, S., Ronchi, G., Udina, E., et al. (2016). Chitosan-film enhanced chitosan nerve guides for long-distance regeneration of peripheral nerves. *Biomaterials* 76, 33–51. doi: 10.1016/j.biomaterials.2015.10.040
- Mian, A., Newaz, G., Vendra, L., Rahman, N., Georgiev, D. G., Auner, G., et al. (2005). Laser bonded microjoints between titanium and polyimide for applications in medical implants. *J. Mater. Sci. Mater. Med.* 16, 229–237. doi: 10.1007/s10856-005-6684-1



- Minev, I. R., Musienko, P., Hirsch, A., Barraud, Q., Wenger, N., Moraud, E. M., et al. (2015). Electronic dura mater for long-term multimodal neural interfaces. *Science* 347, 159–163. doi: 10.1126/science.1260318
- Moore, S. K. (2019). Shape-shifting electrodes for the brain: Materials that have memory could make medical implants easier to place-[News]. *IEEE Spectr.* 56, 10–11. doi: 10.1109/MSPEC.2019.8635803
- Morales, J. M. H., and Clément, C. (2018). “Technical challenges of active implantable medical devices for neurotechnology,” in *2018 IEEE CPMT Symposium Japan* (Kyoto).
- Murphy, B. A. (2008). *A Biocompatibility Study of Aluminum Nitride Packaging for Cortical Implants*. Detroit: Wayne State University.
- Muskovich, M., and Bettinger, C. J. (2012). Biomaterials-based electronics: polymers and interfaces for biology and medicine. *Adv. Healthcare Mater.* 1, 248–266. doi: 10.1002/adhm.201200071
- Nagane, S., Sitarik, P., Wu, Y., Baugh, Q., Chhatre, S., Lee, J., et al. (2020). Functionalized polythiophene copolymers for electronic biomedical devices. *MRS Adv.* 5, 943–956. doi: 10.1557/adv.2020.3
- Nakai, M., Niinomi, M., Zhao, X., and Zhao, X. (2011). Self-adjustment of Young's modulus in biomedical titanium alloys during orthopaedic operation. *Mater. Lett.* 65, 688–690. doi: 10.1016/j.matlet.2010.11.006
- Nam, Y. S., Yoon, J. J., Lee, J. G., and Park, T. G. (1999). Adhesion behaviours of hepatocytes cultured onto biodegradable polymer surface modified by alkali hydrolysis process. *J. Biomater. Sci. Polymer Edn.* 10, 1145–1158. doi: 10.1163/156856299X00801
- Navarro, X., Krueger, T. B., Lago, N., Micera, S., Stieglitz, T., and Dario, P. (2005). A critical review of interfaces with the peripheral nervous system for the control of neuroprostheses and hybrid bionic systems. *J. Peripher. Nerv. Syst.* 10, 229–258. doi: 10.1111/j.1085-9489.2005.10303.x
- Neto, J. P., Baião, P., Lopes, G., Frazão, J., Nogueira, J., Fortunato, E., et al. (2018). Does impedance matter when recording spikes with polytrodes? *Front. Neurosci.* 12:715. doi: 10.3389/fnins.2018.00715
- Niaounakis, M. (2015). *Biopolymers: Applications and Trends*. Norwich, NY: William Andrew.
- Nick, C., Quednau, S., Sarwar, R., Schlaak, H. F., and Thielemann, C. (2014). High aspect ratio gold nanopillars on microelectrodes for neural interfaces. *Microsyst. Technol.* 20, 1849–1857. doi: 10.1007/s00542-013-1958-x
- Oh, S. J., Song, J. K., and Kim, S. J. (2003). Neural interface with a silicon neural probe in the advancement of microtechnology. *Biotechnol. Bioprocess Eng.* 8, 252–256. doi: 10.1007/BF02942274
- Oh, Y. S., Hamagami, J. I., Watanabe, Y., Takata, M., and Yanagida, H. (1993). A novel palladium thin film hydrogen-detector. *J. Ceramic Soc. Japan* 101, 618–620. doi: 10.2109/jcersj.101.618
- Onuki, Y., Bhardwaj, U., Papadimitrakopoulos, F., and Burgess, D. J. (2008). A review of the biocompatibility of implantable devices: current challenges to overcome foreign body response. *J. Diabetes Sci. Technol.* 2, 1003–1115. doi: 10.1177/193229680800200610
- Ordóñez, J. S., Boehler, C., Schuettler, M., and Stieglitz, T. (2013). “Silicone rubber and thin-film polyimide for hybrid neural interfaces—a MEMS-based adhesion promotion technique,” in *2013 6th International IEEE/EMBS Conference on Neural Engineering* (San Diego, CA: NER).
- Ordóñez, J., Schuettler, M., Boehler, C., Boretius, T., and Stieglitz, T. (2012). Thin films and microelectrode arrays for neuroprosthetics. *MRS Bull.* 37, 590–598. doi: 10.1557/mrs.2012.117
- Pal, R. K., Farghaly, A. A., Wang, C., Collinson, M. M., Kundu, S. C., and Yadavalli, V. K. (2016). Conducting polymer-silk biocomposites for flexible and biodegradable electrochemical sensors. *Biosens. Bioelectron.* 81, 294–302. doi: 10.1016/j.bios.2016.03.010
- Pan, A. I., Lin, M.-H., Chung, H.-W., Chen, H., Yeh, S.-R., Chuang, Y.-J., et al. (2016). Direct-growth carbon nanotubes on 3D structural microelectrodes for electrophysiological recording. *Analyst* 141, 279–284. doi: 10.1039/C5AN01750E
- Park, D.-W., Brodnick, S. K., Ness, J. P., Atry, F., Krugner-Higby, L., Sandberg, A., et al. (2016). Fabrication and utility of a transparent graphene neural electrode array for electrophysiology, *in vivo* imaging, and optogenetics. *Nat. Protoc.* 11, 2201–2222. doi: 10.1038/nprot.2016.127
- Park, D.-W., Ness, J. P., Brodnick, S. K., Esquibel, C., Novello, J., Atry, F., et al. (2018). Electrical neural stimulation and simultaneous *in vivo* monitoring with transparent graphene electrode arrays implanted in GCaMP6f mice. *ACS Nano* 12, 148–157. doi: 10.1021/acsnano.7b04321
- Park, D.-W., Schendel, A. A., Mikael, S., Brodnick, S. K., Richner, T. J., Ness, J. P., et al. (2014). Graphene-based carbon-layered electrode array technology for neural imaging and optogenetic applications. *Nat. Commun.* 5:5258. doi: 10.1038/ncomms6258
- Passeri, D., Alippi, A., Bettucci, A., Rossi, M., Tamburri, E., and Terranova, M. L. (2011). Indentation modulus and hardness of polyaniline thin films by atomic force microscopy. *Synth. Met.* 161, 7–12. doi: 10.1016/j.synthmet.2010.10.027
- Patel, P. R., Popov, P., Mohebi, A., Hamid, A., Pettibone, J., Roossien, D., et al. (2017). “Carbon fiber electrode array for the detection of electrophysiological and dopaminergic activity,” in *232nd ECS Meeting (October 1-5, 2017)* (National Harbor, MD: ECS).
- Patel, N. R., and Gohil, P. P. (2012). A review on biomaterials: scope, applications & human anatomy significance. *Int. J. Emerg. Technol. Adv. Eng.* 2, 91–101.
- Patel, P. R., Na, K., Zhang, H., Kozai, T. D. Y., Kotov, N. A., Yoon, E., et al. (2015). Insertion of linear 8.4  $\mu\text{m}$  diameter 16 channel carbon fiber electrode arrays for single unit recordings. *J. Neural Eng.* 12:046009. doi: 10.1088/1741-2560/12/4/046009
- Patel, P. R., Zhang, H., Robbins, M. T., Nofar, J. B., Marshall, S. P., Kobylarek, M. J., et al. (2016). Chronic *in vivo* stability assessment of carbon fiber microelectrode arrays. *J. Neural Eng.* 13:66002. doi: 10.1088/1741-2560/13/6/066002
- Patil, A. C., and Thakor, N. V. (2016). Implantable neurotechnologies: a review of micro- and nanoelectrodes for neural recording. *Med. Biol. Eng. Comput.* 54, 23–44. doi: 10.1007/s11517-015-1430-4
- Patil, A. C., Xiong, Z., and Thakor, N. V. (2020). Toward nontransient silk bioelectronics: engineering silk fibroin for bionic links. *Small Methods* 4:2000274. doi: 10.1002/smt.202000274
- Patolsky, F., Timko, B. P., Yu, G., Fang, Y., Greytak, A. B., Zheng, G. et al. (2006). Detection, stimulation, and inhibition of neuronal signals with high-density nanowire transistor arrays. *Science* 313, 1100–1104.
- Patrick, E., Orazem, M. E., Sanchez, J. C., and Nishida, T. (2011). Corrosion of tungsten microelectrodes used in neural recording applications. *J. Neurosci. Methods* 198, 158–171. doi: 10.1016/j.jneumeth.2011.03.012
- Peled, A., Pevzner, A., Soroka, H. P., and Patolsky, F. (2014). Morphological and chemical stability of silicon nanostructures and their molecular overlayers under physiological conditions: towards long-term implantable nanoelectronic biosensors. *J. Nanobiotechnol.* 12:7. doi: 10.1186/1477-3155-12-7
- Perotto, G., Zhang, Y., Naskar, D., Patel, N., Kaplan, D. L., Kundu, S. C., et al. (2017). The optical properties of regenerated silk fibroin films obtained from different sources. *Appl. Phys. Lett.* 111:103702. doi: 10.1063/1.4998950
- Phan, H. P., Zhong, Y., Nguyen, T. K., Park, Y., Dinh, T., Song, E., et al. (2019). Long-lived, transferred crystalline silicon carbide nanomembranes for implantable flexible electronics. *ACS Nano* 13, 11572–11581. doi: 10.1021/acsnano.9b05168
- Piconi, C., and Maccauro, G. (1999). Zirconia as a ceramic biomaterial. *Biomaterials* 20, 1–25. doi: 10.1016/S0142-9612(98)00010-6
- Pierce, G. F., Mustoe, T. A., Altmann, B. W., Deuel, T. F., and Thomason, A. (1991). Role of platelet-derived growth factor in wound healing. *J. Cell. Biochem.* 45, 319–326. doi: 10.1002/jcb.240450403
- Porrizzo, R., Bellani, S., Luzio, A., Lanzarini, E., Caironi, M., and Antognazza, M. R. (2014). Improving mobility and electrochemical stability of a water-gated polymer field-effect transistor. *Org. Electron.* 15, 2126–2134. doi: 10.1016/j.orgel.2014.06.002
- Pranti, A. S., Schander, A., Bödecker, A., and Lang, W. (2017). Highly stable PEDOT: PSS coating on gold microelectrodes with improved charge injection capacity for chronic neural stimulation. *Proceedings* 1:492. doi: 10.3390/proceedings1040492
- Pranti, A. S., Schander, A., Bödecker, A., and Lang, W. (2018). PEDOT: PSS coating on gold microelectrodes with excellent stability and high charge injection capacity for chronic neural interfaces. *Sens. Actuators B Chem.* 275, 382–393. doi: 10.1016/j.snb.2018.08.007
- Prasad, A., Xue, Q. S., Sankar, V., Nishida, T., Shaw, G., Streit, W. J., et al. (2012). Comprehensive characterization and failure modes of tungsten microwire arrays in chronic neural implants. *J. Neural Eng.* 9:056015. doi: 10.1088/1741-2560/9/5/056015
- Qiang, Y., Artoni, P., Seo, K. J., Culaclii, S., Hogan, V., Zhao, X., et al. (2018). Transparent arrays of bilayer-nanomesh microelectrodes for simultaneous

- electrophysiology and two-photon imaging in the brain. *Sci. Adv.* 4:eaat0626. doi: 10.1126/sciadv.aat0626
- Rao, S. S., Han, N., and Winter, J. O. (2011). Polylysine-modified PEG-based hydrogels to enhance the neuro-electrode interface. *J. Biomater. Sci. Polym. Ed.* 22, 611–625. doi: 10.1163/092050610X488241
- Ratner, B. D., and Bryant, S. J. (2004). Biomaterials: where we have been and where we are going. *Annu. Rev. Biomed. Eng.* 6, 41–75. doi: 10.1146/annurev.bioeng.6.040803.140027
- Rebelo, R., Fernandes, M., and Figueiro, R. (2017). Biopolymers in medical implants: a brief review. *Procedia Eng.* 200, 236–243. doi: 10.1016/j.proeng.2017.07.034
- Ren, L., Xu, S., Gao, J., Lin, Z., Chen, Z., Liu, B., et al. (2018). Fabrication of flexible microneedle array electrodes for wearable bio-signal recording. *Sensors* 18:1191. doi: 10.3390/s18041191
- Rivnay, J., Inal, S., Collins, B. A., Sessolo, M., Stavrinidou, E., Strakosas, X., et al. (2016). Structural control of mixed ionic and electronic transport in conducting polymers. *Nat. Commun.* 7:11287. doi: 10.1038/ncomms11287
- Rivnay, J., Wang, H., Fenno, L., Deisseroth, K., and Malliaras, G. G. (2017). Next-generation probes, particles, and proteins for neural interfacing. *Sci. Adv.* 3:e1601649. doi: 10.1126/sciadv.1601649
- Robinson, J. T., Jorgolli, M., Shalek, A. K., Yoon, M.-H., Gertner, R. S., and Park, H. (2012). Vertical nanowire electrode arrays as a scalable platform for intracellular interfacing to neuronal circuits. *Nat. Nanotechnol.* 7, 180–184. doi: 10.1038/nnano.2011.249
- Rodger, D. C., Fong, A. J., Li, W., Ameri, H., Ahuja, A. K., Gutierrez, C., et al. (2008). Flexible parylene-based multielectrode array technology for high-density neural stimulation and recording. *Sens. Actuat. B Chem.* 132, 449–460. doi: 10.1016/j.snb.2007.10.069
- Rogers, J. A., Someya, T., and Huang, Y. (2010). Materials and mechanics for stretchable electronics. *Science* 327, 1603–1607. doi: 10.1126/science.1182383
- Rousche, P. J., Pellinen, D. S., Pivin, D. P., Williams, J. C., Vetter, R. J., and Kipke, D. R. (2001). Flexible polyimide-based intracortical electrode arrays with bioactive capability. *IEEE Trans. Biomed. Eng.* 48, 361–371. doi: 10.1109/10.914800
- Rubehn, B., and Stieglitz, T. (2010). *In vitro* evaluation of the long-term stability of polyimide as a material for neural implants. *Biomaterials* 31, 3449–3458. doi: 10.1016/j.biomaterials.2010.01.053
- Russell, C., Roche, A. D., and Chakrabarty, S. (2019). Peripheral nerve bionic interface: a review of electrodes. *Int. J. Intell. Robot. Appl.* 3, 11–18. doi: 10.1007/s41315-019-00086-3
- Saddow, S. E., Frewin, C. L., Araujo Cespedes, F., Gazziro, M., Bernadin, E., and Thomas, S. (2016). SiC for biomedical applications. *Mater. Sci. Forum* 858, 1010–1014. doi: 10.4028/www.scientific.net/MSF.858.1010
- Saifuddin, N., Raziah, A. Z., and Junizah, A. R. (2013). Carbon nanotubes: a review on structure and their interaction with proteins. *J. Chem.* 2013:676815. doi: 10.1155/2013/676815
- Saracino, E., Maiolo, L., Polese, D., Semprini, M., Borrachero-Conejo, A. I., Gasparetto, J., et al. (2020). A glial-silicon nanowire electrode junction enabling differentiation and noninvasive recording of slow oscillations from primary astrocytes. *Adv. Biosyst.* 4:1900264. doi: 10.1002/adbi.201900264
- Saunier, V., Flahaut, E., Blatché, C., Bergaud, C., and Maziz, A. (2020). Carbon nanofiber-PEDOT composite films as novel microelectrode for neural interfaces and biosensing. *Biosens. Bioelectron.* 165:112413. doi: 10.1016/j.bios.2020.112413
- Savage, W. (2013). *Joining of Advanced Materials*. New York, NY: Elsevier.
- Scarano, A., Assenza, B., Piattelli, M., Iezzi, G., Leghissa, G. C., Quaranta, A., et al. (2005). A 16-year study of the microgap between 272 human titanium implants and their abutments. *J. Oral Implantol.* 31, 269–275. doi: 10.1563/753.1
- Schander, A., Stemmann, H., Tolstosheeva, E., Roese, R., Biefeld, V., Kempen, L., et al. (2016). Design and fabrication of novel multi-channel floating neural probes for intracortical chronic recording. *Sens. Actuat. A Phys.* 247, 125–135. doi: 10.1016/j.sna.2016.05.034
- Schaubroeck, D., Verplanck, R., Cauwe, M., Cuyppers, D., Baumanns, K., and Op de Beeck, M. (2017). “Polyimide-ALD-polyimide layers as hermetic encapsulant for implants,” in *XXXI International Conference on Surface Modification Technologies (SMT31)* (Mons).
- Schiavone, G., Wagner, F., Fallegger, F., Kang, X., Vachicouras, N., Barra, B., et al. (2018). “Long-term functionality of a soft electrode array for epidural spinal cord stimulation in a minipig model,” in *2018 40th Annual International Conference of the IEEE Engineering in Medicine and Biology Society (EMBC)* (Honolulu, HI).
- Scholten, K., and Meng, E. (2015). Materials for microfabricated implantable devices: a review. *Lab Chip* 15, 4256–4272. doi: 10.1039/C5LC00809C
- Seo, D., Carmenta, J. M., Rabaey, J. M., Alon, E., and Maharbiz, M. M. (2013). Neural dust: an ultrasonic, low power solution for chronic brain-machine interfaces. *arXiv [Preprint]*. arXiv:1307.2196.
- Seo, K. J., Qiang, Y., Bilgin, I., Kar, S., Vinegoni, C., Weissleder, R., et al. (2017). Transparent electrophysiology microelectrodes and interconnects from metal nanomesh. *ACS Nano* 11, 4365–4372. doi: 10.1021/acsnano.7b01995
- Sevil, B., and Zuhail, K. (2010). “Synthesis and characterization of polypyrrole nanoparticles and their nanocomposites with poly (propylene),” in *Macromolecular Symposia* (Wiesbaden: Wiley Online Library), 59–64.
- Seymour, J. P., and Kipke, D. R. (2007). Neural probe design for reduced tissue encapsulation in CNS. *Biomaterials* 28, 3594–3607. doi: 10.1016/j.biomaterials.2007.03.024
- Shen, K., and Maharbiz, M. M. (2019). Design of ceramic packages for ultrasonically coupled implantable medical devices. *IEEE Trans. Biomed. Eng.* 67, 2230–2240. doi: 10.1109/TBME.2019.2957732
- Shen, K., and Maharbiz, M. M. (2020). Ceramic packaging in neural implants. *bioRxiv [Preprint]*. doi: 10.1101/2020.06.26.174144
- Shepherd, R. K., Villalobos, J., Burns, O., and Nayagam, D. A. X. (2018). The development of neural stimulators: a review of preclinical safety and efficacy studies. *J. Neural Eng.* 15:041004. doi: 10.1088/1741-2552/aac43c
- Shih, V. C. Y., Harder, T. A., and Tai, Y. C. (2003). “Yield strength of thin-film parylene-C,” in *Symposium on Design, Test, Integration and Packaging of MEMS/MOEMS 2003* (IEEE), 394–398.
- Shin, D., Bae, S.-K., Yan, C., Kang, J.-M., Ryu, J.-C., Ahn, J.-H., et al. (2012). Synthesis and applications of graphene electrodes. *Carbon Lett.* 13, 1–16. doi: 10.5714/CL.2012.13.1.001
- Shur, M., Fallegger, F., Pirondini, E., Roux, A., Bichat, A., Barraud, Q., et al. (2020). Soft printable electrode coating for neural interfaces. *ACS Appl. Bio Mater.* 3, 4388–4397. doi: 10.1021/acsbm.0c00401
- Sim, J. Y., Haney, M. P., Park, S. I., McCall, J. G., and Jeong, J. W. (2017). Microfluidic neural probes: *in vivo* tools for advancing neuroscience. *Lab Chip* 17, 1406–1435. doi: 10.1039/C7LC00103G
- Siuly, S., and Zhang, Y. (2016). Medical big data: neurological diseases diagnosis through medical data analysis. *Data Sci. Eng.* 1, 54–64. doi: 10.1007/s41019-016-0011-3
- Sofi, H. S., Ashraf, R., Khan, A. H., Beigh, M. A., Majeed, S., and Sheikh, F. A. (2019). Reconstructing nanofibers from natural polymers using surface functionalization approaches for applications in tissue engineering, drug delivery and biosensing devices. *Mater. Sci. Eng. C* 94, 1102–1124. doi: 10.1016/j.msec.2018.10.069
- Sohn, Y.-S., Park, J., Yoon, G., Song, J., Jee, S.-W., Lee, J.-H., et al. (2010). Mechanical properties of silicon nanowires. *Nanoscale Res. Lett.* 5, 211–216. doi: 10.1007/s11671-009-9467-7
- Solarski, S., Ferreira, M., and Devaux, E. (2005). Characterization of the thermal properties of PLA fibers by modulated differential scanning calorimetry. *Polymer* 46, 11187–11192. doi: 10.1016/j.polymer.2005.10.027
- Song, E., Chiang, C. H., Li, R., Jin, X., Zhao, J., Hill, M., et al. (2019a). Flexible electronic/optoelectronic microsystems with scalable designs for chronic biointegration. *Proc. Natl. Acad. Sci. U.S.A.* 116, 15398–15406. doi: 10.1073/pnas.1907697116
- Song, E., Li, J., and Rogers, J. A. (2019b). Barrier materials for flexible bioelectronic implants with chronic stability—current approaches and future directions. *APL Mater.* 7:050902. doi: 10.1063/1.5094415
- Song, E., Li, J., Won, S. M., Bai, W., and Rogers, J. A. (2020). Materials for flexible bioelectronic systems as chronic neural interfaces. *Nat. Mater.* 19, 590–603. doi: 10.1038/s41563-020-0679-7
- Stenger, D. A., and McKenna, T. M. (1994). *Enabling Technologies for Cultured Neural Networks*. Cambridge, MA: Academic Press.
- Stieglitz, T. (2010). Manufacturing, assembling and packaging of miniaturized neural implants. *Microsyst. Technol.* 16, 723–734. doi: 10.1007/s00542-009-0988-x
- Stieglitz, T., Schuetzler, M., and Meyer, J.-U. (2000). Micromachined, polyimide-based devices for flexible neural interfaces. *Biomed. Microdevices* 2, 283–294. doi: 10.1023/A:100995522114

- Strojnik, P., and Peckham, P. H. (2000). "Implantable stimulators for neuromuscular control," in *Biomed. Eng. Handbook*, 2nd Edn (Boca Raton, FL: CRC Press LLC).
- Su, H.-C., Lin, C.-M., Yen, S.-J., Chen, Y.-C., Chen, C.-H., Yeh, S.-R., et al. (2010). A cone-shaped 3D carbon nanotube probe for neural recording. *Biosens. Bioelectron.* 26, 220–227. doi: 10.1016/j.bios.2010.06.015
- Su, X., Wang, P., Chen, W., Zhu, B., Cheng, Y., and Yan, D. (2004). Translucent  $\alpha$ -sialon ceramics by hot pressing. *J. Am. Ceramic Soc.* 87, 730–732. doi: 10.1111/j.1551-2916.2004.00730.x
- Subramanian, B., Muraleedharan, C. V., Ananthakumar, R., and Jayachandran, M. (2011). A comparative study of titanium nitride (TiN), titanium oxy nitride (TiON) and titanium aluminum nitride (TiAlN), as surface coatings for bio implants. *Surf. Coat. Technol.* 205, 5014–5020. doi: 10.1016/j.surfcoat.2011.05.004
- Sun, Y., Akhremitchev, B., and Walker, G. C. (2004). Using the adhesive interaction between atomic force microscopy tips and polymer surfaces to measure the elastic modulus of compliant samples. *Langmuir* 20, 5837–5845. doi: 10.1021/la036461q
- Szostak, K. M., Grand, L., and Constantinou, T. G. (2017). Neural interfaces for intracortical recording: Requirements, fabrication methods, and characteristics. *Front. Neurosci.* 11:665. doi: 10.3389/fnins.2017.00665
- Takeuchi, S., Ziegler, D., Yoshida, Y., Mabuchi, K., and Suzuki, T. (2005). Parylene flexible neural probes integrated with microfluidic channels. *Lab Chip* 5, 519–523. doi: 10.1039/b417497f
- Takmakov, P., Ruda, K., Phillips, K. S., Isayeva, I. S., Krauthamer, V., and Welle, C. G. (2015). Rapid evaluation of the durability of cortical neural implants using accelerated aging with reactive oxygen species. *J. Neural Eng.* 12:26003. doi: 10.1088/1741-2560/12/2/026003
- Tang, J., Xiong, L., Wang, S., Wang, J., Liu, L., Li, J., et al. (2008). Influence of silver nanoparticles on neurons and blood-brain barrier via subcutaneous injection in rats. *Appl. Surf. Sci.* 255, 502–504. doi: 10.1016/j.apsusc.2008.06.058
- Tao, H., Hwang, S.-W., Marelli, B., An, B., Moreau, J. E., Yang, M., et al. (2015). Fully implantable and resorbable wireless medical devices for postsurgical infection abatement. in *2015 28th IEEE International Conference on Micro Electro Mechanical Systems (MEMS)* (Estoril).
- Thukral, A., Ershad, F., Enan, N., Rao, Z., and Yu, C. (2018). Soft ultrathin silicon electronics for soft neural interfaces: a review of recent advances of soft neural interfaces based on ultrathin silicon. *IEEE Nanotechnol. Mag.* 12, 21–34. doi: 10.1109/MNANO.2017.2781290
- Thunemann, M., Lu, Y., Liu, X., Kiliç, K., Desjardins, M., Vandenbergh, M., et al. (2018). Deep 2-photon imaging and artifact-free optogenetics through transparent graphene microelectrode arrays. *Nat. Commun.* 9:2035. doi: 10.1038/s41467-018-04457-5
- Tyler, B., Gullotti, D., Mangraviti, A., Utsuki, T., and Brem, H. (2016). Polylactic acid (PLA) controlled delivery carriers for biomedical applications. *Adv. Drug Deliv. Rev.* 107, 163–175. doi: 10.1016/j.addr.2016.06.018
- Vanhoestenbergh, A., and Donaldson, N. (2011). The limits of hermeticity test methods for micropackages. *Artific. Organs* 35, 242–244. doi: 10.1111/j.1525-1594.2011.01222.x
- Vanhoestenbergh, A., and Donaldson, N. (2013). Corrosion of silicon integrated circuits and lifetime predictions in implantable electronic devices. *J. Neural Eng.* 10:31002. doi: 10.1088/1741-2560/10/3/031002
- Vekinis, G., Ashby, M. F., and Beaumont, P. W. R. (1990). R-curve behaviour of Al<sub>2</sub>O<sub>3</sub> ceramics. *Acta metall. Mater.* 38, 1151–1162. doi: 10.1016/0956-7151(90)90188-M
- Veliev, F., Han, Z., Kalita, D., Briançon-Marjollet, A., Bouchiat, V., and Delacour, C. (2017). Recording spikes activity in cultured hippocampal neurons using flexible or transparent graphene transistors. *Front. Neurosci.* 11:466. doi: 10.3389/fnins.2017.00466
- Viana, A. C. D., de Melo, M. C. C., de Azevedo Bahia, M. G., and Buono, V. T. L. (2010). Relationship between flexibility and physical, chemical, and geometric characteristics of rotary nickel-titanium instruments. *Oral Surg. Oral Med. Oral Pathol. Oral Radiol. Endod.* 110, 527–533. doi: 10.1016/j.tripleo.2010.05.006
- Viventi, J., Kim, D. H., Vigeland, L., Frechette, E. S., Blanco, J. A., Kim, Y. S., et al. (2011). Flexible, foldable, actively multiplexed, high-density electrode array for mapping brain activity *in vivo*. *Nat. Neurosci.* 14:1599. doi: 10.1038/nn.2973
- Vlasov, A. S., and Karabanova, T. A. (1993). Ceramics and medicine. *Glas. Ceram.* 50, 398–401. doi: 10.1007/BF00683586
- Vomero, M., Castagnola, E., Ciarpella, F., Maggolini, E., Goshi, N., Zucchini, E., et al. (2017). Highly stable glassy carbon interfaces for long-term neural stimulation and low-noise recording of brain activity. *Sci. Rep.* 7:40332. doi: 10.1038/srep40332
- Vomero, M., Castagnola, E., Ordóñez, J. S., Carli, S., Zucchini, E., Maggolini, E., et al. (2018). Incorporation of silicon carbide and diamond-like carbon as adhesion promoters improves *in vitro* and *in vivo* stability of thin-film glassy carbon electrocorticography arrays. *Adv. Biosyst.* 2:1700081. doi: 10.1002/adbi.201700081
- Vomero, M., Van Niekerk, P., Nguyen, V., Gong, N., Hirabayashi, M., Cinopri, A., et al. (2016). A novel pattern transfer technique for mounting glassy carbon microelectrodes on polymeric flexible substrates. *J. Micromech. Microeng.* 26:25018. doi: 10.1088/0960-1317/26/2/025018
- Wahl, S. M., Wong, H., and McCartney-Francis, N. (1989). Role of growth factors in inflammation and repair. *J. Cell. Biochem.* 40, 193–199. doi: 10.1002/jcb.240400208
- Wang, J., Ma, F., and Sun, M. (2017). Graphene, hexagonal boron nitride, and their heterostructures: properties and applications. *RSC Adv.* 7, 16801–16822. doi: 10.1039/C7RA00260B
- Wang, J. J., Wang, D. S., Wang, J., Zhao, W. L., and Wang, C. W. (2011). High transmittance and superhydrophilicity of porous TiO<sub>2</sub>/SiO<sub>2</sub> bi-layer films without UV irradiation. *Surf. Coat. Technol.* 205, 3596–3599. doi: 10.1016/j.surfcoat.2010.12.033
- Wang, M., Mi, G., Shi, D., Bassous, N., Hickey, D., and Webster, T. J. (2018). Nanotechnology and nanomaterials for improving neural interfaces. *Adv. Funct. Mater.* 28:1700905. doi: 10.1002/adfm.201700905
- Wang, S., Li, M., Wu, J., Kim, D.-H., Lu, N., Su, Y., et al. (2012). Mechanics of epidermal electronics. *J. Appl. Mech.* 79:031022. doi: 10.1115/1.4005963
- Wang, X., Hirschberg, A. W., Xu, H., Slingsby-Smith, Z., Lecomte, A., Scholten, K., et al. (2020). A parylene neural probe array for multi-region deep brain recordings. *J. Microelectromech. Syst.* 29, 499–513. doi: 10.1109/JMEMS.2020.3000235
- Wang, X.-S., and Feng, X.-Q. (2002). Effects of thickness on mechanical properties of conducting polythiophene films. *J. Mater. Sci. Lett.* 21, 715–717. doi: 10.1023/A:1015737106002
- Wasikiewicz, J. M., Roohpour, N., and Vadgama, P. (2013). "Packaging and coating materials for implantable devices," in *Implantable Sensor Systems for Medical Applications* (Cambridge: Woodhead Publishing), 68–107.
- Wellman, S. M., Eles, J. R., Ludwig, K. A., Seymour, J. P., Michelson, N. J., McFadden, W. E., et al. (2018). A materials roadmap to functional neural interface design. *Adv. Funct. Mater.* 28:1701269. doi: 10.1002/adfm.201701269
- Wiegand, C., Abel, M., Ruth, P., Wilhelms, T., Schulze, D., Norgauer, J., et al. (2009). Effect of the sterilization method on the performance of collagen type I on chronic wound parameters *in vitro*. *J. Biomed. Mater. Res. B Appl. Biomater.* 90, 710–719. doi: 10.1002/jbm.b.31338
- Wijeratne, T., Grisold, W., Trenkwalder, C., and Carroll, A. M. W. (2020). World Brain Day 2020: move together to end Parkinson's disease. *J. Neurol. Sci.* 416:116996. doi: 10.1016/j.jns.2020.116996
- Wild, C., and Wörner, E. (2004). *The CVD Diamond Booklet*. Available online at: [https://accuton.com/application/files/4815/2301/5992/cvd\\_diamond\\_booklet.pdf](https://accuton.com/application/files/4815/2301/5992/cvd_diamond_booklet.pdf) (accessed October 25).
- Williams, D. F. (1986). "European society for biomaterials," in *Definitions in Biomaterials: Proceedings of a Consensus Conference of the European Society for Biomaterials* (Chester).
- Wise, K. D., Anderson, D. J., Hetke, J. F., Kipke, D. R., and Najafi, K. (2004). Wireless implantable microsystems: high-density electronic interfaces to the nervous system. *Proc. IEEE* 92, 76–97. doi: 10.1109/JPROC.2003.820544
- Won, S. M., Song, E., Zhao, J., Li, J., Rivnay, J., and Rogers, J. A. (2018). Recent advances in materials, devices, and systems for neural interfaces. *Adv. Mater.* 30:1800534. doi: 10.1002/adma.201800534
- Woods, V., Trumpis, M., Bent, B., Palopoli-Trojani, K., Chiang, C. H., Wang, C., et al. (2018). Long-term recording reliability of liquid crystal polymer  $\mu$ ECOG arrays. *J. Neural Eng.* 15:066024. doi: 10.1088/1741-2552/aae39d
- Wu, F., Im, M., and Yoon, E. (2011). "A flexible fish-bone-shaped neural probe strengthened by biodegradable silk coating for enhanced biocompatibility," in *2011 16th International Solid-State Sensors, Actuators and Microsystems Conference* (Beijing: IEEE).



- Wu, J., Pike, R. T., and Wong, C. P. (1999). "Interface-adhesion-enhanced bi-layer conformal coating for avionics application," in *Proceedings International Symposium on Advanced Packaging Materials. Processes, Properties and Interfaces* (Braselton).
- Wu, F., Tien, L. W., Chen, F., Berke, J. D., Kaplan, D. L., and Yoon, E. (2014). Silk-backed structural optimization of high-density flexible intracortical neural probes. *J. Microelectromech. Syst.* 24, 62–69. doi: 10.1109/JMEMS.2014.2375326
- Xie, C., Lin, Z., Hanson, L., Cui, Y., and Cui, B. (2012). Intracellular recording of action potentials by nanopillar electroporation. *Nat. Nanotechnol.* 7, 185–190. doi: 10.1038/nnano.2012.8
- Xu, K., Li, S., Dong, S., Zhang, S., Pan, G., Wang, G., et al. (2019). Bioresorbable electrode array for electrophysiological and pressure signal recording in the brain. *Adv. Healthc. Mater.* 8:1801649. doi: 10.1002/adhm.201801649
- Xue, N., Wang, D., Liu, C., Ke, Z., Elia, P., Li, T., et al. (2018). A biodegradable porous silicon and polymeric hybrid probe for electrical neural signal recording. *Sens. Actuatur. B Chem.* 272, 314–323. doi: 10.1016/j.snb.2018.06.001
- Yang, W., Wu, J., Fan, Q. H., and Li, W. (2019a). "Highly conductive, transparent, and antireflective PEDOT: PSS/ITO/Ag/ITO on parylene-C with tunable peak transmittance," in *2019 IEEE 32nd International Conference on Micro Electro Mechanical Systems (MEMS)* (Seoul).
- Yang, J., Kim, D. H., Hendricks, J. L., Leach, M., Northey, R., and Martin, D. C. (2005). Ordered surfactant-templated poly (3, 4-ethylenedioxythiophene)(PEDOT) conducting polymer on microfabricated neural probes. *Acta Biomater.* 1, 125–136. doi: 10.1016/j.actbio.2004.09.006
- Yang, K.-H., and Narayan, R. J. (2019). Biocompatibility and functionalization of diamond for neural applications. *Curr. Opin. Biomed. Eng.* 10, 60–68. doi: 10.1016/j.cobme.2019.03.002
- Yang, W., Broski, A., Wu, J., Fan, Q. H., and Li, W. (2017). Characteristics of transparent, PEDOT: PSS-coated indium-tin-oxide (ITO) microelectrodes. *IEEE Trans. Nanotechnol.* 17, 701–704. doi: 10.1109/TNANO.2017.2785627
- Yang, W., Wu, J., Fan, Q. H., and Li, W. (2019b). "Transparent and ultra-flexible PEDOT: PSS/ITO/Ag/ITO on Parylene thin films with tunable properties," in *Oxide-Based Materials and Devices X* (Bellingham, WA: International Society for Optics and Photonics), 109191W.
- Yen, S.-J., Hsu, W.-L., Chen, Y.-C., Su, H.-C., Chang, Y.-C., Chen, H., et al. (2011). The enhancement of neural growth by amino-functionalization on carbon nanotubes as a neural electrode. *Biosens. Bioelectron.* 26, 4124–4132. doi: 10.1016/j.bios.2011.04.003
- Yoda, R. (1998). Elastomers for biomedical applications. *J. Biomater. Sci. Polym. Ed.* 9, 561–626. doi: 10.1163/156856298X00046
- Yoon, I., Hamaguchi, K., Borzenets, I. V., Finkelstein, G., Mooney, R., and Donald, B. R. (2013). Intracellular neural recording with pure carbon nanotube probes. *PLoS ONE* 8:e65715. doi: 10.1371/journal.pone.0065715
- Yu, K. J., Kuzum, D., Hwang, S.-W., Kim, B. H., Juul, H., Kim, N. H., et al. (2016). Bioresorbable silicon electronics for transient spatiotemporal mapping of electrical activity from the cerebral cortex. *Nat. Mater.* 15, 782–791. doi: 10.1038/nmat4624
- Yu, Z., McKnight, T. E., Ericson, M. N., Melechko, A. V., Simpson, M. L., Morrison, I. I. I., et al. (2012). Vertically aligned carbon nanofiber as nano-neuron interface for monitoring neural function. *Nanomedicine* 8, 419–423. doi: 10.1016/j.nano.2012.02.011
- Yucel, T., Lovett, M. L., and Kaplan, D. L. (2014). Silk-based biomaterials for sustained drug delivery. *J. Control. Release* 190, 381–397. doi: 10.1016/j.jconrel.2014.05.059
- Zambov, L., Weidner, K., Shamamian, V., Camilletti, R., Pernisz, U., Loboda, M., et al. (2006). Advanced chemical vapor deposition silicon carbide barrier technology for ultralow permeability applications. *J. Vac. Sci. Technol. A* 24, 1706–1713. doi: 10.1116/1.2214694
- Zátonyi, A., Fedor, F., Borhegyi, Z., and Fekete, Z. (2018). *In vitro* and *in vivo* stability of black-platinum coatings on flexible, polymer microECog arrays. *J. Neural Eng.* 15:054003. doi: 10.1088/1741-2552/aac71
- Zeng, Q., Xia, K., Sun, B., Yin, Y., Wu, T., and Humayun, M. S. (2017). Electrodeposited iridium oxide on platinum nanocones for improving neural stimulation microelectrodes. *Electrochim. Acta* 237, 152–159. doi: 10.1016/j.electacta.2017.03.213
- Zhang, C., Liu, J.-Q., Tian, H.-C., Kang, X.-Y., Du, J.-C., Rui, Y.-F., et al. (2015). Implantable electrode array with platinum black coating for brain stimulation in fish. *Microsyst. Technol.* 21, 139–145. doi: 10.1007/s00542-013-2017-3
- Zhang, M., Tang, Z., Liu, X., and Van der Spiegel, J. (2020). Electronic neural interfaces. *Nat. Electron.* 3, 191–200. doi: 10.1038/s41928-020-0390-3
- Zhang, Q., Huang, J., Zhao, M., Qian, W., and Wei, F. (2011). Carbon nanotube mass production: principles and processes. *ChemSusChem* 4, 864–889. doi: 10.1002/cssc.201100177
- Zhao, R., Liu, X., Lu, Y., Ren, C., Mehra, A., Komiyama, T., et al. (2018). "3D expandable microwire electrode arrays made of programmable shape memory materials," in *2018 IEEE International Electron Devices Meeting (IEDM)* (San Francisco, CA).
- Zhao, Y., You, S. S., Zhang, A., Lee, J. H., Huang, J., and Lieber, C. M. (2019). Scalable ultrasmall three-dimensional nanowire transistor probes for intracellular recording. *Nat. Nanotechnol.* 14, 783–790. doi: 10.1038/s41565-019-0478-y
- Zhao, Z., Gong, R., Zheng, L., and Wang, J. (2016). *In vivo* neural recording and electrochemical performance of microelectrode arrays modified by rough-surfaced AuPt alloy nanoparticles with nanoporosity. *Sensors* 16:1851. doi: 10.3390/s16111851
- Zhou, H.-B., Li, G., Sun, X.-N., Zhu, Z.-H., Jin, Q.-H., Zhao, J.-L., et al. (2009). Integration of Au nanorods with flexible thin-film microelectrode arrays for improved neural interfaces. *J. Microelectromech. Syst.* 18, 88–96. doi: 10.1109/JMEMS.2008.2011122
- Zöpfl, T., Klare, S., Wachutka, G., and Schrag, G. (2009). "Characterisation of the intrinsic stress in micromachined parylene membranes," in *Smart Sensors, Actuators, and MEMS IV* (Bellingham, WA: International Society for Optics and Photonics), 73621M.

**Conflict of Interest:** The authors declare that the research was conducted in the absence of any commercial or financial relationships that could be construed as a potential conflict of interest.

Copyright © 2021 Yang, Gong and Li. This is an open-access article distributed under the terms of the Creative Commons Attribution License (CC BY). The use, distribution or reproduction in other forums is permitted, provided the original author(s) and the copyright owner(s) are credited and that the original publication in this journal is cited, in accordance with accepted academic practice. No use, distribution or reproduction is permitted which does not comply with these terms.



## GLOSSARY

EEG, Electroencephalogram; ECoG, Electrocorticogram; LFPs, Local field potentials; SNR, Signal-to-noise ratio; ITO, Indium tin oxide; SiC, Silicon carbide; PDMS, Polydimethylsiloxane; LCPs, Liquid crystal polymers; PEDOT:PSS, Poly(3,4-ethylene dioxothiophene):poly(styrene sulfonate); PPy, Poly(pyrrole); ROS, Reactive oxidative species; CPs, Conducting polymers; BDD, Boron-doped polycrystalline diamond; Mo, Molybdenum; ISO, International Organization of Standard; PEG, Polyethylene glycol; PEGMA, Polyethylene glycol methacrylate; GNPs, Gold nanoparticles; Si NM, Silicon nanomembranes; SiO<sub>2</sub>, Silicon dioxide; PBS, Phosphate-buffered saline; DI, De-ionized; PA, Parylene C; PI, Polyimide; SMPs, Shape-memory polymers; Au, Gold; PET, Polyethylene terephthalate; Pt, Platinum; Ir, Iridium; W, Tungsten; Ta, Tantalum; 3D, Three dimensional; 2D, Two dimensional; IrOx, Iridium oxide; EPIC, Electrodeposited a PtIr coating; Si, Silicon; CMOS, Complementary metal-

oxide-semiconductor; FETs, Field-effect transistors; PLGA, Poly(lactic-co-glycolic acid); Ge, Germanium; SiGe, Silicon germanium; IZO, Indium-doped zinc oxide; a-IGZO, Indium-gallium-zinc oxide; ZnO, Zinc oxide; Ra, Average surface roughness; PANi, Poly(aniline); PT, Poly(thiophene); CVD, Chemical vapor deposition; CFs, Carbon fibers; CNTs, Carbon nanotubes; CFMEs, Carbon fiber microelectrodes; CNF, Carbon nanofiber; COC, Cyclic olefin copolymer; fMRI, Functional magnetic resonance imaging; SWCNTs, Single-walled carbon nanotubes; MWCNTs, Multi-walled carbon nanotubes; GC, Glassy carbon; EM, Electromagnetic; Al<sub>2</sub>O<sub>3</sub>, Alumina; AlN, Aluminum nitride; PECVD, Plasma-enhanced chemical vapor deposition; LPCVD, Low-pressure chemical vapor deposition; PMMA, Polymethylmethacrylate; PC, Polycarbonate; PS, Polystyrene; RAA, Reactive accelerated aging; SCS, Specialty Coating System; RGC, Retinal ganglion cell; PBTPA, Bioresorbable polyanhydride-based polymer; PLA, Poly lactic acid; NGF, Nerve growth factor.



OPEN ACCESS

**Edited by:**

Elisa Castagnola,  
University of Pittsburgh, United States

**Reviewed by:**

Jinghua Yin,  
Changchun Institute of Applied  
Chemistry, Chinese Academy  
of Sciences, China  
Carolina Parra,  
Federico Santa María Technical  
University, Chile  
Davide Ricci,  
University of Genoa, Italy

**\*Correspondence:**

Andrea Capasso  
andrea.capasso@inl.int

**Specialty section:**

This article was submitted to  
Nanobiotechnology,  
a section of the journal  
Frontiers in Bioengineering and  
Biotechnology

**Received:** 30 September 2020

**Accepted:** 04 January 2021

**Published:** 27 January 2021

**Citation:**

Santos J, Moschetta M,  
Rodrigues J, Alpuim P and Capasso A  
(2021) Interactions Between 2D  
Materials and Living Matter: A Review  
on Graphene and Hexagonal Boron  
Nitride Coatings.  
Front. Bioeng. Biotechnol. 9:612669.  
doi: 10.3389/fbioe.2021.612669

# Interactions Between 2D Materials and Living Matter: A Review on Graphene and Hexagonal Boron Nitride Coatings

**João Santos<sup>1</sup>, Matteo Moschetta<sup>2</sup>, João Rodrigues<sup>1</sup>, Pedro Alpuim<sup>1,3</sup> and Andrea Capasso<sup>1\*</sup>**

<sup>1</sup> International Iberian Nanotechnology Laboratory, Braga, Portugal, <sup>2</sup> Center for Synaptic Neuroscience and Technology, Istituto Italiano di Tecnologia, Genova, Italy, <sup>3</sup> Centro de Física das Universidades do Minho e do Porto, Braga, Portugal

Two-dimensional material (2DM) coatings exhibit complex and controversial interactions with biological matter, having shown in different contexts to induce bacterial cell death and contribute to mammalian cell growth and proliferation *in vitro* and tissue differentiation *in vivo*. Although several reports indicate that the morphologic and electronic properties of the coating, as well as its surface features (e.g., crystallinity, wettability, and chemistry), play a key role in the biological interaction, these kinds of interactions have not been fully understood yet. In this review, we report and classify the cellular interaction mechanisms observed in graphene and hexagonal boron nitride (hBN) coatings. Graphene and hBN were chosen as study materials to gauge the effect of two atomic-thick coatings with analogous lattice structure yet dissimilar electrical properties upon contact with living matter, allowing to discern among the observed effects and link them to specific material properties. In our analysis, we also considered the influence of crystallinity and surface roughness, detailing the mechanisms of interaction that make specific coatings of these 2DMs either hostile toward bacterial cells or innocuous for mammalian cells. In doing this, we discriminate among the material and surface properties, which are often strictly connected to the 2DM production technique, coating deposition and post-processing method. Building on this knowledge, the selection of 2DM coatings based on their specific characteristics will allow to engineer desired functionalities and devices. Antibacterial coatings to prevent biofouling, biocompatible platforms suitable for biomedical applications (e.g., wound healing, tissue repairing and

regeneration, and novel biosensing devices) could be realized in the next future. Overall, a clear understanding on how the 2DM coating's properties may modulate a specific bacterial or cellular response is crucial for any future innovation in the field.

**Keywords:** antibacterial properties, two-dimensional materials (2D materials), cellular interaction, neuronal interface, tissue engineering

## INTRODUCTION

### Background and Motivation

Other than being present in most of the Earth's habitats, bacteria live in symbiotic and parasitic relationships with plants and animals. Bacteria are ubiquitous in mammals, and while they are necessary for the development of a balanced immune system, the disruption of microbiomes can negatively affect the health of an individual. Nowadays, bacterial pathogenic agents represent a major public health issue (Medzhitov, 2007; Pope et al., 2008; Ali and Keil, 2009; Ling et al., 2015; Begum et al., 2020; WHO, 2020). The use of antibiotics, one of the main and most effective tools for combating bacterial infections, has gradually led to an increase in drug resistance in the microbes responsible for infections, as a consequence of misuse and/or overuse, requiring ever-increasing doses to achieve the same inhibition effect (Medzhitov, 2007; Pope et al., 2008; Ling et al., 2015; WHO, 2020). Alarming predictions state that at the rate by which bacteria are becoming resistant to antibiotics, drug-resistant bacteria could kill more than ten million people/year by 2050, a prediction that is further aggravated by the increasing ease in global mobility (Medzhitov, 2007; Pope et al., 2008; Ali and Keil, 2009; Ling et al., 2015; Begum et al., 2020; WHO, 2020).

Another concern regarding bacteria is their adhesion to surfaces, and the consequent issue of biofouling. Biofouling refers to the formation of a biofilm consisting of a complex community of one or several microbial species on the surface of an object, which can impair its functionality, e.g., by promoting corrosion. Biofouling and related issues can cause damage to objects, equipment and structures, and often lead to significant financial loss (Flemming and Wingender, 2010). In the context of implanted devices, biofouling should be carefully monitored and prevented to preserve the functionality and lifespan of the implants. Current solutions to minimize biofouling can potentially release toxins and have a harmful impact on the environment and marine life. The realization of effective antibacterial and anti-biofilm coatings based on innovative biocompatible materials would greatly contribute to prevent surface contamination and hindering the spreading of bacteria in many contexts (Szunerits and Boukherroub, 2016).

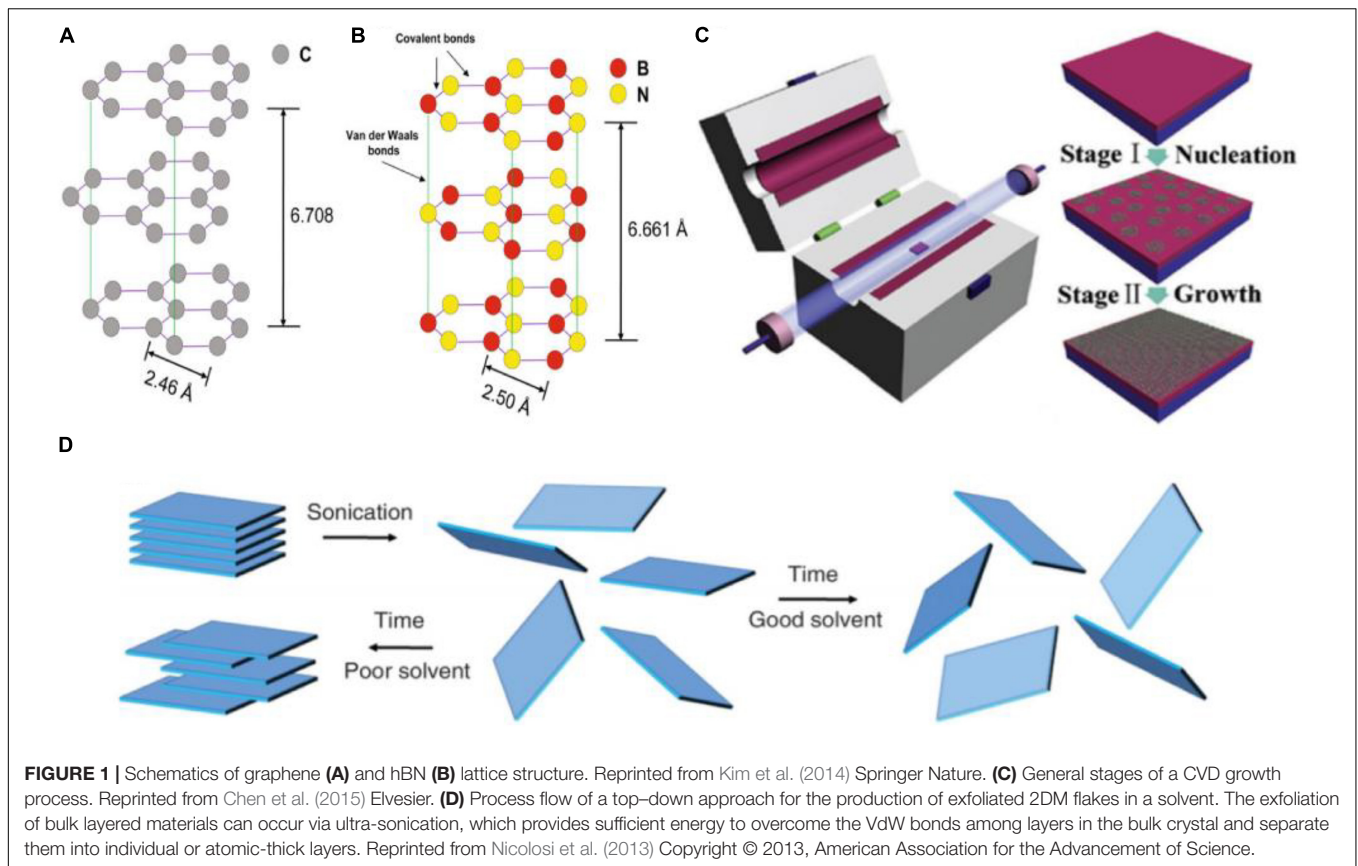
In medicine, degenerative diseases have overtaken infections as the leading cause of death worldwide, with tissue damage caused by ischemia, stroke and neurological pathologies representing the most prevalent cause of mortality in high-income countries (WHO, 2013). In this scenario, traditional pharmacology shows some limits and challenges (Blaschke, 2009; Enna and Williams, 2009). For these reasons, other strategies (e.g., stem cell therapy and advanced nanomaterials) have been

developed with the aim of promoting tissue repair and restoring the correct functionality of the damaged tissue (Howard et al., 2008; Liao et al., 2008; O'Brien, 2011; Wang et al., 2011). Tissue engineering involves replication and regeneration of damaged tissues and organs. To this end, it relies on substrates that mimic the physiological *in vivo* conditions. Suitable substrate materials should be able to guide cell growth and modulation, bioactive molecule delivery, physicochemical cue generation, while having similar mechanical properties to the native tissue (Shin et al., 2016).

Bacteria and mammalian cells have been shown to respond to a wide set of physicochemical signals, such as biochemical, electrical, and magnetic. The interactions with coatings made of different materials have shown to play a role in modulating or tailoring cellular response. Two-dimensional materials (2DMs) are a class of atomic-thick materials that are the subject of intense research efforts, motivated by a wide range of useful properties of high interest in several technological fields (Miró et al., 2014; Bonaccorso et al., 2015; Capasso et al., 2019; Kang et al., 2020). In the biomedical field, applications for 2DMs include bio-sensing (Pumera, 2011), tissue engineering (Goenka et al., 2014), personal protective equipment fabrication (Zhong et al., 2020), and drug or gene delivery (Chimene et al., 2015).

### Graphene and hBN: Structure, Properties, and Role in Bio-Applications

Graphene and hexagonal boron nitride (hBN) are archetypal 2DMs that have drawn the attention of researchers (Randviir et al., 2014; Kang et al., 2020; Khan et al., 2020; Mendelson et al., 2020). Graphene is a carbon allotrope consisting of a single layer of  $sp^2$ -bonded carbon atoms arranged in a hexagonal lattice (**Figure 1A**) (Novoselov et al., 2004; Geim et al., 2005; Allen et al., 2010). Monolayer graphene has a thickness of 0.34 nm and a lattice constant of 2.46 Å. When in graphitic, multilayer form, it shows an interlayer distance of 3.354 Å (Kim et al., 2014). Its atomic bonds, combined with its one-atom thickness, grant graphene properties such as high electrical conductivity, thermal conductivity, mechanical flexibility, and optical transparency (Geim and Novoselov, 2007; Lee et al., 2008; Koh et al., 2010). Furthermore, there is the possibility of surface functionalization with a variety of bioactive molecules (Shin et al., 2016). hBN is a layered material with a honeycomb structure analogous to that of graphene, consisting of covalently bonded boron (B) and nitrogen (N) atoms (**Figure 1B**) (Lynch and Drickamer, 1966). hBN layers have a AA' stacking configuration bonded by van der Waals (VdW) forces (with interlayer distance of 3.33 Å)



(Wang et al., 2017). Having analogous structure but insulating electrical behavior, hBN is sometimes referred to as “white graphene.” hBN features properties such as high hydrophobicity, thermal insulation, electrical insulation, low dielectric constant, resistance to oxidation, high chemical stability, and mechanical strength (Mahvash et al., 2017; Chilkoo et al., 2018; Merlo et al., 2018; Emanet et al., 2019; Mukheem et al., 2019). Due to these properties, 2D BN-based materials have also demonstrated potential in antibacterial coatings (Mukheem et al., 2019), as well as applications in the biomedical field – such as wound healing (Şen et al., 2019), and bone tissue regeneration (Şen et al., 2019; Aki et al., 2020).

Techniques for 2DM production fall within two main categories, defined as bottom-up and top-down (Tour, 2014; Kong et al., 2019; Matsoso et al., 2020). Among the bottom-up techniques, chemical vapor deposition (CVD) allows the production of 2DMs with atomic thickness (i.e., mono- to few-layer) and high crystallinity (Figure 1C) (Lisi et al., 2014; Li et al., 2016; Gnisci et al., 2018; Deng et al., 2019; Faggio et al., 2020). Graphene and hBN are commonly grown on copper (Cu) substrates, which enable a self-limiting growth resulting in monolayer graphene over large areas (Figure 1D) (Faggio et al., 2013; Capasso et al., 2015b; Wu et al., 2015; Deng et al., 2019; Wang L. et al., 2019). After the growth, the 2DMs can be transferred to target substrates via wet etching techniques (Mattevi et al., 2011; Capasso et al., 2014; Backes et al., 2019). CVD is a valid production method

especially to fabricate graphene-based devices for electronics and other applications requiring high reproducibility, although it is still a rather expensive technique which requires high temperatures, full control on parameters, and post-production transfer processes (Backes et al., 2019; Deng et al., 2019). The most common top-down technique is liquid phase exfoliation (LPE). In a LPE process, bulk layered materials (such as graphite or hBN crystals) are exfoliated in a liquid solvent using an external source of energy, such as ultra-sonication or shear mixing, as illustrated in Figure 1D. The energy is required to overcome the weak VdW bonds holding the layered bulk crystal together and disperse the exfoliated layers in the solvent. As-produced dispersions of isolated layers (also called “flakes”) can be adjusted in concentration and size-distribution by successive ultracentrifugation stages. The fluidic properties of the dispersions (e.g., surface tension and viscosity) can also be tuned to comply with specific depositions techniques, such as inkjet or screen printing, spray coating, and flexography (Capasso et al., 2015a; Kim et al., 2019). Overall, LPE is a suitable approach to produce liquid dispersions of 2DMs in large amounts, at the expense of a somehow limited control on the thickness and lateral size distribution, and on the defect level of the flakes.

Research on graphene and hBN toward bio-technology has focused to date on three main objectives: (i) new systems capable of inducing tissue regeneration or restoring cell-to-cell communication; (ii) specific diagnostic tools for the *in vivo* detection of biological markers of pathologies; (iii) supports



for monitoring and modulating excitable cell activity (Fattahi et al., 2014; Marchesan et al., 2017; Scaini and Ballerini, 2018). Graphene in particular has been proposed to engineer innovative biological interfaces able to adapt and interact with the biological matter (Goenka et al., 2014; Reina et al., 2017). However, the physicochemical interaction between graphene and *in vitro* cell cultures still eludes a full and comprehensive understanding, which will finally shed light on the biocompatibility of these materials (Syama and Mohanan, 2016).

Graphene and hBN have been recently found to induce specific cellular responses in different contexts. Taking into consideration the issues related to bacterial infection and the relevance of degenerative diseases, the different biological interactions of these materials can be exploited toward the following aims: (1) inducing bacterial cell death, e.g., to design medical instruments and mitigate the spreading of infections in hospital environment, and to produce anti-biofouling coatings (Parra et al., 2015c, 2017; Zurob et al., 2019); (2) stimulating cellular growth, such as in the case of tissue engineering, wound healing, and bone tissue regeneration (Fernandes et al., 2019; Şen et al., 2019; Aki et al., 2020). Devices such as epidermal electronics, intra-cortical implants for sensing and brain tissue regeneration require intimate contact with biological systems. Desired properties in these materials are softness, allowing to conform and adhere to the tissue's micro-roughness, but also biocompatibility (Jeong et al., 2013; Kabiri Ameri et al., 2017; Campos et al., 2019; Meng et al., 2019; Wang Q. et al., 2019); (3) drug delivery and tissue engineering (Edmondson et al., 2014; Goenka et al., 2014; Kumar and Parekh, 2020). As such, the physicochemical features of graphene and hBN, as well as their respective interactions with cells, must be studied. Concerning graphene-based materials (GBM), most of the studies to date focused on the functionalized forms of graphene such as graphene oxide (GO) and reduced graphene oxide (rGO). These materials, however, should be treated as separated cases due to the significant influence of their functional groups and defects in cellular interaction. Regarding hBN-based materials, research is still discontinuous and incomplete. While some forms of BN, such as BN nanotubes (BNNs) and hBN in liquid dispersion, have been widely investigated in terms of cytotoxicity and possible applications in tissue repairing after injuries (Merlo et al., 2018), 2D hBN coatings for biomedicine are still rather unexplored. Due to the general scarcity of literature regarding hBN, we have decided to extend the review to include more hBN-related materials to provide a more complete outlook.

In this paper, we reviewed the literature describing the various kinds of interactions that pristine graphene and hBN coatings respectively show with different bacterial species and different types of mammalian cells. Following this "Introduction," the section "2DM coatings and cellular interaction" will report and comment on the main interaction mechanisms taking place when graphene and hBN coatings are used to interface bacterial and mammalian cells. The section "Coating applications" will then build on this by detailing the current and prospective applications for such coatings in the biomedical field. In the "Conclusion," the main results and perspectives on the topic will be summarized.

## 2DM COATINGS AND CELLULAR INTERACTION

### Graphene and Bacteria

In this section, we report on the studied interactions between GBM coatings and bacteria, correlating them to the structural and electrical characteristics of the various coatings. Current literature on the antimicrobial mechanisms in GBMs such as GO and rGO, initially reported in 2010 (Akhavan and Ghaderi, 2010; Hu et al., 2010), has been reviewed by Henriques et al. (2018). The antibacterial activity of graphene-containing composites has also been investigated (Zhao et al., 2016). The antibacterial mechanisms exhibited by graphene and GBMs are commonly found in other 2DMs as well (Mei et al., 2020). Contrarily to most existing works in literature, in this review we focus primarily on pristine graphene coatings. Considering that the physicochemical properties of graphene strongly depend on the production and processing methods (**Figure 2A**) (Xia et al., 2019), we direct our enquiry to graphene produced by either CVD (Lisi et al., 2017; Kairi et al., 2018; Lin et al., 2018; Deng et al., 2019; Faggio et al., 2020) or LPE (Hernandez et al., 2008; Nicolosi et al., 2013), two common methods for the production of graphene – provided that in the latter case the exfoliated graphene flakes are deposited on a substrate forming a coating. While CVD-deposited graphene is typically atomically smooth (Gnisci et al., 2018; Zhang et al., 2020), coatings made of LPE graphene are often structurally irregular (Nicolosi et al., 2013; Capasso et al., 2015a; Bonaccorso et al., 2016; Niu et al., 2016), since they consist of randomly oriented stacks of flakes (typically deposited by printing or spray coating technique) (Lee et al., 2019).

In the case of atomically smooth, CVD-grown graphene coatings, the main antibacterial mechanism is determined by its electronic conductivity (**Figures 2B,C**) (Lu et al., 2012; Li et al., 2014). Regarding LPE-graphene, the roughness inherent of these types of coatings has been shown to promote bacterial cell destruction through physical interaction of the cell membrane with the edges of the flakes (**Figures 2D–F**).

In the case of atomically smooth graphene coatings (such as CVD), where the bacterial cells will not be in contact with exposed flake edges, the antibacterial effects have been shown to arise from electronic conductivity of the basal plane, which induces cell oxidation without reactive oxygen species (ROS) production (Lu et al., 2012; Li et al., 2014). This effect is attributed to the oxidative stress that arises from graphene's high electrical conductivity, which through disruption of cellular respiration produces oxidative stress and depletion of ATP levels. The antibacterial activity of the basal plane of graphene is mediated through the charge transfer capacity of the underlying substrates, i.e., bacterial cell death occurs only when the graphene film is coupled with an electrically conductive (such as Cu) or a semiconducting substrate (such as Ge). Gram + (G+) *Staphylococcus aureus* and Gram- (G-) (*Escherichia coli*) were used to investigate the antibacterial properties of monolayer graphene film on Cu, semiconductor Ge and insulator SiO<sub>2</sub>. The study showed that while graphene on Cu and Ge could inhibit the

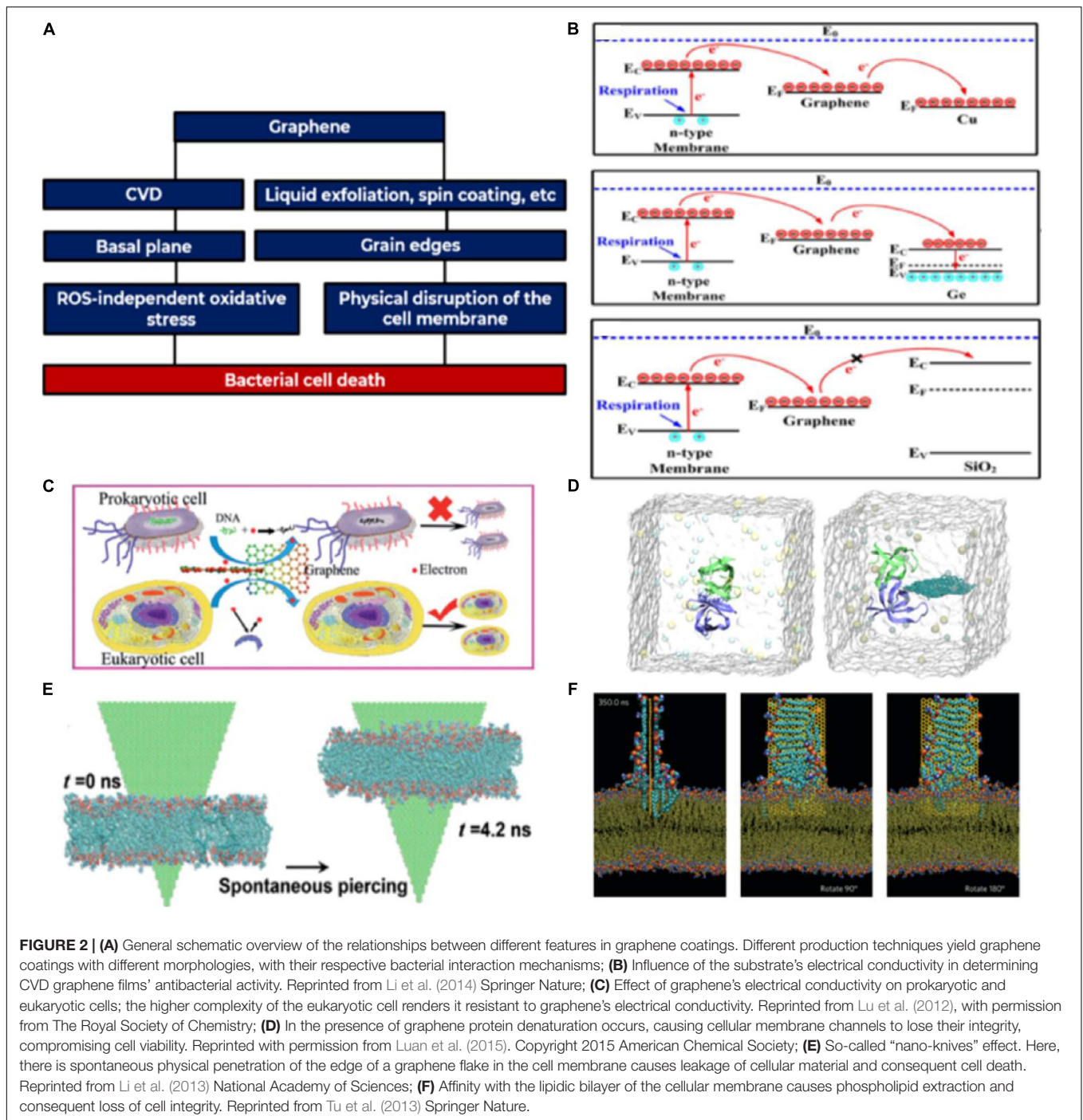


**FIGURE 2 | (A)** General schematic overview of the relationships between different features in graphene coatings. Different production techniques yield graphene coatings with different morphologies, with their respective bacterial interaction mechanisms; **(B)** Influence of the substrate's electrical conductivity in determining CVD graphene films' antibacterial activity. Reprinted from Li et al. (2014) Springer Nature; **(C)** Effect of graphene's electrical conductivity on prokaryotic and eukaryotic cells; the higher complexity of the eukaryotic cell renders it resistant to graphene's electrical conductivity. Reprinted from Lu et al. (2012), with permission from The Royal Society of Chemistry; **(D)** In the presence of graphene protein denaturation occurs, causing cellular membrane channels to lose their integrity, compromising cell viability. Reprinted with permission from Luan et al. (2015). Copyright 2015 American Chemical Society; **(E)** So-called "nano-knives" effect. Here, there is spontaneous physical penetration of the edge of a graphene flake in the cell membrane causes leakage of cellular material and consequent cell death. Reprinted from Li et al. (2013) National Academy of Sciences; **(F)** Affinity with the lipid bilayer of the cellular membrane causes phospholipid extraction and consequent loss of cell integrity. Reprinted from Tu et al. (2013) Springer Nature.

proliferation of both bacteria types, the same did not occur on SiO<sub>2</sub> (Li et al., 2014). On the one hand, G<sup>-</sup> bacteria have shown more vulnerability in samples with Si substrates than on the ones with SiO<sub>2</sub> substrates due to negatively charged cellular membrane which enhanced electron extraction. On the other hand, G<sup>+</sup> bacteria showed more susceptibility to the physical damage exerted by the vertically aligned graphene due to the composition and shape of its cell wall (Wei et al., 2020). The conclusions regarding the conductivity

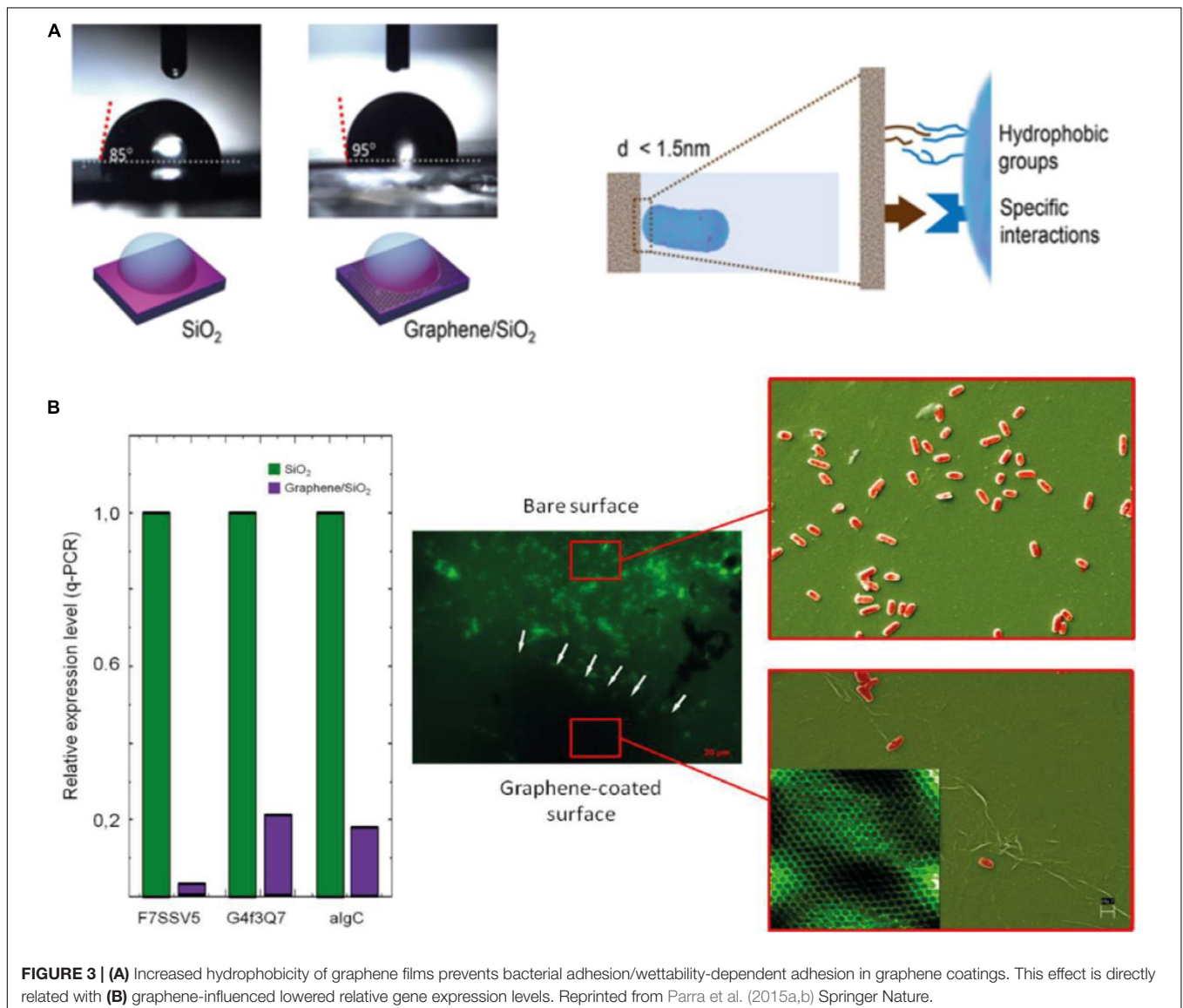
dependent antibacterial activity, however, are not consensual. Bacterial cells incubated on graphene and hBN (grown by CVD on Cu) did not show any decrease in viability after 24 h, contrarily to cells incubated on bare Cu surfaces. Here, both 2DMs equally acted as physical barriers for the cupric ions, preventing the interaction between bacteria and the Cu substrate, successfully protecting it from biocorrosion (Parra et al., 2015c). CVD-graphene on Cu and Au showed no antibacterial activity. Polycrystalline graphene coatings on

Cu, however, allowed for the release of cupric ions due to incomplete substrate coverage, promoting cell death (Dellieu et al., 2015). Proliferation of *E. coli* communities on CVD-grown graphene-on-Au despite the substrate's electrical conductivity has been reported (Szunerits and Boukherroub, 2016). Usually, graphene's antibacterial properties stem from ROS-independent oxidative stress. However, there have been reports of graphene-modified commercial water filtering membrane producing an increase in ROS in bacterial cells (Musico et al., 2014).

Wettability has been reported to play a role in bacterial adhesion. Hydrophilic GO coatings have been compared to hydrophobic rGO and graphene coatings in terms of human plasma proteins and bacterial cells adhesion. Both types of cells showed preferential adhesion to the hydrophobic samples (Henriques et al., 2020). CVD graphene grown on Cu and transferred to SiO<sub>2</sub> presented a wrinkled surface as a result from

the differential thermal expansion on Cu. This situation, coupled with bilayer regions, and micrometric damages resultant from the transfer process, exposed the underlying SiO<sub>2</sub> and contribute to the overall roughness of the material. They have observed that the coatings impact surface energy and electrostatic interactions with bacteria, decreasing bacterial adhesion through reduction of the expression levels of genes related to adhesion in *Halomonas* spp. CAM2, a typical biofilm producing species. In graphene coated SiO<sub>2</sub>, the substrate has a significant surface state density just below the conduction band, which donates electrons to graphene to balance the chemical potential at the interface. This leads to a n-type graphene coating, repelling negatively charged bacteria in solution, and to an observable decrease in wettability (Parra et al., 2015a) (Figure 3).

Based on these reports, bacterial adhesion appears to be dependent on both the surface texture and electronic properties of the substrate.





Many works have referred to the so-called “nano-knives effect.” This expression usually describes several mechanisms that arise from the contact of the cellular membrane with the edge of a graphene flake: (1) physical insertion of the sharp edges in the membrane and subsequent extraction of phospholipids (Tu et al., 2013; Pham et al., 2015); (2) protein–protein bonding disruption, due to the lipophilic nature of graphene sheets that favorably enter the hydrophobic interface between contacting proteins, leading to their destabilization (Luan et al., 2015). Both of these contribute toward the formation of pores in the membrane and occur usually in LPE-type coatings where the edges of the 2DM are exposed. Pham et al. (2015) have studied the interactions between the surface of LPE multilayer graphene with random orientated edges and *P. aeruginosa* and *S. aureus* cell membranes have been studied through both experimental and simulation methods. Graphene samples with different flake size and orientation were used, resulting in coatings with different surface texture. Their results, shown in **Table 1**, highlighted the role of roughness of the graphene coating in moderating *P. aeruginosa* and *S. aureus* death. Coatings with penetration angles closer to 90° (with respect to the surface) have more consistently shown to induce the formation of pores in the cell membrane that lead to osmotic imbalance and death. However, the two types of cells attached to the control surfaces remained viable, contrarily to the two other types of fabricated graphene surfaces – rough (GN-R) and smooth (GN-S). The differences in bactericidal activity in the two surfaces can be accounted for by taking into consideration three parameters: exposed edge length ( $L_{GN}$ ), graphene orientation ( $\theta_{GN}$ ), and edge length density ( $d_{edge}$ ). GN-R exhibits a higher number of viable *S. aureus* cells due to its decreased edge density. *S. aureus* are smaller than *P. aeruginosa*, making it possible for them to colonize the free space between edges (Pham et al., 2015).

This effect is directly related to edge density in the film and the diameter of the bacteria. They have also noted that the number of attached bacteria was variable among the films, with a higher amount being found on smoother surfaces, i.e., pyrolytic graphite surfaces used as control. Pranno et al. (2020) used LPE graphene to improve antimicrobial properties of titanium dental implants, commonly exposed to infections. The graphene flakes were then applied as a coating on the titanium. The lowest % of *S. aureus* biofilm formation was observed in samples with the smaller flake size (obtained with the longest sonication times) (Pranno et al., 2020). Besides bacteria, a physical disruption mechanism has also been recently observed in the case of virus, again via the contact with sharp edges in graphene (Innocenzi and Stagi, 2020). By fully understanding and exploiting these properties, it would be

possible to design coatings to protect surfaces from the effects of biofouling; this is particularly relevant for the biomedical field, where implants are typically subject to this kind of degradation.

## Graphene and Mammalian Cells

### Neuronal Cells

Contrarily to what it has been reported for bacteria, graphene has proven to be suitable for interfacing with mammalian tissues. Despite the existence of a large variety of publications regarding the biocompatibility and the cytotoxicity of GBMs both in *in vitro* (cell lines and primary cultures) and *in vivo* (rodent) models, the majority of them focused on the functionalized forms of graphene: GO and rGO (Pinto et al., 2013; Lalwani et al., 2016). However, the biocompatibility of pristine graphene-coated supports is only partially investigated and usually limited to cell culture models (Li et al., 2011; Park et al., 2011; Tang et al., 2013; He et al., 2016; Veliev et al., 2016; Fischer et al., 2018; Kitko et al., 2018; Pampaloni et al., 2018). Since graphene has been considered as a potential therapeutically tool for neurological diseases treatment, a specific attention has been given to its biocompatibility for neuronal cells (Akhavan, 2016; Bei et al., 2019). Li et al. (2011) fabricated a high-quality CVD graphene coated device and tested its biocompatibility as an interface for primary hippocampal neurons. Authors reported no obvious cytotoxicity, as CVD graphene did not significantly affect cell viability. They speculated that the “friendly” interaction between graphene and neurons is favored by the non-detectability of the catalyst (Cu) contamination traces, usually associated with ROSs formation (Firme and Bandaru, 2010; Li et al., 2011).

Veliev et al. (2016) confirmed the observation by Li et al. (2011) while investigating the development of primary hippocampal neurons plated onto monolayer graphene. In accordance with previous findings, graphene showed a good biocompatibility, but authors attributed that to the high crystalline quality of graphene. It is important to clarify that, in both studies, authors limited the investigation until 5 and 7 days *in vitro* (DIV), respectively (Li et al., 2011; Veliev et al., 2016). More recently, Pampaloni et al. (2018) tested the interaction between monolayer graphene and neurons, again restricting the biocompatibility evaluation to 8–10 DIV. In accordance to previous studies, authors confirmed the excellent biocompatibility of the material, reporting no differences in cell viability. Due to the presence of astrocytes in the primary cultures, authors also evaluated the influence of graphene on astrocytes, indicating no evident cytotoxic effect on glial cells and no changes in neurons/astrocytes ratio (Pampaloni et al., 2018). He et al. (2016) extended the time of cytotoxicity investigation, monitoring neuronal cultures for 21 days: They did not found any evident cytotoxicity and confirmed the excellent biocompatibility of graphene-coated substrates. Indeed, 4 h after the plating, neurons were correctly adhered and spread out compared to ones grown in control conditions. They ascribed the good biocompatibility to the substrate surface morphological characteristics. Starting from the assumption that material surface structure has an impact on cellular adhesion (Li et al., 2010), He et al. (2016) suggested that the

**TABLE 1** | Different coating surface parameters and their antibacterial effect against model species (Pham et al., 2015).

Material	$L_{GN}$	$\theta_{GN}$	$d_{edge}$	Effective against
GN-R	137.3 nm	62.1°	7.7 $\mu\text{m}/\mu\text{m}^2$	<i>P. aeruginosa</i>
GN-S	79.7 nm	37.2°	10.8 $\mu\text{m}/\mu\text{m}^2$	<i>P. aeruginosa</i> <i>S. aureus</i>



presence of ripples and wrinkles might result in an increased mechanical interlocking between graphene and hippocampal neurons. Interestingly, Kitko et al. (2018) ascribed to cholesterol the good neuron adhesion into graphene. Previously, Zhang et al. (2016) had demonstrated through computational modeling that graphene interacts preferentially with cholesterol (specifically localized at the level of the eukaryotic membranes), causing its extraction (Zhang and Wang, 2015). Starting from this assumption, Kitko et al. (2018) confirmed experimentally the computational prediction, demonstrating that graphene is capable to increase cell membrane cholesterol concentration. Authors did not limit their study to neurons, but replicated the experiments taking in consideration fibroblasts. Again, they showed an analogous cholesterol increase in fibroblasts grown onto graphene, concluding that cholesterol should be considered as a graphene effect mediator (Kitko et al., 2018). Specific attention has also been given to human neuronal stem cells (hNSC). Park et al. investigated the effect of graphene-coated solid substrates on hNSCs. Authors did not report any harmful effect of graphene on the progenitor cells that maintained their biochemical properties (positivity to nestin immunostaining), confirming the good biocompatibility of the support (Figure 4) (Park et al., 2011). Same results have been confirmed by Tang et al. (2013). However, in this work, authors grew hNSCs onto graphene nanospheres. They reported that cells tightly adhered to the substrates without any evident cytotoxic response (Tang et al., 2013). Similarly, a graphene-based foam was shown to act as biocompatible scaffold for the culture of human neurons, supporting cell viability and differentiation of human embryonic stem cell-derived cortical neurons (D'Abaco et al., 2018).

A controversial aspect, which is necessary to mention, concerns the common practice of pre-coating graphene-based substrates. The practice of pre-coating graphene with poly-L-lysine (PLL) before neuronal seeding has been used by Li et al. (2011) and later by Veliev et al. (2016). Due to its high hydrophilicity, PLL is known to be an important factor for correct cell adhesion to non-biological substrates, by mimicking the extracellular matrix. Authors suggested that a PLL coating might be an important factor that has favored neuronal adhesion and promoted cell viability. Indeed, neurons grown onto PLL-coated graphene exhibited a larger cell body size and a highly developed dendritic arborization with long and branched neurites (Li et al., 2011; Veliev et al., 2016). Alternately, both Park et al. (2011) and Tang et al. (2013) treated graphene and control glass with laminin to facilitate hNSC adhesion. In addition, He et al. (2016) clearly stated the impossibility of growing neurons onto graphene without coating. Authors excluded the interference of PLL-coating on the presented data and suggested that the good cell adhesion on the substrate is related exclusively to the graphene surface properties (He et al., 2016). Nonetheless, at the same time, Veliev et al. demonstrated the possibility to grow neurons onto bare graphene. In accordance with Veliev et al. and Kitko et al. (2018) managed to properly seed neurons on bare CVD graphene, without the need of a pre-coating treatment. However, authors underlined that the coating absence does not permit a total interaction between neurons and the substrate. Indeed, this approach did not prevent the deposition

of biomolecules (present in the serum containing media) that could form a protein corona (previously demonstrated for GO, Hu et al., 2011). Pampaloni et al. (2018) confirmed the possibility to grow neurons onto graphene without any pre-coating step. But, it is necessary to report that authors used non-pure neuronal cultures (Pampaloni et al., 2018). The presence of glial cells must be seriously considered, since astrocytes are known to favor neuronal adhesion, neurite elongation and synapse formation and maturation (Laming et al., 2000; Chung et al., 2015). Because of the variety of discordant studies, PLL use to promote cell adhesion remains a controversial aspect in the study of the interaction between graphene and mammalian cells. The mechanism by which neuronal cells properly adheres to graphene without a pre-coating treatment is still unclear and needs to be further investigated. Indeed, it becomes necessary to deeply evaluate the chemical interaction between PLL and graphene, to avoid data misinterpretation.

### Non-neuronal Cells

Beyond the possible application in neurological diseases/disorders, graphene also represents an attractive material for non-neuronal tissue engineering. The possibility to use graphene as a platform that supports and promotes cell adhesion, proliferation, and maturation, pushed the researchers to investigate its interaction with non-excitable cells. Kalbacova et al. (2010) tested the capability of human non-neuronal cells to grow onto monolayer and multilayer graphene. Authors plated three distinct types of cells: human osteoblasts, SAOS-2 cells (a cell line) and human mesenchymal stromal cells (MSCs, primary cells). 48 h after the plating, both osteoblasts and MSCs homogeneously covered all the graphene substrate, verifying the biocompatibility of the substrate (Kalbacova et al., 2010). Subsequently, three independent studies reached the same conclusions as Kalbacova et al. (2010). Nayak et al. (2011) verified the biocompatibility of graphene for mesenchymal stromal cells (MSCs), reporting no changes in cell viability between MSCs plated onto graphene-coated and non-coated supports and concluding that cell seeding was not negatively affected by the graphene presence. Aryaei et al. (2014) confirmed the biocompatibility of the graphene supports for osteoblast cells, investigating viability and adhesion. Authors reported no toxic effects of graphene across all substrates independently by the different surface properties (i.e., thickness and roughness) (Aryaei et al., 2014). Park et al. further investigated the CVD-graphene interaction with the mesenchymal stem cells, focusing on the possibility to promote the stem cell differentiation into cardiomyocytes. Firstly, authors displayed that graphene did not alter cell viability. Indeed, no significant changes were showed in terms of living cells between MSCs plated onto graphene-coated or uncoated supports, at different time points. In addition, cells plated onto graphene presented an increased expression of Bcl-2 (anti-apoptotic marker) and a reduced expression of Caspase-3 (pro-apoptotic marker), but the degree of cell proliferation was similar across the conditions (PCNA expression) (Park et al., 2014). In more recent years, Rodriguez et al. (2017) and Xie et al. (2017) studied the biocompatibility of the graphene film for human dental pulp stem cells (DPSC). In both works,

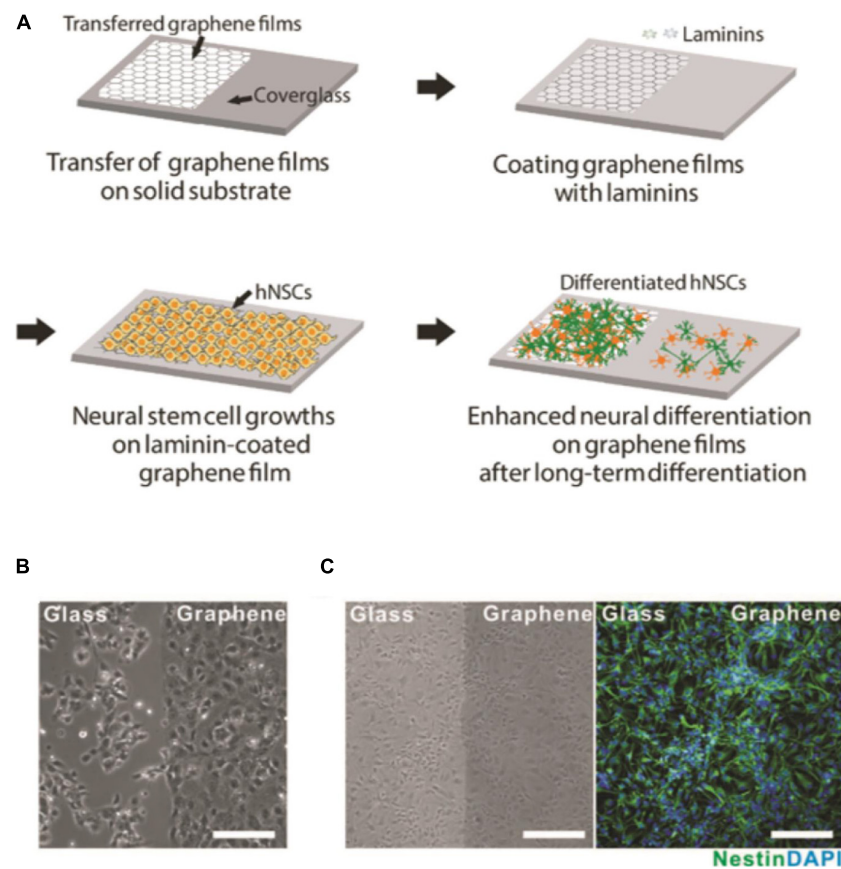


**FIGURE 4 |** Growth of hNSCs on graphene. **(A)** Schematics of the process. **(B)** Bright-field image of hNSCs on the boundary area between glass (left) and graphene (right) 10 h after cell seeding. Note that more hNSCs were attached on graphene region than on glass region at this early period of cell adhesion. **(C)** Bright-field (left) and fluorescence (right) images of hNSCs proliferated for 5 days. Immunostaining markers were nestin (green) for neural stem cells and DAPI (blue) for nuclei. There was no difference in cell numbers between the graphene and glass regions. Note that all the cells were immunopositive for the nestin marker, indicating they exhibited the property of NSCs. All scale bars correspond to 200  $\mu\text{m}$ . Reprinted from Park et al. (2011) Elsevier Ltd.

authors demonstrated that DPSC were able to adhere correctly to graphene coated substrate as early as 1 day after the seeding and properly proliferate, despite material high hydrophobicity (Rodriguez et al., 2017; Xie et al., 2017).

Aiming at an extended knowledge about the interaction of graphene with mammalian cells, it is also useful to study how graphene can interact with cancer cells. In a way similar to its interaction with bacteria, graphene shows toxic effects when put in contact with tumor derived cells. Despite the need for further investigation in this field, in recent years some preliminary studies suggest the possibility to use graphene as anti-neoplastic agent. Zhou et al. (2014) studied the interaction between graphene in a liquid solution and human breast cancer cells (MDA-MB-231). Authors demonstrated that graphene led to the inhibition of electron transfer chains, a consequently reduction in ATP production and impairment of F-actin cytoskeleton assembly, crucial mechanisms to promote migration and invasion of metastatic cells (Zhou et al., 2014). In addition, both GO and B-rGO, also in liquid solution, have shown toxicity toward MCF-7 human breast cancer cells in a dose-dependent manner, as shown by a decreased cell viability,

associated with an increased ROS production and release of lactate dehydrogenase (Gurunathan et al., 2013). However, studies regarding the interaction of graphene with virus and cancer cells are still limited, and further research will be thus needed in the future. Monolayer graphene grown by CVD was studied as a coating for porous Ti substrates for bone repair. The coatings revealed to be biocompatible and to favor cellular growth and adhesion, thus improving the properties of the substrate. The positive results were attributed to the impermeability of graphene to metallic ions, preventing the contact between cells and metal ions in the porous structure (Lascano et al., 2020).

The number of *in vivo* studies investigating the toxicology, distribution and clearance of graphene is gradually increasing. Nonetheless, the vast majority concerns the functionalized form of graphene, in particular GO, given its capability to better interact with the biological matter (Nurunnabi et al., 2015; Lalwani et al., 2016; Lu et al., 2019). For these reasons we extended our attention by including graphene nanosheets and nanoplatelets (GNP). Yang et al. (2011) studied for the first time the long-term *in vivo* distribution and toxicity of 125I-labeled

graphene nanosheets functionalized with polyethylene glycol (PEG). Authors treated intravenously mice with graphene nanosheets at 20 mg/kg for 3 months and demonstrated that the material localized preferentially at the level of the reticuloendothelial system (RES), liver and spleen. Interestingly, graphene nanosheets were gradually cleared by both renal and fecal excretion. No significant toxicity was detected by blood analysis and histological examinations, leading authors to encourage further studies in this field (Yang et al., 2011). Between 2011 and 2013, three independent works investigating the *in vivo* toxicity of graphene at the level of the lung were published (Duch et al., 2011; Schinwald et al., 2012; Ma-Hock et al., 2013). Duch et al. (2011) studied the *in vivo* toxicity of three distinct GBMs: solution of aggregated graphene, dispersed graphene into pluronic acid and GO and administered them intra-tracheally into the lung of young mice. Interestingly, severe tissue injuries were reported in mice treated with GO persisting until 21 days after the administration; on the contrary pristine graphene showed a significant reduction in toxicity. Authors demonstrated that GO induces a covalent oxidation and boosts pulmonary toxicity by enhancing mitochondrial ROS species formation, tissue inflammation and cell apoptosis, concluding that the 2D-graphene is a safer option for a biomedical application (Duch et al., 2011). Schinwald et al. (2012) used commercially available GNPs (consisting in few layers of graphene) and evaluated their breathability, deposition and eventual inflammatory potential. They demonstrate that GNPs (up to 25  $\mu\text{m}$  of diameter) were respirable and deposited beyond the ciliated airways. Interestingly the GNPs revealed to be inflammogenic in both lung and pleural space. Indeed, several inflammatory markers were found after both the bronchoalveolar lavage, the pleural lavage and the *in vitro* assay. Authors stated that GNPs are a potential risk for the human health and the reduction of their diameter is needed for biomedical applications, given the capability of macrophages to phagocyte them (Schinwald et al., 2012). Ma-Hock et al. (2013) exposed male Wistar rats for 6 h per day on 5 consecutive days and evaluated the toxicity after the end and after 3 weeks from the exposure. They reported an increase in the inflammatory processes at exposure concentration of 10  $\text{mg}/\text{m}^3$  (Ma-Hock et al., 2013). The authors of the three works agreed in suggesting a deeper investigation of the *in vivo* cytotoxic of the graphene before any human application. Sasidharan et al. (2015) presented a 3-month report that studied the acute and chronic toxicity of intravenously administered graphene in male Swiss albino mice. For their work, authors choose to administer 20 mg/kg of few layer graphene (FLG) and its derivatives carboxylated FLG and PEGylated FLG. They demonstrated that during the first 24 h graphene accumulated preferentially in the lung, which represented the tissue with the highest uptake and retention. In addition, graphene was found also in spleen, liver, and kidney, but no accumulation was detected in brain, heart, or testis (Figure 5). FLG caused severe cellular and tissue damages. Necrosis, fibrosis, hepatic and renal injuries and glomerular dysfunction were detected in the organs where graphene was accumulated. Molecular analysis revealed that 23 markers of critical inflammation and immune response were altered in gene expression. On the contrary, FLG-PEG

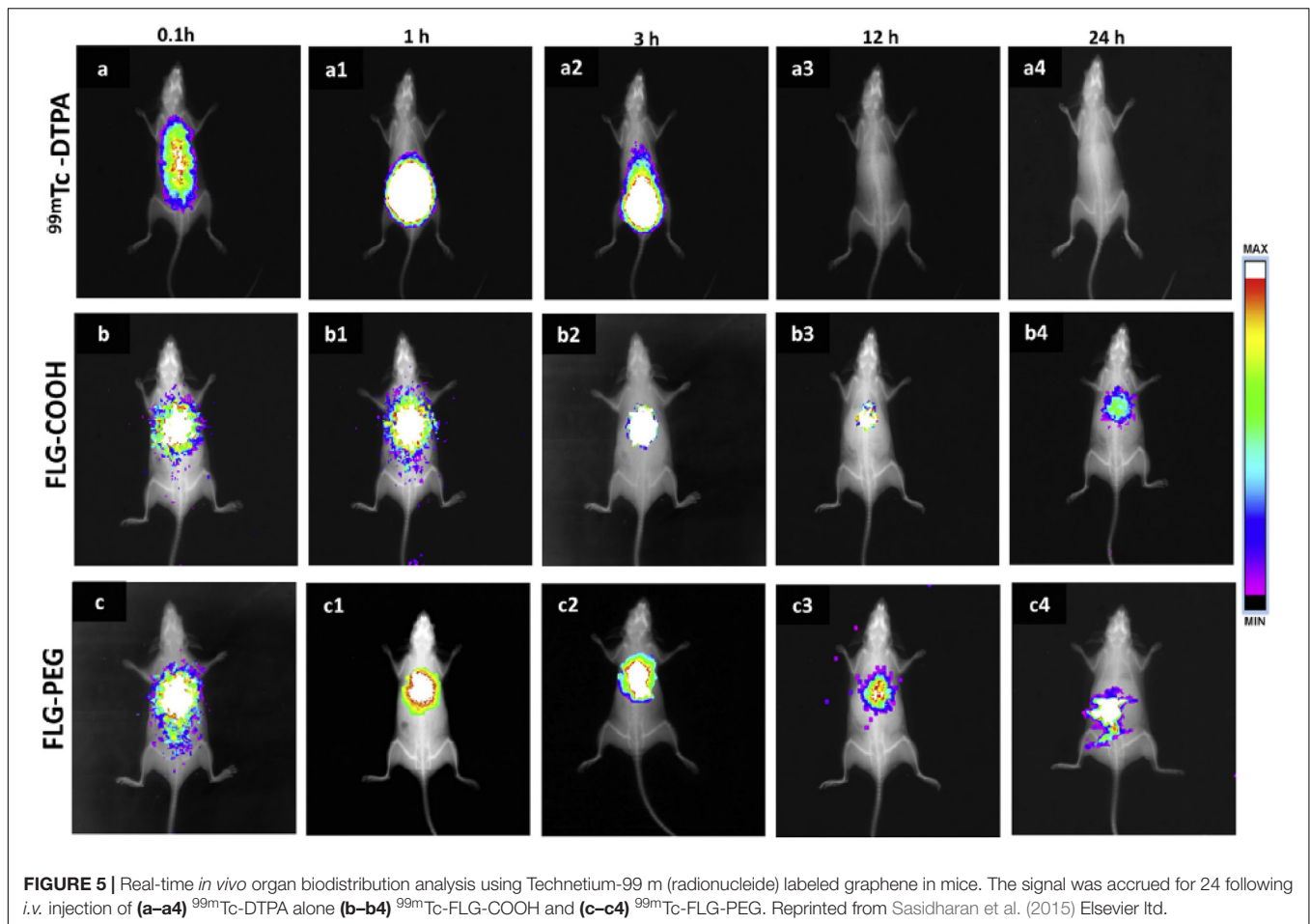
induced no significant toxicity, despite its persistence in liver and spleen after 3 months. Authors concluded that graphene functionalization is the safer root for the biomedical application of this material (Sasidharan et al., 2015).

In the same year, Shin et al. (2015) published a promising work investigating the graphene *in vivo* toxicity by nasal inhalation system Sprague-Dawley rats. Animals were treated for 6 h/day for 5 days and evaluated the recovery for 1, 3, 7, or 28 days. Authors took in consideration three distinct groups: (i) rats treated with control ambient air; (ii) rats treated with a low concentration of graphene (0.68  $\text{mg}/\text{m}^3$ ); and (iii) rats treated with high concentration of graphene (3.86  $\text{mg}/\text{m}^3$ ). No significant alterations were detected in animal and organ weight and in the levels of protein expression (i.e., lactate dehydrogenase and albumin). Despite alveolar macrophage ingestion of graphene was observed in both material-treated groups, no severe toxic effect was detected at the concentration and time points used (Shin et al., 2015). Mao et al. (2016) studied the long-term *in vivo* distribution of graphene in mice after inhalation associated with precise graphene quantification. Authors treated mice with a carbon-14 labeled FLG by oral gavage or intratracheal instillation and quantify the distribution of FLG for up to 3 or 28 days. Mice treated intratracheally showed a FLG retention in the lung of about 47% with a dose-dependent acute lung injury and pulmonary edema. Interestingly the toxicity resulted reduced with time despite the continued presence of FLG in the lung. 1 and 0.18% of FLG was detected in liver and spleen, respectively after 14 days and in feces after 28 days. No gastrointestinal absorption was detected in animals treated with FLG by oral gavage. In this robust work, authors demonstrated the partial persistence of graphene in the lung (causing only transient cytotoxicity) and, in accordance with Yang et al. (2011), its capability to be eliminated by feces (Mao et al., 2016). In Jia et al. (2019) highlighted the *in vitro* (HEK cells) and *in vivo* (zebrafish) toxicity of graphene and GO of three different sizes (small, medium, and large). Authors demonstrated that *in vitro* both the small and the large size of graphene and GO increased DNA damage, ROS formation and the expression of associated critical genetic markers. Injection of both graphene and GO in zebrafish induced ROS generation and developmental alterations. In general, a significant higher toxicity was reported for smaller size graphene (in particular for GO) that showed a stronger ability to decrease the survival rate and induce the acute toxicity (Jia et al., 2019).

## hBN and Bacteria

Compared to graphene, the current literature focusing on the interactions between hBN-based materials with cells is rather limited. For this reason, in addition to hBN-based coatings, in this paragraph we report also on the main studies conducted on hBN materials and nanocomposites dispersed in liquids (i.e., not deposited as coatings in solid state), including other BN structures. Kivanç et al. (2018) investigated the effect of hBN NPs in *S. mutans* 3.3, *S. pasteurii* M3, *Candida* sp.M25, and *S. mutans* ATTC 25175 specimens. The used concentration of hBN NPs did not result in bacterial cell death but inhibited bacterial biofilm growth (Kivanç et al., 2018). Studies





conducted using hBN nanoflakes produced by LPE suggest that they can physically damage bacteria cells by disrupting their membrane and consequentially releasing intracellular material. Zhang et al. (2019), via experiments and molecular dynamics (MD) simulations, revealed that phospholipids are attracted to the surface of BN, leading to the nanosheet insertion and destructive lipid extraction, with the hydrophobic effect having a role in the extraction process. In their work, they modeled the inner and outer membranes of G- specimens and uncovered a phospholipid extraction effect in the presence of hBN flakes, akin to the extraction effect exhibited by graphene (Figure 6) (Zhang et al., 2019).

Similarly, Li Z. et al. (2018) simulated the lipid extraction caused by single BN nanosheets and reported a correlation between changes in the lipid extraction behavior and temperature, due to the lipid membrane phase transition. Pandit et al. (2019) demonstrated that oriented BN flakes in a low-density polyethylene matrix can have bactericidal effects when the extruded nanocomposite is in contact with several types of bacteria. The findings demonstrate that the sharp-edged BN nanoflakes changed the cells envelope morphology due to substantial physical damage, leading to lysis of the bacterial cells (Pandit et al., 2019). Antimicrobial composites were produced by grafting quaternary ammonium compounds

to the surface of hBN nanoplatelets and using the modified nanoplatelets as filler for linear low-density polyethylene. The nanocomposite was 100% effective in inhibiting *E. coli* and *S. aureus* bacterial growth. The excellent antimicrobial activity is attributed to direct contact mechanisms, which allows to avoid the use of biocides and consequently reduce environmental pollution (Xiong et al., 2019). Gudź et al. (2020) showed that both pristine BN films and gentamicin- and amphotericin-loaded films successfully inhibited the growth of antibiotic resistant G- *E. coli* K-261. The immersion of the BN film in normal saline solution generates ROS species, which can lead to accelerated oxidative stress at the site of physical cell damage (Gudź et al., 2020). The antibacterial activity of a polyhydroxyalkanoate, chitosan, and hBN-incorporated nanocomposite was investigated through a time-kill method against multi drug resistant bacteria, such as methicillin-resistant *S. aureus* and *E. coli* (K1 strains) bacteria. The results showed significant antibacterial activity (Mukheem et al., 2019). BN nanosheets produced by chemical exfoliation and subsequently doped with varying concentrations of Cu showed excellent catalytic activity for dye degradation and treatment of industrial wastewater. The Cu-doped BN nanosheets also showed potential as antimicrobial agents against *S. aureus* and *E. coli* bacteria (Ikram et al., 2020).



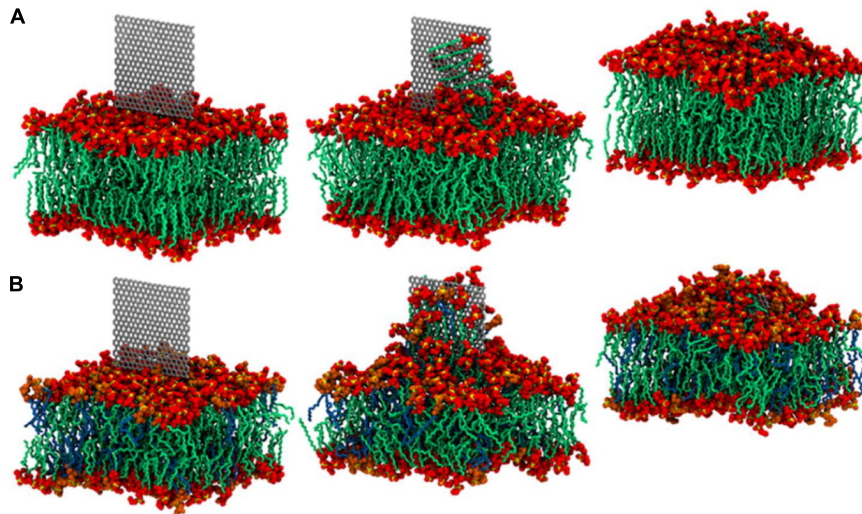


**FIGURE 6 |** hBN flakes cause lipid extraction, as shown through MD simulation. **(A,B)** Represent the outer and inner membranes present in a G-organism, respectively, after 0, 50, and 500 ns. The continuous extraction of phospholipids from the membrane's bilayer causes damage and subsequent loss of integrity. Reprinted with permission from Zhang et al. (2019). Copyright 2019, American Chemical Society.

The current state of the art on the mechanisms of interaction of hBN with bacteria is still in nascent stage. Further research is needed to clarify the mechanisms, possibly in comparative terms to graphene, whose high electrical conductivity seems to play an important role in mediating its interaction with cells.

## hBN and Mammalian Cells

In the last decade, studies on the interaction between mammalian cells and BN nanotubes (BNNTs) have dominated the vast majority of publications, leaving contrasting results, and unanswered questions (Chen et al., 2009; Ciofani et al., 2010a,b, 2014; Lahiri et al., 2010, 2011; Horváth et al., 2011; Jiang et al., 2015). In recent years, the soluble forms of hBNs, i.e., nanoparticles (NPs) and nanosheets, have been considered (Kıvanç et al., 2018; Mateti et al., 2018; Taskin et al., 2020), while the toxicity of 2D hBN films and possible cell interfacing applications were not investigated. Reviews regarding the applications of different BN structures have pointed out important works regarding the interactions with mammalian cells and their cytotoxicity (Pan et al., 2020). hBN and BNNTs in general have been considered as good candidates for a wide range of applications in the biomedicine (e.g., drug and gene delivery, tissue-mimicking biomaterials), pharmaceuticals and cosmetics (Emanet et al., 2019). For these reasons, similarly to the chapter before, we extended the literature survey to hBN materials in solution.

Mateti et al. (2018) studied the biocompatibility of hBN nanosheets and NPs of different dimensions for osteoblast-like cells (SaOS2). They obtained NPs with a diameter range between 100 and 200 nm and two distinct groups of nanosheets (NS1, diameter: 1  $\mu\text{m}$  and thickness: 100 nm; NS2, diameter: 100 nm and thickness: 3 nm). Authors tested the cytotoxicity of the materials for SaOS2 cells and reported a significant decrease in cell viability in presence of both nanosheets and NPs with

the smallest size. They attributed the cytotoxicity of such small NPs to their capability to be internalized by the cell, triggering ROS formation (Mateti et al., 2018). Taskin et al. (2020) studied and tested the biocompatibility of hBN flakes *in vitro* on a mouse hippocampal cell line (mHippo E14). Authors treated cells with hBN and its degradation product (BA), fixing the range of exposure at 4.4–440  $\mu\text{m/mL}$  (for 24 and 72 h). No cytotoxic effects, no changes in cell cycle, ROS production and DNA damage were detected for hBN concentration lower than 22  $\mu\text{m/mL}$ . In addition, both hBN and BA favored the cell survival after exposure to doxorubicin (an anti-neoplastic agent), by reducing oxidative stress (Figure 7) (Taskin et al., 2020).

Kıvanç et al. (2018) investigated the effect of hBN NPs in two mammalian cell lines: human skin fibroblasts (CCD-1094Sk, ATCC® CRL 2120™) and Madin-Darby canine kidney cells. At the highest concentration of 0.4 mg/mL, the hBN NPs caused mild cytotoxic effect on CRL-2120 cells (Kıvanç et al., 2018). Polyvinyl alcohol/hBN/bacterial cellulose (BC), 3D-printed composites have been used as bone tissue scaffolds. Significant increase in human osteoblast cell viability on the scaffolds was observed for composites with specific weight ratios. The work deduced that BC-doped, 3D-printed scaffolds with well-defined porous structures have considerable potential in bone tissue engineering. hBN contributes to improve the mechanical properties of the composite, as well as the thermal stability and swelling degree (Aki et al., 2020). Chemically functionalized BNNTs have shown biocompatibility in *in vitro* assays on fibroblast cells (Ciofani et al., 2012). BNNTs have been investigated as boron atom carriers in boron neutron capture therapy, a treatment for several forms of aggressive cancer, including cerebral glioblastoma multiforme. *In vitro* results have pointed toward selective uptake of these nanotube vectors by glioblastoma multiforme cells, but not by normal human fibroblast (Ciofani et al., 2009).

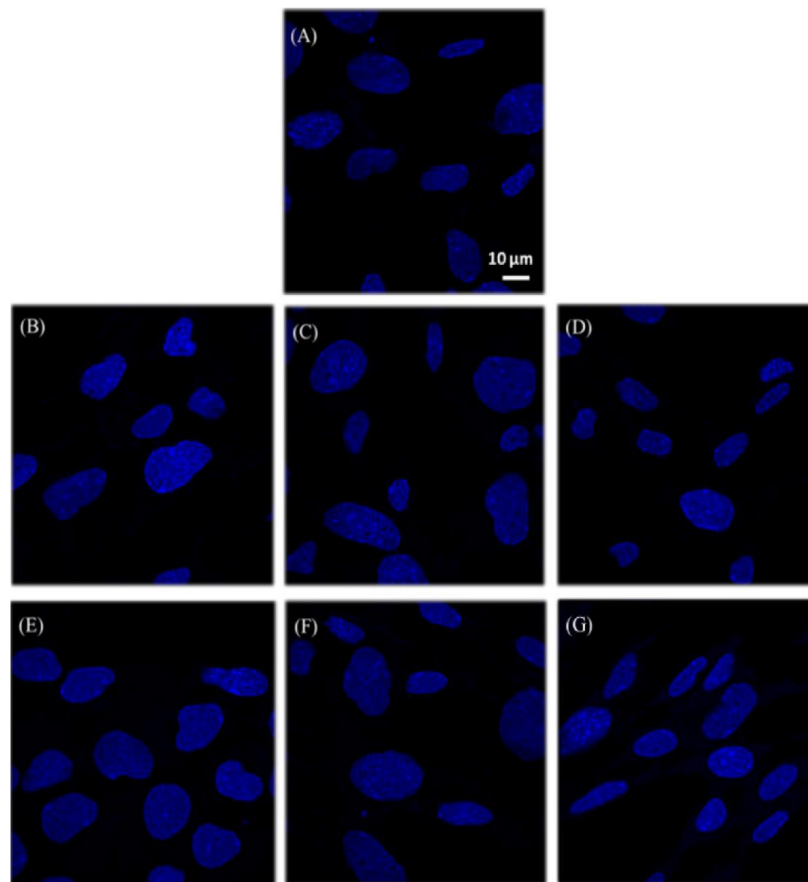


**FIGURE 7 |** Detection of apoptotic bodies on embryonic mouse hippocampal (mHippoE-14) cells treated with hBNs and BA exposed for 72 h. **(A)** Control cells, **(B)** 4.4, **(C)** 22, and **(D)** 44  $\mu\text{g/mL}$  B containing hBNs with 72 h exposure, and **(E)** 4.4, **(F)** 22, and **(G)** 44  $\mu\text{g/mL}$  B containing BA with 72 h exposure. Reprinted from Irem et al. (2019).

hBN synthesized from BA has been used as a therapeutic route in wound healing, due to their biodegradability and ease of dispersion in aqueous environment. Cellular uptake capacities were determined, and human umbilical vein endothelial cells (HUVEC) had higher uptake capacity when compared to human dermal fibroblasts, explaining the different proliferation effect of hBN in these cell lines. Nevertheless, improvement of proliferation and migration in both types of cells was observed. Angiogenesis ability of HUVECs treated with hBN showed promising results. Additionally, it was found that hBN might also improve the wound healing process by lowering ROS due to its antioxidant capacity, similarly to BA; it was found that hBN can rescue cells from apoptosis, and that at low concentrations, it did not depolarize the mitochondria nor disrupt F-actin formation (Şen et al., 2019).

The dose-dependent effect of hBN NPs on biological systems was investigated *in vivo* in Wistar albino rat subjects. Biochemical, hematologic and histopathology parameters were examined for 24 h after intravenous injection of different doses of hBN NPs. Hematological and biochemical parameters showed no changes except in the 1600 and 3200  $\mu\text{g/kg}$  dose groups. Histological detections on these groups indicated the

hBN NP treatment induced significant damage in the liver, kidney, heart, spleen, and pancreas. The results also indicated that hBN NPs with diameter of 121 nm could hold promise in biomedical applications, where low doses between 50 and 800  $\mu\text{g/kg}$  are not toxic (Kar et al., 2020). Parkinson's disease (PD) is an aggressive neurodegenerative disease characterized by the loss of dopamine-sensitive neurons in the substantia nigra region of the brain. hBNs demonstrated neuroprotective properties in the experimental PD model induced by 1-methyl-4-phenylpyridinium ( $\text{MPP}^+$ ). Cell viability tests confirmed that hBNs do not exhibit neurotoxic effects. Flow cytometry analysis determined that hBN significantly decreased apoptotic cells in the experimental PD model (Küçükdoğan et al., 2020). Overall, although less studied than GBMs, hBN, and hBN-based materials have shown promise in a wide range of biomedical applications.

## COATING APPLICATIONS

As detailed in Section “2DM coatings and cellular interaction,” graphene and hBN present complex interaction in biological medium mediated either by the direct edge contact and

membrane disruption, or through electrical conductivity. In the case of bacterial cells, the features of coatings made from these materials have resulted in decreased adhesion and cell destruction. However, in the case of mammalian cells, not only are these mechanisms innocuous, but they are advantageous in promoting tissue growth and cell differentiation through enhanced adhesion. Exploiting these features allow the design of coatings for different ends, with cell-specific tailored interactions. In the following section we show how these materials have a positive impact in preventing biofouling by decreasing cellular adhesion, and how they can be used to enhance mammalian cell growth.

## Graphene and hBN for Antifouling

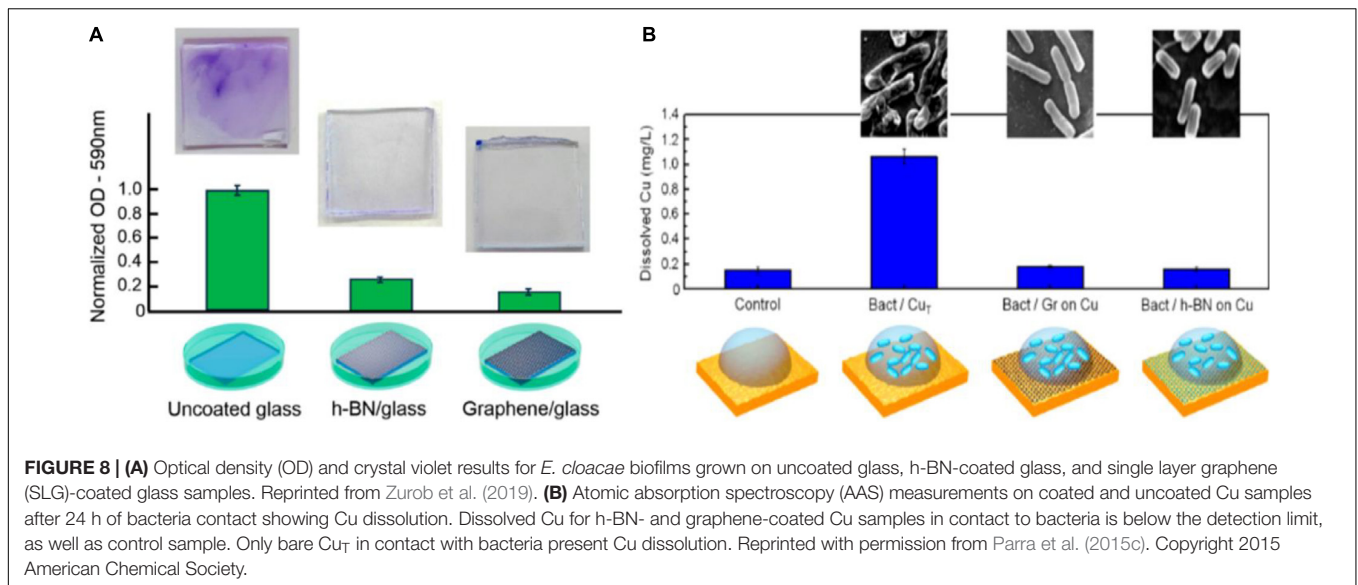
Corrosion accounts for a significant economic cost annually, thus motivating numerous efforts to prevent it (Gerhardus and Brongers, 2010; DNV GL, 2015). One type of corrosion comes from biofouling, which encompasses the formation of a microbial biofilm on a metallic surface. Microorganisms growing on surfaces perform a variety of metabolic reactions, with products that promote the deterioration of the underlying substratum, ultimately leading to the mechanical failure of the surface they are attached to. The biofilm contains exopolymers which impede the diffusion of solutes and gases between the surface and the bulk aqueous phase. These exopolymeric substances are essential for the biofilm since they allow the development of highly structured microbial communities on the surface by enhancing adhesion to the metallic surface and providing stability to the biofilm. The various species can collectively carry out metabolic activities that are potentially more corrosive to the underlying surface than could be achieved by a single species alone. These features of sessile microbial growth represent important prerequisites of biocorrosion. Additionally, bacterial species within the biofilm are more resistant to antibiotic and UV radiation than those in their planktonic or sessile state, thus requiring novel approaches in order to mitigate (Otter et al., 2015). Currently, the techniques used to control biofouling include physical (heat treatments, pulse power-technology, radioactive coatings, flushing, scrubbing and biological control) and chemical methods (biocides, chlorine, marine bioactive compounds, Ag, or Cu alloys). However, these approaches are non-specific, which leads to environmental impact resulting from their effect on species not involved in biofilm formation (Parra et al., 2015a). While typical approaches rely on the application of coatings with bactericidal payloads, these present limitations such as low durability and gradually lead to bacterial resistance development as well as negative environmental impacts (Reed et al., 2019; Zurob et al., 2019). Other control strategies imply the use of polymeric coatings, such as epoxy. This type of coating acts as a barrier against water, oxygen, and corrosive species. Despite their advantageous properties, such as low toxicity, these are a temporary solution, due to their high brittleness, poor impact resistance and flexibility, leading to microscopic cracks and mechanical damage (Parra et al., 2015b; Chhetri et al., 2019).

Here, we contemplate the interaction mechanisms of graphene or hBN with bacterial cells as the basis for effective antibiofouling coatings. These materials have demonstrated

superior functionality in comparison to the other above-mentioned approaches due to their rich biological interaction mechanism, explored in the prior sections, which present the development of more resistant bacteria. Graphene and hBN coatings have shown to be ion impermeable barriers due to their reduced lattice size, which is smaller than the bacteria and their metabolites thus creating a physical barrier that prevents the bacteria from interacting, and consequently corroding the underlying substrate. Parra et al. (2015c, 2017) have shown that this mechanism is effective in controlling MIC in Cu and Ni substrates. Zurob et al. (2019) studied the effect of graphene and hBN coatings on a wild Gram- *Enterobacter cloacae* strain biofilm. Graphene-coated glass exhibits 83.6% less biofilm than uncoated glass. In the case of hBN, a 73.8% suppression of biofilm formation was found (Figure 8). While both coatings contribute to a significant reduction of the biofilm, no bactericidal effects were found, suggesting that the bactericidal effect is independent of the charge transfer capabilities of the substrate, and that biofilm reduction could be attributed to decreased cellular adhesion. The authors mention the influence of electrostatic interactions and surface energy rather than charge transfer in antibacterial properties (Zurob et al., 2019). The performance of CVD hBN and graphene coatings in preventing cellular adhesion are shown in Figure 8. Parra and Zurob agreed that bacterial adhesion inhibition is dependent on surface energy and electrostatic interaction. Simultaneously to the ability to combat microbial corrosion, hBN coatings can be also effective at suppressing galvanic effects due to their insulating nature, unlike graphene, where the local defects act as a cathodic site for anchoring and reducing terminal electron acceptors, enhancing the negative effects of galvanic corrosion. This was demonstrated by Chilkoor et al. (2018) where a CVD-grown monolayer hBN was used to protect a Cu substrate from planktonic and sessile forms of *D. alaskensis* G20, a sulfate-reducing bacterium. The monolayer hBN acted as an impermeable layer for the corrosion effects of the biofilm, blocking the migration of aggressive metabolites to the substrate and subsequent degradation (Chilkoor et al., 2018).

Al-Saadi et al. (2017) reported the beneficial impact from the impregnation of hBN into a silane composite for the purpose of bioimplant coatings, successfully improving the corrosion resistance by nearly fivefold and durability of the Mg alloy. By impregnating specimens into a Hank's solution for 96 h the effects of calcium phosphate deposition were ascertained, with less corrosion products formed and no delamination detected (Al-Saadi et al., 2017). The impact of these findings shows that the incorporation of hBN into composites can improve the corrosion protection and antibacterial properties of biomedical devices, such as Mg-based ones, which have great biocompatibility and suitable mechanical properties for such purposes, but usually lack the necessary lifetime when in presence of human body fluids due to high corrosion rates (Riaz et al., 2019). The study of the approaches taken to tackle this problematic give insight into the dynamics occurring at the interface between these complex biological systems and the surface of the material, providing useful information on how to design better solutions. The action of these 2DM coatings in protecting the underlying substrate





is twofold. On one hand, the reduced lattice size blocks the access of microbial communities to the substrate, thus hindering its corrosion during metabolic activity. On the other hand, the electrostatic properties of these materials have shown to successfully inhibit bacterial adhesion. The double effect here described can be exploited to prevent corrosion of implants.

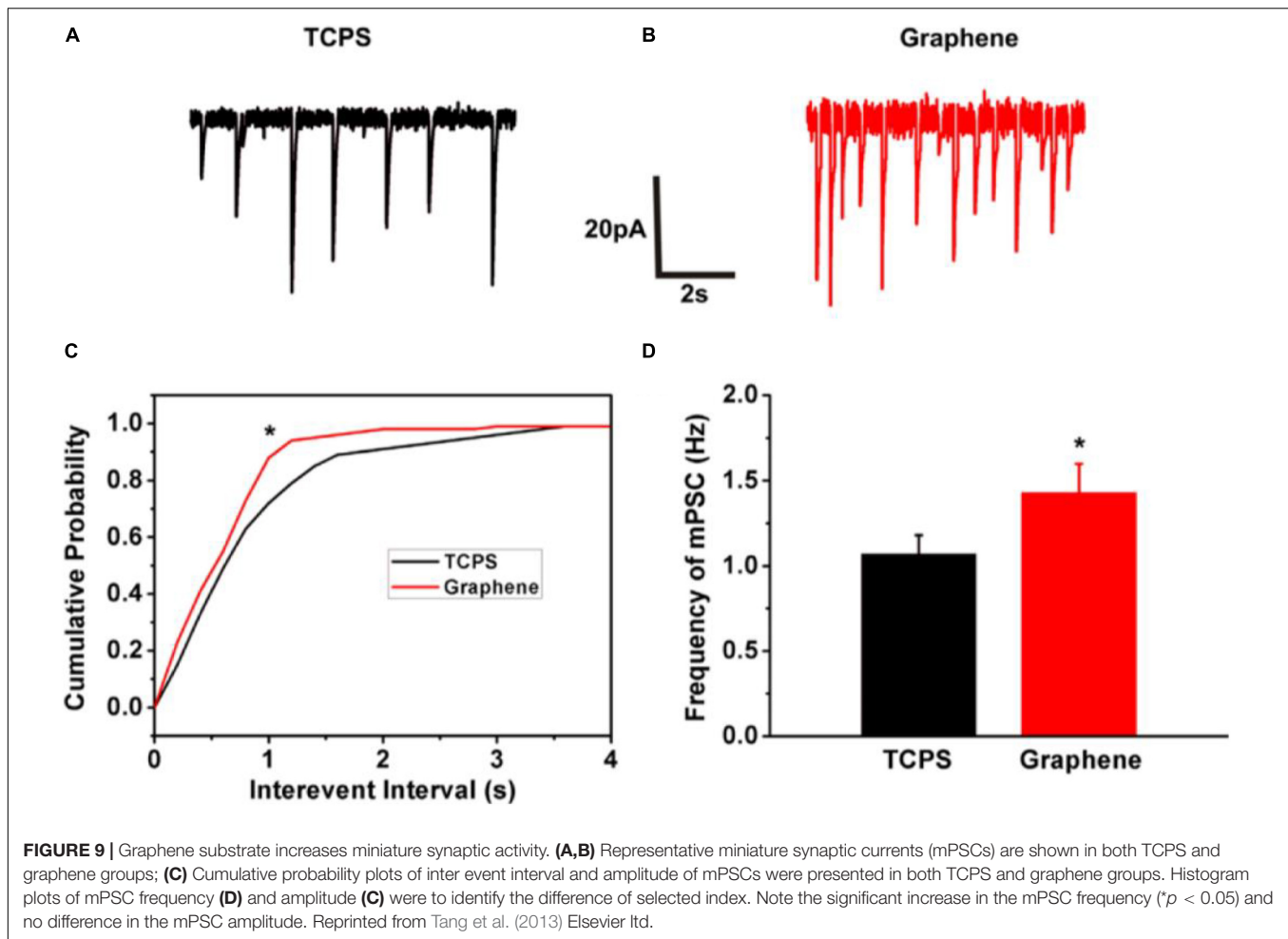
## Graphene as Stem Cell Differentiation Promoter

Tissue engineering is a therapeutic multidisciplinary field that exploits medical, biological, and physical-chemical expertise with the purpose to obtain biomimetic tissues for restoring, recreating or improving the original physiological functions. The advent of nanomaterials represents an extraordinary research opportunity in this field, already featuring a large amount of publications and patents (Hubbell, 1995; Lutolf and Hubbell, 2005; Kohane and Langer, 2008). In the last decade, a large number of papers focusing on the capability of graphene to promote stem cell differentiation have been published. Park et al. investigated the effect of graphene on hNSCs, demonstrating that 10 h after cell feeding the majority of hNSCs adhered preferentially onto graphene, rather than onto glass (Figure 4). Interestingly, after a long-term differentiation process, the number of differentiated cells on graphene was significantly higher, with a large prevalence of neurons instead of astrocytes. Authors concluded that graphene promotes cell adhesion and drives stem cell differentiation toward a neuronal fate by creating a more suitable microenvironment for the stem cells (Park et al., 2011). Also, graphene nano-spheres seem capable to promote NCS differentiation. Tang et al. (2013) displayed that after 1 day in culture, cells properly migrated and started differentiating into mature neurons. The neuronal differentiation, evaluated in terms of neurites growth and extension, was followed until complete neuronal maturation by staining cells with  $\beta$ -tubulin and MAP-2 markers. In addition, through electrophysiological

and live imaging techniques, authors reported that graphene was capable to enhance electrical network signaling (Figure 9) (Tang et al., 2013).

Kalbacova et al. (2010); Nayak et al. (2011), and Park et al. (2014) studied the possibility of promoting mesenchymal stromal cell differentiation using graphene. Kalbacova et al. (2010) showed that, 48 h after the plating, MSCs homogeneously covered all the graphene substrate, while cells plated onto the control support (SiO<sub>2</sub>) formed separated islands. In addition, MSCs seeded onto graphene showed a spindle-shape morphology, allowing a higher proliferation with a possible differentiation toward osteoblast lineage. On the contrary, MSCs plated onto SiO<sub>2</sub> presented a more polygonal cell shape, typical of non-differentiated cells. Author also tested the cell adherence and concluded that cells plated onto graphene showed a weaker and smaller contact with the support, corresponding to an active state of the cells (Kalbacova et al., 2010). Nayak et al. (2011) used CVD graphene, transferred onto four different supports: glass, silicon wafer, PET, and PDMS. Authors reported that mesenchymal cells maintained their peculiar spindle-shape across when plated onto Gr/glass and Gr/SiO<sub>2</sub>. Notably, cells plated onto PET and PDMS (graphene coated or non) showed rounded and irregular morphology, probably due to the poor adhesion. By adding in the maintaining medium a protein cocktail to favor osteogenic differentiation, the cells plated onto the graphene uncoated supports did not express protein markers of differentiation after 15 days of treatment; on the contrary MSCs plated onto graphene coated substrates remarkably differentiated into osteoblasts at a comparable rate to the differentiation with the bone morphogenic protein-2 (BMP-2) (Nayak et al., 2011). In addition, Park et al. (2014) demonstrated that, even in absence of chemical differentiation inducers, graphene presence was sufficient to induce MSC commitment toward the cardiomyogenic lineage. They attributed this phenomenon to the upregulation of extracellular matrix protein and cell signaling molecule expression (Park et al., 2014).





Liu et al. (2016) studied the *in vivo* effects of a CVD-grown monolayer graphene-coated Ti disks implanted in the back subcutaneous area of nude mice. Authors incubated *in vitro* human adipose-derived stem cells (hASCs) and human bone marrow mesenchymal stem cells (hBMSCs) on the top of their support before implanting them into the mice. No evident *in vivo* toxicity was reported; in addition, they demonstrated that CVD graphene favored cell adhesion, proliferation and differentiation toward an osteogenic faith, in accordance with Nayak et al. (2011). By epigenetic analysis, authors revealed that graphene had the ability to upregulate the osteogenesis associated genes by increasing tri-methylation of H3K4 (Nayak et al., 2011; Liu et al., 2016). Between 2017 and 2019, Xie et al. (2017) published two works evaluating the potential of graphene to promote osteogenic differentiation. In the first work, authors studied the possibility for graphene to promote dental pulp stem cell (DPSC) differentiation toward an odontogenic or osteogenic faith. They evaluated mineralization and differentiation of DPSC after 14 and 28 days and reported that cells grown onto graphene presented higher level of mineralization. In addition, odontoblastic genes resulted down-regulated and osteogenic genes and proteins were significantly up-regulated. Interestingly, cells plated onto control glass, but grown with medium obtain from graphene

samples, showed the down regulation of odontoblastic genes, and associated with an increase in bone-related gene and protein. Authors concluded that graphene was not a material suitable for dental reconstruction, but appropriate for bone tissue engineering (Xie et al., 2017). Starting from the previous work, Xie et al. studied the capability of graphene to promote *in vivo* osteogenesis and the molecular mechanisms at the base of this process. Authors generated MSC-impregnated graphene scaffolds and implanted them into immunocompromised (SCID) mice at 28 days of life. Without the addition of any osteogenic inducers, graphene scaffolds were able to promote osteogenic differentiation of MSC by increasing the expression of bone-related markers (RUNX2 and OPN) (Xie et al., 2019). Li K. et al. (2018) investigated the possibility to enhance the surface bioactivation of titanium alloys (Ti6-Al4-V) by a graphene coating to improve osteogenesis and osseointegration in an *in vivo* New Zealand white rabbit femoral condyle defect model. Animals were implanted with both a graphene-coated and a non-coating supports and their capability to enforce osteogenesis after 4, 12, and 24 weeks was evaluated. No evident cytotoxicity was reported in this work. Biomechanical testing, micro-computed tomography (Micro-CT) analyses and histological observations were performed. Authors demonstrated that microstructure

parameters (i.e., bone volume/total volume fraction and mineral apposition rate) and the new bone formation were significantly enhanced in animals implanted with the graphene-coated Ti6-Al4-V (Li K. et al., 2018).

## Graphene as Excitable Cell Activity Enhancer

Due to its biocompatibility and electrical properties, graphene has been regarded as an advanced and viable interface for enhancing neuronal activity or improving the record of electrical cell signal. Li et al. demonstrated that CVD graphene is able to promote neurite sprouting and outgrowth (associated with a significant increase of GAP-43 protein expression), concluding that the graphene-coated substrate could have a prominent impact on the cell early developing stages (Li et al., 2011). In accordance with Li et al. (2011) and He et al. (2016) reported that graphene accelerated neuronal maturation, favoring microtubules formation and growth, and promoted dendritic spine density and maturation with a consequent enhanced synaptic transmission strength. They suggested that the acceleration in microtubules formation (known to play a

pivotal role in neurite and axon specification, Kuijpers and Hoogenraad, 2011), coupled with graphene's high electrical conductivity (as suggested by Tang et al., 2013), might be at the base of all the reported improvements. Kitko et al. (2018) displayed that neurons plated onto graphene showed an enhanced synaptic transmission, related to an increasing in the synaptic vesicle number, probability of release and recycling rate (Kitko et al., 2018). Pampaloni et al. (2018) testing the interaction between neurons and monolayer graphene, partially confirmed the capability of the graphene to enhance postsynaptic current (PSC) strength. In this work, however, the authors clearly demonstrated that the enhancement regarded only spontaneous synaptic transmission, without reporting any alteration in the synaptic bouton numbers and the miniature PSCs. In addition, they displayed that monolayer graphene could also increase neuronal firing activity, by regulation of the extracellular ion distribution around neurons. They demonstrated that neurons grown onto graphene showed a significant increase in potassium currents, responsible for the observed shift from adapting to tonically firing (Figure 10).

Through a theoretical approach, they speculated that monolayer graphene effects on neurons might be maximized

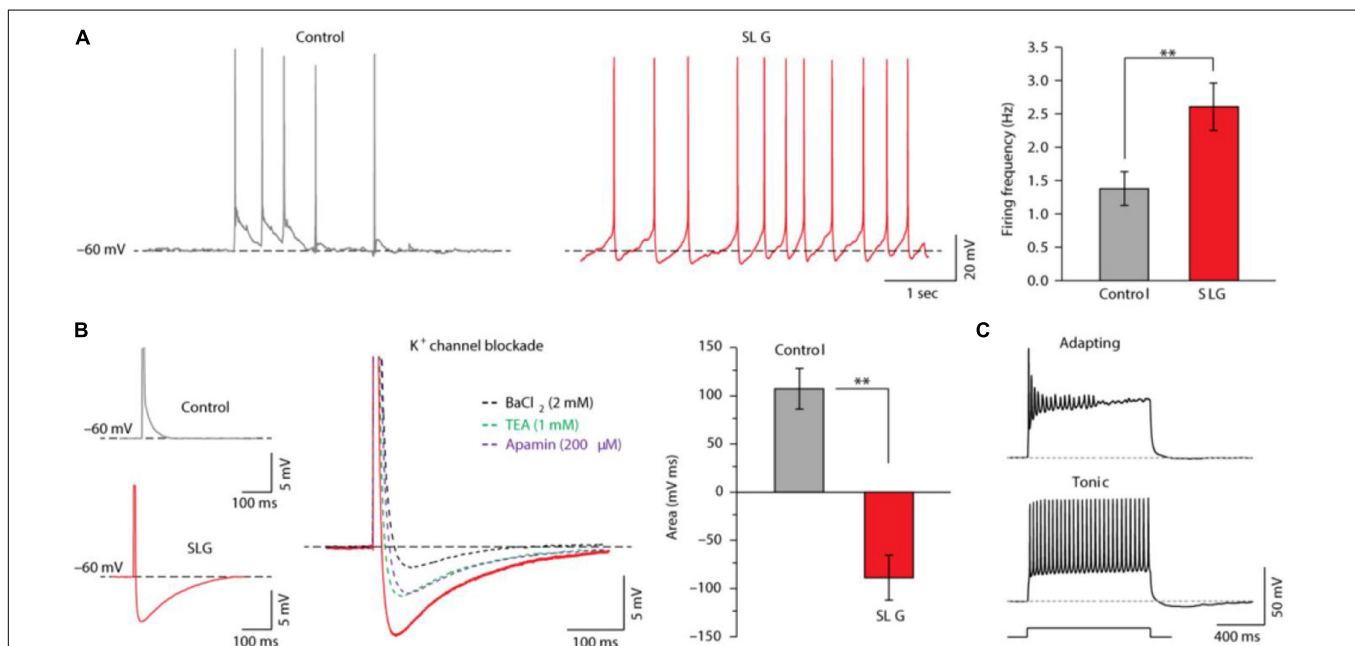


**FIGURE 10 |** SLG triggers changes in single-cell intrinsic excitability. **(A)** Representative current-clamp recordings of hippocampal neurons in culture (10 DIV) in control and SLG. Control and SLG neurons displayed similar resting membrane potentials ( $-52 \pm 10$  mV in SLG;  $-50 \pm 7$  mV in control). When held at  $-60$  mV, the cell's spontaneous action potential firing was measured as summarized in the histograms (right). Note the significantly higher action potential frequency in SLG [ $(2.60 \pm 0.36)$  Hz in SLG,  $n = 21$ ;  $(1.37 \pm 0.26)$  Hz in control,  $n = 19$ ;  $P = 0.0054$ ]. Significance:  $**P < 0.01$ . **(B)** Evoked single action potential in control (top) and SLG (bottom). Note the pronounced AHP in SLG neurons, which was partially abolished by each of the treatments shown:  $\text{BaCl}_2$ , tetra-ethylammonium (TEA) or apamin (right, superimposed tracings). The histogram quantifies the area below the control and SLG post-AP voltage trajectories with respect to the resting membrane potential. The AHP in SLG neurons was significantly different from the ADP detected in control neurons [ $(-86.96 \pm 23.60)$  mV ms in SLG,  $n = 25$ ;  $(+107.12 \pm 21.85)$  mV ms in control,  $n = 20$ ;  $P = 0.0010$ ]. Interestingly, the AHP was reduced (by 88%) by bath-applying  $\text{Ba}_{2+}$  ( $\text{BaCl}_2$ , 2 mM;  $n = 3$ ), which is known to block  $\text{K}_f$  (inward-rectifier) and  $\text{K}_{Ca}$  (calcium-activated) membrane potassium channels (Alger and Nicoll, 1980; Jiang and MacKinnon, 2000; Alagem et al., 2001). The AHP was also reduced (by 58%) by bath-applying TEA (1 mM;  $n = 9$ ), a non-selective blocker of the large majority of voltage-gated  $\text{K}^+$  membrane channels ( $\text{K}_v$  47, including  $\text{BK}_{Ca}$  channels (Hille, 2001). Finally, apamin (200  $\mu\text{M}$ ;  $n = 5$ ), a specific inhibitor of  $\text{SK}_{Ca}$  membrane channels (Hille, 2001), also strongly affected the AHP (47% reduction). **(C)** Current-clamp recordings from neurons in control and SLG revealed different cell-discharge patterns, classified as adapting or tonic. Reprinted from Pampaloni et al. (2018) Springer Nature.

when graphene is deposited in an electrically insulation support (i.e., glass), compared to a suspended condition. Authors concluded that the alteration in the spontaneous synaptic transmission could be justify by the different ratio between cells with adaptive/tonic phenotypes. Notably, authors did not exclude a potential contribution of astrocytes in the surface ion concentration alterations, since astrocytes are able to regulate the extracellular medium between neurons and the substrate (Pampaloni et al., 2018).

In a recent publication, Capasso et al. (2020) questioned the importance of conductivity as a crucial property to foster neuronal activity by investigating the electrical behavior of primary neurons plated onto graphene-based films. The authors prepared two films by CVD with different lattice structure and electrical conductivity. Neurons grown onto both substrates were able to form a highly structured and mature network. Interestingly, low-conductivity graphene seemed to improve the neuronal network architecture without significantly modifying intrinsic electrical activity, compared to pristine graphene. These results indicated that a high electrical conductivity *per se* is not sufficient to promote the electrical activity of neuronal networks, suggesting that other material features (e.g., surface chemistry, roughness, wettability, etc.) have to be taken into account in the design of future graphene-based implants (Capasso et al., 2020). Following this rationale, the same group demonstrated that monolayer graphene with higher hydrophilicity (water contact angle of  $40.7^\circ$  vs.  $83.7^\circ$  of the pristine graphene) improved cell-to-cell communication. The authors fabricated such highly hydrophilic coatings on polyethylene terephthalate using remote plasma hydrogenation, which did not affect graphene's crystallinity allowing to preserve a residual electrical conductivity ( $\sim 3 \text{ k}\Omega/\square$ ). The formation of excitatory synaptic connections increased in hydrogenated graphene with respect to pristine graphene, leading to a doubled miniature excitatory postsynaptic current frequency. This study indicated that wettability might be the key to enable neuronal interfacing (Moschetta et al., 2020).

## Graphene for Biosensing

CVD graphene demonstrated excellent biocompatibility, as shown by its ability to drive neuronal growth and regeneration *in vivo* (Li et al., 2011). Due to its positive impact in cultured neurons, graphene revealed to be a durable and biocompatible material for intracortical probes due to the reduced proliferation of astrocytes and microglia. Healthier neuron network at the implant site provide a sustainable coupling between electrode and target neurons, allowing for chronic recording and to act as scaffolds for regenerative medicine. The acceptance of intracortical implant is crucial for neurorehabilitation applications, since reliable and long-lasting monitoring of single units in freely moving environment are required for replacing disable node of the neural network and restore sensory function or fine motor command (Bourrier et al., 2019a). Monitoring the activity of individual neurons requires the intimate contact of micro and nano electronic devices with cells over mesoscale networks. Gliosis is the immune response of cells and tissues that lead to the rejection of the

penetrating intracortical probes, hindering the realization of neuro-rehabilitation projects. Graphene and other carbon-based nanomaterials have risen as good candidates due to good adhesion, neuron regeneration, and potential to provide highly sensitive devices such as graphene field effect transistors (GFET). Graphene's mechanical properties also allow it to conform to soft tissues, further improving its biocompatibility and contributing to the acceptance of intracortical probes. However, monolayer-based devices could be teared off during implantation and manipulation and might degrade over time within the brain. Bourrier et al. have attempted to address this issue by supporting graphene with a biocompatible and degradable polymeric film (based on hyaluronic acid). The protective polymeric layer does not hinder device's features and function, namely neuron and tissue response (Bourrier et al., 2019b). Veliev et al. have reported on the fabrication of GFETs on various substrates with high sensitivity and low noise level. Experiments carried out *in vitro* showed detection of spontaneous activity of hippocampal neurons (which were grown *in situ* on top of the graphene sensors). The hippocampal neuron cells exhibited healthy morphology and spontaneous electrical activity after 19–21 days in culture. The electrical measurements did not harm the cells. The performance of the GFETs degrades slightly with time (Veliev et al., 2017). The ultimate resolution of neural activity sensing consists of ion channel activity monitoring. Graphene has been used to monitor individual ion channels through field effect detection (Veliev et al., 2018). The advent of e-tattoos, or epidermal electronics, provided non-invasive and high-fidelity sensing, and graphene showed promise in this regard due to its mechanical and electronic properties (Kabiri Ameri et al., 2017). It has been also used in a self-healable tattoo that allows continuous monitoring of electrophysiological signals (e.g., skin temperature and hydration; glucose, urea, sodium, and calcium levels). Graphene has been used to create multifunction ultrathin tattoos. Enabled by graphene's mechanical properties and biocompatibility, these tattoos provide high-fidelity sensing by conforming to the micro-roughness of the skin by matching its modulus. Skin/electrode contact interface is enlarged, lowering contact impedance and higher signal to noise ratios (Wang Q. et al., 2019).

Finally, DNA has been shown to bind directly to graphene without the need of a linker, making it highly interesting for biosensor development (Campos et al., 2018). Field-effect transistors (FET) with two-dimensional channels made of monolayer graphene have been developed to achieve label-free detection of DNA hybridization down to attomolar concentration, while offering at the same time the possibility of discriminating single nucleotide polymorphism (Campos et al., 2019). Additionally, graphene has been used to track DNA hybridization reaction with nanoscale resolution in real time by using nano-photonic effects (Adão et al., 2019).

## CONCLUSION

In this review, we reported on the interaction of graphene and hBN coatings with living cells, both bacterial and mammalian,

focusing on the interaction mechanisms and accounting for current applications. Graphene and hBN are two-dimensional materials with analogous lattice structure and markedly different electrical properties. Although the literature on graphene for biomedical applications is more extensive, we chose to survey relevant research results on hBN to point out the current state of the art on both materials and compare the interaction mechanisms.

In the case of graphene coatings, an active antibacterial mechanism is observed which seems to be strongly dependent on the coating morphology, and consequently on the production method. On the one hand, liquid-phase produced graphene coatings are generally morphologically heterogeneous and present exposed flake edges, which have shown to interact with bacterial cells and lead to cellular impairment. This effect is dependent on orientation of the nanoflakes at the surface and affects certain bacterial species more than others, based on their size and shape, in accordance to the surface texture of the coatings. On the other hand, graphene films produced by chemical vapor deposition are usually planar, making in this case the basal plane at the root of the cellular interaction. Therefore, rather than edge dependent effects, CVD graphene coatings showed antibacterial effects due a high electrical conductivity, which would produce oxidative stress and a consequent depletion of ATP, culminating in bacteria cell death. The effectiveness of this charge transfer mechanism is dependent on the complexity of the cellular membrane.

With regards to mammalian cells, CVD graphene coatings produced revealed to be highly suitable for cell interfacing. Nonetheless, no universal consensus exists yet on the physiochemical mechanism underlying the favorable interaction between cells and graphene, despite some authors attributed the excellent biocompatibility to the absence of ROSs formation or to the capability of graphene of directly interacting with specific molecules in the mammalian cell membrane (i.e., cholesterol). Overall, the absence of an evident *in vivo* cytotoxicity, in addition to the capability of boosting cell activity and stimuli responsivity, makes graphene an excellent candidate for the realization of cellular interfaces. In addition, graphene is found to promote cell adhesion and proliferation, and to drive stem cell differentiation toward both a neuronal and non-neuronal faith (depending on the stem cell subtype), by creating a suitable microenvironment for the stem cells. When interfacing neuronal stem cells, a graphene coating is able *per se* to boost neurite sprouting and maturation and, when interaction with mesenchymal stem cells, drive their maturation specifically toward osteoblast or cardiomyogenic lineage in both *in vitro* and *in vivo* systems. Besides its ability to favor stem cell maturation, when interfacing excitable cells, monolayer graphene films revealed also to enhance synaptic transmission by increasing spontaneous intracellular  $\text{Ca}^{2+}$  spikes and neuronal firing by altering extracellular  $\text{K}^{+}$  concentration. Traditionally, authors attributed these phenomena to the high electrical conductivity graphene. However, this feature alone is not enough to promote the electrical activity of neuronal networks, and hence other characteristics of the coating (e.g., thickness and roughness) must be considered when designing

graphene-based interfaces and implants. As a final and crucial remark, the *in vivo* biocompatibility of graphene is still debated. Few works reported in the last decade alert about the possible *in vivo* toxicity of graphene and its derivatives. A peculiar aspect that troubles the scientific community regards the possibility of graphene to permanently deposits in the organs (lung, spleen and liver), causing chronic inflammatory processes. Nonetheless, the long-term persistence of graphene in the organisms has not been clearly demonstrated and in most of the cases the toxicity reduces over time; in addition, phenomena of graphene clearance through feces has been reported. On the other hand, the possibility to use 2D graphene as an *in vivo* therapeutical tool is still an open question. Graphene-coated prosthesis has been successfully employed to favor bone tissue regeneration; in addition, cancer cell aggregations seem permeable to graphene sheets and capable to retain them. This interesting phenomenon leads researcher to investigate the possibility to use graphene in the antineoplastic therapies.

As a partial conclusion about the mechanisms of interaction with the two kinds of cells, we underline that although a graphene coating in certain conditions can induce bacterial cell death, the mammalian cells seem to be generally unharmed by it. Based on these interactions, applications for graphene have surfaced. CVD graphene coatings have shown to be able to hinder bacterial adherence and coating due to electrostatic interactions at the surface. Additionally, its lattice size allows it to be impermeable to Cu and Ni ions, blocking the bacteria at the surface to metabolize the substrate. CVD graphene has also been used for sensing applications in neuroscience and medicine in the form of sensors, wearable devices and scaffolding due to its softness, electrical conductivity, and biocompatibility.

Due to the limited availability of literature regarding hBN coatings and their interaction with bacteria and cells, we have reviewed not only cases where this material was deposited on a substrate, but also those investigating its behavior in liquid solutions and in nanocomposites, in order to provide a more comprehensive overview. In the case of 2D hBN coatings, studies conducted experimentally with LPE samples and via simulations showed antibacterial effects related to the exposed flake edges (as shown for graphene), which promoted cellular membrane disruption and temperature-dependent lipid extraction. However, studies conducted in atomically smooth hBN coatings (e.g., CVD) have revealed no antibacterial activity of the basal plane, further highlighting the role of a sufficiently high electrical conductivity in bacterial death. Electrostatic interactions seemed to contribute toward an inhibition of bacterial adhesion. Despite their markedly different electrical conductivity, both graphene and hBN coatings have shown to be effective against biocorrosion of metal substrates by reducing the number of adhered bacteria, with the reduced cellular adhesion being consequence of the atomic smoothness of the coatings. In both cases, the small lattice size in graphene and hBN allows them to act as impermeable barriers, blocking the migration of aggressive metabolites and avoiding biocorrosion of the underlying metallic substrate.



With regards to mammalian cells, hBN has shown to be cytotoxic in liquid solution above certain concentrations and in a shape-dependent manner. Cytotoxicity studies conducted with hBN in liquid solution for different nanoflake sizes show that when the size is small enough it becomes possible for mammalian cells to internalize them and cause an increase in ROS production. Overall, 2D hBN materials have shown promise in bone tissue scaffolding, wound healing, and treatment of neurodegenerative diseases such as Parkinson's. For further understanding the potential of this kind of materials, the cytotoxicity will need to be ascertained to address some of the inconsistencies present in literature.

In conclusion, the current scenario suggests that, notwithstanding the substantial amount of studies in the field, further investigation is still needed before two-dimensional materials such as graphene and hBN can fulfill their potential in advanced biomedical applications. This is particularly true in

the case of hBN, where most interactions with living matter still needs to be understood and detailed.

## AUTHOR CONTRIBUTIONS

JS and MM: data acquisition and writing original draft. JR: data revision and support on writing. PA: data interpretation and evaluation. AC: conceptualization, coordination, writing, and funding acquisition. All authors: final writing.

## FUNDING

AC acknowledges the support of the European Union's Horizon 2020 Research and Innovation Program under the Marie Skłodowska-Curie grant agreement no. 713640.

## REFERENCES

- Adão, R. M. R., Campos, R., Figueiras, E., Alpuim, P., and Nieder, J. B. (2019). Graphene setting the stage: tracking DNA hybridization with nanoscale resolution. *2D Mater.* 6:045056. doi: 10.1088/2053-1583/ab41e0
- Akhavan, O. (2016). Graphene scaffolds in progressive nanotechnology/stem cell-based tissue engineering of the nervous system. *J. Mater. Chem. B* 4, 3169–3190. doi: 10.1039/c6tb00152a
- Akhavan, O., and Ghaderi, E. (2010). Toxicity of graphene and graphene oxide nanowalls against bacteria. *ACS Nano* 4, 5731–5736. doi: 10.1021/nn101390x
- Aki, D., Ulag, S., Unal, S., Sengor, M., Ekren, N., Lin, C. C., et al. (2020). 3D printing of PVA/hexagonal boron nitride/bacterial cellulose composite scaffolds for bone tissue engineering. *Mater. Des.* 196:109094. doi: 10.1016/j.matdes.2020.109094
- Alagem, N., Dvir, M., and Reuveny, E. (2001). Mechanism of Ba<sup>2+</sup> block of a mouse inwardly rectifying K<sup>+</sup> channel: differential contribution by two discrete residues. *J. Physiol.* 534, 381–393. doi: 10.1111/j.1469-7793.2001.00381.x
- Alger, B. E., and Nicoll, R. A. (1980). Epileptiform burst afterhyperpolarization: calcium-dependent potassium potential in hippocampal CA1 pyramidal cells. *Science* 210, 1122–1124. doi: 10.1126/science.7444438
- Ali, S. H., and Keil, R. (2009). *Networked Disease: Emerging Infections in the Global City*. Hoboken, NJ: Wiley.
- Allen, M. J., Tung, V. C., and Kaner, R. B. (2010). Honeycomb carbon: a review of graphene. *Chem. Rev.* 110, 132–145. doi: 10.1021/cr900070d
- Al-Saadi, S., Banerjee, P. C., Anisur, M. R., and Raman, R. K. S. (2017). Hexagonal boron nitride impregnated silane composite coating for corrosion resistance of magnesium alloys for temporary bioimplant applications. *Metals* 7:518. doi: 10.3390/met7120518
- Aryaei, A., Jayatissa, A. H., and Jayasuriya, A. C. (2014). The effect of graphene substrate on osteoblast cell adhesion and proliferation. *J. Biomed. Mater. Res. Part A* 102, 3282–3290. doi: 10.1002/jbm.a.34993
- Backes, C., Abdelkader, A., Alonso, C., Andrieux, A., Arenal, R., Azpeitia, J., et al. (2019). *Production and Processing of Graphene and Related Materials To Cite this Version?: HAL Id?: hal-02144563 Production And Processing Of Graphene And Related*. Versailles: UVSQ.
- Begum, S., Pramanik, A., Davis, D., Patibandla, S., Gates, K., Gao, Y., et al. (2020). 2D and heterostructure nanomaterial based strategies for combating drug-resistant bacteria. *ACS Omega* 5, 3116–3130. doi: 10.1021/acsomega.9b03919
- Bei, H. P., Yang, Y., Zhang, Q., Tian, Y., Luo, X., Yang, M., et al. (2019). Graphene-based nanocomposites for neural tissue engineering. *Molecules* 24:658. doi: 10.3390/molecules24040658
- Blaschke, T. F. (2009). Global challenges for clinical pharmacology in the developing world. *Clin. Pharmacol. Ther.* 85, 579–581. doi: 10.1038/clpt.2009.54
- Bonaccorso, F., Bartolotta, A., Coleman, J. N., and Backes, C. (2016). 2D-crystal-based functional inks. *Adv. Mater.* 28, 6136–6166. doi: 10.1002/adma.201506410
- Bonaccorso, F., Colombo, L., Yu, G., Stoller, M., Tozzini, V., Ferrari, A. C., et al. (2015). Graphene, related two-dimensional crystals, and hybrid systems for energy conversion and storage. *Science* 347:1246501. doi: 10.1126/science.1246501
- Bourrier, A., Shkrobatova, P., Bonizzato, M., Rey, E., Barraud, Q., Courtine, G., et al. (2019a). Monolayer graphene coating of intracortical probes for long-lasting neural activity monitoring. *Adv. Healthc. Mater.* 8, 1–13. doi: 10.1002/adhm.201801331
- Bourrier, A., Szarpak-Jankowska, A., Veliev, F., Olarte-Hernandez, R., Shkrobatova, P., Bonizzato, M., et al. (2019b). Introducing a biomimetic coating for graphene neuroelectronics: toward in-vivo applications. *Biomed. Phys. Eng. Express* 7:015006.
- Campos, R., Borme, J., Guerreiro, J. R., Machado, G., Cerqueira, M. F., Petrovykh, D. Y., et al. (2019). Attomolar label-free detection of dna hybridization with electrolyte-gated graphene field-effect transistors. *ACS Sensors* 4, 286–293. doi: 10.1021/acssensors.8b00344
- Campos, R., Machado, G., Cerqueira, M. F., Borme, J., and Alpuim, P. (2018). Wafer scale fabrication of graphene microelectrode arrays for the detection of DNA hybridization. *Microelectron. Eng.* 189, 85–90. doi: 10.1016/j.mee.2017.12.015
- Capasso, A., Bellani, S., Palma, A. L., Najafi, L., Del Rio Castillo, A. E., Curreli, N., et al. (2019). CVD-graphene/graphene flakes dual-films as advanced DSSC counter electrodes. *2D Mater.* 6:035007. doi: 10.1088/2053-1583/ab117e
- Capasso, A., De Francesco, M., Leoni, E., Dikonimos, T., Buonocore, F., Lancellotti, L., et al. (2014). Cyclododecane as support material for clean and facile transfer of large-area few-layer graphene. *Appl. Phys. Lett.* 105:113101. doi: 10.1063/1.4895733
- Capasso, A., Del Rio Castillo, A. E. E., Sun, H., Ansaldo, A., Pellegrini, V., and Bonaccorso, F. (2015a). Ink-jet printing of graphene for flexible electronics: an environmentally-friendly approach. *Solid State Commun.* 224, 53–63. doi: 10.1016/j.ssc.2015.08.011
- Capasso, A., Dikonimos, T., Sarto, F., Tamburrano, A., De Bellis, G., Sarto, M. S., et al. (2015b). Nitrogen-doped graphene films from chemical vapor deposition of pyridine: influence of process parameters on the electrical and optical properties. *Beilstein J. Nanotechnol.* 6, 2028–2038. doi: 10.3762/bjnano.6.206
- Capasso, A., Rodrigues, J., Moschetta, M., Buonocore, F., Faggio, G., Messina, G., et al. (2020). Interactions between primary neurons and graphene films with different structure and electrical conductivity. *Adv. Funct. Mater.* 2005300, 1–11. doi: 10.1002/adfm.202005300
- Chen, X., Wu, P., Rousseas, M., Okawa, D., Gartner, Z., Zettl, A., et al. (2009). Boron nitride nanotubes are noncytotoxic and can be functionalized for

- interaction with proteins and cells. *J. Am. Chem. Soc.* 131, 890–891. doi: 10.1021/ja807334b
- Chen, X., Zhang, L., and Chen, S. (2015). Large area CVD growth of graphene. *Synth. Met.* 210, 95–108. doi: 10.1016/j.synthmet.2015.07.005
- Chhetri, S., Samanta, P., Murmu, N., and Kuila, T. (2019). Anticorrosion properties of epoxy composite coating reinforced by molybdate-intercalated functionalized layered double hydroxide. *J. Compos. Sci.* 3:11. doi: 10.3390/jcs3010011
- Chilkoor, G., Karanam, S. P., Star, S., Shrestha, N., Sani, R. K., Upadhyayula, V. K. K., et al. (2018). Hexagonal boron nitride: the thinnest insulating barrier to microbial corrosion. *ACS Nano* 12, 2242–2252. doi: 10.1021/acsnano.7b06211
- Chimene, D., Alge, D. L., and Gaharwar, A. K. (2015). Two-dimensional nanomaterials for biomedical applications: emerging trends and future prospects. *Adv. Mater.* 27, 7261–7284. doi: 10.1002/adma.201502422
- Chung, W. S., Allen, N. J., and Eroglu, C. (2015). Astrocytes control synapse formation, function, and elimination. *Cold Spring Harb. Perspect. Biol.* 7:a020370. doi: 10.1101/cshperspect.a020370
- Ciofani, G., Danti, S., D'Alessandro, D., Ricotti, L., Moscato, S., Bertoni, G., et al. (2010a). Enhancement of neurite outgrowth in neuronal-like cells following boron nitride nanotube-mediated stimulation. *ACS Nano* 4, 6267–6277. doi: 10.1021/nn101985a
- Ciofani, G., Del Turco, S., Rocca, A., De Vito, G., Cappello, V., Yamaguchi, M., et al. (2014). Cytocompatibility evaluation of gum Arabic-coated ultra-pure boron nitride nanotubes on human cells. *Nanomedicine* 9, 773–788. doi: 10.2217/nnm.14.25
- Ciofani, G., Genchi, G. G., Liakos, I., Athanassiou, A., Dinucci, D., Chiellini, F., et al. (2012). A simple approach to covalent functionalization of boron nitride nanotubes. *J. Colloid Interface Sci.* 374, 308–314. doi: 10.1016/j.jcis.2012.01.049
- Ciofani, G., Raffa, V., Mencias, A., and Cuschieri, A. (2009). Folate functionalized boron nitride nanotubes and their selective uptake by glioblastoma multiforme cells: implications for their use as boron carriers in clinical boron neutron capture therapy. *Nanoscale Res. Lett.* 4, 113–121. doi: 10.1007/s11671-008-9210-9
- Ciofani, G., Ricotti, L., Danti, S., Moscato, S., Nesti, C., D'Alessandro, D., et al. (2010b). Investigation of interactions between poly-L-lysine-coated boron nitride nanotubes and c2c12 cells: up-take, cytocompatibility, and differentiation. *Int. J. Nanomedicine* 5, 285–298. doi: 10.2147/IJN.S9879
- D'Abaco, G. M., Mattei, C., Nasr, B., Hudson, E. J., Alshawaf, A. J., Chana, G., et al. (2018). Graphene foam as a biocompatible scaffold for culturing human neurons. *R. Soc. Open Sci.* 5:171364. doi: 10.1098/rsos.171364
- Dellieu, L., Lawarée, E., Reckinger, N., Didembourg, C., Letesson, J. J., Sarrazin, M., et al. (2015). Do CVD grown graphene films have antibacterial activity on metallic substrates? *Carbon N. Y.* 84, 310–316. doi: 10.1016/j.carbon.2014.12.025
- Deng, B., Liu, Z., and Peng, H. (2019). Toward mass production of CVD graphene films. *Adv. Mater.* 31, 1–25. doi: 10.1002/adma.201800996
- DNV GL (2015). *Assessment of Global Cost of Corrosion. [REPORT] Rep. No. OAPUS310GKOCH (PP110272)-1, Rev. 3, Append., 25.* Oslo: DNV GL.
- Duch, M. C., Budinger, G. R. S., Liang, Y. T., Soberanes, S., Urich, D., Chiarella, S. E., et al. (2011). Minimizing oxidation and stable nanoscale dispersion improves the biocompatibility of graphene in the lung. *Nano Lett.* 11, 5201–5207. doi: 10.1021/nl202515a
- Edmondson, R., Broglie, J. J., Adcock, A. F., and Yang, L. (2014). Three-dimensional cell culture systems and their applications in drug discovery and cell-based biosensors. *Assay Drug Dev. Technol.* 12, 207–218. doi: 10.1089/adt.2014.573
- Emanet, M., Sen, Ö., Taşkın, I. Ç., and Çulha, M. (2019). Synthesis, functionalization, and bioapplications of two-dimensional boron nitride nanomaterials. *Front. Bioeng. Biotechnol.* 7:363. doi: 10.3389/fbioe.2019.00363
- Enna, S. J., and Williams, M. (2009). Challenges in the search for drugs to treat central nervous system disorders. *J. Pharmacol. Exp. Ther.* 329, 404–411. doi: 10.1124/jpet.108.143420
- Faggio, G., Capasso, A., Messina, G., Santangelo, S., Dikonimos, T., Gagliardi, S., et al. (2013). High-temperature growth of graphene films on copper foils by ethanol chemical vapor deposition. *J. Phys. Chem. C* 117, 21569–21576. doi: 10.1021/jp407013y
- Faggio, G., Messina, G., Lofaro, C., Lisi, N., and Capasso, A. (2020). Recent advancements on the CVD of graphene on copper from ethanol vapor. *C J. Carbon Res.* 6:14. doi: 10.3390/c6010014
- Fattahi, P., Yang, G., Kim, G., and Abidian, M. R. (2014). A review of organic and inorganic biomaterials for neural interfaces. *Adv. Mater.* 26, 1846–1885. doi: 10.1002/adma.201304496
- Fernandes, M. M., Carvalho, E. O., and Lanceros-Mendez, S. (2019). Electroactive smart materials: novel tools for tailoring bacteria behavior and fight antimicrobial resistance. *Front. Bioeng. Biotechnol.* 7:277. doi: 10.3389/fbioe.2019.00277
- Firme, C. P., and Bandaru, P. R. (2010). Toxicity issues in the application of carbon nanotubes to biological systems. *Nanomedicine Nanotechnol. Biol. Med.* 6, 245–256. doi: 10.1016/j.nano.2009.07.003
- Fischer, R. A., Zhang, Y., Risner, M. L., Li, D., Xu, Y., and Sappington, R. M. (2018). Impact of graphene on the efficacy of neuron culture substrates. *Adv. Healthc. Mater.* 7:e1701290. doi: 10.1002/adhm.201701290
- Flemming, H. C., and Wingender, J. (2010). The biofilm matrix. *Nat. Rev. Microbiol.* 8, 623–633. doi: 10.1038/nrmicro2415
- Geim, A. K., and Novoselov, K. S. (2007). The rise of graphene. *Nat. Mater.* 6, 183–191. doi: 10.1038/nmat1849
- Geim, A. K., Novoselov, K. S., Jiang, D., Schedin, F., Booth, T. J., Khotkevich, V. V., et al. (2005). Two-dimensional atomic crystals. *Proc. Natl. Acad. Sci. U.S.A.* 102, 10451–10453.
- Gerhardus, H. K., and Brongers, N. G. T. (2010). ACCE international. *J. Clin. Eng.* 35, 185–186. doi: 10.1097/jce.0b013e3181fb9a65
- Gnisci, A., Faggio, G., Messina, G., Kwon, J., Lee, J. Y., Lee, G. H., et al. (2018). Ethanol-CVD growth of sub-mm single-crystal graphene on flat Cu surfaces. *J. Phys. Chem. C* 122, 28830–28838. doi: 10.1021/acs.jpcc.8b10094
- Goenka, S., Sant, V., and Sant, S. (2014). Graphene-based nanomaterials for drug delivery and tissue engineering. *J. Control. Release* 173, 75–88. doi: 10.1016/j.jconrel.2013.10.017
- Gudz, K. Y., Permyakova, E. S., Matveev, A. T., Bondarev, A. V., Manakhov, A. M., Sidorenko, D. A., et al. (2020). Pristine and Antibiotic-Loaded Nanosheets/Nanoneedles-Based Boron Nitride Films as a Promising Platform to Suppress Bacterial and Fungal Infections. *ACS Appl. Mater. Interfaces* 12, 42485–42498. doi: 10.1021/acsami.0c10169
- Gurunathan, S., Han, J. W., Eppakayala, V., and Kim, J. H. (2013). Green synthesis of graphene and its cytotoxic effects in human breast cancer cells. *Int. J. Nanomedicine* 8, 1015–1027. doi: 10.2147/IJN.S42047
- He, Z., Zhang, S., Song, Q., Li, W., Liu, D., Li, H., et al. (2016). The structural development of primary cultured hippocampal neurons on a graphene substrate. *Colloids Surf. B Biointerfaces* 146, 442–451. doi: 10.1016/j.colsurfb.2016.06.045
- Henriques, P. C., Borges, I., Pinto, A. M., Magalhães, F. D., and Gonçalves, I. C. (2018). Fabrication and antimicrobial performance of surfaces integrating graphene-based materials. *Carbon N. Y.* 132, 709–732. doi: 10.1016/j.carbon.2018.02.027
- Henriques, P. C., Pereira, A. T., Pires, A. L., Pereira, A. M., Magalhães, F. D., and Gonçalves, I. C. (2020). Graphene surfaces interaction with proteins, bacteria, mammalian cells, and blood constituents: the impact of graphene platelet oxidation and thickness. *ACS Appl. Mater. Interfaces* 12, 21020–21035. doi: 10.1021/acsami.9b21841
- Hernandez, Y., Nicolosi, V., Lotya, M., Blighe, F. M., Sun, Z., De, S., et al. (2008). High-yield production of graphene by liquid-phase exfoliation of graphite. *Nat. Nanotechnol.* 3, 563–568. doi: 10.1038/nnano.2008.215
- Hille, B. (2001). "Potassium channels and chloride channels," in *Ionic Channels of Excitable Membranes*, ed. B. Hille (Sunderland, MA: Sinauer Associates).
- Horváth, L., Magrez, A., Golberg, D., Zhi, C., Bando, Y., Smajda, R., et al. (2011). In vitro investigation of the cellular toxicity of boron nitride nanotubes. *ACS Nano* 5, 3800–3810. doi: 10.1021/nn200139h
- Howard, D., Buttery, L. D., Shakesheff, K. M., and Roberts, S. J. (2008). Tissue engineering: strategies, stem cells and scaffolds. *J. Anat.* 213, 66–72. doi: 10.1111/j.1469-7580.2008.00878.x
- Hu, W., Peng, C., Luo, W., Lv, M., Li, X., Li, D., et al. (2010). Graphene-based antibacterial paper. *ACS Nano* 4, 4317–4323. doi: 10.1021/nn101097v
- Hu, W., Peng, C., Lv, M., Li, X., Zhang, Y., Chen, N., et al. (2011). Protein corona-mediated mitigation of cytotoxicity of graphene oxide. *ACS Nano* 5, 3693–3700. doi: 10.1021/nn200021j

- Hubbell, J. A. (1995). Biomaterials in tissue engineering. *Bio Technol.* 13, 565–576. doi: 10.1038/nbt0695-565
- Ikram, M., Hussain, I., Hassan, J., Haider, A., Imran, M., Aqeel, M., et al. (2020). Evaluation of antibacterial and catalytic potential of copper-doped chemically exfoliated boron nitride nanosheets. *Ceram. Int.* 46, 21073–21083. doi: 10.1016/j.ceramint.2020.05.180
- Innocenzi, P., and Stagi, L. (2020). Carbon-based antiviral nanomaterials: graphene, C-dots, and fullerenes. A perspective. *Chem. Sci.* 11, 6606–6622. doi: 10.1039/d0sc02658a
- Irem, T., Sen, O., Emanet, M., Culha, M., and Yilmaz, B. (2019). Biocompatibility evaluation of hexagonal boron nitrides on healthy mouse hippocampal cell line and their positive effect on stressed cells. *Beilstein Arch.* 2019:201965. doi: 10.3762/bxiv.2019.65.v1
- Jeong, J. W., Yeo, W. H., Akhtar, A., Norton, J. J. S., Kwack, Y. J., Li, S., et al. (2013). Materials and optimized designs for human-machine interfaces via epidermal electronics. *Adv. Mater.* 25, 6839–6846. doi: 10.1002/adma.201301921
- Jia, P. P., Sun, T., Junaid, M., Yang, L., Ma, Y. B., Cui, Z. S., et al. (2019). Nanotoxicity of different sizes of graphene (G) and graphene oxide (GO) in vitro and in vivo. *Environ. Pollut.* 247, 595–606. doi: 10.1016/j.envpol.2019.01.072
- Jiang, X. F., Weng, Q., Wang, X., Bin Li, X., Zhang, J., Golberg, D., et al. (2015). Recent progress on fabrications and applications of boron nitride nanomaterials: a review. *J. Mater. Sci. Technol.* 31, 589–598. doi: 10.1016/j.jmst.2014.12.008
- Jiang, Y., and MacKinnon, R. (2000). The barium site in a potassium channel by X-ray crystallography. *J. Gen. Physiol.* 115, 269–272. doi: 10.1085/jgp.115.3.269
- Kabiri Ameri, S., Ho, R., Jang, H., Tao, L., Wang, Y., Wang, L., et al. (2017). Graphene electronic tattoo sensors. *ACS Nano* 11, 7634–7641. doi: 10.1021/acsnano.7b02182
- Kairi, M. I., Khavarian, M., Bakar, S. A., Vigolo, B., and Mohamed, A. R. (2018). Recent trends in graphene materials synthesized by CVD with various carbon precursors. *J. Mater. Sci.* 53, 851–879. doi: 10.1007/s10853-017-1694-1
- Kalbacova, M., Broz, A., Kong, J., and Kalbac, M. (2010). Graphene substrates promote adherence of human osteoblasts and mesenchymal stromal cells. *Carbon N. Y.* 48, 4323–4329. doi: 10.1016/j.carbon.2010.07.045
- Kang, S., Lee, D., Kim, J., Capasso, A., Kang, H. S., Park, J.-W., et al. (2020). 2D semiconducting materials for electronic and optoelectronic applications: potential and challenge. *2D Mater.* 7:022003. doi: 10.1088/2053-1583/ab6267
- Kar, F., Hacıoğlu, C., Göncü, Y., Söğüt, İ., Şentürk, H., Burukoğlu Dönmez, D., et al. (2020). In vivo assessment of the effect of hexagonal boron nitride nanoparticles on biochemical, histopathological, oxidant and antioxidant status. *J. Clust. Sci.* [Epub ahead of print]. doi: 10.1007/s10876-020-01811-w
- Khan, K., Tareen, A. K., Aslam, M., Wang, R., Zhang, Y., Mahmood, A., et al. (2020). Recent developments in emerging two-dimensional materials and their applications. *R. Soc. Chem.* 8, 387–440. doi: 10.1039/c9tc04187g
- Kim, K. K., Kim, S. M., and Lee, Y. H. (2014). A new horizon for hexagonal boron nitride film. *J. Korean Phys. Soc.* 64, 1605–1616. doi: 10.3938/jkps.64.1605
- Kim, M., Jeong, J. H., Lee, J. Y., Capasso, A., Bonaccorso, F., Kang, S. H., et al. (2019). Electrically conducting and mechanically strong graphene-poly(lactic acid) composites for 3D printing. *ACS Appl. Mater. Interfaces* 11, 11841–11848. doi: 10.1021/acsmi.9b03241
- Kitko, K. E., Hong, T., Lazarenko, R. M., Ying, D., Xu, Y. Q., and Zhang, Q. (2018). Membrane cholesterol mediates the cellular effects of monolayer graphene substrates. *Nat. Commun.* 9:796. doi: 10.1038/s41467-018-03185-0
- Kıvanç, M., Barutca, B., Koparal, A. T., Göncü, Y., Bostancı, S. H., and Ay, N. (2018). Effects of hexagonal boron nitride nanoparticles on antimicrobial and antibiofilm activities, cell viability. *Mater. Sci. Eng. C* 91, 115–124. doi: 10.1016/j.msec.2018.05.028
- Koh, Y. K., Bae, M. H., Cahill, D. G., and Pop, E. (2010). Heat conduction across monolayer and few-layer graphenes. *Nano Lett.* 10, 4363–4368. doi: 10.1021/nl101790k
- Kohane, D. S., and Langer, R. (2008). Polymeric biomaterials in tissue engineering. *Pediatr. Res.* 63, 487–491. doi: 10.1203/01.pdr.0000305937.26105.e7
- Kong, W., Kum, H., Bae, S.-H., Shim, J., Kim, H., Kong, L., et al. (2019). Path towards graphene commercialization from lab to market. *Nat. Nanotechnol.* 14, 927–938. doi: 10.1038/s41565-019-0555-2
- Küçükoğlu, R., Türkez, H., Arslan, M. E., Tozlu, ÖÖ, Sönmez, E., Mardinoğlu, A., et al. (2020). Neuroprotective effects of boron nitride nanoparticles in the experimental Parkinson's disease model against MPP+ induced apoptosis. *Metab. Brain Dis.* 35, 947–957. doi: 10.1007/s11011-020-00559-6
- Kuijpers, M., and Hoogenraad, C. C. (2011). Centrosomes, microtubules and neuronal development. *Mol. Cell. Neurosci.* 48, 349–358. doi: 10.1016/j.mcn.2011.05.004
- Kumar, S., and Parekh, S. H. (2020). Linking graphene-based material physicochemical properties with molecular adsorption, structure and cell fate. *Commun. Chem.* 3, 1–11. doi: 10.1038/s42004-019-0254-9
- Lahiri, D., Rouzard, F., Richard, T., Keshri, A. K., Bakshi, S. R., Kos, L., et al. (2010). Boron nitride nanotube reinforced polylactide-polycaprolactone copolymer composite: mechanical properties and cytocompatibility with osteoblasts and macrophages in vitro. *Acta Biomater.* 6, 3524–3533. doi: 10.1016/j.actbio.2010.02.044
- Lahiri, D., Singh, V., Benaduce, A. P., Seal, S., Kos, L., and Agarwal, A. (2011). Boron nitride nanotube reinforced hydroxyapatite composite: mechanical and tribological performance and in-vitro biocompatibility to osteoblasts. *J. Mech. Behav. Biomed. Mater.* 4, 44–56. doi: 10.1016/j.jmbbm.2010.09.005
- Lalwani, G., D'Agati, M., Khan, A. M., and Sitharaman, B. (2016). Toxicology of graphene-based nanomaterials. *Adv. Drug Deliv. Rev.* 105(Pt B), 109–144. doi: 10.1016/j.addr.2016.04.028
- Laming, P. R., Kimelberg, H., Robinson, S., Salm, A., Hawrylak, N., Müller, C., et al. (2000). Neuronal-glial interactions and behaviour. *Neurosci. Biobehav. Rev.* 24, 295–340. doi: 10.1016/S0149-7634(99)00080-9
- Lascano, S., Chávez-Vásquez, R., Muñoz-Rojas, D., Aristizabal, J., Arce, B., Parra, C., et al. (2020). Graphene-coated Ti-Nb-Ta-Mn foams: a promising approach towards a suitable biomaterial for bone replacement. *Surf. Coatings Technol.* 401:126250. doi: 10.1016/j.surfcoat.2020.126250
- Lee, C., Wei, X., Kysar, J. W., and Hone, J. (2008). Measurement of the elastic properties and intrinsic strength of monolayer graphene. *Science* 321, 385–388. doi: 10.1126/science.1157996
- Lee, X. J., Hiew, B. Y. Z., Lai, K. C., Lee, L. Y., Gan, S., Thangalazhy-Gopakumar, S., et al. (2019). Review on graphene and its derivatives: synthesis methods and potential industrial implementation. *J. Taiwan Inst. Chem. Eng.* 98, 163–180. doi: 10.1016/j.jtice.2018.10.028
- Li, J., Wang, G., Zhu, H., Zhang, M., Zheng, X., Di, Z., et al. (2014). Antibacterial activity of large-area monolayer graphene film manipulated by charge transfer. *Sci. Rep.* 4:4359. doi: 10.1038/srep04359
- Li, K., Wang, C., Yan, J., Zhang, Q., Dang, B., Wang, Z., et al. (2018). Evaluation of the osteogenesis and osseointegration of titanium alloys coated with graphene: an in vivo study. *Sci. Rep.* 8:1843. doi: 10.1038/s41598-018-19742-y
- Li, N., Zhang, X., Song, Q., Su, R., Zhang, Q., Kong, T., et al. (2011). The promotion of neurite sprouting and outgrowth of mouse hippocampal cells in culture by graphene substrates. *Biomaterials* 32, 9374–9382. doi: 10.1016/j.biomaterials.2011.08.065
- Li, X., Colombo, L., and Ruoff, R. S. (2016). Synthesis of graphene films on copper foils by chemical vapor deposition. *Adv. Mater.* 28, 6247–6252. doi: 10.1002/adma.201504760
- Li, X., MacEwan, M. R., Xie, J., Siewe, D., Yuan, X., and Xia, Y. (2010). Fabrication of density gradients of biodegradable polymer microparticles and their use in guiding neurite outgrowth. *Adv. Funct. Mater.* 20, 1632–1637. doi: 10.1002/adfm.201000146
- Li, Y., Yuan, H., Von Dem Bussche, A., Creighton, M., Hurt, R. H., Kane, A. B., et al. (2013). Graphene microsheets enter cells through spontaneous membrane penetration at edge asperities and corner sites. *Proc. Natl. Acad. Sci. U.S.A.* 110, 12295–12300. doi: 10.1073/pnas.1222761110
- Li, Z., Zhang, Y., Chan, C., Zhi, C., Cheng, X., and Fan, J. (2018). Temperature-dependent lipid extraction from membranes by boron nitride nanosheets. *ACS Nano* 12, 2764–2772. doi: 10.1021/acsnano.7b09095
- Liao, S., Chan, C. K., and Ramakrishna, S. (2008). Stem cells and biomimetic materials strategies for tissue engineering. *Mater. Sci. Eng. C* 28, 1189–1202. doi: 10.1016/j.msec.2008.08.015
- Lin, L., Deng, B., Sun, J., Peng, H., and Liu, Z. (2018). Bridging the gap between reality and ideal in chemical vapor deposition growth of graphene. *Chem. Rev.* 118, 9281–9343. doi: 10.1021/acs.chemrev.8b00325
- Ling, L. L., Schneider, T., Peoples, A. J., Spoering, A. L., Engels, I., Conlon, B. P., et al. (2015). A new antibiotic kills pathogens without detectable resistance. *Nature* 517, 455–459. doi: 10.1038/nature14098



- Lisi, N., Buonocore, F., Dikonimos, T., Leoni, E., Faggio, G., Messina, G., et al. (2014). Rapid and highly efficient growth of graphene on copper by chemical vapor deposition of ethanol. *Thin Solid Films* 571, 139–144. doi: 10.1016/j.tsf.2014.09.040
- Lisi, N., Dikonimos, T., Buonocore, F., Pittori, M., Mazzaro, R., Rizzoli, R., et al. (2017). Contamination-free graphene by chemical vapor deposition in quartz furnaces. *Sci. Rep.* 7, 1–11. doi: 10.1038/s41598-017-09811-z
- Liu, Y., Chen, T., Du, F., Gu, M., Zhang, P., Zhang, X., et al. (2016). Single-layer graphene enhances the osteogenic differentiation of human mesenchymal stem cells in vitro and in vivo. *J. Biomed. Nanotechnol.* 12, 1270–1284. doi: 10.1166/jbn.2016.2254
- Lu, B., Li, T., Zhao, H., Li, X., Gao, C., Zhang, S., et al. (2012). Graphene-based composite materials beneficial to wound healing. *Nanoscale* 4, 2978–2982. doi: 10.1039/c2nr11958g
- Lu, N., Wang, L., Lv, M., Tang, Z., and Fan, C. (2019). Graphene-based nanomaterials in biosystems. *Nano Res.* 12, 247–264. doi: 10.1007/s12274-018-2209-3
- Luan, B., Huynh, T., Zhao, L., and Zhou, R. (2015). Potential toxicity of graphene to cell functions via disrupting protein-protein interactions. *ACS Nano* 9, 663–669. doi: 10.1021/nn506011j
- Lutolf, M. P., and Hubbell, J. A. (2005). Synthetic biomaterials as instructive extracellular microenvironments for morphogenesis in tissue engineering. *Nat. Biotechnol.* 23, 47–55. doi: 10.1038/nbt1055
- Lynch, R. W., and Drickamer, H. G. (1966). Effect of high pressure on the lattice parameters of diamond, graphite, and hexagonal boron nitride. *J. Chem. Phys.* 44, 181–184. doi: 10.1063/1.1726442
- Ma-Hock, L., Strauss, V., Treumann, S., Küttler, K., Wohlleben, W., Hofmann, T., et al. (2013). Comparative inhalation toxicity of multi-wall carbon nanotubes, graphene, graphite nanoplatelets and low surface carbon black. *Part Fibre Toxicol.* 10:23. doi: 10.1186/1743-8977-10-23
- Mahvash, F., Eissa, S., Bordjiba, T., Tavares, A. C., Szkopek, T., and Sij, M. (2017). Corrosion resistance of monolayer hexagonal boron nitride on copper. *Sci. Rep.* 7:42139. doi: 10.1038/srep42139
- Mao, L., Hu, M., Pan, B., Xie, Y., and Petersen, E. J. (2016). Biodistribution and toxicity of radio-labeled few layer graphene in mice after intratracheal instillation. *Part Fibre Toxicol.* 13:7. doi: 10.1186/s12989-016-0120-1
- Marchesan, S., Ballerini, L., and Prato, M. (2017). Nanomaterials for stimulating nerve growth. *Science* 356, 1010–1011. doi: 10.1126/science.aan1227
- Mateti, S., Wong, C. S., Liu, Z., Yang, W., Li, Y., Li, L. H., et al. (2018). Biocompatibility of boron nitride nanosheets. *Nano Res.* 11, 334–342. doi: 10.1007/s12274-017-1635-y
- Matsoso, B., Hao, W., Li, Y., Vuillet-a-Ciles, V., Garnier, V., Steyer, P., et al. (2020). Synthesis of hexagonal boron nitride 2D layers using polymer derived ceramics route and derivatives. *J. Phys. Mater.* 3:034002. doi: 10.1088/2515-7639/ab854a
- Mattevi, C., Kim, H., and Chhowalla, M. (2011). A review of chemical vapour deposition of graphene on copper. *J. Mater. Chem.* 21, 3324–3334. doi: 10.1039/c0jm02126a
- Medzhitov, R. (2007). Recognition of microorganisms and activation of the immune response. *Nature* 449, 819–826. doi: 10.1038/nature06246
- Mei, L., Zhu, S., Yin, W., Chen, C., Nie, G., Gu, Z., et al. (2020). Two-dimensional nanomaterials beyond graphene for antibacterial applications: current progress and future perspectives. *Theranostics* 10, 757–781. doi: 10.7150/thno.39701
- Mendelson, N., Chugh, D., Reimers, J. R., Cheng, T. S., Gottscholl, A., Long, H., et al. (2020). Identifying carbon as the source of visible single-photon emission from hexagonal boron nitride. *Nat. Mater.* [Epub ahead of print]. doi: 10.1038/s41563-020-00850-y
- Meng, Z., Stolz, R. M., Mendecki, L., and Mirica, K. A. (2019). Electrically-transduced chemical sensors based on two-dimensional nanomaterials. *Chem. Rev.* 119, 478–598. doi: 10.1021/acs.chemrev.8b00311
- Merlo, A., Mokkapati, V. R. S. S., Pandit, S., and Mijakovic, I. (2018). Boron nitride nanomaterials: biocompatibility and bio-applications. *Biomater. Sci.* 6, 2298–2311. doi: 10.1039/c8bm00516h
- Miró, P., Audiffred, M., and Heine, T. (2014). An atlas of two-dimensional materials. *Chem. Soc. Rev.* 43, 6537–6554. doi: 10.1039/c4cs00102h
- Moschetta, M., Lee, J.-Y., Rodrigues, J., Podestà, A., Varvicchio, O., Son, J., et al. (2020). Hydrogenated graphene improves neuronal network maturation and excitatory transmission. *Adv. Biol.* [Epub ahead of print].
- Mukheem, A., Shahabuddin, S., Akbar, N., Miskoon, A., Muhamad Sarih, N., Sudesh, K., et al. (2019). Boron nitride doped polyhydroxyalkanoate/chitosan nanocomposite for antibacterial and biological applications. *Nanomaterials* 9:645. doi: 10.3390/nano9040645
- Musico, Y. L. F., Santos, C. M., Dalida, M. L. P., and Rodrigues, D. F. (2014). Surface modification of membrane filters using graphene and graphene oxide-based nanomaterials for bacterial inactivation and removal. *ACS Sustain. Chem. Eng.* 2, 1559–1565. doi: 10.1021/sc500044p
- Nayak, T. R., Andersen, H., Makam, V. S., Khaw, C., Bae, S., Xu, X., et al. (2011). Graphene for controlled and accelerated osteogenic differentiation of human mesenchymal stem cells. *ACS Nano* 5, 4670–4678. doi: 10.1021/nn200500h
- Nicolosi, V., Chhowalla, M., Kanatzidis, M. G., Strano, M. S., and Coleman, J. N. (2013). Liquid exfoliation of layered materials. *Science* 340, 72–75. doi: 10.1126/science.1226419
- Niu, L., Coleman, J. N., Zhang, H., Shin, H., Chhowalla, M., and Zheng, Z. (2016). Production of two-dimensional nanomaterials via liquid-based direct exfoliation. *Small* 12, 272–293. doi: 10.1002/smll.201502207
- Novoselov, K. S., Geim, A. K., Morozov, S. V., Jiang, D., Zhang, Y., Dubonos, S. V., et al. (2004). Electric field in atomically thin carbon films. *Science* 306, 666–669. doi: 10.1126/science.1102896
- Nurunnabi, M., Parvez, K., Nafuijman, M., Revuri, V., Khan, H. A., Feng, X., et al. (2015). Bioapplication of graphene oxide derivatives: drug/gene delivery, imaging, polymeric modification, toxicology, therapeutics and challenges. *RSC Adv.* 5, 42141–42161. doi: 10.1039/c5ra04756k
- O'Brien, F. J. (2011). Biomaterials & scaffolds for tissue engineering. *Mater. Today* 14, 88–95. doi: 10.1016/S1369-7021(11)70058-X
- Otter, J. A., Vickery, K., Walker, J. T., deLancey Pulcini, E., Stoodley, P., Goldenberg, S. D., et al. (2015). Surface-attached cells, biofilms and biocide susceptibility: implications for hospital cleaning and disinfection. *J. Hosp. Infect.* 89, 16–27. doi: 10.1016/j.jhin.2014.09.008
- Pampaloni, N. P., Lottner, M., Giugliano, M., Matruggio, A., D'Amico, F., Prato, M., et al. (2018). Single-layer graphene modulates neuronal communication and augments membrane ion currents. *Nat. Nanotechnol.* 13, 755–764. doi: 10.1038/s41565-018-0163-6
- Pan, D., Su, F., Liu, H., Ma, Y., Das, R., Hu, Q., et al. (2020). The properties and preparation methods of different boron nitride nanostructures and applications of related nanocomposites. *Chem. Rec.* 20, 1314–1337. doi: 10.1002/tcr.202000079
- Pandit, S., Gaska, K., Mokkapati, V. R. S. S., Forsberg, S., Svensson, M., Kádár, R., et al. (2019). Antibacterial effect of boron nitride flakes with controlled orientation in polymer composites. *RSC Adv.* 9, 33454–33459. doi: 10.1039/C9RA06773F
- Park, J., Park, S., Ryu, S., Bhang, S. H., Kim, J., Yoon, J. K., et al. (2014). Graphene-regulated cardiomyogenic differentiation process of mesenchymal stem cells by enhancing the expression of extracellular matrix proteins and cell signaling molecules. *Adv. Healthc. Mater.* 3, 176–181. doi: 10.1002/adhm.201300177
- Park, S. Y., Park, J., Sim, S. H., Sung, M. G., Kim, K. S., Hong, B. H., et al. (2011). Enhanced differentiation of human neural stem cells into neurons on graphene. *Adv. Mater.* 23, H263–H263. doi: 10.1002/adma.201101503
- Parra, C., Dorta, F., Jimenez, E., Henriquez, R., Ramirez, C., Rojas, R., et al. (2015a). A nanomolecular approach to decrease adhesion of biofouling - producing bacteria to graphene - coated material. *J. Nanobiotechnol.* 13:82. doi: 10.1186/s12951-015-0137-x
- Parra, C., Dorta, F., Jimenez, E., Villalobos, P., and Seeger, M. (2015b). *Towards the Suppression of Biocorrosion and Biofouling Through Graphene Coatings*. Hoboken, NJ: Wiley, 4–5.
- Parra, C., Montero-Silva, F., Gentil, D., del Campo, V., da Cunha, T. H. R., Henriquez, R., et al. (2017). The many faces of graphene as protection barrier. Performance under microbial corrosion and Ni allergy conditions. *Materials* 10:1406. doi: 10.3390/ma10121406
- Parra, C., Montero-Silva, F., Henriquez, R., Flores, M., Garín, C., Ramirez, C., et al. (2015c). Suppressing bacterial interaction with copper surfaces through



- graphene and hexagonal-boron nitride coatings. *ACS Appl. Mater. Interfaces* 7, 6430–6437. doi: 10.1021/acsami.5b01248
- Pham, V. T. H., Truong, V. K., Quinn, M. D. J., Notley, S. M., Guo, Y., Baulin, V. A., et al. (2015). Graphene induces formation of pores that kill spherical and rod-shaped bacteria. *ACS Nano* 9, 8458–8467. doi: 10.1021/acs.nano.5b03368
- Pinto, A. M., Gonçalves, I. C., and Magalhães, F. D. (2013). Graphene-based materials biocompatibility: a review. *Colloids Surf. B Biointerfaces* 111, 188–202. doi: 10.1016/j.colsurfb.2013.05.022
- Pope, C. F., O'Sullivan, D. M., McHugh, T. D., and Gillespie, S. H. (2008). A practical guide to measuring mutation rates in antibiotic resistance. *Antimicrob. Agents Chemother.* 52, 1209–1214. doi: 10.1128/AAC.01152-07
- Pranno, N., La Monaca, G., Polimeni, A., Sarto, M. S., Uccelletti, D., Bruni, E., et al. (2020). Antibacterial activity against staphylococcus aureus of titanium surfaces coated with graphene nanoplatelets to prevent peri-implant diseases. An in-vitro pilot study. *Int. J. Environ. Res. Public Health* 17:1568. doi: 10.3390/ijerph17051568
- Pumera, M. (2011). Graphene in biosensing. *Mater. Today* 14, 308–315. doi: 10.1016/S1369-7021(11)70160-2
- Randviir, E. P., Brownson, D. A. C., and Banks, C. E. (2014). A decade of graphene research: production, applications and outlook. *Mater. Today* 17, 426–432. doi: 10.1016/j.mattod.2014.06.001
- Reed, J. H., Gonsalves, A. E., Román, J. K., Oh, J., Cha, H., Dana, C. E., et al. (2019). Ultrascaleable multifunctional nanoengineered copper and aluminum for antiadhesion and bactericidal applications. *ACS Appl. Biol. Mater.* 2, 2726–2737. doi: 10.1021/acsabm.8b00765
- Reina, G., Gonzalez-Dominguez, J. M., Criado, A., Vazquez, E., Bianco, A., and Prato, M. (2017). Promises, facts and challenges for graphene in biomedical applications. *Chem. Soc. Rev.* 46, 4400–4416. doi: 10.1039/c7cs00363c
- Riaz, U., Shabib, I., and Haider, W. (2019). The current trends of Mg alloys in biomedical applications—A review. *J. Biomed. Mater. Res. Part B Appl. Biomater.* 107, 1970–1996. doi: 10.1002/jbm.b.34290
- Rodriguez, C. L. C., Kessler, F., Dubey, N., Rosa, V., and Fecine, G. J. M. (2017). CVD graphene transfer procedure to the surface of stainless steel for stem cell proliferation. *Surf. Coatings Technol.* 311, 10–18. doi: 10.1016/j.surfcoat.2016.12.111
- Sasidharan, A., Swaroop, S., Koduri, C. K., Girish, C. M., Chandran, P., Panchakarla, L. S., et al. (2015). Comparative in vivo toxicity, organ biodistribution and immune response of pristine, carboxylated and PEGylated few-layer graphene sheets in Swiss albino mice: a three month study. *Carbon* N. Y. 95, 511–524. doi: 10.1016/j.carbon.2015.08.074
- Scaini, D., and Ballerini, L. (2018). Nanomaterials at the neural interface. *Curr. Opin. Neurobiol.* 50, 50–55. doi: 10.1016/j.conb.2017.12.009
- Schinwald, A., Murphy, F. A., Jones, A., MacNee, W., and Donaldson, K. (2012). Graphene-based nanoplatelets: a new risk to the respiratory system as a consequence of their unusual aerodynamic properties. *ACS Nano* 6, 736–746. doi: 10.1021/nn204229f
- Şen, Ö., Emanet, M., and Çulha, M. (2019). Stimulatory effect of hexagonal boron nitrides in wound healing. *ACS Appl. Biol. Mater.* 2, 5582–5596. doi: 10.1021/acsabm.9b00669
- Shin, J. H., Han, S. G., Kim, J. K., Kim, B. W., Hwang, J. H., Lee, J. S., et al. (2015). 5-Day repeated inhalation and 28-day post-exposure study of graphene. *Nanotoxicology* 9, 1023–1031. doi: 10.3109/17435390.2014.998306
- Shin, S. R., Li, Y. C., Jang, H. L., Khoshakhlagh, P., Akbari, M., Nasajpour, A., et al. (2016). Graphene-based materials for tissue engineering. *Adv. Drug Deliv. Rev.* 105, 255–274. doi: 10.1016/j.addr.2016.03.007
- Syama, S., and Mohanan, P. V. (2016). Safety and biocompatibility of graphene: a new generation nanomaterial for biomedical application. *Int. J. Biol. Macromol.* 86, 546–555. doi: 10.1016/j.ijbiomac.2016.01.116
- Szunerits, S., and Boukherroub, R. (2016). Antibacterial activity of graphene-based materials. *J. Mater. Chem. B* 4, 6892–6912. doi: 10.1039/C6TB01647B
- Tang, M., Song, Q., Li, N., Jiang, Z., Huang, R., and Cheng, G. (2013). Enhancement of electrical signaling in neural networks on graphene films. *Biomaterials* 34, 6402–6411. doi: 10.1016/j.biomaterials.2013.05.024
- Taskin, I. C., Sen, O., Emanet, M., Culha, M., and Yilmaz, B. (2020). Hexagonal boron nitrides reduce the oxidative stress on cells. *Nanotechnology* 31:215101. doi: 10.1088/1361-6528/ab6f6c
- Tour, J. M. (2014). Top-down versus bottom-up fabrication of graphene-based electronics. *Chem. Mater.* 26, 163–171. doi: 10.1021/cm402179h
- Tu, Y., Lv, M., Xiu, P., Huynh, T., Zhang, M., Castelli, M., et al. (2013). Destructive extraction of phospholipids from *Escherichia coli* membranes by graphene nanosheets. *Nat. Nanotechnol.* 8, 594–601. doi: 10.1038/nnano.2013.125
- Veliev, F., Briçon-Marjollet, A., Bouchiat, V., and Delacour, C. (2016). Impact of crystalline quality on neuronal affinity of pristine graphene. *Biomaterials* 86, 33–41. doi: 10.1016/j.biomaterials.2016.01.042
- Veliev, F., Cresti, A., Kalita, D., Bourrier, A., Belloir, T., Briçon-Marjollet, A., et al. (2018). Sensing ion channel in neuron networks with graphene field effect transistors. *2D Mater.* 5:045020. doi: 10.1088/2053-1583/aad78f
- Veliev, F., Han, Z., Kalita, D., Briçon-Marjollet, A., Bouchiat, V., and Delacour, C. (2017). Recording spikes activity in cultured hippocampal neurons using flexible or transparent graphene transistors. *Front. Neurosci.* 11:466. doi: 10.3389/fnins.2017.00466
- Wang, A., Tang, Z., Park, I. H., Zhu, Y., Patel, S., Daley, G. Q., et al. (2011). Induced pluripotent stem cells for neural tissue engineering. *Biomaterials* 32, 5023–5032. doi: 10.1016/j.biomaterials.2011.03.070
- Wang, J., Ma, F., and Sun, M. (2017). Graphene, hexagonal boron nitride, and their heterostructures: properties and applications. *RSC Adv.* 7, 16801–16822. doi: 10.1039/c7ra00260b
- Wang, L., Xu, X., Zhang, L., Qiao, R., Wu, M., Wang, Z., et al. (2019). Epitaxial growth of a 100-square-centimetre single-crystal hexagonal boron nitride monolayer on copper. *Nature* 570, 91–95. doi: 10.1038/s41586-019-1226-z
- Wang, Q., Ling, S., Liang, X., Wang, H., Lu, H., and Zhang, Y. (2019). Self-healable multifunctional electronic tattoos based on silk and graphene. *Adv. Funct. Mater.* 29, 1–8. doi: 10.1002/adfm.201808695
- Wei, W., Li, J., Liu, Z., Deng, Y., Chen, D., Gu, P., et al. (2020). Distinct antibacterial activity of a vertically aligned graphene coating against Gram-positive and Gram-negative bacteria. *J. Mater. Chem. B* 8, 6069–6079. doi: 10.1039/d0tb00417k
- WHO (2013). *Global Action Plan for the Prevention and Control of Noncommunicable Diseases 2013–2020*. Geneva: WHO.
- WHO (2020). *Coronavirus Disease 2019 (COVID-19) Situation Reports. April 1 2020*. Geneva: WHO.
- Wu, Q., Jang, S. K., Park, S., Jung, S. J., Suh, H., Lee, Y. H., et al. (2015). In situ synthesis of a large area boron nitride/graphene monolayer/boron nitride film by chemical vapor deposition. *Nanoscale* 7, 7574–7579. doi: 10.1039/c5nr00889a
- Xia, M. Y., Xie, Y., Yu, C. H., Chen, G. Y., Li, Y. H., Zhang, T., et al. (2019). Graphene-based nanomaterials: the promising active agents for antibiotics-independent antibacterial applications. *J. Control. Release* 307, 16–31. doi: 10.1016/j.jconrel.2019.06.011
- Xie, H., Cao, T., Franco-Obregón, A., and Rosa, V. (2019). Graphene-induced osteogenic differentiation is mediated by the integrin/FAK axis. *Int. J. Mol. Sci.* 20:574. doi: 10.3390/ijms20030574
- Xie, H., Chua, M., Islam, I., Bentini, R., Cao, T., Viana-Gomes, J. C., et al. (2017). CVD-grown monolayer graphene induces osteogenic but not odontoblastic differentiation of dental pulp stem cells. *Dent. Mater.* 118, 116–117. doi: 10.1016/j.dental.2016.09.030
- Xiong, S. W., Zhang, P., Xia, Y., Fu, P. G., and Gai, J. G. (2019). Antimicrobial hexagonal boron nitride nanoplatelet composites for the thermal management of medical electronic devices. *Mater. Chem. Front.* 3, 2455–2462. doi: 10.1039/c9qm00411d
- Yang, K., Wan, J., Zhang, S., Zhang, Y., Lee, S. T., and Liu, Z. (2011). In vivo pharmacokinetics, long-term biodistribution, and toxicology of pegylated graphene in mice. *ACS Nano* 5, 516–522. doi: 10.1021/nn1024303
- Zhang, J., Lin, L., Jia, K., Sun, L., Peng, H., and Liu, Z. (2020). Controlled growth of single-crystal graphene films. *Adv. Mater.* 32:e1903266. doi: 10.1002/adma.201903266
- Zhang, L., and Wang, X. (2015). Mechanisms of graphyne-enabled cholesterol extraction from protein clusters. *RSC Adv.* 5, 11776–11785. doi: 10.1039/c4ra16944a
- Zhang, L., Xu, B., and Wang, X. (2016). Cholesterol extraction from cell membrane by graphene nanosheets: a computational study. *J. Phys. Chem. B* 120, 957–964. doi: 10.1021/acs.jpcc.5b10330
- Zhang, Y., Chan, C., Li, Z., Ma, J., Meng, Q., Zhi, C., et al. (2019). Nanotoxicity of boron nitride nanosheet to bacterial membranes. *Langmuir* 35, 6179–6187. doi: 10.1021/acs.langmuir.9b00025

- Zhao, C., Deng, B., Chen, G., Lei, B., Hua, H., Peng, H., et al. (2016). Large-area chemical vapor deposition-grown monolayer graphene-wrapped silver nanowires for broad-spectrum and robust antimicrobial coating. *Nano Res.* 9, 963–973. doi: 10.1007/s12274-016-0984-2
- Zhong, H., Zhu, Z., Lin, J., Cheung, C. F., Lu, V. L., Yan, F., et al. (2020). Reusable and recyclable graphene masks with outstanding superhydrophobic and photothermal performances. *ACS Nano* 14, 6213–6221. doi: 10.1021/acsnano.0c02250
- Zhou, H., Zhang, B., Zheng, J., Yu, M., Zhou, T., Zhao, K., et al. (2014). The inhibition of migration and invasion of cancer cells by graphene via the impairment of mitochondrial respiration. *Biomaterials* 35, 1597–1607. doi: 10.1016/j.biomaterials.2013.11.020
- Zurob, E., Dennett, G., Gentil, D., Montero-Silva, F., Gerber, U., Naulín, P., et al. (2019). Inhibition of wild *Enterobacter cloacae* biofilm formation by nanostructured graphene-and hexagonal boron nitride-coated surfaces. *Nanomaterials* 9:49. doi: 10.3390/nano9010049
- Conflict of Interest:** The authors declare that the research was conducted in the absence of any commercial or financial relationships that could be construed as a potential conflict of interest.

Copyright © 2021 Santos, Moschetta, Rodrigues, Alpuim and Capasso. This is an open-access article distributed under the terms of the Creative Commons Attribution License (CC BY). The use, distribution or reproduction in other forums is permitted, provided the original author(s) and the copyright owner(s) are credited and that the original publication in this journal is cited, in accordance with accepted academic practice. No use, distribution or reproduction is permitted which does not comply with these terms.



# Advances in Engineering Human Tissue Models

Chrysanthi-Maria Moysidou, Chiara Barberio and Róisín Meabh Owens\*

Department of Chemical Engineering and Biotechnology, University of Cambridge, Cambridge, United Kingdom

## OPEN ACCESS

### Edited by:

Davide Ricci,  
University of Genoa, Italy

### Reviewed by:

Moo-Yeal Lee,  
Cleveland State University,  
United States  
Giorgia Imparato,  
Center for Advanced Biomaterials for  
Healthcare (IIT), Italy

### \*Correspondence:

Róisín Meabh Owens  
rmo37@cam.ac.uk

### Specialty section:

This article was submitted to  
Biomaterials,  
a section of the journal  
Frontiers in Bioengineering and  
Biotechnology

**Received:** 24 October 2020

**Accepted:** 22 December 2020

**Published:** 28 January 2021

### Citation:

Moysidou C-M, Barberio C and  
Owens RM (2021) Advances in  
Engineering Human Tissue Models.  
Front. Bioeng. Biotechnol. 8:620962.  
doi: 10.3389/fbioe.2020.620962

Research in cell biology greatly relies on cell-based *in vitro* assays and models that facilitate the investigation and understanding of specific biological events and processes under different conditions. The quality of such experimental models and particularly the level at which they represent cell behavior in the native tissue, is of critical importance for our understanding of cell interactions within tissues and organs. Conventionally, *in vitro* models are based on experimental manipulation of mammalian cells, grown as monolayers on flat, two-dimensional (2D) substrates. Despite the amazing progress and discoveries achieved with flat biology models, our ability to translate biological insights has been limited, since the 2D environment does not reflect the physiological behavior of cells in real tissues. Advances in 3D cell biology and engineering have led to the development of a new generation of cell culture formats that can better recapitulate the *in vivo* microenvironment, allowing us to examine cells and their interactions in a more biomimetic context. Modern biomedical research has at its disposal novel technological approaches that promote development of more sophisticated and robust tissue engineering *in vitro* models, including scaffold- or hydrogel-based formats, organotypic cultures, and organs-on-chips. Even though such systems are necessarily simplified to capture a particular range of physiology, their ability to model specific processes of human biology is greatly valued for their potential to close the gap between conventional animal studies and human (patho-) physiology. Here, we review recent advances in 3D biomimetic cultures, focusing on the technological bricks available to develop more physiologically relevant *in vitro* models of human tissues. By highlighting applications and examples of several physiological and disease models, we identify the limitations and challenges which the field needs to address in order to more effectively incorporate synthetic biomimetic culture platforms into biomedical research.

**Keywords:** tissue engineering, scaffold, hydrogel, 3D biology, organoid, organ-on-a-chip

## INTRODUCTION

Cell culture systems represent an indispensable tool for a wide range of biomedical studies. Harrison's first experiments, early in the twentieth century, on development of frog nerve fibers in a dish, the establishment of aseptic technique and subculture methods by Carrell and Ebeling in 1920s and the successful isolation and maintenance of the first immortalized human cell line (HeLa cells) by Gey in the 1950s, made it possible to grow cells in artificial environments, laying the foundation for cell and molecular biology (Taylor and Taylor, 2014; Jedrzejczak-Silicka, 2017; Simian and Bissell, 2017). Cell culture has come a long way since then and is now a vital and invaluable tool for

a vast array of applications, both in academic and industrial settings, including drug development, cancer research and tissue engineering (Przyborski, 2017; Kapałczyńska et al., 2018). In such studies, two-dimensional (2D) cell culture systems dominate, continuing to improve our perception and understanding of cell biology. These cell systems rely mainly on adherent cultures, where cells grow as a monolayer attached to a plastic or glass substrate. Although easy and convenient, 2D cultures exhibit numerous disadvantages. Firstly, they are simplistic imitations of the *in vivo* situation, where cells grow within a complex three-dimensional (3D) microenvironment. The lack of this environmental context and structural architecture excludes physical cues for cell-cell and cell-matrix communication, critical for several cellular processes (e.g., mitosis, self-renewal, and differentiation). These physical constraints also impede cells from organizing naturally and spreading vertically, forcing them to flatten out and grow as monolayers (Fitzgerald et al., 2015; Przyborski, 2017). In turn, gene expression, production of proteins and cytoskeletal structure are altered, resulting in loss of the diverse cell phenotype and thus of the physiological cellular behavior and function (Birgersdotter et al., 2005; Luca et al., 2013; Fontoura et al., 2020). In addition, the absence of oxygen and nutrient gradients in monolayer cultures disrupts cell response to physiological stimuli, further inhibiting basic cellular processes and intercellular crosstalk, while the lack of a heterogeneous cell population in 2D models hinders their potential to form more complex tissue- or organ-like structures. These inherent limitations and shortcomings of 2D cell systems ultimately lead to failures in understanding cell behavior in healthy or diseased states (Duval et al., 2017). The research community is now beginning to seek alternative technologies that will facilitate development of models able to more closely mimic the complexity of whole tissues *in vitro* (Fitzgerald et al., 2015; Przyborski, 2017; Kapałczyńska et al., 2018). To this end, 3D cell cultures can provide a well-controlled *in vivo*-like microenvironment specifically tailored to each application (Chen, 2016; Koledova, 2017; Owens et al., 2017; Przyborski, 2017; Kapałczyńska et al., 2018; Jensen and Teng, 2020).

Although it is thought that the inception of 3D biology was in the 1970s (Schwarz and Bissell, 1977; Bissell, 1981; Bissell and Barcellos-Hoff, 1987), where cells were cultivated in floating collagen gels or agar, in fact, the phrase “three-dimensional cell culture models” was first coined in the studies of Barcellos-Hoff in 1989 and Petersen in 1992, who developed assays to distinguish between healthy and malignant breast epithelial cells grown in laminin-rich matrices (Hamburger and Salmon, 1977; Bissell, 2017; Simian and Bissell, 2017). These studies were followed by a body of research on new technologies focused on enhancing the morphological and physiological relevance of cell culture systems. The increasing number of publications since then, utilizing such cell culture platforms, or suggesting new ones, highlights the transition of the field into 3D cell culture in order to improve the capabilities of experiments performed *in vitro* (Bissell, 2017; Przyborski, 2017; Devarasetty et al., 2020). Over the years, 3D cell culture has become a generalized term, often used to point out the disparities between conventional and new cell culture technologies. Therefore, it is important

to clearly define what is meant—or should be meant—by this term. Broadly speaking, we define 3D cell culture as an *in vitro* tissue-specific microenvironment that enables individual cells to grow, maintaining their 3D shape and functions, as well as to interact with their surroundings and a heterogeneous population of neighboring cells, establishing sufficient signaling networks. In this environment exogenous interference and support should be minimized (e.g., automated media perfusion) to reduce stress and unnatural cell responses and rather enable growth of different cell types to foster the development of more realistic culture systems (Abbott, 2003; Huh et al., 2011; Shamir and Ewald, 2014). 3D cell culture is also used to describe tissue- and organ-like structures emerging from the combination of 3D cell biology with Tissue Engineering (TE) principles. In these studies, researchers are focused on reconstructing organ structure and function *ex vivo* (Figure 1), to produce more reliable and physiologically relevant human-like 3D *in vitro* models (Khademhosseini and Langer, 2016; Caddeo et al., 2017), following the basic TE premise: the appropriate cell types (e.g., primary cells, stem cells) are seeded in biodegradable structures fabricated to mimic the target organ or tissue (i.e., scaffolds) and are supplied with the appropriate cocktail of substances essential for tissue generation (e.g., growth factors and signaling molecules; Langer and Vacanti, 1993). Such tissue-engineered human equivalents represent a promising alternative to the current state-of-the-art and particularly to animal models, which often fail to recapitulate human conditions due to differences in the overall physiology and in the molecular and signaling mechanisms involved in the onset and progression of diseases. This is evidenced by the high failure rates of drugs and therapies to enter clinical trials to get approval from regulatory agencies despite successful tests in animals, underlying the challenges in translating such data to human systems. Besides their greater translational relevance, the development of tissue-engineered *in vitro* models has recently taken off thanks to ethical and economic arguments (Rouwkema et al., 2011; Caddeo et al., 2017). Although the use and welfare of animals in science is protected by national and international legislation (e.g., the principle of 3Rs), there are still vibrant discussions and room for improvements as well as strong encouragement for reduction and replacement. This is also encouraged by an economic point of view, since the actual costs for drug or treatment candidates to become clinical products are huge and the process is time-consuming and labor intensive (Rouwkema et al., 2011; Fitzgerald et al., 2015).

In this review, we focus on bioengineering approaches that seek to integrate TE with 3D cell biology toward more sophisticated and reliable 3D human tissue equivalents, with the potential to (i) enhance the predictive value of preclinical studies, (ii) improve the way we study physiology and pathology and thus to address biological questions that so far necessitated animal models, and (iii) bridge the gap between current (pre-)clinical research tools and human systems by assisting and advancing drug development processes in terms of science, bioethics and economy (Rouwkema et al., 2011; Fitzgerald et al., 2015; Caddeo et al., 2017). Current trends in the field suggest that the choice of the culture format/technology/device that will support the tissue equivalent should take into account the



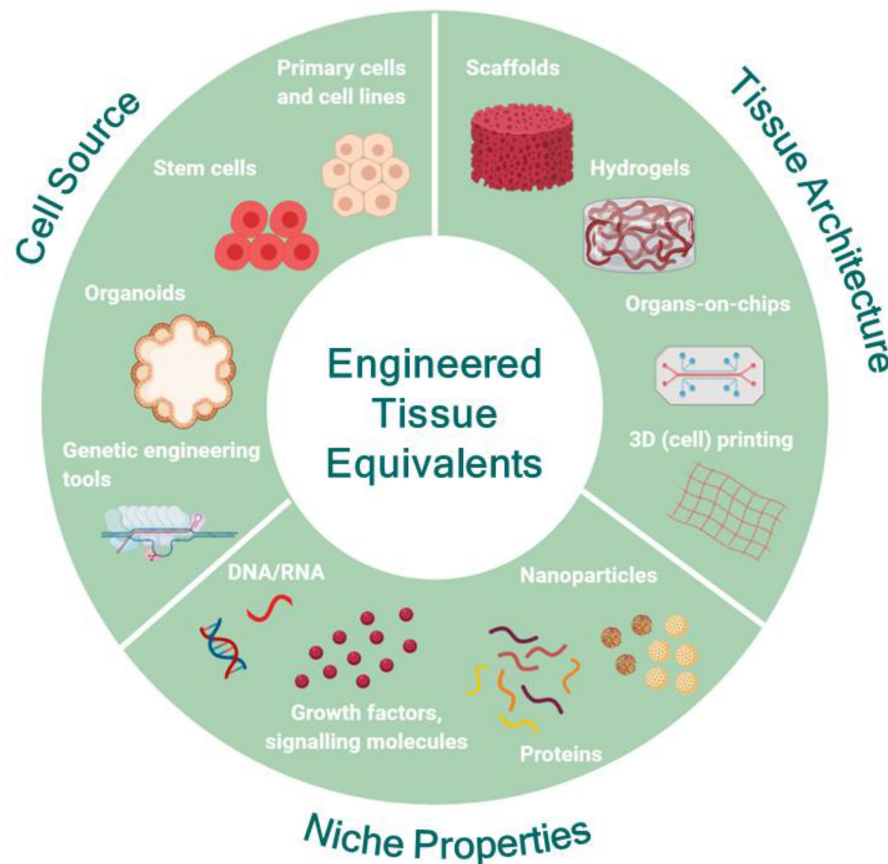


**FIGURE 1 |** Engineering human tissue equivalents *in vitro*: the main premise for the successful development of tissue equivalents is to understand the structural and functional role of each counterpart of the native tissue and to carefully choose the range of features necessary to recapitulate the specific characteristics of the native tissue for each application. Then, the appropriate source of cells can be identified and modulated, if necessary, to capture the desired functionality. In parallel, the most appropriate substrate format can be designed and engineered to match the physicochemical properties and architecture of the native tissue under the conditions of interest and to facilitate coupling with the appropriate biochemical and biophysical cues mimicking the *in vivo* niche. Created with BioRender.com.

constituent parts of the organ(s) to be modeled and the extent to which the *in vivo* complexity will be recapitulated. Various techniques and culture formats have been developed to meet these requirements, however a single format/technology/device that meets the requirements/needs of all 3D cell culture assays does not exist, and indeed should not exist, given the diversity in the morphology and functions of all the different organs/tissues researchers are emulating for different applications (Shamir and Ewald, 2014; Knight and Przyborski, 2015). Based on the format, 3D cell culture platforms can generally be categorized as scaffold-free or scaffold-based systems. Scaffold-based approaches utilize natural or synthetic materials to provide support in the form of a matrix that creates the desired tissue-specific microenvironment for optimal cell growth and differentiation and natural ECM deposition, while preserving the native tissue architecture (Fitzgerald et al., 2015; Przyborski, 2017). Decellularised scaffolds have also been used to culture cells *in vitro* by removing cells from whole tissues/organs or from the scaffold biomaterial surface after culturing cells on it for sufficient time for native

ECM deposition. This way the structural and functional matrix proteins (e.g., collagen, fibronectin, hyaluronic acid, and laminin) remain intact while the exact composition varies according to the origin of tissue/organ or the cells seeded (Fitzgerald et al., 2015). Another category where cell growth and differentiation is supported by biomimetic matrices is hydrogels, which are networks of cross-linked hydrophilic polymers with the unique capability to absorb and retain copious amounts of water without dissolving but rather swelling. Similar to scaffolds, hydrogels can be made from natural or synthetic materials and cross-linked by either physical or chemical means. Due to their particularly soft nature, they are well-suited for soft tissue *in vitro* models (Fitzgerald et al., 2015; Przyborski, 2017). In contrast, scaffold-free culture systems seek the formation of multicellular masses without exogenous input as a framework, but rather by encouraging cells to form aggregates, secrete their own ECM and then self-assemble into 3D microstructures (Przyborski, 2017). This categorization however is quite generalized since the progress in, and convergence of, related disciplines have made

possible the generation of new, improved, and more sophisticated tools for 3D biomimetic cultures. Currently, novel biofabrication methods (e.g., 3D printing) and microscale technologies (e.g., soft lithography), can be combined with advanced biological systems such as organoids and stem cells, resulting in more complex culture systems, tailored for specific applications. In the following sections, we first provide an overview of the current technological bricks available to develop tissue-engineered human models by summarizing the advancements in cell biology, materials science and bioengineering. Then, through examples of the current state-of-the-art, we identify and discuss the advantages, limitations and challenges the field needs to address in order for *in vitro* TE models to be successfully implemented in biomedical research.

## BUILDING BLOCKS FOR DEVELOPING HUMAN TISSUE EQUIVALENTS

### Cell Sources for *in vitro* Tissue Engineering

To successfully design and develop tissue equivalents, it is useful to understand the anatomical and functional characteristics of the tissue of interest, as well as the role and interaction of its constituent parts (Caddeo et al., 2017). Although the end goal is to create organ and tissue equivalents with enhanced biomimicry in the lab, it is important to acknowledge the reductionist nature of these models. In fact, 3D human tissue equivalents are intentionally and necessarily reductionist, carefully designed to capture a specific range of the *in vivo* physiology over time, fit for a specific application. Therefore, a crucial step in the design process is to identify the appropriate factors that must be incorporated in order to model different *in vivo* situations (Chen, 2016). To this end, the source and the number of cells must be carefully chosen as this will determine the ability of the model to capture *in vitro* the desired characteristics of the native tissue at the cell culture level and then establish what the system might or might not recapitulate and to what extent (Chen, 2016; Caddeo et al., 2017).

### Stem Cells

Until recently, TE approaches relied almost exclusively on established cell lines and primary cells. Despite the advantages of using cell lines (e.g., easy to use, inexpensive, unlimited availability, reproducibility, no need of ethics approval), they are not considered ideal sources for modeling human conditions since they do not exhibit normal features, often drifting from the genetic and phenotypic profile of the tissue of origin (Carter and Shieh, 2015a). Primary cells are more representative of the morphological and functional features of the tissue they are derived from, but they can be difficult to obtain and maintain for long-term experiments. Moreover, they have low proliferation rates and must be used in early passage stages because they lose their structural, functional, and self-renewal properties as they undergo senescence processes. Reproducibility of results is an additional issue when using primary cells and donor-to-donor variations must be taken into account (Benam et al., 2015; Caddeo et al., 2017).

To overcome these limitations, stem cells are now being employed for reconstructing tissue/organ structure and function

*in vitro*, due to their unique capabilities to self-renew (stemness) and to differentiate toward one or more specialized cell types (potency), representing a versatile source of cellular substitutes for a wide range of applications (Avior et al., 2016; McKee and Chaudhry, 2017; Rowe and Daley, 2019). Until recently, the only source of stem cells for biomedical research was human-derived embryonic stem cell lines (ESCs). However, the discovery of human induced pluripotent stem cells (iPSCs) in 2007 (Takahashi et al., 2007) substantially altered the field of biomedical research. iPSCs are engineered stem cells generated directly from adult (differentiated) somatic cells by introducing a set of pluripotency-associated genes into cells, or through chemical reprogramming or protein delivery (Khademhosseini and Langer, 2016; Caddeo et al., 2017). These cells exhibit similar stemness and potency characteristics as ESCs and, under certain conditions and depending on their origin, they can differentiate toward various cell types. Among other applications, human iPSCs offer an unlimited supply of cells for *in vitro* TE, disease modeling, cell therapy and pharmaceutical applications. Importantly, as these stem cells can be derived from patients with specific pathology, patient-derived hiPSCs are now used to more accurately model disease and to improve diagnostics and drug discovery, laying the foundations for novel methods of personalized medicine (Cyranoski, 2018; Rowe and Daley, 2019). Despite the great potential of iPSCs to bridge the gap between preclinical studies, animal models and clinical studies, it is important to note that currently most iPSC-derived cell types exhibit immature phenotypes, while some pathologies cause such damage in adult somatic cells that the iPSCs derived from such tissues would not be informative (Benam et al., 2015; Cyranoski, 2018). Ongoing research on establishing protocols for the maturation of iPSC-derived specialized cell types will likely address these challenges via applying different biochemical and biophysical stimuli. TE strategies could be useful in these efforts by providing the appropriate microenvironment (e.g., biomimetic scaffolds) and cues (e.g., ECM rich in growth factors) to guide differentiation and maturation (Benam et al., 2015).

Finally, another type of stem cells that have gained a lot of attention as a cell source for TE are mesenchymal stem/stromal cells (MSCs), mainly due to their therapeutic potential (Rosenbaum et al., 2008; Khademhosseini and Langer, 2016). MSCs are a specific subtype of multipotent stem cells, diversely distributed in the human body including bone marrow, adipose, perinatal tissues, blood, periodontal ligament, and skeletal muscles, from most of which they can be isolated (Rosenbaum et al., 2008; McKee and Chaudhry, 2017; Ullah et al., 2019). Despite having the same capabilities as pluripotent stem cells, MSCs can differentiate toward only a few specific cell types, such as osteogenic, chondrogenic, and adipogenic cell types, depending on the nature and maturity of the tissue of origin (Rosenbaum et al., 2008; McKee and Chaudhry, 2017). Their homing capability has made them very attractive candidates for a wide breadth of preclinical and clinical applications, including tissue regeneration, wound healing, and treatment of autoimmune diseases (Khademhosseini and Langer, 2016; Ullah et al., 2019). Upon injury, MSCs are naturally released in the circulation and migrate to the damaged tissue where they secrete

a pool of cytokines, growth factors and other bioactive molecules with immunomodulatory and angiogenic effects, thus creating a microenvironment that promotes tissue repair and regeneration (Ullah et al., 2019). For *in vitro* TE, MSCs represent a useful resource, mainly due to their ease in isolation, manipulation and differentiation, compared to the longer and more elaborate iPSCs protocols.

## Organoids

The advent of human pluripotent stem cells marked the starting point of the development of “organs in a dish,” also known as organotypic cultures or organoids, a major breakthrough of the past decade (Dutta et al., 2017; Lancaster and Huch, 2019). The term “organoid” is not new; it was used in the 1950s and 1960s to describe structures in cell culture systems that resembled organs (Duryee and Doherty, 1954; Schneider et al., 1963; Wolter, 1967) and more recently in studies where 3D cell aggregates, called spheroids, were defined as organoids despite the fact that they were not fully representative of the native tissue (Dutta et al., 2017). The term has become popularized in *in vitro* biology and evolved to generally refer to tissues or structures that resemble an organ, losing its precision (Dutta et al., 2017; Lancaster and Huch, 2019). A more specific working definition that fulfills the basic definition of organoids was recently proposed, along with several criteria: “(1) a 3D structure containing cells that establish or retain the identity of the organ being modeled; (2) the presence of multiple cell types, as in the organ itself; (3) the tissue exhibits some aspect of the specialized function of the organ; and (4) self-organization according to the same intrinsic organizing principles as in the organ itself” (Lancaster and Huch, 2019). These properties render organoids suitable formats/tools for modeling organ architecture *in vitro*. Because iPSC-derived organoids follow *in vivo* like development, their morphology closely recapitulates the native organ structure, making them particularly apt for studies looking at developmental organogenesis, while tissue-specific adult stem cell organoids are mostly suited for studying tissue homeostasis and maintenance, since naturally in the body they are key players in these processes (Fatehullah et al., 2016; Yin et al., 2016; Lancaster and Huch, 2019).

Currently, several protocols exist for the development of organoids for various organs, derived either from pluripotent stem cells (ESCs and iPSCs) or from organ-specific adult stem cells (ASCs) and progenitor cells (Takebe and Wells, 2019). The establishment of a protocol for a long-term, well-defined, and stable culture of murine intestinal organoids in 2009 by Sato et al. (2009) and subsequent adaptation of the protocol and modifications of the growth factor cocktail in the original organoid culture medium allowed the generation of human organoids from various tissues, such as stomach (Bartfeld et al., 2015), liver (Takebe et al., 2013), esophagus (Li et al., 2018), lung (Dye et al., 2015), and ovaries (Kessler et al., 2015; see Kim et al., 2020, for an extended review). Organoids now represent a powerful tool for a wide spectrum of biomedical applications ranging from basic cell biology studies, organogenesis and tissue homeostasis to disease modeling (see Lancaster and Huch, 2019, for an extended review), drug/therapy development, and

regenerative medicine (Schweiger and Jensen, 2016; Brassard and Lutolf, 2019). However, there are several general shortcomings and challenges in the development and application of organoids, as well as in the interpretation and translation of the derived data. An important issue is the reproducibility and consistency of organoids from batch to batch. The initial culture conditions and the environment in which organoids grow are of paramount importance for their self-organization and the development of the desired emergent tissue (Brassard and Lutolf, 2019). To date, most organoid systems rely on animal-derived ECMs, such as Matrigel, supplemented with growth factors and endogenous signaling molecules (e.g., Wnt, Noggin, and R-spondin). Even though Matrigel works as an artificial niche, mimicking the native tissue environmental cues, its poorly understood composition, heterogenous nature, and batch-to-batch variability hinders the reproducibility and robustness of the organoid systems, often leading to heterogeneity in size, shape, and viability, even between organoids in the same culture (Fatehullah et al., 2016; De Souza, 2018; Brassard and Lutolf, 2019; Lancaster and Huch, 2019; Kim et al., 2020). In addition, although these organotypic cultures are highly biologically relevant, they alone do not necessarily recapitulate the dynamics present in the human system. For example, the majority of organoid culture systems lack essential components of their living counterparts, such as the enteric nervous system, the immune system, as well as luminal flow and peristalsis (In et al., 2016; Tsakmaki et al., 2017; De Souza, 2018; Kim et al., 2020). Also, lack of vascularization in organoid cultures means that their growth and development depends on diffusion of nutrients from the surrounding media. While this might not be an issue for small organoids, in cases of some larger organoids the diffusion of nutrients is limited, resulting in dramatic necrosis in their interior and hence compromising the long-term viability of the system and the validity of the results (McMurtrey, 2016; Grebenyuk and Ranga, 2019; Lancaster and Huch, 2019). To overcome this limitation, culturing organoids under flow within microfluidic chips has been proposed recently, as a means to induce vascularization and hence to improve the morphological and functional characteristics of the bioengineered tissues (Homan et al., 2019).

The tremendous potential of organoid culture systems could not go unnoticed by tissue engineers. Firstly, since organoid systems are designed and developed to recapitulate the environment and properties of the stem cell niche and the tissue progeny with indefinite culture potential, they represent an alternative, more accessible, and scalable source for harnessing stem cells (Yin et al., 2016). Employment of molecular technology and organoids in the service of *in vitro* TE can further enhance the potential of these systems in mimicking the *in vivo* conditions. In particular, genes within organoids can be manipulated using tools, such as CRISPR/Cas-9, to either correct mutations and restore physiological function or to introduce mutations and model various disease phenotypes (Dutta et al., 2017; Lancaster and Huch, 2019; Kim et al., 2020), again providing an alternative source of cells with broad applicability and amenable to manipulation. Additionally, since organoids may contain more than one tissue representative cell type, they



can be used as a single cellular input for tissue-engineered equivalents, allowing them to better capture the cellular diversity of the living counterparts (Kasendra et al., 2018).

Stem cells and organoids are a versatile source of cells for *in vitro* TE applications, thus the convergence of these fields can be mutually beneficial. On one hand the use of human-derived cellular parts enhances the relevance of tissue-engineered equivalents, both in terms of mimicry and data interpretation. On the other hand, tissue engineering provides a broad toolbox to study stem cells and organoids and to address challenges related to engineering the appropriate niche for controlling the culture conditions. It also provides the extrinsic instruction patterns to robustly and elaborately direct self-organization processes. This way TE approaches can aid stem cells and organoids in realizing their full potential as *in vitro* tools for biomedical research (Benam et al., 2015; Chen, 2016; McKee and Chaudhry, 2017; Brassard and Lutolf, 2019).

## Materials for *in vitro* Tissue Engineering

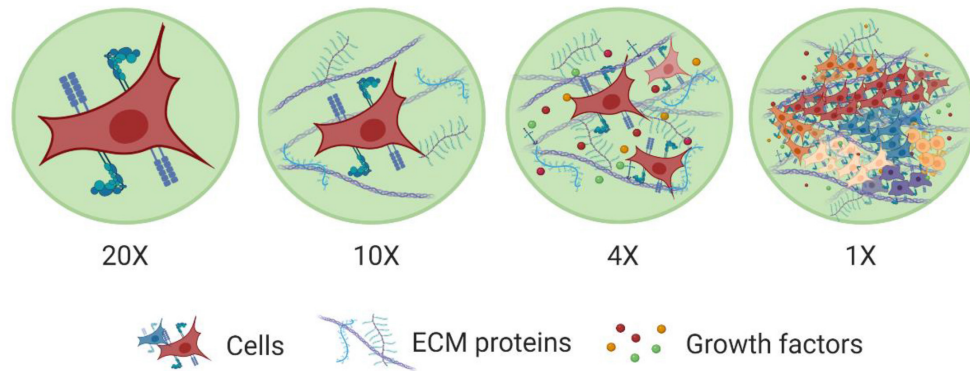
Alongside the appropriate cell type(s), another fundamental element for effectively engineering tissue equivalents is the choice of the suitable biomaterial(s). In the classic TE paradigm, pre-engineered 3D supports/scaffolds, made from natural or synthetic materials, are used as templates for cell attachment, growth and differentiation toward functional living constructs (Vacanti, 2006). As scaffolds act as a synthetic ECM, modifying the biomaterial building blocks to mimic the native tissue ECM is a major challenge. In the body, ECM is a 3D network that consists of various macromolecules, including proteins and polysaccharides, responsible for tissue support and maintenance, cell-cell and cell-ECM communication, diffusion of nutrients metabolites and growth factors. In addition, ECM mediates signaling pathways from soluble factors and other sources, regulating various cellular behaviors, such as migration, adhesion, proliferation, and differentiation (Frantz et al., 2010; Theocharis et al., 2016; Afewerki et al., 2019; **Figure 2**). In this context, the role of biomaterials for tissue engineered equivalents is to provide cells with the appropriate framework/template to adhere, proliferate, differentiate, mature, secrete ECM and form the necessary cell-cell, and cell-scaffold interactions that will enable them to auto-organize as they would *in vivo* (Przyborski, 2017; Afewerki et al., 2019; **Figure 3**). The choice of biomaterial depends on the application and the physiological or pathophysiological conditions the tissue model aims to emulate (Caddeo et al., 2017). However, there are many other properties that need to be considered when selecting biomaterials, including biocompatibility, strength and elasticity, porosity, molecular gradients and mass transport of nutrients and growth factors, oxygenation, adhesion or signaling sites, surface roughness, shape, type (e.g., scaffold or hydrogel), and source (Sitarski et al., 2018), in order to more realistically recapitulate the cues naturally occurring in the native tissue.

A broad range of materials is now available for the fabrication of various types of substrates, the properties of which can be tailored at the micro- and nano-scale to match the requirements of specific applications (Huang et al., 2017; Nikolova and Chavali, 2019; Cembran et al., 2020). A characteristic property

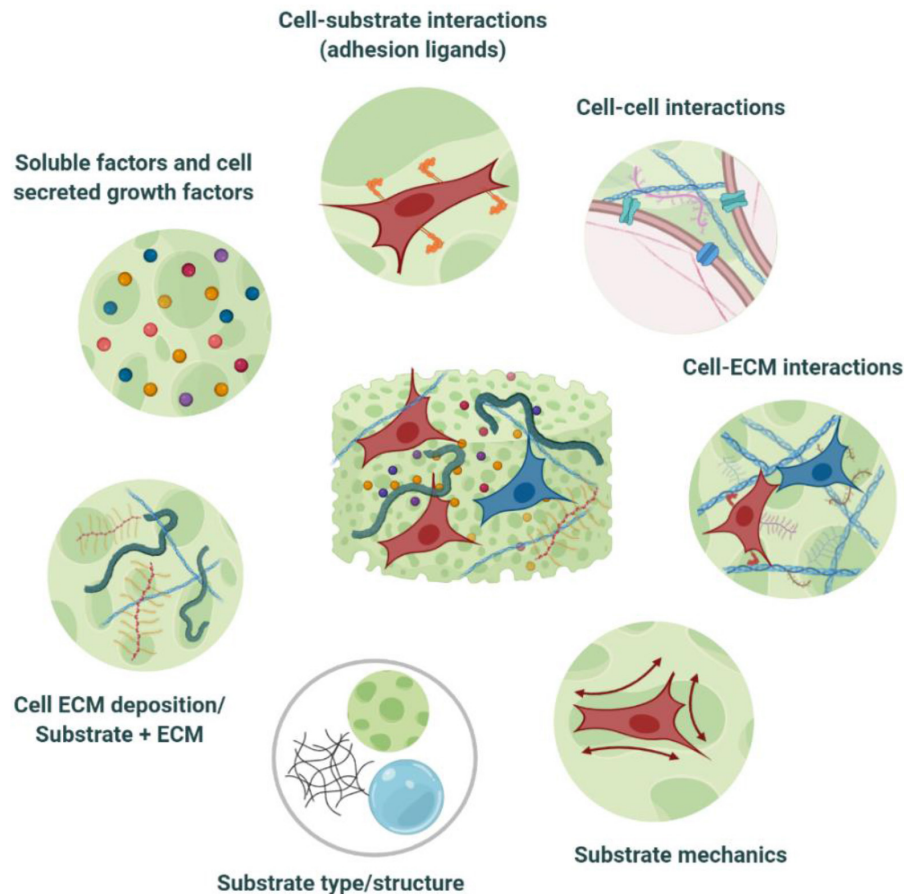
of TE scaffolds that particularly affects primary cell-matrix interactions as well as cell behavior and fate upon seeding, is its topography. It is well-known that micro-topography (1–100  $\mu\text{m}$ ) is responsible for cell recruitment, adhesion, orientation and gene expression, while the submicron and nano- features strongly influence the cytoskeletal arrangement (Hayes and Richards, 2010). Tailoring surface topography of biomaterials has been shown to support and enhance differentiation of MSCs toward specific lineages (Abagnale et al., 2015). Mechanobiology studies have revealed that, amongst other cues, cells are also responsive to the material stiffness (Discher et al., 2005), which can affect intracellular signaling cascades that trigger cell adhesion, phenotype maintenance, cytoskeletal reconstruction, and even stem cell differentiation (Engler et al., 2006; Mao et al., 2016; Cao et al., 2017; Kumar et al., 2017; Vining and Mooney, 2017; Darnell et al., 2018). Therefore, selection of biomaterials with the appropriate stiffness is not only important for matching the native tissue mechanical properties, but can be also used as a tool to control cell phenotypes and thus modulate cell behavior (Khademhosseini and Langer, 2016; Ledo et al., 2020b). Furthermore, materials can undergo several chemical modifications, to improve their physicochemical properties as well as to enable incorporation of biologically relevant molecules and signals necessary for guiding and regulating cell response. For example, proteins from the ECM (e.g., hyaluronic acid, collagen, fibronectin etc.) can be blended or grafted to the material surface to improve cell behavior, by acting as matrix-associated biological cues, regulating cell attachment (e.g., via integrin-mediated binding), as well as proliferation and infiltration within the scaffold (Baker and Chen, 2012). For instance, incorporation of well-known cell binding motifs from ECM-derived proteins, such as RGD (arginine-glycine-aspartate) peptide, can enhance cell spreading, and viability in hydrogels (Gallagher et al., 2020).

Biomaterials may be prepared of natural polymers such as collagen, laminin, and hyaluronic acid, or from synthetic materials such as polyethylene glycol (PEG), propylene glycol diacetate (PGDA), polyvinylidene fluoride (PVDF), or copolymers (Afewerki et al., 2019; Nikolova and Chavali, 2019). Thus, they can be categorized as natural, synthetic, or hybrid biomaterials (see **Table 1** for examples of biomaterials and applications). In most cases, naturally derived biomaterials are amino acid-based or sugar-based biopolymers which can be components of the natural ECM (e.g., collagen, laminin, elastin, and fibrinogen) or not (e.g., chitin, silk fibroin, chitosan, and alginate; Silva et al., 2017; Ahadian et al., 2018). Such materials represent an attractive source for *in vitro* TE applications, due to their microstructure, stability, biocompatibility, and ability to present cells with natural adhesion sites, as well as due to the possibility to tailor and control their properties via physical or chemical treatments (i.e., cross-linking) or by blending them with other biopolymers (Guarino et al., 2016; Ullah and Chen, 2020) to better recapitulate *in vitro* the physiological milieu. A commonly used natural biomaterial in 3D biomimetic cultures and tissues is collagen, as it is a major component of the natural ECM and it is among the main structural proteins of most connective tissues (Ahadian et al., 2018; Sorushanova et al., 2019). The







**FIGURE 2 |** Levels of organization within tissues. The major building block of tissues are cells. Cell membranes are equipped with a wide range of proteins that help them sense and respond to cues in their microenvironment. Cells also interact with other cells and the surrounding ECM network. This ECM network comprises of various macromolecules (e.g., proteins, polysaccharides) and soluble factors (e.g., growth factors) immobilized in its structure, which promote cell-cell and cell-ECM interactions. This way ECM establishes a favorable niche for cells to grow, spread, differentiate, and perform various functions and also to work together with other cells to form more complex structures toward tissues with specific functionalities. Created with BioRender.com.





**FIGURE 3 |** Cell-biomaterial interactions within tissue engineered equivalents. TE substrates constitute an artificial ECM, encompassing *in vivo*-like, tissue-specific biochemical, and biophysical cues. This niche provides a favorable microenvironment for cells to adhere, proliferate, differentiate, mature, and deposit their own ECM, as well as to communicate and to establish the necessary cell-cell, and cell-ECM interactions that will enable them to auto-organize as they would *in vivo*. Modulation of the niche properties can also guide cell behaviour toward the desired phenotypic output. Created with BioRender.com.

**TABLE 1 |** Examples of biomaterials, fabrication methods and cell sources for skin, brain, heart, lung, intestine, bone, and liver biomimetic cultures.

Material(s) and format	Fabrication method	Cell source	References
 <b>Skin biomimetic cultures</b>			
Collagen hydrogel	Gelation/3D bioprinting	Fibroblasts, melanocytes (MCs), and keratinocytes (KCs)	Min et al., 2018
Alginate/Carboxymethyl cellulose/Nanofibrillated cellulose (ALG/CMC/NFC) bioinks		Fibroblasts and KCs	Lee et al., 2009
Collagen I scaffolds	Gelation/vitrification	Human skin fibroblasts (hSF)	Zidarič et al., 2020
		Normal human skin fibroblasts (NhSF), Normal human dendritic cells (NHDC), Normal human epidermal keratinocytes (NHEK)	Uchino et al., 2009
Silk Fibroin/Collagen (SF/COL) scaffolds	Freeze-drying	Primary neonatal foreskin fibroblast (NH), hiNSCs	Vidal et al., 2019
Polycaprolactone (PCL), Polycaprolactone/Collagen (PCL/COL), Polycaprolactone/Poly (L-lactic acid) (PCL/PLLA), Polycaprolactone/Poly (L-lactic acid)/Collagen (PCL/PLLA/COL) scaffolds		MSCs	Rahmani et al., 2018
Polycaprolactone/Aloe vera (PCL/AV), Polycaprolactone/Curcumin (PCL/CUR), Polycaprolactone/Aloe Vera/Tetracycline hydrochloride (PCL/AV/TCH) scaffolds	Electrospinning	Human dermal fibroblasts	Ezhilarasu et al., 2019
Gelatin methacrylate/Nanofibrils (GelMa/NF), Gelatin/Nanofibrils			Rnjak et al., 2009
Milk protein/Polycaprolactone (MP/PCL) scaffolds		Human keratinocytes	Hewitt et al., 2019
Synthetic Elastin (SE) hydrogels		Human dermal fibroblasts, Human keratinocytes	Mao et al., 2018
 <b>Brain biomimetic cultures</b>			
Collagen gels	Gelation	Neuroblastoma cell line (SK-N-BE)	Villasante et al., 2017
Alginate/Collagen hydrogels		hiPSCs	Moxon et al., 2019
Gelatin hydrogels coated with Collagen IV/Fibronectin		hiPSC, human brain microvascular endothelial cells (BMECs)	Faley et al., 2019
Silk fibroin scaffold/Collagen I hydrogels	Silk extraction/Salt-leaching	hiPSCs	Rouleau et al., 2020
Liquid crystal elastomers (LCE) scaffolds	Salt-leaching	SH-SY5Y	Prévô et al., 2018
Silk fibroin (SF) scaffolds	Freeze-drying	hiNSCs	Cairns et al., 2020
Pol(vinyl alcohol)/Sodium alginate (PVA/SA) fibers	Multilayer Coaxial Laminar Flow	hiPSCs	Zhu et al., 2017



(Continued)

TABLE 1 | Continued

Material(s) and format	Fabrication method	Cell source	References
Sodium Alginate/Gelatin (SA/Gel) based bioinks	Gelation/3D bioprinting	SH-SY5Y, hiPSCs	Fantini et al., 2019
Gelatin Methacrylate (GelMa), Glycidyl/Methacrylate/Hyaluronic acid (GM/HA) hydrogels		Neural Stem Cells (NSCs)	Tang et al., 2020
Methacrylated Alginate (AlgMA) hydrogels		Neuroblastoma cell line (SK-N-BE)	Monferrer et al., 2020
Poly(desaminotyrosyl tyrosine ethyl ester carbonate) (pDTEc) nanofibers		Neural reprogrammed stem cells (RN-iPS)	Carlson et al., 2016
Polycaprolactone (PCL) scaffolds		Human neural progenitor stem cells (hNPCs)	Jakobsson et al., 2017
Polyethylene diacrylate (PEGDA) scaffolds	UV polymerization		Murphy et al., 2020
 <b>Heart biomimetic cultures</b>			
Collagen nanofibers	Electrospinning	Human Bone marrow mesenchymal stem cells (hBM-MSC)	Joshi et al., 2018
Poly(vinylidene fluoride)/Trifluoroethylene (PVDF/TrFE) scaffolds		hiPSCs, Cardiomyocytes (CMs)	Adadi et al., 2020
Collagen fibers	Melt electro-wiring	Human umbilical cord vein smooth muscle cells (HUVSMCs)	Saidy et al., 2019
Alginate (Alg) hydrogel nanofibers, Alginate/Gelatin (Alg/GelF/MA) hydrogel nanofibers	Wet-electrospinning	Mesenchymal stem cells enhanced with enhanced green fluorescent protein (hEGFP-MSCs)	Majidi et al., 2018
Gelatin hydrogels	Gelation/3D bioprinting	hMSCs	Tijore et al., 2020
Hyaluronic Acid/Arginin-Glycine-Aspartic Acid (HA/RGD) hydrogels			Gallagher et al., 2020
Gelatin Methacrylate (GelMa) bioinks		HUVECs, CMs	Zhang et al., 2016b
Gelatin Methacrylate/Polyethylene diacrylate (GelMa-PEGDA) bioinks		Induced multipotent stem cells (iMSCs)	Nachlas et al., 2020
Gelatin/Gellan Gum (GG) hydrogels		hiPSC-CMs	Koivisto et al., 2019
Poly(vinyl alcohol) (PVA) scaffolds	Freeze-drying		Dattola et al., 2019
Polycaprolactone films (MacPCL)	Layer-by-layer assembly, Laser perforation	hMSCs	Zhang et al., 2019
Matrigel coated fiber matrices	Two-photon polymerization	hiPSC-CMs	Wang C. et al., 2020
 <b>Lung biomimetic cultures</b>			
Collagen hyaluronate (CHyA-B) scaffolds	Freeze-drying	Bronchial epithelium cells (Calu-3)	O'Leary et al., 2016
Poly(L-lactide-co-glycolide)/Gelatin (PLGA/Gel), Poly(L-lactide-co-glycolide)/Sodium bicarbonate (PLGA-SBC) microparticles		Lung adenocarcinoma cells (A549)	Kuriakose et al., 2019

(Continued)


**TABLE 1 |** Continued

Material(s) and format	Fabrication method	Cell source	References
Hyaluronic Acid-Furan/ Modified methylcellulose with reactive thiols (HA-Furan/MC-SH) hydrogels	Gelation	Smooth muscle cells (SMCs)	Tam et al., 2019
Poly(vinyl chloride)(PVC) sheets	Electrospinning	Lung adenocarcinoma cells (A549)	Simon et al., 2016
Polyethylene terephthalate (PET) nanofibers		Human airway smooth muscle (HASM)	Morris et al., 2014
Polyethylene terephthalate (PET) scaffolds		Lung fibroblasts (MRC5)	Htwe et al., 2015
Polyurethanes/polyhedral oligomeric silsesquioxane (PU/POSS) scaffolds	3D bioprinting	Human bone marrow mesenchymal stem cells (hBM-MSCs)	Wu et al., 2020
 <b>Intestine biomimetic cultures</b>			
Collagen scaffolds	Gelation	Caco-2	Kim et al., 2014
Propylacrylamide (pNIPAM) hydrogels	Freeze-drying	Caco-2, HT29-MTX, hiNSCs	Dosh et al., 2017
Silk fibroin (SF) scaffolds		Human colonoid culture Caco-2	Shaban et al., 2018
			Manousiouthakis et al., 2019
Collagen scaffolds	Curing/gelation		Roh et al., 2019
Polyethylene diacrylate (PEGDA)/Acrylic acid/Fibronectin and composite scaffolds	3D bioprinting		Yu et al., 2012
Polyethylene diacrylate/Alginate acid (PEGDA/AA) scaffolds	UV photo-polymerization		Creff et al., 2019
Polyethylene terephthalate (PET) nanofibrous scaffolds	Electrospinning		Castaño et al., 2019
			Patient et al., 2019
 <b>Bone biomimetic cultures</b>			
Ulvan/gelatin (UG) scaffolds	Gelation/Freeze-drying	Human adipose-derived mesenchymal stem cells (hADMSCs)	Tziveleka et al., 2020
Alginate/Gelatin (Alg/Gel) scaffolds	3D bioprinting	hMSCs	Zhang et al., 2020
Polycaprolactone/Calcium-polyphosphate (PCL/Ca-polyP) microspheres		Human osteoblast-like cells (SAOS-2)	Neufurth et al., 2017
Alginate/Gelatin (Alg/Gel) scaffolds coated with graphene oxide (GO)		hADSCs	Li et al., 2020
Polycaprolactone/Poly(L-lactic acid)/Hyaluronic Acid (PLA/PCL/HA) scaffolds	Casting	Human osteocarcinoma cell line (MG63)	Hassanajili et al., 2019
Gelatin Methacrylate (GelMA)-VEGF hydrogels		MSCs	Byambaa et al., 2017
Keratin sponges		Human osteoblast-like cells (SAOS-2)	Bloise et al., 2020
Poly(L-lactic acid)/Dimethyl sulphoxide (PCL/DMSO) scaffolds		Human bone marrow stromal cells (hBMSCs)	Seok et al., 2020

(Continued)



TABLE 1 | Continued

Material(s) and format	Fabrication method	Cell source	References
Poly(L-lactic acid) (PCL), Poly(L-lactic acid)/Silicate-containing hydroxyapatite (PCL-siHA) scaffolds	Electrospinning	hMSCs	Shkarina et al., 2018
Poly(3,4- ethylene dioxythiophene)/Collagen (PEDOT/COLL) scaffolds	Freeze-drying	Neural crest stem cells (NCSCs)	landolo et al., 2020
Polypyrrole crosslinked (PPY/XCS) scaffolds		hADMSCs /HUVECs	Zhang et al., 2018
Tricalcium phosphate/Alginic acid/Graphene Oxide (TCP/AA/GO) scaffolds	Polymerization/3D bioprinting	Human osteoblast cells (hOB)	Boga et al., 2018
Magnesium- $\beta$ -Tricalcium Phosphate Composite (Mg-TCP) scaffolds	Gelation/ 3D bioprinting	hMSCs, HUVECs	Gu et al., 2019
 <b>Liver biomimetic cultures</b>			
Collagen gels	Gelation	Human hepatocarcinoma cells (HepG2)	Yip and Cho, 2013
Glycyrrhizin /Alginate/Calcium (GL/Alg/Ca) hydrogels	Gelation/Freeze-drying		Tong et al., 2018
Chitosan/Gelatin (CS/Gel) scaffolds			Zhang et al., 2016c
Decellularized extracellular matrix (dECM)based hydrogels	Bioprinting/Gelation/ Freeze-drying		Gong et al., 2014
Gelatin Methacrylate (GelMA) hydrogels	3D bioprinting		Ma et al., 2018
		Human hepatocarcinoma cells (HepG2/C3A)- HUVECs	Massa et al., 2017
Gelatin Methacrylate/Decellularized extracellular matrix (GelMa/dECM) bioinks		Human induced hepatocytes (hiHep)	Mao et al., 2020
Collagen/Hyaluronic Acid (COL/HA) bioinks		Activated hepatic stellate cells (aHSC)	Mazzocchi et al., 2019
Poly(L-lactide-co-glycolide)/Collagen I (PLGA/COL I) nanofibrous scaffolds	Electrospinning	Primary human hepatocytes	Brown et al., 2018
Poly(ethylene glycol)/Alginate/Gelatin (PAG) cryogel matrices	Cryogelation	Human hepatocarcinoma (Huh-7), HepG2	Kumari et al., 2016
Inverted colloidal crystal (ICC) hydrogel scaffolds	UV photo-polymerization	Huh-7	Kim M. H. et al., 2016
Polycaprolactone (PCL) micro-scaffolds	Selective Laser Sintering	HepG2, HUVECs	Pang et al., 2020

Created with BioRender.com.

prevalence of collagen in human tissues, its excellent properties (e.g., low immunogenicity, biocompatibility, biodegradability, hydrophilicity, easy processing, good encapsulation response, etc.; Ahadian et al., 2018; Liu X. et al., 2019) and the advances in preparation and cross-linking methods to boost its physicochemical properties have enabled the fabrication of various types of collagen-based bioactive substrates (e.g., scaffolds, gels, fibers, and sponges; Uchino et al., 2009; Yip and Cho, 2013; Patel et al., 2019; Sorushanova et al., 2019; Ferro et al., 2020). Skin substitute studies, for instance, have extensively employed this natural material for wound healing purposes (Min et al., 2018), while collagen hydrogels have also been shown to effectively support and enhance the growth and survival of primary cortical neurons in a 3D mimetic environment (Evans et al., 2019).

Blends of natural materials with other biomolecules or synthetic polymers are also commonly used for the recapitulation of the tissue milieu, as a means to overcome drawbacks related with the poor mechanical properties of some natural polymers [e.g., collagen (Ullah et al., 2018), gelatin (Han et al., 2014)], the low solubility in water [e.g., keratin (Wang et al., 2016)], their limited biostability (Pedron et al., 2013; Ryan and O'Brien, 2015), as well as source availability, and their uncontrollable biodegradation (Pradhan et al., 2020). In fact, such blends allow for enhancement of the mechanical properties and for better control over the biochemical properties of the engineered substrates according to the requirements of the tissue under development. For example, addition of elastin to porous collagen scaffolds was shown to reduce stiffness and enhance viscoelasticity, while inducing a more contractile-like smooth muscle cell phenotype (Ryan and O'Brien, 2015). Combination of collagen with HA was shown recently to yield a bioink/hydrogel suitable for 3D printing liver tissue constructs containing primary human hepatocytes and liver stellate cells, that were viable and functional for over 2 weeks and able to respond to drugs (Mazzocchi et al., 2019). In addition, PLGA nanofibrous scaffolds treated with type I collagen or fibronectin, as the minimal essential ECM components of the liver microenvironment, were able to accommodate long-term *in vitro* support, maintenance, and function of primary human hepatocytes (Brown et al., 2018).

Another commonly used material is gelatin-polysaccharide composite hydrogels (Afewerki et al., 2019). The chemical similarities of gelatin to the native tissue ECM, its biocompatibility, low antigenicity, cost-effectiveness, and combination with polysaccharides have been shown to produce composite hydrogels with enhanced ECM biomimicry levels, increased mechanical resilience (Afewerki et al., 2019); hydrophilicity (Jansen et al., 2005); and antimicrobial and anti-inflammatory properties (Wang et al., 2007), thus highly promising materials for 3D cell culture and TE applications (Afewerki et al., 2019). This was exemplified by the study of Guan et al., who showed that porous gelatin-chitosan scaffolds, loaded with hyaluronic acid and heparan sulfate, offer a valuable option for neural tissue engineering as they form a suitable 3D microenvironment for the adhesion, growth and differentiation of neural stem and progenitor cells (Guan et al., 2013).

## Engineering Methods to Reconstitute Tissue Architecture *in vitro*

The choice of the most suitable biomaterial is coupled with the fabrication method, as this can also influence the final properties of the 3D matrix supporting the engineered tissue (Mabrouk et al., 2020). Various fabrication methods have been utilized so far, spanning from freeze-drying (Mabrouk et al., 2020) and physical/chemical cross-linking reactions (Hu et al., 2019), for scaffold and hydrogel preparation, respectively, to microscale technologies, such as soft-lithography for microfluidic channel fabrication (Khademhosseini et al., 2006).

Conventional scaffold fabrication approaches have relied on techniques such as freeze-drying (**Figure 4A**), solvent casting/particulate leaching (SCPL) (**Figure 4B**), melt molding and gas foaming with which different porosity levels can be achieved (Wang et al., 2006). Due to the simplicity of established protocols and the relatively low-cost and tunability of scaffold porosity and geometry, these techniques are the standard for fabricating scaffolds (Mabrouk et al., 2020). However, several drawbacks have been reported, including cases of low interconnectivity of the porous network, irregular pore sizes, use of organic solvents with possible toxic effects and lack of precise control over the overall mechanical properties (El-Kady et al., 2012; Hribar et al., 2014). In an attempt to overcome these limitations, several groups employed electrospinning (**Figure 4C**) to fabricate various 3D matrices from both natural or synthetic materials and blends, as this method has been shown to provide better control over the mechanical properties (e.g., porosity and tensile strength), the geometry and the micro- and nano-topography of the fibrous scaffolds (Cui et al., 2010). Htwe et al. (2015) fabricated electrospun polyethylene terephthalate (PET)-based nanofibrous scaffolds, with similar geometry to human lung extracellular matrix, to form 3D cultures of lung fibroblasts as a biologically relevant tool for the investigation of such cells in the pathogenesis of lung inflammation via activating the NF- $\kappa$ B signaling pathway (Htwe et al., 2015). In addition, electrospun PET-based 3D nanofibrous scaffolds, coated with collagen and mimicking the basement membrane structure, were shown to successfully support an *in vitro* model of the human intestinal barrier that exhibited superior performance as a drug-testing platform compared to conventional models (Patient et al., 2019).

Over the last few years, additive manufacturing (AD) approaches have also gained a lot of attention as an alternative fabrication route to organize cells in 3D due to their potential to provide precise spatiotemporal control over biophysical and biochemical cues necessary to reproduce a biomimetic microenvironment (Murr, 2016; Bose et al., 2020; Nikolaev et al., 2020; Sun et al., 2020). AD approaches include techniques such as three-dimensional printing (3DP) (**Figures 4D,E**), light-assisted bioprinting (Trautmann et al., 2018), fused deposition modeling (FDM), selective laser sintering (SLS), that, along with advances in biomaterials and bioinks, enable precise deposition of materials into custom shapes and patterns to replicate complex tissue architectures, not possible using conventional techniques, and with high control and reproducibility (Melchels et al., 2012;

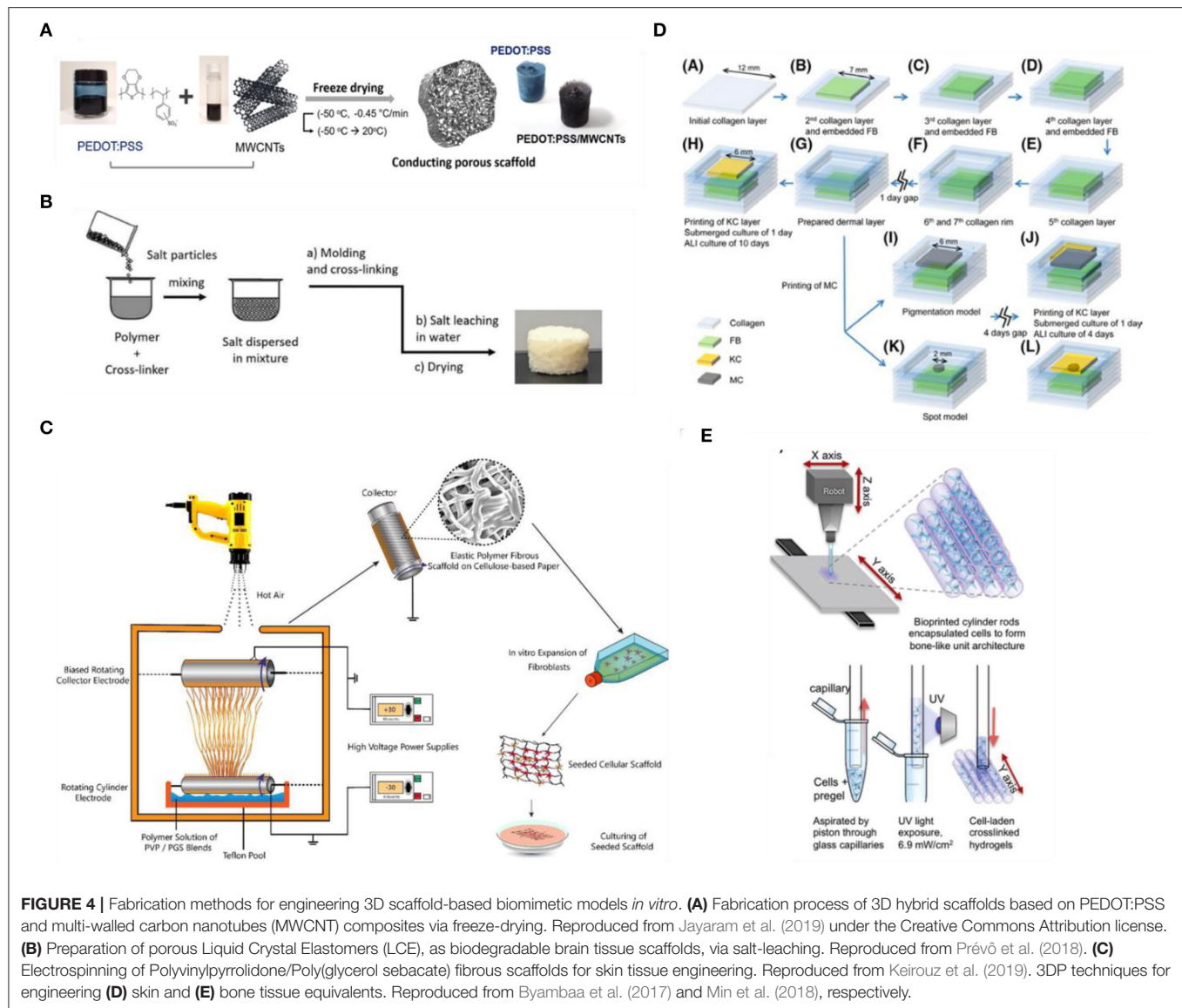


**FIGURE 4 |** Fabrication methods for engineering 3D scaffold-based biomimetic models *in vitro*. **(A)** Fabrication process of 3D hybrid scaffolds based on PEDOT:PSS and multi-walled carbon nanotubes (MWCNT) composites via freeze-drying. Reproduced from Jayaram et al. (2019) under the Creative Commons Attribution license. **(B)** Preparation of porous Liquid Crystal Elastomers (LCE), as biodegradable brain tissue scaffolds, via salt-leaching. Reproduced from Prévôt et al. (2018). **(C)** Electrospinning of Polyvinylpyrrolidone/Poly(glycerol sebacate) fibrous scaffolds for skin tissue engineering. Reproduced from Keirouz et al. (2019). 3DP techniques for engineering **(D)** skin and **(E)** bone tissue equivalents. Reproduced from Byambaa et al. (2017) and Min et al. (2018), respectively.

Cui et al., 2017). Moreover, AD approaches, and specifically 3DP techniques, based on coupling multimaterial printing with high performance bioinks (i.e., hydrogel solutions that act both as cell carriers, and structural components to control and direct cell activity and fate; Chimene et al., 2020) and biomolecules have been developed to obtain highly customisable, biofunctional, and mechanically compliant scaffolds (Chimene et al., 2016). The potential of bioprinting for building such biorelevant models is highlighted in various recent studies, seeking to develop highly biomimetic and functional tissues for disease modeling and drug testing (Kolesky et al., 2014; Horvath et al., 2015; Lee A. et al., 2019; Lee H. et al., 2019; Theodoridis et al., 2019; Daly et al., 2020). However, there are still challenges and limitations to be addressed before this novel approach is fully adopted by researchers. For example, not all biomaterials are compatible with AD fabrication methods for the recapitulation of some complex micro- and nano-features, while printing modules and

parameters, such as print speed, print pressure, and temperature as well as cell density in the bioink, can influence the cell-material dynamics during the printing process (Zhang and Wang, 2019). Nevertheless, as new methods for modulating biomaterial properties (e.g., new cross-linking mechanisms), along with advances in printing technologies—both software and hardware—are developed, we expect to see advances in the convergence of AD manufacturing and *in vitro* TE with the potential to leverage physicochemical cues and hence facilitate the development of more robust tissue equivalents.

Finally, a highly promising and popular method for building tissue equivalents, which has been favored by the emergence of the aforementioned AD manufacturing technology, is modular tissue engineering (Ouyang et al., 2020). Contrary to the top-down approach of the traditional TE paradigm, this bottom-up approach is based on fabricating living building blocks using cells (optionally together with biomolecules and/or biomaterials)

which are then assembled to create more biomimetic customized tissue models (Nichol and Khademhosseini, 2009; Ouyang et al., 2020). Various methods of building and assembling these modular tissue blocks are being explored, including 3DP/bioprinting (Graham et al., 2017; Liu T. et al., 2019; Subbiah et al., 2020), micropatterning (De Gregorio et al., 2018), microfabrication of cell-laden hydrogels (Onoe et al., 2013; Jeon et al., 2019; **Figure 4E**) and scaffolds (de Rutte et al., 2019), and self-assembly (Kato-Negishi et al., 2013; see Ouyang et al., 2020, for an extended review). Among other advantages, bottom-up tissue engineering approaches have gained a lot of attention because they offer a new means to generate vascularized tissues via modular assembly of pre-formed vascularized tissue blocks, a major challenge for tissue engineering at present (Nichol and Khademhosseini, 2009; Marga et al., 2012; Ouyang et al., 2020). In some cases, the versatility of these living tissue blocks allows not only for the modular assembly of vascularized tissues and organs (Homan et al., 2019), but also for the assembly of other complex tissue types (Miller et al., 2012; Magnan et al., 2020). It would be interesting to see if this strategy for vascularization of tissues could be also applied to promote innervation of biofabricated tissues and organs (Das et al., 2020).

## Engineering Methods to Recapitulate the Physicochemical Properties of the Native Niche

As discussed above, progress in materials science and engineering has enabled the development of functional/smart (bio)materials and platforms for TE applications by aiding the reconstruction and control of an environment that mimics key features of the natural niche. In the *in vivo* situation, cells have the capacity to generate, sense, integrate, and respond to systemic and local mechano-chemical cues and through interactions with neighboring cells and the surrounding ECM, they collectively generate tissues/organs with impressive structure and functionality (Brassard and Lutolf, 2019). Therefore, besides the appropriate source of cells and the materials with the appropriate physicochemical properties and microstructure, the exposure to biochemical and biophysical cues is of paramount importance for engineering tissues *in vitro* (Caddeo et al., 2017; Bao et al., 2018; Chen et al., 2019). Biophysical cues include bulk properties (e.g., viscoelasticity, stiffness, and porosity), as well as surface properties (e.g., roughness, guidance cues, charge, and wetting characteristics), while biochemical cues, besides the chemical structure, and composition of the materials, also refer to the presence of gradients of nutrients, signaling molecules, or even reprogramming factors, such as mRNA (Ledo et al., 2020a). In the following section, we discuss recent advances in reconstructing several niche properties and key aspects of the natural biochemical and mechanical signals, known to influence fundamental cellular processes, as well as methods of delivering such stimulants, to simulate the chemical signaling and biological pathways of the native environment and thus promote physiological cell growth and differentiation within the engineered tissue models.

## Chemical/Biochemical Stimuli

*In vivo*, cellular responses are influenced by various spatiotemporal biochemical signals (Caddeo et al., 2017; Park et al., 2019). Within tissues, concentration gradients for soluble components, nutrients, metabolites as well as oxygen and pH exist and are essential for exerting pressures that can stimulate or inhibit basic cellular processes (Przyborski, 2017). The proximity of vasculature and blood vessels, the diffusion of molecules through the surrounding ECM and the metabolic activity of the organ/tissue, which regulate oxygen tension, nutrient consumption and cellular waste secretion and removal, affect these natural gradients and in turn the maintenance of physiological levels of chemotaxis and homeostasis (Langhans, 2018).

Since most tissue-engineered constructs lack a vascular network, cells rely for their survival on diffusion of nutrients and oxygen through the construct (Rouwkema et al., 2009). Along with cell culture media, the engineered (bio-)materials and ECM components of the 3D tissue equivalent can act as a reservoir of such molecules, as well as for soluble components that can enhance, stimulate or inhibit specific cellular functions and guide cells toward the desired output (Caddeo et al., 2017; Afewerki et al., 2019). Essentially, cell culture media is a cocktail of molecules and compounds that range from basic nutrients necessary for cell growth to biochemical stimulants with more specialized role, depending on the needs of the cell line(s) in culture (**Table 2**). For example, glucose is widely used as the main source of energy for cell metabolism, while serum (e.g., fetal bovine serum) forms the basis of culture media as the cocktail of hormones, growth factors and protease inhibitors, supplemented with buffering systems, inorganic salts, amino acids and proteins/peptides that promote cell growth and viability, while also control pH and osmolality of the cell culture environment (Yang and Xiong, 2012; Carter and Shieh, 2015b; Salazar et al., 2016). A type of biomolecule in media formulations with more specialized role is growth factors (GFs). GFs are used as culture media additives due to their key role in multiple signaling pathways between cells and their environment as well as in fundamental cellular processes. For instance, bone morphogenetic proteins (BMPs) stimulate bone cell differentiation, vascular endothelial growth factors (VEGFs) stimulate blood vessel differentiation (angiogenesis), while GFs, such as epidermal growth factor (EGF), regulate a wide variety of functions in both epithelial and mesenchymal cells (De et al., 2013; Yao and Asayama, 2017). In addition to providing a biochemical link for enhancing cell communication (Gonçalves et al., 2013), addition of GFs in the cellular microenvironment is necessary for the reconstruction of the native tissue niche, where they are part of an extensive cross-talk between cell membrane receptors and ECM components (Brizzi et al., 2012). This is particularly important in the case of stem cells as well as for the derivation and maintenance of various types of organoids (Urbischek et al., 2019) the self-organization and maturation processes of which require a spatially homogeneous cocktail of specific growth factors (e.g., R-spondins and Noggin) and other signaling molecules (Brassard and Lutolf, 2019).



**TABLE 2 |** Common biomolecules in conventional cell culture media.

Types of biomolecules	Role	Example
Carbohydrates	Source of energy	Glucose Galactose
Amino acids	Protein synthesis, Secondary source of energy, Regulation of cell proliferation and density, Stimulation of growth and enhancement of cell viability	L-glutamine L-cysteine L-Lysine
Proteins and peptides	Binding of water, salts, free fatty acids, hormones, and vitamins Removal of toxic substances, Protection against proteolysis, Promotion of cell attachment	Albumin Transferrin Fibronectin Aprotinin
Growth factors	Cell signaling and communication, Mediation of processes such as proliferation, differentiation, wound healing, and tissue maturation	Bone morphogenetic proteins (BMPs) Vascular endothelial growth factors (VEGFs) Epidermal growth factor (EGF)
Cytokines	Cell Signaling and communication Stimulation of cells toward differentiation pathways Modeling hematoinmune response of tissues	Interleukins (IL) Tumor necrosis factor a (TNF-a)
Vitamins	Cell growth and proliferation Enzyme co-factors	Vitamin B group

Another class of biomolecules used to engineer the *in vitro* niche and mimic native signaling networks is cytokines. Apart from their modulatory role in the hematoinmune system, cytokines produced by a broad range of cells (e.g., lymphocytes, endothelial cells, and fibroblasts),—depending on the type and state of cell—, have also been found immobilized in the ECM, forming a complex functional network within the body, exerting systemic effects that go beyond their immunomodulatory role (Morán et al., 2013). Hence, they are now being employed to engineer the microenvironment of tissue equivalents, not only as agents that enrich the cell culture media, but also as components of the (bio)material blends used to support the 3D culture system. For example, in a perfusion-based bioreactor model of human bone marrow, addition of hematopoietic cytokines (i.e., thrombopoietin, stem cell factor, and Fms-related tyrosine kinase 3 ligand) significantly aided the establishment of a xeno-free environment that in turn favored the expansion of hematopoietic stem cells (Bourgine et al., 2018), while controlled release of BMP and VEGF blended in bone-mimetic substrates was shown to exert a synergistic effect on stimulation of osteoblasts (Bao et al., 2017). Finally, it is worth noting the efforts on substituting animal derived-sera with human (Muraglia et al., 2017; Heger et al., 2018) or synthetic serum (Ejiri et al., 2015; Patel et al., 2015), as these have been shown to better support cell growth and behavior in 3D without compromising the results (Heger et al., 2018). In addition, standardization of such sera formulations will facilitate the development of completely animal-free cell systems and tissue equivalents, better capturing the native biochemical environment of specific cell types (Ejiri et al., 2015).

### Physical/Biophysical Stimuli

Besides biochemical cues, each cell within the native tissue is subject to a unique mechanical environment defined

by gradients of intracellular and extracellular forces, the interactions with neighboring cells and the surrounding ECM (Caddeo et al., 2017; Brassard and Lutolf, 2019). Via mechanotransduction mechanisms, cells respond to these biophysical stresses and transduce the mechanical stimuli into biochemical signals, modifying their behavior (e.g., proliferation rate, shape, and migration). In addition, cells rearrange their cytoskeleton and cell membrane positioning and produce and exert endogenous contractile forces in the surrounding microenvironment, remodeling the ECM. This dynamic reciprocity of biophysical cues is constantly reshaping cells and the native niche structure and is associated with different cellular functions and tissue homeostasis (Xu et al., 2009; Humphrey et al., 2014; Kratochvil et al., 2019). Along with the physical properties and microarchitectural features of the tissue engineering materials, it has now been established that experimental platforms of tissue equivalents should acknowledge and incorporate the physiological biophysical variables to successfully imitate *in vitro* the dynamic interplay between cells and their exterior (Humphrey et al., 2014; Przyborski, 2017).

Over the last couple of decades, efforts are focusing on better understanding the effects of mechanical stimuli on cells and on addressing the challenges of reconstituting biophysical cues of physiological and diseased conditions *in vitro*. Of particular interest is the application of fluid shear stress that several tissues and cells within the body experience (Delon et al., 2019). For example, blood flow and pressure exert on endothelial cells one of the greatest forces within mammalian organisms (1–5 Pa) (Baeyens et al., 2016). In response to these forces, endothelial cells alter their morphology and orientation, which in turn regulates vessel physiology, function, and remodeling activity accordingly. In addition, endothelial cells transduce the frictional blood flow force into biochemical signals via specialized mechanisms

that shape the ability of the vascular system to effectively perfuse all tissues. Alterations in the nature of these forces or in the mechanotransduction mechanism have been shown to contribute to major vasculature diseases (Kamiya and Ando, 1996; Kadohama et al., 2007; Baeyens et al., 2016; Chistiakov et al., 2017). Epithelial cells also experience fluid shear stress (e.g., peristalsis in the intestine), which affects both their structure and function. Several *in vitro* studies have revealed the importance of this mechanical cue in the formation of microvilli in the apical surface of various epithelial cell types, including intestinal (Delon et al., 2019), lung (Stucki et al., 2018), and placental (Miura et al., 2015), highlighting the importance of incorporating such biophysical cues in bioengineering applications.

The effects of biophysical cues in advancing the relevance of *in vitro* cellular and tissue models has also been explored in the context of stimulating cells to enhance their functional and phenotypical characteristics or to trigger the differentiation of stem cells toward the desired lineage. Mechanical stretching has long been an attractive experimental strategy for controlling cell growth, gene expression, lineage commitment, and differentiation and thus successfully engineering mechanically functional tissues, such as cardiac, lung, vasculature, and bone (Diederichs et al., 2010; Riehl et al., 2012). For example, cyclic stretch was shown to enhance the viability and functional maturation of 3D cardiac tissue constructs based on human embryonic stem cell-derived cardiomyocytes seeded on gelatin-based scaffolds (Mihic et al., 2014). In another study, Fang et al. highlight the potential of mechanical stretch for enhancing stem cell behavior and regulating their fate. By applying cyclic stretch to human adipose-derived stem cells (hADSCs), the authors found that stretching significantly promoted the proliferation, adhesion, and migration of hADSCs, it suppressed apoptosis and adipogenesis, while it enhanced osteogenesis (Fang et al., 2019).

Besides mechanical cues, biophysical cues also involve electrical or magnetic fields, ultrasound stimulation and photostimulation (Ding et al., 2017; Chen et al., 2019). Due to the strong presence of bioelectricity (e.g., cell membrane potential, trans-epithelial potential found in all types of epithelial tissues) and its effects on *in vivo* systems, electrical stimulation has drawn a lot of attention for its potential benefits in tissue engineering (Balint et al., 2013; see McCaig et al., 2005, for an extended review on bioelectricity). Several *in vitro* studies have revealed the effects of electrical stimulation on various biological events both on cellular and tissue level, spanning from improved cellular migration and differentiation to enhanced wound healing and nerve regeneration (Vodovnik et al., 1992; Lluçà-Valldeperas et al., 2015; Snyder et al., 2017; Srirussamee et al., 2019). In the recent years, these effects have also been explored in 3D culture setups. For example, Kumar et al., studied the effect of external dynamic electric field as a guiding cue for osteoblasts seeded on 3D printed porous titanium alloy scaffolds. Their findings suggest that the presence of electric field, under dynamic conditions, had a positive effect on proliferation, growth, and expression level of prominent adhesion and cytoskeletal proteins, as well as on cell-cell interactions (Kumar et al., 2016; Iandolo et al., 2020). However, the emergence of electroactive polymers as a new class of smart materials has brought to the fore the potential of

combining materials suitable for TE with electrical stimulation. Early work on 2D cell culture assays based on polypyrrole, for example, has shown that such materials can support the growth, proliferation, and differentiation of mammalian cells (Zelikin et al., 2002) as well as stimulation of neurite outgrowth (Schmidt et al., 1997) or enhancement of osteogenic commitment of bone marrow stromal cells (Shastri et al., 1999) upon application of electrical fields. Moreover, carbon nanotubes (CNTs) have been shown to promote cardiomyocyte maturation (Martinelli et al., 2012) as well as to enhance the performance of engineered neurons and neural networks (Cellot et al., 2009; Fabbro et al., 2012), among other applications. Nowadays, it is well established that such materials can act both as substrates for cell attachment and tissue growth and as bioactive elements for regulating cellular activities within 3D tissue culture systems (Balint et al., 2013; Chen et al., 2019). The use of conducting materials in regulating stem cell function through electrical stimulation in 3D microenvironments was exemplified recently by co-culturing human adipose-derived MSCs (hADMSCs) and umbilical vein endothelial cells (HUVECs) in an electrically conducting polypyrrole/chitosan scaffold, demonstrating enhanced autocrine signaling, promoting the cellular functions of the co-culture system (Zhang et al., 2018). In another study, Zhu et al. developed carbon nanofibrous scaffolds with enhanced electrical conductivity and mechanical flexibility and demonstrated that sufficient support of stem cell-derived neuron-like cells, while application of biphasic electrical stimulation enhanced differentiation and maturation of these cells, as evidenced by the upregulation of the relevant neuronal biomarkers (Zhu et al., 2018). Finally, earlier this year, Iandolo et al. developed highly porous electroactive PEDOT:PSS and collagen type I composite scaffolds that supported neural crest-derived stem cell (NCSC) culture and osteogenic differentiation, without the need for scaffold pre-conditioning. The modulation of mechanical and electrical properties induced by collagen blending provided a new means for directing cell fate and response, as well as a tool for cell-based monitoring and stimulation applications (Iandolo et al., 2020).

### Spatiotemporal Delivery and Control of Biochemical and Biophysical Cues in Engineered Tissue Equivalents

As discussed in previous sections, advancements in fabrication technologies and material engineering have enabled the development of tissue engineering substrates that can present cells with the necessary cues to finely elicit a plethora of cellular functions and signaling mechanisms (Leijten et al., 2017). However, our understanding of cell-material interactions so far has been based mainly on static culture systems, while the *in vivo* array of biochemical and biophysical signals changes over space and time. Even though mimicking natural gradients in 3D culture platforms is possible, the thickness of the culture construct, as well as the competition of cells, can limit the diffusion of nutrients, oxygen, growth factors, and other signaling molecules and due to inhomogeneous distribution, cells located in the middle of the construct might not have access to sufficient supply of those molecules and thus behave differently from cells

that are closer to the engineered tissue surface (Levorson et al., 2011; Caddeo et al., 2017). In turn, this results in non-uniform cell proliferation and matrix deposition and in inhomogeneous tissue formation (Gholipourmalekabadi et al., 2016). Therefore, a lot of focus has now shifted to developing culture platforms that can dynamically recapitulate *in vitro* the native tissue spatio-temporal variation of signals. Such engineered platforms have the potential to facilitate better understanding and to provide more degrees of flexibility and control over cell function and fate and thus to eventually build tissues that better emulate the dynamics of the *in vivo* conditions (Leijten et al., 2017).

From the materials engineering point of view, even though numerous matrix-based techniques for delivering physicochemical cues, such as blending cell-adhesive ligands within scaffold materials (Gallagher et al., 2020) or micropatterning growth factors in hydrogels (Jeon et al., 2018), have been shown to improve cell behavior, this approach lacks the possibility to fine-tune and precisely control the timing of delivery, which is also important for cell survival and fate. In the case of MSCs, for instance, it has been shown that the RGD cell-adhesive motif is essential for stem cell survival at the early stages of 3D culture in PEG hydrogels, while removal of ligands at later stages does not compromise the viability of cells, but rather improves their differentiation (Kloxin et al., 2009). To overcome limitations in delivering natural cues in a spatiotemporal manner the development of dynamic biomaterials that allow for reversible modulation of the physicochemical properties and on-demand release of the desired molecules via either cell-mediated or user-mediated mechanisms, represents a promising strategy (Willerth et al., 2008; Leijten et al., 2017; Schneeberger et al., 2017; Cimmino et al., 2018; Kratochvil et al., 2019; Xu et al., 2020). A characteristic example where the delivery of physicochemical cues is mediated by cell activity is remodelable 3D hydrogels. Madl et al. showed recently that in elastin-like protein hydrogels, prior to chemically-induced differentiation, a critical amount of matrix remodeling is necessary to maintain the stemness and to enhance the differentiation capacity of neural progenitor cells into astrocytes and mature neurotransmitter-responsive neurons, via a mechanism regulated by cadherin cell-cell contacts and catenin-mediated activation of Yes-Associated Protein (YAP) expression (Madl et al., 2019). These findings highlight the potential of bioresponsive materials as attractive tissue engineering platforms that enable both expansion and subsequent differentiation of stem cells toward the desired tissue within a single cell culture setup. On the other hand, materials can be engineered to respond to user-directed stimuli as a means to fine-tune the presentation of spatiotemporal cues to cells and thus to direct and modulate interactions within the biological system (Cimmino et al., 2018). An example of this approach is the use of protease-cleavable peptides in 3D materials, as shown in a recent publication by Guo et al. The researchers, combining bio-orthogonal click chemistry and protein engineering, developed PEG-based multi-layered hydrogels with spatially-defined regions of immobilized proteins, where exogenous application of enzymes for triggering the temporal release and removal of select proteins was shown to be a promising tool for controlling cellular microenvironments (Guo et al., 2017).

Due to their spatiotemporal tunability, materials responsive to light, temperature or electrical fields have also been called for, to allow triggering of the release of ECM-presented cues from a 3D substrate to the cell culture microenvironment, thus directing advanced cellular fates within tissue engineering platforms (Wylie et al., 2011; Deforest and Tirrell, 2015; Cimmino et al., 2018; Ruskowitz and Deforest, 2018; Kratochvil et al., 2019; Shadish et al., 2019).

Sophisticated bioreactor systems can be used to fine-tune culture parameters and to reproduce an *in vitro* tissue-specific physiological microenvironment capable of overcoming diffusion limits and oxygenation for better control or even coupled delivery of chemical and mechanical cues (Levorson et al., 2011; Hansmann et al., 2013; Schmid et al., 2018). For example, a bioreactor system developed by Zohar et al. enabled the investigation of the direct flow-induced shear stress on vascularization of poly(L-lactic acid)/poly(lactic-co-glycolic acid) (PLLA/PLGA) scaffolds and showed that flow conditions enhance vascular network formation and maturation (Zohar et al., 2018). Charoensook et al. created a bioreactor-based functional *in vitro* model of the neuromuscular junction by cultivation of transdifferentiated myocytes and stem cell-derived motoneurons, where electrical stimulation resulted in improved maturation and function of motoneurons and myocytes, as well as exhibiting physiological response to drugs, thus suggesting its potential as a pharmacological screening platform and controlled studies of neuromuscular diseases (Charoensook et al., 2017). Furthermore, an all-in-one bioreactor approach facilitated the reconstruction and control of a more physiologically relevant 3D cardiac tissue microenvironment by combining, within a single chamber, electrical stimulation of the cardiac tissue, bidirectional interstitial fluid flow and on-line monitoring, and analysis of tissue functionality during culture (Visone et al., 2018).

One of the most promising technologies for bridging the gap between *in vitro* and *in vivo* systems is organs-on-chips (OOCs), alternatively called microphysiological *in vitro* models. OOCs technology has emerged from the combination of recent advances in microengineering and fluidic physics with trends in growing cells in 3D, allowing for the development of models that more faithfully recapitulate key features of specific human tissues and their interactions (Ramadan and Zourab, 2020). The design of the vast majority of OOC models are based on (micro-)fluidic devices, fabricated by soft-lithographic techniques, with continuously perfused chambers inhabited by living cells arranged in a biomimetic manner, while facilitating precise control over delivery of nutrients and spatiotemporal tuning of oxygen and pH gradients (Bein et al., 2018; Ronaldson-Bouchard and Vunjak-Novakovic, 2018). Among the added benefits of using such systems are the continuous supply of nutrients and removal of waste, the unparalleled, independent control over multiple key factors of the cell system, the possibility for *in situ*, high precision and automated monitoring and sample analysis, as well as the ability to interface different cellular compartments for enhanced cell cross-talk and exchange of signaling molecules and growth factors. But, what creates an enormous potential for enhancing the physiological relevance of the *in vitro* cell systems, spurring new, unforeseeable applications

of this technology, is the combination of a biomimetic niche with accurate, precise, and coupled delivery of more complex biochemical and biophysical cues (Bein et al., 2018; Ramadan and Zourob, 2020). Even though most of the attention OOCs have gained is focused on pharmacology and pre-clinical drug screening applications, as low-cost and animal-free alternative tool (Ramadan and Zourob, 2020), it is clear that the principle behind this technology lines perfectly with the TE paradigm and scope: convergence of cells with the advanced chip technology-biomaterials and delivery of physiologically relevant cues toward more robust tissue equivalents. As a result, various research groups around the world, both in the academic and industrial sectors, have developed a broad range of OOCs, mimicking the human gut (Ramadan and Jing, 2016; Kasendra et al., 2018; Shin et al., 2019), liver (Delalat et al., 2018; Jang et al., 2019), kidney (Jang et al., 2013; Chang et al., 2017; Yin et al., 2020), lung (Huh et al., 2012; Stucki et al., 2018; Felder et al., 2019), blood-brain barrier (Kilic et al., 2016; Wevers et al., 2018), bone (Marturano-Kruik et al., 2018), and vasculature (Schimek et al., 2013; Jeon et al., 2015) in both healthy and pathophysiological conditions, such as infection (Villenave et al., 2017; Ortega-Prieto et al., 2018) and cancer (Ayuso et al., 2016; Hassell et al., 2017; Hao et al., 2018; Carvalho et al., 2019), as well as for the interaction of multiple organs, as first showcased by Shuler et al. and more recently by others, toward multi-organ and whole-body microsystems (Miller and Shuler, 2016; Verneti et al., 2017; Edington et al., 2018; Herland et al., 2020), to study collective responses to drugs or disease inducing agents and inter-organ communication.

## APPLICATIONS OF 3D BIOMIMETIC CULTURES AND TISSUE EQUIVALENTS

### Modeling Human Health and Disease

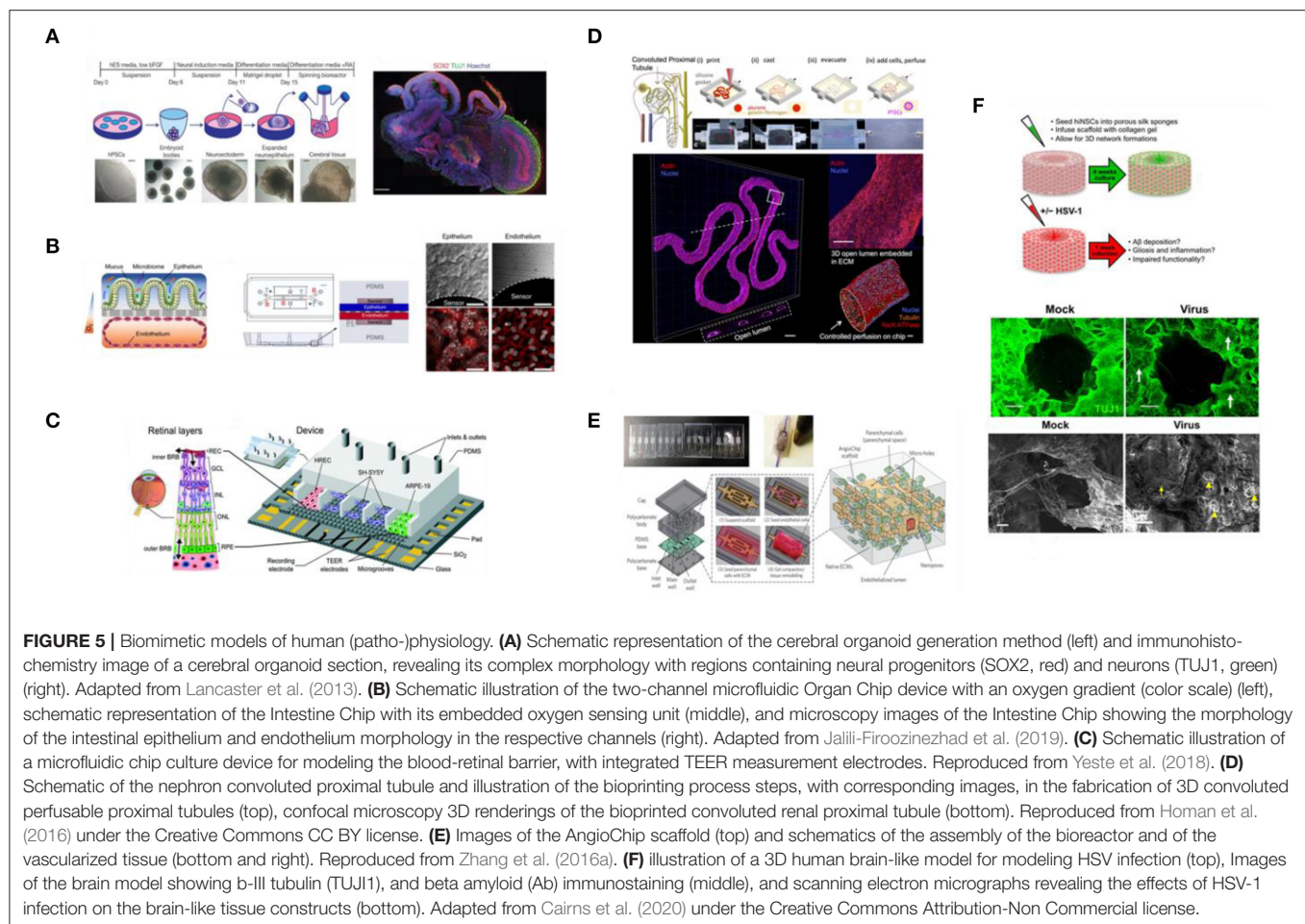
The transformation of the field toward more *in-vivo*-like human models is still ongoing, facilitated by the technological advancements in 3D cell platforms. Their deployment in early biomedical applications has already given prominence to the usefulness and validity of such models, leading to a paradigm shift in our understanding of human cell and tissue biology (Chen, 2016; Przyborski, 2017). Several studies over the past decades have showcased the powerful potential of 3D *in vitro* models in addressing questions specific to the human biology that are challenging, if not impossible, to answer with animal models and conventional biological assays. Additionally, increasing evidence suggests that such models are highly valuable for modeling pathophysiological conditions to study the disease onset and progression mechanisms, to identify pathogenic factors and potential therapeutics in the pre-clinical and clinical level (Chen, 2016).

As discussed earlier, the advent of human organoids as systems strikingly similar to the *in vivo* environment has provided researchers with the unique opportunity to recreate the human physiology and architecture *in vitro* (Kim et al., 2020). A study that laid the foundation for the use of organoids for biomedical applications, was the generation of cerebral organoids in 2013. Lancaster and Knoblich used hiPSCs to

establish an organoid culture system with various discrete, independent brain regions, including the cerebral cortex with progenitor populations, that give rise to mature and functional cortical neuron subtypes, recapitulating the formation of neural tissue in human brain development stages. In addition to this healthy brain tissue, they used patient-specific iPSCs and developed cerebral organoids that bore clear characteristics of the microcephaly neurodevelopmental disorder. This system helped them to address questions about the disease in a way that would not have been possible by growing neurons in flat surfaces or by engineering mouse models, due to lack of the necessary niche and interspecies differences, respectively (Lancaster et al., 2013; **Figure 5A**). Since then, organoids have played a prominent role in enhancing our understanding of various biological phenomena, including development and organogenesis (Karzbrun et al., 2018; Trisno et al., 2018; Vyas et al., 2018; Rossi et al., 2019; Shi et al., 2020), infectious biology (Forbester et al., 2015; Leslie et al., 2015; Karve et al., 2017; Heo et al., 2018; Lamers et al., 2020), cancer (Li et al., 2018; Nagle et al., 2018; Fusco et al., 2019; Ooft et al., 2019), and other diseases. Among others, the recent study by Sachs et al. on long-term expanding lung organoids clearly shows the versatility of these experimental tissue formats in faithfully recapitulating the adult epithelial airway structure and function from both healthy individuals and from patients with cystic fibrosis, lung cancer, and viral infections (Sachs et al., 2019). Finally, the valuable contribution of organoids in disease modeling is also showcased by the great efforts to build novel biomedical resources where samples from minimal amounts of tissue biopsies are used to generate patient-derived organoids, stored for future research, known as living biobanks (Sachs et al., 2018; Yan et al., 2018; Kim et al., 2020; Nelson et al., 2020; Simpson et al., 2020). The potential of such biomedical resources for modeling disease and investigating therapeutic strategies, even at the personalized level, is nicely exemplified in a study published earlier this year that presents methods for generating and biobanking patient-derived glioblastoma organoids (GBOs) that recapitulate and preserve the cellular and mutational diversity of the corresponding glioblastomas, reflecting inter- and intra-tumoral heterogeneity, holding great promise as a precision medicine tool for diagnosis and treatment (Jacob et al., 2020).

In parallel, the growing body of literature over the past years reflects the tremendous effort and progress in bioengineering tissue equivalents that allow for interfacing with vasculature and enable more in-depth investigation of tissue structure, homeostasis and pathophysiology, as well as communication between tissues and their surroundings. As discussed in the previous sections, successful engineering of tissues *in vitro* requires careful consideration of the cell sources, the type of material and the fabrication method as well as of the integration of the relevant biophysical and biochemical cues, all of which highly depend on the native tissue structure and function and on the biological question to be addressed with the model. For example, the delineation of tissue compartments and the regulation of the passage of ions and solutes by epithelia and endothelia are of particular importance for the recreation of such barrier tissues. While early strategies, relied on permeable





supports to separate the apical and basal compartments of the barrier-forming monolayers (Lea, 2015; Pearce et al., 2018), microphysiological systems and OOC approaches are taking this concept a step further, by exploiting novel bioengineering techniques to create compartmentalized barrier models with a more biomimetic interface between endothelial and epithelial tissues, combined with delivery of essential environmental cues (Bein et al., 2018). The work of Huh et al. was among the first attempts to this end. The researchers created a “lung-on-a-chip” that models human lung function in both normal and disease states, by co-culturing microvascular endothelial cells (i.e., bottom, microvascular compartment) and alveolar epithelial cells (i.e., top, alveolar compartment) in parallel microchannels separated by a thin semipermeable membrane, that also enabled the establishment of an air-liquid interface environment, where cell culture medium was perfused via the microvascular channels while the alveolar channel was filled with air. Cyclic stretch of the tissue via application of vacuum to the side compartments of the parallel channels was shown to successfully mimic the breathing motion of the lung, while concurrent administration of the cytokine interleukin-2 (IL-2) to the microvascular channel was shown to compromise the barrier, reproducing the pulmonary leakage, which is a characteristic symptom of the pulmonary

oedema (Huh et al., 2012). Versions of human gut-on-a-chip were also developed with the same device, where the side vacuum chambers and the application of fluid flow were exploited to recreate the peristaltic motions, but were also shown to induce spontaneous formation of the characteristic intestinal villus-crypts structures (Kim and Ingber, 2013). More recently though, this system was modified to accommodate the development of a co-culture of mucus-producing human primary intestinal epithelium in the same compartment with stable communities of the human gut microbiota by applying a hypoxia gradient across the endothelium-epithelium interface, while simultaneously monitoring oxygen levels and intestinal barrier function (Jalili-Firoozinezhad et al., 2019; Figure 5B). In a different approach, Trietsch et al. developed their intestine-on-a-chip model in a membrane-free manner, where a functional intestinal barrier is formed in a lateral channel of a microfluidic chip, at the interface with an ECM gel that supports the basal side of the epithelium and facilitates access to the perfusion channel on the opposite side of the intestinal tubules (Trietsch et al., 2017). Another way to achieve compartmentalization and tissue-tissue interfaces within OOC systems, bypassing the use of membranes, was proposed by Yeste et al. who developed a microfluidic device where cells grow in parallel compartments that are highly interconnected via a grid

of microgrooves, facilitating heterotypic cell-cell contact, and paracrine signaling, while integration of electrodes allows for in-line monitoring of the cell barrier integrity in each compartment. The device successfully supported the generation, maintenance and monitoring of a blood-retinal-barrier model, based on the co-culture of primary retinal endothelial cells (HREC), a human neuroblastoma cell line (SH-SY5Y), and a human retinal pigment epithelial cell line (ARPE-19) (**Figure 5C**), highlighting the necessity of compartmentalization in enhancing the robustness of barrier models as well as the added benefits of integrating in-line monitoring units (Yeste et al., 2018). OOC technology has also significantly contributed in dissecting *in vitro* the mechanisms behind various (patho-)physiological mechanisms of the brain (Haring et al., 2017). Herland et al., for instance, were able to study human neurovascular function and inflammation in a 3D model of the human blood-brain barrier (BBB) within a microfluidic chip and to reveal the distinct contributions of astrocytes and pericytes to neuroinflammation (Herland et al., 2016). Kilic et al. proposed a brain-on-chip model suitable for studying the migration of human neural progenitors in response to chemotactic cues (Kilic et al., 2016), while Park et al., proposed a microfluidic device for the brain-like interstitial perfusion of neurospheroids and tested the toxicity of amyloid- $\beta$ , showcasing the validity of brain-on-chips in modeling and studying neurodegenerative diseases as well (Park et al., 2015).

Although OOC models have been shown to better capture the *in vivo* situation, compared to conventional 2D culture formats, often such models are quasi-3D, forming an intermediate stage between 2D and 3D cell culture microenvironments rather than truly biomimetic tissues. To overcome this limitation, OOC technologies are now going beyond 2D, utilizing gels and scaffolds as tissue growth templates, toward generating 3D tissue equivalents of high biomimicry (Terrell et al., 2020), as shown recently in reports on the fabrication of 3D convoluted, luminal tissue architectures (Massa et al., 2017; Manousiouthakis et al., 2019; Wang X. et al., 2020). For instance, 3D human renal proximal tubules were engineered via combined bioprinting with 3D cell culture and OOC principles. The tissue construct was housed in perfusable chips and embedded within an extracellular matrix that supported the active perfusion, growth, differentiation, and maintenance of the proximal tubule epithelium for over two months, during which the nephron-like tissue exhibited significantly enhanced epithelial morphology and functional properties (e.g., brush border, basement membrane protein deposition, basolateral interdigitations, enhanced cell height, megalin expression, and albumin uptake), as well as *in-vivo*-like response upon delivery of nephrotoxin and cyclosporine A (Homan et al., 2016; **Figure 5D**). Robust 3D vascular models that more faithfully capture the natural milieu have also been called for interfacing with different tissue equivalents (Morgan et al., 2013; Kolesky et al., 2016). In an attempt to overcome the challenges in the choice of material for vasculature engineering as well as to address the challenge of co-cultivating parenchymal cells with vasculature in 3D, Zhang et al. created the AngioChip. This is a stable biodegradable scaffold that consists of a perfusable 3D, branched, luminal microchannel

network with thin, flexible but yet mechanically compliant walls, lined by endothelial cells, and surrounded by a tunable matrix that supports the assembly of parenchymal cells. In addition, the walls feature nano-pores and micro-holes that were shown to enhance permeability, to facilitate efficient molecular exchange, intercellular crosstalk (**Figure 5E**), as well as extravasation of monocytes and endothelial cells upon biomolecular stimulation, as showcased via the successful vascularization of hepatic and cardiac tissues. The precise placement of endothelial and parenchymal cells, in a simple to operate format, the control of the initial architecture of the vasculature as well as the potential to fine-tune the vessel permeability to match the requirements of different organ models, highlight the AngioChip as a versatile tool for cultivating the vasculature in tissue engineering platforms (Zhang et al., 2016a). Progress in modeling the human brain has also been made with the emergence of *in vitro* TE technology. Researchers have long studied the multi-layered, hierarchical brain architecture and complex physiology, but recapitulating the entire brain *in vitro* still remains a huge challenge, in part because of this complexity but also due to the complications associated with the available technology (Lozano et al., 2015). Novel cell sources combined with new materials and technological platforms have yielded new tools for building functional brain-like tissues, pushing further the borders of our understanding of the human brain. This is also particularly important for neurodevelopmental and neurodegenerative studies where translation of findings to the clinic is hindered by interspecies differences (e.g., cognition), among other factors (Hackam and Redelmeier, 2006; Hartung, 2013). For instance, in a pioneering study Tang-Schomer et al. developed a 3D brain-like cortical tissue construct using primary cortical neurons in a silk fibroin/collagen gel composite scaffold as a support for the 3D axon connections, that was able to reproduce the compartmentalization of gray and white matter as well as the *in vivo* relevant biochemical and electrophysiological outcomes necessary for the assessment of both brain physiology and brain disorders (Tang-Schomer et al., 2014). Optimization of this silk-fibroin scaffolds, along with the development of a technique to generate expandable and rapidly differentiating human-induced neural stem cell (hiNSC) lines, has enabled this group to further advance their approach in building 3D brain tissue equivalents that allow for long term studies of neural tissue in various conditions, such as neurodegeneration, brain tumors and injury (Chwalek et al., 2015; Cairns et al., 2016; Cantley et al., 2018; Sood et al., 2019; Rouleau et al., 2020). A remarkable application of this system though was reported earlier this year where the implication of herpes simplex virus type I (HSV-1) as a causative agent of Alzheimer's Disease was investigated. The 3D bioengineered brain model was able to reproduce the herpes-induced AD pathophysiology, encompassing features of the *in vivo* physiological human disease, including A $\beta$  plaque formation, neuronal loss, reactive gliosis, neuroinflammation, and diminished neural network functionality, reflecting the great progress and the tremendous potential of 3D TE approaches to address the critical need in building robust and physiologically relevant 3D human tissues (Cairns et al., 2020; **Figure 5F**).

## Drug and Treatment Development

3D biomimetic systems technology facilitates not only elucidation of disease biology and deeper understanding of the onset and progression mechanisms, but also identification and screening of potential drug candidates and therapies. Implementation of these systems in various stages of drug discovery and development is considered as a powerful alternative for addressing the challenges associated with the poor predictive power of existing preclinical models that, more often than not, is responsible for the high attrition rates of clinical trials (Roth and Singer, 2014; Caddeo et al., 2017; Ronaldson-Bouchard and Vunjak-Novakovic, 2018). 3D biomimetic cultures in the format of spheroids, organoids, hydrogels and scaffolds that more closely capture the disease physiology have already demonstrated the validity of this technology for drug development, screening, and toxicology assays (Sobrinho et al., 2016; Wan et al., 2016; Villasante et al., 2017; Plummer et al., 2019; Han et al., 2020). However, OOCs in particular have gained a lot of attention for their potential to produce more predictive and accurate data by resolving the discrepancies in drug safety and efficacy observed between models currently used in preclinical and clinical stages of drug testing and hence accelerate the translational process (Haring et al., 2017; Low and Tagle, 2017; Ronaldson-Bouchard and Vunjak-Novakovic, 2018). The precise control of multicellular activities, the spatiotemporal distribution/delivery of relevant cues and the interface between different tissue types that OOCs offer has been exploited for the evaluation of novel anticancer therapies (Sontheimer-Phelps et al., 2019), among others (Ribas et al., 2016; Mittal et al., 2018). For example, Bai et al. demonstrated that a microfluidic platform, interfacing lung or bladder carcinoma aggregates with vessel-like structures, can serve as an *in vivo*-like surrogate for anti-invasive and anti-metastatic drug screening, revealing the role of signaling pathways involved in the drug action mechanism (Bai et al., 2015). More recently, a tumor-on-a-chip platform, where the efficiency and toxicity of gemcitabine-loaded nanoparticles on Matrigel-embedded human colon cancer cells in contact with a 3D vessel-like colonic endothelium was successfully evaluated, was proposed as a precision onco-nanomedicine tool (Carvalho et al., 2019; **Figure 6A**). Despite the fact that oxygenation, a highly important parameter for the cancer microenvironment, is not taken into account in terms of monitoring and evaluation, both studies reflect the important developments made toward more accurate and precise screening of cancer therapeutics utilizing OOCs.

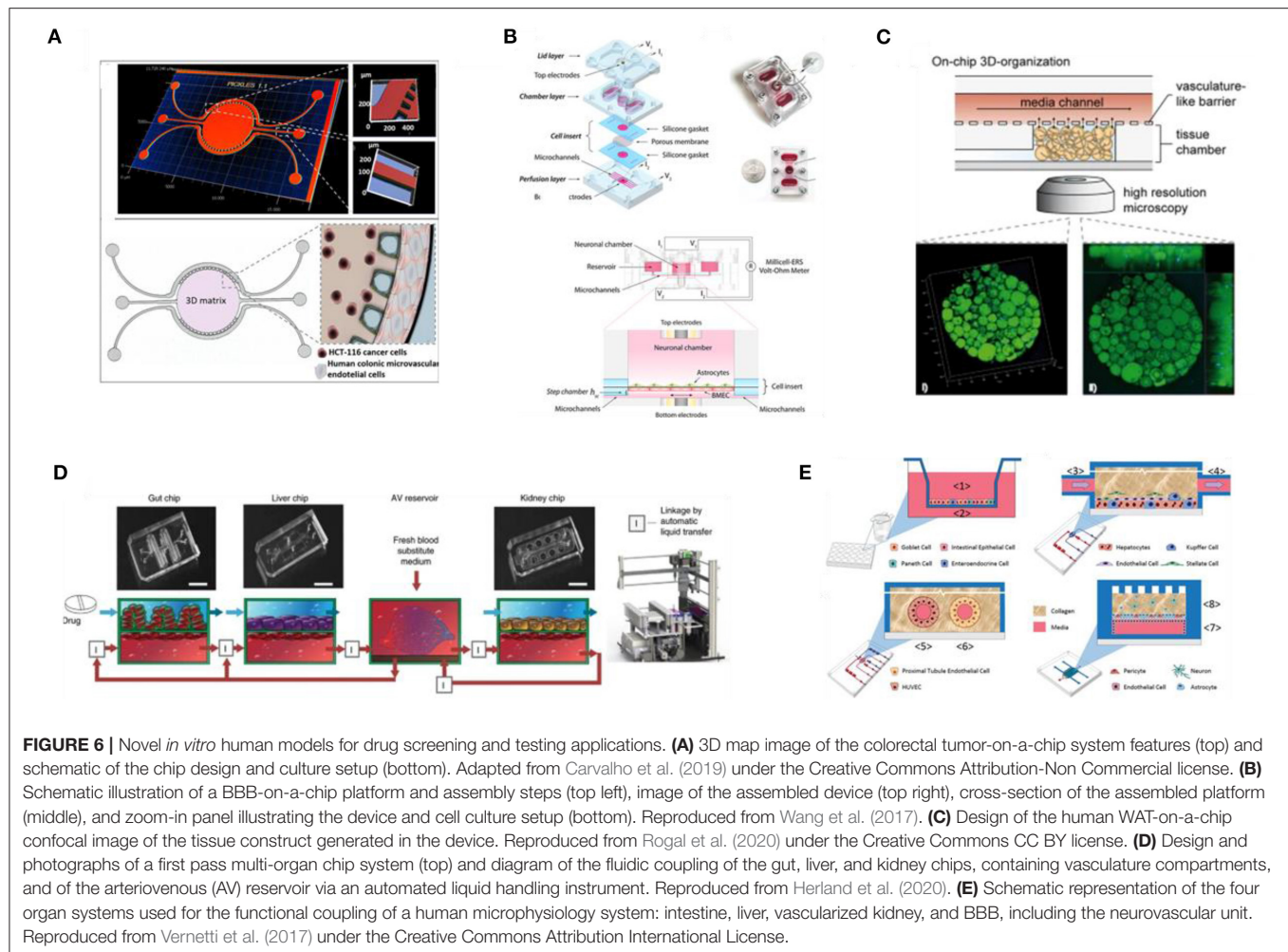
OOC platforms are also highly relevant for testing drug permeability and transport across the blood-brain-barrier (BBB). This distinctive tissue structure is made up of neurons, astrocytes, oligodendrocytes, microglia, smooth muscle cells, brain epithelial and endothelial cells, and pericytes embedded in the brain extra-cellular matrix (ECM), and bears the responsibility of maintaining brain homeostasis by supporting the neuronal activity and by tightly regulating the passage of metabolites, drugs, and other solutes from the peripheral blood into the central nervous system (Griep et al., 2013; Wang et al., 2017; Vatine et al., 2019). As OOC approaches

allow for better compartmentalization and efficient assembly of the corresponding cellular components and environmental cues, thus more realistic reconstitution of the native tissue (Booth and Kim, 2012; Adriani et al., 2017; Wang et al., 2017; Campisi et al., 2018; Vatine et al., 2019), their utility in modeling various features of the BBB and their implementation in preclinical drug evaluation studies has gained a lot of attention recently, particularly for testing whether a drug designed to treat neurological diseases can actually cross the BBB to reach its target (Ronaldson-Bouchard and Vunjak-Novakovic, 2018). This was showcased by Wang et al. who proposed the fabrication of a BBB-on-a-chip with integrated TEER sensors for *in situ* monitoring of the barrier tissue integrity (**Figure 6B**). Even though the authors utilized primary astrocytes derived from rats, in a co-culture with human iPSC-derived brain microvascular endothelial cells (BMECs), their BBB microfluidic chip was able to generate drug permeability data comparable with *in vivo* values (Wang et al., 2017). In a different application, a compartmentalized, multilayer OOC device was shown to successfully maintain and monitor functional human white adipose tissue and fatty acid metabolism while also being applicable for testing tissue responsiveness to therapeutic compounds, useful for diabetes, and obesity studies (Rogal et al., 2020; **Figure 6C**).

Ultimately, what renders 3D biomimetic tissues and particularly OOCs even more attractive alternatives for drug and therapy development is their ability to be linked via their endothelium/vascular channel, in a way that mimics the drug distribution within the body, toward multi-organ systems for simulating pharmacokinetic and pharmacodynamic drug responses (Prantil-Baun et al., 2018; Ronaldson-Bouchard and Vunjak-Novakovic, 2018). This possibility has been recently explored by various studies, where different tissues were fluidically coupled to model the *in-vivo*-like organ interactions (Zhang et al., 2009; Maschmeyer et al., 2015a,b; Tsamandouras et al., 2017). A very recent characteristic example of such a multi-organ system was reported earlier this year, comprising organ-on-chip models of the gut, liver and kidney. The models were linked by their endothelium-lined channels through a robotic system circulating a common blood substitute that represents the systemic circulation, stored in a fluid-mixer reservoir that represents the arteriovenous (**Figure 6D**). The system was then used to model first-pass absorption, distribution, metabolism, excretion and toxicity of nicotine and cis-platin and quantitatively predict pharmacodynamics, and pharmacokinetic parameters, with results matching clinical data (Herland et al., 2020). In the same concept, Verneti et al. coupled human MPS models representing the major absorption, metabolism and clearance organs (the jejunum, liver, and kidney) along with skeletal muscle and neurovascular models and evaluated the organ-specific processing, pharmacokinetic, and toxicity of terfenadine, trimethylamine (TMA)—as a potentially toxic microbiome metabolite—and vitamin D3. Their findings were consistent with clinical data, while they also discovered that trimethylamine-N-oxide (TMAO) can pass through the BBB (Verneti et al., 2017; **Figure 6E**).

Without a doubt, this technology has the potential to transform drug discovery and development. However, there





are still several challenges that should be addressed before the field realizes its tremendous potential. For example, with a few exceptions, most scaffold/hydrogel-based 3D models and OOCs primarily utilize cell lines, which in some cases may drift from the normal genotypic and phenotypic profile of the tissue of origin (Carter and Shieh, 2015a). Populating next-generation models with more relevant cells, such as iPSCs and organoid-derived patient specific cells can help overcome this limitation and better capture the tissue phenotype and thus to better mimic drug responses. This should be in line with the biological question the model is trying to address, recapitulating the specific features of the pathophysiology of interest. In addition, current OOC and MPS systems are fabricated predominantly with polydimethylsiloxane (PDMS), due to its ease-of-use, elasticity, optical transparency, and low-cost microfabrication. But issues related to the absorption of small hydrophobic molecules by this material severely compromise the validity of such systems in drug screening studies, pushing for transition to alternative, non-absorptive materials (Campbell et al., 2020). Also, 3D tissue equivalents and OOCs, as more sophisticated and multi-parametric models, require close control and synchronism of these different parameters to achieve the necessary functionality,

particularly when long-term viability is the case (Sontheimer-Phelps et al., 2019). Moreover, in multi-organ systems, besides *in-vivo*-like sequential coupling of each counterpart, scaling must also be taken into account, to match flow volume and rate with cultured tissue mass in order to mimic the native conditions and to achieve the required level to support functionality (Wikswow et al., 2013; Bhatia and Ingber, 2014; Ronaldson-Bouchard and Vunjak-Novakovic, 2018; Ramadan and Zourob, 2020). Finally, for this technology to live up to its potential and to be successfully implemented in the drug development process, it is necessary to move from the proof-of-concept laboratory models toward more widely available prototypes to facilitate high-throughput screening and further validation that the models effectively mimic *in vivo* drug responses. Since OOCs is a multidisciplinary field, the overall progress of this technology and its implementation in drug development, among other applications, heavily relies on parallel advancements in the field of cell biology, materials, microengineering, and microfluidics. Toward this direction, the introduction of commercially available systems is already taking place, promoting the production of more automated, user-friendly OOCs, and will definitely help resolve current limitations (Zhang and Radisic, 2017).



Nevertheless, to more efficiently employ this technology, more deep understanding of cell-material and cell-cell interactions and functions, as well as better understanding of the effects of biochemical and biophysical stimuli on the overall tissue structure and function is required.

## Sensing and Monitoring

As discussed during the previous sections, novel technologies for 3D TE *in vitro* offer unprecedented control over various parameters for the development and maintenance of the tissue equivalent of interest. In addition to fine-tuning the biological system parameters, this technology allows for the integration of in-line sensors that report not only on system parameters (e.g., flow rate, O<sub>2</sub> levels, and pH), but also provide feedback on cellular activity, thus facilitating the study of a broad range of physiological phenomena (Bhatia and Ingber, 2014). Despite their inherent limitations, the majority of current approaches rely heavily on optical transducers, such as fluorescence microscopy, which is more a qualitative assay, that requires labeling (Kim S. et al., 2016; Sobrino et al., 2016), combined with downstream analysis of effluents to detect changes in gene expression and metabolite production (Curto et al., 2017; Roh et al., 2019). The use of invasive probes and the terminal nature of these assays, which sometimes requires harsh and lengthy protocols for sample preparation prior to imaging and analyzing, can be bypassed by advanced imaging techniques. For example, Raman spectroscopy has emerged as a suitable tool for non-invasive, *in situ* quality control of cells and substrates, as well as for real-time monitoring of physiologically relevant metabolites (Pudlas et al., 2011; Zbinden et al., 2020). Two-photon excitation microscopy is also being employed now as an alternative to confocal microscopy for 3D and deep tissue imaging, obviating the need for sectioning of 3D tissue-engineered constructs that sometimes can compromise the sample quality (Gioiella et al., 2016; Hume et al., 2018).

Besides new imaging assays, electrical transducers have been also shown to provide a wealth of real-time information through non-invasive and dynamic interfacing with biological systems (Rivnay et al., 2018). A well-established tool for rapid monitoring of cells *in vitro*, especially for drug toxicology studies, is Electrochemical Impedance Spectroscopy (EIS), with which it is possible to obtain information about cell adhesion, proliferation, and differentiation over time. In fact, EIS is widely used for monitoring Transepithelial/Transendothelial Electrical Resistance (TEER), a commonly used parameter to quantitatively characterize the function and integrity of tissue barriers with fast, non-invasive measurements (Benson et al., 2013; De León et al., 2020). van der Helm et al. recently developed an intestinal OOC with integrated electrodes that allowed for transepithelial barrier function and tissue differentiation monitoring via impedance spectroscopy, while combination with electrical simulation showed that this method can be adapted within any organ-on-chip to better monitor cell activity and to also enable comparisons between different platforms (van der Helm et al., 2019; **Figure 7A**). Integration of electrical transducers has also been reported recently in 3D biomimetic cultures (Pas et al., 2017; Zhang et al., 2017; Curto et al., 2018;

Jahnke et al., 2019; Li et al., 2019). Kalmykov et al., for example, developed an “organ-on-e-chip” where they interfaced human cardiac spheroids with 3D self-roll biosensor arrays, which operated either as microelectrodes for EIS monitoring or as field-effect transistors, enabling acquisition of continuous multiplex recordings that allowed for real-time monitoring of cardiac tissue maturation (Kalmykov et al., 2019; **Figure 7B**). A high-density multi-electrode array was also proposed for real-time and automated impedimetric monitoring of cell migration out of human breast microtumours (Jahnke et al., 2019; **Figure 7C**). Despite the great progress made, most of these models fail to achieve intimate electrode-cell coupling which is necessary to accurately record a signal, since they utilize electrodes that are designed for planar culture of cells and are thus ill-adapted for monitoring complex 3D tissues (Inal et al., 2017; Jahnke et al., 2019). To overcome this limitation, conducting polymer scaffolds can be used instead, as evidenced recently by their remarkable performance as tissue building blocks (Wan et al., 2015; Guex et al., 2017; Iandolo et al., 2020). However, what makes these materials more attractive as TE substrates is that in addition to more seamless integration with complex cell cultures, they also allow for more intimate cell-electrode coupling, necessary for accurate signal transduction, and hence more effective monitoring of cell status and tissue formation (Inal et al., 2017; del Agua et al., 2018; Jayaram et al., 2019). We recently explored the potential of these materials for *in vitro* TE applications and organ-on-chip platforms. In particular, we fabricated tubular 3D macroporous electroactive scaffolds, based on the conducting polymer poly(3,4-ethylenedioxythiophene) doped with poly(styrene sulfonate) (PEDOT:PSS), the electrical, mechanical and biochemical properties of which we were able to fine-tune. We then integrated these tubular PEDOT:PSS scaffolds into a transistor configuration (i.e., transistor in a tube: Tubistor) and showed proof of principle for continuous monitoring of a simple 3D co-culture of mammalian cells over a period of 4 days. The real-time electrical readouts, cross-validated with optical analysis, enabled us to closely monitor cellular activity and even distinguish between cell adhesion and barrier tissue formation in a non-destructive, label-free manner, highlighting the added benefits of integrating in-line sensing components within engineered tissues for building more robust and sophisticated TE models (Pitsalidis et al., 2018; **Figure 7D**).

## CONCLUSIONS AND OUTLOOK

The implementation of TE concepts and methods into biomimetic tissue models, originally directed at regenerative medicine applications, is an accelerating trend. As summarized here, 3D *in vitro* models of various human tissues and organs have been successfully developed, thanks to the synergistic progress and advances in all disciplines that converge to give rise to more sophisticated tissue and disease models with enhanced structural and functional accuracy. Although many challenges are yet to be resolved, the advent of hiPSCs and organoids has, without a doubt, provided bioengineers with unlimited sources of tissue-specific cells, genetic engineering of which

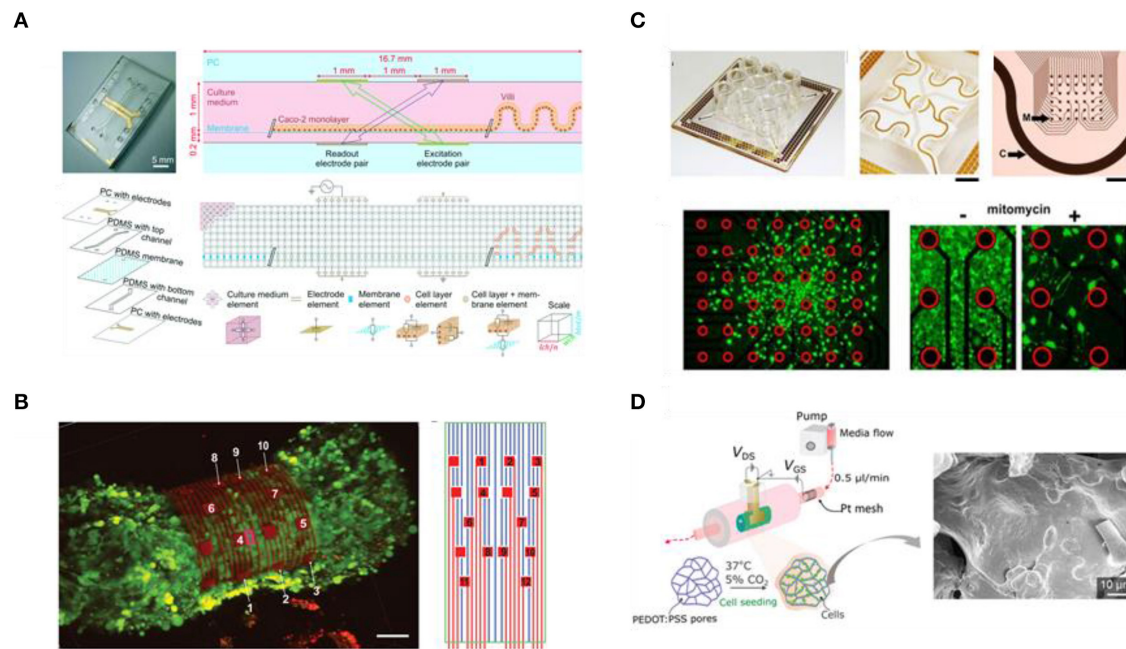


**FIGURE 7 |** Biomimetic *in vitro* models of human tissues with integrated sensing and monitoring units. **(A)** Design and operation principles of a gut-on-chip device, along with the equivalent electrical circuit used for impedance monitoring of the intestinal barrier and the corresponding simulations. Reproduced from van der Helm et al. (2019) under the Creative Commons Attribution-Non Commercial License. **(B)** A 3D confocal microscopy image of 3D cardiac spheroid labeled with  $\text{Ca}^{2+}$  indicator dye (Fluo-4, green fluorescence) encapsulated by a self-roll biosensor array for electrical recordings; organ-on-a-chip (left) and 2D map of the microelectrodes of the biosensor array (right). Reproduced from Kalmykov et al. (2019) under the Creative Commons Attribution-Non Commercial license. **(C)** Image and design of a novel multi-well high-dense microelectrode array for cell migration studies (top), cell migration pattern for mitomycin C treated human breast cancer cells on the microelectrode array (bottom left), and comparative magnification to mitomycin C untreated cells (red circles mark electrodes) (bottom right). Adapted from Jahnke et al. (2019) under the Creative Commons Attribution International License. **(D)** Schematic representation of the setup of a 3D transistor in a tube (Tubistor), based on electroactive scaffolds (left), for hosting and concurrently monitoring 3D cell cultures. Reproduced from Pitsalidis et al. (2018) under the Creative Commons Attribution-Non Commercial license.

enables further modifications (e.g., insert/delete mutations in healthy/diseased cells) to guide phenotypic behaviors. This provides an excellent opportunity for transforming drug development routes by accelerating the process, and generating data more accurate and relevant to human systems. In addition, the use of patient-specific cells facilitates studies of rare diseases, as well as precision and personalized medicine approaches for the development of drugs and therapies optimized for specific patient biology. Smart biomaterials have now been designed to more faithfully recapitulate the chemical, mechanical and topographical properties of the complex human tissues and their microenvironment. Advanced fabrication methods have additionally enabled arrangement of tissue counterparts and environmental cues with unprecedented control and accuracy. These features have combined to generate complex biological structures of high fidelity, matching the *in vivo* situation. A key challenge remains however: monitoring and characterization of such models still relies predominantly on end-point, invasive assays, delaying the validation of results, particularly for drug screening, and toxicology studies. Integration of electrical components in tissue engineering platforms can help resolve this limitation. Such tools enable dynamic, non-invasive and continuous monitoring of cells, offering rapid insight into different biological events

within these systems. Standardization of components such as media formulation is a non-trivial additional challenge, for maintaining the survival and function of multiple cell types, which combined with spatiotemporal delivery of tissue-specific and application-specific (i.e., homeostatic or pathophysiological conditions) environmental cues, offer a novel means for dynamically controlling and directing tissue generation and maturation *in vitro*. Without a doubt *in vitro* tissue engineered systems have shown great promise for revolutionizing many aspects of biomedical research. As more sophisticated and human relevant *in vitro* models appear in literature, in parallel with commercialization of platforms for hosting such models, we expect to see a paradigm shift in our understanding of human biology as well as in disease diagnosis and treatment.

## AUTHOR CONTRIBUTIONS

C-MM and CB wrote the text and prepared the figures. RMO wrote the text and edited the manuscript and secured the funding. All authors contributed to the article and approved the submitted version.

## FUNDING

The authors wish to acknowledge funding from the European Research Council (ERC) under the European Union's Horizon 2020 research and innovation programme (grant agreement

no. 723951 to RO, C-MM, and CB). The authors also wish to acknowledge funding by the Engineering and Physical Sciences Research Council Centre for Doctoral Training in Sensor Technologies and Applications (EP/L015889/1 to CB).

## REFERENCES

- Abagnale, G., Steger, M., Nguyen, V. H., Hersch, N., Sechi, A., Jousen, S., et al. (2015). Surface topography enhances differentiation of mesenchymal stem cells towards osteogenic and adipogenic lineages. *Biomaterials* 61, 316–326. doi: 10.1016/j.biomaterials.2015.05.030
- Abbott, A. (2003). Biology's new dimension. *Nature* 424, 870–872. doi: 10.1038/424870a
- Adadi, N., Yadi, M., Gal, I., Asulin, M., Feiner, R., Edri, R., et al. (2020). Electrospun fibrous PVDF-TrFe scaffolds for cardiac tissue engineering, differentiation, and maturation. *Adv. Mater. Technol.* 5:1900820. doi: 10.1002/admt.201900820
- Adriani, G., Ma, D., Pavesi, A., Kamm, R. D., and Goh, E. L. K. (2017). A 3D neurovascular microfluidic model consisting of neurons, astrocytes and cerebral endothelial cells as a blood-brain barrier. *Lab Chip* 17, 448–459. doi: 10.1039/C6LC00638H
- Afewerki, S., Sheikhi, A., Kannan, S., Ahadian, S., and Khademhosseini, A. (2019). Gelatin-polysaccharide composite scaffolds for 3D cell culture and tissue engineering: towards natural therapeutics. *Bioeng. Transl. Med.* 4, 96–115. doi: 10.1002/btm2.10124
- Ahadian, S., Civitarese, R., Bannerman, D., Mohammadi, M. H., Lu, R., Wang, E., et al. (2018). Organ-on-a-chip platforms: a convergence of advanced materials, cells, and microscale technologies. *Adv. Healthc. Mater.* 7:1700506. doi: 10.1002/adhm.201700506
- Avior, Y., Sagi, I., and Benvenisty, N. (2016). Pluripotent stem cells in disease modelling and drug discovery. *Nat. Rev. Mol. Cell Biol.* 17, 170–182. doi: 10.1038/nrm.2015.27
- Ayuso, J. M., Virumbrales-Muñoz, M., Lacueva, A., Lanuza, P. M., Checa-Chavarria, E., Botella, P., et al. (2016). Development and characterization of a microfluidic model of the tumour microenvironment. *Sci. Rep.* 6:36086. doi: 10.1038/srep36086
- Baeyens, N., Bandyopadhyay, C., Coon, B. G., Yun, S., and Schwartz, M. A. (2016). Endothelial fluid shear stress sensing in vascular health and disease. *J. Clin. Invest.* 126, 821–828. doi: 10.1172/JCI183083
- Bai, J., Tu, T. Y., Kim, C., Thiery, J. P., and Kamm, R. D. (2015). Identification of drugs as single agents or in combination to prevent carcinoma dissemination in a microfluidic 3D environment. *Oncotarget* 6, 36603–36614. doi: 10.18632/oncotarget.5464
- Baker, B. M., and Chen, C. S. (2012). Deconstructing the third dimension-how 3D culture microenvironments alter cellular cues. *J. Cell Sci.* 125, 3015–3024. doi: 10.1242/jcs.079509
- Balint, R., Cassidy, N. J., and Cartmell, S. H. (2013). Electrical stimulation: a novel tool for tissue engineering. *Tissue Eng. Part B Rev.* 19, 48–57. doi: 10.1089/ten.teb.2012.0183
- Bao, M., Xie, J., and Huck, W. T. S. (2018). Recent advances in engineering the stem cell microniche in 3D. *Adv. Sci.* 5:1800448. doi: 10.1002/advs.201800448
- Bao, X., Zhu, L., Huang, X., Tang, D., He, D., Shi, J., et al. (2017). 3D biomimetic artificial bone scaffolds with dual-cytokines spatiotemporal delivery for large weight-bearing bone defect repair. *Sci. Rep.* 7:7814. doi: 10.1038/s41598-017-08412-0
- Bartfeld, S., Bayram, T., Van De Wetering, M., Huch, M., Begthel, H., Kujala, P., et al. (2015). *In vitro* expansion of human gastric epithelial stem cells and their responses to bacterial infection. *Gastroenterology* 148, 126.e6–136.e6. doi: 10.1053/j.gastro.2014.09.042
- Bein, A., Shin, W., Jalili-Firoozinezhad, S., Park, M. H., Sontheimer-Phelps, A., Tovaglieri, A., et al. (2018). Microfluidic organ-on-a-chip models of human intestine. *Cell. Mol. Gastroenterol. Hepatol.* 5, 659–668. doi: 10.1016/j.jcmgh.2017.12.010
- Benam, K. H., Dauth, S., Hassell, B., Herland, A., Jain, A., Jang, K.-J., et al. (2015). Engineered *in vitro* disease models. *Annu. Rev. Pathol. Mech. Dis.* 10, 195–262. doi: 10.1146/annurev-pathol-012414-040418
- Benson, K., Cramer, S., and Galla, H.-J. (2013). Impedance-based cell monitoring: barrier properties and beyond. *Fluids Barriers CNS* 10:5. doi: 10.1186/2045-8118-10-5
- Bhatia, S. N., and Ingber, D. E. (2014). Microfluidic organs-on-chips. *Nat. Biotechnol.* 32, 760–772. doi: 10.1038/nbt.2989
- Birgersdotter, A., Sandberg, R., and Ernberg, I. (2005). Gene expression perturbation *in vitro* - a growing case for three-dimensional (3D) culture systems. *Semin. Cancer Biol.* 15, 405–412. doi: 10.1016/j.semcancer.2005.06.009
- Bissell, M. J. (1981). The differentiated state of normal and malignant cells or how to define a “normal” cell in culture. *Int. Rev. Cytol.* 70, 27–100. doi: 10.1016/S0074-7696(08)61130-4
- Bissell, M. J. (2017). Goodbye flat biology – time for the 3rd and the 4th dimensions. *J. Cell Sci.* 130, 3–5. doi: 10.1242/jcs.200550
- Bissell, M. J., and Barcellos-Hoff, M. H. (1987). The influence of extracellular matrix on gene expression: is structure the message? *J. Cell Sci.* 1987, 327–343. doi: 10.1242/jcs.1987.supplement\_8.18
- Blaise, N., Patrucco, A., Bruni, G., Montagna, G., Caringella, R., Fassina, L., et al. (2020). *In vitro* production of calcified bone matrix onto wool keratin scaffolds via osteogenic factors and electromagnetic stimulus. *Materials* 13:3052. doi: 10.3390/ma13143052
- Boga, J. C., Miguel, S. P., de Melo-Diogo, D., Mendonça, A. G., Louro, R. O., and Correia, I. J. (2018). *In vitro* characterization of 3D printed scaffolds aimed at bone tissue regeneration. *Colloids Surfaces B Biointerfaces* 165, 207–218. doi: 10.1016/j.colsurfb.2018.02.038
- Booth, R., and Kim, H. (2012). Characterization of a microfluidic *in vitro* model of the blood-brain barrier (μBBB). *Lab Chip* 12, 1784–1792. doi: 10.1039/c2lc40094d
- Bose, S., Koski, C., and Vu, A. A. (2020). Additive manufacturing of natural biopolymers and composites for bone tissue engineering. *Mater. Horizons* 7, 2011–2027. doi: 10.1039/d0mh00277a
- Bourguin, P. E., Klein, T., Paczulla, A. M., Shimizu, T., Kunz, L., Kokkalis, K. D., et al. (2018). *In vitro* biomimetic engineering of a human hematopoietic niche with functional properties. *Proc. Natl. Acad. Sci. U.S.A.* 115, E5688–E5695. doi: 10.1073/pnas.1805440115
- Brassard, J. A., and Lutolf, M. P. (2019). Engineering stem cell self-organization to build better organoids. *Cell Stem Cell* 24, 860–876. doi: 10.1016/j.stem.2019.05.005
- Brizzi, M. F., Tarone, G., and Defilippi, P. (2012). Extracellular matrix, integrins, and growth factors as tailors of the stem cell niche. *Curr. Opin. Cell Biol.* 24, 645–651. doi: 10.1016/j.ceb.2012.07.001
- Brown, J. H., Das, P., DiVito, M. D., Ivancic, D., Tan, L. P., and Wertheim, J. A. (2018). Nanofibrous PLGA electrospun scaffolds modified with type I collagen influence hepatocyte function and support viability *in vitro*. *Acta Biomater.* 73, 217–227. doi: 10.1016/j.actbio.2018.02.009
- Byambaa, B., Annabi, N., Yue, K., Trujillo-de Santiago, G., Alvarez, M. M., Jia, W., et al. (2017). Bioprinted osteogenic and vasculogenic patterns for engineering 3D bone tissue. *Adv. Healthc. Mater.* 6:1700015. doi: 10.1002/adhm.201700015
- Caddeo, S., Boffito, M., and Sartori, S. (2017). Tissue engineering approaches in the design of healthy and pathological *in vitro* tissue models. *Front. Bioeng. Biotechnol.* 5:40. doi: 10.3389/fbioe.2017.00040
- Cairns, D. M., Chwalek, K., Moore, Y. E., Kelley, M. R., Abbott, R. D., Moss, S., et al. (2016). Expandable and rapidly differentiating human induced neural stem cell



- lines for multiple tissue engineering applications. *Stem Cell Rep.* 7, 557–570. doi: 10.1016/j.stemcr.2016.07.017
- Cairns, D. M., Rouleau, N., Parker, R. N., Walsh, K. G., Gehrke, L., and Kaplan, D. L. (2020). A 3D human brain-like tissue model of herpes-induced Alzheimer's disease. *Sci. Adv.* 6:eay8828. doi: 10.1126/sciadv.aay8828
- Campbell, S. B., Wu, Q., Yazbeck, J., Liu, C., Okhovatian, S., and Radisic, M. (2020). Beyond polydimethylsiloxane: alternative materials for fabrication of organ-on-a-chip devices and microphysiological systems. *ACS Biomater. Sci. Eng.* doi: 10.1021/acsbomaterials.0c00640
- Campisi, M., Shin, Y., Osaki, T., Hajal, C., Chiono, V., and Kamm, R. D. (2018). 3D self-organized microvascular model of the human blood-brain barrier with endothelial cells, pericytes and astrocytes. *Biomaterials* 180, 117–129. doi: 10.1016/j.biomaterials.2018.07.014
- Cantley, W. L., Du, C., Lomoio, S., Depalma, T., Peirent, E., Kleinknecht, D., et al. (2018). Functional and sustainable 3D human neural network models from pluripotent stem cells. *ACS Biomater. Sci. Eng.* 4, 4278–4288. doi: 10.1021/acsbomaterials.8b00622
- Cao, X., Ban, E., Baker, B. M., Lin, Y., Burdick, J. A., Chen, C. S., et al. (2017). Multiscale model predicts increasing focal adhesion size with decreasing stiffness in fibrous matrices. *Proc. Natl. Acad. Sci. U.S.A.* 114, E4549–E4555. doi: 10.1073/pnas.1620486114
- Carlson, A. L., Bennett, N. K., Francis, N. L., Halikere, A., Clarke, S., Moore, J. C., et al. (2016). Generation and transplantation of reprogrammed human neurons in the brain using 3D microtopographic scaffolds. *Nat. Commun.* 7:10862. doi: 10.1038/ncomms10862
- Carter, M., and Shieh, J. (2015a). *Guide to Research Techniques in Neuroscience*. Elsevier. Available online at: [https://zu.edu.jo/UploadFile/Library/E\\_Books/Files/LibraryFile\\_91258\\_7.pdf](https://zu.edu.jo/UploadFile/Library/E_Books/Files/LibraryFile_91258_7.pdf)
- Carter, M., and Shieh, J. (eds.). (2015b). "Chapter 14 - cell culture techniques," in *Guide to Research Techniques in Neuroscience*, 2nd Edn (Academic Press), 295–310. doi: 10.1016/B978-0-12-800511-8.00014-9
- Carvalho, M. R., Barata, D., Teixeira, L. M., Giselbrecht, S., Reis, R. L., Oliveira, J. M., et al. (2019). Colorectal tumor-on-a-chip system: a 3D tool for precision onco-nanomedicine. *Sci. Adv.* 5:eaaw1317. doi: 10.1126/sciadv.aaw1317
- Castaño, A. G., García-Díaz, M., Torras, N., Altay, G., Comelles, J., and Martínez, E. (2019). Dynamic photopolymerization produces complex microstructures on hydrogels in a moldless approach to generate a 3D intestinal tissue model. *Biofabrication* 11:025007. doi: 10.1088/1758-5090/ab0478
- Cellot, G., Cilia, E., Cipollone, S., Rancic, V., Supcane, A., Giordani, S., et al. (2009). Carbon nanotubes might improve neuronal performance by favouring electrical shortcuts. *Nat. Nanotechnol.* 4, 126–133. doi: 10.1038/nnano.2008.374
- Cembran, A., Bruggeman, K. F., Williams, R. J., Parish, C. L., and Nisbet, D. R. (2020). Biomimetic materials and their utility in modeling the 3-dimensional neural environment. *iScience* 23:100788. doi: 10.1016/j.isci.2019.100788
- Chang, S. Y., Weber, E. J., Sidorenko, V. S., Chapron, A., Yeung, C. K., Gao, C., et al. (2017). Human liver-kidney model elucidates the mechanisms of aristolochic acid nephrotoxicity. *JCI Insight* 2:e95978. doi: 10.1172/jci.insight.95978
- Charoensook, S. N., Williams, D. J., Chakraborty, S., Leong, K. W., and Vunjak-Novakovic, G. (2017). Bioreactor model of neuromuscular junction with electrical stimulation for pharmacological potency testing. *Integr. Biol.* 9, 956–967. doi: 10.1039/c7ib00144d
- Chen, C., Bai, X., Ding, Y., and Lee, I. S. (2019). Electrical stimulation as a novel tool for regulating cell behavior in tissue engineering. *Biomater. Res.* 23, 1–12. doi: 10.1186/s40824-019-0176-8
- Chen, C. S. (2016). 3D biomimetic cultures: the next platform for cell biology. *Trends Cell Biol.* 26, 798–800. doi: 10.1016/j.tcb.2016.08.008
- Chimene, D., Kaunas, R., and Gaharwar, A. K. (2020). Hydrogel bioink reinforcement for additive manufacturing: a focused review of emerging strategies. *Adv. Mater.* 32:1902026. doi: 10.1002/adma.201902026
- Chimene, D., Lennox, K. K., Kaunas, R. R., and Gaharwar, A. K. (2016). Advanced bioinks for 3D printing: a materials science perspective. *Ann. Biomed. Eng.* 44, 2090–2102. doi: 10.1007/s10439-016-1638-y
- Chistiakov, D. A., Orekhov, A. N., and Bobryshev, Y. V. (2017). Effects of shear stress on endothelial cells: go with the flow. *Acta Physiol.* 219, 382–408. doi: 10.1111/apha.12725
- Chwalek, K., Tang-Schomer, M. D., Omenetto, F. G., and Kaplan, D. L. (2015). *In vitro* bioengineered model of cortical brain tissue. *Nat. Protoc.* 10, 1362–1373. doi: 10.1038/nprot.2015.091
- Cimmino, C., Rossano, L., Netti, P. A., and Ventre, M. (2018). Spatio-temporal control of cell adhesion: toward programmable platforms to manipulate cell functions and fate. *Front. Bioeng. Biotechnol.* 6:190. doi: 10.3389/fbioe.2018.00190
- Creff, J., Courson, R., Mangeat, T., Foncy, J., Souleille, S., Thibault, C., et al. (2019). Fabrication of 3D scaffolds reproducing intestinal epithelium topography by high-resolution 3D stereolithography. *Biomaterials* 221:119404. doi: 10.1016/j.biomaterials.2019.119404
- Cui, H., Nowicki, M., Fisher, J. P., and Zhang, L. G. (2017). 3D bioprinting for organ regeneration. *Adv. Healthc. Mater.* 6:1601118. doi: 10.1002/adhm.201601118
- Cui, W., Zhou, Y., and Chang, J. (2010). Electrospun nanofibrous materials for tissue engineering and drug delivery. *Sci. Technol. Adv. Mater.* 11:014108. doi: 10.1088/1468-6996/11/1/014108
- Curto, V. F., Ferro, M. P., Mariani, F., Scavetta, E., and Owens, R. M. (2018). A planar impedance sensor for 3D spheroids. *Lab Chip* 18, 933–943. doi: 10.1039/c8lc00067k
- Curto, V. F., Marchiori, B., Hama, A., Pappa, A.-M., Ferro, M. P., Braendlein, M., et al. (2017). Organic transistor platform with integrated microfluidics for in-line multi-parametric *in vitro* cell monitoring. *Microsystems Nanoeng.* 3:17028. doi: 10.1038/micronano.2017.28
- Cyranoski, D. (2018). How human embryonic stem cells sparked a revolution. *Nature*. Available online at: <https://www.nature.com/articles/d41586-018-03268-4> (accessed September 24, 2020).
- Daly, A., Davidson, M., and Burdick, J. (2020). 3D bioprinting of high cell-density heterogeneous tissue models through spheroid fusion within self-healing hydrogels. *bioRxiv* doi: 10.1101/2020.05.21.103127
- Darnell, M., Gu, L., and Mooney, D. (2018). RNA-seq reveals diverse effects of substrate stiffness on mesenchymal stem cells. *Biomaterials* 181, 182–188. doi: 10.1016/j.biomaterials.2018.07.039
- Das, S., Gordián-Vélez, W. J., Ledebur, H. C., Mourikioti, F., Rompolas, P., Chen, H. I., et al. (2020). Innervation: the missing link for biofabricated tissues and organs. *npj Regen. Med.* 5:11. doi: 10.1038/s41536-020-0096-1
- Dattola, E., Parrotta, E. I., Scalise, S., Perozziello, G., Limongi, T., Candeloro, P., et al. (2019). Development of 3D PVA scaffolds for cardiac tissue engineering and cell screening applications. *RSC Adv.* 9, 4246–4257. doi: 10.1039/C8RA08187E
- De Gregorio, V., Imparato, G., Urciuolo, F., and Netti, P. A. (2018). Micro-patterned endogenous stroma equivalent induces polarized crypt-villus architecture of human small intestinal epithelium. *Acta Biomater.* 81, 43–59. doi: 10.1016/j.actbio.2018.09.061
- De León, S. E., Pupovac, A., and McArthur, S. L. (2020). Three-Dimensional (3D) cell culture monitoring: opportunities and challenges for impedance spectroscopy. *Biotechnol. Bioeng.* 117, 1230–1240. doi: 10.1002/bit.27270
- de Rutte, J. M., Koh, J., and Di Carlo, D. (2019). Scalable high-throughput production of modular microgels for *in situ* assembly of microporous tissue scaffolds. *Adv. Funct. Mater.* 29:1900071. doi: 10.1002/adfm.201900071
- De Souza, N. (2018). Organoids. *Nat. Methods* 15:23. doi: 10.1038/nmeth.4576
- De, P., Dey, N., and Leyland-Jones, B. (2013). "Growth factor and signaling networks," in *Brenner's Encyclopedia of Genetics*, 2nd Edn. (Elsevier Inc.), 365–369.
- Deforest, C. A., and Tirrell, D. A. (2015). A photoreversible protein-patterning approach for guiding stem cell fate in three-dimensional gels. *Nat. Mater.* 14, 523–531. doi: 10.1038/nmat4219
- del Agua, I., Marina, S., Pitsalidis, C., Mantione, D., Ferro, M., Iandolo, D., et al. (2018). Conducting polymer scaffolds based on poly(3,4-ethylenedioxythiophene) and xanthan gum for live-cell monitoring. *ACS Omega* 3, 7424–7431. doi: 10.1021/acsomega.8b00458
- Delalat, B., Cozzi, C., Rasi Ghaemi, S., Polito, G., Kriel, F. H., Michl, T. D., et al. (2018). Microengineered bioartificial liver chip for drug toxicity screening. *Adv. Funct. Mater.* 28:1801825. doi: 10.1002/adfm.201801825
- Delon, L. C., Guo, Z., Oszmiana, A., Chien, C. C., Gibson, R., Prestidge, C., et al. (2019). A systematic investigation of the effect of the fluid shear stress on Caco-2 cells towards the optimization of epithelial organ-on-chip models. *Biomaterials* 225:119521. doi: 10.1016/j.biomaterials.2019.119521
- Devarasetty, M., Forsythe, S. D., Shelley, E., and Soker, S. (2020). *In vitro* modeling of the tumor microenvironment in tumor organoids. *Tissue Eng. Regen. Med.* 17, 759–771. doi: 10.1007/s13770-020-00258-4



- Diederichs, S., Böhm, S., Peterbauer, A., Kasper, C., Scheper, T., and van Griensven, M. (2010). Application of different strain regimes in two-dimensional and three-dimensional adipose tissue-derived stem cell cultures induces osteogenesis: implications for bone tissue engineering. *J. Biomed. Mater. Res. Part A* 94A, 927–936. doi: 10.1002/jbm.a.32772
- Ding, S., Kingshott, P., Thissen, H., Pera, M., and Wang, P.-Y. (2017). Modulation of human mesenchymal and pluripotent stem cell behavior using biophysical and biochemical cues: a review. *Biotechnol. Bioeng.* 114, 260–280. doi: 10.1002/bit.26075
- Discher, D. E., Janmey, P., and Wang, Y. L. (2005). Tissue cells feel and respond to the stiffness of their substrate. *Science* 310, 1139–1143. doi: 10.1126/science.1116995
- Dosh, R. H., Essa, A., Jordan-Mahy, N., Sammon, C., and Le Maitre, C. L. (2017). Use of hydrogel scaffolds to develop an *in vitro* 3D culture model of human intestinal epithelium. *Acta Biomater.* 62, 128–143. doi: 10.1016/j.actbio.2017.08.035
- Duryee, W. R., and Doherty, J. K. (1954). Nuclear and cytoplasmic organoids in the living cell. *Ann. N. Y. Acad. Sci.* 58, 1210–1231. doi: 10.1111/j.1749-6632.1954.tb45904.x
- Dutta, D., Heo, I., and Clevers, H. (2017). Disease modeling in stem cell-derived 3D organoid systems. *Trends Mol. Med.* 23, 393–410. doi: 10.1016/j.molmed.2017.02.007
- Duval, K., Grover, H., Han, L. H., Mou, Y., Pegoraro, A. F., Fredberg, J., et al. (2017). Modeling physiological events in 2D vs. 3D cell culture. *Physiology* 32, 266–277. doi: 10.1152/physiol.00036.2016
- Dye, B. R., Hill, D. R., Ferguson, M. A., Tsai, Y. H., Nagy, M. S., Dyal, R., et al. (2015). *In vitro* generation of human pluripotent stem cell derived lung organoids. *Elife* 4:e05098. doi: 10.7554/eLife.05098
- Edington, C. D., Chen, W. L. K., Geishecker, E., Kassiss, T., Soenksen, L. R., Bhushan, B. M., et al. (2018). Interconnected microphysiological systems for quantitative biology and pharmacology studies. *Sci. Rep.* 8:4530. doi: 10.1038/s41598-018-22749-0
- Ejiri, H., Nomura, T., Hasegawa, M., Tatsumi, C., Imai, M., Sakakibara, S., et al. (2015). Use of synthetic serum-free medium for culture of human dermal fibroblasts to establish an experimental system similar to living dermis. *Cytotechnology* 67, 507–514. doi: 10.1007/s10616-014-9709-0
- El-Kady, A. M., Rizk, R. A., Abd El-Hady, B. M., Shafaa, M. W., and Ahmed, M. M. (2012). Characterization, and antibacterial properties of novel silver releasing nanocomposite scaffolds fabricated by the gas foaming/salt-leaching technique. *J. Genet. Eng. Biotechnol.* 10, 229–238. doi: 10.1016/j.jgeb.2012.07.002
- Engler, A. J., Sen, S., Sweeney, H. L., and Discher, D. E. (2006). Matrix elasticity directs stem cell lineage specification. *Cell* 126, 677–689. doi: 10.1016/j.cell.2006.06.044
- Evans, M. G., Al-Shakli, A., and Chari, D. M. (2019). Electrophysiological properties of neurons grown on soft polymer scaffolds reveal the potential to develop neuromimetic culture environments. *Integr. Biol.* 11, 395–403. doi: 10.1093/intbio/zyz033
- Ezhilarasu, H., Ramalingam, R., Dhand, C., Lakshminarayanan, R., Sadiq, A., Gandhimathi, C., et al. (2019). Biocompatible aloe vera and tetracycline hydrochloride loaded hybrid nanofibrous scaffolds for skin tissue engineering. *Int. J. Mol. Sci.* 20:5174. doi: 10.3390/ijms20205174
- Fabbro, A., Bosi, S., Ballerini, L., and Prato, M. (2012). Carbon nanotubes: artificial nanomaterials to engineer single neurons and neuronal networks. *ACS Chem. Neurosci.* 3, 611–618. doi: 10.1021/cn300048q
- Faley, S. L., Neal, E. H., Wang, J. X., Bosworth, A. M., Weber, C. M., Balotin, K. M., et al. (2019). iPSC-derived brain endothelium exhibits stable, long-term barrier function in perfused hydrogel scaffolds. *Stem Cell Rep.* 12, 474–487. doi: 10.1016/j.stemcr.2019.01.009
- Fang, B., Liu, Y., Zheng, D., Shan, S., Wang, C., Gao, Y., et al. (2019). The effects of mechanical stretch on the biological characteristics of human adipose-derived stem cells. *J. Cell. Mol. Med.* 23, 4244–4255. doi: 10.1111/jcmm.14314
- Fantini, V., Bordoni, M., Scocozza, F., Conti, M., Scarian, E., Carelli, S., et al. (2019). Bioink composition and printing parameters for 3D modeling neural tissue. *Cells* 8:830. doi: 10.3390/cells8080830
- Fatehullah, A., Tan, S. H., and Barker, N. (2016). Organoids as an *in vitro* model of human development and disease. *Nat. Cell Biol.* 18, 246–254. doi: 10.1038/ncb3312
- Felder, M., Trueeb, B., Stucki, A. O., Borcard, S., Stucki, J. D., Schnyder, B., et al. (2019). Impaired wound healing of alveolar lung epithelial cells in a breathing lung-on-a-chip. *Front. Bioeng. Biotechnol.* 7:3. doi: 10.3389/fbioe.2019.00003
- Ferro, M. P., Heilshorn, S. C., and Owens, R. M. (2020). Materials for blood brain barrier modeling *in vitro*. *Mater. Sci. Eng. R Rep.* 140:100522. doi: 10.1016/j.mser.2019.100522
- Fitzgerald, K. A., Malhotra, M., Curtin, C. M., O'Brien, F. J., and O'Driscoll, C. M. (2015). Life in 3D is never flat: 3D models to optimise drug delivery. *J. Control. Release* 215, 39–54. doi: 10.1016/j.jconrel.2015.07.020
- Fontoura, J. C., Viezzer, C., dos Santos, F. G., Ligabue, R. A., Weinlich, R., Puga, R. D., et al. (2020). Comparison of 2D and 3D cell culture models for cell growth, gene expression and drug resistance. *Mater. Sci. Eng. C* 107:110264. doi: 10.1016/j.msec.2019.110264
- Forbester, J. L., Goulding, D., Vallier, L., Hannan, N., Hale, C., Pickard, D., et al. (2015). Interaction of salmonella enterica serovar Typhimurium with intestinal organoids derived from human induced pluripotent stem cells. *Infect. Immun.* 83, 2926–2934. doi: 10.1128/IAI.00161-15
- Frantz, C., Stewart, K. M., and Weaver, V. M. (2010). The extracellular matrix at a glance. *J. Cell Sci.* 123, 4195–4200. doi: 10.1242/jcs.023820
- Fusco, P., Parisatto, B., Rampazzo, E., Persano, L., Frasson, C., Di Meglio, A., et al. (2019). Patient-derived organoids (PDOs) as a novel *in vitro* model for neuroblastoma tumours. *BMC Cancer* 19:970. doi: 10.1186/s12885-019-6149-4
- Gallagher, L. B., Dolan, E. B., O'Sullivan, J., Levey, R., Cavanagh, B. L., Kovarova, L., et al. (2020). Pre-culture of mesenchymal stem cells within RGD-modified hyaluronic acid hydrogel improves their resilience to ischaemic conditions. *Acta Biomater.* 107, 78–90. doi: 10.1016/j.actbio.2020.02.043
- Gholipourmalekabadi, M., Zhao, S., Harrison, B. S., Mozafari, M., and Seifalian, A. M. (2016). Oxygen-generating biomaterials: a new, viable paradigm for tissue engineering? *Trends Biotechnol.* 34, 1010–1021. doi: 10.1016/j.tibtech.2016.05.012
- Gioiella, F., Urciuolo, F., Imparato, G., Brancato, V., and Netti, P. A. (2016). An engineered breast cancer model on a chip to replicate ECM-activation *in vitro* during tumor progression. *Adv. Healthc. Mater.* 5, 3074–3084. doi: 10.1002/adhm.201600772
- Gonçalves, A. I., Rodrigues, M. T., Lee, S. J., Atala, A., Yoo, J. J., Reis, R. L., et al. (2013). Understanding the role of growth factors in modulating stem cell tenogenesis. *PLoS ONE* 8:e83734. doi: 10.1371/journal.pone.0083734
- Gong, H., Agustin, J., Wootton, D., and Zhou, J. G. (2014). Biomimetic design and fabrication of porous chitosan-gelatin liver scaffolds with hierarchical channel network. *J. Mater. Sci. Mater. Med.* 25, 113–120. doi: 10.1007/s10856-013-5061-8
- Graham, A. D., Olof, S. N., Burke, M. J., Armstrong, J. P. K., Mikhailova, E. A., Nicholson, J. G., et al. (2017). High-resolution patterned cellular constructs by droplet-based 3D printing. *Sci. Rep.* 7:7004. doi: 10.1038/s41598-017-06358-x
- Grebenyuk, S., and Ranga, A. (2019). Engineering organoid vascularization. *Front. Bioeng. Biotechnol.* 7:39. doi: 10.3389/fbioe.2019.00039
- Griep, L. M., Wolbers, F., De Wagenaar, B., Ter Braak, P. M., Weksler, B. B., Romero, I. A., et al. (2013). BBB on CHIP: microfluidic platform to mechanically and biochemically modulate blood-brain barrier function. *Biomed. Microdevices* 15, 145–150. doi: 10.1007/s10544-012-9699-7
- Gu, Y., Zhang, J., Zhang, X., Liang, G., Xu, T., and Niu, W. (2019). Three-dimensional printed Mg-Doped  $\beta$ -TCP bone tissue engineering scaffolds: effects of magnesium ion concentration on osteogenesis and angiogenesis *in vitro*. *Tissue Eng. Regen. Med.* 16, 415–429. doi: 10.1007/s13770-019-00192-0
- Guan, S., Zhang, X.-L., Lin, X.-M., Liu, T.-Q., Ma, X.-H., and Cui, Z.-F. (2013). Chitosan/gelatin porous scaffolds containing hyaluronic acid and heparan sulfate for neural tissue engineering. *J. Biomater. Sci. Polym. Ed.* 24, 999–1014. doi: 10.1080/09205063.2012.731374
- Guarino, V., Cirillo, V., and Ambrosio, L. (2016). Bicomponent electrospun scaffolds to design extracellular matrix tissue analogs. *Expert Rev. Med. Devices* 13, 83–102. doi: 10.1586/17434440.2016.1126505
- Guex, A. G., Puetzer, J. L., Armgarth, A., Littmann, E., Stavrinidou, E., Giannelis, E. P., et al. (2017). Highly porous scaffolds of PEDOT:PSS for bone tissue engineering. *Acta Biomater.* 62, 91–101. doi: 10.1016/j.actbio.2017.08.045
- Guo, C., Kim, H., Ovadia, E. M., Mourafetis, C. M., Yang, M., Chen, W., et al. (2017). Bio-orthogonal conjugation and enzymatically triggered

- release of proteins within multi-layered hydrogels. *Acta Biomater.* 56, 80–90. doi: 10.1016/j.actbio.2017.04.002
- Hackam, D. G., and Redelmeier, D. A. (2006). Translation of research evidence from animals to humans. *J. Am. Med. Assoc.* 296, 1731–1732. doi: 10.1001/jama.296.14.1731
- Hamburger, A. W., and Salmon, S. E. (1977). Primary bioassay of human tumor stem cells. *Science* 197, 461–463. doi: 10.1126/science.560061
- Han, F., Dong, Y., Su, Z., Yin, R., Song, A., and Li, S. (2014). Preparation, characteristics and assessment of a novel gelatin-chitosan sponge scaffold as skin tissue engineering material. *Int. J. Pharm.* 476, 124–133. doi: 10.1016/j.ijpharm.2014.09.036
- Han, S., Kim, S., Chen, Z., Shin, H. K., Lee, S.-Y., Moon, H. E., et al. (2020). 3D bioprinted vascularized tumour for drug testing. *Int. J. Mol. Sci.* 21:2993. doi: 10.3390/ijms21082993
- Hansmann, J., Groeber, F., Kahlig, A., Kleinhans, C., and Walles, H. (2013). Bioreactors in tissue engineering-principles, applications and commercial constraints. *Biotechnol. J.* 8, 298–307. doi: 10.1002/biot.201200162
- Hao, S., Ha, L., Cheng, G., Wan, Y., Xia, Y., Sosnoski, D. M., et al. (2018). A spontaneous 3D bone-on-a-chip for bone metastasis study of breast cancer cells. *Small* 14:1702787. doi: 10.1002/sml.201702787
- Haring, A. P., Sontheimer, H., and Johnson, B. N. (2017). Microphysiological human brain and neural systems-on-a-chip: potential alternatives to small animal models and emerging platforms for drug discovery and personalized medicine. *Stem Cell Rev. Rep.* 13, 381–406. doi: 10.1007/s12015-017-9738-0
- Hartung, T. (2013). Food for thought; look back in anger - what clinical studies tell us about preclinical work. *ALTEX* 30, 275–291. doi: 10.14573/altex.2013.3.275
- Hassanajili, S., Karami-Pour, A., Oryan, A., and Talaei-Khozani, T. (2019). Preparation and characterization of PLA/PCL/HA composite scaffolds using indirect 3D printing for bone tissue engineering. *Mater. Sci. Eng. C* 104:109960. doi: 10.1016/j.msec.2019.109960
- Hassell, B. A., Goyal, G., Lee, E., Sontheimer-Phelps, A., Levy, O., Chen, C. S., et al. (2017). Human organ chip models recapitulate orthotopic lung cancer growth, therapeutic responses, and tumor dormancy *in vitro*. *Cell Rep.* 21, 508–516. doi: 10.1016/j.celrep.2017.09.043
- Hayes, J. S., and Richards, R. G. (2010). Surfaces to control tissue adhesion for osteosynthesis with metal implants: *in vitro* and *in vivo* studies to bring solutions to the patient. *Expert Rev. Med. Devices* 7, 131–142. doi: 10.1586/erd.09.55
- Heger, J. I., Froehlich, K., Pastuschek, J., Schmidt, A., Baer, C., Mrowka, R., et al. (2018). Human serum alters cell culture behavior and improves spheroid formation in comparison to fetal bovine serum. *Exp. Cell Res.* 365, 57–65. doi: 10.1016/j.yexcr.2018.02.017
- Heo, I., Dutta, D., Schaefer, D. A., Iakobachvili, N., Artagiani, B., Sachs, N., et al. (2018). Modelling Cryptosporidium infection in human small intestinal and lung organoids. *Nat. Microbiol.* 3, 814–823. doi: 10.1038/s41564-018-0177-8
- Herland, A., Maoz, B. M., Das, D., Somayaji, M. R., Prantil-Baun, R., Novak, R., et al. (2020). Quantitative prediction of human pharmacokinetic responses to drugs via fluidically coupled vascularized organ chips. *Nat. Biomed. Eng.* 4, 421–436. doi: 10.1038/s41551-019-0498-9
- Herland, A., van der Meer, A. D., FitzGerald, E. A., Park, T.-E., Sleetboom, J. J. F., and Ingber, D. E. (2016). Distinct contributions of astrocytes and pericytes to neuroinflammation identified in a 3D human blood-brain barrier on a chip. *PLoS ONE* 11:e0150360. doi: 10.1371/journal.pone.0150360
- Hewitt, E., Mros, S., McConnell, M., Cabral, J. D., and Ali, A. (2019). Melt-electrowriting with novel milk protein/PCL biomaterials for skin regeneration. *Biomed. Mater.* 14:055013. doi: 10.1088/1748-605X/ab3344
- Homan, K. A., Gupta, N., Kroll, K. T., Kolesky, D. B., Skylar-Scott, M., Miyoshi, T., et al. (2019). Flow-enhanced vascularization and maturation of kidney organoids *in vitro*. *Nat. Methods* 16, 255–262. doi: 10.1038/s41592-019-0325-y
- Homan, K. A., Kolesky, D. B., Skylar-Scott, M. A., Herrmann, J., Obuobi, H., Moisan, A., et al. (2016). Bioprinting of 3D convoluted renal proximal tubules on perfusable chips. *Sci. Rep.* 6:34845. doi: 10.1038/srep34845
- Horvath, L., Umehara, Y., Jud, C., Blank, F., Petri-Fink, A., and Rothen-Rutishauser, B. (2015). Engineering an *in vitro* air-blood barrier by 3D bioprinting. *Sci. Rep.* 5:7974. doi: 10.1038/srep07974
- Hribar, K. C., Soman, P., Warner, J., Chung, P., and Chen, S. (2014). Light-assisted direct-write of 3D functional biomaterials. *Lab Chip* 14, 268–275. doi: 10.1039/c3lc50634g
- Htwe, S. S., Harrington, H., Knox, A., Rose, F., Aylott, J., Haycock, J. W., et al. (2015). Investigating NF- $\kappa$ B signaling in lung fibroblasts in 2D and 3D culture systems. *Respir. Res.* 16:144. doi: 10.1186/s12931-015-0302-7
- Hu, W., Wang, Z., Xiao, Y., Zhang, S., and Wang, J. (2019). Advances in crosslinking strategies of biomedical hydrogels. *Biomater. Sci.* 7, 843–855. doi: 10.1039/c8bm01246f
- Huang, G., Li, F., Zhao, X., Ma, Y., Li, Y., Lin, M., et al. (2017). Functional and biomimetic materials for engineering of the three-dimensional cell microenvironment. *Chem. Rev.* 117, 12764–12850. doi: 10.1021/acs.chemrev.7b00094
- Huh, D., Hamilton, G. A., and Ingber, D. E. (2011). From 3D cell culture to organs-on-chips. *Trends Cell Biol.* 21, 745–754. doi: 10.1016/j.tcb.2011.09.005
- Huh, D., Leslie, D. C., Matthews, B. D., Fraser, J. P., Jurek, S., Hamilton, G. A., et al. (2012). A human disease model of drug toxicity-induced pulmonary edema in a lung-on-a-chip microdevice. *Sci. Transl. Med.* 4:159ra147. doi: 10.1126/scitranslmed.3004249
- Hume, R. D., Berry, L., Reichelt, S., D'Angelo, M., Gomm, J., Cameron, R. E., et al. (2018). An engineered human adipose/collagen model for *in vitro* breast cancer cell migration studies. *Tissue Eng. Part A* 24, 1309–1319. doi: 10.1089/ten.tea.2017.0509
- Humphrey, J. D., Dufresne, E. R., and Schwartz, M. A. (2014). Mechanotransduction and extracellular matrix homeostasis. *Nat. Rev. Mol. Cell Biol.* 15, 802–812. doi: 10.1038/nrm3896
- Iandolo, D., Sheard, J., Karavitas Levy, G., Pitsalidis, C., Tan, E., Dennis, A., et al. (2020). Biomimetic and electroactive 3D scaffolds for human neural crest-derived stem cell expansion and osteogenic differentiation. *MRS Commun.* 10, 179–187. doi: 10.1557/mrc.2020.10
- In, J. G., Foulke-Abel, J., Estes, M. K., Zachos, N. C., Kovbasnjuk, O., and Donowitz, M. (2016). Human mini-guts: new insights into intestinal physiology and host–pathogen interactions. *Nat. Rev. Gastroenterol. Hepatol.* 13, 633–642. doi: 10.1038/nrgastro.2016.142
- Inal, S., Hama, A., Ferro, M., Pitsalidis, C., Ozat, J., Iandolo, D., et al. (2017). Conducting polymer scaffolds for hosting and monitoring 3D cell culture. *Adv. Biosyst.* 1:1700052. doi: 10.1002/adbi.201700052
- Jacob, F., Salinas, R. D., Zhang, D. Y., Nguyen, P. T. T., Schnoll, J. G., Wong, S. Z. H., et al. (2020). A patient-derived glioblastoma organoid model and biobank recapitulates inter- and intra-tumoral heterogeneity. *Cell* 180, 188.e22–204.e22. doi: 10.1016/j.cell.2019.11.036
- Jahnke, H. G., Mewes, A., Zitzmann, F. D., Schmidt, S., Azendorf, R., and Robitzki, A. A. (2019). Electrochemical live monitoring of tumor cell migration out of micro-tumors on an innovative multiwell high-dense microelectrode array. *Sci. Rep.* 9:13875. doi: 10.1038/s41598-019-50326-6
- Jakobsson, A., Ottosson, M., Zalis, M. C., O'Carroll, D., Johansson, U. E., and Johansson, F. (2017). Three-dimensional functional human neuronal networks in uncompressed low-density electrospun fiber scaffolds. *Nanomed. Nanotechnol. Biol. Med.* 13, 1563–1573. doi: 10.1016/j.nano.2016.12.023
- Jalili-Firoozinezhad, S., Gazzaniga, F. S., Calamari, E. L., Camacho, D. M., Fadel, C. W., Bein, A., et al. (2019). A complex human gut microbiome cultured in an anaerobic intestine-on-a-chip. *Nat. Biomed. Eng.* 3, 520–531. doi: 10.1038/s41551-019-0397-0
- Jang, K.-J., Mehr, A. P., Hamilton, G. A., McPartlin, L. A., Chung, S., Suh, K.-Y., et al. (2013). Human kidney proximal tubule-on-a-chip for drug transport and nephrotoxicity assessment. *Integr. Biol.* 5, 1119–1129. doi: 10.1039/c3ib40049b
- Jang, K. J., Otieno, M. A., Ronxhi, J., Lim, H. K., Ewart, L., Kodella, K. R., et al. (2019). Reproducing human and cross-species drug toxicities using a Liver-Chip. *Sci. Transl. Med.* 11:eaax5516. doi: 10.1126/scitranslmed.aax5516
- Jansen, E. J. P., Sladek, R. E. J., Bahar, H., Yaffe, A., Gijbels, M. J., Kuijter, R., et al. (2005). Hydrophobicity as a design criterion for polymer scaffolds in bone tissue engineering. *Biomaterials* 26, 4423–4431. doi: 10.1016/j.biomaterials.2004.11.011
- Jayaram, A. K., Pitsalidis, C., Tan, E., Moysidou, C.-M., De Volder, M. F. L., Kim, J.-S., et al. (2019). 3D hybrid scaffolds based on PEDOT:PSS/MWCNT composites. *Front. Chem.* 7:363. doi: 10.3389/fchem.2019.00363
- Jedrzejczak-Silicka, M. (2017). “History of cell culture,” in *New Insights into Cell Culture Technology*, ed S. J. Thatha Gowder (InTech). Available online at: <https://www.intechopen.com/books/new-insights-into-cell-culture-technology/history-of-cell-culture>. doi: 10.5772/66905

- Jensen, C., and Teng, Y. (2020). Is it time to start transitioning from 2D to 3D cell culture? *Front. Mol. Biosci.* 7:33. doi: 10.3389/fmolb.2020.00033
- Jeon, J. S., Bersini, S., Gilardi, M., Dubini, G., Charest, J. L., Moretti, M., et al. (2015). Human 3D vascularized organotypic microfluidic assays to study breast cancer cell extravasation. *Proc. Natl. Acad. Sci. U.S.A.* 112, 214–219. doi: 10.1073/pnas.1417115112
- Jeon, O., Lee, K., and Alsberg, E. (2018). Spatial micropatterning of growth factors in 3D hydrogels for location-specific regulation of cellular behaviors. *Small* 14:1800579. doi: 10.1002/smll.201800579
- Jeon, O., Lee, Y. B., Hinton, T. J., Feinberg, A. W., and Alsberg, E. (2019). Cryopreserved cell-laden alginate microgel bioink for 3D bioprinting of living tissues. *Mater. Today Chem.* 12, 61–70. doi: 10.1016/j.mtchem.2018.11.009
- Joshi, J., Brennan, D., Beachley, V., and Kothapalli, C. R. (2018). Cardiomyogenic differentiation of human bone marrow-derived mesenchymal stem cell spheroids within electrospun collagen nanofiber mats. *J. Biomed. Mater. Res. Part A* 106, 3303–3312. doi: 10.1002/jbm.a.36530
- Kadohama, T., Nishimura, K., Hoshino, Y., Sasajima, T., and Sumpio, B. E. (2007). Effects of different types of fluid shear stress on endothelial cell proliferation and survival. *J. Cell. Physiol.* 212, 244–251. doi: 10.1002/jcp.21024
- Kalmykov, A., Huang, C., Bliley, J., Shiwarski, D., Tashman, J., Abdullah, A., et al. (2019). Organ-on-a-chip: three-dimensional self-rolled biosensor array for electrical interrogations of human electrogenic spheroids. *Sci. Adv.* 5:eaax0729. doi: 10.1126/sciadv.aax0729
- Kamiya, A., and Ando, J. (1996). “Responses of vascular endothelial cells to fluid shear stress: mechanism,” in *Biomechanics*, eds K. Hayashi, A. Kamiya, and K. Ono (Tokyo: Springer), 29–56. doi: 10.1007/978-4-431-68317-9\_2
- Kapalczyńska, M., Kolenda, T., Przybyła, W., Zajackowska, M., Teresiak, A., Filas, V., et al. (2018). 2D and 3D cell cultures – a comparison of different types of cancer cell cultures. *Arch. Med. Sci.* 14, 910–919. doi: 10.5114/aoms.2016.63743
- Karve, S. S., Pradhan, S., Ward, D. V., and Weiss, A. A. (2017). Intestinal organoids model human responses to infection by commensal and Shiga toxin producing *Escherichia coli*. *PLoS ONE* 12:e0178966. doi: 10.1371/journal.pone.0178966
- Karzbrun, E., Kshirsagar, A., Cohen, S. R., Hanna, J. H., and Reiner, O. (2018). Human brain organoids on a chip reveal the physics of folding. *Nat. Phys.* 14, 515–522. doi: 10.1038/s41567-018-0046-7
- Kasendra, M., Tovaglieri, A., Sontheimer-Phelps, A., Jalili-Firoozinezhad, S., Bein, A., Chalkiadaki, A., et al. (2018). Development of a primary human Small Intestine-on-a-Chip using biopsy-derived organoids. *Sci. Rep.* 8:2871. doi: 10.1038/s41598-018-21201-7
- Kato-Negishi, M., Morimoto, Y., Onoe, H., and Takeuchi, S. (2013). Millimeter-sized neural building blocks for 3D heterogeneous neural network assembly. *Adv. Healthc. Mater.* 2, 1564–1570. doi: 10.1002/adhm.201300052
- Keirouz, A., Fortunato, G., Zhang, M., Callanan, A., and Radacsi, N. (2019). Nozzle-free electrospinning of Poly(vinylpyrrolidone)/Poly(glycerol sebacate) fibrous scaffolds for skin tissue engineering applications. *Med. Eng. Phys.* 71, 56–67. doi: 10.1016/j.medengphy.2019.06.009
- Kessler, M., Hoffmann, K., Brinkmann, V., Thieck, O., Jackisch, S., Toelle, B., et al. (2015). The Notch and Wnt pathways regulate stemness and differentiation in human fallopian tube organoids. *Nat. Commun.* 6:8989. doi: 10.1038/ncomms9989
- Khademhosseini, A., and Langer, R. (2016). A decade of progress in tissue engineering. *Nat. Protoc.* 11, 1775–1781. doi: 10.1038/nprot.2016.123
- Khademhosseini, A., Langer, R., Borenstein, J., and Vacanti, J. P. (2006). *Microscale Technologies for Tissue Engineering and Biology*. Available online at: [www.pnas.org/cgi/doi/10.1073/pnas.05076811102](http://www.pnas.org/cgi/doi/10.1073/pnas.05076811102) (accessed September 25, 2020).
- Kilik, O., Pamies, D., Lavell, E., Schiapparelli, P., Feng, Y., Hartung, T., et al. (2016). Brain-on-a-chip model enables analysis of human neuronal differentiation and chemotaxis. *Lab Chip* 16, 4152–4162. doi: 10.1039/c6lc00946h
- Kim, H. J., and Ingber, D. E. (2013). Gut-on-a-Chip microenvironment induces human intestinal cells to undergo villus differentiation. *Integr. Biol.* 5:1130. doi: 10.1039/c3ib40126j
- Kim, J., Koo, B. K., and Knoblich, J. A. (2020). Human organoids: model systems for human biology and medicine. *Nat. Rev. Mol. Cell Biol.* 21, 571–584. doi: 10.1038/s41580-020-0259-3
- Kim, M. H., Kumar, S. K., Shirahama, H., Seo, J., Lee, J. H., Zhdanov, V. P., et al. (2016). Biofunctionalized hydrogel microcavities promote 3D hepatic sheet morphology. *Macromol. Biosci.* 16, 314–321. doi: 10.1002/mabi.201500338
- Kim, S., Chung, M., Ahn, J., Lee, S., and Jeon, N. L. (2016). Interstitial flow regulates the angiogenic response and phenotype of endothelial cells in a 3D culture model. *Lab Chip* 16, 4189–4199. doi: 10.1039/c6lc00910g
- Kim, S. H., Chi, M., Yi, B., Kim, S. H., Oh, S., Kim, Y., et al. (2014). Three-dimensional intestinal villi epithelium enhances protection of human intestinal cells from bacterial infection by inducing mucin expression. *Integr. Biol.* 6, 1122–1131. doi: 10.1039/c4ib00157e
- Kloxin, A. M., Kasko, A. M., Salinas, C. N., and Anseth, K. S. (2009). Photodegradable hydrogels for dynamic tuning of physical and chemical properties. *Science* 324, 59–63. doi: 10.1126/science.1169494
- Knight, E., and Przyborski, S. (2015). Advances in 3D cell culture technologies enabling tissue-like structures to be created *in vitro*. *J. Anat.* 227, 746–756. doi: 10.1111/joa.12257
- Koivisto, J. T., Gering, C., Karvinen, J., Maria Cherian, R., Belay, B., Hyttinen, J., et al. (2019). Mechanically biomimetic gelatin-gellan gum hydrogels for 3D culture of beating human cardiomyocytes. *ACS Appl. Mater. Interfaces* 11, 20589–20602. doi: 10.1021/acsami.8b22343
- Koledova, Z. (2017). “3D cell culture: an introduction,” in *Methods in Molecular Biology*, ed Z. Kiledova (New York, NY: Humana Press Inc.), 1–11. doi: 10.1007/978-1-4939-7021-6\_1
- Kolesky, D. B., Homan, K. A., Skylar-Scott, M. A., and Lewis, J. A. (2016). Three-dimensional bioprinting of thick vascularized tissues. *Proc. Natl. Acad. Sci. U.S.A.* 113, 3179–3184. doi: 10.1073/pnas.1521342113
- Kolesky, D. B., Truby, R. L., Gladman, A. S., Busbee, T. A., Homan, K. A., and Lewis, J. A. (2014). 3D bioprinting of vascularized, heterogeneous cell-laden tissue constructs. *Adv. Mater.* 26, 3124–3130. doi: 10.1002/adma.201305506
- Kratochvil, M. J., Seymour, A. J., Li, T. L., Paşca, S. P., Kuo, C. J., and Heilshorn, S. C. (2019). Engineered materials for organoid systems. *Nat. Rev. Mater.* 4, 606–622. doi: 10.1038/s41578-019-0129-9
- Kumar, A., Nune, K. C., and Misra, R. D. K. (2016). Understanding the response of pulsed electric field on osteoblast functions in three-dimensional mesh structures. *J. Biomater. Appl.* 31, 594–605. doi: 10.1177/0885328216658376
- Kumar, A., Placone, J. K., and Engler, A. J. (2017). Understanding the extracellular forces that determine cell fate and maintenance. *Development* 144, 4261–4270. doi: 10.1242/dev.158469
- Kumari, J., Karande, A. A., and Kumar, A. (2016). Combined effect of cryogel matrix and temperature-reversible soluble-insoluble polymer for the development of *in vitro* human liver tissue. *ACS Appl. Mater. Interfaces* 8, 264–277. doi: 10.1021/acsami.5b08607
- Kuriakose, A. E., Hu, W., Nguyen, K. T., and Menonid, J. U. (2019). Scaffold-based lung tumor culture on porous PLGA microparticle substrates. *PLoS ONE* 14:e0217640. doi: 10.1371/journal.pone.0217640
- Lamers, M. M., Beumer, J., Vaart, J., Van, Der, Knoops, K., Puschhof, J., Breugem, T. I., et al. (2020). SARS-CoV-2 productively infects human gut enterocytes. *Science* 369, 50–54. doi: 10.1126/science.abcl1669
- Lancaster, M. A., and Huch, M. (2019). Disease modelling in human organoids. *Dis. Model. Mech.* 12:dmm039347. doi: 10.1242/dmm.039347
- Lancaster, M. A., Renner, M., Martin, C.-A., Wenzel, D., Bicknell, L. S., Hurles, M. E., et al. (2013). Cerebral organoids model human brain development and microcephaly. *Nature* 501, 373–379. doi: 10.1038/nature12517
- Langer, R., and Vacanti, J. P. (1993). Tissue engineering. *Science* 260, 920–926. doi: 10.1126/science.8493529
- Langhans, S. A. (2018). Three-dimensional *in vitro* cell culture models in drug discovery and drug repositioning. *Front. Pharmacol.* 9:6. doi: 10.3389/fphar.2018.00006
- Lea, T. (2015). “Epithelial cell models; general introduction,” in *The Impact of Food Bioactives on Health: in vitro and ex vivo models*, 95–102. Available online at: [https://link.springer.com/content/pdf/10.1007%2F978-3-319-16104-4\\_9.pdf](https://link.springer.com/content/pdf/10.1007%2F978-3-319-16104-4_9.pdf) (accessed March 27, 2018).
- Ledo, A. M., Senra, A., Rilo-Alvarez, H., Borrajo, E., Vidal, A., Alonso, M. J., et al. (2020a). mRNA-activated matrices encoding transcription factors as primers of cell differentiation in tissue engineering. *Biomaterials* 247:120016. doi: 10.1016/j.biomaterials.2020.120016
- Ledo, A. M., Vining, K. H., Alonso, M. J., Garcia-Fuentes, M., and Mooney, D. J. (2020b). Extracellular matrix mechanics regulate transfection and SOX9-directed differentiation of mesenchymal stem cells. *Acta Biomater.* 110, 153–163. doi: 10.1016/j.actbio.2020.04.027



- Lee, A., Hudson, A. R., Shiwarski, D. J., Tashman, J. W., Hinton, T. J., Yerneni, S., et al. (2019). 3D bioprinting of collagen to rebuild components of the human heart. *Science* 365, 482–487. doi: 10.1126/science.aav9051
- Lee, H., Chae, S., Kim, J. Y., Han, W., Kim, J., Choi, Y., et al. (2019). Cell-printed 3D liver-on-a-chip possessing a liver microenvironment and biliary system. *Biofabrication* 11:25001. doi: 10.1088/1758-5090/aaf9fa
- Lee, W., Debasitis, J. C., Lee, V. K., Lee, J. H., Fischer, K., Edminster, K., et al. (2009). Multi-layered culture of human skin fibroblasts and keratinocytes through three-dimensional freeform fabrication. *Biomaterials* 30, 1587–1595. doi: 10.1016/j.biomaterials.2008.12.009
- Leijten, J., Seo, J., Yue, K., Trujillo-de Santiago, G., Tamayol, A., Ruiz-Esparza, G. U., et al. (2017). Spatially and temporally controlled hydrogels for tissue engineering. *Mater. Sci. Eng. R Rep.* 119, 1–35. doi: 10.1016/j.mser.2017.07.001
- Leslie, J. L., Huang, S., Opp, J. S., Nagy, M. S., Kobayashi, M., Young, V. B., et al. (2015). Persistence and toxin production by *Clostridium difficile* within human intestinal organoids result in disruption of epithelial paracellular barrier function. *Infect. Immun.* 83, 138–145. doi: 10.1128/IAI.02561-14
- Levorson, E. J., Kasper, F. K., and Mikos, A. G. (2011). “Scaffolds: flow perfusion bioreactor design,” in *Comprehensive Biomaterials*, ed P. Ducheyne (Elsevier), 1–11. doi: 10.1016/b978-0-08-055294-1.00154-9
- Li, J., Liu, X., Crook, J. M., and Wallace, G. G. (2020). 3D printing of cytocompatible graphene/alginate scaffolds for mimetic tissue constructs. *Front. Bioeng. Biotechnol.* 8:824. doi: 10.3389/fbioe.2020.00824
- Li, Q., Nan, K., Le Floch, P., Lin, Z., Sheng, H., and Liu, J. (2019). Cyborg organoids: implantation of nanoelectronics via organogenesis for tissue-wide electrophysiology. *bioRxiv* 697664. doi: 10.1101/697664
- Li, X., Francies, H. E., Secrier, M., Perner, J., Miremedi, A., Galeano-Dalmau, N., et al. (2018). Organoid cultures recapitulate esophageal adenocarcinoma heterogeneity providing a model for clonality studies and precision therapeutics. *Nat. Commun.* 9:2983. doi: 10.1038/s41467-018-05190-9
- Liu, T., kun, Pang, Y., Zhou, Z., zhen, Yao, R., and Sun, W. (2019). An integrated cell printing system for the construction of heterogeneous tissue models. *Acta Biomater.* 95, 245–257. doi: 10.1016/j.actbio.2019.05.052
- Liu, X., Zheng, C., Luo, X., Wang, X., and Jiang, H. (2019). Recent advances of collagen-based biomaterials: multi-hierarchical structure, modification and biomedical applications. *Mater. Sci. Eng. C* 99, 1509–1522. doi: 10.1016/j.msec.2019.02.070
- Llucíà-Valdeperas, A., Sanchez, B., Soler-Botija, C., Gálvez-Montón, C., Prat-Vidal, C., Roura, S., et al. (2015). Electrical stimulation of cardiac adipose tissue-derived progenitor cells modulates cell phenotype and genetic machinery. *J. Tissue Eng. Regen. Med.* 9, E76–E83. doi: 10.1002/term.1710
- Low, L. A., and Tagle, D. A. (2017). Tissue chips-innovative tools for drug development and disease modeling. *Lab Chip* 17, 3026–3036. doi: 10.1039/c7lc00462a
- Lozano, R., Stevens, L., Thompson, B. C., Gilmore, K. J., Gorkin, R., Stewart, E. M., et al. (2015). 3D printing of layered brain-like structures using peptide modified gellan gum substrates. *Biomaterials* 67, 264–273. doi: 10.1016/j.biomaterials.2015.07.022
- Luca, A. C., Mersch, S., Deenen, R., Schmidt, S., Messner, I., Schäfer, K.-L., et al. (2013). Impact of the 3D microenvironment on phenotype, gene expression, and EGFR inhibition of colorectal cancer cell lines. *PLoS ONE* 8:e59689. doi: 10.1371/journal.pone.0059689
- Ma, X., Yu, C., Wang, P., Xu, W., Wan, X., Lai, C. S. E., et al. (2018). Rapid 3D bioprinting of decellularized extracellular matrix with regionally varied mechanical properties and biomimetic microarchitecture. *Biomaterials* 185, 310–321. doi: 10.1016/j.biomaterials.2018.09.026
- Mabrouk, M., Beherei, H. H., and Das, D. B. (2020). Recent progress in the fabrication techniques of 3D scaffolds for tissue engineering. *Mater. Sci. Eng. C* 110:110716. doi: 10.1016/j.msec.2020.110716
- Madl, C. M., LeSavage, B. L., Dewi, R. E., Lampe, K. J., and Heilshorn, S. C. (2019). Matrix remodeling enhances the differentiation capacity of neural progenitor cells in 3D hydrogels. *Adv. Sci.* 6:1801716. doi: 10.1002/adv.201801716
- Magnan, L., Labrunie, G., Fénelon, M., Dusserre, N., Foulc, M. P., Lafourcade, M., et al. (2020). Human textiles: a cell-synthesized yarn as a truly “bio” material for tissue engineering applications. *Acta Biomater.* 105, 111–120. doi: 10.1016/j.actbio.2020.01.037
- Majidi, S. S., Slemming-Adamsen, P., Hanif, M., Zhang, Z., Wang, Z., and Chen, M. (2018). Wet electrospun alginate/gelatin hydrogel nanofibers for 3D cell culture. *Int. J. Biol. Macromol.* 118, 1648–1654. doi: 10.1016/j.ijbiomac.2018.07.005
- Manousiouthakis, E., Chen, Y., Cairns, D. M., Pollard, R., Gerlovin, K., Dente, M. J., et al. (2019). Bioengineered *in vitro* enteric nervous system. *J. Tissue Eng. Regen. Med.* 13, 1712–1723. doi: 10.1002/term.2926
- Mao, A. S., Shin, J. W., and Mooney, D. J. (2016). Effects of substrate stiffness and cell-cell contact on mesenchymal stem cell differentiation. *Biomaterials* 98, 184–191. doi: 10.1016/j.biomaterials.2016.05.004
- Mao, Q., Wang, Y., Li, Y., Juengpanich, S., Li, W., Chen, M., et al. (2020). Fabrication of liver microtissue with liver decellularized extracellular matrix (dECM) bioink by digital light processing (DLP) bioprinting. *Mater. Sci. Eng. C* 109:110625. doi: 10.1016/j.msec.2020.110625
- Mao, W., Kang, M. K., Shin, J. U., Son, Y. J., Kim, H. S., and Yoo, H. S. (2018). Coaxial hydro-nanofibrils for self-assembly of cell sheets producing skin bilayers. *ACS Appl. Mater. Interfaces* 10, 43503–43511. doi: 10.1021/acsami.8b17740
- Marga, F., Jakab, K., Khatriwala, C., Shepherd, B., Dorfman, S., Hubbard, B., et al. (2012). Toward engineering functional organ modules by additive manufacturing. *Biofabrication* 4:022001. doi: 10.1088/1758-5082/4/2/022001
- Martinelli, V., Cellot, G., Toma, F. M., Long, C. S., Caldwell, J. H., Zentilin, L., et al. (2012). Carbon nanotubes promote growth and spontaneous electrical activity in cultured cardiac myocytes. *Nano Lett.* 12, 1831–1838. doi: 10.1021/nl204064s
- Marturano-Kruik, A., Nava, M. M., Yeager, K., Chramiec, A., Hao, L., Robinson, S., et al. (2018). Human bone perivascular niche-on-a-chip for studying metastatic colonization. *Proc. Natl. Acad. Sci. U.S.A.* 115, 1256–1261. doi: 10.1073/pnas.1714282115
- Maschmeyer, I., Hasenberg, T., Jaenicke, A., Lindner, M., Lorenz, A. K., Zech, J., et al. (2015a). Chip-based human liver-intestine and liver-skin co-cultures - a first step toward systemic repeated dose substance testing *in vitro*. *Eur. J. Pharm. Biopharm.* 95, 77–87. doi: 10.1016/j.ejpb.2015.03.002
- Maschmeyer, I., Lorenz, A. K., Schimek, K., Hasenberg, T., Ramme, A. P., Hübner, J., et al. (2015b). A four-organ-chip for interconnected long-term co-culture of human intestine, liver, skin and kidney equivalents. *Lab Chip* 15, 2688–2699. doi: 10.1039/c5lc00392j
- Massa, S., Sakr, M. A., Seo, J., Bandaru, P., Arneri, A., Bersini, S., et al. (2017). Bioprinted 3D vascularized tissue model for drug toxicity analysis. *Biomicrofluidics* 11:044109. doi: 10.1063/1.4994708
- Mazzocchi, A., Devarasetty, M., Huntwork, R., and Soker, S. (2019). Optimization of collagen type I-hyaluronan hybrid bioink for 3D bioprinted liver microenvironments. *Biofabrication* 11:015003. doi: 10.1088/1758-5090/aac543
- McCaig, C. D., Rajnicek, A. M., Song, B., and Zhao, M. (2005). Controlling cell behavior electrically: current views and future potential. *Physiol. Rev.* 85, 943–978. doi: 10.1152/physrev.00020.2004
- McKee, C., and Chaudhry, G. R. (2017). Advances and challenges in stem cell culture. *Colloids Surfaces B Biointerfaces* 159, 62–77. doi: 10.1016/j.colsurfb.2017.07.051
- McMurtrey, R. J. (2016). Analytic models of oxygen and nutrient diffusion, metabolism dynamics, and architecture optimization in three-dimensional tissue constructs with applications and insights in cerebral organoids. *Tissue Eng. Part C Methods* 22, 221–249. doi: 10.1089/ten.tec.2015.0375
- Melchels, F. P. W., Domingos, M. A. N., Klein, T. J., Malda, J., Bartolo, P. J., and Huttmacher, D. W. (2012). Additive manufacturing of tissues and organs. *Prog. Polym. Sci.* 37, 1079–1104. doi: 10.1016/j.progpolymsci.2011.11.007
- Mihic, A., Li, J., Miyagi, Y., Gagliardi, M., Li, S. H., Zu, J., et al. (2014). The effect of cyclic stretch on maturation and 3D tissue formation of human embryonic stem cell-derived cardiomyocytes. *Biomaterials* 35, 2798–2808. doi: 10.1016/j.biomaterials.2013.12.052
- Miller, J. S., Stevens, K. R., Yang, M. T., Baker, B. M., Nguyen, D. H. T., Cohen, D. M., et al. (2012). Rapid casting of patterned vascular networks for perfusable engineered three-dimensional tissues. *Nat. Mater.* 11, 768–774. doi: 10.1038/nmat3357
- Miller, P. G., and Shuler, M. L. (2016). Design and demonstration of a pumpless 14 compartment microphysiological system. *Biotechnol. Bioeng.* 113, 2213–2227. doi: 10.1002/bit.25989



- Min, D., Lee, W., Bae, I. H., Lee, T. R., Croce, P., and Yoo, S. S. (2018). Bioprinting of biomimetic skin containing melanocytes. *Exp. Dermatol.* 27, 453–459. doi: 10.1111/exd.13376
- Mittal, R., Woo, F. W., Castro, C. S., Cohen, M. A., Karanxha, J., Mittal, J., et al. (2018). Organ-on-chip models: Implications in drug discovery and clinical applications. *J. Cell. Physiol.* 234, 8352–8380. doi: 10.1002/jcp.27729
- Miura, S., Sato, K., Kato-Negishi, M., Teshima, T., and Takeuchi, S. (2015). Fluid shear triggers microvilli formation via mechanosensitive activation of TRPV6. *Nat. Commun.* 6:8871. doi: 10.1038/ncomms9871
- Monferrer, E., Martín-Vañó, S., Carretero, A., García-Lizarriar, A., Burgos-Panadero, R., Navarro, S., et al. (2020). A three-dimensional bioprinted model to evaluate the effect of stiffness on neuroblastoma cell cluster dynamics and behavior. *Sci. Rep.* 10:35367. doi: 10.1038/s41598-020-62986-w
- Morán, G. A. G., Parra-Medina, R., Cardona, A. G., Quintero-Ronderos, P., and Rodríguez, É. G. (2013). *Cytokines, Chemokines and Growth Factors*. Available online at: <https://www.ncbi.nlm.nih.gov/books/NBK459450/> (accessed September 24, 2020).
- Morgan, J. P., Delnero, P. F., Zheng, Y., Verbridge, S. S., Chen, J., Craven, M., et al. (2013). Formation of microvascular networks *in vitro*. *Nat. Protoc.* 8, 1820–1836. doi: 10.1038/nprot.2013.110
- Morris, G. E., Bridge, J. C., Eltobi, O. M. I., Knox, A. J., Aylott, J. W., Brightling, C. E., et al. (2014). Human airway smooth muscle maintain *in situ* cell orientation and phenotype when cultured on aligned electrospun scaffolds. *Am. J. Physiol. Lung Cell. Mol. Physiol.* 307, L38. doi: 10.1152/ajplung.00318.2013
- Moxon, S. R., Corbett, N. J., Fisher, K., Potjewyd, G., Domingos, M., and Hooper, N. M. (2019). Blended alginate/collagen hydrogels promote neurogenesis and neuronal maturation. *Mater. Sci. Eng. C* 104:109904. doi: 10.1016/j.msec.2019.109904
- Muraglia, A., Nguyen, V. T., Nardini, M., Moggi, M., Coviello, D., Dozin, B., et al. (2017). Culture medium supplements derived from human platelet and plasma: cell commitment and proliferation support. *Front. Bioeng. Biotechnol.* 5:66. doi: 10.3389/fbioe.2017.00066
- Murphy, A. R., Haynes, J. M., Laslett, A. L., Cameron, N. R., and O'Brien, C. M. (2020). Three-dimensional differentiation of human pluripotent stem cell-derived neural precursor cells using tailored porous polymer scaffolds. *Acta Biomater.* 101, 102–116. doi: 10.1016/j.actbio.2019.10.017
- Murr, L. E. (2016). Frontiers of 3D printing/additive manufacturing: from human organs to aircraft fabrication. *J. Mater. Sci. Technol.* 32, 987–995. doi: 10.1016/j.jmst.2016.08.011
- Nachlas, A. L. Y., Li, S., Streeter, B. W., De Jesus Morales, K. J., Sulejmani, F., Madukauwa-David, D. I., et al. (2020). A multilayered valve leaflet promotes cell-laden collagen type I production and aortic valve hemodynamics. *Biomaterials* 240:119838. doi: 10.1016/j.biomaterials.2020.119838
- Nagle, P. W., Plukker, J. T. M., Muijs, C. T., van Luijk, P., and Coppes, R. P. (2018). Patient-derived tumor organoids for prediction of cancer treatment response. *Semin. Cancer Biol.* 53, 258–264. doi: 10.1016/j.semcancer.2018.06.005
- Nelson, L., Tighe, A., Golder, A., Littler, S., Bakker, B., Moralli, D., et al. (2020). A living biobank of ovarian cancer *ex vivo* models reveals profound mitotic heterogeneity. *Nat. Commun.* 11:822. doi: 10.1038/s41467-020-14551-2
- Neufurth, M., Wang, X., Wang, S., Steffen, R., Ackermann, M., Haep, N. D., et al. (2017). 3D printing of hybrid biomaterials for bone tissue engineering: calcium-polyphosphate microparticles encapsulated by polycaprolactone. *Acta Biomater.* 64, 377–388. doi: 10.1016/j.actbio.2017.09.031
- Nichol, J. W., and Khademhosseini, A. (2009). Modular tissue engineering: Engineering biological tissues from the bottom up. *Soft Matter* 5, 1312–1319. doi: 10.1039/b814285h
- Nikolaev, M., Mitrofanova, O., Brogiere, N., Geraldo, S., Dutta, D., Tabata, Y., et al. (2020). Homeostatic mini-intestines through scaffold-guided organoid morphogenesis. *Nature* 585, 574–578. doi: 10.1038/s41586-020-2724-8
- Nikolova, M. P., and Chavali, M. S. (2019). Recent advances in biomaterials for 3D scaffolds: a review. *Bioact. Mater.* 4, 271–292. doi: 10.1016/j.bioactmat.2019.10.005
- O'Leary, C., Cavanagh, B., Unger, R. E., Kirkpatrick, C. J., O'Dea, S., O'Brien, F. J., et al. (2016). The development of a tissue-engineered tracheobronchial epithelial model using a bilayered collagen-hyaluronate scaffold. *Biomaterials* 85, 111–127. doi: 10.1016/j.biomaterials.2016.01.065
- Onoe, H., Okitsu, T., Itou, A., Kato-Negishi, M., Gojo, R., Kiriya, D., et al. (2013). Metre-long cell-laden microfibres exhibit tissue morphologies and functions. *Nat. Mater.* 12, 584–590. doi: 10.1038/nmat3606
- Ooft, S. N., Weeber, F., Dijkstra, K. K., McLean, C. M., Kaing, S., van Werkhoven, E., et al. (2019). Patient-derived organoids can predict response to chemotherapy in metastatic colorectal cancer patients. *Sci. Transl. Med.* 11:eaay2574. doi: 10.1126/scitranslmed.aay2574
- Ortega-Prieto, A. M., Skelton, J. K., Wai, S. N., Large, E., Lussignol, M., Vizcay-Barrena, G., et al. (2018). 3D microfluidic liver cultures as a physiological preclinical tool for hepatitis B virus infection. *Nat. Commun.* 9:682. doi: 10.1038/s41467-018-02969-8
- Ouyang, L., Armstrong, J. P. K., Salmeron-Sanchez, M., and Stevens, M. M. (2020). Assembling living building blocks to engineer complex tissues. *Adv. Funct. Mater.* 30:1909009. doi: 10.1002/adfm.201909009
- Owens, R. M., Iandolo, D., and Wittmann, K. (2017). A (bio) materials approach to three-dimensional cell biology. *MRS Commun.* 7, 287–288. doi: 10.1557/mrc.2017.102
- Pang, Y., Sutoko, S., Wang, Z., Horimoto, Y., Montagne, K., Horiguchi, I., et al. (2020). Organization of liver organoids using Raschig ring-like micro-scaffolds and triple co-culture: Toward modular assembly-based scalable liver tissue engineering. *Med. Eng. Phys.* 76, 69–78. doi: 10.1016/j.medengphys.2019.10.010
- Park, J., Lee, B. K., Jeong, G. S., Hyun, J. K., Lee, C. J., and Lee, S. H. (2015). Three-dimensional brain-on-a-chip with an interstitial level of flow and its application as an *in vitro* model of Alzheimer's disease. *Lab Chip* 15, 141–150. doi: 10.1039/c4lc00962b
- Park, S. M., Eom, S., Hong, H., Yoon, J., Lee, S. J., Kim, B. C., et al. (2019). Reconstruction of *in vivo*-like *in vitro* model: enabling technologies of microfluidic systems for dynamic biochemical/mechanical stimuli. *Microelectron. Eng.* 203–204, 6–24. doi: 10.1016/j.mee.2018.10.010
- Pas, J., Pitsalidis, C., Koutsouras, D. A., Quilichini, P. P., Santoro, F., Cui, B., et al. (2017). Neurospheres on patterned PEDOT:PSS microelectrode arrays enhance electrophysiology recordings. *Adv. Biosyst.* 2:1700164. doi: 10.1002/adbi.201700164
- Patel, A. K., Celiz, A. D., Rajamohan, D., Anderson, D. G., Langer, R., Davies, M. C., et al. (2015). A defined synthetic substrate for serum-free culture of human stem cell derived cardiomyocytes with improved functional maturity identified using combinatorial materials microarrays. *Biomaterials* 61, 257–265. doi: 10.1016/j.biomaterials.2015.05.019
- Patel, M., Nakaji-Hirabayashi, T., and Matsumura, K. (2019). Effect of dual-drug-releasing micelle-hydrogel composite on wound healing *in vivo* in full-thickness excision wound rat model. *J. Biomed. Mater. Res. Part A* 107, 1094–1106. doi: 10.1002/jbm.a.36639
- Patient, J. D., Hajiali, H., Harris, K., Abrahamsson, B., Tannergren, C., White, L. J., et al. (2019). Nanofibrous scaffolds support a 3D *in vitro* permeability model of the human intestinal epithelium. *Front. Pharmacol.* 10:456. doi: 10.3389/fphar.2019.00456
- Pearce, S. C., Coia, H. G., Karl, J. P., Pantoja-Feliciano, I. G., Zachos, N. C., and Racicot, K. (2018). Intestinal *in vitro* and *ex vivo* models to study host-microbiome interactions and acute stressors. *Front. Physiol.* 9:1584. doi: 10.3389/fphys.2018.01584
- Pedron, S., Becka, E., and Harley, B. A. C. (2013). Regulation of glioma cell phenotype in 3D matrices by hyaluronic acid. *Biomaterials* 34, 7408–7417. doi: 10.1016/j.biomaterials.2013.06.024
- Pitsalidis, C., Ferro, M. P., Iandolo, D., Tzounis, L., Inal, S., and Owens, R. M. (2018). Transistor in a tube: a route to three-dimensional bioelectronics. *Sci. Adv.* 4:eaat4253. doi: 10.1126/sciadv.aat4253
- Plummer, S., Wallace, S., Ball, G., Lloyd, R., Schiapparelli, P., Quiñones-Hinojosa, A., et al. (2019). A Human iPSC-derived 3D platform using primary brain cancer cells to study drug development and personalized medicine. *Sci. Rep.* 9:1407. doi: 10.1038/s41598-018-38130-0
- Pradhan, S., Brooks, A. K., and Yadavalli, V. K. (2020). Nature-derived materials for the fabrication of functional biodevices. *Mater. Today Bio.* 7:100065. doi: 10.1016/j.mtbio.2020.100065
- Prantl-Baun, R., Novak, R., Das, D., Somayaji, M. R., Przekwas, A., and Ingber, D. E. (2018). Physiologically based pharmacokinetic and pharmacodynamic analysis enabled by microfluidically linked

- organs-on-chips. *Annu. Rev. Pharmacol. Toxicol.* 58, 37–64. doi: 10.1146/annurev-pharmtox-010716-104748
- Prévo, M. E., Andro, H., M., Alexander, S. L., Ustunel, S., Zhu, C., Nikolov, Z., et al. (2018). Liquid crystal elastomer foams with elastic properties specifically engineered as biodegradable brain tissue scaffolds. *Soft Matter* 14:354. doi: 10.1039/c7sm01949a
- Przyborski, S. (2017). *Technology Platforms for 3D Cell Culture*. Wiley-Blackwell. Available online at: <https://www.wiley.com/en-gb/Technology+Platforms+for+3D+Cell+Culture:+A+User's+Guide-p-9781118851500> (accessed January 8, 2018).
- Pudlas, M., Koch, S., Bolwien, C., Thude, S., Jenne, N., Hirth, T., et al. (2011). Raman spectroscopy: a noninvasive analysis tool for the discrimination of human skin cells. *Tissue Eng. Part C Methods* 17, 1027–1040. doi: 10.1089/ten.tec.2011.0082
- Rahmani, A., Bakhshayesh, D., Mostafavi, E., Alizadeh, E., Asadi, N., Akbarzadeh, A., et al. (2018). Fabrication of three-dimensional scaffolds based on nano-biomimetic collagen hybrid constructs for skin tissue engineering. *ACS Omega* 3, 8605–8611. doi: 10.1021/acsomega.8b01219
- Ramadan, Q., and Jing, L. (2016). Characterization of tight junction disruption and immune response modulation in a miniaturized Caco-2/U937 coculture-based *in vitro* model of the human intestinal barrier. *Biomed. Microdevices* 18:11. doi: 10.1007/s10544-016-0035-5
- Ramadan, Q., and Zourob, M. (2020). Organ-on-a-chip engineering: Toward bridging the gap between lab and industry. *Biomicrofluidics* 14:41501. doi: 10.1063/5.0011583
- Ribas, J., Sadeghi, H., Manbachi, A., Leijten, J., Brinegar, K., Zhang, Y. S., et al. (2016). Cardiovascular organ-on-a-chip platforms for drug discovery and development. *Appl. Vitro. Toxicol.* 2, 82–96. doi: 10.1089/aivt.2016.0002
- Riehl, B. D., Park, J. H., Kwon, I. K., and Lim, J. Y. (2012). Mechanical stretching for tissue engineering: two-dimensional and three-dimensional constructs. *Tissue Eng. Part B Rev.* 18, 288–300. doi: 10.1089/ten.teb.2011.0465
- Rivnay, J., Inal, S., Salles, A., Owens, R. M., Berggren, M., and Malliaras, G. G. (2018). Organic electrochemical transistors. *Nat. Rev. Mater.* 3:17086. doi: 10.1038/natrevmats.2017.86
- Rnjak, J., Li, Z., Maitz, P. K. M., Wise, S. G., and Weiss, A. S. (2009). Primary human dermal fibroblast interactions with open weave three-dimensional scaffolds prepared from synthetic human elastin. *Biomaterials* 30, 6469–6477. doi: 10.1016/j.biomaterials.2009.08.017
- Rogal, J., Binder, C., Kromidas, E., Roos, J., Probst, C., Schneider, S., et al. (2020). WAT-on-a-chip integrating human mature white adipocytes for mechanistic research and pharmaceutical applications. *Sci. Rep.* 10:6666. doi: 10.1038/s41598-020-63710-4
- Roh, T. T., Chen, Y., Paul, H. T., Guo, C., and Kaplan, D. L. (2019). 3D bioengineered tissue model of the large intestine to study inflammatory bowel disease. *Biomaterials* 225:119517. doi: 10.1016/j.biomaterials.2019.119517
- Ronaldson-Bouchard, K., and Vunjak-Novakovic, G. (2018). Organs-on-a-chip: a fast track for engineered human tissues in drug development. *Cell Stem Cell* 22, 310–324. doi: 10.1016/j.stem.2018.02.011
- Rosenbaum, A. J., Grande, D. A., and Dines, J. S. (2008). The use of mesenchymal stem cells in tissue engineering: a global assessment. *Organogenesis* 4, 23–27. doi: 10.4161/org.6048
- Rossi, G., Boni, A., Guiet, R., Girgin, M., Kelly, R., and Lutolf, M. (2019). Embryonic organoids recapitulate early heart organogenesis. *bioRxiv* 802181. doi: 10.1101/802181
- Roth, A., and Singer, T. (2014). The application of 3D cell models to support drug safety assessment: opportunities and challenges. *Adv. Drug Deliv. Rev.* 69–70, 179–189. doi: 10.1016/j.addr.2013.12.005
- Rouleau, N., Cantley, W. L., Liaudanskaya, V., Berk, A., Du, C., Rusk, W., et al. (2020). A Long-living bioengineered neural tissue platform to study neurodegeneration. *Macromol. Biosci.* 20:e2000004. doi: 10.1002/mabi.202000004
- Rouwkema, J., Gibbs, S., Lutolf, M. P., Martin, I., Vunjak-Novakovic, G., and Malda, J. (2011). *In vitro* platforms for tissue engineering: implications for basic research and clinical translation. *J. Tissue Eng. Regen. Med.* 5, e164–e167. doi: 10.1002/term.414
- Rouwkema, J., Koopman, B. F. J. M., Blitterswijk, C. A. V., Dhert, W. J. A., and Malda, J. (2009). Supply of nutrients to cells in engineered tissues. *Biotechnol. Genet. Eng. Rev.* 26, 163–178. doi: 10.5661/bger-26-163
- Rowe, R. G., and Daley, G. Q. (2019). Induced pluripotent stem cells in disease modelling and drug discovery. *Nat. Rev. Genet.* 20, 377–388. doi: 10.1038/s41576-019-0100-z
- Ruskowicz, E. R., and Deforest, C. A. (2018). Photoresponsive biomaterials for targeted drug delivery and 4D cell culture. *Nat. Rev. Mater.* 3:17087. doi: 10.1038/natrevmats.2017.87
- Ryan, A. J., and O'Brien, F. J. (2015). Insoluble elastin reduces collagen scaffold stiffness, improves viscoelastic properties, and induces a contractile phenotype in smooth muscle cells. *Biomaterials* 73, 296–307. doi: 10.1016/j.biomaterials.2015.09.003
- Sachs, N., de Ligt, J., Kopper, O., Gogola, E., Bounova, G., Weeber, F., et al. (2018). A living biobank of breast cancer organoids captures disease heterogeneity. *Cell* 172, 373.e10–386.e10. doi: 10.1016/j.cell.2017.11.010
- Sachs, N., Papaspyropoulos, A., Zomer-van Ommen, D. D., Heo, I., Böttinger, L., Klay, D., et al. (2019). Long-term expanding human airway organoids for disease modeling. *EMBO J.* 38:e100300. doi: 10.15252/embj.2018100300
- Saidy, N. T., Wolf, F., Bas, O., Keijnders, H., Hutmacher, D. W., Mela, P., et al. (2019). Biologically inspired scaffolds for heart valve tissue engineering via melt electrowriting. *Small* 15:e1900873. doi: 10.1002/smll.201900873
- Salazar, A., Keusgen, M., and Von Hagen, J. (2016). Amino acids in the cultivation of mammalian cells. *Amino Acids* 48, 1161–1171. doi: 10.1007/s00726-016-2181-8
- Sato, T., Vries, R. G., Snippert, H. J., van de Wetering, M., Barker, N., Stange, D. E., et al. (2009). Single Lgr5 stem cells build crypt-villus structures *in vitro* without a mesenchymal niche. *Nature* 459, 262–265. doi: 10.1038/nature07935
- Schimek, K., Busek, M., Brincker, S., Groth, B., Hoffmann, S., Lauster, R., et al. (2013). Integrating biological vasculature into a multi-organ-chip microsystem. *Lab Chip* 13:3588. doi: 10.1039/c3lc50217a
- Schmid, J., Schwarz, S., Meier-Staude, R., Sudhop, S., Clausen-Schaumann, H., Schieker, M., et al. (2018). A perfusion bioreactor system for cell seeding and oxygen-controlled cultivation of three-dimensional cell cultures. *Tissue Eng. Part C Methods* 24, 585–595. doi: 10.1089/ten.tec.2018.0204
- Schmidt, C. E., Shastri, V. R., Vacanti, J. P., and Langer, R. (1997). Stimulation of neurite outgrowth using an electrically conducting polymer. *Proc. Natl. Acad. Sci. U.S.A.* 94, 8948–8953. doi: 10.1073/pnas.94.17.8948
- Schneeberger, K., Spee, B., Costa, P., Sachs, N., Clevers, H., and Malda, J. (2017). Converging biofabrication and organoid technologies: the next frontier in hepatic and intestinal tissue engineering? *Biofabrication* 9:013001. doi: 10.1088/1758-5090/aa6121
- Schneider, H., Muirhead, E. E., and Zydeck, F. A. (1963). Some unusual observations of organoid tissues and blood elements in monolayer cultures. *Exp. Cell Res.* 30, 449–459. doi: 10.1016/0014-4827(63)90322-7
- Schwarz, R. I., and Bissell, M. J. (1977). Dependence of the differentiated state on the cellular environment: modulation of collagen synthesis in tendon cells. *Proc. Natl. Acad. Sci. U.S.A.* 74, 4453–4457. doi: 10.1073/pnas.74.10.4453
- Schweiger, P. J., and Jensen, K. B. (2016). Modeling human disease using organotypic cultures. *Curr. Opin. Cell Biol.* 43, 22–29. doi: 10.1016/j.ceb.2016.07.003
- Seok, J. M., Rajangam, T., Jeong, J. E., Cheong, S., Joo, S. M., Oh, S. J., et al. (2020). Fabrication of 3D plotted scaffold with microporous strands for bone tissue engineering. *J. Mater. Chem. B* 8, 951–960. doi: 10.1039/c9tb02360g
- Shaban, L., Chen, Y., Fasciano, A. C., Lin, Y., Kaplan, D. L., Kumamoto, C. A., et al. (2018). A 3D intestinal tissue model supports *Clostridioides difficile* germination, colonization, toxin production and epithelial damage. *Anaerobe* 50, 85–92. doi: 10.1016/j.anaerobe.2018.02.006
- Shadish, J. A., Benuska, G. M., and DeForest, C. A. (2019). Bioactive site-specifically modified proteins for 4D patterning of gel biomaterials. *Nat. Mater.* 18, 1005–1014. doi: 10.1038/s41563-019-0367-7
- Shamir, E. R., and Ewald, A. J. (2014). Three-dimensional organotypic culture: Experimental models of mammalian biology and disease. *Nat. Rev. Mol. Cell Biol.* 15, 647–664. doi: 10.1038/nrm3873
- Shastri, V. P., Rahman, N., Martin, I., and Langer, R. (1999). Application of conductive polymers in bone regeneration. *Mater. Res. Soc. Symp. Proc.* 550, 215–219. doi: 10.1557/proc-550-215

- Shi, Y., Sun, L., Wang, M., Liu, J., Zhong, S., Li, R., et al. (2020). Vascularized human cortical organoids (vOrganoids) model cortical development *in vivo*. *PLoS Biol.* 18:e3000705. doi: 10.1371/journal.pbio.3000705
- Shin, W., Wu, A., Massidda, M. W., Foster, C., Thomas, N., Lee, D.-W., et al. (2019). A Robust longitudinal co-culture of obligate anaerobic gut microbiome with human intestinal epithelium in an anoxic-oxic interface-on-a-chip. *Front. Bioeng. Biotechnol.* 7:13. doi: 10.3389/fbioe.2019.00013
- Shkarina, S., Shkarin, R., Weinhardt, V., Melnik, E., Vacun, G., Kluger, P., et al. (2018). 3D biodegradable scaffolds of polycaprolactone with silicate-containing hydroxyapatite microparticles for bone tissue engineering: high-resolution tomography and *in vitro* study. *Sci. Rep.* 8:8907. doi: 10.1038/s41598-018-27097-7
- Silva, S. S., Fernandes, E. M., Pina, S., Silva-Correia, J., Vieira, S., Oliveira, J. M., et al. (2017). "2.11 polymers of biological origin," in *Comprehensive Biomaterials II*, ed P. Ducheyne (Elsevier), 228–252. Available online at: <https://www.sciencedirect.com/referencework/9780081006924/comprehensive-biomaterials-ii>
- Simian, M., and Bissell, M. J. (2017). Organoids: a historical perspective of thinking in three dimensions. *J. Cell Biol.* 216, 31–40. doi: 10.1083/jcb.201610056
- Simon, K. A., Mosadegh, B., Minn, K. T., Lockett, M. R., Mohammady, M. R., Boucher, D. M., et al. (2016). Metabolic response of lung cancer cells to radiation in a paper-based 3D cell culture system. *Biomaterials* 95, 47–59. doi: 10.1016/j.biomaterials.2016.03.002
- Simpson, K. L., Stoney, R., Frese, K. K., Simms, N., Rowe, W., Pearce, S. P., et al. (2020). A biobank of small cell lung cancer CDX models elucidates inter- and intratumoral phenotypic heterogeneity. *Nat. Cancer* 1, 437–451. doi: 10.1038/s43018-020-0046-2
- Sitarski, A. M., Fairfield, H., Falank, C., and Reagan, M. R. (2018). 3D tissue engineered *in vitro* models of cancer in bone. *ACS Biomater. Sci. Eng.* 4, 324–336. doi: 10.1021/acsbomaterials.7b00097
- Snyder, S., DeJulius, C., and Willits, R. K. (2017). Electrical stimulation increases random migration of human dermal fibroblasts. *Ann. Biomed. Eng.* 45, 2049–2060. doi: 10.1007/s10439-017-1849-x
- Sobrinho, A., Phan, D. T. T., Datta, R., Wang, X., Hachey, S. J., Romero-López, M., et al. (2016). 3D microtumors *in vitro* supported by perfused vascular networks. *Sci. Rep.* 6:31589. doi: 10.1038/srep31589
- Sontheimer-Phelps, A., Hassell, B. A., and Ingber, D. E. (2019). Modelling cancer in microfluidic human organs-on-chips. *Nat. Rev. Cancer* 19, 65–81. doi: 10.1038/s41568-018-0104-6
- Sood, D., Tang-Schomer, M., Pouli, D., Mizzoni, C., Raia, N., Tai, A., et al. (2019). 3D extracellular matrix microenvironment in bioengineered tissue models of primary pediatric and adult brain tumors. *Nat. Commun.* 10:4529. doi: 10.1038/s41467-019-12420-1
- Sorushanova, A., Delgado, L. M., Wu, Z., Shologu, N., Kshirsagar, A., Raghunath, R., et al. (2019). The collagen suprafamily: from biosynthesis to advanced biomaterial development. *Adv. Mater.* 31:1801651. doi: 10.1002/adma.201801651
- Srirusamee, K., Mobini, S., Cassidy, N. J., and Cartmell, S. H. (2019). Direct electrical stimulation enhances osteogenesis by inducing Bmp2 and Spp1 expressions from macrophages and preosteoblasts. *Biotechnol. Bioeng.* 116, 3421–3432. doi: 10.1002/bit.27142
- Stucki, J. D., Hobi, N., Galimov, A., Stucki, A. O., Schneider-Daum, N., Lehr, C. M., et al. (2018). Medium throughput breathing human primary cell alveolus-on-chip model. *Sci. Rep.* 8:14359. doi: 10.1038/s41598-018-32523-x
- Subbiah, R., Hipfinger, C., Tahayeri, A., Athirasala, A., Horsophonphong, S., Thrivikraman, G., et al. (2020). 3D printing of microgel-loaded modular microcages as instructive scaffolds for tissue engineering. *Adv. Mater.* 32:2001736. doi: 10.1002/adma.202001736
- Sun, H., Jia, Y., Dong, H., Dong, D., and Zheng, J. (2020). Combining additive manufacturing with microfluidics: an emerging method for developing novel organs-on-chips. *Curr. Opin. Chem. Eng.* 28, 1–9. doi: 10.1016/j.coch.2019.10.006
- Takahashi, K., Tanabe, K., Ohnuki, M., Narita, M., Ichisaka, T., Tomoda, K., et al. (2007). Induction of pluripotent stem cells from adult human fibroblasts by defined factors. *Cell* 131, 861–872. doi: 10.1016/j.cell.2007.11.019
- Takebe, T., Sekine, K., Enomura, M., Koike, H., Kimura, M., Ogaeri, T., et al. (2013). Vascularized and functional human liver from an iPSC-derived organ bud transplant. *Nature* 499, 481–484. doi: 10.1038/nature12271
- Takebe, T., and Wells, J. M. (2019). Organoids by design. *Science* 364, 956–959. doi: 10.1126/science.aaw7567
- Tam, R. Y., Yockell-Lelièvre, J., Smith, L. J., Julian, L. M., Baker, A. E. G., Choey, C., et al. (2019). Rationally designed 3D hydrogels model invasive lung diseases enabling high-content drug screening. *Adv. Mater.* 31:1806214. doi: 10.1002/adma.201806214
- Tang, M., Xie, Q., Gimple, R. C., Zhong, Z., Tam, T., Tian, J., et al. (2020). Three-dimensional bioprinted glioblastoma microenvironments model cellular dependencies and immune interactions. *Cell Res.* 30, 833–853. doi: 10.1038/s41422-020-0338-1
- Tang-Schomer, M. D., White, J. D., Tien, L. W., Schmitt, L. I., Valentin, T. M., Graziano, D. J., et al. (2014). Bioengineered functional brain-like cortical tissue. *Proc. Natl. Acad. Sci. U.S.A.* 111, 13811–13816. doi: 10.1073/pnas.1324214111
- Taylor, M. W., and Taylor, M. W. (2014). "A history of cell culture," in *Viruses and Man: A History of Interactions* (Cham: Springer International Publishing), 41–52. doi: 10.1007/978-3-319-07758-1\_3
- Terrell, J. A., Jones, C. G., Kabandana, G. K. M., and Chen, C. (2020). From cells-on-a-chip to organs-on-a-chip: Scaffolding materials for 3D cell culture in microfluidics. *J. Mater. Chem. B* 8, 6667–6685. doi: 10.1039/d0tb00718h
- Theocharis, A. D., Skandalis, S. S., Gialeli, C., and Karamanos, N. K. (2016). Extracellular matrix structure. *Adv. Drug Deliv. Rev.* 97, 4–27. doi: 10.1016/j.addr.2015.11.001
- Theodoridis, K., Aggelidou, E., Vavilis, T., Manthou, M. E., Tsimponis, A., Demiri, E. C., et al. (2019). Hyaline cartilage next generation implants from adipose-tissue-derived mesenchymal stem cells: comparative study on 3D-printed polycaprolactone scaffold patterns. *J. Tissue Eng. Regen. Med.* 13, 342–355. doi: 10.1002/term.2798
- Tijore, A., Irvine, S. A., and Sarig, U. (2020). Contact guidance for cardiac tissue engineering using 3D bioprinted gelatin patterned hydrogel. *Biofabrication* 10:025003. doi: 10.1088/1758-5090/aaa15d
- Tong, X. F., Zhao, F. Q., Ren, Y. Z., Zhang, Y., Cui, Y. L., and Wang, Q. S. (2018). Injectable hydrogels based on glycyrrhizin, alginate, and calcium for three-dimensional cell culture in liver tissue engineering. *J. Biomed. Mater. Res. Part A* 106, 3292–3302. doi: 10.1002/jbm.a.36528
- Trautmann, A., Lemke, H.-D., Hellmann, R., Walther, T., and Rüth, M. (2018). "Large 3D direct laser written scaffolds for tissue engineering applications," in *Nanophotonics Australasia 2017*, eds J. W. M. Chon and B. Jia (SPIE), 186. doi: 10.1117/12.2282417
- Trietsch, S. J., Naumovska, E., Kurek, D., Setyawati, M. C., Vormann, M. K., Wilschut, K. J., et al. (2017). Membrane-free culture and real-time barrier integrity assessment of perfused intestinal epithelium tubes. *Nat. Commun.* 8:262. doi: 10.1038/s41467-017-00259-3
- Trisno, S. L., Philo, K. E. D., McCracken, K. W., Catá, E. M., Ruiz-Torres, S., Rankin, S. A., et al. (2018). Esophageal organoids from human pluripotent stem cells delineate Sox2 functions during esophageal specification. *Cell Stem Cell* 23, 501.e7–515.e7. doi: 10.1016/j.stem.2018.08.008
- Tsakmaki, A., Fonseca Pedro, P., and Bewick, G. A. (2017). 3D intestinal organoids in metabolic research: virtual reality in a dish. *Curr. Opin. Pharmacol.* 37, 51–58. doi: 10.1016/j.coph.2017.09.003
- Tsamandouras, N., Chen, W. L. K., Edington, C. D., Stokes, C. L., Griffith, L. G., and Cirit, M. (2017). Integrated gut and liver microphysiological systems for quantitative *in vitro* pharmacokinetic studies. *AAPS J.* 19, 1499–1512. doi: 10.1208/s12248-017-0122-4
- Tziveleka, L. A., Sapalidis, A., Kikionis, S., Aggelidou, E., Demiri, E., Kritis, A., et al. (2020). Hybrid sponge-like scaffolds based on ulvan and gelatin: design, characterization and evaluation of their potential use in bone tissue engineering. *Materials* 13, 1–20. doi: 10.3390/ma13071763
- Uchino, T., Takezawa, T., and Ikarashi, Y. (2009). Reconstruction of three-dimensional human skin model composed of dendritic cells, keratinocytes and fibroblasts utilizing a handy scaffold of collagen vitrigel membrane. *Toxicol. Vitro* 23, 333–337. doi: 10.1016/j.tiv.2008.12.003
- Ullah, M., Liu, D. D., and Thakor, A. S. (2019). Mesenchymal stromal cell homing: mechanisms and strategies for improvement. *iScience* 15, 421–438. doi: 10.1016/j.isci.2019.05.004
- Ullah, S., and Chen, X. (2020). Fabrication, applications and challenges of natural biomaterials in tissue engineering. *Appl. Mater. Today* 20:100656. doi: 10.1016/j.apmt.2020.100656



- Ullah, S., Zainol, I., Chowdhury, S. R., and Fauzi, M. B. (2018). Development of various composition multicomponent chitosan/fish collagen/glycerin 3D porous scaffolds: effect on morphology, mechanical strength, biostability and cytocompatibility. *Int. J. Biol. Macromol.* 111, 158–168. doi: 10.1016/j.ijbiomac.2017.12.136
- Urbischek, M., Rannikmae, H., Foets, T., Ravn, K., Hyvönen, M., and de la Roche, M. (2019). Organoid culture media formulated with growth factors of defined cellular activity. *Sci. Rep.* 9:6193. doi: 10.1038/s41598-019-42604-0
- Vacanti, C. A. (2006). The history of tissue engineering. *J. Cell. Mol. Med.* 10, 569–576. doi: 10.1111/j.1582-4934.2006.tb00421.x
- van der Helm, M. W., Henry, O. Y. F., Bein, A., Hamkins-Indik, T., Crounce, M. J., Leineweber, W. D., et al. (2019). Non-invasive sensing of transepithelial barrier function and tissue differentiation in organs-on-chips using impedance spectroscopy. *Lab Chip* 19, 452–463. doi: 10.1039/C8LC00129D
- Vatine, G. D., Barrile, R., Workman, M. J., Sances, S., Barriga, B. K., Rahnama, M., et al. (2019). Human iPSC-derived blood-brain barrier chips enable disease modeling and personalized medicine applications. *Cell Stem Cell* 24, 995.e6–1005.e6. doi: 10.1016/j.stem.2019.05.011
- Verneti, L., Gough, A., Baetz, N., Blutt, S., Broughman, J. R., Brown, J. A., et al. (2017). Functional coupling of human microphysiology systems: intestine, liver, kidney proximal tubule, blood-brain barrier and skeletal muscle. *Sci. Rep.* 7:42296. doi: 10.1038/srep42296
- Vidal, S. E. L., Tamamoto, K. A., Nguyen, H., Abbott, R. D., Cairns, D. M., and Kaplan, D. L. (2019). 3D biomaterial matrix to support long term, full thickness, immuno-competent human skin equivalents with nervous system components. *Biomaterials* 198, 194–203. doi: 10.1016/j.biomaterials.2018.04.044
- Villasante, A., Sakaguchi, K., Kim, J., Cheung, N. K., Nakayama, M., Parsa, H., et al. (2017). Vascularized tissue-engineered model for studying drug resistance in neuroblastoma. *Theranostics* 7:42296. doi: 10.7150/thno.20730
- Villanave, R., Wales, S. Q., Hamkins-Indik, T., Papafragkou, E., Weaver, J. C., Ferrante, T. C., et al. (2017). Human gut-on-a-chip supports polarized infection of coxsackie B1 virus *in vitro*. *PLoS ONE* 12:e0169412. doi: 10.1371/journal.pone.0169412
- Vining, K. H., and Mooney, D. J. (2017). Mechanical forces direct stem cell behaviour in development and regeneration. *Nat. Rev. Mol. Cell Biol.* 18, 728–742. doi: 10.1038/nrm.2017.108
- Visone, R., Talò, G., Lopa, S., Rasponi, M., and Moretti, M. (2018). Enhancing all-in-one bioreactors by combining interstitial perfusion, electrical stimulation, on-line monitoring and testing within a single chamber for cardiac constructs. *Sci. Rep.* 8:16944. doi: 10.1038/s41598-018-35019-w
- Vodovnik, L., Miklavčič, D., and Serša, G. (1992). Modified cell proliferation due to electrical currents. *Med. Biol. Eng. Comput.* 30, CE21–CE28. doi: 10.1007/BF02446174
- Vyas, D., Baptista, P. M., Brovold, M., Moran, E., Gaston, B., Booth, C., et al. (2018). Self-assembled liver organoids recapitulate hepatobiliary organogenesis *in vitro*. *Hepatology* 67, 750–761. doi: 10.1002/hep.29483
- Wan, A. M. D., Inal, S., Williams, T., Wang, K., Leleux, P., Estevez, L., et al. (2015). 3D conducting polymer platforms for electrical control of protein conformation and cellular functions. *J. Mater. Chem. B* 3, 5040–5048. doi: 10.1039/c5tb00390c
- Wan, X., Li, Z., Ye, H., and Cui, Z. (2016). Three-dimensional perfused tumour spheroid model for anti-cancer drug screening. *Biotechnol. Lett.* 38, 1389–1395. doi: 10.1007/s10529-016-2035-1
- Wang, B., Yang, W., McKittrick, J., and Meyers, M. A. (2016). Keratin: structure, mechanical properties, occurrence in biological organisms, and efforts at bioinspiration. *Prog. Mater. Sci.* 76, 229–318. doi: 10.1016/j.pmatsci.2015.06.001
- Wang, C., Koo, S., Park, M., Vangelatos, Z., Hoang, P., Conklin, B. R., et al. (2020). Maladaptive contractility of 3D human cardiac microtissues to mechanical nonuniformity. *Adv. Healthc. Mater.* 9:1901373. doi: 10.1002/adhm.201901373
- Wang, D. A., Varghese, S., Sharma, B., Strehin, I., Fermanian, S., Gorham, J., et al. (2007). Multifunctional chondroitin sulphate for cartilage tissue-biomaterial integration. *Nat. Mater.* 6, 385–392. doi: 10.1038/nmat1890
- Wang, X., Guo, C., Chen, Y., Tozzi, L., Szymkowiak, S., Li, C., et al. (2020). Developing a self-organized tubulogenesis model of human renal proximal tubular epithelial cells *in vitro*. *J. Biomed. Mater. Res. Part A* 108, 795–804. doi: 10.1002/jbm.a.36858
- Wang, X., Li, W., and Kumar, V. (2006). A method for solvent-free fabrication of porous polymer using solid-state foaming and ultrasound for tissue engineering applications. *Biomaterials* 27, 1924–1929. doi: 10.1016/j.biomaterials.2005.09.029
- Wang, Y. I., Abaci, H. E., and Shuler, M. L. (2017). Microfluidic blood-brain barrier model provides *in vivo*-like barrier properties for drug permeability screening. *Biotechnol. Bioeng.* 114, 184–194. doi: 10.1002/bit.26045
- Wevers, N. R., Kasi, D. G., Gray, T., Wilschut, K. J., Smith, B., van Vught, R., et al. (2018). A perfused human blood-brain barrier on-a-chip for high-throughput assessment of barrier function and antibody transport. *Fluids Barriers CNS* 15:23. doi: 10.1186/s12987-018-0108-3
- Wiksw, J. P., Curtis, E. L., Eagleton, Z. E., Evans, B. C., Kole, A., Hofmeister, L. H., et al. (2013). Scaling and systems biology for integrating multiple organs-on-a-chip. *Lab Chip* 13, 3496–3511. doi: 10.1039/c3lc50243k
- Willerth, S. M., Rader, A., and Sakiyama-Elbert, S. E. (2008). The effect of controlled growth factor delivery on embryonic stem cell differentiation inside fibrin scaffolds. *Stem Cell Res.* 1, 205–218. doi: 10.1016/j.scr.2008.05.006
- Wolter, J. R. (1967). Proliferating pigment epithelium: producing a simple organoid structure in the subretinal space of a human eye. *Arch. Ophthalmol.* 77, 651–654. doi: 10.1001/archophth.1967.00980020653016
- Wu, L., Magaz, A., Huo, S., Darbyshire, A., Loizidou, M., Emberton, M., et al. (2020). Human airway-like multilayered tissue on 3D-TIPS printed thermoresponsive elastomer/collagen hybrid scaffolds. *Acta Biomater.* 113, 177–195. doi: 10.1016/j.actbio.2020.07.013
- Wylie, R. G., Ahsan, S., Aizawa, Y., Maxwell, K. L., Morshead, C. M., and Shoichet, M. S. (2011). Spatially controlled simultaneous patterning of multiple growth factors in three-dimensional hydrogels. *Nat. Mater.* 10, 799–806. doi: 10.1038/nmat3101
- Xu, G., Ding, Z., Lu, Q., Zhang, X., Zhou, X., Xiao, L., et al. (2020). Electric field-driven building blocks for introducing multiple gradients to hydrogels. *Protein Cell* 11, 267–285. doi: 10.1007/s13238-020-00692-z
- Xu, R., Boudreau, A., and Bissell, M. J. (2009). Tissue architecture and function: dynamic reciprocity via extra- and intra-cellular matrices. *Cancer Metastasis Rev.* 28, 167–176. doi: 10.1007/s10555-008-9178-z
- Yan, H. H. N., Siu, H. C., Law, S., Ho, S. L., Yue, S. S. K., Tsui, W. Y., et al. (2018). A comprehensive human gastric cancer organoid biobank captures tumor subtype heterogeneity and enables therapeutic screening. *Cell Stem Cell* 23, 882.e11–897.e11. doi: 10.1016/j.stem.2018.09.016
- Yang, Z., and Xiong, H.-R. (2012). “Culture Conditions and Types of Growth Media for Mammalian Cells,” in *Biomedical Tissue Culture*, eds L. Ceccherini-Nelli and B. Matteoli (Intech). doi: 10.5772/52301
- Yao, T., and Asayama, Y. (2017). Animal-cell culture media: History, characteristics, and current issues. *Reprod. Med. Biol.* 16, 99–117. doi: 10.1002/rmb.2.12024
- Yeste, J., García-Ramírez, M., Illa, X., Guimerà, A., Hernández, C., Simó, R., et al. (2018). A compartmentalized microfluidic chip with crisscross microgrooves and electrophysiological electrodes for modeling the blood-retinal barrier. *Lab Chip* 18, 95–105. doi: 10.1039/c7lc00795g
- Yin, L., Du, G., Zhang, B., Zhang, H., Yin, R., Zhang, W., et al. (2020). Efficient drug screening and nephrotoxicity assessment on co-culture microfluidic kidney chip. *Sci. Rep.* 10:6568. doi: 10.1038/s41598-020-63096-3
- Yin, X., Mead, B. E., Safaei, H., Langer, R., Karp, J. M., and Levy, O. (2016). Engineering stem cell organoids. *Cell Stem Cell* 18, 25–38. doi: 10.1016/j.stem.2015.12.005
- Yip, D., and Cho, C. H. (2013). A multicellular 3D heterospheroid model of liver tumor and stromal cells in collagen gel for anti-cancer drug testing. *Biochem. Biophys. Res. Commun.* 433, 327–332. doi: 10.1016/j.bbrc.2013.03.008
- Yu, J., Peng, S., Luo, D., and March, J. C. (2012). *In vitro* 3D human small intestinal villous model for drug permeability determination. *Biotechnol. Bioeng.* 109, 2173–2178. doi: 10.1002/bit.24518
- Zbinden, A., Marzi, J., Schlünder, K., Probst, C., Urbanczyk, M., Black, S., et al. (2020). Non-invasive marker-independent high content analysis of a microphysiological human pancreas-on-a-chip model. *Matrix Biol.* 85–86, 205–220. doi: 10.1016/j.matbio.2019.06.008
- Zelikin, A. N., Lynn, D. M., Farhadi, J., Martin, I., Shastri, V., and Langer, R. (2002). Erodible conducting polymers for potential biomedical applications. *Angew. Chemie Int. Ed.* 41, 141–144. doi: 10.1002/1521-3773(20020104)41:1<141::AID-ANIE141>3.0.CO;2-V



- Zhang, B., Montgomery, M., Chamberlain, M. D., Ogawa, S., Korolj, A., Pahnke, A., et al. (2016a). Biodegradable scaffold with built-in vasculature for organ-on-a-chip engineering and direct surgical anastomosis. *Nat. Mater.* 15, 669–678. doi: 10.1038/nmat4570
- Zhang, B., and Radisic, M. (2017). Organ-on-a-chip devices advance to market. *Lab Chip* 17, 2395–2420. doi: 10.1039/c6lc01554a
- Zhang, C., Zhao, Z., Abdul Rahim, N. A., van Noort, D., and Yu, H. (2009). Towards a human-on-chip: culturing multiple cell types on a chip with compartmentalized microenvironments. *Lab Chip* 9:3185. doi: 10.1039/b915147h
- Zhang, J., Neoh, K. G., and Kang, E. (2018). Electrical stimulation of adipose-derived mesenchymal stem cells and endothelial cells co-cultured in a conductive scaffold for potential orthopaedic applications. *J. Tissue Eng. Regen. Med.* 12, 878–889. doi: 10.1002/term.2441
- Zhang, J., Wehrle, E., Adamek, P., Paul, G. R., Qin, X. H., Rubert, M., et al. (2020). Optimization of mechanical stiffness and cell density of 3D bioprinted cell-laden scaffolds improves extracellular matrix mineralization and cellular organization for bone tissue engineering. *Acta Biomater.* 114, 307–322. doi: 10.1016/j.actbio.2020.07.016
- Zhang, S., and Wang, H. (2019). Current progress in 3D bioprinting of tissue analogs. *SLAS Technol.* 24, 70–78. doi: 10.1177/2472630318799971
- Zhang, W., Wang, Z., Xie, C., Wang, X., Luo, F., Hong, M., et al. (2019). Scaffold with micro/macro-architecture for myocardial alignment engineering into complex 3D cell patterns. *Adv. Healthc. Mater.* 8:1901015. doi: 10.1002/adhm.201901015
- Zhang, Y., Wang, Q.-S., Yan, K., Qi, Y., Wang, G.-F., and Cui, Y.-L. (2016c). Preparation, characterization, and evaluation of genipin crosslinked chitosan/gelatin three-dimensional scaffolds for liver tissue engineering applications. *J. Biomed. Mater. Res. Part A* 104, 1863–1870. doi: 10.1002/jbm.a.35717
- Zhang, Y. S., Aleman, J., Shin, S. R., Kilic, T., Kim, D., Shaegh, S. A. M., et al. (2017). Multisensor-integrated organs-on-chips platform for automated and continual *in situ* monitoring of organoid behaviors. *Proc. Natl. Acad. Sci. U.S.A.* 114, E2293–E2302. doi: 10.1073/pnas.1612906114
- Zhang, Y. S., Arneri, A., Bersini, S., Shin, S. R., Zhu, K., Goli-Malekabadi, Z., et al. (2016b). Bioprinting 3D microfibrinous scaffolds for engineering endothelialized myocardium and heart-on-a-chip. *Biomaterials* 110, 45–59. doi: 10.1016/j.biomaterials.2016.09.003
- Zhu, W., Ye, T., Lee, S. J., Cui, H., Miao, S., Zhou, X., et al. (2018). Enhanced neural stem cell functions in conductive annealed carbon nanofibrous scaffolds with electrical stimulation. *Nanomedicine Nanotechnology, Biol. Med.* 14, 2485–2494. doi: 10.1016/j.nano.2017.03.018
- Zhu, Y., Wang, L., Yin, F., Yu, Y., Wang, Y., Liu, H., et al. (2017). A hollow fiber system for simple generation of human brain organoids. *Integr. Biol.* 9, 774–781. doi: 10.1039/c7ib00080d
- Zidarič, T., Milojević, M., Gradišnik, L., Kleinschek, K. S., Maver, U., and Maver, T. (2020). Polysaccharide-based bioink formulation for 3D bioprinting of an *in vitro* model of the human dermis. *Nanomaterials* 10:733. doi: 10.3390/nano10040733
- Zohar, B., Blinder, Y., Mooney, D. J., and Levenberg, S. (2018). Flow-induced vascular network formation and maturation in three-dimensional engineered tissue. *ACS Biomater. Sci. Eng.* 4, 1265–1271. doi: 10.1021/acsbomaterials.7b00025

**Conflict of Interest:** The authors declare that the research was conducted in the absence of any commercial or financial relationships that could be construed as a potential conflict of interest.

Copyright © 2021 Moysidou, Barberio and Owens. This is an open-access article distributed under the terms of the Creative Commons Attribution License (CC BY). The use, distribution or reproduction in other forums is permitted, provided the original author(s) and the copyright owner(s) are credited and that the original publication in this journal is cited, in accordance with accepted academic practice. No use, distribution or reproduction is permitted which does not comply with these terms.



# Foreign Body Reaction to Implanted Biomaterials and Its Impact in Nerve Neuroprosthetics

Alejandro Carnicer-Lombarte<sup>1</sup>, Shao-Tuan Chen<sup>1</sup>, George G. Malliaras<sup>1\*</sup> and Damiano G. Barone<sup>1,2\*</sup>

<sup>1</sup> Electrical Engineering Division, Department of Engineering, University of Cambridge, Cambridge, United Kingdom, <sup>2</sup> Division of Neurosurgery, Department of Clinical Neurosciences, University of Cambridge, Cambridge, United Kingdom

## OPEN ACCESS

### Edited by:

Elisa Castagnola,  
University of Pittsburgh, United States

### Reviewed by:

Jennifer Patterson,  
Instituto IMDEA Materiales, Spain  
PaYaM ZarrinTaj,  
Oklahoma State University,  
United States

### \*Correspondence:

George G. Malliaras  
gm603@cam.ac.uk  
Damiano G. Barone  
dgb36@cam.ac.uk

### Specialty section:

This article was submitted to  
Biomaterials,  
a section of the journal  
Frontiers in Bioengineering and  
Biotechnology

**Received:** 28 October 2020

**Accepted:** 19 March 2021

**Published:** 15 April 2021

### Citation:

Carnicer-Lombarte A, Chen S-T,  
Malliaras GG and Barone DG (2021)  
Foreign Body Reaction to Implanted  
Biomaterials and Its Impact in Nerve  
Neuroprosthetics.  
Front. Bioeng. Biotechnol. 9:622524.  
doi: 10.3389/fbioe.2021.622524

The implantation of any foreign material into the body leads to the development of an inflammatory and fibrotic process—the foreign body reaction (FBR). Upon implantation into a tissue, cells of the immune system become attracted to the foreign material and attempt to degrade it. If this degradation fails, fibroblasts envelop the material and form a physical barrier to isolate it from the rest of the body. Long-term implantation of medical devices faces a great challenge presented by FBR, as the cellular response disrupts the interface between implant and its target tissue. This is particularly true for nerve neuroprosthetic implants—devices implanted into nerves to address conditions such as sensory loss, muscle paralysis, chronic pain, and epilepsy. Nerve neuroprosthetics rely on tight interfacing between nerve tissue and electrodes to detect the tiny electrical signals carried by axons, and/or electrically stimulate small subsets of axons within a nerve. Moreover, as advances in microfabrication drive the field to increasingly miniaturized nerve implants, the need for a stable, intimate implant-tissue interface is likely to quickly become a limiting factor for the development of new neuroprosthetic implant technologies. Here, we provide an overview of the material-cell interactions leading to the development of FBR. We review current nerve neuroprosthetic technologies (cuff, penetrating, and regenerative interfaces) and how long-term function of these is limited by FBR. Finally, we discuss how material properties (such as stiffness and size), pharmacological therapies, or use of biodegradable materials may be exploited to minimize FBR to nerve neuroprosthetic implants and improve their long-term stability.

**Keywords:** foreign body reaction, nerve neuroprosthetics, neural implants, neural interface, peripheral nerve stimulation, biocompatibility

## INTRODUCTION

Implantable devices constitute a class of treatments for disease or dysfunction with unique therapeutic potential. By remaining implanted for long periods of time while delivering a therapy directly into the affected tissue, implants can target the source of a dysfunction with great accuracy and for as long as required. One of the most versatile class of implants are nerve neuroprosthetics: implantable devices which interface with the peripheral nerves of the body. Nerves serve as communication bridges between the brain and all peripheral structures, transmitting information between the two. Whether by activating nerves through electrical stimulation or by reading their electrical signals, nerve neuroprosthetics offer a myriad of applications such as the control

of bladder function (Brindley et al., 1982), management of depression (Nemeroff et al., 2006), and restoration of sensory perception in amputees (D'Anna et al., 2019). While implantable technologies—and in particular nerve neuroprosthetics—have extensively evolved over the last few decades by drawing on advancements in biomaterials and manufacturing techniques, the clinical use of implants continues to be severely hampered by the challenges arising from the hostile environment of the body.

The aim of this review is to highlight one of the major challenges to the clinical translation of implantable materials and devices: the foreign body reaction (FBR). The slow onset of this reaction triggered by the body and its dynamic profile (beginning with an acute inflammatory attack and transitioning to a long-term fibrotic response) make it difficult to predict and test for during the design and development of implantable devices. Research often focuses on the optimisation of implantable technologies for good function over a period of days to weeks after implantation. While it is impractical to test new technologies for longer periods of time at every step, clinical devices have to remain implanted in human patients for years or decades. In order to facilitate bench-to-bedside translation of new technologies, it is therefore crucial to consider the effects that FBR will have on both the implanted device and the surrounding tissue.

In this review we present an overview of the cellular events leading to and maintaining FBR in order to provide an understanding of the processes involved in this reaction and the challenges presented to implanted devices, and discuss some of the general design principles that can be followed to minimize the impact of FBR. We discuss the impact of FBR in the emerging field of nerve neuroprosthetics—how nerve neuroprosthetic designs have evolved over the years and addressed the challenges posed by FBR. Finally, we look at the future of the field by discussing novel strategies being developed to combat FBR to implants, and how these may be implemented in nerve neuroprosthetic devices.

## IMPLANTATION OF BIOMATERIALS AND THE FOREIGN BODY REACTION

Foreign body reaction (FBR) is an unavoidable process which takes place whenever any material becomes implanted into the body. The process of implantation injures the tissue around the foreign object, which triggers an inflammatory process. Over a period of weeks to months this inflammatory process develops into a fibrotic response, which envelops and

isolates the implanted material. When the foreign material is implanted with the aim of delivering a therapy, both the acute (predominantly inflammatory) and chronic (fibrotic) stages of FBR pose significant challenges to its integrity and therapeutic function. The complex timeline of FBR is summarized in **Figure 1**, and exemplified in **Figure 2**.

### Acute FBR

The acute phase of FBR begins immediately after implantation. The tissue damage and extravasation of blood which inevitably occurs during the implantation process triggers an immediate rush of inflammatory-mediating cells to the area. Within seconds of implantation, proteins—many of which are derived from extravasated blood, such as albumin and fibrinogen—become non-specifically adsorbed to the surface of the implant (**Figure 1**—protein binding). This layer of proteins becomes a provisional matrix, through which cells gathering in the area can identify and interact with the foreign body. As time progresses, proteins of this provisional matrix undergo a dynamic process of adsorption-desorption, through which the smaller proteins which are initially found around the implant surface (such as albumin) are progressively replaced by larger ones. This process—known as the Vroman effect—can vary in protein composition and time course for different implanted materials, leading to differences in FBR across different materials even at this early stage (Wilson et al., 2005; Xu and Siedlecki, 2007).

The implantation process marks the beginning of a cascade of cellular events that make up FBR. Within minutes of implantation, neutrophils—the early responders in any type of tissue injury—migrate into the area. Neutrophils adhere to the protein layer surrounding the implant and begin to release factors which promote the progression of the inflammatory process (such as reactive oxygen species and proteolytic enzymes, **Figure 1**—neutrophil recruitment, **Figure 2**). Together with similar chemical signals resulting from blood clotting and mast cell activation, these factors increase vascular permeability and attract monocytes into the site of implantation. Once arrived, monocytes begin to differentiate into macrophages, which in turn proliferate and populate the lesion (**Figure 1**—monocyte recruitment and differentiation to macrophages, **Figure 2**). Within two days of implantation the initial wave of neutrophils has completely disappeared to give way to a population of macrophages (Anderson et al., 2008; Franz et al., 2011), which self-sustains itself by continuously proliferating and releasing chemoattractants that recruit further macrophages. These macrophages also mediate the core of the inflammatory response, releasing pro-inflammatory actors such as TNF $\alpha$  (tumor necrosis factor  $\alpha$ ), and interleukins IL-1b, IL-6, and IL-8 (Jones et al., 2007; Mesure et al., 2010). Up to this stage the inflammatory response to device implantation is very similar to that occurring in any injury—neutrophils rush to the area and recruit macrophages, which first eliminate invading threats and then mediate tissue repair. However, as macrophages populate the site of implantation, this initial acute inflammatory response develops into FBR.

As macrophages populate the lesion site they begin to adhere to and cover the exposed surface of the implant. This

**Abbreviations:** CNS, Central nervous system; DAPI, 4',6-diamidino-2-phenylindole; ECM, Extracellular matrix; FBGC, Foreign body giant cell; FBR, Foreign body reaction; FINE, Flat interface nerve electrode; IL-1 $\beta$ , Interleukin 1 beta; LIFE, Longitudinally implanted intrafascicular electrode; NF, Neurofilament; PDGF, Platelet-derived growth factor; PDMS – Polydimethylsiloxane; PET, Polyethylene terephthalate; PLA, Poly(lactic acid); PLGA, Poly(lactic-co-glycolic acid); PMMA, Poly(methyl methacrylate); PNS, Peripheral nervous system; ROS, Reactive oxygen species; SEM, Scanning electron microscope; SPINE, Slowly penetrating interfascicular nerve electrode; TGF- $\beta$ , Transforming growth factor beta; TIME, Transverse intrafascicular multichannel electrode; TNF $\alpha$ , Tumor necrosis factor alpha; VEGF, Vascular endothelial growth factor.

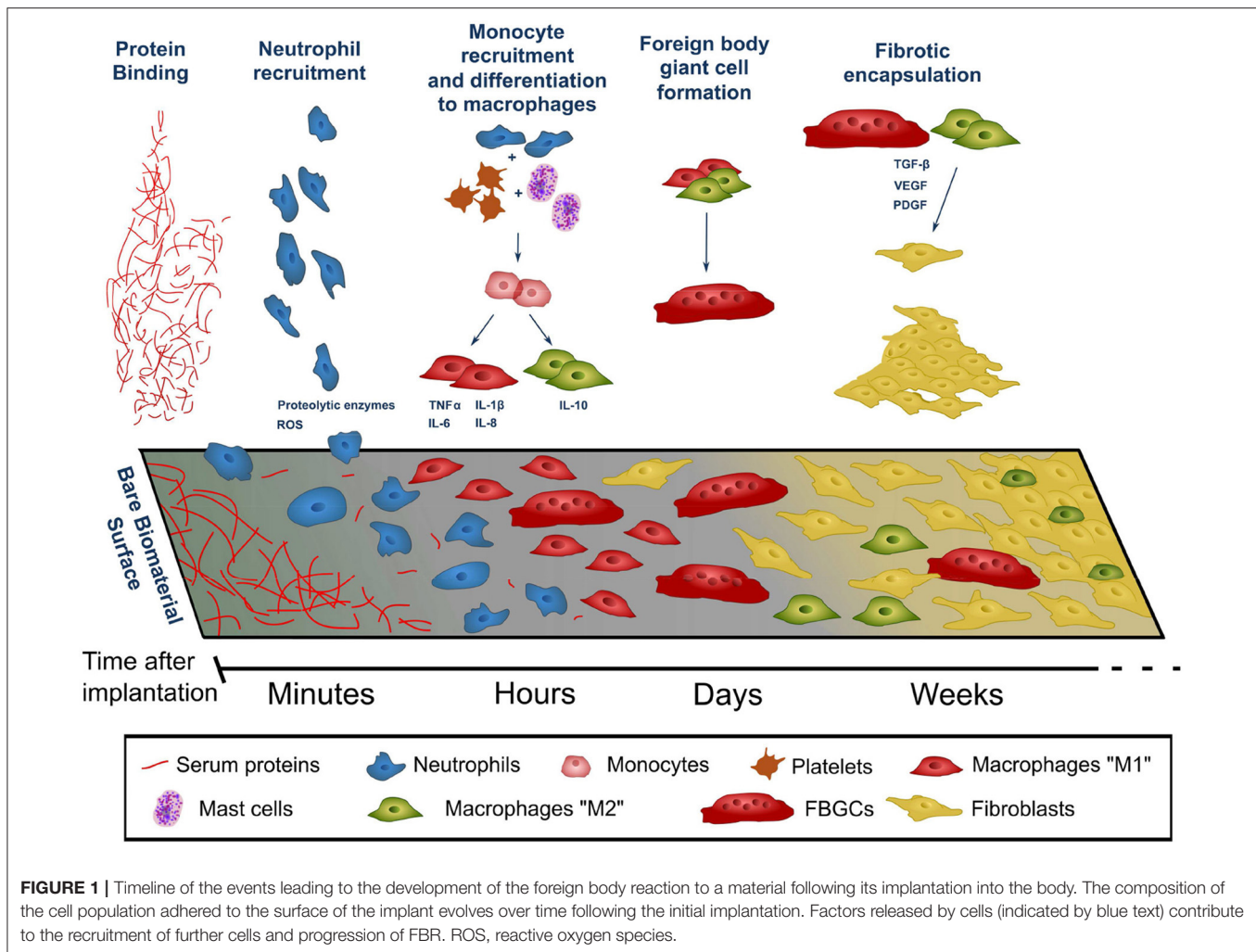


**FIGURE 1 |** Timeline of the events leading to the development of the foreign body reaction to a material following its implantation into the body. The composition of the cell population adhered to the surface of the implant evolves over time following the initial implantation. Factors released by cells (indicated by blue text) contribute to the recruitment of further cells and progression of FBR. ROS, reactive oxygen species.

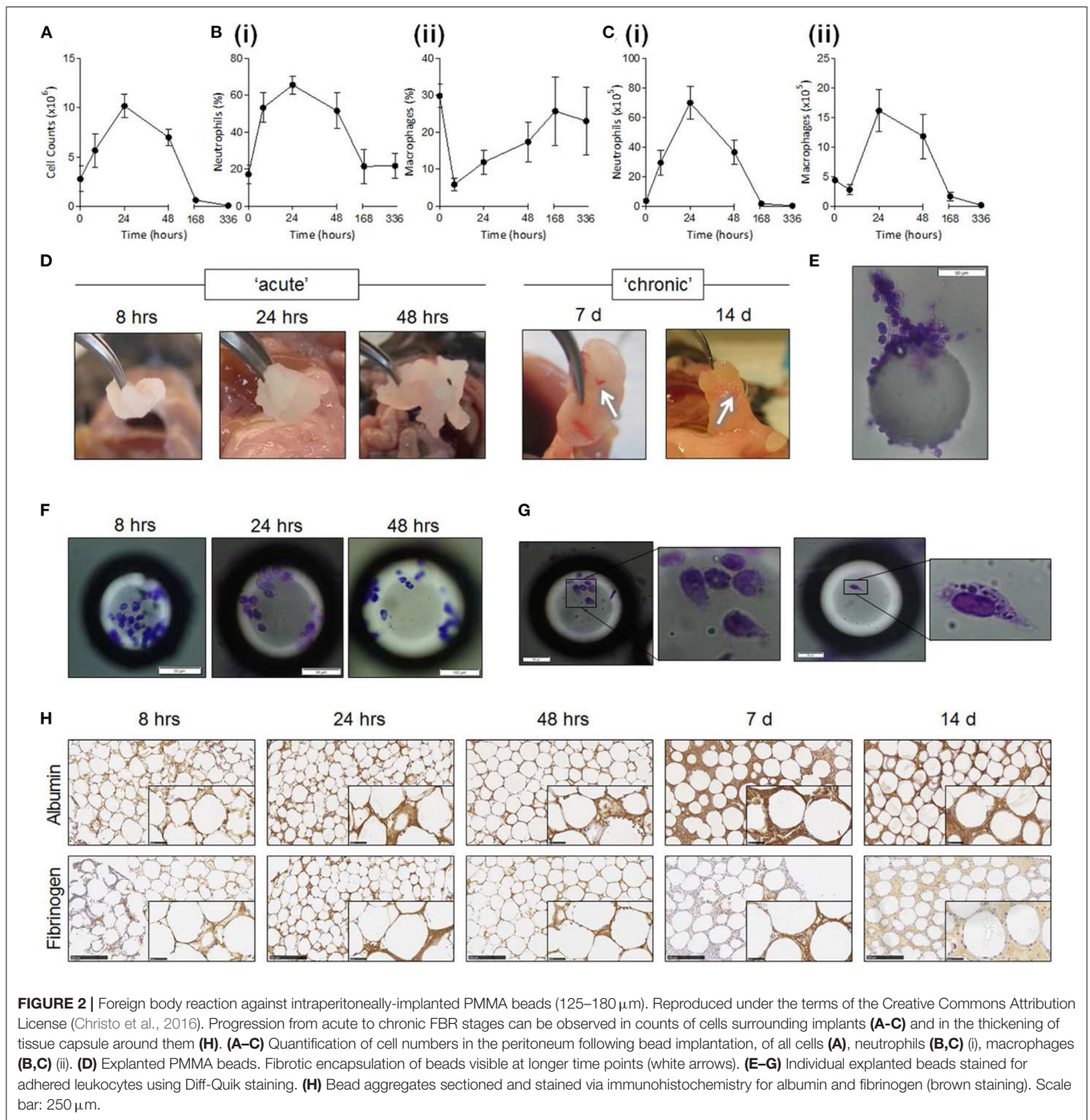
adhesion process is thought to be a critical component of FBR initiation, and occurs through integrins—a broad class of transmembrane proteins which bind to other proteins of the tissue environment—that specifically bind to the proteins adsorbed to the implant's surface. In particular,  $\alpha$ M $\beta$ 2 integrin is considered crucial for this initial adhesion stage as it specifically binds to serum proteins of the implant surface such as fibronectin and fibrinogen (Anderson et al., 2008). Following this initial adhesion stage macrophages undergo cytoskeletal remodeling. Bound macrophages flatten over the surface of the implant in an attempt to engulf and phagocytose it, and extend podosomes—structures specialized in proteolysis and extracellular matrix remodeling. Bound and activated macrophages also secrete chemoattractive factors which continue to recruit macrophages even after the initial implantation injury has resolved (Crowe et al., 2000).

The macrophage layer forming around the implant creates a defined and isolated space. Being unable to phagocytose the entire implant due to its large size, macrophages instead secrete factors into this space in an attempt to break down the foreign body and instead phagocytose the resulting

fragments. The factors released by macrophages as a result of this frustrated phagocytosis include degrading enzymes and reactive oxygen species (Hansen and Mossman, 1987; Anderson, 2001). This macrophage attack poses a significant challenge to implant stability. Otherwise stable biomaterials can exhibit surface degradation and cracking when exposed to the hostile inflammatory environment created by macrophages (Labow et al., 2001; Wiggins et al., 2001), which may cause a breakdown of the implant or the leaching of toxic species into the tissue from the underlying layers.

If macrophages successfully degrade and phagocytose the implant during this acute phase of FBR, the reaction ends, and the tissue slowly returns to normal. Some implantable devices are designed to exploit this inflammatory process to degrade after they have carried out their therapeutic role. A common example of this are regeneration conduits: implants inserted into lesioned tissue designed to guide tissue regrowth and be degraded as the tissue heals (Arslantunali et al., 2014). In many cases, however, implants are required to remain implanted indefinitely to continue carrying out their therapeutic role. When in these cases macrophages





fail to degrade the implant, FBR transitions into its chronic stage.

## Chronic FBR

The chronic phase of FBR is characterized by a transition from solely inflammatory to a fibrotic process. In contrast to the direct challenges to an implant's survivability posed by acute FBR, the chronic stage of FBR involves the encapsulation of the implant in a layer of fibrous tissue. This fibrotic layer acts as a

barrier between the implant and the host tissue into which it was implanted, and can greatly difficult the delivery of any therapy into the surrounding tissue. FBR progressively transitions into its chronic fibrotic stage over the course of weeks after implantation and, unless the implant is destroyed or removed, it remains active indefinitely.

During the transition to the chronic stage of FBR macrophages switch from a pro-inflammatory activation phenotype (M1 macrophages) to an anti-inflammatory and tissue generation

phenotype (M2 macrophages) (Mantovani et al., 2004; Lawrence and Natoli, 2011; Sridharan et al., 2015). This phenotypic transition is often observed as part of the normal wound healing process, marking the switch from the elimination of foreign threats in an injury to the healing of the tissue (Brown et al., 2012; Hesketh et al., 2017). During FBR, however, M2 macrophages instead play a role in the formation of a fibroblast and ECM-rich capsule that covers and isolates the implant.

M2 macrophages become central orchestrators of fibrosis during FBR, attracting and organizing fibroblasts to the implant's surface. M2 macrophages decrease inflammatory activity by releasing anti-inflammatory cytokines such as IL-10 (Klopfleisch, 2016). TGF- $\beta$  released by these macrophages attracts local fibroblast populations, and induces their activation on arrival (Ignatz and Massagué, 1986). These activated fibroblasts adhere to the implant's surface and begin depositing layers of extracellular matrix proteins (**Figure 1**—fibrotic encapsulation). The activation of fibroblasts involves their transdifferentiation into myofibroblasts—a cell type also responsible for the formation of scar tissue and commonly found in wound healing (Hinz et al., 2007). PDGF—also released by macrophages—induces the proliferation of myofibroblasts, which over time cover the entire surface of the implant (Bonner, 2004).

A hallmark of FBR is also the fusion of macrophages into polynucleate foreign body giant cells (FBGCs) on the surface of the implant. Within days of implantation macrophages adhered to the implant begin to fuse with each other into much larger cells (**Figure 1**—foreign body giant cell formation), capable of phagocytosing larger particles ( $> 10\ \mu\text{m}$ , in contrast to the  $< 5\ \mu\text{m}$  that macrophages can phagocytose) (Anderson et al., 2008). The dynamics of the fusion process of macrophages into FBGCs appears to be tightly tied to the composition of the layer of proteins adsorbed to the implants surface, and therefore to the properties of the material itself (McNally and Anderson, 2002). While capable of phagocytosing larger particles than their non-fused counterparts, FBGCs release similar degradative and chemoattractive factors, and do not appear to play a unique role in FBR. Their striking morphology, almost exclusive to FBR, is however a useful tool for the identification of this reaction in tissue samples in both research and clinic.

The combination of macrophages, fibroblasts, and laid down extracellular matrix build up to create and entirely new tissue—the FBR capsule. As the capsule develops into a new tissue compartment new blood vessels have to extend into it in order to supply it with nutrients. VEGF and PDGF, released by the capsule tissue as it becomes anoxic, act as pro-angiogenic factors drawing in newly-forming blood vessels (Luttikhuisen et al., 2006). Further cell proliferation and ECM deposition allow the capsule to progressively thicken over months, until the implant becomes isolated from the surrounding tissue (**Figure 2**). The capsule eventually reaches a steady-state where macrophage activity is no longer intense enough to continue driving fibrosis further away from the implant. The thickness of the capsule and the time needed to reach this point varies greatly, and depends on multiple factors such as implant materials, size of implant, and location in the body. However, the capsule remains a living tissue—since the source of FBR remains present the capsule is

capable of regrowing if damaged or removed, and can adapt if the properties of the enclosed implant change.

It is worth noting that the described process of FBR can differ in certain tissues. The most notable example is the central nervous system. Due to the tight control the body exerts over cell and molecule crossing from the bloodstream into the central nervous system, FBR here is driven by different cell types. Namely, inflammation is mediated by CNS-resident microglia (rather than macrophages), while fibrosis is driven by astrocytes instead of fibroblasts (Polikov et al., 2005; Salatino et al., 2017). Despite these differences, the general principles underlying FBR and the consequences (formation of a fibrotic capsule, inflammatory damage to the surrounding tissue) still apply (Polikov et al., 2005; Salatino et al., 2017). Despite the similarities in tissue composition and function that the central and peripheral nervous systems share, FBR in peripheral nerves is not driven by microglia and astrocytes, but by macrophages and fibroblasts like in most other tissues.

The FBR capsule poses a significant challenge to the therapeutic function of implantable devices. While the chronic stage of FBR involves a less aggressive immune attack to the implanted materials, the growing fibrotic capsule forms a physical barrier that interferes with the delivery of agents or sensing of signals in the surrounding tissue. While certain classes of implants—such as those carrying out a structural role, or delivering large amounts of therapeutic agents to large volumes of tissue—are less affected by the FBR capsule, its presence is an increasingly relevant problem. As implantable technologies continue to progress toward more refined devices capable of interacting with ever smaller subsets of tissue, the disruption of the tissue-implant interface by FBR becomes a leading cause of failure (Salatino et al., 2017; Spearman et al., 2018). Moreover, as this failure is likely to occur at chronic implantation timepoints (months), identification of the problem and optimisation of implant design at preclinical testing stages is challenging. Understanding FBR and implementing design choices that account for it therefore becomes a crucial step in the development of medical implants.

While the cellular processes of FBR are well characterized the properties of an implantable material that initially tag it as foreign are not understood. As a result, FBR to implants cannot be entirely avoided. Instead, a successful implant capable of carrying out its therapeutic function for its intended lifetime needs to accommodate some degree of FBR, and implement design choices to ensure that this severity is not exceeded.

## Implant Design Considerations for FBR

FBR is fundamentally tied to tissue trauma (Wang et al., 2015; Klopfleisch and Jung, 2017). Not only is the initial implantation of a device the trigger that begins the cellular events leading to FBR, but subsequent trauma around the implanted device leads to further inflammation and worsens ongoing FBR. Consequently, one of the most effective strategies to reduce FBR is designing implants that minimize tissue trauma.

Implants begin interacting with the body at the moment they undergo insertion into tissue. While implant design is often tailored to the location in the body which it will inhabit

for its therapeutic lifetime, it is important to remember that delivering the implant to that location is a key step with consequences for the device's performance. Tissue damage during implantation is responsible for the initial inflammatory wave attracting cells to the area, and the resulting extravasated blood proteins provide the first interface for the cells to interact with the implant. It is therefore unsurprising that the degree of implantation trauma is linked to the degree of FBR (Wang et al., 2015). While implantation trauma cannot be totally eliminated, implants can be designed accounting for the surgical implantation procedure. For example, some brain probe designs incorporate biodegradable stiff material shanks that enable easy penetration into tissue, degrading thereafter and leaving behind the softer probe (Kozai et al., 2014). Such designs simplify the implantation procedure, eliminating the need for bulkier, more damaging tools which may otherwise be necessary to deliver the probe, and are associated with a lower amount of tissue damage (Kozai et al., 2014). Alternatively, flexible implants can be designed to be combined with purposely-designed shuttle tools for low trauma implantation into tissue (Figure 3). Implants that take into consideration the mechanics of the implantation procedure and ease of surgical handling can minimize implantation trauma and FBR. Strategies not directly related to the implant itself can also aid in reducing implantation trauma, such as targeting of more easily accessible tissues. Imaging-guided surgical systems can be used to avoid major blood vessels and reduce blood extravasation (Spetzger et al., 1995), optimizing the implantation procedure.

Once implanted, devices continue to interact with the surrounding tissue—often in damaging ways. Tissue is subject to continuous motion at various rates and length scales, due to the host's breathing, blood pumping, movement, and locomotion. While implanted devices will also experience these movements, differences in mechanical properties between implant and surrounding tissue will lead to a mismatch in how the two move and deform in response. As implants fail to move together with tissue, the compression and sliding along the interface causes damage to the surrounding tissue (Goldstein and Salcman, 1973; Sharp et al., 2009; Barrese et al., 2016). This not only leads to local inflammation—therefore further exacerbating FBR—but can also permanently destroy the surrounding target tissue which may be the therapeutic target of the implant. This mechanical mismatch is particularly relevant for implants containing electronic components, as silicon-based components are orders of magnitude stiffer than biological tissues. In order to minimize FBR, implants have begun to experience a shift toward soft or flexible designs, capable of mechanically coupling with their local tissue environment. Particularly in neuroprostheses implanted in nervous tissue—some of the softest tissue in the body—implants implementing flexible or stretchable materials can achieve a much lower degree of FBR and tissue damage when chronically implanted (Nguyen et al., 2014; Minev et al., 2015; Lacour et al., 2016; Capogrosso et al., 2018). Smoother implant designs, avoiding sharp corners which can be particularly damaging to tissue when motion between the two occurs, can also be implemented to decrease tissue damage and chronic FBR (Veisheh et al., 2015).

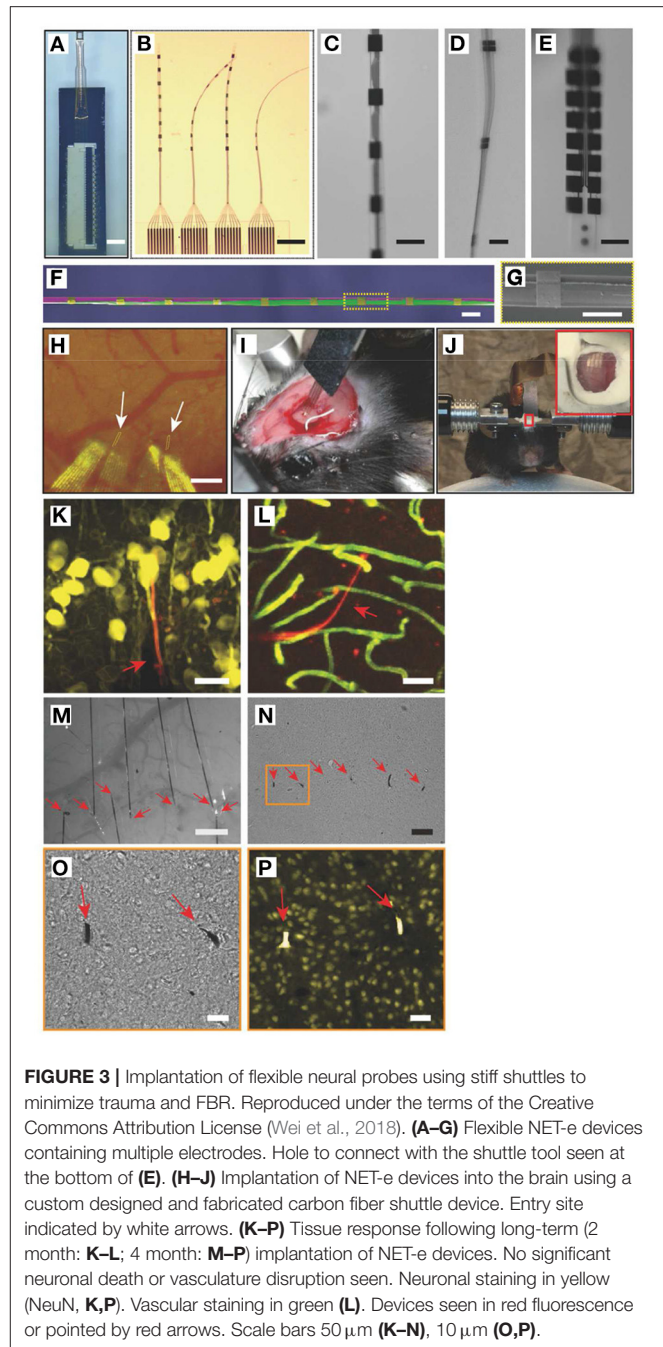


**FIGURE 3 |** Implantation of flexible neural probes using stiff shuttles to minimize trauma and FBR. Reproduced under the terms of the Creative Commons Attribution License (Wei et al., 2018). (A–G) Flexible NET-e devices containing multiple electrodes. Hole to connect with the shuttle tool seen at the bottom of (E). (H–J) Implantation of NET-e devices into the brain using a custom designed and fabricated carbon fiber shuttle device. Entry site indicated by white arrows. (K–P) Tissue response following long-term (2 month: K–L; 4 month: M–P) implantation of NET-e devices. No significant neuronal death or vasculature disruption seen. Neuronal staining in yellow (NeuN, K,P). Vascular staining in green (L). Devices seen in red fluorescence or pointed by red arrows. Scale bars 50  $\mu$ m (K–N), 10  $\mu$ m (O,P).

Material chemistry is also tightly linked to the body response and FBR. Implantable materials need to be carefully chosen to not contain any toxic species which may damage host tissue or promote inflammation—a feature generally englobed under the term “biocompatible” (Williams, 2008). This not only includes material chemistry at the surface of the implant, but also components which may leach from within overtime or become exposed to the body if surface cracking occurs. Over decades of work, the field of implantable material research has selected materials that exhibit good biocompatibility, including polymers (e.g., silicones, polyethylene, polyimide), metals (e.g., platinum,



gold) and ceramics. Certain features of material chemistry can also be exploited to beneficially influence FBR, such as the use of low-fouling materials which prevent FBR-triggering non-specific protein adsorption (**Figure 1**) (Zhang et al., 2013; Xie et al., 2018). A deeper discussion of the interactions between material chemistry and FBR, and of the choices of materials in different implants, are beyond the scope of this review and are discussed elsewhere (Williams, 2008; Hassler et al., 2011; Zarrintaj et al., 2018; Mariani et al., 2019).

In recent decades, more active steps have begun to be taken to directly tackle FBR. Active strategies meant to directly interfere with the cellular events leading to FBR have been implemented in implantable devices since the incorporation of anti-inflammatory compounds in pacemaker leads in the late twentieth century (Mond et al., 2014). Inflammation, however, plays an active role in other biological processes such as repair of tissue damaged around the implantation site, making the use of anti-inflammatory compounds not always possible. In recent years, as the finer molecular network underlying FBR are becoming better understood, new and more specific targets to interfere with FBR have become available. This new generation of active FBR treatments (contrasting with the passive strategies relating to implant design discussed above) are discussed later in this review.

## NERVE NEUROPROSTHETICS AND FBR

Neuroprosthetic implantable devices deliver a therapy to a patient by interfacing and interacting with their nervous tissue. This interface is typically electrical in nature—electrodes in the implant record the action potential activity in the nearby neuronal population, and/or activate nearby neurons through electrical stimulation. While potentially able to address a myriad of conditions, neuroprosthetics are a class of implantable device particularly vulnerable to FBR. The fibrotic capsule forming around the implant not only damages and displaces the target neuronal tissue, but also forms a high-impedance layer that dampens the weak electrical signals produced by neurons and dissipates stimulating electrode currents. FBR is currently the key culprit behind chronically-implanted neuroprosthetic implant failure (Polikov et al., 2005; Salatino et al., 2017), and poses a major hurdle to the clinical translation of new neuroprosthetic technologies.

Neuroprosthetics have frequently been targeted to the central nervous system, for purposes such as the treatment of Parkinson's disease and tremor symptoms (Anderson and Lenz, 2006), restoration of hearing (Colletti et al., 2009), or treatment of epilepsy (Sprengers et al., 2017). The peripheral nervous system, however, is becoming an increasingly attractive target for the delivery of therapies to restore lost or abnormal function. Nerves form a fine network of pathways through which the brain communicates with all structures around the body. By targeting the correct nerve, an implant can activate, modulate, or monitor a specific body structure—such as organs (e.g., bladder, pancreas), muscles (inducing movement), or skin (tactile sensation).

Despite its great therapeutic potential, the peripheral nervous system is particularly vulnerable to FBR. Unlike the brain and spinal cord, which are enclosed in protective bony structure, nerves run between muscles and organs. Body movements, as caused by normal activities such as locomotion or limb movements, subject nerves to constant tensile and compressive forces. When an implant is present, these mechanical challenges can lead to nerve trauma, exacerbating FBR—particularly when stiff implant materials, contrasting with the very soft nerve tissue, are present (Lacour et al., 2016). Additionally, while the CNS is considered an immune privileged site (Louveau et al., 2015) where inflammation and fibrosis are more subdued than elsewhere in the body, the peripheral nervous system develops the typical severity of FBR (Spearman et al., 2018).

Nerve neuroprosthetic technologies are very varied, with different designs eliciting different kinds of responses in tissue (**Table 1**). The degree of nerve invasiveness is often used as a metric to group together different classes of neuroprosthetics. Nerves are complex structures formed by three main types of tissue. The nerve endoneurium houses the axons of neurons, projecting throughout the entire length of the nerve and transmitting signals across the body in the form of action potentials. The endoneurium is bundled by a tightly packed layer of cells, making the nerve perineurium. While some nerves contain a single of these endoneurial bundles, others contain multiple distinct bundles which are individually referred to as nerve fascicles. Finally, the entire nerve is wrapped in a layer of ECM-rich tissue—the epineurium—which provides structural support and mechanical protection to the nerve (**Figure 4**).

Due to this structure, more invasive implant designs with electrodes positioned close to axons in the endoneurium can achieve better electrical recording/stimulation, and may selectively target specific subpopulations of axons (e.g., individual fascicles within the same nerve). More invasive implants, however, can lead to trauma and FBR closer to the fragile nerve axons, potentially leading to the long-term failure of the implant (**Figure 5**). This invasiveness-selectivity trade-off is a key factor influencing the design of nerve neuroprosthetic implants.

Based on the degree of invasiveness nerve neuroprosthetic designs can be categorized into three different groups (summarized in **Figures 4, 5**). Epineurial cuff electrodes are the least invasive, placed around the outside of the nerve without breaching the epineurium. Intraneural penetrating electrodes locally breach the epineurium and perineurium of the nerve, piercing into the endoneurial compartment. Finally, the most invasive group are regenerative nerve electrodes, which exploit the regenerative properties of the peripheral nervous system in order to remain embedded in regrowing nerve tissue following an injury. While there is a wide range of nerve implant designs covering the entire invasiveness-selectivity spectrum, these subdivisions provide a useful and commonly used way of categorizing implants (Navarro et al., 2005) and discuss their implications in the context of FBR.

### Epineurial Cuff Electrodes

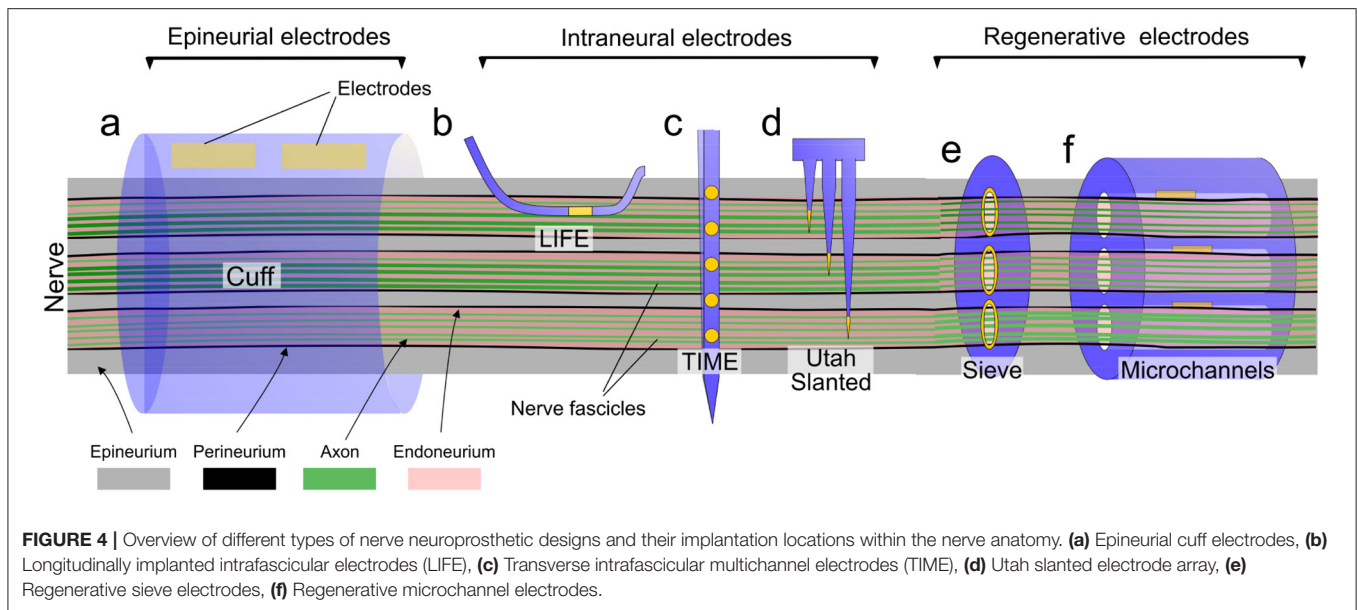
Cuff electrodes are the simplest type of neuroprosthetic design. Cuff implants typically consist of a hollow cylinder of insulating



**TABLE 1** | Summary and comparison of the nerve response and FBR to various classes of nerve neuroprosthetics.

Nerve neuroprosthetic type	Implant material	Implantation period	Nerve tissue and FBR response	Fibrotic area/thickness	Animal model	References
Cuff	Silicone	133–137 days	Nerve structure reorganized to match cylindrical cuff. FBR capsule developed around inner edge of cuff. Collagen-rich tissue growth between FBR capsule and nerve fascicles.	2.13–2.65 mm <sup>2</sup>	Cat	Romero et al., 2001
Spiral cuff	Silicone	28–34 weeks	Nerve morphology deformed by presence of cuff. Abundance of abnormally thinly-myelinated axons. Thinning of the perineurium. Extensive fibrosis in epineurium. FBR capsule around the inside of cuff.	n.m.	Cat	Grill and Mortimer, 2000
Spiral cuff	Silicone	18 hours, 7 days, 1 month	Reshaping of nerve morphology seen as soon as 18 hours. Fibrotic capsule seen from 7 day time point. Upregulation of inflammatory markers at 18 hours and 7 days, which decreased by 1 month.	n.m.	Rat	Vince et al., 2005
Cuff	Hydrogel or PET	6 weeks, 2 months	Soft (hydrogel) cuffs led to no inflammation or any perceivable fibrotic thickening of the nerve epineurium. Stiff (PET) cuffs developed extensive nerve inflammation and fibrosis, and some loss of axons.	n.m.	Rat	Liu et al., 2019, 2020
FINE cuff	Silicone	3 months	FINE cuffs lead to a fibrotic thickening of the epineurium, without axonal damage as long as only moderate pressure is applied.	4.33–4.36 mm <sup>2</sup>	Cat	Leventhal et al., 2006
LIFE	Polyimide	3 months	No substantial nerve or axon damage. Focal but chronic inflammation and scar formation around implant.	0.04 mm <sup>2</sup>	Rat	Lago et al., 2007
TIME	Polyimide	2 months	No significant loss of axons or nerve activity. Thin fibrotic capsule seen surrounding the implant intraneurally.	n.m.	Rat	Badia et al., 2011b
LIFE	Parylene C	Up to 32 weeks	Inflammation (macrophage presence) increased in the nerve following implantation, reaching a maximum at 2 weeks post-implantation. A fibrotic capsule developed surrounding the implant and thickening over time.	~50 μm by 32 weeks	Rat	de la Oliva et al., 2018
SELINE	Polyimide	Up to 165 days	Inflammation (macrophage presence) and fibrosis increased in the weeks after implantation, but decreased by 165 days post-implantation. Loss of axons close to the implant at chronic time points.	~0.07 mm <sup>2</sup> at 28 days, ~0.04 mm <sup>2</sup> at 165 days	Rat	Wurth et al., 2017
Slanted Utah array	Silicon	Up to 350 days	Axonal degeneration in fascicles penetrated by the array shanks. Extensive inflammation surrounding the shanks, particularly close to the base.	n.m.	Cat	Christensen et al., 2014
Sieve	Polyimide	2 to 12 months	Nerve fiber regeneration took place between 2 to 6 months post-implantation. Axon numbers declined (axonal death) 6 to 12 months post-implantation.	n.m.	Rat	Lago et al., 2005
Microchannel	Silicone	3, 6, and 12 months	Axon regeneration through microchannels was robust in the first 3 months. This was followed by a decrease in axon number as the thickness of the fibrotic capsule around the inner channel wall increased.	34 μm	Rat	FitzGerald, 2016

Studies that did not report on the response of tissue following implantation have not been included. N.m., FBR capsule thickness not measured in study; PET, Polyethylene terephthalate; LIFE, longitudinally implanted intrafascicular electrodes; TIME, transverse intrafascicular multichannel electrodes; FINE, flat interface nerve electrode; SELINE, self-opening neural interface.



material containing one or more pair of electrodes along its inner surface, which is wrapped around the outermost layer of the nerve (the epineurium) during surgical implantation. Their low invasiveness, simple design and simpler implantation procedure has made them arguably the most successful type of nerve neuroprosthesis in reaching the human clinic. Their low invasiveness makes them ineffective at selectively recording electrical signals from subsets of axons within a nerve, as the connective tissue of the epineurium dissipates the low amplitude axon action potentials. Cuff electrodes are, however, effective at providing a therapeutic effect through whole nerve electrical stimulation.

Nerve stimulation carried out through implantable nerve cuffs is currently used at the clinical level to treat a variety of conditions. These include sacral nerve stimulation to restore bladder and bowel function (Brindley et al., 1982; Johnston et al., 2005) and peroneal nerve stimulation for the treatment of foot drop (Liberson et al., 1961; Burridge et al., 2007). Electrical stimulation of the vagus nerve—a cranial nerve connecting the brain with many of the body's organs—is also becoming an increasingly popular choice for the treatment of conditions such as epilepsy (Uthman et al., 2004) and depression (Schachter, 2002; Nemeroff et al., 2006). Phrenic nerve stimulation, also known as diaphragm pacing, has also been recently introduced into clinical practice as an aid for ventilation in spinal cord injury patients (Hirschfeld et al., 2008).

Outside of the clinic, nerve recordings using cuff electrodes are also being explored as potential therapeutic avenues. Although more challenging to carry out compared to nerve stimulation due to the distance between electrodes and the weak electrical signals transmitted by axons, with an ECM-rich epineurium separating the two, motor and sensory nerve signals gathered using cuff electrodes have been used to guide and fine-tune prostheses such as artificial limbs in human patients (Micera et al., 2001; Navarro et al., 2005; Raspopovic et al., 2010).

The comparatively large size of cuff electrodes and their ease of use have also made cuff electrodes a popular platform for the development of new neuroprosthetic-related technologies, such as wireless ultrasound-driven nerve stimulation (Piech et al., 2020), self-wrapping designs (Zhang et al., 2019), and self-healing, stretchable devices that accommodate for tissue growth as an animal grows (Liu et al., 2020).

Due to the position in which cuff electrodes are implanted, FBR to these cuffs develops predominantly in the epineurium of the host nerve. While this is useful to avoid damage to the fragile neuronal axons in the endoneurium as a consequence of inflammation, the epineurium already poses a significant barrier to communication between nerve and electrodes. A thickening of the epineurium as part of FBR can dissipate the already weak electrical signals transmitted by axons, limiting the use of these devices for electrical recording applications in long-term implantations (Navarro et al., 2005). This effect can be compounded when the cuff fits the nerve too loosely. Gaps between the nerve epineurium and implant are prone to filling with fibrotic tissue (Romero et al., 2001), and can increase trauma to the nerve due to mechanical shear damage during movement.

While tightly fit cuffs can offer better results, excessive nerve compression can severely impact long-term nerve health. Although the nerve connective tissue absorbs tensile forces along its axis, compressive forces around the nerve are transmitted to the fragile axons in the endoneurium. Nerve compression is associated with axonal death and inflammation (Krarup et al., 1989; Grill and Mortimer, 2000; Vince et al., 2005), which can in turn exacerbate FBR to the implant (Romero et al., 2001). Long-term nerve compression can also contribute to the development of neuropathic pain (Campbell and Meyer, 2006; Yalcin et al., 2014).

Flexible and stretchable materials such as PDMS have been an effective option to build the body of the cuff, able to gently squeeze around the nerve epineurium without excessive

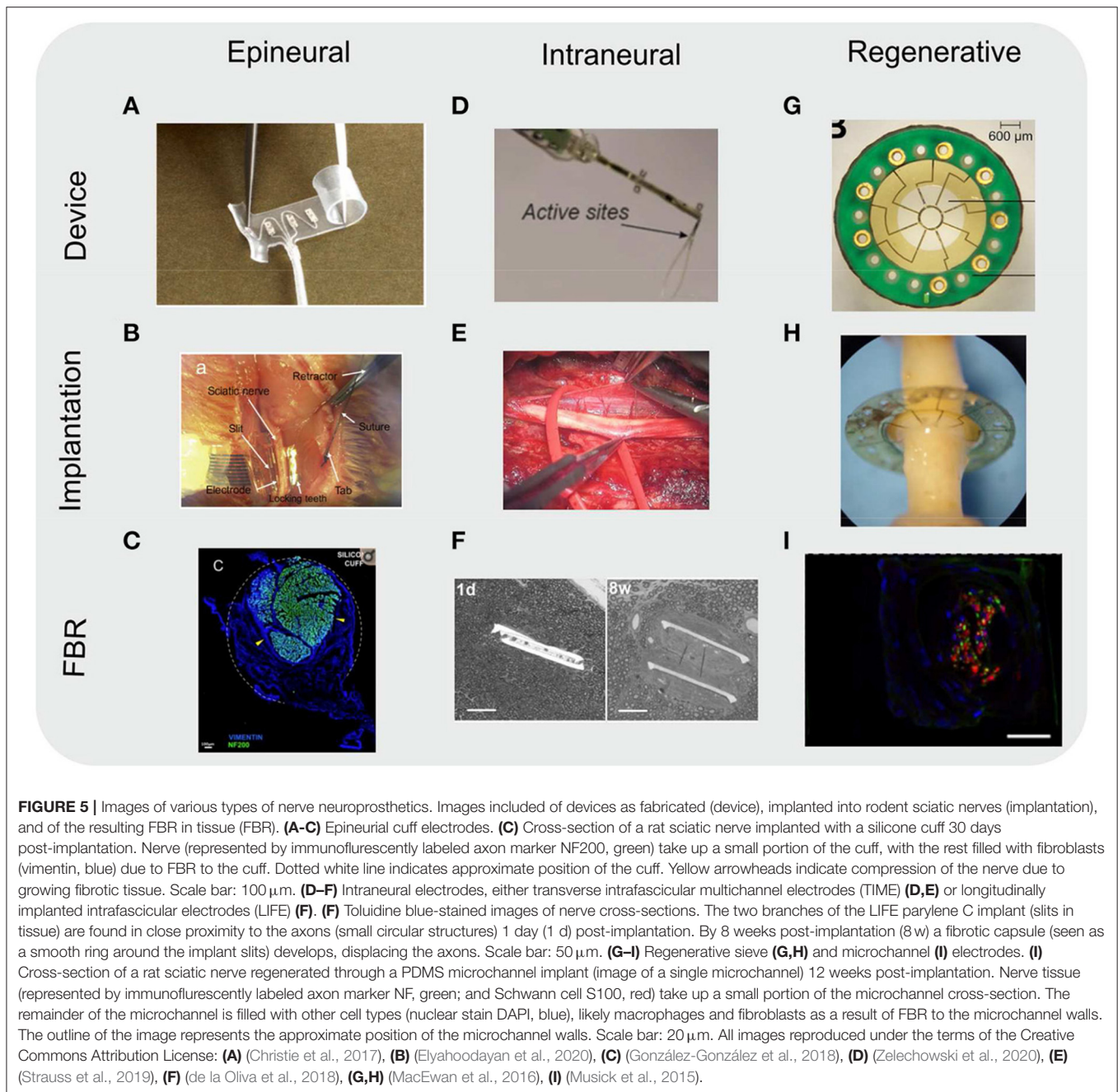
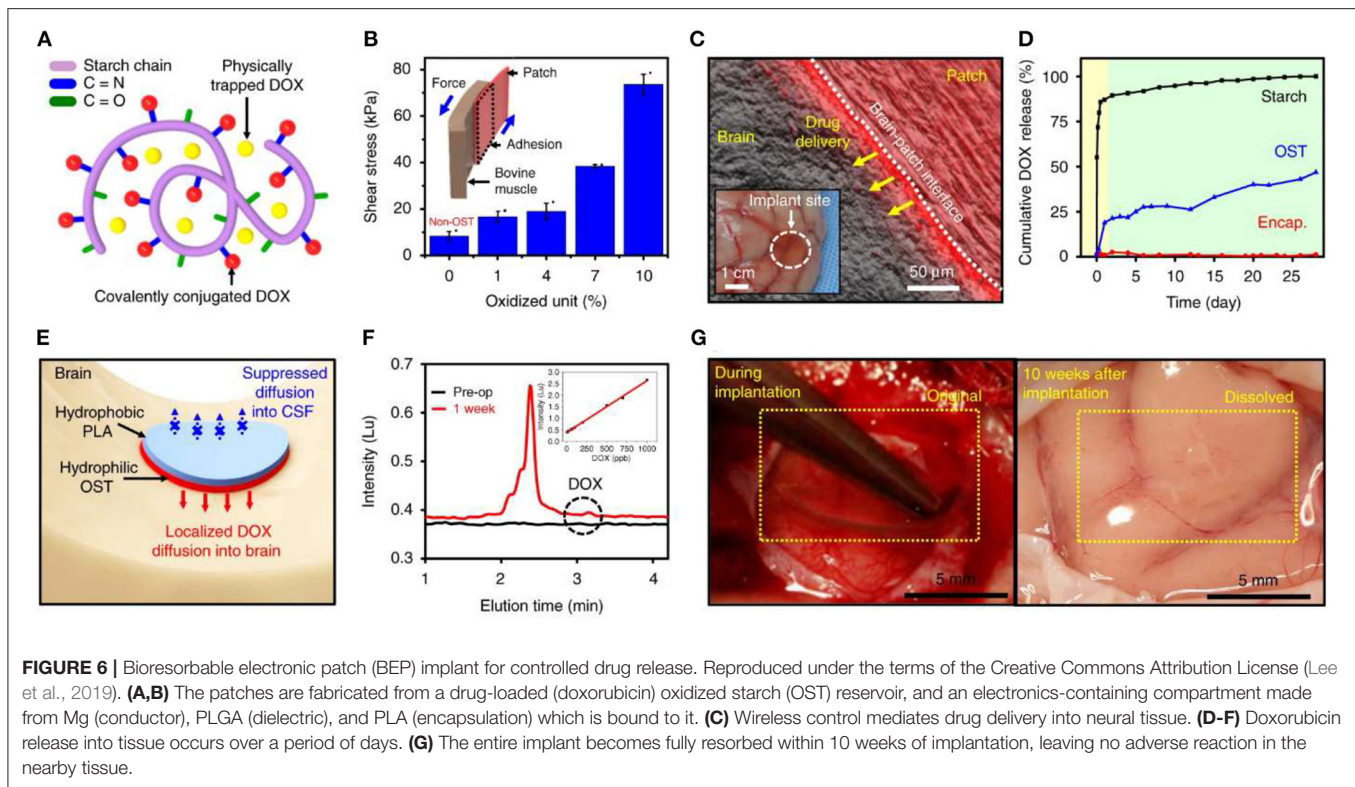


**FIGURE 5 |** Images of various types of nerve neuroprosthetics. Images included of devices as fabricated (device), implanted into rodent sciatic nerves (implantation), and of the resulting FBR in tissue (FBR). **(A–C)** Epineural cuff electrodes. **(C)** Cross-section of a rat sciatic nerve implanted with a silicone cuff 30 days post-implantation. Nerve (represented by immunofluorescently labeled axon marker NF200, green) take up a small portion of the cuff, with the rest filled with fibroblasts (vimentin, blue) due to FBR to the cuff. Dotted white line indicates approximate position of the cuff. Yellow arrowheads indicate compression of the nerve due to growing fibrotic tissue. Scale bar: 100  $\mu\text{m}$ . **(D–F)** Intraneural electrodes, either transverse intrafascicular multichannel electrodes (TIME) **(D,E)** or longitudinally implanted intrafascicular electrodes (LIFE) **(F)**. **(F)** Toluidine blue-stained images of nerve cross-sections. The two branches of the LIFE parylene C implant (slits in tissue) are found in close proximity to the axons (small circular structures) 1 day (1 d) post-implantation. By 8 weeks post-implantation (8 w) a fibrotic capsule (seen as a smooth ring around the implant slits) develops, displacing the axons. Scale bar: 50  $\mu\text{m}$ . **(G–I)** Regenerative sieve **(G,H)** and microchannel **(I)** electrodes. **(I)** Cross-section of a rat sciatic nerve regenerated through a PDMS microchannel implant (image of a single microchannel) 12 weeks post-implantation. Nerve tissue (represented by immunofluorescently labeled axon marker NF, green; and Schwann cell S100, red) take up a small portion of the microchannel cross-section. The remainder of the microchannel is filled with other cell types (nuclear stain DAPI, blue), likely macrophages and fibroblasts as a result of FBR to the microchannel walls. The outline of the image represents the approximate position of the microchannel walls. Scale bar: 20  $\mu\text{m}$ . All images reproduced under the terms of the Creative Commons Attribution License: **(A)** (Christie et al., 2017), **(B)** (Elyahoodayan et al., 2020), **(C)** (González-González et al., 2018), **(D)** (Zelechowski et al., 2020), **(E)** (Strauss et al., 2019), **(F)** (de la Oliva et al., 2018), **(G,H)** (MacEwan et al., 2016), **(I)** (Musick et al., 2015).

compression. From a chemical perspective, PDMS is well characterized to be inert and biocompatible, not releasing toxic species of exacerbating the inflammatory response and being well-suited for long-term implantation (Williams, 2008; Hassler et al., 2011). PDMS is now the material of choice for most nerve cuffs in clinical practice, including those for vagus nerve (Ben-Menachem et al., 2015) and sacral nerve stimulation (Brindley et al., 1982; Johnston et al., 2005). PDMS cuffs develop lower degrees of trauma and FBR than cuffs made from other flexible materials such as metallic meshes (Christensen and Tresco, 2018), matching the pattern seen in other low-stiffness materials

(Liu et al., 2019, 2020). However, deformable substrates such as PDMS pose difficulties for the fabrication of electronics (Lacour et al., 2016). This becomes an increasingly relevant challenge as nerve neuroprosthetics evolve into more elaborate designs, aiming to achieve higher resolution communication with the host nerves.

Despite the sensitivity of nerves to poor-fitting nerve cuffs, certain cuff electrode designs purposely apply compressive forces to the nerve in order to achieve better interfacing. Specifically, the FINE (flat interface nerve electrode) is designed with a flattened, elliptical bore in order to flatten out large cylindrical



nerves. Large sensorimotor nerves often contain axons bundled into separate fascicles each leading to a different muscle, which can each be targeted for better therapeutic selectivity. However, fascicles are typically packed tightly together in the nerve cross-section, and classical cuff designs struggle to selectively stimulate individual fascicles. FINE cuffs are designed to flatten the nerve, distributing its fascicles over a wider cross-section, making them accessible to sets of electrodes lining the inner surface of the cuff. This designed has been used to selectively restore sensory perception in human arm amputee patients (Tan et al., 2014). While excessive compressive forces are associated with axonal death and increased FBR, moderate nerve reshaping with FINE implants does not seem exert sufficient force to cause axon death or more connective tissue deposition than seen in wider nerve cuffs (Tyler and Durand, 2003; Leventhal et al., 2006).

Advances in fabrication technologies are also opening new possibilities for the development of better long-term performing cuff implants. Nerves can be scanned in reconstructed in three dimensions in order to later 3D print cuffs perfectly adapted to their anatomy (Johnson et al., 2015), potentially minimizing mechanical trauma and FBR at the nerve-implant interface. 3D printed implants can be compatible with electrode manufacturing techniques (Haghighashtiani and McAlpine, 2017), opening the door for future perfect-fit epineurial cuff electrodes suitable for clinical use.

## Intraneural Penetrating Electrodes

Intraneural electrodes are designed to penetrate the outer layers of the nerve and position the electrodes in closer proximity to

the axons—often directly inside the endoneurial compartment. The need to penetrate through connective tissue layers in order to reach neuronal tissue places similar design needs to those of penetrating electrodes used in the brain, and indeed some intraneural nerve electrodes stem from designs used in brain applications. Penetrating electrodes are placed in closer proximity to axons and without the presence of electrically insulating connective tissue layers. Their location in the nerve anatomy allows them to carry out good quality electrical recordings, potentially being able to distinguish between signals from different groups of axons within one same nerve fascicle. Being embedded within the nerve tissue, penetrating electrodes are also better anchored to their target tissue which prevents slippage between the two and ensures that the same groups of axons can be monitored over time. While also useful for electrically stimulating small groups of axons within the nerve, the small size of electrodes and the manufacturing techniques used in penetrating devices make them less effective at delivering widespread current for whole nerve activation. For nerve stimulation at the clinical level, epineurial cuffs remain the preferred choice (Navarro et al., 2005).

Penetrating electrodes, however, face a disadvantage in the need to rupture through nerve compartments during implantation. This process not only generates more trauma than an epineurial device, but also localizes the trauma closer to axons. This can not only lead to the development of a fibrotic capsule deep within the nerve tissue, but can also lead to nearby axon death due to the inflammation associated with FBR. Moreover, by remaining implanted within the nerve tissue, shear damage



due to mechanical mismatch between the two becomes a major source of further trauma that can potentially worsen axon death and fibrosis.

While intraneural penetrating electrode designs have not yet reached widespread use in the human clinic, a wide range of designs have been developed over the years in the research environment. Longitudinal-interfascicular electrodes (LIFE), consisting of a long flexible body with a single electrode implanted into the endoneurium of a nerve fascicle with the aid of a rigid needle, were one of the earliest penetrating designs developed (Malmstrom et al., 1998). More recently, updated LIFE designs manufactured using microfabrication technology and containing multiple electrodes along its length have also been developed (thin-film LIFE) (Navarro et al., 2007). LIFE implants are effective for long-term recording and stimulation applications, having for example been used in humans for the recording of volitional limb movement and to elicit skin sensation of touch/pressure (Dhillon et al., 2004, 2005; Micera et al., 2008).

While LIFE implants are limited to interfacing with a single nerve fascicle, transverse intrafascicular multichannel electrodes (TIMEs) are designed to penetrate through the entire nerve cross-section and establish connection with multiple nerve fascicles. By stimulating one or multiple fascicles simultaneously, TIMEs are able to produce a wider range of distinct nerve activation patterns. This can, for example, be used to reproduce a wider range of distinct sensory perceptions in amputee patients (Strauss et al., 2019). TIME implants are also fabricated from flexible materials such as polyimide, and are also inserted with the aid of a microneedle which is removed after surgical implantation (Boretius et al., 2010). TIMEs are able to both stimulate (Badia et al., 2011b) and record from Badia et al. (2016) separate nerve fascicles within nerves independently, and coupled with artificial hand prostheses have been used to restore sensory perception in human hand amputee patients (Raspopovic et al., 2014; D'Anna et al., 2019). Stimulating TIMEs have also been used to restore sensory perception in leg amputees, combined with pressure sensor-equipped leg prosthetics (Petrini et al., 2019).

LIFE and TIME nerve neuroprosthetics share a key similarity in their design: the use of flexible materials. Flexible implants are able to better deform with the nerve tissue, as the two move around together during normal body activity. Flexible implants in general show improved tissue compatibility compared to stiffer equivalents, minimizing trauma and FBR arising from shear damage (Lacour et al., 2016; Salatino et al., 2017). This is particularly relevant for soft and fragile tissues, or tissues which are constantly exposed to movement—two characteristics which apply to the peripheral nervous system. Though LIFE and TIME implants still induce a substantial amount of trauma during the implantation procedure, they elicit a limited degree of FBR. While a thin fibrotic capsule forms around these flexible devices over chronic implantation time points, the degree of fibrosis is mild enough to permit stable long-term recordings, with no widespread inflammation or axon damage seen (Lago et al., 2007; Badia et al., 2011a). The mechanical matching with tissue renders these implants very robust, exhibiting very little damage or delamination after implantation (Cvančara et al.,

2020). Self-deploying anchors can also be incorporated into intraneural designs, minimizing movement and the associated trauma following implantation, as seen with self-opening neural interface (SELINE) devices (Cutrone et al., 2015), and generating minimal FBR (Wurth et al., 2017). Combined with potential improvements in the implantation procedure, flexible penetrating nerve implants such as these hold great potential for long-term therapeutic applications and translation into clinical use, as highlighted by the several recent uses of TIMEs in human patients (D'Anna et al., 2019; Petrini et al., 2019).

Most of the materials used in these flexible devices are chosen to have well-established biocompatibility—being chemically inert to the body and remaining so for long periods of implantation—while also being compatible with thin-film fabrication techniques. Polyimide is particularly popular for nervous system implant applications—including the PNS. Polyimide is biocompatible and exhibits low cytotoxicity *in vitro*, and remains stable for long periods of implantation (Richardson et al., 1993; Rubehn and Stieglitz, 2010; Hassler et al., 2011). Parylene C has recently arisen as a good material option for peripheral nerve devices (de la Oliva et al., 2018), and has a well-established history of biocompatibility and biostability (Chang et al., 2007; Winslow et al., 2010; Hassler et al., 2011).

Stiff material penetrating arrays have also seen widespread use as nerve neuroprosthetics. Utah arrays were developed in the early 1990s as a means to deploy large numbers of electrodes to deep layers of the brain (Normann and Fernandez, 2016), and have since been adapted for use in nerves (Branner and Normann, 2000; Branner et al., 2001). These implants consist of arrays of stiff silicon shanks with individual electrodes exposed at their tips. During implantation the shank array is pierced directly into the neural tissue. The variety fabricated for use in nerves has shanks of variable depth, allowing electrodes to be deployed into different fascicles and giving them the name of slanted Utah arrays. In contrast to other penetrating probes, Utah arrays incorporate up to 100 electrodes which can be deployed across the entire cross-section of the nerve—ensuring that the entire nerve axon population can be interfaced with. Slanted Utah arrays have been used for both stimulation (restoration of sensory perception) and recording (monitoring of motor activity) applications in human hand amputee patients (Clark et al., 2014; Davis et al., 2016; Wendelken et al., 2017). Nerve recordings with these implants were able to guide the movement of a virtual hand prosthesis over a period of 30 days, indicating that robust recordings can still be achieved during the onset of the chronic stages of FBR (Davis et al., 2016).

Despite the success of Utah arrays in producing high quality multi-site recordings in both CNS and PNS, from a long-term stability and FBR perspective these implants are more problematic than other penetrating designs. While as a material silicon is chemically inert and biocompatible, permitting cell growth and not causing particular adverse reactions in tissue over long implantation periods (Bayliss et al., 1999; Shin et al., 2019), its high stiffness leads to poor tissue compatibility when applied to such an invasive format. Utah arrays rupture nerve tissues when implanted for each of the many electrodes it contains, greatly increasing insertion trauma. Moreover, their stiff material

body contributes to greater mechanical shear damage around each of the shanks, worsening long-term trauma and FBR. This mechanical damage is severe enough to damage not only the fragile nervous tissue, but also the probes themselves. In the CNS, a tissue less exposed to movement than peripheral nerves, a study determined that 90% of Utah arrays implanted in non-human primates failed over a 6 year chronic implantation period, with most of failures seen within a year of implantation (Barrese et al., 2016). Slanted Utah arrays implanted into nerves cause large amounts of tissue damage, which over long-term implantation periods lead to larger FBR responses and chronic inflammation (Christensen et al., 2014, 2016).

Slanted Utah arrays continue to be of great value as research tools, and show promise for the translation of new therapies to the clinic. Recently, slanted Utah arrays implanted into the median and ulnar nerves of a hand amputee patient. Through stimulation of the nerves, and in combination with muscle recordings, the patient was able to drive and receive sensory feedback from a bionic hand (George et al., 2019). Despite this and other prior translational successes (Clark et al., 2014; Davis et al., 2016; Wendelken et al., 2017), the large degree of trauma and FBR associated with current Utah array designs poses difficult challenges for their widespread clinical use.

While most penetrating electrodes are designed to pierce directly into the endoneurial compartment, certain designs employ a less invasive approach. Slowly penetrating interfascicular nerve electrodes (SPINs), for example, consist of a nerve cuff incorporating penetrating electrode-equipped flaps over its inner surface, which slowly penetrate into the nerve cross-section after implantation. While piercing into the ECM-rich epineurium, these flaps settle between fascicles and do not pierce the perineurium. By bypassing part of the epineurium, these electrodes achieve a decrease in stimulation threshold and can achieve better selectivity than traditional epineurial cuff designs (Tyler and Durand, 1994, 1997). Although SPIN designs achieve some of the advantages of intrafascicular designs, they can exhibit better long-term stability by localizing fibrosis and inflammation due to FBR to the outer, more robust, layers of the nerve architecture.

On the other end of the spectrum, certain types of nerve neuroprosthetics achieve fascicle recordings by more severely disrupting the tissues of the nerve. Microchannel implants—devices made up of multiple electrode-containing channels designed to each host a subset of the nerve's axons, and more commonly used as regenerative nerve electrodes—have also been used to interface with healthy nerves. Implantation of these devices involves the surgical disruption of the nerve epineurium, followed by the gentle teasing of the axons within into small bundles which are then enclosed within the implant's channels. While the severe implantation trauma caused by the full dissection of the epineurium can lead to axon damage, certain nerves are able to support this implantation procedure (Chew et al., 2013). Such microchannel electrodes have, for example, been implanted in nerves at locations very proximal to the dorsal root ganglia to monitor bladder function in rodents at long-term implantation time points (Chew et al., 2013). However, the implanted nerves experienced a steady loss

of axons over a 3 month period, likely a consequence of the implantation trauma combined with subsequent damage caused by the proximity of the implant walls to the fragile axons. Their good recording properties and ease of use have, however, found use for them in *ex vivo* applications such as nerve-on-a-chip platforms (Gribi et al., 2018).

## Regenerative Nerve Electrodes

The last class of implants are regenerative nerve electrodes, which exploit the regenerative capacity of peripheral nerves in order to embed electrodes deeply into nerve tissue. In contrast to the central nervous system, peripheral nerves are capable of undergoing some degree of regeneration when injured. When a nerve is damaged axons past the lesion site degenerate, while axons proximal to the lesion begin regrowing across it in an attempt to reconnect with their distal target. If an implant containing electrodes is introduced into a nerve lesion, these axons will often grow through the implant as part of their regenerative response. This strategy can be used to position large numbers of electrodes throughout the entire cross-section of the nerve and, once the regenerating axons reconnect to their targets at the distal end of the nerve, the array of electrodes can be used to stimulate or record the electrical activity of small axon subsets.

While regenerative implants are effective at tightly interfacing large numbers of electrodes with a nerve, they are also associated with the largest amount of implantation trauma. Whether occurring accidentally or purposely induced (in research models), regenerative implants require a nerve lesion to be present. Most commonly this is in the form of a full nerve transection, where the two ends of the nerve are cleanly separated and a gap forms between the two (Navarro et al., 2005; Thompson et al., 2015). Lesioning brings with it large amounts of inflammation and fibrosis which, although initially directed toward guiding axon regeneration and repairing the nerve tissue, can later worsen FBR around the implant.

The first widely used type of regenerative nerve neuroprosthetics to be developed were sieve electrodes. Early sieve electrode designs were fabricated from rigid silicon wafers perforated with an array of holes, each of which contained an electrode (Edell, 1986; Akin et al., 1994; Navarro et al., 1996). Silicon is bioinert as a material, permitting cell growth (Bayliss et al., 1999) and remaining stable for long periods of implantation without causing adverse tissue reactions (Shin et al., 2019). However, the high stiffness of silicon can lead to mechanical damage surrounding silicon implants. Silicon sieves were observed to lead to extensive axon death after implantation and were replaced by more flexible materials such as polyimide in later designs (Shimatani et al., 2003; Ramachandran et al., 2006). Upon implantation into a transected nerve axons would regenerate through the sieve's holes, allowing stimulation or monitoring of their electrical activity. While holes with diameters as small as individual axons (2–10  $\mu\text{m}$ ) could theoretically have allowed individual recordings of single regenerated axons, axon regeneration fails through such small holes (Navarro et al., 1998). Instead, holes of 40–65  $\mu\text{m}$  were typically preferred (Navarro et al., 1998). Sieve electrodes implanted into regenerating nerves in rodent models have been successfully used to record gustatory

(Shimatani et al., 2003) as well as sensorimotor (Ramachandran et al., 2006) signals weeks after implantation. More recently, additional features such as the incorporation of porous “transit” zones in the center of the sieve and the use of glial derived neurotrophic factor (GDNF) to improve nerve regeneration and survival have been implemented (MacEwan et al., 2016).

Aside from the injury-associated trauma related to the implantation of a regenerative implant, sieve electrodes are also vulnerable to further long-term tissue trauma and FBR. The narrow holes through which axons regenerate become a choke point where trauma and fibrosis can easily develop. Implanted sieve electrodes made of polyimide experience a steady increase in axonal numbers over the first 6 months post-implantation, as all axons slowly regenerate through the implant and into the distal nerve stump. This is, however, followed by a sharp decline in axon numbers at the 12 month time point (Lago et al., 2005). Inflammation, characterized by an accumulation of macrophages around the edges of the sieve holes, appears to peak 6 months into implantation followed by a moderate decline—possibly as the holes become filled with fibroblasts and ECM (Klinge et al., 2001).

A more recent evolution of the sieve electrode design are microchannel electrodes, composed of a solid cylinder of material perforated by an array of long channels, each housing within them one or more electrodes. Microchannel devices exploit the fact that fully transected nerves are capable of regenerating across up to centimeter-long gaps left between the nerve stumps (Deal et al., 2012). Microchannel devices are typically several millimeters in length, and have channels of  $\sim 100\ \mu\text{m}$  diameter. While microchannel electrodes might at first look like a longitudinally-extended version of the sieve electrode design, microchannels offer a number of advantages. The walls of the microchannels—made from insulating materials—serve to amplify the weak axon electrical signals, and shield the electrodes from external noise (Fitzgerald et al., 2008). While originally made from polyimide (FitzGerald et al., 2012), more recent microchannel designs are built from stretchable and softer materials such as PDMS (Musick et al., 2015; Lancashire et al., 2016). Microchannel devices have been used to record sensorimotor nerve signals in rodent models (Gore et al., 2015; Srinivasan et al., 2015b), and have been shown to work even in absence of a regeneration target in full amputation models (Srinivasan et al., 2015a).

While many of the same implications for FBR that apply sieve electrodes also apply to microchannel electrodes, microchannels both offer some advantages and face additional challenges. On one hand, microchannel devices are often made from stretchable materials, such as PDMS. These materials allow the channel walls to deform, in contrast to sieve polyimide sieve electrodes which can only bend within the nerve cross-sectional plane. This can minimize the degree of long-term damage caused to the nerve tissue within the channels, decreasing FBR and axon death. Studies have achieved long-term recordings in freely moving animals using microchannel devices for periods 4 months post-implantation (Gore et al., 2015), while only small signals in response to electrical stimulation have been recorded at such chronic timepoint with sieve electrodes (Ramachandran et al.,

2006). The channels in microchannel devices are, however, orders of magnitude longer than the holes of a sieve electrode. This creates a need to fully vascularise the tissue within the channels to supply the axons with nutrients and prevent their death, which makes them more vulnerable to the slow build-up of fibrotic tissue during chronic FBR. While axon regeneration can occur in microchannel devices with channels as small as small as  $55\ \mu\text{m}$  in diameter (similar to sieve electrode dimensions), optimal axon regeneration is seen when coupled with growth of one or more blood vessel, requiring larger microchannels of  $100\ \mu\text{m}$  diameter (Lacour et al., 2009). Once regeneration has occurred, however, the progressive narrowing of the channel diameter as FBR develops over its inner wall leads to the eventual occlusion of these blood vessels, depriving axons of their nutrient supply. By 6 months post-implantation PDMS microchannel devices can develop capsules within the channels  $28\ \mu\text{m}$  in thickness which, while still leaving a large portion of the channel diameter unoccluded, lead to the death of the majority of the axons (FitzGerald, 2016).

While sieve and microchannel electrodes are the most distinct regenerative nerve designs, specifically developed to be used in regenerating nerves, many other classes of implantable nerve neuroprosthetics can be used as regenerative devices. Cuff electrodes can be inserted into the gap of a nerve lesion and the nerve allowed to grow through it, rather than wrapping the cuff around a healthy nerve (Lotfi et al., 2011; Stoyanova et al., 2013; Thompson et al., 2015). Regenerative designs ensure that tissue always perfectly surrounds the implant, providing tighter interfacing and higher quality electrical stimulation/recording properties without accidentally excessively compressing the nerve. Similarly, cylindrical conduits implanted into a gap lesion can also be equipped with penetrating implants facing its bore, allowing axons to regrow around them for better interfacing (Musallam et al., 2007; Clements et al., 2013). Thin-film devices can also be incorporated into bridging conduits to split the bore into two or more channels, achieving some of the higher-selectivity benefits provided by microchannel designs (Delgado-Martínez et al., 2017). Although these devices may perform better than their non-regenerative counterparts, the large amount of trauma and subsequent inflammation and FBR are unlikely to be worthwhile trade-off unless a nerve lesion has already occurred.

## LOOKING AHEAD—NEW MATERIALS AND STRATEGIES TO MINIMIZE FBR

The development of a foreign body reaction in response to the implantation of materials into nerves has been reported in literature for decades (Kim et al., 1976). Over the years, a wide range of nerve neuroprosthetic designs have been developed and tested. This has provided a wealth of data on the advantages and disadvantages of different designs, including their effect on FBR and tissue trauma. While a lot can be learned from past designs for the development of implants with better long-term stability and tissue compatibility, there has also been an increasing interest in gaining a deeper understanding of the

**TABLE 2 |** Summary of factors influencing FBR to implants and strategies employed to minimize it.

Implant properties and downstream effects influencing FBR	Strategies to minimize FBR
Chemical biocompatibility and material degradation	<ul style="list-style-type: none"> <li>• Bioinert and long-term stable materials.</li> <li>• Degradable materials that are removed from the body before FBR progresses into its chronic stage.</li> </ul>
Biofouling of the implant	<ul style="list-style-type: none"> <li>• Low fouling materials or coatings at the implant surface.</li> </ul>
Implant size and shape	<ul style="list-style-type: none"> <li>• Microfabrication of smaller implants and use of designs better suited for their nerve environment.</li> </ul>
Implant stiffness	<ul style="list-style-type: none"> <li>• Soft and flexible materials or implant coatings.</li> </ul>
Tissue inflammation	<ul style="list-style-type: none"> <li>• Anti-inflammatory compounds, particularly locally delivering through the implant.</li> <li>• Compounds targeting FBR-specific inflammation.</li> </ul>
Fibrosis and capsule formation	<ul style="list-style-type: none"> <li>• Anti-fibrotic compounds.</li> <li>• Suppressants of vascular growth.</li> </ul>

*Note certain factors contributing to FBR have more than one strategy FBR-reduction strategy associated.*

causes and pathways underlying FBR—and ways of directly tackling this reaction (Table 2).

FBR occurs in response to any material that is implanted into the body (Anderson et al., 2008; Salatino et al., 2017). However, certain material properties can exacerbate or decrease FBR. Implantable materials must exhibit good biocompatibility, being chemically inert to tissue to minimize inflammation and cell death (Williams, 2008; Hassler et al., 2011; Mariani et al., 2019), and remain so for the necessary long implantation periods. Even if used materials are chosen to be biocompatible, mechanical factors such as the size and geometry of implanted bodies fabricated from these also has a direct impact on the severity of the FBR. Trauma is intimately tied to FBR, as the inflammation resulting from tissue damage will attract immune cells to the area which can join the reaction against the implant (monocyte/macrophage recruitment step, Figure 1). Different size and shape implants will trigger different amounts of FBR based on the degree of mechanical trauma they cause in when moving in their implanted location. However, even when these variables are eliminated—for example by implanting a mass of spherical implants of different sizes into the peritoneal cavity of rodent models—size appears to directly impact on FBR. Spherical implants of 0.5 mm diameter generate higher degrees of FBR than larger 1.5 mm ones, an effect which is consistent for a wide range of materials (Veisheh et al., 2015). Similarly, shape appears to directly influence FBR, with sharper edges generating more fibrosis than spherical implants (Veisheh et al., 2015). Very small implants—with dimensions smaller than individual cells—such as injectable mesh electrodes seem to generate minimal amounts of FBR, potentially largely bypassing this response by preventing cells (neutrophils, macrophages and fibroblasts in Figure 1) from fully spreading on their surface and becoming activated (Zhou

et al., 2017). Interference with cell adhesion can also be achieved through chemical means. Low fouling materials minimize the adsorption of proteins to their surface—the first step leading to FBR—and coating implants with these can greatly diminish FBR (Xie et al., 2018).

Material stiffness also greatly contributes to FBR, with softer materials (closer in stiffness to that of biological tissues) generating less mechanical trauma and therefore less FBR (Lacour et al., 2016; Salatino et al., 2017). However, similarly to implant size, stiffness also appears to play a direct role in guiding FBR independently of the mechanical damage caused during movement. Nerve implants coated with a range of very low stiffness materials develop less fibrosis and inflammation than those coated with less soft materials (Carnicer-Lombarte et al., 2019). How properties such as size, geometry and stiffness directly guide FBR is not understood. While no specific mechanism has been identified, mechanotransduction (the conversion of mechanical cues into biochemical signals) is thought to play a role. Cells such as macrophages are known to actively interact with their mechanical environment and modulate their inflammatory activity in response (Iskratsch et al., 2014).

Pharmacological therapies also have great potential to target the downstream consequences of FBR. FBR is primarily mediated by inflammation—macrophages respond to the presence of the implant and orchestrate the fibrotic response that leads to its encapsulation. Anti-inflammatory compounds can directly inhibit FBR by dampening this inflammatory response. A decrease in macrophage activity around the implant decreases both their adherence and proliferation around the implant and the recruitment of capsule-forming fibroblasts (Figure 1). Dexamethasone—a commonly used anti-inflammatory corticosteroid drug—has found great success in pacemaker stimulator implants used in the clinic, where it is incorporated into the material surrounding the electrodes and elutes over time into the surrounding tissue to hamper FBR and improve implant life-time and stability (Mond et al., 2014). Dexamethasone has also been tested for control of FBR in nerve neuroprosthetics. Regenerative microchannel implants incorporating dexamethasone show a decrease in the thickness of the fibrotic capsule and avoid the death of axons over time seen in un-treated implants (FitzGerald, 2016). Dexamethasone administered systemically has also been shown to improve the electrical stimulation properties using TIME implants over a 3-month implantation period (Oliva et al., 2019). Despite its effectiveness, dexamethasone hampers all processes mediated by inflammation—including tissue healing. Dexamethasone use can limit tissue healing following implantation trauma and the chronic trauma associated with the indwelling implant, which can be particularly detrimental in regenerative implants relying on the regrowth of nerve tissue into the implant (FitzGerald, 2016). Similar to dexamethasone, other general anti-inflammatory drugs such as aspirin (Malik et al., 2011) and rapamycin (Takahashi et al., 2010) have also been shown effective for the reduction of FBR. However, although the pathway underlying FBR in inflammation has not been characterized, certain mediators are beginning to be identified



and provide new pharmacological targets against FBR. CSF1 receptor has been recently identified as playing a unique role in FBR-associated inflammation, with its inhibition using both implant-encapsulated and systemically-delivered small molecule compounds leading to a decrease in macrophage activity and fibrosis around implanted materials without impacting wound healing (Doloff et al., 2017; Farah et al., 2019).

Further downstream in the FBR process, fibrosis can also be targeted as a means to eliminate some of the more severe consequences of FBR (fibrotic encapsulation, the last step of FBR—**Figure 1**). TGF- $\beta$  lies at the heart of the fibrotic response in FBR, driving the activation of fibroblasts surrounding the implant into myofibroblasts (Ignatz and Massagué, 1986). Local inhibition of TGF- $\beta$  through injection of anti-sense oligonucleotides has been shown to decrease capsule formation in subcutaneous implants (Mazaheri et al., 2003). Suppressors of TGF- $\beta$  are entering the clinic for the management of fibrotic diseases, offering an opportunity for their use in FBR (King et al., 2014). Growth of the fibrotic capsule also requires the extension of new blood vessels into the newly forming tissue. Local scavenging of VEGF around implants, a stimulator of endothelial growth released by anoxic tissue, can inhibit the extension of new blood vessels necessary to support the fibrotic capsule and decrease fibrotic encapsulation (Dondossola et al., 2017).

Apart from surface modification or adjusting the invasiveness of the implants, devices made of biodegradable and bioresorbable materials have been increasingly gathering momentum as a viable class of bioelectronics to minimize the effect of FBR when implanted (Veisheh and Vegas, 2019) (**Figure 6**). The fibrotic components of FBR develop to chronically-indwelling implants. Biodegradable implants prevent the development of fibrosis by allowing the acute inflammatory phases of FBR to degrade part or the entirety of the implant once its therapeutic role is complete. Biodegradable and bioresorbable devices offer a unique opportunity to simultaneously perform targeted diagnosis and therapy *in vivo* with minimal long-term FBR consequences (Grossen et al., 2017).

For applications where the functions of the implants are only necessary for a predefined period of time, this class of so-called transient electronics employ a layered design (Hwang et al., 2012) where degradable polymeric materials act as an encapsulation layer, with functional inorganic materials such as zinc, magnesium, or silicon enclosed inside. While the active layers can remain long-term *in vivo* (producing a much smaller, lower trauma-inducing device than the original implanted one), they can also themselves be degradable. Not only does the degradable device prevent any need for later surgical extraction once the device lifetime has expired (Mattina et al., 2020), biodegradable devices also provide an alternative route for the immune system to process the device and lead to a much lower degree of FBR. Both the degradation time and rate of degradation can be adjusted by modulating the thickness between the active and encapsulation layers, allowing the devices to remain *in vivo* from days, weeks, to months depending on the applications (Choi et al., 2016).

Rogers and colleagues have designed and fabricated a class of biodegradable sensors to monitor relevant physiological parameters such as cerebral temperature and oxygenation (Bai et al., 2019), spatiotemporal neural activities in the cerebral cortex (Yu et al., 2016), and intracranial pressure (Kang et al., 2016). Biodegradable therapeutic devices such as electronic stents for controlled drug releases for endovascular diseases (Son et al., 2015), or wireless tissue heating for infection treatment (Tao et al., 2014) both demonstrated the high specificity and efficacy of targeted implantable devices while avoiding the negative tissue encapsulation due to FBR.

However, some studies still reported moderate degrees of FBR at the implantation sites of biodegradable bioelectronics (Xue et al., 2014). These studies postulated that the FBR might be due to incomplete degradation of the polymeric materials, and/or the accumulation of debris after the materials are degraded. As a result, careful design and modulating between the active/encapsulating layers of the biodegradable electronics is essential to the success of mitigating FBR in this class of implantable electronics.

## THE FUTURE OF NERVE NEUROPROSTHETICS

Despite its unavoidable presence, FBR has until recently been an acceptable side effect of the implantation of nerve neuroprosthetics. In the clinic, nerve cuffs have bypassed its effect by delivering larger stimulating currents to entire nerves, while in the research environment shorter implantation time points have allowed the development of implantable technologies without allowing fibrosis to develop. However, nerve neuroprosthetics continue to evolve with advances in knowledge of materials and manufacturing techniques, leading to higher resolution designs requiring more intimate interfacing with neuronal tissues. Together with a growing interest in the translation of these technologies into human clinical use (Wendelken et al., 2017; D'Anna et al., 2019; Petrini et al., 2019), FBR has become a dominant problem that needs to be actively addressed at the implant design stage.

Since its infancy, the field of nerve neuroprosthetics has overall transitioned from stiff materials, well suited for traditional microfabrication techniques, to flexible devices. While cuffs have been the predominant choice for widespread clinical stimulation applications, newer ultraflexible devices such as the TIME are seeing great success in humans (D'Anna et al., 2019; Petrini et al., 2019). The success of these devices can serve to inspire the design of new flexible nerve implant designs and drive a push for the translation of existing ones toward human use. CNS neural interfaces are experiencing a similar shift toward soft/flexible designs (Salatino et al., 2017). Low FBR designs developed for brain applications may be adapted for use in peripheral nerves, such as injectable mesh electrodes (Zhou et al., 2017) or ultraflexible non-penetrating transistor arrays (Khodagholy et al., 2013). Neural tissue is some of the softest in the body (Cox and Erler, 2011), and remains orders of magnitude softer than many materials commonly regarded as soft (Lacour

et al., 2016), leaving ample room for the improvement of current soft designs into even more biocompatible and FBR-minimizing ones.

A transition to soft nerve neuroprosthetics will bring with it fabrication challenges. The field of neuroprosthetics has greatly benefitted from microfabrication technology used in the semiconductor industry, which does not easily translate to soft or flexible substrates. This becomes particularly relevant as implant designs become smaller in scale and increasingly elaborate in order to record signals from small subsets of axons within a nerve. A range of strategies are being developed with this objective, such as the use of stiff but also thin and therefore flexible materials (Khodagholy et al., 2015), the engineering of defects in stiff materials to render them deformable (Vachicouras et al., 2017), or the encapsulation of electronics in soft materials (Liu et al., 2019).

An alternative—or more likely a complementary—strategy for future nerve neuroprosthetic designs will be the incorporation of compounds or materials that actively target FBR. Several FBR-targeting compounds are already progressing toward use in humans (King et al., 2014; Farah et al., 2019), and as our understanding of FBR continues to evolve this repertoire will likely continue to expand. Future nerve neuroprosthetics will likely be multimodal, containing not only electrode arrays to electrically communicate with tissue, but also mechanisms to chemically interact with it in the form of FBR-modulating compounds. The delivery of these compounds may occur through engineered structures such as microfluidic channels, or provided through material-oriented solutions such as immobilization of compounds on their surface or encapsulation within materials. The field of surgical nerve repair already employs implants actively modulating biological processes (Carvalho et al., 2019), and may be a useful source for the

development of new-generation nerve neuroprosthetics. Other novel strategies, such as the incorporation of cells or tissue within devices to transform them into living implants, interacting with and integrating into the host (Rochford et al., 2020), may also provide unique avenues to address FBR. While the inclusion of these additional modalities introduces further challenges for the manufacturing of neuroprosthetics, the therapeutic potential of implantable devices capable of stable, fine resolution recording and stimulation over decades far outweigh the costs.

## DATA AVAILABILITY STATEMENT

The original contributions generated for the study are included in the article/supplementary material, further inquiries can be directed to the corresponding author/s.

## AUTHOR CONTRIBUTIONS

AC-L and DB designed the paper and analyzed the literature. AC-L and S-TC wrote the paper. GM and DB revised the paper. All the authors read and approved the manuscript.

## FUNDING

This work was supported by the Engineering and Physical Sciences Research Council (EPSRC; 27 EP/S009000/1). AC-L acknowledges support from the Wellcome Trust (Wellcome Trust Junior 28 Interdisciplinary Fellowship). S-TC acknowledges support from the Cambridge Trust. DB is supported by Health Education England and the National Institute for Health Research HEE/ NIHR ICA Program Clinical Lectureship (CL-2019-14-004).

## REFERENCES

- Akin, T., Najafi, K., Smoke, R. H., and Bradley, R. M. (1994). A micromachined silicon sieve electrode for nerve regeneration applications. *IEEE Trans. Biomed. Eng.* 41, 305–313. doi: 10.1109/10.284958
- Anderson, J. M. (2001). Biological responses to materials. *Annu. Rev. Mater. Res.* 31, 81–110. doi: 10.1146/annurev.matsci.31.1.81
- Anderson, J. M., Rodriguez, A., and Chang, D. T. (2008). Foreign body reaction to biomaterials. *Semin. Immunol.* 20, 86–100. doi: 10.1016/j.smim.2007.11.004
- Anderson, W. S., and Lenz, F. A. (2006). Surgery Insight: deep brain stimulation for movement disorders. *Nat. Rev. Neurol.* 2, 310–320. doi: 10.1038/ncpneu0193
- Arslantunali, D., Dursun, T., Yucel, D., Hasirci, N., and Hasirci, V. (2014). Peripheral nerve conduits: technology update. *Med. Devices Auckl. NZ* 7, 405–424. doi: 10.2147/MDER.S59124
- Badia, J., Boretius, T., Andreu, D., Azevedo-Coste, C., Stieglitz, T., and Navarro, X. (2011a). Comparative analysis of transverse intrafascicular multichannel, longitudinal intrafascicular and multipolar cuff electrodes for the selective stimulation of nerve fascicles. *J. Neural Eng.* 8:036023. doi: 10.1088/1741-2560/8/3/036023
- Badia, J., Boretius, T., Pascual-Font, A., Udina, E., Stieglitz, T., and Navarro, X. (2011b). Biocompatibility of chronically implanted transverse intrafascicular multichannel electrode (TIME) in the rat sciatic nerve. *IEEE Trans. Biomed. Eng.* 58, 2324–2332. doi: 10.1109/TBME.2011.2153850
- Badia, J., Raspopovic, S., Carpaneto, J., Micera, S., and Navarro, X. (2016). Spatial and functional selectivity of peripheral nerve signal recording with the transversal intrafascicular multichannel electrode (TIME). *IEEE Trans. Neural Syst. Rehabil. Eng.* 24, 20–27. doi: 10.1109/TNSRE.2015.2440768
- Bai, W., Shin, J., Fu, R., Kandela, I., Lu, D., Ni, X., et al. (2019). Bioresorbable photonic devices for the spectroscopic characterization of physiological status and neural activity. *Nat. Biomed. Eng.* 3, 644–654. doi: 10.1038/s41551-019-0435-y
- Barrese, J. C., Aceros, J., and Donoghue, J. P. (2016). Scanning electron microscopy of chronically implanted intracortical microelectrode arrays in non-human primates. *J. Neural Eng.* 13:026003. doi: 10.1088/1741-2560/13/2/026003
- Bayliss, S. C., Buckberry, L. D., Fletcher, I., and Tobin, M. J. (1999). The culture of neurons on silicon. *Sens. Actuators Phys.* 74, 139–142. doi: 10.1016/S0924-4247(98)00346-X
- Ben-Menachem, E., Revesz, D., Simon, B. J., and Silberstein, S. (2015). Surgically implanted and non-invasive vagus nerve stimulation: a review of efficacy, safety and tolerability. *Eur. J. Neurol.* 22, 1260–1268. doi: 10.1111/ene.12629
- Bonner, J. C. (2004). Regulation of PDGF and its receptors in fibrotic diseases. *Cytokine Growth Factor Rev.* 15, 255–273. doi: 10.1016/j.cytogfr.2004.03.006
- Boretius, T., Badia, J., Pascual-Font, A., Schuettler, M., Navarro, X., Yoshida, K., et al. (2010). A transverse intrafascicular multichannel electrode (TIME) to interface with the peripheral nerve. *Biosens. Bioelectron.* 26, 62–69. doi: 10.1016/j.bios.2010.05.010
- Branner, A., and Normann, R. A. (2000). A multielectrode array for intrafascicular recording and stimulation in sciatic nerve of cats. *Brain Res. Bull.* 51, 293–306. doi: 10.1016/s0361-9230(99)00231-2

- Branner, A., Stein, R. B., and Normann, R. A. (2001). Selective stimulation of cat sciatic nerve using an array of varying-length microelectrodes. *J. Neurophysiol.* 85, 1585–1594. doi: 10.1152/jn.2001.85.4.1585
- Brindley, G. S., Polkey, C. E., and Rushton, D. N. (1982). Sacral anterior root stimulators for bladder control in paraplegia. *Paraplegia* 20, 365–381. doi: 10.1038/sc.1982.65
- Brown, B. N., Ratner, B. D., Goodman, S. B., Amar, S., and Badylak, S. F. (2012). Macrophage polarization: an opportunity for improved outcomes in biomaterials and regenerative medicine. *Biomaterials* 33, 3792–3802. doi: 10.1016/j.biomaterials.2012.02.034
- Burridge, J., Haugland, M., Larsen, B., Pickering, R. M., Svaneborg, N., Iversen, H. K., et al. (2007). Phase II trial to evaluate the ActiGait implanted drop-foot stimulator in established Hemiplegia. 39, 212–218. doi: 10.2340/16501977-0039
- Campbell, J. N., and Meyer, R. A. (2006). Mechanisms of neuropathic pain. *Neuron* 52, 77–92. doi: 10.1016/j.neuron.2006.09.021
- Capogrosso, M., Gandar, J., Greiner, N., Moraud, E. M., Wenger, N., Polina, S., et al. (2018). Advantages of soft subdural implants for the delivery of electrochemical neuromodulation therapies to the spinal cord. *J. Neural Eng.* 15:026024. doi: 10.1088/1741-2552/aaa87a
- Carnicer-Lombarte, A., Barone, D. G., Dimov, I. B., Hamilton, R. S., Prater, M., Zhao, X., et al. (2019). Mechanical matching of implant to host minimises foreign body reaction. *bioRxiv* 82:9648. doi: 10.1101/829648
- Carvalho, C. R., Oliveira, J. M., and Reis, R. L. (2019). Modern trends for peripheral nerve repair and regeneration: beyond the hollow nerve guidance conduit. *Front. Bioeng. Biotechnol.* 7:337. doi: 10.3389/fbioe.2019.00337
- Chang, T. Y., Yadav, V. G., De Leo, S., Mohedas, A., Rajalingam, B., Chen, C.-L., et al. (2007). Cell and protein compatibility of parylene-C surfaces. *Langmuir* 23, 11718–11725. doi: 10.1021/la7017049
- Chew, D. J., Zhu, L., Delivopoulos, E., Mineev, I. R., Musick, K. M., Mosse, C. A., et al. (2013). A microchannel neuroprosthesis for bladder control after spinal cord injury in rat. *Sci. Transl. Med.* 5, 210ra155–210ra155. doi: 10.1126/scitranslmed.3007186
- Choi, S., Lee, H., Ghaffari, R., Hyeon, T., and Kim, D.-H. (2016). Recent advances in flexible and stretchable bio-electronic devices integrated with nanomaterials. *Adv. Mater. Deerfield Beach Fla* 28, 4203–4218. doi: 10.1002/adma.201504150
- Christensen, M. B., Pearce, S. M., Ledbetter, N. M., Warren, D. J., Clark, G. A., and Tresco, P. A. (2014). The foreign body response to the Utah Slant Electrode Array in the cat sciatic nerve. *Acta Biomater.* 10, 4650–4660. doi: 10.1016/j.actbio.2014.07.010
- Christensen, M. B., and Tresco, P. A. (2018). The foreign body response and morphometric changes associated with mesh-style peripheral nerve cuffs. *Acta Biomater.* 67, 79–86. doi: 10.1016/j.actbio.2017.11.059
- Christensen, M. B., Wark, H. A. C., and Hutchinson, D. T. (2016). A histological analysis of human median and ulnar nerves following implantation of Utah slanted electrode arrays. *Biomaterials* 77, 235–242. doi: 10.1016/j.biomaterials.2015.11.012
- Christie, B. P., Freeberg, M., Memberg, W. D., Pinault, G. J. C., Hoyen, H. A., Tyler, D. J., et al. (2017). “Long-term stability of stimulating spiral nerve cuff electrodes on human peripheral nerves.” *J. NeuroEngineering Rehabil.* 14:3. doi: 10.1186/s12984-017-0285-3
- Christo, S. N., Diener, K. R., Manavis, J., Grimbaldston, M. A., Bachhuka, A., Vasilev, K., et al. (2016). Inflammation components ASC and AIM2 modulate the acute phase of biomaterial implant-induced foreign body responses. *Sci. Rep.* 6:20635. doi: 10.1038/srep20635
- Clark, G. A., Wendelken, S., Page, D. M., Davis, T., Wark, H. A. C., Normann, R. A., et al. (2014). “Using multiple high-count electrode arrays in human median and ulnar nerves to restore sensorimotor function after previous transradial amputation of the hand,” in *2014 36th Annual International Conference of the IEEE Engineering in Medicine and Biology Society (Chicago, IL: IEEE)*, 1977–1980. doi: 10.1109/EMBC.2014.6944001
- Clements, I. P., Mukhatyar, V. J., Srinivasan, A., Bentley, J. T., Andreasen, D. S., and Bellamkonda, R. V. (2013). Regenerative Scaffold Electrodes for Peripheral Nerve Interfacing. *IEEE Trans. Neural Syst. Rehabil. Eng.* 21, 554–566. doi: 10.1109/TNSRE.2012.2217352
- Colletti, V., Shannon, R. V., Carner, M., Veronese, S., and Colletti, L. (2009). Progress in restoration of hearing with the auditory brainstem implant. *Prog. Brain Res.* 175, 333–345. doi: 10.1016/S0079-6123(09)17523-4
- Cox, T. R., and Erler, J. T. (2011). Remodeling and homeostasis of the extracellular matrix: implications for fibrotic diseases and cancer. *Dis. Model. Mech.* 4, 165–178. doi: 10.1242/dmm.004077
- Crowe, M. J., Doetschman, T., and Greenhalgh, D. G. (2000). Delayed Wound Healing in Immunodeficient TGF- $\beta$ 1 Knockout Mice. *J. Invest. Dermatol.* 115, 3–11. doi: 10.1046/j.1523-1747.2000.00010.x
- Cutrone, A., Valle, J. D., Santos, D., Badia, J., Filippeschi, C., Micera, S., et al. (2015). A three-dimensional self-opening intraneural peripheral interface (SELINE). *J. Neural Eng.* 12:016016. doi: 10.1088/1741-2560/12/1/016016
- Cvančara, P., Boretius, T., López-Álvarez, V. M., Maciejasz, P., and Andreu, D., Raspopovic, S., et al. (2020). Stability of flexible thin-film metallization stimulation electrodes: analysis of explants after first-in-human study and improvement of *in vivo* performance. *J. Neural Eng.* 17:046006. doi: 10.1088/1741-2552/ab9a9a
- D’Anna, E., Valle, G., Mazzoni, A., Strauss, I., Iberite, F., Patton, J., et al. (2019). A closed-loop hand prosthesis with simultaneous intraneural tactile and position feedback. *Sci. Robot.* 4:eaau8892. doi: 10.1126/scirobotics.aau8892
- Davis, T. S., Wark, H. A. C., Hutchinson, D. T., Warren, D. J., O’Neill, K., Scheinblum, T., et al. (2016). Restoring motor control and sensory feedback in people with upper extremity amputations using arrays of 96 microelectrodes implanted in the median and ulnar nerves. *J. Neural Eng.* 13:036001. doi: 10.1088/1741-2560/13/3/036001
- de la Oliva, N., Mueller, M., Stieglitz, T., Navarro, X., and del Valle, J. (2018). On the use of Parylene C polymer as substrate for peripheral nerve electrodes. *Sci. Rep.* 8:5965. doi: 10.1038/s41598-018-24502-z
- Deal, N. D., Griffin, J. W., and Hogan, M. V. (2012). Nerve conduits for nerve repair or reconstruction. *J. Am. Acad. Orthop. Surg.* 20, 63–68. doi: 10.5435/JAAOS-20-02-063
- Delgado-Martínez, I., Righi, M., Santos, D., Cutrone, A., Bossi, S., D’Amico, S., et al. (2017). Fascicular nerve stimulation and recording using a novel double-aisle regenerative electrode. *J. Neural Eng.* 14:046003. doi: 10.1088/1741-2552/aa6bac
- Dhillon, G. S., Krüger, T. B., Sandhu, J. S., and Horch, K. W. (2005). Effects of short-term training on sensory and motor function in severed nerves of long-term human amputees. *J. Neurophysiol.* 93, 2625–2633. doi: 10.1152/jn.00937.2004
- Dhillon, G. S., Lawrence, S. M., Hutchinson, D. T., and Horch, K. W. (2004). Residual function in peripheral nerve stumps of amputees: implications for neural control of artificial limbs. No benefits in any form have been received or will be received from a commercial party related directly or indirectly to the subject of this article. *J. Hand Surg.* 29, 605–615. doi: 10.1016/j.jhbs.2004.02.006
- Doloff, J. C., Veisheh, O., Vegas, A. J., Tam, H. H., Farah, S., Ma, M., et al. (2017). Colony stimulating factor-1 receptor is a central component of the foreign body response to biomaterial implants in rodents and non-human primates. *Nat. Mater.* 16, 671–680. doi: 10.1038/nmat4866
- Dondossola, E., Holzapfel, B. M., Alexander, S., Filippini, S., Huttmacher, D. W., and Friedl, P. (2017). Examination of the foreign body response to biomaterials by nonlinear intravital microscopy. *Nat. Biomed. Eng.* 1:0007. doi: 10.1038/s41551-016-0007
- Edell, D. J. (1986). A peripheral nerve information transducer for amputees: long-term multichannel recordings from rabbit peripheral nerves. *IEEE Trans. Biomed. Eng.* BME-33, 203–214. doi: 10.1109/TBME.1986.325892
- Elyahoodayan, S., Larson, C., Cobo, A. M., Meng, E., and Song, D. (2020). Acute *in vivo* testing of a polymer cuff electrode with integrated microfluidic channels for stimulation, recording, and drug delivery on rat sciatic nerve. *J. Neurosci. Methods* 336:108634. doi: 10.1016/j.jneumeth.2020.108634
- Farah, S., Doloff, J. C., Müller, P., Sadraei, A., Han, H. J., Olafson, K., et al. (2019). Long-term implant fibrosis prevention in rodents and non-human primates using crystallized drug formulations. *Nat. Mater.* 1:5. doi: 10.1038/s41563-019-0377-5
- FitzGerald, J. J. (2016). Suppression of scarring in peripheral nerve implants by drug elution. *J. Neural Eng.* 13:026006. doi: 10.1088/1741-2560/13/2/026006
- Fitzgerald, J. J., Lacour, S. P., McMahon, S. B., and Fawcett, J. W. (2008). Microchannels as axonal amplifiers. *IEEE Trans. Biomed. Eng.* 55, 1136–1146. doi: 10.1109/TBME.2007.909533
- FitzGerald, J. J., Lago, N., Benmerah, S., Serra, J., Watling, C. P., Cameron, R. E., et al. (2012). A regenerative microchannel neural interface for recording



- from and stimulating peripheral axons *in vivo*. *J. Neural Eng.* 9:016010. doi: 10.1088/1741-2560/9/1/016010
- Franz, S., Rammelt, S., Scharnweber, D., and Simon, J. C. (2011). Immune responses to implants – a review of the implications for the design of immunomodulatory biomaterials. *Biomaterials* 32, 6692–6709. doi: 10.1016/j.biomaterials.2011.05.078
- George, J. A., Kluger, D. T., Davis, T. S., Wendelken, S. M., Okorokova, E. V., He, Q., et al. (2019). Biomimetic sensory feedback through peripheral nerve stimulation improves dexterous use of a bionic hand. *Sci. Robot.* 4:2352. doi: 10.1126/scirobotics.aax2352
- Goldstein, S. R., and Salzman, M. (1973). Mechanical factors in the design of chronic recording intracortical microelectrodes. *IEEE Trans. Biomed. Eng.* 20, 260–269. doi: 10.1109/TBME.1973.324190
- González-González, M. A., Kanneganti, A., Joshi-Imre, A., Hernandez-Reynoso, A. G., Bendale, G., Modi, R., et al. (2018). Thin film multi-electrode softening cuffs for selective neuromodulation. *Sci. Rep.* 8:16390. doi: 10.1038/s41598-018-34566-6
- Gore, R. K., Choi, Y., Bellamkonda, R., and English, A. (2015). Functional recordings from awake, behaving rodents through a microchannel based regenerative neural interface. *J. Neural Eng.* 12:016017. doi: 10.1088/1741-2560/12/1/016017
- Gribi, S., du Bois de Dunilac, S., Ghezzi, D., and Lacour, S. P. (2018). A microfabricated nerve-on-a-chip platform for rapid assessment of neural conduction in explanted peripheral nerve fibers. *Nat. Commun.* 9:4403. doi: 10.1038/s41467-018-06895-7
- Grill, W. M., and Mortimer, J. T. (2000). Neural and connective tissue response to long-term implantation of multiple contact nerve cuff electrodes. *J. Biomed. Mater. Res.* 50, 215–226. doi: 10.1002/(sici)1097-4636(200005)50:2<215::aid-jbm17>3.0.co;2-a
- Grossen, P., Witzigmann, D., Sieber, S., and Huwyler, J. (2017). PEG-PCL-based nanomedicines: a biodegradable drug delivery system and its application. *J. Control. Release Off. J. Control. Release Soc.* 260, 46–60. doi: 10.1016/j.jconrel.2017.05.028
- Haghiashiani, G., and McAlpine, M. C. (2017). Sensing gastrointestinal motility. *Nat. Biomed. Eng.* 1, 775–776. doi: 10.1038/s41551-017-0146-1
- Hansen, K., and Mossman, B. T. (1987). Generation of superoxide (O<sub>2</sub><sup>-</sup>) from alveolar macrophages exposed to asbestiform and nonfibrous particles. *Cancer Res.* 47, 1681–1686.
- Hassler, C., Boretius, T., and Stieglitz, T. (2011). Polymers for neural implants. *J. Polym. Sci. Part B Polym. Phys.* 49, 18–33. doi: 10.1002/polb.22169
- Hesketh, M., Sahin, K. B., West, Z. E., and Murray, R. Z. (2017). Macrophage phenotypes regulate scar formation and chronic wound healing. *Int. J. Mol. Sci.* 18:1545. doi: 10.3390/ijms18071545
- Hinz, B., Phan, S. H., Thannickal, V. J., Galli, A., Bochaton-Piallat, M.-L., and Gabbiani, G. (2007). The myofibroblast. *Am. J. Pathol.* 170, 1807–1816. doi: 10.2353/ajpath.2007.070112
- Hirschfeld, S., Exner, G., Luukkaala, T., and Baer, G. A. (2008). Mechanical ventilation or phrenic nerve stimulation for treatment of spinal cord injury-induced respiratory insufficiency. *Spinal Cord* 46, 738–742. doi: 10.1038/sc.2008.43
- Hwang, S.-W., Tao, H., Kim, D.-H., Cheng, H., Song, J.-K., Rill, E., et al. (2012). A physically transient form of silicon electronics. *Science* 337, 1640–1644. doi: 10.1126/science.1226325
- Ignatz, R. A., and Massagué, J. (1986). Transforming growth factor-beta stimulates the expression of fibronectin and collagen and their incorporation into the extracellular matrix. *J. Biol. Chem.* 261, 4337–4345.
- Iskratsch, T., Wolfenson, H., and Sheetz, M. P. (2014). Appreciating force and shape—the rise of mechanotransduction in cell biology. *Nat. Rev. Mol. Cell Biol.* 15, 825–833. doi: 10.1038/nrm3903
- Johnson, B. N., Lancaster, K. Z., Zhen, G., He, J., Gupta, M. K., Kong, Y. L., et al. (2015). 3D printed anatomical nerve regeneration pathways. *Adv. Funct. Mater.* 25, 6205–6217. doi: 10.1002/adfm.201501760
- Johnston, T. E., Betz, R. R., Smith, B. T., Benda, B. J., Mulcahey, M. J., Davis, R., et al. (2005). Implantable FES system for upright mobility and bladder and bowel function for individuals with spinal cord injury. *Spinal Cord* 43, 713–723. doi: 10.1038/sj.sc.3101797
- Jones, J. A., Chang, D. T., Meyerson, H., Colton, E., Kwon, I. K., Matsuda, T., et al. (2007). Proteomic analysis and quantification of cytokines and chemokines from biomaterial surface-adherent macrophages and foreign body giant cells. *J. Biomed. Mater. Res. A* 83A, 585–596. doi: 10.1002/jbma.a.31221
- Kang, S. K., Murphy, R. K. J., Hwang, S. W., Lee, S. M., Harburg, D. V., Krueger, N. A., et al. (2016). Bioresorbable silicon electronic sensors for the brain. *Nature* 530, 71–76. doi: 10.1038/nature16492
- Khodagholy, D., Doublet, T., Quilichini, P., Gurfinkel, M., Leleux, P., Ghestem, A., et al. (2013). *In vivo* recordings of brain activity using organic transistors. *Nat. Commun.* 4:1575. doi: 10.1038/ncomms2573
- Khodagholy, D., Gelinas, J. N., Thesen, T., Doyle, W., Devinsky, O., Malliaras, G. G., et al. (2015). NeuroGrid: recording action potentials from the surface of the brain. *Nat. Neurosci.* 18, 310–315. doi: 10.1038/nn.3905
- Kim, J. H., Manuelidis, E. E., Glenn, W. W. L., and Kaneyuki, T. (1976). Diaphragm pacing: histopathological changes in the phrenic nerve following long-term electrical stimulation. *J. Thorac. Cardiovasc. Surg.* 72, 602–608. doi: 10.1016/S0022-5223(19)40049-4
- King, T. E., Bradford, W. Z., Castro-Bernardini, S., Fagan, E. A., Glaspole, I., Glassberg, M. K., et al. (2014). A phase 3 trial of pirfenidone in patients with idiopathic pulmonary fibrosis. *N. Engl. J. Med.* 370, 2083–2092. doi: 10.1056/NEJMoa1402582
- Klinge, P. M., Vafa, M. A., Brinker, T., Brandis, A., Walter, G. F., Stieglitz, T., et al. (2001). Immunohistochemical characterization of axonal sprouting and reactive tissue changes after long-term implantation of a polyimide sieve electrode to the transected adult rat sciatic nerve. *Biomaterials* 22, 2333–2343. doi: 10.1016/S0142-9612(00)00420-8
- Klopfleisch, R. (2016). Macrophage reaction against biomaterials in the mouse model—phenotypes, functions and markers. *Acta Biomater.* 43, 3–13. doi: 10.1016/j.actbio.2016.07.003
- Klopfleisch, R., and Jung, F. (2017). The pathology of the foreign body reaction against biomaterials. *J. Biomed. Mater. Res. A* 105, 927–940. doi: 10.1002/jbma.a.35958
- Kozai, T. D. Y., Gugel, Z., Li, X., Gilgunn, P. J., Khilwani, R., Ozdoganlar, O. B., et al. (2014). Chronic tissue response to carboxymethyl cellulose based dissolvable insertion needle for ultra-small neural probes. *Biomaterials* 35, 9255–9268. doi: 10.1016/j.biomaterials.2014.07.039
- Krarup, C., Loeb, G. E., and Pezeshkpour, G. H. (1989). Conduction studies in peripheral cat nerve using implanted electrodes: III. The effects of prolonged constriction on the distal nerve segment. *Muscle Nerve* 12, 915–928. doi: 10.1002/mus.880121108
- Labow, R. S., Meek, E., and Santerre, J. P. (2001). Hydrolytic degradation of poly(carbonate)-urethanes by monocyte-derived macrophages. *Biomaterials* 22, 3025–3033. doi: 10.1016/s0142-9612(01)00049-7
- Lacour, S. P., Courtine, G., and Guck, J. (2016). Materials and technologies for soft implantable neuroprostheses. *Nat. Rev. Mater.* 1:16063. doi: 10.1038/natrevmats.2016.63
- Lacour, S. P., Fitzgerald, J. J., Lago, N., Tarte, E., McMahon, S., and Fawcett, J. (2009). Long micro-channel electrode arrays: a novel type of regenerative peripheral nerve interface. *IEEE Trans. Neural Syst. Rehabil. Eng.* 17, 454–460. doi: 10.1109/TNSRE.2009.2031241
- Lago, N., Ceballos, D. J., Rodriguez, F., Stieglitz, T., and Navarro, X. (2005). Long term assessment of axonal regeneration through polyimide regenerative electrodes to interface the peripheral nerve. *Biomaterials* 26, 2021–2031. doi: 10.1016/j.biomaterials.2004.06.025
- Lago, N., Yoshida, K., Koch, K. P., and Navarro, X. (2007). Assessment of biocompatibility of chronically implanted polyimide and platinum intrafascicular electrodes. *IEEE Trans. Biomed. Eng.* 54, 281–290. doi: 10.1109/TBME.2006.886617
- Lancashire, H. T., Vanhoestenbergh, A., Pendegrass, C. J., Ajam, Y. A., Magee, E., Donaldson, N., et al. (2016). Microchannel neural interface manufacture by stacking silicone and metal foil laminae. *J. Neural Eng.* 13:034001. doi: 10.1088/1741-2560/13/3/034001
- Lawrence, T., and Natoli, G. (2011). Transcriptional regulation of macrophage polarization: enabling diversity with identity. *Nat. Rev. Immunol.* 11, 750–761. doi: 10.1038/nri3088
- Lee, J., Cho, H. R., Cha, G. D., Seo, H., Lee, S., Park, C.-K., et al. (2019). Flexible, sticky, and biodegradable wireless device for drug delivery to brain tumors. *Nat. Commun.* 10:5205. doi: 10.1038/s41467-019-13198-y



- Leventhal, D. K., Cohen, M., and Durand, D. M. (2006). Chronic histological effects of the flat interface nerve electrode. *J. Neural Eng.* 3, 102–113. doi: 10.1088/1741-2560/3/2/004
- Liberson, W. T., Holmquest, H. J., Scot, D., and Dow, M. (1961). Functional electrotherapy: stimulation of the peroneal nerve synchronized with the swing phase of the gait of hemiplegic patients. *Arch. Phys. Med. Rehabil.* 42, 101–105.
- Liu, Y., Li, J., Song, S., Kang, J., Tsao, Y., Chen, S., et al. (2020). Morphing electronics enable neuromodulation in growing tissue. *Nat. Biotechnol.* 2, 1–6. doi: 10.1038/s41587-020-0495-2
- Liu, Y., Liu, J., Chen, S., Lei, T., Kim, Y., Niu, S., et al. (2019). Soft and elastic hydrogel-based microelectronics for localized low-voltage neuromodulation. *Nat. Biomed. Eng.* 3:58. doi: 10.1038/s41551-018-0335-6
- Lotfi, P., Garde, K., Chouhan, A. K., Bengali, E., and Romero-Ortega, M. I. (2011). Modality-specific axonal regeneration: toward selective regenerative neural interfaces. *Front. Neuroengineering* 4:11. doi: 10.3389/fneng.2011.00011
- Louveau, A., Harris, T. H., and Kipnis, J. (2015). Revisiting the concept of CNS immune privilege. *Trends Immunol.* 36, 569–577. doi: 10.1016/j.it.2015.08.006
- Luttikhuisen, D. T., Harmsen, M. C., and Luyn, M. J. A. V. (2006). Cellular and molecular dynamics in the foreign body reaction. *Tissue Eng.* 12, 1955–1970. doi: 10.1089/ten.2006.12.1955
- MacEwan, M. R., Zellmer, E. R., Wheeler, J. J., Burton, H., and Moran, D. W. (2016). Regenerated sciatic nerve axons stimulated through a chronically implanted macro-sieve electrode. *Front. Neurosci.* 10:557. doi: 10.3389/fnins.2016.00557
- Malik, A. F., Hoque, R., Ouyang, X., Ghani, A., Hong, E., Khan, K., et al. (2011). Inflammasome components Asc and caspase-1 mediate biomaterial-induced inflammation and foreign body response. *Proc. Natl. Acad. Sci. U.S.A.* 108, 20095–20100. doi: 10.1073/pnas.1105152108
- Malmstrom, J. A., McNaughton, T. G., and Horch, K. W. (1998). Recording properties and biocompatibility of chronically implanted polymer-based intrafascicular electrodes. *Ann. Biomed. Eng.* 26, 1055–1064. doi: 10.1114/1.35
- Mantovani, A., Sica, A., Sozzani, S., Allavena, P., Vecchi, A., and Locati, M. (2004). The chemokine system in diverse forms of macrophage activation and polarization. *Trends Immunol.* 25, 677–686. doi: 10.1016/j.it.2004.09.015
- Mariani, E., Lisignoli, G., Borzi, R. M., and Pulsatelli, L. (2019). Biomaterials: foreign bodies or tuners for the immune response? *Int. J. Mol. Sci.* 20:636. doi: 10.3390/ijms20030636
- Mattina, A. A. L., Mariani, S., and Barillaro, G. (2020). Bioresorbable materials on the rise: from electronic components and physical sensors to *in vivo* monitoring systems. *Adv. Sci.* 7:1902872. doi: 10.1002/adv.201902872
- Mazaheri, M. K., Schultz, G. S., Blalock, T. D., Caffee, H. H., and Chin, G. A. (2003). Role of connective tissue growth factor in breast implant elastomer capsular formation. *Ann. Plast. Surg.* 50, 263–268; discussion 268. doi: 10.1097/01.sap.0000046781.75625.69
- McNally, A. K., and Anderson, J. M. (2002). Beta1 and beta2 integrins mediate adhesion during macrophage fusion and multinucleated foreign body giant cell formation. *Am. J. Pathol.* 160, 621–630. doi: 10.1016/s0002-9440(10)64882-1
- Mesure, L., Visscher, G. D., Vranken, I., Lebacqz, A., and Flameng, W. (2010). Gene expression study of monocytes/macrophages during early foreign body reaction and identification of potential precursors of myofibroblasts. *PLoS ONE* 5:e12949. doi: 10.1371/journal.pone.0012949
- Micera, S., Jensen, W., Sepulveda, F., Riso, R. R., and Sinkjaer, T. (2001). Neuro-fuzzy extraction of angular information from muscle afferents for ankle control during standing in paraplegic subjects: an animal model. *IEEE Trans. Biomed. Eng.* 48, 787–794. doi: 10.1109/10.930903
- Micera, S., Navarro, X., Carpaneto, J., Citi, L., Tonet, O., Rossini, P. M., et al. (2008). On the use of longitudinal intrafascicular peripheral interfaces for the control of cybernetic hand prostheses in amputees. *IEEE Trans. Neural Syst. Rehabil. Eng.* 16, 453–472. doi: 10.1109/TNSRE.2008.2006207
- Minev, I. R., Musienko, P., Hirsch, A., Barraud, Q., Wenger, N., Moraud, E. M., et al. (2015). Electronic dura mater for long-term multimodal neural interfaces. *Science* 347, 159–163. doi: 10.1126/science.1260318
- Mond, H. G., Helland, J. R., Stokes, K., Bornzin, G. A., and McVE, N. E. S., R. (2014). The electrode-tissue interface: the revolutionary role of steroid-elution. *Pacing Clin. Electrophysiol.* 37, 1232–1249. doi: 10.1111/pace.12461
- Musallam, S., Bak, M. J., Troyk, P. R., and Andersen, R. A. (2007). A floating metal microelectrode array for chronic implantation. *J. Neurosci. Methods* 160, 122–127. doi: 10.1016/j.jneumeth.2006.09.005
- Musick, K. M., Rigosa, J., Narasimhan, S., Wurth, S., Capogrosso, M., Chew, D. J., et al. (2015). Chronic multichannel neural recordings from soft regenerative microchannel electrodes during gait. *Sci. Rep.* 5:14363. doi: 10.1038/srep14363
- Navarro, X., Calvet, S., But, í, M., Gómez, N., Cabruja, E., Garrido, P., et al. (1996). Peripheral nerve regeneration through microelectrode arrays based on silicon technology. *Restor. Neurol. Neurosci.* 9, 151–160. doi: 10.3233/RNN-1996-9303
- Navarro, X., Calvet, S., Rodríguez, F. J., Stieglitz, T., Blau, C., But, í, M., et al. (1998). Stimulation and recording from regenerated peripheral nerves through polyimide sieve electrodes. *J. Peripher. Nerv. Syst. JPNS* 3, 91–101.
- Navarro, X., Krueger, T. B., Lago, N., Micera, S., Stieglitz, T., and Dario, P. (2005). A critical review of interfaces with the peripheral nervous system for the control of neuroprostheses and hybrid bionic systems. *J. Peripher. Nerv. Syst.* 10, 229–258. doi: 10.1111/j.1085-9489.2005.10303.x
- Navarro, X., Lago, N., Vivo, M., Yoshida, K., Koch, K. P., Poppendieck, W., et al. (2007). “Neurobiological evaluation of thin-film longitudinal intrafascicular electrodes as a peripheral nerve interface,” in 2007 *IEEE 10th International Conference on Rehabilitation Robotics* (Noordwijk: IEEE), 643–649. doi: 10.1109/ICORR.2007.4428492
- Nemeroff, C. B., Mayberg, H. S., Krah, S. E., McNamara, J., Frazer, A., Henry, T. R., et al. (2006). VNS therapy in treatment-resistant depression: clinical evidence and putative neurobiological mechanisms. *Neuropsychopharmacology* 31, 1345–1355. doi: 10.1038/sj.npp.1301082
- Nguyen, J. K., Park, D. J., Skousen, J. L., Hess-Dunning, A. E., Tyler, D. J., Rowan, S. J., et al. (2014). Mechanically-compliant intracortical implants reduce the neuroinflammatory response. *J. Neural Eng.* 11:056014. doi: 10.1088/1741-2560/11/5/056014
- Normann, R. A., and Fernandez, E. (2016). Clinical applications of penetrating neural interfaces and Utah Electrode Array technologies. *J. Neural Eng.* 13:061003. doi: 10.1088/1741-2560/13/6/061003
- Oliva, N., de la, Valle, J., del, Delgado-Martínez, I., Mueller, M., Stieglitz, T., and Navarro, X. (2019). Long-term functionality of transversal intraneural electrodes is improved by dexamethasone treatment. *IEEE Trans. Neural Syst. Rehabil. Eng.* 56:1–1. doi: 10.1109/TNSRE.2019.2897256
- Petrini, F. M., Bumbasirevic, M., Valle, G., Ilic, V., and Mijović, P., Cvančara, P., et al. (2019). Sensory feedback restoration in leg amputees improves walking speed, metabolic cost and phantom pain. *Nat. Med.* 25, 1356–1363. doi: 10.1038/s41591-019-0567-3
- Piech, D. K., Johnson, B. C., Shen, K., Ghanbari, M. M., Li, K. Y., Neely, R. M., et al. (2020). A wireless millimetre-scale implantable neural stimulator with ultrasonically powered bidirectional communication. *Nat. Biomed. Eng.* 4, 207–222. doi: 10.1038/s41551-020-0518-9
- Polikov, V. S., Tresco, P. A., and Reichert, W. M. (2005). Response of brain tissue to chronically implanted neural electrodes. *J. Neurosci. Methods* 148, 1–18. doi: 10.1016/j.jneumeth.2005.08.015
- Ramachandran, A., Schuettler, M., Lago, N., Doerge, T., Koch, K. P., Xavier, N., et al. (2006). Design, *in vitro* and *in vivo* assessment of a multi-channel sieve electrode with integrated multiplexer. *J. Neural Eng.* 3:114. doi: 10.1088/1741-2560/3/2/005
- Raspopovic, S., Capogrosso, M., Petrini, F. M., Bonizzato, M., Rigosa, J., Pino, G. D., et al. (2014). Restoring natural sensory feedback in real-time bidirectional hand prostheses. *Sci. Transl. Med.* 6, 222ra19–222ra19. doi: 10.1126/scitranslmed.3006820
- Raspopovic, S., Carpaneto, J., Udina, E., Navarro, X., and Micera, S. (2010). On the identification of sensory information from mixed nerves by using single-channel cuff electrodes. *J. NeuroEngineering Rehabil.* 7:17. doi: 10.1186/1743-0003-7-17
- Richardson, R. R., Miller, J. A., and Reichert, W. M. (1993). Polyimides as biomaterials: preliminary biocompatibility testing. *Biomaterials* 14, 627–635. doi: 10.1016/0142-9612(93)90183-3
- Rochford, A. E., Carnicer-Lombarte, A., Curto, V. F., Malliaras, G. G., and Barone, D. G. (2020). When bio meets technology: biohybrid neural interfaces. *Adv. Mater.* 32:1903182. doi: 10.1002/adma.201903182
- Romero, E., Denef, J. F., Delbeke, J., Robert, A., and Veraart, C. (2001). Neural morphological effects of long-term implantation of the self-sizing spiral cuff nerve electrode. *Med. Biol. Eng. Comput.* 39, 90–100. doi: 10.1007/BF02345271
- Rubehn, B., and Stieglitz, T. (2010). In vitro evaluation of the long-term stability of polyimide as a material for neural implants. *Biomaterials* 31, 3449–3458. doi: 10.1016/j.biomaterials.2010.01.053

- Salatino, J. W., Ludwig, K. A., Kozai, T. D. Y., and Purcell, E. K. (2017). Glial responses to implanted electrodes in the brain. *Nat. Biomed. Eng.* 1, 862–877. doi: 10.1038/s41551-017-0154-1
- Schachter, S. C. (2002). Vagus nerve stimulation: where are we? *Curr. Opin. Neurol.* 15:201. doi: 10.1097/00019052-200204000-00013
- Sharp, A. A., Ortega, A. M., Restrepo, D., Curran-Everett, D., and Gall, K. (2009). *In vivo* penetration mechanics and mechanical properties of mouse brain tissue at micrometer scales. *IEEE Trans. Biomed. Eng.* 56, 45–53. doi: 10.1109/TBME.2008.2003261
- Shimatani, Y., Nikles, S. A., Najafi, K., and Bradley, R. M. (2003). Long-term recordings from afferent taste fibers. *Physiol. Behav.* 80, 309–315. doi: 10.1016/j.physbeh.2003.08.009
- Shin, J., Yan, Y., Bai, W., Xue, Y., Gamble, P., Tian, L., et al. (2019). Bioresorbable pressure sensors protected with thermally grown silicon dioxide for the monitoring of chronic diseases and healing processes. *Nat. Biomed. Eng.* 3, 37–46. doi: 10.1038/s41551-018-0300-4
- Son, D., Lee, J., Lee, D. J., Ghaffari, R., Yun, S., Kim, S. J., et al. (2015). Bioresorbable electronic stent integrated with therapeutic nanoparticles for endovascular diseases. *ACS Nano* 9, 5937–5946. doi: 10.1021/acsnano.5b00651
- Spearman, B. S., Desai, V. H., Mobini, S., McDermott, M. D., Graham, J. B., Otto, K. J., et al. (2018). Tissue-engineered peripheral nerve interfaces. *Adv. Funct. Mater.* 28:1701713. doi: 10.1002/adfm.201701713
- Spetzger, U., Laborde, G., and Gilsbach, J. M. (1995). Frameless neuronavigation in modern neurosurgery. *Minim. Invasive Neurosurg. MIN* 38, 163–166. doi: 10.1055/s-2008-1053478
- Sprengers, M., Vonck, K., Carrette, E., Marson, A. G., and Boon, P. (2017). Deep brain and cortical stimulation for epilepsy. *Cochrane Database Syst. Rev.* 7:CD008497. doi: 10.1002/14651858.CD008497.pub3
- Sridharan, R., Cameron, A. R., Kelly, D. J., Kearney, C. J., and O'Brien, F. J. (2015). Biomaterial based modulation of macrophage polarization: a review and suggested design principles. *Mater. Today* 18, 313–325. doi: 10.1016/j.mattod.2015.01.019
- Srinivasan, A., Tahilramani, M., Bentley, J. T., Gore, R. K., Millard, D. C., Mukhatyar, V. J., et al. (2015a). Microchannel-based regenerative scaffold for chronic peripheral nerve interfacing in amputees. *Biomaterials* 41, 151–165. doi: 10.1016/j.biomaterials.2014.11.035
- Srinivasan, A., Tipton, J., Tahilramani, M., Kharbouch, A., Gaupp, E., Song, C., et al. (2015b). A regenerative microchannel device for recording multiple single unit action potentials in awake, ambulatory animals. *Eur. J. Neurosci.* doi: 10.1111/ejn.13080
- Stoyanova, I. I., Wezel, R. J. A., van, and Rutten, W. L. C. (2013). In vivo testing of a 3D bifurcating microchannel scaffold inducing separation of regenerating axon bundles in peripheral nerves. *J. Neural Eng.* 10:066018. doi: 10.1088/1741-2560/10/6/066018
- Strauss, I., Valle, G., Artoni, F., D'Anna, E., Granata, G., Di Iorio, R., et al. (2019). Characterization of multi-channel intraneural stimulation in transradial amputees. *Sci. Rep.* 9:19258. doi: 10.1038/s41598-019-55591-z
- Takahashi, H., Wang, Y., and Grainger, D. W. (2010). Device-based local delivery of siRNA against mammalian target of rapamycin (mTOR) in a murine subcutaneous implant model to inhibit fibrous encapsulation. *J. Controlled Release* 147, 400–407. doi: 10.1016/j.jconrel.2010.08.019
- Tan, D. W., Schiefer, M. A., Keith, M. W., Anderson, J. R., Tyler, J., and Tyler, D. J. (2014). A neural interface provides long-term stable natural touch perception. *Sci. Transl. Med.* 6, 257ra138–257ra138. doi: 10.1126/scitranslmed.3008669
- Tao, H., Hwang, S.-W., Marelli, B., An, B., Moreau, J. E., Yang, M., et al. (2014). Silk-based resorbable electronic devices for remotely controlled therapy and *in vivo* infection abatement. *Proc. Natl. Acad. Sci. U.S.A.* 111, 17385–17389. doi: 10.1073/pnas.1407743111
- Thompson, C. H., Zoratti, M. J., Langhals, N. B., and Purcell, E. K. (2015). Regenerative electrode interfaces for neural prostheses. *Tissue Eng. Part B Rev.* 22, 125–135. doi: 10.1089/ten.teb.2015.0279
- Tyler, D. J., and Durand, D. M. (1994). Interfascicular electrical stimulation for selectively activating axons. *IEEE Eng. Med. Biol. Mag.* 13, 575–583.
- Tyler, D. J., and Durand, D. M. (1997). A slowly penetrating interfascicular nerve electrode for selective activation of peripheral nerves. *IEEE Trans. Rehabil. Eng.* 5, 51–61. doi: 10.1109/86.559349
- Tyler, D. J., and Durand, D. M. (2003). Chronic response of the rat sciatic nerve to the flat interface nerve electrode. *Ann. Biomed. Eng.* 31, 633–642. doi: 10.1114/1.1569263
- Uthman, B. M., Reichl, A. M., Dean, J. C., Eisenschenk, S., Gilmore, R., Reid, S., et al. (2004). Effectiveness of vagus nerve stimulation in epilepsy patients: A 12-year observation. *Neurology* 63, 1124–1126. doi: 10.1212/01.WNL.0000138499.87068.C0
- Vachicouras, N., Tringides, C. M., Campiche, P. B., and Lacour, S. P. (2017). Engineering reversible elasticity in ductile and brittle thin films supported by a plastic foil. *Extreme Mech. Lett.* 15, 63–69. doi: 10.1016/j.eml.2017.05.005
- Veisheh, O., Doloff, J. C., Ma, M., Vegas, A. J., Tam, H. H., Bader, A. R., et al. (2015). Size- and shape-dependent foreign body immune response to materials implanted in rodents and non-human primates. *Nat. Mater.* 14, 643–651. doi: 10.1038/nmat4290
- Veisheh, O., and Vegas, A. J. (2019). Domesticating the foreign body response: recent advances and applications. *Adv. Drug Deliv. Rev.* 144, 148–161. doi: 10.1016/j.addr.2019.08.010
- Vince, V., Thil, M.-A., Gérard, A.-C., Veraart, C., Delbeke, J., and Colin, I. M. (2005). Cuff electrode implantation around the sciatic nerve is associated with an upregulation of TNF-alpha and TGF-beta 1. *J. Neuroimmunol.* 159, 75–86. doi: 10.1016/j.jneuroim.2004.10.010
- Wang, Y., Vaddiraju, S., Gu, B., Papadimitrakopoulos, F., and Burgess, D. J. (2015). Foreign body reaction to implantable biosensors. *J. Diabetes Sci. Technol.* 9, 966–977. doi: 10.1177/1932296815601869
- Wei, X., Luan, L., Zhao, Z., Li, X., Zhu, H., Potnis, O., et al. (2018). Nanofabricated ultraflexible electrode arrays for high-density intracortical recording. *Adv. Sci.* 5:1700625. doi: 10.1002/advs.201700625
- Wendelken, S., Page, D. M., Davis, T., Wark, H. A. C., Kluger, D. T., Duncan, C., et al. (2017). Restoration of motor control and proprioceptive and cutaneous sensation in humans with prior upper-limb amputation via multiple Utah Slanted Electrode Arrays (USEAs) implanted in residual peripheral arm nerves. *J. NeuroEngineering Rehabil.* 14:4. doi: 10.1186/s12984-017-0320-4
- Wiggins, M. J., Wilkoff, B., Anderson, J. M., and Hiltner, A. (2001). Biodegradation of polyether polyurethane inner insulation in bipolar pacemaker leads. *J. Biomed. Mater. Res.* 58, 302–307. doi: 10.1002/1097-4636(2001)58:3<302::aid-jbm1021>3.0.co;2-y
- Williams, D. F. (2008). On the mechanisms of biocompatibility. *Biomaterials* 29, 2941–2953. doi: 10.1016/j.biomaterials.2008.04.023
- Wilson, C. J., Clegg, R. E., Leavesley, D. I., and Percy, M. J. (2005). Mediation of biomaterial-cell interactions by adsorbed proteins: a review. *Tissue Eng.* 11, 1–18. doi: 10.1089/ten.2005.11.1
- Winslow, B. D., Christensen, M. B., Yang, W.-K., Solzbacher, F., and Tresco, P. A. (2010). A comparison of the tissue response to chronically implanted Parylene-C-coated and uncoated planar silicon microelectrode arrays in rat cortex. *Biomaterials* 31, 9163–9172. doi: 10.1016/j.biomaterials.2010.05.050
- Wurth, S., Capogrosso, M., Raspopovic, S., Gandar, J., Federici, G., Kinany, N., et al. (2017). Long-term usability and bio-integration of polyimide-based intra-neural stimulating electrodes. *Biomaterials* 122, 114–129. doi: 10.1016/j.biomaterials.2017.01.014
- Xie, X., Doloff, J. C., Yesilyurt, V., Sadraei, A., McGarrigle, J. J., Omami, M., et al. (2018). Reduction of measurement noise in a continuous glucose monitor by coating the sensor with a zwitterionic polymer. *Nat. Biomed. Eng.* 2, 894–906. doi: 10.1038/s41551-018-0273-3
- Xu, L.-C., and Siedlecki, C. A. (2007). Effects of surface wettability and contact time on protein adhesion to biomaterial surfaces. *Biomaterials* 28, 3273–3283. doi: 10.1016/j.biomaterials.2007.03.032
- Xue, A. S., Koshy, J. C., Weathers, W. M., Wolfswinkel, E. M., Kaufman, Y., Sharabi, S. E., et al. (2014). Local foreign-body reaction to commercial biodegradable implants: an *in vivo* animal study. *Craniofacial Trauma Reconstr.* 7, 27–34. doi: 10.1055/s-0033-1364199
- Yalcin, I., Megat, S., Barthas, F., Waltisperger, E., Kremer, M., Salvat, E., et al. (2014). The sciatic nerve cuffing model of neuropathic pain in mice. *J. Vis. Exp. JoVE*. doi: 10.3791/51608
- Yu, K. J., Kuzum, D., Hwang, S.-W., Kim, B. H., Juul, H., Kim, N. H., et al. (2016). Bioresorbable silicon electronics for transient spatiotemporal mapping of electrical activity from the cerebral cortex. *Nat. Mater.* 15, 782–791. doi: 10.1038/nmat4624

- Zarrintaj, P., Saeb, M. R., Ramakrishna, S., and Mozafari, M. (2018). Biomaterials selection for neuroprosthetics. *Curr. Opin. Biomed. Eng.* 6, 99–109. doi: 10.1016/j.cobme.2018.05.003
- Zelechowski, M., Valle, G., and Raspopovic, S. (2020). A computational model to design neural interfaces for lower-limb sensory neuroprostheses. *J. NeuroEngineering Rehabil.* 17:24. doi: 10.1186/s12984-020-00657-7
- Zhang, L., Cao, Z., Bai, T., Carr, L., Ella-Menye, J.-R., Irvin, C., et al. (2013). Zwitterionic hydrogels implanted in mice resist the foreign-body reaction. *Nat. Biotechnol.* 31, 553–556. doi: 10.1038/nbt.2580
- Zhang, Y., Zheng, N., Cao, Y., Wang, F., Wang, P., Ma, Y., et al. (2019). Climbing-inspired twining electrodes using shape memory for peripheral nerve stimulation and recording. *Sci. Adv.* 5:eaaw1066. doi: 10.1126/sciadv.aaw1066
- Zhou, T., Hong, G., Fu, T.-M., Yang, X., Schuhmann, T. G., Viveros, R. D., et al. (2017). Syringe-injectable mesh electronics integrate seamlessly with minimal chronic immune response in the brain. *Proc. Natl. Acad. Sci.* 114, 5894–5899. doi: 10.1073/pnas.1705509114
- Conflict of Interest:** The authors declare that the research was conducted in the absence of any commercial or financial relationships that could be construed as a potential conflict of interest.

Copyright © 2021 Carnicer-Lombarte, Chen, Malliaras and Barone. This is an open-access article distributed under the terms of the Creative Commons Attribution License (CC BY). The use, distribution or reproduction in other forums is permitted, provided the original author(s) and the copyright owner(s) are credited and that the original publication in this journal is cited, in accordance with accepted academic practice. No use, distribution or reproduction is permitted which does not comply with these terms.



# Explant Analysis of Utah Electrode Arrays Implanted in Human Cortex for Brain-Computer-Interfaces

Kevin Woeppel<sup>1,2</sup>, Christopher Hughes<sup>1,2,3</sup>, Angelica J. Herrera<sup>1,2,3</sup>, James R. Eles<sup>1</sup>, Elizabeth C. Tyler-Kabara<sup>2,4</sup>, Robert A. Gaunt<sup>1,2,3,5</sup>, Jennifer L. Collinger<sup>1,2,3,5</sup> and Xinyan Tracy Cui<sup>1,2\*</sup>

<sup>1</sup>Department of Bioengineering, University of Pittsburgh, Pittsburgh, PA, United States, <sup>2</sup>Center for the Neural Basis of Cognition, Pittsburgh, PA, United States, <sup>3</sup>Rehab Neural Engineering Labs, Pittsburgh, PA, United States, <sup>4</sup>Department of Neurosurgery, The University of Texas at Austin, Austin, TX, United States, <sup>5</sup>Department of Physical Medicine and Rehabilitation, University of Pittsburgh, Pittsburgh, PA, United States

## OPEN ACCESS

### Edited by:

Valentina Castagnola,  
Italian Institute of Technology (IIT), Italy

### Reviewed by:

Gaëlle Piret,  
Institut National de la Santé et de la  
Recherche Médicale (INSERM), France  
Dan Wu,

Zhejiang University of Technology,  
China

Stefano Carli,  
University of Ferrara, Italy

### \*Correspondence:

Xinyan Tracy Cui  
xic11@pitt.edu

### Specialty section:

This article was submitted to  
Biomaterials,  
a section of the journal  
Frontiers in Bioengineering and  
Biotechnology

**Received:** 16 August 2021

**Accepted:** 29 October 2021

**Published:** 07 December 2021

### Citation:

Woeppel K, Hughes C, Herrera AJ, Eles JR, Tyler-Kabara EC, Gaunt RA, Collinger JL and Cui XT (2021) Expant Analysis of Utah Electrode Arrays Implanted in Human Cortex for Brain-Computer-Interfaces. *Front. Bioeng. Biotechnol.* 9:759711. doi: 10.3389/fbioe.2021.759711

Brain-computer interfaces are being developed to restore movement for people living with paralysis due to injury or disease. Although the therapeutic potential is great, long-term stability of the interface is critical for widespread clinical implementation. While many factors can affect recording and stimulation performance including electrode material stability and host tissue reaction, these factors have not been investigated in human implants. In this clinical study, we sought to characterize the material integrity and biological tissue encapsulation via explant analysis in an effort to identify factors that influence electrophysiological performance. We examined a total of six Utah arrays explanted from two human participants involved in intracortical BCI studies. Two platinum (Pt) arrays were implanted for 980 days in one participant (P1) and two Pt and two iridium oxide (IrOx) arrays were implanted for 182 days in the second participant (P2). We observed that the recording quality followed a similar trend in all six arrays with an initial increase in peak-to-peak voltage during the first 30–40 days and gradual decline thereafter in P1. Using optical and two-photon microscopy we observed a higher degree of tissue encapsulation on both arrays implanted for longer durations in participant P1. We then used scanning electron microscopy and energy dispersive X-ray spectroscopy to assess material degradation. All measures of material degradation for the Pt arrays were found to be more prominent in the participant with a longer implantation time. Two IrOx arrays were subjected to brief survey stimulations, and one of these arrays showed loss of iridium from most of the stimulated sites. Recording performance appeared to be unaffected by this loss of iridium, suggesting that the adhesion of IrOx coating may have been compromised by the stimulation, but the metal layer did not detach until or after array removal. In summary, both tissue encapsulation and material degradation were more pronounced in the arrays that were implanted for a longer duration. Additionally, these arrays also had lower signal amplitude and impedance. New biomaterial strategies that minimize fibrotic encapsulation and enhance material stability should be developed to achieve high quality recording and stimulation for longer implantation periods.

**Keywords:** brain-computer interface, human participant, Utah array, neural electrical stimulation, neural electrode array, explant analysis



# 1 INTRODUCTION

Intracortical brain-computer interfaces (BCIs) can restore function for people affected by significant paralysis by allowing the user to control an effector or assistive device with signals recorded in the brain. In recent years intracortical implants in motor cortex have been used for BCI control in primates and human participants with up to 10 degrees of freedom (Hochberg et al., 2006; Santhanam et al., 2006; Velliste et al., 2008; Collinger et al., 2013; Wodlinger et al., 2014; Bouton et al., 2016; Ajiboye et al., 2017). More recently, somatosensory feedback has also been added to these systems by stimulating through electrodes in the somatosensory cortex (Flesher et al., 2016; Armenta Salas et al., 2018; Fifer et al., 2020; Hughes et al., 2020; Flesher et al., 2021; Hughes et al., 2021). Given that intracortical BCIs require surgical implantation, they must be stable over many years to be clinically viable. This issue has been studied in both humans and primates, demonstrating that signals can be reliably recorded from electrodes in the motor cortex for over 6 years when devices do not fail, although there is considerable inter-subject variability and signals typically deteriorate over time (Suner et al., 2005; Chestek et al., 2011; Simeral et al., 2011; James et al., 2013; Downey et al., 2018; Bullard et al., 2020; Hughes et al., 2021).

Changes in recorded activity can be caused by many factors including movements of the electrodes relative to the brain, encapsulation of the electrode sites, as well as material degradation and failure (Prasad et al., 2014; Kozai et al., 2015; Woeppel et al., 2017). These factors can be broadly grouped into multiple failure categories, including material and biological failure (James et al., 2013).

Biological failures can occur as a result of the host tissue reactions to the implant. The traumatic nature of the implant leads to glial activation and encapsulation of the implant in a glial sheath (Polikov et al., 2005; Salatino et al., 2017). The glial sheath creates a physical barrier between the electrode and the neurons, while the extensive inflammation damages healthy neurons and may cause a neuron dead zone around the implant (Buzsáki, 2004; Schwartz et al., 2006). One recent study examining brain tissue from a human patient implanted with a Utah microelectrode array for 7 months found a substantial degree of tissue damage which correlated with decreased recording performance (Szymanski et al., 2021). In addition to central nervous system (CNS) reactions, the meninges can grow under the electrode. Meningeal encapsulation is highly collagenous and originates from non-CNS tissues. Substantial undergrowth of meningeal tissues can result in displacement of the electrode sites or complete ejection of the device from the CNS (Woolley et al., 2013). Subsequent device ejection is the most prevalent cause of chronic device failure in non-human primates, accounting for nearly 30% of chronic failure (Barrese et al., 2016; Dunlap et al., 2020). Longer experimental times increase the chance of meningeal undergrowth and eventual ejection of the recording device from the host tissues (Rousche and Normann, 1998; Barrese et al., 2016; Degenhart et al., 2016).

Material failures include metal corrosion, insulation cracking, and insulation delamination. These material failure modes often

increase in likelihood as time progresses. The parylene-C insulation commonly used for Utah style intracortical arrays can crack and delaminate, shunting current to the biological tissues (Schmidt et al., 1988; Prasad et al., 2014; Xie et al., 2014; Caldwell et al., 2020). The metal tips of Utah arrays, most commonly platinum or iridium oxide, are generally stable *in vitro*, but may be eroded away by aggressive stimulation (Negi et al., 2010) or the comparatively harsh *in vivo* environment (Negi et al., 2010). Furthermore, use of the electrodes for stimulation can impact the rate of tip degradation (Cogan, 2008; Gilgunn et al., 2013).

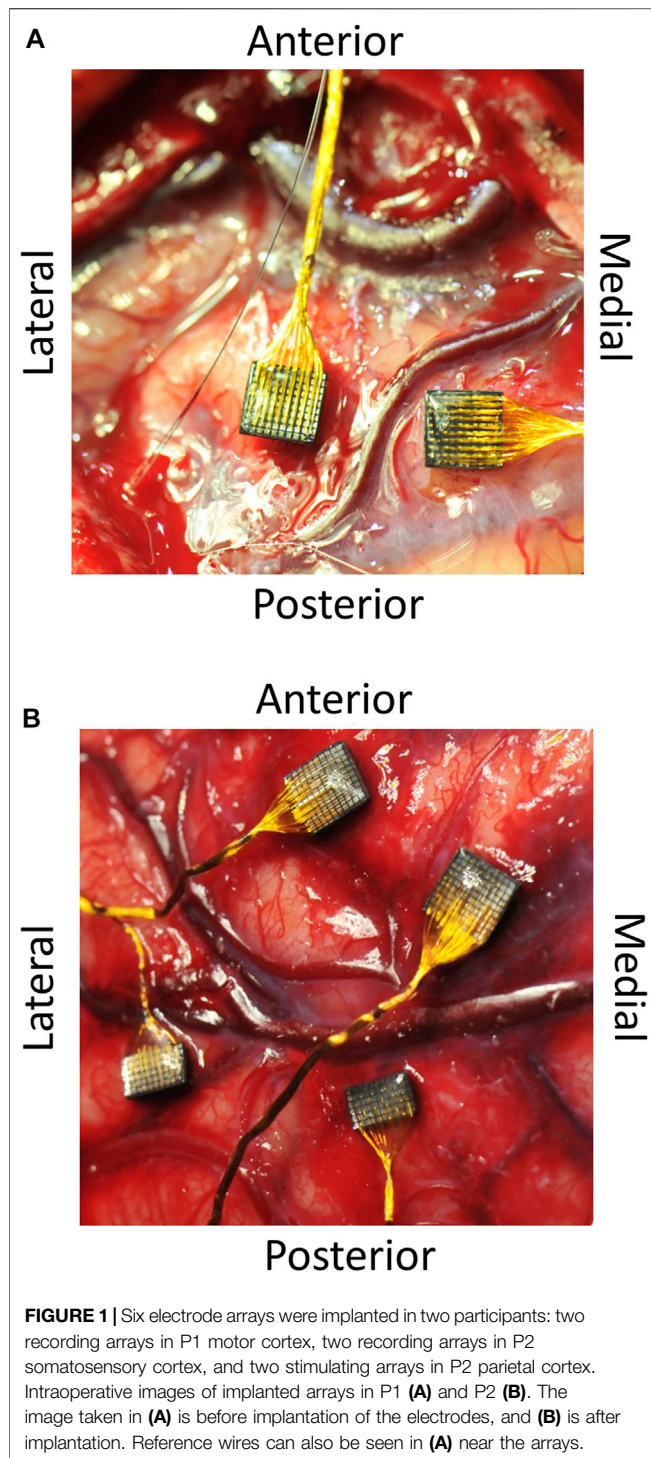
To establish stimulation limits for these clinical studies, experiments were performed in non-human primates and showed that frequent microstimulation over 6 months did not cause more loss of neurons around the electrode tips than insertion of the devices themselves and that stimulation had no behavioral effect for tasks that required tactile feedback (Chen et al., 2014; Kim et al., 2015). Using these established parameters, we would not expect stimulation to cause further damage to the brain tissue after implantation or have deleterious effects on behavior. In fact, stimulation over 5 years in a participant with these established parameters has not resulted in significant differences in signal between stimulated and non-stimulated arrays and detection thresholds have improved over time (Hughes et al., 2021). However, to our knowledge there have been no post-implant examinations of the material properties of intracortical arrays implanted in humans. Here we examine the extent to which any material degradation occurred on explanted human intracortical electrodes, which will aid in the design and development of robust BCIs for long-term clinical use.

In this work, electrodes explanted from two human participants were examined to determine the extent of tissue encapsulation and material failure and to assess how these factors affected chronic recording performance. These electrodes were implanted for different lengths of time and were surgically explanted: 987 days for the two arrays in participant 1 (P1) and 182 days for the four arrays in participant 2 (P2). Both arrays in P1 and two of the arrays in the P2 had platinum (Pt) tips and were used for recording only, while the other two of the arrays in P2 had sputtered iridium oxide (IrOx) tips and were used for both stimulating and recording (Negi et al., 2010). First, the extent and nature of the tissue encapsulation of the arrays was investigated using optical microscopy and two-photon microscopy (TPM). Following this, the electrode arrays were examined with scanning electron microscopy (SEM) and energy-dispersive x-ray spectroscopy (EDS) to evaluate the extent of material damage. Finally, we compared the results of these analyses to endpoint recording performance of the devices and characterized the relationship between electrical stimulation and material degradation.

## 2 METHODS

### 2.1 Participants

These studies (NCT01894802 and NCT01364480) were conducted under Investigational Device Exemptions from the



U.S. Food and Drug administration and were approved by the Institutional Review Boards at the University of Pittsburgh (Pittsburgh, PA) and the Space and Naval Warfare Systems Center Pacific (San Diego, CA). Informed consent was obtained before any study procedures were conducted. Two participants were implanted with microelectrode arrays in the brain. The first subject (P1) was implanted with two intracortical

Pt microelectrode arrays (4 mm × 4 mm, Blackrock Microsystems, Salt Lake City, UT, United States) each with 96 wired electrode shanks (length 1.5 mm) in a 10 × 10 grid in the participant's left motor cortex (**Figure 1**). The second subject (P2) was implanted with two Pt microelectrode arrays (Blackrock Microsystems, Salt Lake City, UT) in the left somatosensory cortex and two IrOx microelectrode arrays in the left parietal cortex. Each Pt array in the somatosensory cortex consisted of 88 wired electrodes in a 10 × 10 grid while each IrOx array in the parietal cortex consisted of 32 wired electrodes distributed throughout a 6 × 10 grid (**Figure 1**). Following implantation of the arrays into P2, it was discovered that the implant locations were posterior to the intended sites. Following which, the pedestals were removed, and a second implantation was performed 2 months later. This second set of implants are not within the scope of this study and are still implanted in the participant as of October 2021. A timeline for the arrays from implant to final analysis can be found in **Table 1**.

## 2.2 Neural Recording and Signal Quality Metrics

Neural data were collected for both P1 and P2 using Neuroport Neural Signal Processors (Blackrock Microsystems, Salt Lake City, UT). At the beginning of each test session, a threshold for all channels was set at  $-5.25$  (P1 before day 565) and  $-4.5$  (all other test sessions) times the root-mean-square voltage. Data were collected across 287 sessions spanning 33 months for P1 and 40 sessions across 4 months for P2. No recordings were done for the final 2 months of P2's implant as the percutaneous pedestal connectors had been removed to prepare for the reimplant.

One of the main goals of the clinical study was to provide the participants with high degree-of-freedom control of a robotic arm. To accomplish this, participants performed a brain-computer interface calibration paradigm at the beginning of a test session. We used 3 min of data collected during this calibration procedure to run spike sorting analyses offline. The sorting method, described in detail in Downey et al. (2018) used principal component analysis (PCA) to separate units, defined as threshold crossings from an individual electrode, based on the similarity of their waveform shape. Characteristics for each unit were then calculated. Peak-to-peak voltage ( $V_{pp}$ ) was defined as the voltage difference between the peak and the trough of the average waveform for each unit. Since there could be more than one unit identified per electrode, the unit with the maximum  $V_{pp}$  was chosen to represent the signal quality for the given electrode. Electrodes were considered to be viable if they contained waveforms with a minimum  $V_{pp}$  of  $20 \mu V$  in P1 and  $30 \mu V$  in P2 and a minimum firing rate of 0.25 Hz. We chose these lower amplitude thresholds rather than being more conservative because lower amplitude multiunit recordings can still be used for decoding, although very low amplitude recordings may be more indicative of noise.

### 2.2.1 Impedances

Electrode impedances were measured for both participants using the NeuroPort patient cable data acquisition system (Blackrock

**TABLE 1 |** Timeline of implantation, procedures, and explant analysis.

Electrode	Length of implant	Used for stimulation	Reason for explantation	Post explant optical imaging	Fixation	Staining	Two photon microscopy	Enzymatic cleaning	SEM	EDS
P1 Medial and Lateral Recording arrays	987 days	No	Retraction of skin around pedestal	Immediately after explant ( <b>Figure 3</b> )	Formalin, immediately after explant	Hoechst (cell nuclei), 20-min at 1:1,000 22C	Yes following staining	Yes following TPM	Yes, environmental SEM then standards SEM ( <b>Figure 6</b> )	Yes, last procedure performed
P2 Medial and Lateral Recording Arrays	182 days	No	Undesired implant location	Immediately after explant ( <b>Supplementary Figure S1</b> )	Formalin, 2 months after explant	None	Yes, following staining	No	Yes, standard SEM only ( <b>Figure 6</b> )	Yes, last procedure performed
P2 Medial and Lateral Stimulating Arrays	182 days	Yes, 7 times over first 30 days	Undesired implant location	Immediately after explant ( <b>Supplementary Figure S1</b> )	Formalin, 2 months after explant	None	No	No	Yes, standard SEM only ( <b>Figure 6</b> )	Yes, last procedure performed ( <b>Figure 7</b> )

Microsystems, Salt Lake City, UT). For P1, impedances were measured at the beginning of a test session once a month. Impedances values for P2 were measured at the beginning of each test session. The system delivered a 1 kHz, 10 nA peak-to-peak sinusoidal current to each implanted electrode for 1 s.

### 2.2.2 Intracortical Stimulation and Calculated Metrics

Seven test sessions across approximately 1 month involved microstimulation on the IrOx arrays. Stimulation was delivered using a CereStim R96 multichannel microstimulation system (Blackrock Microsystems, Salt Lake City, UT). Pulse trains consisted of cathodal phase first, current-controlled, charge-balanced pulses delivered at frequencies from 20 to 300 Hz and at amplitudes from 1 to 100  $\mu$ A. The cathodal phase was 200  $\mu$ s long, the anodal phase was 400  $\mu$ s long, and the anodal phase was set to half the amplitude of the cathodal phase. The phases were separated by a 100  $\mu$ s interphase period. Stimulus pulse trains were varied in terms of amplitude, frequency, and train duration.

The voltage transients associated with each stimulus pulse were recorded using National Instruments data acquisition modules. Voltage traces were displayed in real time using LabView and saved to disk for analysis. Interphase voltage was measured as the voltage at the end of the interphase period immediately prior to the anodal phase for a given stimulation pulse. The total charge delivered to each electrode was calculated across all stimulation experiments using the charge delivered during the cathodal phase.

## 2.3 Explanted Array Handling Before Imaging

The two Pt arrays in P1 were explanted on day 987 post-implant and the four arrays in P2 were explanted on day 182. Following explantation, all arrays were removed from their wire bundles by clipping the wires proximal to the probe and were washed with saline. The P1 arrays were immediately fixed in formalin and then

transferred to PBS bath for storage. Immunohistochemical staining procedure was performed on these two arrays with the goal of identifying neuron (NeuN) and microglia/macrophage (Iba-1). The staining process involves incubation of the arrays with primary antibodies solutions overnight, with secondary antibodies for 4 h followed by Hoescht solution for 20 min for nuclei staining. The antibody staining was unsuccessful, and only nuclei stain was used for the tissue analysis. The P2 arrays were fixed 2 months post-implant, and one of the Pt arrays had visible tissue encapsulation and was imaged using TPM. Because these arrays were not immediately fixed, we did not perform immunostaining, and only characterized the collagen structure, which can be stable without the fixation.

After optical and TPM imaging, two arrays explanted from P1 were sent to the FDA for initial analysis. The arrays were initially imaged with an environmental SEM, then enzymatically cleaned with Asepti-Zyme neutral pH enzymatic instrument presoak/cleaner (4 ml in 250 ml saline) at 37°C for 90 min, followed by Getinge Clean Enzymatic detergent (1 ml in 250 ml saline) at 37°C for 90 min, and then by MetriZyme detergent (1 ml in 250 ml saline) 37°C for 90 min. Samples were then thoroughly washed with water and air dried, ready for SEM imaging. This process was effective at removing some of the tissue and revealing the electrode tip/shank for material analysis. Arrays from P2 did not undergo the enzymatic cleaning procedure. All arrays were stored adhered to copper tape, tips up.

## 2.4 Electrode Imaging

Explanted electrodes were first characterized by optical and two-photon microscopy to assess the degree of tissue encapsulation. For TPM, we used a two-photon laser scanning microscope with a Bruker scan head (Prairie Technologies, Madison, WI), TI: sapphire laser tuned to 920 nm (Mai Tai DS; Spectra-Physics, Menlo Park, CA), light collection through non-descanned photomultiplier tubes (Hamamatsu Photonics KK, Hamamatsu, Shizuoka, Japan), and a 10x or 16x, 0.8



numerical aperture water immersion objective (Nikon Inc., Milville, NY). Laser power was maintained between 20 and 40 mW. For each electrode tip, Z-stacks were collected with filters to resolve second harmonic generation (SHG) at half the laser wavelength (~460 nm), which enabled intrinsic imaging of collagen-I representing the meningeal encapsulation. Images along the length of the electrode shanks were collected as Z-stacks. Z-stack images were either collected at specific regions of interest, or in a grid at all locations across the face of the electrode array. Grid images were automated by the Prairie software with a 10% overlap between images. All image stitching and subsequent image processing was conducted with ImageJ software (NIH). Electrode integrity was characterized by scanning electron microscopy (SEM) and energy-dispersive x-ray spectroscopy (EDS). Samples were washed, dried under alcohol, and sputter-coated with 4 nm Au/Pd. Images were taken by JSM 6335F electron microscope. EDS was taken by Zeiss Sigma 500VP, excluding Au and Pd from quantification.

Using the SEM and optical images, a qualitative category of “non-degraded/unencapsulated” or “degraded/encapsulated” was assigned to each electrode based on the degree of damage to the tip or shank, or the level of encapsulation around the electrode. Arrays explanted from P1 were more extensively cleaned prior to imaging, and the encapsulation score was based on optical images of the explanted arrays. Encapsulation on arrays from P2 was determined by examining the SEM images. Degraded electrode tips were defined as having obvious and substantial surface defects in the metal coating, including pitting of the metal, flaking of the metal, and exposure of the underlying silicon. Degraded shanks were defined relative to the parylene insulation, with defects including insulation cracking along the shank, peeling of the insulation away from the shank near the tip, and other obvious defects in or below the insulation. These categories were compared to EDS images, confirming the presence/absence of metalation at the tip (Pt/IrOx). Electrodes which could not be quantified, due to breakage during removal or gross encapsulation, were assigned a null score and excluded from analysis.

## 2.5 Statistics

Changes in signal and impedances over time were assessed using linear regression. For impedances, data were log-transformed because data did not follow a linear trend. For P2 impedances and Vpp, we excluded data prior to day 30 for regression because the impedances measured in this range were highly variable.

Total charge delivered, minimum interphase voltages, and charge delivered after exceeding an interphase voltage of -0.6 V were compared between the two electrode arrays that had received stimulation using Mann-Whitney tests. We used a non-parametric test because the data was determined to not be normally distributed using an Anderson-Darling test. We used a Fisher exact test to determine if there was a significant relationship between an electrode's material properties (undamaged or damaged) and the length of implantation (Pt arrays in P1 vs. P2) or if it received stimulation (P2 IrOx arrays, yes or no). We further quantified if there was a relationship between both total charge injected and charge injected with

interphase voltages below -0.6 V on stimulated electrodes and their material properties (undamaged or damaged) using logistic regression. Electrode categories were compared to impedances and Vpp using Mann-Whitney tests. We used a non-parametric test because the variances between groups were not the same.

## 3 RESULTS

### 3.1 Signal Amplitude and Impedances Decreased Over Time

Changes in the impedances and peak-to-peak voltages over time were observed on implanted electrodes in both participants (**Figure 2**). Impedances decreased over time on electrodes implanted in P1 ( $p < 0.001$ , log-transformed linear regression, **Figure 2A**). For P2, the starting impedances of IrOx electrodes were lower than the platinum electrodes, which is consistent with the manufacturer's specification (Negi et al., 2010). From day 1–20 we observed an increase in impedances. The initial increase in impedance reversed after 1 month (30 days), and a significant downward trend in impedances was observed until the end of recording for both the IrOx ( $p < 0.001$ , linear regression) and platinum arrays ( $p < 0.001$ , linear regression). Impedances gathered from P1 eventually stabilized after approximately 2 years. The difference between the final impedance values recorded in P1 and P2 can be explained by the difference in length of implantation. Previous studies have determined that impedance values of stimulated and non-stimulated intracortical electrodes decrease dramatically over the first couple of years after implantation in humans (Hughes et al., 2021) and monkeys (Suner et al., 2005; Chestek et al., 2011). Since P2 was implanted for a significantly shorter period, we would expect the electrode impedance values to be larger and more variable, which the data supports.

In the same manner as the impedance measurements, an initial increase in Vpp was observed for both P1 and P2. However, after an increase in the first 30 days, the measured Vpp from P1 and P2 exhibited a downward trend ( $p < 0.001$ , linear regression, **Figures 2C,D**). The rates of decrease in the Vpp between day 30 and 120 for P1 and P2 were -4.0  $\mu\text{V}/\text{month}$  and -4.86  $\mu\text{V}/\text{month}$ , respectively. Median Vpp decreased by 52% across 550 days in P1 and by 14% across 90 days in P2. The median Vpp for P1 leveled off at approximately 25–30  $\mu\text{V}$ .

Comparing across patients, the platinum arrays performed similarly over the first months of implantation. Impedances of the Pt arrays in both P1 and P2 were both initially higher than the IrOx arrays (**Figure 2E**). Recorded unit amplitudes were similar across all arrays regardless of material or patient (**Figure 2F**).

### 3.2 Encapsulating Tissues Were Apparent on Multiple Arrays

Based on the gross optical micrographs, both P1 arrays had a significant degree of adherent tissue on the electrode base and shanks. The nature of the encapsulating tissue was examined with TPM, measuring the second harmonic signal characteristic of collagen. For the more heavily encapsulated P1 arrays, the



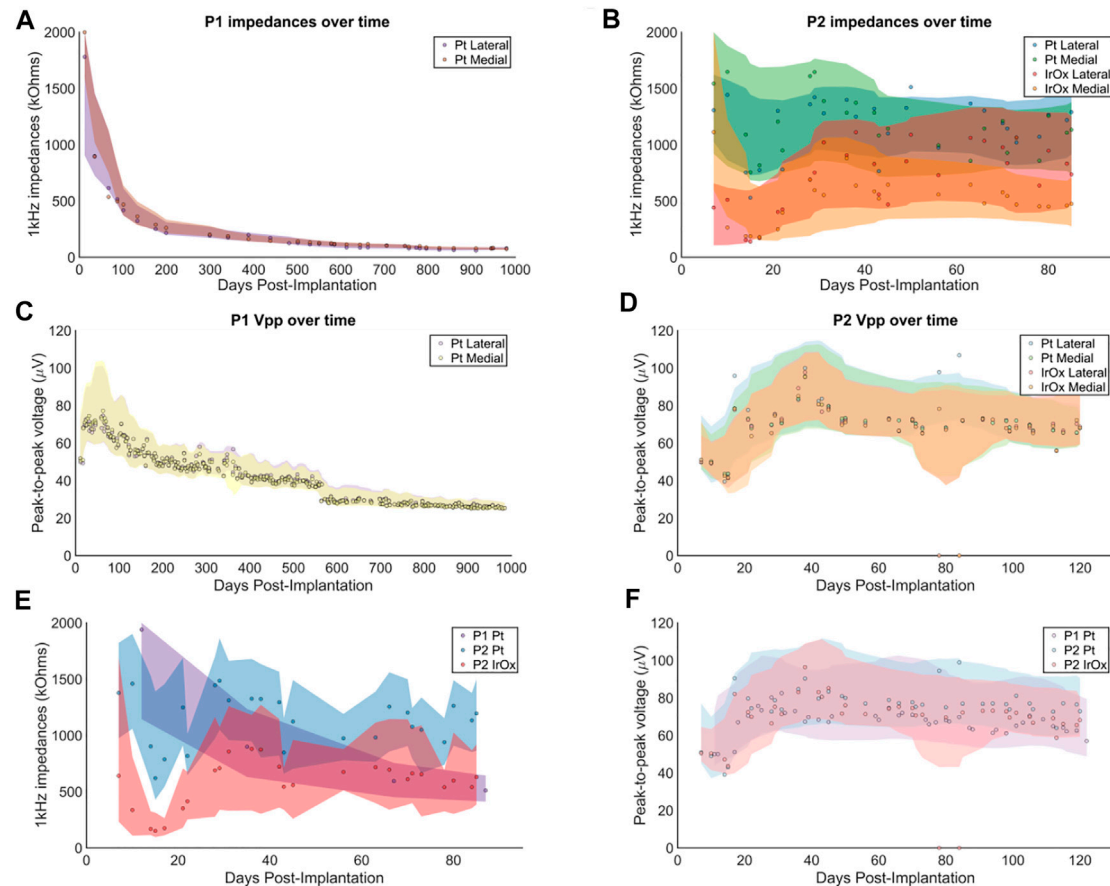
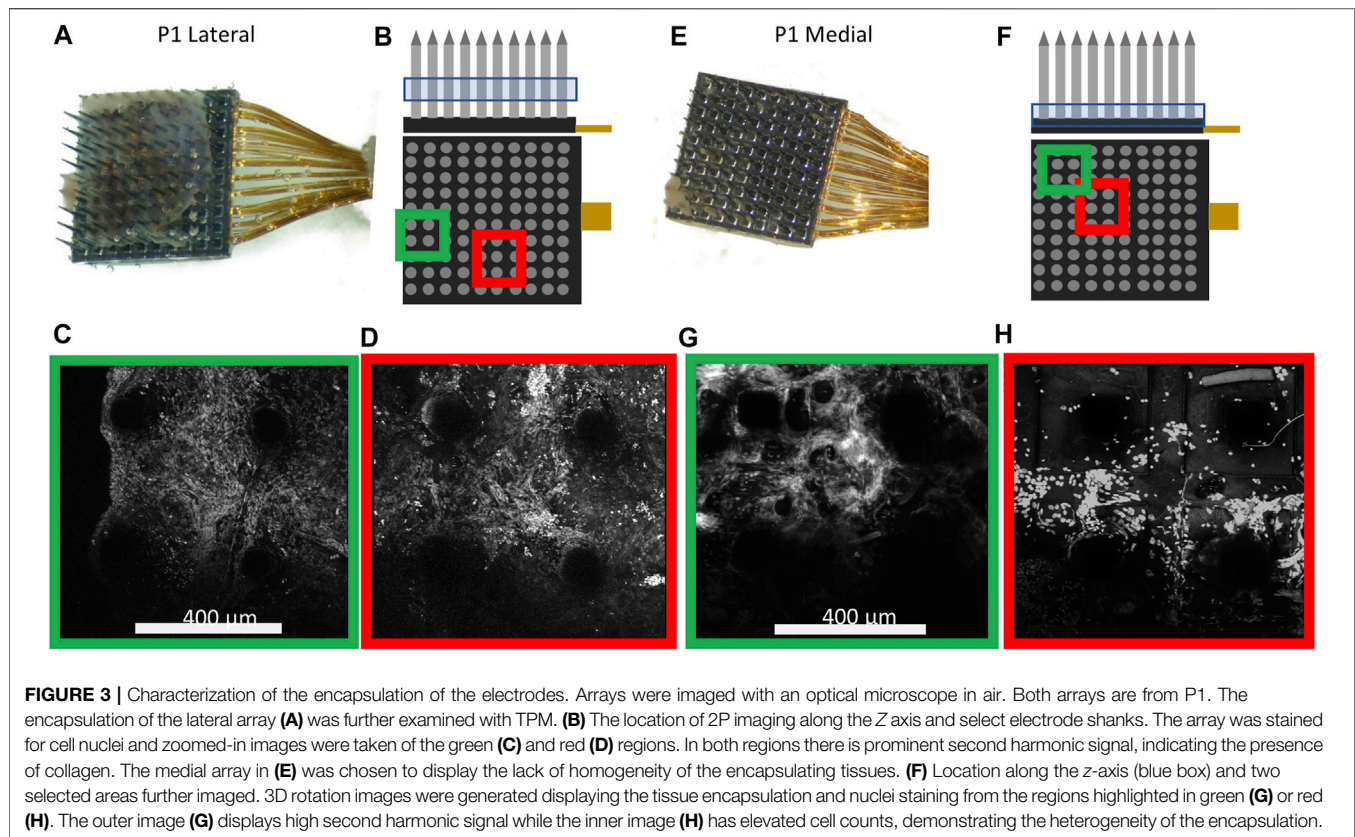


**FIGURE 2 |** Impedances and peak-to-peak voltages decreased over time. Data points represent the median across electrodes for a given test date. The shaded regions show the interquartile ranges smoothed with a nine-point moving average filter with a triangular kernel. Median impedances recorded on **(A)** P1 electrodes and **(B)** P2 electrodes across the length of implant. Impedance measurements on P1 were not conducted with the same temporal resolution as P2. Different colors represent platinum or IrOx for P2 as indicated in the legend. Vpp recorded on **(C)** P1 electrodes and **(D)** P2 electrodes across the length of implant. For P1, there was a discontinuity in the Vpp at day post-implant 550 due to a change in the RMS threshold from  $-5.25$  to  $-4.5$ . Overlaid impedances and Vpp for P1 and P2 are shown in **(E)** and **(F)**, respectively.

encapsulation sheet was found both along the shanks of the array (**Figures 3A–D**) and at the base (**Figures 3E–H**). The lateral array (**Figure 3A**) exhibited strong second-harmonic signal within the tissue sheet confirmed that it was primarily composed of collagen-I fibers (**Figures 3C,D**). After further examining the indicated electrodes and staining for cell nuclei, we observed that the encapsulation was highly cellularized (**Figures 3C,D**). In addition, the encapsulation continued down the shank of the electrode, with cellular and collagenous material detected along the shanks and tips of the array. Upon examining the medial array (**Figure 3E**), we observed that the encapsulation was not homogenous, instead exhibiting greater second harmonic signals nearer to the edges (**Figure 3G**) while having greater cell density nearer the center (**Figure 3H**). SHG imaging is also a good tool for detecting blood vessels because of the strong presence of collagen in the vessel wall, however we did not observe clear blood vessel structure in the P1 explants.

We examined relationship between the preimplant location of the medial Pt array of P2 (**Figure 4A**) and the tissue present on

the explanted array. For the medial Pt array in P2, the encapsulation tissue covers the whole array (**Figure 4B**; **Supplementary Figure S1**) and the TPM imaging from the side revealed significant tissue covering the majority of the electrode tips (**Figure 4C**). Here, we identified clear vascular architecture in the encapsulation tissue with SHG imaging (**Figure 4D**, highlighted in blue). The blood vessel in the encapsulation tissue was traced and super-imposed to the image of pial vasculature observed pre-implantation (**Figure 4E**). As can be seen in **Figure 4F**, the blood vessel traces match the pia vasculature. This indicates that the blood vessels observed to be at the tip of this array were pial blood vessels. Two mechanisms may lead to this: 1) the array did not fully penetrate the pia at the time of implantation; 2) the array was successfully implanted in the brain parenchyma and the pia membrane was pulled out with the array. Since we were able to obtain high Vpp recordings from this array in the region coinciding with the vasculature (**Figure 2D**), the first potential mechanism was ruled out. Therefore, we conclude that not all the



tissue present on the device is fibrotic scar in nature, and that at least some of the tissue on this explant is pia membrane that was pulled out with the device.

### 3.3 Length of Implantation Impacts the Degree of Material Degradation and Fibrous Encapsulation

Based on the optical and SEM images, electrodes were assigned a binary score for the tip, shank, and degree of fibrous encapsulation (Figure 5). The electrode scores and images are shown in Figure 6, and summary data for each group are displayed in Table 2, excluding electrodes which were not wired or used for recording or stimulation. Electrodes that appeared to be broken or damaged by implantation/explantation were excluded from analysis. Tips and shanks were evaluated separately to examine the effects of both tip metallization and electrode insulation on device performance. Differences in the total number of electrodes receiving a tip category, shank category, and encapsulation are due to damage to the electrodes or excess encapsulation preventing the assignment of a proper.

Categories assigned to P1 and P2 platinum arrays were compared to identify any potential changes in material deterioration or encapsulation which may be attributed to the length of implantation (Table 3). We found that both measures of material degradation (tip and shank damage) were more prominent for longer implantation times (27.8% tip damage

for P1 and 11.1% for P2, 15.2% shank damage for P1 and 1.8% for P2,  $p < 0.001$  for both). We also found that the degree of encapsulation is more significant for longer implants with 72.4% for the P1 arrays and 50% for the P2 arrays ( $p < 0.001$ ).

### 3.4 Stimulation Resulted in Electrode Damage on One Stimulating Array but Not the Other

Two IrOx arrays implanted in P2 received a low amount of total charge ( $<160 \mu\text{C}$  per electrode site). Each of the two stimulated IrOx arrays had 60 electrodes, half of which were electrically connected and used for stimulation. Preimplant optical images of the arrays did not show any variation between arrays. The stimulated electrode sites are arranged primarily in a checkerboard fashion. SEM shows that the lateral array had a high degree of tip and shank degradation (Figure 7A). Interestingly, tips and shanks showing visible damage appeared to coincide with the electrodes that were used for stimulation. Furthermore, EDS revealed that stimulated tips had lower iridium counts than non-stimulated tips as illustrated by the lower intensity of the magenta coloring (Figure 7B). The loss of metallization for the lateral stimulating array occurred predominantly on the electrodes used for stimulation. The medial array did not show this pattern (Figure 7C). The damage scores for each electrode tip and shank are summarized in Figures 7D,E. The checkerboard

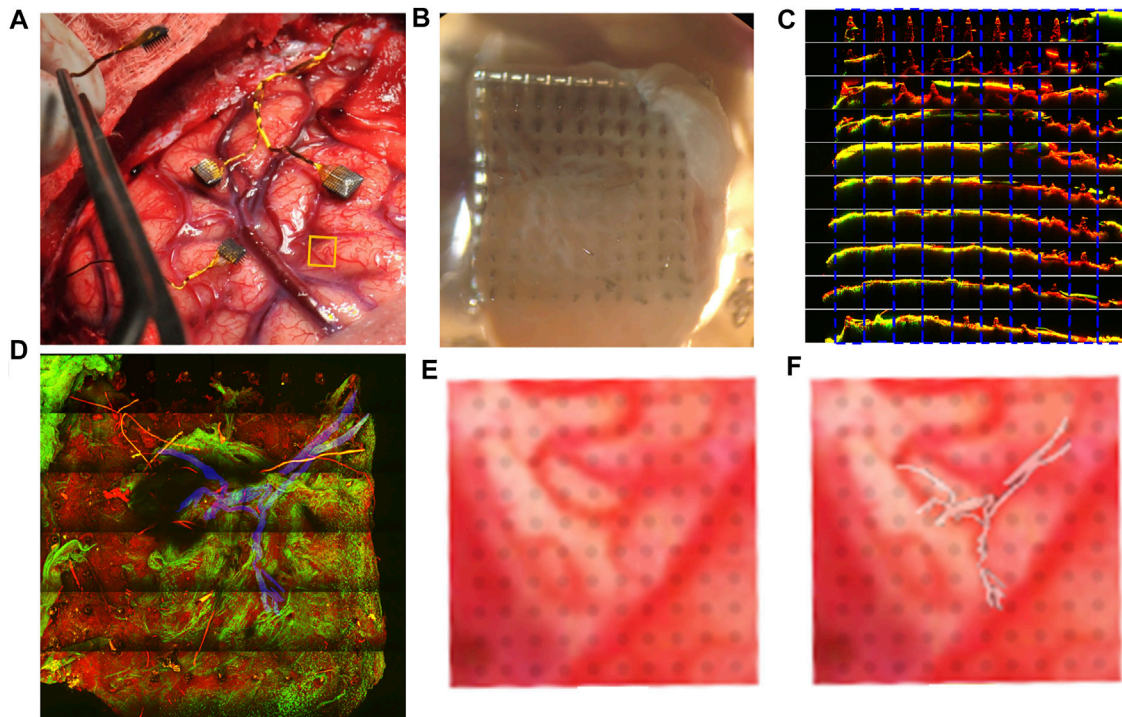


**FIGURE 4 |** Brain vascularization can be visualized on the medial Pt array from P2. The pre-implant location is indicated with a yellow box (A). (B) Optical image of the array showing tissue coverage. (C) TPM of the shanks of the electrode, with green denoting second harmonic signal from collagen and red denoting the autofluorescence of the device. Each electrode was imaged and separated by row (side view). Most of the electrode tips are covered by collagenous tissue. (D) TPM image of the array looking from the tips downward, with a portion of vasculature marked in blue as determined by SHG imaging. (E) zoomed in image from (A) where electrode shanks are superimposed on the underlying vasculature. (F) The vasculature visualized in (D) is superimposed on (E), showing similar trajectory, demonstrating that the vasculature structure identified in the tissue on the explanted array is likely of pial origin.

pattern of damages of the lateral array is clearly seen, which correspond very well with arrangement of the stimulation electrodes. The medial stimulating array has overall much less observable material damage but more tissue encapsulation. Of the 62 electrodes used for stimulation on both arrays, 56 were analyzed, of which 23 had notable tip degradation, 21 of which were located on the lateral electrode array. Metal loss, and the corresponding decrease in iridium signal, was not observed on any non-stimulated electrodes. These results are summarized in **Table 4**.

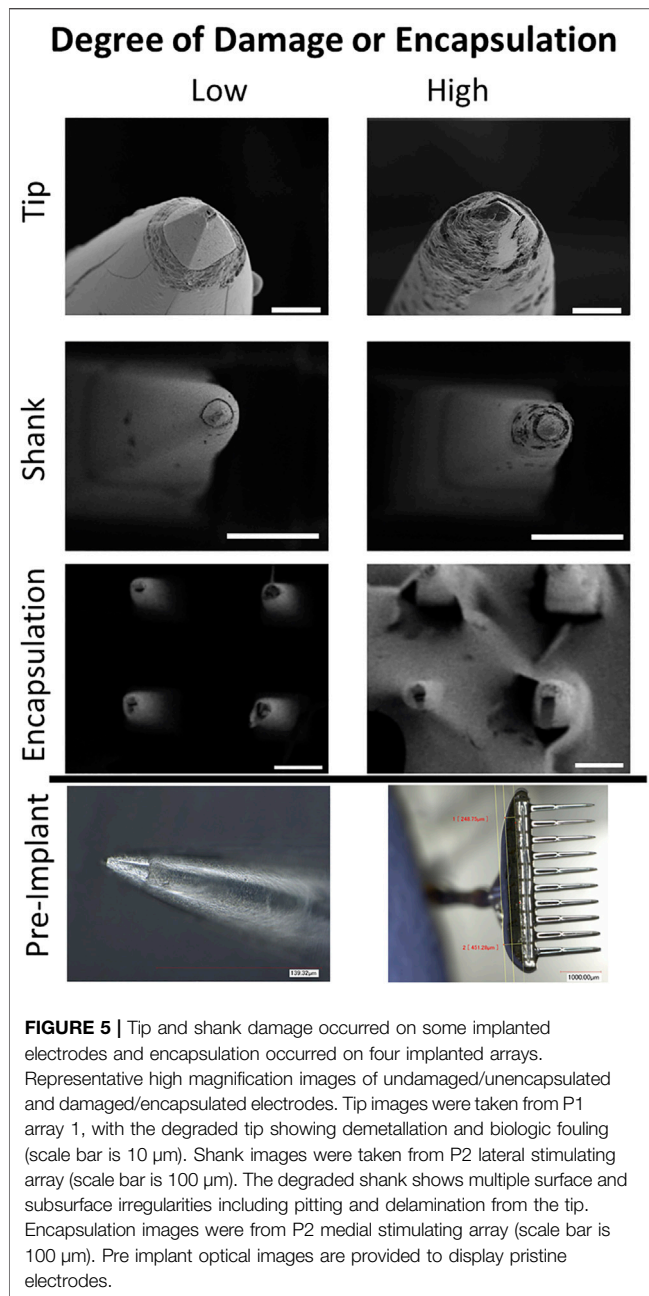
Delivered charge and measured interphase voltages were compared to the material degradation. The amount of stimulation provided was quantified by both the total charge delivered and number of pulses delivered. Although the mean amount of charge injected on the lateral array was greater, it was not significantly different than the mean charge injected on the medial array (Mann-Whitney test,  $p = 0.22$ ). The medial array contained the three electrodes with the most charge delivered, none of which displayed observable material degradation. However, we examined the minimum voltage during the interphase period (**Figure 7F**) and found that the lateral array electrodes experienced higher voltage excursions on average than the medial array electrodes (mean minimum voltage was  $-1.7$  V for the lateral, and  $-1.1$  V for the medial array). Furthermore,

there was a significant relationship between the total charge injected at voltages more negative than  $-0.6$  V (**Figure 7G**) and the tip score ( $p = 0.025$ , crit- $p = 0.034$ , logistic regression) and shank category ( $p = 0.023$ , crit- $p = 0.034$ , logistic regression) on the lateral stimulating array. There was no relationship between total charge injected at voltages less than  $-0.6$  V and tip category ( $p = 0.60$ , logistic regression) or shank category ( $p = 1$ , logistic regression) on the medial array (**Figure 7H**). We found no significant differences in recording quality ( $V_{pp}$ ) (**Figure 7I**) between the damaged and non-damaged electrodes on the two stimulation arrays, after excluding the encapsulated electrodes.

## 4 DISCUSSION

In order for BCIs to become a viable therapy, the longevity of the devices and mechanisms of failure must be well understood. Effective electrode design requires knowledge of the stability of the materials in the harsh *in vivo* environment and the effects of gradually accumulating damage to the device. However, the relationships between chronic material degradation and device performance are poorly understood. The effects of material degradation on performance in human subjects is further complicated by the limited number of human subjects and the





even smaller amount of explanted human BCI arrays. In this work, the *in vivo* performance of human neural electrode arrays was compared to the material integrity after explantation. We have found signs of material degradation on all electrode arrays, with longer implantation times correlating with an increased number of degraded electrodes (Table 3). Additionally, biological tissue encapsulation on the explanted device was also documented as another potential factor to influence recording quality. The biological encapsulation tissues were highly collagenous and also highly cellularized, and appear to form in a time dependent manner, increasing with the length of implantation. A similar form of tissue response has been observed in a post mortem analysis of tissue surrounding a

MEA implanted for 7 months (Szymanski et al., 2021). Further, the nature of the encapsulation at the periphery of the array and the center is different. Together, these results suggest that the encapsulation originated from the meninges, as opposed to the CNS.

#### 4.1 Encapsulation and Material Degradation Were Both Related to the Length of Implantation

Material and biological failure modes are most common on longer time scales (James et al., 2013), and it was expected that material degradation and collagenous encapsulation would increase with longer implant times. Indeed, we observed that the arrays implanted in P1 exhibited greater degrees of material degradation and encapsulation than those in P2 which were implanted for a much shorter length. We also observed a characteristic decline in recording performance and impedances with longer implantation times.

Impedance measurements are often used to determine the integrity of electrodes, while also serving as a method of investigating the interface between the electrode and the host tissues (Thakore et al., 2012; Lago et al., 2016). Previously, we have reported that in rats, complete fibrous encapsulation of the electrode resulted in lower 1 kHz impedance compared to partial encapsulation (Cody et al., 2018). Complex impedance spectra analysis performed in the aforementioned study revealed unique features in the Nyquist plot that corresponds to an extracellular resistance component, which is smaller in the fully encapsulated device than the partially encapsulated device. This may be counterintuitive initially, but can be explained by a few mechanisms. First, the composition of the encapsulation tissue is high in collagen and less resistive than highly cellular and myelin rich brain tissue. Secondly, if the fibrotic growth at the base pushes the array up, a liquid filled gap will be formed between cone shaped shanks and the tract, creating a less resistive current path. Due to the limitation in our instrumentation in this study, impedance data were only obtained at 1 kHz preventing us from measuring complex impedances, but it is plausible that a similar effect may have occurred here. Full spectrum impedance recording in future studies could dissect the contributions from tissue encapsulation and material changes and determine whether the same factors are relevant here. However, such measurement needs to meet the regulatory requirements associated with clinical studies.

The decreases in impedance over time could also be a result of degradation of the electrode tips and shank insulation which leads to increased electrochemical surface area. Interestingly, we found no relationships between the impedance of the electrode at 1 kHz and the  $V_{pp}$  during recording for Pt arrays (Supplementary Figure S2). This is not surprising as impedance is only a measure of the electrochemical properties of the electrode and the electrode/tissue interface and does not account for biological variables such as distance from the electrode to the neuron or health of the host tissues, which are more relevant to  $V_{pp}$ . Impedance has previously been shown to be an unreliable



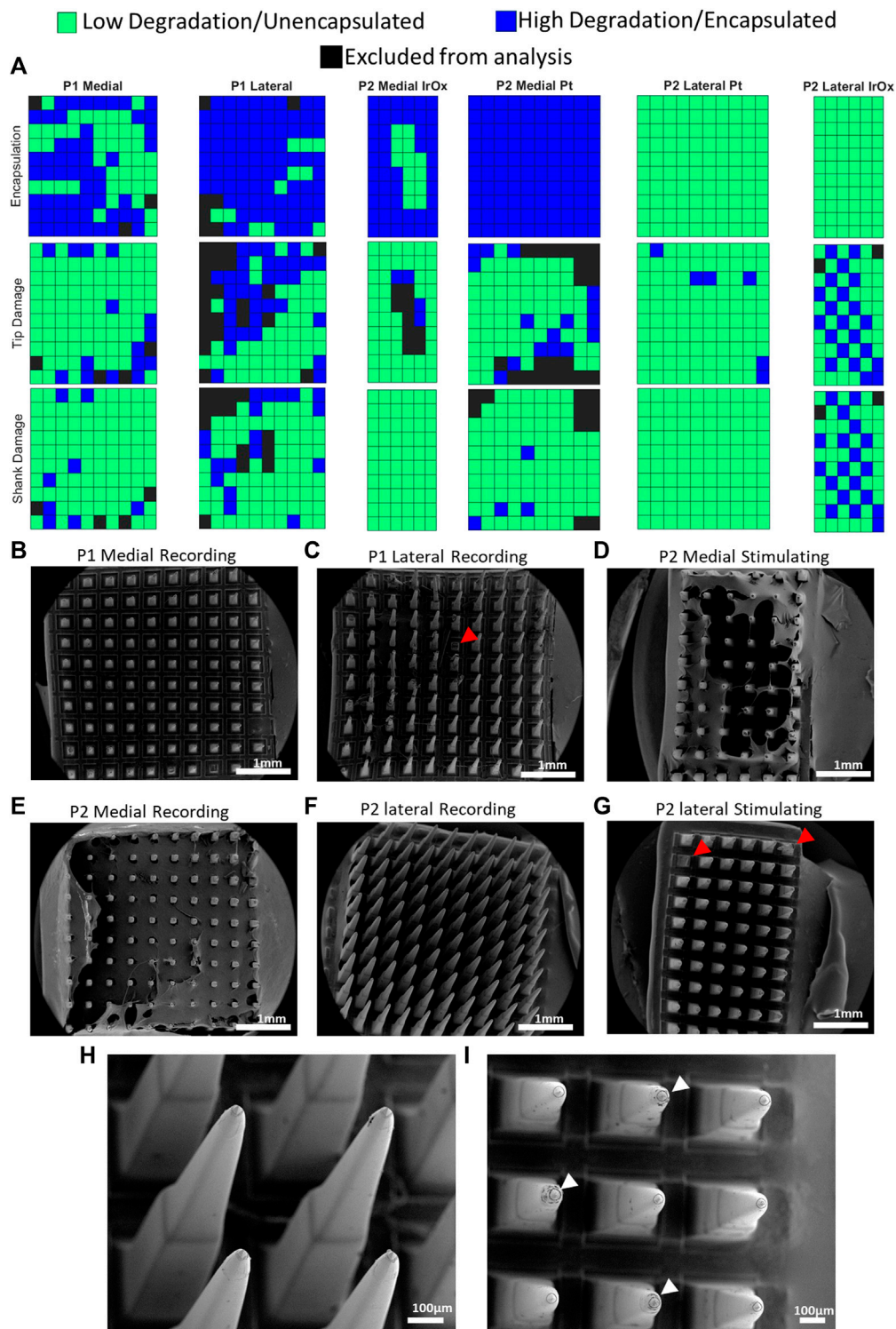


**FIGURE 6 |** Categories assigned to each electrode site. **(A)** Each site was assigned a category with respect to their material integrity or degree of encapsulation. Black sites were not able to be categorized and were excluded from the analysis. Encapsulation was determined by examining the optical images of the arrays for P1 and SEM images for P2. This is due to the enzymatic digestion of the encapsulating tissues that was performed prior to SEM imaging for P1. **(B,C)** Recording arrays implanted into P1 after enzymatic treatment. **(D)** Medial stimulating array implanted into P2. **(E,F)** Medial and lateral recording arrays implanted into P2. **(G)** Lateral stimulating array implanted into P2. **(H,I)** Higher magnification images of recording array in **(F)** and stimulating arrays in **(G)**, respectively. White arrows indicate electrodes which were used for stimulation. Red arrows indicate representative electrodes which were excluded from analysis.

**TABLE 2 |** Number of electrically connected electrodes that were classified as undamaged/unencapsulated or damaged/encapsulated based on tip degradation, shank degradation, and tissue encapsulation.

	Tip degradation		Shank degradation		Encapsulation	
	Low (%)	High (%)	Low (%)	High (%)	Low (%)	High (%)
P1 Medial	77 (83.7)	15 (16.3)	84 (91.3)	8 (8.7)	41 (43.6)	53 (56.4)
P1 Lateral	45 (58.4)	32 (41.6)	67 (79.8)	17 (20.2)	10 (11.0)	81 (89.0)
P2 Pt Medial	59 (81.9)	13 (18.1)	82 (96.5)	3 (3.5)	0 (0)	88 (100)
P2 Pt Lateral	85 (96.6)	3 (3.4)	88 (100)	0 (0)	88 (100)	0 (0)
P2 IrOx Medial	26 (92.9)	2 (7.1)	32 (100)	0 (0)	6 (18.8)	26 (81.2)
P2 IrOx Lateral	7 (25)	21 (75)	9 (32.1)	19 (67.9)	30 (100)	0 (0)
Excluded	45		21		7	

**TABLE 3 |** Differences observed between patients with different length of implant (980 days for P1 and 182 days for P2) on material degradation and encapsulation for electrically connected platinum recording electrode arrays.

	P1 (%)	P2 Pt (%)	Fisher exact <i>p</i> value
Degraded Tips	27.8	11.1	<0.001
Degraded Shank	15.2	1.8	<0.001
Encapsulated	72.4	50	<0.001

predictor of recording performance in rodents and non-human primates (Jiang et al., 2014; Cody et al., 2018). Another important material factor that likely contribute to the uniform reduction of impedance on all arrays is the silicone hermetic sealing failure above the arrays from the wire bundle to the pedestal, which should be characterized in future studies.

The observed collagenous encapsulation of the arrays has been observed in rodent and non-human primate studies (James et al., 2013; Degenhart et al., 2016; Cody et al., 2018). Encapsulation of the electrode tip region can isolate the electrode from nearby neurons, resulting in a lowered  $V_{pp}$ . In addition, the collagenous material grown at the base of the array platform can lift the electrode up and away from the original target neurons, also resulting in  $V_{pp}$  decrease (Degenhart et al., 2016; Cody et al., 2018). Both tissue growth at the tips and the base have been observed from the explanted devices which may contribute to the degradation of  $V_{pp}$  over time in human subjects.

## 4.2 Stimulation at More Negative Voltages May Drive Material Damage Under Certain Circumstances

The stimulation parameters used in this study were based on studies from non-human primates showing that these parameters had no additional effects on cortical tissue apart from implanting the devices themselves, had no behavioral effect on the animal, and had limited effects on the electrode tissue interface (Chen et al., 2014; Kim et al., 2015). Here, we found that electrical stimulation induced damage on one of the two devices. On the lateral array, de-metallization was visible under SEM and detected by EDS on the stimulated electrodes, indicating that stimulation was the cause of the metal loss. The reason that stimulation

caused material damage on the lateral array but not the medial array is unclear. While the specific reason for this cannot be determined, impedances were lower on the medial array (Supplementary Figure S3). The decrease in impedance then could have resulted in lower amplitude voltage excursions during stimulation, decreasing the likelihood of material damage. Indeed, we found that the lateral array had more negative interphase voltages (mean =  $-1.7$  V) when compared to the medial array (mean =  $-1.1$  V).

More material damage was found on the lateral stimulating array in P2 which experienced higher cathodic interphase voltage amplitude. The interphase voltage is analogous to the maximum cathodic electrode potential ( $E_{mc}$ ) measured during charge injection limit (CIL) experiments performed *in vitro*.  $E_{mc}$  with values more negative than  $-0.6$  V (vs. Ag/AgCl) are often considered to be unsafe due to irreversible water hydrolysis occurring at the electrode which could cause hydrogen gas production and pH increases (Cogan et al., 2005). Such reactions could lead to delamination of the IrOx coating even with a small number of pulses. We do not expect the median interphase voltage to be directly comparable to *in vitro* CIL measurements due to the two-electrode setup and increased variables introduced from the biological environment, but we expect the general relationship between voltage and interfacial reactions to hold. Besides the fact that lateral array experienced higher voltage excursion on average, we found a significant correlation between the charge injected below  $-0.6$  V and damage on the lateral stimulating array (Figure 7H). These results indicate that stimulation, beyond a certain voltage threshold, may damage electrodes in a dose (charge) dependent manner.

Partial and complete loss of SIROF from Utah arrays upon continuous stimulation has been reported in previous *in vitro* studies (Negi et al., 2010), but the stimulation doses in these previous studies applied were much higher (7 h of continuous stimulation above 60 nC). One potential explanation is that the stimulation on the lateral array only weakened the adhesion of the IrOx coating and the coating was stripped from the electrode during or after explantation. Alternatively, variations could also be a result of batch-to-batch difference in fabrication where the lateral array received poorly adhered IrOx coating. Notably, the electrodes damaged by stimulation performed just as well in recording as the undamaged electrodes. This interesting result

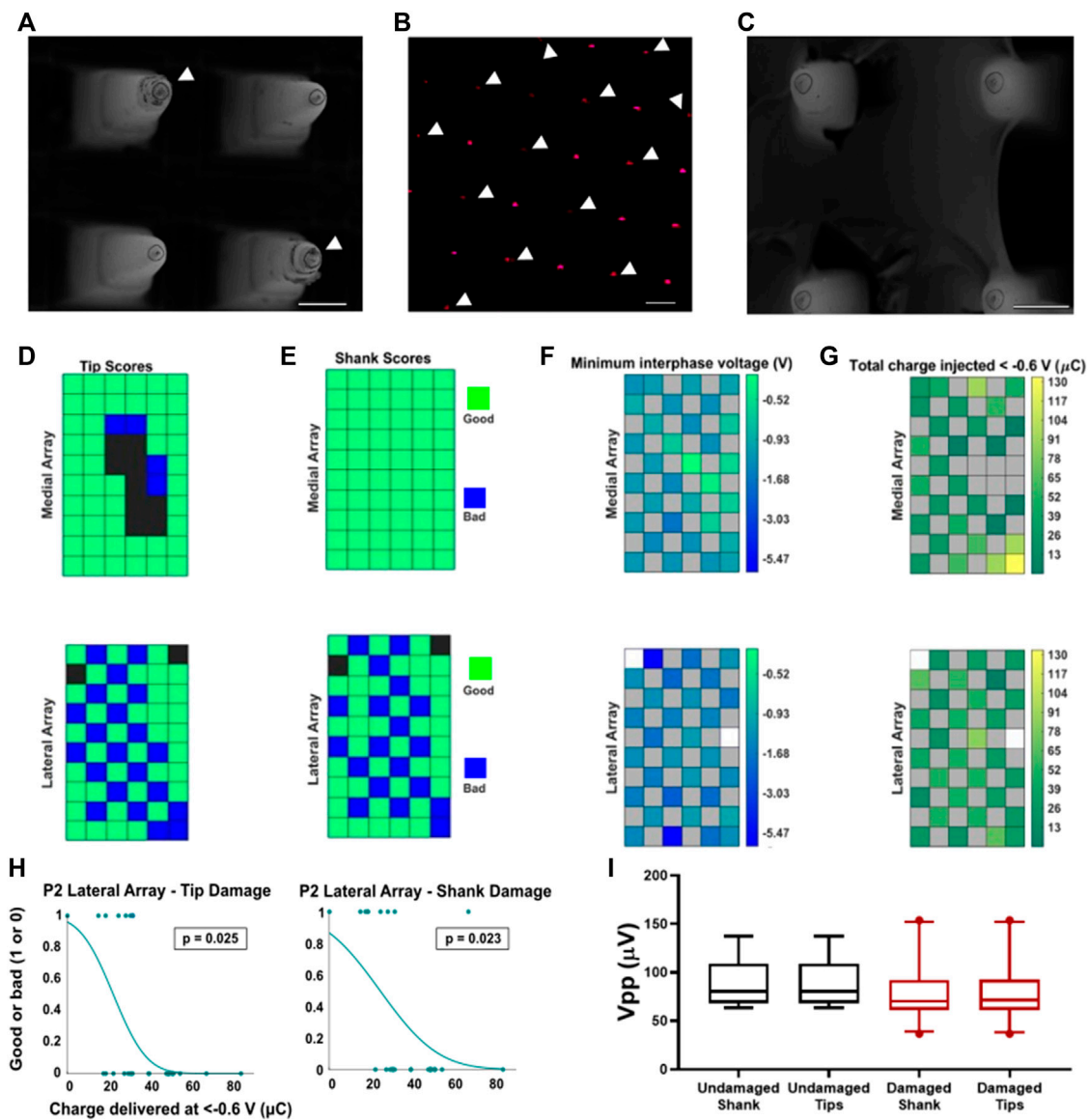


**FIGURE 7 |** Stimulation-induced material damage on one of the two arrays. **(A)** SEM image of four shanks of the lateral array, tip damages are found on the stimulated electrodes marked with white arrows. **(B)** EDS of the stimulating electrodes for the lateral array showing reduced presence of iridium (magenta) on most of the stimulated sites (white arrows). **(C)** SEM image of the medial stimulating array tips. No differences were observed between the non-stimulated and stimulated tips on this array. Scale bars are 100  $\mu\text{m}$ . **(D,E)** Arrays showing the measured material properties on the stimulation arrays including tip categories **(D)** and shank categories **(E)**. Green spaces show electrodes categorized as undamaged/unencapsulated, blue spaces show electrodes categorized as damaged, and black spaces show electrodes that were excluded from analysis. **(F,G)**. Medial (top) and lateral (bottom) stimulating arrays showing **(F)** minimum interphase voltage **(G)** and total charge injected below  $-0.6\text{ V}$ . The color bar for the minimum interphase voltages is log-transformed to emphasize differences between electrodes. Grey spaces indicate unwired electrodes. White spaces indicate wired electrodes that were never stimulated. **(H)** Logistic regression for charge injected over  $-0.6\text{ V}$  and damage to tips (left) or shanks (right). **(I)** Measured peak-to-peak voltages on stimulated electrodes after removing electrodes which were encapsulated with fibrous tissues. There were no significant differences observed in the measured unit amplitudes (Mann-Whitney non-parametric test).

indicates that despite the IrOx delamination and insulation cracking, the electrode is capable of recording neural signal. While electrodes receiving stimulation have previously been shown to be able to record signal for up to 1,500 days (Hughes et al., 2021), whether this recording capability is

maintained over periods of time greater than this remains to be investigated.

The biocompatibility of IrOx coatings has been widely studied and validated for stimulation and recording applications (Lee et al., 2002; Cogan et al., 2005; Cogan 2008; Negi et al., 2010; Negi

**TABLE 4 |** Effect of stimulation on material degradation and encapsulation for IrOx arrays. Non-stimulated tips were not electrically connected.

	Stimulated (%)	Non-stimulated (%)	$\chi^2$ statistic	p value
Damaged tips	41.1	5.6	14.7	<0.001
Damaged shank	33.3	0.0	19.3	<0.001
High encapsulation	43.3	39.7	0.1	>0.05

et al., 2010; Hughes et al., 2021). In another of our studies, stimulating electrodes for over 5 years in a human participant did not result in worse signal recordings when compared to recording electrodes (Hughes et al., 2021). Furthermore, the ability to evoke sensation on stimulated electrodes only improved over time. Based on our observations here, this could be because 1) the material damage caused by stimulation is idiosyncratic, and stimulation didn't result in damage on the arrays of this 5-years study or 2) material damage caused by stimulation had no effect on the electrode's ability to record or stimulate. Discerning between the two is difficult, as studying the *in vivo* properties of the electrodes in parallel with the material properties is not possible in humans. Analysis will need to be conducted on these arrays that received much higher levels of stimulation after explant. Additionally, further animal studies using the stimulus parameters used in our study and assessing damage and changes in recording over time could provide insight here.

### 4.3 Implications for Future Intracortical Electrode Arrays

Overall, our results show that both material integrity and recording performance of human intracortical electrodes decrease over time. Degradation was observed on both the electrode tips and the shank insulation. We have also observed different degrees of tissue encapsulation both at the array base, middle of the shank, and the tips of the arrays. Since we do not have real time data of these material and tissue changes, and explant analysis only provides a partial picture at the end point, we cannot accurately correlate material and biological factors to recording outcome. Multiple human studies have demonstrated that intracortical electrode recordings can enable brain-computer interface control of computer cursor and robotic arms for years after implant, (Bullard et al., 2020) yet the observations in the current study support the need for strategies for increasing material durability and decreasing fibrous encapsulation in order to further improve human BCI recording quality and longevity. Additionally, on one implanted array, we observed clear iridium loss as a result of stimulation, which correlated to more charge injected at more negative voltages. Further research on improving metal adhesion and developing real time electrode potential monitoring methods during stimulation may eliminate such incidences.

### DATA AVAILABILITY STATEMENT

The raw data supporting the conclusion of this article will be made available by the authors, without undue reservation.

### ETHICS STATEMENT

The studies involving human participants were reviewed and conducted under Investigational Device Exemptions from the Food and Drug Administration and were approved by Institutional Review Boards at the University of Pittsburgh Space and the Naval Warfare Systems Center Pacific. The participants provided their written informed consent to participate in this study.

### AUTHOR CONTRIBUTIONS

All authors provided significant intellectual contribution to the manuscript. KW performed the SEM imaging, elemental analysis, writing, and data analysis for **Sections 3.2–3.4**. CH and AH were involved in the ephys data acquisition, writing, and data analysis for **Sections 3.1, 3.4**, JE performed the two photon imaging and analysis, ET performed the surgical procedures on the human participants. RG led the stimulation experiments, JC led the recording study and XC led the explant analysis. All authors have edited, revised and proofread the manuscript.

### FUNDING

The recording and stimulation study was partly funded by the Defense Advanced Research Projects Agency's (Arlington, VA, United States) Revolutionizing Prosthetics program (contract number N66001-10-C-4056). The views expressed herein are those of the authors and do not represent the official policy or position of the Department of Defense or US Government. The explant materials and tissue analysis were supported by the National Institutes of Health grant R01NS110564, R01NS062109 and R01NS089688

### ACKNOWLEDGMENTS

We thank the participants for their dedication to this study. We thank Pavel Takmakov of the Food and Drug Administration for the initial discussion and cleaning protocols for SEM.

### SUPPLEMENTARY MATERIAL

The Supplementary Material for this article can be found online at: <https://www.frontiersin.org/articles/10.3389/fbioe.2021.759711/full#supplementary-material>



## REFERENCES

- Ajiboye, A. B., Willett, F. R., Young, D. R., Memberg, W. D., Murphy, B. A., Miller, J. P., et al. (2017). Restoration of Reaching and Grasping Movements through Brain-Controlled Muscle Stimulation in a Person with Tetraplegia: a Proof-Of-Concept Demonstration. *The Lancet* 389, 1821–1830. doi:10.1016/S0140-6736(17)30601-3
- Armenta Salas, M., Bashford, L., Kellis, S., Jafari, M., Jo, H., Kramer, D., et al. (2018). Proprioceptive and Cutaneous Sensations in Humans Elicited by Intracortical Microstimulation. *eLife* 7, e32904. doi:10.7554/eLife.32904
- Barrese, J. C., Aceros, J., and Donoghue, J. P. (2016). Scanning Electron Microscopy of Chronically Implanted Intracortical Microelectrode Arrays in Non-human Primates. *J. Neural Eng.* 13, 026003. doi:10.1088/1741-2560/13/2/026003
- Bouton, C. E., Shaikhouni, A., Annetta, N. V., Bockbrader, M. A., Friedenber, D. A., Nielson, D. M., et al. (2016). Restoring Cortical Control of Functional Movement in a Human with Quadriplegia. *Nature* 533, 247–250. doi:10.1038/nature17435
- Bullard, A. J., Hutchison, B. C., Lee, J., Chestek, C. A., and Patil, P. G. (2020). Estimating Risk for Future Intracranial, Fully Implanted, Modular Neuroprosthetic Systems: A Systematic Review of Hardware Complications in Clinical Deep Brain Stimulation and Experimental Human Intracortical Arrays. *Neuromodulation: Techn. Neural Interf.* 23, 411–426. doi:10.1111/ner.13069
- Buzsáki, G. (2004). Large-scale Recording of Neuronal Ensembles. *Nat. Neurosci.* 7, 446–451. doi:10.1038/nn1233
- Caldwell, R., Street, M. G., Sharma, R., Takmakov, P., Baker, B., and Rieth, L. (2020). Characterization of Parylene-C Degradation Mechanisms: *In Vitro* Reactive Accelerated Aging Model Compared to Multiyear *In Vivo* Implantation. *Biomaterials* 232, 119731. doi:10.1016/j.biomaterials.2019.119731
- Chen, K. H., Dammann, J. F., Boback, J. L., Tenore, F. V., Otto, K. J., Gaunt, R. A., et al. (2014). The Effect of Chronic Intracortical Microstimulation on the Electrode-Tissue Interface. *J. Neural Eng.* 11, 026004. doi:10.1088/1741-2560/11/2/026004
- Chestek, C. A., Gilja, V., Nuyujukian, P., Foster, J. D., Fan, J. M., Kaufman, M. T., et al. (2011). Long-term Stability of Neural Prosthetic Control Signals from Silicon Cortical Arrays in Rhesus Macaque Motor Cortex. *J. Neural Eng.* 8, 045005. doi:10.1088/1741-2560/8/4/045005
- Cody, P. A., Eles, J. R., Lagenaur, C. F., Kozai, T. D. Y., and Cui, X. T. (2018). Unique Electrophysiological and Impedance Signatures between Encapsulation Types: An Analysis of Biological Utah Array Failure and Benefit of a Biomimetic Coating in a Rat Model. *Biomaterials* 161, 117–128. doi:10.1016/j.biomaterials.2018.01.025
- Cogan, S. F. (2008). Neural Stimulation and Recording Electrodes. *Annu. Rev. Biomed. Eng.* 10, 275–309. doi:10.1146/annurev.bioeng.10.061807.160518
- Cogan, S. F., Troyk, P. R., Ehrlich, J., and Plante, T. D. (2005). *In Vitro* comparison of the Charge-Injection Limits of Activated Iridium Oxide (AIROF) and Platinum-Iridium Microelectrodes. *IEEE Trans. Biomed. Eng.* 52, 1612–1614. doi:10.1109/TBME.2005.851503
- Collinger, J. L., Wodlinger, B., Downey, J. E., Wang, W., Tyler-Kabara, E. C., Weber, D. J., et al. (2013). High-performance Neuroprosthetic Control by an Individual with Tetraplegia. *The Lancet* 381, 557–564. doi:10.1016/S0140-6736(12)61816-9
- Degenhart, A. D., Eles, J., Dum, R., Mischel, J. L., Smalianchuk, I., Endler, B., et al. (2016). Histological Evaluation of a Chronically-Implanted Electrocorticographic Electrode Grid in a Non-human Primate. *J. Neural Eng.* 13, 046019. doi:10.1088/1741-2560/13/4/046019
- Downey, J. E., Schwed, N., Chase, S. M., Schwartz, A. B., and Collinger, J. L. (2018). Intracortical Recording Stability in Human Brain-Computer Interface Users. *J. Neural Eng.* 15, 046016. doi:10.1088/1741-2552/aab7a0
- Dunlap, C. F., Colachis, S. C., Meyers, E. C., Bockbrader, M. A., and Friedenber, D. A. (2020). Classifying Intracortical Brain-Machine Interface Signal Disruptions Based on System Performance and Applicable Compensatory Strategies: A Review. *Front. Neurobot.* 14, 558987. doi:10.3389/fnbot.2020.558987
- Fifer, M. S., McMullen, D. P., Thomas, T. M., Osborn, L. E., Nickl, R. W., Candrea, D. N., et al. (2020). Intracortical Microstimulation Elicits Human Fingertip Sensations. *medRxiv* 05, 20117374. doi:10.1101/2020.05.29.20117374
- Flesher, S. N., Collinger, J. L., Foldes, S. T., Weiss, J. M., Downey, J. E., Tyler-Kabara, E. C., et al. (2016). Intracortical Microstimulation of Human Somatosensory Cortex. *Sci. Transl. Med.* 8, 361ra141. doi:10.1126/scitranslmed.aaf8083
- Flesher, S. N., Downey, J. E., Weiss, J. M., Hughes, C. L., Herrera, A. J., Tyler-Kabara, E. C., et al. (2021). A Brain-Computer Interface that Evokes Tactile Sensations Improves Robotic Arm Control. *Science* 372, 831–836. doi:10.1126/science.abd0380
- Gilgunn, P. J., Ong, X. C., Flesher, S. N., Schwartz, A. B., and Gaunt, R. A. (2013). “Structural Analysis of Implanted Microelectrode Arrays,” in 2013 6th International IEEE/EMBS Conference on Neural Engineering (NER), November 6–8, 2014. doi:10.1109/NER.2013.6696035
- Hochberg, L. R., Serruya, M. D., Friehs, G. M., Mukand, J. A., Saleh, M., Caplan, A. H., et al. (2006). Neuronal Ensemble Control of Prosthetic Devices by a Human with Tetraplegia. *Nature* 442, 164–171. doi:10.1038/nature04970
- Hughes, C., Herrera, A., Gaunt, R., and Collinger, J. (2020). “Bidirectional Brain-Computer Interfaces,” in *Handbook of Clinical Neurology* (Oxford, UK: Elsevier), 168, 163–181. doi:10.1016/b978-0-444-63934-9.00013-5
- Hughes, C. L., Flesher, S. N., Weiss, J. M., Downey, J. E., Boninger, M., Collinger, J. L., et al. (2021). Neural Stimulation and Recording Performance in Human Sensorimotor Cortex over 1500 Days. *J. Neural Eng.* 18 (4), 045012. doi:10.1088/1741-2552/ac18ad
- James, C. B., Naveen, R., Kaivon, P., Corey, T., Carlos, V.-I., Lachlan, F., et al. (2013). Failure Mode Analysis of Silicon-Based Intracortical Microelectrode Arrays in Non-human Primates. *J. Neural Eng.* 10, 066014. doi:10.1088/1741-2560/13/2/026003
- Jiang, J., Willett, F. R., and Taylor, D. M. (2014). “Relationship Between Microelectrode Array Impedance and Chronic Recording Quality of Single Units and Local Field Potentials,” in 2014 36th Annual International Conference of the IEEE Engineering in Medicine and Biology Society, August 26–30, 2014. doi:10.1109/EMBC.2014.6944265
- Kim, S., Callier, T., Tabot, G. A., Gaunt, R. A., Tenore, F. V., and Bensmaia, S. J. (2015). Behavioral Assessment of Sensitivity to Intracortical Microstimulation of Primate Somatosensory Cortex. *Proc. Natl. Acad. Sci. USA* 112, 15202–15207. doi:10.1073/pnas.1509265112
- Kozai, T. D. Y., Catt, K., Li, X., Gugel, Z. V., Olafsson, V. T., Vazquez, A. L., et al. (2015). Mechanical Failure Modes of Chronically Implanted Planar Silicon-Based Neural Probes for Laminar Recording. *Biomaterials* 37, 25–39. doi:10.1016/j.biomaterials.2014.10.040
- Lago, N., Cester, A., Wrachien, N., Natali, M., Quiroga, S. D., Bonetti, S., et al. (2016). A Physical-Based Equivalent Circuit Model for an Organic/electrolyte Interface. *Org. Electro.* 35, 176–185. doi:10.1016/j.orgel.2016.05.018
- Lee, I., Whang, C.-N., Choi, K., Choo, M.-S., and Lee, Y.-H. (2002). Characterization of Iridium Film as a Stimulating Neural Electrode. *Biomaterials* 23, 2375–2380. doi:10.1016/S0142-9612(01)00373-8
- Negi, S., Bhandari, R., Rieth, L., and Solzbacher, F. (2010). *In Vitro* comparison of Sputtered Iridium Oxide and Platinum-Coated Neural Implantable Microelectrode Arrays. *Biomed. Mater.* 5, 015007. doi:10.1088/1748-6041/5/1/015007
- Negi, S., Bhandari, R., Rieth, L., Van Wagenen, R., and Solzbacher, F. (2010). Neural Electrode Degradation from Continuous Electrical Stimulation: Comparison of Sputtered and Activated Iridium Oxide. *J. Neurosci. Methods* 186, 8–17. doi:10.1016/j.jneumeth.2009.10.016
- Polikov, V. S., Tresco, P. A., and Reichert, W. M. (2005). Response of Brain Tissue to Chronically Implanted Neural Electrodes. *J. Neurosci. Methods* 148, 1–18. doi:10.1016/j.jneumeth.2005.08.015
- Prasad, A., Xue, Q.-S., Dieme, R., Sankar, V., Mayrand, R. C., Nishida, T., et al. (2014). Abiotic-biotic Characterization of Pt/Ir Microelectrode Arrays in Chronic Implants. *Front. Neuroeng.* 7, 2. doi:10.3389/fneng.2014.00002
- Rousche, P. J., and Normann, R. A. (1998). Chronic Recording Capability of the Utah Intracortical Electrode Array in Cat Sensory Cortex. *J. Neurosci. Methods* 82, 1–15. doi:10.1016/S0165-0270(98)00031-4
- Salatino, J. W., Ludwig, K. A., Kozai, T. D. Y., and Purcell, E. K. (2017). Glial Responses to Implanted Electrodes in the Brain. *Nat. Biomed. Eng.* 1, 862–877. doi:10.1038/s41551-017-0154-1
- Santhanam, G., Ryu, S. I., Yu, B. M., Afshar, A., and Shenoy, K. V. (2006). A High-Performance Brain-Computer Interface. *Nature* 442, 195–198. doi:10.1038/nature04968

- Schmidt, E. M., McIntosh, J. S., and Bak, M. J. (1988). Long-term Implants of Parylene-C Coated Microelectrodes. *Med. Biol. Eng. Comput.* 26, 96–101. doi:10.1007/BF02441836
- Schwartz, A. B., Cui, X. T., Weber, D. J., and Moran, D. W. (2006). Brain-Controlled Interfaces: Movement Restoration with Neural Prosthetics. *Neuron* 52, 205–220. doi:10.1016/j.neuron.2006.09.019
- Simeral, J. D., Kim, S.-P., Black, M. J., Donoghue, J. P., and Hochberg, L. R. (2011). Neural Control of Cursor Trajectory and Click by a Human with Tetraplegia 1000 Days after Implant of an Intracortical Microelectrode Array. *J. Neural Eng.* 8, 025027. doi:10.1088/1741-2560/8/2/025027
- Suner, S., Fellows, M. R., Vargas-Irwin, C., Nakata, G. K., and Donoghue, J. P. (2005). Reliability of Signals from a Chronically Implanted, Silicon-Based Electrode Array in Non-human Primate Primary Motor Cortex. *IEEE Trans. Neural Syst. Rehabil. Eng.* 13, 524–541. doi:10.1109/TNSRE.2005.857687
- Szymanski, L. J., Kellis, S., Liu, C. Y., Jones, K. T., Andersen, R. A., Commins, D., et al. (2021). Neuropathological Effects of Chronically Implanted, Intracortical Microelectrodes in a Tetraplegic Patient. *J. Neural Eng.* 18, 0460b9. doi:10.1088/1741-2552/ac127e
- Thakore, V., Molnar, P., and Hickman, J. J. (2012). An Optimization-Based Study of Equivalent Circuit Models for Representing Recordings at the Neuron-Electrode Interface. *IEEE Trans. Biomed. Eng.* 59, 2338–2347. doi:10.1109/TBME.2012.2203820
- Velliste, M., Perel, S., Spalding, M. C., Whitford, A. S., and Schwartz, A. B. (2008). Cortical Control of a Prosthetic Arm for Self-Feeding. *Nature* 453, 1098–1101. doi:10.1038/nature06996
- Wodlinger, B., Downey, J. E., Tyler-Kabara, E. C., Schwartz, A. B., Boninger, M. L., and Collinger, J. L. (2014). Ten-dimensional Anthropomorphic Arm Control in a Human Brain-machine Interface: Difficulties, Solutions, and Limitations. *J. Neural Eng.* 12, 016011. doi:10.1088/1741-2560/12/1/016011
- Woepfel, K., Yang, Q., and Cui, X. T. (2017). Recent Advances in Neural Electrode-Tissue Interfaces. *Curr. Opin. Biomed. Eng.* 4, 21–31. doi:10.1016/j.cobme.2017.09.003
- Woolley, A. J., Desai, H. A., and Otto, K. J. (2013). Chronic Intracortical Microelectrode Arrays Induce Non-uniform, Depth-Related Tissue Responses. *J. Neural Eng.* 10, 026007. doi:10.1088/1741-2560/10/2/026007
- Xie, X., Rieth, L., Williams, L., Negi, S., Bhandari, R., Caldwell, R., et al. (2014). Long-term Reliability of Al<sub>2</sub>O<sub>3</sub> and Parylene C Bilayer Encapsulated Utah Electrode Array Based Neural Interfaces for Chronic Implantation. *J. Neural Eng.* 11, 026016. doi:10.1088/1741-2560/11/2/026016

**Conflict of Interest:** The authors declare that the research was conducted in the absence of any commercial or financial relationships that could be construed as a potential conflict of interest.

**Publisher's Note:** All claims expressed in this article are solely those of the authors and do not necessarily represent those of their affiliated organizations, or those of the publisher, the editors and the reviewers. Any product that may be evaluated in this article, or claim that may be made by its manufacturer, is not guaranteed or endorsed by the publisher.

Copyright © 2021 Woepfel, Hughes, Herrera, Eles, Tyler-Kabara, Gaunt, Collinger and Cui. This is an open-access article distributed under the terms of the Creative Commons Attribution License (CC BY). The use, distribution or reproduction in other forums is permitted, provided the original author(s) and the copyright owner(s) are credited and that the original publication in this journal is cited, in accordance with accepted academic practice. No use, distribution or reproduction is permitted which does not comply with these terms.

# Advantages of publishing in Frontiers



## OPEN ACCESS

Articles are free to read  
for greatest visibility  
and readership



## FAST PUBLICATION

Around 90 days  
from submission  
to decision



## HIGH QUALITY PEER-REVIEW

Rigorous, collaborative,  
and constructive  
peer-review



## TRANSPARENT PEER-REVIEW

Editors and reviewers  
acknowledged by name  
on published articles

## Frontiers

Avenue du Tribunal-Fédéral 34  
1005 Lausanne | Switzerland

Visit us: [www.frontiersin.org](http://www.frontiersin.org)

Contact us: [frontiersin.org/about/contact](http://frontiersin.org/about/contact)



## REPRODUCIBILITY OF RESEARCH

Support open data  
and methods to enhance  
research reproducibility



## DIGITAL PUBLISHING

Articles designed  
for optimal readership  
across devices



## FOLLOW US

@frontiersin



## IMPACT METRICS

Advanced article metrics  
track visibility across  
digital media



## EXTENSIVE PROMOTION

Marketing  
and promotion  
of impactful research



## LOOP RESEARCH NETWORK

Our network  
increases your  
article's readership